Lecture Notes in Electrical Engineering 303

Jiadong Sun
Wenhai Jiao
Haitao Wu
Mingquan Lu
Editors

China Satellite Navigation Conference (CSNC) 2014 Proceedings: Volume I

Springer

Lecture Notes in Electrical Engineering

Volume 303

For further volumes:
http://www.springer.com/series/7818

About this Series

"Lecture Notes in Electrical Engineering (LNEE)" is a book series which reports the latest research and developments in Electrical Engineering, namely:

- Communication, Networks, and Information Theory
- Computer Engineering
- Signal, Image, Speech and Information Processing
- Circuits and Systems
- Bioengineering

LNEE publishes authored monographs and contributed volumes which present cutting edge research information as well as new perspectives on classical fields, while maintaining Springer's high standards of academic excellence. Also considered for publication are lecture materials, proceedings, and other related materials of exceptionally high quality and interest. The subject matter should be original and timely, reporting the latest research and developments in all areas of electrical engineering.

The audience for the books in LNEE consists of advanced level students, researchers, and industry professionals working at the forefront of their fields. Much like Springer's other Lecture Notes series, LNEE will be distributed through Springer's print and electronic publishing channels.

Jiadong Sun · Wenhai Jiao
Haitao Wu · Mingquan Lu
Editors

China Satellite Navigation Conference (CSNC) 2014 Proceedings: Volume I

Springer

Editors
Jiadong Sun
China Aerospace Science
and Technology Corporation
Chinese Academy of Sciences
Beijing
China

Wenhai Jiao
China Satellite Navigation Office
Beijing
China

Haitao Wu
Navigation Headquarters
Chinese Academy of Sciences
Beijing
China

Mingquan Lu
Department of Electronic Engineering
Tsinghua University
Beijing
China

ISSN 1876-1100 ISSN 1876-1119 (electronic)
ISBN 978-3-642-54736-2 ISBN 978-3-642-54737-9 (eBook)
DOI 10.1007/978-3-642-54737-9
Springer Heidelberg New York Dordrecht London

Library of Congress Control Number: 2014937269

Printed on acid-free paper

Springer is part of Springer Science+Business Media (www.springer.com)

Preface

China's BDS Navigation Satellite System (BDS) has been independently developed, which is similar in principle to global positioning system (GPS) and compatible with other global satellite navigation systems (GNSS). The BDS will provide highly reliable and precise positioning, navigation and timing (PNT) services as well as short-message communication for all users under all-weather, all-time, and worldwide conditions.

China Satellite Navigation Conference (CSNC) is an open platform for academic exchanges in the field of satellite navigation. It aims to encourage technological innovation, accelerate GNSS engineering, and boost the development of the satellite navigation industry in China and in the world.

The 5th China Satellite Navigation Conference (CSNC 2014) is held on May 21–23, 2014, Nanjing, China. The theme of CSNC 2014 is BDS Application—Innovation, Integration and Sharing, which covers a wide range of activities, including technical seminars, academic exchange, forum, exhibition, lectures, as well as ION panel. The main topics are as:

1. BDS/GNSS Navigation Applications
2. Satellite Navigation Signal System, Compatibility and Interoperability
3. Precise Orbit Determination and Positioning
4. Atomic Clock Technique and Time-Frequency System
5. Satellite Navigation Augmentation and Integrity Monitoring
6. BDS/GNSS Test and Assessment Technology
7. BDS/GNSS User Terminal Technology
8. Satellite Navigation Models and Methods
9. Integrated Navigation and New Methods

The proceedings have 171 papers in nine topics of the conference, which were selected through a strict peer-review process from 479 papers presented at CSNC 2014.

We thank the contribution of each author and extend our gratitude to 165 referees and 36 session chairmen who are listed as members of an editorial board. The assistance of CNSC 2014's organizing committees and the Springer editorial office is highly appreciated.

Jiadong Sun

Editorial Board

The 5th China Satellite Navigation Conference (CSNC 2014)

Scientific Committee

Chairman
Jiadong Sun, China Aerospace Science and Technology Corporation

Vice-Chairman
Rongjun Shen, China
Jisheng Li, China
Qisheng Sui, China
Zuhong Li, China Academy of Space Technology
Shusen Tan, Beijing Satellite Navigation Center, China

Executive Chairman
Jingnan Liu, Wuhan University
Yuanxi Yang, China National Administration of GNSS and Applications
Shiwei Fan, China

Committee Members (By Surnames Stroke Order)
Xiancheng Ding, China Electronics Technology Group Corporation
Qingjun Bu, China
Liheng Wang, China Aerospace Science and Technology Corporation
Yuzhu Wang, Shanghai Institute of Optics and Fine Mechanics, Chinese Academy of Sciences
Guoxiang Ai, National Astronomical Observatories, Chinese Academy of Sciences
Shuhua Ye, Shanghai Astronomical Observatories, Chinese Academy of Sciences
Zhaowen Zhuang, National University of Defense Technology
Qifeng Xu, PLA Information Engineering University
Houze Xu, Institute of Geodesy and Geophysics, Chinese Academy of Sciences
Guirong Min, China Academy of Space Technology
Xixiang Zhang, China Electronics Technology Group Corporation
Lvqian Zhang, China Aerospace Science and Technology Corporation

Junyong Chen, National Administration of Surveying, Mapping and Geoinformation
Benyao Fan, China Academy of Space Technology
Dongjin Luo, China
Guohong Xia, China Aerospace Science and Industry Corporation
Chong Cao, China Research Institute of Radio Wave Propagation (CETC 22)
Faren Qi, China Academy of Space Technology
Sili Liang, China Aerospace Science and Technology Corporation
Shancheng Tu, China Academy of Space Technology
Rongsheng Su, China
Zhipeng Tong, China Electronics Technology Group Corporation
Ziqing Wei, Xi'an Institute of Surveying and Mapping

Organizing Committee

Secretary General
Haitao Wu, Navigation Headquarters, Chinese Academy of Sciences

Vice-Secretary General
Wenhai Jiao, China Satellite Navigation Office
Tao Peng, Academy of Satellite Application, China Aerospace Science and Technology Corporation
Wenjun Zhao, Beijing Satellite Navigation Center
Tao Peng, Satellite Application Research Institute of China Aerospace Science and Technology Corporation
Chuang Shi, Wuhan University
Weina Hao, Navigation Headquarters, Chinese Academy of Sciences

Committee Members (By Surnames Stroke Order)
Qun Ding, Xi'an Institute of Navigation Technology
Miao Yu, Beijing Institute of Space Science and Technology Information
Yinhu Ma, Navigation Satellite Systems Engineering Center, China Academy of Aerospace Electronics Technology
Ying Liu, China Satellite Navigation System Administration Office
Hao Zhang, International Cooperation of China Satellite Navigation System Administration Office
Wangming Yang, Nan Jing High Technology Industrial Development Zone Management Committee
Mingquan Lu, Tsinghua University
Xiuwan Chen, Peking University

Shuanggen Jin, Shanghai Astronomical Observatories, Chinese Academy of Sciences
Xiang'an Zhao, China Defense Science and Technology Information Center
Jing Zhao, Ministry of Science and Technology National Remote Sensing Center
Yuehu Hu, China Aerospace Science and Technology Corporation 20th Institute
Zhong Dou, National Time Service Center of Chinese Academy of Sciences

Contents

Part I
BDS/GNSS Navigation Applications

Chapter 1
Preliminary Results of Tropospheric Wet Refractivity Tomography Based on GPS/GLONASS/BDS Satellite Navigation System

Xiaoying Wang, Ziqiang Dai, Li Wang, Yunchang Cao and Lianchun Song

Abstract Up until the end of October 2012, the Chinese BeiDou navigation satellite system (BDS) had launched 16 satellites, and then started providing formal operation services for China and surrounding regions from the beginning of 2013. It is of theoretical and practical significance to do research on Tropospheric wet refractivity tomography based on BeiDou system. The simulation experiment is conducted based on the ephemeris obtained from two line elements (TLE) and SDP4 model, Shenzhen-Hongkong GNSS network and standard atmosphere. The multiplicative algebraic reconstruction techniques (MART) are used to solve tomography equations to obtain tropospheric wet refractivity field. The results show that for the Shenzhen-Hongkong area the tomography precision has not improved obviously by the signals fusion of GPS/GLONASS/BeiDou, and the tropospheric wet refractivity field can be obtained with high precision based purely on the BeiDou system when GPS/GLONASS become unavailable due to certain factors.

X. Wang · L. Wang
School of Remote Sensing, Nanjing University of Information Science and Technology, Nanjing 210044, China
e-mail: wyzhwxl@163.com

X. Wang
NASG Key Laboratory of Land Environment and Disaster Monitoring, Xuzhou 221116, China

Z. Dai
The 28th Research Institute, China Electronics Technology Group Corporation, Nanjing 210007, China

Y. Cao
Meteorological Observation Center, China Meteorological Administration, Beijing 100081, China

L. Song (✉)
National Climate Center, China Meteorological Administration, Beijing 100081, China
e-mail: songlc_cma@163.com

J. Sun et al. (eds.), *China Satellite Navigation Conference (CSNC) 2014 Proceedings: Volume I*, Lecture Notes in Electrical Engineering 303,
DOI: 10.1007/978-3-642-54737-9_1, © Springer-Verlag Berlin Heidelberg 2014

Keywords BeiDou · Wet refractivity tomography · Algebraic reconstruction techniques

1.1 Introduction

Water vapour plays an important role in the atmospheric process and climate research. The GNSS technology provides a new means for detection of atmospheric water vapor. With the features of a real-time continuity, all-weather conditions and high precision, it can provide water vapour for the need of the weather prediction model. It is a pity that although the precision of the precipitable water vapor (PWV) above the GNSS receives can reach 1–2 mm [1], unfortunately it is still in its innovation for perfect 4D water vapour tomography [2]. The primary cause is that the number of on-orbit satellites is limited, the spatial structure between satellites and stations is weak and the effective SWDs are not enough to obtain the 4D tropospheric water vapor field.

Up until the end of October 2012, the Chinese BeiDou navigation satellite system (BDS) had launched 16 satellites, and then started providing formal operation services for China and surrounding regions from the beginning of 2013. The conditions for water vapor tomography has been mature based on the BDS system, but so far there has little research on atmospheric water vapor detecting based on BDS system yet [3]. This paper gives the preliminary results of the tropospheric wet refractivity tomography based on GPS/GLONASS/BDS system, using multiplicative algebraic reconstruction techniques (MART) iteration method and simulation data from Shenzhen and Hongkong (SH) GNSS network.

1.2 Data and Method

Experimental data are selected from the SH GNSS network with a latitude range of 22°12'–22°36' and a longitude range of 113°53'–114°17' as shown in Fig. 1.1. There are totally 15 stations, including 4 stations (Nanshan, Zhuzilin, Jianyi and Shatoujiao) in Shenzhen and 11 stations in Hong Kong.

The simulation experiment is based on the ephemeris obtained from two line elements (TLE) and SDP4 model, the SH GNSS network and the standard atmosphere. The simulation data is from 0:00 to 24:00 on July 1, 2013 (UTC).

During the data processing, equal to 3 % of the ZWD is the error of the ZWD, and the SWD error with elevation is set to $\sigma_{ZWD} \cdot \sin \alpha^{-1}$. A unified 50 % system error is added to the true value of wet refractivity field as initial value for iteration.

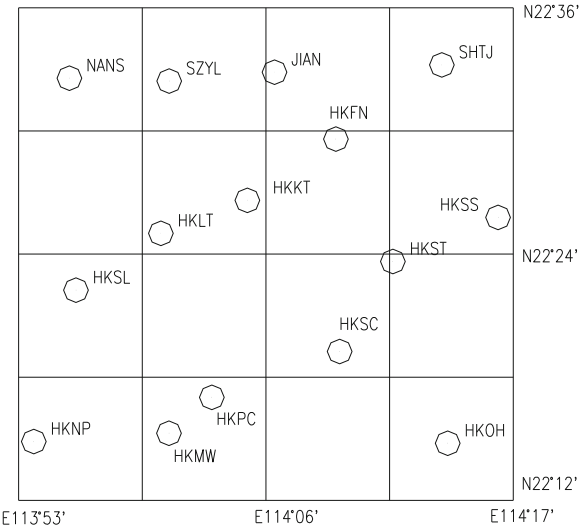

Fig. 1.1 Geographic distribution of the SH GNSS network

There are four voxels in east-west direction with 10 km per voxel. So is in the north-south direction. There are 16 voxels in each layer. The height of the tropopause is set to 10 km and 500 m per layer. Thus there are totally 20 layers in the vertical direction and altogether 320 voxels.

Details for MART can be seen in Bender et al. [4]. The paper proposes two improvements for MART, one is that the Gaussian constraint is realized to update the value of the voxels not penetrated by any SWD, the other is that two new parameters of Bias and RMS, calculated from the result of all the voxels, are adopted to evaluate the precision of the tomography results of the whole grid, whereas the existing δ and σ parameters can only evaluate the precision of the voxels penetrated by SWDs. The Bias and RMS parameters are calculated as shown in Eqs. (1.1) and (1.2),

$$Bias = \frac{1}{n}\sum_{i=1}^{n}\left(Nw_i^k - Nw_i\right) \tag{1.1}$$

$$RMS = \sqrt{\frac{1}{n-1}\sum_{i=1}^{n}\left(\left\{Nw_i^k - Nw_i\right\} - Bias\right)^2} \tag{1.2}$$

In the above equations, Nw denotes voxel wet refractivity; n denotes the total number of voxels and k denotes the kth iterations.

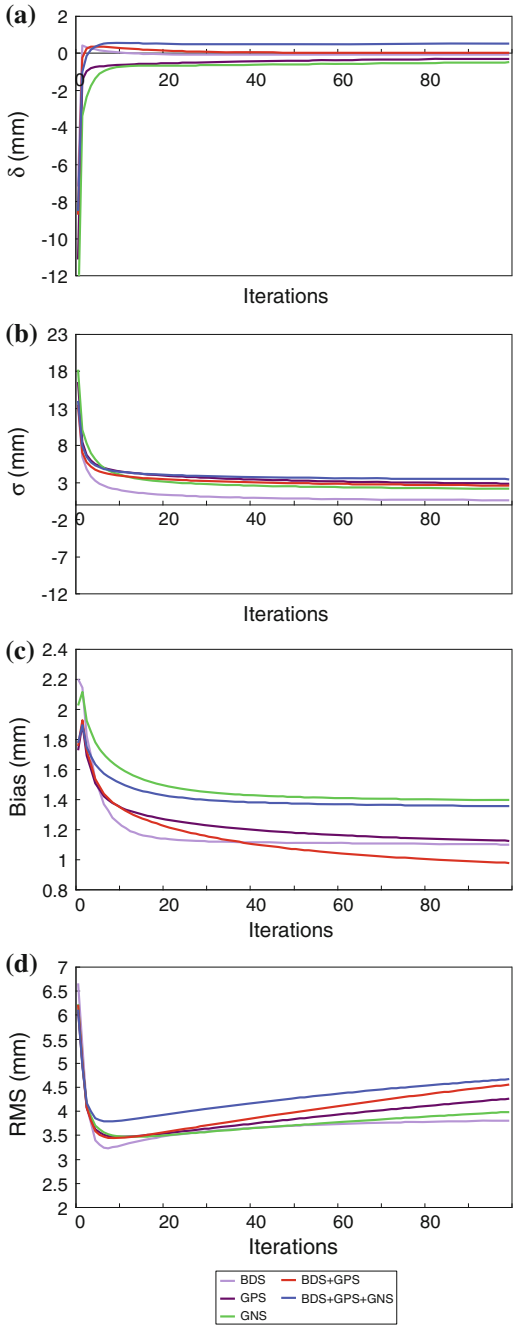

Fig. 1.2 The change of **a** δ, **b** σ, **c** bias and **d** RMS with iteration times using MART based on pure BDS, pure GPS, pure GNS, BDS + GPS and BDS + GPS + GNS mode. The simulated period of time is from 12:00 to 12:30 on July 1, 2013, 100 times of iteration are used

Table 1.1 Statistic results of different modes (the simulation time and iterations are same to that in Fig. 1.2)

mode	BDS	GPS	GNS	BDS + GPS	BDS + GPS + GNS
Total number of SWDs	9,000	11,172	11,244	20,172	31,416
Valid number of SWDs	2,772	2,920	2,624	5,692	8,316
Number of voxels penetrated by SWDs	305	313	310	313	314
δ (mm)	−0.1	−0.3	−0.5	0.1	0.5
σ (mm)	0.6	2.8	2.1	2.6	3.4
Bias (mm)	1.1	1.1	1.4	1.0	1.3
RMS (mm)	3.8	4.3	4.0	4.5	4.7

1.3 Results

The simulation results, from 12:00 to 12:30 on July 1, 2013 (UTC), respectively based on BDS system, GPS system GLONASS(GNS) system, BDS + GPS system, and BDS + GPS + GNS system, are shown in Fig. 1.2. During the simulation time the information such as the number of valid SWDs penetrating out of the top of the grid and that of voxels penetrated by SWDs in three modes are shown as Table 1.1. Figure 1.2 and Table 1.1 show that the precision of tropospheric wet refractivity based on purely BDS system (only 14 satellites are used) is superior to that based on the other four modes, and the signal fusion of multi-navigation systems has no contribution to the precision improvement of tropospheric wet refractivity.

In order to make the conclusion more convincing, Fig. 1.3 gives the results for simulation time from 00:00 to 24:00 on July 1, 2013 (UTC). The δ, σ, Bias and RMS on the 100th iteration are given in Fig. 1.3a–d respectively. The tomography process in conducted per half an hour, and there are 48 samples in one day. Figure 1.3 gives the same conclusions to the Fig. 1.2, indicating that for the SH network, in most of the time, no matter based on the precision parameters δ and σ, or on the Bias and RMS, the pure BDS system can achieve the best tomography precision.

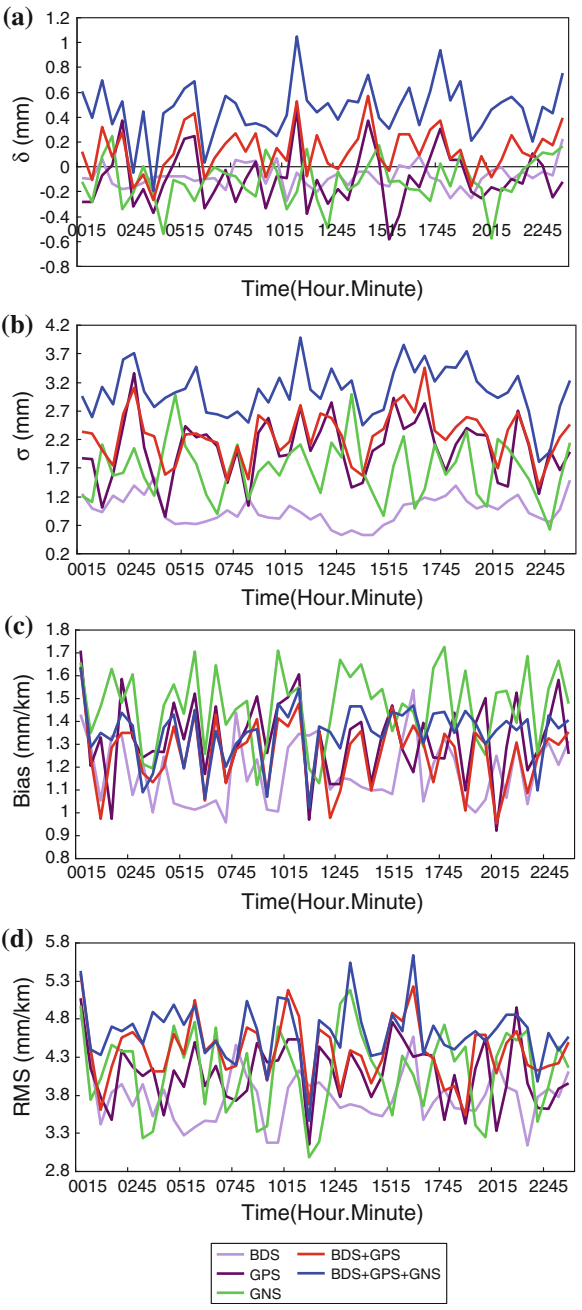

Fig. 1.3 The change of **a** δ, **b** σ, c bias and **d** RMS at the 100th iteration with time (UTC) during 2013/07/01 using MART based on pure BDS, pure GPS,pure GNS, BDS + GPS and BDS + GPS + GNS mode. The simulated period of time is from 00:00 to 24:00 on July 1, 2013

1.4 Conclusion

From the simulation experiment based on the ephemeris obtained from two line elements (TLE) and SDP4 model, Shenzhen-Hongkong GNSS network and standard atmosphere, we can see the good prospect of BDS system used in the atmospheric research. It is promising that the tropospheric water vapor tomography based on the BDS system will be comparable to or better than that based on the GPS or GLONASS systems with its continuous satellite constellating in 2010 for China area, which is of great significance for Chinese ground-based BDS meteorology.

Acknowledgments The paper is supported by the Scientific Research Foundation for Jiangsu Key Laboratory of Meteorological Observation and Information Processing (No.KDXS1305), the Scientific Research Foundation for NASG Key Laboratory of Land Environment and Disaster Monitoring (No. LEDM2012B08), and the Natural Science Foundation of the Jiangsu Higher Education Institutions of China (Grant No. 13KJB170011).

References

1. Rocken C, Van Hove T, Ware RH (1997) Near real-time GPS sensing of atmospheric water vapor. Geophys Res Lett 24:3221–3224
2. Rohm W, Bosy J (2011) The verification of GNSS tropospheric tomography model in a mountainous area. Adv Space Res 47(10):P1721–P1730
3. Wang XY, Wang XL, Dai ZQ, Ke FY, Cao YC, Wang FF, Song LC (2014) Tropospheric wet refractivity tomography based on the BeiDou satellite system. Adv Atmos Sci in press. doi:10.1007/s00376-013-2311-0
4. Bender M, Stosiusa R, Zusa F et al (2011) GNSS water vapour tomography—expected improvements by combining GPS, GLONASS and Galileo observations. Adv Space Res 47(5):886–897

Chapter 2
Analysis of Polar Ionospheric Scintillation Characteristics Based on GPS Data

Lijing Pan and Ping Yin

Abstract Ionospheric scintillation is one of the important factors that affect the performance of satellite navigation system, so ionospheric scintillation monitoring has been drawn more attention. Based on ionospheric scintillation monitoring data at South Pole station in Antarctica, we are able to investigate ionospheric scintillation characteristics over there. Through analyzing scintillation data of 354 days at this site in the year of 2011 we can estimate the statistical occurrence rate of phase scintillation and amplitude scintillation. The temporal, diurnal, monthly and seasonal variations of the characteristics of ionospheric phase scintillation have been studied, as well as the correlation between phase scintillation and geomagnetic disturbance index (Kp). Statistical results show that phase scintillation activities are more pronounced than amplitude scintillation activities at South Pole. The Antarctic ionospheric scintillation were relatively quiet and the phase scintillation index (Sigma phi) with Sigma phi >0.3 took place infrequently only with the occurrence rate of is 0.14 % throughout the year. The occurrence rate of phase scintillation in March, April, September and October is higher than that in other months. The highest occurrence rate is in April and October and the lowest in January. In April, September and October, phase scintillation mainly appeared on the 12–18 UTC, and the different intensities of phase scintillation have a similar time variation characteristics. As shown in the results, higher kp always correlates with stronger phase scintillation.

Keywords Ionospheric scintillation · Antarctica · Statistical analysis · GPS · Sigma phi

L. Pan (✉) · P. Yin
College of Electronic and Information Engineering, Civil Aviation University of China, Tianjin, China
e-mail: lijingpan9130@163.com

P. Yin
e-mail: pyin@cauc.edu.cn

J. Sun et al. (eds.), *China Satellite Navigation Conference (CSNC) 2014 Proceedings: Volume I*, Lecture Notes in Electrical Engineering 303,
DOI: 10.1007/978-3-642-54737-9_2,

2.1 Introduction

The region between 60 and 1,000 km above the Earth's surface, known as the ionosphere, is produced by ionizing radiation. When radio waves propagate through ionosphere, they are refracted, reflected, scattered and absorbed resulting in the loss of energy. Various scales of irregular structures in ionosphere can cause the satellite navigation systems, such as the global positioning system (GPS) signals fluctuate, which is referred to the ionospheric scintillation. Ionospheric scintillation will make greatly influence on the tracking performance of the satellite navigation receivers. It will lead to signal interruption when ionospheric scintillation has a severe interference on communication and the radio broadcast. When the problem gets more serious, it even affects the positioning accuracy and reliability of the satellite navigation system [1]. With the extensive application of space-based satellite communications and navigation systems, the effects of ionospheric scintillation on ground-air communication systems can be effectively avoided or reduced by carrying out monitoring of the ionospheric scintillation. Therefore, monitoring the ionospheric activity and obtained the change law of ionospheric activities are of great significance.

The electron density and Total Electron Content (TEC) of the ionosphere are constantly changing over time and space, so the real-time monitoring is very difficult. By means of the scintillation data measured by the GPS receiver, it is possible to study the characteristics of ionospheric scintillation. Generally, scintillation activity can be roughly divided into three zones: the high latitude regions, low latitude regions and the regions between low latitude regions and high latitude regions [2]. It is shown that the ionospheric scintillation predominates at high latitudes and low latitude equator zone [3]. The ionosphere structure in the low-latitude equatorial regions is unstable due to the magnetic equator Rayleigh-Taylor instability over night, which makes the low-latitude equatorial region become one of the strongest area of the world's scintillation activity [4, 5]. Polar regions connect the Earth geographic pole with geomagnetic pole. The polar ionosphere which has a special physical form and mechanism, connects directly the Earth's magnetosphere and interplanetary space. Occurrence rate of scintillation is high in the polar region. So the research of ionospheric scintillation is more and more important [6, 7].

Currently ionospheric scintillation monitoring mostly focuses on low-latitude equatorial regions, and the scintillation data measured at high latitudes is very little. Foreign study of ionospheric scintillation start early, for a lot of research for the ionospheric scintillation, Hunsucker and others to achieve the ionosphere and its influence on the radio waves propagation to do the research; Spogli waiting for polar ionospheric scintillation research. In this paper, statistical analysis of ionospheric scintillation in Antarctic is made with 3,000,000 data samples over 354 days in 2011. The observed data is taken by a scintillation receiver in the

South Pole Station in Antarctica. The statistical characteristics of ionospheric scintillation in Antarctica region, obtained in the study, will make a certain foundation for a better understanding of ionospheric phase scintillation in this region and for making a model in the future.

2.2 Data and Analysis

Scintillation data for this study is obtained by a scintillation receiver GSV4004 installed in the Antarctica South Pole station (geographic latitude of −90°/magnetic latitude of −74°, geographic longitude 0°). GPS satellites signals have two L-band carrier frequencies, i.e., L1 (1,575.42 Hz) and L2 (1,227.6 Hz). The GSV4004 receiver can receive 11 GPS satellite signals. The main purpose of GSV4004 is to collect ionospheric scintillation data, TEC data of all visible satellites and output data, etc. GSV4004 receiver output two kinds of data, One is a kind of parameter data, computing good S4, sigma phi namely; Another kind is the original data; In this paper, the parameter data [8].

In research of ionospheric scintillation, measure of scintillation intensity index is the amplitude scintillation index S4 and phase scintillation index sigma phi. S4 index is defined as standard deviation of the average of the normalized signal intensity. The index reflects the change in the intensity of the signal amplitude. It is calculated once per minute, which is calculated as

$$S4 = \sqrt{\frac{\langle S_I^2 \rangle - \langle S_I \rangle^2}{\langle S_I \rangle^2}}$$

where, $\langle S_I \rangle$ represents the signal intensity average value. The S4 index in the analysis is the elimination of surrounding noise, which is the correction value of S4. When ionospheric scintillation enhances, S4 index will increase. When S4 index is equal to 1, it is considered as saturation of scintillation in this time. Traditionally, $S4 < 0.3$ is a weak scintillation, and $S4 > 0.6$ is the strong scintillation.

Sigma phi is defined as the standard deviation of the carrier phase in radians. The parameter is obtained by the power spectral density of the carrier phase, which represents the phase change of the satellite signal severity level caused by ionospheric scintillation. The equation is:

$$sigmaphi = \sqrt{E(\phi^2) - E(\phi)^2}$$

where, ϕ is the carrier phase, $E(\phi)$ is expectation of ϕ, outputted by GSV4004 with interval of 60 s.

Table 2.1 Occurrence rate of various levels of sigma phi and S4 of 1 year

Rate Level	Sigma phi (%)	S4 (%)
0–0.1	94.14	97.58
0.1–0.2	5.15	2.34
0.2–0.3	0.57	0.09
0.3–1	0.14	0

2.3 Results and Discussion

Using the data in the year of 2011 from South Pole station, the temporal, monthly and seasonal variations of the statistical characteristics of ionospheric phase scintillation have been studied. Analysis of the occurrence rate between amplitude scintillation and phase scintillation is made. The correlation between phase scintillation index and Kp index is studied in this region. According to the previous experience, the minimum elevation GPS satellites is limited to 20° in order to reduce the effects of multipath and other low-elevation effects.

In this paper, according to previous experience about high latitudes ionospheric scintillation observations, actual observations in Antarctica and 2011 as solar activity low activity, the scintillation of sigma phi <0.3 is considered as weak phase scintillation, sigma phi >0.3 for the strong phase scintillation.

Table 2.1 shows the intensity of the different phase and amplitude of occurrence rate in year. The occurrence rate is defined as the ratio of the number of scintillation greater than a specified value in period of time to the number of all scintillation during the same period. As can be seen in the table, the phase scintillation is stronger than the amplitude scintillation. Hence, we focus on analyzing the characteristics of the phase scintillation in the following sections.

2.3.1 Monthly Variations of Phase Scintillation

Figure 2.1 illustrates the monthly occurrence rate of various levels of phase scintillation in the year 2011. As can be seen from the preliminary results of the measured data, scintillation in the year 2011 is mainly weak phase scintillation with sigma phi <0.3, and strong phase scintillation with sigma phi >0.3 has a lower occurrence rate. As can be seen from the figure, scintillation has obvious seasonal variation characteristic and has a peak in spring and autumn, and has a lower rate in winter and summer. The lowest occurrence rate is in January. In February and March, scintillation significantly increases and has a peak in April. The occurrence rate is low in May and June. In September, October, scintillation significantly enhances and get the maximum. Phase scintillation at different intensity has a good consistency.

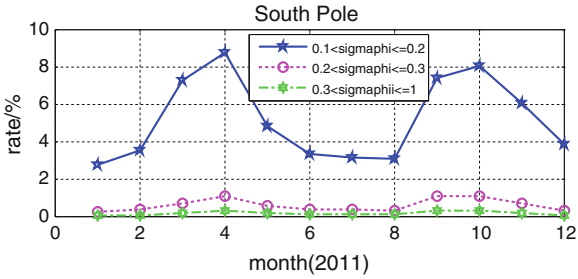

Fig. 2.1 Month-to-month variability of the occurrence rate of different levels of the phase scintillation

2.3.2 Temporal Variations of Phase Scintillation

Figure 2.2 shows the occurrence rate of sigma phi >0.2 with UTC time from January 2011 to December 2011. The axis represents the phase scintillation occurrence rate. Can be seen from the figure in March to may, From September to November blink rate significantly stronger than the June to August, December to February, March to May, From September to November sigma phi >0.2 twinkle incidence peak appeared in UTC 12–18 UTC in this period of time.

2.3.3 Relationship Between Scintillation Index and the Kp

3-hr Kp index can be used to represent the intensity of geomagnetic disturbances. In order to study the correlation between geomagnetic disturbances and scintillation index in Antarctica, we use 2011 kp value that we obtain from SPIDR database [9] to analyse.

The relationship is analyzed among geomagnetic activity index Kp, ionosphere phase scintillation and occurrence rate of phase scintillation. We all on January to November 2011 Kp value processing, take a day of Kp is greater than a maximum of five data, as the days of ionospheric disturbance index of Kp, from all the Kp value in the statistical data of Kp is greater than 5, and will get Kp's statistics and the corresponding time of sigma phi >0.3 strong flicker frequency and the corresponding flashing incidence trend of correlation analysis. The Kp index and phase scintillation have a good relationship in the Antarctic generally. Six representative days from statistics date of kp >5 are selected to draw the figure of the Kp and phase scintillation with UTC time to do a specific analysis, as shown in Fig. 2.3.

In Fig. 2.3, the histogram plots the change of Kp values with time. The axis is UTC time and the axis is the Kp value. The other plots are the temporal variation of phase scintillation. The axis is the value of sigma phi. The circle represents values of sigma phi of the satellite in that time. As can be seen from the figure, large Kp always corresponds with severe phase value scintillation. It is interesting to note that October 25, strong phase scintillation took place with Kp up to 7.3,

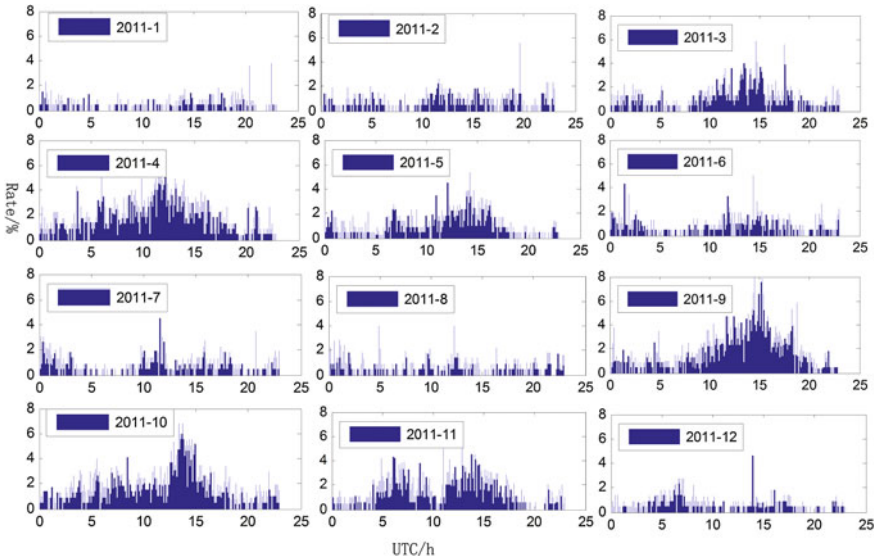

Fig. 2.2 Variability of the occurrence rate of the phase scintillation with sigma phi >0.2

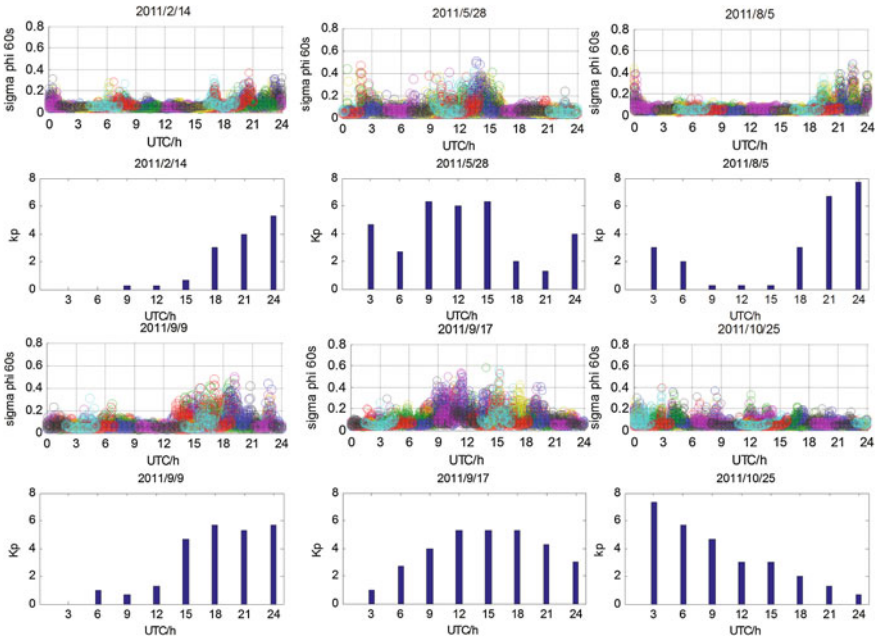

Fig. 2.3 The relationship between the sigma phi and Kp

Table 2.2 The relationship between the sigma phi and Kp

Day	4/2	14/2	1/3	11/3	29/4	28/5	29/5	4/6	5/6	5/8
Kp	5.7	5.3	5.3	5.7	5.3	6.3	5.3	5.3	6.3	7.7
Sigma phi >0.3	16	5	55	13	36	60	13	5	30	39
Rate %	0.15	0.05	0.50	0.12	0.33	0.56	0.12	0.05	0.28	0.36
Day	6/8	9/9	10/9	17/9	26/9	27/9	29/9	24/10	25/10	
Kp	6.3	5.7	5.7	5.3	6.3	5.7	5.7	7	7.3	
Sigma phi >0.3	25	78	12	176	295	17	4	45	13	
Rate %	0.23	0.73	0.11	1.64	2.79	0.16	0.04	0.42	0.12	

however, on September 26 with Kp no more than 7, phase scintillation seems to be more stronger. The underlying mechanism will be our future work (Table 2.2).

2.4 Conclusion

By analyzing GPS scintillation data of 354 days in the year of 2011 at South Pole in Antarctic, a preliminary statistics in Antarctic is made about ionospheric scintillation characteristics and correlation between geomagnetic activity index and phase scintillation index. The results show that phase scintillation is obviously stronger than amplitude scintillation in this region. In 2011, phase scintillation is dominated with weak scintillation of sigma phi <0.3, and the occurrence rate of sigma phi >0.3 is very low, which is the consistent with findings of Spogli et al. [10] research in polar ionospheric scintillation.

Phase scintillation of 0.1< sigma phi <0.2 and 0.3< sigma phi <1 has a significant seasonal variation. The lowest occurrence rate is in January. In February, March, scintillation significantly enhances and peak occurs in April. The occurrence rate of May and June declines. In September, October, scintillation significantly enhances and attaches to the maximum. Scintillation occurred mainly in 1,200–1,800 UTC and this research conclusions are consistent with Spogli et al. [10], Li et al. [11], Gwal and Jain [12].

There is a good correlation between phase scintillation index and Kp. The greater the value of Kp is, the more severe phase scintillation will be. But there is a particular case which is mentioned above, it will be carried out in subsequent Antarctic ionospheric scintillation monitoring and further study.

Acknowledgements In this paper, the data provided by the University of Bath, Professor Mitchell's research group, supported by the United States Siena College. The author is grateful to them. The funding for this issue was provided by the State Department of Education returned Scientific Research Fund.

References

1. Hunsucker RD, Hargreaves JK (2003) The high latitude ionosphere and its effects on radio propagation. Cambridge University Press, Cambridge
2. Aarons J (1982) Global morphology of the ionospheric scintillations. J Proc IEEE 70(4):360–378
3. Aarons J (1997) 50 years of radio-scintillation observations. Aaten Prop Mag 39(6):7–12
4. Weber EJ, Aarons J, Johnson AL (1983) Conjugate studies of an isolated equatorial irregularity region. J Geophys Res 88(A3):3175–3180
5. Basu S, Groves KM et al (1999) A comparison of TEC fluctuations and scintillations at Ascension Island. J Atmos Solar-Terr Phys 61(11):1219–1226
6. Shunlin Liu (2005) Features of ionosphere F region at Antarctic Zhongshan station. Wuhan University, Wuhan
7. Yang Meng et al (2008) Research of polar TEC fluctuations and polar patches during magnetic storm using GPS. Chin J Geophys 51(1):17–24
8. GSV GPS Silicon Valley (2007) GSV4004B GPS ionospheric scintillation & TEC monitor (GISTM) User's Manual
9. http://spidr.ngdc.noaa.gov/
10. Spogli L, Alfonsi L, De Franceschi G, Romano V, Aquino MHO, Dodson A (2009) Climatology of GPS ionospheric scintillations over high and mid-latitude European regions. Ann Geophys 27(9):3429–3437
11. Li G, Ning B, Ren Z, Hu L (2010) Statistics of GPS ionospheric scintillation and irregularities over polar regions at solar minimum. GPS Solutions 14(4):331–341
12. Gwal AK, Jain A (2011) GPS scintillation studies in the arctic region during the first winter-phase 2008 Indian Arctic expedition. Polar Sci 4(4):574–587

Chapter 3
Study on Onboard Engine Thrust Estimation Based on GNSS Precision Orbit Determination Technology

Chen Shanshan, Yue Fuzhan, Jiang Yong and Li Dongjun

Abstract Electric propulsion technology which has the advantages of high specific impulse, small thrust becomes the preferred way of space exploration in future. To ensure the safety and effectiveness of electric propulsion technology applications, the assessment of its performance is needed. The GNSS technology is now used for orbit determination, time service and so on, and it can be used for onboard thrust estimation. The paper gives the thrust model first. Then it gives the method to estimate the thrust for low and circle satellite orbit and the workflow using GNSS precision orbit determination Technology. At last, the simulation is made to analyse the semi-major axis variation under the thrust in the velocity direction. The result of Grace real time orbit and precision orbit is also give to prove the validity of the method in paper. The paper puts forward a suggestion that the real time orbit determination technology can be used for onboard engine thrust rapid assessment.

Keywords Precision orbit determination · GNSS · Electric thruster · Real time orbit determination

3.1 Introduction

In order to shorten the time to reach the planet or star and carry more scientific observation instruments with less propellant in space exploration, we need to find a more efficient propulsion technology than rocket engine. Electric propulsion

C. Shanshan · Y. Fuzhan · J. Yong · L. Dongjun (✉)
Space Star Technology, Beijing 100086, China
e-mail: dongjunli@126.com

C. Shanshan
e-mail: chenshanshan522@163.com

J. Sun et al. (eds.), *China Satellite Navigation Conference (CSNC) 2014 Proceedings: Volume I*, Lecture Notes in Electrical Engineering 303,
DOI: 10.1007/978-3-642-54737-9_3,

technology research and development and its application has attracted the attention of space powers. Electric thruster which can repeat the start and has high specific impulse, small thrust, light weight and long life characteristics, has been used on many satellites. For example, Boeing Company has delivered eighteen satellites for military and commercial satellite applications [1] used the electric thruster. Currently electric propulsion technology is mainly used to keep track position, and when the satellite main propulsion system is invalid, electric propulsion will play an important role in the transfer orbit, such as the U.S. Air Force "Advanced Extremely High Frequency satellite"-1 (AEHF-1) and the Japanese "Hayabusa" for asteroid detection and so on.

Electric propulsion technology is the preferred way forward for the future of space exploration. In order to ensure the effectiveness of its use, pre-test is needed to be carried out to evaluate its performance. The paper use the precision orbit determination technology with spaceborne GPS dual frequency data to complete the engine thrust Estimation. The paper gives the Engine thrust estimation principle first, and the method to estimate the thrust for low and circle satellite orbit. Then the simulation data and GRACE-A [2] data is used to verify the validity of the method. Engine thrust Estimation based on GNSS precision orbit determination can get high accuracy, but it do not have real-time characteristic. So the paper puts forward a suggestion that the real time orbit determination technology can be used for onboard engine thrust rapid assessment at last.

3.2 Engine Thrust Estimation Principle

3.2.1 Mathematical Model of Electric Thruster

In general, the equation of satellite motion [3] in the inertial coordinate system can be described by the following equation:

$$\ddot{\vec{r}} = \vec{a}_g + \vec{a}_{ng} + \vec{a}_{emp} \tag{3.1}$$

where, $\vec{r}$ represents the position vector of the satellite center of mass, $\vec{a}_g$ represents the sum of the acceleration caused by conservative forces on satellites, $\vec{a}_{ng}$ represents the sum of the acceleration caused by non-conservative forces on satellites, $\vec{a}_{emp}$ represents empirical acceleration. Aside from the natural forces discussed above, the motion of a spacecraft may also be affected by the action of onboard thruster system. Despite the variety of satellite thruster system, the thruster model can be described using impulsive thrust model and constant thrust model [4].

1. Impulsive thrust model: the thrust duration is small as compared to the orbit period, so the thrust change with time can be approximated as a function of the pulse function (equal to impulse multiplied the Dirac-δ function). Satellite motion may conveniently be treated as instantaneous velocity increments.

2. Constant thrust model: the thrust duration is long and even comparable to the orbit period. The equation of satellite motion can be described by the following equation:

$$\ddot{\vec{r}} = \vec{a}_g + \vec{a}_{ng} + \vec{a}_{emp} + \vec{a}_E \tag{3.2}$$

where, $\vec{a}_E$ represents the acceleration caused by thrust forces.

Electric thruster has high specific impulse, small thrust and other characteristics. Typical ion propulsion thrust is 20–40 mN with propellant consumption of 0.8 mg/s. The thrust acceleration is expressed as follows:

$$\vec{a}_E = \frac{\vec{F}_E}{m} = \frac{F_E \vec{e}_E}{m_0\left(1 + \frac{\dot{m}}{m}t\right)} \tag{3.3}$$

where, F_E represents engine thrust, m represents satellite mass, $\dot{m}$ represents the propellant consumption, m_0 represents the satellite initial mass, t represents the thrust duration. Consider electric propulsion engine propellant consumption is relatively small than the mass of the satellite, so we can ignores the satellite mass change during the maneuver. The thrust acceleration is expressed as follows:

$$\vec{a}_E = \frac{F_E \vec{e}_E}{m} \tag{3.4}$$

3.2.2 Electric Thrust Estimation Principle and Precision Analysis

3.2.2.1 Orbit Semi-major Axis Changes Under the Tangential Perturbation

Under the two-body problem, the trajectory of the satellite is an ellipse which can be descripted using six orbital elements. But the satellite actually is affected by the sun and moon gravity perturbation, atmospheric drag and so on which makes the orbital elements change with time. The orbit semi-major axis changes [5] as follows:

$$\frac{da}{dt} = \frac{2}{n\sqrt{1-e^2}}\sqrt{1 + 2e\cos f + e^2}U \tag{3.5}$$

where, a, e, n, f respectively represent the satellite orbit semi-major axis, eccentricity, satellite mean motion, true anomaly, U represent the satellite perturbation in the tangential direction component. While n satisfy the following relation:

$$n^2 a^3 = \mu \tag{3.6}$$

where μ represent the constant of Earth gravitation. Taking the (3.6) into (3.5), we obtain:

$$\frac{da}{dt} = \frac{2a\sqrt{a}}{\sqrt{\mu(1-e^2)}}\sqrt{1+2e\cos f+e^2}U \tag{3.7}$$

Formula (3.7) shows that, the engine thrust along the velocity direction will cause changes of the satellite orbit semi-major axis over time and the rate of change also is the function of orbital eccentricity, semi-major axis and true anomaly.

3.2.2.2 Model Simplification of Circular LEO Orbit

First, the eccentricity of the orbit nearly circle is approximately zero, formula (3.7) can be simplified to:

$$\frac{da}{dt} = \frac{2U}{\sqrt{\mu/a^3}} \tag{3.8}$$

In this case, semi-major axis change is only in relation with the engine thrust and semi-major axis and its partial derivative to the semi-major axis is as follows:

$$\frac{\partial}{\partial a}\left(\frac{da}{dt}\right) = \frac{3U}{\sqrt{\mu}}\sqrt{a} \tag{3.9}$$

When the orbit semi-major axis changes Δa, its impact on the rate of change of the semi-major axis measured by the following formula:

$$\frac{\frac{\partial}{\partial a}\left(\frac{da}{dt}\right)\cdot\Delta a}{da/dt} = \frac{3U\sqrt{a}\Delta a/\sqrt{\mu}}{2U/\sqrt{\mu/a^3}} = \frac{3\Delta a}{2a} \tag{3.10}$$

When consider the semi-major axis of the LEO satellite is 500 km and Δa is 20 km, the impact above is less than 0.44 %. So we can consider the semi-major axis is a constant in the semi-major axis change computation and the constant can be substituted by the mean satellite semi-major axis a_m. The change of the orbit semi-major axis by time during Δt is as follows:

$$\Delta a = \frac{2U}{\sqrt{\mu/a_m^3}}\Delta t \tag{3.11}$$

Then the engine thrust can be estimated by the follows:

$$F_E = \frac{m\sqrt{\mu/a_m^3}}{2\Delta t}\Delta a \tag{3.12}$$

The relationship between engine thrust estimation precision and semi-major axis precision is as follows:

$$\sigma_{F_E} = \frac{m\sqrt{\mu/a_m^3}}{2\Delta t}\sigma_{\Delta a} \tag{3.13}$$

3.2.3 Electrical Thrust Estimation Based on GNSS Precision Orbit Determination

The problem of electrical thrust estimation has became the semi-major axis determination problem, then we can make it by orbit determination technology. With the development of GNSS technology, GPS receiver is mounted on a wide range of low-orbit satellites for real-time and precision orbit determination [6]. The workflow to estimate the electrical thrust based on GNSS observation data is as follows:

1. According electric current or voltage of spaceborne electric thruster we divide the GNSS data into the data before maneuver and the data after the maneuver;
2. Use the data before maneuver and the data after the maneuver for precision orbit determination;
3. Integrate the two orbit into the whole maneuver arc;
4. Compare the two orbit and estimate the engine thrust.

3.3 Simulation of Electric Thrust Effect and Analysis of the Orbit Determination Result

The following first simulate the semi-major axis change under the electric thrust of 40 mN in 790 kg, 500 km orbit altitude of the satellite. Then the dual-frequency GPS data of GRACE-A is used for precision orbit determination to validate the feasibility of the estimation method.

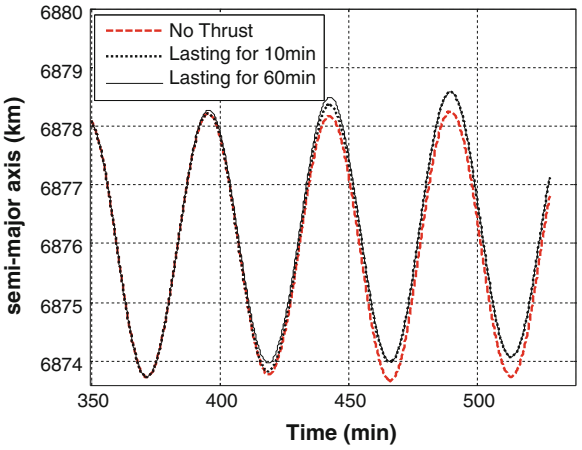

Fig. 3.1 Semi-major axis compare between different lasting time

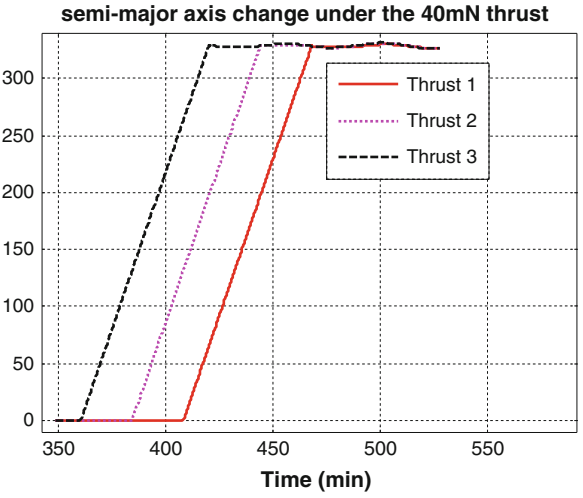

Fig. 3.2 Semi-major axis change at different begin time

3.3.1 Impact of Electric Thrust on Satellite Orbit

First it simulated a 500 km nearly circle orbit of a satellite whose mass is 790 kg. Then the 40 mN thrust along the velocity direction is added at different time and different lasting time. The compare between the initial and changed orbit is as follows (Figs. 3.1, 3.2, 3.3).

Figure 3.2 shows that, semi-major axis change with time under the thrust is approximately linear relationship. Figure 3.3 shows that the change rate of semi-major axis change becomes faster over time; the change rate of semi-major axis change is variety at different added time of thrust; the change rate of semi-major

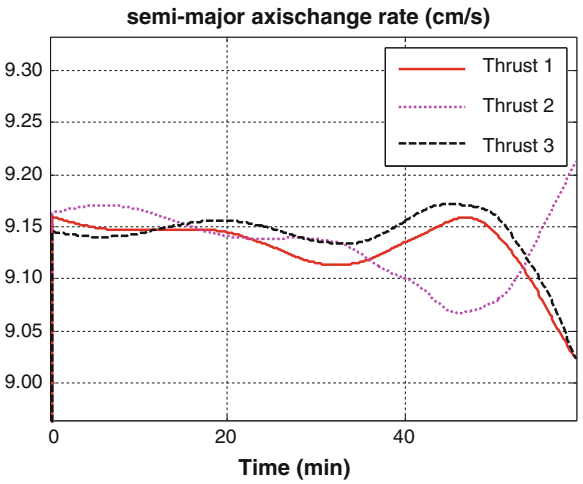

Fig. 3.3 Semi-major axis change rate between at different begin time

axis is approximately a constant value in short time such as 10 min. The relationship between engine thrust estimation precision and semi-major axis precision is as follows:

$$\sigma_{F_E} = \frac{m\sqrt{\mu/a^3}}{2\Delta t}\sigma_{\Delta a} = 0.0073\sigma_{\Delta a} \tag{3.14}$$

3.3.2 *Estimation Accuracy of the Electrical Thrust Based on Dual-Frequency GPS Precise Orbit Determination*

GRACE (Gravity Recovery and Climate Experiment) program is cooperated by NASA and the German DLR. The project has two 220 km away from the nearly circular orbit satellites. In July 2010, GRACE-A satellite orbit altitude is about 460 km. Using the GPS dual-frequency observation data for precise orbit determination, location accuracy and the corresponding semi-axis precision are shown in Figs. 3.4 and 3.5.

The precise orbit accuracy of GRACE-A using dual-frequency data is 5.183 cm. Semi-axis precision is 2.839 cm and the max semi-axis error is 9.13 cm, so the corresponding thrust estimation precision is respectively 0.296 and 1.33 mN. To a 40 mN thruster the relative precision is 0.74 and 3.33 %.

The calculating results of GRACE-A data shows, when using GPS dual-frequency observation data to estimate the thrust of a 40 mN electric thruster, the calibration accuracy can reach 1 %.

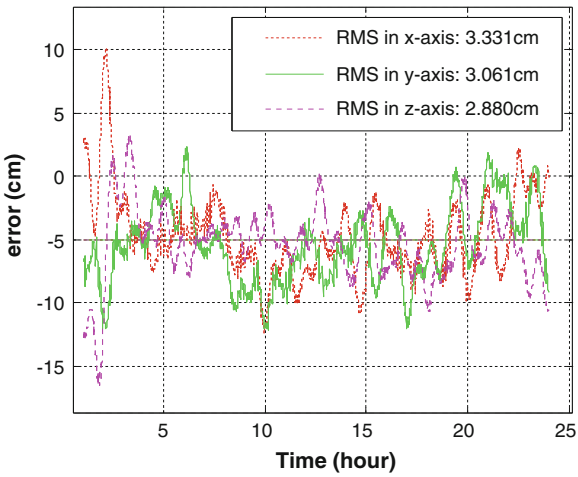

Fig. 3.4 GRACE-A precise orbit accuracy in 3-axis

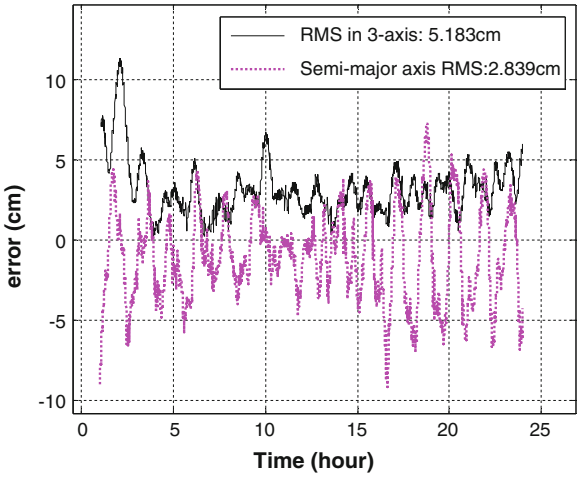

Fig. 3.5 GRACE-A precise orbit accuracy of position and semi-major axis

3.4 Feasibility Using Real-Time Orbit Determination Method for Orbit Control

Precision orbit determination method for electrical thrust estimation can get high accuracy, but do not have the real-time characteristics. The real time orbit determination technology using Kalman arithmetic can estimate satellite state in real time, and it can be used for electric engine thrust Estimation. The GRACE-A result using real time determination algorithms are shown in Figs. 3.6 and 3.7.

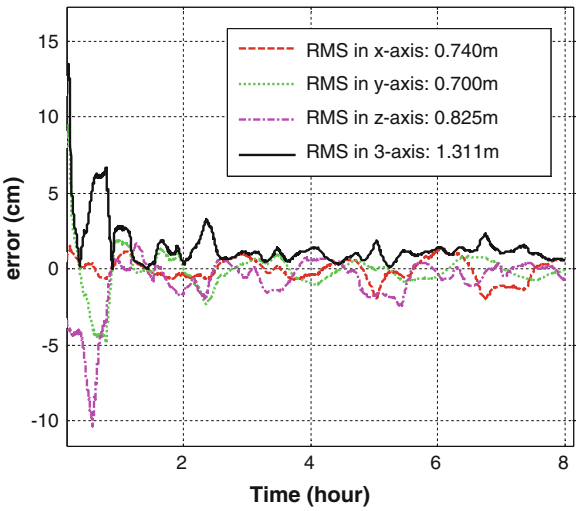

Fig. 3.6 GRACE-A real time orbit accuracy in 3-axis

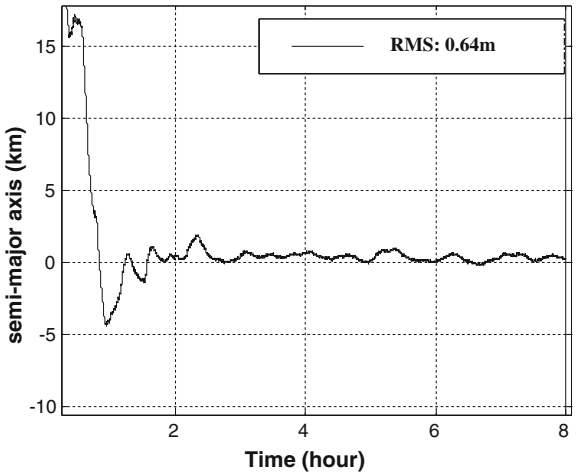

Fig. 3.7 GRACE-A real time orbit accuracy of semi-axis

Figure 3.7 shows that, the filter converges to a stable level of precision an hour later. The orbit accuracy is 1.3 m and semi-axis accuracy is 0.64 m. To a 40 mN thruster the relative precision is approximately 2 %.

3.5 Summary

The method of engine thrust estimation based on the GPS precision orbit determination technology was proposed and proved with GRACE-A data in this paper. The result showed that the method used in 40 mN engine thruster could reach 1 % accuracy in nearly circle LEO satellite. The paper also gives the result of real time orbit determination which has the semi-axis accuracy of 1 m after 1 h filtering.

As the satellite orbit determination is a nonlinear problem, the EKF filter need a long convergence time. Then the use of more advanced filter such as UKF may shorten the time needed for thrust rapid assessment. And also we can add the engine thrust to the filter state vector in order to realize the real time estimation of the electric engine thrust.

References

1. Chi H (2012) The new trend of full electric engine satellite and commercial communication satellite. Space Explor 7:P40–P42
2. Chen J (2007) On precise orbit determination of low earth orbiters. PHD thesis, Tongji University, Shanghai
3. Liu L (2000) Spacecraft orbit theory. National Defence Industry Press, Beijing
4. Yang J (2009) Aerospace dynamics and control. China Aerospace Press, Beijing
5. Liu L, Hu S, Wang X (2006) Introduction of astrodynamics. Nanjing University Press, Nanjing
6. Wang J (1997) GPS precision orbit determination and positioning. Tongji University Press, Shanghai

Chapter 4
Implementation of GNSS Attitude Determination Receiver

Xiang Ao, Xiaowei Cui and Gang Liu

Abstract In this paper a specialized GNSS attitude determination receiver is implemented using homologous RF platform, the receiver uses identical RF circuits which are driven by the same one crystal oscillator, so it has a better correlation between different signal paths. Receiver baseband signal processing is divided into Master RF signal path and Slaver RF signal path. The Master RF signal path completes acquisition and tracking task and the Slaver RF signal path deals with measurements extraction. Different from the traditional independent receiver, carrier phase measurements are extracted independently from the Master signal path. So a unique filter could be used to smooth observed measurements in order to enhance the overall performance and output higher accuracy carrier phase measurements. Higher accuracy of carrier phase measurement will improve the possibility of the success of ambiguity search. Therefore attitude determination receiver has a higher processing performance. Meanwhile the receiver's measurement extraction accuracy is independent from the Master RF signal path, so it can be measured at the time that the Master RF signal path entering the tracking state and the receiver can output measurements as short as possible. When integrated with the INS, attitude determination receiver not only provides position, velocity, but also outputs attitude information. Moreover, INS provides reference attitude information to assist determining carrier ambiguity, so attitude determination receiver has a better performance in the robustness in harsh environments.

X. Ao (✉) · X. Cui
Department of Electronic Engineering, Tsinghua University, Beijing 100084, China
e-mail: xiang.xao@gmail.com

G. Liu
Department of Precision Instruments and Mechanology, Tsinghua University, Beijing, China

G. Liu
Department of Control Engineering, Naval Aeronautical and Astronautical University, Yantai, China

J. Sun et al. (eds.), *China Satellite Navigation Conference (CSNC) 2014 Proceedings: Volume I*, Lecture Notes in Electrical Engineering 303,
DOI: 10.1007/978-3-642-54737-9_4, © Springer-Verlag Berlin Heidelberg 2014

Dynamic experiment is carried out where the GNSS attitude determination receiver and the INS are mounted on a car. The navigation results show that the receiver has a better carrier phase output capacity, and provides more information in the subsequent attitude determination.

Keywords Attitude determination · Homologous RF platform · Carrier phase measurement

4.1 Background

The attitude determination from GNSS signal is to calculate the relative distance between two or more antennas and then convert to the attitude angle, by using carrier phase difference algorithm. When GNSS antenna is located at both the two ends of the platform, one can calculate the baseline vector and then convert to the attitude angle. Presently, multiple GNSS OEM boards are used to generate carrier phase observations independently, based on which carrier phase difference algorithm is used to calculate the attitude angle. The method separates the receiver design from the carrier algorithm, thus reducing the overall performance.

Based on the considerations above, researchers [1–3] have proposed homologous RF platform which take advantage of the correlation between each RF signal path and combine the receiver design with the carrier difference algorithm to achieve a better performance of the attitude determination. This paper implements an attitude determination receiver based on homologous RF platform and verifies its performance.

4.2 Attitude Determination Receiver

4.2.1 Receiver RF

Homologous RF attitude determination receiver shares the same oscillator for frequency synthesizing, frequency down-conversion and AD sampling, thus the RF front-end processing module has the same information processing characteristics. The receiver RF structure [2] is shown in Fig. 4.1.

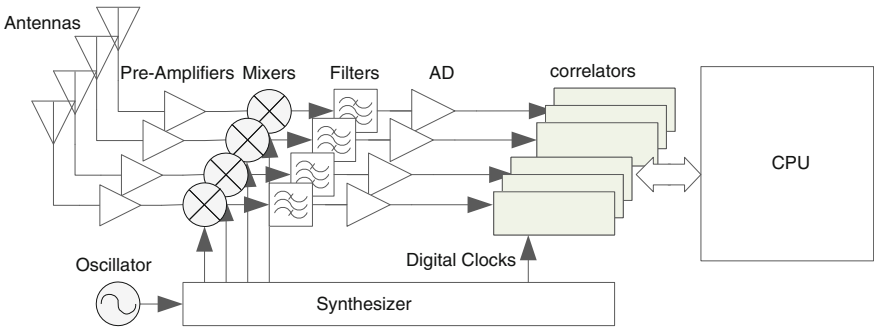

Fig. 4.1 Receiver RF structure

4.2.2 Signal Model

GNSS signal on the L1 band can be expressed in (4.1) at the receiving end.

$$S_{L1}(t) = \sqrt{2P_C}C(t-\tau)D(t-\tau)\cos(2\pi(f_{RF}+f_d)t+\varphi_{\mathrm{RF}}) \tag{4.1}$$

After down-conversion, we can get:

$$S_{IF}(t) = \frac{1}{2}\sqrt{2P_C}C(t-\tau)D(t-\tau)\cos\left(2\pi(f_{IF}+f_d)t+\varphi_{IF}\right) \tag{4.2}$$

As GNSS signal power is quite weak, it is necessary to use coherent integration operation in the baseband signal processing, thus obtaining a higher spreading gain. Assuming the input signal is continuous, pre-detection integration results are expressed as:

$$\begin{aligned} I_k &= \sqrt{2(C/N_0)T_c}\mathrm{sinc}(\pi\Delta f_k T_c)\mathrm{R}(\Delta\tau_k)D\cos(\pi\Delta f_k T_c+\Delta\varphi_k)+\eta_{I,k} \\ Q_k &= \sqrt{2(C/N_0)T_c}\mathrm{sinc}(\pi\Delta f_k T_c)\mathrm{R}(\Delta\tau_k)D\sin(\pi\Delta f_k T_c+\Delta\varphi_k)+\eta_{Q,k} \end{aligned} \tag{4.3}$$

where k represents the k-th channel RF path; C/N_0 is the signal carrier to noise ratio, Δf_k is the Doppler frequency of the local signal, $\Delta\varphi_k$ is the phase error of the receiver with a local signal, R is the autocorrelation function of the spread spectrum signal, D is the current navigation message symbol and η is the coherent integration noise.

4.2.3 Model Analysis

The signal processing for homologous RF attitude determination makes use of Mast RF signal path and Slaver RF signal path. The Master RF signal path is

responsible for signal acquiring and tracking while the Slave RF signal path is responsible for extracting the measurements by using differential carrier phase discriminator. Pre-detection vector of each RF path is expressed as:

$$r_k = I_k + jQ_k = A_k e^{j(\pi \Delta f_k T_c + \Delta \varphi_k)} \tag{4.4}$$

Multiply the Master RF Pre-detection vector r_1 with conjugate of the Slaver RF Pre-detection vector r_2:

$$r_1 \overline{r_2} = A_1 A_2 e^{j(\pi(\Delta f_1 - \Delta f_2)T_c + (\Delta \varphi_1 - \Delta \varphi_2))} \tag{4.5}$$

The differential carrier phase measurements can be expressed as:

$$\Delta \varphi_{21} = \pi(\Delta f_2 - \Delta f_1)T_c + (\Delta \varphi_2 - \Delta \varphi_1) \tag{4.6}$$

As each RF signal path uses the same local carrier phase and pseudo-code phase, differential phase measurements can be expressed as:

$$\begin{aligned} \Delta \varphi_2 - \Delta \varphi_1 &= (\varphi_{\mathrm{IF2}} - \varphi_{loc}) - (\varphi_{\mathrm{IF1}} - \varphi_{loc}) \\ &= (\varphi_{\mathrm{RF2}} - \varphi_{mix2} - \varphi_{loc}) - (\varphi_{\mathrm{RF1}} - \varphi_{mix1} - \varphi_{loc}) \\ &= (\varphi_{\mathrm{RF2}} - \varphi_{\mathrm{RF1}}) - (\varphi_{mix2} - \varphi_{mix1}) \\ &= (\varphi_{\mathrm{RF2}} - \varphi_{\mathrm{RF1}}) - \Delta \varphi_{mix} \end{aligned} \tag{4.7}$$

where RF1 represents the Mast signal path, RF2 represents the Slaver signal path; $\Delta\varphi$ is the phase difference between the received signal and the local signal; φ_{loc} is the local signal phase, φ_{IF} is the IF signal phase, φ_{mix} is the mixer signal phase, $\Delta\varphi_{mix}$ is the constant time delay of the output phase caused by the different of master-slave radio mixer paths.

The observation of differential carrier Doppler can be expressed as:

$$\begin{aligned} \Delta f_2 - \Delta f_1 &= (f_{\mathrm{IF2}} + f_{\mathrm{d2}} - f_{loc}) - (f_{\mathrm{IF1}} + f_{\mathrm{d1}} - f_{loc}) \\ &= (f_{\mathrm{RF2}} + f_{\mathrm{d2}} - f_{mix} - f_{loc}) - (f_{\mathrm{RF1}} + f_{\mathrm{d1}} - f_{mix} - f_{loc}) \\ &= (f_{\mathrm{d2}} - f_{\mathrm{d1}}) \\ &= \Delta f_{\mathrm{d}} \end{aligned} \tag{4.8}$$

where f_{IF} is the IF frequency; f_{d} is the relative motion Doppler frequency; f_{loc} is the local signal frequency; f_{RF} is the Satellite Carrier Frequency; f_{mix} is the mixer frequency.

Considering the different line delay from the mixer input to the RF signal, as well as the mismatch in the length of signal processing path, the baseband output

for each phase of the differential RF channel contains a line delay deviation, therefore the differential carrier phase observations can be expressed as:

$$\begin{aligned}\Delta\varphi_{21} &= \pi(f_{\mathrm{d2}} - f_{\mathrm{d1}})T_{\mathrm{c}} + (\varphi_{\mathrm{RF2}} - \varphi_{\mathrm{RF1}}) - (\Delta\varphi_{mix} + \Delta\varphi_{\mathrm{line}}) \\ &= \pi\Delta f_{\mathrm{d}} T_c + \Delta\varphi_{\mathrm{RF}} - \Delta N_{21} - \Delta\varphi_{bias}\end{aligned} \tag{4.9}$$

Therefore the absolute deviation of the carrier phase of each antenna can be expressed as:

$$\mathrm{L}_{\varphi} = \pi\Delta f_{\mathrm{d}} T_c + \Delta\varphi_{\mathrm{RF}} = \Delta\varphi_{21} + \Delta N_{21} + \Delta\varphi_{bias} \tag{4.10}$$

where Δf_d represents the Doppler difference between the two antennas and the satellite motion component; $\Delta\varphi_{\mathrm{RF}}$ represents the relative absolute phase deviation of two antennas at the satellite distance; $\Delta\varphi_{21}$ represents differential carrier phase measurements between the Master RF signal path and the Slaver RF signal path; ΔN_{21} represents the initial ambiguity; $\Delta\varphi_{bias}$ represents the mismatch carrier phase.

As can be seen from Eq. (4.10), in order to recover the absolute distance between the two antennas, it is necessary to obtain the three observations ($\Delta\varphi_{21}$, ΔN_{21}, $\Delta\varphi_{bias}$). Phase difference $\Delta\varphi_{21}$ is the output of the differential carrier phase discriminator. The initial ambiguity ΔN_{21} can be searched by integer least squares method. Mismatch phase $\Delta\varphi_{bias}$ related to the current work environment, and it is a constant value when the environment has determined. At the start initial vector can be used to calculate the mismatched phase, which will then be used as a fixed offset compensation for each satellite.

4.2.4 Signal Loop Design

The measurement extraction of homologous RF attitude determination receiver is different from that in the independent receiver, where the Master RF signal path acquires and tracks the signal and the Slaver RF signal path correlate the carrier and the spread code derived from the Master RF signal path, and then extract the carrier phase measurement by differential carrier phase discriminator.

For traditional receiver, the full carrier phase measurements output need to verify the current message bit status, which can be implemented by the navigation frame synchronization process.

For Homologous RF attitude determination receiver, the Master RF signal path and the Slaver RF signal path make correlation with the same carrier and the spread code. The carrier phase measurements output is regardless of the local carrier frequency and phase, and the carrier phase measurements are independent of the Master channel loop. When the Master channel loop detects a signal and adjusts the frequency and pseudo-code to the correct point, full differential carrier phase measurements can be obtained as output, which needs only 50 ms.

4.3 Baseline Solution

The raw carrier phase measurement output of the Homologous RF attitude determination receiver is the differential carrier phase of the different antenna in the same satellite. The observation equation of the various antennas and satellite are provided,, where the Master RF signal path (label 1) is used as a starting point, the Slaver signal path (label 2) linearized at the same point, the difference between the stations linear observation equation is obtained:

$$\lambda\Delta\varphi_{21}^{j} = -\lambda\Delta N_{21}^{j} + \Delta\rho_{21}^{j^0} + A^{j}X_{21} + \Delta\varphi_{bias} + \Delta\varepsilon_{\varphi}^{j} \tag{4.11}$$

where j represents satellite label; $\Delta\varphi_{21}^{j}$ represents differential carrier phase measurements; ΔN_{21}^{j} represents initial ambiguity; $\Delta\rho_{21}^{j^0}$ represents linearized different distant; A^{j} represents line of sight Matrix; X_{21} represents baseline vector; $\Delta\varphi_{bias}$ represents carrier phase mismatch of different RF signal path; $\Delta\varepsilon_{\varphi}^{j}$ represents the noise carrier phase measurement.

4.3.1 Baseline Solution Model

As can be seen from Eq. (4.11), the carrier phase differential solution model mainly deal with the three parts: the initial ambiguity ΔN_{21}^{j}, the baseline vector X_{21} and the phase mismatch $\Delta\varphi_{bias}$.

The observation equation can be written in the form of a matrix

$$L_{\varphi} = AX + BN + BL_{\text{bias}} \tag{4.12}$$

where L_{φ} represents carrier phase linearized observation vector; B represents ambiguity coefficient matrix; L_{bias} represents phase mismatch vector, the same value ($\Delta\varphi_{bias}$) for each satellite.

If the current baseline vector is known, the current satellite ambiguity parameter equation can be written as:

$$B(N + L_{\text{bias}}) = L_{\varphi} - AX \tag{4.13}$$

At this moment the float ambiguities can be calculated. And then by using the integer ambiguity characteristics, one can determine the current ambiguity N and the carrier phase mismatch $\Delta\varphi_{bias}$.

If the current ambiguity is known, the current baseline vector and the phase mismatch equation can be written as:

$$L_{\varphi} - BN = AX + BL_{\text{bias}} \tag{4.14}$$

Since L_{bias} share the same value ($\Delta\varphi_{bias}$) for each satellite, it can be set as the 4th parameters to complete the baseline vector solving, and finally obtain the baseline vector and phase mismatch.

If the current ambiguity phase mismatching is known, the current baseline vector parameter equation can be written as:

$$L_{\varphi} - BN - BL_{\text{bias}} = AX \tag{4.15}$$

At this point the baseline vector can be solved.

Based on carrier phase observation Eqs. (4.13)–(4.15), there are three processes under the homologous RF attitude determination receiver for Baseline Solution.

Firstly, based on Eq. (4.12), a double difference equation can be established to calculate the current baseline vector and the double difference ambiguity. Then based on Eq. (4.13), single difference ambiguity N and initial phase mismatch $\Delta\varphi_{bias}$ can be calculated. Finally, based on Eq. (4.14), Kalman filter can be designed to complete baseline vector and phase mismatch solution.

The first two processes mentioned above are mainly for initialization process, the third process is for receiver working state, and the finally process filtering algorithm determine the accuracy of receiver and harshness of the operating environment.

4.3.2 Baseline Filter Equation

Independent receiver phase measurements filtering algorithm is implemented by the realization of phase-locked tracking, which is correlated with the accuracy of the output phase measurements. The differential carrier phase measurements extraction in homologous RF attitude determination receiver is independent to the Master channel tracking loop. So the filters can be designed separately to complete the processing of observations. Considering the case that, with compensate of constant bias, the differential carrier phase measurements of various satellites have single difference integer ambiguity characteristics. From this aspect, it could design a single satellite observations vector Kalman filter completed smoothing measurements and estimated baseline vector. Kalman filter state vector can be taken: baseline vector and the rate of baseline vector and carrier phase mismatch. Baseline vector uses a constant velocity model; while the carrier phase mismatching uses a first-order random walk model.

The Kalman filter state equation is:

$$\begin{aligned} \hat{X}_{k+1}(-) &= \mathrm{F}_k^{k+1}\hat{X}_k(+) \\ \mathrm{P}_{k+1}(-) &= \mathrm{F}_k^{k+1}\mathrm{P}_{k+1}(+)\mathrm{F}_k^{k+1\,T} + Q_k^{k+1} \end{aligned} \tag{4.16}$$

where X represents state vector; F_k^{k+1} represents state transition matrix; P_{k+1} represents state covariance matrix; Q_k^{k+1} represents system model noise.

State vector:

$$X = \begin{pmatrix} r^T & v^T & \lambda\varphi_{bias} \end{pmatrix}^T \tag{4.17}$$

State transition matrix:

$$\mathrm{F}_k^{k+1} = \begin{bmatrix} I_{3\times3} & T_{3\times3} & 0 \\ 0 & I_{3\times3} & 0 \\ 0 & 0 & 1 \end{bmatrix} \tag{4.18}$$

where r^T represents baseline vector; v^T represents the rate of baseline; $\lambda\varphi_{bias}$ represents phase mismatch in distance.

The Kalman filter measurement equation is:

$$\begin{aligned} \hat{X}_k(+) &= \hat{X}_k(-) + K_k Z_k \\ \mathrm{P}_k(+) &= (I - K_k H_k)\mathrm{P}_k(-) \\ K_k &= \mathrm{P}_k(-)H_k\left(H_k\mathrm{P}_k(-)H_k^T + R_k\right)^{-1} \end{aligned} \tag{4.19}$$

where H_k represents measurement update matrix; Z_k represents new measurement vector; R_k represents measurement noise covariance matrix.

And the measurement update matrix is:

$$H_k = \begin{bmatrix} A_{n\times3} & 0_{n\times3} & 1_{n\times1} \end{bmatrix} \tag{4.20}$$

where n represents the number of satellites; $A_{n\times3}$ represents line of sight Matrix; $1_{n\times1}$ represents unit vector.

Mew measurement vector Z_k is extracted by de satellite differential carrier phase measurements $\Delta\varphi$.

$$Z_k = L_\varphi - BN - H_k\hat{X}_{k+1}(-) \tag{4.21}$$

where L_φ represents linearized observation vector (calculated by the difference carrier phase measurements); B represents ambiguity coefficient matrix; N represents single difference integer ambiguity.

4.3.3 Noise Performance Analysis

In the vehicle attitude determination by using GNSS receivers, the primary kind of error comes from the noise in the carrier phase measurement, including loop tracking error, multipath error and oscillator noise. For independent receiver's attitude measurement system, each of which directly affect the error of the carrier

phase measurements, thereby affecting the attitude measurement accuracy. In terms of the homologous RF attitude determination receivers, the carrier phase observations are extracted directly from the loop, making the modulation of error different form the independent receivers.

The Homologous RF attitude determination receiver uses a vector Kalman filter, where the baseline vector motion model is considered in the filtering of carrier phase measurements. Which the accuracy of carrier phase measurements are higher than the independent receiver. Baseline vector is obtained directly through the carrier phase measurements, single satellite multipath error impact on baseline vector became weaken. In addition Homologous RF attitude determination receiver using the same RF circuit configuration, oscillator common noise mode could completely eliminated in the carrier phase different process. Oscillator differential noise mode in constant value is set as a state vector Kalman filter, and the first order differential noise component as a filter in the random walk model, the remaining high order differential noise component will affect the accuracy of carrier phase measurements.

4.4 Experiment

There is a car Experiment using the Homologous RF attitude determination receiver. The receiver use two piece of MAX2769 to receive GPS L1 C/A signal shares the same oscillator. In the experiment, the Master antenna is mounted on the front portion of the experiment car and the Slaver antenna is mounted on the rear of the car. Trying to keep the line in the middle of the car, and the baseline distance is approximately 1.55 m. Also there are two IMU system on the roof of the car, both gyro drift accuracy are 30°/h. IMU1 is an independent inertial navigation system, synchronization with the receiver for analysis and post processing; IMU2 is a combination navigation system which integrates a Novatel board, and it is used for comparison with the attitude determination verification.

Experimental car and raw data output from the Master antenna single point positioning tracing point of post-processing shown in Fig. 4.2.

Satellite Chart show shown and the entire experiment process observation satellite signal quality in Fig. 4.3.

It can be seen, the observation in a poor environment, there are tall building around road blocking satellite signal, and the lower elevation angle of the satellite frequent loss of lock. Most of time there are only four or five satellite in sight for measurements, sometimes there are only three satellites for measurements.

There are three static state points in this experiment, which keep about 15 s. In Fig. 4.4, there are two static state point output yaw angle enlarged, and it can be seen that the Homologous RF attitude determination receiver has 0.3° error. Considering the harsh environment and only 4–5 satellites for most of the observation time, the Homologous RF attitude determination receiver has better yaw angle accuracy.

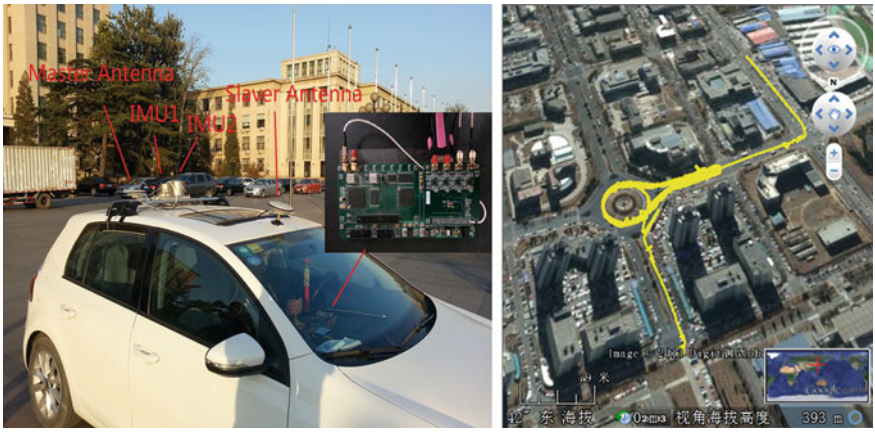

Fig. 4.2 Experimental platform and tracing point

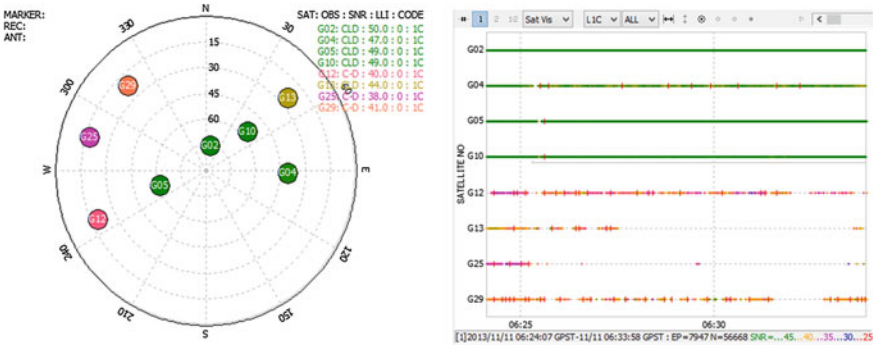

Fig. 4.3 Satellite chart and signal quality

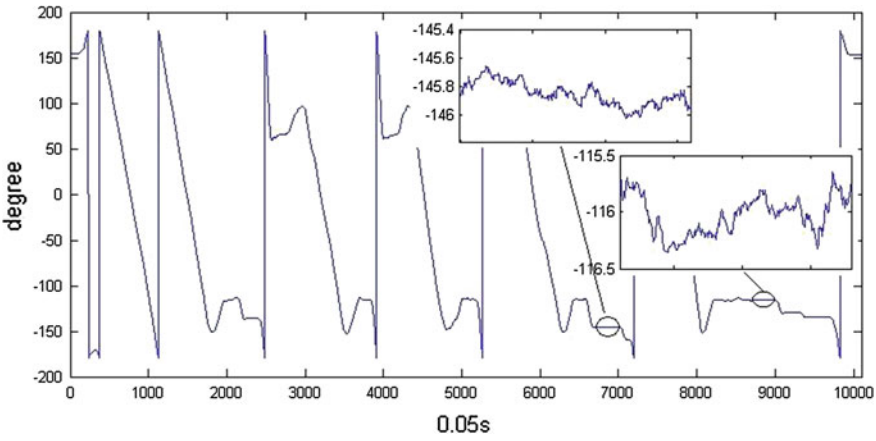

Fig. 4.4 Attitude receiver output yaw angle

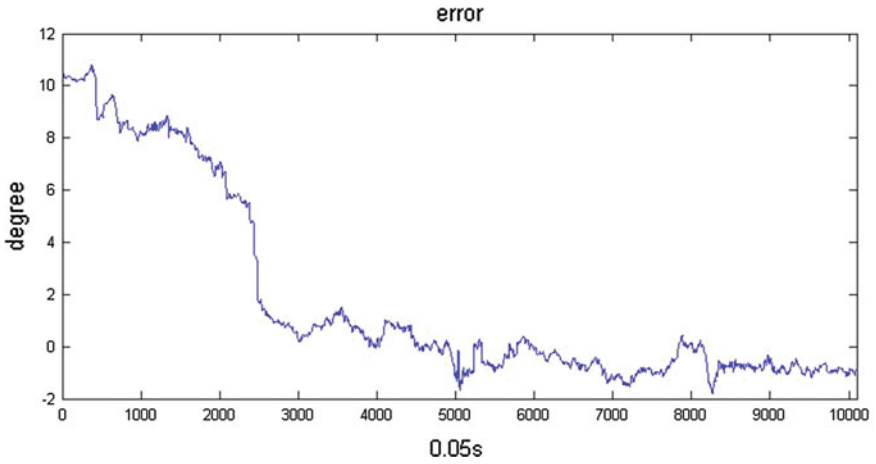

Fig. 4.5 Difference between two yaw angles

IMU2 integrated navigation system, which integrates with the Novatel receiver that outputs pseudorange and pseudorange rate for deeply combine navigation. It has being verified that IMU2 integrated navigation system output angle error is 1°.

Figure. 4.5 shows that the difference between two yaw angles is within 2°. Which has been compensated for misalignment angle between the two systems, and the system time is about its accuracy 2 ms. Considering the poor environmental of observations, the correction of the output the basic yaw angle can be verified for the two systems.

4.5 Conclusions

Experiment results show that the homologous RF attitude determination receiver has a better accuracy in attitude measurement and stronger ability in working in harsh environments.

References

1. Parkinson BW, Spilker JJ (2006) Global positioning system: theory and application, 2 edn. American Institute of Aeronautics and Astronautics,Inc., Washington, DC
2. Cohen CE (1992) Attitude determination using GPS. PhD thesis, Department of Aeronautics and Astronautics, Standford University
3. Keong JH (1999) GPS/GLONASS attitude determination with a common clock using a single difference approach. In: ION GPS 99 conference, Nashville, 14–17 Sept

Chapter 5
Application of Geo-image to Vehicle Navigation

Yibo Si, Fengjuan Wu and Lei Deng

Abstract Geo-image navigation is a new type of navigation. It's based on the geographical image as its main background data and the digital map as its supplemented background data. It provides users with intuitive, rich navigation background information, thereby enhancing the navigation visual effect. The paper shows the concept and characteristics of geo-image navigation. To improve the response speed, the organization of geo-image data in server–side of the dynamic application which relying on network is be studied. In order to improve the display efficiency, the data acquisition and display of the client are researched. The study can be ensuring real-time demand of navigation.

Keywords Geo-image · Vehicle navigation · Dynamic scenes expression

5.1 Geo-image Concept and Characteristics

Vehicle Navigation System utilizes map as data base. Vehicle positioning, navigation and search functions must be achieved by matching with the map. Currently, Vehicle Navigation System uses mostly a digital map, which is characterized by simple, small amount of data, but there are obvious shortcomings. First, traditional digital map navigation uses simple two dimensional point, line, plane to describe object, which is abstract and broad; however, its visual effect is relatively poor, monotonous, and boring. In addition, users will find it difficult to recognize the map with the actual environment. Second, due to long operating cycle and low efficiency, the traditional digital map is not able to meet the needs of the rapid development of the modern city. Compared to traditional GIS that relies

Y. Si (✉) · F. Wu · L. Deng
Beijing Satellite Navigation Center, Beijing, China
e-mail: siyibo@163.com

J. Sun et al. (eds.), *China Satellite Navigation Conference (CSNC) 2014 Proceedings: Volume I*, Lecture Notes in Electrical Engineering 303,
DOI: 10.1007/978-3-642-54737-9_5,

highly on two dimensional descriptions, Geo-image has the advantage of high practicality, and display the true geographical landscape. It is a huge technology innovation.

Geo-image navigation, based on geography image as main background data and digital map as assisted background data, is a new type of navigation. Navigation related geographic information search, path planning, navigation tips and other functions are operated in a scene of image background. The application of Geo-image is the trend of navigation technology. Geo-image navigation fully represents the advantages of image and vector, has a short update cycle and timeliness strong advantage, overthrows the traditional map navigation application, and brings a brand-new visual enjoyment.

5.2 Geo-image Dynamic Application Mode

Studying the trend and history of vehicle navigation system, the first generation products have been developed to the second, and is being rapidly transited to third [1]. Network based new navigation mode and the use of multi-layer structured "server and client" is an essential feature of the third generation of navigation system. The system consists of three parts: navigation data centre, user terminal and communication network. The navigation data centre is the "server" of the entire system which is responsible for the distribution and process of navigation information. With the support of current internet technology, it achieves navigation service such as management of navigation geographic data, distribution of information, and so on. The user terminal is the "client" that can download data from the "server" through live internet, so users are able to access live data and to receive various supports of the centre. The mobile communication network and etc. is the main transmission medium of navigation information. It provides communication service for the dynamic application, and acts as the channel of data transmission.

5.3 Navigation Data Storage at Server Terminal

In navigation applications, in order to improve system response speed, real-time and high-speed call and display need to manage the geo-image storage effectively by using multi-resolution image pyramid model and image blocking. The specific methods are: first, use Mercator projection to transform images; second, divide the transformed images equally; then, process the image data by using the hierarchical pyramid method. The whole process is shown in Fig. 5.1. Combined with the Multi-source remote sensing image data, it helps determine the data sources of multi-level gird image, as shown in Table 5.1.

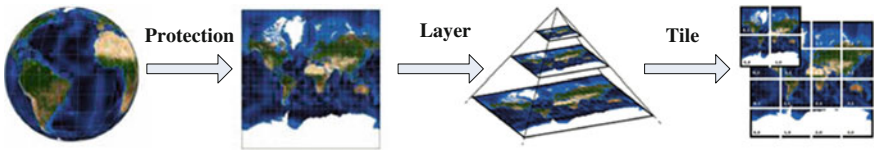

Fig. 5.1 Space divide process of Geo-image

Table 5.1 Multi-level grid tile resolution

Layer number	Width and height (pixel)	Tile resolution (m/pixel)	Map scale (take 96dpi for example)	Data sources
12th floor	1,048,576	38.2185	1:144,447.93	SPOT-4
13th floor	2,097,152	19.1093	1:72,223.96	SPOT-4
14th floor	4,194,304	9.5546	1:36,111.98	SPOT-5
15th floor	8,388,608	4.7773	1:18,055.99	SPOT-5
16th floor	16,777,216	2.3887	1:9,028.00	IKONOS
17th floor	33,554,432	1.1943	1:4,514.00	IKONOS
18th floor	67,108,864	0.5972	1:2,257.00	World view

Based on geographic divided area, Navigation Layer (12th to 18th layers) stores high-resolution image data in corresponding server group. It uses network topology structure to calculate the distance between nodes based on IP address and is able to select closer local data storage server, in order to avoid resource shortage or connection delay.

Index server is a "bridge" connected navigation geographic data server to user. When the user sends data requires to the index server (spatial query dimensions, the required resolution image layers or path planning result, etc.), the index server traversal tile four-tree-index, and build tile coding. Then, it retrieves result from Data Server IP Chart, and determines the address of the target server.

5.4 Navigation Data Acquisition Process

During navigation, users must interact with the server to obtain the required data. The process for requiring data is as follows: (1) users send a calculation request to the routing server (or via user terminal automatically); (2) based on the path planning results (or based on screen size to calculate required data tiles), users send a data "request" to the server; (3) index server locates the garget data server via "index" and sends a scheduling request to the target server; (4) data server reads the corresponding data and sends it directly to the user; (5) user now can "download" and display the data.

Table 5.2 Road classification

Road level	Description
Level 1	High grade roads (highways, national highways)
Level 2	Provincial roads
Level 3	Inter-county roads and city roads
Level 4	Passable roads (street roads)

5.4.1 The Adaptive Switching Strategy for Multi-resolution Images

Before sending requests to the server, users need to specify the resolution of image in which can meet the navigation requirements as well as to determine the spatial dimensions.

Elements of transportation are core geographic information in geo-image navigation. The navigation function must base on road information network. General design and production of digital navigation map should be set up according to requirements of different scales to finish cartographic layers and cartographic generalization. For example, intercity navigation map only need a smaller scale to include main city roads such as city, provincial, and national highways and other elements including main residential areas and road service facilities in which the roads pass through. However, for city navigation, a larger scale is needed to include detailed road network and POI information [2]. Corresponds to geo-image navigation, high-resolution images have unique advantages in areas with complex environments in which surroundings, intersections, or POI are examined meticulously. In less environmental complex areas, such as on highways where speed is relatively high and surrounding environment is less relevant, low resolution images can satisfy its navigation needs. In addition, switching resolution manually may distract the attention of the driver and thus affect safety.

The adaptive visualization operation of navigation information depends on the user's operation behaviors. These behaviors can be discriminated and described to extract a set of adaptive trigger conditions. By setting up the rules for switching, users can request images of different scales from the server automatically to achieve adaptive switching purposes [3]. The rules are as followings.

1. Roads are divided into four levels according to vehicle capacity, as shown in Table 5.2.
2. The scales and resolutions of navigation geographic data and images for each level are shown in Table 5.3.
3. Route is calculated via two-way search method [4]. Calculations are based on the distance between the place of departure and the destination, as shown in Table 5.4.

Table 5.3 Road level and navigation data layer

Road level	Vector map scale	Image LOD layer
Level 1	1:250,000	12
Level 2	1:100,000	13, 14
Level 3	1:25,000 (or 1:50,000)	15, 16
Level 4	1:10,000 (or 1:5,000)	17, 18

Table 5.4 Path planning results and road level

Distance (km)	Instructions	Road level
>500	Interprovincial	Level 1
100–500	General equal to a Provincial administrative area	Level 2
50–100	General equal to a city administrative area	Level 3
<50	General within the city	Level 4

4. When the place of departure and/or the destination are not in the computing layer, the computing layer will increase one layer by one layer until reaching the corresponding node. This node is used as a starting point to compute the nearest node in lower layer, and the cycle goes on until the calculation is completed.

5.4.2 Multi-scale Scenes Expression Strategy

To ensure the efficiency of the interactive response, it is necessary to reduce the amount of data involved in the processing of the scene to a minimum without affecting display quality of the scene details. It has been proved that organizing and scheduling scene data according to the rules of human visual cognition is an effective method. The organization and schedule of scene data are largely dependent on the organization of the scene detail levels and the schedule among data at all levels associated with the viewpoint.

During the navigation process, viewpoint of the user is usually used as the frame of reference. That is, when the user moves, the relative position of the viewpoint on the map remains unchanged and the map takes "incremental loading, dynamic delete" strategy for display. According to human visual habits, region close to the range of vision and consistent with the direction of the travel is of the most concern to the user, whereas the distant region does not require careful judgment. The three-dimensional perspective principle states that using the viewpoint as a starting point, the range of vision increases gradually toward the viewing direction and as objects become more distant they appear smaller and more virtual. Using this as a basis, the field of view can be divided by region to build realistic visual scenes, as shown in Fig. 5.2.

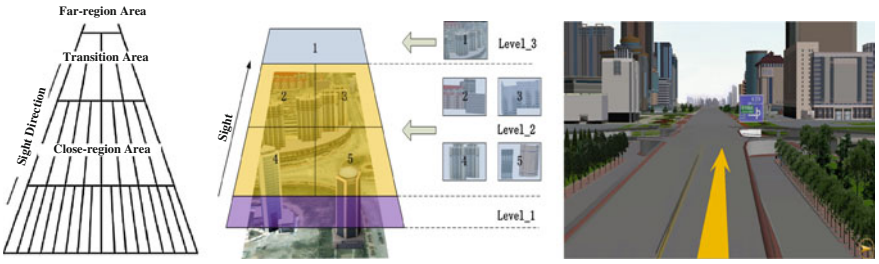

Fig. 5.2 3D scene zoning and visual effect

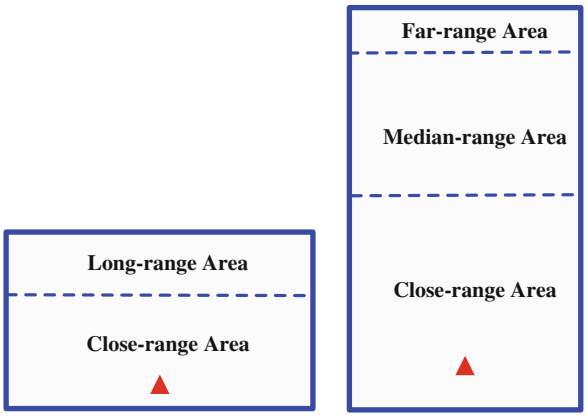

Fig. 5.3 User terminal display by regions

Drawing from three-dimensional multi-scale modeling, the user terminal can display by regions. Use the most commonly used navigation terminal, 400 × 800 resolution, as an example. As shown in Fig. 5.3, rectangles represent terminal devices and the arrows (approximately 1/6 on the screen) represent the locations of the user. The multi-scale scenes expression strategy refers to using a variety of image resolutions to reconstruct the scene within a single navigation scene. High-resolution images are used for close-range and low-resolution images are used for median- and long-range in order to decrease the amount of exchanged data and refresh frequency while increase visual effects at the same time. During navigation, refresh frequency for close-range images are higher than that for median- and long-range images, and the volume of downloaded data is smaller than using single-scale scene method.

In Fig. 5.4, a real navigation case is used to illustrate how the multi-scale scenes expression strategy works. Both horizontal and vertical screen display modes are shown. First, route planning belongs to level 4 roads. Single-scale scene method uses 18th navigation layer image to display across all regions. Using multi-scales scene method, navigation layer images decreases by two layers for each region displayed.

Table 5.5 Comparison: single-scale and multi-scales display

Scene scale	Screen mode	Number of data tiles	Data loaded (kB)	Display effect
Single-scale	Horizontal screen display	18th floor:8	112	Figure 5.5
	Vertical screen display	18th floor:8	111	Figure 5.6
Multi-scales	Horizontal screen display	18th floor:4 16th floor:3	71	Figure 5.7
	Vertical screen display	18th floor:4 16th floor:2 14th floor:2	77	Figure 5.8

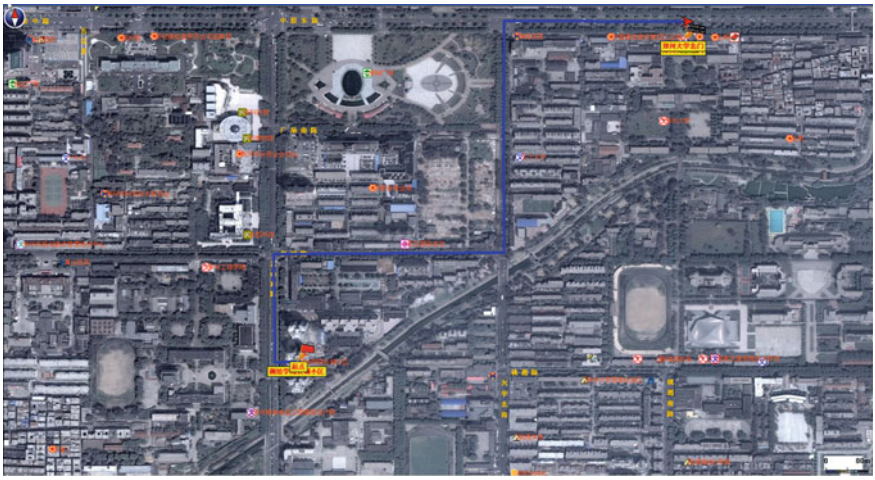

Fig. 5.4 A real Geo-image navigation case

Fig. 5.5 *Horizontal scene* data loaded and display of single-scale

Table 5.5 shows the comparison between single-scale scene method and multi-scales scene method of both horizontal and vertical screen display modes by required data blocks, amount of downloaded data, and display effects.

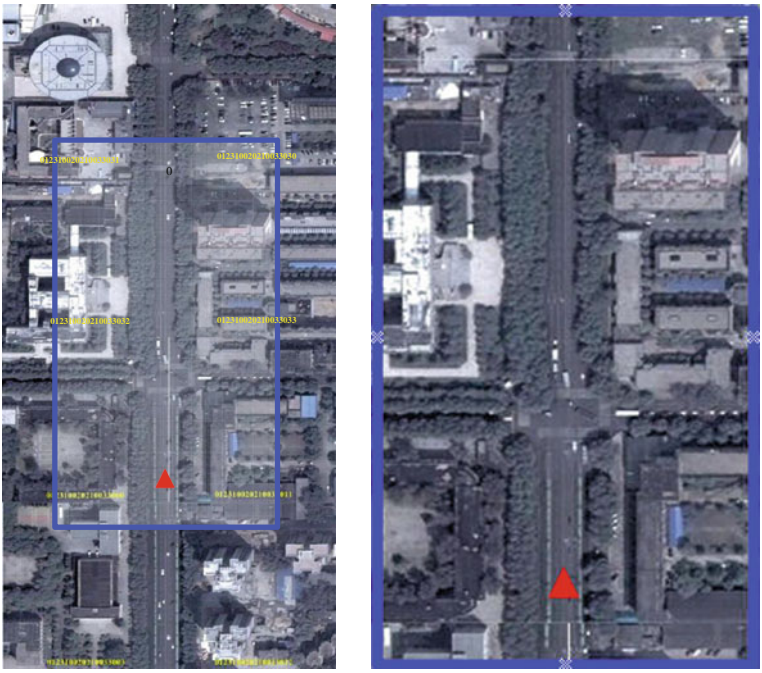

Fig. 5.6 *Vertical scene* data loaded and display of single-scale

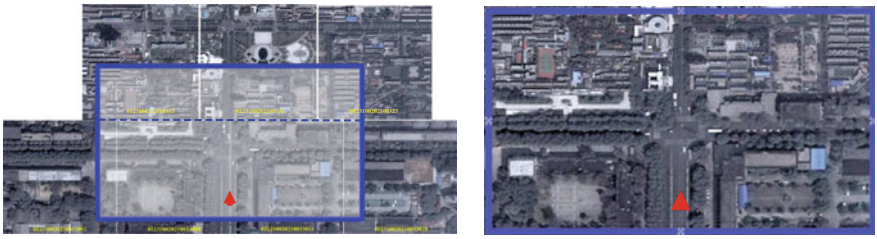

Fig. 5.7 *Horizontal scene* data loaded and display of multi-scales

The multi-scales scene expression strategy has higher display efficiency. A low-resolution tile contains a wider range. The amount of downloaded data is smaller than a full image of higher resolution because lower resolution images require a smaller amount of data than high-resolution images do. Moreover, the refresh frequency is relatively low and thus reduces the burden of display on the user's terminal. In terms of display effects, this strategy meets user's requirements that close-range images are displayed with higher visual quality than long-range images by presenting more distant objects smaller, which is more in line with human visual perception.

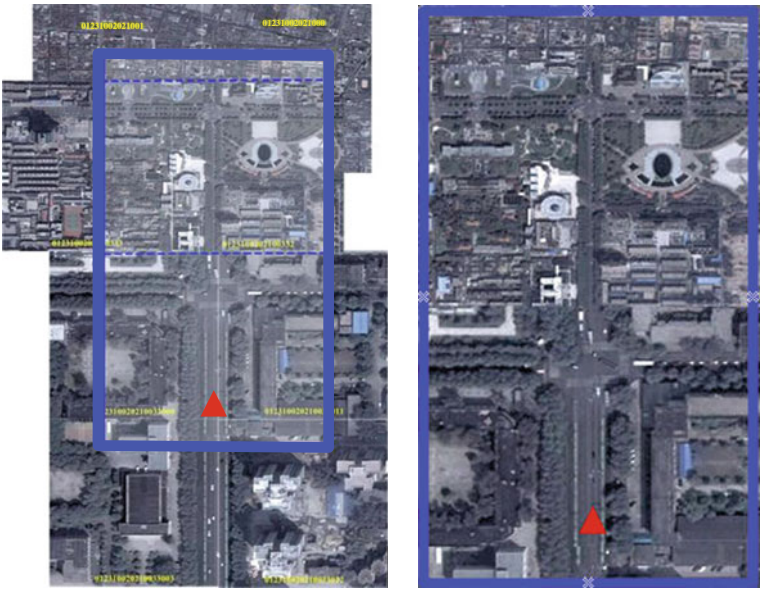

Fig. 5.8 *Vertical scene* data loaded and display of multi-scales

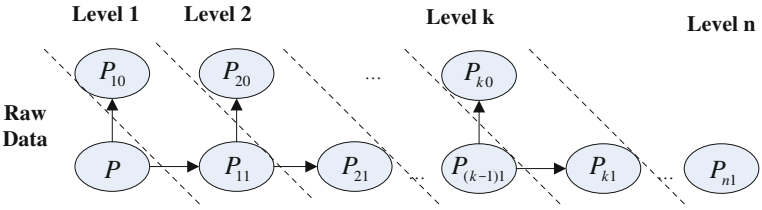

Fig. 5.9 Multi-resolution structure of Geo-image data based on binary-tree model

5.4.3 Progressive Transmission Strategy

Progressive transmission is a method in which the image profile data is transferred first before the details of the image are sent and data is decoding while transferring. This method overcomes diamonds effect due to transmission in line and high compression ratios that traditional image compression technology has. Images begin to decode and appear before data transfer is complete, and therefore improves the transmission efficiency and enhances system adaptability. It is particularly applicable to a wireless communication network environment.

Progressive transmission is based on multi-resolution image data organization of the binary tree model [5]. The model is shown in Fig. 5.9. First, organize multi-resolution image data according to the principle of resolution halved. That means, a level's resolution is a half of its parent level. That means, a level's resolution is a

Table 5.6 Example: progressive transmission based on binary-tree model

Transmission times	Transmission data (kB)	Display resolution (m)
1	2	16
2	2	8
3	4	4
4	8	2
5	16	1

Table 5.7 Transmission case on 16th floor image in some area

	No road buffer	Inside road buffer	Outside road buffer
Tile data	64	24	40
Amount (kB)	596	296	75

Note The image outside the road buffer is divided into two levels, and just transmit the 1st time's data, namely 1/4 initial data amount, the same as the resolution

half of its parent level. In this way, divide the image into N level parts according to the network transmit bandwidth. The lower bandwidth means the bigger N. After finishing the multi-resolution image data organization in level, the image can be composed in reverse combination. Namely, the k + 1 level's image data $P_{(k+1)0}$ and $P_{(k+1)1}$ can make the k level's image data P_{k1}. In this way, the whole image comes back to the initial state. Using the principle of half decreasing multi-scales scene method, navigation layer images decreases by two layers for each region displayed.

According to the request of the user, the data server searches the relative image tiles, make them into a binary tree model, and transmit progressively. The user terminal displays as soon as it received the data. This course is the reverse process of hierarchical organization of Multi-resolution image data and reduce the user's waiting time. Suppose that there is a piece of image tile with 1 m resolution which have a 32K amount of data. It will be transmitted by 5 times according to binary-tree model, Table 5.6 shows the amount of data transmitted and display resolution every time.

When network condition is not optimal (wireless signal or speed is smaller than certain thresholds), there are two application conditions of progressive transmission:

1. During navigation, roads and surround POI are of the main concern to the user, and objects in long-range are less of a concern. For example, on the border areas of city and countryside, many objects and features along the road require careful judgment and thus high-resolution images should be used. On the other hand, for farmland and scattered residential buildings in the far distance, contour information would be enough. Therefore, a buffer zone can be set up based on the typology and attributes of the roads. That is, using the road as a

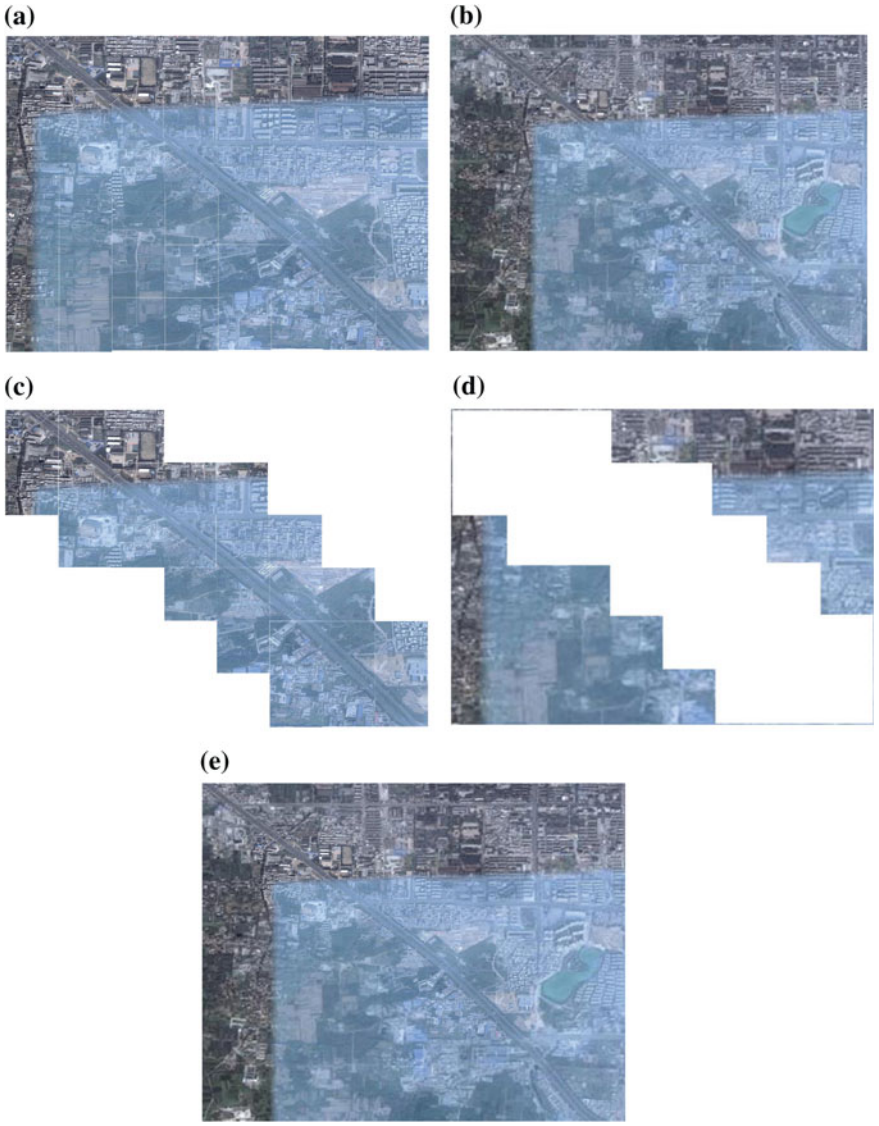

Fig. 5.10 Real application case: progressive transmission on road buffer zone. **a** Raw Geo-image mosaic of 16th floor. **b** Low-resolution Geo-image mosaic of 16th floor. **c** Raw Geo-image mosaic within the road buffer zone. **d** Low-resolution Geo-image (progressive transmission) mosaic outside the road buffer zone. **e** Geo-image mosaic of Client display

reference and expanding a certain range on both sides of the road as the buffer zone, high-resolution images are used within the buffer zone and low-resolution images are used outside the buffer zone. The vector information of image tiles is used to identify the priority: tiles belong to the buffer zone are transferred

with the desired resolution; tiles outside the buffer zone are transferred using the progressive transmission strategy. According to the network condition, only one or a few levels of resolution images are transferred.

A real case is illustrated to show how it works, as seen in Table 5.7 and Fig. 5.10.

As can be seen, the use of a buffer zone to categorize data transmission can effectively reduce the amount of data transferred while does not affect navigation quality.

2. When the tiles have the same priority, estimated transmission time for both progressive transmission and single tile (raw data) transmission will be calculated by the system (represented by T_1 and T_2). Progressive transmission is adopted first if $T_1 > T_2$. Under this method, if network transmission speed is relatively high, transmission may start from a certain level of resolution in the middle range rather than from the highest level.

References

1. Zhu S, Ma Y, Zhu B, Cao W (2008) The current situation and technical analysis of 3D navigation. J Geomatics Sci Technol 25(5):443–445
2. Zhang Y, Su X (2008) The key technologies and solution of in-vehicle digital navigation map. J Geomatics Sci Technol 25(4):267–270
3. Wang H, Ai T, Zhu G (2004) Adaptive strategy on the visualization of electronic map. Geomatics Inf Sci Wuhan Univ 29(6):525–528
4. Chen N, Gao Y (2002) Several technical problems on applications of digital map to vehicle navigation systems Geomatics Inf Sci Wuhan Univ 27(2):143–147
5. Li H, Zhu C, Chen J (2008) Progressive transmission technique of web-based massive image data with multi-resolution. Comput Eng 266–268

Chapter 6
A Correlate-Based GPS Multipath Time Delay Estimation Algorithm

Jian Li, Wenyi Wang, Dan Lu, Lu Wang and Renbiao Wu

Abstract Multipath effect of signals is one of the main causes of the global positioning system positioning error. Although the differential technology can improve the positioning accuracy of navigation system. However, due to the reference station and the user's geographical location is different; Differential GPS (DGPS) system still does not eliminate multipath effects of the satellite signal. The conventional narrow correlator method can reduce positioning error. But it assumes that the bandwidth of channel is unlimited. It can not be met in practice. That is its limitations. In this paper, we consider the characteristics of GPS signal model and the multipath effect In GPS system. We introduce a least-squares iterative multipath super-resolution (LIMS) delay estimation algorithm and propose a multipath signal delay estimation algorithm based on correlation model on this basis. The algorithm takes the correlation output of received signal correlates and the local C/A code as the model, estimates the direct signal and the multipath signal delay accurately in the condition of signal delay is unknown. As can be seen from the simulation results, the multipath interference suppression algorithm we propose outperforms the traditional narrow correlator method and LIMS algorithms.

Keywords Global Positioning System · Multipath effect · Time delay estimate

6.1 Introduction

Navigation satellite system is a star base radio navigation system which takes satellites as a beacon, can provide all-weather, high precision of 3D position, velocity and time information. So that it makes safe and convenient for the global

J. Li (✉) · W. Wang · D. Lu · L. Wang · R. Wu
Tianjin Key Lab for Advanced Signal Processing, Civil Aviation University of China, Tianjin, China
e-mail: mpirecauc@sina.com

J. Sun et al. (eds.), *China Satellite Navigation Conference (CSNC) 2014 Proceedings: Volume I*, Lecture Notes in Electrical Engineering 303,
DOI: 10.1007/978-3-642-54737-9_6,

land, sea, air and other kinds of military and civilian users. American spent heavily to build and maintain the Global Positioning System (Global Positioning System, GPS). GLONASS was developed by Russian Global Navigation Satellite System (Global Navigation Satellite System, GLONASS). Chinese Beidou Satellite Navigation System (Beidou Navigation Satellite System). Europe's Galileo Positioning System (Galileo Positioning System, Galileo) plan. Japan decided to develop a quasi zenith Satellite System (QZSS) and India had the approval of India regional Navigation Satellite System (IRNSS) major projects. Above examples show that Satellite Navigation and Positioning System Occupies the important position in the field of military or civil [1, 2].

Now the GPS chip was already embedded in the cell phone to realize the positioning function. China's Beidou satellite navigation system played an indelible role in the rescues of WenChuan earthquake because of its peculiar characteristics of short message. Therefore, Satellite navigation has been an indispensable part of daily life. However, the positioning systems above, will suffer all kinds of interference from the outside world inevitably, which affect their positioning accuracy. The most significant is the multipath interference. As we know that multipath effect takes most part in the global positioning system (GPS) precision positioning error. The multipath effect is caused by the multipath transmission of satellite signal, that is to say, the receiver antenna received more than just the direct signal and all kinds of medium around once or multiple reflected signals. The reflection signals interfere the direct signal, which makes the observation value deviates from the true value, thus the interference caused time delay effect [3].

The multipath suppression methods commonly are used by changing the receiving antenna and data processing. The method based on antenna can inhibit the multipath signals come from the ground, but it can't work for multipath signals from the top of the antenna. Signal processing methods often have two kinds, one kind is the most common is narrow correlator technology, but narrow correlator method assumes that the channel wireless wide, however, it can not meet in practice [4, 5]. The second way is multipath estimation methods, that is, to detect the multipath signal and estimate the parameters of each multipath signal components. We are mainly interested in signal time delay estimation generally, then according to the parameters of multipath which are estimated, to fix the received composite signal and restore the direct signal. The main methods are the least squares estimation, maximum likelihood estimation and Bayes estimation methods [6–9]. In this paper, we introduce a kind of multipath time delay estimation method and put forward a new method on the basis of it. The main idea of new method is to circular relate the received signal and the local C/A code, then use signal separation method to estimate the interested signal time delay.

6.2 System Model

In order to analyze conveniently, this paper consider using a single reflection path, when there are multiple paths, this method works similarly. When there is only a multipath signals for receiver. We can get

$$y(t) = \sum_{p=1}^{2} \alpha_p c(t-\tau_p) d(t-\tau_p) e^{j\omega_p (t-\tau_p)} + e(t) \tag{6.1}$$

Among them, $d(t)$ is the navigation message, the value is ± 1 in satellite navigation, $c(t)$ is C/A code of satellite signal, $e(t)$ is receiver thermal noise. α_1, τ_1, ω_1 is direct signal amplitude, time delay and frequency respectively. α_2, τ_2, ω_2 is the multipath signal amplitude, time delay and frequency. In convenience of analysis, we regardless of the navigation message, and assume that the frequency of direct signal and multipath signals are equal, both are ω_d. Then the received signal is

$$y(t) = \sum_{p=1}^{2} \alpha_p c(t-\tau_p) e^{i\omega_d (t-\tau_p)} + e(t) \tag{6.2}$$

First, make circular correlation between $c(t)$ and $y(t)$, and samples the related results in $\{0, T_s, \ldots, (N-1)T_s\}$, so that, we can get

$$p(n) = \sum_{p=1}^{2} \alpha_p r(nT_s - \tau_p) + w(n) \tag{6.3}$$

Among them, N are the sample points, and T_s is sample interval.

$$\mathrm{r}(\tau) = \begin{cases} \dfrac{\tau}{T_c}, -T_c < \tau \le 0, \\ \dfrac{-\tau}{T_c}, 0 < \tau \le T_c \\ 0, \text{其他} \end{cases} \quad 6.4$$

$$w(\varsigma) = \frac{1}{T_i} \int_0^{T_i} e(t) c^*(t-\varsigma) dt \tag{6.5}$$

$r(\tau)$ is auto correlation function of C/A code, T_c is the period of C/A code. $w(n)$ is the output of the related samples between $e(t)$ and $c(t)$. T_i is the integration time.

6.3 Multipath Signal Suppression

6.3.1 LIMS Multipath Estimation Method

The main idea of LIMS (Least-Square-Based Iterative Multipath Super-Resolution Technique) algorithm [10] is to consider the autocorrelation function of GPS C/A code is the triangle. So we can use C/A code autocorrelation function to fit the real correlation function. Then we will get the amplitude and time delay estimation. Nonlinear least squares cost function of LIMS algorithm is written as

$$\begin{aligned}\{\boldsymbol{\alpha}, \mathbf{t}\} &= \arg\min_{\alpha,t} ||\mathbf{Gp} - \mathbf{GA}(\mathbf{t})\boldsymbol{\alpha}||^2 \\ &= \arg\min_{\alpha,\mathbf{t}} ||\mathbf{Gp} - \mathbf{G}(\mathbf{B}(\boldsymbol{\alpha}, \mathbf{t})\mathbf{t} + \mathbf{b}(\boldsymbol{\alpha}, \mathbf{t}))||^2\end{aligned} \tag{6.6}$$

where, $\mathbf{G}$ is a nonsingular albino noise matrix. $\mathbf{G} = \mathbf{C}^{-\frac{1}{2}}$, $\mathbf{C}$ is the covariance matrix of the noise vector.

$$[\mathbf{C}]_{k,j} = \frac{T_i}{N_0} E\left\{w_{k-1} w_{j-1}^*\right\} = r((k-j)T_s) \tag{6.7a}$$

$$\begin{aligned}&(1 \le k, j \le \mathrm{N}) \\ &[\mathbf{A}(\mathbf{t})]_{n+1,m+1} = r(nT_s - t_m)\end{aligned} \tag{6.7b}$$

$$[\mathbf{B}(\boldsymbol{\alpha},\mathbf{t})]_{n+1,m+1} = \begin{cases} \dfrac{-\alpha_m}{T_c}, & \dfrac{t_m - T_c}{T_s} < n < \dfrac{t_m}{T_s} \\ \dfrac{\alpha_m}{T_c}, & \dfrac{t_m}{T_s} < n < \dfrac{t_m + T_c}{T_s} \\ 0, & \text{其他} \end{cases} \tag{6.7c}$$

$$\mathbf{b}(\mathbf{a}, \mathbf{t}) = \sum_{m=0}^{M-1} \mathbf{b}(\alpha_m, t_m) \tag{6.7d}$$

$$[\mathbf{b}(\alpha_m, t_m)]_{n+1} = \begin{cases} \alpha_m \cdot (1 + \dfrac{nT_s}{T_c}), & \dfrac{t_m - T_c}{T_s} < n < \dfrac{t_m}{T_s} \\ \alpha_m \cdot (1 - \dfrac{nT_s}{T_c}), & \dfrac{t_m}{T_s} < n < \dfrac{t_m + T_c}{T_s} \\ 0, & \text{其他} \end{cases} \tag{6.7e}$$

where, p is correlator output sampled at N lags {0, Ts,…, (N − 1)Ts}. m is the number of the signals. $\boldsymbol{\alpha} = [\alpha_0, \ldots, \alpha_{M-1}]^T$, $\mathbf{t} = [[t_0, \ldots, t_{M-1}]^T$, is the signal amplitude and delay which is ready for estimation respectively.

The first formula of (6.6) is a least squares cost function about α. When α is known and $\mathbf{B}(\boldsymbol{\alpha}, \mathbf{t})$ and $\mathbf{b}(\boldsymbol{\alpha}, \mathbf{t})$ can be seen as the approximate constant in a small time period, so that the second formula of (6.6) the is a least squares cost function about t. To solve the two least squares cost function and get the iterative equation obtained by using the gradient descent method.

$$\boldsymbol{\alpha}_m = \boldsymbol{\alpha}_{m-1} + \gamma \hat{\mathbf{A}}(\mathbf{t}_{m-1}) \cdot \left(\hat{\mathbf{p}} - \hat{\mathbf{A}}(\mathbf{t}_{m-1}) \boldsymbol{\alpha}_{m-1} \right) \tag{6.8}$$

$$\mathbf{t}_m = \mathbf{t}_{m-1} + \beta \cdot real\left\{ \hat{\mathbf{B}}^H(\boldsymbol{\alpha}_m, \mathbf{t}_{m-1}) \cdot \left(\hat{\mathbf{p}} - \hat{\mathbf{A}}(\mathbf{t}_{m-1}) \boldsymbol{\alpha}_m \right) \right\} \tag{6.9}$$

$\hat{\mathbf{A}}(\mathbf{t}) = \mathbf{GA}(\mathbf{t})$, $\hat{\mathbf{p}} = \mathbf{Gp}$, $\hat{\mathbf{B}}(\alpha, \mathbf{t}) = \mathbf{GB}(\alpha, \mathbf{t})$. γ, β is step size of the two equation respectively. $real(\cdot)$ is to get the real part of the vector. We can get the estimation value of amplitude $\hat{\boldsymbol{\alpha}}_m$ and time delay $\hat{\mathbf{t}}_m$.

6.3.2 Correlate-Based Multipath Signal Estimation Algorithm

LIMS algorithm considers that the GPS C/A code of autocorrelation function is the triangle shape. So we can use it to fitting the real correlation function, and finally estimate the time delay and amplitude through the two least squares cost function. The downside of this approach is that the initial value of the demand is stricter. At the same time the two iteration steps are hard to choose so that the time delay estimation accuracy is not very high. The new multipath estimation algorithm mentioned below can estimate the amplitude and latency of the direct signal and multipath signal one-time. And the resulting estimate error will be smaller than the LIMS algorithm.

We can be seen from expression (6.3), the correlate output includes time delay and amplitude information. So we can consider using this correlate model to get the time delay and amplitude estimation through the adoption of WRELAX method. The specific process is as follow.

Using the discrete Fourier transform to the expression (6.3) correlate output can be obtained

$$P(k) = R(k) \sum_{p=1}^{2} \alpha_p e^{j\omega_p k} + W(k) \tag{6.10}$$

Among them, $P(k)$, $R(k)$ and $W(k)$ are the result of the discrete Fourier transform of $p(n)$, $R(n)$ and $w(n)$ respectively. $\omega_p = -2\pi\tau_p / NT_s$, T_s is the sampling frequency. So we can get the nonlinear least squares cost function of the time delay estimation and the amplitude estimation.

$$C_1\left(\{\hat{\omega}_p, \hat{\alpha}_p\}_{p=1}^2\right) = \sum_{k=-N/2}^{N/2} \left\| P(k) - R(k) \sum_{p=1}^{2} \alpha_p e^{jw_p k} \right\|^2 \tag{6.11}$$

By minimizing the cost function $C_1(\{\hat{\omega}_p, \hat{\alpha}_p\})$ can obtain the unknown parameters estimation. But for the unknown parameters $\{\hat{\omega}_p, \hat{\alpha}_p\}$, the cost function is a nonlinear least squares. Here we use WRELAX method to obtain the parameter estimation.

$$\mathbf{a}(\omega_p) = \left[e^{j\omega_p(-N/2)}, e^{j\omega_p(-N/2+1)}, \ldots, e^{j\omega_p(N/2-1)}\right]^T \tag{6.12}$$

$$\mathbf{P} = [P(-N/2), P(-N/2+1), \ldots, P(N/2-1)]^T \tag{6.13}$$

$$\mathbf{R} = diag\{R(-N/2), R(-N/2+1), \ldots, R(N/2-1)\} \tag{6.14}$$

So the cost function above can be converted to

$$C_1\left(\{\hat{\omega}_p, \hat{\alpha}_p\}_{p=1}^2\right) = \sum_{k=-N/2}^{N/2} \left\| \mathbf{P} - \sum_{p=1}^{2} \alpha_p \mathbf{R}\mathbf{a}(\omega_p) \right\|^2 \tag{6.15}$$

We assume that $\{\hat{\omega}_q, \hat{\alpha}_q\}_{q=1,q\neq p}^2$ has been estimated, so we can get

$$\mathbf{P}_p = \mathbf{P} - \sum_{\substack{q=1 \\ q\neq p}}^{2} \alpha_q [\mathbf{R}\mathbf{a}(\omega_p)] \tag{6.16}$$

Use (6.16) into the cost function, and can get

$$C_2\left(\{\hat{\omega}_p, \hat{\alpha}_p\}_{p=1}^2\right) = \sum_{k=-N/2}^{N/2} \left\| \mathbf{P}_p - \alpha_p \mathbf{R}\mathbf{a}(\omega_p) \right\|^2 \tag{6.17}$$

And minimize the cost function C_2 and the estimated value of the $\hat{\omega}_p$ and $\hat{\alpha}_p$ respectively.

$$\hat{\omega}_p = \arg\max_{\omega_p} \left| \mathbf{a}^H(\omega_p) \mathbf{R}^* \mathbf{P}_p \right|^2 \tag{6.18}$$

$$\hat{\alpha}_p = \left. \frac{\left| \mathbf{a}^H(\omega_p) \mathbf{R}^* \mathbf{P}_p \right|}{\|\mathbf{R}\|_F^2} \right|_{\omega_p = \hat{\omega}_p} \tag{6.19}$$

where $(\cdot)^{\mathrm{H}}$ stands conjugate transpose, and $(\cdot)^{*}$ stands the complex conjugate norm and $\|\cdot\|_F$ stands Frobenius norm.

The step of amplitude and time delay estimation $\{\hat{\omega}_p, \hat{\alpha}_p\}_{p=1}^{2}$ as follow:

Step 1: We assume there is diameter signal only that is to say $p = 1$. Then and calculate (**R** * **P**) according the expression (6.18), then find maximum position of the result of fast Fourier transform (FFT), so that we can get a rough idea of time delay estimation. And we use MATLAB fminbnd function to make a coarse search for this rough time delay in a certain range and get more accurate time delay estimation. FFT points can be as an integer power of 2 through zero padding. And estimate $\{\hat{\omega}_p, \hat{\alpha}_p\}_{p=1}^{2}$ through the expression (6.18), (6.19).

Step 2: We suppose there are two signals, use the $\{\hat{\omega}_1, \hat{\alpha}_1\}$ and **R** get from step one and minus the first signal according to the type (6.16), then get the second signal $\mathbf{P}_2$. Then using $\mathbf{P}_2$ and **R** can get the second signal estimation value $\{\hat{\omega}_2, \hat{\alpha}_2\}$. Then recycling and using $\{\hat{\omega}_2, \hat{\alpha}_2\}$ and **R** according to type (6.16) minus the second signal to estimate $\mathbf{P}_1$ again. Then estimate $\{\hat{\omega}_1, \hat{\alpha}_1\}$again and again by using $\mathbf{P}_1$ and **R**. Repeat the process until the convergence, so that you can calculate the estimate value $\{\hat{\omega}_p, \hat{\alpha}_p\}_{p=1}^{2}$. With type $\omega_p = -2\pi\tau_p/NT_s$ we can work out the signal time delay estimation $\hat{\tau}_p$.

6.4 Numerical Results

Using GPS simulator generates a direct signal of satellite and a multipath signal, sampling frequency is 20 MHz, intermediate frequency is 1.25 MHz, DLL loop noise bandwidth is 2 MHz. Signal-to-noise ratio SNR range for −24 to −16 dB. Then we compare conventional wide relevant methods, the traditional narrow-band algorithms, LIMS time delay estimation algorithm and this paper algorithm about the time delay estimation error.

When multipath signals relative to the direct signal delay is 700 ns, which were about 0.7chip, the multipath signal amplitude attenuation is 0.3 times that of the direct signal. The direct signal time delay estimation error as the change of signal-to-noise ratio SNR curve by using LIMS estimation algorithm this paper promoted estimation algorithm, the traditional narrow-band relevant methods (spacing d = 0.1chip) and conventional wide relevant methods (spacing d = 1chip). As shown in Fig. 6.1, it can be seen that with the increase of signal-to-noise ratio SNR, the time delay estimation error of four algorithms tend to decrease. So we can prove that reducing the correlator spacing method can improve the estimation error, suppress the influence of multipath signal. And the algorithm in this paper is obviously better than the LIMS time delay estimate algorithm and traditional

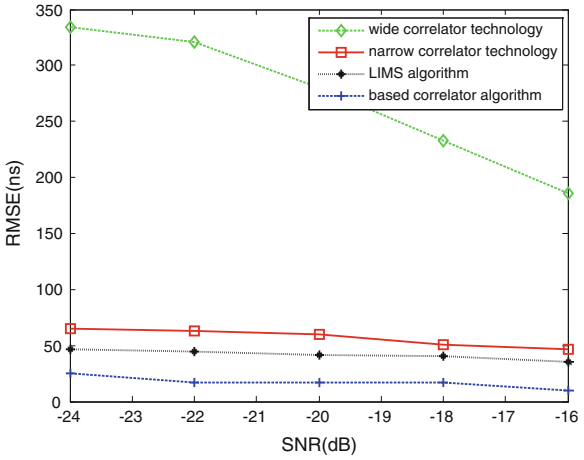

Fig. 6.1 Time delay estimation error with signal to noise ratio (*SNR*)

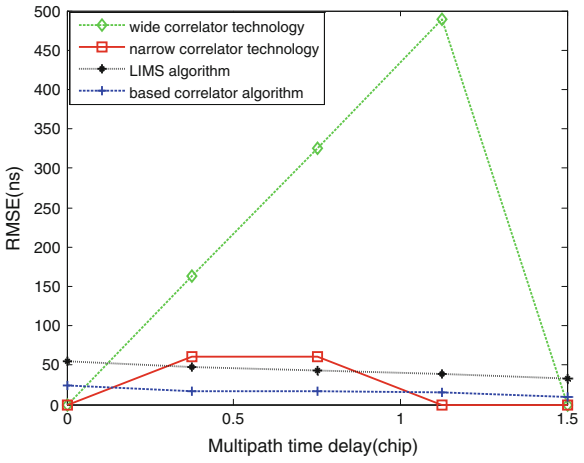

Fig. 6.2 Time delay estimation error with the relative delay

narrow-band related algorithm on the estimation error. So it demonstrates that the algorithm in this paper has a better multipath suppression performance.

When signal-to-noise ratio SNR $= -20$ dB, as shown in Fig. 6.2, the multipath signals relative time delay are in different situations. Conventional wide relevant method (spacing d $=$ 1chip), narrow band correlation method (spacing d $=$ 0.1chip), LIMS time delay estimation algorithm and the algorithm in this paper on time delay estimation error. We also can be seen from the picture that the narrow correlator can inhibit multipath within a certain range, reduce the multipath time delay error. Based on the related characteristics of the pseudo random code, if the times delay of multipath signal relatives to the direct signal beyond the time of a chip, as long as the direct signal locked by phase-locked loop and irrelevant with the local code, multipath effect can be ignored. So the multipath effect on the

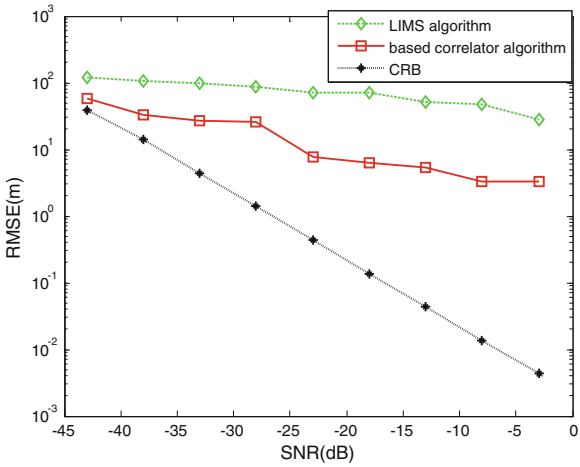

Fig. 6.3 Different algorithms and compared the CRB

receiver mainly in a chip. We can be seen from Fig. 6.2, when the multipath delay in 0.1–1chip, the algorithm in this paper is better than LIMS time delay estimation algorithm and narrowband related algorithm and has a small signal time delay estimation error. It can estimate the direct signal delay more accurately, so as to reduce the influence of the multipath signal to a receiver positioning error.

Figure 6.3 shows in a larger range of signal-to-noise ratio, the comparison of the LIMS time delay estimation algorithm, the algorithm in this paper and the CRB industry. The CRB is unbiased estimation of lower bound, can be used as a standard which can decide the performance of a estimation algorithm is good or not. We can see by the picture, the algorithm in this paper compared with LIMS time delay estimation algorithm is more close to the CRB, that is to say it has the better estimation performance. But the deficiency is that the algorithm still has a certain distance estimation error against the CRB, we still need to continue to improve the accuracy of estimation, and this will be done at the next step [11].

6.5 Conclusion

According to the characteristics of the GPS multipath signal model, analyzes the LIMS time delay algorithm and its performance and puts forward a new algorithm based on the related multipath signal model. It relates the received signal and the local produce C/A code signal through the receiver, and then we can get the direct signal time delay estimation by the mind of signal separation estimated. Seen from the simulation results in this paper, the algorithm in this paper is superior to the LIMS and narrowband related algorithm on the multipath suppression performances.

References

1. Xie G (2009) GPS principle and the design of receiver. Electronic industry press, Beijing
2. Bian S, Li W (2005) An introduction to a satellite navigation system. Electronic industry press, Beijing
3. Xia L (2001) The multipath effect in GPS observation theory research and numerical results. Wuhan University
4. Li J, Wu RB (1998) An efficient algorithm for time delay estimation. IEEE Trans Signal Process 46(8):2231–2235
5. LI J, Wu R (2011) The GPS multipath suppression algorithm based on signal estimation theory. Signal Process 27(12)
6. Liu H, Xu X, Wang X (2005) Multipath signal pn code in spread spectrum ranging system tracking error analysis and elimination of technology. Glob Positioning Syst 30(6):34–38
7. Parada ER, Chastellain F, Botteronetal C (2009) Design of a GPS and Galileo multi-frequency front-end. In: IEEE 69th vehicular technology conference, Barcelona, Spain, pp 1–5
8. Cote FD, Psaromiligkos IN, Gross WJ (2011) GNSS modulation: a unified statistical description. IEEE Trans Aerosp Electron Syst 47(3):1814–1836
9. GPS Navstar Global Positioning System (1995) Interface control document. Revision C, Navstar
10. Nam W, Kong SH (2013) Least-squares-based iterative multipath super-resolution technique. IEEE Trans Signal Process 519–529
11. Li Y (2009) Weak multipath signal time delay estimation technology research. Huazhong university of science and technology, Wuhan

Chapter 7
Based on BeiDou (COMPASS) Build the Environmental Protection Services System of Hainan Marine Fisheries Production Safety

Yubo Lv, Jianfeng Xu, Linhao Xu and Chengye Qi

Abstract Integrating of existing Hainan Province vessels dynamic management information system, to build the environmental protection services system of Hainan marine fisheries production safety, making direct services to all types of marine fishery production safety environment thematic services and products, through the BeiDou system sends real-time to the majority of maritime operations fishing boats and fishermen in the hands, enhancing the overall security environment marine fisheries production support capabilities. The system uses technologies of BeiDou, GIS, network communications, etc., to achieve the dynamic vessels monitoring, producing marine forecast and warning products, forecast and warning message intelligent publishing, initiative to provide accurate early warning for the marine fisheries production safety management, which can effectively reduce marine disasters caused personnel and property damage.

Keywords Marine fisheries · Safety manufacture · COMPASS · Forecast and warning · Environmental protection

Y. Lv
Ocean Monitoring and Forecasting Center of Hainan Province, Haikou, China
e-mail: lvyubohappy@126.com

J. Xu
Department of Ocean and Fisheries of Hainan Province, Haikou, China
e-mail: xujianfenghappy@126.com

L. Xu · C. Qi (✉)
BDStar Information Service Co., Ltd, Beijing, China
e-mail: chyqi@navchina.com

J. Sun et al. (eds.), *China Satellite Navigation Conference (CSNC) 2014 Proceedings: Volume I*, Lecture Notes in Electrical Engineering 303,
DOI: 10.1007/978-3-642-54737-9_7,

7.1 Demand of the Environmental Protection Services System of Hainan Marine Fisheries Production Safety

Our country is a Marine power, Marine fishery occupies an important position in the Marine economy of our country. According to incomplete statistics, there were all kinds of marine fishing vessels of about 310,000, more than 1,000 various types of fishing ports, aquaculture area of over 1,500 ha, more than 800 million people engaged in fishing. Statistics show that in 2011 the total marine production in Hainan Province reached 612 billion yuan, accounting for 27 % of the province's GDP, fishery economic output, value added amounted to 29.5 billion yuan and 18 billion yuan, marine and fisheries economy has become an important pillar of the national economy in Hainan Province.

Marine fisheries production safety is related to the vital interests of the fishermen, and is also highly concerned about the levels of government. After years of construction, Hainan has now set up a dynamic management information system, which covers the province's 6000 medium-sized ocean vessels, realized the Marine fishery ship dynamic monitoring and comprehensive management of Hainan province provide effective guarantee for safe production of fishery and play an important role in fishing boat shelter, emergency, command scheduling.

National marine sector plays an important role in the marine environment observation forecast and marine disaster warning released, the majority of fishermen and fishing are important clients marine warning newspaper work [1]. Aim at the south sea fisheries Forecast and warning failed to business, not unified and not timely forecast source, how will the Marine department station reported Forecast and warning content integration into the existing fishing vessel dynamic management information system, the active for Marine fisheries production safety management to provide accurate warning, is of great significance to reduce disaster losses.

7.2 System Construction Goal

The environmental protection services system of Hainan marine fisheries production safety is the national Marine fisheries production safety environmental protection service system of provincial node system, is a important component.

The environmental protection services system of National marine fisheries production safety construction goal is to build the country, the sea area and the provincial level three-fies system, fusing the Marine station reported Forecast and warning information that is closely related to fisheries production safety, to implement the dynamic monitoring of fishing boat fishing port and aquaculture area, Marine environmental protection services, auxiliary decision-making functions for Marine fishery production, to improve our country's Marine fishery environment comprehensive guarantee ability, effectively reduce the economic

loss and casualties in Marine fishery production, promote the healthy development of China's Marine fishery production [1].

The environmental protection services system of Hainan marine fisheries production safety to ensure the safety of fishery production oriented, with Marine forecasting service in fishery production as the main line, real-time positioning by fishing boats, Marine project station reported Forecast and warning, communication network technology integration, building the environmental protection services system of Hainan marine fisheries production safety that can cover Hainan key fishing waters [2]. This system integration has built Hainan sea fishing vessel dynamic management information system, based on existing Marine environmental forecasting expand and deepen the service, and fishermen fishing areas and fishing ports to make direct services in the fisheries production safety of the Marine environment project service products, in real time to the sea fishing boats and fishermen, improve environmental protection to the safety of fishery production ability.

7.3 System Architecture Design

The environmental protection services system of national marine fisheries production safety adopts the country, area, the provincial level three-fies system of the network structure design, connection between nodes at all levels (Fig. 7.1) [1].

Environmental protection services system of Hainan marine fisheries production safety join hands with has been built in Hainan province of Marine fishing vessel dynamic management information system, this system can be made of fine station reported an alert products sent to the fishing boat through the BeiDou system, realized the ocean station reported an alert products can truly for the purpose of service for fishermen. System works such as Fig. 7.2.

System design divided into multiple function relatively single software modules, each do its independent task, through the message, network, file to data exchange, to access and upload ship static data, dynamic position data, station reported Forecast and warning product, to production and upload station reported warning products. System composition such as Fig. 7.3.

7.4 The Main Construction Contents

7.4.1 Marine Forecast and Warning Products Produced and Pushed

Marine forecast and warning products produced module is based on GIS visualization technology, realizing fine mesh wind, wave and other marine forecast and warning products of Hainan's coastal waters produced, and through standard

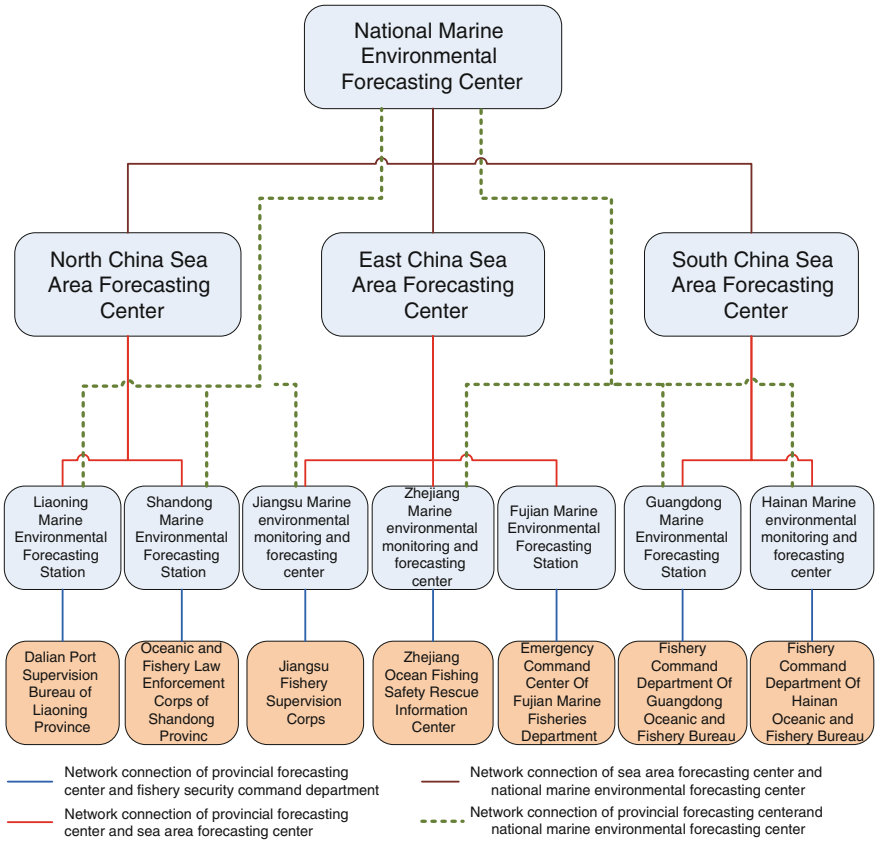

Fig. 7.1 The country, the sea area and the provincial three level system network structure

interface of network transmissing software, upload it to the National Marine Environmental Forecasting Center, South China Sea Forecasting Center, sharing resources of forecast and warning product data.

7.4.1.1 Data Acquisition

Producing of fine mesh wind, wave and other marine forecast and warning products of Hainan's coastal waters, is based on the large surface products issued by the National Marine Environmental Forecasting Center, and the fishery products issued by the South China Sea Forecasting Center, release these two products at the same time every day, then via the storage middleware and file transfer software, finally, the data stored in the database of this systems. Warning Production and Releasement module via proxy module can be automatically or manually downloaded products to the local. Large surface forecast and warning

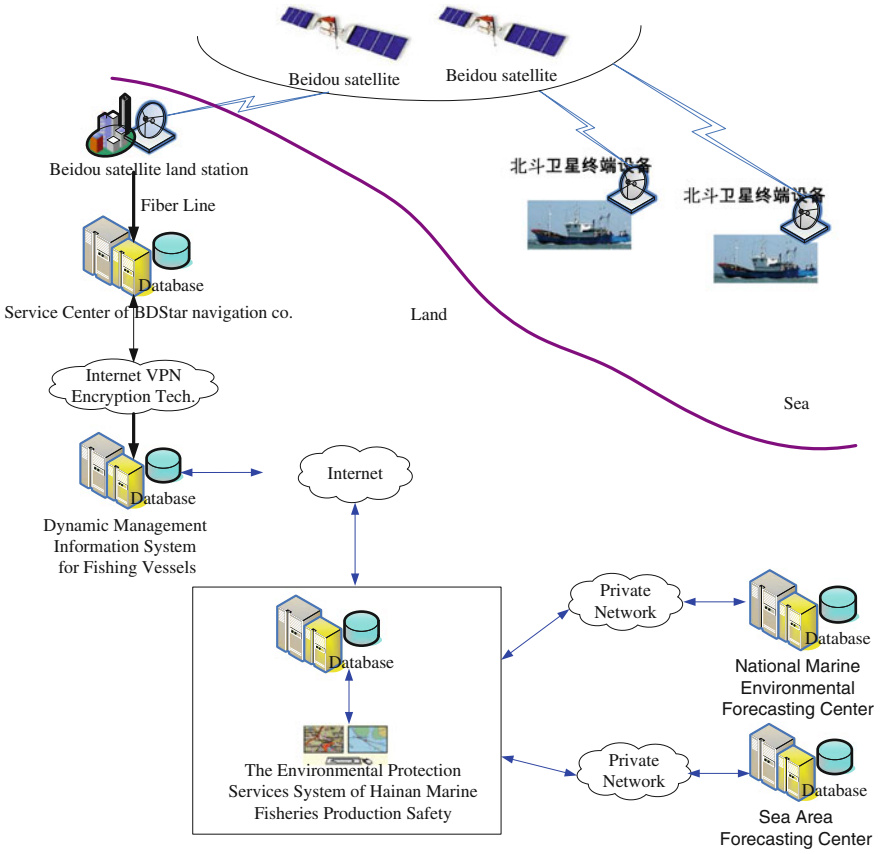

Fig. 7.2 The working principle of the system

products use SHAPE file formats, for easy handling, fishery forecast and warning products converted to XML file formats. The process as shown in Fig. 7.4.

7.4.1.2 Fine Wind and Wave Warning Products Production

System implements two ways of forecasting and warning products production: split sea area product mode and hand-painted mode. First mode is based on the fishery products issued by South China Sea forecasting Center, split it and create initial fishery forecasting and warning product of Hainan Province, then make manual adjustments to produce a final fishery forecasting and warning product; Hand-painted mode is drawing levels contour of the waves height or surface wind power on GIS charts, through the exact algorithm to calculate the wave height or wind power of each fishery, generating Hainan fishery forecast and warning products.

The effect of Hand-painted mode such as shown in Fig. 7.5.

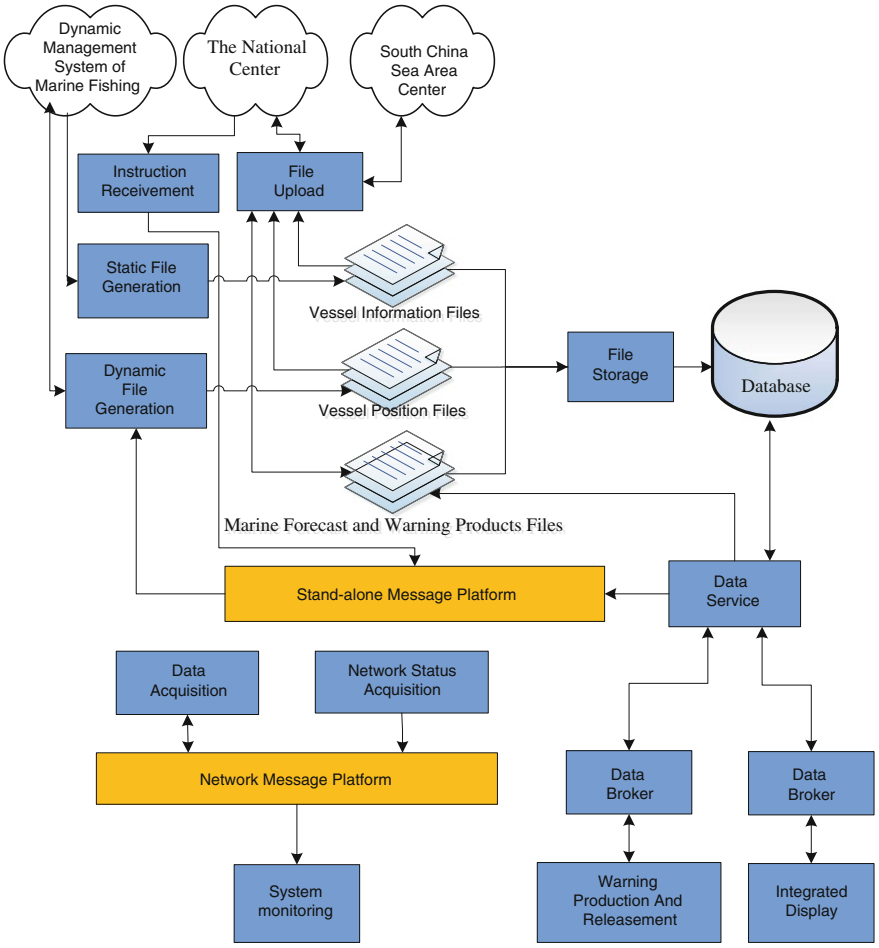

Fig. 7.3 The system composition diagram

7.4.1.3 Forecast and Warning Products's Publishing and Transferring

The forecast and warning products produced by this system stored in the form of EXCEL file and upload it to the server, the file preprocessing module package and make three copies, one for file storage program for its parsed into the library, the other two are uploaded to the National Center and the South China Sea Area Center by the data transfer middleware, with processes as shown in Fig. 7.6.

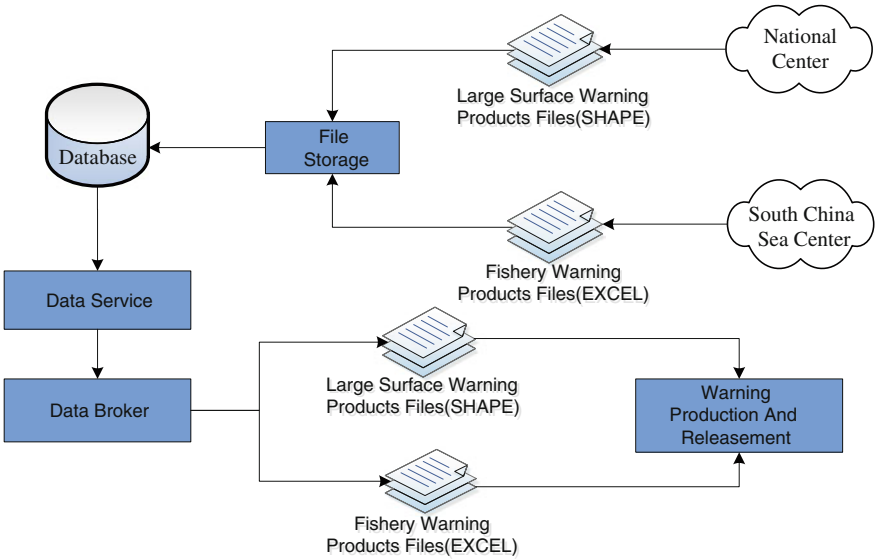

Fig. 7.4 Forecast and warning data acquisition process

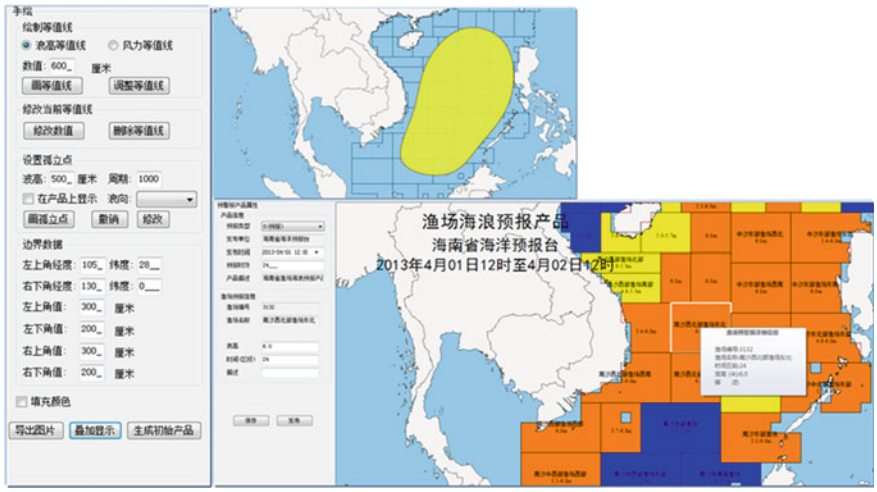

Fig. 7.5 Hand-painted produced forecast and warning products

7.4.2 Display the Marine Forecasting and Warning Products

Marine forecast and warning products display in the integrated display platform module. Platform supports forecast and warning products of shape format superimposed on electronic chart. Including chart display, forecast and warning

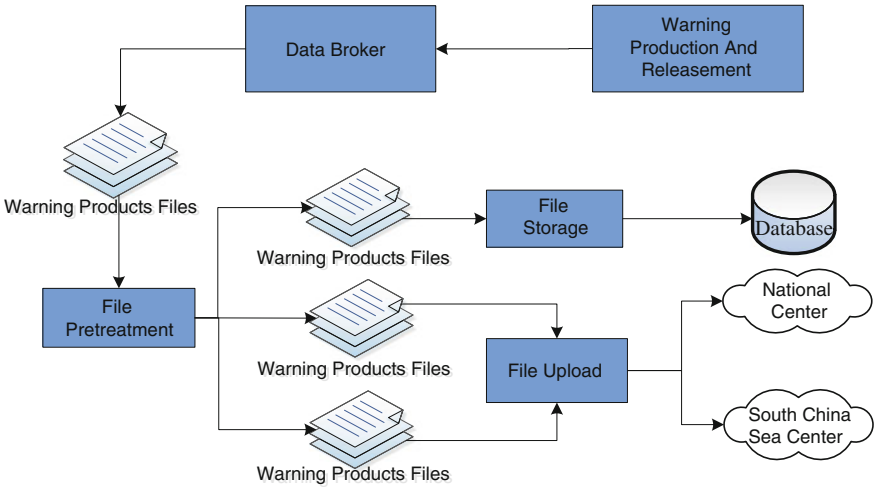

Fig. 7.6 Forecast and warning product release and transport processes

products superimpose, fishing target display, sends the getting ship's position commands, sends forecast and warning SMS, statistics ship online rate, statistics issued instructions etc. functions.

7.4.2.1 A Variety of Chart Display and Fishing Boat Display

The system supports S57 format and SHAPE format charts display, and supports display strategy of multi terminal fusion in fishing target display specification formulated by Ministry of Agriculture.

Under the S57 format chart, the effect of vessels target display shown in "Fig. 7.7 Fishing boat display in S57 format chart".

7.4.2.2 Forecast and Warning Products Overlay Display

The system supports two types of products superimposed on the GIS map: large surface products issued by the National Center, fishery products issued by Sea Area Center and the Provincial station, large surface warning products for the SHAPE format, fishery products for the EXCEL format.

Large surface forecast and warning products display as shown in Fig. 7.8.

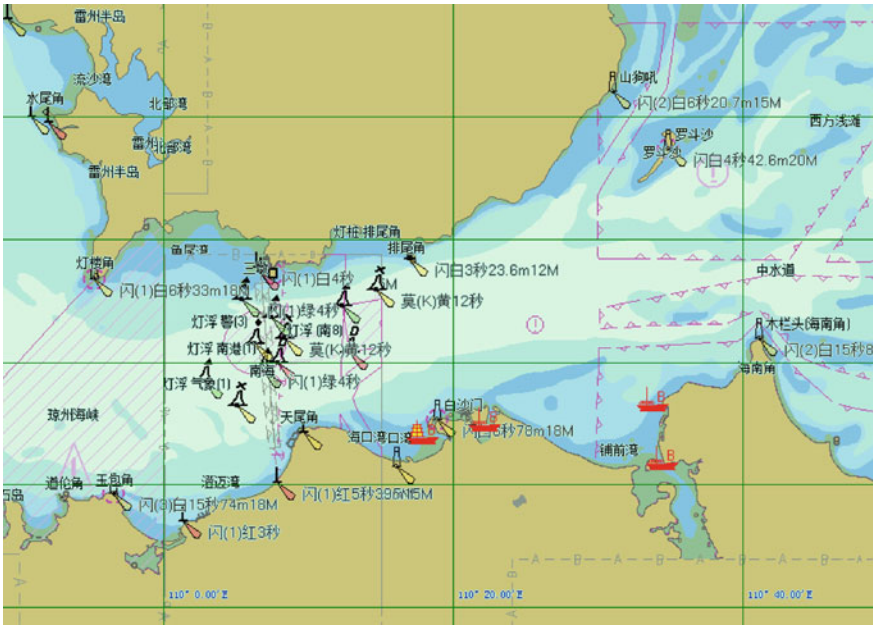

Fig. 7.7 Fishing boat display in S57 format chart

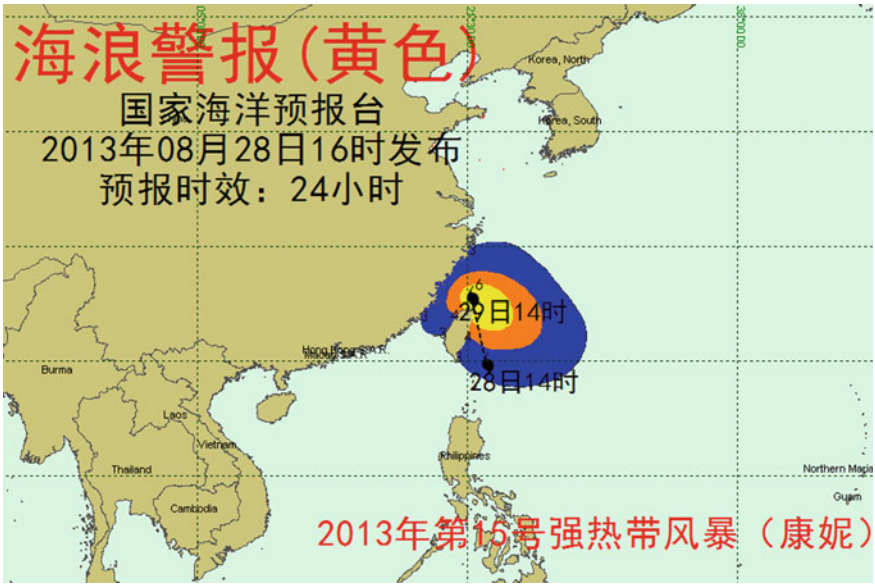

Fig. 7.8 Large surface wave warning product overlapping display

7.4.2.3 Forecast and Warning Messages Produced and Pushed

The system get the dynamic position of fishing vessels through BeiDou, analyzing the type of forecast and warning product, the level and range to achieve release forecast and warning messages based on location intelligence capabilities.

For forecast and warning products the affected fishing can be analyzed in different grades or wind waves grade range, for fisheries forecast and warning products, can be analyzed the affected fishing vessels within range of user-selected. According to the results, the system intelligence generates detailed report warning messages, and through the BeiDou system will send warning messages to the fishing boats and fishermen reported the hands of real-time, effective pre-disaster warning, to protect the safety of fishermen production operations.

7.4.3 System Performance Monitoring

7.4.3.1 Network Status Monitoring

Collected using protocols such as SNMP routers and other network equipment network connection status in different colors respectively connect and disconnect status. Target acquisition can be configured in the form of configuration files stored locally, read the software for the next start. For network anomalies in log mode records to the database.

7.4.3.2 Data Transfer Monitoring

The push process of various types of data visualization monitoring, logging and exception handling the abnormal of document reads and transfer status. By collecting data upload middleware components, data processing log analysis d-ata storage member, including data collection compression, network transmission, data analysis, the time information storage, the information is normal or not, and the number of information data processing, data transmission queue information on HMI, histogram, curves and other forms displayed to the attendant.

7.4.3.3 Server Running Status Monitoring

Through Windows programming interface, access to the specified server and running related processes, including CPU usage, memory usage and so on. And processing server can be configured as a file is saved to the local time for the software to read the next start. When the process is abnormal, through pop-up dialog, playback duty prompted alarm sounds. Create a table in the database corresponding to record abnormal process alarm time occurs, the target machine IP address, the alarm process name, etc., for use in future queries.

Fig. 7.9 Ship's position daily collection and sending curve

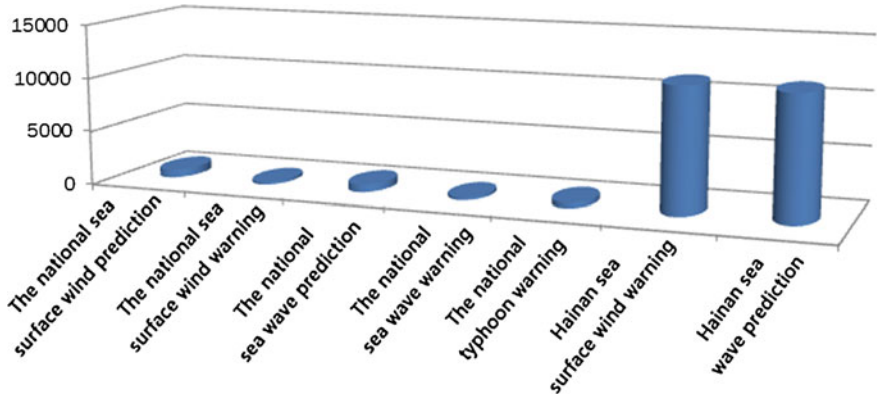

Fig. 7.10 Distribution and reception of forecast and warning products

7.5 Application

The National environmental protection services system of marine fisheries production safety in June 1, 2012 entered operational phase of trial operation, July 3, 2013 by the National Oceanic overall acceptance. Since the system operational test run collected information on all installed fishing BeiDou satellite positioning terminal of Hainan, and a variety of marine warnings on packets of information sent to the affected vessels in the marine fisheries production safety has played a significant role. During the 2013 typhoon affected departments make use of the system sending promptly report warning messages to vessels, effectively reducing staff because of the typhoon disaster and may cause property damage.

As of October 31, 2013, the systematic collection of information on vessels fishing in Hainan 6143, which matches the terminal has reported 6120. Form 2012 June 1 to October 31 nodes collect and South China Sea Area Center, National Center sends a dynamic ship's position daily as Fig. 7.9 Ship's position daily collection and sending curve.

One of the system since June 1, 2012 to October 31, 2013 to receive the National Marine Environmental Forecasting Center production of sea surface wind, wave warning report 1904, which forecast 1399, alarm 505, making 521 typhoon warning. By the Hainan Marine forecast surf forecast produced refined products 11,344, fine sea surface wind forecast products 11462 (Fig. 7.10).

7.6 Conclusion

By using BeiDou system to send the SMS of the marine environment report warning to the hands of fishermen to achieve a marine disaster early warning, which can effectively reduce property damage and casualties caused by tolls. The system is developed to achieve the integration and full use of existing resources, goals, both to tap the potential of the BeiDou system in the marine fisheries sector disaster early warning, but also for future expansion into other industries played a good role model, is the Big Dipper in the civil try an innovative application areas. The system will continue to deepen the subsequent increase forecast and warning products, such as the type and extension of the forecast period will be extended to the forecast and warning service levels in coastal cities and counties in Hainan Province, to expand the scope of services to provide a more comprehensive environmental protection services for the marine fisheries production safety.

References

1. State Oceanic Administration People's Republic of China (2011) The technical specifications for the environmental protection services system of national marine fisheries production safety
2. Department of Ocean and Fisheries of Hainan Province (2012) The overall construction plan for the environmental protection services system of Hainan marine fisheries production safety

Chapter 8
Quasi-Real Time Determination of 2013 Lushan Mw 6.6 Earthquake Epicenter, Trigger Time and Magnitude Using 50 Hz GPS Observations

Meng Li, Dingfa Huang, Li Yan, Weifeng Chen, Hua Liao, Tie Gu and Na Chen

Abstract 50 HZ Global Positioning System (GPS) high rates data of 8 Continual Operation Reference System (CORS) sites nearby Lushan are used to analyze the earthquake trigger time, epicenter and magnitude. All sites position time series on N, E directions are resolved with the track software, and horizontal accuracy can reach to 2 cm at least. Horizontal position time series analyses show that the earthquake mainly affects QLAI, SCTQ, YAAN sites, the horizontal peak amplitudes can reach to 50 mm, the maximum instantaneous velocity can reach to 72.36 mm/s and the maximum instantaneous acceleration have reached to 105.9 mm/s^2. Analyzing the position time series by the method of S transformation, the arrival time of seismic wave is estimated. With seismic wave arriving time and coordinates of three sites which are first detecting the seismic wave, the earthquake's epicenter and trigger time can be fast determined by three-dimensional search method. Moreover, the earthquake magnitude can also be estimated by horizontal peak amplitudes from the sites using the regression method. These suggest exiting GPS infrastructure could be developed into an effective component of earthquake assessment.

Keywords Lushan Earthquake · CORS · High rate GPS · Epicenter · Magnitude

M. Li · D. Huang (✉) · L. Yan · N. Chen
Faculty of Geosciences and Environment Engineering, Southwest Jiaotong University, Chengdu 610031, China
e-mail: dfhuang@home.swjtu.edu.cn

M. Li
e-mail: nemon818@163.com

W. Chen · H. Liao · T. Gu
Disaster Relief Research Institute, Sichuan Seismological Bureau, Chengdu 610041, China

J. Sun et al. (eds.), *China Satellite Navigation Conference (CSNC) 2014 Proceedings: Volume I*, Lecture Notes in Electrical Engineering 303,
DOI: 10.1007/978-3-642-54737-9_8,

8.1 Introduction

The 20 April 2013 Lushan earthquake with the magnitude of Mw 6.6 occurred on the southern segment of the Longmen Shan fault in Sichuan, China. Nearly 200 persons were killed and the economic loss was reached to 170 billion yuan. Once a destructive seismic event occurs, the magnitude determination, the nucleation location, and the seismic event trigger time will be essential for earthquake relief. However, to estimate a reliable and rapid measurement of the magnitude of an earthquake is a challenge, especially for earthquake magnitude is above 8.0 ($M > 8$) [6].

As the technique High-rate GPS whereby positions are estimated at a rate of once per second or higher using the high-precision phase observations of the GPS. In addition, comparing to seismometers, GPS has the unprecedented advantage on estimating the position time series without titling, saturation. Using GPS on seismology has become a new subject, GPS seismology [5]. This new subject springs up at the beginning of the 21th century, Developed only in the last few 5 years, and this technique has been widely used to determine the time-dependent surface displacements induced by the 2008 Wenchuan earthquake in Sichuan of China [9, 12], the 2010 Mw 8.8 Maule Megathrust Earthquake of Central Chile [4], and the 2010 Mw 7.2 El Mayor-Cucapah earthquake [2, 13]. Many researchers have pointed out the need for 10-sps GPS (or even higher sampling rate) data in seismology studies. Several 10-sps GPS seismograms from the 2009 earthquake in L'Aquila, Italy (Mw 6.3) have been used to study strong ground motions and earthquake source mechanisms [1].

Since the CORS' sites of Sichuan, China have integrity and precisely recorded the data through Lushan earthquake occurred, we mainly investigate the potential usage of high rates GPS in earthquake relief by this case in our study.

8.2 Data Processing and Horizontal Movement Characteristics

The raw observation data from Crustal Movement Observation Network of China and Seismological Bureau of Sichuan Province have recorded the detailed ground motion through Lushan Earthquake. All the receivers of CORS sites are Trimble Net8 and the receiver antennas are TRM59800. The geographical location of the CORS sites have been shown as Fig. 8.1.

Epoch-to-epoch processing of the very high rate GPS data (VHRGPS) has been described to analyze the quasi real time displacements of CORS stations in Sichuan during the Lushan earthquake. We use the teqc software provided by UNAVCO (http://www.unavco.org/) and the runpkr00 software provided by Trimble company covert the 50 Hz Trimble T02 data to rinex data, and then the high sampling rate data (50 Hz) were processed using the TRACK software of

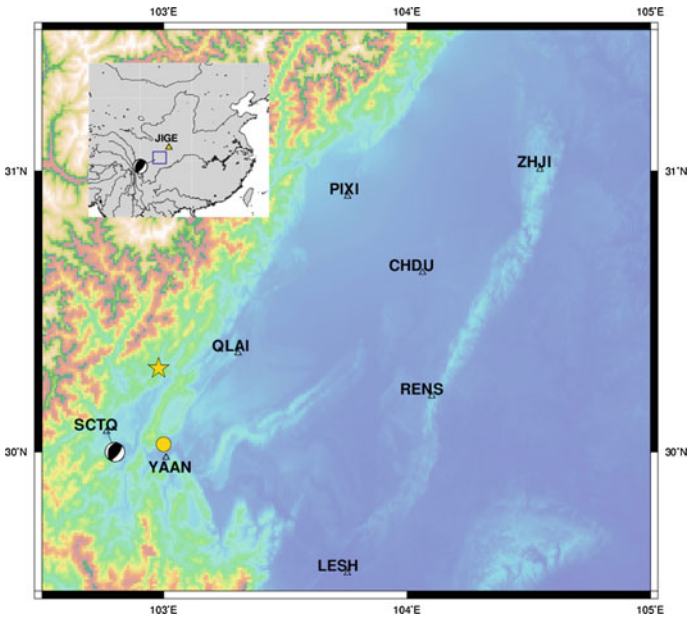

Fig. 8.1 Location of the CORS sites (Beach ball represents focal mechanism was provided by USGS, *yellow Five-pointed star* was the epicenter location provided by Chinese Seismological Bureau, *yellow circle* was the epicenter calculated in this paper, JIGE is the reference station)

GAMIT developed at MIT. The LC combination and IGS precise orbits, and apply a smoothing filter on the backward solution to estimate the atmospheric delays using the whole 24 h data and fix any non-integer biases to a constant value. Because TRACK computes a relative position with respect to a fixed reference station, we choose to use the same for all moving sites.

Since the site JIGE of our CORS network is far enough from the epicenter, the surface wave which shake this station arrives late enough so that the first 200 s are unaffected by this motion, we picked it as the base station. The JIGE site is calculated for check the motion of PENX whether the site has been affected by Lushan Earthquake. In general, it is difficult to assess the accuracy of HRGPS. Some low frequency biases related to atmosphere drift or satellite configuration changes may show, depending on the length of the baseline to the reference station. This does not affect the co-seismic step since it is an almost instantaneous displacement, but renders difficult the chase for pre-seismic or rapid post-seismic signal.

The linear terms of CORS sites deformations have been treated as useless noise and therefore removed. Velocity, acceleration of CORS sites motion have been calculated by signal and double differential of the position time series, respectively. The detailed horizontal displacement, velocity and acceleration time series have been shown by Figs. 8.2, 8.3 and 8.4. Since the accuracies of vertical position time

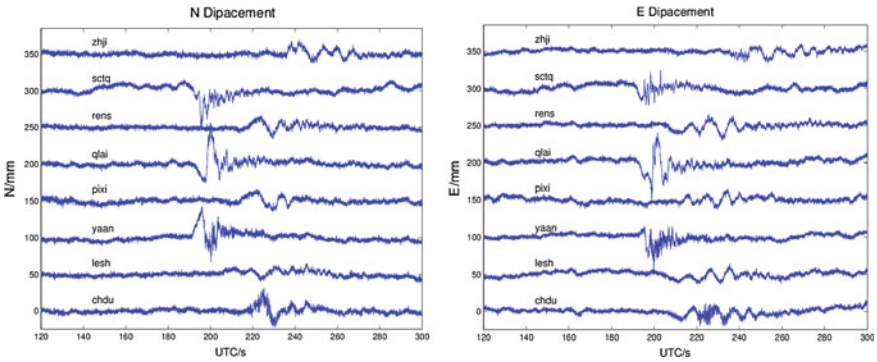

Fig. 8.2 The variety of site displacement during Lushan earthquake

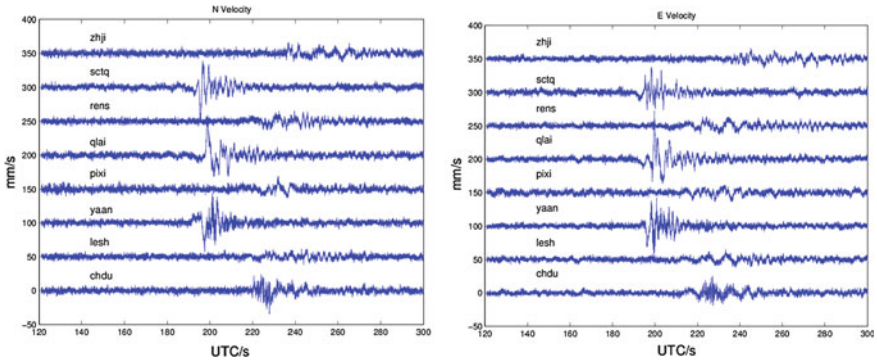

Fig. 8.3 The variety of site velocity during Lushan earthquake

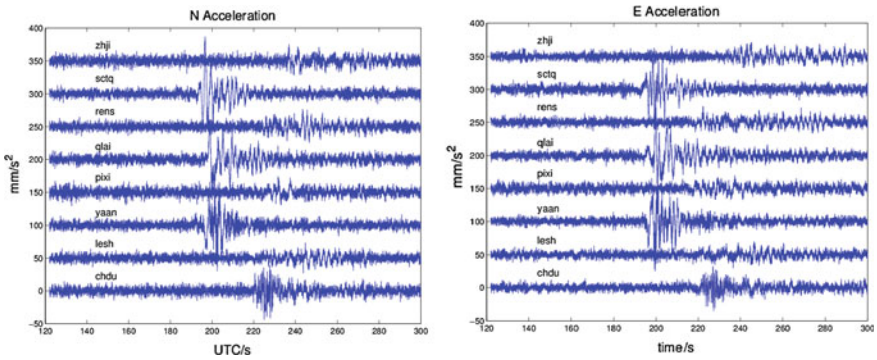

Fig. 8.4 The variety of site acceleration during Lushan earthquake

Table 8.1 The impaction of site movement caused by earthquake

Site	Epicentral distance (km)	Peak amplitude (mm)		Peak velocity (mm/s)		Peak acceleration (mm/s^2)	
		N	E	N	E	N	E
CHDU	123	31.23	20.04	33.99	25.11	43.4	35.2
LESH	113	14.86	14.99	12.14	15	23.1	20.4
PIXI	112	15.99	14.87	18.33	13.79	24.5	19.9
QLAI	56	55.8	53.04	58.91	72.36	59	105.90
RENS	126	16.16	20.76	15.45	13.78	26.6	24.1
SCTQ	29	51.6	24.05	49.75	37.53	86.70	58.7
YAAN	21	42.38	48.72	43.64	42.18	69.8	82
ZHJI	195	19.07	15.66	16.43	15.58	25.2	20.5

series are not good, speared from 4–5 cm, we ignore the vertical displacements during Lushan Earthquake. The statistical table (Table 8.1) mainly shows the impaction of sites movement caused by earthquake. With carefully processed time series, the huge difference between different sites have been described below: the sites QLAI, SCTQ and YAAN nearby the epicenter are most activity, and peak displacement amplitudes of these sites have reached as high as 50 mm. Comparing to the rest sites, CHDU peak displacement amplitude on N direction is the biggest, which have reached 31 mm, and the peak accelerate has reached 105.9 mm/s^2, on E direction at QLAI site. However, GPS accelerate result would be quite smaller than accelerometer's result because of the ground resistance. While, comparing to displacement time series, the acceleration time series enlarge the impaction of earthquake, from which we can check the arriving time and lasting time of seismic wave more easily.

8.3 Analysis of Lushan Earthquake

8.3.1 Arriving Time of the P Wave

When the surface wave of a moderate-magnitude earthquake is treated as some kinds of energy from the model of point source, we can check it from the sites' acceleration time series. To check the arriving time of seismic wave (usually were treated as P wave), the method of S transform has been used. As a time–frequency distribution, S transform was developed in 1994 for analyzing geophysics data [10, 11]. In this way, the S transform is a generalization of the short-time Fourier transform (STFT), extending the continuous wavelet transform and overcoming some of its disadvantages. The improvement is the modulation sinusoids are fixed with respect to the time axis; this localizes the scalable Gaussian window dilations and translations in S transform. Moreover, the S transform doesn't have a cross-term

problem and yields a better signal clarity than Gabor transform. In our study, we used a fast S Transform algorithm invented by Brown in 2010. It reduces the computational time and resources by at least 4 orders of magnitude. The S transform function is showed as below:

$$S(\tau, f) = \int_{-\infty}^{\infty} h(t)w(\tau - t, f)\exp(-2\pi ift)d\tau \tag{8.1}$$

$$\omega(\tau - t, f) = \frac{|f|}{\sqrt{2\pi}}\exp\left(\frac{-f^2(\tau - t)^2}{2}\right) \tag{8.2}$$

In the equation, the $h(t)$ represents the raw time series, $\omega(\tau - t, f)$ represents Gaussian window function, t, f, τ represent time, frequency, time scale factor using in the Gaussian window respectively.

In our experiment, we focus on the points at detect the energy of acceleration changing and the arriving time of P wave. The threshold value choosing is based on the method from document [11]. We find the result perform better by using S transform of these sites nearby Lushan epicenter comparing to the sites far away. That is mainly because when the epicentral distance is increased, the energy of P wave is getting less, which will cause the arriving time difficult to distinguish. We just list the figures of sites QLAI, SCTQ and YAAN, which have been showed from Figs. 8.5, 8.6 and 8.7. Since the arriving time of P wave at N direction and E direction is not the same, we employ a simple variable (horizontal displacement) which is defined as $dS = \sqrt{dN^2 + dE^2}$ to describe the movement characteristics, and the S transform has also been used at the acceleration of horizontal displacement to get the P wave arriving time. The first arrival time of seismic wave deriving from acceleration have been showed in Table 8.2.

From Table 8.2, we could find the P wave first arrive at YAAN site, the lag time for the seismic wave to CHDU is about 26 s. The differential time between YAAN and CHDU is very short but quite valuable. It can be definitely affirmed that the high rates GPS also have a huge potential usage in mainland early earthquake warning.

8.3.2 Rapid Epicenter Estimate

Crowell et al. [3] investigated the epicenter estimation only using the GPS data. They demonstrated that it is possible to estimate earthquake epicenter solely using GPS data. Utilizing high rates GPS to hypocenter location determination is a new approach which should be helpful. The classic method of determining hypocenter location attributes to Geiger and various linear methods based on it, such as the joint hypocenter determination, simultaneous structure and hypocenter determination,

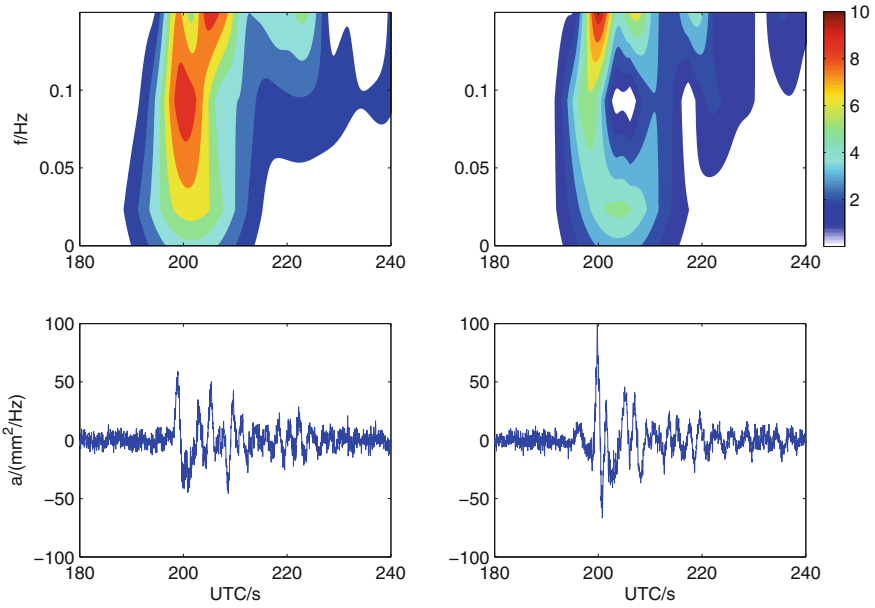

Fig. 8.5 The co-seismic frequency-domain on acceleration of QLAI site

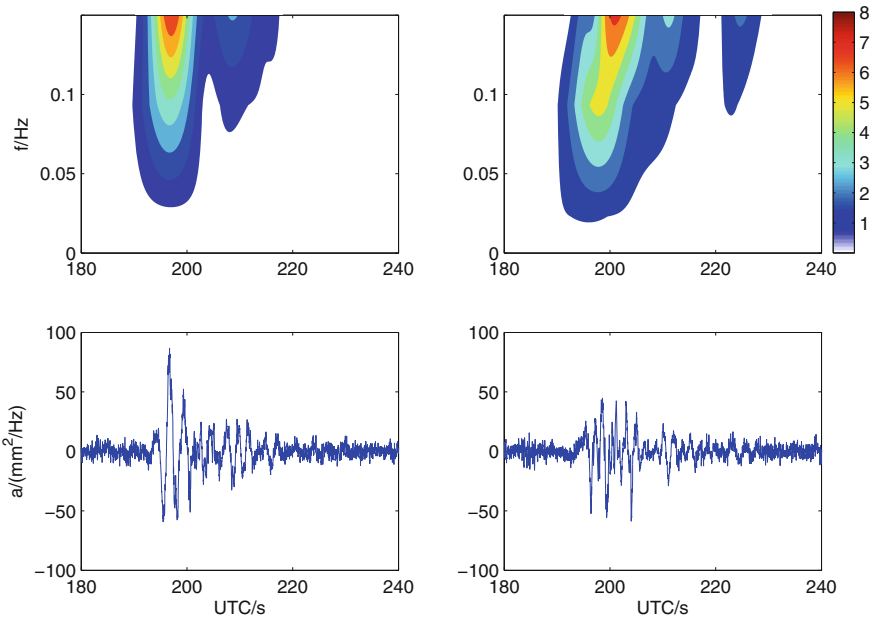

Fig. 8.6 The co-seismic frequency-domain on acceleration of SCTQ site

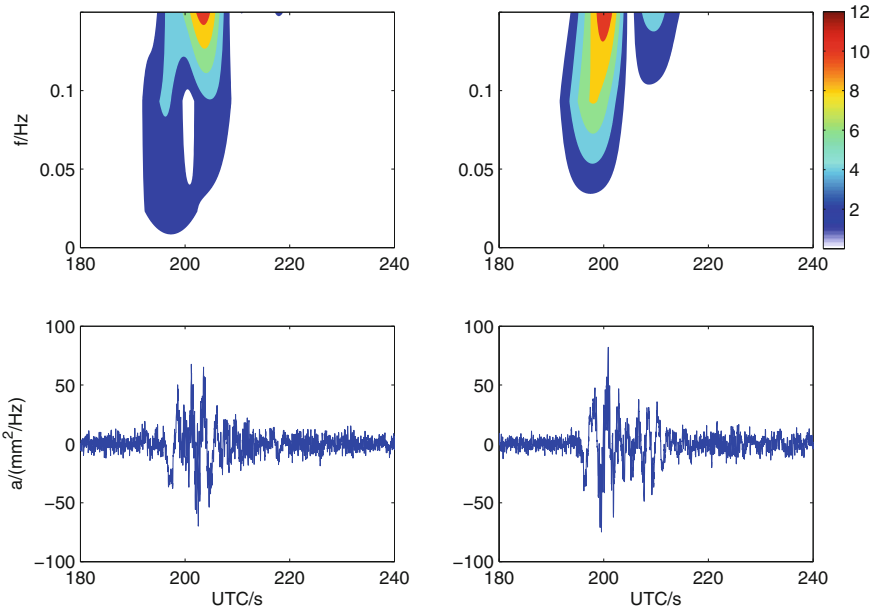

Fig. 8.7 The co-seismic frequency-domain on acceleration of YAAN site

Table 8.2 The arrival time of seismic wave deriving from acceleration

Sites	The offset time of acceleration (s)			
	N	E	Average	Horizontal displacement
CHDU	217.74	216.02	216.88	216.24
LESH	227.2	225.62	226.41	228.92
PIXI	226.76	223.46	225.11	228.34
QLAI	193.22	192.24	192.73	192.46
RENS	224.18	222.74	223.46	221.1
SCTQ	191.34	193.28	192.31	191.7
YAAN	190.98	190.52	190.75	190.8
ZHJI	233.32	234.94	234.13	235.4

relative location technique, and double-difference location algorithm. By using the classic approach state above, at least four well geographic distribution sites' location coordinates are needed to invert the accurate hypocenter location. While, in our study, in order to determine the hypocenter fast and precisely, we use a geometry approach of searching in three-dimension to check the appropriate point source. An equation which using a least-squares fitting algorithm to invert the hypocenter location and the seismic event start time have been established as below:

$$f(T_0, N_0, E_0, U_0) = \min \sum_{i=1}^{n} d_i^2 \tag{8.3}$$

$$d_i = \sqrt{(N_i - N_0)^2 + (E_i - U_0)^2 + (U_i - U_0)^2} - v(t_i - T_0) \tag{8.4}$$

where t_i is the seismic P wave arrival time at site i, N_i, E_i, U_i is the coordinate of site i, T_0, N_0, E_0, U_0 represent the seismic event trigger time and the coordinate in NEU components respectively.

Once three sites have detected the seismic wave, the equation would have a unique solution which can be treated as the initial point source location and seismic event time. However, as the epicentral distance increased, the weight factors of the other sites shall be down because of the uncertainty of P wave velocity. Here, for quasi real-time determine the hypocenter location position, we invert the initial seismic location position and nuclear time just by using three sites at which P wave is first arriving. Since YAAN site have first detected the P wave, we take it as the origin center point. A range of 2° on latitude and longitude out of the center point, and 30 km depth has been chosen. To search for the optimal hypocenter location, we take Eq. (8.3) as the judgment rule. The search steps of horizontal direction is set at 1°, 0.5°, 0.1°, 0.01° respectively, and the depth step is set at 5, 1, 0.5, 0.1 km respectively. After the optimal grid searching, an appropriate location position has been determined as the position of (30.04N, 103.05E), at the depth of 16.7 km, and the initial seismic event time as GPS Time 183.71 s. If added 16 leap seconds from 1982, covert to Beijing time it is 8:02:47.71. The seismic P wave velocity is about 7.11 km/s to YAAN site, 7.02 km/s to SCTQ site, and 7.01 km/s to QLAI site respectively. Therefore, the average spread speed is 7.05 km/s, quite confirms to the seismic P wave's characteristics. The spread time to the three sites is 4.11, 6.71 and 9.05 s respectively.

8.3.3 Magnitude Inversion

As high rate GPS data can provider with a high signal-to-noise ratio (SNR) and precisely determine the peak horizontal displacement, but not sensitive to the P wave. We just investigate the surface wave magnitude derived by GPS. A general form for surface wave magnitude scales can be defined as [8]:

$$M = \log(\mathrm{A}/\mathrm{T}) + a\log(\Delta) + \mathrm{b} \tag{8.5}$$

where A is the peak displacement (including the N E U component) caused by the seismic waves, T is the dominant period of the measured waves, a is the coefficient correction for epicentral distance, and b is a constant. The logarithmic scale is usually used because the seismic wave amplitudes of earthquakes vary enormously.

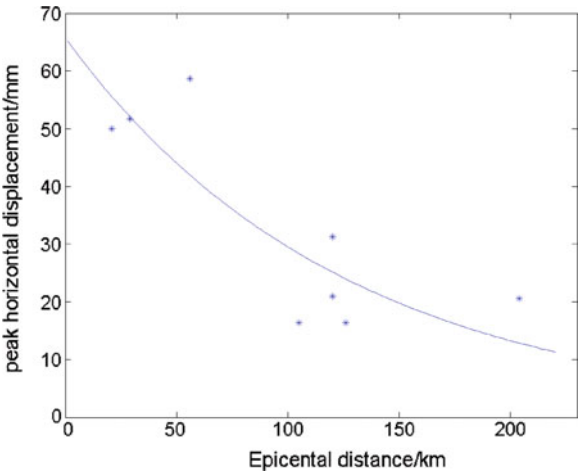

Fig. 8.8 Relationship between peak horizontal displacements and epicentral distance

Table 8.3 Magnitude statistic of sites derived from the surface wave

Sites	Peak displacements (mm)	Epicentral distance (degree)	Magnitude
CHDU	31.17	0.98	6.48
PIXI	27.41	0.89	6.36
QLAI	57.69	0.27	5.82
RENS	21.31	0.96	6.30
SCTQ	51.16	0.30	5.85
YAAN	49.31	0.32	5.87
ZHJI	21.13	1.51	6.62
Regression			6.18

Recent studies have shown that the displacement waveforms derived from high-rate GPS data are consistent with those measured by strong-motion records [2, 13]. Thus, no matter if the displacement waveforms are measured by a seismometer or by GPS, the empirical relation-ship Eq. (8.5) is appropriate for magnitude estimates based on far-field surface waves. Gutenberg (1945) deduced an empirical relationship between peak displacement, distance and magnitude by utilizing the strong-motion [7]. He used an empirical regression method to resolve the coefficient correction a and constant b by the amplitude of surface waves from a set of earthquakes that occurred in California, namely

$$M = \log(\mathrm{A}) + 1.66\log(\Delta) + 2.0, \tag{8.6}$$

Here, which is different from Eq. (8.5), A is the peak horizontal displacement derived from surface waves in units of micrometer, Δ is the epicentral distance in units of degree. M is the magnitude. We use the empirical relationship to build a magnitude evaluate figure, as shown in Fig. 8.8 (Table 8.3).

8.4 Conclusion Remarks

Study shows that 50 Hz GPS measurements have the potential usage on seismic relief, the epicenter, trigger time can be determined quickly about 60 s. Magnitude size also could be determined within nearly 300 s. The searching result of epicenter location is quite close to USGS' results (as shown in Fig. 8.1), and the seismic event start time is 1.71 s less. While, the magnitude determining is different from the announce result of China Seismological Bureau. Especially when the epicentral distance is below 0.5°, the magnitude size estimate is lower apparently. We consider that it may be caused by the assuming empirical equation developed by Gutenberg is not quite suitable in Sichuan, China, from which we consider the GPS observation shall be built at a new equation for magnitude determine.

Dense VHRGPS networks will be very helpful to detect significant variations in the seismic wave propagation, that could be related to rupture dynamics or otherwise hidden geologic heterogeneities and as an earthquake magnitude is bigger, the outcome will be better observed. We find although the seismic wave first arrive YAAN site, the site coordinate time series which impacted most intensity is QLAI site. The phenomena could relate to the hidden geologic heterogeneities.

Acknowledgements The authors hereby acknowledge with thanks to the financial supporting from National Natural Science Foundation of China (no. 41374032), National Hi-Tech Research and Development Program (863) (no. 2012AA12A209) ,and a grant from Spark Program of China Seismological Bureau (No. XH12039). The thanks are also extended to Sichuan Seismological Bureau for the supporting of GNSS CORS observations.

References

1. Avallone A, Marzario M, Cirella A, Piatanesi A, Rovelli A, Di Alessandro C, D'Anastasio E, D'Agostino N, Giuliani R, Mattone M (2011) Very high rate (10 Hz) GPS seismology for moderate-magnitude earthquakes: the case of the Mw 6.3 L'Aquila (central Italy) event. J Geophys Res Solid Earth 116:B2305
2. Bock Y, Crowell BW, Kedar S, Melgar Moctezuma D, Squibb MB, Webb F, Yu E, Clayton RW (2010) Observations and modeling of the Mw 7.2 2010 El Mayor-Cucapah Earthquake with real-time high-rate GPS and accelerometer data: implications for earthquake early warning and rapid response, vol 1, p 5
3. Crowell BW, Bock Y, Squibb MB (2009) Demonstration of earthquake early warning using total displacement waveforms from real-time GPS networks. Seismol Res Lett 80:772–782
4. Delouis B, Nocquet J, Vallée M (2010) Slip distribution of the February 27, 2010 Mw = 8.8 Maule Earthquake, central Chile, from static and high-rate GPS, InSAR, and broadband teleseismic data. Geophys Res Lett 37:L17305
5. Larson KM (2009) GPS seismology. J Geodesy 83:227–233
6. Larson KM, Bilich A, Axelrad P (2007) Improving the precision of high-rate GPS. J Geophys Res Solid Earth (1978–2012) 112
7. Gutenberg B (1945) Amplitudes of surface waves and magnitudes of shallow earthquakes. Bulletin of the eismological Society of America, 35(1): 3-12

8. Richter CF (1935) An instrumental earthquake magnitude scale. Bull Seism Soc Am 25:1–32
9. Shi C, Lou Y, Zhang H, Zhao Q, Geng J, Wang R, Fang R, Liu J (2010) Seismic deformation of the Mw 8.0 Wenchuan earthquake from high-rate GPS observations. Adv Space Res 46:228–235
10. Stockwell RG (2007) Why use the S-transform. AMS Pseudo Differ Operators Partial Differ Eqn Time Freq Anal 52:279–309
11. Stockwell RG, Mansinha L, Lowe RP (1996) Localisation of the complex spectrum: the S transform. J Assoc Explor Geophysicists 17:99–114
12. Yin H, Wdowinski S, Liu X, Gan W, Huang B, Xiao G, Liang S (2013) Strong ground motion recorded by high-rate GPS of the 2008 Ms 8.0 Wenchuan Earthquake, China. Seismol Res Lett 84:210–218
13. Zheng Y, Li J, Xie Z, Ritzwoller MH (2012) 5 Hz GPS seismology of the El Mayor-Cucapah earthquake: estimating the earthquake focal mechanism. Geophys J Int 190:1723–1732

Chapter 9
Simulations and Analysis of BeiDou Navigation Satellite System (BDS)-Relectometry Delay-Doppler Maps for Vegetation

Xuerui Wu and Shuanggen Jin

Abstract Global Positioning System-Reflectometry (GPS-R) is a new promising technique, which uses the reflected signals of the GPS constellation to remotely sense the geophysical parameters of the ocean and land surface. Some initial results were obtained from GPS-R in ocean surface characteristics and soil moisture, while, vegetation sensing is paid attention recently. With the development of Chinese independent Beidou Satellite Navigation System (BDS), it will play a key role in positioning, navigation and timing as well as potential applications of BDS-Reflectometry (BDS-R), e.g. vegetation monitoring using the Delay-Doppler Map (DDM) of BDS-R. Therefore, it is extremely necessary to simulate the vegetation BDS-R DDM maps. Z–V model is a commonly used GPS-R scattering model and its applications include the sea wind, oil slick and soil moisture. In this paper, it is the first time for vegetation DDM simulations from BDS-R, while the vegetation scattering properties are simulated using the modified Bi-mimics model, which can be used to calculate any transmit and receive polarization combinations, assuming that the received power is coming from the first Fresnel zone. The theoretical simulations of DDM are helpful for the further BDS-R vegetation parameters retrieval, and some discussions and analysis are further given.

Keywords BDS-R · Vegetation · Z–V · Bi-mimics · DDM

X. Wu (✉) · S. Jin
Shanghai Astronomical Observatory, Chinese Academy of Sciences,
Shanghai 200030, China
e-mail: xrwu@shao.ac.cn

S. Jin
e-mail: sgjin@shao.ac.cn

X. Wu
Department of Environment Resources and Management, Chifeng University,
Chifeng, Inner, Mongolia 024000, China

J. Sun et al. (eds.), *China Satellite Navigation Conference (CSNC) 2014 Proceedings: Volume I*, Lecture Notes in Electrical Engineering 303,
DOI: 10.1007/978-3-642-54737-9_9,

9.1 Introduction

GNSS-Reflectometry (GNSS-R) was first proposed by Martin-Neira in the early 1990s for altimetry measurement [1]. In the following years, its applications were extended from mesoscale ocean [2] to land surface [3] as well as snow/ice remote sensing [4, 5]. As for the land scenario, soil moisture and vegetation characteristics study are the main purposes [3]. With the development of Chinese independent BeiDou Navigation Satellite System (BDS), it will play a key role in positioning, navigation and timing as well as potential applications of BDS-Reflectometry (BDS-R), e.g. vegetation monitoring using the BDS-R DDM maps. Z–V scattering model was first developed by Zavorotny and Voronovich in 2000 for ocean wind remote sensing [2], which is commonly used for DDM simulations. An efficient algorithm of ZV model was proposed in 2009 for the resource computation consideration (both time and memory) [6]. At present, GNSS-R delay-doppler maps simulations commonly use the Z–V model, such as DDM simulations of ocean wind and oil slick [7]. As for land part, the reflected signal waveform was initially modeled by Masters [8] using Z–V model. KA-GO model was used for soil scattering calculations. However, the Delay Doppler Map simulations of vegetation analysis are still not yet.

This paper focuses on the vegetation DDM simulations using modified Z–V model from BDS-R. The Bi-mimics model [9] is used for vegetation scattering calculations and then Z–V model is used for DDM waveform simulations [2]. In Sect. 9.2, the Bi-mimics model is described and the Z-V model is presented in Sect. 9.3. Initial simulations results are given in Sect. 9.4. And finally, some discussions and conclusions are given in Sect. 9.5.

9.2 Bi-mimics Model

As for GNSS-R remote sensing, GNSS constellations are the source of transmitted signals and the corresponding receiver collects the reflected signals, which form a typical bistatic/multi-static radar working mode. The bistatic scattering model Bi-mimics [9] is adopted in our work to calculate vegetation scattering characteristics.

9.2.1 Basic Formulations

The Bi-mimics model is a bistatic forest scattering model [9], which is based on the first order radiative transfer MIMICS (Michigan Microwave Canopy Scattering) model [10]. The canopy structure is modeled as crown layer and trunk layer over a dielectric ground surface. Assuming that I_i and I_s are the incident intensity and scattering intensity, respectively and (θ_i, φ_i) and (θ_s, φ_s) are the corresponding

incident and scattering angles, the first-order fully polarimetric transformation matrix T is used to relate I_i and I_s.

$$I_s(\theta_s, \varphi_s) = T(\theta_s, \varphi_s) I_i(\theta_i, \varphi_i) \tag{9.1}$$

T is given in terms of the extinction and phase matrices, which are calculated by the average modified Mueller matrices. Note that there are eight scattering mechanisms in this model. Contributions from layers of crown, trunk and ground amount to the final scattering.

9.2.2 Wave Synthesis

As for GNSS-R remote sensing, the transmitted signals are the Right-Hand Circular Polarization (RHCP) polarization, which is different from the original linear polarizations used in conventional microwave techniques. Therefore, we need to make it possible for the circular polarization calculation using Bi-mimics model [9–11].

As we know, the Bi-mimics model is a fully polarimetric model. The bistatic scattering cross section for any combinations of transmit and receive polarizations can be achieved by Eq. (9.2)

$$\sigma_{rt}(\psi_r, \chi_r, \psi_t, \chi_t) = 4\pi \tilde{Y}_m^r M Y_m^t \tag{9.2}$$

where M is the Muller matrix by a 4 × 4 real matrix, see Eq. (9.3–9.5), $\tilde{R}$ is the transpose of R, as shown in Eq. (9.5), and Y_m^t and Y_m^r are the modified Stokes vectors in Eq. (9.6).

$$M = \tilde{R}^{-1} W R^{-1} \tag{9.3}$$

$$W = \begin{bmatrix} S_{vv}S_{vv}^* & S_{vh}S_{vh}^* & S_{vv}S_{vh}^* & S_{vh}S_{vv}^* \\ S_{hv}S_{hv}^* & S_{hh}S_{hh}^* & S_{hv}S_{hh}^* & S_{hh}S_{hv}^* \\ S_{vv}S_{hv}^* & S_{vh}S_{hh}^* & S_{vv}S_{hh}^* & S_{vh}S_{hv}^* \\ S_{hv}S_{vv}^* & S_{hh}S_{vh}^* & S_{hv}S_{vh}^* & S_{hh}S_{vv}^* \end{bmatrix} \tag{9.4}$$

$$R = \begin{bmatrix} 1 & 1 & 0 & 0 \\ 1 & -1 & 0 & 0 \\ 0 & 0 & 1 & 1 \\ 0 & 0 & -j & j \end{bmatrix} \tag{9.5}$$

$$Y_m^t = \begin{bmatrix} \frac{1}{2}(1+\cos 2\psi_t \cos 2\chi_t) \\ \frac{1}{2}(1-\cos 2\psi_t \cos 2\chi_t) \\ \sin 2\psi_t \cos 2\chi_t \\ \sin 2\chi_t \end{bmatrix} \quad Y_m^r = \begin{bmatrix} \frac{1}{2}(1+\cos 2\psi_r \cos 2\chi_r) \\ \frac{1}{2}(1-\cos 2\psi_r \cos 2\chi_r) \\ \sin 2\psi_r \cos 2\chi_r \\ \sin 2\chi_r \end{bmatrix} \tag{9.6}$$

where (ψ_r, χ_r) are the orientation and ellipcity angles for transmitted signals and (ψ_t, χ_t) are the corresponding angles for the received signals.

Using the above mentioned wave synthesis technique, the scattering coefficients of any combination polarization can be achieved. In this paper, RR and RV polarization of Aspen [10] is selected, and only two single scatters are needed, branch and trunk.

9.3 Z–V Model

9.3.1 Scattering Geometry

To simplify our analysis and focus on the problem itself, we do not care about the curvature of the Earth. We should define the coordinate system at first. The specular point is at the origin of the system, Z-axis is vertical and the x-y plane is the plane tangent to the surface. The scattering geometry is depicted in Fig. 9.1. The h0 and h are the height of the transmitter and receiver, and γ is the elevation angle.

$\vec{R}_t$ is the position from transmitter to the origin of the system. $\vec{R}_r$ is the position from the receiver to the origin of the system. $\vec{R}_{sp}$ is the position of the specular point.

$$\vec{R}_t = \begin{bmatrix} \vec{i} & \vec{j} & \vec{k} \end{bmatrix} \begin{bmatrix} 0 \\ h_0 \cot\gamma \\ h_0 \end{bmatrix} \quad \vec{R}_r = \begin{bmatrix} \vec{i} & \vec{j} & \vec{k} \end{bmatrix} \begin{bmatrix} 0 \\ -h \cot\gamma \\ h \end{bmatrix} \quad \vec{R}_{sp} = \begin{bmatrix} \vec{i} & \vec{j} & \vec{k} \end{bmatrix} \begin{bmatrix} 0 \\ 0 \\ 0 \end{bmatrix} \tag{9.7}$$

$R_{0,sp}$ is the distance from transmitter to the specular point. R_{sp} is the distance from the receiver to the specular point.

$$R_{0,sp} = \sqrt{(h_0 \cot\gamma)^2 + h_0^2}, \quad R_{sp} = \sqrt{(h \cot\gamma)^2 + h^2} \tag{9.8}$$

9.3.2 Z–V Model

The final form of GNSS-R scattering model is shown in the Eq. (9.9). Essentially, it's the integral form of bistatic radar equation.

Fig. 9.1 Scattering geometry

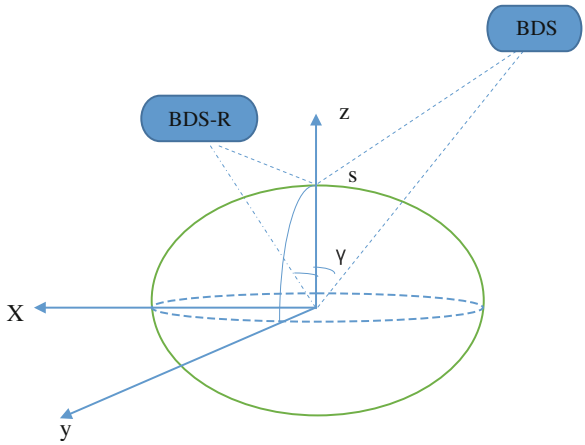

The scattered power is determined by four zones. The first one is the equi-range zones or Fresnel Zone decided by the triangular function, it is a series of elliptical areas with the transmitter and receiver as foci, their interaction with the ocean surface thus forming equi-range. The second one is the Doppler zone determined by the correlation function S, it is a series of hyperbolic curves. The reflected surface roughness is related to the glistening zone. And the function of G is used to define the effective coverage area of the antenna. The final integral region is defined by the above four functions.

As for the ocean part, its roughness scale is comparable or larger than the incoming wavelength, there is a large glistening zone and it may extend several delays away from the specular point. Therefore, not only the quasi-specular scattering component contribute to the aggregate GPS scattering signals, but also the diffractions scattering or Bragg scattering exerts an important role for the finally received waveform.

However, as for land scenario, its roughness scales are well below L-band wavelength, and it does not own a glistening zone, therefore only the coherent part of specular directions are contributed to the overall received GNSS reflected signals. The final contribution to the received GPS signals were thought to come from the first Fresnel Zone. That is to say, only the first elliptical contributed to the final received signals. Here we thought vegetation is uniform in this elliptical area, we use a specular scattering coefficient to represent the total scattering coefficients. And it is calculated by the modified Bi-mimics model.

The final form of Z–V model [2] is shown in Eq. (9.9).

$$\left\langle |Y(\tau)|^2 \right\rangle = T_i^2 \int \frac{D^2(\vec{\rho})\Lambda^2[\tau - (R_0 + R)/c]}{4\pi R_0^2 R^2} \times |S[f_D(\vec{\rho}) - f_c]|^2 \sigma_0(\vec{\rho}) d^2\rho \quad (9.9)$$

where T_i is coherence time. As for the low gain antenna, D is assumed to be unity here (D = 1). Ambiguity function χ is approximated by the triangular function Λ

(also known as pseudorandom code autocorrelation function) and the Doppler filter function S,

$$\chi(\delta\tau, \delta f) = \Lambda(\delta\tau) S(\delta f) \tag{9.10}$$

where $\delta\tau = \tau - \left[R_{0,sp} + R_{sp}\right]/c$ and δf is the Doppler shift due to motions of transmitter and receiver. As for ocean part, intrinsic motions of the surface should be considered. But as for land surface, it is static and there is no need for the consideration of intrinsic surface motions.

$$\delta f(t_0 + \tau) = f_D(t_0 + \tau) = \left[\vec{V}_t \cdot \vec{m} - \vec{V}_r \cdot \vec{n}\right]/\lambda \tag{9.11}$$

where $\vec{V}_t$ and $\vec{V}_r$ are the velocities of transmitter and receiver, $\vec{m}$ and $\vec{n}$ are the unit vectors the incident wave and scattered wave. As for the Doppler shift function S, it is depicted in the following equation,

$$s(\Delta f) = \chi(0, \Delta f) = \frac{\sin(\pi \Delta f T_i)}{(\pi \Delta f T_i)} e^{-\pi i \Delta f T_i} \tag{9.12}$$

As for the triangular function, when $\Delta\tau$ is equal or smaller than τ_c, it is approximated as $1 - \frac{|\Delta\tau|}{\tau_c}$, otherwise, it is 0.

$$\Lambda(\Delta\tau) = \chi(\Delta\tau, 0) \approx \begin{cases} 1 - \frac{|\Delta\tau|}{\tau_c}, & |\Delta\tau| \le \tau_c \\ 0, & |\Delta\tau| > \tau_c \end{cases} \tag{9.13}$$

We have pointed out that only the scattered signals coming from the first Fresnel Zone contribute to the final GNSS-R scattering power. Therefore, we need not integrate as in the ocean part. And the final form of Z–V model is simplified.

9.4 Simulations and Results

This section will give the simulations specular scattering of Aspen and its DDM. As for airborne GNSS-R flight, the commonly incident angles vary between 5° and 45°. Theoretical and experimental data have proven that V polarization is more compatible for the reflected signals. Azimuth angle effects is not considered here and $\varphi_s = \varphi_i = 0°$. That is to say, the incident wave and the scattered wave are in the same plane.

We can see from the simulations (Fig. 9.2) that the co-polarization RR is larger than the cross one RV. For the incident angles vary from 5° to 45°, the differences of scattering coefficient are about 4.4–7.2 dB.

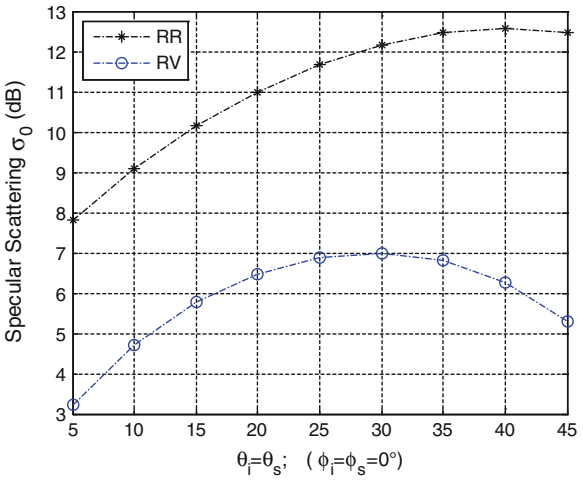

Fig. 9.2 Specular scattering versus specular incident angles

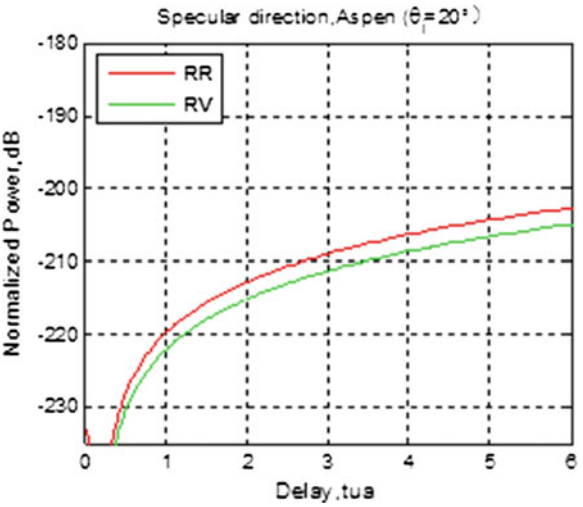

Fig. 9.3 Normalized power versus time delay $\theta_i = 20°$

The Figs. 9.3, 9.4 give the DDM of Aspen, where $\theta_i = 20°$ (Fig. 9.3) and $\theta_i = 40°$ (Fig. 4). The normalized power at $\theta_i = 40°$ is larger than $\theta_i = 20°$ and the power at RR pol is larger than at the RL pol. As the delay increases, the power increases. But it increase sharply when delay is small (0–1). The magnitude of the power is comparable to the theoretical simulations, which use the basic bistatic radar equation [12].

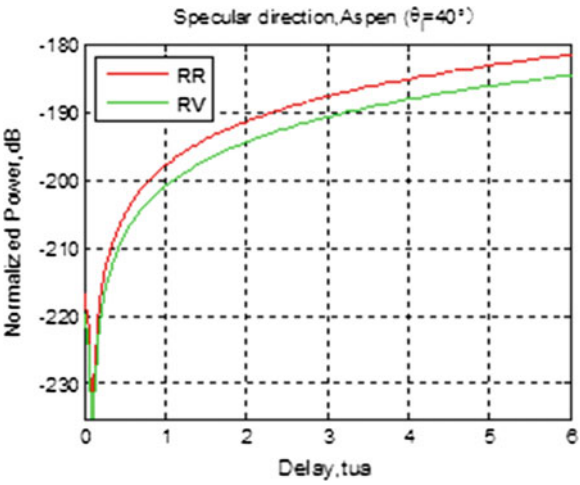

Fig. 9.4 Normalized power versus time delay ($\theta_i = 40°$)

9.5 Conclusions

GNSS-R is a new promising remote sensing technique, particularly in land surface applications due to its L-band working frequency, which is a better bandwidth for penetration and suitable of soil moisture and vegetation monitoring. In this paper, the DDM is the first simulated using the Z–V model for the land surface, here vegetation as an example. The Bi-mimics is used for the calculations of vegetation scattering coefficient. DDM of RR and RV pol at the specular directions are simulated. The results show that DDM forms in the land surface are very different from the ocean surface, whose glistening zone is much larger than the land surface.

Acknowledgments The work is supported by the Natural Science Foundation of the Inner Mongolia Autonomous Region (Grant No. 2013MS0602), Main Direction Project of Chinese Academy of Sciences (Grant No.KJCX2-EW-T03) and National Natural Science Foundation of China (NSFC) Project (Grant No. 11173050 and 11373059).

References

1. Martin-Neira M (1993) A passive reflectometry and interferometry system (PARIS): application to ocean altimetry. ESA J 17:331–355
2. Zavorotnyy V, Voronovich AG (2000) Scattering of GPS signals from the ocean with wind remote sensing application. IEEE Trans Geosci Remote Sens 38(3):951–964
3. Rodriguez-Alvarez N, Camps A, Vall-llossera M et al (2011) Land geophysical parameters retrieval using the interference pattern GNSS-R technique. IEEE Trans Geosci Remote Sens 49(1):71–84. doi:10.1109/TGRS.2010.2049023
4. Cardellach E, Fabra F, Nogués-Correig O, Vall-llossera M et al (2011) GNSS-R ground-based and airborne campaigns for ocean, land, ice, and snow techniques: application to the GOLD-RTR data sets. Radio Sci 46:RS0C04. doi:10.1029/2011RS004683

5. Jin SG, Komjathy A (2010) GNSS reflectometry and remote sensing: new objectives and results. Adv Space Res 46(2):111–117. doi:10.1016/j.asr.2010.01.014
6. Marchán-Hernández JF, Camps A, Rodríguez-Álvarez N et al (2009) An efficient algorithm to the simulation of delay–Doppler maps of reflected global navigation satellite system signals. IEEE Trans Geosci Remote Sens 47(8):2733–2740
7. Valencia E, Camps A, Rodriguez-Alvarez N et al (2013) Using GNSS-R imaging of the ocean surface for oil slick detection. IEEE J Sel Top Appl Earth Obs Remote Sens 6(1):217–223
8. Masters D, Axelrad P, Katzberg S (2004) Initial results of land-reflected GPS bistatic radar soil moisture measurements in SMEX02. Remote Sens Environ 92:507–520
9. Liang P, Pierce LE, Moghaddam M (2005) Radiative transfer model for microwave bistatic scattering from forest canopies. IEEE Trans Geosci Remote Sens 43:2470–2483
10. Ulaby FT, Sarabandi K, McDonald K et al (1990) Michigan microwave canopy scattering model. Int J Remote Sens 11:1223–1253
11. Ulaby FT, Elachi C (1990) Radar polarimetry for geoscience applications. Artech House Publishers, Norwood, MA, USA
12. Ferrazzoli P, Guerriero L, Pierdicca N et al (2010) Forest biomass monitoring with GNSS-R: theoretical simulations. Adv Space Res doi:10.1016/j.asr.2010.04.02

Chapter 10
Ionospheric Anomalies During the March 2013 Geomagnetic Storm from BeiDou Navigation Satellite System (BDS) Observations

Rui Jin, Shuanggen Jin and Xuelin Tao

Abstract Earth's ionosphere disturbances triggered by the geomagnetic storm usually affect the propagation of radio electromagnetic wave. The mid-geomagnetic storm occurred in March 2013 with Dst index of up to −132 nT, which may disturb signal tracking and positioning results of Global Navigation Satellite Systems (GNSS). Unfortunately, LOS TEC series derived from GPS observations contain the ionospheric horizontal gradient information due to the satellites' movement. Geosynchronous Earth orbit (GEO) satellites of BeiDou navigation satellite system (BDS) give us an opportunity to detect ionospheric variations without horizontal gradient of electron density affection. In this paper, the Beidou stations' data provided by multi-GNSS experiments (MGEX) from IGS are the first time used to analyze the geomagnetic storm effects on Beidou navigation system (BDS) and ionospheric anomalous behaviors during 15–21 March 2013. The total electron content (TEC) variations are investigated during this geomagnetic storm using carrier phase measurements from BeiDou GEO satellites in B1 and B2. Dramatic TEC decrease is observed at the main storm and then increases gradually. Hourly TEC scintillation enhances greatly in the next hours of Storm Sudden Commencements (SSC). Although geomagnetic storm effect is global and regional, anomalies difference also can be detected by BDS-GEO TEC observations.

Keywords BDS · Total electron content · Geomagnetic storm · Ionospheric behaviors

R. Jin (✉)
Shanghai Astronomical Observatory, Chinese Academy of Sciences, Shanghai, China
e-mail: ruijin@shao.ac.cn

R. Jin · S. Jin
Graduate University of Chinese Academy of Sciences, Beijing, China
e-mail: sgjin@shao.ac.cn

X. Tao
School of Civil Engineering, Hefei University of Technology, Hefei, China

J. Sun et al. (eds.), *China Satellite Navigation Conference (CSNC) 2014 Proceedings: Volume I*, Lecture Notes in Electrical Engineering 303,
DOI: 10.1007/978-3-642-54737-9_10,

10.1 Introduction

As we know, Earth's ionosphere is dispersive medium. Phases and amplitudes of electro-magnetic wave will be disturbed during its propagation in the ionosphere. Basing on the refraction principles, the dual-frequencies observation of Global Navigation Satellite Systems (GNSS) can be used to monitor the Earth's ionosphere [1–3]. After the recent decades development, GNSS ionosphere monitoring has been become one of the most important GNSS applications. Comparing to traditional ionosphere detection, GNSS ionosphere monitoring has better temporal-spatial resolution. Up to now, GNSS ionosphere monitoring has two approaches through GNSS observations. One is the Earth's ionosphere total electron content (TEC) modelling from ground-based GNSS observations, another way is used by the space-borne GNSS radio occultation. Since 1998, International GNSS Services (IGS) has been continually providing Global TEC maps derived from global consciously operating GNSS stations' data [4, 5]. Regional TEC models with high temporal-spatial resolution has also been built up using GNSS dual-frequencies data with the advent of dense GNSS network, such as continuous GPS network in Japan (GEONET) [6]. The ground-based GNSS derived TEC models not only play an important role in error correction of GNSS positioning, navigation and timing (PNT), especially for single-frequencies users, but also are a reliable source for the study of large and middle scale ionospheric variations. What's more GNSS ionospheric TEC has been the important input of international reference ionosphere model (IRI) [7, 8]. The GNSS ionosphere study mainly focuses on anomaly analysis of TEC along the GNSS signal travelling light of sight (LOS), such as ionospheric effects of solar activities, geomagnetic storms, earthquakes, tsunami, ballistic missiles and some other natural and artificial events [9–13]. Most of GNSS TEC models used for ionospheric delay correction can work well during quiet days, while its precision will be decreased on disturbed days due to the ionospheric effects caused by the events mentioned above. Therefore, on one hand, GNSS ionospheric monitoring can improve ionospheric delay correction of electro-magnetic wave propagation. On the other hand, it has great potentials in disaster warning and space weather motoring.

Usually, the LOS TEC from GPS is used for small scale ionospheric anomaly and rapid change analysis. Unfortunately, LOS TEC series derived from GNSS observations contains the ionospheric horizontal gradient information due to the satellites' movement. It is difficult to divide the TEC variations at one pierce point accurately in Earth Centered Earth Fixed coordinate system (ECEF). Geosynchronous orbit (GEO) satellites of BDS give us an opportunity to detect ionospheric variations without horizontal gradient of electron density affection. In this paper, we analyze the rapid ionospheric behaviours and responses to the geomagnetic storm happened in March 2013 using BDS data from multi-GNSS experiment (MGEX). In Sect. 10.2, the sub-storm in March 2013 is introduced and BDS-GEO TEC estimates are given. Section 10.3 shows the ionospheric effects detected by BDS GEO observations during this geomagnetic storm. And Sect. 10.4 is the summary and conclusions.

10.2 Geomagnetic Storm in March 2013 and BDS-GEO TEC Monitoring

A moderate geomagnetic storm occurred in the middle of March in 2013. Figure 10.1 shows the Dst, AE and Ap index variation in March 2013. Dst and AE data is provided by World Data Center (WDC) for Geomagnetism, Kyoto (http://wdc.kugi.kyoto-u.ac.jp/). Dst index released by WDC is derived by the observations of geomagnetic field horizontal component H getting from magnetic observatories, Hermanus, Kakioka, Honolulu, and San Juan, which are located around the 20°S and 20°N where are sufficiently far from the auroral and equatorial electrojets. Dst index is a good indicator for the disturbance of mid-latitude and near-equatorial geomagnetic field. AE index is extracted from the magnetic field horizontal component observed by 10–13 magnetic observatories located in auroral zone in the northern hemisphere, which reflects the magnetic field variation in the auroral region as the result of electric currents flowing in the high-latitude ionosphere. Ap index presented in Fig. 10.1 is provided by GeoForschungsZentrum (GFZ) (http://www.gfz-potsdam.de/). Ap index is a linear scale from Kp index, which is derived from magnetic field horizontal field components observed by 13 subauroral magnetic stations. As shown in Fig. 10.1, the main disturbances of Dst, AE and Ap index appear on March 17. The Earth's magnetic field is disturbed dramatically in the near-equatorial, mid-latitude and auroral regions. The peak value of Dst index is up to −136 nT. This event is a moderate geomagnetic storm according to NOAA space weather scales.

Here we intend to use BDS-GEO TEC to analyze the ionospheric effects. Three MGEX BDS tracking stations are used (Table 10.1). All of these BDS stations have a good view for BDS GEO satellites.

The TEC along the signal propagation path can be derived from BDS dual-frequencies observations using Eq. (10.1). Here high-orders of refraction index and path differences in two bands are ignored [14].

$$TEC = \frac{f_1^2 f_2^2}{40.28\left(f_1^2 - f_2^2\right)}\left(L_1 - L_2 + const_L\right) = \frac{f_1^2 f_2^2}{40.28\left(f_2^2 - f_1^2\right)}\left(P_1 - P_2 - const_P\right) \tag{10.1}$$

where f stands for signal frequency, L and P stand for BDS carries phase and pseudorange measurements, $const_L$ and $const_P$ are constant items for one continuous observation arc, such as clock error, instrument biases, ambiguity (only for $const_L$) and multipath effects. Based on the thin shell ionosphere assumption, TEC can be converted to vertical TEC using the simple cosine mapping function as follow [15]:

$$vTEC = TEC * \cos\left(\arcsin\left(\frac{R\sin z}{R+H}\right)\right) \tag{10.2}$$

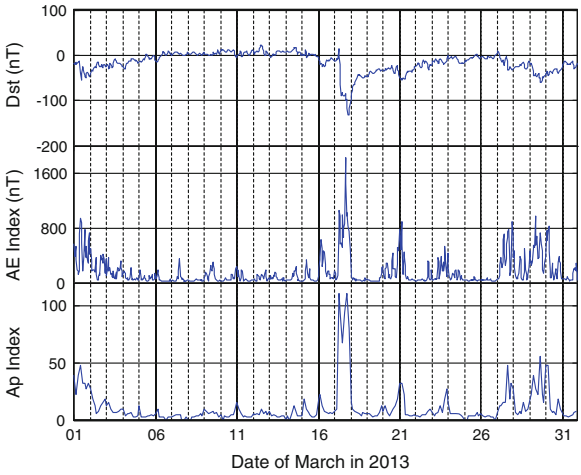

Fig. 10.1 Dst, AE and Ap index variations during March in 2013. The Dst and AE index data are provided by WDC center, while Ap index is provided by GFZ

Table 10.1 Basic information of the 3 chosen MGEX BDS stations

Station name	Latitude/°	Longitude/°	Height/m	Receiver	Country
cut0	−32.00	115.50	24.0	Trimble NetR9	Australia
gmsd	30.56	131.02	142.6	Trimble NetR9	Japan
jfng	30.52	114.49	71.3	Trimble NetR9	China

where R is the radius of Earth, z is zenith distance of signal path at the ionospheric pierce point, and H is the thin shell ionosphere height. Usually the height is set as 300–500 km that is the maximum electron density height of F2 layer. Here the height of 350 km is used. We use carrier phase observations to get TEC values because of its higher precision when compared to pseudorange observations. The relative location between BDS stations and BDS GEO satellites almost do not change. GEO satellites will be available permanently for BDS stations when the satellites and tracking stations are operating normally. For one continuous arc, the constant item in Eq. (10.1) will not change (ignore the measurement error of carrier phase observations). It can be removed by adding the difference between the TEC series derived from global ionosphere map (GIM). The ionospheric effects of moderate geomagnetic storm occurred in March 2013 will be analyzed using BDS-GEO TEC in next section.

10.3 Results and Discussion

Figure 10.2 shows the TEC time series derived from C01 (GEO-1) satellite's dual frequencies carrier phase observations on band B1 and B2 at MGEX cut0 station during the geomagnetic storm in March 2013. The location of cut0 station is shown in Table 10.1. BDS C01 is on the Earth-synchronous orbit with 140°E. The IPP is located at 29.7°S, 118.1°E. In quiet days, for one fixed point in ECEF, TEC values vary at about a constant with small floating amplitude at the same epoch of adjacent days. In general, one point TEC variation at same epoch of days is floating quasi-random around a constant in short period. So it is reasonable to use 2 times of standard deviation of previous 5 days corresponding TEC value as the anomaly threshold. When the TEC values are out of the 2 times standard deviation range, we thought the ionospheric anomaly occurs. As shown in Fig. 10.2 (left), the blue line is the upper boundary that is the sum of mean value and 2 times standard deviation of the same epoch observations of 5 days before the current day. And the red line is the lower boundary that is the difference of mean value and 2 times standard deviation. The boundary lines are incomplete during March 15–17, which is caused by lacking observation on corresponding epochs. The green line stands for the TEC variation from March 15 to March 21. The black dash line is the Storm Sudden Commencements (SSC) released by International Association of Geomagnetism and Aeronomy (IAGA). Dramatic TEC decrease can be found after the SSC and then increase gradually. This trend contains the effect of solar radio flux variation caused by Carrington rotation whose period is nearly 27 days. However it will not cause a sudden decease in normal condition. It is clear to see that the TEC value is out of the 2 times standard deviation from the SSC to the early of March 18. The difference of TEC values and its upper and lower threshold and the radio between the difference and mean values of pervious 5 days are shown on the right panel of Fig. 10.2. The negative anomalies can even be up to about 20 TECU, which is approximately 60 % of the mean value of previous days.

Figures 10.3 and 10.4 for stations gmsd and jfng are similar with Fig. 10.2. These two stations are almost located on the same latitude line. Their anomaly amplitude is similar with about 5 TECU (10–20 %). The anomalies mainly occur on 1–2 days after the SSC. Comparing to quasi conjunction IPP observed by cut0–C01, the anomaly amplitude is much smaller. In general, the ionospheric effects of geomagnetic storm in March 2013 is negative anomalies occurring on 1–2 days after the SSC, while the anomalies amplitudes is difference at different locations.

Figure 10.5 is the hourly standard deviation of the detrended TEC rate (TECU/min) at these three IPPs from March 15 to March 21. Comparing to the same time of pervious and next days, hourly TEC scintillation enhancement in the several hours after SSC can be seen, especially for IPP (29.8°S, 118.1°E) observed by cut0–C01. For IPP (29.8°S, 118.1°E), the enhancement starts from UT 8–20. For the other two IPPs, the enhancement is mainly occurring at UT 10–13.

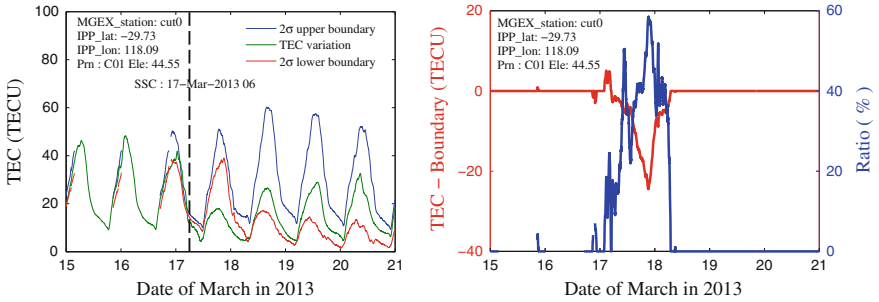

Fig. 10.2 TEC variation at MGEX station cut0 during the geomagnetic storm in March 2013. The *upper* and *lower* boundary is derived from the same epoch of 5 days observations before the event. The *black dash line* stands for storm sudden commencements provided by international service of geomagnetic indices

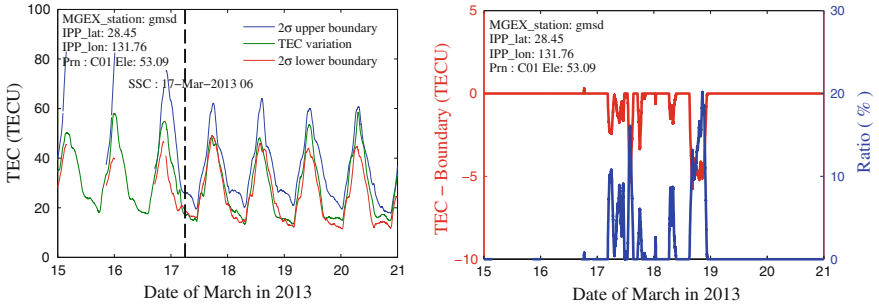

Fig. 10.3 MGEX station gmsd TEC anomalies during the geomagnetic storm in March 2013

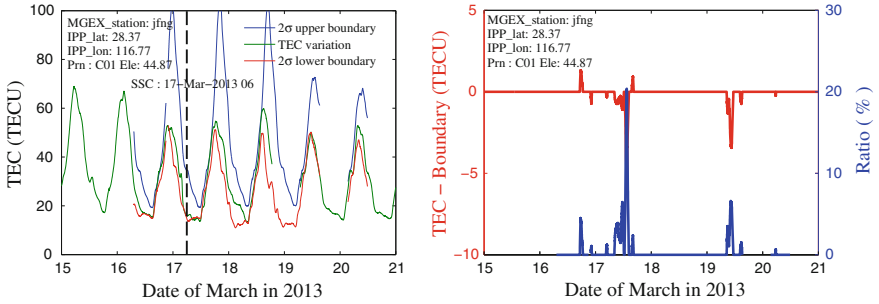

Fig. 10.4 MGEX station jfng absolute TEC variation during the geomagnetic storm in March 2013

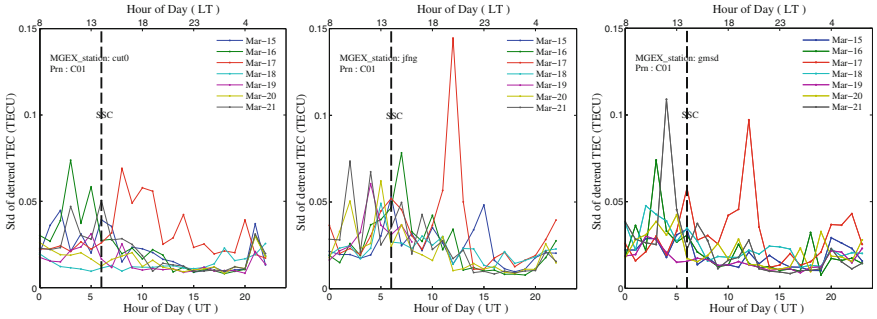

Fig. 10.5 Hourly standard deviation of the detrended TEC rate at MGEX statiosn cut0 (*left*), jfng (*middle*) and gmsd (*right*) with C01 (GEO-1). The *bottom* x-axis stands for the Universal Time (*UT*) while the *top* x-axis stands for local time corresponding to the IPP location

As shown in Fig. 10.5, during UT 1–6, the hourly standard deviation is higher than other periods and its difference between adjacent days is also much larger, which may be related to the local time variation.

10.4 Summary and Conclusions

This paper is the first time to use BDS-GEO observations to analyze the ionospheric effect of a moderate geomagnetic storm. Since the location of GEO satellites and the BDS tracking station in ECEF almost do not change, it provides us a unique opportunity to measure continuous TEC variations at one point without TEC horizontal gradient caused by IPP's variation. Three MGEX BDS stations cut0, gmsd and jfng are used to study the TEC variation in Asia/Pacific region during the storm. The results show that TEC values decrease dramatically after the SSC and increase gradually during the recovery phase of the storm. Obvious anomalies mainly occur during 1–2 days after the SSC, especially for the IPP (29.8°S, 118.1°E) whose negative anomalous peak value is even up to about 20 TECU on March 17. The anomaly amplitude is much difference at different latitudes. Not only the absolute TEC values are disturbed corresponding to the SSC, but also the hourly standard deviation of the rate of TEC is varied in the next hours of SSC.

As BDS is under construction without many continuous operating tracking stations up to now, BDS GEO TEC monitoring is just at beginning stage. However it has its own advantage for Earth's ionosphere sounding due to its quasi-persistent observation geometry. With the increase of the number of BDS tracking stations, more and more one point TEC series can be obtained with a high time resolution. BDS-GEO TEC monitoring will be greatly contribute to the Earth's ionosphere research, and even become a sensitive detector of ionospheric disturbance in Asia/Pacific region.

References

1. Hoffmann-Wellenhof B, Lichtenegger H, Collins J (1994) GPS: theory and practice, 3rd edn. Springer, New York
2. Jin SG, Luo O, Park P (2008) GPS observations of the ionospheric F2-layer behavior during the 20th November 2003 geomagnetic storm over South Korea. J Geodesy 82(12):883–892. doi:10.1007/s00190-008-0217-x
3. Jin SG, Wang J, Zhang H, Zhu WY (2004) Real-time monitoring and prediction of the total ionospheric electron content by means of GPS observations. Chin Astron Astrophys 28(3):331–337. doi:10.1016/j.chinastron.2004.07.008
4. Mannucci AJ, Wilson BD, Yuan DN, Ho CH, Lindqwister UJ, Runge TF (1998) A global mapping technique for GPS-derived ionospheric total electron content measurements. Radio Sci 33(3):565–582
5. Schaer S (1999) Mapping and predicting the Earth's ionosphere using the global positioning system. Geod-Geophys Arb Schweiz 59:59
6. Otsuka Y (2001) A new technique for mapping of total electron content using GPS network in Japan. Doctoral dissertation, Kyoto University
7. Hernández-Pajares M, Juan JM, Sanz J, Orus R, Garcia-Rigo A, Feltens J, Krankowski A (2009) The IGS VTEC maps: a reliable source of ionospheric information since 1998. J Geodesy 83(3–4):263–275
8. Bilitza D, McKinnell LA, Reinisch B, Fuller-Rowell T (2011) The international reference ionosphere today and in the future. J Geodesy 85(12):909–920
9. Liu JY, Lin CH, Chen YI, Lin YC, Fang TW, Chen CH, Hwang JJ (2006) Solar flare signatures of the ionospheric GPS total electron content. J Geophys Res: Space Phys 111(A5) (1978–2012)
10. Kumar S, Singh AK (2011) GPS derived ionospheric TEC response to geomagnetic storm on 24 August 2005 at Indian low latitude stations. Adv Space Res 47(4):710–717
11. Occhipinti G, Rolland L, Lognonné P, Watada S (2013) From Sumatra 2004 to Tohoku-Oki 2011: the systematic GPS detection of the ionospheric signature induced by tsunamigenic earthquakes. J Geophys Res Space Phys 118(6):3626–3636
12. Liu JY, Tsai YB, Ma KF, Chen YI, Tsai HF, Lin CH, Lee CP (2006) Ionospheric GPS total electron content (TEC) disturbances triggered by the 26 December 2004 Indian Ocean tsunami. J Geophys Res Space Phys 111(A5) (1978–2012)
13. Ozeki M, Heki K (2010) Ionospheric holes made by ballistic missiles from North Korea detected with a Japanese dense GPS array. J Geophys Res Space Phys 115(A9) (1978–2012)
14. Li ZH, Huang JS (2005) GPS surveying and data processing. Wuhan University Press, China, Wuhan (in Chinese)
15. Datta-Barua S, Walter T, Blanch J, Enge P (2008) Bounding higher-order ionosphere errors for the dual-frequency GPS user. Radio Sci 43(5)

Chapter 11
Earth Rotation Parameter Estimation from GNSS and Its Impact on Aircraft Orbit Determination

Lihua Wan, Erhu Wei and Shuanggen Jin

Abstract Earth rotation parameters (ERP) play a key role in connecting the International Celestial Reference Frame (ICRF) and the International Terrestrial Reference Frame (ITRF). Furthermore, high precision orbit determination and positioning need the precise ERPs, while ERPs are closely related the geophysical fliud mass redistribution and geodynamics. In this paper, global uniformly distributed 75 IGS stations with more than 60 sites tracking GPS+GLONASS simultaneously are selected to estimate Earth Rotation Parameters. Accuracy and method to improve ERP from only IGS stations in and neighboring China are also analyzed in order to provide the reference for BeiDou ERP estimation. The results show that the precision of Polar motion (PM) estimated from daily GPS and GLONASS observations can be achieve at the precision of 0.066 and 0.157 mas, respectively and the precision of length of day (LOD) can achieve at 0.0283 and 0.0289 ms when compared to IERS C04 solutions, respectively. The precision of PM and LOD from regional stations with daily GPS (GLONASS) observations are better than 0.178 mas (0.365 mas) and 0.0291 ms (0.0360 ms), respectively. The precision of PM and LOD from combined GPS+GLONASS are better than 0.153 mas and 0.0292 ms. In addition, the impact of ERP error on aircraft orbit is

L. Wan (✉) · E. Wei
School of Geodesy and Geomatics, Wuhan University, Wuhan 430079 Hubei, China
e-mail: lh.wan@whu.edu.cn

E. Wei
Key Laboratory of Geospace Environment and Geodesy, Ministry of Education, Wuhan 430079 Hubei, China
e-mail: ehwei@whu.edu.cn

S. Jin
Shanghai Astronomical Observatory, Chinese Academy of Sciences, Shanghai 200030, China
e-mail: sgjin@shao.ac.cn

J. Sun et al. (eds.), *China Satellite Navigation Conference (CSNC) 2014 Proceedings: Volume I*, Lecture Notes in Electrical Engineering 303,
DOI: 10.1007/978-3-642-54737-9_11,

furthermore discussed. The impact on the LOD is greater than the PM. The orbital error can respectively reach 1, 1 and 0.1 m in X, Y and Z direction with 0.5 mas error in PM and 0.5 ms error in LOD.

Keywords ERP · GNSS · Aircraft orbit · Variance components estimation

11.1 Introduction

Earth Rotation Parameters (ERPs) consist of Polar motion and Length of Day as well as Precession and Nutation, which play a key role in the transformation between ICRF and ITRF. Up to now, several Precession and Nutation Model have been built, e.g. IAU1976 precession, IAU 1980 Nutation, IAU 2000, IAU 2000A and IAU 2006. With the accumulation of more geodetic observation data and the improvement of measurement precision, the new precession and nutation model will be constructed with higher precision. The accuracy of the coefficient of IAU 2006 model is achieved with up to 1 μas at J2000.0 [1], which is good enough to realize high precision of coordinate transformation, so ERPs of Polar motion and Length of Day are the most important parameters to limit the current accuracy of conversion between the two coordinate frames.

The first international organization that aimed at determining ERPs is International Latitude Service (ILS), which renamed International Polar Motion Service (IPMS) later. However, due to the limitation of classic optical technologies and instruments, the accuracy of polar motion was about 1 meter. International Time Bureau (BIH) used the Doppler observation data in 1972 and the accuracy was improved to 50 cm [2]. Later the Very Long Baseline Interferometry (VLBI) and Satellite Laser Range (SLR) techniques were used gradually to determined ERP and the relevant precision was improved to 10–20 cm. In 1988, IPMS was replaced by International Earth Rotation Service (IERS) that brought GPS observation to calculate ERP in 1994. Up to now, IERS has used the VLBI, LLR (Lunar Laser Ranging), SLR, GPS and DORIS (Doppler Orbitography by Radiopositioning Integrated on Satellite) observation data to estimate ERPs with a precision of sub-centimeter [3]. A number of estimates and studies on ERP have been conducted from different technologies such as GPS, VLBI, SLR [4–6]. With the development of Global Navigation Satellite Systems (GNSS), the number of International GNSS Service (IGS) tracking stations is increased rapidly. As a result, we have massive GNSS observation data that make possible to calculate ERPs with high precision and high temporal resolution [7]. This paper mainly uses observation data from global uniformly distributed GPS and GLONASS stations to determine ERPs, which are assessed with comparing to the IERS C04 solutions. Furthermore, the impact of ERP errors on aircraft orbit is analyzed and discussed. In addition, ERPs are determined by GNSS data only from regional IGS tracking stations in China and its surrounding areas. Method to improve the precision of

ERP calculated by only regional GPS data is also analyzed in order to test ERP estimate with BeiDou regional navigation system with a limited tracking stations at this stage.

11.2 Principle of ERP Determination and Its Impact on Orbit

11.2.1 Principle of ERP Determination

As it is well known, the observation equation of GNSS satellites is related to the polar motion and rotation, so the ERPs can be determined using GNSS observation. The vector of observation ($\vec{\rho}$) from station to satellite can be expressed by the state vector of satellite ($\vec{r}$) and the position vector of station P ($\vec{r}_P$) in the celestial reference system as follows [8, 9]:

$$\vec{\rho} = f(\vec{r}, \dot{\vec{r}}, \vec{r}_P) \tag{11.1}$$

where $\dot{\vec{r}}$ is the derivative of $\vec{r}$. The vector $\vec{r}_P$ in the inertial coordinate system thus can be expressed by the position vector $\vec{r}_{P0}$ of station in the terrestrial reference system as:

$$\vec{r}_P = PNRW\,\vec{r}_{P0} = P(t)R_1(\Delta\varepsilon)R_2(-\Delta\psi\sin\varepsilon_0)R_3(-\theta_{GM})R_1(y_p)R_2(x_p) \tag{11.2}$$

where P, N, R and W are the matrix of precession, nutation, earth rotation and polar motion, respectively. The parameters of polar motion (x_p, y_p) and LOD (replaced by Earth rotation angle θ) are included in the matrix W and R, respectively. $\Delta\varepsilon$ and $\Delta\psi$ are precession and nutation. Linearized to one order, Eq. (11.1) can be rewritten as:

$$\begin{aligned}\vec{\rho} &= f(\vec{r}, \dot{\vec{r}}, \vec{r}_P) = f_0(\vec{r}, \dot{\vec{r}}, \vec{r}_p) + \frac{\partial f}{\partial x_p}x_p + \frac{\partial f}{\partial y_p}y_p + \frac{\partial f}{\partial \theta}\theta \\ &= f_0(\vec{r}, \dot{\vec{r}}, \vec{r}) + \frac{\partial f}{\partial \vec{r}_p}\frac{\partial \vec{r}_P}{\partial x_p}x_p + \frac{\partial f}{\partial \vec{r}_p}\frac{\partial \vec{r}_P}{\partial y_p}y_p + \frac{\partial f}{\partial \vec{r}_p}\frac{\partial \vec{r}_P}{\partial \theta}\theta\end{aligned} \tag{11.3}$$

where $f_0(\vec{r}, \dot{\vec{r}}, \vec{r})$ is the approximate value calculated by initial ERPs and $\partial f/\partial \vec{r}_p$ is related to the type of observation and expressed by Eq. (11.2). Ignoring the micro items, $\frac{\partial \vec{r}_P}{\partial x_p}$, $\frac{\partial \vec{r}_P}{\partial y_p}$ and $\frac{\partial \vec{r}_P}{\partial \theta}$ can be deduced according to Eq. (11.2) as follows:

$$\frac{\partial f}{\partial \vec{r}_p} = \frac{\vec{r} - \vec{r}_p}{\vec{\rho}} \tag{11.4}$$

$$\frac{\partial \vec{r}_P}{\partial x_p} = PNR\frac{\partial W}{\partial x_p}\vec{r}_{P0} = PNRW\begin{pmatrix} -z \\ 0 \\ x \end{pmatrix} \tag{11.5}$$

$$\frac{\partial \vec{r}_P}{\partial y_p} = PNR\frac{\partial W}{\partial y_p}\vec{r}_{P0} = PNRW\begin{pmatrix} -x_p y \\ x_p x + z \\ -y \end{pmatrix} \tag{11.6}$$

$$\frac{\partial \vec{r}_P}{\partial \theta} = \frac{\partial \vec{r}_P}{\partial \theta_g}\frac{\partial \theta_g}{\partial \theta} = PN\frac{\partial R}{\partial \theta_g}W\vec{r}_{P0}\frac{\partial \theta_g}{\partial \theta} = 2\pi(1+k)(t-t_0)PNRW\begin{pmatrix} -y - y_p z \\ x - x_p z \\ y_p x + x_p y \end{pmatrix} \tag{11.7}$$

where θ_g is the Greenwich Apparent Sidereal Time (GAST) and can be expressed as:

$$\theta_g = GAST = 2\pi[GMST(UT0) + (1+k)UT1] + \Delta\psi\cos\xi \tag{11.8}$$

$$\begin{aligned} GMST(UT0) = {} & (24110.54841 + 8640184.812866T + 0.093104T^2 \\ & - 6.2\times 10^{-6}T^3)/86400 \end{aligned} \tag{11.9}$$

$$UT1 = UTC + (UT1 - UTC)_0 + \theta(t - t_0) \tag{11.10}$$

The T is the Julian century of observation epoch. $(1+k)$ can be calculated at a given T. $(UT1 - UTC)_0$ is the value of $(UT1 - UTC)$ at epoch t_o. Assuming n satellites with observing by m stations and substituting Eq. (11.4)–(11.7) into Eq. (11.3), we can acquire the error equation set as:

$$\underset{m\times n,1}{V} = \underset{m\times n,3}{B}\ \underset{3,1}{X} - \underset{m\times n,1}{l} \qquad \underset{m\times n,m\times n}{P} \tag{11.11}$$

where P is the matrix of weight and other items are expressed as follow:

$$\underset{m\times n,3}{B} = \begin{pmatrix} \frac{\partial f_1^1}{\partial x_p} & \frac{\partial f_1^1}{\partial y_p} & \frac{\partial f_1^1}{\partial \theta} \\ \cdots & \cdots & \cdots \\ \frac{\partial f_i^j}{\partial x_p} & \frac{\partial f_i^j}{\partial y_p} & \frac{\partial f_i^j}{\partial \theta} \\ \cdots & \cdots & \cdots \\ \frac{\partial f_m^n}{\partial x_p} & \frac{\partial f_m^n}{\partial y_p} & \frac{\partial f_m^n}{\partial \theta} \end{pmatrix},\ \underset{m\times n,1}{l} = \begin{pmatrix} \vec{\rho}_1^1 - f_1^1(\vec{r},\dot{\vec{r}},\vec{r}) \\ \cdots \\ \vec{\rho}_i^j - f_i^j(\vec{r},\dot{\vec{r}},\vec{r}) \\ \cdots \\ \vec{\rho}_m^n - f_m^n(\vec{r},\dot{\vec{r}},\vec{r}) \end{pmatrix},\ \underset{m\times n,1}{v} = \begin{pmatrix} v_1^1 \\ v_1^2 \\ v_i^j \\ \cdots \\ v_m^n \end{pmatrix},\ \underset{3,1}{X} = \begin{pmatrix} x_p \\ y_p \\ \theta \end{pmatrix}.$$

Thus according to least-square method, we can determine the value of ERP and assess its precision:

$$X = \left(B^T P B\right)^{-1}\left(B^T P l\right) = \left(\sum_{i=1}^{i=k} B_i^T P_i B_i\right)^{-1}\sum_{i=1}^{i=k} B_i^T P_i l_i \tag{11.12}$$

$$Q = \sigma_0^2\left(\sum_{i=1}^{i=k} B_i^T P_i B_i\right)^{-1} \tag{11.13}$$

$$\sigma_0^2 = \frac{V^T V}{n-t} \tag{11.14}$$

where $(n-t)$, V, σ_0 and Q are the degree of freedom, residual error, unit weighted variance and coefficient matrix, respectively.

11.2.2 Impact of ERP on Orbit Determination

Geocentric Celestial Reference System (GCRS) is a good quasi-inertial reference frame with its axis fixed, so the orbits of the satellites or spacecraft are estimated in the coordinate system. And then coordinates of satellites are converted to the International Terrestrial Reference System (ITRS) using the Earth Orientation Parameters. The transformation equation can be expressed as Eq. (11.2). Transformation matrix P and N can be calculated according to IAU2000A model with a maximum error less than 0.2 μas [10], which equals to 2.6 cm for navigation satellite orbit. So the orbital errors caused by nutation error and precession error are often ignored. However, the orbital error caused by the changes in polar motion and length of day may reach tens of centimeters or even meters which should be considered in the determination of aircraft orbit or autonomous navigation. Omitting complicated derivation, Eq. (11.15) can represent the orbital error affected by ERP errors. More information can be referred to [11, 12].

$$\begin{bmatrix} \Delta X \\ \Delta Y \\ \Delta Z \end{bmatrix} = \begin{bmatrix} Y'_S \cdot \Delta\theta + Z'_S \cdot \Delta X_p \\ -X'_S \cdot \Delta\theta - Z'_S \cdot \Delta Y_p \\ -X'_p \cdot Y'_S \cdot \Delta\theta - Y'_p \cdot X'_S \cdot \Delta\theta - X'_S \cdot \Delta X_p + Y'_S \cdot \Delta Y_p \end{bmatrix} = \begin{bmatrix} Y'_S \cdot \Delta\theta + Z'_S \cdot \Delta X_p \\ -X'_S \cdot \Delta\theta - Z'_S \cdot \Delta Y_p \\ -X'_S \cdot \Delta X_p + Y'_S \cdot \Delta Y_p \end{bmatrix} \tag{11.15}$$

where ΔX_p, ΔY_p and $\Delta\theta$ are the error in polar motion and the error in Earth rotation angel calculated by LOD. $(X'_s,\ Y'_s,\ Z'_s)$ represents the coordinate of satellite in inertial system. $X'_p \cdot \Delta\theta$ and $Y'_p \cdot \Delta\theta$ are micro items which can be ignored.

11.3 GNSS Data Processing and Result

11.3.1 ERP Determination from Global Distribution GNSS Stations

In this paper, 75 IGS tracking stations with global uniform distribution are selected and more than 60 stations can track both GPS and GLONASS. ERPs are determined for 60 days (January 1 to March 1, 2013) using GPS and GLONASS

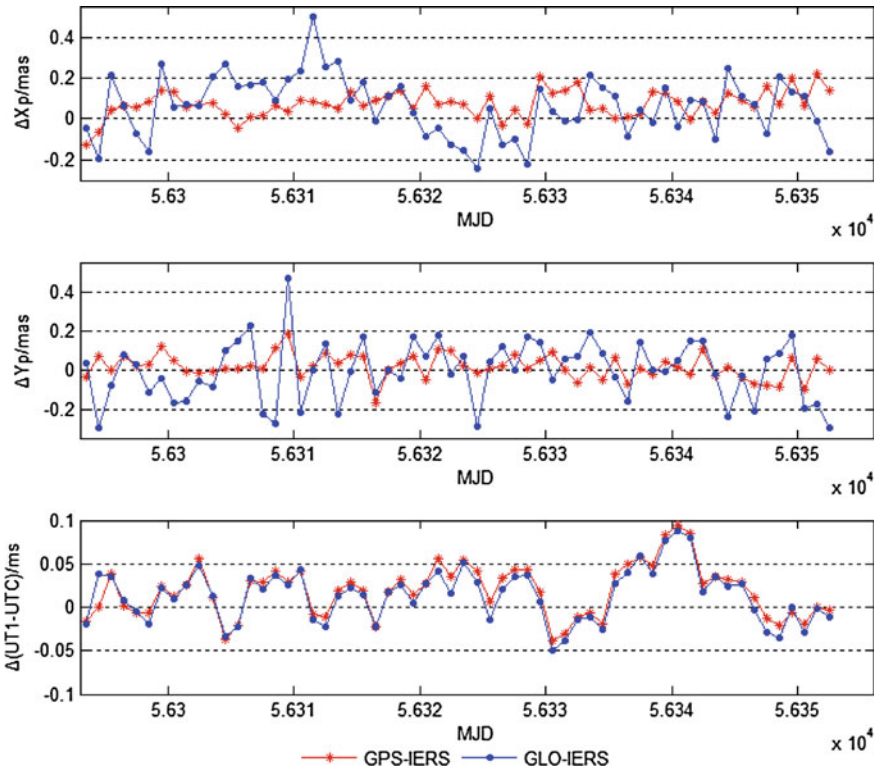

Fig. 11.1 Differences of global experiment results w.r.t IERS C04 solutions

Table 11.1 Statistics results of global GNSS estimated ERPs w.r.t IERS C04

	Polar motion in X/mas		Polar motion in Y/mas		Length of day/ms	
	|Max|	STD	|Max|	STD	|Max|	STD
GPS	0.2172	0.0655	0.1877	0.0627	0.0946	0.0283
GLONASS	0.5017	0.1473	0.4777	0.1571	0.0886	0.0289

observations. Double-difference mode from Bernese GPS Software is chosen during the data processing with strong constraint of orbit elements and solar pressure. Apart from ERPs, troposphere parameters, stations coordinates and clock error are estimated simultaneously. Other models or strategies are used, including the quasi ionosphere free (QIF), IAU 2000 Precession/Nutation, IERS 2000 sub-daily polar model, OT_CSRC ocean tide file, FES2004 ocean loading correction. Differences of experiment results with respect to IERS C04 solutions at the same time (UTC 12:00:00) are showed in Fig. 11.1. Table 11.1 gives the precision statistic results.

According to the results, it is clear to see that ERPs estimated from GPS observations are much better than those from GLONASS observations in polar motion. The two results are compared with IERS C04. The standard deviations are 0.065 mas and 0.150 mas, respectively. However, the two results present a certain relationship with a similar trend and their precisions are the same in LOD (0.0283 ms and 0.0289 ms). Due to correlations with the orbital elements, LOD is not directly connected to GNSS observations. But it's possible to estimate the drift in UT1-UTC through adding a constant value to UT1 and adapting the ascending nodes of the satellite orbits by a corresponding value without affecting the ranges between stations and satellites [13]. In addition, satellites orbits are fixed with the precise ephemeris from IGS products and we chose the same baselines during processing the GPS and GLONASS data, which may be responsible for the correlation between the two results in LOD.

11.3.2 ERPs Estimated from Regional Distribution Stations

In order to analyze the accuracy of ERP from regional distribution stations, 18 stations in China and its surrounding areas are chosen for testing (from Jan 1 to May 31). These stations are bjfs, bjnm, chan, guao, kunm, lhaz, shao, tnml, twtf, urum, wuhn, alic (Australia), hyde (India), kit3 (Uzbekistan), nuts (Singapore), pert (Australia), pimo (Philippines), ulab (Mongolia). The results from regional GPS observations are compared to IERS C04, and the differences are shown in Fig. 11.2.

ERPs are also estimated from regional 11 stations with simultaneously tracking GLONASS (bjfs, bjnm, lhaz, urum, wuhn, alic, hyde, kit3, nuts, pert, ulab). In addition, variance components estimation is used to estimate ERPs from combined GPS+GLONASS observation. Results are compared to the IERS C04 and the differences are shown in Fig. 11.2. Table 11.2 gives the precision statistic of the results from regional observation.

The results show the precision of ERPs from regional stations is lower than that from global stations, especially in polar motion. It's not only related to the number of stations, but also the distribution of stations plays a important role. However, the ERP has been improved dramatically by combined GPS and GLONASS. The combined results has been improved by 15.9 % (x_p), 13.6 % (y_p) and 0.0 % (LOD) when compared to the result from only GPS. It's more significant when compared to the result from GLONASS with 51.5 % (x_p), 58.1 % (y_p) and 19.7 % (LOD). So we can conclude that combined method improves the ERP precision with respect to both GPS and GLONASS alone, which is a good reference when estimating ERPs from regional BDS navigation system observations.

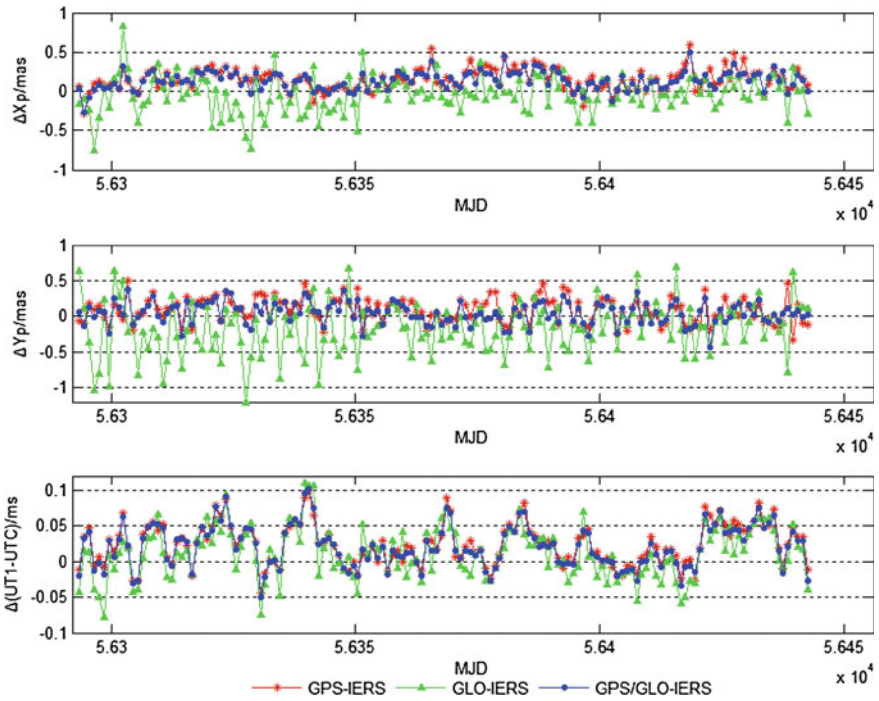

Fig. 11.2 Differences of regional experiment results w.r.t IERS C04 solutions

Table 11.2 Statistics result of regional experiment estimate w.r.t IERS C04

	Polar motion in X/mas		Polar motion in Y/mas		Length of day/ms	
	|Max|	STD	|Max|	STD	|Max|	STD
GPS	0.5945	0.1356	0.4928	0.1775	0.1006	0.0291
GLONASS	0.8331	0.2350	1.2101	0.3651	0.1109	0.0361
GPS+GLONASS	0.4954	0.1140	0.4421	0.1529	0.1016	0.0292

11.3.3 Impact of ERP Error on Aircraft Orbit Determination

In order to analyze the impact of ERP error on aircraft orbit, ERP values of different precision are used to determinate the orbit of aircraft. Because the impacts from ERP are mainly reflected in the coordinates transformation between ICRF and ITRF, so this paper main focus on this session. Figure 11.3 shows the orbital error of GPS satellites with 0.5 mas error in polar motion and 0.5 ms error in LOD with respect to precise ephemeris from IGS products on September 1, 2013. As shown in Fig. 11.3, ERP has more impact on X and Y direction than Z direction. Although the maximum error is less than 10 cm in Z direction, the error in X and Y direction can reaches to 100 cm. In addition, the orbit is more easily affected by LOD than

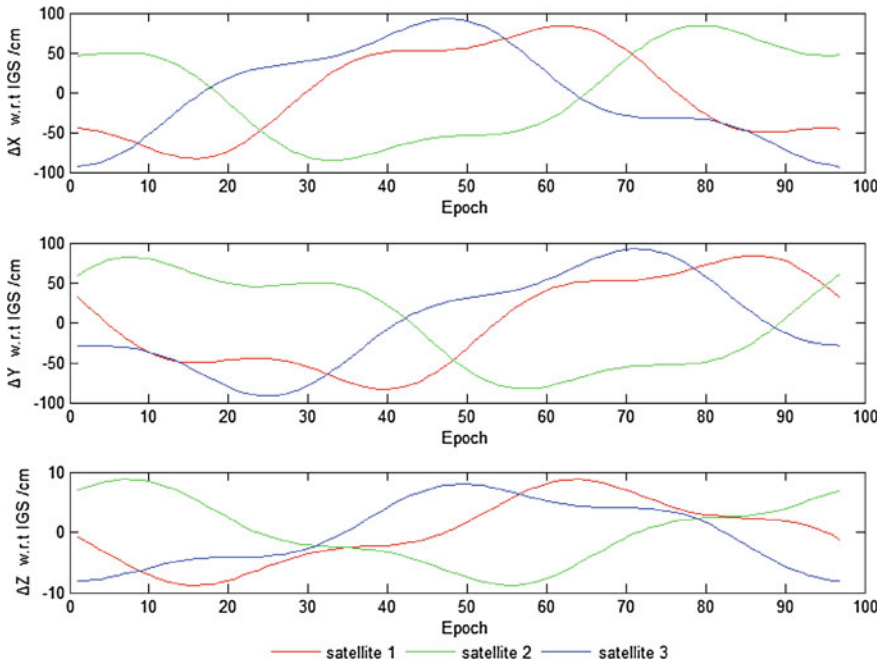

Fig. 11.3 Errors of orbits due to the effect of ERP error

polar motion which can be interpreted by Eq. (11.15). Because the orbit errors in X and Y direction are caused by LOD and polar motion parameters, however, the orbit error in Z direction is caused only by polar motion parameters. According to the further study, in order to satisfy requirement of centimeter-level accuracy for navigation satellite orbit determination, the error in polar motion should be less than 0.05 mas and error in LOD must be less than 0.01 ms, and the orbit error will be less than 2 cm in every X, Y or Z direction in this case.

11.4 Conclusions

Continuous GNSS observations can be used to estimate the ERPs of high precision and high temporal resolution. In this paper, ERP are estimated using GNSS observation in different cases and some conclusions can be drawn.

1. Precision of polar motion can be improved dramatically with more stations and better distribution of stations. However, precision of LOD can't be improved much only by increasing the number of stations.
2. Due to correlation with the orbital elements, LOD is not directly related to GNSS observations. But UT1-UTC can be acquired by adding a constant to UT1 with a certain correlation.

3. Precision of ERPs estimated from regional GNSS stations is relatively low but can be improved by combined multi-system observations. Combined GPS+GLONASS results in polar motion are improved by 15 % with respect to GPS alone and by 50 % with respect to GLONASS alone.
4. LOD has more effects on satellite orbit than polar motion. In order to satisfy requirement of centimeter-level accuracy for orbit determination of navigation satellite, the error in polar motion should be less than 0.05 mas and the error in LOD must be less than 0.01 ms.

References

1. Li ZHH, Wei EH, Peng BB et al (2010) Space geodesy. Wuhan University Press, Wuhan
2. Zhao M, Gu ZN (1986) Comparison and comment on the techniques for determining ERP. Acta Astron Sin 27:181
3. Zhu YL, Feng CG, Zhang FP (2006) Earth orientation parameter solved by lageos Chinese SLR data. Acta Astron Sin 47:441–449
4. Wang Q, Dang Y, Xu T (2013) The method of earth rotation parameter determination using GNSS observations and precision analysis. In: Proceedings of the China Satellite Navigation Conference (CSNC). Springer, Berlin, pp 247–256
5. Wei EH, Li XC, Yi H et al (2010) On EOP parameters based on 2008 VLBI observation data. Geomatics Inf Sci Wuhan Univ 35(8):988–990
6. Zhu YL, Feng CG (2005) Earth orientation parameter and the geocentric variance during 1993–2002 solved with Lageos SLR data. Cehui Xuebao/Acta Geod et Cartographica Sin 34(1):19–23
7. Rothacher M, Beutler G, Weber R et al (2001) High frequency variations in earth rotation from global positioning system data. J Geophys Res Solid Earth (1978–2012) 106(B7):13711–13738
8. Xu G (2007) GPS: theory, algorithms, and applications. Springer, Berlin Heidelberg
9. Yang ZHK, Yang XH, Li ZHG et al (2010) Estimation of earth rotation parameters by GPS observations. J Time Freq 33(001):69–76
10. McCarthy DD, Petit G (2004) IERS conventions (2003). International Earth Rotation and Reference Systems Service (IERS), Germany
11. Li ZHH, Gong XY, Liu WK et al (2011) Correction of earth rotation parameters in AOD of navigation satellites. China Satellite Navigation Conference (CSNC)
12. Cao F, Yang XG, Li ZG et al (2011) The effect of earth rotation parameters on geostationary satellite. China Satellite Navigation Conference (CSNC)
13. Dach R, Hugentobler U, Fridez P et al (2007) Bernese GPS software version 5.0. Astronomical Institute, University of Bern, p 640

Chapter 12
Fusion Positioning of BDS/GPS Based on Variance Component Estimation and Its Application for Geodetic Control Network

Yifan Jing, Anmin Zeng and Tianhe Xu

Abstract Beidou Satellite Navigation System (BDS), developed by China, is an independent satellite navigation system, which is recognized as one of the four major Global Navigation Satellite System (GNSS) in the world. Now, BDS has a constellation of fourteen navigation satellites and the regional satellite navigation system of BDS has been constructed. The system can provide high quality services in China and its surrounding areas, and is extending into global. In this paper, the current status of BDS and GPS is introduced at first. And then, the algorithm of high precision fusion positioning with combination of BDS and GPS is studied based on variance component estimation. Finally, a GNSS geodetic control network is performed as an example, which contains eight points with corresponding baselines ranged from 40 to 200 km. It is proved that, combining BDS and GPS data can present better results than that of any single navigation system using the proposed algorithm and the accuracies of position are better than 1 cm.

Keywords BDS · Fusion positioning · Variance component estimate · Geodetic control network

Y. Jing (✉)
Institute of Navigation and Aerospace Engineering, Information Engineering University, No. 62 Kexue Street, Zhengzhou 450001, Henan, China
e-mail: jing_yi_fan@163.com

A. Zeng
Institute of Surveying and Mapping, Information Engineering University, No. 62 Kexue Street, Zhengzhou 450001, Henan, China

A. Zeng · T. Xu
Xi'an Research Institute of Surveying and Mapping, No. 1 Yanta Road, Xi'an 710054, Shanxi, China

A. Zeng · T. Xu
State Key Laboratory of Geo-information Engineering, No. 1 Yanta Road, Xi'an 710054, Shanxi, China

J. Sun et al. (eds.), *China Satellite Navigation Conference (CSNC) 2014 Proceedings: Volume I*, Lecture Notes in Electrical Engineering 303,
DOI: 10.1007/978-3-642-54737-9_12,

12.1 Introduction

Beidou Satellite Navigation System (BDS) as one of the four Global Navigation Satellite Systems (GNSS) in the world, developed by China independently, is recognized as the third satellite navigation system that can provide positioning service, besides GPS (USA) and GLONASS (Russian). At present, BDS is available for users in China and its surroundings to access to high quality services for positioning, navigating, timing and short message communication. The point-positioning precision of BDS has basically reached the same level as GPS [1].

The same problem that influences the precision of positioning and navigation for every GNSS, including BDS, is the number of visible satellites. It is inevitable in application when no enough visible satellites can be available due to the limitation of constellations. Therefore, using more navigation satellites and realizing multi-GNSS data fusion is urgent. It is very significant to study on fusion positioning of BDS/GPS for enhancing the positioning precision in China and promoting the application of BDS.

In terms of multi-GNSS data fusion, there are many studies especially in the combination of GPS and GLONASS [2, 3]. With the development of BDS, a lot of related experiments and researches come out [1, 4–6]. Most of them are focused on applications in relative positioning under single and short baseline mode. Yet, there is no result reported on BDS/GPS geodetic control networks with middle and long baselines.

In the field of geodetic data fusion, many achievements in theory and application have been made [7]. These studies mainly focus on kinematic multi-sensor navigation systems, such as integrated navigation system based on federated filter [8], adaptive integrated navigation based on static and dynamic filter [9] and integrated navigation by using variance component estimation of multi-sensor measurements [10].

In this paper, our main aim is to test the positioning performance of BDS under current constellation and the performance of BDS/GPS fusion positioning in geodetic control networks. Status of BDS and GPS is introduced and compared at first, and then two types of BDS and GPS fusion models are presented. The fusion algorithm based on variance component estimation is given in details and a practical GNSS network is performed as an example to verify the validation of the proposed algorithm. Finally, some analysis and summary are given.

12.2 Comparisons Between BDS and GPS

GPS is the second generation of the U.S. satellite navigation system and it is the most widely used system in the world. With the increasing development of the satellite navigation industry, many countries have developed their own systems (including global system and regional system). GPS is no longer the only choice

for users and its application market is facing a huge challenge. To maintain its dominant position, U.S. government began to modernize GPS in the 1990s, which include the following main measures: cancelling Selective Availability (SA) policies, increasing civil signals, and launching new-generation satellites [11]. The accuracy of civilian GPS navigation and positioning service already has a great improvement, and its quality will become better and better along with the process of modernization.

Chinese satellite navigation system, known as BDS, is developing rapidly. According to the three-step development strategy [12], the verification system (Beidou I) and the regional satellite navigation system (first stage of Beidou II) has been completed. The global satellite navigation system (second stage of Beidou II) is being constructed. Currently, five geostationary earth orbit (GEO) satellites, five inclined geostationary earth orbit (IGSO) satellites and four medium earth orbit (MEO) satellites are working in orbits of BDS. The system already has capabilities in precise positioning and navigation and will be improved in the construction process further. Meanwhile, it is proved by simulation experiments that the amounts of visible satellites for GNSS users will increase by 50 % when the final BDS constellation with 35 satellites is completed, which will have a great contribution to the quality of global PNT (Positioning, Navigation and Timing) service [13].

Characteristics of BDS and GPS are compared in Table 12.1 [14, 15].

12.3 Methods of BDS/GPS Fusion Positioning

The combination of BDS and GPS can be divided into two modes [7, 16]: one is a combination based on the original observations and the other is based on the baseline solution.

12.3.1 Fusion on the Original Observation Level

The algorithm that realizes BDS/GPS fusion on the original observation level is similar to the one used in a single system. The observation equations of pseudo range and carrier phase need to be extended to form total equations that contain observations of BDS and GPS. And then, error equations, normal equation and solutions will be gained based on the principle of least squares.

The basic normal equation can be described as [4]

$$\begin{bmatrix} \Delta \boldsymbol{a}^B & \boldsymbol{b}^B & \boldsymbol{0} \\ \Delta \boldsymbol{a}^G & \boldsymbol{0} & \boldsymbol{b}^G \end{bmatrix} \begin{bmatrix} d\boldsymbol{X} \\ \Delta\nabla \boldsymbol{N}^B \\ \Delta\nabla \boldsymbol{N}^G \end{bmatrix} = \begin{bmatrix} \Delta\nabla \boldsymbol{L}^B \\ \Delta\nabla \boldsymbol{L}^G \end{bmatrix} \tag{12.1}$$

Table 12.1 Comparisons of characteristics between BDS and GPS

	GPS	BDS (under construction)
Constellation	24MEO	27MEO+3IGSO+5GEO
Orbit number	6	3 (MEO)
Orbit altitude	20,200 km	21,528 km (MEO) 35,786 km (IGSO) 35,786 km (GEO)
Orbit inclination	55°	55° (MEO, IGSO)
Cycle	11 h 58 min	12 h 50 min
Carrier frequency	L1:1,575.42 MHz L2:1,227.60 MHz L5:1,176.45 MHz	B1:1,561.09 MHz B1-2:1,589.74 MHz B2:1,207.14 MHz
Communication system	CDMA	CDMA
Time system	GPST	BDT
Coordinate system	WGS-84	CGCS2000

where B and G represent BDS and GPS; $d\boldsymbol{X}$ is the coordinate correction; Δ is the single-difference operator and $\Delta\nabla$ is double-difference operator; $\boldsymbol{N}$ is the integer ambiguity vector; $\boldsymbol{L}$ is the observation vector; $\boldsymbol{a}$ and $\boldsymbol{b}$ is coefficient matrix corresponding to $d\boldsymbol{X}$ and $\Delta\nabla\boldsymbol{N}$.

Fusion methods based on original observation can make good use of data from the two systems and it is effective to eliminate the ionosphere delay using different frequency data. The difficulty and key issue of the method is how to unify coordinate and time datum to achieve the conversion of CGCS2000 and WGS84, and the conversion of BDT and GPST [3]. In addition, problems of weighting for different system observations need to be considered.

12.3.2 Fusion on the Baseline Solution Level

The step of fusion algorithm based on baselines is as following: BDS and GPS make their own baseline solutions and then they are regarded as virtual observations to build a new error equation. The process is essentially combined using co-adjustments of BDS and GPS.

Compared to fusion of original observations, the fusion of baseline solutions is easier without coordinate transformation between BDS and GPS. The reason is that CGCS2000 and WGS-84 can be maintained at a consistent of several centimetre levels [17], this difference can be ignored in the fusion of baseline solutions. In this mode, the main contribution of multi observation data on positioning is improved and it is useful in geodetic control networks.

Weight determination of baseline solutions of BDS and GPS is similar to that when fusing various geodetic observations [7, 18]. There are many related algorithms in which the most commonly used one is based on variance component

estimation. Since the precision of BDS and GPS data is different, in such case, adjusting variance factors by variance component estimation is effective for balancing the contribution of different type observation on navigation and positioning.

12.4 BDS/GPS Fusion Positioning Based on Variance Component Estimation

The Helmert estimation is one of the types of variance component estimation [19]. The principle of BDS/GPS fusion positioning based on Helmert variance component estimation can be described as the following.

The observation vectors of BDS and GPS are assumed to be $\boldsymbol{L}_i$ ($i = 1, 2$) and the corresponding error equations can be written as

$$\begin{cases} \boldsymbol{V}_1 = \boldsymbol{A}_1\hat{\boldsymbol{X}} - \boldsymbol{L}_1 \\ \boldsymbol{V}_2 = \boldsymbol{A}_2\hat{\boldsymbol{X}} - \boldsymbol{L}_2 \end{cases} \tag{12.2}$$

where $\hat{\boldsymbol{X}}$ is a $m \times 1$ parameter vector needed to be estimated; $\boldsymbol{V}_i$ is residual vectors corresponding to $\boldsymbol{L}_i$; $\boldsymbol{A}_i$ is $n_i \times m$ design matrices corresponding to $\boldsymbol{L}_i$ and n_i is number of observation of the ith type.

The prior weight matrices of $\boldsymbol{L}_i$ are assumed to be $\boldsymbol{P}_i$. Since $\boldsymbol{L}_1$ and $\boldsymbol{L}_2$ are obtained by two different systems, BDS and GPS, they are independent from each other. That is

$$\mathrm{cov}(\boldsymbol{\Delta}_1, \boldsymbol{\Delta}_2) = 0 \tag{12.3}$$

where $\boldsymbol{\Delta}_i$ is the observation error vector. $\boldsymbol{P}_i$ is determined by

$$\boldsymbol{P}_i = \sum_{\Delta_i}^{-1} \tag{12.4}$$

The combined design matrix and the combined prior weight matrix can be described as

$$\boldsymbol{A} = \begin{bmatrix} \boldsymbol{A}_1 \\ \boldsymbol{A}_2 \end{bmatrix} \quad \boldsymbol{P} = \begin{bmatrix} \boldsymbol{P}_1 & \\ & \boldsymbol{P}_2 \end{bmatrix} \tag{12.5}$$

And the combined normal matrix and sub normal matrix corresponding to $\boldsymbol{L}_i$ can be written as

$$\boldsymbol{N} = \boldsymbol{A}^T\boldsymbol{P}\boldsymbol{A} \quad \boldsymbol{N}_i = \boldsymbol{A}_i^T\boldsymbol{P}_i\boldsymbol{A}_i \tag{12.6}$$

An approximate Helmert estimator of the variance component can be expressed as [20]

$$\hat{\sigma}_i^2 = \frac{\boldsymbol{V}_i^T\boldsymbol{P}_i\boldsymbol{V}_i}{n_i - tr(\boldsymbol{N}^{-1}\boldsymbol{N}_i)} \tag{12.7}$$

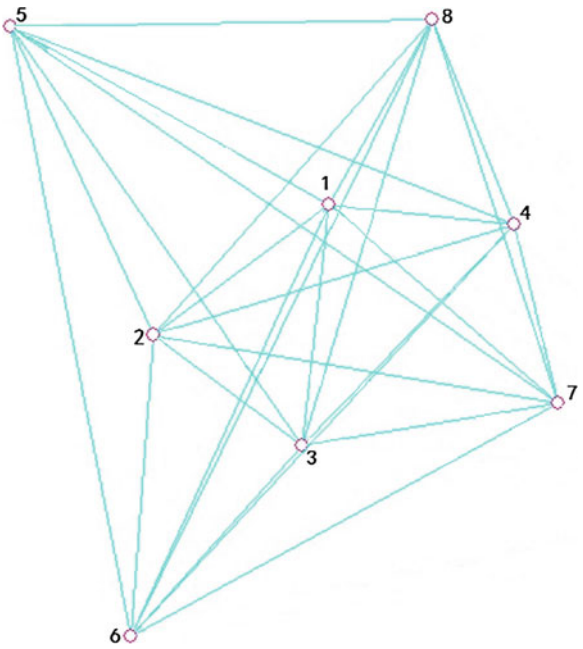

Fig. 12.1 Distribution of stations

where $\hat{\sigma}_i^2$ is the variance factor.

Finally, the solution of fusion positioning is

$$\hat{\boldsymbol{X}} = \left(\sum_{i=1}^{2} \boldsymbol{A}_i^T \tilde{\boldsymbol{P}}_i \boldsymbol{A}_i\right)^{-1} \left(\sum_{i=1}^{2} \boldsymbol{A}_i^T \tilde{\boldsymbol{P}}_i \boldsymbol{L}_i\right) \tag{12.8}$$

where $\tilde{\boldsymbol{P}}_i$ is weight matrix adjusted by Helmert estimator, which is known as

$$\widetilde{\boldsymbol{P}}_i = \hat{\sigma}_i^2 \sum_{\Delta_i}^{-1} \tag{12.9}$$

If some outliers occur among observations, then the robust estimation can be involved in the Helmert variance component estimation by using the equivalent weight [21].

12.5 Computation and Analysis

A practical GNSS network is performed as an example, which contains eight stations with one fixed station (No.1). The distribution of stations is illustrated in Fig. 12.1. Compatible receivers of BDS/GPS were used and each four sets of BDS and GPS data were collected during February 1st to 4th, 2013. Every set contains 56 independent baselines. The baselines length in this GNSS network is from 40 to

Table 12.2 Comparison on mean deviation and RMS of four schemes

Schemes	Mean deviation in B vector (m)	Mean deviation in L vector (m)	Mean deviation in H vector (m)	RMS_B (m)	RMS_L (m)	RMS_H (m)
A	0.0105	0.0267	0.0396	0.0123	0.0290	0.0518
B	0.0019	0.0038	0.0056	0.0024	0.0049	0.0069
C	0.0023	0.0049	0.0063	0.0030	0.0064	0.0078
D	0.0018	0.0037	0.0052	0.0023	0.0050	0.0066

Table 12.3 Comparison of RMS among four schemes for eight points

Points	Schemes	RMS_E (m)	RMS_N (m)	RMS_U (m)	Points	Schemes	RMS_E (m)	RMS_N (m)	RMS_U (m)
1	A	0.0000	0.0000	0.0000	5	A	0.0169	0.0167	0.0421
	B	0.0000	0.0000	0.0000		B	0.0039	0.0026	0.0039
	C	0.0000	0.0000	0.0000		C	0.0036	0.0041	0.0043
	D	0.0000	0.0000	0.0000		D	0.0037	0.0028	0.0032
2	A	0.0324	0.0125	0.0726	6	A	0.0172	0.0105	0.0391
	B	0.0057	0.0023	0.0050		B	0.0047	0.0039	0.0028
	C	0.0075	0.0026	0.0070		C	0.0055	0.0038	0.0061
	D	0.0060	0.0021	0.0037		D	0.0047	0.0034	0.0030
3	A	0.0259	0.0084	0.0131	7	A	0.0352	0.0104	0.0813
	B	0.0009	0.0023	0.0067		B	0.0020	0.0014	0.0101
	C	0.0032	0.0021	0.0062		C	0.0064	0.0017	0.0128
	D	0.0010	0.0021	0.0060		D	0.0025	0.0012	0.0098
4	A	0.0217	0.0133	0.0549	8	A	0.0248	0.0149	0.0203
	B	0.0032	0.0014	0.0078		B	0.0029	0.0027	0.0080
	C	0.0042	0.0028	0.0088		C	0.0053	0.0047	0.0055
	D	0.0031	0.0018	0.0076		D	0.0034	0.0031	0.0061

200 km. Each set of data has high precision baseline solutions and the average residuals are less than 0.01 m. The baseline solutions are regarded as no outliers.

The following four schemes are performed:

Scheme A: least squares using BDS data;
Scheme B: least squares using GPS data;
Scheme C: least squares using BDS and GPS data;
Scheme D: Helmert's variance component estimation using BDS and GPS data.

Results in Table 12.2 show the mean values of absolute difference between the estimated value and the reference of four sets and their RMSs. The mean RMS values of four sets in the station-origin coordinate system (ENU) are presented in Table 12.3.

From the results, the following conclusions can be drawn:

(1) The results of BDS solution with least squares estimation, the average absolute error of points is less than 0.05 m and the average RMS is 0.03 m. It is due to

that the constellation is still incomplete and hasn't as many satellites as GPS. Furthermore, because of using GPS solutions as reference of comparison, there may be systematic deviations between reference and the results of BDS.

(2) The results of combing BDS and GPS solution by least squares are no better than single GPS solutions. It is caused by the unreasonable weight determination between BDS and GPS data.

(3) The results of combing BDS and GPS solution using Helmert variance component estimation are more effective than the other three schemes and the average absolute error of points is less than 0.01 m. It proves that variance component estimations are more reasonable in the combination of baselines solutions of BDS and GPS.

12.6 Conclusions

Fusion positioning of BDS and GPS with baselines solutions gets a better performance than any single navigation system under the condition of determining the relative weight reasonably. It is good for the improvement of solutions of geodetic control networks. Now, BDS is still under construction and cannot provide as many satellites as GPS, which influences the positioning precision. When BDS is finally completed, the constellation will be optimized and the positioning precision will be improved further. It can be concluded that the performance of fusion positioning of BDS and GPS will also be enhanced further.

Acknowledgments This work is supported by the Natural Science Foundation of China (4102014404 and 41104022), the National High Technology Research and Development Program of China (2013AA122501).

References

1. Wang S, Bei J, Li D (2013) The algorithm research on GPS/BDS relative positioning. China geodetic surveying conference
2. Duan J, Sheng Y (2012) An algorithm of combined GPS/GLONASS static relate positioning. Acta Geodaet et Cartographica Sin 41(6):825–830+917
3. Wang J (1999) Stochastic modeling for real-time kinematic GPS/GLONASS positioning. J Inst Navig 46(4):297–305
4. Gao X, Guo J, Cheng P et al (2012) Fusion positioning of compass/GPS based on spatio temporal system unification. Acta Geod Cartographica Sin 41(5):743–748+55
5. Wang X, Bei J (2013) GPS/BDS static baseline processing method and result. J Navig Positioning 1(2):71–73
6. He H, Li J, Yang Y et al (2013) Performance assessment of single- and dual-frequency Beidou/GPS single-epoch kinematic positioning. GPS Solutions 1–11
7. Yang Y, Zeng A (2008) Fusion modes of various geodetic observations and their analysis. Geom Inf Sci Wuhan Univ 33(8):771–774

8. Carlson NA (1988) Federated filter for fault-tolerant integrated navigation system. In: Proceedings of position location and navigation symposium, DLANS, Orlando, 1988
9. Yang Y (2003) Kinematic and static filtering for multi—sensor navigation systems. Geom Inf Sci Wuhan Univ 28(4):386–388+96
10. Yang Y, Gao W (2004) Integrated navigation by using variance component estimates of multi-sensor measurements and adaptive weights of dynamic model information. Acta Geod Cartogr Sin 33(1):22–26
11. Liu J, Zeng P, Zhao W et al (2010) Theory and application of navigation system. Northwestern Polytechnical University Press, Xian
12. Yuanxi YANG (2010) Progress, contribution and challenges of compass/Beidou satellite navigation system. Acta Geod Cartogr Sin 39(1):1–6
13. Yang Y, Li J, Xu J et al (2011) Contribution of the compass satellite navigation system to global PNT users. Chin Sci Bull 56(21):1734–1740
14. Beidou Navigation Satellite System Signal in Space Interface Control Document (version 1.0) (2012)
15. Zeng P, Liu J, Hu Q et al (2011) Research on Beidou and GNSS multi-constellation integrated navigation. GNSS World Chin 1:53–57
16. Yao Y, Xie M, Niu W (2006) Research on the combination of multi-frequency and multi-mode GNSS. GNSS World Chin 5:16–20
17. Li Z, Huang J (2005) GPS measurements and data processing. Wuhan University press, Wuhan
18. Zhang L, Zhang Q, Zeng A (2010) Integrated data processing methods for various geodetic observations and their comparison. Geomatics Sci Eng 30(1):19–23
19. Weibin Huang (1990) Modern adjustment theory and its application. Chinese People's Liberation Army Publishing House, Beijing
20. Yang Y, Xu T, Song L (2005) Robust estimation of variance components with application in global positioning system network adjustment. J Surv Eng 131(4):107–112
21. Yuanxi Yang (1993) Robust estimation theory and its application. Chinese People's Liberation Army Publishing House, Beijing

Chapter 13
Test and Analysis of Interference Effects on Dual Frequency GNSS Receiver

Feng Li, He Huang, Haiqiang Yang, Hong Liu, Min Liu and Haisong Jiao

Abstract High accuracy GNSS receivers generally eliminate ionospheric delay by adopting dual or multi frequency error correction model to obtain desirable positioning results. However, dual-frequency GNSS receivers also face with radio frequency interference (RFI) in actual application, especially in complicated electromagnetic environment. In this paper, the analysis of carrier to noise ratio (C/N_0) and standard deviation of positioning in interference was introduced, and a test on the actual performance of a typical dual-frequency GPS receiver in interference at the two working frequencies was presented. The test results showed that: as the intensity of interference increased, the C/N_0 of signal descends obviously, thereupon the pseudo-range measurement precision for viewed satellites declined, leading to the loss of positioning accuracy. DGPS carrier phase measurement was recommended under interference condition in this article. By the carrier phase differential approach, the measurement error caused in the course of RFI was eliminated, and better results can be achieved if the number of satellites viewed is favorable.

Keywords Interference · Dual-frequency · Pseudo-range positioning · Carrier phase differential

13.1 Introduction

High accuracy GNSS receivers generally eliminate ionospheric delay by adopting dual or multi frequency error correction model. A dual-frequency receiver could eliminate more than 90 % error caused by ionospheric delay [1], obtain desirable and required positioning results in accurate navigation, precision positioning, map

F. Li (✉) · H. Huang · H. Yang · H. Liu · M. Liu · H. Jiao
Luoyang Electronic Equipments Test Center, Luoyang, People's Republic of China
e-mail: amyliu978@gmail.com

J. Sun et al. (eds.), *China Satellite Navigation Conference (CSNC) 2014 Proceedings: Volume I*, Lecture Notes in Electrical Engineering 303,
DOI: 10.1007/978-3-642-54737-9_13,

surveying, etc. However, dual-frequency GNSS receivers also face radio frequency interference (RFI) during the application in complicated electromagnetic environment. Under the impact of deliberate or unintentional interference, the performance in signal acquisition and tracking degrades, or even worse, the receiver loses lock with carrier signals, leading to less reliable surveying results as a result.

There are a number of studies on the performance of GPS receivers, mostly single frequency receiver, in interference; many researches have presented mainly focus on the signal processing. For example, Su et al. testified the feasibility of deliberate interference on GPS, introduced the frequency characteristics of jamming signal. Results showed that GPS signal can be jammed by deliberate interference, even if the interference is sine wave signal [2]. Feng et al. [3] studied the jamming frequency characteristics of receiver further. Zhou et al. has analyzed pseudo-range measurement accuracy and performance of DLL/PLL in interference mainly focus on the receiver signal processing. Results showed that the influence of interference is to increase the internal noise, and to reduce the value of C/N_0, eventually lead to the loss of accuracy [4, 5]. Jiao and Dou carried out studies mainly focused on the anti-jamming effectiveness evaluation of GPS receivers [6, 7].

In this paper, a test on the actual performance of a typical dual-frequency GPS receiver in RFI at two center frequencies was presented, the impact of interference on pseudo-range positioning accuracy and the causes of the error were analyzed.

13.2 Analysis of the Impact of Interference on Receiver

- Carrier to Noise Ratio

In the signal processing, the signal quality of GNSS receivers was indicated as carrier to noise ratio (C/N_0).The carrier to noise ratio density under the condition of jamming is as follow [8].

$$[C/N_0]_{eq} = \frac{1}{\frac{1}{C/N_0} + \frac{J/S}{QR_c}} \tag{13.1}$$

C/N_0 for the carrier to noise density without interference. J/S is a ratio for the jamming power. R_C for basic code rate of pseudo random noise (PRN). Q for the adjustment coefficient of spread spectrum gain.

Formula (13.1) showed that the C/N_0 of signal will decline as the interference occurs, and signal acquisition, carrier tracking, data demodulation will deteriorate simultaneously.

- The Standard Deviation

The standard deviation was used to depict the measurement precision of the receiver. According to Ref. [6], standard deviations of pseudo-range measurement and carrier phase measurement were functions of C/N_0. Pseudo-range measurement deviation and carrier phase measurement deviation are as follows [6]:

$$\rho_{\mathrm{pr}}^2 = \Delta^2 \frac{\mathrm{B}_{DLL} 2d^2}{C/N_0} \left| 2(1-d) + \frac{B_{ID} 4d}{C/N_0} \right| = \Delta^2 \left| \frac{\mathrm{B}_{DLL} 4d^2(1-d)}{C/N_0} + \frac{\mathrm{B}_{DLL} B_{ID} 8d^3}{(C/N_0)^2} \right| \tag{13.2}$$

Δ for code length, B_{DLL} for noise bandwidth of DLL; d for the distance between front correlator and the real-time correlator, B_{ID} for the noise bandwidth of integrate and dump filter.

$$\sigma_{dr} = \sqrt{\left(\frac{B_{PLL}}{C/N_0} + \frac{B_{PLL} B_{ID}}{2(C/N_0)^2} \right)} \left(\frac{\lambda}{2\pi} \right) \tag{13.3}$$

B_{PLL} for noise bandwidth of PLL; B_{ID} for noise bandwidth of integrate and dump filter. λ for the wavelength of the carrier.

In interference, the value of C/N_0 is much larger than B_{DLL}, B_{ID} and B_{DLL}, thus formula (13.2) and (13.3) will be simplified as follows.

$$\rho_{\mathrm{pr}}^2 \approx \Delta^2 \left| \frac{\mathrm{B}_{DLL} 4d^2(1-d)}{C/N_0} \right| \tag{13.4}$$

$$\sigma_{dr} \approx \sqrt{\left(\frac{B_{PLL}}{C/N_0} \right)} \left(\frac{\lambda}{2\pi} \right) \tag{13.5}$$

Interference will increase the thermal noise of the GPS receiver, making pseudo-range measurement error and carrier phase measurement error increased.

13.3 Test of the Impact of Interference on Pseudo-range Measurement

To study the variation of pseudo-range measurement accuracy in interference, a HP8642 signal generator was used as jamming resource, sending out sine wave signal, which arrived at the antenna of GPS receiver. Meanwhile we use a spectrum analyzer to monitor the intensity of interference.

Test object was a NovAtel RT2 dual-frequency GPS receiver, yields accuracies of 10 m (SEP).

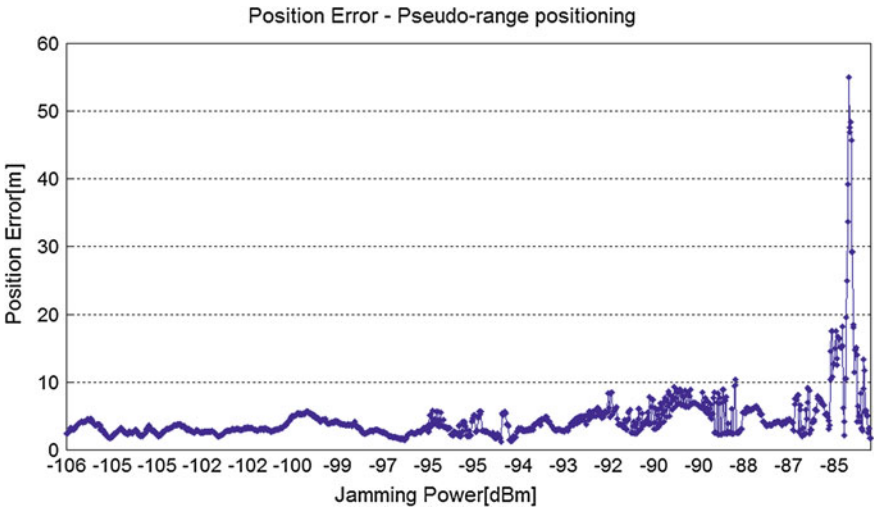

Fig. 13.1 Curve variation of pseudo-range positioning error in the interference at L1 frequency

13.3.1 Impact of Interference at L1 Frequency on Pseudo-range Measurement

Firstly, we send jamming signal at L1 frequency (1,575.42 MHz), increased jamming power 1 dB each time step-by-step until navigation signals were completely shielded, observed the positioning accuracy and stored satellites observation for data processing.

13.3.1.1 Pseudo-range Positioning Accuracy

Results showed that the serial of pseudo-range point positioning error can be divided into three stages (Fig. 13.1):

- In the interval [−106 dBm, −97 dBm], the variation of pseudo-range point positioning error was kept within 10 m, the impact of jamming can be ignored.
- In the interval [−96 dBm, −87 dBm], the serial of position error showed that the receiver was influenced by jamming for a certain extent, and there came out same outliers in pseudo-range positioning data.
- Error became even larger as the increasing signal density. When the jamming power reached −82 dBm, the receiver was out of service.

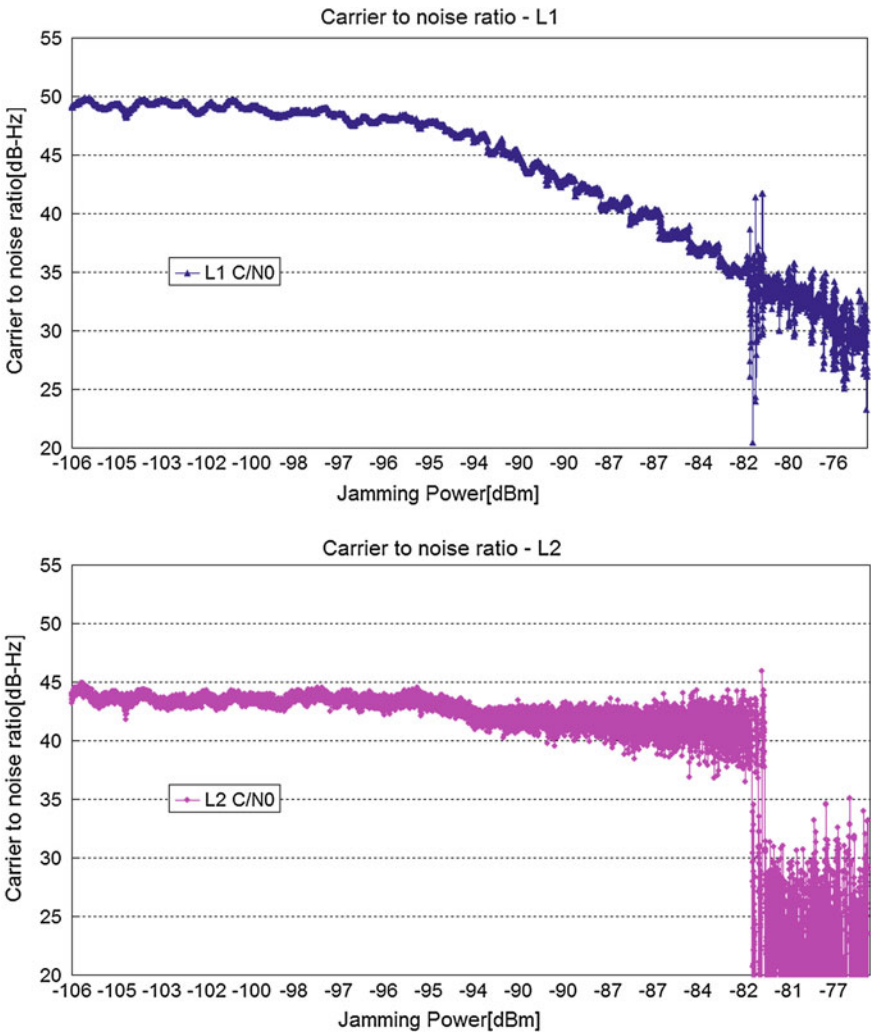

Fig. 13.2 Curve variation of carrier to noise ratio (C/N_0) of L1 and L2 carrier in the interference at L1 frequency

13.3.1.2 Analysis

On the basis of formula (13.4) and (13.5), C/N_0 and standard deviation were key indicators of GPS receivers; therefore they were extracted from observation data for analysis.

From Figs. 13.2 and 13.3 we can see that:

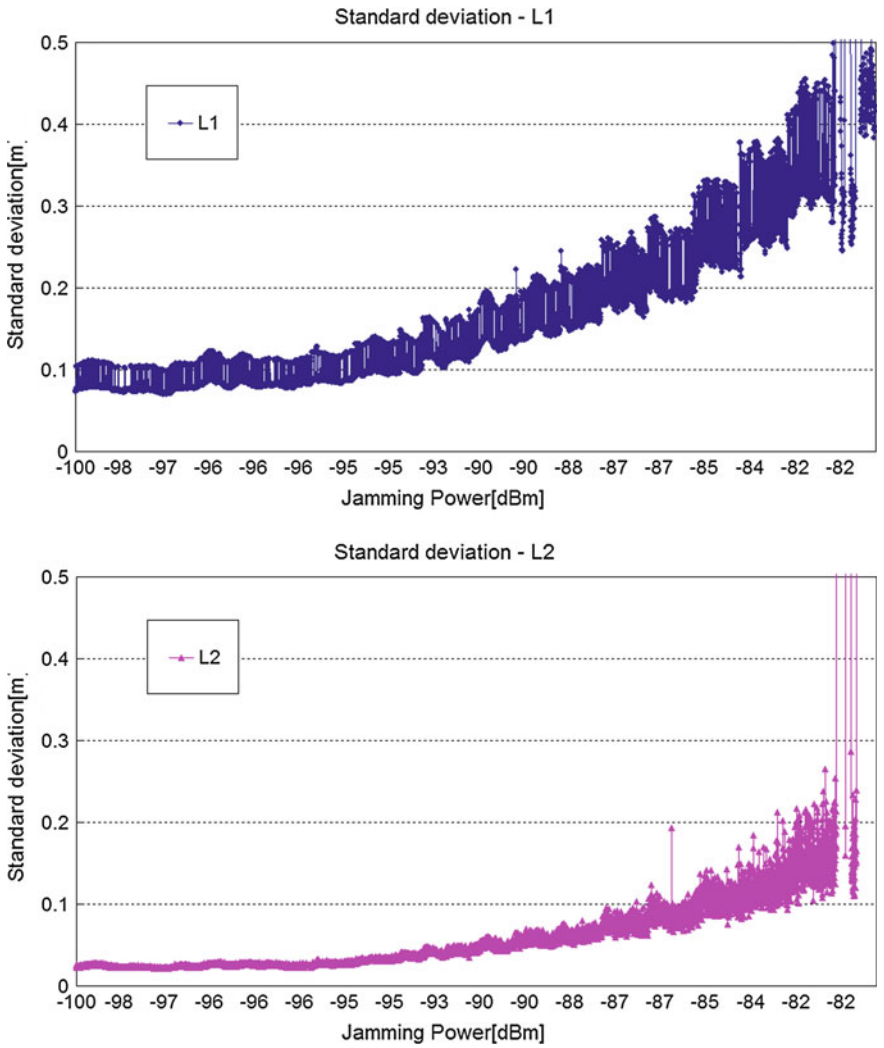

Fig. 13.3 Curve variation of pseudo-range measurement standard deviation of L1 and L2 carrier in the interference at L1 frequency

- The C/N_0 of L1 signal declined relatively slowly and the C/N_0 of L2 signal hardly decreased while jamming power was less than −97 dBm, the standard deviations were stable.
- Then in the interval [−96 dBm, −82 dBm], the C/N_0 of L1 signal showed an evident downward trend and the C/N_0 of L2 signal began to fluctuate, the pseudo-range measurement standard deviations of both L1 and L2 signals became larger simultaneously. When the jamming power was larger than −82 dBm, the quality

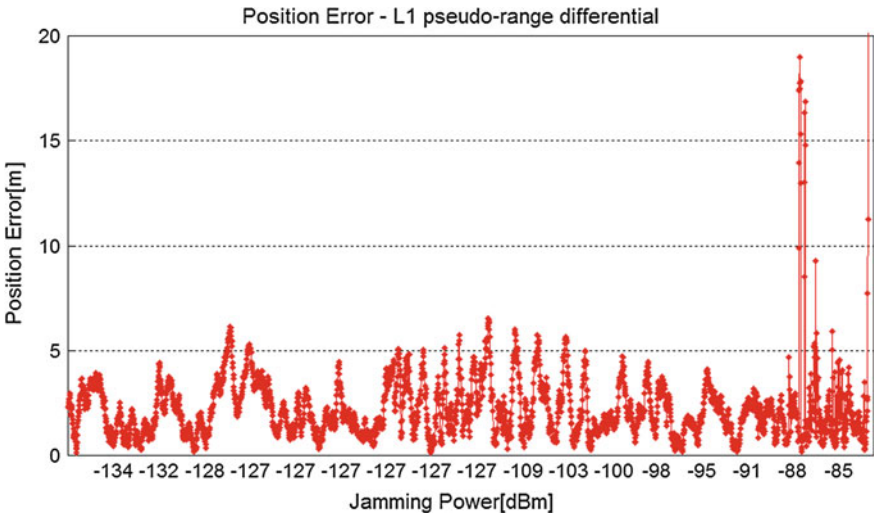

Fig. 13.4 Curve variation of pseudo-range differential measurement error in the interference at L1 frequency

of two carrier signals deteriorate, and the standard deviations were out of normal range.

In the process of point positioning, firstly dual-frequency GPS receivers finish the acquisition of the coarse acquisition code (C/A), then C/A code will guide the acquisition of the precision code (P) to realize frame synchronization; the tracking of P code still need C/A code for synchronization. Therefore, when the impact on the receiver could not be eliminated, the L2 carrier signal would be affected evidently as the C/N_0 of L1 carrier signal declined.

13.3.1.3 Pseudo-range Differential Measurement

According to spatial correlation of the error caused through signal propagation within short distance, pseudo-range differential measurement calculate position of the rover station on the principle of relative position by receiving pseudo-range correction (PRC) and range rate correction (RRC) given by the reference station. Figure 13.4 showed the variation of pseudo-range differential measurement accuracy in the interference at L1 frequency.

In the interval [−134 dBm, −90 dBm], pseudo-range differential position error was kept within 6.5 m. As interference power increased, observed satellites of the rover decreased thereupon, the pseudo-range differential measurement accuracy became deteriorated.

Interference was not the common source of error, it merely affected the rover station, and thus the correction for the interference was not given by the reference

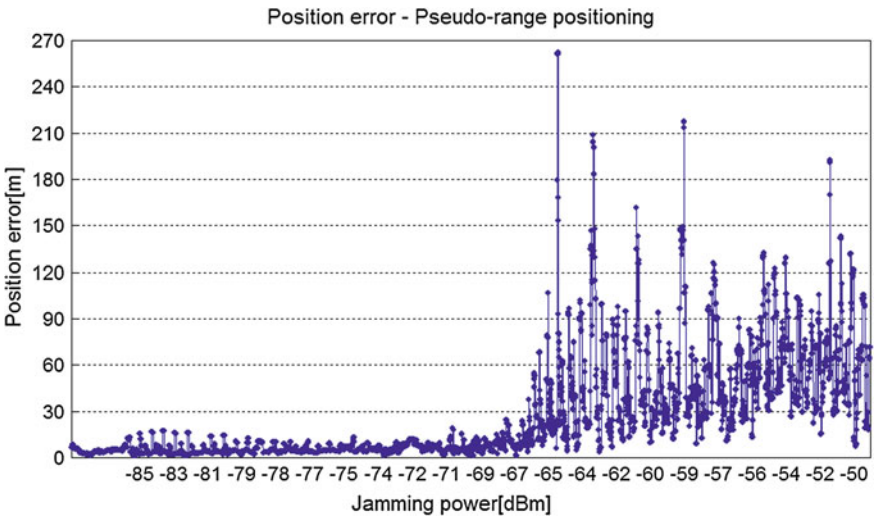

Fig. 13.5 Curve variation of pseudo-range positioning error in the interference at L2 frequency

station. However, results showed the error was eliminated after data processing if observed satellites were enough for pseudo-range differential.

Analysis found that the Impact of interference is similarly to the effects of signal masking, will reduce the number of satellites, make the distribution of satellites worse and reduce the value of position dilution of precision (PDOP), lower measurement accuracy. Therefore, the conclusion is pseudo-range differential measurement approach will improve the quality of position if the number of viewed satellites is favorable, otherwise the error can not be eliminated.

13.3.2 Impact of Interference at L2 Frequency on Pseudo-range Measurement Accuracy

Then, we adjust the jamming signal frequency to 1,227.60 MHz, increased signal intensity step-by-step, the test results are as follows.

13.3.2.1 Pseudo-range Pointing Accuracy

- In the interval [−85 dBm, −72 dBm], the variation of pseudo-range positioning accuracy kept within 20 m, the effects was relatively small.
- The error increased rapidly as the increasing of jamming power, the maximum error was over 200 m. Nevertheless, the receiver was able to keep tracking satellites in the whole process. The receiver came back to normal soon after the jamming signal stopped (Fig. 13.5).

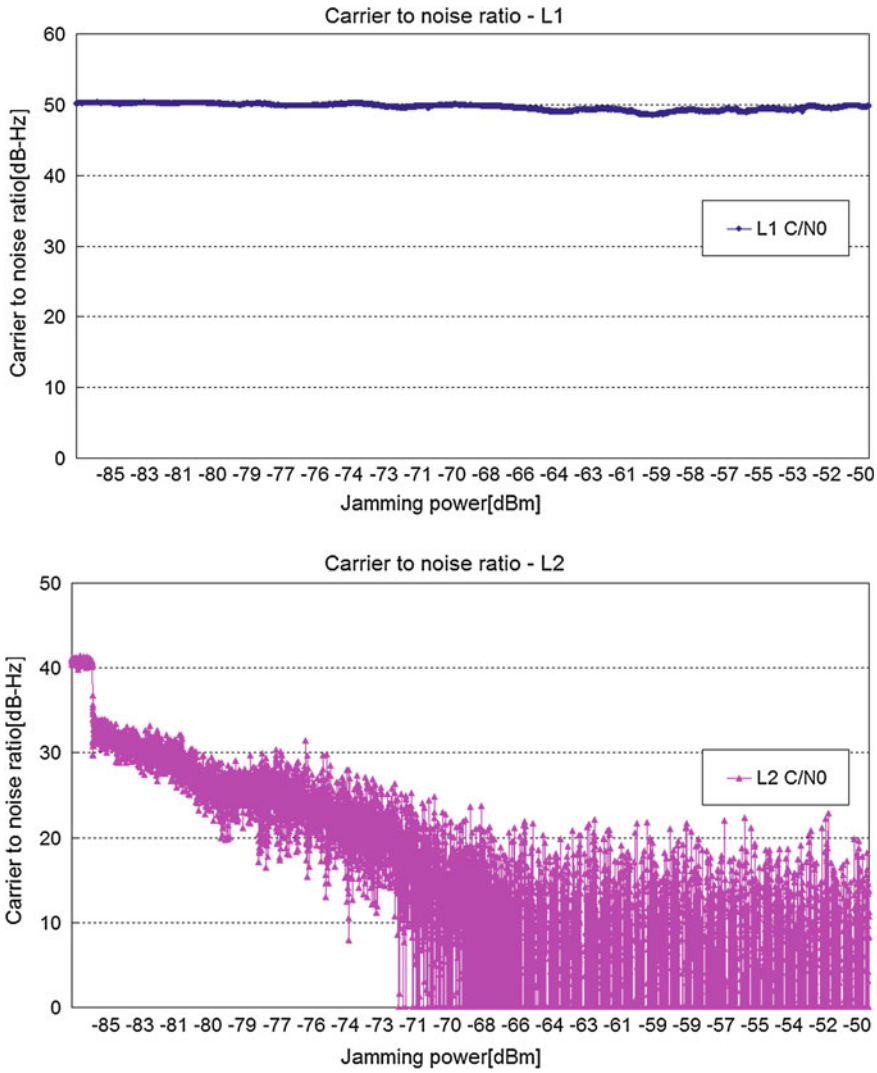

Fig. 13.6 Curve variation of carrier to noise ratio (C/N_0) of L1 carrier and L2 carrier in the interference at L2 frequency

13.3.2.2 Analysis

- The quality of L2 carrier signal deteriorated rapidly, the variation of its C/N_0 showed an evident trend in the interval [−85 dBm, −72 dBm]; while L1 carrier signal was not affected from beginning to end (Fig. 13.6). The standard deviations were basically consistent with the C/N_0 value.

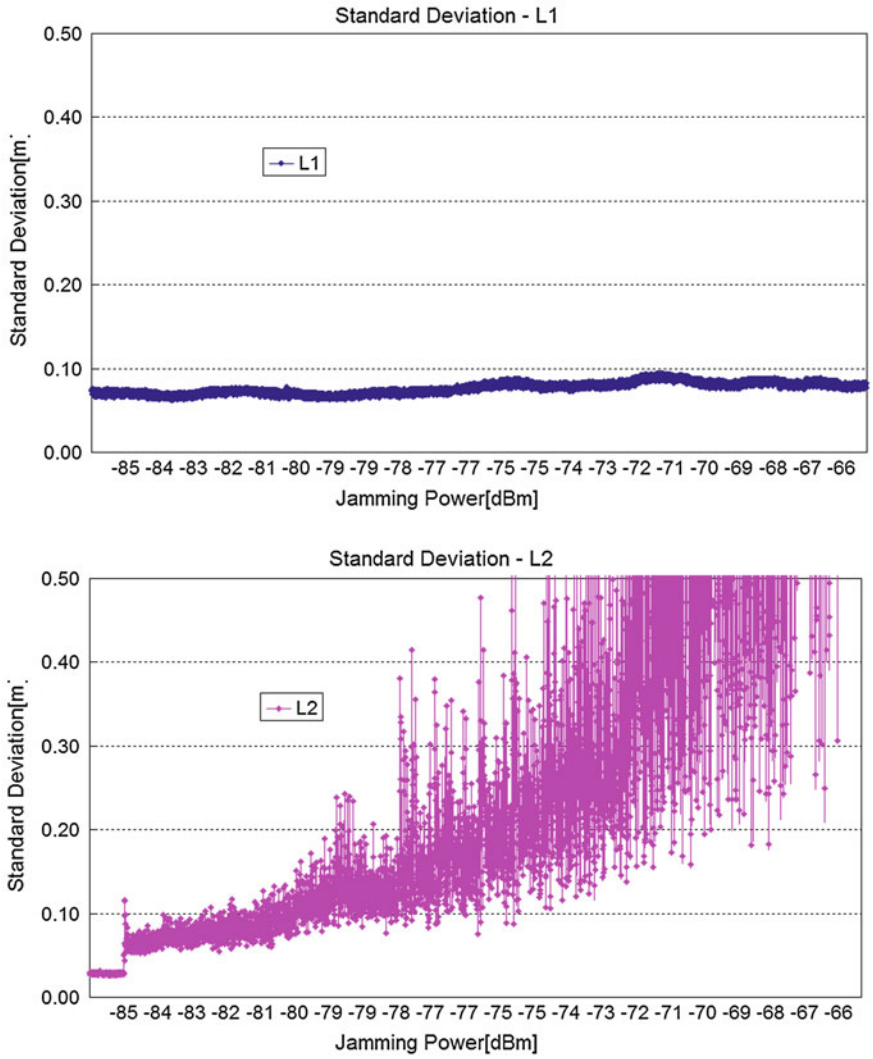

Fig. 13.7 Curve variation of pseudo-range measurement standard deviation of L1 carrier and L2 carrier in the interference at L2 frequency

- As the density of jamming signal continuously increased, the value of C/N_0 and standard deviations of L2 signal became larger simultaneously (Fig. 13.7).

Dual-frequency receivers correct pseudo-range measurement error by using the following mathematical model [8]:

$$\rho_0 = \rho_{f1} - \delta\rho_{f1} = \rho_{f1} - \left(\delta\rho_{f1} - \delta\rho_{f1}\right)\left(\frac{f_2^2}{f_1^2 - f_2^2}\right) \tag{13.6}$$

ρ_0 for the real distance from satellite to the rover. ρ_{f1} and ρ_{f2} for pseudo-range measurement value of L1 and L2 carrier. $\delta_{\rho f1}$ and $\delta_{\rho f2}$ for pseudo-range measurement deviation of L1 and L2 carrier. f_1 and f_2 for the frequency of L1 and L2 carrier.

In the interference at L2 frequency, pseudo-range measurement by L1 signal was not affected, ρf1 and $\delta\rho_{f1}$ were not affected by interference, so the loss of pseudo-range measurement accuracy was due to the variation of $\delta\rho_{f2}$ in the interference at L2 frequency.

13.3.2.3 Pseudo-range Differential Measurement

After data processing, the error was eliminated with the correction given by the reference, while C/N_0 of L1 carrier was not affected by the interference, its corresponding observations were normal, error can be eliminated in the process of differential, and therefore the measurement accuracy was actually improved. The conclusion is that we can get reliable measurement results by using pseudo-range differential in the case of less demanding precision (Fig. 13.8).

13.4 The Verification of the Phase Differential Scheme on Error Elimination in Interference

There are two types of differential positioning algorithms: pseudo-range and carrier phase. Under the conditions of short baseline, the results based on the double difference of the carrier phase are two grades higher than those based on pseudo-range differential, therefore the carrier phase differential scheme plays a dominant role in higher accuracy applications.

On the analysis hereinabove, the influence of interference is to increase the internal noise, and to enlarge measurement error; however the error caused by thermal noise in phase-locked loop is much smaller than that in the code tracking loop. Thus error caused in the interference can be eliminated based on the double difference of the carrier phase.

13.4.1 Carrier Phase Differential Measurement in the Interference at L1 Frequency

The variation of phase differential measurement showed that when jamming power was less than −86 dBm, the position derivation was within 5 cm. As the intensity of interference increased, satellites which can be observed by the rover reduced, and precision of measurement deteriorated (Fig. 13.9). It is concluded that the quality of the differential positioning solution generally decreases with the number

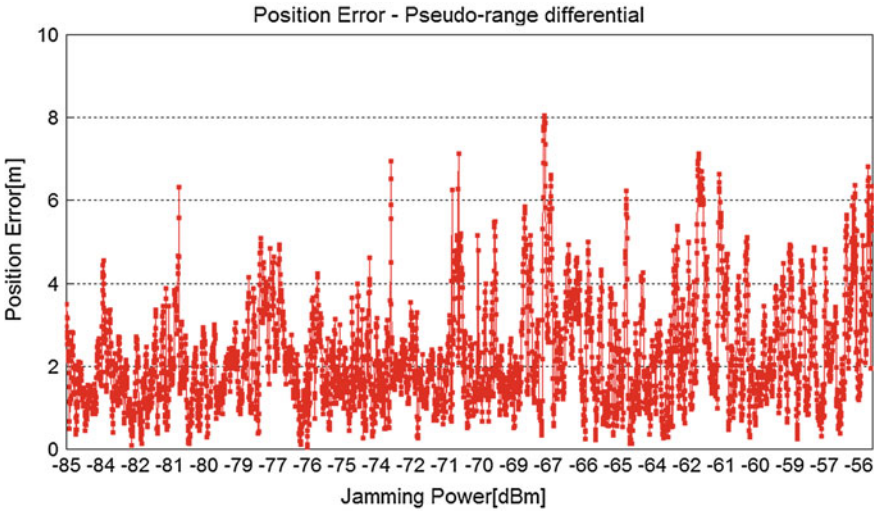

Fig. 13.8 Curve variation of pseudo-range differential measurement error in the interference at L2 frequency

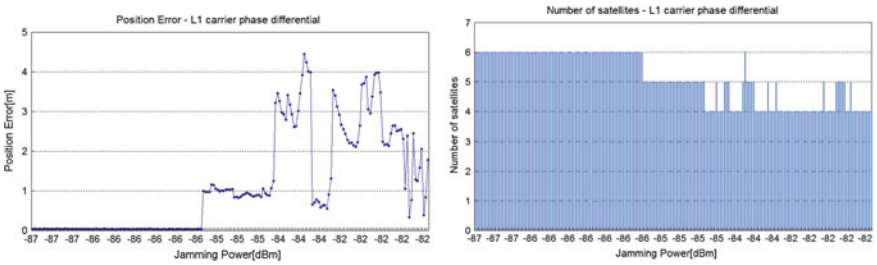

Fig. 13.9 Curve variation of carrier phase differential error in the interference at L1 frequency (*left*) and number of satellites participated in differential (*right*)

of satellites which can be simultaneously viewed by both the reference and remote station receivers. As well, the quality of the positioning solution decreases if the distribution of satellites in the sky is not favorable.

13.4.2 Carrier Phase Differential Measurement in the Interference at L2 Frequency

By Using carrier phase scheme, the error caused in interference was eliminated effectively, the overall position deviation kept within 3 cm in interval [−85 dBm, −72 dBm]. As the intensity of interference increased, there appeared several

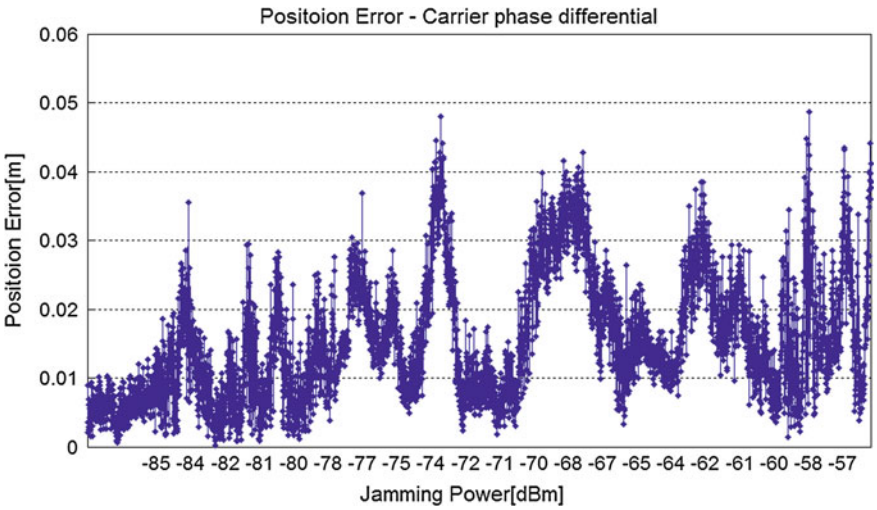

Fig. 13.10 Curve variation of carrier phase differential error in the interference at L2 frequency

outliers, who can be identified through comparison and statistic. Therefore the phase differential scheme is helpful to improve the accuracy in interference (Fig. 13.10).

13.5 Conclusion

Test showed that when the interference is at two working frequencies of dual-frequency GPS receivers, it may affect the performance of receivers, make the noise of signal, which was amplified after received, increased, lower the accuracy of delay lock loops (DLL) and Phrase Locked Loops (PLL).

When the L1 carrier was jammed, the carrier to noise ratio (C/N_0) of both L1 and L2 carrier signals declined simultaneously, the deviation of pseudo-range measurement for satellites increased, and the number of satellite viewed decreased, the accuracy of pseudo-range positioning and pseudo-range differential measurement would be affected eventually. By the carrier phase differential scheme, the impact of RFI was eliminated for a certain extent; yet, the reduction of viewed satellites would lead to the loss of measurement accuracy.

In the interference at L2 frequency, the receiver was able to keep tracking L1 signals, its pseudo-range differential measurement results were not influenced, however the pseudo-range pointing error increased obviously. With the help of carrier phase differential algorithms, we can eliminate error in the interference at L2 carrier frequency.

In practical application, it is recommended that the monitoring of RF signals in GNSS frequency domain should be enhanced, and frequency protection in application area be implemented if possible. Measurement in the complex electromagnetic environment should be avoided; or anti-interference means be adopted if required in jamming. In interference environment, make sure enough observation data was stored, and process data by using DGPS carrier phase differential approach to acquire desirable measurement results.

References

1. Tan SS (2010) The engineering of satellite navigation and positioning. National Defense Industry Press, Beijing
2. Su JJ, Li ZH (2002) Study of deliberate interference on GPS. Space Electron Coun 4:17–20
3. Feng Q, Lu B, Chang Zhu et al (2009) Study on the jamming frequency characteristics to GPS receiver. Space Electron Coun 25(3):4–6
4. Zhou KF, Yang Y et al (2005) Influence of jamming to pseudo-range measurement precision of GPS receiver. Electron Coun Tech 20(3):25–28
5. Zhou KF, Zhou XR, Yu JH (2006) Analysis of DLL/PLL of GPS receiver and its anti-jamming capability. Electron War Tech 21(2):36–39
6. Jiao X et al (2003) Effectiveness evaluation of the implementation of the GPS receiver to suppress interference. Space Electron Coun 3:11–14
7. Dou Y, Zhang WM, Chen J (2006) Analysis of Anti-interference performance of GPS receiver. Ordnance Ind Autom 25(11):50–52
8. Elliott D (2012) Understanding GPS: principles and applications. Publishing house of Electronic Industry, Beijing

Chapter 14
Study on the Personal Information Anonymization Method for the Releasing of Navigation Data

Jiannan Gao, Rendong Ying, Peilin Liu and Wenxian Yu

Abstract In this paper we give a quantitative calculation of personal information anonymization in the released navigation data based on the information theory. Individual personal information privacy index is defined and calculated based on the Markov chain model. The simulation of special state model shows that the proposed algorithm can be used to evaluate the ambiguity of different individuals from the navigation data. The simulation is based on Markov chain model, while the proposed personal information privacy metric algorithm does not depend on the motion model, one can apply it to other more accurate individual motion models and provide a quantitative basis for the personal information anonymization for the releasing of navigation data.

Keywords Navigation · Information privacy metri · Entropy · Information theory · Markov model

14.1 Introduction

Along with the development of mobile communication technology, satellite navigation technology and data mining theory, the mobile services based on the location information develop rapidly in recent years. Personal location information is used in different areas and provides customers with convenient and efficient information services including traffic analysis and optimization, mall pedestrian flow analysis, advertising, etc.

J. Gao (✉) · R. Ying (✉) · P. Liu · W. Yu
Shanghai Jiao Tong University, Shanghai 200240, China
e-mail: jiannan.gao@gmail.com

R. Ying
e-mail: rdying@sjtu.edu.cn

J. Sun et al. (eds.), *China Satellite Navigation Conference (CSNC) 2014 Proceedings: Volume I*, Lecture Notes in Electrical Engineering 303,
DOI: 10.1007/978-3-642-54737-9_14,

However, numerous utilizations of location-based services (LBS) also bring privacy and security issues. Once the personal location information is stolen, it is likely to cause the leakage of behavioral patterns, hobbies, living habits and other information, more likely to cause personal security threats. Therefore, LBS information privacy protection is becoming the hotspot and trends of the theoretical study of LBS currently. Most of the existing algorithms based on k-anonymous technologies meet the needs of location information privacy protection of single query users, while for continuous query users, those technologies do not work well because from the analysis of the trajectory, some privacy can still be revealed. When additional ancillary information is provided, it is readily to identify an individual. Therefore, resulting in the leakage of personal privacy.

There are already some trajectory information anonymization technologies including personalized k-anonymous technology [1], the silent period technology [2], the PRIVE method [3] and MOBIHIDE method [4]. SP. Li puts forward the anonymity measurement based on entropy theory [5].

In this paper, a new anonymity measurement is proposed, which is based on the changing of entropy of trace data with time. Besides by utilizing the Markov motion model, personal information anonymization problem during the navigation trajectory information dissemination is also studied in this article.

14.2 Problem Description

The scenes of this study are described as follows. Given a known initial location data of target A, and a target movement trajectory, how to avoid associating target A and the moving trajectory?

An example of application is that a large shopping mall, manager of the mall needs to optimize the layout of the shops by the analysis of the moving trajectory of customers in the store. But the customer does not want the shopping mall to associate their personal information with their trajectory, namely: the shopping mall can get the trajectory data, but is not able to identify the customers.

From a practical point of view, at some specific locations of a shopping mall, such as the elevators with video camera or the cashier section, the identity and location of customer can be known simultaneously. Therefore, to avoid this kind of information binding, the navigation information at these locations should be masked. Suppose that at time 0, the location of individual target is C_0, in order to avoid the association between the published trajectory data and the target, one need to eliminate the trajectory data between the time 0 and T. The question is: what's the minimal value of T. In the following section we will discuss the mathematic model that defined the ambiguity index with the change of time T.

14.3 Mathematic Model

We define the ambiguity of trajectory data and individual goals from the perspective of probability. Assume that at time T, there are M people ($M > 1$) at the position u. the probability distribution of the identity of the person appearing at this moment and this position can be used to infer his identity. This probability is a function of T, $\mathbf{u}$ and the individual identity m, as:

$$p(m; T, \mathbf{u}) \tag{3.1}$$

where $m = 1, 2, \ldots, M$ represent the identity of each person and u is the location an identity can appear. So for different individual m, the variation or flatness of its probability $p(m; T, \mathbf{u})$ can be used to evaluate the ambiguity of each individual. In view of the information theory, the ambiguity can be evaluated by the entropy, namely:

$$h(T; \mathbf{u}) = -\sum\nolimits_m p(m; T, \mathbf{u}) \log p(m; T, \mathbf{u}) \tag{3.2}$$

The entropy $h(T; u)$ reaches the maximum when $p(m; T, u)$ is constant for different m, i.e. each identity looks the same from the point of view of probability. Since the entropy $h(T; u)$ is a function of time T, therefore, it represents the level of personal information anonymization during the navigation trajectory

Considering the actual situation, the customers will not always linger in one area, and with the increase of T they will eventually leave the area, which means that for large enough T,

$$\sum\nolimits_m p(m; T, \mathbf{u}) < 1 \tag{3.3}$$

In order to make the definition of ambiguity in the formula (3.1) meaningful, it is necessary to "normalize" entropy, which gives the definition of the "information privacy metric" as below:

$$g(T; \mathbf{u}) = -\frac{1}{a}\sum\nolimits_m p(m; T, \mathbf{u}) \log \frac{p(m; T, \mathbf{u})}{a} \tag{3.4}$$

where $a = \sum_m p(m; T, \mathbf{u})$ is the normalization factor. For in the scenarios of M individuals, the maximum of $g(T; \mathbf{u})$ is $\log M$.

In order to find the relationship between $g(T; \mathbf{u})$ and T or $\mathbf{u}$, we need to calculate the probability $p(m; T, \mathbf{u})$. In order to define the following motion model we first discretize the time and denote each time step by integers ($n = 0, 1, 2, \ldots$). Then the first-order Markov chain model is selected as the simplified motion model for individuals. An example of the model is shown in Fig. 14.1.

In the state transition model shown above, each state represent a location, therefor 5 locations (u_k, $k = 1, 2, 3, 4, 5$) are considered in the model. Among these locations, u_5 is special, which represents the case that customers leave the mall and don't come back, namely "absorbing state". In this model the position vector of all the identite $\mathbf{u}(n)$ at any moment only depends on the position at

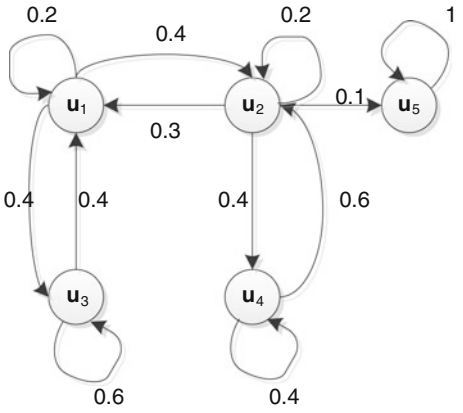

Fig. 14.1 Markov model of personal motion position

former moment $\mathbf{u}(n-1)$ with the transfer probability matrix of the Markov chain model. Numbers on the arrows of the figure represents the probability from one location to another location, which is also the state transition probability. Consider the case when there is only one person in the store, denote $\mathbf{p}(n)$ the probability that this person at time n in each position in the map, thus resulting in the state transition equation below:

$$\mathbf{p}(n) = \mathbf{p}(n-1)\mathbf{H} \tag{3.5}$$

where the matrix $\mathbf{H}$ is the state transition probability matrix. Corresponding to the example shown in Fig. 14.1, the value of $\mathbf{H}$ is given by:

$$\mathbf{H} = \begin{bmatrix} 0.2 & 0.4 & 0.4 & 0 & 0 \\ 0.3 & 0.2 & 0 & 0.4 & 0.1 \\ 0.4 & 0 & 0.6 & 0 & 0 \\ 0 & 0.6 & 0 & 0.4 & 0 \\ 0 & 0 & 0 & 0 & 1 \end{bmatrix} \tag{3.6}$$

Based on state transfer formula, and the probability distribution of the initial position $\mathbf{p}(0)$, the probability $\mathbf{p}(n)$ of every individual's potion at any time n can be achieved from the above model, namely:

$$\mathbf{p}(n) = \mathbf{p}(0)\mathbf{H}^n \tag{3.7}$$

Denote

$$\mathbf{p}(0) = [0 \quad \cdots \quad \underset{i\text{th}}{0} \quad 1 \quad 0 \quad \cdots \quad 0] \tag{3.8}$$

the initial probability vector that individual m in position u_i at the initial moment, thus the jth element of $\mathbf{p}(n)$ representing the probability of individual m appear at position u_j at the time n, namely $p(m, n, u_j)$ in the formula 3.1. So calculate the

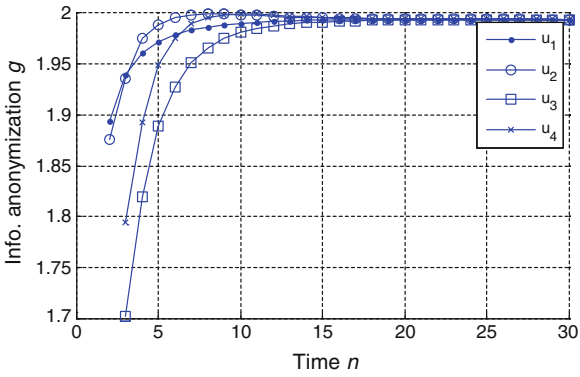

Fig. 14.2 Change of $g(n, u_i)$ with time n. At the initial time four persons are in the positions u_1–u_4, respectively

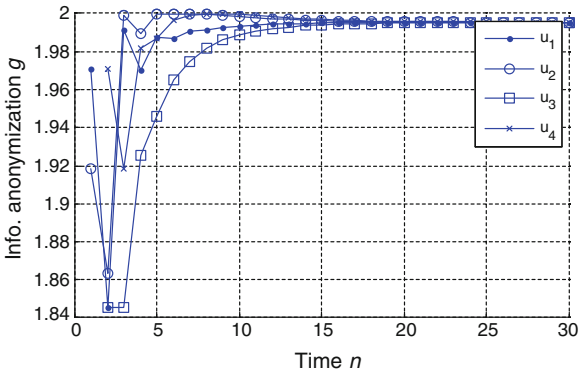

Fig. 14.3 Change of $g(n, u_i)$ with time n. At the initial time, two persons are in u_1 and the other two are in u_2

formula 3.4 and get the personal information anonymization degree function $g(n, u_i)$, and decide whether to release trajectory information at time n according to the proximity of the function and the maximum possible values.

14.4 Model Simulation

The simulation is based on Markov motion model assumptions and state transition matrix. Here is the simulation. Suppose that there are four people at the initial moment, respectively in the four position u_1–u_4. With the passage of time, the information privacy metric is showed in Fig. 14.2.

The "information privacy metric" function in the figure increases with the increasing time n, reflecting the phenomenon of the gradually rising of the difficulty to judge corresponding individual from the location information.

The three diagrams (Figs. 14.3, 14.4, 14.5) are given respectively: (1) At initial time two persons are in u_1 and the other two are in u_2; (2) At initial time one person is in u_1 and the other three are in u_2; (3) At initial time four persons are all

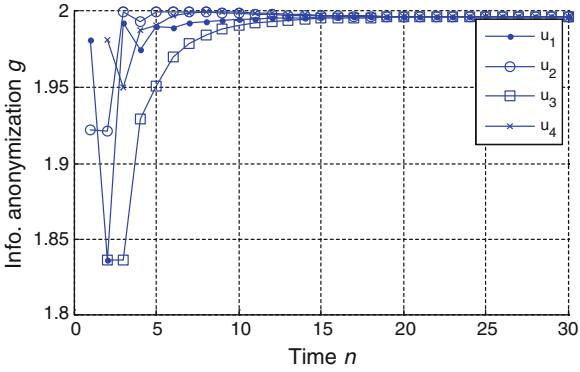

Fig. 14.4 Change of $g(n, u_i)$ with time n. At initial time one person is in u_1 and the others in u_2

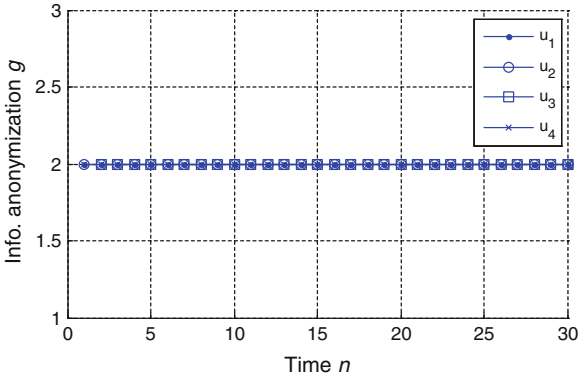

Fig. 14.5 Change of $g(n, u_i)$ with time n. At initial time all the persons are in u_2

in u_2. The diagram shows that "privacy metric" function of g increases with the concentration at initial time, which reflects the fact that at the initial moment the more concentrated the people are, the more difficult to distinguish different individuals by the trajectory.

14.5 Conclusion

In this paper we discuss the method to evaluate the extension of personal information anonymization during the navigation trajectory based on Markov chain model. Besides, this paper defines a function of "personal information privacy metric" based on the information entropy. With this function, the degree of association between data and personal information can be evaluated quantitatively, and the degree of personal information privacy is shown to be function of time and can be calculated with the person motion model. A Markov chain motion model based simulation is given in this paper, which shows the change of ambiguity of person with time and initial locations. The Markov chain model in the simulation

is a simplified model, for more accurate individual motion models, it is necessary to analysis large amount of trajectory informations, which will be the future work of this paper. The calculation method of "personal information privacy metric" proposed in this paper can be readily extended to other motion models to get more accurately evaluation result, and it provides a quantitative basis for the personal information anonymization in the publication of navigation data.

Acknowledgments The research work has been jointly funded by Beidou Navigation Satellite System Management Office (BDS office) and the Science and Technology Commission of Shanghai Municipality; the funding project number is BDZX005.

References

1. Gedik B, Liu L (2008) Protecting location privacy with personalized k-anonymity: architecture and algorithms. IEEE Trans Mob Comput 7(1):1–18
2. Huang L, Matsuura K, Yamane H (2005) Enhancing wireless location privacy using silent period. In: Proceedings of the IEEE wireless communications and networking conference, 2005, pp 1187–1192
3. Gabrial G, Panos K, Spiros S (2007) Prive: anonymous location-based queries in distributed mobile system. In: Proceedings of the 16th international conference on World Wide Web, 2007, pp 371–380
4. Gabrial Q, Panos K, Spiros S (2007) MobiHide: a mobile peer-to-peer system for anonymous location-based queries. In: Proceedings of the 10th international symposium on advances in spatial and temporal databases, 2007, pp 221–238
5. Lin X, Li SP, Yang ZH (2009) Attacking algorithms against continuous queries in LBS and anonymity measurement. J Softw 20(4):1058–1068. http://www.jos.org.cn/1000-9825/3428.htm

Chapter 15
A BDS Observation Preprocessing Method Considering the Influence of Frequent Clock Jump

Min Wang, Hongzhou Chai, Zongpeng Pan and Haifeng Zhu

Abstract Because of frequent clock jump introduced by the BDS receiver, the continuity of observation series is broken and the validity of slip detection process is undermined. After analyzing the impact mechanism of clock jump on cycle slip detection, a clock jump detection and repairing method is proposed. Validated by real BDS data, this method can effectively recover the consistency of pseudorange and phase observation and therefore avoid frequent ambiguity re-initialization, which leads to better and more stable precise point positioning solution with BDS observation.

Keywords Receiver clock jump · BDS · Cycle slip

15.1 Introduction

Cheap crystal oscillator provides the internal time reference of most surveying GNSS receiver. Due to the poor stability of such kind of oscillator, the receiver clock offset grows fast. To synchronize the receiver and GPS time reference, the receiver has to adjust the internal clock offset to keep it within a certain limitation. The clock jump is the abrupt clock value added to receiver clock offset to control its variation range [3].

When the receiver clock offset is introduced, the continuity of corresponding raw observation series or time tag is broken. If the clock jump happens on both the phase and pseudorange observation, the consistency of them remains. However, when it only happens on pseudorange observation, the consistency of phase and pseudorange observation is broken. As a result, the clock jump may be mistakenly

M. Wang (✉) · H. Chai · Z. Pan · H. Zhu
Zhengzhou Institute of Surveying and Mapping, Zhengzhou, China
e-mail: difzibo@163.com; different9@163.com

J. Sun et al. (eds.), *China Satellite Navigation Conference (CSNC) 2014 Proceedings: Volume I*, Lecture Notes in Electrical Engineering 303,
DOI: 10.1007/978-3-642-54737-9_15,

detected as cycle slip by phase and pseudorange combination method. Different from cycle slip, the clock jump influences every satellite observation of the same epoch. If the clock jump left undetected, the positioning result will be re-initialized frequently and the accuracy and reliability of positioning result can no longer be guaranteed [6]. Unfortunately, we find that frequent millisecond level clock jumps are not rare in observations output by some current BDS/GPS receivers.

In this paper, a BDS preprocessing method that is resistant to clock jump impact is introduced. By using virtual phase observation composed of raw phase observation, the second-order ionosphere delay is canceled to improve the accuracy of clock jump detection. Validated by real BDS observation, this method can effectively repair the frequent millisecond level clock jump and prevent its influence on cycle slip detection. After preprocessing BDS observation with this method, the frequent re-initialization of ambiguity parameter can be avoided, which lays a good foundation for further positioning estimation.

15.2 Classification of BDS Clock Jump

The clock steering mechanism varies between different receiver manufacturers. However, according to its influence on time tag, pseudorange and phase observation, the receiver clock jump can be classified as four types defined in Table 15.1 [4].

All the BDS data used in this paper are collected by COMPASS Experimental Tracking Network (CETN) established by the GNSS Research Center, Wuhan University. All the stations of CETN are equipped with UR240 dual-frequency BDS/GPS receivers manufactured by Unicore Communications Incorporation. Even though the receiver types of all the stations are the same, the firmware version may vary, which results in different clock offset steering mechanism. Therefore, the clock jump behavior of same type receiver may be different.

As shown in Fig. 15.1, the B1 phase observation series of LASA station in day of year (DOY) 93, 2013 has a smooth variation trend, meanwhile the pseudorange observation abruptly jumps nearly every 1,500 s. The corresponding clock offset value derived with pseudorange observations resets at exactly same epoch of observation jump. When the receiver clock offset value reaches ± 0.5 ms, a 1 ms abrupt clock jump is introduced to keep the absolute value of clock offset within 0.5 ms. Because the value jump that happens to pseudorange observation does not occurs to phase observation, it is a type 3 clock jump illustrated in Table 15.1.

Different from the clock steering method within receiver used in LASA station, as illustrated in Fig. 15.2, both the phase and pseudorange raw observation of HRBN station in DOY 93, 2013 are adjusted to leave a room for the type four clock jump. The frequent clock jumps cause a sawtooth signature of the observation. After analyzing observations from all the CETN stations, we find that

Table 15.1 Four types of clock jump

Type	Time tag	Pseudorange	Phase
1	Jumpy	Smooth	Smooth
2	Jumpy	Jumpy	Smooth
3	Smooth	Jumpy	Smooth
4	Smooth	Jumpy	Jumpy

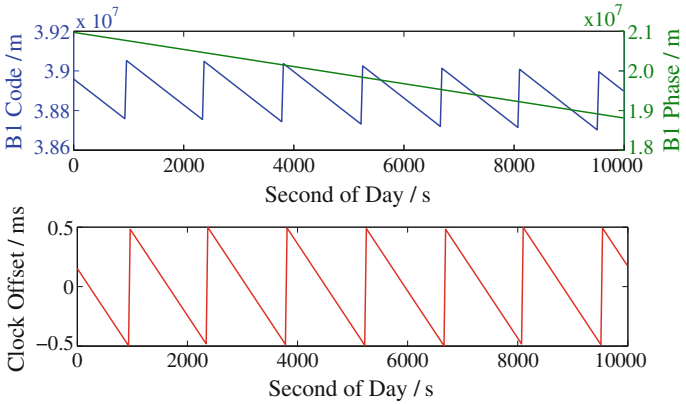

Fig. 15.1 B1 pseudorange and phase observation and corresponding receiver clock offset series of C01 satellite for LASA station

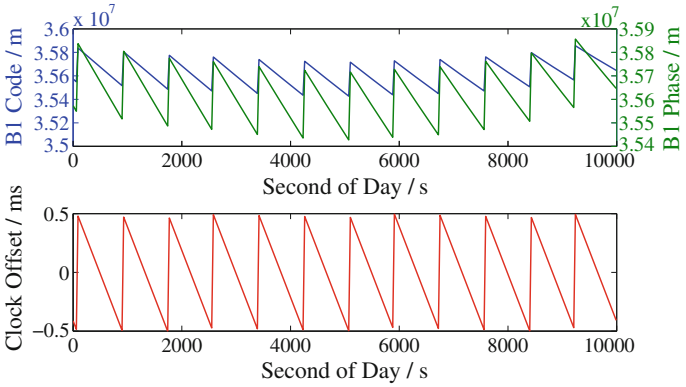

Fig. 15.2 B1 pseudorange and phase observation and corresponding receiver clock offset series of C06 satellite for HRBN station

except for LASA and HRBN station, the type two and four millisecond level clock jump exist in some other stations. In this paper, we focus on handling those types of clock jump.

15.3 Influence of BDS Observation Clock Jump on Cycle Slip Detection

The influence of clock jump on cycle slip detection depends on the type of clock jump. In general, the raw GNSS pseudorange and phase observation can be represented as Eqs. (15.1)–(15.3):

$$\Phi_{\mathrm{i}}(t) = g(t) - I_{\mathrm{i}}(t) + \lambda_{\mathrm{i}} N_{\mathrm{i}}^{\mathrm{j}}(t) + \varepsilon_{\Phi,\mathrm{i}} \tag{15.1}$$

$$P_{\mathrm{i}}(t) = g(t) + I_{\mathrm{i}}(t) + \varepsilon_{\mathrm{P,i}} \tag{15.2}$$

$$g(t) = \rho(t) + c \cdot dt_{\mathrm{r}}(t) - c \cdot dt^{\mathrm{s}}(t) + T(t) \tag{15.3}$$

where $\Phi_{\mathrm{i}}(t)$ and $P_{\mathrm{i}}(t)$ are i frequency phase and pseudorange observation at epoch t separately, $g(t)$ includes satellite-to-station geometry distance and other frequency-irrelevant delay like receiver antenna phase center offset and troposphere delay, $dt_{\mathrm{r}}(t)$ is receiver clock offset, $dt^{\mathrm{s}}(t)$ is satellite clock offset, $T(t)$ is troposphere delay, $I_{\mathrm{i}}(t)$ is second-order ionosphere delay for frequency i, $N_{\mathrm{i}}^{\mathrm{j}}(t)$ is ambiguity for satellite j and frequency i, $\varepsilon_{\Phi,\mathrm{i}}$ and $\varepsilon_{\mathrm{P,i}}$ are the corresponding phase and pseudorange observation noise separately.

For duo-frequency observation, the ionosphere delay on different frequency can be converted using following relationship:

$$I_2(t) = \gamma I_1(t) \tag{15.4}$$

where $\gamma = \frac{f_1^2}{f_2^2}$, f_{i} is the frequency value for frequency i.

In general, the cycle slip detection uses certain type of cycle slip detection observation computed with raw observation. The cycle slip is detected by checking the time difference of cycle slip detection observation. Most cycle slip detection methods eliminate or decrease other observation series variety influence like satellite-station geometry distance and satellite clock offset by observation combination or time difference. Different combinations of raw observation e.g. ionosphere residual method, geometry-free method and MW combination method may output different cycle slip detection result [9]. Moreover, single cycle slip detection observation has certain insensitive cycle slip, so it is wise to use different observation combinations for cycle slip detection simultaneously.

Depend on the selection of cycle slip detection observation, the cycle slip detection methods also have different sensibility to clock jump. For example, when applying geometry-free method to cycle slip detection for a duo-frequency receiver, corresponding cycle slip detection observation is composed as Eq. (15.5):

$$\Delta L_{\mathrm{GF}} = \Delta\Phi_1 - \Delta\Phi_2 = \Delta N_1 - \Delta N_2 + \varepsilon_{\mathrm{GF}} \tag{15.5}$$

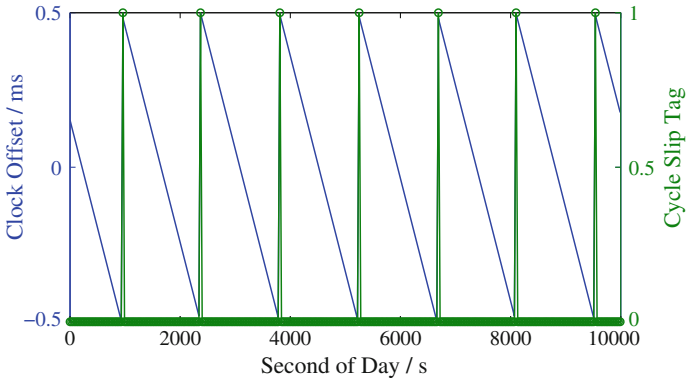

Fig. 15.3 Cycle slip detection result using original MW combination for LASA station

where, Δ is time difference operator, ε_{GF} is corresponding geometry-free combination noise. Only phase observation is used in this combination and receiver clock has been eliminated, so clock jump will cause no trouble to this cycle slip detection method.

For another common cycle slip detection method MW combination method, the cycle slip detection observation is computed as followings:

$$\Delta L_{MW} = \lambda_w(\Delta N_1 - \Delta N_2) + \Delta g_{sum} + \varepsilon_{MW} \tag{15.6}$$

$$\Delta g_{sum} = \Delta g_\Phi - \Delta g_P \tag{15.7}$$

where λ_w is wavelength of widelane combination, Δg_Φ and Δg_P are the time difference of $g(t)$ for phase and pseudorange observation separately, Δg_{sum} is the sum of those two items, ε_{MW} is noise of MW combination observation. Type one and four clock jump will do no harm to cycle slip detection because the jump value caused by clock jump is eliminated by combination process. In general, the Δg_{sum} value should be around zero. However, when type two and three clock jump happen, because the consistency of phase and code observation is broken up, the Δg_{sum} value series will have an abrupt jump, which makes the clock jump mistakenly detected as cycle slip.

The Fig. 15.3 demonstrates the MW combination cycle slip detection result without clock jump detection for LASA station in DOY 93, 2013. For cycle slip detection, the cycle slip tag one represents there is a cycle slip detected and zero represents normal observation. All the clock jumps have been detected as cycle slips. Different from cycle slip, the clock jump occurs to all the observations at same epoch. The false cycle slip detection result will cause frequent initialization of ambiguity parameter and influence the result stability and accuracy in further processing. Because the MW combination is sensitive to type two and three clock jump, it needs to detect and repair clock jump firstly to improve the correctness and reliability of cycle slip detection [1].

15.4 BDS Data Preprocessing Method Immune to Clock Jump

Guo [3] pointed out that the receiver clock jump has two basic characteristics. Frist, the same amount of steep jump value contributed to receiver clock jump can be seen in all satellites observations of the same epoch. Second, for millisecond level clock jump, the value of clock jump is an integer number by millisecond. The general idea of our method is to exploit these two characteristics to distinguish clock jump from cycle jump and repair them correctly.

15.4.1 BDS Clock Jump Detection Method

For our observation reprocessing method, two virtual phase observation are built firstly, the virtual phase observation for frequency i is $L_{\mathrm{i}}^{*\mathrm{j}}$ [8]:

$$\begin{aligned} L_1^{*\mathrm{j}} &= (1+\alpha)L_1 - \alpha L_2 \\ &= g(t) + I_1(t) + (1+\alpha)\lambda_1 N_1^{\mathrm{j}}(t) - \alpha\lambda_2 N_2^{\mathrm{j}}(t) \end{aligned} \tag{15.8}$$

$$\begin{aligned} L_2^{*\mathrm{j}} &= \beta L_1 - (\beta-1)L_2 \\ &= g(t) + I_2(t) + \beta\lambda_1 N_1^{\mathrm{j}}(t) - (\beta-1)\lambda_2 N_2^{\mathrm{j}}(t) \end{aligned} \tag{15.9}$$

where, α and β are conversion coefficient, $\alpha = \frac{2}{\gamma-1}$, $\beta = \frac{2\gamma}{\gamma-1}$. After conversion of Eqs. (15.8) and (15.9), the sign of ionosphere delay in virtual observation is same as that of pseudorange observation. When $L_{\mathrm{i}}^{*\mathrm{j}}$ minus corresponding pseudorange, the second-order ionosphere delay and its influence on clock jump detection can be mitigated.

After acquiring the virtual phase observation $L_{\mathrm{i}}^{*\mathrm{j}}$, the clock jump detection observation $S_{\mathrm{i}}^{\mathrm{j}}(t)$ can be formed as Eq. (15.10):

$$S_{\mathrm{i}}^{\mathrm{j}}(t) = \frac{\Delta P_{\mathrm{i}}^{\mathrm{j}} - \Delta L_{\mathrm{i}}^{*\mathrm{j}}}{c_{\mathrm{S}}} = \frac{-\Delta N_{\mathrm{s}} + \Delta g + \varepsilon_{\mathrm{S}}}{c_{\mathrm{S}}} \tag{15.10}$$

where c_{S} is the unit conversion coefficient form meter to millisecond, $c_{\mathrm{S}} = c \times 10^3$, c is the speed of light, ΔN_{s} is the time difference of $L_{\mathrm{i}}^{*\mathrm{j}}$ ambiguity, Δg is other frequency-irrelevant delay that has not been eliminated, ε_{S} is clock jump detection observation noise. Because the second-order ionosphere delay is eliminated during the combination process, the abrupt change of ionosphere delay like ionosphere scintillation will not influence the clock jump detection. Moreover, when clock jump happens, all the clock jump detection observations at same epoch will have a sudden jump and we can make use of this character to distinguish cycle slip from clock jump.

Every clock jump detection observation at certain epoch should be checked with following equation:

$$\left|S_{\mathrm{i}}^{\mathrm{j}}(t)\right| < k_1 \tag{15.11}$$

k_1 is the detection threshold, $k_1 = 10^{-3}\, c - 3\sigma$, σ reflects the noise level of detection observation, the value is 3–5 m [4]. If the Eq. (15.11) is met, then Eq. (15.12) will be used to test if all satellites are influenced.

$$n = Na \tag{15.12}$$

where, n is the number of clock jump detection observation meeting Eq. (15.11), Na is the number of the valid clock jump detection observation at certain epoch.

To confirm there is a clock jump in current epoch, other two detection value h_1 and h_2 have to be checked [2]:

$$h_1 = \frac{\arctan(q_1/q_2)}{2\pi} \tag{15.13}$$

$$q_1 = \sum^{n} \sin(S_{\mathrm{i}}^{\mathrm{j}}(t)) \tag{15.14}$$

$$q_2 = \sum^{n} \cos(S_{\mathrm{i}}^{\mathrm{j}}(t)) \tag{15.15}$$

where, h_1 is the fractional part of clock jump detection observation. The computation method is initially come up by Gabor and Nerem to compute the fractional cycle bias (FCB).

Other detection observation h_2 is used to test if all the clock jump detection observation $S_{\mathrm{i}}^{\mathrm{j}}(t)$ can be reasonably rounded to same integer. Equation (15.16) tells the definition of h_2:

$$h_2 = \sum_{i=2}^{n} |S_i - \mathrm{round}(S_1)| \tag{15.16}$$

where S_1 is the first detection observation and n is the number of observations at current epoch. When all the two conditions in Eq. (15.17) are satisfied, the existence of clock jump can be confirmed.

$$\begin{cases} h_1 < k_2 \\ h_2 < k_3 \end{cases} \tag{15.17}$$

The values of two detection threshold k_2 and k_3 should reflect the noise level of pseudorange observation and account for the reliability of detection results. In this paper, the k_2 is set as 10^{-5} ms and $k_3 = \sqrt{n-1} \cdot k_2$, n is the number of valid clock jump detection observation.

When a clock jump is detected, we should first determine the size of clock jump and then try to repair it. Through test of Eq. (15.17), all the clock jump detection observation can be rounded to same integer value. Because the clock jump has integer value characteristic, we can acquire the exact value of clock jump value M by simply round the first clock jump detection observation S_1 to its nearest integer:

$$M = \text{round}(S_1) \tag{15.18}$$

After determining the value of clock jump, the consistency of phase and pseudorange observation can be recovered by add the clock jump value to original phase observation [5].

$$\widehat{L} = L + M \cdot c_S \tag{19}$$

15.4.2 BDS Data Reprocessing Scenario

An effective BDS observation preprocessing method has to consider insensitive cycle slip of different cycle slip detection observation and to arrange the order of different preprocessing procedure accordingly. If possible, both the clock jump and cycle slip should be detected and repaired to avoid their influence on further data processing.

Figure 15.4 shows the preprocessing data flow come up by this paper, every observation of same epoch is looped over. Firstly, the geometry-free combination observation that is insensitive to clock jump is used to detect obvious blunder and cycle slip. And then the observations will be detected for clock jump with the method proposed in Sect. 15.3. When there is a clock jump detected, the phase observation will be adjusted to recover the consistency of phase and pseudorange observation. At last, the MW combination will be used to detect the remaining cycle slip which is insensitive to geometry-free combination. Because clock jump has been detected and repaired, the reliability of cycle slip detection procedure is improved.

15.5 Results and Analysis

Figure 15.5 shows the comparison of MW combination observation series for station LEID before and after clock jump detection. The blue and red curves represent original and repaired MW combination observation series separately. The LEID station also belongs to CETN mentioned in Sect. 15.2. Because frequent clock jumps undermine the consistency of pseudorange and phase observation,

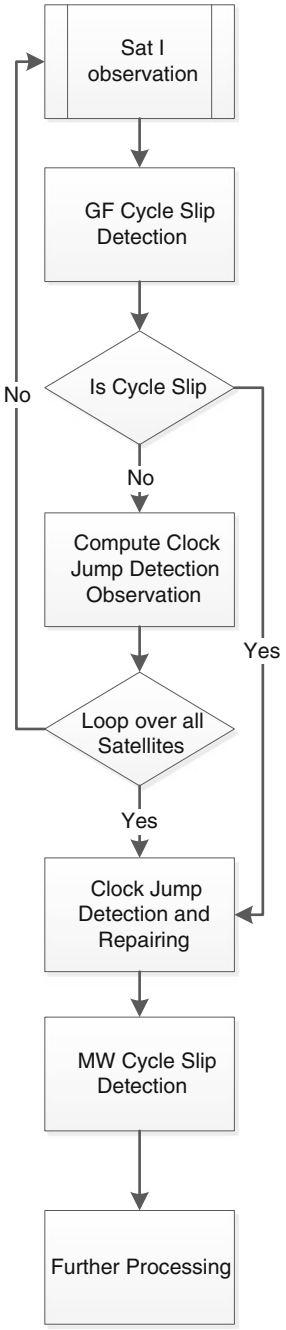

Fig. 15.4 Flowchart of BDS observation preprocessing

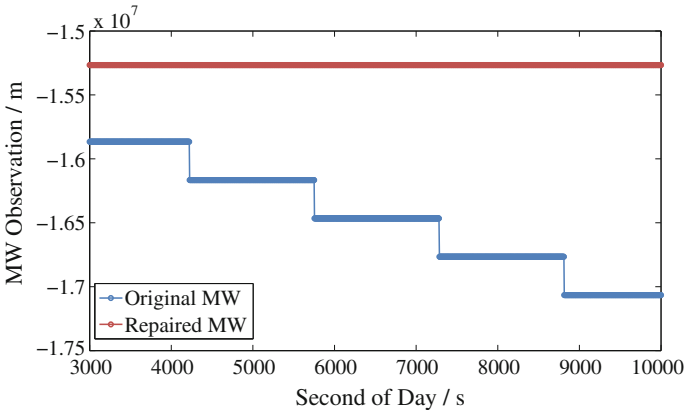

Fig. 15.5 Original and repaired MW combination observation series for station LEID and C05 satellite

the blue original MW combination observation series decrease by a constant stepwise value introduced by clock jump and the steadiness of MW combination is lost. After applying clock jump repairing, the red repaired MW combination series can keep stable, which means no clock jump will be detected as fault cycle slip any more.

To test the preprocessing method proposed by this paper, we compare this method with the common preprocessing method that does not consider the influence of clock jump. Kinematic precise point positioning (PPP) method is carried out to test the influence of different preprocessing scenario on final positioning results. In our experiment, first preprocessing scenario just uses geometry-free combination and MW combination for cycle slip detection. The second scenario uses the preprocessing method introduced in Sect. 15.4. Other estimation configurations are identical between two scenario. The cut-off angle is set as 10° and the position state is modeled as Gauss white noise [7]. The BDS satellite precise ephemeris is provided by GNSS research center, Wuhan University.

As illustrated in Fig. 15.6, without clock jump repairing, the phase observations for LASA station in DOY 93, 2013 are detected as cycle slip about every 20 min, which leads to frequent re-initialization of ambiguity. The positioning result cannot converge at all and the average positioning accuracy is only at meter level.

The Fig. 15.7 demonstrates that after clock jump detection and repairing, the positioning accuracy of LASA station is improved. The clock jump repairing process can make the MW combination steadier and not interrupted by clock jump. The frequent re-initialization is avoided, so after the convergence period, the positioning accuracy can keep within 30 cm at most of time.

Comparing the positioning result of Figs. 15.6 and 15.7, we can safely conclude that the clock jump detection and repairing procedure is necessary for specific

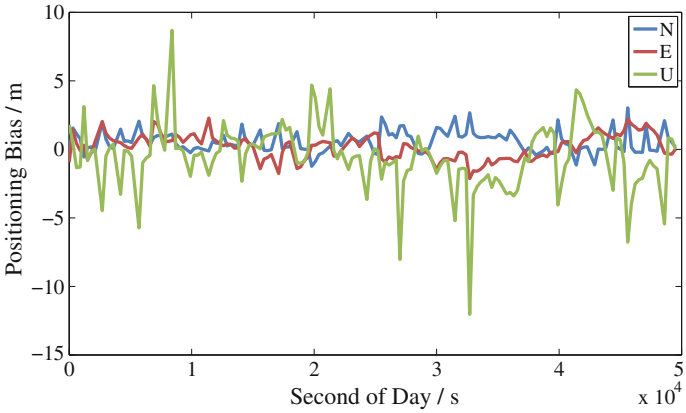

Fig. 15.6 Kinematic PPP positioning result before clock jump repairing for station LASA

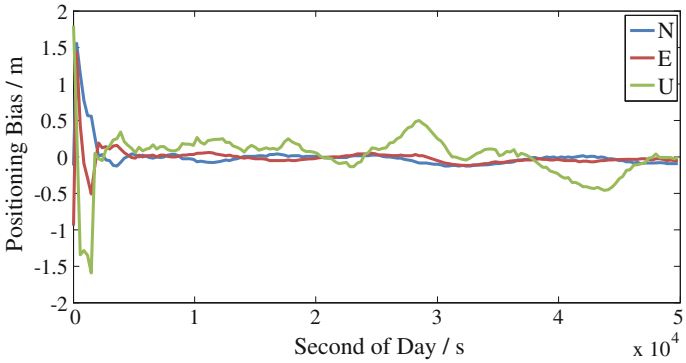

Fig. 15.7 Kinematic PPP positioning result after clock jump repairing for station LASA

GPS/BDS receivers. Only after mitigating the influence of clock jump on cycle slip detection, the reliable and accuracy positioning results can be expected.

15.6 Conclusions

An effective data preprocessing scenario is a precondition for further observation processing and utilizing. In this paper, to avoid the influence of frequent clock jump on cycle slip detection and improve the positioning accuracy, an observation preprocessing method that resistant to clock jump is come up. After detecting and repairing of clock jump, reliability of the cycle slip detection is guaranteed, which lays a good foundation for positioning estimation.

Limited by observation data volume we collected, the method proposed by this paper mainly focus on duo-frequency observation preprocessing. Further research will study adapting this method for triple-frequency observation preprocessing.

Acknowledgments GNSS Research Centre of Wuhan University is gratefully acknowledged for providing BDS data and precise ephemeris. This work is supported by China National Natural Science Foundation of China (No.: 41274045).

References

1. Dai Z (2012) MATLAB software for GPS cycle-slip processing. GPS Solutions 16(2):267–272
2. Gabor MJ, Nerem RS (1999) GPS carrier phase ambiguity resolution using satellite-satellite single differences. In: Proceedings of ION GPS 99, Nashville, TN, 14–17 Sept 1999, pp 1569–1578
3. Guo F (2013) Theory and methodology of quality control and quality analysis for GPS precise point positioning. Wuhan University, Wuhan
4. Guo F, Zhang X (2014) Real-time clock jump compensation for precise point positioning. GPS Solutions 18(1):41–50
5. Heo YJ, Cho J, Heo MB (2012) An approach for GPS clock jump detection using carrier phase measurements in real-time. J Electr Eng Technol 7(3):429–435
6. Kim HS, Lee HK (2012) Elimination of clock jump effects in low-quality differential GPS measurements. J Electr Eng Technol 7(4):626–635
7. Leandro RF (2009) Precise point positioning with GPS: a new approach for positioning, atmospheric studies, and signal analysis. University of New Brunswick, Fredericton, NB
8. Leick A (2004) GPS satellite surveying. Willey, Hoboken, New Jersey
9. Liu Z (2010) A new automated cycle slip detection and repair method for a single dual-frequency GPS receiver. J Geodesy 85(3):171–183

Chapter 16
Analysis of Precipitable Water Vapor (PWV) Data Derived from Multiple Techniques: GPS, WVR, Radiosonde and NHM in Hong Kong

Biyan Chen and Zhizhao Liu

Abstract Water vapor is a highly variable component in the atmosphere and plays a key role in many atmospheric processes. Accurate measurement of water vapor is vital for improving the predictability of regional precipitation, weather and visibility, especially for highly moist metropolis like Hong Kong. In this paper, we analyze precipitable water vapor (PWV) data in Hong Kong derived from four techniques, i.e. radiosonde, water vapor radiometer (WVR), Global Positioning System (GPS) and numerical weather prediction (NWP)'s non-hydrostatic model (NHM) during a period of approximately 6-month. Radiosonde observations have a low temporal resolution and the observation interval is usually 12 h. The quality of WVR PWV measurements is affected by rainy weather. GPS can provide PWVs at a relatively high temporal resolution, but the vertical resolution is poor. NWP's NHM is developed based on sophisticated physical and numerical models. The Hong Kong Polytechnic University (PolyU) and Hong Kong Observatory (HKO) collaborate to perform three-dimensional (3D) water vapor modeling using PWV data derived from multiple techniques including GPS, WVR and radiosonde, with an aim to assimilate 3D water vapor data into NWP being run at HKO. This will allow the improvement of weather forecasting capability in Hong Kong. However, it is important to understand the quality and characteristics of the water vapor data obtained from various techniques prior to data assimilation. We analyze the correlation and comparison results of the four water vapor observation techniques. It is found that the correlation coefficients between PWVs from GPS, WVR, NHM and radiosonde data are 0.979, 0.983 and 0.975, respectively. Moreover, the correlation coefficients between NHM and GPS, NHM and WVR, WVR and GPS are 0.975, 0.962 and 0.968, respectively. Intercomparison results indicate that

B. Chen · Z. Liu (✉)
Department of Land Surveying and Geo-Informatics, The Hong Kong Polytechnic University, 11 Yuk Choi Road, Hung Hom, Kowloon, Hong Kong, China
e-mail: lszzliu@polyu.edu.hk

B. Chen
e-mail: 12901813r@connect.polyu.hk

J. Sun et al. (eds.), *China Satellite Navigation Conference (CSNC) 2014 Proceedings: Volume I*, Lecture Notes in Electrical Engineering 303,
DOI: 10.1007/978-3-642-54737-9_16,

water vapor data derived from these four techniques have very good agreements with each other, with root mean squares error (RMS) ranging from 2.474 to 4.259 mm. Among the four techniques, we find that WVR and radiosonde water vapor observations have the best agreement, with a bias and RMS error of 0.176 and 2.474 mm, respectively.

Keywords Water vapor · Precipitable water vapor (PWV) · Global positioning system (GPS) · Water vapor radiometer (WVR) · Radiosonde · Non-hydrostatic model (NHM)

16.1 Introduction

Water vapor is a key atmospheric greenhouse gas and makes a great contribution to many atmospheric processes such as the cloud formation, hydrological cycle and radiative balance [1–3]. Knowledge of water vapor variations is essential for regional weather forecasting and global climate study. Precipitable water vapor (PWV) is an important parameter that can directly reflect the content of water vapor in the atmosphere [4]. Accurate estimates of PWV can improve the predictability of rainfalls and thunderstorms, thereby reducing the impacts caused by these short-term severe weather events. This is especially significant for a highly populated and at the same time highly humid city as Hong Kong. However, PWV is highly variable in space and time. It is a big challenge to obtain accurate water vapor information with high spatial and temporal resolution by using a single type of instrument or technique alone.

In the past few decades, many techniques have been developed to measure the water vapor in atmosphere. Among them, the most traditional water vapor observation technique is the radiosonde. Radiosonde provides the longest archive of water vapor data and has been employed as a major source to study the long-term tropospheric water vapor trend [5–7]. In addition, since the radiosonde can measure PWV with an accuracy of a few millimeters, it is often used as an accuracy standard to evaluate the performances of other water vapor sensors [8, 9]. Unfortunately, subject to sparse spatial distribution of radiosonde stations and low temporal resolution (usually only twice launches of balloon daily), water vapor data derived from radiosonde is difficult to meet the demand for short-term weather forecasting. Another accurate technique to retrieve atmospheric water vapor is water vapor radiometer (WVR) that is often used to calibrate wet tropospheric delay for geodetic observations such as very-long-baseline interferometry (VLBI) [10, 11]. A great advantage of WVR is that it can make observations with a much higher frequency (e.g. 15 min) at various elevations and azimuths [12]. However, during conditions of rainfalls, due to the detrimental effect of liquid water drops on the optics, the brightness temperatures will be in error, resulting in unreliable PWV measurements [8, 13, 14]. Obviously, this shortcoming restricts its applications in monitoring water

vapor variations for a region like Hong Kong where rain is often encountered. GPS technique has successfully demonstrated its ability to retrieve PWV with both high spatial and temporal resolutions. This technique, GPS or GNSS meteorology, was first published in Bevis et al. [4]. Subsequently, many studies have worked on water vapor retrieval from GNSS data and research results show that GNSS-derived PWV can reach an accuracy of few millimeters [8, 14–18]. Nevertheless, PWV estimated from GNSS data represents only the integrated water vapor above a certain station, and vertical distribution information of water vapor is poor. Another approach to obtain high spatial resolution water vapor data is to use numerical weather prediction (NWP) models. By processing and analyzing weather observation data with computer models, NWP is able to forecast the future weather state [19, 20]. NWP is developed based on complicated physical models and it has been evidenced that assimilation of water vapor data from other independent sensors into the NWP can improve the capability in severe weather phenomena forecasting [21, 22].

Many studies have been made to compare the measurements of PWV obtained from multiple techniques. For example, Niell et al. [8] did a systematic study on the comparison of water vapor data derived from radiosonde, WVR, GPS and VLBI. Their research showed that PWV obtained from these four techniques agreed within 1 mm. Li et al. [23] compared water vapor data obtained by radiosonde, GPS and moderate-resolution imaging spectroradiometer (MODIS) and they indicated that the MODIS PWV products should be calibrated before being utilized in tropospheric wet delay correction for geodetic observations such as interferometric synthetic aperture radar (InSAR). By using PWV measurements collected by GPS, radiosonde and WVR at several sites in Canada and Alaska during an 8-year period, Bokoye et al. [24] revealed that the root mean square (RMS) of the differences among these three techniques was about 2 mm . Ning et al. [14] conducted comparisons of water vapor data derived from observations made over a 10-year-long period by VLBI, WVR, radiosonde and the reanalysis product of the European Centre for Medium-Range Weather Forecasts (ECMWF). They found that the zenith wet delay (ZWD) derived from GPS, VLBI, WVR and ECMWF agreed within 7 mm. Vázquez et al. [25] assessed the quality of GPS derived PWV with respect to radiosonde and NWP data. Liu et al. [3] compared the water vapor products from radiosonde, MODIS and Aerosol Robotic NETwork (AERONET) sunphotometer at Hong Kong region. PWV derived from 6 years of AERONET agreed well with radiosonde with a RMS error of 2.89 mm. Their study also indicated that MODIS products are not suitable for the short-term weather forecasting since they have a low temporal resolution.

The Hong Kong Polytechnic University (PolyU) is in collaboration with the Hong Kong Observatory (HKO) to perform three-dimensional (3D) water vapor modelling using PWV data from multiple techniques including a network of GPS receivers, WVR and radiosonde instruments, with an ultimate goal to assimilate the 3D water vapor data into the NWP that is daily running at HKO. At the Hong Kong Polytechnic University, a PWV real-time monitoring system (PWVRMS) has been developed and in automated operation since 19 April 2012. This PWVRMS analyzes the GPS/GNSS data collected from the Hong Kong Satellite

Positioning Reference Station Network (SatRef). SatRef is a GPS/GNSS network of 12 stations that are managed and operated by the Lands Department, the Government of Hong Kong Special Administrative Region (HKSAR). The PWVRMS can provide PWV information of each station with a temporal resolution of 10 min [26]. However these GPS water vapor data have not been evaluated using collocated radiosonde data. The previous PWV comparison had a large distance separation between GPS station and radiosonde station [26].

For this study, one GPS receiver was installed nearby the radiosonde station at King's Park, Hong Kong in June 2013. The test is designed so that a GPS-radiosonde collocation water vapor observation system can evaluate the GPS-derived PWV accuracy using radiosonde data. The PWV comparison of this collocation system is valuable to provide a realistic accuracy assessment of a large amount of real-time water vapor data obtained from the PWVRMS system, which are used in 3D water vapor modeling. The 3D water vapor data are planned to be assimilated into the NWP being run at the Hong Kong Observatory in the future. It is expected that the assimilation of 3D water vapor into NWP will allow the improvement of weather forecasting capability in Hong Kong. However, it is important to understand the quality and characteristics of the water vapor data obtained from various techniques prior to their assimilation into NWP.

In this study, the PWV derived from NWP's non-hydrostatic model (NHM), WVR, radiosonde and GPS in Hong Kong over a 6-month-period (June to November 2013) are analyzed. This research aims to evaluate the quality of water vapor data obtained from multiple sensors with an aim to prepare the water vapor data assimilation into the NWP conducted in Hong Kong Observatory's daily operations. This will be particularly beneficial to the short-term weather forecasting in Hong Kong region. Section 16.2 describes the four water vapor observation techniques including GPS, radiosonde, WVR and NHM. Comparison results of PWV are presented in Sect. 16.3, followed by the discussions and conclusions in Sect. 16.4.

16.2 Description of Multiple Water Vapor Observations

16.2.1 GPS

A GPS signal from a distant satellite received by ground GPS receiver is delayed by the troposphere in atmosphere. Unlike the ionosphere, the tropospheric delay cannot be eliminated by GPS observations at two different frequencies because of the non-dispersive characteristic of troposphere [26]. On the other hand, due to the refraction effect on radio signals by the troposphere, we are able to estimate the tropospheric delay from GPS observations. Basically, the zenith tropospheric delay (ZTD) can be estimated from two different GPS data processing techniques, namely precise point positioning (PPP) and double-differencing [16, 18, 27, 28].

Usually, the ZTD can be split into two components: zenith hydrostatic delay (ZHD) and zenith wet delay (ZWD). ZHD can be calculated with surface pressure and temperature at a reasonable good accuracy using empirical models such as Saastamoinen model [29]. Thus, ZWD can be derived by removing the ZHD from ZTD. ZWD can be readily converted into PWV by using the formula below [30]:

$$PWV = k \cdot ZWD \tag{16.1}$$

where k is the conversion factor and is a function of the weighted mean temperature of the atmosphere [4]. Based on the analysis of 8-year radiosonde data, Chen et al. indicated the best conversion factor k is equal to 0.162 without the need of using the surface temperature in Hong Kong [30]. The GPS station, equipped with a GPS/GLONASS receiver (model: Eclipse II R320) that was donated by its manufacturer Hemisphere GPS Inc. to the authors for this research, is collocated with the radiosonde station at the King's Park (22.32°N, 114.17°E) in Hong Kong. This GPS/GLONASS receiver and radiosonde collocation observation system was built on 7 June 2013 and it is the first such system in Hong Kong. In this study, GPS data are processed by Bernese 5.0 software to obtain the PWV measurements.

16.2.2 Radiosonde

The radiosonde station in Hong Kong is situated at the King's Park (22.32°N, 114.17°E) and this is the only one in the Hong Kong region. Radiosonde balloons are launched twice per day by the Hong Kong Observatory (HKO) at UTC 0:00 and 12:00 (Local hour UTC+8), respectively. The radiosonde instrument used by the HKO is the Vaisala RS92, which claims to have a reproducibility of better than 2 %. Radiosonde is able to measure meteorological parameters such as pressure, temperature and relative humidity at various altitudes from the balloon-borne platform. By using these meteorological parameters, PWV (unit:mm) in a layer is calculated as [5]:

$$WV = \frac{1}{g} \int_{p_1}^{p_2} \frac{0.622 \cdot e}{p - e} d_p \tag{16.2}$$

where WV is the PWV in a layer bounded by pressure p_1 and p_2 (unit:Pascal) that are measured at two altitudes. g is the acceleration of gravity (i.e. 9.806 m s^{-2}). p and e are the atmosphere pressure (unit:Pascal) and water vapor pressure (unit:Pascal), respectively. PWV measurements derived from radiosonde data are often used as accuracy standard to evaluate water vapor data from other independent sensors. Because of its expensive operation cost, radiosonde data have a low temporal data rate that restricts its applications in short-term weather forecasting.

16.2.3 WVR

The WVR used in this study is located at the headquarters of the HKO, which is about 1 km from the radiosonde station [31]. WVR data are acquired with an interval of 15 min. Seven oxygen channels and seven water vapor channels are used to measure the temperature, humidity and liquid water vapor profiles up to a height of 10 km in zenith model [32]. HKO employs the neural network approach to retrieve the water vapor data from observations at various frequency channels on the basis of using radiosonde data [32]. Because WVR data accuracy is degraded by liquid water drops on the optics, PWV measurements collected under the conditions of rainfalls are discarded in the data analysis.

16.2.4 NHM

Based on the NHM developed by the Japan Meteorological Agency (JMA), HKO has been operating a new NWP system from 2010 [33]. The mesoscale NHM is now running at a horizontal resolution of 10 km with a configuration of $585 \times 405 \times 50$ (vertical) grid points. The NHM data are updated every 3 h and have an ability to provide forecast up to 72 h ahead [34]. After several experimental trials, it is shown that NHM is able to improve the capability of prediction of severe weather and mesoscale convective systems for Hong Kong region [33, 34]. NHM is operated with sophisticated physical schemes and the initial condition is from the JMA Global Spectral Model (GSM), JNoVA-3DVAR (JMA Non-hydrostatic model based Variational data Assimilation system) and the Local Analysis and Prediction System (LAPS) cloud moisture analysis [34]. It is expected that by ingesting water vapor data obtained from other observations such as GPS, radiosonde and WVR into the NHM, the NWP can improve its capability in short-term severe weather prediction. This is exactly the research motivation of this paper.

16.3 PWV Comparisons Among GPS, Radiosonde, WVR and NHM

Intercomparisons have been conducted among all four techniques for PWV time series measurements. In our study, PWV time series measurements derived from the four techniques during the period from 7 June 2013 to 24 November 2013 were used in comparisons. Before the analysis, outliers that may be due to instrumental error or record error are rejected from the PWV time series measurements. In this study, an outlier is determined when the absolute difference between its value and the mean is greater than 3σ, where σ represents the standard deviation [23]. In addition, it should be noted that the differences of PWV derived from two

different techniques larger than triple standard deviation were considered as outliers and were discarded in data analysis. Thus, all statistics given below were based on data after outlier screening.

16.3.1 Comparisons of GPS, WVR and NHM with Radiosonde

The PWV measurements derived from the GPS and WVR have temporal resolutions of 30 and 15 min, respectively. The estimates from NHM have a temporal resolution of 3 h. Radiosonde observations are made with an interval of 12 h. Figure 16.1 presents the time series of PWV measurements retrieved from GPS, WVR, NHM, and radiosonde during the time period from 7 June 2013 to 24 November 2013 in Hong Kong. Over the approximately 6-month period, there are a total of 332 radiosonde observations. For comparison purpose, only PWV measurements obtained at 0 and 12 h UTC from the GPS, WVR and NHM are adopted. Because of the high accuracy of radiosonde data, it is often employed as a reference to evaluate water vapor data retrieved from other techniques [3, 8, 9, 35]. Thus, by comparing water vapor data derived from GPS, WVR, and NHM with radiosonde data, it is clear to understand the performance of these three techniques.

Figure 16.2 shows the comparison of PWV obtained from the GPS and radiosonde observations. GPS PWV measurements agree with radiosonde data at a correlation coefficient $r = 0.979$. The bias, standard deviation (STD), and root mean square (RMS) error are -1.101, 2.589, and 2.810 mm, respectively (see also Table 16.1). The maximum (Max) and minimum (Min) differences of PWV between GPS and radiosonde are 5.031 and -7.211 mm, respectively (see also Table 16.1). As shown in Fig. 16.3, we can observe that PWV derived from WVR agree well with radiosonde data, with a high correlation coefficient $r = 0.983$. The bias, STD, and RMS error between the two observation techniques are 0.176, 2.468, and 2.474 mm, respectively. In Fig. 16.4, we present the PWV comparison between the NHM and radiosonde. The bias, STD, and RMS error for the two techniques are 1.682, 2.729, and 3.207 mm, respectively (see also Table 16.1). The correlation coefficient between the NHM and radiosonde technique is $r = 0.975$. We can clearly find that PWV obtained from WVR have the best agreement with radiosonde data. This may be because that the HKO utilizes the radiosonde data as references to retrieve the water vapor data from the WVR observations. Moreover, in this study only the WVR observations measured under no rains adopted in the comparison, this may also lead to the good agreement between the WVR and radiosonde. The relative poor performance of NHM can be explained by the fact that NHM water vapor is derived from physical models instead of actual observations. The fact that GPS-derived and WVR-derived water vapor data have an accuracy higher than NHM water vapor data implies that the

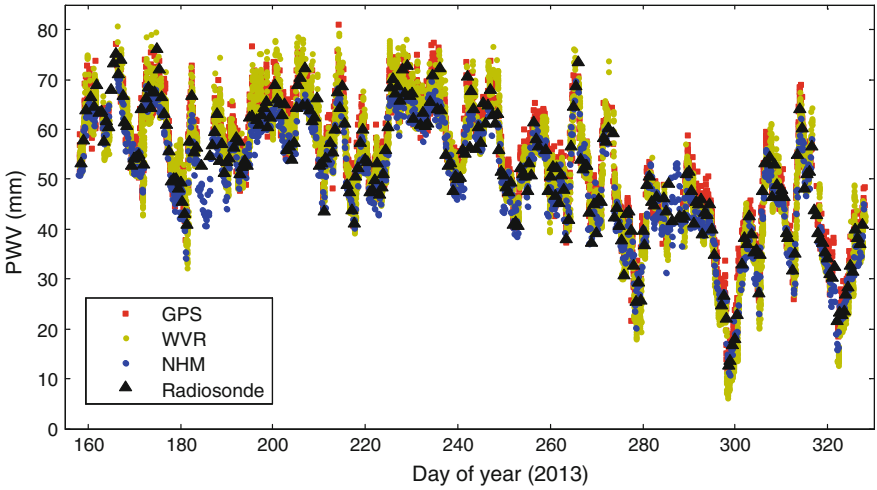

Fig. 16.1 PWV time series measurements derived from GPS, WVR, NHM, and radiosonde during the time period from 7 June 2013 to 24 November 2013 in Hong Kong

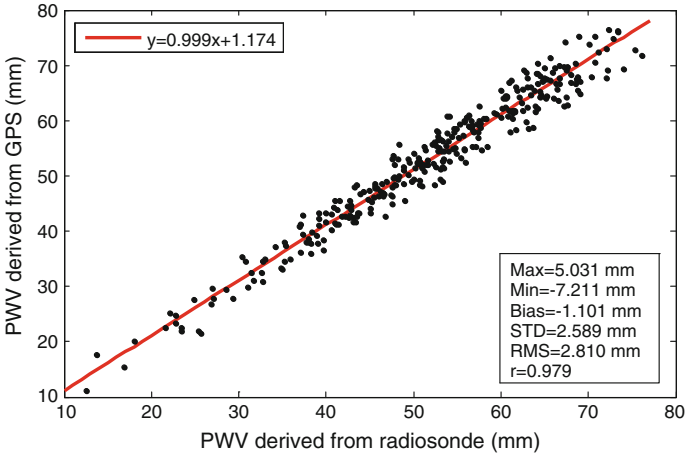

Fig. 16.2 Comparison of PWV between GPS and radiosonde measurements

assimilation of water vapor data observed from multiple techniques (e.g. GPS, WVR, and radiosonde) into the NHM can further enhance the NWP's weather forecasting performance. In addition, we notice that GPS PWV measurements show a good agreement with radiosonde data. Since GPS technique has a much higher spatial resolution (horizontally) and lower operation cost, it will be an important approach to monitor the water vapor distribution in meteorological research. We also compared the water vapor retrieved from GPS, WVR, and NHM

Table 16.1 Intercomparisons of the PWV estimated from GPS, radiosonde, WVR, and NHM data for the time period from 7 June 2013 to 24 November 2013 in Hong Kong

Comparison	Bias (mm)	STD (mm)	RMS error (mm)	Maximum difference (mm)	Minimum difference (mm)	Correlation coefficient r
Radiosonde-GPS	−1.101	2.589	2.810	5.031	−7.211	0.979
Radiosonde-WVR	0.176	2.468	2.474	6.650	−8.586	0.983
Radiosonde-NHM	1.682	2.729	3.207	7.961	−4.102	0.975
NHM-GPS	−3.155	2.859	4.259	3.424	−9.764	0.975
NHM-WVR	−1.855	3.754	4.188	7.970	−14.705	0.962
GPS-WVR	1.182	3.462	3.658	12.414	−11.034	0.968

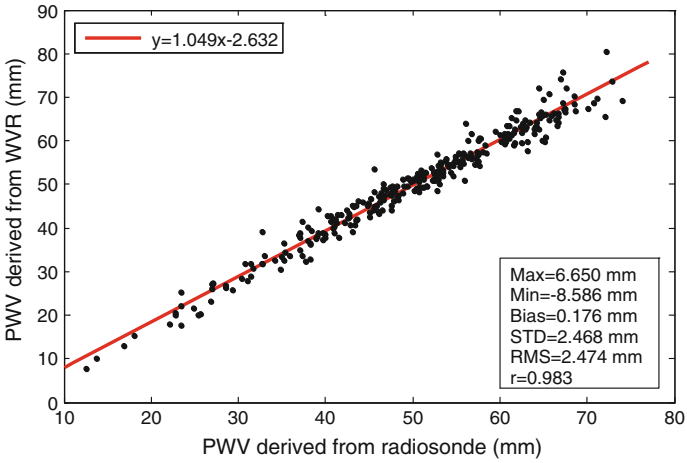

Fig. 16.3 Comparison of PWV between WVR and radiosonde measurements

with radiosonde data on a monthly scale. As shown in Table 16.2 and Fig. 16.5, we can find that biases and RMS errors of all the comparisons vary in different months. Generally, the RMS errors in summer months (June, July, and August) are larger than those in autumn months (September, October, and November). This is because summer is the most humid season of the year in Hong Kong and the water vapor in summer experiences much larger variations than other seasons.

Some previous studies have shown that there are day-night differences in the radiosonde observations [23, 36, 37]. In this study, in order to investigate the day-night differences of the radiosonde measurements, we compare the PWV derived from GPS, WVR, and NHM with radiosonde data separately for day and night cases. Table 16.3 gives the details of the statistical results. In daytime, RMS errors of 2.867, 2.670, and 3.512 mm were yielded for radiosonde-GPS, radiosonde-WVR, and radiosonde-NHM, respectively. Their correlation coefficients are 0.978, 0.979, and 0.973, respectively. Using only the nighttime measurements, the RMS

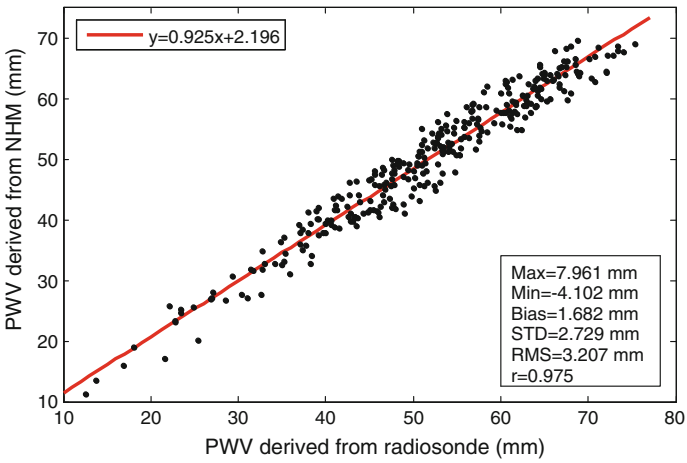

Fig. 16.4 Comparison of PWV between NHM and radiosonde measurements

Table 16.2 Monthly comparisons of PWV between radiosonde to GPS, WVR, NHM data in Hong Kong (unit:mm)

Comparison		June	July	August	September	October	November
Radiosonde-GPS	Bias	0.316	−2.098	−1.461	−1.706	−0.407	−0.897
	RMS	2.963	3.682	2.959	2.825	2.035	2.141
Radiosonde-WVR	Bias	0.367	−0.476	−0.436	−0.517	1.066	0.983
	RMS	2.492	2.947	2.176	2.149	2.602	2.438
Radiosonde-NHM	Bias	2.011	2.186	1.609	1.228	1.601	1.520
	RMS	3.295	3.413	3.269	3.274	3.114	2.894

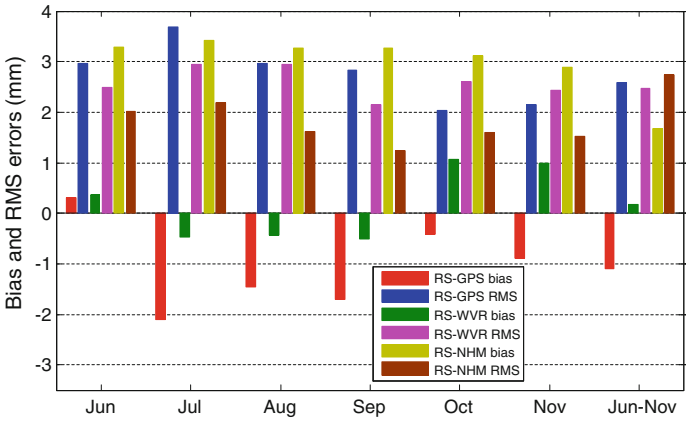

Fig. 16.5 Statistics of PWV comparisons between radiosonde and GPS (*RS-GPS*), radiosonde and WVR (*RS-WVR*), radiosonde and NHM (*RS-NHM*) for the months of June, July, August, September, October, November, and June to November

Table 16.3 Day-night differences of the comparisons between radiosonde and GPS, WVR, NHM data for the time period from 7 June 2013 to 24 November 2013 in Hong Kong

Comparison		Bias (mm)	STD (mm)	RMS error (mm)	Maximum difference (mm)	Minimum difference (mm)	Correlation coefficient r
Radiosonde-GPS	Day	−0.815	2.748	2.867	5.031	−6.055	0.978
	Night	−1.360	2.147	2.775	4.445	−7.211	0.985
Radiosonde-WVR	Day	−0.361	2.646	2.670	5.629	−8.586	0.979
	Night	0.667	2.189	2.289	6.650	−5.095	0.988
Radiosonde-NHM	Day	1.608	2.938	3.512	7.961	−4.102	0.973
	Night	1.755	2.512	3.068	7.923	−3.478	0.978

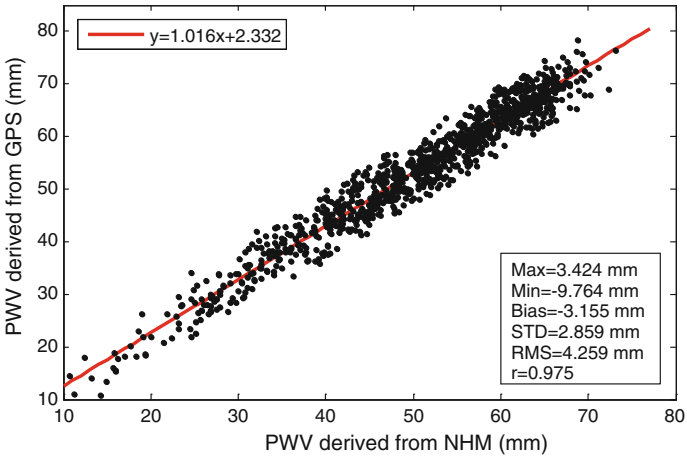

Fig. 16.6 Comparison of PWV between GPS and NHM measurements

errors between radiosonde and GPS, radiosonde and WVR, radiosonde and NHM are 2.775, 2.289, and 3.068 mm, respectively. In addition, the nighttime correlation coefficients for radiosonde-GPS, radiosonde-WVR, and radiosonde-NHM are 0.985, 0.988, and 0.978, respectively. Obviously, we can find that the RMS errors of PWV differences in the daytime are larger than those in nighttime. This may due to the impact of solar radiation to the radiosonde sensors in the daytime. The solar radiation can heat the relative humidity (RH) sensor, which results in a smaller reading of relative humidity values [23, 38].

16.3.2 Comparisons of GPS and WVR with NHM

NHM has a temporal resolution of 3 h that is much lower than GPS and WVR techniques. During the 6-month period, a total of 1346 NHM observations can be used in the comparison. As shown in Figs. 16.6 and 16.7, the correlation

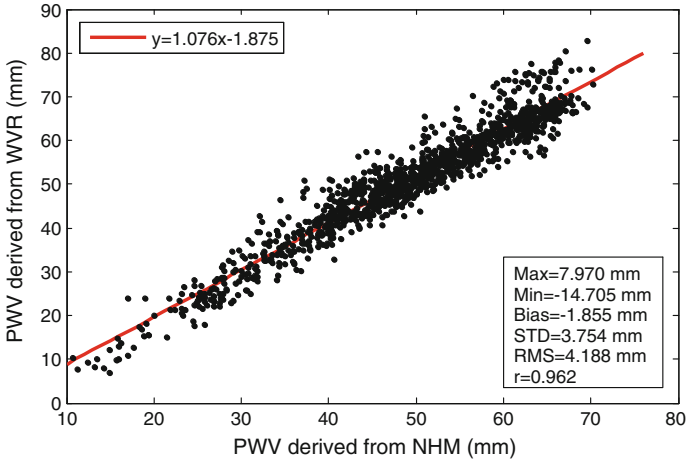

Fig. 16.7 Comparison of PWV between WVR and NHM measurements

coefficients between GPS PWV and NHM PWV, WVR PWV and NHM PWV, are 0.975 and 0.962 respectively (see also Table 16.1). The bias, STD, and RMS error between GPS PWV and NHM PWV are −3.155, 2.859, and 4.259 mm, respectively (see also Table 16.1). Compared the water vapor data derived from WVR with NHM data, statistical results show that the bias, STD, and RMS error are −1.855, 3.754, and 4.188 mm, respectively (see Table 16.1 and Fig. 16.7). We can observe that the RMS of NHM with respect to GPS is larger than that with respect to WVR data. This indicates that PWV derived from NHM agree slightly better with WVR data than with GPS data. Nevertheless, as discussed above, both GPS and WVR water vapor products have higher accuracies than the NHM water vapor, if the radiosonde water vapor data are used as reference.

16.3.3 Comparisons Between GPS and WVR Data

In our study, GPS PWV measurements have a temporal resolution of 30 min and WVR data are available with an interval of 15 min. The PWV values derived from WVR during 30 min (i.e. two WVR PWV measurements) were averaged for comparison with GPS. Figure 16.8 shows the comparison of GPS and WVR PWV. It can be clearly seen that the bias, STD, and RMS error between the two observation techniques are 1.182, 3.462, and 3.658 mm, respectively (see also Table 16.1). The maximum and minimum difference of GPS PWV and WVR PWV are 12.414 and −11.034 mm, respectively (see also Table 16.1). The correlation coefficient between the two techniques is $r = 0.983$, which is lower than those of GPS PWV respect to radiosonde and NHM data (see Table 16.1). It can

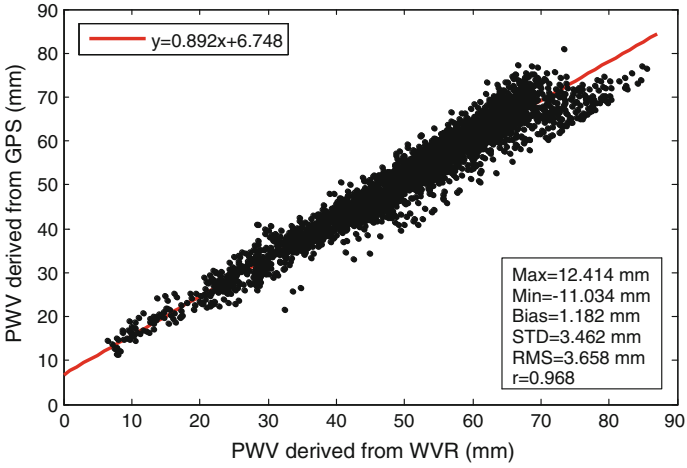

Fig. 16.8 Comparison of PWV between GPS and WVR measurements

be possibly explained by the different observation intervals. As mentioned before, the temporal resolutions for WVR, GPS, NHM, and radiosonde PWV are 15, 30 min, 3 and 12 h, respectively.

16.4 Discussion and Conclusion

Due to their crucial role in meteorological research, intercomparisons of PWV estimates derived from GPS, radiosonde, WVR, and NHM are carried out for an approximate 6-month time period in 2013 at the Hong Kong Observatory. The comparisons between the GPS, radiosonde, WVR, and NHM PWV data show RMS errors of 2.474–4.259 mm. All the statistical results show that water vapor data derived from these four observation techniques have good agreements with each other.

Using the radiosonde data as a reference, the accuracies of water vapor data derived from GPS, WVR, and NHM are carefully evaluated. Results show that the RMS error of radiosonde-GPS PWV, radiosonde-WVR PWV, and radiosonde-NHM PWV are 2.810, 2.474, and 3.207 mm, respectively. The correlation coefficients between radiosonde and GPS, radiosonde and WVR, radiosonde and NHM, are 0.979, 0.983 and 0.975, respectively. The statistical results demonstrated that WVR can retrieve the PWV with a high accuracy. For the GPS derived PWV measurements, many previous studies showed that the comparison of PWV derived from GPS with radiosonde is consistent at the level of 1–2 mm [8, 23, 39, 40]. In our study, the RMS error between GPS derived PWV and radiosonde data is 2.810 mm. It is slightly higher than other studies. After a numerical data

analysis, we conclude this is due to the impact of phase center variation (PCV) of the Hemisphere GPS receiver antenna. In our research, the antenna we used is the Hemisphere (A52 WB ANTENNA). Unfortunately no PCV calibration data for this type of antenna are available in the International GNSS Service (IGS) antenna calibration database (refer to ftp://ftp.unibe.ch/aiub/BSWUSER50/GEN/PHAS_COD.I08). Therefore no antenna PCV is adopted during the GPS water vapor estimation in this study. We did several tests to evaluate the impact of PCV on the estimates of PWV by using Bernese 5.0 software. In our experiments, the antenna used is the Leica AR25.R4 LEIT and its PCV calibration data is available in the IGS antenna calibration database (see ftp://ftp.unibe.ch/aiub/BSWUSER50/GEN/PHAS_COD.I08). We compared the PWVs estimated considering PCV calibration with those without PCV calibration and found that there is a bias of 1.84 mm between the two PWV estimates. This is consistent with Zhang's study which showed that PCV can result in a bias of 1–2 mm to the estimates of PWV [41]. Thus, we conclude the relatively large RMS error between the GPS and radiosonde yielded in our study is attributed to unavailability of antenna PCV information. We also compared the PWV measurements derived from GPS and WVR with NHM data. The RMS errors between GPS, WVR and NHM are 4.259 and 4.188 mm, respectively. The relatively high RMS errors may probably due to the fact that NHM is developed based on complicated physical models and that NHM lacks enough actually measured meteorological data. Furthermore, comparisons between PWV measurements derived from GPS and WVR data were performed. The bias, STD, RMS error, and correlation coefficient between the two observation techniques are 1.182, 3.462, 3.658 mm, and 0.968, respectively.

Over the past decade, owing to high level of greenhouse gas emissions from the Pearl-River-Delta region, Hong Kong has suffered increased air pollution and high concentrations of water vapor leading to more uncertainties in reliable weather forecasting. It is now urgent to improve the capability of short-term severe weather prediction, such as hails, rainfalls and thunderstorms. The numerical weather prediction model NHM, which is daily operated at HKO, has the ability to provide forecast up to 72 h ahead for Hong Kong region. Our study shows that water vapor data obtained from GPS and WVR have higher accuracies than the water vapor data generated from the NHM model itself. Thus it is reasonable to expect that after assimilating the GPS-derived and WVR-derived water vapor data into the NHM, its ability of short-term weather prediction can be improved. Especially for GPS, its advantages of high temporal and horizontal resolution, and low operation cost will enable it to play an important role in the short-term weather forecasting and long-term climate change research in Hong Kong.

Acknowledgments This work is supported by the Hong Kong Research Grants Council (RGC) General Research Fund (GRF) project B-Q28F. The supports from the National Natural Science Foundation of China (NSFC No. 41274039) are gratefully acknowledged. Mr. Sai Tick Chan, Mr. Wang Chun Woo and Mr. P. W. Chan from the Hong Kong Observatory, the Government of Hong Kong Special Administrative Region (HKSAR), are acknowledged for providing the WVR and NHM data. The authors also thank the Department of Atmospheric Science of University of

Wyoming for providing the Hong Kong radiosonde data. The Lands Department of the Government of Hong Kong Special Administrative Region (HKSAR) is thanked for providing GPS/GNSS data from the Hong Kong Satellite Positioning Reference Station Network (SatRef).

References

1. Ohtani R, Naito I (2000) Comparisons of GPS-derived precipitable water vapors with radiosonde observations in Japan. J Geophys Res 105(D22):26917–26929
2. Mattar C, Sobrino JA, Julien Y, Morales L (2011) Trends in column integrated water vapour over Europe from 1973 to 2003. Int J Climatol 31(12):1749–1757
3. Liu Z, Wong MS, Nichol J, Chan PW (2013) A multi-sensor study of water vapour from radiosonde, MODIS and AERONET: a case study of Hong Kong. Int J Climatol 33(1):109–120
4. Bevis M, Businger S, Herring TA, Rocken C, Anthes RA, Ware RH (1992) GPS meteorology: remote sensing of atmospheric water vapor using the Global Positioning System. J Geophys Res Atmos 1984–2012 97(D14):15787–15801
5. Ross RJ, Elliott WP (1996) Tropospheric water vapor climatology and trends over North America: 1973-93. J Clim 9:3561–3574
6. Zhai P, Eskridge RE (1997) Atmospheric water vapor over China. J Clim 10(10):2643–2652
7. Ross RJ, Elliott WP (2001) Radiosonde-based northern hemisphere tropospheric water vapor trends. J Clim 14:1602–1612
8. Niell AE, Coster AJ, Solheim FS, Mendes VB, Toor PC, Langley RB et al (2001) Comparison of measurements of atmospheric wet delay by radiosonde, water vapor radiometer, GPS, and VLBI. J Atmos Ocean Technol 18:830–850
9. Adeyemi B, Joerg S (2012) Analysis of water vapor over Nigeria using radiosonde and satellite data. J Appl Meteorol Climatol 51(10):1855–1866
10. Beckman B (1985) A water-vapor radiometer error model. IEEE Trans Geosci Remote Sens 4:474–478
11. Elgered G, Davis JL, Herring TA, Shapiro II (1991) Geodesy by radio interferometry: water vapor radiometry for estimation of the wet delay. J Geophys Res Solid Earth 1978–2012 96(B4):6541–6555
12. Liu Z, Li M, Zhong W, Wong MS (2013) An approach to evaluate the absolute accuracy of WVR water vapor measurements inferred from multiple water vapor techniques. J Geodyn (Internet), Available from: http://linkinghub.elsevier.com/retrieve/pii/S0264370713001348
13. Guiraud FO, Howard J, Hogg DC (1979) A dual-channel microwave radiometer for measurement of precipitable water vapor and liquid. IEEE Trans Geosci Electron 17(4):129–136
14. Ning T, Haas R, Elgered G, Willén U (2011) Multi-technique comparisons of 10 years of wet delay estimates on the west coast of Sweden. J Geod 86(7):565–575
15. Rocken C, Ware R, Van Hove T, Solheim F, Alber C, Johnson J et al (1993) Sensing atmospheric water vapor with the global positioning system. Geophys Res Lett 20(23):2631–2634
16. Duan J, Bevis M, Fang P, Bock Y, Chiswell S, Businger S et al (1996) GPS Meteorology: direct estimation of the absolute value of precipitable water. J Appl Meteorol 35(6):830–838
17. Raja MKRV, Gutman SI, Yoe JG, McMillin LM, Zhao J (2008) The validation of AIRS retrievals of integrated precipitable water vapor using measurements from a network of ground-based GPS receivers over the contiguous United States. J Atmos Ocean Technol 25(3):416–428
18. Lee S-W, Kouba J, Schutz B, Kim DH, Lee YJ (2013) Monitoring precipitable water vapor in real-time using global navigation satellite systems. J Geod 87(10–12):923–934

19. Stephens GS (1984) The parameterization of radiation for numerical weather prediction and climate models. Mon Weather Rev 112:826–867
20. Kimura R (2002) Numerical weather prediction. J Wind Eng Ind Aerodyn 90(12):1403–1414
21. Gendt G, Dick G, Reigber C, Tomassini M, Liu Y, Ramatschi M (2004) Near real time GPS water vapor monitoring for numerical weather prediction in Germany. J Meteorol Soc Jpn 82(1B):361–370
22. De Haan S, Holleman I, Holtslag AAM (2009) Real-time water vapor maps from a GPS surface network: construction, validation, and applications. J Appl Meteorol Climatol 48(7):1302–1316
23. Li Z, Muller JP, Cross P (2003) Comparison of precipitable water vapor derived from radiosonde, GPS, and Moderate-Resolution Imaging Spectroradiometer measurements. J Geophys Res 108(D20). Available from: http://doi.wiley.com/10.1029/2003JD003372
24. Bokoye AI, Royer, A, O'Neill NT, Cliche P, McArthur LJB, Teillet PM (2003) Multisensor analysis of integrated atmospheric water vapor over Canada and Alaska. J Geophys Res 108(D15). Available from: http://doi.wiley.com/10.1029/2002JD002721
25. Vázquez BGE, Grejner-Brzezinska DA (2012) GPS-PWV estimation and validation with radiosonde data and numerical weather prediction model in Antarctica. GPS Solutions 17(1):29–39
26. Liu Z, Li M (2013) The first PPP-based GPS water vapor real-time monitoring system in Pearl-River-Delta Region, China. In: Sun J, Jiao W, Wu H, Shi C (eds) Proceedings of China satellite navigation conference (CSNC) 2013 [Internet]. Springer Berlin, Heidelberg (cited 26 Nov 2013), pp 71–87. Available from: http://link.springer.com/10.1007/978-3-642-37398-5_7
27. Wielgosz P, Cellmer S, Rzepecka Z, Paziewski J, Grejner-Brzezinska DA (2011) Troposphere modeling for precise GPS rapid static positioning in mountainous areas. Meas Sci Technol 22(4):045101
28. Tao W (2008) Near real-time GPS PPP-inferred water vapor system development and evaluation. University of Calgary, Calgary. Available from: http://www.ucalgary.ca/engo_webdocs/YG/08.20275.WenyouTao.pdf
29. Saastamoinen J (1972) Atmospheric correction for the troposphere and stratosphere in radio ranging satellites. AGU, Washington, DC, pp 247–251. Available from: http://dx.doi.org/10.1029/GM015p0247
30. Chen Y, Liu Y, Wang X, Li P (2007) GPS real-time estimation of precipitable water vapor-Hong Kong experiences. Acta Geod Cartogr Sin 36:9–12
31. Chan PW (2009) Nowcasting applications of a microwave radiometer in Hong Kong. Delft, The Netherlands
32. Chan PW (2010) The use of neural network retrieval for thermodynamic profiles of a ground-based microwave radiometer. Washington, DC, USA
33. Chan ST, Chan TF, Wong WK (2010) An intercomparison of WRF-ARW and JMA-NHM performance in prediction of tropical cyclones over the South China Sea in 2008. In: 29th conference on hurricanes and tropical meteorology American Meteorological Society. Available from: http://203.129.68.41/publica/reprint/r887.pdf
34. Wong WK (2010) Development of operational rapid update non-hydrostatic NWP and data assimilation systems in the Hong Kong Observatory. In: The 3rd international workshop on prevention and mitigation of meteorological disasters in Southeast Asia, pp 1–4. Available from: http://203.129.68.5/publica/reprint/r882.pdf
35. Soden BJ (2004) An analysis of satellite, radiosonde, and lidar observations of upper tropospheric water vapor from the Atmospheric Radiation Measurement Program. J Geophys Res 109(D4). Available from: http://doi.wiley.com/10.1029/2003JD003828
36. Park C-G, Roh K-M, Cho J-H (2012) Radiosonde sensors bias in precipitable water vapor from comparisons with Global Positioning System Measurements. J Astron Space Sci 29(3):295–303
37. Vaisala radiosonde RS92 performance in the WMO intercomparison of high quality radiosonde systems, Yangjiang, China 2010, 2013, pp 17

38. Miloshevich LM, Vömel H, Whiteman DN, Leblanc T (2009) Accuracy assessment and correction of Vaisala RS92 radiosonde water vapor measurements. J Geophys Res 114(D11). Available from: http://doi.wiley.com/10.1029/2008JD011565
39. Elgered G, Johansson JM, Rönnäng BO (1997) Measuring regional atmospheric water vapor using the Swedish permanent GPS network. Geophys Res Lett 24(21):2663–2666
40. Tregoning P, Boers R, O'Brien D, Hendy M (1998) Accuracy of absolute precipitable water vapor estimates from GPS observations.pdf. J Geophys Res 103(D22):28701–28710
41. Zhang S (2009) Research and application of remote sensing water vapor using ground based GPS/Met. Wuhan University, Wuhan

Chapter 17
The Implementation of Rapid Acquisition Algorithm for GPS Weak Signal by Using FPGA

Yuanlei Wang, Yang Gao and Meng Wang

Abstract The traditional acquisition technology of low orbit GPS signal has been widely applied in the design of GPS navigation receiver. However, navigation receiver can only accept the navigation signal which comes from the other end of the earth when running above the navigation constellation, which results the decline of GPS navigation visibility and signal power, and the navigation signal power from high orbit navigation receiver will reduce 10 dB at least than low orbit navigation receiver and traditional fast acquisition design can not meet design requirements of high orbit navigation receiver. Therefore, this paper present a design which increase times of coherent integration to improve ratio of carrier and noise of received signal, at the same time, it uses full link simulation by simulink to verify feasibility of the design, the final design of weak signal acquisition, through the test of Xilink company Virtex4 series FPGA chip based on the weak signal acquisition sensitivity up to −176 dB. Because the GLONASS navigation system and BDS navigation and GPS navigation system using spread spectrum communication system, different with GPS navigation system in production of presucode ratio and presurange and the carrier frequence parameters. Therefore, this fast acquisition algorithm for GPS weak signal adapt to the design of GLONASS navigation receiver and BDS navigation receiver.

Keywords GPS · Weak signal · Fast acquisition · High orbit

Y. Wang (✉) · Y. Gao · M. Wang
Space Star Technology Co., Ltd, Beijing 100094, China
e-mail: Sandao650@126.com

J. Sun et al. (eds.), *China Satellite Navigation Conference (CSNC) 2014 Proceedings: Volume I*, Lecture Notes in Electrical Engineering 303,
DOI: 10.1007/978-3-642-54737-9_17,

17.1 Preface

Satellites running in high orbit can only receive GPS signal from the other side of the earth. Because of the shield of earth and energy loss through free space field, the visibility and signal intensity of GPS satellites decline very much for user satellites. There may be zero to three visible GPS satellites under this circumstances, even the visible GPS signal can hardly be received [1]. There are several features of high orbit satellites as follow:

Weak visibility of GPS satellite:
Satellites running in high orbit can receive GPS signal. Because the GPS satellites antenna point to the earth, the GPS receiver fixed on high orbit satellites can only receive the signal from the other side of the earth, resulting the weak visibility of GPS signal.

Low signal power:
Long distance transmission with atmosphere damping and ionosphere delay give rise to low signal power to be received.

Difficulty of signal capture:
Low GPS signal power make the capture of visible satellite a troublesome. For this reason, the study of GPS weak signal capture contributes much to the independent positioning of high orbit satellites and has important engineering application value.

17.2 Code Phase Compensation

To improve the capture sensitivity of GPS signal, the pre-detection integral time must be extend (pre-detection integral time need to be less half of navigation message bit). But in this way, the main problem is that code phase drift caused by code Doppler result in the damping, shifting or widening of correlation peak, affecting the capture performance. Therefore it is necessary to make some compensation, namely code Doppler compensation [2]. Figures 17.1, 17.2 give the output of correlation with code Doppler compensation or not. It is obvious that the correlation become widening and the energy decline.

Code Doppler is caused by the relative movement between satellite and receiver. Its calculation formula is as follow:

$$f_{D,C} = f_c \times \eta = f_c \times \frac{f_{D,1}}{f_{RF}} \tag{17.1}$$

where f_c is code rate.

During the pre-detection integral time, relative phase drift between received code and local code is:

$$\Delta p = f_{D,C} \times N_{nc} T_{coh} = f_{D,c} \times T_{PIT} \tag{17.2}$$

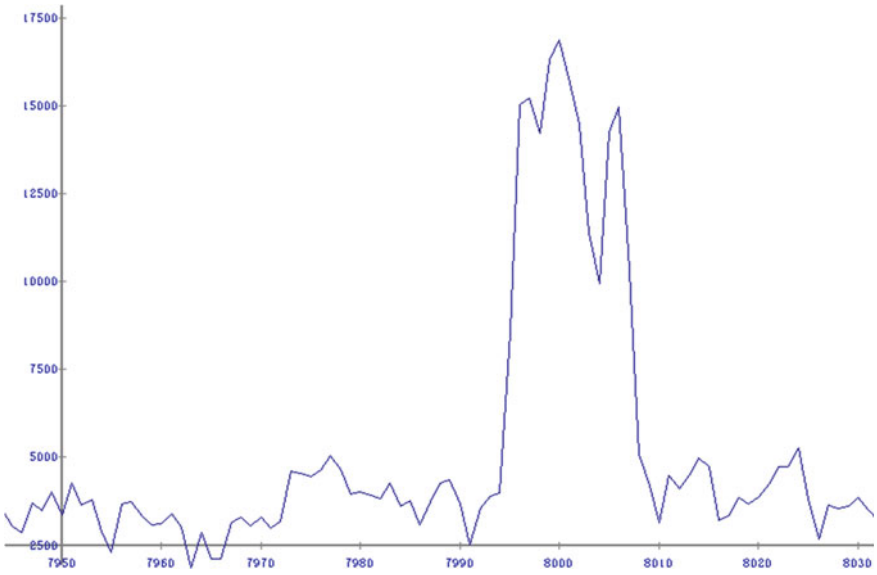

Fig. 17.1 No using code Doppler compensation correlation peak

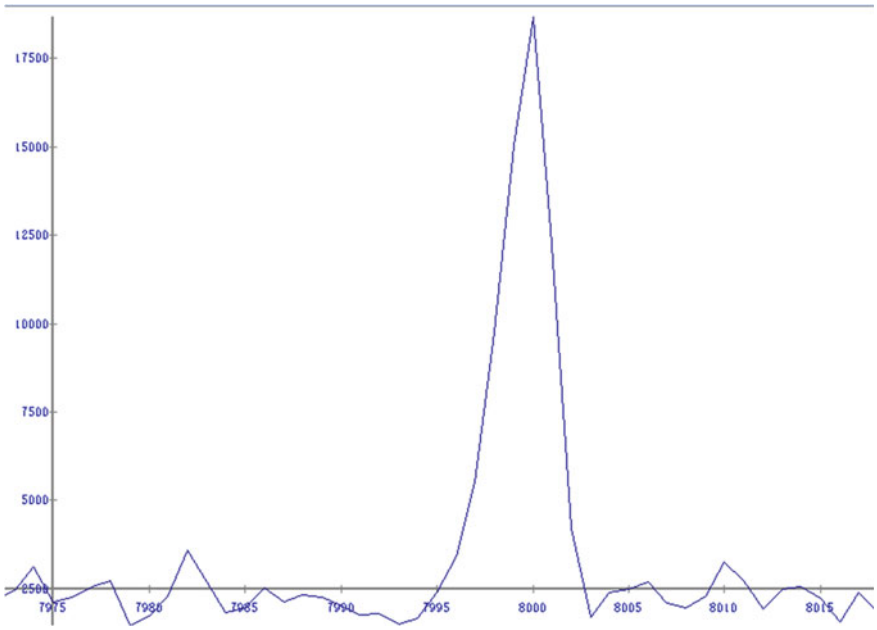

Fig. 17.2 Using code Doppler compensation correlation peak

where $T_{PIT} = N_{nc}T_{coh}$ is pre-detection integral time. Code phase drift lead to damping, shifting or widening of code self-correlation peak. GPS signal capture is three-dimensional search including C/A code number, C/A code phase and carrier frequency. Using time domain signal correlation capture GPS signals can not meet the requirements of real-time GPS capture. Taken parallel capture technology based on FFT (Fast Fourier Transform) can effectively improve the efficiency of capture.

17.3 Parallel Frequency Acquisition

Parallel frequency search algorithms capture process goes as follows: first, the input digital IF signal and the internal copied carrier mix each other, then correlation operate with the copied C/A. So I and Q correlation results thus obtained is a matter of self-correlation function $R(\tau)$ and the residual carrier frequency loss factor functions in $\sin c(f_e T_{coh})$ of the product; then, the correlation results $i + jq$ in the time domain by the Fourier transform of the signal transformed to the frequency domain, which reflects the intensity of each frequency component of the correlation results $i + jq$; finally, the frequency field amplitude of the signal is analyzed to find out the value of the residual frequency f_e and a received signal corresponding to the carrier frequency. If the copied C/A code phase is different from the received signal C/A code phase, the low correlation between them will suppress the amplitude of the signal before the Fourier transform and transform such fourier leaves no change in the results of a large amplitude, so the receiver may conclude that the received signal is not located on this search code phases corresponding to the band. Only when the copying C/A code phase and the received C/A code phase are aligned, the amplitude of the output of the Fourier transform may be an obvious peak, and the peak corresponding to the frequency band of the Fourier transform is the estimated value of the frequency error, and the copied C/A code phase signal is naturally an estimate of the number of the received signal phase. Thus the two-dimensional search used Fourier transform converts to a one-dimensional code phase search, thus improving the signal acquisition time [3] (Fig. 17.3).

17.4 Parallel Code Phase Acquisition

Similar to the way of the parallel search for frequency, when the frequency is be searched by sliding, the parallel search of code can be achieved. The algorithm for parallel search and capture of code is as follows: when the digital IF signals were respectively mixed with the carrier signal for the copy of sinusoidal and cosine which respectively belong to I branch and Q branch, parallel code phase search algorithm is not these results are correlated with C/A by digital correlator directly,

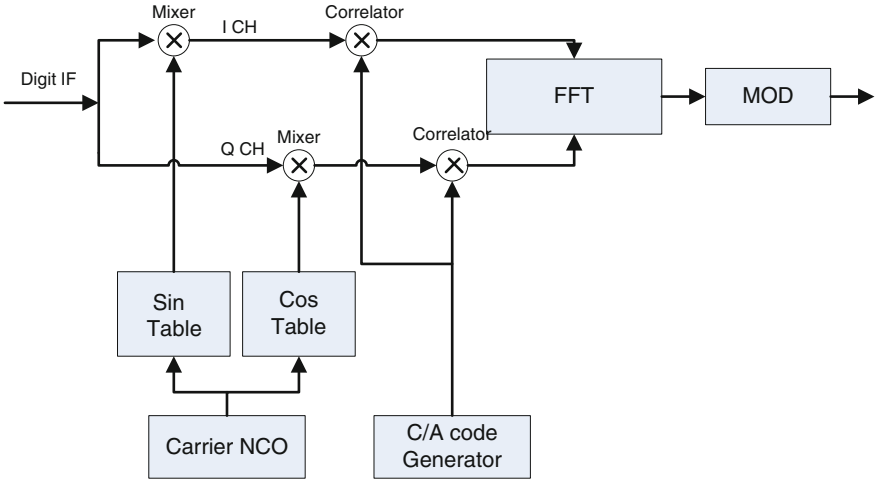

Fig. 17.3 Frequency parallel capture diagram

but doing fourier transform for the plural mixing results $i + jq$, and then the transform results are multiplied with the conjugate value of fourier transform for copy C/A code. Then, the multiplication results input the module of Inverse Fourier transform obtained in the time dimensions of correlation results. Finally, the correlation value is detected by analyzing the result of the determination signal is being or not. When completed the currently of band search and detection. The receiver then let the carrier numerically controlled oscillator copied to another sin and cos values with carrier frequency. Next, a similar frequency band to complete the search and detection (Fig. 17.4).

Compared parallel frequency acquisition and parallel code phase acquisition: for example, for the same two-dimensional search range, 41 search bands and 2,046 search code with a total of 83,886 (41 × 2,046) search unit. Two-dimensional search need to search for 83,886 times, parallel frequency search needs to search 2,046 times, parallel code phase search just search 41 times, but search speed is consumed by costs in exchange for a share of hardware resources required the large amount of RAM storage resources when achieved parallel code phase acquisition algorithm. This is also the reasons of parallel code phase search algorithm does not being widely used, however, the high-capacity FPGA chip is introduced, Parallel code phase acquisition algorithm has the effective realization of the hardware platform.

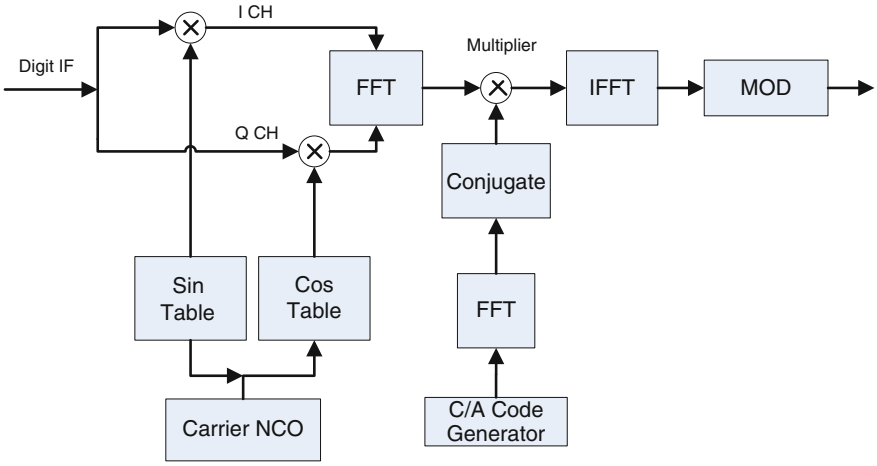

Fig. 17.4 Code parallel capture diagram

17.5 System Design for GPS Signal Capture Algorithm

To achieve high sensitivity to capture fast, so use the parallel code phase search acquisition mode for fast capture, combined with the carrier phase compensation and code Doppler compensation technique to achieve weak GPS signal capture algorithm [4]. Weak signal capture baseband processing module (circuit) structure chart as follows: signal capture circuit consists of preprocess, the relevant calculation mode, non-coherent accumulation and peak search and so on (Fig. 17.5).

17.5.1 AD Sampling Data Preprocess

Finished the AD sampling after data entering signal capture channels, in order to be able to adapt to the requirements of the signal capture algorithm, the ADC sample preprocess data will be into data preprocessing module. In addition, to avoid data bit flip, using 10 ms coherent accumulation, this module mainly to complete: In AD signal mixed to the baseband signal, a low pass filter, down sampling and 10 ms data buffer (Fig. 17.6).

17.5.2 Doppler Filtering and Removing Modules

Filter select comb filter, the 10 ms data was accumulated by the adder 1 ms data for increase signal fast capture sensitivity. Due to the Doppler frequency, leading

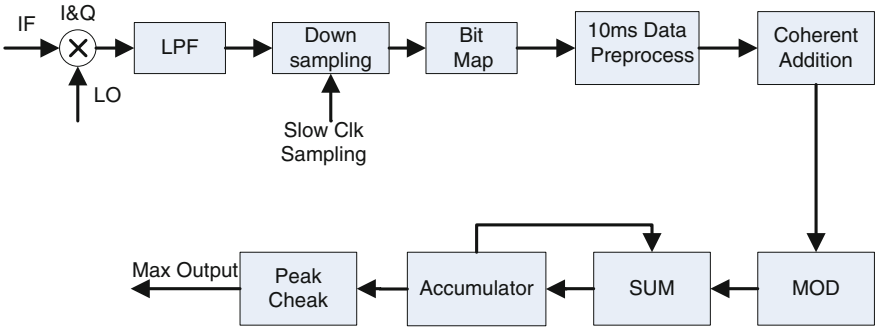

Fig. 17.5 Code parallel signal capture processing flow diagram

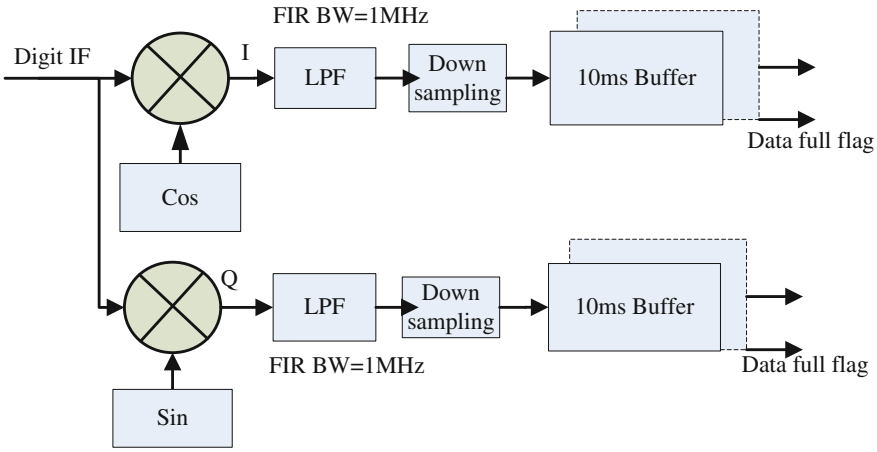

Fig. 17.6 AD sampling data pre-processing flow diagram

to phase of the carrier was changed in the time of 1 ms, then need carrier phase compensation during the signal processing. After the carrier phase compensation, according to the stepping frequency to remove the carrier Doppler frequency operation. Then performed of Down-sampling operation as in Fig. 17.7.

Assuming during a starting position in the n-th sampling point during 1 ms. Removed if carrier phase after removal of:

$$\theta(\tau_n) = \pi f_a \tau_n^2 + 2\pi f_d \tau_n + \theta_\Delta \tag{17.3}$$

so the k-th sample point in the m-th of 1 ms, after removal of the carrier frequency carrier phase is:

$$\begin{aligned}\theta(\tau_m + kT_{S_d}) = {} & \pi f_a (\tau_m + kT_{S_d})^2 \\ & + 2\pi f_d (\tau_m + kT_{S_d}) + \theta_\Delta\end{aligned} \tag{17.4}$$

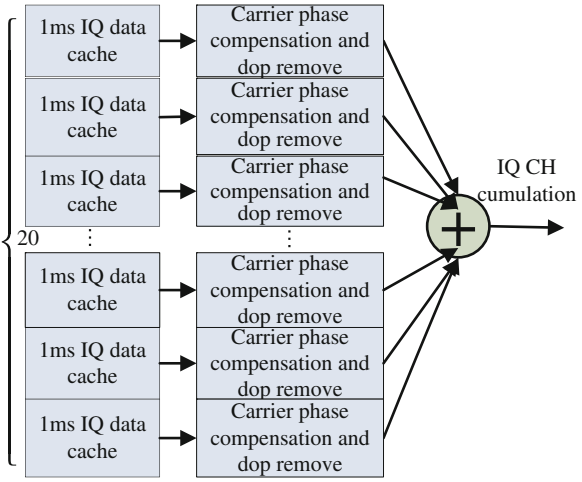

Fig. 17.7 Doppler filtering and removing structural diagram

Removed Carrier Doppler and the results of the carrier Doppler compensation is:

$$\theta'(\tau_m + kT_{S_d}) \approx \theta(\tau_n) \tag{17.5}$$

Therefore, construct the following correction:

$$\Delta\theta(m,k,n) = \theta(\tau_m + kT_{S_d}) - \theta(\tau_n) \tag{17.6}$$

The carrier Doppler remove and compensation results is:

$$\begin{aligned} \theta'(\tau_m + kT_{S_d}) &\approx \theta(\tau_n) \\ &= \theta(\tau_m + kT_{S_d}) - \Delta\theta(m,k,n) \end{aligned} \tag{17.7}$$

Next, the value of study formula $\Delta\theta(m,k,n)$:
Can be obtained:

$$\begin{aligned} \Delta\theta(m,k,n) &= \theta(\tau_m + kT_{S_d}) - \theta(\tau_n) \\ &= \pi f_a\left[(\tau_m + kT_{S_d})^2 - \tau_n^2\right] + 2\pi f_d(\tau_m - \tau_n + kT_{S_d}) \end{aligned} \tag{17.8}$$

Can be obtained:

$$\tau_m - \tau_n \approx (m-n)T_p \tag{17.9}$$

Therefore, can be obtained:

$$\Delta\theta(m,k,n) \approx 2\pi f_d\left[(m-n)T_p + kT_{S_d}\right] \tag{17.10}$$

Local estimated Doppler frequency shift $\hat{f}_d$. The phase correction amount is:

$$\Delta\hat{\theta}(m,k,n) \approx 2\pi\hat{f}_d\left[(m-n)T_p + kT_{S_d}\right] \tag{17.11}$$

Elimination of the carrier and the carrier Doppler compensation results is:

$$\theta'(\tau_m + kT_{S_d}) = \theta(\tau_m + kT_{S_d}) - 2\pi\hat{f}_d\left[(m-n)T_p + kT_{S_d}\right] \tag{17.12}$$

17.5.3 Non-coherent Accumulation Module

In order to achieve the capture of weak signals, by increasing the non-coherent accumulate times, to obtain high signal gain. Local C/A code generator by a fixed code rate code phase offset in 10 ms coherent accumulate is smaller, impact can be negligible for the coherent integration [5, 6], multiple non-coherent accumulation times due to the code phase offset is relatively large. Therefore, the code phase offset must be compensated, assuming the correlation function is:

$$\begin{aligned} r(\varepsilon) &= r(\tau_r - \tau_l) \\ &= E\{c(t+\tau_r)c(t+\tau_l)\} \end{aligned} \tag{17.13}$$

Within the $nN_{coherent}T_p$ seconds, correlation function of the sequence of the formula is obtained by FFT operation:

$$\begin{aligned} R_{0,k}(\varepsilon_0) &= E\{c(mT_S + \tau_r)c(mT_S + \tau_r + kT_S)\} \\ &= r(\tau_r - \tau_r - kT_S) = r(\varepsilon_0 - kT_S) \\ R_{n,k}(\varepsilon_0) &= r\left(\tau_r - \tau_r + \varepsilon^{\Delta}_{nN_{coherent}T_p} - kT_S\right) \\ &= r\left(\varepsilon_0 + \varepsilon^{\Delta}_{nN_{coherent}T_p} - kT_S\right) \end{aligned} \tag{17.14}$$

Clearly visible:

$$R_{n,k}(\varepsilon_0) = R_{0,k}\left(\varepsilon_0 + \varepsilon^{\Delta}_{nN_{coherent}T_p}\right) \tag{17.15}$$

In the above formula:

$$\varepsilon^{\Delta}_{nN_{coherent}T_p} \approx n\frac{f_d}{f_L}N_{coherent}T_p \tag{17.16}$$

Assume:

$$\varepsilon^{\Delta}_{nN_{coherent}T_p} \approx uT_S \tag{17.17}$$

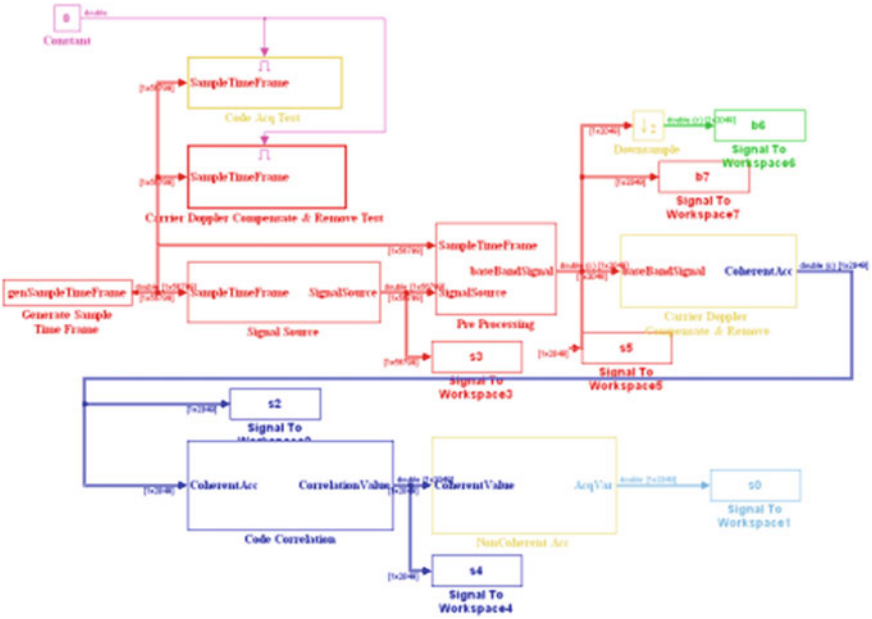

Fig. 17.8 SimulinkFull link simulation diagram

Then:

$$\begin{aligned} R_{n,k}(\varepsilon_0) &= r\left(\varepsilon_0 + \varepsilon^{\Delta}_{nN_{coherent}T_p} - kT_S\right) \\ &\approx r(\varepsilon_0 + uT_S - kT_S) \\ &= R_{0,k-u}(\varepsilon_0) \end{aligned} \tag{17.18}$$

Or:

$$R_{0,k}(\varepsilon_0) \approx R_{n,k+u}(\varepsilon_0) \tag{17.19}$$

17.6 Link Simulation and Hardware Implementation

After Simulink simulation link verification, the link including an analog signal source GPS signal pre-processing, the carrier Doppler removed, the carrier phase offset, the code phase offset, non-coherent accumulation module, through this link simulation, the simulation output results meet design requirements.

Significant correlation peak, Amplitude without attenuation, Width done not extended; Signal is achieved captured. When the antenna signal power of −185 dBW (Figs. 17.8, 17.9).

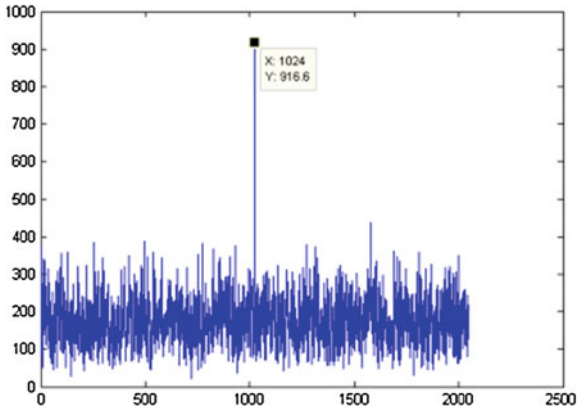

Fig. 17.9 Matlab simulation results of the analysis of the correlation peak

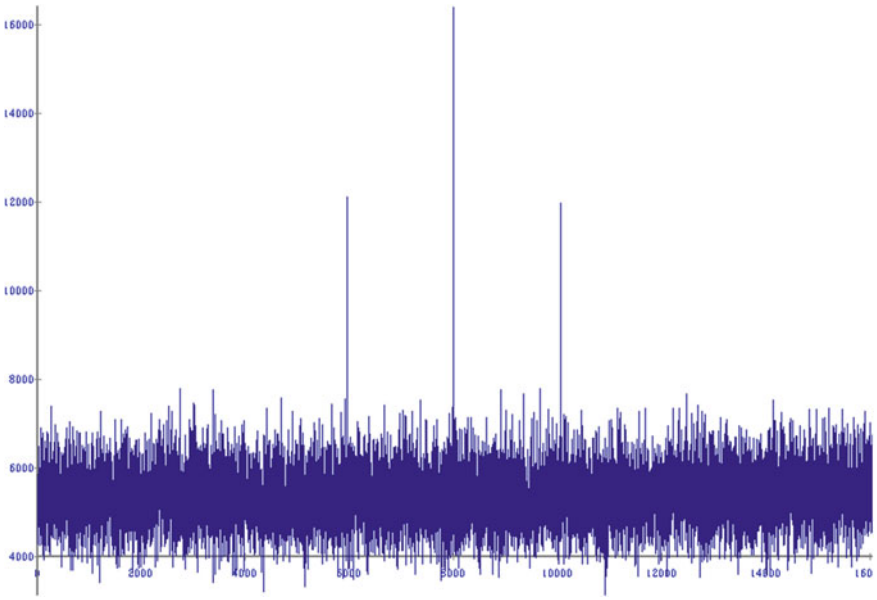

Fig. 17.10 Signal power −166 dBW (without antenna gain) to capture the peak

Ultimately based on Xilinx's FPGA chip of Virtex4 series for verify weak signal capture designs. Use Spirent simulator source, run static satellite navigation orbit, signal Doppler is 0, the satellite number is 1, the signal power is −176 dBW (without antenna gain), you can see the correlation peak is obvious. And satisfies the sinc envelope waveform, the largest correlation peak when the Doppler frequency search is 0 Hz, Doppler search frequency offset 50 Hz (10 ms coherent

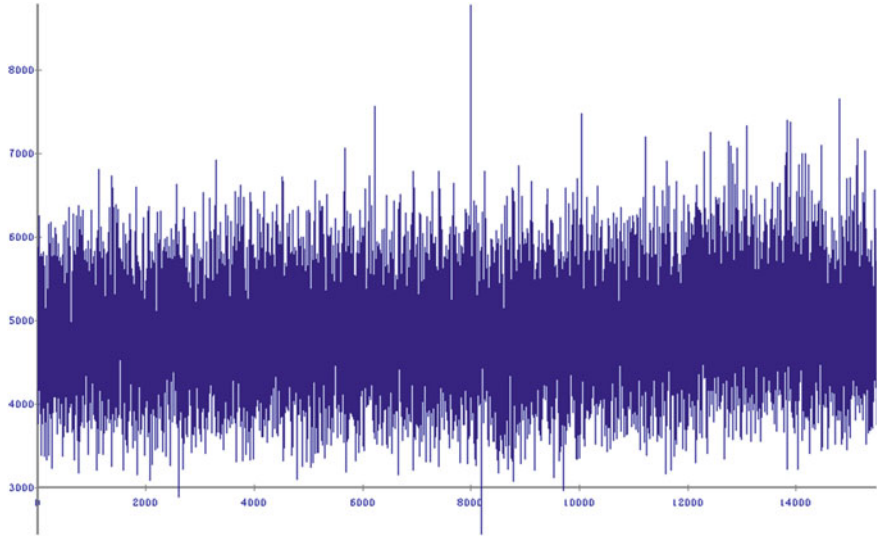

Fig. 17.11 Signal power −172 dBW (without antenna gain) to capture the peak

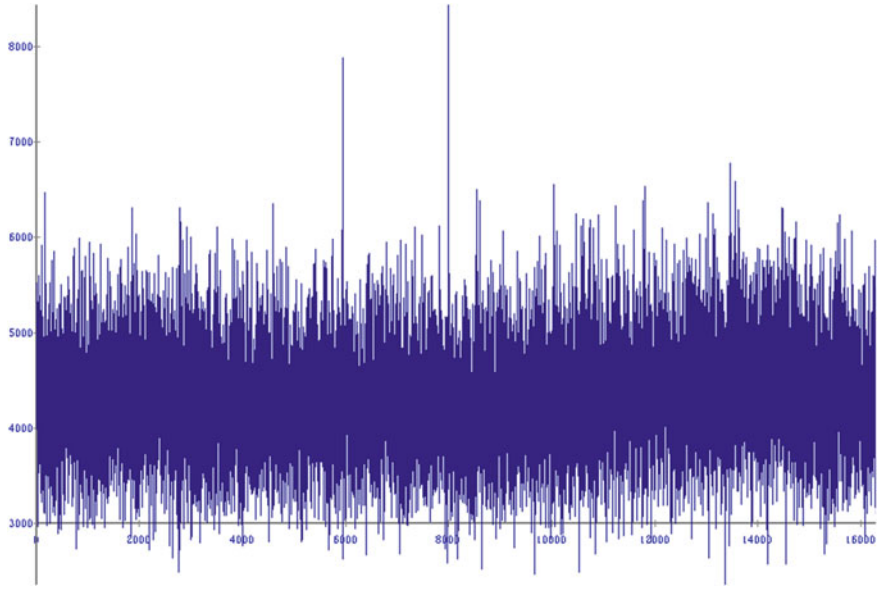

Fig. 17.12 Signal power −169 dBW (without antenna gain) to capture the peak

accumulation), the second largest correlation peak; 100 Hz Doppler shift frequency search (10 ms coherent accumulation), correlation peak was drowned in the noise, the results meet the theoretical sinc envelope waveform.

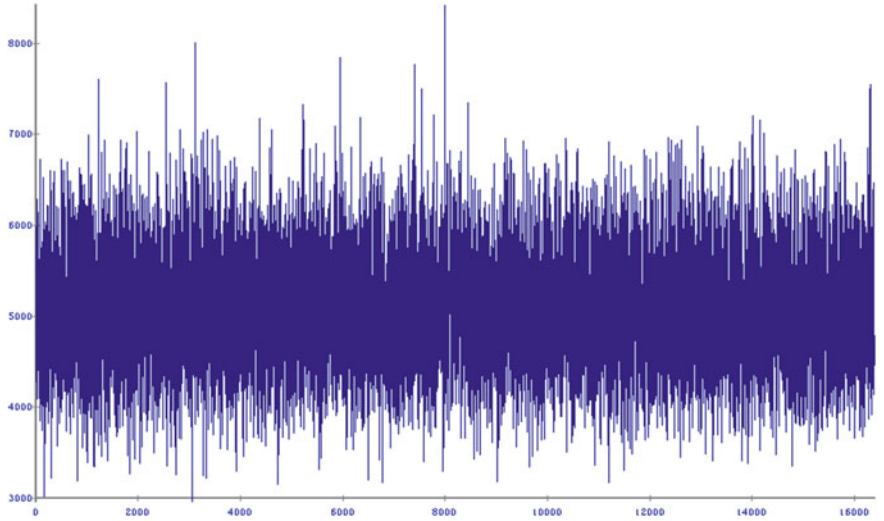

Fig. 17.13 Signal power −176 dBW (without antenna gain) to capture the peak

In order to facilitate seen in weak signal conditions correlation peak, use FPGA debugging tools (Chip scope) to view accumulator, the results as shown (Figs. 17.10, 17.11, 17.12, 17.13).

17.7 Conclusion

This paper analyzes two kinds of GPS signal quickly capture technology and GPS weak signal acquisition code Doppler compensation, Application of Matlab Simulink simulation tool to build full link verify code parallel fast capture algorithm and code Doppler compensation algorithm can be realized. By this method can improve the acquisition sensitivity of the GPS signal. The signal power of the antenna can be effective capture when GPS signals power is −185 dBW.

References

1. Hou W, Chou P, Zhao M (2010) The research of high sensitivity GNSS capture technology. The paper of Zhejiang University Degree, pp 49–53
2. Zhang L, Li H, Cui X, Lu M (2013) Doppler code compensation and local clock biased with weak GNSS signal acquisition. Simul Comput 8
3. Xie G (2009) GPS principle and receiver design. Electronic Industry Press, Beijing, pp 366–374

4. Wang S, Mao Z, Xie C (2009) Base on GPS signal research and pre-capture hardware implementation research: microelectronics and computer
5. Fast fourier transform v3.2, Xilinx logicore data sheet, 2005.09
6. GP2015 GPS Receiver RF Front End.Zarlink semiconductor data sheet, 2005.05

Chapter 18
Typhoon Wind Speed Observation Utilizing Reflected Signals from BeiDou GEO Satellites

Weiqiang Li, Dongkai Yang, Fran Fabra, Yunchang Cao and Wei Yang

Abstract Typhoon monitoring utilizing reflected GNSS signals is a new application of GNSS-R technique. Coastal observations are an efficient way for the model of geophysical parameters retrieval in Typhoon and identified as a promising complementary technique with respect to the satellite instruments. However, the relationship between GNSS-R observables and the sea surface wind speed in Typhoon could not be fully described through theoretical models for the coastal regions. Meanwhile the instability of the coastal GNSS-R geometry makes it difficult to optimize an empirically calibrated model. The BeiDou GEO satellites could provide stable geometry and better coverage capability in mid- and low-latitude region where most of the typhoons occur. Based on this consideration, ocean reflected signals from BeiDou GEO satellites are exploited for coastal Typhoon observation in this paper. The relationship between reflected waveform parameters, such as coherent time, and the ocean geophysics parameters, such as wind speed is analysed. Preliminary analysis of the BeiDou reflected signal collected during the TIGRIS experiment shows good agreement between the GNSS-R measured wind speeds and the in situ measurements, the average deviation is 1.6 m/s with the root-mean-square error of 2.4 m/s.

Keywords BeiDou · GEO satellite · Reflection · Wind speed · Correlation time

W. Li (✉) · D. Yang · Y. Cao
Lab 202, Beihang University, Beijing 100191, China
e-mail: weiqiang.li.buaa@gmail.com

F. Fabra
Earth Observation Research Group, Institut d'Estudis Espacials de Catalunya (ICE-CSIC/IEEC), Barcelona 08193, Spain

W. Yang
CMA Meteorological Observation Centre, CMA, Beijing 100081, China

J. Sun et al. (eds.), *China Satellite Navigation Conference (CSNC) 2014 Proceedings: Volume I*, Lecture Notes in Electrical Engineering 303,
DOI: 10.1007/978-3-642-54737-9_18,

18.1 Introduction

The use of reflected signals from GNSS systems as a source of opportunity for remote sensing, known as GNSS-R technique, has been a research area of increasing interest. It was first proposed in 1993 for ocean altimetry [1], and has also been proved for many other remote sensing applications on the ocean [2], land [3] and sea ice [4].

The potential of reflected GPS signal on wind sensing was proposed and demonstrated in 1998 from aircraft experiments [2], some of the results measured during hurricane indicated that reflected GPS signals are also sensitive to ocean surface winds over 40 m/s [5]. With the ongoing improvements the theoretical description and modelling of the ocean scattered GNSS signals such as Z-V model [6] and the reception and use of GPS reflected signals from space with UK-DMC satellite [7], NASA has recently approved the CYGNSS mission, consisting of a constellation of 8 LEO satellites, to obtain GNSS-R wind speed estimations while monitoring tropical cyclones with high spatial and temporal resolution and improve their forecast [8]. Since 1990s, the scientist in China have began to study GNSS-R technique, several airborne [9] and coastal experiment [10] have been performed and theoretical analysis on the performance of typhoon observation utilizing space based GNSS-R has been studied [11].

The model of GNSS-R observable over typhoons and corresponding geophysical parameters retrieval methods becomes crucial for future research on GNSS-R based typhoon monitoring, which depends on long term observation to accumulate data. Coastal observations are an efficient way for the long term observation of typhoons, which is also identified as a promising complementary technique with respect to the satellite instruments [12].

The SWH measurement using coastal GNSS-R has been demonstrated through several experiments [10, 13]. However, the relationship between GNSS-R observables and the sea surface wind speed in Typhoon could not be fully described through theoretical models for the coastal regions. Meanwhile, the instability of the coastal GNSS-R geometry makes it difficult to optimize an empirically calibrated model.

The BeiDou system consists of an IGSO/MEO/GEO hybrid constellation, in which the GEO satellites could provide stable geometry for GNSS-R technique and better coverage capability in mid- and low-latitude region, where most of the typhoons occur. Based on this consideration, ocean reflected signals from BeiDou GEO satellites are exploited for coastal typhoon observation in this paper. The relationship between reflected waveform parameters, such as coherent time, and the ocean geophysics parameters, such as wind speed is analysed. Preliminary data processing results shows the potential of this method for sea state monitoring during typhoons.

18.2 Principles and Methods

Due to the weakness of the reflected signal, the received reflected GNSS signal $u_R(t)$ should be correlated with the local generated replicas with different time delays as

$$w_R(t,\tau) = \int_0^{T_c} u_R(t+t'+\tau)c(t+t')D(t)e^{j2\pi f_R t'}\mathrm{d}t' \tag{18.1}$$

in which τ is the time delay relative to the delay of the specular points, T_C is the coherent integration time, $c(\cdot)$ is the local generated PRN code, $D(\cdot)$ is the data bit and f_R is the carrier frequency of the reflected signal.

In airborne and spaceborne applications, the size of the glistening zone are comparable with the first iso-range area and the trailing edge of the reflected power waveform, i.e. $|w_R(t,\tau)|^2$ will significantly be distorted with the increasing of the wind speed. The wind speed could be retrieved through the fitting between the measured waveforms and the theoretical ones. However, the power waveforms collected in coastal applications have no significant distortion with respect to the direct one, and it's difficult to retrieve the wind speeds through the above mentioned methods. Nevertheless, the correlation time of the reflected signals received from the coastal instruments is longer, which makes it possible to be utilized for wind speed retrieval. The correlation function of the complex waveforms at the specular point could be defined as [14]

$$R(\Delta t,0) = \frac{\langle w_R(t,0)w_R(t+\Delta t,0)\rangle_t}{\langle w_R(t,0)w_R(t,0)\rangle_t} \tag{18.2}$$

and the correlation time could be calculated through

$$\tau_w = \int_0^{\infty} R(\Delta t)\mathrm{d}\Delta t \tag{18.3}$$

In developed sea, the relationship between the correlation time and the wind speed could be found in [15] as

$$\tau_w \approx 3\frac{\lambda}{U_{10}}erf^{-\frac{1}{2}}\left(2.7\frac{\rho}{U_{10}^2}\right) \tag{18.4}$$

in which U_{10} is the wind speed at 10 m above the sea surface, $erf(\cdot)$ is the error function and ρ is the size of the observed area determined by the antenna's footprint and the geometry of the observation.

However, the relationship between correlation time and the sea surface wind speed in Typhoon could not be fully described through the theoretical models for the coastal regions due to the development of the wave spectrum and the depth of the sea in coastal regions. Moreover, the instability of the coastal GNSS-R

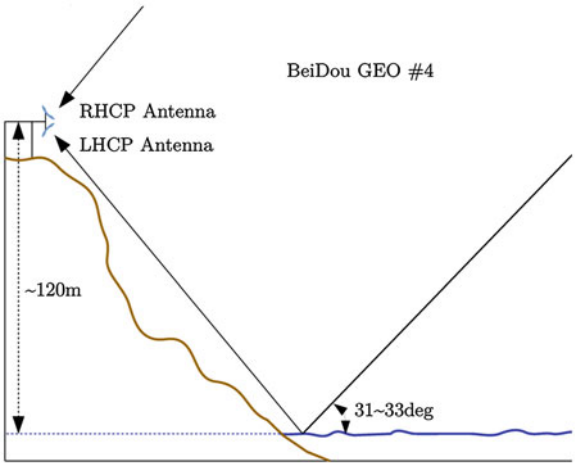

Fig. 18.1 Description of the experimental site

geometry makes it difficult to optimize an empirically calibrated model, which corresponds to the results from other coastal experiments. The BeiDou GEO satellites could provide stable geometry, i.e. the elevation and azimuth change little during the whole observation period, which could simplify the wind speed retrieval model and provide good opportunities for coastal wind speed measurement.

18.3 Experiment and Data Processing

18.3.1 Description on the Experiment

Taking into account the historical tracks of the typhoons in the North–West Pacific basin and the experimental environment, the campaign took place in Hailing Island (21.57°N, 111.86°E), South–East of China, from the beginning of July until end of September 2013. The setup was installed in a coastal location ($\sim$120 m above sea level and $\sim$170 m away from the coastline) as shown in Fig. 18.1. The view angle is 10–35° in elevation and 80–116° in azimuth in which the BeiDou GEO PRN 4 satellite (elevation: 31–33°, azimuth: 108–109°) is located.

The omnidirectional RHCP antenna was compatible with both BeiDou and GPS systems to collect direct signals from the BeiDou satellites, and the high-gain (13 dB) narrow beam-width (38°) LHCP antenna was collecting their corresponding reflections from the sea surface. The received direct and reflected BeiDou signals are amplified, filtered, down-converted, sampled and stored as the digital intermediate frequency (IF) with a central frequency of 3.996 MHz and a sampling frequency of 16.369 MHz. Both the L.O. frequency and the bandwidth of

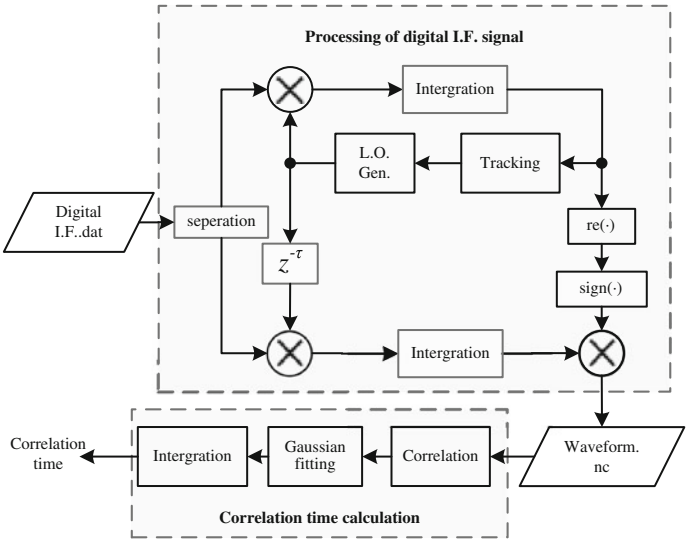

Fig. 18.2 Data Processing Scheme of BeiDou reflected signal

the RF-frontend are reconfigurable to collect the raw signals of both BeiDou and GPS. During the experiment, the in situ measurements from the nearby meteorological station were also collected.

18.3.2 Data Processing Scheme

The detailed block diagram of the data processing software is designed as shown in Fig. 18.2. There are two main blocks: the digital signal process unit and the correlation time calculation unit.

The digital signal processing unit is designed accord with the BeiDou signal structures. The direct and reflected raw samples are separated and correlated with the local generated replica whose delay and Doppler are estimated through the tracking loop of direct signal and the satellite-receiver geometry. The complex correlation values are then stored as the waveform files. Figure 18.3 illustrates the comparison between the direct and reflected power waveform, we could notice that the path delay between the waveforms' peaks is around 134.5 m which shows moderate agreement with the theoretical prediction, i.e. 130.7 m. On the other hand, the waveform has no significant distortion with respect to the direct one even in high wind speed which agrees with the analysis in Sect. 18.2.

The correlation time calculation unit extracts the maximum of those waveforms as the representative point. Then, the autocorrelations of 60,000 (i.e. 1 min) complex value of this points are calculated according to (18.2) and fitted with the Gaussian function. At last, the correlation time of the reflected signal could be calculated through (18.3).

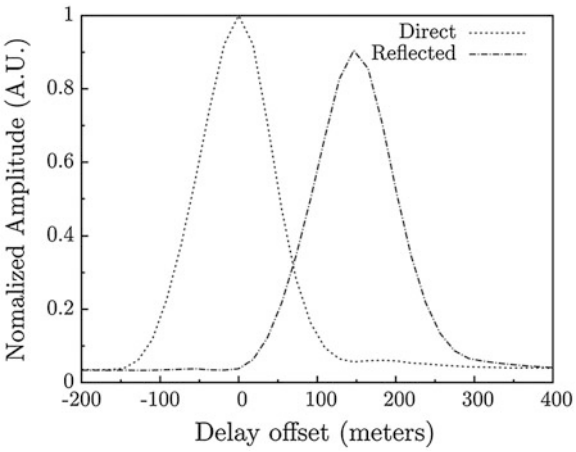

Fig. 18.3 Power waveforms of direct and reflected signals from BeiDou #4 satellite

18.4 Analysis of the Data Collected During Typhoons

During the experiment, there were two typhoons, i.e. JEBI (201309) and UTOR (201311) which had significant effects on the sea surface around the experimental site. Within the BeiDou reflected signal collecting window, the tracks of the two typhoons [16] are illustrated in Fig. 18.4. The equipment began to operate 10 h before the landfall of JEBI over which the duration of the observation is around 80 h. The observation on UTOR was interrupted 3 h before its landfall due to the problem of the power supply, and the duration of the observation is 42 h.

The correlation times of the reflected signals from the BeiDou PRN 4 satellite and the in situ wind speed measurements during the two typhoons are compared in Fig. 18.5. During observation of JEBI, it was in the decaying stage and the typhoon center moved away from the experimental site, so the observed wind speed showed a decreasing trend. During observation of UTOR, it was in the mature stage and the typhoon center moved toward the experimental site, the observed wind speed showed an increasing trend. The correlation times of the reflected signal are inversely proportional to the wind speeds as expected. Based on this relationship and theoretical model in (18.4), an empirically calibrated model was adopted as

$$U_{10} = a\tau_w^b + k \tag{18.5}$$

in which a, b and k are empirical coefficients. Taking into account of the range of the wind speed in typhoons and the distribution of the observed data, the weighted least squares fitting is adopted, with the wind speeds as the weight coefficient, to improve the applicability and the retrieval accuracy for the high wind speed. As shown in Fig. 18.6, the empirical coefficients are determined though the correlation times and wind speeds observed during JEBI as: $a = 3.253\times10^5$, $b = -2.388$, $k = 1.343$. The retrieved wind speed and the in situ measurement

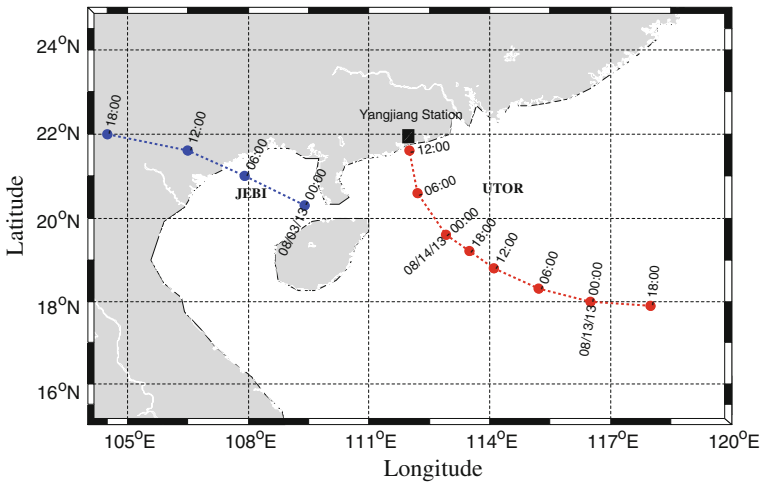

Fig. 18.4 Tracks of JEBI and UTOR during the collecting period of BeiDou reflected signal

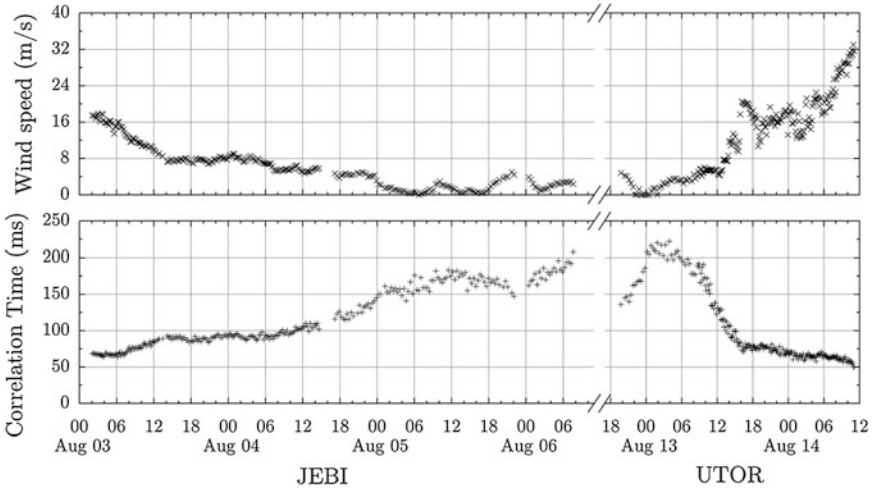

Fig. 18.5 Correlation time of BeiDou reflected signal and in situ measured wind speed during JEBI and UTOR

during JEBI are compared in Fig. 18.7, in which the average deviation is 0.7 m/s with the root-mean-square error of 1.2 m/s.

With the correlation times collected during UTOR, the wind speed was retrieved through expression (18.5). The retrieved wind speeds and the in situ measurements are compared in Fig. 18.7, which shows good agreement between them. And the average deviation is 1.6 m/s with the root-mean-square error of 2.4 m/s.

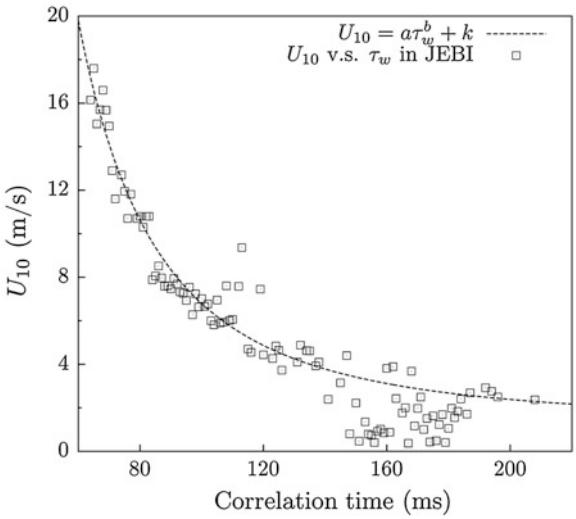

Fig. 18.6 Relationship between the correlation time and the wind speeds during JEBI

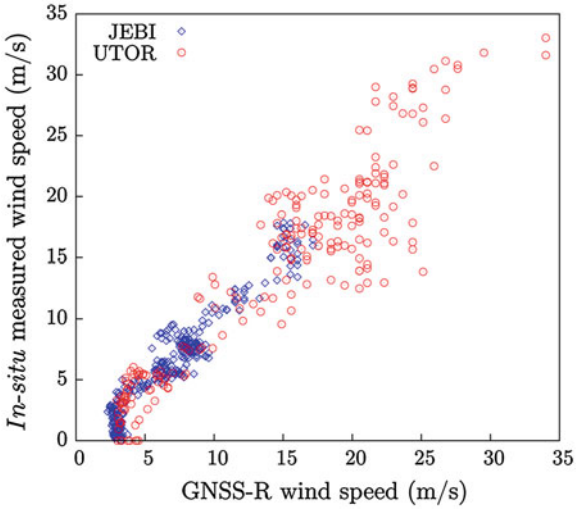

Fig. 18.7 Comparison between the wind speeds retrieved from BeiDou reflected signal and in situ measurement

18.5 Conclusion

The BeiDou GEO satellites could provide stable geometry and better coverage capability in mid- and low-latitude region. This paper takes such advantages and exploited ocean reflected signals from BeiDou GEO satellites for coastal Typhoon observation. The proposed method was verified through the analysis of data collected during TIGRIS experiment in 2013. The main conclusions of the paper include:

- The power waveforms collected in coastal applications have no significant distortion with respect to the direct one, it's difficult to retrieve the wind speeds through fitting the measured waveforms with the theoretical ones.
- The correlation time of the reflected signals is sensitive to the wind speed and could be utilized for wind speed retrieval in coastal observations.
- The stable geometry of BeiDou GEO satellites could simplify the wind speed retrieval model and provide good opportunities for coastal GNSS-R based sea state measurement.

The empirically calibrated model will be refined by further collecting and processing of the experimental data. And the study on the relationship between the waveform parameters and other geophysics parameters, such as SSH and SWH is ongoing.

This is the first report of the receiving, processing of application of the reflected BeiDou signals. The proposed methods could also be extended to other applications, such as ground based soil moisture and coastal sea ice monitoring, which could spread the applications of BeiDou system in the meteorological and oceanographic fields.

Acknowledgments The authors would like to thank Prof. Xia Qing and Prof. Li Huang from China Meteorological Administration during the experiment and the preparation of this paper. The authors would also like to acknowledge the support of colleagues at Guangdong Meteorological Administration and Shenzhen Meteorological Administration during the experiment. The work of W. Li was supported by China Postdoctoral Science Foundation funded project (2013M530513). This work was supported in part by the National High Technology Research and Development Program of China (863 Program) (SS2013AA120602) and the BeiDou Application Program (GFZX03030303).

References

1. Martin-Neira M (1993) A passive reflectometry and interferometry system (PARIS)—application to ocean altimetry. ESA J 17(4):331–355
2. Garrison JL, Katzberg SJ, Hill MI (1998) Effect of sea roughness on bistatically scattered range coded signals from the global positioning system. Geophysical Research Letter 25(13):2257–2260
3. Katzberg SJ, Torres O, Grant MS et al (2006) Utilizing calibrated GPS reflected signals to estimate soil reflectivity and dielectric constant: Results from SMEX02. Remote Sens Environ 100(1):17–28
4. Fabra F, Cardellach E, Rius A et al (2011) Phase altimetry with dual polarization GNSS-R over sea ice. IEEE Trans Geosci Remote Sens 50(6):2112–2121
5. Katzberg SJ, Torres O, Ganoe GG (2006) Calibration of reflected GPS for tropical storm wind speed retrievals. Geophys Res Lett 33:L18602
6. Zavorotny VU, Voronovich AG (2000) Scattering of GPS signals from the ocean with wind remote sensing application. IEEE Trans Geosci Remote Sens 38(2):951–964
7. Gleason S, Hodgart S, Sun Y et al (2000) Detection and processing of bistatically reflected gps signals from low earth orbit for the purpose of ocean remote sensing. IEEE Trans Geosci Remote Sens 43(6):1229–1241

8. Ruf C, Lyons A, Unwin M et al (2013) CYGNSS: enabling the future of hurricane prediction [remote sensing satellites]. IEEE Geosci Remote Sens Mag 1(2):52–67
9. Li WQ, Yang DK, Zhang B et al (2011) Real-time processing of reflected GNSS signals for remote sensing: system and experiments. J Navig 64(S1):127–140
10. Wang X, Sun Q, Zhang XJ et al (2008) First China ocean reflection experiment using coastal GNSS-R. Chin Sci Bull 53(7):1117–1120
11. Li WQ, Martin-Neira M, D'Addio S (2013) Typhoon Observations with the PARIS In-Orbit Demonstration Mission. Geophys Res Abstr 15, EGU2013-10395
12. Li H, Xia Q, Yin C et al (2013) The current status of research on GNSS-R remote sensing technology in China and future development. J Radars 2(4):389–399
13. Valencia E, Camps A, Marchan-Hernandez JF et al (2010) Experimental determination of the sea correlation time using GNSS-R coherent data. IEEE Geosci Remote Sens Lett 7(4):675–679
14. Cardellach E, Rius A, Martín-Neira M et al (2013) Consolidating the precision of interferometric GNSS-R ocean altimetry using airborne experimental data. IEEE Trans Geosci Remote Sens . doi:10.1109/TGRS.2013.2286257
15. Frasier SJ, Camps A (2001) Dual-beam interferometry for ocean surface current vector mapping. IEEE Trans Geosci Remote Sens 39(2):401–414
16. Digital Typhoon: Typhoon Images and Information. http://agora.ex.nii.ac.jp/digital-typhoon/index.html.en, 2013

Chapter 19
An Analysis of the Temporal and Spatial Variations of the Global Tropopause with COSMIC Radio Occultation Bending Angles

Pan Gao, Xiaohua Xu and JinCheng Guo

Abstract As the transition layer between the troposphere and the stratosphere, the structure of the tropopause is closely related to the weather and climate of the near-surface layer. The variation of the tropopause parameters including the height, the temperature and the pressure of the tropopause are sensitive indicators of climate variability and global change. Characterized by the advantages of high vertical resolution, low-cost, global coverage, and all-weather capability, the Global Positioning System (GPS) radio occultation (RO) technology provides rich observation data for the study of the global tropopause structure. The precise identification of the tropopause height is the prerequisite for the accurate determination of the tropopause temperature and pressure. The tropopause height identified from GPS RO temperature profile will be affected by the errors brought out by the assumptions and the prior atmosphere background applied in the inversion process of the temperature profile. To determine the tropopause height directly from RO bending angle profile is an effective way to avoid such errors. In this paper, the natural logarithm objective covariance transform method is used to identify the tropopause height from GPS RO bending angle profiles. With the GPS RO data from the Constellation Observing System for Meteorology, Ionosphere and Climate (COSMIC) mission, the spatial and temporal variations of the global tropopause parameters included height, temperature and pressure are analyzed. It is found that the latitudinal distribution characteristics of the tropopause parameters

This study was supported by National Natural Science Foundation of China (Grant No. 4137 4036, 41074024, 40904002, 41204030) and National 973 Project China (Grant No. 2013CB7 33301).

P. Gao (✉) · X. Xu · J. Guo
School of Geodesy and Geomatics, Wuhan University, 129 Luoyu Road,
Wuhan 430079, China
e-mail: gaopan@whu.edu.cn

J. Sun et al. (eds.), *China Satellite Navigation Conference (CSNC) 2014 Proceedings: Volume I*, Lecture Notes in Electrical Engineering 303,
DOI: 10.1007/978-3-642-54737-9_19,

are distinct and the seasonal variation trends of the tropopause structure are significant. It is also found that the temporal and spatial distributions of the tropopause parameters are asymmetric over the northern and the southern hemispheres.

Keywords Tropopause · COSMIC · Bending angle · GPS radio occultation

19.1 Introduction

As a transition layer between the troposphere and the stratosphere, the tropopause is an important indicator of the physical, chemical and thermal dynamics change between the troposphere and the stratosphere. Research shows that vertical mixing ratio, static stability, trace gases (mainly water vapor and ozone) and the thermodynamic equilibrium have significantly different characteristics in the troposphere and the stratosphere [1]. Some researchers presented that the tropopause height increased due to global warming [2–4]. Tropopause height variation are caused by many complex physical mechanisms [5, 6]. One of the physical mechanism is that the warm in the tropospheric (due to increase of greenhouse gases) and cool in the stratospheric(due to the decrease of the ozone) leads to the increase of the tropopause height [4]. At the same time, the tropopause temperature, pressure and other parameters will be changed. The structural variations of the tropopause are considered to be an effective indicator to study the global climate change [7–9]. The traditional data to research the tropopause are the radiosonde data [10, 11] and the reanalysis data, such as the European Centre for Medium-Range Weather Forecasts (ECMWF) and National Centers for Environmental Prediction (NCEP) [12, 13]. However, these data sources have some disadvantage. The vertical resolution of the reanalysis data is low, which will lead errors to determine the tropopause. Although the radiosonde observations have high vertical resolution, the spatial resolution is low and the distribution of the radiosonde stations is uneven.

Since the mid-1990s of 20th century, as a new type of earth's atmosphere detection technology, the GPS radio occultation technique attracts more and more attention. GPS radio occultation technology can provide the atmospheric parameters profiles with all-weather, high-precision, high vertical resolution, global coverage and long-term stability, which are ideal data source to study the tropopause structural changes [14, 15]. With the GPS/MET occultation data, Randel et al. [14] studied the thermodynamics transform of the tropopause in the tropics. They revealed the construction and varying pattern of the tropical cold point tropopause [14]. By use the temperature data from CHAMP occultation mission from September 2001 to August 2006, Borsche et al. [12] analyzed the distribution and variation of the tropical tropopause height and temperature. The features of the tropopause structure in Australian region were presented by Khandu et al. [2], by combination of the CHAMP, GRACE and COSMIC occultation temperature data.

In the studies mentioned above, the tropopauses which a were mainly the cold point tropopause (CPT) or lapse rate tropopause (LRT), were determined by the temperature profiles of the GPS occultation data, which were retrieved from the bending angle profile of the GPS occultation data. However, some assumptions are used in the process of the inversion of the temperature profiles from the GPS occultation bending profiles, such as, hydrostatic equilibrium equation, the equation of state of the ideal gas, the atmosphere spherical symmetry and the dry atmosphere instead of the entire atmospheric [16, 17]. In addition, a priori temperature profile should be provided by the numeric weather modelm (NWP) or some other observations at the process of the inversion of the variational assimilation. The accuracy of the occultation temperature profilers will be affected by the error of the priori temperature profile. Therefore, the tropopause height determined by the occultation temperature profiles may be affected by the errors of the impact of these various factors.

In order to avoid the influence of tropopause structure caused by the temperature inversion errors due to the assumptions mentioned above, in recent years, some researchers proposed some methods to determine the tropopause height directly from the bending angle profiles. Rao first use the angle gradient to determine the tropopause which are compared with the CPT and the LRT determined from the temperature profiles of the corresponding RO events, as well as the CPT and the LRT derived from the radiosonde observations occur within 300 km and 3 h of the RO events [17]. Lewis puts forward another method to determine tropopause by bending angle covariance transforms which is more robust than Rao's method [16].

In recent years, global climate change anomaly, extreme cold weather happed frequently in some local areas. However, the tropopause structure is closely linked to the global climate change. The research to the variations of tropopause parameters is significance in context of global climate change anomaly. A wealth of observational data of COSMIC occultation mission has been accumulated to study the tropopause structure. Thus, in the current global climate change anomaly, this paper use the COSMIC bending angle data to study the global tropopause, based on the method to determine the tropopause height directly from the bending angle profiles proposed by Lewis [16].

19.2 Data and Method

19.2.1 Data

Constellation Observing System for Meteorology, Ionosphere and Climate (COSMIC) is a collaboration developed by American and Taiwan, China, consist of six small satellites. They can provide maximum 2,500 observation events per day. Since its successful launch in April 2006, it attracts extensive attention from various research institutions and scholars. The data provided by the COSMIC are

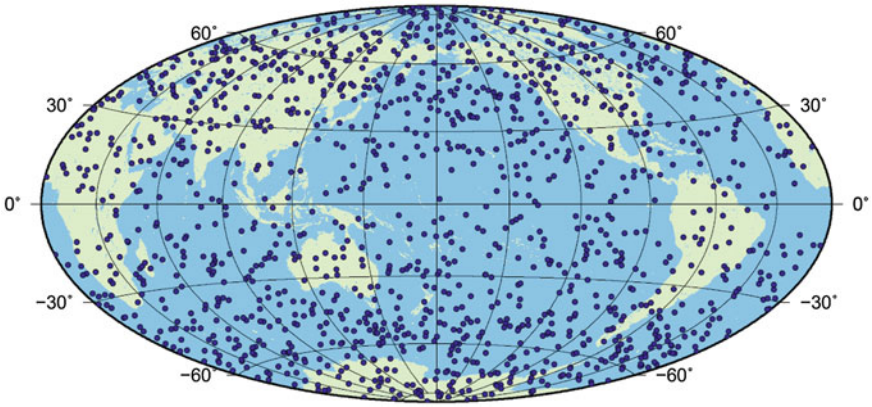

Fig. 19.1 The distribution of COSMIC radio occultation events occurred on January 8th, 2008

important data source to study the global tropopause structure. In this paper, the bending angle observation data are downloaded from the COSMIC Data Analysis and Archive Center (CDAAC) from 1 July 2006 to 29 April 2013. Figure 19.1 shows distribution of global COSMIC occultation events on January 8, 2008. From the we can see that the number occultation events is rich and global uniform coverage in general.

19.2.2 Method to Determine the Tropopause

In this paper we determine the tropopause height directly from the bending angle profiles proposed by Lewis [16]. The basic principle is as follows:

For a occultation events, the natural logarithm of the bending angle profile $\alpha(z)$ is ln $\alpha(z)$. The localised covariance transform of ln $\alpha(z)$ is as follows:

$$W_{\ln\alpha}(a,b) = \frac{1}{a}\cdot\int_{z_b}^{z_t} \ln\ \alpha(z)\cdot h\left(\frac{z-b}{a}\right)\cdot \mathrm{d}z \tag{19.1}$$

In Eq. (19.1), z is the height of the profiles, z_b and z_t are the bottom and top of the profiles, is the height between z_b and z_t. $h\left(\frac{z-b}{a}\right)$ is a gradient function defined as:

$$h\left(\frac{z-b}{a}\right) = \begin{cases} \ln\alpha(z) - \ln\alpha(b), & b-\frac{a}{2} \le \mathrm{z} \le b+\frac{a}{2} \\ 0, & z < b-\frac{a}{2} \quad \text{or} \quad \mathrm{z} > b+\frac{a}{2} \end{cases} \tag{19.2}$$

a is the vertical scale. A transition from steep to shallower gradients with increasing height is identified by a maximum of $W_{\ln\alpha}(a,b)$. The height of the maximum of $W_{\ln\alpha}(a,b)\ b = b_p$ is the tropopause height.

Compared different values of a, we choose 35 km of a. This choice for a identifies the larger scale tropopause transition and filters small scale variations associated with lower troposphere temperature and humidity gradients [4, 16].

19.2.3 Statistical Method

In order to analyze the tropopause variation by latitude, we divide the globe into 18 latitude bands with 10° interval. Every latitude band has 144 grid cells of 5° × 5° (longitude × latitude). Then calculate the average $L_{i,j}$ of the tropopause height, temperature and pressure in every grid cells

$$L_{i,j} = \frac{1}{n_{i,j}} \cdot \sum_{k=1}^{n_{i,j}} L_{i,j,k} \quad (i = 1, 2, 3 \ldots 18;\ j = 1, 2, 3 \ldots 144) \tag{19.3}$$

$L_{i,j}$ is the mean value of the tropopause height, temperature and pressure of the jth grid cells of ith latitude band. $n_{i,j}$ is the number of occultation events in the 5° × 5° grid cell. $L_{i,j,k}$ is the kth tropopause height, temperature and pressure of the 5° × 5°grid cell.

19.3 Result and Analysis

19.3.1 Tropopause Structure Changes with Latitude and Longitude

Figure 19.2 shows the latitudinal variations of tropopause height, temperature and pressure by using the COSMIC occultation bending angle profiles.

Figure 19.2a shows the global distribution of tropopause height changes with latitude. From the figure, we can see that the tropopause height reaches its maximum in the tropical regions near the equator, which is consistent with the results by Nishida et al. [18], who used the GPS/MET occultation temperature profiles. Tropical tropopause layer (TTL) is the gate from the troposphere to the stratosphere [19]. Tropopause height decreases from the equator to the north and the south direction, and the minimum height is at the arctic pole. In subtropical region between 20 and 40, the tropopause height decreases sharply with latitude from the equator to high latitude zones. This may be influenced by the subtropical jet (STJ) and the movement of latitude direction from the tropical tropopause to the pole tropopause [20]. In the STJ zones the probability of occurrence of the multi-tropopause is maximum [20, 21]. In the tropical regions near the equator and the poles, the height of the tropopause is relatively flat with latitude. In the zones from

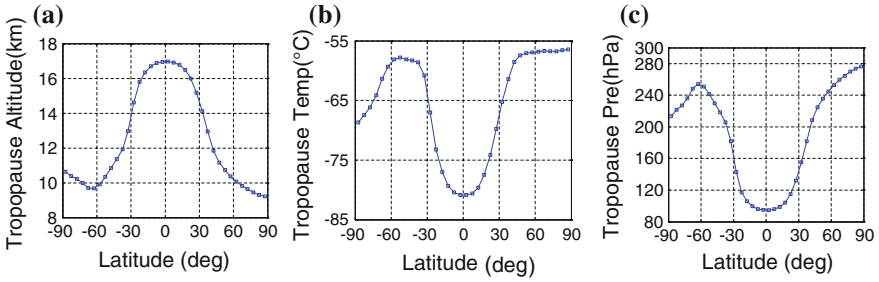

Fig. 19.2 (**a**) The latitudinal variations of tropopause height, (**b**) temperature, and (**c**) pressure

the equator to the latitude 60°, the tropopause height changes by latitude is symmetry in southern and northern hemisphere. In the zone from the 60° to the poles, this symmetry changes. The tropopause height in the antarctic circle higher than that in the arctic circle, which is consistent with the results by Schmidt et al. [22], who used the CHAMP temperature profiles.

Figure 19.2b shows the global distribution of tropopause temperature changes with latitude. From the picture we can see that the tropopause temperature variation with latitude is u-shaped distribution, which is just opposite with the tropopause height variation shown in Fig. 19.2a. The tropopause temperature is lowest at the equator zones. In the tropical regions near the equator, the tropopause temperature increases gradually with increasing latitude. In subtropical regions, the tropopause temperature rises sharply with increasing latitude. In the mid-latitude region the tropopause temperature increases with latitude is relatively flat. In the Antarctic Circle the tropopause temperature decreases with latitude, while in the Arctic Circle, the tropopause temperature continues to rise with latitude. This indicates that the tropopause temperature in southern and northern hemisphere is asymmetry, which is consistent with Schmidt et al. [22].

Figure 19.2c shows the global distribution of tropopause pressure changes with latitude. From the picture, we can see that the tropopause pressure change with latitude is just opposite with that of the tropopause height, but consistent with that of the tropopause temperature. The tropopause pressure of about 950 h Pa in the equator is lowest. In the Arctic, the pressure is highest of about 280 h Pa. From the equator to 60°, the tropopause pressure increases with latitude. In the Antarctic Circle, the tropopause pressure decreases with latitude, while in the Arctic Circle, tropopause pressure continues to rise with latitude. This also indicates that the tropopause pressure on both hemisphere is asymmetry. The pressure in the Southern Hemisphere (SH) is lower than that in the Northern Hemisphere (NH). Which is consistent with Hoinka [23], who use the reanalysis data ECMWF, and Schmidt et al. [22], who use the CHAMP occultation temperature profiles.

In order to further analyze the features of spatial distribution of the tropopause parameters, Fig. 19.3 gives the global tropopause parameters change with latitude and longitude. Figure 19.3a shows that global tropopause height mainly changes

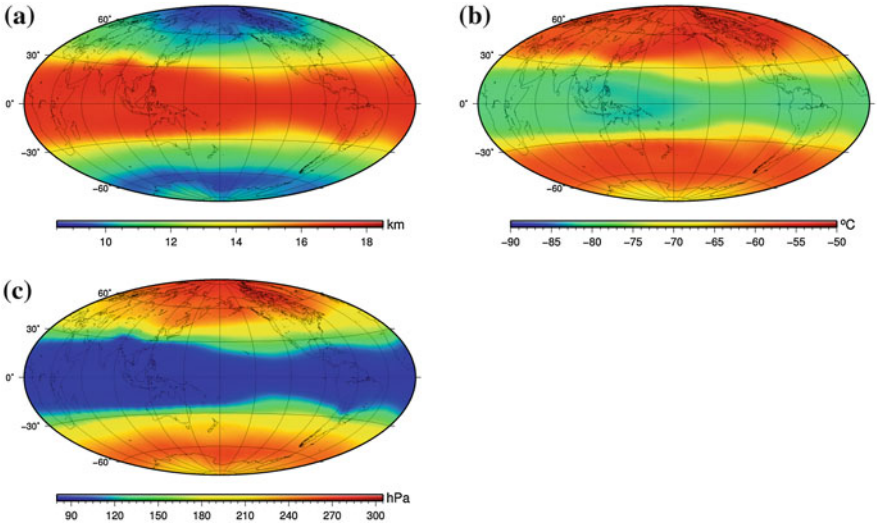

Fig. 19.3 (**a**) The global distribution of tropopause height, (**b**) temperature, and (**c**) pressure

with latitude rather than with longitude. The tropopause is highest of about 17 km in the equator zones and is lowest of about 9 km in the Arctic Pole. In the zones from the equator 30° in both hemisphere, the tropopause height is relative flat of about 16–18 km. However, the tropopause height decreases sharply in the subtropical region. From subtropical to high latitudes, the tropopause is decreases gradually. Figure 19.3b shows the spatial distribution of the global tropopause temperature. From the picture we can see that the tropopause temperature is coldest in the tropical regions near the equator. With increasing of the latitude, the tropopause temperature increases gradually. This is because that the atmosphere in the low latitudes zones near the equator can absorb more solar radiation, which drives the strengthen of the atmosphere convection that results in high and cold tropopause in these zones. On the contrary, the atmosphere at high latitudes regions absorbs less solar radiation. So, the atmospheric convection is weak, which leads to low and warm tropopause [24]. Figure 19.3b also shows that tropopause temperature is mainly changes with latitude and just changes with longitude in local areas. In the tropics, the tropopause temperature over the land is lower than that over the ocean. The lowest tropopause temperature is located over the zone between Oceania and the Eurasian continent. The tropopause temperature over the Pacific Ocean higher than that over the other zones at the same latitude band. This is mainly caused by the different nature of the underlying surface.

Figure 19.3c shows the spatial distribution of the global tropopause pressure. From the picture we can see that the tropopause pressure is lowest in the tropical regions, higher in poles and highest in Arctic Circle. The tropopause pressure increases gradually from the equator to the poles. The tropopause pressure change with longitude and latitude is asymmetry in two hemispheres. The variation in the

NH is more complex than that in the SH, which is consistent with Hoinka [23]. Who indicate that the tropopause pressure is streamlined distribution in the SH and zonal distribution in the NH.

19.3.2 Seasonal Changes of the Global Tropopause Structure

To analyze the seasonal changes of the global structure of the tropopause, we applied a method to determine the tropopause from RO bending angle profiles with COSMIC RO bending angle profiles data. Using this method we obtained the seasonal average of the global tropopause parameters. Figures 19.4, 19.5, 19.6 were given the changes in the global tropopause height, temperature and pressure in different seasons with the latitude and longitude distribution.

Figure 19.4 shows the global tropopause seasonal changes in height. In Fig. 19.4a–d respectively donate the latitude and longitude distributions of global tropopause height changes in spring, summer, autumn and winter. Comparing with the four sub-graph in Fig. 19.4, the maximum of tropopause height distributed in winter near the equator and seasonal changes of the tropopause height near the equator are small. The minimum of tropopause height distributes in the Arctic in spring. Seasonal changes of the tropopause height in the North and south poles and subtropicals are the largest throughout the year. Figure 19.4 also shows that seasonal changes of the tropopause height are asymmetry in the Northern Hemisphere (SH) and Southern Hemisphere (SH), in NH the tropopause height changes with the seasons are more complex, especially in eastern Asia and North America. In SH tropopause height changes with the seasons is relatively simpler, in summer and autumn, in the southern of 30°S tropopause height changes gently with latitude and longitude and the differences between the regions are small. The asymmetry of NH and SH tropopause height changes in time and space is mainly due to the different impact of NH and SH underlying surface and human activities [24], NH is with more complex land-sea distribution, more land area and more densely populated, while in SH land-sea distribution is relatively simple, less land area, population sparse.

Figure 19.5 shows the seasonal global tropopause temperatures changes. In Fig. 19.4a–d respectively donate the latitude and longitude distributions of global tropopause temperature changes in spring, summer, autumn and winter. Comparing with the four sub-graph in Fig. 19.4, the NH tropopause temperature changes with the seasons are more complicated, affected by frequently human activities; while tropopause temperature seasonal changes over Antarctica are unique, the deference of tropopause temperature seasonal changes is large between NH and SH. The tropopause temperature seasonal changes are asymmetries. From spring to summer, the tropopause temperature near the equatorial, in the north and south subtropical regions and northern regions of the NH subtropical increases, while the tropopause temperature in the southern regions of the SH subtropical

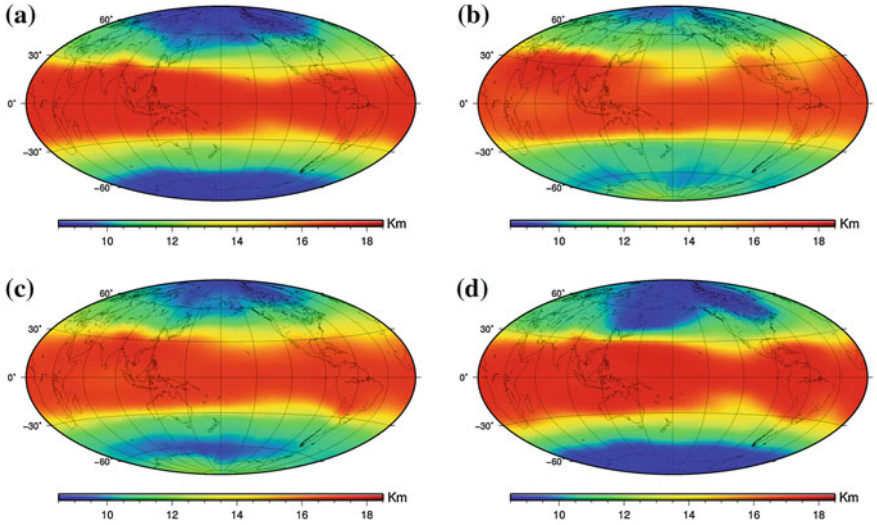

Fig. 19.4 (**a**) The global distribution of the tropopause height in spring, (**b**) summer, (**c**) autumn, and (**d**) winter

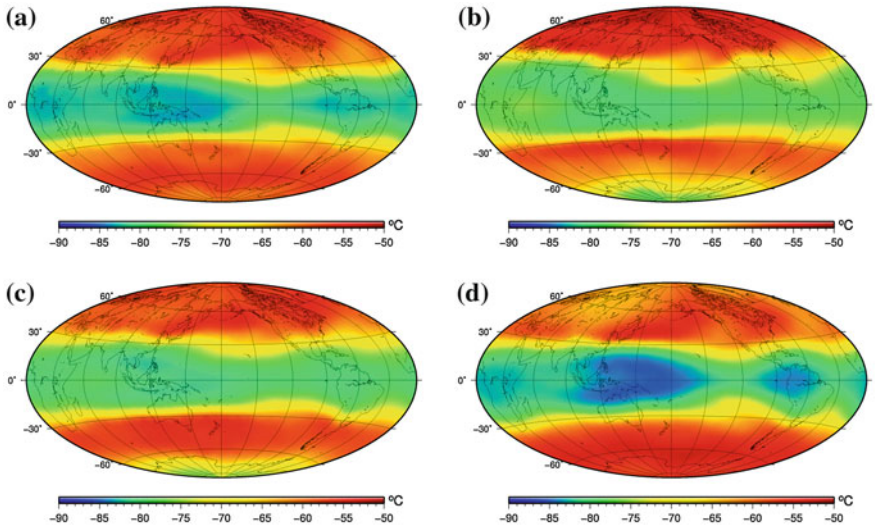

Fig. 19.5 (**a**) The global distribution of the tropopause temperature in spring, (**b**) summer, (**c**) autumn, and (**d**) winter

decreases. In particular, the Antarctic tropopause temperature drop is particularly evident. In the spring, the Antarctic Circle tropopause temperature is higher than other regions in SH; while in the summer, over the Antarctic continent tropopause temperature drops lower than in SH subtropics and southern regions of the

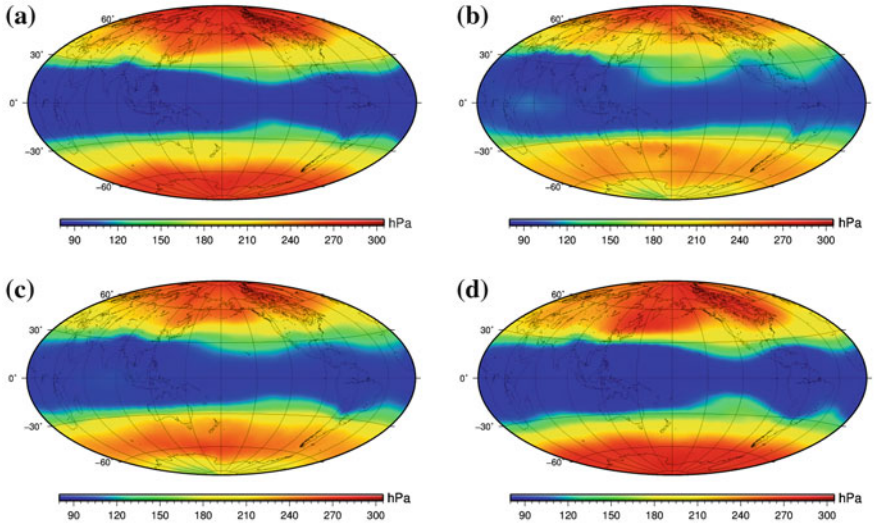

Fig. 19.6 (**a**) The global distribution of the tropopause pressure in spring, (**b**) summer, and (**c**) autumn, and (**d**) in winter

subtropical. Tropopause structure over the Antarctic continent has its own unique variations, Antarctica can be studied as a separate region in the study of global climate change, which is consistent with Han et al. [24].

Figure 19.6 shows the seasonal global tropopause pressure changes. In Fig. 19.4a–d respectively donate the latitude and longitude distributions of global tropopause pressure changes in spring, summer, autumn and winter. Comparing with the four sub-graph in Fig. 19.4, in the spring, tropopause pressure maximum distributes in the Arctic while the minimum in the equatorial regions. The largest difference of global tropopause pressure is in the spring, the larger is in the winter, difference of summer and fall global tropopause pressure is relatively small. Seasonal tropopause pressure changes of SH and NH is asymmetry. Seasonal tropopause pressure changes in SH is more regular, while in NH is more complex, with significant geographical variation, especially in winter and the Pacific west coast of North America, which mainly due to the presence of high level jet stream in the North American winter [23, 25].

19.4 Conclusions

The tropopause is a key region for the material and energy exchange between the troposphere and stratosphere, the study of tropopause parameters and structure changes is significantly important to the study of global climate changes. As one of the most advanced space exploration technology in the 21st century, GNSS radio

occultation technique with its high vertical resolution, low-cost, global coverage, quasi-real-time, all-weather advantages, provides a new detection technology for study of the tropopause. But presently methods to determine the tropopause using the GPS RO data are mainly based on the definition of LRT and CPT from temperature profiles. While retrieval of temperature profiles from the RO bending angle profiles applied to the state equation of ideal gas, a spherical symmetry and hydrostatic equilibrium equation assumptions [16, 17]. In addition, a priori temperature profile should be provided by the NWP or some other observations at the process of the inversion of the variational assimilation. The accuracy of the occultation temperature profilers will be affected by the error of the priori temperature profile. However, the tropopause determined directly from the bending angle profiles can avoid the influence of the assumption to retrieve the temperature profiles.

In this paper we determine the tropopause height directly from the bending angle profiles from the COSMIC occultation mission based on the method proposed by Lewis [16]. We divide the globe into 36 × 72 grid cells with 5° × 5°. We also divide the globe into 18 latitude bands with 10° interval. We analyze the tropopause parameters variations by latitude. We find that in the tropics the tropopause height is highest, the temperature and pressure is lowest. From the equator to the poles the tropopause height decreases, but the temperature and pressure decrease. The spatial distribution features of the global tropopause parameters are analyzed by calculating the average of the tropopause height, temperature and pressure in every 5° × 5° grid cell. We find that the latitudinal distribution characteristics of the tropopause parameters are distinct. The seasonal variation of the tropopause parameters are also analyze by calculating the seasonal means of the tropopause parameters. We find that the spatial distribution and seasonal variation of the tropopause parameters are asymmetry. The tropopause parameters variations in the NH is more complex than that in the SH, especially, in the Eastern Asia and North America in winter in the NH.

With the development of Beidou systems and Galileo systems and the improvement of GLONASS systems, receivers loaded on low-orbit satellites will receive signal from the GPS, Beidou, Galileo and GLONASS. Then more occultation data can be obtained, which will drive to generate more achievement about the atmosphere included the tropopause.

Acknowledgments The authors would like to acknowledge UCAR (USA) and NSPO (Taiwan) for the free COSMIC data.

References

1. Mehta SK, Ratnam MV, Murthy BVK (2010) Variability of the tropical tropopause over Indian monsoon region. J Geophys Res 115:D14120. doi:10.1029/2009JD012655
2. Awange JL, Wickert J, Schmidt T, Sharifi MA, Heck B, Fleming K (2011) GNSS remote sensing of the Australian tropopause. Clim Change 105:597–618

3. Schmidt T, Wickert J, Beyerle G (2008) Global tropopause height trends estimated from GPS radio occultation data. Geophys Res Lett 35(L11806). doi:10.1029/2008GL 034012
4. Schmidt T, Wickert J, Haser A (2010) Variability of the upper troposphere and lower stratosphere observed with GPS radio occultation bending angles and temperatures. Adv Space Res 46:150–161
5. Santer BD, Wigley TM, Simmons AJ (2004) Identification of anthropogenic climate change using a second-generation reanalysis. J Geophys Res 109:D21104. doi:10.1029/2004JD005075
6. Shepherd TG (2002) Issues in stratosphere-troposphere coupling. J Meteorol Soc Jpn 4B:769–792
7. Santer, BD, Wehner MF, Wigley TML, Sausen R, Meehl GA, Taylor KE, Ammann C, Arblaster J, Washington WM, Boyle JS, Brüggemann W (2003) Contributions of anthropogenic and natural forcing to recent tropopause height changes. Science 301:479–483. doi:10.1126/science.1084123,2003
8. Sausen R, Santer BD (2003) Use of changes in tropopause height to detect human influences on climate. Meteorol Z 12:131–136. doi:10.1127/0941-2948/2003/0012-0131.2003
9. Son SW, Polvani LMD, Waugh W, Birner T, Akiyoshi H, Garcia RR, Gettelman A, Plummer DA, Rozanov E (2009) The impact of stratospheric ozone recovery on tropopause height trends. J Clim 22:429–445. doi:10.1175/2008JCLI2215.1.2009
10. Seidel DJ, Rebecca JR, Angell JK (2001) Climatological characteristics of the tropical tropopause as revealed by radiosondes. J Geophys Res 106:7857–7887
11. Seidel DJ, Randel WJ (2006) Variability and trends in the global tropopause estimated from radiosonde data. J Geophys Res 111
12. Borsche M, Kirchengast G, Foelsche U (2007) Tropical tropopause climatology as observed with radio occultation measurements from CHAMP compared to ECMWF and NCEP analyses. Geophys Res Lett 34:L03702. doi:10.1029/2006GL027918
13. Randel WJ, Wu F, Gaffen DJ (2000) Interannual variability of the tropical tropopause derived from radiosonde data and NCEP reanalyses. J Geophys Res 105(D12):15509–15523
14. Randel WJ, Wu F, Rios WR (2003) Thermal variability of the tropical tropopause region derived from GPS/MET observations. J Geophys Res 108(D1). doi: 10.1029/2002JD002595,2003
15. Xu X, Luo J, Zhang K (2011) An analysis of the structure and variation of the tropopause over China with GPS radio occultation. J Navig 64:103–111
16. Lewis HW (2009) A robust method for tropopause altitude identification using GPS radio occultation data. Geophys Res Lett 36:L12808. doi:10.1029/2009GL039231
17. Rao DN, Ratnam MV, Murthy BVK (2007) Identification of tropopause using bending angle profile from GPS radio occultation (RO) a radio tropopause. Geophys Res Lett 34:L15809. doi:10.1029/2007GL029709
18. Nishida M, Shimizu A, Tsuda T (2000) Seasonal and longitudinal variations in the tropical tropopause observed with the GPS occultation technique (GPS/MET). J Meteorol Soc Jpn 78(6):691–700
19. Fueglistaler S, Dessler AE, Dunkerton TJ, Folkins I, Fu Q, Mote PW (2009) Tropical tropopause layer, Rev Geophys 47(RG1004):31
20. Añel JA, Antuña JC, Torre L, Castanheir JM, Gimeno L (2008) Climatological features of global multiple tropopause events. J Geophys Res 113(D00B08) doi:10.1029/2007JD009697
21. Randel WJ, Seide DJl, Pan LL (2007) Observational characteristics of double tropopauses. J Geophys Res 112(D07309). doi:10.1029/2006JD007904,Apr.,2007
22. Schmidt T, Wickert J, Beyerle G (2004) Tropical tropopause parameters derived from GPS radio occultation measurements with CHAMP. J Geophys Res 109(D13105). doi:10.1029/2004JD004566

23. Hoinka K (1998) Statistics of the global tropopause pressure, Mon. Weather Rev. 3303–3325
24. Han T, Ping J, Zhang S (2011) Global features and trends of the tropopause derived from GPS/CHAMP RO data. Sci China Phys, Mech Astron 54(2):365–374. doi: 10.1007/s11433-010-4217-5
25. Peixoto JP, Oort AH (1992) Physics of climate. American Institute of Physics, New York, pp 520

Chapter 20
The Simulation and Analysis of BeiDou Satellite Usability Under the Condition of Missile's Pitch Attack

Jianxun Li, Chengfeng Wu, Feng Li, Shipin Hong, Zheng Liu, Zhu Cheng and Ji Xin

Abstract Compass Navigation Satellite System is a precise satellite navigation which is independently created by Chinese scientists. Base on its characteristics of providing all-weather, continuous, real time and high accuracy three-dimensional positioning, it has been widely concerned on military and the civilian. At present, the first phase of Beidou second generation satellite system has been put into trial operation and the second phase of Beidou second generation satellite system is speeding up research and development. The number of received satellites under

J. Li (✉)
Beijing Automation Control Equipments Institute, Feihangstr. 1, Beijing 100074, China
e-mail: ljx_neu@163.com

C. Wu
Beijing Automation Control Equipmets Institute, Feihangstr. 2, Beijing 100074, China
e-mail: asoka7879@gmail.com

F. Li
Beijing Automation Control Equipmets Institute, Feihangstr. 3, Beijing 100074, China
e-mail: lifeng600@sohu.com

S. Hong
Beijing Automation Control Equipmets Institute, Feihangstr. 4, Beijing 100074, China

Z. Liu
Beijing Automation Control Equipmets Institute, Feihangstr. 5, Beijing 100074, China

Z. Cheng
National University of Defense Technology. 6, Changsha 410073, China

J. Xin
Air Force Military Representative Office of FengTai region in Beijing. 7, Beijing 100074, China

J. Sun et al. (eds.), *China Satellite Navigation Conference (CSNC) 2014 Proceedings: Volume I*, Lecture Notes in Electrical Engineering 303,
DOI: 10.1007/978-3-642-54737-9_20,

natural condition with different time and different places can be predicted through Ephemeris. However, it generally requires that the satellite positioning receiver can position stably while the missile's attitude keeps changing in missile's application field. The satellite usability under the condition that missiles in different poses, especially under the condition of big pitch attitude is very important to navigation and guidance scheme design. This paper formulates reasonable simulation scheme with Beidou satellite constellation distribution, typical microstrip antenna directional diagram and typical ballistic. It focus on the simulation of some key parameters, such as the number of Beidou satellites, geometric distribution and positioning success rate of Beidou area navigation system and Beidou global navigation system in different time and places when the single antenna or dual antenna layout scheme has been adopted, which under the condition of great pitching against missiles or in different course. Meanwhile, it gives the analysis of satellite availability and guidance. The simulation scheme and the result of simulation and analysis in this paper has important engineering significance to make full use of the Beidou satellite in the process of missile trajectory planning and navigate tactic designing.

Keywords Large pitching angle · Satellite constellation · Simulation · Beidou

20.1 Introduction

The availability of navigation system refers to the percentage of the time used in system service [1]. The content of availability includes precision availability and good availability. The difference of client position and measuring time leads to the difference of the navigation satellite number and satellite geometric structure, and observed error. Thus, the availability of system is different with different space-time point. Usually the decision condition for availability analysis depends on the geometry dilution of precision GDOP, which reflects proportional coefficient between the pseudo-range measurement and user's location error caused by satellite geometry relationship [2]. The availability of the satellite information in the end of the missile flight is related to such parameters as the anti-interference ability of satellite positioning system, satellite navigation precision, satellite coverage region, projectile attitude and on-board antenna design scheme. In this paper, we carry out simulation and analysis on availability of Beidou satellite navigation system and Beidou global navigation system used in the terminal guidance by simulating typical ballistic and considering parameters that influence the end of navigation.

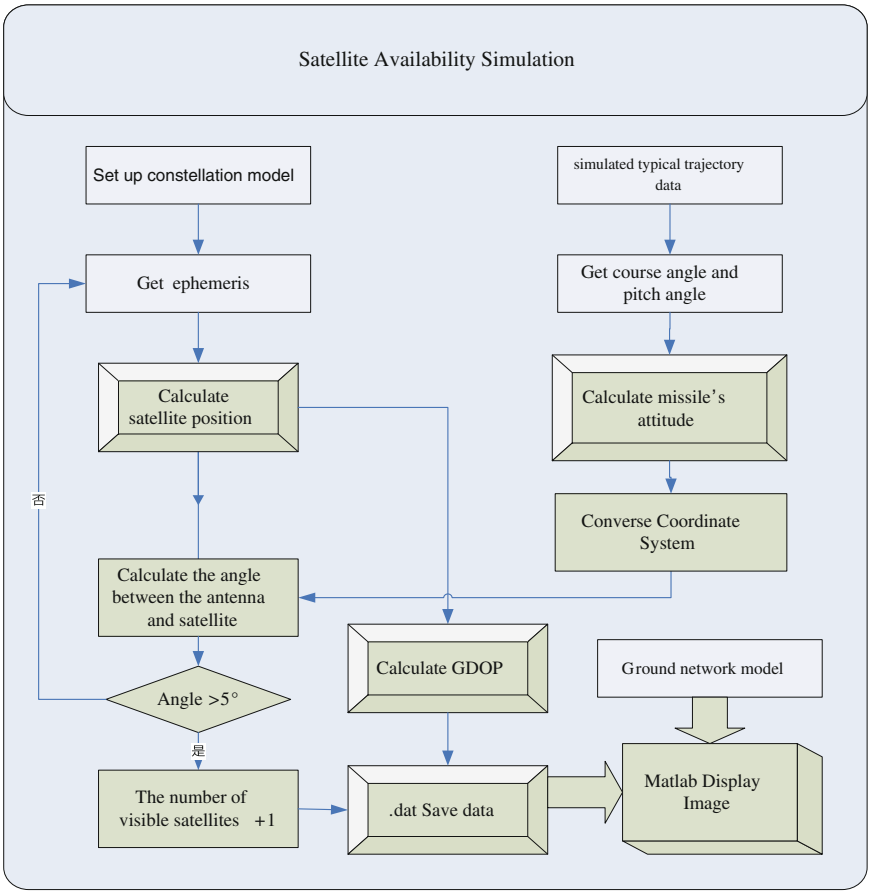

Fig. 20.1 Main framework of simulation system

20.2 Satellite Availability Simulation System Design for the Missile's Ending Guidance

20.2.1 Simulation System Design

The simulation system is mainly composed of Beidou satellite constellation model, ground network model, simulated typical trajectory data and satellite availability simulation algorithm. At last, the system will display the image by using Matlab. The main algorithm includes satellite position calculation, attitude calculation and dilution of precision calculation. The diagram of the simulation system's main framework is shown in Fig. 20.1.

20.2.2 Modelling of Global Surface Network

In order to assess the availability of Beidou satellite navigation system, we need to model the ground network with the global surface and divide the ground network in global scope according to certain latitude and longitude and take a certain observation period of time in a certain sampling interval. Then, we analyze the data. Consequently, we can obtain the availability of the system by concluding all the availability results from all the ground grid points in all the sampling time. Normally, there are two grid division methods, one of which is equal longitude and latitude division and the other of which is equal area division [3].

In this article, equal latitude and longitude division method is adopted to model the ground network and the global surface is divided into 60 and 120 equal pieces, which means the global surface is divided into $3^{\circ} \times 3^{\circ}$ global grid map. Each grid point on the net is corresponding to the position of the ground. We take central positions in each grid region as representative points, of which the availability is the system's availability for the whole grid regions.

20.2.3 Attitude Calculation: Coordinate Transformation

Owing to different trajectory design and the missile's attitude keeps changing with different attacking times and different antenna's pitch angle, the angle of the antenna receiving stars keeps changing. Also, it influences the antenna's range of receiving stars. When simulating the availability of satellite, we mainly consider such parameters as azimuth, course angle and pitch angle. The core algorithm is to calculate the attitude of the missile, the importance of which is coordinate transformation. First, the surface coordinate (The inertial coordinate system refers to the ground coordinate system in the pitch attack phase.) is used to determine the centroid position of the missile and space attitude benchmark. The origin is usually projection point of the centroid position of the missile. Then the dynamic coordinates are set up by fixing the missile coordinates and velocity, the origin of which is the centroid of the missile [4]. Consequently, the attitude angle can be determined by missile coordinates and ground coordinate system. Then we can calculate the angle between the aerial and satellite and obtain the number of visible stars by masking the attitude angle and aerial angle by transforming them into WGS-84 ground coordinate system. The missile coordinate system and WGS-84 ground coordinate system both belong to the space rectangular coordinates. For any two space rectangular coordinates, they can be overlapped one translation and three rotations. During each rotation of the coordinates, it is related to one angle, such as head angle, pitch angle and rotation angle. It is assumed that the angle rotated by OX is γ, rotated by OY is φ and rotated by OZ is θ. Then the rotation matrix can be represented by

$$L_x(\gamma) = \begin{pmatrix} 1 & 0 & 0 \\ 0 & \cos\gamma & \sin\gamma \\ 0 & -\sin\gamma & \cos\gamma \end{pmatrix} \tag{20.1}$$

$$L_y(\varphi) = \begin{pmatrix} \cos\varphi & 0 & -\sin\varphi \\ 0 & 1 & 0 \\ \sin\varphi & 0 & \cos\varphi \end{pmatrix} \tag{20.2}$$

$$L_z(\theta) = \begin{pmatrix} \cos\theta & \sin\theta & 0 \\ -\sin\theta & \cos\theta & 0 \\ 0 & 0 & 1 \end{pmatrix} \tag{20.3}$$

After coordinate transformation, the system will calculate the missile's position and the satellite's position that calculated by the simulated Beidou constellation. If the angle is larger than 5°, it is within the visible stars and vice versa.

20.2.4 Calculation of Dilution of Precision for GDOP

Geometric dilution of precision GDOP is an important factor to the accuracy of position and it represents the distance vector amplification factor between the receiver and satellite which caused by GPS ranging errors. GDOP is determined by the geometrical relationship which is calculated by the position of the receiver and the satellite. It only depends on the geometrical position of the satellite, resulting in direct addition operation without considering the pseudo-range. The geometrical distribution of the satellite is an important factor that influences the positional accuracy. This factor can be analyzed quantitatively in terms of dilution of precision (DOP) [5]. The least square solution for four satellites and more than four satellites is shown as

$$\begin{aligned} \Delta\hat{\boldsymbol{x}} &= \boldsymbol{A}^{-1}\Delta\boldsymbol{\rho} \\ \Delta\hat{\boldsymbol{x}} &= (\boldsymbol{A}^{T}\boldsymbol{A})^{-1}\boldsymbol{A}^{T}\Delta\boldsymbol{\rho} \end{aligned} \tag{20.4}$$

In this formula, $\Delta\hat{\mathbf{x}}$ is unknown vector. $\Delta\boldsymbol{\rho}$ is the observed noise vector, and A is the observed matrix, which is composed of the direction cosine of the observed vector from the satellite to the receiver. After transforming into the local geometrical coordinates represented by satellite azimuth and satellite altitude, the observed matrix can be expressed by

$$A = \begin{bmatrix} \cos(E_1)\sin(A_{Z1}) & \cos(E_1)\cos(A_{Z1}) & \sin(E_1) & 1 \\ \cos(E_2)\sin(A_{Z2}) & \cos(E_2)\cos(A_{Z2}) & \sin(E_2) & 1 \\ \vdots & \vdots & \vdots & \vdots \\ \cos(E_n)\sin(A_{Zn}) & \cos(E_n)\cos(A_{Zn}) & \sin(E_n) & 1 \end{bmatrix} \tag{20.5}$$

By Eq. (20.4), we can get the variance of the position error as

$$\begin{aligned} \mathrm{E}[\Delta\hat{\boldsymbol{x}}\Delta\hat{\boldsymbol{x}}^{\mathrm{T}}] &= \boldsymbol{A}^{-\boldsymbol{1}} \cdot \boldsymbol{E}[\Delta\boldsymbol{\rho}\Delta\boldsymbol{\rho}^{\mathrm{T}}] \cdot \boldsymbol{A}^{-\mathrm{T}} \quad \boldsymbol{k} = \boldsymbol{4} \\ \mathrm{E}[\Delta\hat{\boldsymbol{x}}\Delta\hat{\boldsymbol{x}}^{\mathrm{T}}] &= (\boldsymbol{A}^{\mathrm{T}}\boldsymbol{A})^{-\boldsymbol{1}}\boldsymbol{A}^{\boldsymbol{T}} \cdot \boldsymbol{E}[\Delta\boldsymbol{\rho}\Delta\boldsymbol{\rho}^{\boldsymbol{T}}] \cdot \boldsymbol{A}(\boldsymbol{A}^{\mathrm{T}}\boldsymbol{A})^{-\boldsymbol{1}} \quad \boldsymbol{k} > \boldsymbol{4} \end{aligned} \tag{20.6}$$

Assuming that all the value of $\Delta\rho$ is zero mean observation noise and has the same variance $\sigma^2(m^2)$, we can get such relationships as

$$\begin{aligned} \mathrm{E}[\Delta\boldsymbol{\rho}_i\,\Delta\boldsymbol{\rho}_j^{\mathrm{T}}] &= \sigma^2, \quad i = j \\ \mathrm{E}[\Delta\boldsymbol{\rho}_i\,\Delta\boldsymbol{\rho}_j^{\mathrm{T}}] &= 0, \quad i \neq j \end{aligned} \tag{20.7}$$

Using Eqs. (20.6) and (20.7), the variance can be simplified as

$$\mathrm{E}[\Delta\hat{x}\,\Delta\hat{x}^{T}] = \sigma^2 \cdot (A^{T}A)^{-1} \tag{20.8}$$

As can be seen, GPS positional accuracy is related to such two main parameters as observed accuracy σ affected by error source and geometrical distribution from the satellite and receiver. Those two factors that affect the GPS precision is relative but not absolute. For example, when the value of DOP is low, it is possible that the observed accuracy σ is high, leading to bad positional accuracy. Simultaneously, it is possible that the value of DOP is high but the error accuracy is good, resulting in high value of positional accuracy. The weighting coefficient matrix Q can be expressed by

$$Q = \left(A^{\mathrm{T}}A\right)^{-1} = \begin{bmatrix} Q_{11} & Q_{12} & Q_{13} & Q_{14} \\ Q_{21} & Q_{22} & Q_{23} & Q_{24} \\ Q_{31} & Q_{32} & Q_{33} & Q_{34} \\ Q_{41} & Q_{42} & Q_{43} & Q_{44} \end{bmatrix} \tag{20.9}$$

Thus, we can get the formula to calculate the value of DOP

Horizontal Dilution of Precision, HDOP:

$$\mathrm{HDOP} = \sqrt{Q_{11} + Q_{22}} \tag{20.10}$$

Vertical Dilution of Precision, VDOP:

$$\mathrm{VDOP} = \sqrt{Q_{33}} \tag{20.11}$$

Time Dilution of Precision, TDOP:

$$\mathrm{TDOP} = \sqrt{Q_{44}} \tag{20.12}$$

Geometrical Dilution of Precision, GDOP:

$$\begin{aligned} \mathrm{GDOP} &= \sqrt{\mathrm{VDOP}^2 + \mathrm{HDOP}^2 + \mathrm{TDOP}^2} \\ \Rightarrow \mathrm{GDOP} &= \sqrt{Q_{11} + Q_{22} + Q_{33} + Q_{44}} \end{aligned} \tag{20.13}$$

20.3 Simulation Analysis of Satellite Availability in Large Pitch Condition

In the experiments, we consider the distribution of Beidou satellite, microstrip antenna pattern and the ballistic simulation. We mainly focus on the simulation of Beidou satellite number, geometrical distribution, and positioning success rate of Beidou local navigation system and global navigation system in different time and different locations when the missile has different head angles and in large pitch attack condition.

20.3.1 Simulation Condition

The experiments are carried out in Beidou local and global system. In order to obtain a stable distribution of the stars, we set a simulation cycle to five days (120 h). In each hour, we simulate the position information of the missile. The azimuth angle of the carrier is in east, south, west and north direction. The conditions above will be simulated with the whole big pitch attacking period that contains 48 pitch angles (per second). The antenna scheme of the carrier respectively adopts single antenna scheme (Vertical axis and heading to the sky), Up–Down-Double-Antenna (install on the upper and down surface of the carrier which is vertical to the axis of the carrier) and Tail-Double-Antenna (One antenna is vertical to the axis of the carrier and points to the sky, but the other is in the tail). Considering the angle problem when the antenna receives the information, the antenna pattern is shown in Fig. 20.2.

The number of the visible satellites, Geometrical Dilution of Precision (GDOP) and the positioning success rate of the current region of the carrier are presented by $3^{\circ} \times 3^{\circ}$ global grid maps according to the simulation results with the number of the visible satellites no less than 4 and the GDOP no more than 20. The data simulation in this paper uses simulated ballistic data in the stage of big pitch attack. The simulation of satellite availability is based on the track and flight time in the ballistic data, aiming at the attitude at different time. In the result, three pictures are defined as a triad, among which "*.gdop" is Geometrical Dilution of Precision, "*.n.sat" is the number of the visible satellites and "*.success rate map" is positioning success rate in 120 h, respectively.

20.3.2 Single Antenna Scheme for Satellite Availability Simulation

The position distribution and the number of satellites are different in different satellite navigation constellation, resulting in the difference of the number of

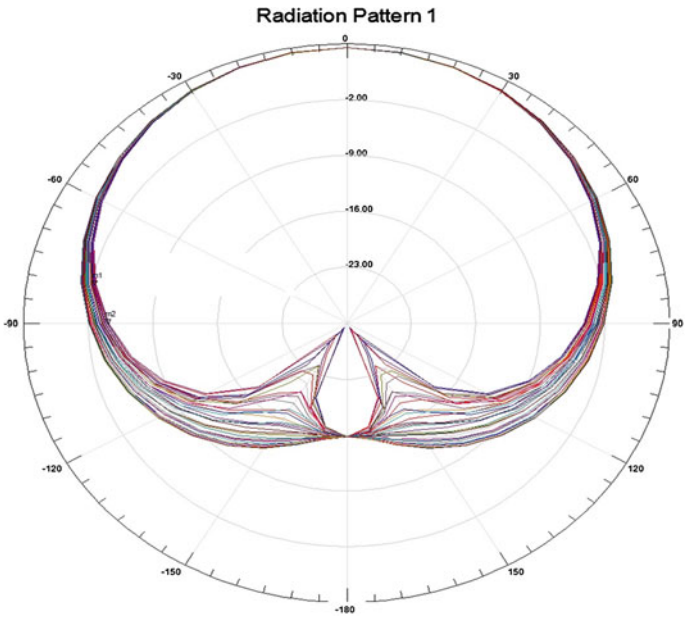

Fig. 20.2 Geometrical dilution of precision

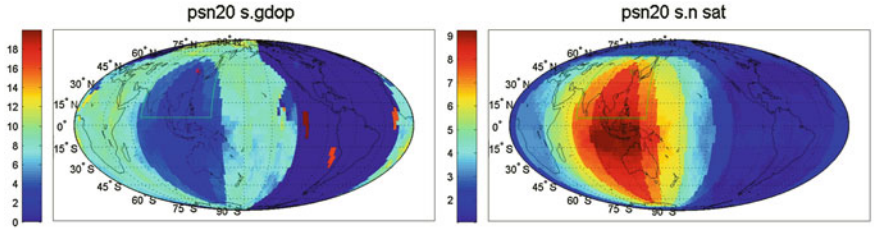

Fig. 20.3 Simulation result: geometrical dilution of precision (*left*) and number of visible satellite (*right*)

visible satellites under the same condition, which affects the positioning in practice. The simulation trail is under the condition of single antenna design scheme (Vertical axis and heading to the sky). The availability simulation which based on simulated ballistic and the four course of east, south, west and north in the whole diving attack stage is carried out in the Beidou local and Beidou global positioning system. In the Beidou local positioning system, the simulated ballistic direction is north. When the pitch angle of missile is 23°, the simulation results of the availability are presented in the following triad. The global geometrical dilution of precision and the global number of visible satellite distribution with special attitude of the missile is shown in the Fig. 20.3.

The global positioning success rate distribution result is shown in Fig. 20.4.

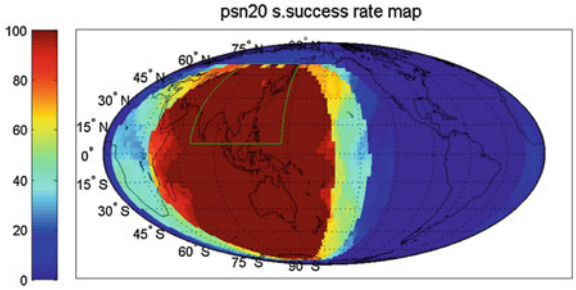

Fig. 20.4 Positioning success rate

The simulation results above shows that the body of missile itself shades the reception of satellites signals in the ending stage of the diving. According to the microstrip antenna pattern, the received signal strength is different under different attitudes of the missile. The normal receiving stars rate under Beidou local navigation system of the Asian-Pacific region in the Western Hemisphere approaches 100 % when the elevation angle of the missile is 23°. The normal receiving stars rate of the Western Hemisphere apart from equatorial region is about 80–95 %. However, at latitude 60° N, due to the distribution of satellites in Beidou local system and number of satellites, the elevation angle between antenna and satellite is less than 5°, which makes the positioning success rates reduce.

In Beidou global positioning system, the dilution of satellites is in a wide range and in a huge number. Thus, the positioning success rate of the western hemisphere can be 100 % in the same condition of missile's attitude.

20.3.3 Dual-Antenna Scheme for Satellite Availability Simulation

The availability of a satellite in the navigational satellite system mainly depends on the elevation angle between antenna and the satellite. Thus, the design of antenna has great influences to the simulation results of satellite availability. The simulation trial of dual-antenna scheme aims at two programs: Up–Down-Double-Antenna design scheme and Tail-Double-Antenna design scheme. The availability simulation with four course of east, south, west and north in the diving attack stage is carried out in the Beidou local positioning system. The results of positioning success rate of Up–Down-Double-Antenna design scheme and Tail-Double-Antenna design scheme in the condition of the same attitude of missile are shown in the Fig. 20.5.

When Up–Lower-Double-Antenna design scheme is adopted and the course is north, the results that global positioning success rate of missile's each pitch angle throughout the whole end attack stage is shown in the Table 20.1.

According to the simulation results the following conclusions could be drawn: from the global positioning success rate distribution results, when Up–Down-Double-Antenna design scheme is adopted and the pitch angle in the range of −31

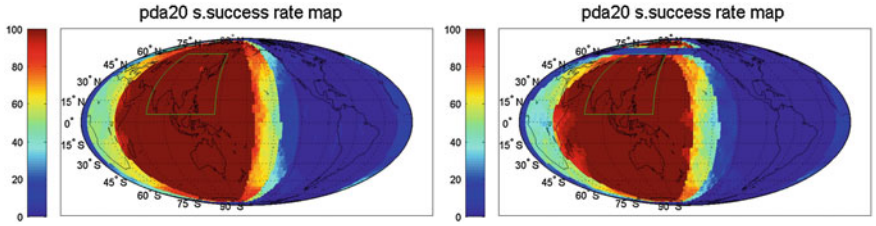

Fig. 20.5 Positioning success rate of Up–Down-Antenna design scheme (*left*) and Tail-Double-Antenna design scheme (*right*)

Table 20.1 Positioning success rate of every time

Time/s (°)	Simulate position		Course	Positioning success rate %
	Latitude	Longitude		
70–85	48	95	北	100
66–69				95.83
43–63				100
42				55.83
33–41				18.33
31				83.33
30				100

to −42°, because of satellite distribution and missile's body occlusion, the antenna's receiving stars range has been sharply reduced and it leads positioning success rate decreased. However, if Tail-Double-Antenna design scheme is adopted, this question could be effectively avoided and the positioning success rate of the whole end attack stage can reach 100 %. At present, when the Tail-Double-Antenna design scheme is selected the positioning success rate throughout the whole end attack stage is higher than Up–Down-Double-Antenna design scheme in the Beidou local navigation system. Meanwhile, the effect of receiving stars when the double antenna scheme is selected is better than the condition that single-antenna scheme is selected and the success rate is higher than 30 %. It can ensure that the normal receiving star rate when the pitch angle reach to 80° could be the same as horizontal state when the double-antenna is adopted.

20.4 Conclusion

This paper put forward the satellite availability simulation scheme under the condition of missile's big pitch attacking with the characters of missile's micro-strip antenna and satellite constellation distribution of Beidou local navigation system and Beidou global navigation system. It focus on the simulation of some key parameters, such as the number of Beidou satellites, geometric distribution and

positioning success rate when the satellite receiver in different time and in different places, which under the condition of great pitching against missiles or in different course. In view of single antenna and dual antenna layout scheme that commonly used in actual project, it analyses and compares the availability of Beidou local navigation system and Beidou global navigation system. Also, it gives the key conclusion. In the end of the missile flight, because the elevation of on-board antenna changes greatly, the coverage characteristics of the receiver antenna to the space keeps changing. In order to ensure that satellite signals can be received normally with different postures of the missile, the dual-antenna layout program has more advantages than the single antenna scheme. The simulation scheme and the conclusion of simulation in this paper has important engineering significance to make full use of the Beidou satellite in the process of missile trajectory planning and navigate tactic designing.

References

1. Federal radionavigation Plan (2001) DOD/DOT. DOT-VNTSC-RSPA-01-3.1/DOD-4650, 5 Mar 2002
2. Yu CC, Bian SF (2012) Usability analysis of Beidou satellite navigation system at the present stage. Hydrogr surveying charting 32(5):1671–3044
3. Yuanfeng L, Yan Z, Falin W (2010) Analysis of global availability for Beidou 2nd generation navigation system. Electron Measur Technol 33(2):15–17
4. Zhang A, Xu H, Cui L (2010) Application of coordinate transform in hardware-in-the-loop simulation of anti-ship missile. Comput Simul 27(10):64–65
5. Cong L, Abidat Al, Tan ZZ (2006) Analysis and simulation of the GDOP of satellite navigation. Acta Electronica Sinica 34(12):2204–2205

Chapter 21
Research on the Maintenance of Ascending Node Longitude of IGSO Satellite

Cheng-long Peng, Yuan-lan Weng and Zhi Zhang

Abstract IGSO satellite plays important part to COMPASS Navigation Satellite System and its position significantly impacts performance of the whole navigation system service. With various of perturbations and initial orbit error, ascending node longitude of IGSO satellite drift continued, which varies service area of navigation system. It's necessary to amendment longitude of the satellite ascending node to keep navigation precision periodically. Control strategies were analyzed alone, and offset of semi-major axis is determined base d on the change law of ascending node longitude. Optimum control velocity increment to amendment orbit by the means of Lagrange multiplier and a control method to maintain satellite orbit are presented. Simulation results have verified the effectiveness and convenience. This paper also provides reference of Maintenance of navigation constellation.

Keywords IGSO · Ascending node longitude · Position maintenance · Optimization control

21.1 Introduction

In order to improve the performance of satellite navigation system, a feasible way is that inclined geosynchronous orbit (IGSO) satellite joins in the satellite network, which ground track is theoretically the word of '8' across the northern and southern hemispheres with intersection crossing on the equator, and orbital inclination determines the maximum latitude of the sub-satellite point. Actually, the ground track is not a closed '8' owing to the effect of disturbing force. When the orbit drifts eastward, the intersection locates in the southern hemisphere and on the contrary in the northern hemisphere, which is not conducive to maintaining the

C. Peng (✉) · Y. Weng · Z. Zhang
College of Aerospace Science and Engineering, National University of Defense Technology, Changsha 410073, China
e-mail: pengcl987@163.com

J. Sun et al. (eds.), *China Satellite Navigation Conference (CSNC) 2014 Proceedings: Volume I*, Lecture Notes in Electrical Engineering 303,
DOI: 10.1007/978-3-642-54737-9_21,

intersection of location and has a great impact on the navigation performance of the system. Therefore, it must be implemented to control the ascending node (AN) to prevent substantial drift. This paper studies the Maintenance method of AN Longitude of IGSO Satellite to ensure it to be near some longitude.

In some satellite navigation systems, such as active GPS, GALILEO and GLONASS; medium earth orbit (MEO) satellites are used, while COMPASS Navigation Satellite System (CNSS) adds the IGSO satellites to improve the navigation performance, so study on IGSO satellite orbital characteristics has important theoretical and engineering value which can lay a solid foundation for the construction and improvement of (CNSS). On IGSO satellite characteristics and optimal control problem, some scholars have done the appropriate research and demonstration. Reference [1] discusses the evolution law of AN longitude drift on the equator owing to the combined effect of various orbit perturbing forces and the initial orbit deviation on IGSO satellite, and proposes some maintenance policy. Reference [2] also analyzes the satellite constellation and coverage characteristics of IGSO satellite in orbit. Reference [3] studies the optimal maneuver to seek the global optimal solution of the problem based on functional analysis; Reference [4–7] focuses on the optimal control problem based on double-pulse tracks with minimum fuel. Reference [8] describes control policy model of the optimal path planning on perturbed satellite orbit.

Based on the aforementioned studies, the control method of AN longitude of IGSO satellite is proposed. Through a comprehensive analysis of effect characteristics of perturbation on IGSO, drift rate of AN longitude is deduced, accordingly, orbital elements correction offset is determined quantitatively, and the optimal control pulse of orbit correction obtained by Lagrange multiplier method. Finally simulation verifies the validity of the method and feasibility of implementation.

21.1.1 Intersection of Longitude Drift Law

Due to small change in the orbital eccentricity and inclination, IGSO can be approximated as a circular orbit with constant inclination. But the drift of the AN longitude mainly impacts service performance of CNSS, and the drift affected by initial semi-major axis deviation (SMAD) δa contains mainly linear items, while the drift affected by perturbing force is the nonlinear part. After correction of initial SMAD, correction of semi-major axis and eccentricity variation caused by perturbation is mainly control correction for long-term control in orbit.

The average angular velocity of the satellite motion is

$$n = \sqrt{\frac{\mu}{a^3}} \tag{21.1}$$

where μ is earth gravitational constant, a is designed for a nominal orbit semi-major axis, n is the average angular velocity of the satellite motion.

Of the partial derivative of formula (21.1), the average deviation of the satellite orbit angular velocity owing to SMAD can be

$$\delta n = -\frac{3}{2}\frac{n}{a}\delta a \tag{21.2}$$

δa is deviation of in-orbit semi-major axis difference from designed nominal orbital semi-major axis.

With effect of deviations in the initial orbit and orbital perturbation effects, a period of IGSO satellite passing AN is actually not equal to the Earth's rotation period, a small deviation δt exists, which causes differences δn between actual average angular velocity of the satellite n and the Earth 's rotation angular velocity ω_e

$$\delta n = n - \omega_e \tag{21.3}$$

The time difference that the satellite and the Earth's rotation run for a period may be expressed as

$$\delta t = \left(1 - \frac{\omega_e}{n}\right)\frac{2\pi}{\omega_e} \tag{21.4}$$

From (21.2) (21.3) (21.4), the drift of AN longitude affected by initial SMAD after IGSO satellites runs for a period is derived

$$\dot{\lambda}_{error} = \delta t \cdot \omega_e = \left(1 - \frac{\omega_e}{n}\right) \cdot 2\pi \tag{21.5}$$

Formula (21.5) shows that the change of AN longitude of IGSO satellite contains a linear drift part with time, which is mainly caused by the initial orbit deviation and the variation of orbital semi-major axis caused by orbit perturbation. The difference between the actual average angular velocity n of the satellite and the Earth's rotation rate ω_e determines linear drift slope of AN longitude, that is drift speed.

To resolve the variation λ of AN longitude, it is necessary to consider the longitude variable rate of AN $\ddot{\lambda}$ in different locations and angular velocity deviation δn related to initial orbit bias and orbital perturbation. IGSO satellite with orbital altitude of 42,164 km is a high-orbit satellite, which orbital perturbation of oblateness of the earth, lunisolar gravitational perturbation should be considered.

When IGSO satellite suffered perturbing force is denoted f, which is denoted by the radial component f_r, transverse component f_t, the rate of orbital semi-major axis is

$$\frac{da}{dt} = \frac{2}{n\sqrt{1-e^2}}[e\sin M \cdot f_r + (1 + e\cos M)f_t] \tag{21.6}$$

where M is mean anomaly, the satellite orbit can be approximated as a circular one, namely $e \approx 0$;

Then (21.6) is simplified to

$$\frac{da}{dt} = \frac{2}{n} f_t \tag{21.7}$$

To find the (21.5) derivative was

$$\ddot{\lambda}_1 = \frac{2\pi\omega_e}{n_1^2}\frac{dn_1}{dt} \tag{21.8}$$

To integrate (21.2) (21.7) and (21.8), we obtain

$$\ddot{\lambda}_1 = -6\pi a^2 \frac{\omega_2}{\mu} \cdot f_t \tag{21.9}$$

IGSO AN will occur orbital resonance phenomenon affected by the Earth's Tesseral harmonic terms perturbation, mainly caused by entries resonance $J_{2.2}$ that leads to long-period variation of orbit semi-major axis, namely long-period variation of average angular velocity.

Under the action of item $J_{2.2}$, the long-period variation of orbit semi-major axis semi-major due to the orbital resonance can be written as

$$\frac{da}{dt} = \frac{3R_e J_{2.2}}{a} n(1 + \cos\ i)^2 \sin\ 2\left(\lambda_f - \lambda_{2.2}\right) \tag{21.10}$$

where i the satellite orbit inclination; R_e equatorial radius of the earth; λ_f longitude of the ascending node; $\lambda_{2.2}$ longitude of the symmetry axis to the equatorial ellipse under $J_{2.2}$. The corresponding average rate of the angular velocity can be obtained by the formula (21.8)

$$\frac{dn_2}{dt} = -\frac{9R_e J_{2.2}}{2a^2} n_2^2 (1 + \cos i)^2 \sin 2\left(\lambda_f - \lambda_{2.2}\right) \tag{21.11}$$

Of partial derivative of (21.5), drift velocity rate of AN longitude $\ddot{\lambda}_2$ caused by the entry $J_{2.2}$ can be expressed as

$$\ddot{\lambda}_2 = \frac{2\pi\omega_e}{n_2^2}\frac{dn_2}{dt} \tag{21.12}$$

By (21.9) (21.10), we obtain

$$\ddot{\lambda}_2 = -9\pi J_{2.2} \frac{R_e}{a^2} (1 + \cos i)^2 \sin 2\left(\lambda_f - \lambda_{2.2}\right) \tag{21.13}$$

where $\ddot{\lambda}_1$, $\ddot{\lambda}_2$ namely long-term variation rate of RAAN caused by the Earth's Tesseral harmonic terms perturbation and the Earth's oblateness perturbation. Long-term variation rate of RAAN caused by Earth's oblateness perturbation and unisolar gravitational perturbation was main item. From the above equation,

variation of the position of the ascending node of IGSO satellite contains part of linear change with time and nonlinear drift part with the time square, the satellite longitude of AN can expressed as

$$\lambda = \lambda_o + \dot{\lambda}_{error} t + \frac{1}{2}(\ddot{\lambda}_1 + \ddot{\lambda}_2)t^2 \tag{21.14}$$

where λ_o initial AN longitude, so the value of the AN longitude drift $\Delta\lambda$ is

$$\Delta\lambda = \dot{\lambda}_{error} t + \frac{1}{2}\left(\ddot{\lambda}_1 + \ddot{\lambda}_2\right)t^2 \tag{21.15}$$

From (21.15), a quadratic function can be expressed as

$$f(\lambda) = At + Bt^2 \tag{21.16}$$

The linear drift part caused by the initial orbit deviation can be eliminated by orbit semi-major axis bias. For nonlinear drift partially caused by the orbital perturbations, an ascending node longitude drift ring can be designed, so that IGSO satellite is controlled when the ascending node drifts to ring edges.

Using a linear drift part and longitude perturbation caused by the drift of the second-order change part, a control is Exerted so that the AN drifts in the opposite direction when the AN drifts to the edge of the ring, to keep AN to be the specified range.

For a quadratic function $f(\lambda)$, when $B < 0$, parabola $f(\lambda)$ opens down, AN drifts westward, control clicks on the west side of the ring, after the control is applied, AN drifts eastward, the AN drifts eastward gradually slowly and vanishes, and turn back to the west side of the ring, then next control begins. When $B > 0$, the opposite is the case.

The linear drift with the time of satellite's AN can be eliminated using semi-major axis offset Δa

$$\Delta a = \frac{2a}{3\omega_e}\dot{\lambda}_{error} \tag{21.17}$$

from (21.5), then Δa is expressed as

$$\Delta a = \frac{4\pi a}{3\omega_e}\left(1 - \frac{\omega_e}{n}\right) \tag{21.18}$$

21.1.2 Intersection of Longitude Control

Variation of IGSO satellite AN contains linear drift with time and nonlinear changes with time squared. The former can be eliminated by using semi-major axis offset. For the latter, Eq. (21.12) shows that the latter leads to the change of AN,

which is related to position of AN. For the nonlinear impact part of J_{22}, a corresponding amount of bias δa is derived from the previous section.

With Gaussian orbital perturbation equations, the orbit control is divided into two independent parts, one is control of the orbital elements in plane, that is tangential control F_t and radial control F_r; Another is control of the plane, that is normal control F_n of the orbit plane, for the law of control. Because IGSO satellite eccentricity is small as a circular orbit approximately, namely $e \approx 0$, so the tangential control maintains the orbital elements in plane, and the normal control corrects the orbital inclination.

If radial control $F_r = 0$, orbit control equation is simplified

$$\begin{cases} \dfrac{da}{dt} = \dfrac{2}{n} F_t \\ \dfrac{di}{dt} = \dfrac{1}{na} F_n \cos u \\ \dfrac{d\lambda}{dt} = \dfrac{1}{na \sin i} F_n \sin u \\ \dfrac{de_x}{dt} = \dfrac{2}{na} F_t \cos u \\ \dfrac{de_y}{dt} = \dfrac{2}{na} F_t \sin u \\ \dfrac{du}{dt} = n - \cos i \dfrac{d\Omega}{dt}. \end{cases} \tag{21.19}$$

From Eq. (21.19), orbit control equation is divided into two groups: one is control equation in plane only with tangential control F_t related to a, e_x, e_y, and another is control equation outside of plane only with the normal control F_n related i, Ω, which is decouple. So orbit control can be decomposed into two decoupled maneuver: the orbital plane elliptical orbit control and directional control of the plane.

Plane equations can be written as

$$\begin{cases} \dfrac{da}{dt} = \dfrac{2}{n} F_t \\ \dfrac{de_x}{dt} = \dfrac{2}{na} F_t \cos u \\ \dfrac{de_y}{dt} = \dfrac{2}{na} F_t \sin u. \end{cases} \tag{21.20}$$

Since the orbit control amount is small, the required thrust is small, and control duration is short, it can be regarded as impulse control, and integral pulse with time can regarded as velocity increment, the orbit control equations in plane can be

written increments equation. The following formula represents for a single control pulse

$$\begin{cases} \dfrac{\Delta a}{a} = \dfrac{2}{na}\Delta v_t \\ \Delta e_x = \dfrac{2}{na}\Delta v_t \cos u \\ \Delta e_y = \dfrac{2}{na}\Delta v_t \sin u. \end{cases} \tag{21.21}$$

From (21.20), it can be seen that: there are three independent variables $\Delta a, \Delta e_x, \Delta e_y$ in the plane, but the single pulse velocity in plane have two components, three independent variables can not be corrected on one time. While the two speeds pulses have four components, full correction can be achieved. The question is that: how to determine the size and location of twice the speeds pulse so that the two pulses complete the full correction factor within the orbital plane and the fuel consumption is minimized, which is an optimal orbit control design problems.

From the Eq. (21.21), the twice speed pulse, the orbit control increment equations are expressed as

$$\begin{cases} \dfrac{\Delta a}{a} = \dfrac{2}{na}(\Delta v_{t_1} + \Delta v_{t_2}) \\ \Delta e_x = \dfrac{2}{na}(\Delta v_{t_1} \cos u_1 + \Delta v_{t_2} \cos u_2) \\ \Delta e_y = \dfrac{2}{na}(\Delta v_{t_1} \sin u_1 + \Delta v_{t_2} \sin u_2). \end{cases} \tag{21.22}$$

Optimal control problem described as: seeking $\Delta v_{t_1}, \Delta v_{t_2}, u_1, u_2$ to meet constraints that makes the index function minimum.

$$J = \min_{\Delta \bar{v}_{t_1}, \Delta \bar{v}_{t_2}, u_1, u_2} (|\Delta v_{t_1}| + |\Delta v_{t_2}|) \tag{21.23}$$

This is required under the constraints of a typical function extreme problems that can be solved by Lagrange multiplier method strictly. For IGSO orbit, the eccentricity is small and it is considered $\Delta e < \frac{\Delta a}{a}$ that situation is called degradation. Two desired velocity pulse is applied, the first location u_1 may be any one, and when this position is selected, the corresponding speed increment Δv_{t_1}, and a second increment Δv_{t_2} and its location u_2 will be subsequently completely determined

$$\begin{cases} \Delta v_{t_1} = \dfrac{na}{4} \dfrac{\left(\frac{\Delta a}{a}\right)^2 - \left(\Delta e_x^2 + \Delta e_y^2\right)}{\frac{\Delta a}{a} - \left(\Delta e_x \cos u_1 + \Delta e_y \sin u_1\right)} \\ \Delta v_{t_2} = \dfrac{na\Delta a}{2a} - \Delta v_{t_1} \\ \cos u_2 = \dfrac{na}{2\Delta v_{t_2}} \left(\Delta e_x - \dfrac{2\Delta v_{t_1}}{na} \cos u_1\right) \\ \sin u_2 = \dfrac{na}{2\Delta v_{t_2}} \left(\Delta e_y - \dfrac{2\Delta v_{t_1}}{na} \sin u_1\right). \end{cases} \tag{21.24}$$

From the above equation, It can be seen that the twice speed increments is in the same direction, that is, when $\Delta a > 0$, the twice speed increments are acceleration, when $\Delta a < 0$, they are deceleration. Corresponding Semi-major axis offset is positive or negative.

The drift direction of AN needs to be determined before revision control. When AN drift westward to border of control ring, the actual Semi-major axis is greater than the nominal one, then the control is exerted modified speed increment of $\Delta v < 0$; amended AN will drift eastward, and vice versa.

21.2 Numerical Simulation

In the following simulation, the orbital drift of IGSO satellite is analyzed with orbital control and with absence of orbital control, respectively.

Initial IGSO satellite orbit parameters:

Semi-major axis	$a_o = 42{,}164{,}169.637135$ m
Eccentricity	$e = 0.00$
Orbital inclination	$i = 55.0°$
RAAN	$\lambda = 118.00°$
Argument of perigee	$\omega = 0.00°$
Mean anomaly	$M = 0.00°$

the average orbital parameters in the simulation are used in the calculation of orbit, which can reflect approximated orbit characteristics of the long-term movement of the satellites.

With the absence of orbital control, longitude drift of AN simulation of IGSO satellite is shown in Fig. 21.1.

As shown from Fig. 21.1, the ground track of AN longitude drifts to 62.3°E from the designed nominal position 118°E over one year duration without orbit maintenance, the satellite into the ascending node longitude, and the coverage area of the satellite has deviated from the mission area, which does not meet the requirements of a satellite mission obviously.

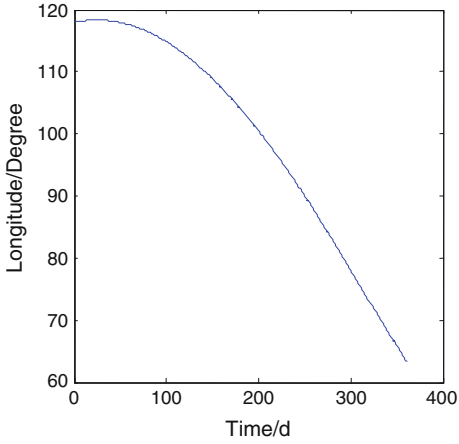

Fig. 21.1 AN drift law without control

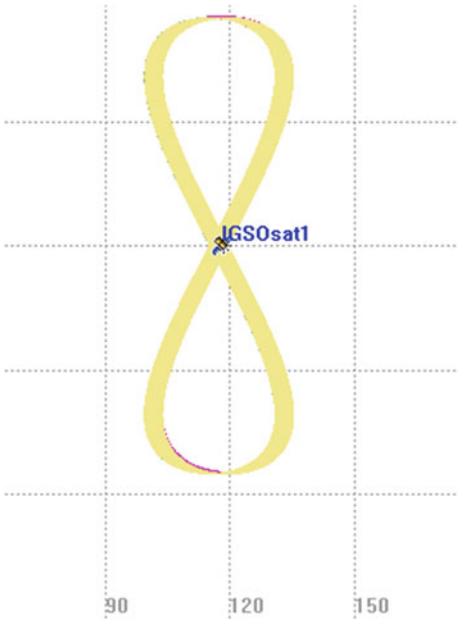

Fig. 21.2 Variation law of sub-satellite track of controlled satellite

For the control status of IGSO satellite, AN drifts freely to the edge of control ring (118°E ± 1.0°) after a period of time, namely to the threshold of control, then the one pulse control is exerted when $u_1 = 0$, the another pulse control is also exerted in the time of u_2, which keeps AN to return to the control ring. Afterward, AN of satellite continues to drift, the second control is implemented, the time interval of twice controls is the period of satellite control.

Through three times of orbital control based on the above methods, the control results, such as sub-satellite track, drift of AN longitude, are shown from Figs. 21.2, 21.3, 21.4.

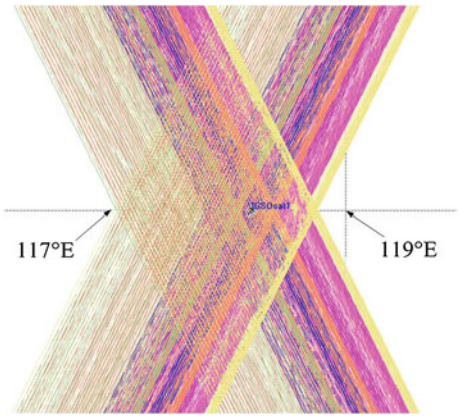

Fig. 21.3 Amplification of sub-satellite track (Intersection)

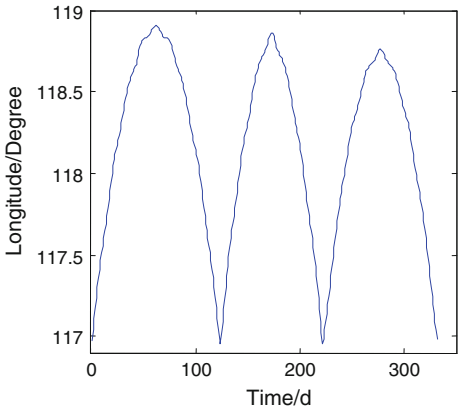

Fig. 21.4 Drift law of AN longitude with three controls

As shown from Fig. 21.4, when the satellite orbit is controlled, AN longitude of the satellite relative to the nominal position is kept within a certain range (±1°), which meets the mission requirements. The duration of three times of orbital controls is 331 days, of which the first period of satellite control holds 122 days, the second 99 days, and the third 110 days, and their differences is mainly affected by small changes in orbital eccentricity, which magnitude is shown in Fig. 21.5, so the orbit may be regarded as nearly circular one, the simulation result is verified to be valid.

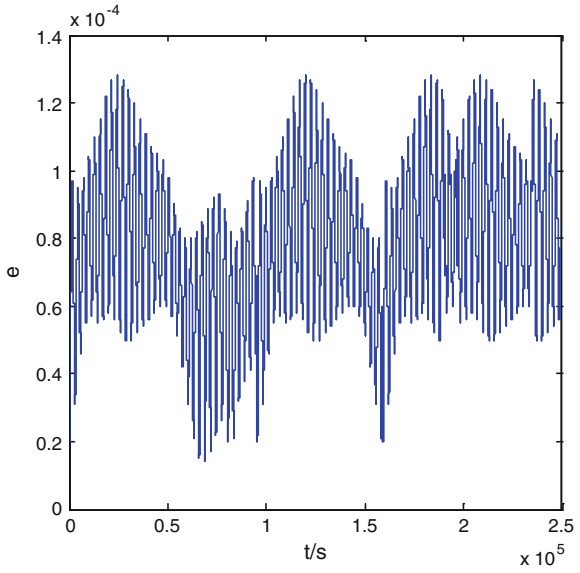

Fig. 21.5 Variation law of orbit eccentricity

21.3 Conclusion

Based on analyzing the impact of various perturbation of the IGSO satellite on the drift of AN longitude, the method of double-pulse control is used, the optimal pulse speed and the direction of thrust is derived. The three times of IGSO satellite orbit control is simulated, which results meet mission requirements. That shows that the control method is simple and feasible to implement. That AN of satellite is maintained in control ring verifies the effectiveness of the control method, and result is significant to the control of IGSO satellite.

References

1. Zhu M, Hu S (2009) Location evolution and keeping of IGSO cross node. Chin Space Sci Technol (1):41–45
2. Jiang Y, Yang S (2011) Coverage performance analysis on combined-GEO-IGSO satellite constellation. J Electron 28(2):228–234
3. Tan W, Jen TC (2008) The function approximation method applied in MEO and IGSO satellites optimal maneuver. In: Proceedings of 46th AIAA Aerospace Sciences Meeting, Reno Nevada, USA, 7–10 Jan 2008
4. Luo C, Gao D (2006) Double impulse fuel-optimal control for formation reconfiguration. J Astronaut 27(6):1211–1216
5. Chang Y, Zhou J (2008) Optimal two-impulse formation keeping control in near circular orbit based on J_2 invariant perturbation conditions. Aerosp Control 26(6):3–8
6. Katsuhiko Yamada (2011) Fuel-optimal eccentricities for precise formation keeping of spacecraft on Keplerian orbits. Acta Astronaut 68:1811–1819

7. Yoshihiro I, Akira I (2008) Optimal impulsive relative orbit transfer along a circular orbit. J Guidance Control Dyn 31(4):1014–1027
8. Mohammad A, Ramin V (2012) Stabilizing chaotic system on periodic orbits using multi-interval and modern optimal control strategies. Commun Nonlinear Sci Numer Simulat 17:3832–3842

Part II
BDS/GNSS Test and Assessment Technology

Chapter 22
A Research of Multi-antenna Spoofing Detection Technology

Guangwei Fan, Baoguo Yu, Zhixin Deng and Zhenhua Wang

Abstract This paper presented a method that supports multi-element signal direction finding through power augmentation after the spoofing jamming signals are despread with the local codes, which is compared with the satellite position acquired by ephemeris calculating. The conventional spoofing–jamming detection methods are only effective to specific spoofing jamming. This algorithm utilizes the priori knowledge that the satellite navigation receiving system already has detected a number of spoofing jamming with the high-resolution direction-finding method. The simulation results show that this algorithm has good detection performance on both active spoofing and passive spoofing.

Keywords GNSS · Direction of arrival · Spoofing jamming · Despread

22.1 Introduction[1]

In recent years, with the evolution of electronic technology and the improvement of navigation frequency protection policy, spoofing jamming is becoming the major threat to Beidou Navigation System (Compass) in the civil navigation field [1]. The spoofing jamming results in severely affection on the regional navigation, positioning and time service quality of Compass; therefore, it is necessary to detect and eliminate spoofing jamming. Spoofing jamming refers to the jamming action

[1] National High Technology Research and Development Program of China (No:2012AA121802).

G. Fan (✉) · B. Yu · Z. Deng · Z. Wang
The 54th Research Institute of CETC, Shijiazhuang, China
e-mail: fgweihb@163.com

G. Fan · B. Yu · Z. Deng · Z. Wang
Satellite Navigation Technology and Equipment Engineering, Shijiazhuang, Hebei, China

J. Sun et al. (eds.), *China Satellite Navigation Conference (CSNC) 2014 Proceedings: Volume I*, Lecture Notes in Electrical Engineering 303,
DOI: 10.1007/978-3-642-54737-9_22,

that transmits spurious signal of the same parameters with the satellite navigation signal (but different information code) to the satellite navigation receiver and makes the receiver generate wrong positioning information. Spoofing jamming can be divided into two types: active spoofing jamming [2, 3] and passive spoofing jamming [3].

The spoofing on navigation system are drawing more and more attention. It is always an important topic in the ICG of Global Satellite Navigation Systems' annual conferences to discuss the technologies of spoofing detection and elimination. Some detection methods for spoofing jamming have been proposed, e.g., Huang et al. [4]. Systematic introduced the spoofing detection methods, Zhou et al. [5]. Summarized and prospected the counter-spoofing technology of satellite navigation system; Nielsen [6] proposed a detection method for spoofing using a handheld single-antenna receiver; Montgomery [7], a scholar in Texas University proposed a technique to detect spoofing by sensing the phase difference variation received with two antennas. As per our summary of these approaches, the known detection and identification techniques of spoofing jamming are mainly based on such parameters as power change rate of satellite, absolute value of Carrier to noise ratio (CNR), relative power of signal at different frequency points, pseudo-range change rate, rate of Doppler frequency shift change, cross-correlation between L1 and L2, L1–L2 pseudo-range differential or jump of observed quantity.

Base on analysis and summary of the existing algorithms, this paper proposed a spoofing detection and identification algorithm utilizing the correlation gain of acquired and tracked navigation signal based on direction finding of multi-element antenna. In addition to the design principle and the implementation process, the algorithm was also validated through simulations.

22.2 Spoofing Model

This research took the civil signal of branch I at B1 frequency point as reference, of which the transmitted signal is expressed as follows:

$$\begin{aligned} S^j = {} & A_C C^j(t) D_C^j(t) \cos\left(2\pi f t + \varphi_C^j\right) \\ & + A_P P^j(t) D_P^j(t) \sin\left(2\pi f t + \varphi_P^j\right) \end{aligned} \tag{22.1}$$

where

J represents satellite ID number,
A_C represents the ranging code amplitude modulated in carrier branch Q at frequency point B1,
C represents the ranging code in branch I,
P represents the ranging code in branch Q,
D_C represents the data code modulated with the ranging code in branch I,
D_P represents the data code modulated with the ranging code in branch Q,

f represents the carrier frequency at frequency point B1,
φ_C represents the initial phase of carrier branch I at frequency point B1, and
φ_P represents the initial phase of carrier branch Q at frequency point B1.

The civil signal received at the receiving end is expressed as follows:

$$x(t) = \sum_{j=1}^{M} A_C^j C^j(t-\tau_j) D_C^j(t-\tau_j) \cos\left(2\pi f_j(t-\tau_j) + \varphi_C^j\right) + N(t) \tag{22.2}$$

where

τ_j represents the delay of signal on arrival of receiver from the jth satellite,
M represents the number of visible satellites,
f_j represents the frequency of signal containing Doppler frequency shift on arrival of receiver from the jth satellite, and
$N(t)$ represents the system noise of receiver.

Active spoofing jamming is achieved by generating highly realistic spoofing signals with interference generator. Active spoofing jamming must know the code type of satellite navigation signal and the navigation message to be simulated at the moment. It is applicable to civil signal of public code type, but difficult for military signal that is encrypted.

The active spoofing jamming model for civil code at B1 frequency point can be considered as the civil signal at B1 frequency point plus certain Doppler frequency shift. When the receiving end is exposed in passive spoofing jamming, the signal received at the receiving end can be expressed as follows:

$$\begin{aligned} x(t) = & \sum_{j=1}^{M} A_c^j C^j(t-\tau_j) D_C^j(t-\tau_j) \cos\left(2\pi f_j(t-\tau_j) + \varphi_C^j\right) \\ & + \sum_{l=1}^{L} A_C^l C^l(t-\tau_l) D_C^l(t-\tau_l) \cos\left(2\pi f_v(t-\tau_l) + \varphi_C^l\right) \\ & + N(t) \end{aligned} \tag{22.3}$$

where

L represents the number of active spoofing jamming sources,
A_C^l represents the amplitude of the lth spoofing jamming, which is typically 5 to 10 dB higher than the true signal,
$D_C^l(t)$ represents the data code modulated for spoofing jamming, and
f_v represents the carrier frequency with certain Doppler frequency shift relative to B1 frequency point.

As for passive spoofing jamming, it is required to receive satellite navigation signals from the sky utilizing the natural prolongation of navigation signal and

directly broadcast them after delay and amplification processing. It is relatively simple to implement delay jamming, for it does not require knowing the coding form of satellite navigation signal and the navigation message at the moment. However, the jamming signals have to reach the receiver in not more than 90 ms after the delay, for the time that satellite navigation signal takes to arrive at the earth is typically within the range of 70–90 ms. In the event of passive spoofing jamming, the model of the signal received by the receiving end can be expressed as follows:

$$\begin{aligned} x(t) = & \sum_{j=1}^{M} A_c^j C^j\left(t-\tau_j\right) D_C^j\left(t-\tau_j\right) \cos\left(2\pi f_j\left(t-\tau_j\right)+\varphi_C^j\right) \\ & + \sum_{j=1}^{M'} A_c^{j'} C^j\left(t-\tau_j-\tau_{j'}\right) D_C^{j'}\left(t-\tau_j-\tau_{j'}\right) \cos\left(2\pi f_v\left(t-\tau_j-\tau_{j'}\right)+\varphi_C^j\right) \\ & + N(t) \end{aligned} \tag{22.4}$$

where $A_c^{j'}$ represents the amplitude and $\tau_{j'}$ represents the delay of passive spoofing jamming.

Taking the civil code of Compass B1 signal for example, after the received signal of one pseudo-code period is correlated with the SS code $c_i(t-\tau_i)$ of the desired satellite signal, the resultant signal can be expressed as follows:

$$y(\tau) = \frac{1}{2{,}046T_c} \int_{t=0}^{2{,}045} x(t) c_i(t-\tau_i) \cos(2\pi f_i(t-\tau_i)+\varphi_i) dt \tag{22.5}$$

where T_c represents the time width of every chip in pseudo code and f_i represents the same frequency as that of the received signal. After the above correlation despreading to each satellite, the power of desired signal may be improved effectively.

Figure 22.1 shows the correlation function of the pseudo-code signal corresponding to B1I-branch civil code in one period. Specifically, Fig. 22.1a shows the autocorrelation function with a certain chip delay and Fig. 22.1b shows the autocorrelation function with the same pseudo-code initial phase but different superposition. Figure 22.1c shows the cross-correlogram between pseudo code in one period and the pseudo codes in other branches. As shown in the figures, autocorrelation could generate a certain gain, the pseudo codes at different initial phase could generate correlation peak with the same pseudo code at known initial phase, but different pseudo codes would not generate correlation peak. spoofing jamming to receiver is achieved with the aid of the spread-spectrum gain that is acquired after pseudo codes are correlated and despread with the local codes in different channels. Generally, passive spoofing jamming is achieved by forwarding the satellite signals received by the receiver and broadcasting them after they are

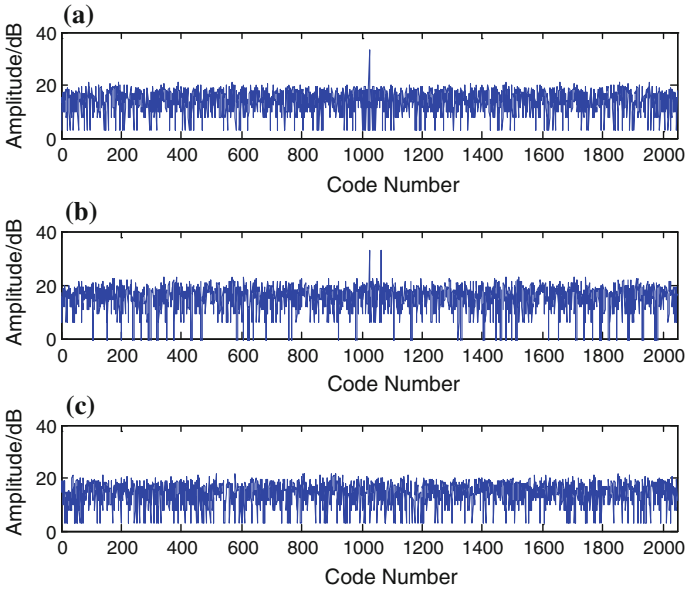

Fig. 22.1 Pseudo-code correlation function

delayed and amplified. Therefore, two peaks emerge in the interfered channel of receiver after correlation processing. By contrast, active spoofing jamming is to simulate the satellite navigation signals and Ephemeris that receiver can not receive for now. The correlated peak emerges in the channel that signals are not supposed to be acquired.

22.3 Performance Test of the OEM Board

Assuming that the receiving array of Compass receiver adopts uniform linear arrays, of which P identical omnidirectional elements are aligned along a straight line with equal element separations, the steering vector of the P-element uniform linear array can be expressed as follows:

$$a(\theta_i) = [1, e^{-j\omega_i}, \ldots, e^{-j(p-1)\omega_i}]^T \tag{22.6}$$

where

$$\omega_i = 2\pi \sin \theta_i d/\lambda,$$

λ represents the signal wavelength, and
d represents the separation distance between adjacent elements, typically $d \leq \lambda/\lambda 2$.

If there are a total of M signals including both spoofing signal and normal navigation signal, then the signal received by the pth element can be expressed as:

$$x_p(t) = \sum_{i=1}^{M} a_p(\theta_i)s_i(t) + n_p(t) \tag{22.7}$$

The received signal, after correlated with the local code, can be expressed as:

$$h_p(\tau) = \sum_{i=1, i\neq j}^{M} a_p(\theta_i)q_i(t) + a_p\left(\theta_j\right)y_j(t) + n_p(t) \tag{22.8}$$

where

j represents the jth correlation channel of receiver,
$q_i(t)$ represents the result of other satellite signal correlating with the local code of the jth channel, and
$y_j(t)$ represents the result of the jth satellite signal correlating with the local code of the jth channel.

Since receiver has different receiving channels in response to different satellites to receive the correlation with the local code, the signals of other channel received by the corresponding channel are negligible relative to the local channel, i.e., $q_i(t) << y_j(t)$. Therefore, Eq. (22.8) may be simplified as:

$$h_p^j(\tau) = a_p\left(\theta_j\right)y_j(t) + n_p(t) \tag{22.9}$$

Generally, the length of correlation integral is one pseudo-code period. To select a number of pseudo-code periods, non-coherent accumulation is required.

The data that are correlated with the ith channel of P elements constitute a data vector, which can be expressed as:

$$H^j(\tau) = [h_1^j(\tau), \ldots, h_p^j(\tau)]^H \tag{22.10}$$

The correlated covariance matrix is expressed as follows:

$$R_{hh}^j = E\left[H^j(t)H^j(t)^H\right] = AR_{yy}A^H + \sigma_N^2 I \tag{22.11}$$

where

$R_S = E[y_j(t)y_j(t)^H]$ represents the complex envelope covariance matrix of signal,
I represents the single-element array of P dimensions, and
σ_N^2 represents the noise power of array element.

According to the subspace resolution theory, if the number of signal sources is fewer than the number of array elements, then the signal component of the array data will be located in 1 low-rank space of array covariance matrix R. After

correlation with subchannel, if only navigation signal exists without spoofing jamming or only active spoofing jamming exists, then there is only one large signal component; if passive spoofing jamming exists as well, then it is possible to have two large signal components. Theoretically, it is possible to extract large eigen component by means of eigen decomposition as long as the number of array elements is more than 2. Therefore, run a eigen decomposition to R and arrange the eigenvectors in descending order as per the magnitude of eigen value to get:

$$\begin{aligned} R &= U_s \sum_s U_s^H + U_n \sum_n U_n^H \\ &= \sum_{m=1}^{K} \zeta_m e_m e_m^H + \sum_{m=K+1}^{M} \zeta_m e_m e_m^H \end{aligned} \tag{22.12}$$

The larger eigen values $\zeta_1, \ldots, \zeta_K$ in R corresponds to the signal term while the smaller eigen values $P - K$ correspond to the noise term. Therefore, it is possible to form a signal subspace with K eigen vectors $e_1, e_2, \ldots, e_K$; besides, $P - K$ eigen vectors $e_{K+1}, \ldots, e_M$ form a noise subspace. Since the space spanned by the direction vectors $a_i(\theta)$ of signal and the space spanned by eigen vectors U_s are the same, and the signal subspace and the noise subspace are orthogonal with each other; therefore, $a_i(\theta)$ is orthogonal with the noise subspace U_n. Considering the nature that the projection of signal subspace in noise subspace is zero, it is possible to acquire the super-resolution estimation of the signal wave arrival direction by establishing spectrum peak search.

Finally, the spatial spectrum estimation is achieved as per the equation below:

$$P_{MUSIC} = \frac{1}{a^H(\theta)(I - SS^H)a(\theta)} \tag{22.13}$$

.

22.4 Spoofing Jamming Detection and Identification Algorithm

Among the spoofing jamming detection and identification algorithms, the multi-element spoofing jamming detection technique is also based on the 60–70 dB correlation gain after the spoofing jamming is correlated. In other words, the direction of spoofing jamming in multi-element channels can be detected with the aid of the high correlation gain achieved after the pseudo codes tracking satellite are decomposed. By comparing it with the satellite position resolved from Ephemeris, it is possible to implement detection and identification of spoofing jamming.

The detection and identification process is as shown in Fig. 22.2. Firstly, a multi-element receiver receives the navigation signals and spoofing jamming from the sky, which are amplified to appropriate amplitude via RF link.

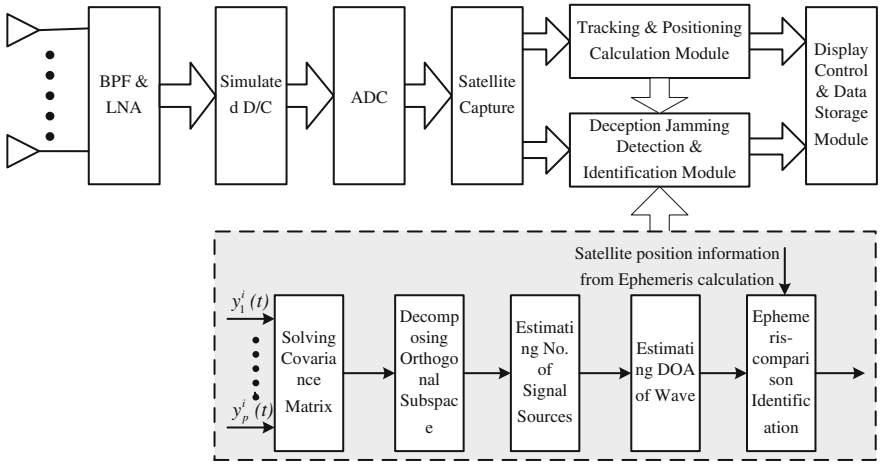

Fig. 22.2 Detection and identification flow chart of spoofing jamming

And then, the signal frequency is converted to the required output frequency before the output signals are converted into digital signals through an AD converter.

Thirdly, the receiver of each channel completes acquiring and tracking of the corresponding receive channel separately.

Fourthly, the receivers duplicate the corresponding carriers and pseudo codes internally at the same time, which must be synchronized with the counterparts of the received satellite signal.

Fifthly, the replicate carrier and the received signal go through a frequency mixing process to complete carrier decomposition and signal despreading. At the end of this step, only data code is left in the received signal.

Sixthly, carry out direction finding with MUSIC algorithm with the aid of the resultant gain after correlation and considering the integrated data of receivers after correlating with different satellite channels.

Finally, compare the angle information acquired from direction-finding process with the satellite position information acquired from position calculation to complete detection and identification of spoofing jamming.

The algorithm verification is mainly purposed to verify the direction-finding detection performance after correlation; therefore, it is allowed to simplify the acquiring and tracking process in receiver. Assuming that the frequency and the pseudo-code initial phase of received signal are known, the detection and identification algorithm process of spoofing jamming on the basis of multi-element reception can be described as follows:

- Initialize all the parameter settings.
- Despread the signals received via corresponding channels using Eq. (22.8).
- Work out the correlated covariance matrix with Eqs. (22.10) and (22.11).

- Decompose the covariance matrix to get the signal subspace and the noise subspace.
- Figure out the arrival direction of signal with Eq. (22.13).
- Compare the detected direction with the satellite position worked out by means of Ephemeris calculating to determine the signal is spoofing jamming or navigation signal.
- Repeat steps 2 through 6 to traverse all the receiving channels until all the spoofing jamming existing in the received signal are detected.

22.5 Simulation and Performance Analysis of Algorithm

To verify the algorithm performance, the following simulation was given with reference to the Compass civil signal at B1 frequency point. In the simulation, Gold code of 2046 bit length was taken as the spread-spectrum code of navigation signal and modulated at B1 frequency point in BPSK mode on the noise background of additive white Gaussian noise. With the code rate of 2.046 MHz/s, the input SNR of −25 dB and 12-element linear array model, the simulation model did not consider the effects from the spoofing jamming in the same channel and the true satellite signals at different frequencies.

We assumed that satellite signals entered channels 1, 2 and 3 of multi-antenna receiver at the incidence angles of 10, 30 and −60° respectively. And the satellite signals in channels 1 and 2 were interfered by a passive spoofing–jamming source in the direction of −70°, of which the ratio of interference power relative to noise power was −20 dB. Besides, an active spoofing jamming entered Channel 4 at the incidence angle of 60° and with the SINR of −20 dB. Multi-element integrated direction-finding process was given after correlation with different channels, to get the direction-finding result, as shown in Fig. 22.3.

Figure 22.3 shows the direction finding in Channel 1 after correlation processing. Two incident signals were detected at the angles of 10 and −70° respectively. They got higher correlation gains after correlating with the local codes in receiver channels. In the mean time, the cross-correlation gain between the signals in other channel and the local code in the local channel was too little and negligible. If a channel receives the same correlation signals from two different directions, it implies that channel is subject to the effect of passive spoofing jamming. By comparing the findings with the Ephemeris information resolved from satellite Ephemer, it is possible to determine the signal in which direction is passive spoofing jamming.

Figure 22.4 shows the direction finding after correlation processing with Channel 2. It can be seen in the diagram that the correlated direction-finding algorithm proposed in this paper detected two signal directions satisfactorily for the purpose of identifying spoofing jamming, though the incident direction of passive spoofing jamming and the incident direction of satellite signal were close to each other.

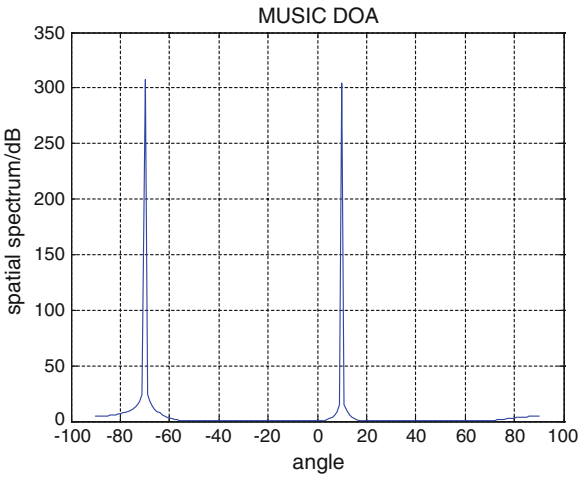

Fig. 22.3 Direction finding in channel 1 after correlation processing

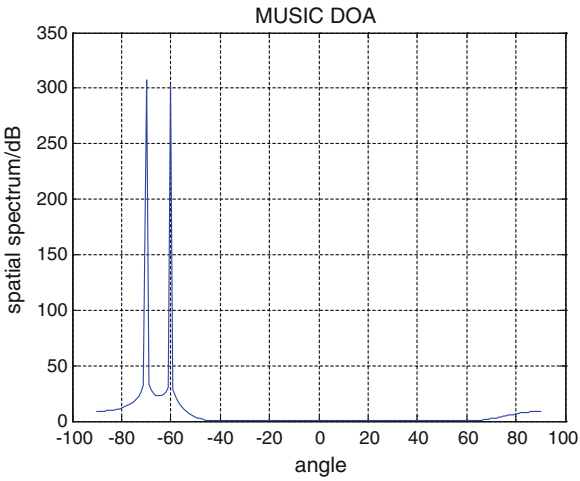

Fig. 22.4 Direction finding in channel 2 after correlation processing

Figure 22.5 shows the direction finding in Channel 3 after correlation processing. It can be seen in the diagram that the spoofing jamming aiming at other channel would not interfere with the local channel if no spoofing jamming aimed at the local channel.

Figure 22.6 shows that a signal entered Channel 4 after correlated direction finding at the angle of 60^{o}. Since the Ephemeris of active spoofing jamming in the incident direction is hard to be exactly the same as that of the simulated satellite signal, it is feasible to detect and identify active spoofing jamming by means of Ephemeris comparison.

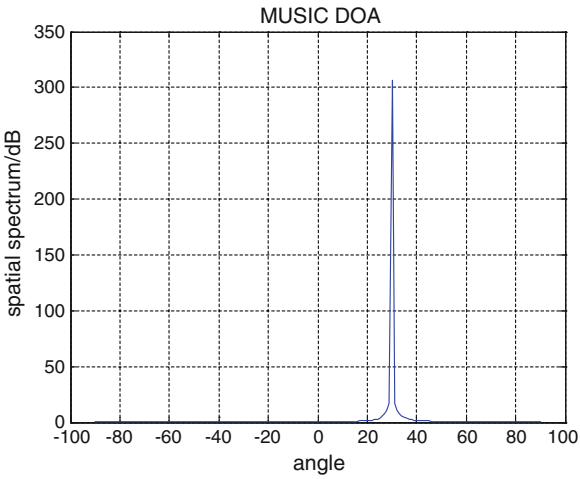

Fig. 22.5 Direction finding in channel 3 after correlation processing

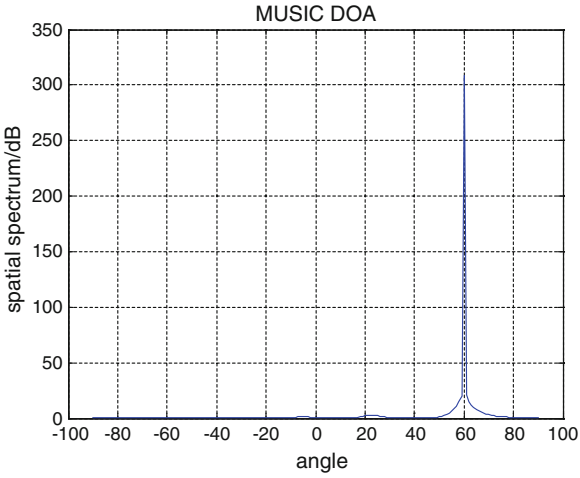

Fig. 22.6 Direction finding in channel 4 after correlation processing

To verify the estimation performance of the correlated direction-finding and identification algorithm proposed in this paper, the root mean square error (RMSE) was used to describe the direction-finding performance of the algorithm. The RMSE is defined as follows:

$$\mathrm{RMSE} = \sqrt{E\left\{(\theta' - \theta)^2\right\}} \tag{22.14}$$

Where, θ' represents the direction of estimated signal and θ represents the direction of true signal.

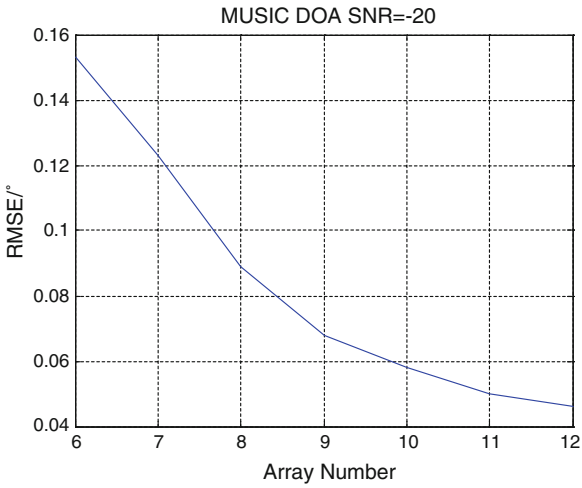

Fig. 22.7 Effect of element number to angle measurement error

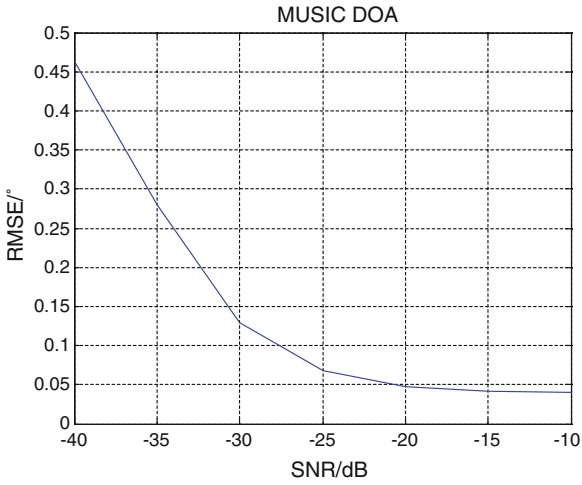

Fig. 22.8 Effect of signal power to angle measurement error

The effects of different element numbers to the correlated direction-finding performance were simulated. Set the incident direction of signal to 30°, the SNR to −20 dB and the element number to 6 through 12 separately in addition to linear array model. The simulation result is as shown in Fig. 22.7.

Figure 22.7 shows the effect of changed element number to direction-finding accuracy. It can be seen in the diagram that the correlated angle measurement performance climbed up along with the increase of element number. The correlated angle measurement accuracy has already reached 0.15° more or less when the array was made up of 6 elements, able to satisfy the detection and identification requirements of spoofing jamming.

The effects of different SNRs to the correlated direction-finding performance were simulated. Set the incident angle of signal to 30°, the SNR to −20 dB, the linear array model to 12 elements and the SNR changing from −40 to −10 dB in steps of 5 dB. The simulation result is as shown in Fig. 22.8.

Figure 22.8 shows the effect of signal power to angle measurement error. It can be seen in the curve diagram that the angle measurement accuracy climbed up along with the increase of SNR and approached 0.1° at the SNR of −25 dB. The SNR of typical navigation signal is within the range of −25 to −20 dB and the power of spoofing jamming is a little bit higher than that of navigation signal; therefore, the correlated direction-finding algorithm proposed in this paper has good direction-finding performance to either spoofing jamming or satellite signal, capable of detecting and identifying various spoofing jamming and satellite navigation signals.

22.6 Summary

With reference to Beidou civil signal at B1 frequency point, this paper described the receiving models of passive and active spoofing. Based on the high-resolution direction-finding algorithm and the spread-spectrum gain after correlation despreading of received signal, a multi-antenna detection and identification algorithm of spoofing was proposed. After signal correlation despreading, this algorithm can estimate the direction of arrival signal and compare it with the satellite position acquired by ephemeris calculating to recognize spoofing jamming from normal navigation signal. The simulation results show that the proposed algorithm has good detection performance for either passive spoofing jamming or active spoofing jamming within the power range of navigation signal in addition to good universality. In the condition of few receiving channels, it is still capable of providing high measurement accuracy. This algorithm effectively improves the detection performance of spoofing.

References

1. Basker S (2010) Jamming: a clear and present danger. GPS World 21(4):8–9
2. He S, Li T, Han Y (2004) A research of GPS jamming technology in navigation wars. Shipboard Electr Countermeasure 27(1):24–27
3. Humphreys TE, Ledvina BM, Psiaki ML, et al (2008) Assessing the spoofing threat: Development of a portable GPS civilian spoofer. In: Proceedings of the ION GNSS international technical meeting of the satellite division. 55–56
4. Huang L, Tang X, Wang F (2011) A research of anti-spoofing methods in satellite navigation receiver. J Wuhan University (Information Science Edition) 36(11):1344–1347

5. Zhou X, Li GX, Cai DB, et al (2013) review and outlook of counter-spoofing technologies in satellite navigation system. In: Proceedings of the 4th China GNSS academic annual conference: S7 Compass/GNSS User Terminal Technologies
6. Nielsen J, Broumandan A, Lachapelle G (2012) GNSS spoofing detection for single antenna handheld receivers. Navigation 58(4):335–344
7. Montgomery PY, Humphreys TE, Ledvina BM (2009) A Multi-Antenna Detection. Inside GNSS 4(2):40–46

Chapter 23
Research on Testing Method and Influence of GlONASS Inter-frequency Biases

Xue Zhang, Huijun Zhang and Xiaohui Li

Abstract GLONASS adopts FDMA signal mechanism, some inter-frequency biases generated at the receiver end make difficult to the implementation and application of multi-mode navigation, which is an important subject having to be considered and resolved. First, in this paper, GNSS simulator was implemented based on the study on the testing approach for GLONASS inter-frequency biases, the experimental data from two kinds of brand receiver (Septentrio PolaRx 4 and Novatel OEMV_3G_L1L2s) was obtained and analyzed in details. The results from receivers show that there is a difference in inter-frequency bias between the two, whose increasing presents a linear trend. Second, the multi-station measured data comparison was experimented, influence of GLONASS inter-frequency biases on the results from GLONASS independent positioning, GPS/GLONASS integrated positioning and system time offset monitoring are analyzed. The experiment result indicates that correction in GLONASS inter-frequency bias during location solution and system time offset monitoring can improve the accuracy of positioning and the precision of system time offset monitoring significantly, the performance is related to the type of receiver.

Keywords GLONASS · Inter-frequency biases · GPS/GLONASS integrated positioning · System time offset

X. Zhang (✉) · H. Zhang · X. Li
National Time Service Center, Chinese Academy of Sciences, Xi'an 710600, China
e-mail: yingtaoxinyu@126.com

X. Zhang · H. Zhang · X. Li
Key Laboratory of Precision Navigation Positioning and Timing, Chinese Academy of Sciences, Xi'an 710600, China

X. Zhang
University of Chinese Academy of Sciences, Beijing 100039, China

J. Sun et al. (eds.), *China Satellite Navigation Conference (CSNC) 2014 Proceedings: Volume I*, Lecture Notes in Electrical Engineering 303,
DOI: 10.1007/978-3-642-54737-9_23,

23.1 Introduction

The U.S. GPS maintains the leading position in the development and application of Global Navigation Satellite System at present, but a single GNSS system has its limitation because of few satellites observed, it's difficult to meet requirements of positioning especially in deep mountain gorge and between urban high-rises. Actually, almost all of commercial high-end GNSS receivers have the function of multi-system joint location in order to increase the number of observable satellites, to improve the observation geometry and the reliability and accuracy in positioning. Joint positioning using multi-system satellite navigation has become one of the major trends in the development of navigation.

However, multi-system joint positioning also brings about a series of problems such as compatibility and interoperation etc., one of which is about pseudo code and carrier wave [1]. Each of GNSS adopts a different signal system, the code division multiple access method is for GPS, while the frequency division multiple access mode is for GLONASS with inter-frequency biases generated at the receiver end. Implementation and application of multi-mode navigation are brought difficulties, which needs a significant concern and resolution.

23.2 Research on Testing Methods of GLONASS Inter-frequency Biases

23.2.1 GLONASS Inter-frequency Biases

Modern receivers can receive and record the satellite signals through multiple channels at the same time. The value of receiver channel retardation deviation depends on the obtained signal changes in frequency. For GPS with CDMA signal system, frequencies of carrier wave from satellites are same(inter-frequency biases generated by different signals from same satellite won't be discussed in this paper), in the case of ignoring channel retardation deviation caused by the power of received signal, retardation deviation with a sub-millimeter size between each channel is negligible [2]. While FDMA signal system for GLONASS, channel delays inside is different from each other for satellite signals of different frequency point to results in some bias, which is called inter-frequency biases. In order to improve the accuracy of positioning and the precision of GNSS time difference detection, it's necessary to measure GLONASS inter-frequency biases precisely in advance.

The inter-frequency biases of GLONASS are related to hardware, especially the type of receiver. For inter-frequency biases of GLONASS from different types of receiver, Wanninger [3] took advantage of single-difference carrier phase to observe and compute the GLONASS inter-frequency biases of 133 receivers from 9 different vendors, he pointed out that the difference between adjacent frequency

ranges from mm to cm, while the GLONASS inter-frequency biases present similar to gather together. GNSS data analysis center of Shanghai astronomical observatory (SHA) [4] classified GLONASS hardware relay in different observation stations, created models for inter-frequency biases from different kinds of receiver and forecasted.

23.2.2 Testing Methods of GLONASS Inter-frequency Biases Based on GNSS Simulator

Considering inter-frequency biases, the pseudorange equation of GLONASS satellite, at a frequency number i can be expressed as (23.1):

$$\rho_i = r_i + pd_i + c(dT_i + DCB_i - dt_i) + d(ion)_i + d(trop)_i + Ep_i \tag{23.1}$$

where ρ_i is the pseudorange from receiver to GLONASS satellite, r_i represents the geometric distance between satellite and ground, pd_i represents the track error, dT_i represents the receiver clock error, DCB_i represents a different channel delay for different GLONASS satellites, dt_i represent the satellite clock error, $d(ion)_i$ represents the ionospheric delay, $d(trop)_i$ represents tropospheric delay, Ep_i is the other errors and c is the speed of light. At this time, $IFDB_{i,j}$ is the GLONASS inter-frequency bias between frequency number i and j can be expressed as:

$$IFDB_{i,j} = DCB_i - DCB_j \tag{23.2}$$

Using the GNSS simulator to measure the GLONASS inter-frequency biases, it can provide the GNSS RF signals for receiver. At the simulator end, setting the GLONASS satellites of different frequencies to the GEO satellites and at the same point, GPS satellites are set to the default. GPS satellites can not be closed at this time, for two reasons: (1) GNSS simulator does not work properly in the case of all the GPS satellites are closed. (2) GLONASS satellites located at the same point, the receiver can not meet the positioning needs if all the GPS satellites are closed.

During the test, atmospheric delays of simulator are closed in order to reduce the effects of noise paths, adjusting the power level of GNSS signals until the best signal to noise ratio at receiver side. In the ideal case, the pseudorange value output from receiver by different frequencies of GLONASS satellites should be the same value, nonetheless, due to the channel delay biases between GLONASS different frequencies, pseudorange be biased at the receiver side for different frequency points of GLONASS satellites. Consequently, GLONASS inter-frequency biases can be calculated by comparing its pseudorange difference.

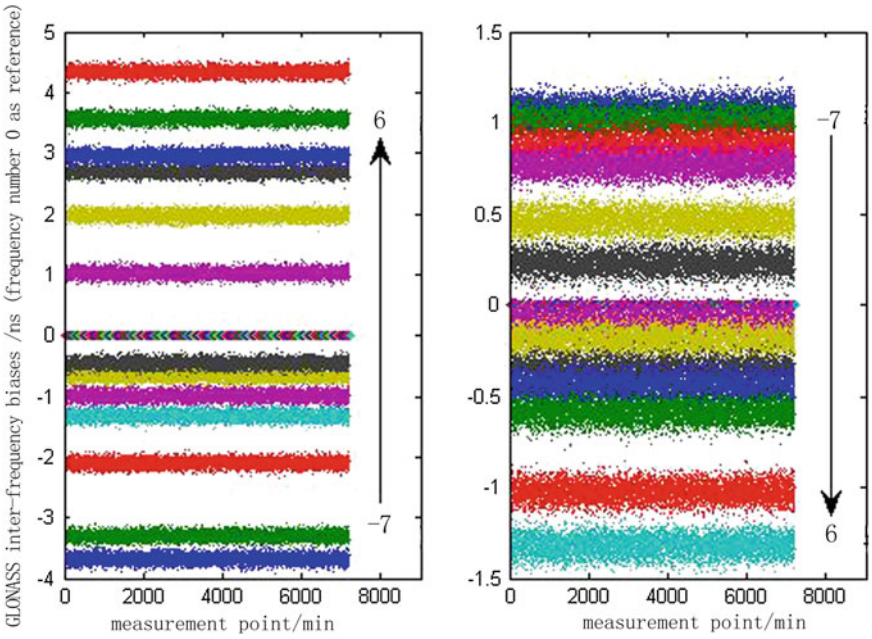

Fig. 23.1 Comparison of GLONASS inter-frequency biases between different receivers

23.3 Analysis of Testing Results of GLONASS Inter-frequency Biases

GLONASS has 14 frequency points, the sub-bands are identified by frequency numbers k, from −7 to 6. The GLONASS L1 carrier frequency, in hertz, at a frequency number k are defined by:

$$f_{L1}^{K}[Hz] = 1602 \cdot 10^{6} + k \cdot 562500 \tag{23.3}$$

The use of GNSS simulator to test the GLONASS L1 carrier signal inter-frequency biases of Septentrio PolaRx 4 receiver and Novatel OEMV_3G_L1L2s receiver, take the receiver channel which receives the GLONASS satellites of frequency number 0 as reference channel, the inter-frequency biases of other channels can be calculated relative to the reference channel, thus the results were compared to be analyzed.

Figure 23.1 shows the Comparison of GLONASS inter-frequency biases between two different receivers (Septentrio and Novatel) at different frequency numbers. Figure 23.2 shows the results of GLONASS inter-frequency biases of two receivers. It can be seen from Fig. 23.1 intuitively, whether Septentrio or Novatel receiver, GLONASS inter-frequency biases of any frequency numbers are

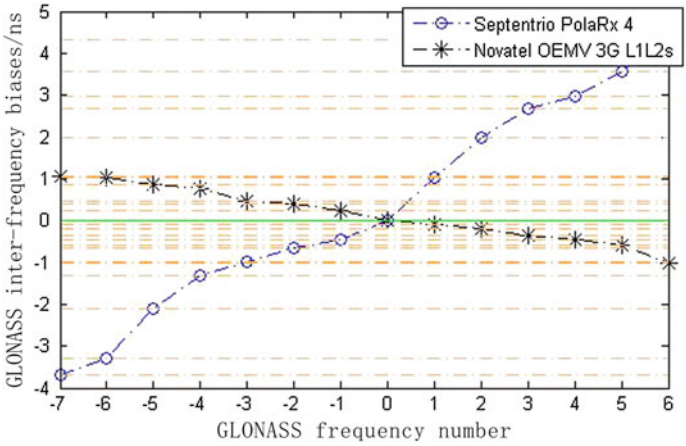

Fig. 23.2 Results of GLONASS inter-frequency biases of two different receivers

very stable with respect to the frequency of 0 GLONASS satellites. The fluctuation range changes with time is very small and substantially unchanged in a short time.

In Fig. 23.2, the inter-frequency biases seem to vary with the frequency number, although the magnitude of change is uncertain, differences between adjacent frequencies about millimetres to centimetres level. For the purposes of Septentrio receiver, the inter-frequency biases exhibit linear increasing trend along with frequency number is increasing in general, and in the range between −5 to +5 ns. However, For Novatel receiver, the value exhibits linear decreasing trend with the increasing frequency numbers, which the range is less than Septentrio receiver, is about −1.5 to +1.5 ns. This shows that the inter-frequency biases between the different types of receivers is not the same [3], there are some differences, which may be related to the hardware configuration of the receiver [5].

23.4 GLONASS Inter-Frequency Biases Affect the Positioning Results

23.4.1 Positioning Models for Considering the GLONASS Inter-frequency Biases

Currently, in the conventional data processing of single GLONASS system, we do not consider the effect of GLONASS inter-frequency biases generally that all GLONASS satellite receiver hardware delays are the same, no need for calibration of channel delay, so that the deviation will be absorbed by the receiver clock error parameters. In the case of conventional multimode observation, GLONASS inter-frequency biases is much smaller than the delay between GLONASS/GPS system,

so the data processing are generally not considered GLONASS inter-frequency biases [6]. However, the conclusions from the previous section shows that, for some receivers, such as Septentrio receiver, its GLONASS inter-frequency deviation span relatively large deviations, the value between the minimum frequency point −7 and maximum frequency point 6 more than 3 m (−5 to +5 ns), in order to improve the positioning accuracy and precision, it is necessary to consider the GLONASS inter-frequency biases.

By Eq. (23.2), GLONASS channel delay DCB_i of frequency number i can expressed as [7]:

$$DCB_i = DCB_0 + IFDB_{i,0} \tag{23.4}$$

where DCB_0 is the GLONASS channel delay of frequency number 0, $IFDB_{i,0}$ is the GLONASS inter-frequency bias value of number i relative to the number 0. Superscripts g and r represent the GPS and GLONASS. GPS/GLONASS navigation positioning error equation after corrected is as follows:

$$\begin{cases} \rho^g = r^g + pd^g + c(dT + DCB^g - dt^g) + d(ion)^g + d(trop)^g + Ep^g \\ \rho^r = r^r + pd^r + c(dT + DCB_0^r - dt^r) + c^*IFDB_{i,0} + d(ion)^r + d(trop)^r + Ep^r \end{cases} \tag{23.5}$$

In the GPS/GLONASS integrated positioning, GPS inter-frequency biases in the sub-millimeter level, is negligible. It should be emphasized that, DCB^g, DCB_0^r will be absorbed by the receiver clock error parameters will not affect the positioning results in either positioning mode. But GLONASS inter-frequency biases will affect the positioning accuracy [8].

23.4.2 Analysis of Positioning Results for Considering the Inter-frequency Biases

Using the pseudorange observation data of Lintong, Changchun, Kashi three cities for GLONASS independent positioning and GPS/GLONASS integrated positioning, different types of receivers and antennas are used and receiver coordinates are known, analyzing the impact of GLONASS inter-frequency biases by comparing the positioning results in these three cities.

Experimental scenario (1): Positioning without introducing GLONASS inter-frequency biases; Experiment scenario (2): introduction of GLONASS inter-frequency biases in the position resolution. We can measure the impact of the inter-frequency bases between RMS values of positioning error.

Table 23.1 3D position RMS errors in GLONASS positioning of three different stations

positioning mode	Station	Type of receiver	Type of antenna	3D RMS (m)	
				Scenario 1	Scenario 2
GLONASS	Lintong	Septentrio PolaRx 4	ZEPHYR GEODETIC model 2	5.07	3.81
	Kashi			4.79	3.69
	Changchun			5.12	3.92

Table 23.2 3D position RMS errors in GLONASS positioning of two different receivers in Lintong station

Positioning mode	Station	Type of receiver	Type of antenna	3D RMS (m)	
				Scenario 1	Scenario 2
GLONASS	LinTong	Septentrio PolaRx 4	ZEPHYR GEODETIC model 2	5.07	3.81
		Novatel OEMV_3G_L_1L_2s	GPS-702-GG	5.94	5.37

23.4.2.1 GLONASS Independent Positioning

Lintong, Kashi, Changchun stations are using the same receiver and antenna, receiver type is Septentrio PolaRx 4, antenna type is ZEPHYR GEODETIC Model 2, the satellite elevation cut-off angle of 10°, RMS values of the 3D position deviation for GLONASS independent positioning in both experimental program as shown in Table 23.1. In Lintong station, using two different types of receivers and antennas, one using the Septentrio PolaRx 4 receiver and ZEPHYR GEODETIC Model 2 antenna, and the other using the Novatel OEMV_3G_L1L2s receiver and GPS-702-GG antenna, the RMS error values as shown in Table 23.2.

As can be seen from Table 23.1, using Septentrio receiver, the introduction of inter-frequency biases compared with no introduction, the RMS error values of three stations were reduced by more than 20 %. It is thus clear that for the Septentrio receiver, the positioning accuracy and precision can effectively improving by introducing inter-frequency biases, However, this conclusion is not correct for all receivers, At the same station, using Novatel receiver, the accuracy was found to be improved not obviously by introducing inter-frequency biases as shown in Table 23.2, it is result from the Novatel receiver is not sensitive to the inter-frequency biases, which span of only about 1 m.

From Tables 23.1 and 23.2 we can see: using the receiver of sensitive inter-frequency biases, the accuracy can be improved effectively; otherwise, they have poor little effect on the positioning results.

Table 23.3 3D position RMS errors in GPS/GLONASS positioning of three different stations

Positioning mode	Station	Type of receiver	Type of antenna	3D RMS (m)	
				Scenario 1	Scenario 2
GPS/ GLONASS	Lintong	Septentrio PolaRx 4	ZEPHYR GEODETIC	2.91	2.59
	Kashi			2.56	2.35
	Changchun			3.08	2.87

Table 23.4 3D position RMS errors in GPS/GLONASS positioning of two different receivers in lintong station

Positioning mode	Station	Type of receiver	Type of antenna	3D RMS (m)	
				Scenario 1	Scenario 2
GPS/ GLONASS	LinTong	Septentrio PolaRx 4	ZEPHYR GEODETIC model 2	2.91	2.59
		Novatel OEMV_3G_L_1L_2s	GPS-702-GG	3.12	3.01

23.4.2.2 GPS/GLONASS integrated positioning

Although there are differences in many aspects between the GLONASS and GPS system, such as coordinate systems, time systems, signal structure, but the single positioning system does not guarantee the RAIM [9] for uses worldwide, for this, GPS/GLONASS combined positioning has the important practical significance. Using the same protocol as the Sect. 23.4.2.1, introducing GLONASS inter-frequency biases in the GPS/GLONASS positioning, the 3D RMS error values as shown in Tables 23.3 and 23.4.

It can be seen from Tables 23.3 and 23.4, GPS/GLONASS positioning combinations can effectively improving the positioning accuracy. For Septentrio receiver, RMS value is reduced by about 10 % by introducing inter-frequency bias, but for Novatel receiver, it is only reduced by about 5 %. So the effect of GLONASS inter-frequency biases in the GPS/GLONASS positioning is much smaller, this is because in GPS/GLONASS dual-mode observations, existing delay deviation between this two navigation systems, its value is different for different receiver and about several tens of meters [6], higher than GLONASS inter-frequency biases for one or two orders of magnitude. Therefore, It can clearly be seen that introduction of inter-frequency biases can improve the accuracy of positioning in GPS/GLONASS integrated positioning, but the performance is less than GLONASS independent positioning.

23.5 Impact of GNSS Systems Offset Monitoring Results for Considering GLONASS Inter-frequency Biases

23.5.1 GNSS System Time Offset Monitoring Methods for Space Signal Reception

Nowadays, there are two main methods for GNSS system time offset monitoring: (1) Building a comparison link between two GNSS systems. (2) Other satellites space signal reception [1].

The system time offset monitoring principle by receiving space signals is as follows: the standard frequency signal of the National Time Service Center as a frequency reference, the standard time signal as the reference time scale, the difference between UTC (NTSC) and GNSST was be measured. As be shown in Fig. 23.3, in the precise known of GNSS receiver antenna phase center, each navigation system spatial navigation signals received by timing receiver, the receiver pseudo-range and high-precision time interval counter measurement value are used so as to calculate the difference between UTC (NTSC) and each navigation system, it can be expressed as [10]:

$$\begin{aligned} UTC(NTSC) - GNSST = (\rho - \mathrm{r} \ + dt - \mathrm{pd} - \mathrm{d(ion)} - \mathrm{d(trop)} - \mathrm{Ep})/\mathrm{c} \\ - TICValue - \Delta ChDelay + \Delta ISDB \end{aligned} \tag{23.6}$$

where GNSST is the GNSS system time, TICValue is the measurement value of precision time interval counter, ΔChDelay indicates that the receiver relative channel delay bias, ΔISDB represents the inter-system hardware delay biases.

23.5.2 Application of GLONASS Inter-frequency Biases in GNSS System Time Offset Monitoring

In Lintong station, Using Septentrio receiver to build the monitoring system for GPS/GLONASS system time offset determination. The inter-frequency biases should be eliminated based on the GLONASS frequency number value because its variation range of Septentrio receiver is large. At this time, UTC (NTSC)-GLONASS is calculated on the basis of the formula (23.6), which should deducted the $\mathrm{IFDB}_{\mathrm{i},0}$. In order to analyze the accuracy of the monitoring system time offset, the results are compared with circular T.

From Figs. 23.4 and 23.5, UTC (NTSC)-GLONASST monitoring results are consistent with trends of Circular T whether the introduction of GLONASS inter-frequency biases. The monitoring accuracy has slightly improved by introducing it, but the improvement is not obvious for the RMS value drops 3.24 ns from 3.84 ns. This is due to the GLONASS inter-frequency biases exhibit linear trend

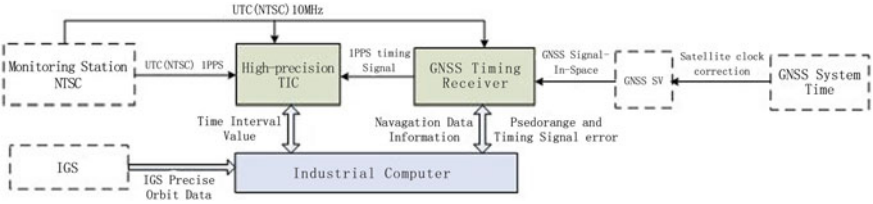

Fig. 23.3 Schematic diagram of monitoring GNSS system time offset for space signal reception

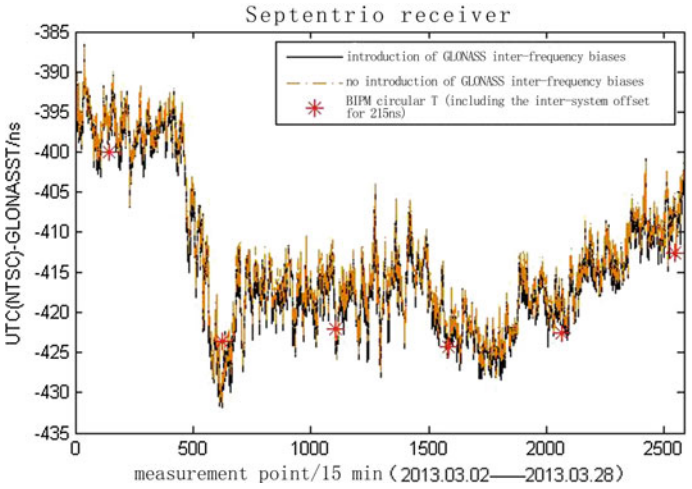

Fig. 23.4 Comparison of UTC(NTSC)-GLONASST results

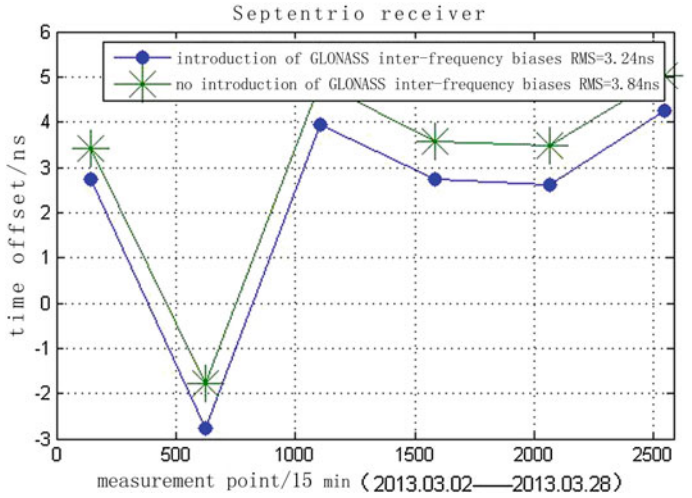

Fig. 23.5 Results of UTC(NTSC)-GLONASST compared with the circular T

and have symmetric relation with respect to the frequency number 0, GLONASS inter-frequency biases will be partly eliminated in system time offset calculation processing.

23.6 Conclusions

First, the test approach for GLONASS inter-frequency biases is studied in this paper, the experimental data from two kinds of brand receiver (Septentrio PolaRx 4 and Novatel OEMV_3G_L1L2s) was obtained and analyzed in details. Second, GLONASS inter-frequency biases are introduced into GLONASS single system positioning, GPS/GLONASS integrated positioning and system time difference monitoring. The experiment result indicates that considering GLONASS inter-frequency biases in location solution and system time monitoring can improve the accuracy of positioning and the precision of system time offset monitoring, the performance is related to the type of receiver.

References

1. Wu H, Li X, Lu X (2011) Time of the satellite navigation system. Science Press, Beijing
2. Li JW, Hao JM, Li JZ, Zhang JJ (2004) GNSS world of China 3:48–51
3. Wanninger L (2012) Carrier-phase inter-frequency biases of GLONASS receivers. J Geodesy 86(2):139–148. doi:10.1007/s00190-011-0502-y
4. Shanghai Observatory GNSS Analysis Center [DB/OL]. http://www.shao.ac.cn/shao_gnss-ac
5. Sleewagen J, Simsky A, Wilde WD et al (2012) Demystifying GLONASS inter-frequency carrier phase biases. InsideGNSS
6. Xiao P, Chen JP, Wang JX (2013) Improving user navigation performance with GLONASS IFDB. J Geodesy Geodyn 33(3):102–105
7. Kim HS, Lee JY (2013) Receiver Inter-channel bias search technique based on LAMBDA. In: IGNSS symposium, Outrigger Gold Coast, Qld Australia
8. Wanninger L, Wallstab-Freitag S (2007) Combined processing of GPS, GLONASS, and SBAS code phase and carrier phase measurements. In: ION GNSS, pp 866–875
9. Xu LX, Li XH (2009) The methods to deal with time offset and an analysis of their effect to positioning accuracy in multi-mode satellite navigation system. Chin J Sci Instrum 30(10):192–195
10. Lin Z (2013) Research on one-station and multi-station combined monitoring method of GNSS system time offset. University of Chinese Academy of Sciences, Beijing

Chapter 24
Analyzing the Impact of Satellite Clock-TGD Coupled Error on BDS Positioning Accuracy

Zhouzheng Gao, Hongping Zhang, Qile Zhao, Zhigang Hu and Wenbin Shen

Abstract BeiDou Navigation Satellite System (BDS) has got the ability of real-time navigation and high accuracy positioning services for the Asian-Pacific regions by the end of 2012 with the constellation of 5GEOs + 5IGSOs + 4MEOs. Currently, although BDS can provide positioning service better than 10 m, there remains a problem that the positions calculated with B1 and B2 pseudo-range ionosphere-free combination (BC) are a little worse in accuracy than those obtained from B1 pseudo-range only. This phenomena can be partly explained with the observing errors (white noise and multi-path), and the accuracy of ionosphere model. Besides, the coupled error for BDS satellite clock-TGD would be another important factor. Here we analyze this coupled error and its effect on BDS real-time positioning based on BDS precise clock and BDS satellites DCB provided by GNSS Research Center (GRC), Wuhan University. 12 days' BDS observations from BeiDou experimental tracking stations (BETS) have been processed and investigated with the precise products by GRC and broadcast ephemeris. Results indicate that the coupled error between BDS broadcast satellite clock and TGD of BC is 5.04 ns, which is about 3 times larger than that of B1 (1.79 ns). And it is a system bias that results BC positioning accuracy worse than that of B1. In additional, by analyzing BDS observations' multi-path noise, it shows the multi-path noise is one of the facts leading to BDS BC positioning accuracy a litter worse than B1 positioning accuracy. We also find that the receiver noise is the main reason affecting BDS velocity accuracy.

Keywords BDS real-time positioning · BDS TGD · Clock-TGD coupled errors

Z. Gao (✉) · W. Shen
School of Geodesy and Geomatics, Wuhan University, 129 Luoyu Road, Wuhan 430079, China
e-mail: zhouzhenggao@whu.edu.cn

Z. Gao · H. Zhang · Q. Zhao · Z. Hu
GNSS Research Center, Wuhan Uiversity, 129 Luoyu Road, Wuhan 430079, China

J. Sun et al. (eds.), *China Satellite Navigation Conference (CSNC) 2014 Proceedings: Volume I*, Lecture Notes in Electrical Engineering 303,
DOI: 10.1007/978-3-642-54737-9_24,

24.1 Introduction

BeiDou Navigation Satellite System (BDS) built by China independently has got the ability applying standard navigation and precise positioning services for the Asian-Pacific regions since Nov. 27, 2012. Currently, BDS constellation consists of 5GEOs, 5IGSOs, and 4MEOs. According to China government's plan, the full constellation of BDS will include 5GEOs, 3IGSOs and 27MEOs by the end of 2020, which will provide global navigation service similar to GPS and GLONASS. In additional, BDS adopts China Geodetic Coordinate System 2000 (CGCS2000) keeping compatibility with WGS-84 for real-time navigation, and BeiDou Time System (BDT) with a difference of 14 s and 1,356 weeks comparing to GPST [1]. Currently, meter level (better than 10 m) real-time navigation and centimeter level precise positioning service can be obtained using BDS in Asian-Pacific region. Which is very close to GPS performance [2–4]. However, as reference 4 and 5 indicate, this performance is mainly influenced by the quality of BDS pseudo-range and carrier-phase, and the distribution of BDS DOP. Currently, there two main problems should be answered for BDS's widely application. One is to find the reason why the BDS's velocity accuracy is not as good as GPS velocity accuracy in same region. Another problem is to get the answer why there is an abnormal that the standard point positioning (SPP) service of BDS B1 frequency is better than that of B1 and B2 ionosphere-free (IF) combination while using observations collected by same receiver in BDS real-time navigation.

Usually, the multi-path noise of BDS observations is considered as the major facts leading to the abnormal problem in BDS real-time positioning. But we insist there are some other facts in it. That are the accuracy of BDS satellites' Time Group Delay (TGD) and the coupled error between BDS satellite broadcast clock and TGD. According to Matsakis's research in 2007 [5], the positioning accuracy of GNSS can be affected by TGD directly. And the influence of Differential Code Bias (DCB) (equal to TGD) to GPS precise positioning is several centimetres [6]. So, if BDS TGD's accuracy is not high enough, then it will impact on BDS positioning accuracy. Besides, as it knows, BDS satellite clocks are based on B3 frequency, so the coupled error between clock and TGD may be another fact leading to the abnormal problem.

To analyse the reason leading to this abnormal problem in BDS navigation, the BDS data collected by BETS and precise satellites orbit and clock products with interval of 30 s applied by Wuhan University are used in this paper. The coupled error between satellites clock and TGD and TGD accuracy are mainly analysed. Besides, the receiver observing noise and multi-path noise are also analyzed in this paper. Then conclusions about the reason resulting the abnormal problems in BDS real-time navigation application are obtained.

24.2 BDS SPP Mathematic Model

Usually, pseudo-range and Doppler observation are used in BDS navigation, the observation equations on B1 frequency can be defined as:

$$\rho = \mathrm{B1} + \mathrm{c} \cdot (\delta t^s + Tgd_1 - \delta t_r) - \rho_{ion} - \rho_{trop} - \rho_{mp} + \varepsilon_{B1} \tag{24.1}$$

$$\dot{\rho} = \mathrm{D1} \cdot \lambda_1 + \mathrm{c} \cdot (\delta \dot{t}^s - \delta \dot{t}_r) - \dot{\rho}_{ion} - \dot{\rho}_{trop} - \dot{\rho}_{mp} + \varepsilon_{D1} \tag{24.2}$$

where, B1, D1 and λ_1 are pseudo-range, Doppler and carrier-phase wavelength of B1 frequency respectively; ρ and $\dot{\rho}$ represents distance between satellites and user and pseudo-range rate; c is light speed in vacuum; δt^s and $\delta \dot{t}^s$ are satellite clock bias and drift; δt_r and $\delta \dot{t}_r$ are receiver clock bias and drift; Tgd_1 is the TGD between B1 and B3 frequency; $\rho_{ion}(\dot{\rho}_{ion}), \rho_{trop}(\dot{\rho}_{trop})$, and $\rho_{mp}(\dot{\rho}_{mp})$ are ionosphere delay, troposphere delay and multi-path (changing rate of these errors); ε_{B1} *and* ε_{D1} are the observation noise and un-modeled errors. Generally, the IF combination function can be expressed as:

$$\rho = \alpha \cdot (B1 + c \cdot Tgd_1) - \beta \cdot (B2 + c \cdot Tgd_2) - \rho_{trop} - \rho_{mp} + \varepsilon_{BC} \tag{24.3}$$

To keep consistent in writing with GPS IF combination, Eq. (24.3) can also be written as:

$$\rho = (\alpha \cdot B1 - \beta \cdot B2) + \alpha \cdot c \cdot Tgd_1 - \beta \cdot c \cdot Tgd_2 - \rho_{trop} - \rho_{mp} + \varepsilon_{BC} \tag{24.4}$$

where, $\alpha = f_1^2/(f_1^2 - f_2^2)$, $\beta = f_2^2/(f_1^2 - f_2^2)$; f_1 and f_2 are the frequency of B1 and B2. For GPS, the satellites clock is calculated based on observations IF combinations. Therefore, the TGD for IF combination has been included in GPS broadcast satellite clock. But BDS satellites clock is calculated based on B3, so while using B1 and B2 observations forming IF combinations, the influence of TGD of B1 and B2 should be considered carefully. What's more, if there is a coupled error between satellite clock and TGD, this coupled error will be enlarged 1.5–2.5 times while forming BDS pseudo-range IF combination which will impact on BDS IF SPP position accuracy obviously.

24.2.1 BDS Receiver Noise

Receiver noise is considered as the most important reason leading to BDS low accuracy velocity. So it is necessary to analyze the influence of receiver noise in BDS SPP and velocity. Usually, receiver noise of pseudo-range (B1) and Doppler (D1) can be analyzed by zero-baseline. The function of pseudo-range and Doppler observations can be expressed as:

$$\nabla\Delta B1 = B1_k^i - B1_k^j - \left(B1_m^i - B1_m^j\right) \tag{24.5}$$

$$\nabla\Delta D1 = D1_k^i - D1_k^j - \left(D1_m^i - D1_m^j\right) \tag{24.6}$$

where, $\nabla\Delta$ represents double difference; i and j are BDS satellite i and satellite j; m and k represent station m and station k.

24.2.2 BDS Multi-path Noise

Besides, multi-path is considered as an important reason leading to the abnormal problem in BDS real-time navigation. The function of multi-path of pseudo-range on BDS B1 and B2 frequency can be defined as [1]:

$$MP_1 = B_1 - \frac{f_1^2 + f_2^2}{f_1^2 - f_2^2} L_1 + \frac{2f_2^2}{f_1^2 - f_2^2} L_2 \tag{24.7}$$

$$MP_C = \frac{f_1^2}{f_1^2 - f_2^2}(B_1 - L_1) - \frac{f_2^2}{f_1^2 - f_2^2}(B_2 - L_2) \tag{24.8}$$

where, L_1 and L_2 represents BDS carrier-phase observations. In Eqs. (24.7) and (24.8), most of the error is eliminated except receiver noise and multi-path. As it knows, multi-path for carrier-phase is very small and receiver noise is white noise. Therefore, Eqs. (24.7) and (24.8) can express the strength of multi-path on B1 and B2 frequency directly. In additional, average value is adopted to eliminate the effect of carrier-phase ambiguity in Eqs. (24.7) and (24.8).

24.2.3 BDS TGD Analyzing

The accuracy of TGD is very important for BDS SPP service. However, there is no effective method to get the accuracy of TGD in current. Usually, standard deviation (STD) or variance is used to assess satellites TGD accuracy [7]. So, in this paper, the accuracy of BDS TGD will be verified by analyzing the convergence time and initial positioning accuracy of un-differential un-combined Precise Point Positioning with ionosphere-delay and receiver DCB constrained (IC-PPP) [8]. In IC-PPP model, DCB (or TGD) is used to eliminate the time delay caused by satellite hardware. If BDS DCB accuracy is better than TGD, the convergence time and initial positioning accuracy of IC-PPP adopting DCB will be better than that of IC-PPP using TGD. Otherwise, the convergence time and initial positioning of IC-PPP using TGD will be better. Because, PDOP is the same for a group observations, so the convergence time and initial positioning accuracy is determined by pseudo-range quality (DCB or TGD accuracy) directly. In this paper, based on IC-

PPP model, we use BDS satellites precise orbit and clock products applied Wuhan University, BDS broadcast TGD and BDS DCB calculated by Wuhan University to analyze TGD's accuracy.

24.2.4 Coupled Error Between BDS Clock and TGD

As it knows, GPS satellite clocks are based on pseudo-range ionosphere-free combination. TGD is used to transform the clock bias to L1 for single frequency GPS users. But BDS satellite clocks in the broadcast ephemeris is based on B3. So, while using pseudo-range IF combination for BDS SPP, the TGD for B1 and B2 frequency should be corrected firstly but forming IF combination directly. Therefore, if there is a bias for B1 and B2 satellites TGD, usually the same part (system bias) of satellites TGD will be absorbed by receiver clock in parameters estimating. But the different part will influence BDS SPP accuracy and will be reflected as pseudo-range residual. When using pseudo-range IF combinations for BDS SPP, the influence of the bias will be enlarged about 3 times, which can lead the position accuracy of single SPP better than that of IF SPP.

To research the coupled error between satellite clock and TGD BDS precise orbit and clock based on IF combinations and BDS satellites' DCB provided by Wuhan University are used as reference. In this paper, the satellite clock and TGD coupled error of B1 and IF combination (BC) is presented mainly. The satellite clock of BDS broadcast ephemeris $\delta t^s_{B1,whu}$ and precise clock $\delta t^s_{B1,brdc}$ on B1 frequency can be written as:

$$\begin{cases} \delta t^s_{B1,brdc} = \delta t^s + Tgd_1 \\ \delta t^s_{B1,whu} = \delta t^s_{whu} + DCB_{B1B2} \cdot \beta \end{cases} \tag{24.9}$$

Similarly, BC satellite clock can be expressed as:

$$\begin{cases} \delta t^s_{BC,brdc} = \delta t^s + Tgd_1 \cdot \alpha - Tgd_2 \cdot \beta \\ \delta t^s_{BC,whu} = \delta t^s_{whu} \end{cases} \tag{24.10}$$

where, DCB_{B1B2} is the DCB between B1 and B2; δt^s_{whu} is BDS precise clock based on GPST system which leads *to* system bias $d\delta t^s_{B1}$ and $d\delta t^s_{BC}$ for B1 and BC clocks while data analyzing, respectively. The difference between precise clocks and broadcast clocks can be written as:

$$\begin{cases} d\delta t^s_{B1} = \delta t^s_{B1,brdc} - \delta t^s_{B1,whu} \\ d\delta t^s_{BC} = \delta t^s_{BC,brdc} - \delta t^s_{BC,whu} \end{cases} \tag{24.11}$$

In additional, because the system bias is a constant for each BDS satellites, so it can be absorbed by receiver clock while parameter estimating, and it will have no

impact on BDS positioning accuracy. To make data analyze clearly, the constant $d\hat{\delta}t^s_{B1}$ for B1 frequency can be eliminated by Eq. (24.12):

$$\begin{cases} d\hat{\delta}t^s_{B1} = \frac{1}{n}\sum_{i=0}^{n} d\delta t^s_{B1,i} \\ \Delta\delta t^s_{B1,i} = d\delta t^s_{B1,i} - d\hat{\delta}t^s_{B1} \end{cases} \tag{24.12}$$

And similarly, the constant $d\hat{\delta}t^s_{BC}$ can be ignored by Eq. (24.13):

$$\begin{cases} d\hat{\delta}t^s_{BC} = \frac{1}{n}\sum_{i=0}^{n} d\delta t^s_{BC,i} \\ \Delta\delta t^s_{BC,i} = d\delta t^s_{BC,i} - d\hat{\delta}t^s_{BC} \end{cases} \tag{24.13}$$

Then, the satellite clock and TGD coupled error of B1 and BC can be obtained by the statistics result of Eqs. (24.12) and (24.13).

24.3 Data Analyzing

Based on mathematic model presented above, we processed some BDS data between day of year (DOY) 139 and 150 in 2013 collected by BETS equipped with Unicore UR-240 receiver. The detail information are shown in Table 24.1 and BDS constellation with 5GEOs, 5IGSOs, and 4MEOs are shown in Fig. 24.1. The data will be processed as follow schemes.

1. Adopting zero-baseline model, analyse receiver noise of Trimble R9 and UR-240.
2. According to Eqs. (24.7) and (24.8), analyse multi-path noise of Beijing and Wuhan station.
3. Using IC-PPP model and BDS precise products, analyse the accuracy of BDS TGD.
4. Following Eqs. (24.9)–(24.13), analyse the accuracy of BDS orbit, TGD, and the coupled error between clock and TGD, and it impact on BDS SPP performance.

While data processing, the observations with satellite elevation low than 10° are ignored and observation error source including troposphere delay, ionosphere delay, pseudo-range time group delay, earth rotation, relativity, satellite clock and receiver clock are considered.

Table 24.1 Information for data used in this paper

Data type	From	Interval
BDS observation	BETS	30 s
BDS broadcast orbit	BDS system	1 h
BDS broadcast clock	BDS system	1 h
BDS broadcast TGD	BDS system	–
BDS precise orbit	Wuhan University	30 s
BDS precise clock	Wuhan University	30 s
BDS DCB	Wuhan University	–
Ionosphere GIM	CODE	2 h

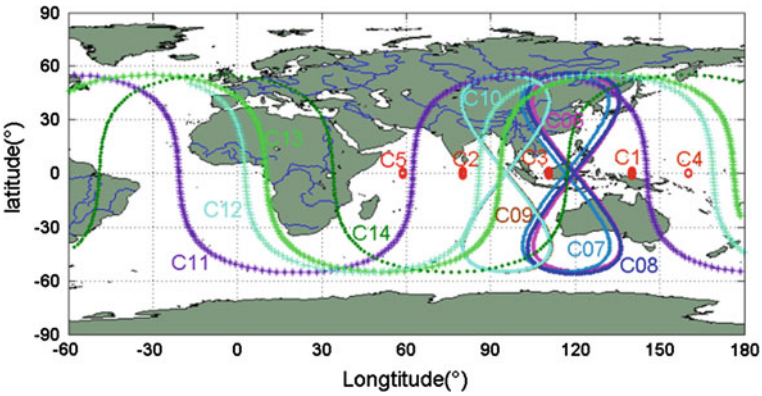

Fig. 24.1 BDS satellites constellation with 5GEO + 5IGSO + 4MEO

24.3.1 BDS Receiver Noise

As it knows, all the observing errors are eliminated in zero-baseline except receiver noise. As Figs. 24.2 and 24.3 showing, UR-240 receiver's pseudo-range noise and Doppler noise are 0.657 and 0.175 m, respectively. R9 receiver's pseudo-range noise and Doppler noise are 0.365 and 0.037 m. Obviously, UR-240 receiver noise is much larger than that of R9, especially the Doppler noise. That means the quality of UR-240 observations is lower than that of R9. And it will lead to BDS navigation result using UR-240 observations worse than the result using R9 observations, especially for BDS velocity.

Figure 24.4 shows BDS velocity accuracy in static using UR-240 observation and R9 observation, respectively. The velocity RMS of UR-240 receiver in North, East, and Up is 0.219, 0.098, and 0.273 m/s. And R9 receiver's velocity RMS is 0.054, 0.014, and 0.083 m/s for North, East, and Up component respectively. According to Eq. (24.2), the accuracy of BDS velocity depends on Doppler's quality directly. Therefore, the reason why UR-240 receiver's velocity accuracy is worse than R9's is because UR-240 Doppler noise is larger than R9 Doppler noise.

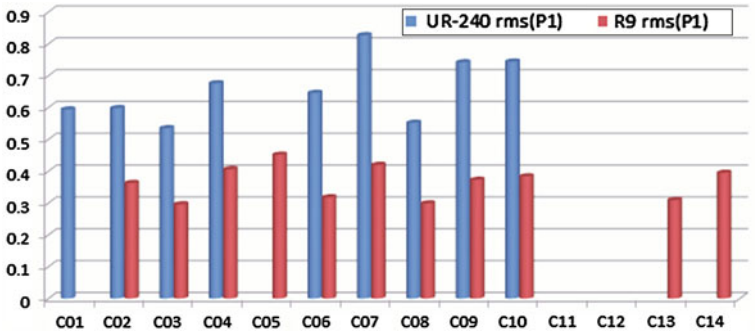

Fig. 24.2 RMS of B1 pseudo-range observations noise for UR-240 receiver and R9 receiver (unit: meter)

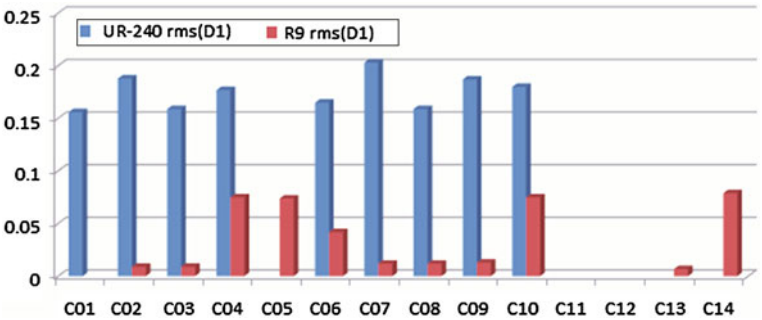

Fig. 24.3 RMS of D1 doppler observations noise for UR-240 receiver and R9 receiver (unit: meter)

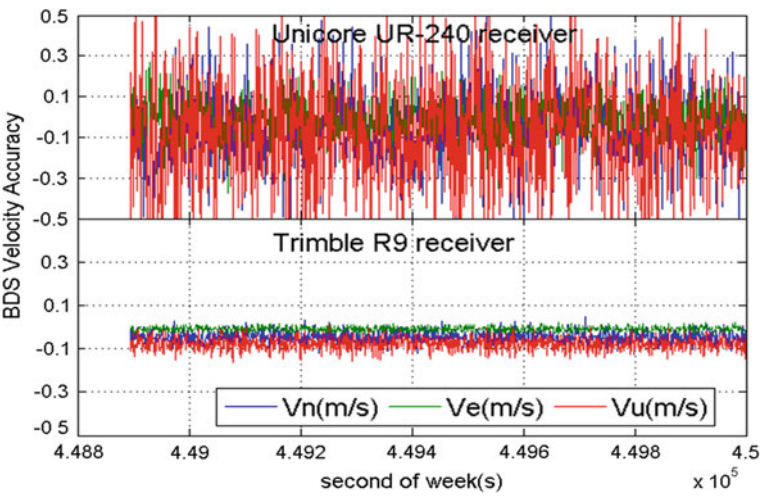

Fig. 24.4 BDS velocity accuracy calculated by receiver UR-240 and R9 in static

Table 24.2 Positioning accuracy of BDS for Beijing and Wuhan station

Station	Beijing		Wuhan	
Type	BC	B1	BC	B1
NE (95 % m)	8.079	4.871	5.699	5.215
3D (95 % m)	12.632	8.464	8.993	10.882

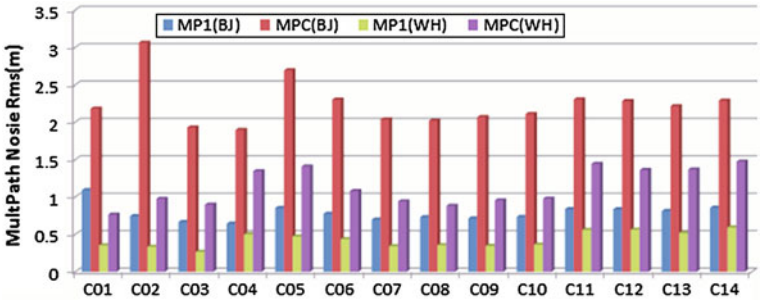

Fig. 24.5 Multipath noise for BC combination and B1 frequency of BDS in Beijing and Wuhan station

24.3.2 BDS Multi-path Noise

To analyse the impact of multi-path noise on BDS SPP positioning accuracy, Beijing (BJ) and Wuhan (WH) station BDS observations are processed in same way. Table 24.2 shows BDS SPP positioning accuracy of Beijing and Wuhan station using BC and B1 observation respectively. In Beijing station, B1 pseudo-range position accuracy (95 %) is 4.871 and 8.464 m in horizon and 3D component. While using BC combination, the position accuracy is 8.079 and 12.632 m in horizon and 3D component. In Wuhan station, B1 pseudo-range position accuracy (95 %) is 5.215 and 10.882 m for horizon and 3D component. While using BC combination, the position accuracy is 5.699 and 8.993 m for horizon and 3D component, respectively. Obviously, the positioning accuracy of BC is worse than B1 positioning accuracy. But in Wuhan station, the positioning accuracy of BC is better than that of B1. In additional, the PDOP of Beijing (2.858) is very close to Wuhan PDOP (2.679). Besides, the receiver used in both Beijing and Wuhan station is UR-240. Reasonably, the effect of PDOP and receiver noise on BDS positioning accuracy can be ignored. Therefore, the multi-path must be the most possible fact leading the abnormal positioning results in Beijing station.

According Eqs. (24.7) and (24.8), BDS satellites multi-path noise of Beijing and Wuhan station is calculated and its statistics results are shown in Fig. 24.5. Clearly, the multi-path noise in Wuhan station is lower than that of Beijing station. In Beijing station, the multi-path noise for B1 and BC pseudo-range is 0.786 and 2.244 m. And the multi-path noise for B1 and BC is 0.431 and 1.136 m in Wuhan

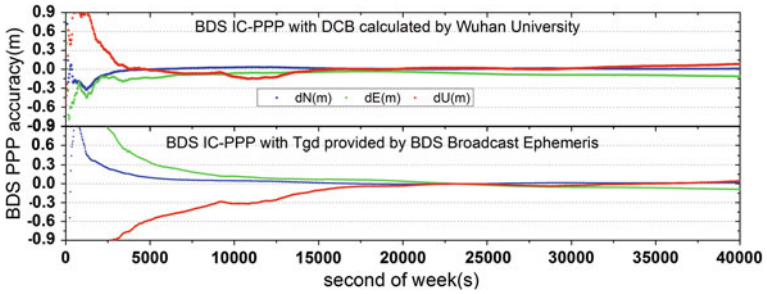

Fig. 24.6 Impact of BDS TGD on positioning accuracy and convergence of BDS IC-PPP

station. Obviously, the ionosphere-free combination makes multi-path noise 3 times bigger than that of B1. Besides, the multi-path noise of both B1 and BC in Beijing station is about 2 times bigger than that of Wuhan station. Which leads the position accuracy of BC in Beijing is worse than B1 positioning accuracy directly. Meanwhile, because the multi-path noise of Wuhan station is very low (very close to receiver noise) and ionosphere-free combination can ignored first order ionosphere delay completely. So, Wuhan station's BC 3D positioning accuracy is improved obviously comparing to B1 3D positioning accuracy.

24.3.3 BDS TGD Accuracy

Because the convergence time and initial positioning accuracy of IC-PPP is affected by pseudo-range quality directly. Therefore, while using TGD applied by BDS and satellite DCB applied by Wuhan University in BDS IC-PPP respectively, if IC-PPP adopting DCB needs less convergence time and expresses better initial positioning accuracy, it means TGD accuracy is worse. Otherwise, BDS TGD accuracy is better. According to the result showing in Fig. 24.6, in Beijing station the convergence time of IC-PPP using DCB applied by Wuhan University is 1.76 h less than IC-PPP using BDS TGD (4.23 h). Meanwhile, the initial positioning accuracy of IC-PPP using DCB is 2.0 m better than IC-PPP using TGD (5.0 m). It illustrates that BDS satellites' TGD accuracy is high enough currently and it can be improved better and better in the feature.

24.3.4 Clock and TGD Coupled Error

Coupled error between satellite clock and TGD and satellite orbit accuracy are another facts affect BDS SPP positioning accuracy. As Fig. 24.7 shows, the orbit accuracy of IGSO and MEO is better than 2.0 m in X–Y–Z components. GEO

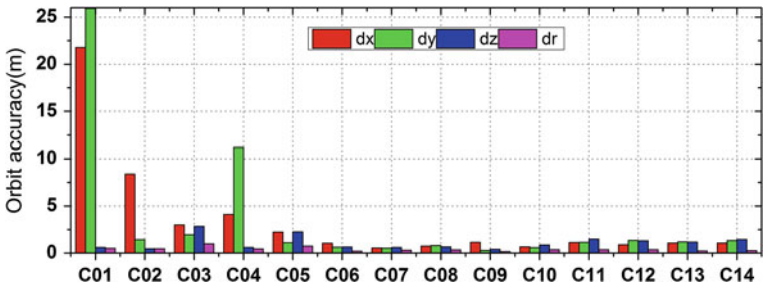

Fig. 24.7 BDS's orbit accuracy of broadcast ephemeris

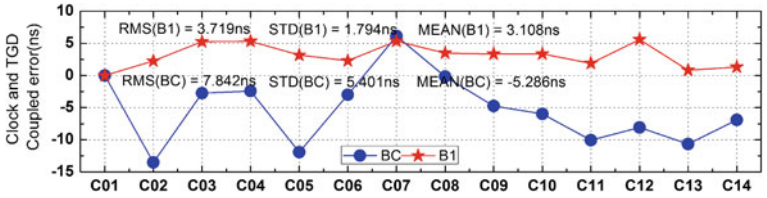

Fig. 24.8 BDS clock-TGD coupled error on BC combination and B1 frequency

orbit accuracy is a litter worse, especially satellites C01 (25.93 m), C02 (8.39 m) and C04 (11.04 m). All BDS satellite orbit accuracy in Radial direction is better than 0.5 m, except GEO C03 (0.982 m) and C05 (0.744 m). Figure 24.8 shows the coupled error of B1 and BC between BDS satellite clock and TGD. The statistics illustrate that the RMS of B1 satellite clock is 3.719 ns, and the RMS of BC satellite clock is 7.842 ns. Obviously, there is a same system bias for both B1 and BC satellite clock. Usually, the system bias can be absorbed by receiver clock while parameter estimation and will have no effect on BDS positioning accuracy. But the coupled error of both B1 and BC satellite clock expressed as STD in Fig. 24.8 will affect BDS SPP positioning accuracy. As results show, the coupled error of B1 is 1.794 ns (0.54 m), and the coupled error of BC is 5.401 ns (1.62 m). Clearly, the coupled error of BC is about 3 times bigger than that of B1. And it can be an important fact that leads to BDS BC positioning accuracy worse than B1 positioning accuracy.

24.4 Summary

In this paper, we focus on the abnormal problem that leads to BDS B1 positioning accuracy better than BC positioning accuracy. By analysing receiver noise, multi-path noise, BDS satellite orbit accuracy, and coupled error between satellite clock and TGD, the results illustrate that:

1. BDS has the ability to provide SPP positioning result better than 10 m and provide velocity result better than 0.1 m/s, currently.
2. The velocity accuracy of BDS is affected by receiver Doppler noise. As shown in this paper, the Doppler noise of UR-240 is larger than that of R9. Which leads to the velocity accuracy of UR-240 lower than that of R9. It expresses that BDS provide velocity accuracy better than 0.1 m/s if receiver Doppler noise is not too large.
3. Multi-path noise is one of the facts leads to BDS BC positioning accuracy worse than B1 positioning accuracy.
4. The accuracy of BDS satellite orbit is better than 2.0 m in X–Y–Z component and better than 0.5 m in Radial direction. And GEO satellites orbit accuracy is not good enough.
5. The accuracy of BDS TGD is not high enough, and it leads to the coupled error between satellite clock and TGD of BC (5.041 ns) is about 3 times larger than that of B1 (1.794 ns). And it is an important facts leading to BDS B1 positioning accuracy better than BC positioning accuracy.

References

1. Shi C, Zhao Q, Hu Z et al (2013) Precise relative positioning using real tracking data from COMPASS GEO and IGSO satellites. GPS Solutions 17(1):103–119
2. Zhou S, Gao Y, Zhou J et al (2012) Positioning accuracy assessment for the 4GEO/5IGSO/2MEO constellation of COMPASS. Sci China Phys Mech Astron 55(22)
3. Montenbruck O, Hauschild A, Steigenberger P et al (2012) Initial assessment of the COMPASS/BeiDou-2 regional navigation satellite system. GPS Solutions 1–12
4. Yang YX, Li JL, Wang AB et al (2013) Preliminary assessment of the navigation and positioning performance of BeiDou regional navigation satellite system. Sci China Earth Sci 1–9
5. Matsakis D (2007) The timing group delay (TGD) correction and GPS timing biases. In: Proceeding of the 63rd annual meeting of the institute of navigation, Cambridge, MA
6. Ruan R (2009) Study on GPS precise point positioning using un-differenced carrier phase. PLA Information Engineering University
7. Xing N, Wu X, Hu X, et al. (2012) Secular changes in differential code bias of COMPASS system. In: China Satellite Navigation Conference (CSNC) 2012 Proceedings Lecture notes in electrical engineering, vol 160. pp 243–251
8. Zhang H, Gao Z, Ge M et al (2013) On the convergence of ionospheric constrained precise point positioning (IC-PPP) based on undifferential uncombined raw GNSS observations. Sensors 13:15708–15725. doi:10.3390/s131115708u

Chapter 25
General Computing Platform Based GNSS Signal Simulator Architecture: Design, Implementation and Validation

Zhenyi Wei, Hong Li, Zheng Yao and Mingquan Lu

Abstract In the process of GNSS (Global Navigation Satellite System) signal design and validation of receiver algorithm, a GNSS signal simulator is needed for generating a predetermined signal format, and at the time of both signal design and receiver algorithm validation, testing and verification in a number of different scenarios are needed, which requires flexible configuration and features convenient expansion of the simulator. In recent years, the software platform based GNSS signal simulator is becoming an important development direction under such a fast and flexible request. In the process of signal generation, the simulation is ending up with a huge amount of data even if there is only one signal to be generated, when we consider more signals and bandwidth issues, the computing becomes a disaster, and the requirements of long-time simulation from system and signal validation make it worse. So how to generate such huge amount of GNSS signals on software platforms in nearly real-time, along with better flexibility and scalability, is a technical difficulty. Focusing on this problem, a new software framework for GNSS signal simulator is proposed. The main idea of the new framework includes two aspects: First, after reconsidering the signal generation process and application scenarios, responsibilities of each part of the GNSS signal simulator are re-analyzed to form several layers, and layers are stratified using a unified interface and rules. In this division, the core layer, which undertakes arduous computing tasks and data throughput, is no longer involved in user interaction and system calls, and is no longer affected by adding new signals. Second, for the huge amount of data throughput and computational issues, the core layer will be placed on a general-purpose computing platform like graphics card, taking full advantage of its high parallel computing capabilities along with scalability, to generate signal output under the unified signal generation structure and processes. Finally, under the appropriate given application scenarios, the signal simulator output is validated by

Z. Wei (✉) · H. Li · Z. Yao · M. Lu
Department of Electronic Engineering, Tsinghua University, Beijing 100084, China
e-mail: weizhenyi03@yeah.net

J. Sun et al. (eds.), *China Satellite Navigation Conference (CSNC) 2014 Proceedings: Volume I*, Lecture Notes in Electrical Engineering 303,
DOI: 10.1007/978-3-642-54737-9_25,

software receiver, the results show that the results of the new framework could meet the design requirements, and it can be used as a tool for testing and validating.

Keywords GNSS · Signal simulator · General-purpose computing platform · Parallel computing

25.1 Introduction

Recent years, position and navigation services provided by GNSS (Global Navigation Satellite System) are becoming key services in daily life for everyone. As a result, the research on signals, navigation data and modulation goes deeper and deeper, which provides more support for the design of new signals on new frequent point. In this process, GNSS signal simulators (hereinafter, simulators) with more flexibility and extensibility are thirstily needed, which are also the necessary tools for rapid and statically design for signals and systems.

One of the main difficulty in front of the simulator is the massive computing amount, especially for new signals with a bandwidth of over 20 MHz, in which case 40 Mbyte data is generated and outputted within a single second. Besides that, when multi-system and multi-frequency scenarios are considered, it is resulting in an amount of over 400 M sps (samples per second), or even 1 G sps. In order to meet this requirement, there are several methods coming out in the process of signal simulating development. Firstly, hardware signal simulator is developed, which mostly use one FPGA as the core device with several DSP to simulating GNSS signals. The advantages are obvious, hardware signal simulators are usually real-time systems. Nevertheless, long-time developing, complicated debugging and relative fixed functioning exist in the hardware development process, which makes the disadvantages also obvious for hardware signal simulators. Thinking of that, after great development of hardware technologies on computer science, software signal simulator starts to become a new direction from then on.

In the early days, there are two kinds of software signal simulator. One is using scripts, toolboxes or Simulink on Matlab platform, and the other is based on lower programming language, like C language. These software signal simulators turns out to be very impressive, especially in flexibility and extensibility, which means software signal simulator could certainly be a tool of verification and prototype design for signals and systems. However, the above two software signal simulators are still using the traditional computing architecture, which is based on CPU (Central Processing Unit). Because of the character in CPU architecture, which has relatively small percentage of the wafer area to calculate, software system with CPU as its core calculating unit suffers in low calculating speed, which is too slow to simulating in real-time systems.

In the next few years, software signal simulator could not be a standalone tool for its incompleteness, until calculating on GPU (Graphic Processing Unit) platform is taken.

Instead of too much thinking of fast response, GPUs use most of their wafer area to calculate, which meets the initial requirements when GPU coming to the world, that is, large amount of calculation during graphics display. As a result, GPU has far more calculating units than CPU, for the relative fixed calculating process and much less complicated flow control. For NVIDIA Geforce GTX 780Ti (hereinafter, 780Ti), it has a memory bandwidth of 288 GB/s [1], on the other hand, CPU has a memory bandwidth of nearly 10 GB/s, depending on the CPU and memory unit used. As a result, GPU yields big performance benefits. At the same time, the parallel processing capabilities also benefit from the large amount of processing units in processing cores, for 780Ti, there are 2,880 CUDA cores [1]. It is far more in number than processing units within CPUs, which is usually less than 10.

Based on the facts above, it is possible to use GPU to gain the massively parallel computing ability.

Prototypes of GNSS signal simulator based on GPU appeared in 2011 [2], when the base implementation of signal simulator based on GPU is proposed, focusing on the core difficulties, and along with the discussion of general improvement on the performance. Another discussion focuses on the performance of GNSS signal simulator and a method of performance measurements is also proposed [3]. Both jobs provide enough basis and principles for sampling computing of simulation, which clears the obstacles in front of the implementation of GNSS signal simulator.

Under the premise that processing performance is not the most significant limiting factor, a new GNSS signal simulator architecture based on GPU platform is proposed, mainly focusing on flexibility and extensibility in the scenario of multi-system and multi-frequency.

In terms of content, GPU platform and main developing tools are introduced first, and main scenarios about GNSS signal simulators are analysed to find out the core difficulty in the design process. After that, a new architecture in the multi-system and multi-frequency scenarios is proposed, with signal models as well. Then main improvements in the implementation are explained. In the end an example will be given for verification.

25.2 GPU and CUDA

There are plenty of descriptions of the architecture, performance and main development methods about GPU and CUDA [2–4], which is the main development tool on NIVIDIA GPUs. For not importing misunderstanding and ambiguity, a simple description about GPU and CUDA is also provided here.

GNSS signal simulator mentioned in this paper is developed on GPU platform, identified as Geforce GTX 780Ti, which is a member of NIVIDIA GPU series [1]. It is noted that other NIVIDA GPUs share the same core architecture and design thought, but might result in different performance estimations by the specific type and version of GPUs.

CUDA (Compute Unified Device Architecture) is a developing language on GPU platform invented by NIVIDA Corporation, used to develop massive parallel computing program, and finally turn GPUs to general computing platform. Because of the aiming at computing performance with massive parallel tiny threads, GPU has totally different behavior than CPU. CPU focuses on the flow control, such as instruction pretreatment, out-of-order execution, and pipeline, which costs most of CPU wafer area. Nevertheless GPU focuses on fixed and simpler computing processes, which save most of GPU wafer area for computing, giving GPU extremely large number of computing units and massive parallel computing capability which is never reachable for CPU. For example, there are 2,880 CUDA cores inside of 780Ti, comparing with 4 physical cores within Intel i7 4,770 K.

Although GPU has great power on parallel computing, it is impossible to finish the entire job using only GPU. Because of the lacking of complete instruction control, GPU has poor performance on complicated instruction sequence. Generally, GPU is appropriate for core computing platform, cooperating with main control codes on CPU [5, 6].

While computing in GPU, the key point is the parallelization. Normally parallelization is focused on data, which means every single thread in GPU computes one piece of data or relative some pieces. In order to gain high parallelization, the organization of processes in GPU has to be considered. In GPU, processes are organized in three levels called Grid, Block and thread. Threads are organized as Blocks in two-dimension, while blocks are organized as Grids in two-dimension [5].

25.3 Signal Simulator Design

As a software verification tool, signals generated by GNSS signal simulator include various influence factors about antenna, space, atmosphere, multipath, and so on, as shown in Fig. 25.1.

In this section, scenarios for GNSS signal simulators are analysed, followed by the architecture of simulators, and then the signal model.

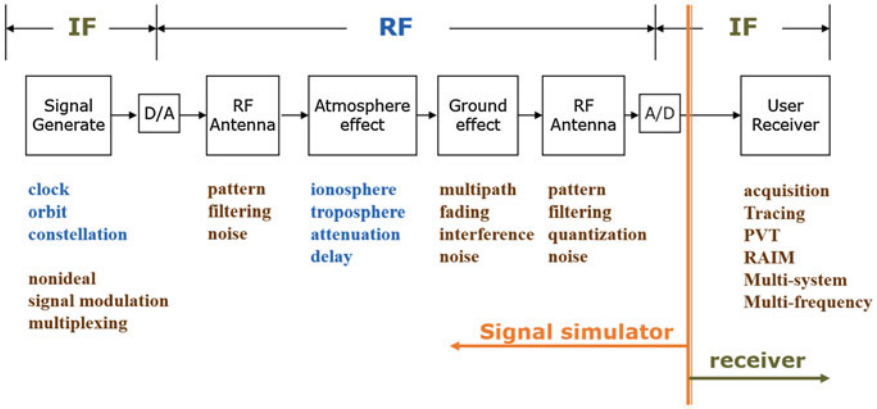

Fig. 25.1 Content of GNSS signal simulator

25.3.1 Scenarios of Application and Analysis of Performance

There are three main parts in simulator architecture, that is, simulation definition, signal definition and signal samples definition [3]. The primary computing pressure lies in the samples definition part, while in history samples definition part is the main difficulty to shut the traditional software simulators out of real-time simulating scenario. However, after using GPU, massive parallel computing ability improved so much that the main focuses under different scenarios should be reconsidered to make the simulating system, not sampling definition part itself, meet requirements better.

For GNSS signal simulators, there are two main application scenarios:

- Generate signal data as fast as could, and analyse the output data file for fast verification
- Be part of a system including hardware or software receiver, and working together with real-time receivers for testing and verification under the effects of multipath, environment, and constellation, etc.

Under the first scenario, the main output type is data file, as shown in Fig. 25.2.

In this process, the main performances of each step are shown as below (in low-cost PC platform)

- Throughput bandwidth of GPU: 288 GB/s
- Throughput bandwidth of PCI-E 3.0: 16 GB/s (for 16 channels)
- Writing speed for SATA 3.0: 0.75 GB/s (6 Gbit per second).

It is clear that GPU has the best performance in all steps, which means if common low cost PC platform is used to simulate GNSS signals in the first scenario, the bottleneck is the writing speed through PCI-E and SATA. Even using

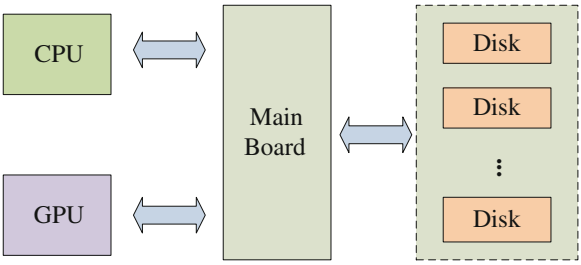

Fig. 25.2 Scenario 1 of GNSS signal simulator

special technique like RAID (Redundant Arrays of Independent Disks), it is still too much to close the 384-time gap in speed.

Under the second scenario, the type of outputting is network, link Ethernet, optical fibre or IB (InfiniBand), as shown in Fig. 25.3.

On the other side, if it is a hardware receiver, then it requires the normal speed, which is not a problem for simulators using GPU. If it is a software receiver, especially receiver also using GPU to do the correlation computing, it might require much higher data speed. However, just like the first scenario, the data speed is clearly limited by the PC platform and connecting types, which are shown as below:

- Throughput bandwidth of GPU: 288 GB/s
- Throughput bandwidth of PCI-E 3.0: 16 GB/s (for 16 channels)
- Bandwidth of Ethernet: 1.25 GB/s (10Gbps)
- Bandwidth of optical fibre: 1 GB/s (8Gbps)
- Bandwidth of IB: 5 GB/s (40 Gbps).

It is clear that GPU also has the best performance in all these steps and connection techniques.

At the same time, GPU has a performance of up to several TFlops (Tera Floating-point operations per second) for float point computing [1, 6, 7], which is much more than sufficient for signal simulating.

According to the analysis above, it could come to the conclusion that samples definition with computing on GPU has not been the performance bottleneck of GNSS signal simulators.

As a result, when designing the architecture of GNSS signal simulators base on GPU, the computing performance and throughput ability are not the most important limitation any more. On the other hand, ensuring the speed requirements met, considerations about flexibility and extensibility are becoming more and more important.

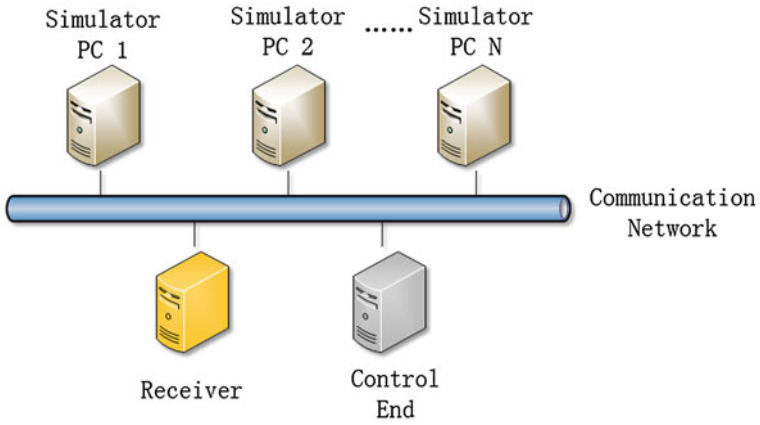

Fig. 25.3 Scenario 2 of GNSS signal simulator

25.3.2 Architecture of Signal Simulator

In the three parts of GNSS signal simulator architecture, the first two are not main topic discussed in this paper. For sampling definition, when considering scenarios of multi systems and multi frequencies, 1-D flattening design is not appropriate any more.

In multi-system and multi-frequency scenarios, different signals have various modulation types. At the same time, with the growth of signal number, multiplex technique becomes more complicated. It turns out to be a main difficulty to generally consider the different modulations and Multiplex techniques, and describe them with a consistent architecture.

First, in multi-system and multi-frequency scenarios, the content of GNSS signal simulating process is organized in four layers as below:

- Signal: generating signals with various modulation type, directly dealing with navigation message, pseudo-random code, sub-carrier and carrier, and returning the generated signal result on every sampling point.
- Frequency point: implementation of multiplexing
- System: actual GNSS systems, main differences between systems lie in the constellation and navigation message
- Task: a complete GNSS signal simulation, summing results from all channel, and returning output data with noise and quantization.

In the entire process, as the constellation and navigation message could be stored beforehand, system layer and frequency point layer could merge as one frequency point layer. Then the simulation process contains three layers: task, frequency point and signal.

Existed simulators mainly focus on the signal layer, to make the entire simulating process flattened in channels. But in multi-system and multi-frequency

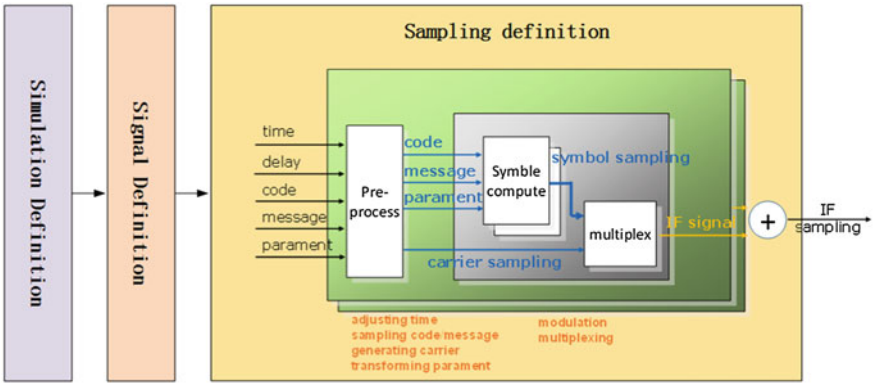

Fig. 25.4 Structure of GNSS signal simulator

scenario, with more consideration of flexibility and extensibility, the architecture mainly focuses on the frequency point layer, that is, it is flattened in frequency point layer other than signal layer.

As a result, the minimum unit in GPU is not signals, which stand as specific system, frequency point, signal and path, but frequency points, which stand as specific system, frequency point and path. At the same time, multiplexing based on phase lookup table is used in signal generating process, to improve the flexibility and extensibility of the architecture, especially for adding new signals on new frequency points.

Block diagram of the simulator architecture is shown as Fig. 25.4.

25.3.3 Model of Signals

In the view of intermediate receivers, received signals belong to several frequency points of several systems, including interference between each other, so the architecture should provide more support for simulating in multi-system and multi-frequency scenarios.

For these simulators, besides the traditional descriptions about navigation message, pseudo-random code and carrier, a more general description including various modulation types is needed for signal modelling.

POCET (Phase-optimized constant-envelope transmission) looks signal multiplexing again from a new point of view [8]. GNSS signal multiplexing is generally taken as the distribution of phases. In this theory, output signal is taken as phase modulation to the intermediate carrier with phases matching corresponding samples. As a result, phase to be modulated could be looked up from a stored table. Then signal in specific satellite and specific frequency point could be expressed as below

$$s_{1,1,1}(t) = A(t) \cdot \cos[2\pi f(t - \tau - \tau_{MP}) + \varphi(t - \tau - \tau_{MP}) + \theta(t)] \tag{25.1}$$

where t is the local time of receivers, τ is the transmission delay, τ_{MP} is the multipath delay, A is the amplitude, f is the intermediate frequency, θ is the carrier phase.

It is noted that φ is the lookup result of the phase table, which is loaded beforehand, $\varphi(t)$ indexes as $n(t)$.

$$n(t) = \sum_{m=1}^{M} b_m(t) * 2^{m-1}$$

Under the architecture taking frequency point as simulating core inside GPU, output signal summing all frequency points and all satellites is expressed as below

$$s(t) = \sum_{n=1}^{N_F} \sum_{h=1}^{N_{ch}(n,m)} \sum_{m=1}^{N_S(n)} A_{n,m,h}(t) \cdot \cos \begin{bmatrix} 2\pi f_n(t - \tau_m - \tau_h) \\ +\varphi_{n,m}(t - \tau_m - \tau_h) \\ +\theta_n(t) \end{bmatrix} \tag{25.2}$$

where N_F is the number of frequency points, $N_S(n)$ is the numbers of visible satellites in frequency n, $N_{ch}(n,m)$ is the number of paths for signals of satellite m, $A_{n,m,h}$ is the amplitude, f_n is the equivalent intermediate frequency, $\varphi_{n,m}$ is phase result looked up from the table.

25.4 Implementation of Signal Simulator

General thoughts about implementation based on GPU are becoming accordance [2–4]. Based on these thoughts, considering special requirements in the scenario of multi-system and multi-frequency, an improved architecture for simulators is proposed. The improvements mainly features in three points: calculation inside of threads, organization of threads, and load of resource.

25.4.1 Calculation Inside of Threads

Following the principles based on frequency points, CUDA threads are designed to computing all signals in the same frequency point, including multiplexing, inside of which a lookup table is used for phase modulation. It is shown in Fig. 25.5.

Before simulating, different lookup tables could be chosen by different signal combinations, without changing the computing flow inside threads. At the same time, when adding new signals, the mainly work lies in changing the lookup tables.

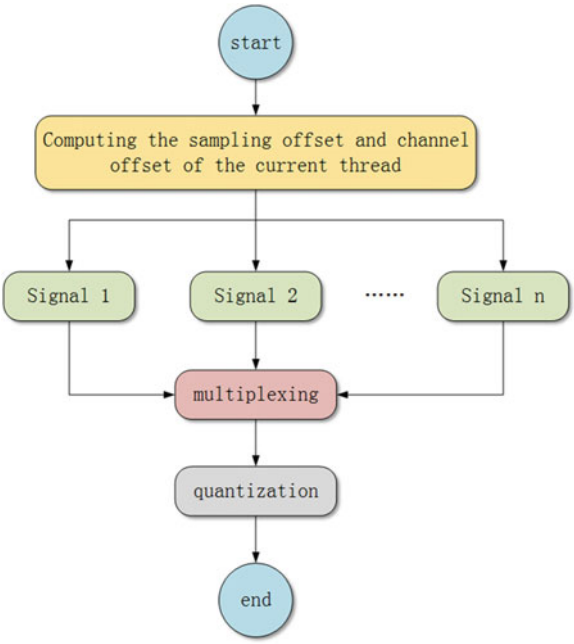

Fig. 25.5 Flow chart of processing in GPU threads

On the other hand, computing pressure inside single thread becomes heavier. However, as computing results of sampling points in different frequencies are stored in different memory addresses on GPU, which means there are no interlace in address accessing. As a result, there is not significant influence [5, 6].

Under new architecture, new 2-D computing organization takes place of the old 1-D flattened one.

When using 1-D organization, the number of channels is calculated by:

$$N_{Channel} = N_{SV} \cdot N_{MP} \cdot N_F \cdot N_{SIG}$$

In 2-D organization, channel number is:

$$N_{Channel} = N_{SV} \cdot N_{MP} \cdot N_F$$

From this point, to finish the same computing amount, fewer CUDA threads are needed, with each thread bearing more computing work.

25.4.2 Threads Organization

In the implementation before, warp in CUDA is usually used to compute as many sampling points in a channel as possible [3], which is intuitionistic and efficient. However, the same batch of wrap should be executed in the same multiprocessor

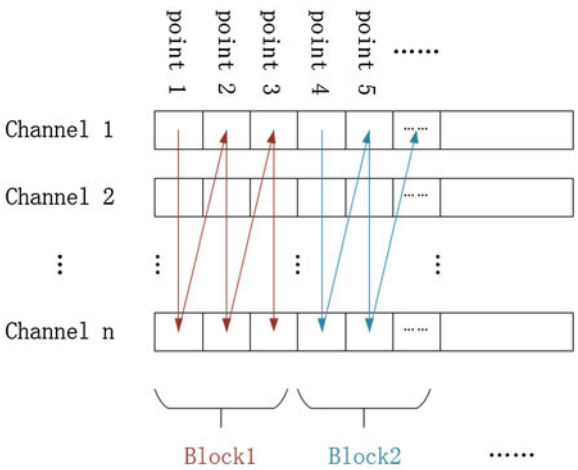

Fig. 25.6 Concept of thread organization in new architecture

[5, 6], so these warps should be in the same block, which limits the number of channels:

$$n_{Channel} \leq N_{Channel} = \left\lfloor \frac{N_{BD}}{W_{SIZE}} \right\rfloor$$

where $N_{Channel}$ is the maximum channel number, N_{BD} is the maximum thread number per block, W_{SIZE} is the thread number per warp.

For 780Ti, $N_{BD} \leq 1{,}024$ $W_{SIZE} = 32$ [1, 7], so $N_{Channel} = 32$. According to the fact above, for multi-system and multi-frequency simulators, the upper limit of channel number is too small, even without considering multipath effect.

At the same time, when $n_{Channel} < N_{Channel}$, because the thread number is less than the maximum thread number per block, computing performance is reduced actually. That is, the thread using efficiency in single block $\eta_{Block} = \frac{n_{Channel}}{N_{Channel}} < 1$, which means computing process is not taking use of full capacity of CUDA.

To settle this question, reorganization of CUDA threads is needed. Considering the constraint of using share memory inside block to sum thread data efficiently [6], channel number to be summed is limited by the size of block, which is usually less than 1,024. At a result, to enlarge the percentage of thread using in single block, thread organization is raised as Fig. 25.6.

Where, for sampling points in channels, threads in CUDA block are arranged by channels first and then sampling points, which is called channel first architecture. Accordingly the old architecture is called sampling first architecture. Then available sampling points in a single block is:

$$n_{Sample} \leq N_{Sample} = \left\lfloor \frac{N_{BD}}{n_{Channel}} \right\rfloor \tag{25.3}$$

where N_{Sample} is the upper limit of available sampling points in a single block.

Channel computing could be accomplished only if $n_{Sample} \geq 1$, and then available channels in a block is $n_{Channel} \leq N_{Channel} = 1{,}024$, which means all 1,024 could participate in the computing. At the same time, because of the 2-D organization of threads, thread number needed for computing also reduces. As a result, the new thread organization would enlarge simulation ability efficiently.

Besides, the block using efficiency increases as well. When all threads in a CUDA block could not be divided by channel number, the number of thread remaining is less than $n_{Channel}$, then the lower limit of block using efficiency is:

$$\begin{aligned} \eta_{Block} &= \frac{n_{Channel} \cdot n_{Sample}}{N_{BD}} \\ &= 1 - \frac{\mathrm{mod}(N_{BD}, n_{Channel})}{N_{BD}}. \\ &> 1 - \frac{n_{Channel}}{N_{BD}} \end{aligned} \tag{25.4}$$

If $n_{Channel}$ is equal to that when using sampling first architecture, which means $n_{Channel} \leq 32$, it is more efficient to use channel first architecture than to use sampling first architecture. Besides, another advantage of channel first architecture is the adaptability of more channels when $n_{Channel} > 32$, which seems more important in multi-system and multi-frequency scenarios.

In channel first architecture, the sampling offset and channel offset used by computing inside threads are:

$$i_{Sample} = i_B \cdot n_{Sample} + \tilde{i}_{Sample} \tag{25.5}$$

$$i_{Channel} = \mathrm{mod}(i_T, n_{Channel}) \tag{25.6}$$

where i_{Sample} is the sampling offset of current thread, $\tilde{i}_{Sample}$ is the sampling offset in current block, i_B is the 1-D offset of current block, $i_{Channel}$ is the channel offset of current thread in current block, i_T is the 1-D offset of current thread in current block. The details is as below

$$\begin{aligned} \tilde{i}_{Sample} &= \lfloor i_T / n_{Channel} \rfloor \\ i_B &= i_{By} \cdot N_{Bx} + i_{Bx} \\ i_T &= i_{Ty} \cdot N_{Tx} + i_{Tx} \end{aligned}$$

i_{Bx} and i_{By} are the x-coordinate and y-coordinate of the 2-D identification of current block respectively, i_{Tx} and i_{Ty} are the x-coordinate and y-coordinate of the 2-D identification of current thread respectively, N_{Bx} and N_{Tx} are the capacity of current block and current thread in the xx direction respectively.

25.4.3 Resource Loading

Because of the change of thread organization, resource loading should change according to that. The most significant change is the changeable of sampling point number in a CUDA block. When using sampling first architecture, the sampling pint number in a CUDA block fixes to 32, which is the thread number per warp, while the number is n_{sample} using channel first architecture. At the same time, for computing according to configured parameters, results of all threads are stored in shared memory and then summed as needed. For float type, this will cost $4 \cdot N_{BD}$ in share memory, which is less than the nominal size of 48 Kb. So the design is practicable.

According to the three changes above, the computing process in GPU under new architecture could adapt the simulation in multi-system and multi-frequency scenarios.

25.5 Simulation and Verification

The biggest advantages of the new architecture are flexibility and extensibility, now it is verified by a new type of signal which is being designed.

The detail information of the new signal is as below:

- modulation: BPSK
- intermediate frequency: 0 MHz
- code length: 2,046
- code frequency: 2.046 MHz
- message frequency: 1 KHz
- number of visible satellites: 9
- channel number: 36
- sample frequency: 5 MHz
- quantization: 8 bit.

Verifying the data file generated by the signal simulator, and the PSD (Power Spectrum Density) of the output signal is shown in Fig. 25.7, where the theoretical envelope is shown in red dashed line.

The signal in time domain is shown in Fig. 25.8. Acquisition result from a software receiver for a single channel is shown in Fig. 25.9, and the tracing result is shown in Fig. 25.10.

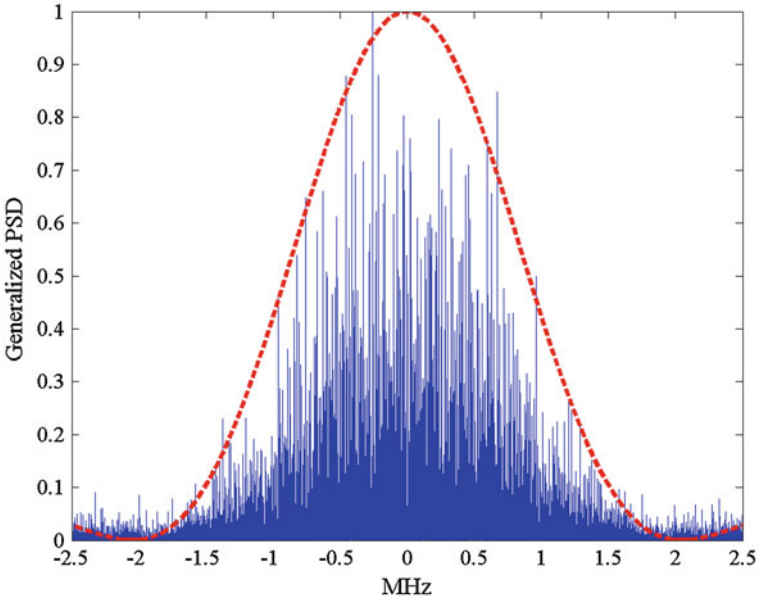

Fig. 25.7 PSD of single channel data generated

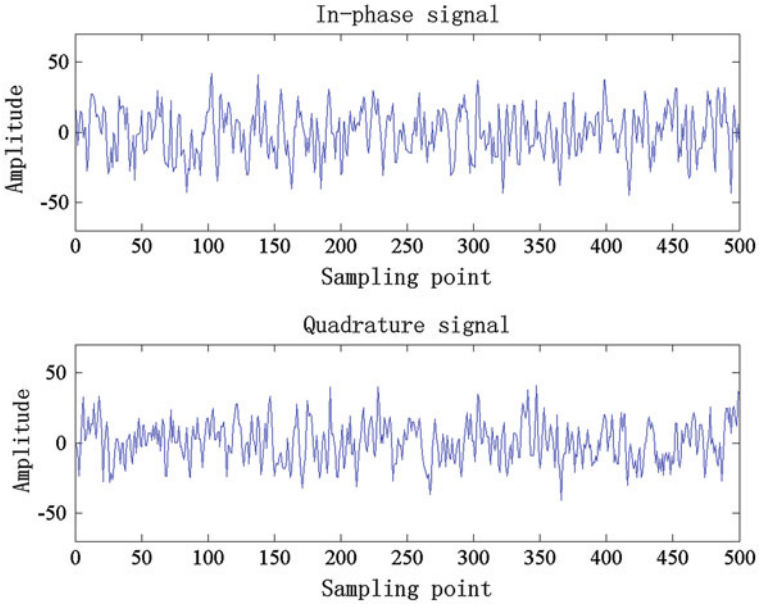

Fig. 25.8 Generated signal for all channels in time domain

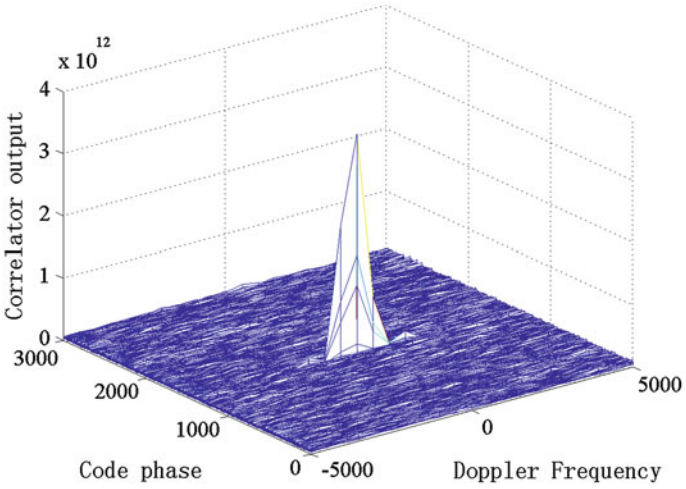

Fig. 25.9 Acquisition result of single channel

Fig. 25.10 Tracking result of single channel

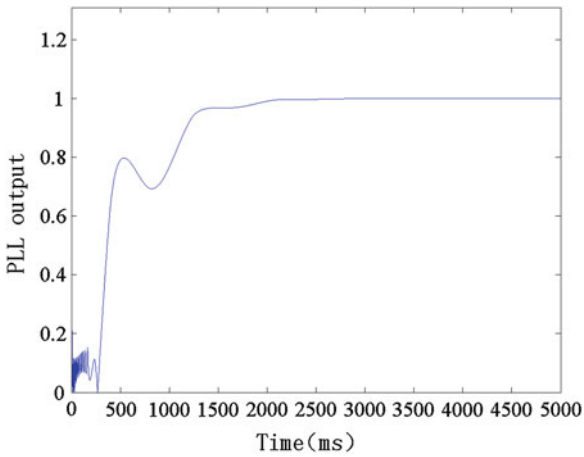

25.6 Conclusion

A new architecture of GNSS signal simulator based on GPU is proposed in this paper, followed by implementation and verification.

The architecture is designed for the multi-system and multi-frequency scenarios, which requires more channel number and more flexibility. GPU is still used for massive parallel computing on sampling points, but the calculating in CUDA threads and threads organization are improved for the focused scenarios.

CUDA threads are used to generate signals on the same frequency point instead of simple signals, that is, multiplexing is done inside of threads. As a result of this

new view, CUDA threads are reorganized to channel-first architecture, which enlarges the maximum channel number to 1,024, without significant reducing to the entire performance of the simulator. In the end, this new architecture is verified by a new signal being designed.

At current moment, the design of this new architecture is mostly finished and main models are implemented. Future work includes verification for other signals and combined signals from different frequencies, while moving signal implementations of older architecture to the new architecture. The final purpose is to construct a rapid GNSS signal simulating platform using massive parallelization of GPU and proper strategy of organization and arrangement.

References

1. Corporation N (2013) Geforce GTX 780Ti specifications
2. Li Q, Yao Z, Li H, Lu M (2012) A CUDA-based real-time software GNSS IF signal simulator. In: Proceedings of China Satellite Navigation Conference (CSNC). Springer
3. Bartunkova I, Eissfeller B (2001) Massive parallel algorithms for software GNSS signal simulation using GPU. In: Proceedings of the 25th international technical meeting of the satellite division of the Institute of Navigation (ION GNSS 2012)
4. Li Q, Yao Z, Lu M (2013) Design and optimization of GPU-based real-time software GNSS signal simulator. Comput Simul 30(1):120–123
5. Nvidia C (2009) C programming best practices guide. Cuda Toolkit 2
6. Staff N (2011) NVIDIA CUDA C programming guide. NVIDIA Corporation
7. Kepler Compatibility Guide for CUDA Applications. NVIDIA Corporation, 2013
8. Dafesh P, Cahn C (2001) Phase-optimized constant-envelope transmission (POCET) modulation method for GNSS signals. In: Proceedings of the 22nd international technical meeting of the satellite division of the Institute of Navigation (ION GNSS 2009)

Chapter 26
A High Precision Real-Time Low Order Polynomial Interpolation Method for GNSS Satellite Orbit

Xin Zhang, Jing Pang, Yingxue Su, Guozhu Zhang and Gang Ou

Abstract As an important testing method for integrated navigation receiver and hardware-in-loop simulation, real-time closed-loop navigation signal simulator needs to make the input external trace presented on output signal in ms. While constellation orbital calculation plays an important role in signal parameters generation, its computing efficiency has an important influence on time performance of simulator. The calculation load distribution of simulator constellation orbit interpolation based on sliding newton interpolation method is analyzed, and it's pointed out that the interpolating polynomial calculation efficiency is an important factor affecting the calculation load. A real-time precision satellite orbit low order polynomial interpolation method is proposed, which reduces the calculation load significantly without decreasing precision. The results also show that the new method speed up calculation six times than the direct 7-order sliding newton interpolation method for position error less than millimeter and velocity error less than 10^{-5} m/s, and obviously promoting the real-time performance.

Keywords Satellite navigation · Real-time closed-loop · Navigation signal simulator · Orbit interpolation · Real-time performance

26.1 Introduction

High precision real-time closed-loop navigation signal simulator can receive real-time external trajectory data and synchronize with external system by hardware triggering events, so as to complete relative motion simulation between satellite constellation and users with low delay and high precision. It can be widely used in

X. Zhang (✉) · J. Pang · Y. Su · G. Zhang · G. Ou
College of Electronic Science and Engineering, National University of Defense Technology, Changsha 410073, Hunan, People's Republic of China
e-mail: marmy@163.com

J. Sun et al. (eds.), *China Satellite Navigation Conference (CSNC) 2014 Proceedings: Volume I*, Lecture Notes in Electrical Engineering 303,
DOI: 10.1007/978-3-642-54737-9_26,

the R&D and testing of integrated navigation terminals, as well as in guidance and control of real-time closed-loop testing in semi-physical simulation system.

The real-time generation of pseudorange and its change rate in real-time closed-loop navigation signal simulator is one of the key technologies, because it is difficult to guarantee the real-time performance by calculating satellite orbit directly using satellite ephemeris or orbit integral method. Therefore, the ephemeris interpolation and fitting methods [1], including many kinds of polynomial interpolation methods [2–9] are generally used to improve the real-time performance of satellite position and velocity of calculation.

Generally, High orders (about nine orders) are required in polynomial interpolation with large node intervals (900–300 s), and "window" is needed to overcome the Runger Phenomenon [4, 5]. In [10], low-order Hermite Interpolation of satellite position and velocity are researched. Although the low-order Hermite Interpolation can significantly reduce the calculation complexity of the interpolation, the node interval must be small enough to ensure the interpolation precision, which results in initial calculation complexity greatly increased by adding more nodes.

After the calculation load analysis of satellite orbit calculation method in navigation signal simulator based on interpolation, this paper presents a high precision real-time low order polynomial interpolation method, which reduces the total calculation complexity and improves the real-time performance of the simulator with the interpolation precision kept.

26.2 Calculation Load Analysis of Satellite Orbit

The interpolation calculation of satellite orbit in the navigation signal simulator includes satellite position and velocity calculation at any moment. In [1], the procedure of traditional sliding high-order Newton polynomial interpolation method used for orbit calculation is summarized. As show in Fig. 26.1, the entire calculation process can be divided into two parts, including weak real-time part and strong real-time part. The calculation of the standard nodes by ephemeris and generation of interpolation polynomial coefficients are finished in the weak real-time part. Then, the calculation of satellite location and velocity at any moment by using polynomial interpolation is carried out in strong real-time part. The weak real-time part calculation is only performed in time of simulation initialization and ephemeris update, and has low running frequency and weaker real-time requirements. However, the polynomial interpolation has a strong real-time requirement and must be completed within the specified time limit to meet the pseudorange calculation requirement.

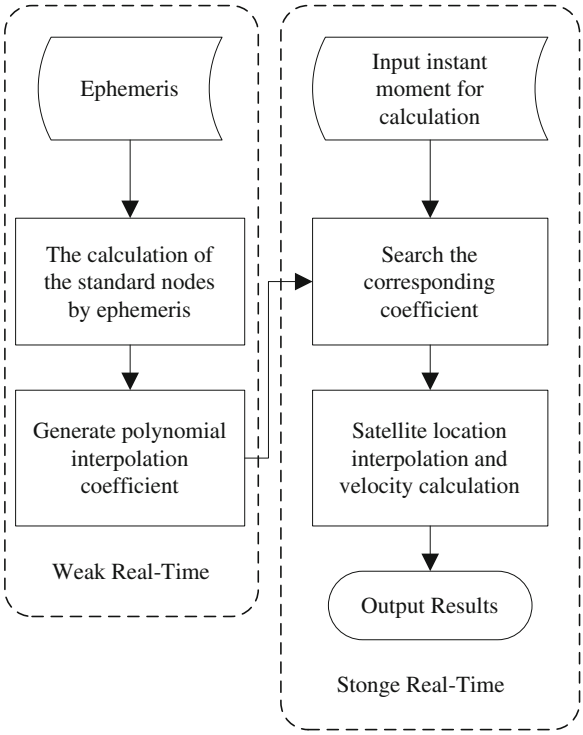

Fig. 26.1 Satellite orbit calculation procedure in simulator

26.2.1 Calculation Load Analysis of Weak Real-Time Part

In case of navigation signal simulator initialization or ephemeris update, satellite ephemeris date is needed for satellite position calculation. Taking direct GPS ephemeris calculation as an example, during the calculation process, the ephemeris and a large number of complex calculation, including floating-point multiplication, iterative arithmetic and trigonometric function arithmetic are needed. The specific calculation procedure is given in [11]. If the numerical integration method is used, the calculation procedure will be more complicated. Furthermore, the interpolation polynomial coefficient table is required to be calculated after the calculation of standard nodes.

It can be seen from the calculation process that the calculation load of each standard node by using ephemeris data in weak real-time part is larger. More standard nodes to be calculated will result in longer initialization time and greatly increased calculation load when ephemeris update, which will consequently affect the real-time calculation of strong real-time part. Therefore, the standard nodes in real-time closed-loop navigation simulator always have large node interval, which reduces calculation load of weak real-time part.

26.2.2 Calculation Load Analysis of Strong Real-Time Part

The calculation in strong real-time part is mainly due to the prolonged continuous interpolation of satellite orbit in navigation signal simulator.

Generally, the interpolation of satellite orbit uses piecewise polynomial interpolation method. The category of piecewise polynomial interpolation methods and their calculation effectiveness analysis are studied in [1–5, 10]. Newton interpolation and cubic-order Hermite interpolation are commonly regarded as two piecewise polynomial interpolation methods with the best efficiency. However, due to the lower order of cubic-order Hermite interpolation, if the interval between two nodes is large, the interpolation error is also large. So the cubic-order Hermite interpolation is generally not used in orbit interpolation.

Assuming that $f(t)$ is the location function of satellite in Earth Centered Earth Fixed System (ECEF), and t is the time. When the equality of interpolation interval is ignored, the nth-order Newton interpolation polynomial can be expressed as:

$$f_{Nn}(t) = f[t_0] + f[t_0, t_1] \cdot (t - t_0) + \cdots + f[t_0, t_1, \ldots, t_n] \cdot \prod_{i=0}^{n-1} (t - t_i) \tag{26.1}$$

where t_0, t_1, … t_n and their corresponding $f(t_0)$, $f(t_1)$, … $f(t_n)$ are called the interpolation nodes, $|t_{k+1} - t_k|$ is defined as node space, $f[t_0, t_1, \ldots t_n]$ is the nth-order difference quotient of $f(t)$, and $f[t_0] = f(t_0)$. The difference quotient can be calculated by:

$$f[t_0, t_1, \ldots, t_k] = \frac{f[t_0, \ldots t_{k-2}, t_k]}{t_k - t_{k-1}} - \frac{f[t_0, t_1, \ldots, t_{k-1}]}{t_k - t_{k-1}} \tag{26.2}$$

From (26.1) and (26.2), nth-order Newton interpolation polynomial may be obtained by adding a higher order term to $n - 1$ order polynomial. And when t changes between $t_0, t_1, \ldots t_n$, the difference quotient does not need to be recalculated. In case of interpolation intervals are equal, $h = |t_n - t_{n-1}| = \cdots = |t_1 - t_0|$, the interpolation formula in difference quotient form can be replaced by that in differential form in Newton interpolation, which can simplify the calculation process without affecting the calculation precision. The difference quotient in (26.2) calculated by forward difference can be given by:

$$f[t_0, t_1, \ldots t_k] = \frac{\Delta^k f_0}{k! h^k} \tag{26.3}$$

where Δ is the forward difference operator, and $\Delta^k f_0$ shall meet:

$$\Delta f_i = f(t_i + h) - f(t_i) \tag{26.4}$$

$$\Delta^k f_0 = \Delta^{k-1} f_1 - \Delta^{k-1} f_0 \tag{26.5}$$

Let $t = t_0 + \lambda h$, and substitute (26.2) by (26.3) to get:

$$f_{Nh}(\lambda) = f(t_0) + \sum_{k=1}^{n} \left(\frac{\Delta^k f_0}{k!} \cdot \prod_{i=0}^{k-1} (\lambda - i) \right) \tag{26.6}$$

During piecewise Newton interpolation, reasonable sliding "window" needs to be used to avoid interpolation precision degradation and "Runge phenomenon". However, this will increase the calculation complexity caused by sliding. Moreover, the velocity of satellites cannot be directly achieved by sliding higher order Newton interpolation, thus it shall be calculated by the velocity defined in (26.7), where s is the time interval.

$$v(t) = f'(t) = \lim_{s \to 0} \frac{f\left(t + \frac{s}{2}\right) - f\left(t - \frac{s}{2}\right)}{s} \tag{26.7}$$

If cubic-order Hermite interpolation polynomial is used for interpolation, the value of $f(t)$ at interpolation node t_i and t_{i+1}, and their first order derivative are needed. Then, the interpolation polynomial can be expressed as:

$$f_{H3}(t) = a_i + b_i(t - t_i) + c_i(t - t_i)^2 + d_i(t - t_i)^3 \tag{26.8}$$

where

$$a_i = f(t_i), b_i = f'(t_i),\ c_i = \frac{3f[t_i, t_{i+1}] - 2f'(t_i) - f'(t_{i+1})}{t_{i+1} - t_i}$$
$$d_i = \frac{f'(t_i) - 2f[t_i, t_{i+1}] - f'(t_{i+1})}{(t_{i+1} - t_i)^2}$$

$f[\cdot]$ can be calculated by (26.2). The satellite velocity can be obtained by (26.9) with cubic-order Hermite interpolation.

$$v_{H3}(t) = b_i + 2c_i(t - t_i) + 3d_i(t - t_i)^2 \tag{26.9}$$

The satellite location and velocity calculation with piecewise polynomial interpolation is always happened company with signal parameter update. Due to the iteration process of pseudorange calculation, the polynomial interpolation always needs to be called several times in the process of signal parameters update calculation each time.

With a real-time requirement of 10 ms, assuming that the polynomial interpolation is called m times on the average in the process of each satellite signal parameters update, and there are more than 100 satellites in GPS, GLONASS, Galileo and Beidou system, so more than 100 m times interpolation calculation must be completed within a time limit of far less than 10 ms, considering various channel errors calculation, communication and control of the simulator.

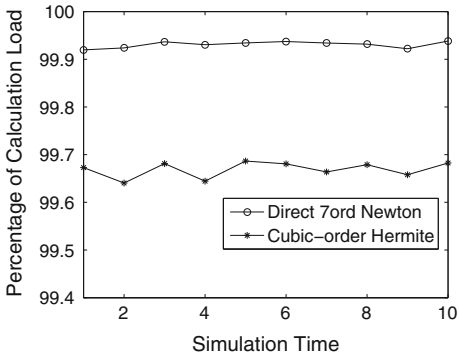

Fig. 26.2 Percentage of calculation load in strong real-time part

26.2.3 Calculation Load Distribution

According to calculation load analysis of strong and weak real-time parts, the calculation and storage of standard nodes of satellite orbit and polynomial interpolation coefficient by ephemeris are mainly carried out in the weak real-time part. Whereas the calculation of satellite orbit parameters at any time instant is mainly achieved in the strong real-time part. Due to there is time sequence in interpolation coefficient searching, the time consumed by interpolation coefficient searching can be ignored. Therefore, the main calculation load of the interpolation depends on the calculation process of the interpolation polynomial.

According to the conclusion in [1], the percentage of calculation load of satellite orbit parameters is simulated and analyzed, which 7-order Newton interpolation with the sliding window and cubic-order Hermite interpolation are applied in respectively. All the simulations use GPS Ephemeris to calculate the standard nodes with interval of 600 s.

As shown in Fig. 26.2, the calculation load of strong real-time part with 7-order Newton interpolation method applied takes more than 99.9 % of the satellite orbit calculation load. On the other hand, more than 99.6 % calculation load is taken when cubic-order Hermite interpolation method applied. All results show that the interpolation operation occupies the majority of the calculation load.

The percentage decrease when cubic-order Hermite interpolation is applied is due to its significant decrease in calculation complexity compared with 7-order Newton interpolation, and it also decrease the overall calculation load in orbit calculation.

However, the interpolation error of satellite location can be controlled below 10^{-5} m with 7-order Newton interpolation, and the approximate error of satellite velocity when $s = 0.01$ can also be controlled below 10^{-5} m/s. Whereas the interpolation error of satellite location with cubic-order Hermite interpolation satellite location can reach meters, which cannot meet the calculation precision requirements of the simulator.

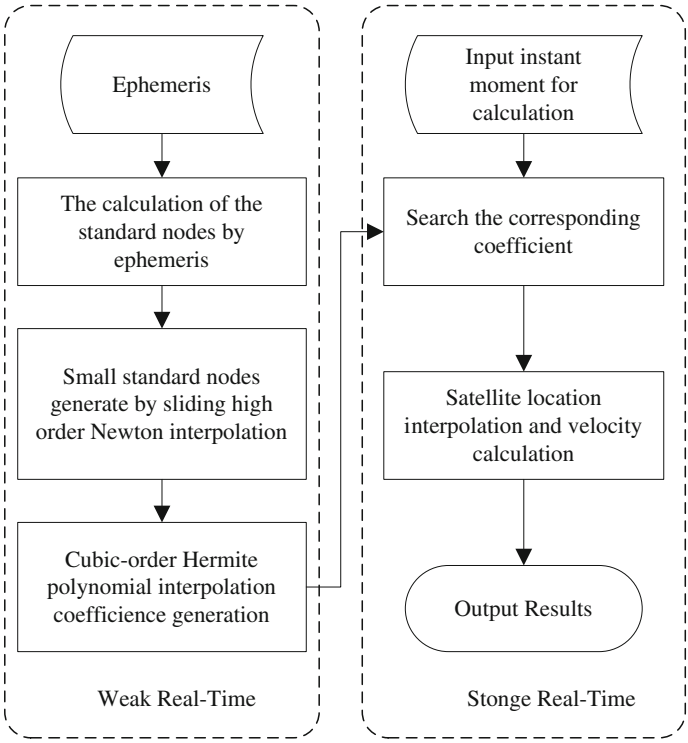

Fig. 26.3 Improved calculation procedure for satellite orbit in simulator

26.3 Improved Interpolation Method for Orbit

On the basis of the calculation load distribution analysis for multi-constellation satellite orbit, an improved low order interpolation method for orbit is presented. The complete process is shown in Fig. 26.3.

The whole procedure can be divided into the following steps:

1. Data preparation for standard nodes with large interval: The position of satellites with standard large interval is directly calculated using ephemeris.
2. Generating small interval standard nodes with sliding high order Newton polynomial interpolation: Standard nodes with smaller interval can be achieved using sliding high order Newton interpolation, and the velocity of each standard node is calculated by (26.7).
3. Preparation of cubic-order Hermite interpolation polynomial coefficients: The corresponding interpolation coefficients for each cubic-order Hermite interpolation interval are calculated and numbered.

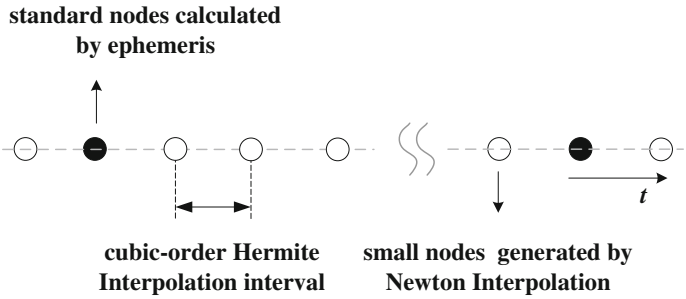

Fig. 26.4 The small nodes and large standard node in the improved method

4. Interpolation polynomial coefficients searching: According to the input time instant for satellite location calculation, the appropriate interpolation polynomial coefficients are searched.
5. Calculate the satellite location and velocity at the time instant with cubic-order Hermite interpolation.

The relationship between each large standard node and the small node in the improved procedure is shown in Fig. 26.4. The nodes with large standard interval obtained by ephemeris are interpolated, new nodes with smaller intervals are generated, and velocities of all nodes are calculated. All the work generating small nodes in weak real-time part adds only a small amount of calculation complexity.

By executing orbit interpolation in the strong real-time part with low order interpolation method, the calculation efficiency is higher than that with high order interpolation. Moreover, when stronger real-time requirements is needed, the calculation complexity increment of low order interpolation will be slowed down significantly compared with that of high order interpolation.

26.4 Result Analysis of Numerical Examples

The real-time calculation performance is analyzed in this paper with a satellite location error less than millimeter and velocity error less than 10^{-5} m/s. The ephemeris of GPS Satellite PRN 14 at 0:00 on September 10th, 2011 are used to calculate the satellite location and velocity with different parameter refresh time interval, which can be used as the true values of satellite orbit parameters. Then the location and velocity of the satellite are calculated with sliding 7-order Newton interpolation and the proposed improved interpolation method, respectively. The calculation loads of the two mentioned methods are compared in MATLAB. The parameter refresh time interval are set to be 20, 10, 4 and 2 ms, respectively, with corresponding time interval types called 1, 2, 3 and 4.

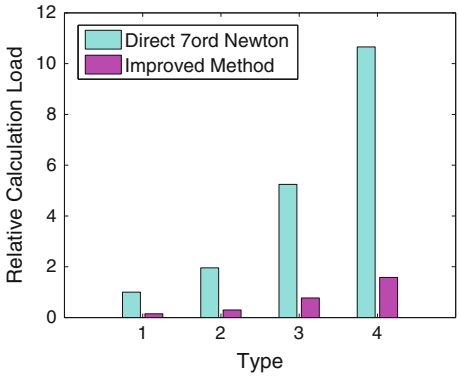

Fig. 26.5 Comparison of relative calculation load of the two interpolation methods

The standard node interval calculated directly by ephemeris in weak real-time part is 600 s, and interpolated standard nodes with 30 s interval is generated with 9th-order sliding Newton interpolation. The comparison result of relative calculation load of the two interpolation methods with different parameter refresh time interval types are shown in Fig. 26.5, and the relative calculation load is defined as the ratio of different calculation load to the calculation load of direct 7-order Newton interpolation under 20 ms.

It can be seen that the calculation load of the improved method presented in this paper is always about 1/6 that of direct sliding 7-order Newton interpolation method. With the decrease of parameter refresh time interval, the increase of calculation load of proposed method in the strong real-time part is significantly lower than that of direct 7-order sliding Newton interpolation method.

26.5 Conclusion

By calculation load analysis of satellite orbit in real-time closed-loop navigation signal simulator, we can draw the following conclusions:

1. A single-time calculation complexity of the weak real-time part is large, but the total calculation load can be limited to low level. The piecewise polynomial interpolation in the strong real-time part is frequently called, its calculation load accounts for the vast majority of the total calculation load (over 99 %).
2. Since the piecewise interpolation coefficients can be calculated and stored in sequence, the order of the polynomial interpolation has a key impact on the calculation efficiency of the strong real-time part.
3. An improved interpolation method for satellite orbit is presented. In the weak real-time part, sliding high-order Newton interpolation is used for generating small nodes. In the strong real-time part, cubic-order Hermite polynomial is used for piecewise interpolation of satellite orbit. While the calculation load increment of the weak real-time part can be ignored, the calculation load of the

strong real-time part can be significantly reduced. Under the condition that satellite positioning error less than millimeter and velocity error less than 1e−5 m/s, the calculation load of proposed method can be reduced to about 1/6 that of direct sliding 7-order Newton interpolation method.

References

1. Tong HB, Sha H, Zhang GZ, Ou G (2012) A high-precision and real-time interpolation method for satellite orbit in GNSS. J Nat Univ Def Technol 34(2):59–63
2. Wei EH, Chai H (2006) The comparison research on GPS precise ephemeris interpolation methods. GNSS World China 31(5):13–15
3. Schenewerk M (2003) A brief review of basic GPS orbit interpolation strategies. GPS Solut 6(4):265–267
4. Horemuz M, Andersson JV (2006) Polynormial interpolation of GPS satellite coordinates. GPS Solut 10(1):67–72
5. Hong Y, Ou JK, Peng BB (2006) Three interpolation methods for precise ephemeris and clock offset of GPS satellite. Geomatics Inf Sci Wuhan Univ 31(6):516–518
6. Ding WW, Liu WK, Li ZH (2007) Polynomial fitting of GPS satellite coordinates based on broadcast ephemeris. Hydrogr Surveying Charting 27(6):4–9
7. Wu JZ, Gao JQ, Li MF (2009) Research on interpolation method for IGS precise ephemeris and clock bias. Geotech Invest Surveying 7:52–54
8. Gong HC, Li QH (2009) The interpolation methods for satellite coordinate and clock offset based on IGS precise ephemeris. GNSS World China 34(5):24–27
9. Zhang SJ, Li JC, Xing LL et al (2007) Comparative analysis on two methods for IGS precise ephemeris interpolation. J Geodesy Geodyn 27(2):80–83
10. Korvenoja P (2000) Efficient satellite orbit approximation. In: ION GPS, Salt Lake, pp 1930–1937
11. Kaplan ED (1996) Understanding GPS: principles and applications. Artech House, Boston, pp 30–40

Chapter 27
TD-AltBOC Signal Generation and Multipath Simulation on FPGA-Based Platform

Jihui Cui, Zhigang Huang and Jianlei Yang

Abstract The proposition of Time Division Alternative Binary Offset Carrier (TD-AltBOC) provides a new solution for COMPASS B2 navigation signal. Relative to AltBOC, TD-AltBOC has higher multiplexing efficiency, lower reception complexity and higher ranging accuracy when greater frontend bandwidth is used. However, the assessment of TD-AltBOC modulation performance is still in the theoretical period. It is needed to test the properties of TD-AltBOC actually in the highly realistic and complex spatial simulation environment. To solve this problem, this paper proposes methods of generating TD-AltBOC signal and simulating the simple multipath scenario on the FPGA-based hardware platform. TD-AltBOC is generated using lookup table method based on the basic modulation principles. By converting the value of the parameter k in the lookup table, this paper achieves the key technology that the phase of subcarrier flips with 180° at the even chips spot. The multipath signal is composed of direct signal, reflected signal and reference signal. The MDR and multipath delay can be controlled precisely. This article has tested the code tracking performance and anti-multipath performance of the generated signal. The testing results match the theory. The methods of signal generation and multipath simulation this paper proposes can meet the demand of performance assessment.

Keywords Performance assessment · TD-AltBOC · Signal generation · Multipath simulation

J. Cui (✉) · Z. Huang · J. Yang
Institute of Electronic and Information Engineering, Beihang University, Beijing 100191, China
e-mail: 1034906278@qq.com; quanchenger2010@gmail.com

J. Sun et al. (eds.), *China Satellite Navigation Conference (CSNC) 2014 Proceedings: Volume I*, Lecture Notes in Electrical Engineering 303,
DOI: 10.1007/978-3-642-54737-9_27,

27.1 Introduction

TD-AltBOC [1] (Time Division-Alternative Binary Offset Carrier) is a new navigation signal modulation like AltBOC. It can transmit four different signals (its upper sideband and lower sideband have a data channel and a pilot channel respectively). Relative to AltBOC, TD-AltBOC modulation makes the data channel and pilot channel time division multiplexed. Constant envelope modulation can be achieved despite no product signal generated. Multiplexing efficiency is 100 %. The complexity of signal generation and reception is similar with that of BOC. When receiver with wider bandwidth is used to receive more high-order harmonics, performance can be improved.

The test and assessment to the performance of TD-AltBOC signal is on-going gradually. The reference [1 – 3] made some preliminary theoretical analysis on the performance of TD-AltBOC. However, the actual hardware test is still in shortage. This paper analyzes the method of generating TD-AltBOC signal and implements it on the FPGA platform, helping set up hardware signal simulator for the test and assessment on the diverse properties of TD-AltBOC. It also introduces the method of simulating the dual multipath scenarios. At the same time, the article shows the means and the results of testing the tracking performance and anti-multipath performance and compares the results with the theoretical curves.

27.2 TD-AltBOC Modulation Principle

The mathematical expression of the TD-AltBOC baseband signal is following:

$$\begin{aligned} s(t) = {} & [d_A(t)c_{AD}(t) + c_{AP}(t)]\left[SC_{B,\cos}(t) - jSC_{B,\sin}(t)\right] \\ & + [d_B(t)c_{BD}(t) + c_{BP}(t)]\left[SC_{B,\cos}(t) + jSC_{B,\sin}(t)\right] \end{aligned} \tag{27.1}$$

In which, $SC_{B,\cos}(t)$ is binary cosine subcarrier. $SC_{B,\sin}(t)$ is binary sine subcarrier. Their definitions are following:

$$\begin{aligned} SC_{B,\cos}(t) &= sign(\cos(2\pi f_s t)), \\ SC_{B,\sin}(t) &= sign(\sin(2\pi f_s t)), \end{aligned} \tag{27.2}$$

$d_{\mathrm{A}}(t)$ and $c_{\mathrm{AD}}(t)$ are the bit and PN code waveform of the data channel of the lower band respectively. $c_{\mathrm{AP}}(t)$ is the PN code waveform of the pilot channel of the lower band. $d_{\mathrm{B}}(t)$ and $c_{\mathrm{BD}}(t)$ are the bit and PN code waveform of the data channel of the upper band respectively. $c_{\mathrm{BP}}(t)$ is the PN code waveform of the pilot channel of the upper band. They are expressed as follows:

$$
\begin{aligned}
c_{AD}(t) &= \sum_{l=-\infty}^{+\infty} \sum_{k=0}^{N_{AD}-1} C_{AD}(k)p(t-(2N_{AD}l+2k)T_c), \\
c_{AP}(t) &= \sum_{l=-\infty}^{+\infty} \sum_{k=0}^{N_{AP}-1} C_{AP}(k)p(t-(2N_{AP}l+2k+1)T_c), \\
c_{BD}(t) &= \sum_{l=-\infty}^{+\infty} \sum_{k=0}^{N_{BD}-1} C_{BD}(k)p(t-(2N_{BD}l+2k)T_c), \\
c_{BP}(t) &= \sum_{l=-\infty}^{+\infty} \sum_{k=0}^{N_{BP}-1} C_{BP}(k)p(t-(2N_{BP}l+2k+1)T_c),
\end{aligned}
\tag{27.3}
$$

In which, C_{AD}, C_{AP}, C_{BD} and C_{BP} are the PN codes (± 1) of the four channels respectively. The corresponding code lengths are N_{AD}, N_{AP}, N_{BD} and N_{BP}. Tc is the width of one code chip. $p(t)$ is a rectangular pulse defined as follows:

$$
p(t) = \begin{cases} 1, & 0 \le t < T_c \\ 0, & others \end{cases} \tag{27.4}
$$

From the PN code waveform expressions of the upper and lower data channels and pilot channels, it can be seen that the data channel and pilot channel on the same band are time division multiplexed. Data channel is transmitted at the odd time spot and pilot channel is transmitted at the even time spot. The time spot allocation of TD-AltBOC signal components is depicted in Fig. 27.1.

When $2f_s/f_c$ (f_s is the frequency of the subcarrier and f_c is the frequency of PN code) is odd, the power spectral density (PSD) of TD-AltBOC signal is the Eq. (27.5). When $2f_s/f_c$ is even, the PSD is the Eq. (27.6).

$$
G_{AD}^{odd}(f) = \frac{R_c}{(\pi f)^2}\cos^2\left(\frac{\pi f}{R_c}\right)\sin^2\left(\frac{\pi f}{4f_s}\right) \Big/ \sin^2\left(\frac{1}{4}\pi + \frac{\pi f}{4f_s}\right) \tag{27.5}
$$

$$
G_{AD}^{even}(f) = \frac{R_c}{(\pi f)^2}\sin^2\left(\frac{\pi f}{R_c}\right)\sin^2\left(\frac{\pi f}{4f_s}\right) \Big/ \sin^2\left(\frac{1}{4}\pi + \frac{\pi f}{4f_s}\right) \tag{27.6}
$$

The PSD of TD-AltBOC is depicted in the Fig. 27.2.

27.3 Generation Method with FPGA

The generation principle block of the TD-AltBOC(15,10) signal is showed in Fig. 27.3. In this scheme, the highest clock rate is 122.76 MHz. It drives the cosine and sine generators. The time division multiplexers of the data channel and the pilot channel use the clock of 10.23 MHz as drivers. And the clock rate of the PN code generators is 5.115 MHz.

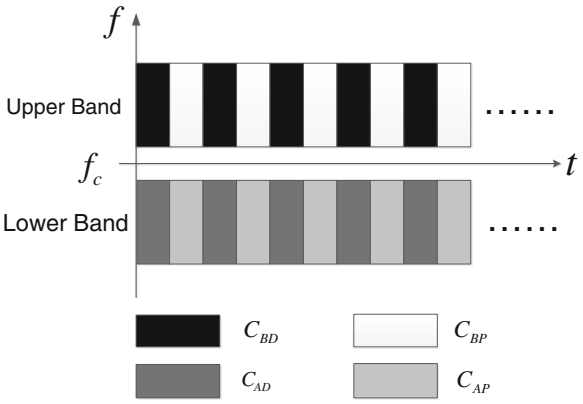

Fig. 27.1 Time spot allocation of TD-AltBOC signal components

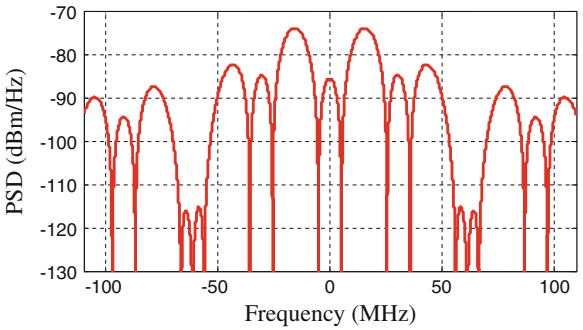

Fig. 27.2 Normalized power spectral density of TD-AltBOC signal

The program in FPGA mainly uses lookup table to generate TD-AltBOC signal. The Table 27.1 is the lookup table [4] of the TD-AltBOC module.

In the generation process of the TD-AltBOC(15,10), $f_s/f_c = 1.5$, in the other words, one PN code chip corresponds to 1.5 cycles of subcarriers. In order to maintain the continuity of the subcarrier, it is needed that the odd code chips correspond to the 1.5 cycles of subcarriers with the initial phase of 0° and the even code chips correspond to the 1.5 cycles of subcarriers with the initial phase of 180°. In the other words, when the lookup table is used during the even chips period, the lookup Table 27.1 should be reversed with 180°. Then the values of the k in the Table 27.1, 1 and 2, should be exchanged with 3 and 4 respectively. Other processes of even code chips are the same with those of the odd code chips.

In the FPGA program, PN code sequences are read out from RAM with 10.23 MHz clock rate. Then the data channels are multiplied by navigation message but the pilot channels have no change. The four channels get the signals of E_{a-I}, E_{a-P}, E_{b-I} and E_{b-P} respectively. And then two sequences of the four (E_{a-I} and E_{b-I} or E_{a-P} and E_{b-P}) are used to look up the table. The IQ expanded

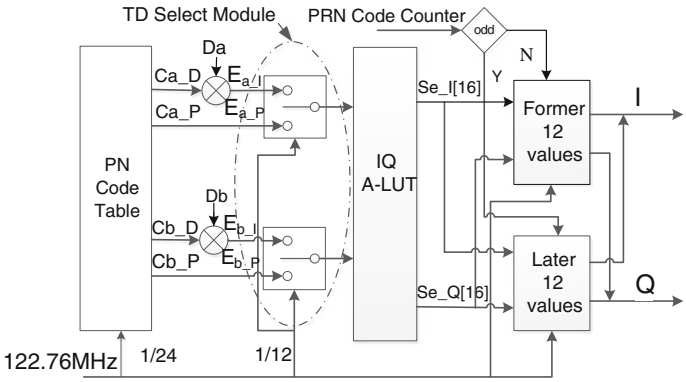

Fig. 27.3 Generation block diagram of TD-AltBOC(15,10) signal. A-LUT is short of amplitude lookup table

Table 27.1 Lookup table of TD-AltBOC(15,10)

		Input							
Ea_I		−1	−1	+1	+1	–	–	–	–
Eb_I		−1	+1	−1	+1	–	–	–	–
Ea_P		–	–	–	–	−1	−1	+1	+1
Eb_P		–	–	–	–	−1	+1	−1	+1
iTs	$t' = t$ modulo *Ts*	*k* according to $s(t) = \exp(jk\pi/2)$(normalized)							
	t'								
0	[0, *Ts*/8]	4	1	3	2	4	1	3	2
1	[*Ts*5/8, 2 *Ts*5/8]	4	1	3	2	4	1	3	2
2	[2 *Ts*/8, 3 *Ts*/8]	2	1	3	4	2	1	3	4
3	[3 *Ts*/8, 4 *Ts*/8]	2	1	3	4	2	1	3	4
4	[4 *Ts*/8, 5 *Ts*/8]	2	3	1	4	2	3	1	4
5	[5 *Ts*/8, 6 *Ts*/8]	2	3	1	4	2	3	1	4
6	[6 *Ts*/8, 7 *Ts*/8]	4	3	1	2	4	3	1	2
7	[7 *Ts*/8, *Ts*]	4	3	1	2	4	3	1	2

Note Ea_I $= d_A(t)c_{AD}(t)$, Eb_I $= d_B(t)c_{BD}(t)$, Ea_P $= c_{AP}(t)$, Eb_P $= c_{BP}(t)$. '–' represents nonsense

amplitude lookup table in the Fig. 27.3 is slightly different from the lookup Table 27.1. It corresponds to the amplitudes of the phase and quadrature components and is expanded to two cycles of the subcarrier (it has 16 values and the former 8 values are the same with the latter 8 values). In the FPGA program, the amplitudes are quantified with 16 bits. During the odd code chips period, the former 12 values are sent out sequentially with 122.26 MHz rate. During the even code chips period, however, the latter 12 values are sent out sequentially. As a result, it can be achieved that the phase reverses with 180° during the even code chips period.

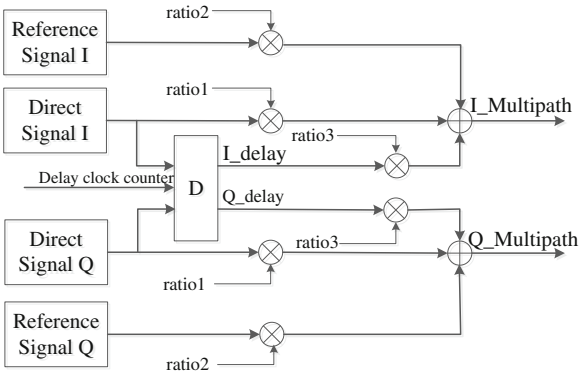

Fig. 27.4 Simulation of dual multipath scenario

27.4 Simulation Method of Multipath

This paper proposes a simulation method of multipath scenario with single reflected signals. This scenario can be used to test the anti-multipath performance of the signal system with different multipath signal and direct signal power ratios (MDR) and different multipath delay conditions. The simulation method is showed in the Fig. 27.4.

In Fig. 27.4, the direct signal and reference signal use two quadrature PN code sequences. They use TD-AltBOC(15,10) modulation, the generation method of which is showed above. The reflected signal is generated by delaying the direct signal. The delayed clocks are controlled by the parameter 'counter'. Ratio1, ratio2 ratio3 are the control parameters of amplitude. Simulating multipath scenarios with different MDR conditions can be achieved by fixing parameters ratio1, ratio2 (i.e., fixing the power of the direct signal and reference signal) and adjusting the parameter ratio3 (i.e., adjusting the power of reflected signal). Similarly, simulating multipath scenarios with different multipath delays can be achieved by changing the parameter 'counter'.

Reference signal is designed for anti-multipath performance testing considerations. Software receiver uses two PN code sequences to receive and process the multipath signal respectively at the same time. The code tracking error can be gotten by make subtraction between the two corresponding code phases.

27.5 Testing Results

27.5.1 Power Spectral Density of TD-AltBOC(15,10)

The I channel and Q channel baseband signals of TD-AltBOC(15,10) are converted into analog signals by DAC (i.e., converter from digital to analog). The output

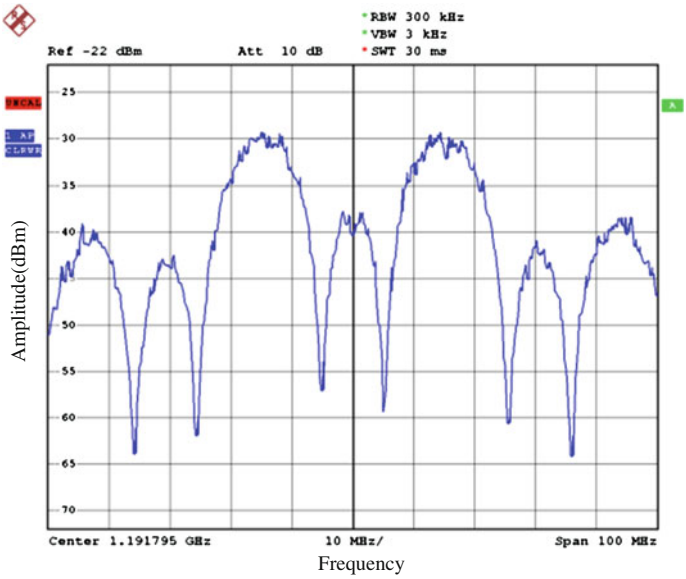

Fig. 27.5 PSD of RF TD-AltBOC(15,10) signal

baseband analog signals are changed into a RF signal by frequency up conversion. The PSD of RF TD-AltBOC(15,10) is showed in Fig. 27.5.

27.5.2 Code Tracking Accuracy

The signal generated from FPGA needs to go through frequency up conversion, adjustable attenuators, frequency down conversion and sampling device module. Eventually, the sampled data is stored as a file the soft receiver can handle. As a result, the code tracking accuracy of TD-AltBOC(15,10) can be tested with software in different CN0 conditions by adjusting the amplitude of the attenuator.

The Fig. 27.6 shows the code tracking of TD-AltBOC(15,10) with SSB (Single Sideband) reception and process in different CN0 conditions. The theoretical curve is showed in this figure as well. The software uses second-order PLL and non-coherent early-late loop to track the code and carrier. The bandwidth of front-end is 70 MHz. The carrier loop bandwidth is 6 Hz. The coherent integration time and the non-coherent accumulation are 1 ms and 1 time respectively. The code loop bandwidth is 2 Hz and the relevant interval (i.e., interval between early code and late code) is Tc (Tc is the code length).

In the Fig. 27.6, from the curve of code tracking accuracy-CN0, it can be seen that when the CN0 of TD-AltBOC(15,10) is in the range of 42–52 dB-Hz, the test result is basically consistent with the theory and the tracking accuracy is better than 0.5 m. However, when the CN0 is lower than 42 dB-Hz, the code tracking

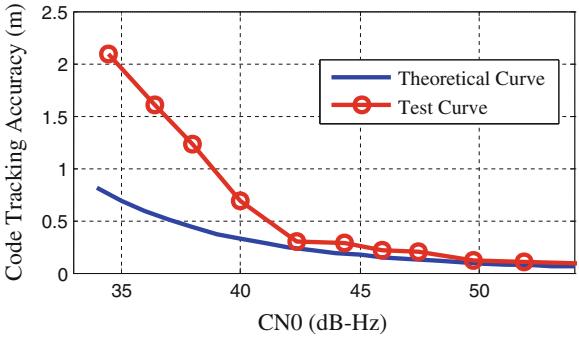

Fig. 27.6 Impact of the CN0 on the code track accuracy

accuracy is deteriorating rapidly and the gap between the test result and the theory is increasing. Analysis of the reasons, the theoretical curve is based on code tracking accuracy model of the non-coherent early-late loop [3]. However, the theoretical model doesn't take consider that the phase detector will enter the nonlinear region when the CN0 is lower, which causes the deterioration of the code tracking accuracy. As a result, the test curve doesn't match the theoretical curve when the CN0 lower than 42 dB-Hz. The code tracking accuracy model of the non-coherent early-late loop is shown in the Eq. (27.7).

$$\sigma^2_{\text{Code,NELP}} = \frac{B_{\text{L}}(1-0.5B_{\text{L}}T_{\text{I}})\int_{-B}^{B} G_{in}(f)\sin^2(\pi f\Delta)df}{\frac{P}{N_0}\left(2\pi\int_{-B}^{B} fG_{in}(f)\sin(\pi f\Delta)df\right)^2}\left(1+\frac{\int_{-B}^{B} G_{c_{in}}(f)\cos^2(\pi f\Delta)df}{\frac{P}{N_0}T_I\left(\int_{-B}^{B} G_{c_{\text{in}}}(f)\cos(\pi f\Delta)df\right)^2}\right) \tag{27.7}$$

In which, B_{L} is the bandwidth of code loop. T_{I} is the integration time. $2B$ is the front bandwidth. $G_{in}(f)$ is the PSD of signal. Δ is the interval of early-late codes. P is the signal power. N_0 is the PSD of Gaussian white noise.

27.5.3 Multipath Test

The multipath signal of TD-AltBOC(15,10) is generated based on the above mentioned multipath simulation method. It then go through all the middle module. Eventually, the multipath signal and the reference signal are received and tracked by the software receivers respectively at the same time. By calculating the difference between the code phases of the multipath signal and the reference signal, the code tracking error can be gotten.

In the process of multipath simulation, the control coefficients of amplitude are quantified by 16 bits. So the accuracy is 1/65,536, about −96 dB. The system clock is 122 MHz. So the accuracy of the code delay is 1/(122.76 MHz), about 8 ns. In short, the simulation accuracy can meet the need of test.

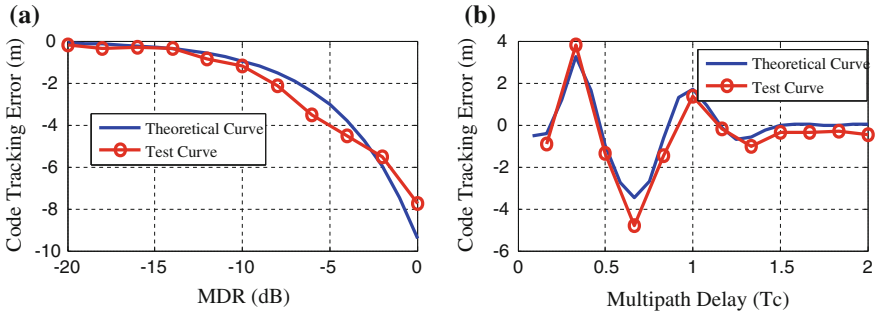

Fig. 27.7 Multipath test result. **(a)** Impact of multipath intensity on the code track error (**b**) Impact of multipath delay on the code track error

The Fig. 27.7a and b are the code tracking error of TD-AltBOC(15,10) with different MDRs (the multipath delay is fixed as half of Tc) and different multipath delays (the MDR is fixed as −10 dB) respectively.

As the Fig. 27.7b shows, the code tracking error fluctuates up and down with the changing of multipath delay, which is different from the envelop waveform in some other papers. The reason is that in the test the reflected signal has code delays relative to the direct signal and the subcarrier of the reflected is delayed as well. For TD-AltBOC(15,10) signal, one code chip corresponds to 1.5 cycles of subcarriers. So when one code chip is delayed, the phase of the subcarrier is delayed with 1.5 cycles (i.e., 540° delay), which causes the conversion between the positive and the negative of code tracking error. However, the curve of multipath delay in some related papers is depicted with a fixed phase delay of the carrier. The theoretical curve of multipath error in the Fig. 27.7b is drawn based on the envelope model [5] (as the Eq. 27.8 shows) of multipath error with the phase flip of carrier taken in count.

$$\varepsilon_\tau = \frac{\pm \widetilde{a_1} \int_{-\beta_r/2}^{\beta_r/2} S(f) \sin(2\pi f \widetilde{\tau_1}) \sin(\pi f d) df}{2\pi \int_{-\beta_r/2}^{\beta_r/2} f S(f) \sin(\pi f d) \left[1 \pm \widetilde{a_1} \cos(2\pi f \widetilde{\tau_1})\right] df} \tag{27.8}$$

In the Eq. (27.8), $\widetilde{a_1}$ represents the amplitude ratio between multipath and direct signal. When the phase difference between the multipath and direct signal is 0°, ± becomes +. And when the phase difference is 180°, ± becomes −. S(f) is the signal PSD. $\widetilde{\tau_1}$ is the multipath delay. β_r represents the front bandwidth of the receiver and d represents the interval of early-late codes.

The test result matches the theory basically. The code tracking error which is caused by multipath signal increases with the MDR. When the MDR is lower than −10 dB, the code tracking error is within 2 m. The code tracking error is impacted greatly by the phase gap between the reflected signal and direct signal. When the phase gap is 0 or 180°, the code tracking error is greatest and when the code delay is greater than 1.5 chips, the code tracking error is almost zero.

27.6 Summery

This article uses the lookup table method to generate TD-AltBOC(15,10) signal and proposes a simulation method of multipath scenarios. The test results of code tracking accuracy and anti-multipath performance match the theories. The platform can provide a source simulator for test and assessment on signal system. The multipath simulation method can achieve the precise control of the parameters, which can reduce the statistical uncertainty of the conventional multipath simulation method. This is good for the test of anti-multipath performance. To test and assess other properties of TD-AltBOC signal, it is needed that the more complex scenarios of higher simulating level are achieved on the basis of the signal generation method this article proposes.

References

1. Tang Z, Zhou H (2011) TD-AltBOC: a new COMPASS B2 modulation. Huazhong University of Science and Technology, Wuhan, pp 1014–1021
2. Yan T, Wei J (2013) Performance analysis on single sideband of TD-AltBOC modulation signal. In: CSNC, pp 91–100
3. Yang Z (2013) Research on key technology of GNSS signals performance assessment. Beihang University, Beijing, pp 75–76
4. Wang L, Li P, Liu C (2011) Study on AltBOC navigation signal technology, In: CSNC
5. Zuping Tang (2009) Research on relevant theory for GNSS signal design and evaluation. Huazhong University of Seience and Technology, Wuhan

Chapter 28
Analysis Method for GNSS Signal Quality Based on Constellation Diagram

Ying Wang, Zhe Su, Yansong Meng and Xiaoxia Tao

Abstract Modern Global Navigation Satellite System (GNSS) signals commonly use very complex modulation and combining method to get diversified and high quality service of navigation, positioning and timing. For that reason, analysis methods of communication signal are not sufficient to reflect navigation signal quality. Based on the analysis of differences between navigation signal and general communication signal, this paper noted concerns and research method of constellation diagram, through real signal generation system, analysed the differences between real signal and ideal signal, proved the method is intuitive and credible through other signal quality analysis methods, and can display more problems of signal generation system and signal quality.

Keywords Constellation diagram · Satellite navigation · Signal quality

28.1 Introduction

Users' receivers realize navigation, positioning and timing function, relying on the signal broadcasted by satellite navigation system, so the quality of satellite navigation signals plays a key role in the evaluation of a satellite navigation system

Y. Wang (✉) · Z. Su · Y. Meng · X. Tao
China Academy of Space Technology (Xi'an), Xi'an 710100, China
e-mail: eaglesoars@126.com

Z. Su
e-mail: eaglesoars@126.com

Y. Meng
e-mail: eaglesoars@126.com

X. Tao
e-mail: eaglesoars@126.com

J. Sun et al. (eds.), *China Satellite Navigation Conference (CSNC) 2014 Proceedings: Volume I*, Lecture Notes in Electrical Engineering 303,
DOI: 10.1007/978-3-642-54737-9_28,

performance. China Beidou Satellite Navigation System (BDS) is rapidly developed recently, and plans to use more complex modulation and combining method. In this case, the general vector signal analyzers and other instruments are not sufficient to fully reflect the signal performance, and therefore it is necessary to develop an intuitive vector signal quality measurement method. In this study, the satellite navigation signals were compared with the general communication signals, and the constellation diagram was proposed for the analysis of satellite navigation signal quality. This method is suitable for the evaluation of signal design and signal transmission signal quality when high SNR (Signal to Noise Ratio) and a large amount of data conditions. The method can be integrated and more finely examines the amplitude and phase information of all the signals added to one frequency carrier, analyzes the error between the theoretical limit and real signal, and evaluates the phase relationship between the signals from various quarters in the combined signal.

28.2 Features of Satellite Navigation Signals

Constellation diagram is developed from the motion of signal along with time and any one-dimension signal can be expressed as a time-variable function of the amplitude and phase. This paper will be focused on the baseband signal.

28.2.1 The Difference from the Communication Signal

Constellation diagram is an analysis method for digital modulation communication signals. It characterizes the signal amplitude and phase distribution with time by description of the accumulated points of two-dimension signal vector points. When many signals were composited, constellation diagram can reflect the phase relationship between the signals. Therefore it is suitable for satellite navigation signal to analysis and the time delay and the channel characteristic.

1. In the communication field, it need to be concerned about the distance between the signal constellation points, and achieve maximum discrimination within the minimum distance, so that the communication signal constellation points generally show distribution, symmetry and other characteristics. The goal is to more fully utilize the limited bandwidth for the transmission data, and to reduce the error rate. The satellite navigation signals are generally transmitted signal bandwidth is sufficient information broadcast message data, and more bandwidth is used to characterize the pseudo-code transition edge to get a more accurate and consistent time portrayed accuracy. So little attention to the information communication system signal transition edge, people only concern signal eye opening for greater tolerance to clock jitter on the sampling time.

For satellite navigation signals, there are two important performance indicators related to correlation peak: an overall height of the correlation peak, it reflects the correlation length and the signal to noise ratio (SNR) of the received signal; another is the sharp characteristic of the correlation peak, which reflects the timing accuracy and precision that receiver can track and achieve. The performance is associated with the design itself and the transition process of the actual received signal transition edges. In addition, due to the correlation operation occurred in all the regions of pseudo-code signal cycle (ideally correlation), a jitter clock showed greater affect.

2. A communication receiver generally received all the data of one frequency or time slot. The modulation scheme is generally simpler. Usually the satellite navigation receivers use a simple way of BPSK or QPSK modulation to receive a part of signal in the complex signals, and these signals independently sufficient for data extraction and ranging for positioning.
3. Navigation satellites need to be long life, high reliability, and considering power amplifier efficiency, the satellite navigation systems often transmit several signals via one channel. It is necessary to modulate by constant envelope technology. The satellite navigation signal is typically a composite signal, the rate of each signal, the power ratio is different, and joined modulation component to form constant envelope modulation, often resulting in an uneven distribution of the position of the satellite navigation signal point in constellation diagram (it is symmetry to center).

28.2.2 Navigation Signal Constellation Concerns

The correlation performance of satellite navigation signals, power amplifier efficiency, and the correlation delay characteristic make major concern requirements focus on these points:

1. IQ vector magnitude consistency (constant envelope performance). After the quantization processing, digital filtering and digital-analog converter (DAC), a noise signal is added and the constellation point is no longer the ideal transition. Hence it is needed to use other methods to assess constant envelope losses such as PAPR.
2. The straight and finesse characteristic when signal constellation point jumping. When the signal constellation point jump, the jumping path of the ideal signal or the signal that through linear systems of group delay constant is always straight. In the time domain, the combined signal component of each channel is always the same clock transition driven (or remains); in the frequency domain, which reflects the symmetry of the signal spectrum. Further, the signal constellation points in time between jumps should overlap each track, reflecting the stability of the signal delay.

3. Signal constellation point symmetry, and the degree of overlap of a circle. This reflects the results of signal distortion channel characteristics of signal amplitude and phase. Such as band-pass filter makes the power attenuation of the signal component far from the center frequency larger, making the ratio of signal power changes, while constant envelope properties are also changed.

28.3 Signal Model

Usually, the first, each base-band satellite navigation signal is generated, and then QPSK, Interplex, CASM, majority voting or other composite method is used to form constant envelope signals.

The baseband signal can be expressed as

$$\tilde{s}_{BB}(t) = s_{IBB}(t) + js_{QBB}(t) \tag{28.1}$$

where $s_{IBB}(t)$ is the in-phase component and $s_{QBB}(t)$ is the quadrature component. The envelope of the composite signal is theoretically constant, so it can be normalized as 28.1. The signal modulated by Intermediate frequency carrier, becomes

$$\tilde{s}_{IF}(t) = \tilde{s}_{BB}(t)e^{j(2\pi f_{IF}t+\varphi)} \tag{28.2}$$

Typically, the baseband signals and IF carrier signals are generated and modulated in the digital domain. So the signal sent to DAC is

$$s_{IF}(t) = \mathrm{Re}[\tilde{s}_{IF}(t)] \tag{28.3}$$

Then the quality of the IF signal can be tested and validated. After the carrier is removed, the signal is given by

$$\tilde{s}_{BIF}(t) = s'_{IF}(t)e^{j(2\pi f_{IF}t+\varphi')} = s_{IIF}(t) + js_{QIF}(t) \tag{28.4}$$

where $s'_{IF}(t)$ is the IF signal into a digital IF signal acquisition device after quantization, digital filtering, digital to analog conversion, analog channel, analog-digital conversion.

After the signal is sent to the DAC converter and filters, combiners and other units, finally it is sent to the amplifier transmitted by the antenna system. For amplifiers and other characteristics described in [1, 2] and so the simulation and the impact on navigation signal quality. Here the simulation and analysis only related in the previous system.

Under-sampling the RF signal, a baseband signal which is removed carrier is given by

$$\tilde{s}_{BRF}(t) = s'_{RF}(t)e^{j(2\pi f_{RF}t+\varphi')} = s_{IRF}(t) + js_{QRF}(t) \tag{28.5}$$

Thus, $s_{IBB}(t)$ and $s_{QBB}(t)$, $s_{IIF}(t)$ and $s_{QIF}(t)$, $s_{IRF}(t)$ and $s_{QRF}(t)$, adding filtering operation, were analyzed and compared.

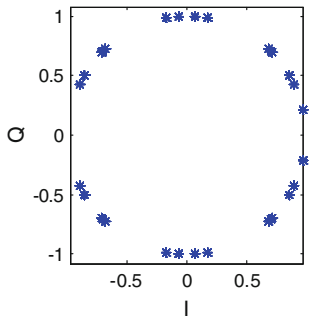

Fig. 28.1 Signal constellation (candidate)

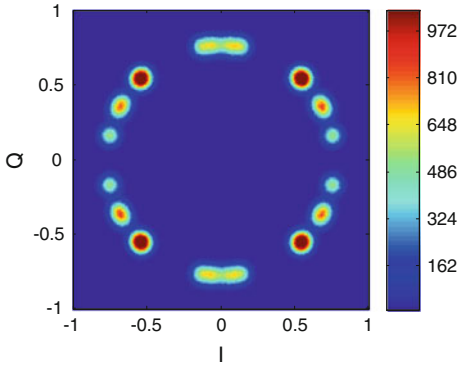

Fig. 28.2 Signal constellation (and noise)

28.3.1 Ideal Signals

Tan et al. [3], presented the signal of Beidou Satellite Navigation System (BDS), which the use of Interplex method, the ideal signal constellation can be shown in Fig. 28.1. The constellation vector can jump between any points and the signal is constant envelope.

Due to the high concentration of the ideal signal constellation point, it is not conducive to doing color temperature distribution analysis. Therefore appropriate to add white Gaussian noise, the color temperature distribution is shown in Fig. 28.2 (normalized to the maximum modulus value). The color of different constellation points is different, but good symmetry.

Under normal circumstances, IF carrier and baseband signal are generated in the digital domain, accompanied by a series of spurious and harmonics. It needs to be low pass filtered for enhancing the desired signal power, suppressing the useful signal band and the power of the unwanted signal. So a 40.92 MHz bandwidth digital linear phase FIR filter is implemented in the generation system for the IF signal. Similarly, for comparison, a real 20.46 MHz baseband filter is used for the ideal signal. After filtering, the constellation diagram is shown in Fig. 28.3. The symmetry is still good, but a large number of transition points appeared, some

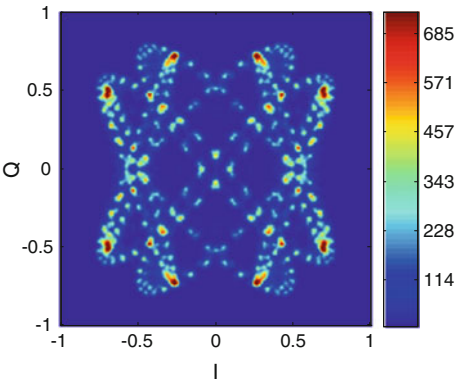

Fig. 28.3 Signal constellation (and filter)

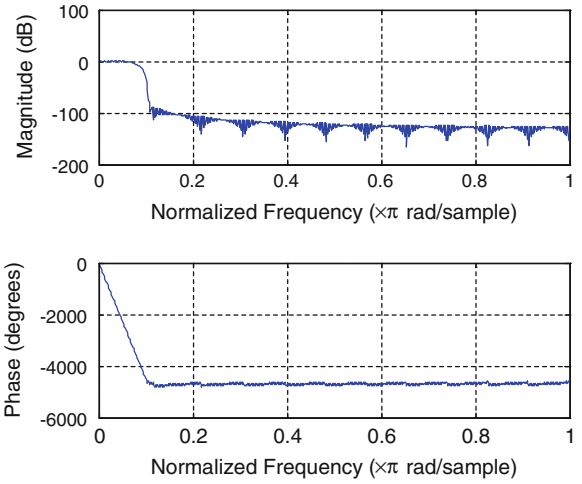

Fig. 28.4 Low pass filter

constellation points moved, meanwhile constant envelope performance dropped. The ideal signal, sampling frequency of 500 MHz, 10 ms length, double-precision floating-point, is generated. The filter is shown in Fig. 28.4. The same filters were used for IF and RF.

28.3.2 IF Signal Analysis

Using the same sample rate for ideal signal and homologous clock, the signal after DAC is acquired. Then Eq. 28.4 is used to convert it to a baseband signal. The constellation diagram is shown in Fig. 28.5. At this time, the '+' frequency component which need filter is contained in the high-frequency part. The signal added filter is shown in Fig. 28.6.

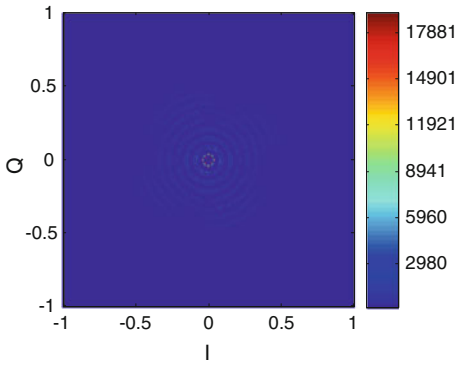

Fig. 28.5 Real signal constellation

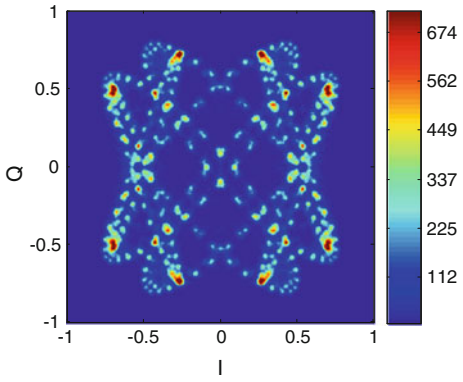

Fig. 28.6 Real signal constellation (add filter)

By filter shown in Fig. 28.4, compared with Fig. 28.3, the constellation diagram is similar, and the symmetry is still good, but the movement locus of the signal points appear bent. In the vector form of the signal constellation diagram, counterclockwise rotation shows the frequency components above the carrier frequency and clockwise rotation shows the frequency components below the carrier frequency.

In the bad case of the symmetry of the spectrum as well as when the delay changes in the time domain, the transition state of bending and rotation will occur. Figure 28.6 shows higher consistency with Fig. 28.3.

The time domain signal is processed of the real part are shown in Fig. 28.7. The time-domain signal has a considerable similarity. As presented, the actual received signal and the ideal signal properties are very close.

The statistical analysis of the data error is shown in Figs. 28.8, and 28.9. The error in the distribution is close to Gaussian distribution. However, by the spectral analysis, the spectral is not white, that means the error contains signal components.

By comparing the power spectral density (PSD) of ideal signal and the measured signal, as shown in Fig. 28.10, we can see the difference is small but obvious. Though it is not easy to locate the problem, but more visually illustrate the gap between the actual signal and the ideal signal.

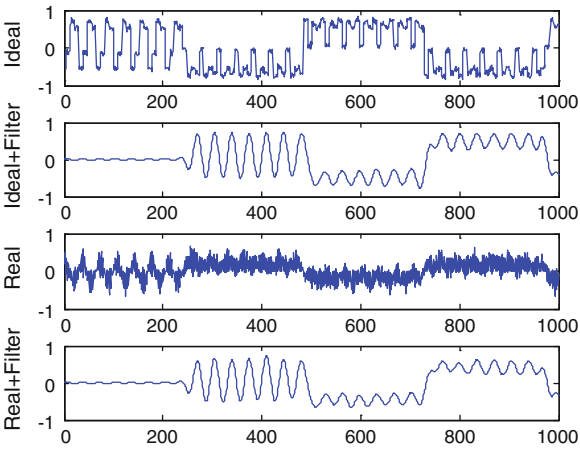

Fig. 28.7 Real part of the ideal and real signal

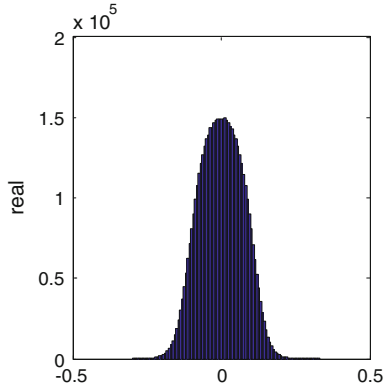

Fig. 28.8 Error histogram

28.3.3 RF Signal Analysis

Compared to the IF signal, after a large number of analog devices, these devices have more or less impact on the RF signal amplitude and phase characteristics. These effects generally are all linear distortion that can be compensated using a filter. The filter usually is asymmetric, variable group delay, complex filter structure. If the channel characteristics are ideal or the hardware resource is not enough, the channel can use linear phase or real filter to compensate.

Then the RF signal is sampled, converted to baseband, using the same filtering policy, a constellation shown in Fig. 28.11. Serious distortion of the signal constellation is shown. The constant envelope properties have heavy losses, followed by the loss of symmetry and with serious deterioration of signal quality. Nonetheless, the constellation points are clear and the center of symmetry is still good, which is the key that signal can be demodulated.

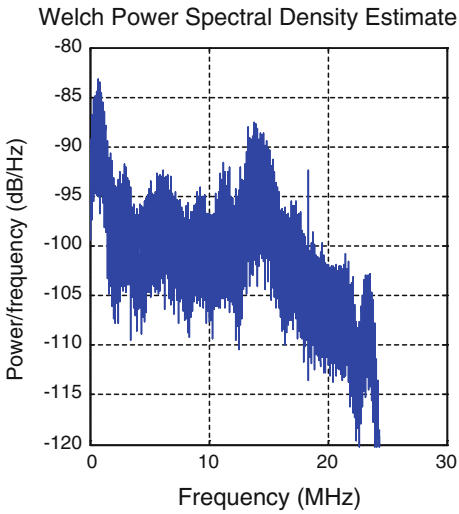

Fig. 28.9 PSD (error)

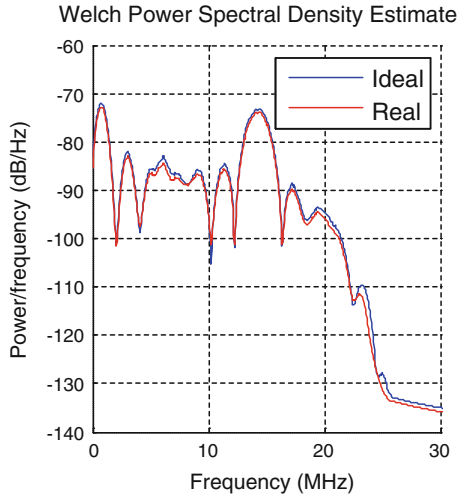

Fig. 28.10 PSD (signal)

The channel amplitude and group delay characteristic parameters are extracted, then the digital signal is processed for pre-distortion using the least squares method to design filters in frequency domain. The RF signal is captured and analyzed. As shown in Fig. 28.12, the constellation symmetry is significantly improved; bilateral symmetry has also been improved to some extent. So we can predict that the correlation characteristics of the signal, PAPR, and the relative delay of each signal has also been greatly improved.

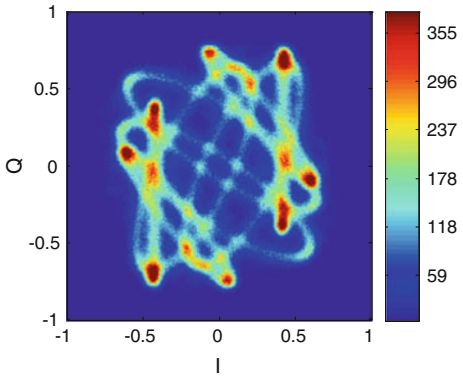

Fig. 28.11 Signal constellation

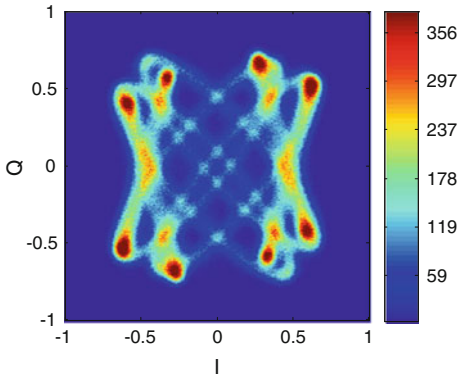

Fig. 28.12 Signal constellation (pre-distortion)

28.4 Testing and Validation

After the analysis, other factors of signal quality need to be considered. This paper selected a few key parameters to be measured and compared.

28.4.1 PAPR

PAPR (Peak-to-average power ratio) is an important parameter to evaluate performance of the constant envelope signals, which make signal PAPR amplifier efficiency greatly improved. Through the statistics of the four signals, the PAPR can prove the constellation expressed intuitive performance. The PAPR statistics are shown in Table 28.1 (unit is 1), the results of each segment are consistent with the constellation of visual expression.

Table 28.1 Peak-to-average power ratio (*PAPR*)

Ideal	IF	Mixer out	Combiner out	Pre-distortion
1.5637	1.6177	1.8214	1.8465	1.7515

Table 28.2 Correlation loss/dB

Ideal	IF	Mixer out	Combiner out	Pre-distortion
0	0.0183	0.0620	0.1646	0.0563

Table 28.3 Delay between B1CD and B1A code/ns

Ideal	IF	Mixer out	Combiner out	Pre-distortion
0	−0.1632	−0.7810	−1.0566	−0.4407

Table 28.4 Delay between B1CD and B1A carrier phase/rad

Ideal	IF	Mixer out	Combiner out	Pre-distortion
0	0.0210	−0.0152	0.2277	0.0613

28.4.2 Correlation Loss

Correlation loss is the main parameter related to satellite navigation signal channel characteristics. Correlation loss cannot be too big for devices which are used in satellite navigation signal generation system. The correlation loss at each stage of treatment is shown in Table 28.2.

28.4.3 Code Phase Consistence

More than one satellite navigation signals are added to a composite signal, so the phase consistency of the signal is directly expressed in constellation diagram. By using time domain correlation algorithm, B1A and B1CD signals relative delays are calculated in Table 28.3.

28.4.4 Carrier Phase Consistence

The consistency of the carrier phase from the single signal including in constant envelope signal, is an important indicator of the signal delay. By calculating the time domain in-phase and quadrature branch compliance with the ideal signal, the signal relative carrier phase delay of B1CD and B1A is shown in Table 28.4.

28.5 Conclusions

This paper analyzed the characters of satellite navigation signal, simulated the signal constellation diagram of complex modulation satellite navigation signal. Constellation diagram analysis method is proved feasible and reliable, and can systematically reflect more aspects of the problems of signal generation system and signal quality than amplitude-frequency testing method.

References

1. Soellner M, Kohl R, Luetke W (2002) The impact of linear and non-linear signal distortions on Galileo code tracking accuracy. In: ION GPS, Portland
2. Huang X, Hu X, Tang Z (2009) Impact of satellite's high power amplifiers on spectrum of navigation signals and PRN tracking accuracy. Chin J Electron 37(3):P640–P645
3. Tan S, Zhou B, Guo S, Liu Z (2010) Design of China global satellite navigation signals. In: CSNC, Beijing

Chapter 29
Navigation Satellite Fault Diagnosis, Prognosis and Evaluation System for On-orbit Application

Jia Guo, Yuqian Pan, Chonghua Liu and Wenjing Feng

Abstract As the core of spacecraft health management, fault diagnosis and prognosis are important for on-orbit reliability. Ground system is necessary due to limited on-board processing resource and infrequent fault data. A navigation satellite fault diagnosis, prognosis and evaluation system is proposed for on-orbit application. The system includes data interface module, satellite data simulation module, fault diagnosis, prognosis and evaluation module, system control and graphical user interface module, database module. To support analysis of on-orbit data, telemetry data interface is provided. Fault simulation is embedded for generating normal and fault data as data supporting for technology verification. The distributed system provides various fault diagnosis and prognosis methods with extensibility.

Keywords Navigation satellite · On-orbit application · Fault diagnosis · Fault prognosis · Dynamic evaluation

29.1 Introduction

Navigation satellite system based on multi-satellite constellation requires continuous and stable operation. If on-orbit satellite failure occurs without timely processing, it may result in deterioration of system service availability, even in direct impact on system applications effect. Therefore, timely and effective fault diagnosis and prognosis is important for guaranteeing high reliability and stable operation of on-orbit satellites [1–3].

J. Guo (✉) · Y. Pan · C. Liu · W. Feng
Institute of Spacecraft System Engineering, China Academy of Space Technology, Beijing, China
e-mail: guojia.gm@gmail.com; guojia_email@163.com

J. Sun et al. (eds.), *China Satellite Navigation Conference (CSNC) 2014 Proceedings: Volume I*, Lecture Notes in Electrical Engineering 303,
DOI: 10.1007/978-3-642-54737-9_29,

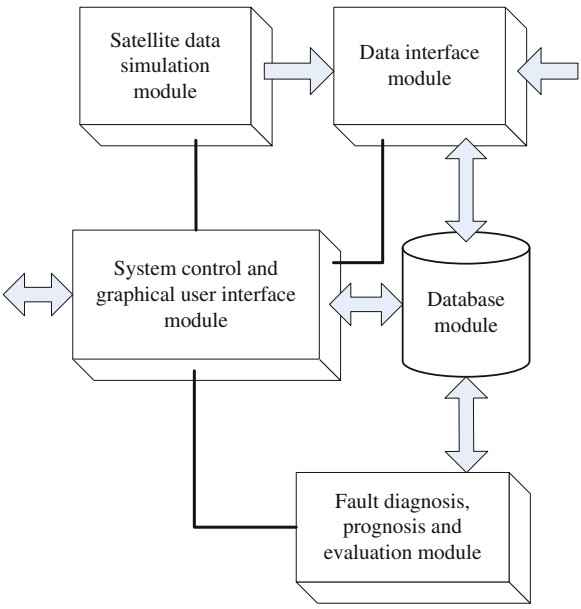

Fig. 29.1 Block diagram of system architecture

Currently, ground system is necessary for fault diagnosis and prognosis due to limited on-board processing resource and infrequent fault data, only a small amount of health management tools are implemented on-board [4, 5]. On-orbit telemetry data reflects the health status of satellite. This paper proposes a navigation satellite fault diagnosis, prognosis and evaluation system for on-orbit application using telemetry data to achieve timely diagnosis and prognosis of faults, and provide necessary technical means for on-orbit dynamic evaluation.

29.2 System Architecture and Functionality

29.2.1 System Architecture

The system includes data interface module, satellite data simulation module, fault diagnosis, prognosis and evaluation module, system control and graphical user interface module, database module. Figure 29.1 shows the system architecture.

Distributed system platform is constructed to guarantee long-term reliable operation of the system, and system expandability to meet the demand for the large number of satellites in navigation satellite system and the characteristics of complex data types. Each component module can be arranged separately in different nodes, as required to achieve predetermined functionality. Information flows through the shared network of nodes. The system can assign task to multiple nodes, reducing system's reliance on single node. During maintenance of node,

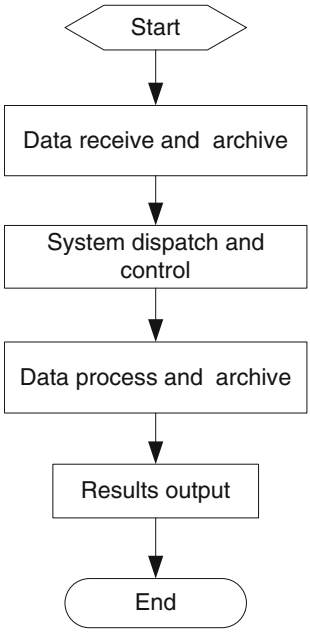

Fig. 29.2 System workflow

normal operation of the system can be achieved. Overall system operation should not be affected by failure of a small number of nodes to safeguard long-term reliable operation.

Main functionalities of the system modules are illustrated below.

- Data interface module—Information interaction with internal and external data source.
- Satellite data simulation module—Using fault simulation technology to simulate generation of satellite normal and fault data.
- Fault diagnosis, prognosis and evaluation module—Providing various fault diagnosis, prognosis and evaluation methods.
- System control and graphical user interface module—Implementation system task allocation, human-computer interaction and visualization.
- Database module—Supporting various types of data storage, query and output.

29.2.2 System Functionality

The system implements fault diagnosis and prognosis based on telemetry data, and provide necessary technical means for on-orbit dynamic evaluation. Typical system workflow is illustrated in Fig. 29.2.

- Data interface module receives telemetry data from on-orbit satellite ground system (or satellite data simulation module). After deframing, unpacking and

format converting according to telemetry data protocol, data is archived to database. Telemetry data definition and telemetry data protocol stored in database are invoked by data interface module.
- System control and graphical user interface module pre-read system work plan from database to sent scheduling control commands to fault diagnosis, prognosis and evaluation module, and monitor the progress of system work plan.
- Fault diagnosis, prognosis and evaluation module reads telemetry data and algorithms configuration data from database under scheduling control commands, and invokes built-in algorithms to implement fault diagnosis and prognosis. After completion of current processing task, the processing results should be timely archived into database, and completion situation should be transmitted.
- System control and graphical user interface module, according to user settings, visualize processing results, output files, etc.

29.3 Key Module Design

29.3.1 Data Interface Module

Data interface module implements information interaction with internal and external data source, using external data interface with on-orbit satellite ground systems to support fault diagnosis and prognosis analysis based on actual operating data. Meanwhile, the module receives simulation data using internal data interface with satellite data simulation module. Data interface module includes data converter sub-module and database operation sub-module.

Data converter sub-module receives the telemetry data stream, decomposes to telemetry frames according to preset telemetry protocol, deframes and unpacks the frames according to frame format, converts to engineering data with physical meaning according to telemetry data definition.

Database operation sub-module reads the preset data in database for data converter sub-module using when data interface module initializes. Upon completion of data conversion, database operation sub-module archives all the engineering data and original data for further analysis in fault diagnosis, prognosis and evaluation module.

Figure 29.3 shows the workflow of data interface module.

29.3.2 Satellite Data Simulation Module

Using principles and empirical models, satellite data simulation module can simulate the real satellite health status and generate normal and fault status, then send data in the form of telemetry data to data interface module. The module

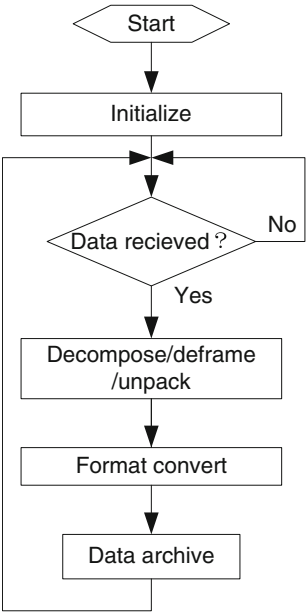

Fig. 29.3 Data interface module workflow

provides necessary technical data to support pre-verification and analysis of algorithms.

Simulated data within the simulation module should have interchangeability with external data from on-orbit satellite. All the data format definition should follow the uniform telemetry protocols. In practical application, system users can choose to use different data source according to the needs.

In the process of using the system, the data generating models in satellite data simulation module can be further modified to improve simulation accuracy by comparison of the simulated data and real data from on-orbit satellite.

29.3.3 Fault Diagnosis, Prognosis and Evaluation Module

Fault diagnosis, prognosis and evaluation module is the core module of the system, implementing fault diagnosis and prognosis through reading telemetry data and algorithms configuration data. The module includes algorithm control sub-module, threshold determination sub-module, complex diagnosis sub-module, and prognosis module.

Algorithm control sub-module invokes algorithm sub-modules under scheduling control commands. After processing, the sub-module transmits completion situation to system control and graphical user interface module, and then continues to wait for the next command.

Threshold determination sub-module quickly determines the received real-time telemetry data in which threshold range according to the preset value of the

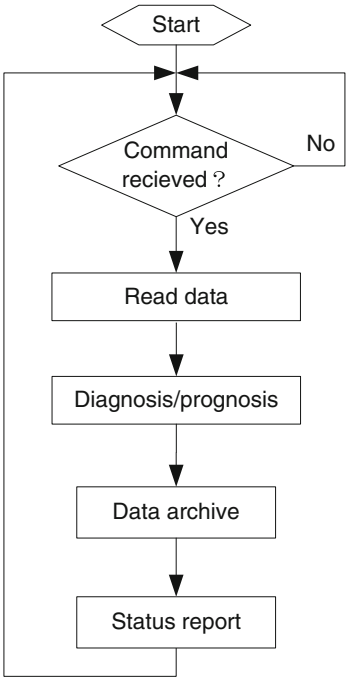

Fig. 29.4 Diagnosis and prognosis workflow

interval, and accordingly transmits the corresponding alarm level to database. Threshold determination algorithm is simple and fast, can be adopted to monitor on-orbit satellite telemetry data in real-time. Threshold judgment can be preliminary diagnosis to quickly determine whether a single telemetry data is failure.

For complex associated fault problems, the same fault will lead to changes in a number of telemetry data, using a single telemetry data cannot be adequate for accurate diagnosis. Complex diagnosis sub-module can further improve the diagnosis accuracy, to obtain more detailed diagnostic information. Algorithms built in the sub-module are complex and difficult to achieve real-time diagnosis, generally gives a comprehensive diagnosis result based on telemetry data in specific time period according to system schedule and control commands. Built-in algorithms include Chaotic Analysis, Kalman Filtering, Artificial Neural Networks, Support Vector Machines and other diagnostic algorithms with extensibility.

Effectively predict before failure, and accordingly take actions in advance, that can be beneficial for stable operation of on-orbit satellites. Prognosis module predicts future data trends to make failure prediction based on the results. Built-in algorithms include Regression Analysis, Kalman Filtering, Gray System Model, Hidden Markov Model, Artificial Neural Networks, Support Vector Machines and other prognostic algorithms with extensibility.

Figure 29.4 shows the workflow of fault diagnosis, prognosis and evaluation module.

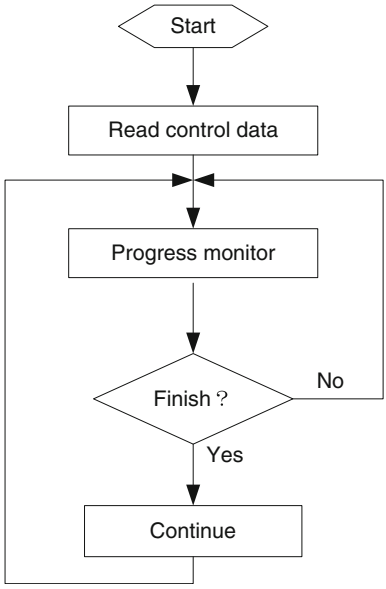

Fig. 29.5 System control workflow

29.3.4 System Control and Graphical User Interface Module

System control and graphical user interface module controls fault diagnosis, prognosis and evaluation module to complete task combined with progress of task arrangement. The module includes scheduling sub-module, progress monitor sub-module, database operation sub-module, interaction and visualization sub-module.

Scheduling sub-module send control commands in order by system scheduling data sheets and data processing progress. Progress monitor sub-module can monitor task progress, immediately arrange for the next step when the current task is completed. Typical scheduling process is shown in Fig. 29.5.

Interaction and visualization sub-module implements the graphical user interface, supports data query, write/read, delete and other operations by database operation sub-module, and visualizes data processing results.

29.3.5 Database Module

Database module is the system data hub, including telemetry format definition table, telemetry data table, algorithm configuration table, system scheduling table, data processing results table and other tables.

Telemetry format definition table is read when data interface module is initializing for pre-processing, data frame and data definition are adopted after receiving telemetry data.

Telemetry data table is data sources for diagnosis and prognosis consisted of pre-processed telemetry data. Algorithm configuration table is read by fault diagnosis, prognosis and evaluation module.

System control and graphical user interface module reads system scheduling table to send control commands. Task scheduling data includes algorithms currently used, data processing objects, and time labels, etc.

Data processing results table is designed for storing results generated by fault diagnosis, prognosis and evaluation module.

29.4 Conclusion

This paper proposes a navigation satellite fault diagnosis, prognosis and evaluation system for on-orbit application using telemetry data to implement timely fault diagnosis, prognosis and evaluation. With the gradual accumulation of on-orbit data, built-in algorithms can be further expanded and enhanced to improve system performance.

References

1. Carlos G, Alan C (2005) Health management and automation for future space systems. In: AIAA 2005–6803. AIAA, Washington
2. Baroth E (2001) IVHM techniques for future space vehicles. AIAA 2001–3523. AIAA, Washington
3. Saha B, Saha S, Goebel K (2009) A distributed prognostic health management architecture. In: Proceedings of MFPT
4. Gordon B (2005) A review of system health state determination methods. In: AIAA 2005–2528. AIAA, Washington
5. Inseok H, Sungwan K, Youdan K, Seah C (2010) A survey of fault detection, isolation and reconfiguration methods. IEEE Trans Control Syst Technol 18(3):636–653

Chapter 30
Investigation/Research and Implementation of Trajectory Generation in GNSS Simulation

He Li, Chengdong Xu and Pengfei Zhang

Abstract GNSS (Global Navigation Satellite System) simulation system is a powerful tool for designing GNSS and researching the related problem of that efficiently. The trajectory and motion information generation of vehicles is an important part of scenario design in GNSS simulation system. In this part, the trajectory generation based on waypoint data is the most complicated. It involves the trajectory planning, vehicle kinematics, solution of geodetic problem and other related research fields. The trajectory generation based on waypoint set by the user is an inverse solution of geodetic problem actually. According to the study and comparison of different solutions of geodetic problem, and taking into account the requirement of the vehicle trajectory accuracy and computation complexity in GNSS simulation system, an inverse solution of geodetic problem based on the local earth reference ellipsoid and partial spherical assumption is put forward in this paper. Compared with the existing algorithms, a certain availability of the inverse solution in this paper within the limits is verified. Given the kinematics characteristics of vehicles, ships and aircrafts, the corresponding method of waypoint trajectory generation is designed. At last, the solution mentioned above is implemented by C#, and it has also been applied to a GNSS simulation platform successfully.

Keywords GNSS · Simulation · Trajectory generation · Geodetic problem · Implementation

H. Li (✉) · C. Xu · P. Zhang
Key Laboratory of Dynamics and Control of Flight Vehicle, Ministry of Education, School of Aerospace Engineering, Beijing Institute of Technology, Beijing, China
e-mail: chinabv@sina.com

J. Sun et al. (eds.), *China Satellite Navigation Conference (CSNC) 2014 Proceedings: Volume I*, Lecture Notes in Electrical Engineering 303,
DOI: 10.1007/978-3-642-54737-9_30,

30.1 Introduction

GNSS (Global Navigation Satellite System) simulation system is a powerful tool for designing GNSS and researching the related problem of that efficiently. Scientists and engineers can make use of the simulation system for research on fields of satellite navigation, and it is beneficial in cost and efficiency. Meanwhile, a large number of researchers have focused on the research object. In a GNSS simulation system, the trajectory and motion information generation of vehicles is an important part of scenario design. In this part, the trajectory generation based on waypoint data is the most complicated. It involves the trajectory planning, vehicle kinematics, solution of geodetic problem and other related research fields.

The trajectory generation based on the known waypoints is an inverse solution of geodetic problem actually. Since more than one hundred years, many mathematicians and geodetic scientists come up with a wide variety of calculating formulas and methods of geodetic problem [1]. According to incomplete statistics, there are more than 70 kinds of calculating formulas and methods of geodetic problem used in space technology and national defense, aviation and marine, etc. [2]. According to the theoretical basis for these solutions, the existing solutions of geodetic problem can be divided into five categories: (1) a solution suitable for short distance (less than 200 km) based on geodetic line differential equation in the geodetic coordinate system, such as a Gaussian average argument method [2]; (2) a solution based on the auxiliary spherical projection, such as a Bessel method and a nested coefficient method [2]; (3) a solution based on a map projection, such as a TAyMAH projection formula [3]; (4) a solution with numerical integration of geodetic line differential equation directly [4]; (5) a solution based on the other lines beyond the geodetic line, such as a chord line method and a normal cutting line method [5]. Different solutions have their own characteristics, some solutions have heavy steps which need iterative calculating repeatedly; some solutions have singular results, it cannot be solved when two waypoints locate on the equator or the longitude circle at the same time; some other solutions only apply to the situation of short line, a larger error will be brought in the situation of a longer line.

According to the analysis and summary of the previous studies, combined with the application of geodetic problem in GNSS simulation system, and taking into account the requirement that the vehicle trajectory generated is not very close to the geodetic line and the algorithm is needed to be simple with less calculation for real-time simulation, a simplified algorithm for an inverse solution of geodetic problem is proposed in this paper. Based on this algorithm, this paper designs a trajectory generation method with waypoint data combined with the kinematics characteristics of different vehicles.

30.2 Inverse Solution of Geodetic Problem

30.2.1 A Simplified Algorithm for Inverse Solution of Geodetic Problem

The starting point P_k and ending point P_{k+1} of motion for vehicle are known, and the geodetic coordinates of them are (λ_k, φ_k) and $(\lambda_{k+1}, \varphi_{k+1})$ respectively, where λ is longitude and φ is latitude. Then, the inverse solution of geodetic problem is to calculate the length of geodetic line between P_k and P_{k+1}, the azimuth angle $\psi_{k,k+1}$ at the starting point P_k and the back azimuth angle $\psi_{k+1,k}$ at the ending point P_{k+1}.

As shown in Fig. 30.1, the position of the ending point P_{k+1} relative to the starting point P_k can be represented in four situations as A, B, C and D, namely P_{k+1} is respectively located in the northeast, southeast, southwest and northwest of P_k. In Fig. 30.1, M is an intersection point of the longitude circle through P_k and the big circle through A and D which is located on the minor arc between A and D; N is an intersection point of the longitude circle through P_k and the big circle through B and C which is located on the minor arc between B and C; MP_kN is a meridian circle; DMA and CNB are both prime vertical circles.

Regulation: east longitude is positive, west longitude is negative; north latitude is positive and south latitude is negative. Because of the influence of the latitude and longitude with positive or negative values, it is divided into four kinds of situations to solve according to the position of ending point P_{k+1} on reference ellipsoid and the relative position of P_k and P_{k+1}. The four situations are as follows:

(a) The ending point P_{k+1} is located in the northern hemisphere and to the north of the starting point P_k, namely $\varphi_{k+1} \geq 0, \varphi_{k+1} \geq \varphi_k$;
(b) The ending point P_{k+1} is located in the northern hemisphere and to the south of the starting point P_k, namely $0 \leq \varphi_{k+1} \leq \varphi_k$;
(c) The ending point P_{k+1} is located in the southern hemisphere and to the south of the starting point P_k, namely $\varphi_{k+1} \leq \varphi_k, \varphi_{k+1} \leq 0$;
(d) The ending point P_{k+1} is located in the southern hemisphere and to the north of the starting point P_k, namely $0 \geq \varphi_{k+1} \geq \varphi_k$.

Now the geodetic problem is solved in the situation of (a) as an example, the results of other situations are presented directly.

Figure 30.2 is a profile view along the meridian plane MP_kN, where point P'_{k+1} is the projection of the ending point P_{k+1} on the meridian plane MP_kN, the geodetic coordinate of it is $(\lambda_k, \varphi_{k+1})$; a is the length of AO; b is the length of AB.

According to the main curvature radius formula, the following equation can be obtained.

$$OP_k = R_e[1 - 2e + 3e\sin^2(\varphi_k)] \tag{30.1}$$

where R_e is the reference radius of the earth, e is the eccentricity of the reference ellipsoid.

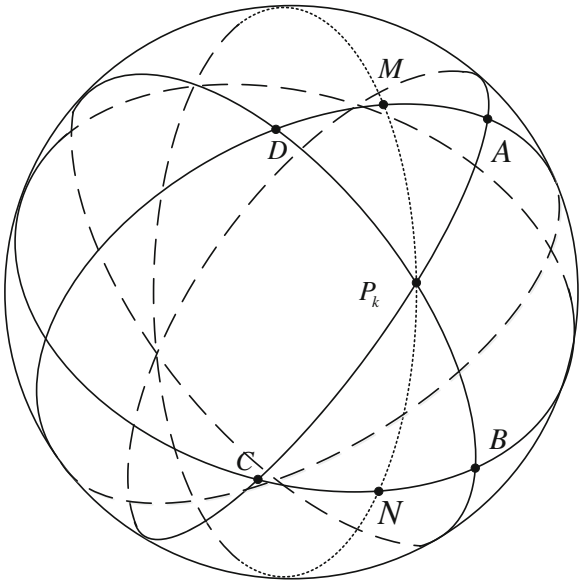

Fig. 30.1 The relative position of starting point and ending point

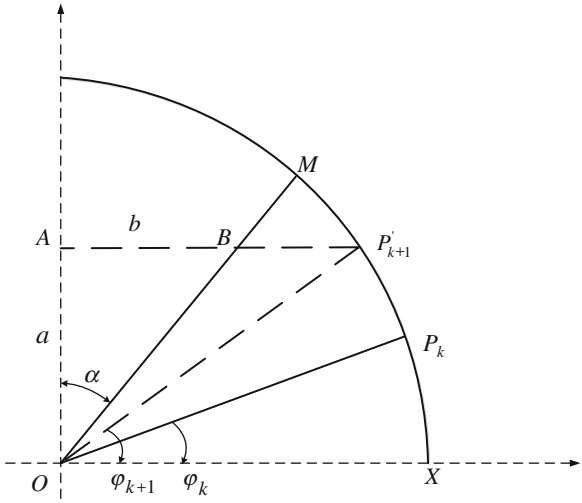

Fig. 30.2 Profile view of the meridian plane

In general, the waypoints selected are relatively close within 10 km [6], meanwhile, the eccentricity of the reference ellipsoid is lesser, so it can be seen $OP_k = OX = OM$ approximately.

As shown the geometric relationship in Fig. 30.2:

$$\angle MOP_k = \pi/2 - \alpha - \varphi_k \tag{30.2}$$

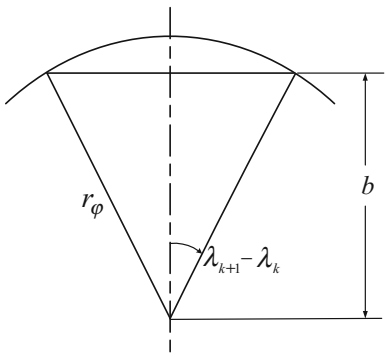

Fig. 30.3 Profile view of the parallel plane

$$\angle AP'_{k+1}O = \angle P'_{k+1}OX = \varphi_{k+1} \tag{30.3}$$

then

$$a = OP'_{k+1} \cdot \sin(\varphi_{k+1}) = OP_k \cdot \sin(\varphi_{k+1}) \tag{30.4}$$

From the profile view of the parallel plane through P_k (as shown in Fig. 30.3), the value of b can be got.

$$b = r_\varphi \cdot \cos(\lambda_{k+1} - \lambda_k) \tag{30.5}$$

Where r_φ is the radius of the parallel circle.

$$r_\varphi = OP_{k+1} \cdot \cos(\varphi_{k+1}) \tag{30.6}$$

Then

$$\alpha = \arctan\left(\frac{b}{a}\right) \tag{30.7}$$

According to the above formulas and on the basis of partial spherical assumption, the following formula can be obtained.

$$\overset{\frown}{P_kM} = \frac{\pi}{2} - \varphi_k - \arctan\left[\frac{\cos(\varphi_{k+1}) \cdot \cos(\lambda_{k+1} - \lambda_k)}{\sin(\lambda_{k+1})}\right] \tag{30.8}$$

Similarly, the following conclusions can be got according to a similar derivation process:

(a) P_{k+1} is located in the northern hemisphere, and it is to the north of P_k:

$$\overset{\frown}{P_kM} = \frac{\pi}{2} - \varphi_k - \arctan\left[\frac{\cos(|\varphi_{k+1}|) \cdot \cos(|\lambda_{k+1} - \lambda_k|)}{\sin(|\varphi_{k+1}|)}\right] \tag{30.9}$$

(b) P_{k+1} is located in the northern hemisphere, and it is to the south of P_k:

$$\overset{\frown}{P_kM} = -\frac{\pi}{2} + \varphi_k + \arctan\left[\frac{\cos(|\varphi_{k+1}|) \cdot \cos(|\lambda_{k+1} - \lambda_k|)}{\sin(|\varphi_{k+1}|)}\right] \tag{30.10}$$

(c) P_{k+1} is located in the southern hemisphere, and it is to the north of P_k:

$$\overset{\frown}{P_kM} = -\frac{\pi}{2} - \varphi_k + \arctan\left[\frac{\cos(|\varphi_{k+1}|) \cdot \cos(|\lambda_{k+1} - \lambda_k|)}{\sin(|\varphi_{k+1}|)}\right] \tag{30.11}$$

(d) P_{k+1} is located in the southern hemisphere, and it is to the south of P_k:

$$\overset{\frown}{P_kM} = \frac{\pi}{2} + \varphi_k - \arctan\left[\frac{\cos(|\varphi_{k+1}|) \cdot \cos(|\lambda_{k+1} - \lambda_k|)}{\sin(|\varphi_{k+1}|)}\right] \tag{30.12}$$

So far, $\overset{\frown}{P_kM}$ has been expressed. DMA and MP_kN are two orthogonal circles, so the spherical angle $\angle AMP_k = \pi/2$. The problem can be solved based on the partial spherical assumption only when $\overset{\frown}{MA}$ is obtained.

As shown in Fig. 30.4, θ represents the great arc $\overset{\frown}{AM}$.

From the geometric relationship shown in Fig. 30.4, it can be seen that:

$$r_1 \cdot \sin(|\lambda_k - \lambda_{k+1}|) = r_2 \cdot \sin\theta \tag{30.13}$$

where

$$\frac{r_1}{r_2} = \cos(|\varphi_{k+1}|) \tag{30.14}$$

so

$$\theta = \arcsin\left(\cos(|\varphi_{k+1}|) \cdot \sin(|\lambda_k - \lambda_{k+1}|)\right) \tag{30.15}$$

namely

$$\overset{\frown}{AM} = \theta = \arcsin\left(\cos(|\varphi_{k+1}|) \cdot \sin(|\lambda_k - \lambda_{k+1}|)\right) \tag{30.16}$$

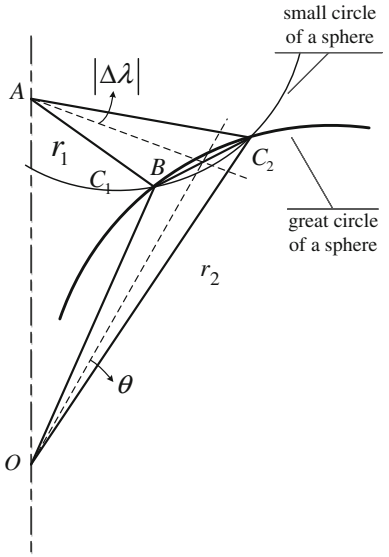

Fig. 30.4 Calculate the length of the great arc

Based on the partial spherical assumption, spherical angle $\angle MP_kA$ can be got according to the spherical triangle theorem.

According to the spherical triangle cosine theorem,

$$\cos \overset{\frown}{AP_k} = \cos \overset{\frown}{MA} \cdot \cos \overset{\frown}{MP_k} + \sin \overset{\frown}{MA} \cdot \sin \overset{\frown}{MP_k} \cos(\angle AMP_k) \tag{30.17}$$

where $\angle AMP_k = \pi/2$, so

$$\overset{\frown}{AP_k} = \arccos\left(\cos \overset{\frown}{MA} \cdot \cos \overset{\frown}{MP_k}\right) \tag{30.18}$$

and by the spherical triangle sine theorem,

$$\angle MP_kA = \arcsin\left(\sin \overset{\frown}{MA} / \sin \overset{\frown}{AP_k}\right) \tag{30.19}$$

The relative position between P_k and P_{k+1} is uncertain, so $\psi_{k,k+1}$ can be expressed as follows according to the position relationship between the starting point and the ending point which is shown in Fig. 30.1:

the case with point A: $\psi_{k,k+1} = \angle MP_kA$;
the case with point B: $\psi_{k,k+1} = \pi - \angle MP_kA$;
the case with point C: $\psi_{k,k+1} = \pi + \angle MP_kA$;
the case with point D: $\psi_{k,k+1} = 2\pi - \angle MP_kA$.

Calculate the mean radius R

$$R = \frac{OP_k + OP_{k+1}}{2} \tag{30.20}$$

The mean radius can be replaced by that of the middle latitude. In the case of the latitude with larger span, it is more accurate, namely

$$R = R_{(\varphi_k + \varphi_{k+1})/2} \tag{30.21}$$

then the quasis geodetic length S of geodetic line arc $\overset{\frown}{AP_k}$ is

$$S = R \cdot \overset{\frown}{AP_k} \tag{30.22}$$

So far, the problem has been solved.

30.2.2 Examples and Results Analysis

Inspired by the paper of He Ju from Wuhan University [7], the algorithm proposed in this paper is implemented based on MATLAB development platform. In this paper, 5 examples are selected, and the results are got and analyzed.

30.2.2.1 Examples

Following the references [7–10], 5 examples are set, where the 1st example [8] is short distance example, the 2nd example [8] is middle distance example and the 3rd–5th examples are long distance example. The data of the 1st and the 2nd examples cite the book "Ellipsoid Geodesy Research" written by Zhao [8]; the data of the 3rd example cites the book "Ellipsoid Geodesy" written by Chen and Chao [9]; the data of the 4th example cites Ref. [10]; the data of the 5th example cites Ref. [7]. Where the 3rd example shows that the longitudes are just opposite in sign and the 4th example shows that the latitudes are just opposite in sign; the 5th example is that the starting point and the ending point are located on the equator together.

30.2.2.2 Results and Analysis

As shown in Table 30.1, the results of the 5 examples in the above solution of geodetic problem are presented. Analyzing the results, we can see that the scale error ratio (the ratio between the absolute value and the reference value, where the absolute value is that of the difference between the result of the solution and the reference value, namely, $\gamma = |S - S_R|/|S_R|$) of the solution are all less than 0.5 %, and the least one is just 0.0000000008 %. The results when the starting point is

Table 30.1 Examples of the inverse solution of geodetic problem

Examples	80 km level	410 km level	8,000 km level	15,000 km level	Equator point
Reference ellipsoid	Krasovsky	Krasovsky	Krasovsky	Krasovsky	International ellipsoid 1975
λ_k	130°10′12.2676″	115°10′00.0000″	33°05′00.0000″	90°00′00.1100″	100°00′00.0000″
φ_k	40°02′35.6784″	40°02′35.6784″	68°58′00.0000″	35°00′00.2200″	00°00′00.0000″
λ_{k+1}	130°12′1.104″	118°10′03.000″	−122°26′00.0057″	215°59′04.3380″	10°00′00.0000″
φ_{k+1}	40°45′47.9027″	43°00′55.8784″	37°44′59.9755″	−30°29′20.9640″	00°00′00.0000″
S (m)	79,804.965	413,356.407	7,960,499.005	14,976,684.272	10,018,758.8838
$\psi_{k,k+1}$	01°49′49.6691″	36°13′51.7682″	339°05′11.1169″	98°55′09.8936″	270°00′00.0000″
S_R (m)	80,000.000	414,306.538	7,999,606.380	15,000,000.200	10,018,758.883
$\psi_{(k,k+1)R}$	01°49′43.004″	36°12′01.027″	339°49′56.385″	100°00′00.3300″	270°00′00.0000″
Scale error ratio	0.002437932680945	0.002293304099928	0.004888662448621	0.001554381864492	0.000000000008

located in the low or middle latitudes are better than that in the high latitudes. However, the precision is enough to satisfy the requirement of the accuracy of the trajectory generated in scenario design in GNSS simulation system.

In Table 30.1, S_R and $\psi_{(k,k+1)R}$ are reference values.

The algorithm proposed by this paper can meet the inverse solution of geodetic problem whatever in the following situations: across the equator, across the eastern and western hemispheres, and the starting point and ending point are both located on the equator, more importantly, there will not be a singular phenomenon. There are some advantages among the current solutions: Bessel algorithm cannot solve the problem when the starting point and ending point are both located on the equator [7]; Gaussian average argument method has a larger error in the situation of long distance than that of the algorithm proposed by this paper. In addition, in this paper, the algorithm is relatively simple, it doesn't need heavy and complicated calculation, and the implementation by program is relatively simple.

30.3 Trajectory Generation and Implementation

Vehicles cannot move along the broken line, that is to say there cannot be a sudden change in the azimuth angle of the vehicle, so the situation that the azimuth angle of the vehicle is not equal to that of expectation ($\psi_{k,k+1}$ mentioned above) should be taken into consideration, when the above algorithm is applied to vehicle trajectory generation.

30.3.1 Methods of Trajectory Generation

Based on the consideration that the initial azimuth angle of the vehicle may not be equal to the expectant azimuth angle, a turning movement should be added at the initial period of the vehicle movement along the waypoints, and the actual azimuth angle of the vehicle should be adjusted to the expectant azimuth angle, then the vehicle continues to move along the quasi geodetic line.

According to the algorithm of the inverse solution of geodetic problem proposed by this paper, the expectant azimuth angle $\psi_{k,k+1}$ at the starting point and the length of quasi geodetic line S can be solved firstly, and then the corresponding turning process and the movement along geodetic line can be designed based on the kinematic characteristics of different vehicles. For aircraft, due to the dynamic and kinematic characteristics are complicated, bank-to-turn model which is used in general is applied to design turning process, the turning model can be expressed as follows:

$$\dot{\psi} = -\frac{g_0 \cdot \sin\gamma}{V \cdot \cos\gamma} \tag{30.23}$$

where $\dot{\psi}$ is yaw angular velocity, γ is roll angle, V is the velocity of aircraft. The velocity V can be got according to the previous flight status, and then $\dot{\psi}$ can be solved based on γ designed by user. However, the position of the aircraft is changing with the rotation of the aircraft, so the inverse geodetic problem should be solved in real time so that each instantaneous expectant azimuth angle $\psi_{k,k+1}$ and the length of quasi geodetic line S can be got until the expectant azimuth angle is equal to the current azimuth angle.

For cars and ships, the dynamic and kinematic characteristics (ignore the influence and constraints of road and sea conditions on the movement firstly, and then add them separately after solving them, namely default that the car movement is not restricted by terrain, the yawing, heaving and rolling of ships produced by sea conditions have few influence on the movement along waypoints) are more simple than that of aircraft relatively, so the turning movement of them can be expressed as follows:

$$\omega = \frac{V}{r} \tag{30.24}$$

where ω is the angular velocity, r is the turning radius. In the same way, the inverse geodetic problem should be solved in real time during the turning adjustment of cars and ships.

The movement along quasi geodetic line can be started after the azimuth angle of the vehicle has been adjusted. According to the current S and V, the time of the movement along geodetic line can be got $t = S/(V \cdot \cos\theta)$ (θ is the pitch angle of the vehicle), the vehicle moves along geodetic line in t and adjusts the height. The aircraft flies in cruise speed among waypoints in general, so the velocity should be adjusted to cruise speed before the aircraft starts the movement along quasi geodetic line.

30.3.2 An Example of Implementation

We take Visual Studio 2010 from the Microsoft Company as a development platform and take C# as a programming language, the movement of aircrafts, cars and ships along waypoints is implemented according to the above method, and it has been applied to a GNSS simulation platform successfully. The flight of aircraft along waypoints is taken as an example, the flight mission is shown in Table 30.2.

According to the mission shown in Table 30.2, combined with the method of trajectory generation along waypoints proposed by this paper, the flight trajectory along the waypoints of the aircraft is shown in Fig. 30.5.

Table 30.2 Flight mission list

Waypoints	Coordinates (longitude, latitude, height)
Starting point	(E116°34′26.61″, N40°04′27.21″, 32 m)
Waypoint 1	(E127°06′54.28″, N35°34′01.34″, 8,000 m)
Waypoint 2	(E139°46′10.25″, N35°33′33.61″, 8,000 m)
Ending point	(E121°33′52.94″, N25°04′08.91″, 4 m)

The starting point is the capital airport runway L36, and the ending point is the Taipei Songshan airport

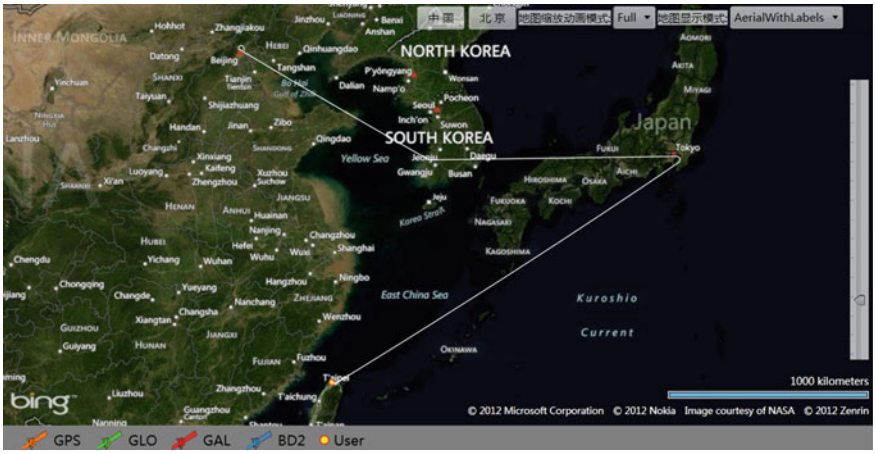

Fig. 30.5 Flight trajectory along waypoints

30.4 Conclusion

The algorithm proposed by this paper can apply to the inverse solution of geodetic problem in any situation and any distance, and the singular phenomenon cannot be produced. It is simple and easy to implement by program, the scale error ratio is less than 0.5 %. It can satisfy the requirement of the trajectory generated in scenario design of GNSS simulation system, and it can be applied to trajectory generation of vehicles along waypoints.

The method of trajectory generation along waypoints in GNSS simulation system proposed by this paper is in conformity with the actual movement rule of vehicles. In addition, it is implemented simply and it has been applied to a GNSS simulation platform successfully.

Acknowledgments This work was supported by the National High-Tech. R&D Program, China (No. 2011AA120505) and the National Natural Science Foundation, China (No. 61173077).

References

1. Zhou Z, Guo G, Jia X (2007) A review on solution of geodetic problem. Sci Surveying Mapp 32(4):P190–P191 (in Chinese)
2. Kong X, Guo J, Liu Z (2010) Foundation of geodesy. Wuhan University Press, Wuhan (in Chinese)
3. Huang J (1994) The new solving process TAyMAH projection formula geodesic inverse problem. J PLA Inst Surveying Map 11(2):P94–P100 (in Chinese)
4. Fan Y, Wang J, Liu H (2007) Numerical methods of geodesic problem. Geotech Invest Surveying 1:P61–P63 (in Chinese)
5. Xu S (1990) The Chord Method for the precise calculation formulas of direct and inverse geodetic problems 15(1):P19–P27 (in Chinese)
6. Li H, Wang R (2009) Great ellipse nautical method and its navigation parameters calculation. J Naval Univ Eng 21(4):P7–12 (in Chinese)
7. Ju H, Hu P, Hu H (2006) Investigation and experiment of algorithm fitting arbitrary distance. Sci Surveying Map 31(2):P29–P31 (in Chinese)
8. Zhao W (1997) Ellipsoid geodesy research. Wuhan University of Geosciences Press, Wuhan (in Chinese)
9. Chen J, Chao D (1986) Ellipsoid geodesy. Surveying and Mapping Press, Beijing (in Chinese)
10. Zhou J, Miao Y, Cheng W, Sun G (2002) An effective algorithm based on Bessel's formula for inverse solution of geodetic problem. Acta Geodaetica et Cartographics Sinica 5(6):P108–P111 (in Chinese)

Chapter 31
Simulation Method and Effect Analysis of Multi-GNSS System Time Offsets

Zhicheng Lv, Jing Pang, Jing Peng, Guozhu Zhang and Feixue Wang

Abstract In multi-system compatibility and interoperability application, time offsets between different navigation systems is an important factor affecting the service performance. To verify the correctness and effectiveness of algorithm that how to deal with system time offsets in multi-mode receivers, GNSS navigation signals simulator is required the system time offset simulation function. The simulation algorithm and the effect on the navigation services performance of system time offsets were discussed. Firstly, the time offset parameters in navigation message and its physical meaning were described. Then, proposed a unified multi-GNSS system time offsets simulation method base on UTC and given system time offsets parameter simulation algorithm. Finally, according to different application scenarios, the impact on the performance of the navigation service availability of two system time offsets processing method-system level and user level-were analyzed and compared.

Keywords Satellite navigation · Compatibility and interoperability · Time offset between different navigation systems · Navigation signal simulator

31.1 Introduction

With the continuously upgrade and improve of GPS and GLONASS and rapid development of emerging navigation systems such as Galileo and COMPASS, the compatibility and interoperability among multiple global navigation satellite system (GNSS) is gradually becoming the future GNSS application development trends [1]. Compared with a single navigation system, using of multiple GNSS

Z. Lv (✉) · J. Pang · J. Peng · G. Zhang · F. Wang
College of Electronic Science and Engineering, National University of Defense Technology, Changsha 410073, Hunan, People's Republic of China
e-mail: chifeng21@163.com

J. Sun et al. (eds.), *China Satellite Navigation Conference (CSNC) 2014 Proceedings: Volume I*, Lecture Notes in Electrical Engineering 303,
DOI: 10.1007/978-3-642-54737-9_31,

navigation will not only increase the number of visible satellites, can also increase the amount of redundant observations and raise the level of integrity testing.

Since different navigation systems use different time reference frames, the time offsets exist when they are transformed each other. Usually, the magnitude of time offsets is about dozens of NS and change slowly with time [2]. Research results show that the system time offset has become one of the key factors affecting the positioning accuracy of multi-system receiver and the effect degree is not only related to the estimated accuracy of system time offset, but also closely associate with the approach adopted to deal with the system time offset [3].

There are two aspects including information and signal layers must be considered in system time offsets simulation of signal simulator [4]. The information layer means creating the system time offset correction parameters which will be broadcast in the navigation message. The signal layer represents that downward navigation signals must join the effect of system time offsets.

The paper is organized as follow. Section 31.2 describes the time offset parameters in navigation message and its physical meaning. Section 31.3 proposes a unified multi-GNSS system time offsets simulation method base on UTC and given system time offsets parameter simulation algorithm. Finally, according to different application scenarios, the impact on the performance of the navigation service availability of two system time offsets processing method-system level and user level-were analyzed and compared in Sect. 31.4. The investigation is summarized in Sect. 31.5.

31.2 Time Offset Parameters in Navigation Message

The system time offset parameters have been listed in navigation message, such that receivers can correct observations when they demodulate the message. Table 31.1 lists the layout of system time offset parameters in navigation broadcast message, in which UTO, GTO, RTO, ETO and BTO mean GNSS to UTC time offset, GNSS to GPS time offset, GNSS to GLONASS time offset, GNSS to Galileo time offset and GNSS to COMPASS time offset. It can be seen that both the construction of new systems and the improvement of working systems are taking into account the needs of interoperable application, and conduct technical subjects, such as the time difference measurement and correction system research [5, 6].

31.2.1 GNSS to UTC Time Offset Parameters

GNSS time (except GLONASSS) is a continuous time scale, while UTC implements leap seconds which is announced and published regularly by International Earth Rotation Service (IERS). In addition, it shows the drift of slow changes over time between GNSS time and UTC time which includes deterministic component

Table 31.1 The layout of time offset parameters in GNSS navigation message[a]

System	Message	UTO	GTO	RTO	ETO	BTO
GPS	LNAV	√	–			
	CNAV	√	–	√	√	+
	CNAV-2	√	–	√	√	+
GLONASS	NAV	√	√	–		
Galileo	F/NAV	√	√		–	
	I/NAV	√	√		–	
COMPASS	NAV	√	√	√	√	–

[a] : '√' Implies that the parameter has been defined, '+' Implies that the parameter has been set aside to expand

and stochastic component. The characterization of the deterministic component can generally be determined using a piecewise least-square polynomial fitting method. And the stochastic component can be modelled by a power law spectrum [7]. GNSS time is synchronized with UTC at 1 μs level (modulo 1 s), but actually is kept within 50 ns (95 %).

The relationship of time offset between GNSS and UTC is generally indicated by seven parameters, as A_{0UTC}, A_{1UTC}, A_{2UTC}, Δt_{LS}, WM_{LSF}, DN and Δt_{LSF}. The physical meaning of these parameters is as follows:

A_{0UTC} The time offset between GNSS time and UTC
A_{1UTC} The frequency offset between GNSS time and UTC
A_{2UTC} The linear frequency drift between GNSS time and UTC
Δt_{LS} Delta time due to leap seconds
WM_{LSF} The week number at the end of which the leap second becomes effective
DN The day number at the end of which the leap second becomes effective
Δt_{LSF} The scheduled future value of the delta time due to leap seconds

Therefore, deviations between the GNSS time and UTC time can be expressed as:

$$\Delta t_{UTC} = \Delta t_{LS} + A_{0UTC} + A_{1UTC} t_E + A_{2UTC} t_E^2 \tag{31.2.1}$$

where t_E is GNSS time as estimated by the user.

Unlike GPS, Galileo or Compass, GLONASS time scale implements leap seconds, like UTC. GLONASS Time (GLONASST) is generated by the GLONASS Central Synchroniser and the difference between the UTC(SU) and GLONASST should not exceed 1 ms plus 3 h, but τ is typically better than 1 μs, namely:

$$T_{GLONASS} = T_{UTC(\mathrm{SU})} + 3^{\mathrm{h}}00^{\mathrm{m}}00^{\mathrm{s}} - \tau, \quad |\tau| < 1\,\mathrm{ms} \tag{31.2.2}$$

In GLONASS navigation message, word KP is notification on forthcoming leap second correction of UTC (±1 s).

31.2.2 Time Offset Parameters Between GNSS

To provide continuous and stable navigation services, each navigation system builds an independent time system which is maintained by control segment. The difference of atomic clock type and performance lead to time offset between GNSS time, including fixed whole seconds deviation as well as time-variant component changed over time.

The fixed whole seconds deviation between GNSS time are due to the different zero time-point of GNSS which is steered to UTC time and the leap second of UTC time. The time-variant component between GNSS time is mainly produced by the different frequencies characteristic of atomic clocks which can be modeled by a piecewise least-square polynomial fitting method and a power law spectrum. In navigation message, GNSS time synchronization parameters are always quantified for five variable: A_{0GGTO}, A_{1GGTO}, A_{2GGTO}, t_{GGTO} and WN_{GGTO}, where

A_{0GGTO}	The time offset between GNSS time
A_{1GGTO}	The frequency offset between GNSS time
A_{2GGTO}	The linear frequency drift between GNSS time
t_{GGTO}	GNSS time synchronization parameters reference time of week
WM_{GGTO}	GNSS time synchronization parameters reference week number.

Therefore, time difference between GNSS time can be expressed as

$$\begin{aligned}\Delta t_{GGTO} = {} & A_{0GGTO} \\ & + A_{1GGTO}(604800(WN_E - WN_{GGTO}) + t_E - t_{GGTO}) \\ & + A_{2GGTO}(604800(WN_E - WN_{GGTO}) + t_E - t_{GGTO})^2\end{aligned} \tag{31.2.3}$$

where t_E is the GNSS time as estimated by the user and WN_E is the week number to which t_E is referenced.

Monitoring results show that time offsets between GPS and GLONASS can be up to 150–180 ns [8]. Therefore, in order to support compatibility and interoperability, GPS and Galileo systems advertised with each other in their respective navigation message broadcast time offset parameters (GGTO). The Galileo Systems Requirements Document specified that the GGTO shall be accurate to within 5 ns/24 h (2-sigma) [9].

31.3 Time Offsets Simulation

Multi-GNSS signal simulator outputs GPS, GLONASS, Galileo and COMPASS downlink navigation signals synchronously. An unified multi-GNSS system time offsets simulation method base on UTC and parameter simulation algorithm is proposed. Its basic thought is that using UTC as the reference time benchmark, the

Table 31.2 System time offsets parameters

Parameter	Unit	Definition
WN_0	Week	Reference week number
t_0	s	Reference time of week
$A_{0BDS\text{-}UTC}$	s	Time offset between COMPASS and UTC
$A_{1BDS\text{-}UTC}$	s/s	Frequency offset between COMPASS and UTC
$A_{2BDS\text{-}UTC}$	s/s^2	Linear frequency drift between COMPASS and UTC
$A_{0GPS\text{-}UTC}$	s	Time offset between GPS and UTC
$A_{1GPS\text{-}UTC}$	s/s	Frequency offset between GPS and UTC
$A_{2GPS\text{-}UTC}$	s/s^2	Linear frequency drift between GPS and UTC
$A_{0GLO\text{-}UTC}$	s	Time offset between GLONASS and UTC
$A_{1GLO\text{-}UTC}$	s/s	Frequency offset between GLONASS and UTC
$A_{2GLO\text{-}UTC}$	s/s^2	Linear frequency drift between GLONASS and UTC
$A_{0GAL\text{-}UTC}$	s	Time offset between Galileo and UTC
$A_{1GAL\text{-}UTC}$	s/s	Frequency offset between Galileo and UTC
$A_{2GAL\text{-}UTC}$	s/s^2	Linear frequency drift between Galileo and UTC

time offsets between GNSS is calculated through the time offsets between GNSS and UTC. Then, the effect of GNSS time offsets is added to pseudo-range and carrier-phase observations using simulation model mentioned above.

31.3.1 Simulation of Time Offset Parameters

According to the system time offset parameters in navigation message introduced in Chap. 2, a set of parameters witch represent the relationship between GNSS time are put forward, as shown in Table 31.2. WN_0 and t_0 are the reference time of parameters which can be specified for any navigation system time in practice. In this paper, they are defined as the COMPASS system time.

Thus, the time offset parameters between COMPASS and other GNSS systems at reference time can be calculated by:

$$\Delta A_{0BDS-GNSS} = A_{0BDS-UTC} - A_{0GNSS-UTC} \tag{31.3.1}$$

$$\Delta A_{1BDS-GNSS} = A_{1BDS-UTC} - A_{1GNSS-UTC} \tag{31.3.2}$$

$$\Delta A_{2BDS-GNSS} = A_{2BDS-UTC} - A_{2GNSS-UTC} \tag{31.3.3}$$

Similarly, time offset parameters between GNSS can be calculated at reference time, and will not repeat them here. The calculation results of time offset parameters are arranged to navigation message. It needs to be aware of that due to the reference time is defined as COMPASS time, it must take into account leap seconds and transform to GNSS time when disposing other GNSS system navigation message.

Time offset parameters between GNSS and UTC in the navigation message-A_{0UTC}, A_{1UTC} and A_{2UTC} are defined in Table 5 and can be directly assigned. Δt_{LS}, WM_{LSF}, DN and Δt_{LSF} must be adjusted real-time according to the simulation time and transcripts of UTC leap seconds.

31.3.2 Simulation of Observations

In multi-GNSS signal simulator, the pseudo-range observation equations to a common satellite at time t can be expressed as:

$$d_0(t) = r(t) + d_{iono}(t) + d_{trop}(t) + d_{clock}(t) \tag{31.3.4}$$

where $r(t)$ is the geometric distance between satellite and receiver, $d_{iono}(t)$ is the signal path delay due to the ionosphere, $d_{trop}(t)$ is the signal path delay due to the troposphere, $d_{clock}(t)$ is the satellite clock offset with respect to system time. In multi-GNSS application, the system time offsets $d_{time-offset}(t)$ must be added to observations. The pseudo-range observation equations thus rewrites to:

$$d(t) = d_0(t) + d_{time-offset}(t) \tag{31.3.5}$$

with

$$d_{time-offset}(t) = a(t) + \varphi(t) \tag{31.3.6}$$

where $a(t)$ is the deterministic component which can be computed by system time offset parameters:

$$\begin{aligned} a(t) = {} & A_{0GNSS-UTC} \\ & + A_{1GNSS-UTC}[t - t_0 + 604800(WN - WN_0)] \\ & + A_{2GNSS-UTC}[t - t_0 + 604800(WN - WN_0)]^2 \end{aligned} \tag{31.3.7}$$

$\varphi(t)$ is the stochastic component and can be modelled by a power law spectrum:

$$S_y(t) = \sum_{\alpha=0}^{4} h_\alpha f^\alpha \tag{31.3.8}$$

where $S_y(t)$ is the frequency-fluctuation noise power spectral density, f is the Fourier frequencies, h_α is the coefficient of energy spectrum of noise intensity as the noise figure α. The values 0–4 of α represent RWFM, FFM, WFM, FPM and WPM respectively. The modeling component implementations can reference [7].

31.4 Time Offsets Effect Analysis

In multi-GNSS receivers, there are two methods to diminish or eliminate the system time offsets. One approach is known as the system-level processing method, in which the system time offset will be calculated by time offset parameters broadcasting in navigation message. The positioning precision is relative to the precision of time offset parameter and accuracy of model when using system-level processing method. Another method is known as the user-level processing method, in which the system time offset will be calculated as an unknown together with the PVT solution in the navigation equations. This method requires at least $4 + (\mathrm{N} - 1)$ visible satellites, where N is the number involved in the solution of navigation systems.

By linearizing the pseudo-range observation equations, the difference between the estimated pseudo-range and measured pseudo-range can be expressed as

$$\Delta\rho = H\Delta X + v \tag{31.4.1}$$

where $\Delta\rho$ is the difference vector between the estimated and measured pseudo-range, H is the matrix that contains the direction cosines of unit vectors pointing from the receiver to the satellite, ΔX is the correction vector of the position and time evolution of the system, The vector v accounts for the measurement noises.

It is assumed that the number of satellites of COMPASS, GPS and Galileo in view is l, m and n respectively. This paper mainly analyses the positioning performance of two system time offsets processing methods.

31.4.1 Time Offset Processing Method at System-Level

For the system-level processing method, the system time offsets are seen as known parameters which can be obtained from the broadcast messages. So only the 3D position and the time biases between the receiver and the navigation systems need to be determined. Taking system time offsets into account, the observation matrix and correction vector are defined by:

$$H = \begin{bmatrix} \alpha_{x_1,bds} & \beta_{y_1,bds} & \gamma_{z_1,bds} & 1 & 0 & 0 \\ \cdots & \cdots & \cdots & \cdots & \cdots & \cdots \\ \alpha_{x_l,bds} & \beta_{y_l,bds} & \gamma_{z_l,bds} & 1 & 0 & 0 \\ \alpha_{x_1,gps} & \beta_{y_1,gps} & \gamma_{z_1,gps} & 0 & 1 & 0 \\ \cdots & \cdots & \cdots & \cdots & \cdots & \cdots \\ \alpha_{x_m,gps} & \beta_{y_m,gps} & \gamma_{z_m,gps} & 0 & 1 & 0 \\ \alpha_{x_1,gal} & \beta_{y_1,gal} & \gamma_{z_1,gal} & 0 & 0 & 1 \\ \cdots & \cdots & \cdots & \cdots & \cdots & \cdots \\ \alpha_{x_n,gal} & \beta_{y_n,gal} & \gamma_{z_n,gal} & 0 & 0 & 1 \\ 0 & 0 & 0 & 1 & -1 & 0 \\ 0 & 0 & 0 & 1 & 0 & -1 \end{bmatrix} \tag{31.4.2}$$

$$\Delta X = [\,\Delta x \quad \Delta y \quad \Delta z \quad \Delta t_{bds} \quad \Delta t_{gps} \quad \Delta t_{gal}\,]^T \tag{31.4.3}$$

where the measurements made with COMPASS, GPS and Galileo are marked with the index *bds, gps* and *gal* respectively. Assuming that the measurement errors from different satellites do not contain a bias and are independent from each other, then the covariance matrix can be represented as a diagonal matrix form:

$$R(\Delta\rho) = T(\sigma^2_{1,bds}, \ldots, \sigma^2_{l,bds}, \sigma^2_{1,gps}, \ldots, \sigma^2_{m,gps}, \sigma^2_{1,gal}, \ldots, \sigma^2_{n,gal}, \sigma^2_{BGTO}, \sigma^2_{BETO}) \tag{31.4.4}$$

where σ_i^2 is the variance of the i-th measurement error on row i. σ^2_{BGTO} is the variance of BGTO (COMPASS to GPS time offset), σ^2_{BETO} is the variance of BETO (COMPASS to Galileo time offset).

Based on least square theory, the covariance matrix of ΔX can be defined by:

$$R(\Delta X) = (H^T H)^{-1} H^T R(\Delta\rho) H (H^T H)^{-1} \tag{31.4.5}$$

Therefore, the geometric dilution of precision of navigation solutions need to be redefined as the dimension of the matrix H has changed:

$$\begin{aligned} GDOP &= \sqrt{\sigma^2_{11} + \sigma^2_{22} + \sigma^2_{33} + \sigma^2_{44} + \sigma^2_{55} + \sigma^2_{66}} \\ PDOP &= \sqrt{\sigma^2_{11} + \sigma^2_{22} + \sigma^2_{33}} \\ HDOP &= \sqrt{\sigma^2_{11} + \sigma^2_{22}} \\ VDOP &= \sqrt{\sigma^2_{33}} \\ TDOP &= \sqrt{\sigma^2_{44} + \sigma^2_{55} + \sigma^2_{66}} \end{aligned} \tag{31.4.6}$$

where α_{ij} is the element at position of row i and column j in $R(\Delta X)$.

31.4.2 Time Offset Processing Method at User-Level

When using the user-level processing method, the system time offset will be calculated by the receiver as unknown from the equations of navigation. Generally, we set one navigation system time as the reference time, and other GNSS time is convert and formed deviations between the reference time. Assuming that

COMPASS system time is selected as the reference time, so the observation matrix and estimating parameter vector can be expressed as:

$$H = \begin{bmatrix} \alpha_{x_1,bds} & \beta_{y_1,bds} & \gamma_{z_1,bds} & 1 & 0 & 0 \\ \cdots & \cdots & \cdots & \cdots & \cdots & \cdots \\ \alpha_{x_l,bds} & \beta_{y_l,bds} & \gamma_{z_l,bds} & 1 & 0 & 0 \\ \alpha_{x_1,gps} & \beta_{y_1,gps} & \gamma_{z_1,gps} & 1 & -1 & 0 \\ \cdots & \cdots & \cdots & \cdots & \cdots & \cdots \\ \alpha_{x_m,bds} & \beta_{y_m,bds} & \gamma_{z_m,bds} & 1 & -1 & 0 \\ \alpha_{x_1,gal} & \beta_{y_1,gal} & \gamma_{z_1,gal} & 1 & 0 & -1 \\ \cdots & \cdots & \cdots & \cdots & \cdots & \cdots \\ \alpha_{x_n,gal} & \beta_{y_n,gal} & \gamma_{z_n,gal} & 1 & 0 & -1 \end{bmatrix} \tag{31.4.7}$$

$$\Delta X = [\,\Delta x \quad \Delta y \quad \Delta z \quad \Delta t_{bds} \quad \Delta BGTO \quad \Delta BETO\,] \tag{31.4.8}$$

where $\Delta BGTO$ is the COMPASS to GPS time offset, $\Delta BETO$ is the COMPASS to Galileo time offset. Assuming that the measurement errors from different satellites do not contain a bias and are independent from each other, then the covariance matrix can be represented by:

$$R(\Delta\rho) = T(\sigma^2_{1,bds}, \ldots, \sigma^2_{l,bds}, \sigma^2_{1,gps}, \ldots, \sigma^2_{m,gps}, \sigma^2_{1,gal}, \ldots, \sigma^2_{n,gal}) \tag{31.4.9}$$

The new precision errors, influenced by system time offsets are defined by:

$$\begin{aligned} GDOP &= \sqrt{\sigma^2_{11} + \sigma^2_{22} + \sigma^2_{33} + \sigma^2_{44} + \sigma^2_{55} + \sigma^2_{66}} \\ PDOP &= \sqrt{\sigma^2_{11} + \sigma^2_{22} + \sigma^2_{33}} \\ HDOP &= \sqrt{\sigma^2_{11} + \sigma^2_{22}} \\ VDOP &= \sqrt{\sigma^2_{33}} \\ TDOP &= \sqrt{\sigma^2_{44}} \end{aligned} \tag{31.4.10}$$

At the same time, the dilution of precision of $\Delta BGTO$ and $\Delta BETO$ can be defined when the system time offsets are determined by the receiver:

$$BGTDOP = \sqrt{\sigma^2_{55}} \tag{31.4.11}$$

$$BETDOP = \sqrt{\sigma^2_{66}} \tag{31.4.12}$$

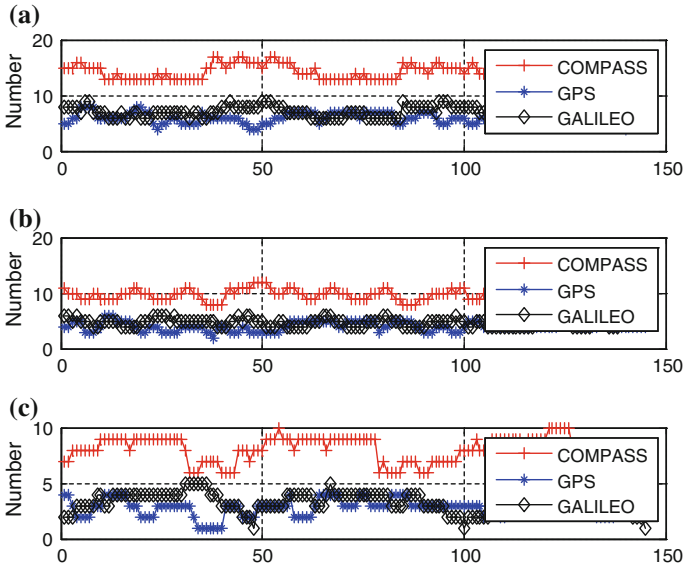

Fig. 31.1 The number of visible satellites in different environment mask angle **a** 15°, **b** 30°, **c** 40°

31.4.3 Influence Analysis of Time Offsets

This section mainly compared and analyzed the influence of navigation service performance in different system time offset level and different system time offset processing method through simulation technique. The simulation constellation is composed of COMPASS(5GEO+5IGSO+27MEO), GPS(24MEO) and Galileo(27MEO). A static user located at (E112.989988°, N28.221251°, H100 m) in Changsha is simulated. The performance of navigation service have been tested in different system time offset parameter precision and different system time offset processing method in typical environmental conditions, such as the open areas (mask angles is 15°), common blocks (mask angles is 30°) and urban canyons (mask angles is 40°).

Simulating continuously 24 h with 1 min sampling interval, we get a set of observations total of 1,440. Figure 31.1 draws the curve of visible satellites number of GNSS in different mask angle at 10 min intervals. It can be seen that GPS and Galileo will not meet the minimum position requirements of at least four visible satellites in part of time at mask angle 40°. Therefore, using GPS or Galileo alone can not provide continuous navigation and positioning services.

The availability of satellite navigation system is defined as the percentage of time of navigation system providing available navigation services, which generally is equivalent to the percentage of time when GDOP under a certain threshold. This article takes the experience value GDOP = 6.3 as positioning availability threshold. The statistics results of availability when each navigation system works

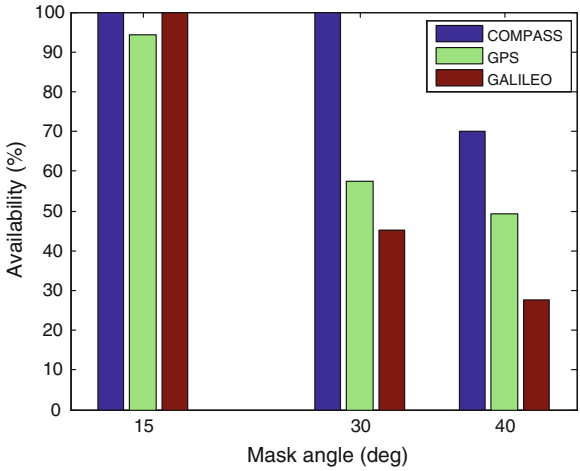

Fig. 31.2 Availability of navigation service in different environment

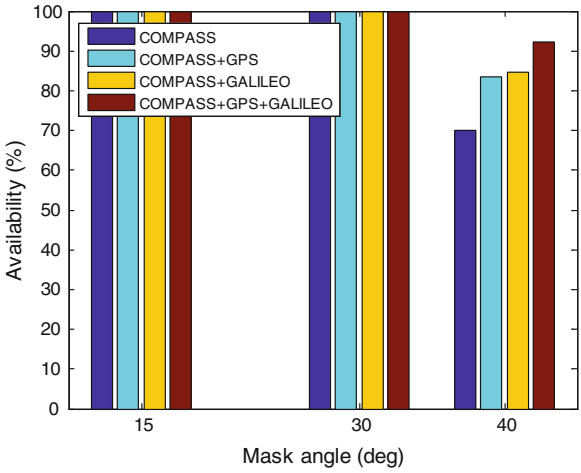

Fig. 31.3 Availability of regardless of the system time offset

alone in different mask angles are shown in Fig. 31.2. The results show that, the availability performance gradually declined when the mask angle increase. The decrease on the number of visible satellite number is one of the important factors which lead to the availability become worse. Using of combined GNSS navigation services can increase the number of visible satellites and improve space geometry configuration.

The availability results of single COMPASS, the dual-system of COMPASS+GPS and COMPASS+Galileo, and the triple-system of COMPASS+GPS+Galileo under the condition of regardless of the system time offset, time offset processing method at system-level and time offset processing method at user-level are shown in Figs. 31.3, 31.4 and 31.5 respectively. Compared with using a single navigation system (see Fig. 31.2), multiple combinations can improve the

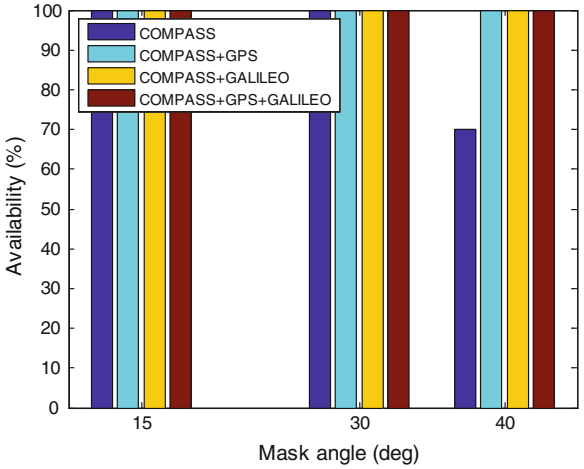

Fig. 31.4 Availability of system-level processing

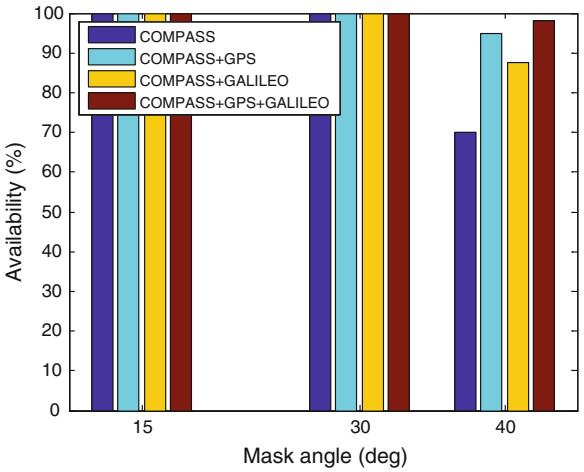

Fig. 31.5 Availability of user-level processing

navigation service availability levels. Results show that availability levels can be reached 100 % in mask angle 30°, and increased to 80 % in mask angel 40°. Using system-level processing method, time offset is a known which is obtained from navigation message directly. It will increase the number of visible satellite without altering the number of estimating parameters and reducing the geometric dilution of precision. Therefore, availability level can reach 100 % in mask angle 40°. In user-level processing method, time offset must be treated as an unknown together with PVT information solution. So, the performance enhancing effect is slightly worse than system-level processing method. The availability of COMPASS, GPS and Galileo combining application can reach to 92.2 % in mask angle 40°.

Xu and Li [3] simulated and analyzed the effects of the above two time offset processing methods on the positioning accuracy. Simulation results indicate that when the error broadcasted by navigation messages is about 5 ns, it's more advisable to handle by receiver. In environment of blocking serious, where the number of visible satellite is less than common blocks, using systems-level processing method can obtain better performance. In practice, we can choose system time offset treatment by considering the number of visible satellite, the precision of time offset parameters and DOP value together.

31.5 Concluding Remarks

In practical application, system time offset is one of the important factors that affect the performance of navigation and positioning services. Aiming at the question of system time offset simulation in multi-GNSS signal simulator, this paper proposes a unified multi-GNSS system time offsets simulation method base on UTC and specific algorithms which can be used to guide the design of multi-GNSS signal simulator. The effects of the two system time processing methods–system-level and user-level-on the availability performance are compared and analyzed. Finally, the implementation strategy of dealing with the system time offset in multi-GNSS receivers is discussed.

References

1. Shusen TAN (2010) The engineering of satellite navigation and positioning, 2nd edn. National Defense Industry Press, Beijing
2. Moudrak A (2004) GPS Galileo time offset: how it affects positioning accuracy and how to cope with it. In: Proceedings of ION GNSS 17th international technique meeting of the satellite division, pp 660–669
3. L Xu, X Li (2009) The methods to deal with time offset and an analysis of their effect to positioning accuracy in multi-mode satellite navigation system. Chin J Sci Instrum 30(10):192–195
4. Hahn J, Powers E (2004) GPS and Galileo timing interoperability. In: Proceedings of GNSS 2004
5. Hahn J, Powers E (2005) Implementation of the GPS to Galileo time offset (GGTO). In: Proceedings of the 2005 joint IEEE international frequency control symposium and precise time and time interval (PTTI) systems and applications meeting, 29–31 Aug 2005, pp 33–212
6. Sesia I, Orgiazzi D, Tavella P (2005) Determination of GPS/Galileo time offset (GGTO), insights from the Galileo system test bed V1 results, poster session at EFTF
7. Y Jiao, Y Kou (2011) Analysis, modeling and simulation of GPS satellite clock errors. Sci Sin Phys Mech Astron 41:596–601 (in Chinese)
8. Pei X (2013) GPS/GLONAS combined positioning. Tongju University, p 2
9. Ririz R, Tobias G et al (2008) GPS/GIOVE interoperability: GGTO and timing biases. ENC-GNSS Toulouse, France, 2008

Chapter 32
The Effects of Non Ideal Channel for Navigation Signal and Research on Pre-distortion Methods

Zhimei Yang, Qibing Xu and Lixin Zhang

Abstract In order to provide high-precision satellite navigation services, continuous, high-precision and high-integrity signals should be provided. Non ideal property of each module will result in a certain degree of distortion to the navigation signals and affect. In this paper, channel simulation model based on the actual transmission channel is established firstly. Then, the analysis of independent simulation and that of combining simulation are applied to measure the impact of each module and the whole channel on signal quality. Finally, the corresponding pre-distortion method is put forward to compensate the distortion effects, simultaneously, simulations are compared to verify the performance. The research based on E1 signal is to assess the degree of distortion and the pre-distortion performance using constellation, power spectrum, SCB curve and correlation loss. Simulation results indicate that the program can Improve the constellation by inhibiting the band spectrum of the signal, optimize SCB curve, reduce correlation loss, eliminate the effect on the quality of signals caused by the transmission channel and increase the precision of positioning accuracy, which has great significances and prospects in satellite communication system.

Keywords E1 signal · Non ideal channel · Pre-distortion · Evaluation parameters

32.1 Introduction

From the GPS of American, GLONASS of Russia, GALILEO of Europe to Beidou (COMPASS) system of China, the satellite navigation system plays a more and more important role in national life and military field. In order to provide

Z. Yang (✉) · Q. Xu · L. Zhang
Xi'an Institute of Space Radio Technology, Xi'an 710100, China
e-mail: yangzhimei1988@163.com

J. Sun et al. (eds.), *China Satellite Navigation Conference (CSNC) 2014 Proceedings: Volume I*, Lecture Notes in Electrical Engineering 303,
DOI: 10.1007/978-3-642-54737-9_32,

high-precision satellite navigation services, continuous, high-precision and high-integrity signals should be provided by satellites. As the non ideal property of independent devices, it will cause a certain degree of distortion when the navigation signals go through the navigation channel, which is bound to affect the performance of the navigation system. China and other countries are researching on the distortion of signals caused by the non ideal characters of transmission module components. In paper [1], a simplify satellite channel base band simulation model is proposed, including the ideal signal generator module, satellite channel module and receiver module, the satellite channel module is simplified into a front filter, HPA and post filter to evaluate the effect of linear amplitude, phase, group delay distortion and high power amplifier (HPA) nonlinear distortion on tracking accuracy of BPSK signal. Correspond evaluation parameters are timing offset and S curve offset. The effect of linear and nonlinear distortion to several candidate BOC modulation signals are analyzed in paper [2], at the same time, the power loss and correlation loss are discussed brought by the limit of bandwidth of the filter. The distortion of high power amplifier for BOC and its derivative signals are analyzed and the joint effects brought about by the bandwidth limitation and nonlinear factors are presented in paper [3].

Thus, the distortion effect of non ideal property of navigation satellite channel on signals can not be ignored. So far, most study focus on the impact of the channels, while eliminating the influence of distortion is rare. Digital pre-distortion is a good way to compensate distortion, but the current pre-distortion method are mostly applied to the compensation of nonlinear effects in power amplifier, the transmission channel pre-distortion can hardly be referred. In this paper, the model of the transmission channel is established, simulation analysis based on Galileo E1 signals (CBOC (6,1,1/11) and BOC (15,2.5) signals are modulated by the combined INTERPLEX) show the influence on signals in non ideal channel, the corresponding pre-distortion method is proposed to compensate the distortion effects, meanwhile the compare of simulation results and its effectiveness are verified by a set of evaluation parameters.

32.2 The Model of Navigation Transmission Channel

General model of Navigation transmission channel as shown in Fig. 32.1.

Ideal signal generator, digital filtering and D/A is integrated a digital signal generator module. The part of frequency conversion is equivalent to a pre-filter, Through the adjustment of the amplitude and phase frequency response, the channel characteristics before HPA is simulated. The multiplexer and antenna after HPA is unified into a post-filter for the simulation of the channel characteristics after HPA. So the general model of Navigation transmission channel is acquired. The following part is the analysis of the filter and HPA models.

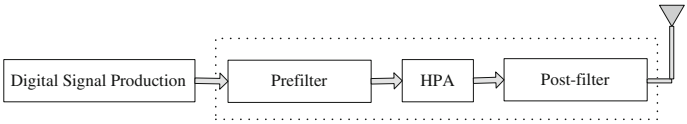

Fig. 32.1 General model of navigation transmission channel

Fig. 32.2 Simulation block diagram

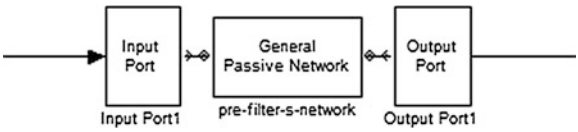

32.2.1 Model of Pre-filter/Post-filter

The effect of filter modeling is to analyze the influence of filter bandwidth, amplitude-frequency and group delay characteristic to the. In view of the above requirements, two models of filter are established to analyze the influence of the signal distortion.

One way to design filter is using the FDAtool attached to matlab/simulink. This method can produce both FIR filter and IIR filter, the group delay of FIR filter is related to the Filter order, simultaneously the uneven distribution situation exists in the group delay of FIR filter.

Another way to design filter is according to the actual S-parameter of filter, whose simulation Block Diagram as shown in Fig. 32.2.

Analog signal is transformed into RF analog voltage signal in the module Input Port, and the module General Passive Network which is the main part of filter can be simulated by inputting S file directly. The load impedance of S-parameter model is set up in the module Output port. This model is mainly used for simulating amplitude-frequency and group delay characteristics of actual filter, which selected S21 parameter as shown in Fig. 32.3.

32.2.2 Model of HPA

HPA model mainly imitates the AM-AM and AM-PM properties in HPA system. There are two kinds of typical HPA simulation analysis model: Saleh model based on tube wave HPA of TWTA and Rapp model based on solid state HPA of SSPA. Saleh model has the advantages of simple structure and high performance, which is a classical and practical model. Its amplitude and phase mathematical can be expressed as:

$$A(r) = \frac{\alpha_a r}{1 + \beta_a r^2}, \quad \Phi(r) = \frac{\alpha_\phi r^2}{1 + \beta_\phi r^2} \tag{32.1}$$

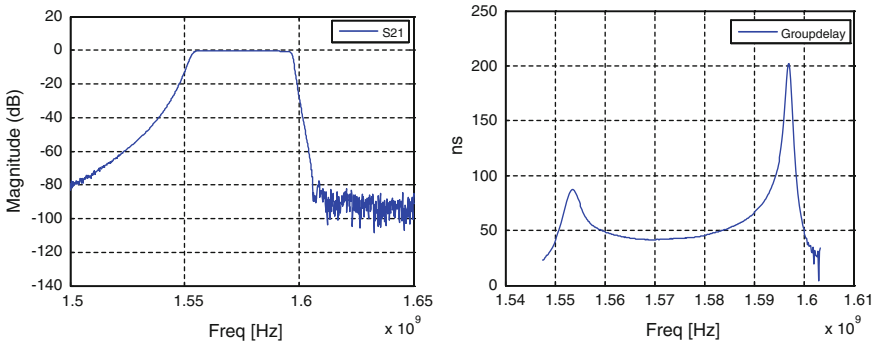

Fig. 32.3 S21 parameter

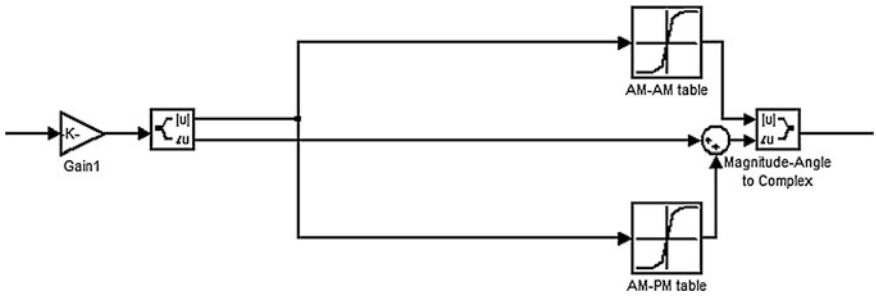

Fig. 32.4 High power amplifier lookup table model

The Saleh model can be established by measuring the voltage as well as the phase and loading the parameters.

In order to improve the tube wave HPA model, we generate AM-AM and AM-PM charts using the power of the input signal, output signal and the phase offset of output signal, meanwhile, the data are expanded by inserting methods. Then we get the corresponding output powers and phase offsets. The simulation block diagram is shown in Fig. 32.4.

Characteristics of the look-up table is different from the Saleh model because the data are derived from actual devices, which are more credible. Figure 32.5 shows the comparison between AM-AM and AM-PM:

32.3 Evaluation Indicators

In order to assess the degree of signal distortion caused by transmission channel, four evaluation indicators are used in the article, such as constellation, power spectrum, correlation loss and SCB curve. Constellation and power spectrum are well-known for us, so the following part briefly introduces correlation loss and SCB curve.

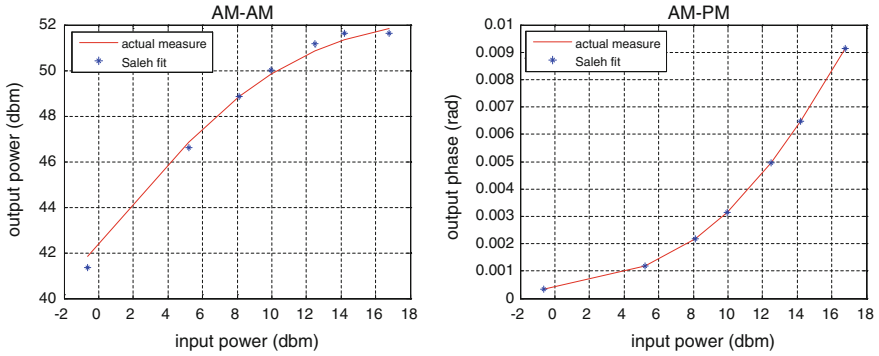

Fig. 32.5 AM-AM and AM-PM *curves*

Correlation introduction: as an important indicator of navigation signal, correlation is used to evaluate the attenuation degree of actual transmit power of navigation signal. Correlation (CL) is defined as:

$$CL\ (\mathrm{dB}) = P_{\underset{Ideal}{CCF}}(\mathrm{dB}) - P_{\underset{SIS}{CCF}}(\mathrm{dB})$$

where

$$P_{CCF}(\mathrm{dB}) = \max(20 \cdot \log_{10}(|CCF(\varepsilon)|))$$

$$CCF(S_{\mathrm{out}}, S_{in,k}, \tau) = \frac{\int_0^T s_{out}(t) \cdot s_{in,k}^*(t+\tau)dt}{\sqrt{\left(\int_0^T |s_{out}(t)|^2 dt\right) \cdot \left(\int_0^T |s_{in}(t)|^2 dt\right)}}$$

CCF is the normalized cross-correlation function of ideal signal $S_{in}(t)$ with period T and distortion signal $S_{out}(t)$. And $S_{in,k}(t)$ refers to the k-th signal component in $S_{in}(t)$.

Measure of correlation is obtained in the case of removing IF and Doppler shift in I/Q channels. The max absolute of correlation function is regarded as the estimates of correlation peak, which is obtained by calculating the correlation of shifted local reproduction signal and input signal [4].

SCB curve introduction: For the PN ranging system, Correlation function of spreading code is no longer symmetrical around after linear and nonlinear distortion. The bias can be generated between the zero crossing of phase detector and the autocorrelation function maximum of current code, which is defined as zero offset. So we can acquire the definitions of SCB curve by plotting the zero offset with different lead and lag time.

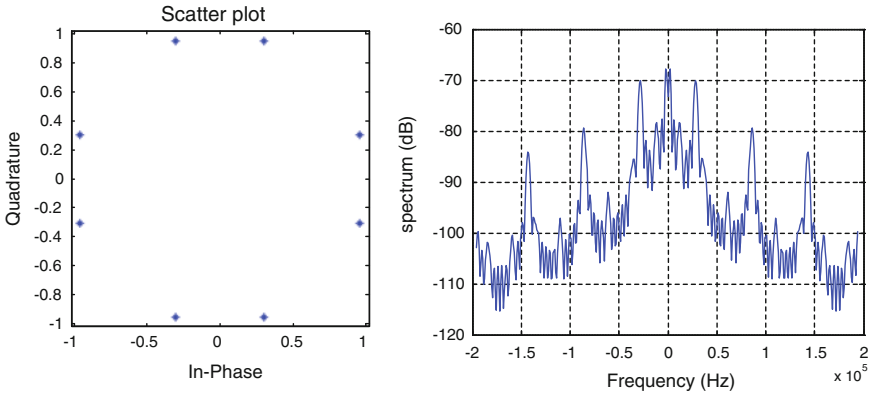

Fig. 32.6 The ideal E1 signal

32.4 Simulation Results and Analysis

The E1 signal is synthesized by INTERPLEX modulation of CBOC (6,1,1/11) and BOC (15,2.5) signals. The ideal E1 signal constellation and power spectrum are shown in Fig. 32.6.

Independent simulation analysis is used on condition that there only exiting a filter or HPA while combined simulation analysis is applied to the whole channel. The corresponding pre-distortion method is put forward to compensate the distortion effects and simulation results are compared. Simulation based on Galileo E1 signal is designed to analyze the losses of system distortion and pre-distortion performance through indices including the constellation diagram, power spectrum, SCB curve and correlation loss.

32.4.1 Filter

We discuss the filter's impact on the signal and pre-distortion performance below assuming that there only exiting filter in the channel. The filter is designed with S parameter model in the process of simulation. The distortion of signals caused by filters is mainly caused by the bandwidth of the filter, amplitude frequency property and the group delay property, thus, a pre-distortion filter which has the opposite property of amplitude frequency property and phase frequency property. The basic principle of the corresponding pre-distortion algorithm is to load the group delay curve and amplitude frequency property curve of S parameters and convert filter's system function to amplitude frequency property and phase frequency property of each frequency grid by interpolating. Data are imported using the fitting algorithm to calculate the amplitude and phase of each frequency

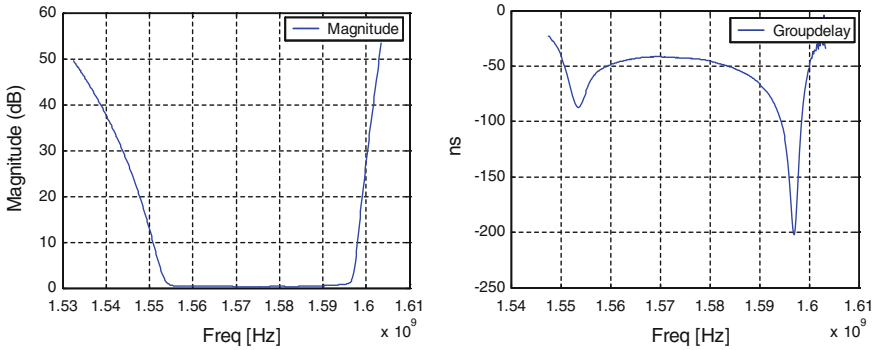

Fig. 32.7 The amplitude frequency property and group delay property of pre-distortion filter

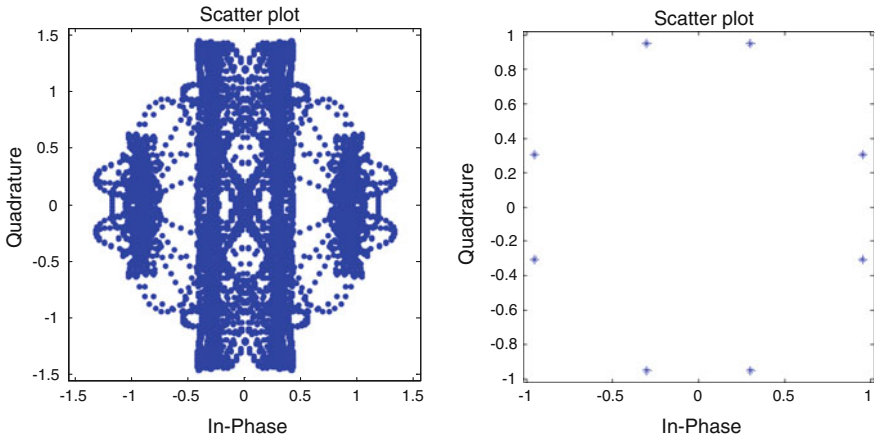

Fig. 32.8 Constellation [without pre distortion (*left*), pre-distortion (*right*)]

point, after IFFT, we can achieve filter coefficient by calculating corresponding pre-distortion filter. The amplitude frequency property and group delay property are shown in Fig. 32.7.

Figure 32.8 display the comparison between the distortion signal and that of adding the pre-distortion algorithm (Figs. 32.9, 32.10, Table 32.1).

The constellation reveals that filter distortion has leading to the divergence of constellation points and bringing the band region. The region is brought mainly due to the removing of high harmonics, making the signal's phase a slow process of change rather than a idea one. After pre-distortion processing, the distribution of constellation can be improved obviously.

From the power spectrum, we know the effect of removing and restricting on the signals out of band is just like what we expected, which can be recovered after pre-distortion processing.

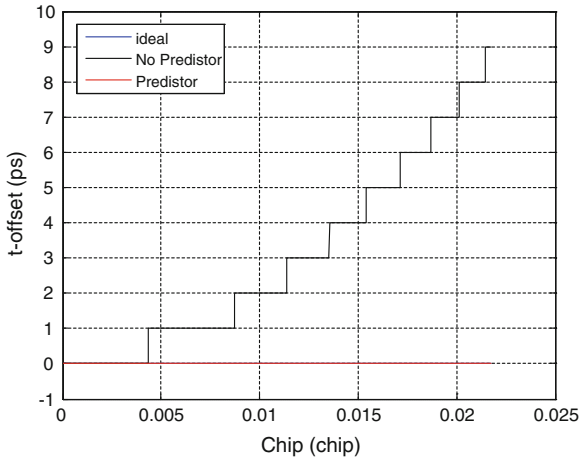

Fig. 32.9 SCB *curve*

Fig. 32.10 Power spectrum

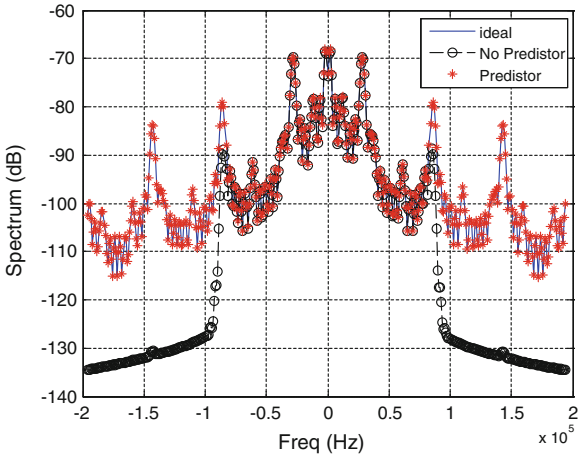

Table 32.1 Correlation loss

Without pre-distortion (dB)	4.528714e+000
Pre-distortion (dB)	−9.458155e−014

The correlation loss shows that the value caused by this filter is 4.528 dB, Fig. 32.8 become very low when adding pre-distortion part. The value should be non negative, however, the imaginary part of the complex signal is not strictly for 0, but a small volume when the real part is imported into the process, lead to the correlation loss negative.

We can achieve from SCB curve that SCB is 9 ps when the filter is introduced, while the SCB is 0 ps by adding the pre-distortion part after, which is coincident with the idea SCB.

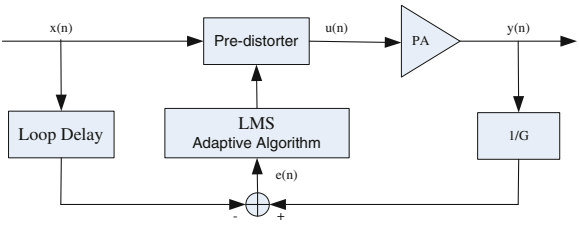

Fig. 32.11 The pre-distortion structure diagram

32.4.2 HPA

The impact of HPA on the signal and pre-distortion performance is discussed in this section in case that there only exiting HPA in the channel. High power amplifier model is established using look-up table method and pre-distort part is constructed by polynomial fitting method. The parameters of the polynomial can be adjusted using the LMS algorithm.

In Fig. 32.11, X(n) is the input signal at time n, y(n) is the output signal of the power amplifier, the response of the whole system is expressed as D(n), G is the linear magnification. When the equation e(n) = d(n) − y(n) accord with the convergence of the algorithm E(n) = 0, the output power is the linear function of input signal, Y(n) = G * x(n).

The pre-distorter for polynomial mathematical model:

$$\mathrm{u}(n) = \sum_{k=1}^{K} a_k x(n)|x(n)|^{k-1} \tag{32.2}$$

a_{kq} is the coefficient of the polynomial, whose accuracy determines the performance of the pre-distorter. Update coefficients can be obtained by LMS algorithm [5].

Figure 32.12 shows the compare between the effect of signal's distortion handled by the amplifier and the effect adding the pre-distortion algorithm (Figs. 32.13, 32.14, Table 32.2).

The constellation reveals that filter distortion has leading to the rotation of constellation points and it is not symmetry, which is caused by AM/AM and AM/PM of HPA. The rotation is eliminated after pre-distortion processing, but the divergence of constellation points also exist.

From the power spectrum, we know the signal power is significantly enlarged and spectrum spread caused by the HPA nonlinear effects, new frequency components appear out of the band. After adding the pre-distortion, the spread spectrum out of band can be effectively inhibited, the power spectrum power can be close to the ideal signal spectrum

The correlation loss shows that the value caused by HPA is 9.01e −9 dB, Fig. 32.12 increase to 4.77e−5 dB when adding pre-distortion part.

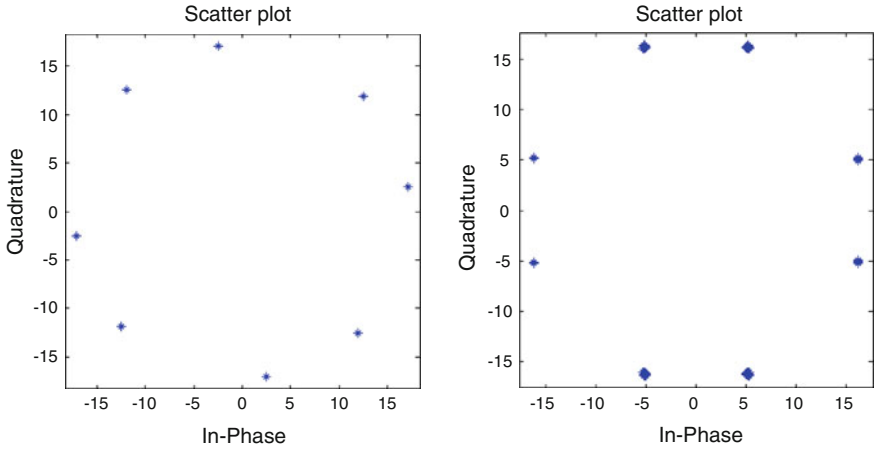

Fig. 32.12 Constellation [without pre distortion (*left*), pre-distortion (*right*)]

Fig. 32.13 SCB curve

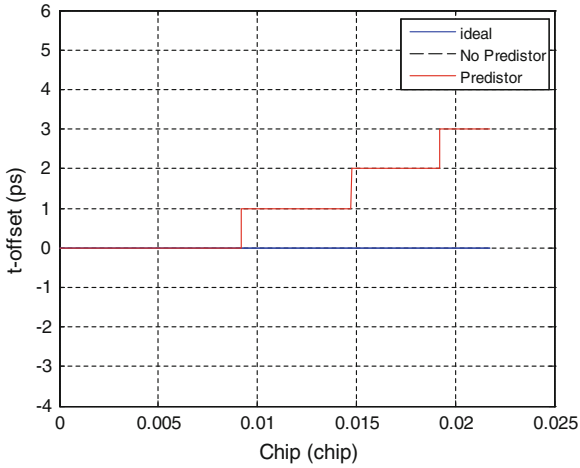

We can achieve from SCB curve that SCB is 0 ps caused by HPA which is accord with the idea value. SCB change to 3 ps after the pre-distortion part.

The effect of high power amplifier distortion caused by the loss of correlation and SCB curve is very small, which indicate that high power amplifier for some indicators do not necessarily have a worse effect, but have improved that to some extent. In Sect. 32.4.3, the improvement of correlation loss and SCB caused by HPA can be better reflected. The two indices could not mean the high power amplifier causes small signal distortion, which can be achieved through the constellation diagram and power spectrum. It is a normal phenomenon that the values of these two indices increase within a narrow range after adding the pre-distortion part.

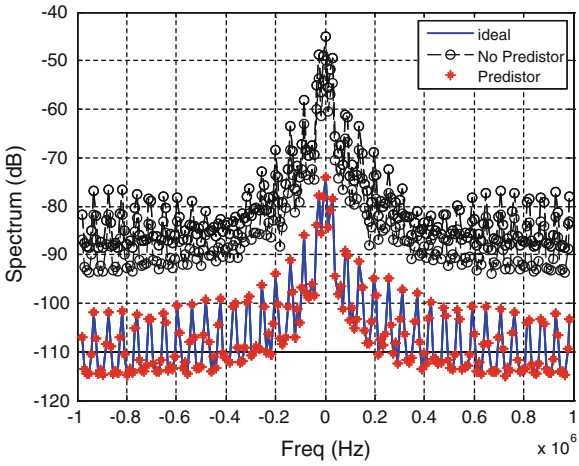

Fig. 32.14 Power spectrum

Table 32.2 Correlation loss

Without pre-distortion (dB)	9.015557e−009
Pre distortion (dB)	4.770860e−005

32.4.3 The Whole Transmitting Channel

The analysis in this section displays the distortion caused by the whole transmitting channel (pre-filter + HPA + post-filter) and the compare between the distortion signal and that of adding the pre-distortion algorithm. Assuming the pre-filter and post-filter are similar in using parameters of S model and high power amplifier uses look-up table model. This pre-distortion method combine previous method of pre-filter and that of HPA, the simulation results are shown as in Figs. 32.15, 32.16, 32.17 and Table 32.3.

The constellation reveals that band-limited property of the filter will destroy the constant envelope of signals, lead to the divergence of constellation points and bring the band region when signals go through the pre-filter. HPA part cause the rotation of constellation points and it is not symmetry. Finally, the post-filter cause the constellation divergence more obvious and deteriorating the band region. While pre-distortion part can improve the constellation effectively.

From the power spectrum, we know the spectrum spread is eliminated when the post-filter is introduced, but the distortion is preserved when the nonlinear property of HPA is serious. Post-filter can only remove noises in the outer band rather than improve distortion of inner band spectrum. While adding pre-distortion process, power spectrum is close to the ideal one.

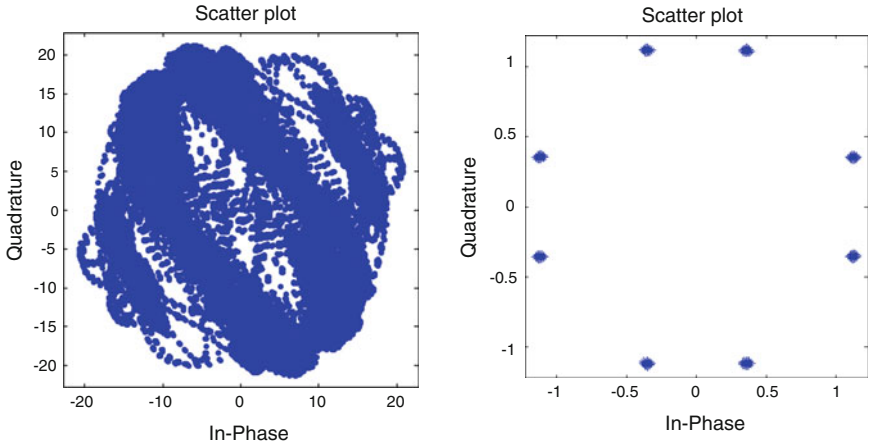

Fig. 32.15 Constellation [without pre distortion (*left*), pre-distortion (*right*)]

Fig. 32.16 SCB *curve*

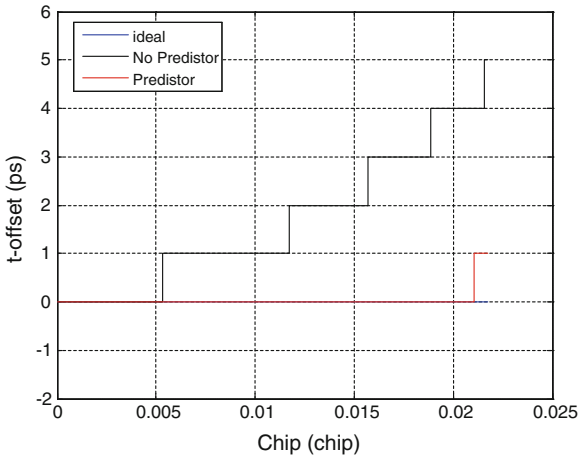

The correlation loss shows that the value caused by the whole transmitting channel is 21.52 dB, Fig. 32.15 decrease to 1.30e−4 dB when adding pre-distortion part.

We can achieve from SCB curve that SCB is 5 ps caused by the whole transmitting channel. The SCB reduces to 1 ps after the pre-distortion part.

Obviously, the filter has a larger impact on constellation loss and SCB, while the nonlinearity of HPA can improve the two indices.

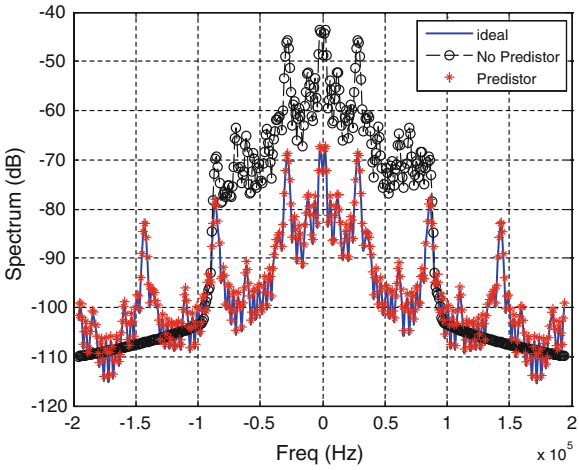

Fig. 32.17 Power spectrum

Table 32.3 Correlation loss

Without pre-distortion (dB)	2.152373e+001
Pre-distortion (dB)	1.303963e−004

32.5 Conclusion

Simulations and analyses in this paper are based on E1 signals, the parameters of the simulation model for the filter and high power amplifier are actually measured so that the corresponding pre-distortion processing possesses some practical value in engineering field.

References

1. Rapisarda M, Angeletti P, Casini E (2007) A simulation framework for the assessment of navigation payload non-idealities. In: 2nd workshop on GNSS signal and signal processing, 24–25 April 2007, ESTEC
2. Soellner M, Kohl R, Luekte W et al (2002) The impact of linear and non-linear signal distortions on Galileo code tracking accuracy. ION GPS 2002. ION, Portland, pp 1270–1285
3. Huang X, Hu X, Tang Z (2009) Impact of Satellite's high power amplifiers on spectrum of navigation signals and PRN tracking accuracy. Chin J Electron (3):640–645
4. Soellner M, Kurzhals C, Kogler W, Erker S, Thölert S, Meurer M (2008) One year in orbit GIOVE-B signal quality assessment from launch to now
5. Zheng T, Wei D, Tang H (2005) Adaptive signal processing in communication. Electronic Industry Press
6. Slifka MK, Whitton JL (2000) Clinical implications of dysregulated cytokine production. J Mol Med. doi:10.1007/s001090000086

Chapter 33
Application of Real-Time Multipath Estimation on the GEO Satellite Dual-Frequency Ionospheric Delay Monitoring

Wei Zhao, Min Li, Zhixue Zhang, Jinxian Zhao, Caibo Hu, Na Zhao and Hui Ren

Abstract Due to the orbit characteristics of the GEO satellite in Compass constellation, the multipath error in pseudorange measure cannot only be eliminated by the receiver, but also be amplified in the elimination of the ionosphere delay by dual frequency pseudorange combination, resulting in the accuracy deterioration of ionosphere delay monitoring by the monitor stations. Based on the slow-change characteristics of the GEO satellite orbit, this paper proposes a method of using real-time multipath estimation, which is extracted from previous days' pseudorange measurements, to correct the multipath error in real-time ionosphere delay computation. Experiment results demonstrate that this method can eliminate the fluctuations in GEO satellite dual frequency ionospheric delay measurements caused by multipath error and enhance the dual frequency ionospheric delay measurements accuracy of low azimuth GEO satellites by 55.7 %.

Keywords Compass system · GEO satellite · Real-time multipath estimation · Dual-frequency ionospheric delay monitoring

33.1 Introduction

Compass satellite navigation system constellation is GEO, IGSO, MEO satellite mixed constellation. Limited by the number of satellites (five GEO satellites, five IGSO satellite, and four MEO satellite) and satellite orbits, IGSO and MEO satellite are invisible for region users, so the GEO satellites are important for user positioning and ionosphere delay monitoring. Dual-frequency pseudorange is the main measure of monitoring ionosphere delay variety; foreign satellite-based

W. Zhao (✉) · M. Li · Z. Zhang · J. Zhao · C. Hu · N. Zhao · H. Ren
Beijing Institute of Spacecraft System Engineering, Beijing, China
e-mail: joypla@163.com

J. Sun et al. (eds.), *China Satellite Navigation Conference (CSNC) 2014 Proceedings: Volume I*, Lecture Notes in Electrical Engineering 303,
DOI: 10.1007/978-3-642-54737-9_33,

augmentation system experts discovered the "standing multipath error" phenomenon in GEO satellite pseudorange in GEO navigation signals ranging study [1]. This is because of the characteristic of GEO satellite obit that results in the multipath error in pseudorange difficult to eliminate in terminal end, on the contrary, it will be amplified in dual-frequency ionosphere monitoring, bring about the phenomenon of the precision of dual-frequency positioning lower than single-frequency [2]. The method of combination of pseudorange and carrier phase can mitigate multipath error effectively, but affected by carrier phase ambiguity resolution and cycle slip, this method cannot be applied in real-time ionosphere delay monitoring.

Due to the position of ionosphere delay monitoring is fixed, and the obit of GEO satellite only moves 0.08°, in the condition of no great change of the circumstance and architecture of the station surrounding, the multipath of GEO satellite can regarded as stable. The history pseudorange multipath error of specific station can be calculated by post processing, combined with the characteristic of GEO satellite obit, the real-time correction for multipath error in pseudorange can be achieved.

33.2 Analysis of the GEO Multipath Error Impact on Ionosphere Delay Monitoring

33.2.1 Multipath Signal Error Characteristic

In satellite navigation system, the navigation signal will emerge the phenomena of attenuation, reflection and phase of deflection due to buildings, trees, and other obstacles on the entire propagation way from satellite to receiver, so that the signal arrives at the receiver antenna is a plurality of several propagation path signal. Owing to different transmission paths, there are relative phase and relative delay, and amplitude characteristics differences between direct signal and the reflected signal, resulting in signal distortion which entry into the receiving loop and the offset of correlation peak identification curve zero, and then affecting the user range measuring accuracy. At the same time, due to different environmental characteristics, there are no spatial correlations between the multipath signals, and because the incident angle of the signal relative to antenna phase center varies with satellite-ground relative positions changes, result in multipath signal also changes with time. The generation mechanism and variation rule of multipath signal cannot be described by specific environmental model due to the random characteristics mentioned above [3].

33.2.2 Analysis of the Amplification Effect of Dual-Frequency Ionosphere Delay Calculation on Multipath Error

In the B1B2 dual-frequency pseudorange positioning mode, B1 frequency ionospheric delay is calculated as follows:

$$\Delta Ion_{B1} = \left(\frac{f_{B2}^2}{f_{B2}^2 - f_{B1}^2}\right)(\rho_{B1} - \rho_{B2}) \tag{33.1}$$

where ΔIon_{B1} is the ionospheric delay value in the B1 pseudorange measurement, f_{B1} is the frequency value of B1, f_{B2} is the frequency value of B3, ρ_{B1} and ρ_{B2} are the pseudorange measuring value of B1 and B2. So the B2 ionosphere delay value can be expressed below.

$$\Delta Ion_{B2} = (f_{B1}/f_{B2})^2 \cdot \Delta Ion_{B1} \tag{33.2}$$

Assuming that the pseudorange measurement error and receiver noise on B1, B2 frequency point are uncorrelated and have equal mean square deviation, and then the relationship between ionosphere delay error by dual-frequency pseudorange method and the measurement error of pseudorange is as below.

$$\Delta Ion = \sqrt{2} \cdot \left(\frac{f_{B2}^2}{f_{B1}^2 - f_{B2}^2}\right) \cdot \Delta\rho \tag{33.3}$$

It can be seen from formula above, the calculation error of ionosphere delay for B1/B2 dual-frequency combined pseudorange is 2.1 times than the single-frequency pseudorange measurement error.

To review the amplification effect of dual-frequency ionosphere calculation on multipath error, the ionosphere monitoring result of one ground monitoring station for a GEO satellite of Compass system is analyzed, as shown in Fig. 33.1. The blue curve is the calculation results of ionosphere delay for the corresponding GEO satellite using dual-band carrier phase, the green curve is the calculation results of ionosphere delay using dual-band pseudorange. When receiver make navigation signals related matching and tracking lock, the final range of error caused by multipath effects has been determined, which the width will not be more than a symbol of code pseudorange, or phase will not exceed 1/4 of the carrier wavelength in theory. Therefore, the multipath effects affect carrier phase measurements much less than pseudorange measurements. The measurement errors on pseudorange measurement caused by multipath signal are up to several meters or even tens of meters, while measurement errors on carrier phase do not exceed 1/4 wavelength (4–6 cm), with respect to the multipath error on pseudoranges, carrier phase multipath error is negligible. From Fig. 33.1, it can be seen that the ionosphere error calculated by dual-frequency pseudorange has more chattering amplitude than the result calculated by dual-frequency carrier phase, the ionosphere delay calculation error of dual-band pseudorange is 9.83 TECU.

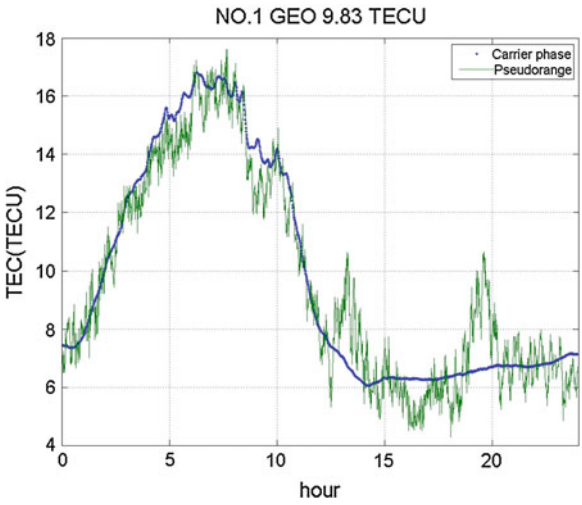

Fig. 33.1 Stat: the ionosphere delay monitoring results of one ground station for the GEO satellite in 24 h

33.3 Analysis of the Pseudorange Multipath Error of the GEO Satellite

33.3.1 Analysis of the Orbit Characteristic of the GEO Satellite

GEO satellite is also called "geosynchronous earth orbit satellite". Its orbit height is 36,000 km. Its inclination and eccentricity is zero. Observed from an earth station, GEO satellite seems to be static, that's where the name origins. In satellite navigation system, multipath error is related to satellite elevation and azimuth. Therefore, we simulated the elevation and azimuth of an GEO satellite from an earth station located in Beijing. The simulation period is 1 week. In Fig. 33.2, the green line stands for azimuth, and the red line stands for elevation. It can be seen that, to the same earth station, the azimuth of GEO changes less than 0.2° during 2 days, and the elevation of GEO changes less than 0.4° during 2 days.

33.3.2 Analysis of the Pseudorange Multipath Error of the GEO Satellite

To correct the multipath error from pseudorange in real time, we need to analyze the change of multipath error in a period. This paper uses the method proposed by Kee and Prof. Parkinson [4], which extracts multipath error from the combination observations of dual-frequency pseudorange and carrier phase, expressed in the following formula:

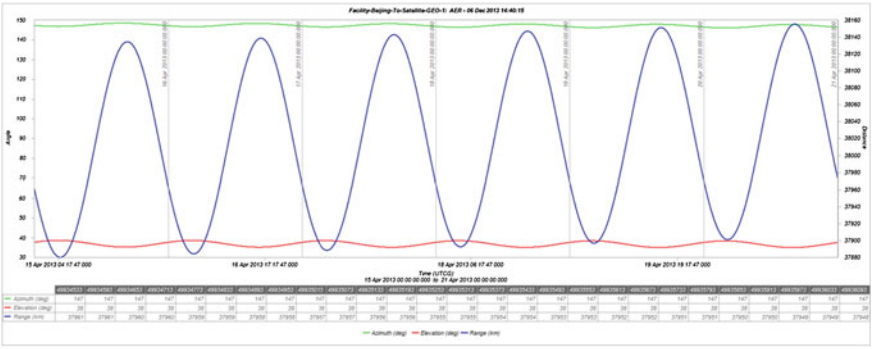

Fig. 33.2 The azimuth and elevation angle of GEO satellite from an earth station

$$MP_1 = \rho_1 + \frac{1+\alpha_{12}}{1-\alpha_{12}}\varphi_1 \cdot \lambda_1 - \frac{2}{1-\alpha_{12}}\varphi_2 \cdot \lambda_2 \tag{33.4}$$

$$MP_2 = \rho_2 + \frac{2\alpha_{12}}{1-\alpha_{12}}\varphi_1 \cdot \lambda_1 - \frac{1+\alpha_{12}}{1-\alpha_{12}}\varphi_2 \cdot \lambda_2 \tag{33.5}$$

In the above formula, $\rho_1\rho_2$ is the pseudorange observations of B1B2 frequency, $\varphi_1\varphi_2$ is the carrier phase observations, $\lambda_1\lambda_2$ is the wavelength of two frequency, $\alpha_{12} = f_1^2/f_2^2, f_1 f_2$ is the frequency.

Experiment data is collected by observing a GEO satellite named SV03 of Compass system from an Ionosphere monitor station located in north China during 2012 Dec 1 to 2012 Dec 3. The extracted multipath error is shown in Fig. 33.3.

It can be seen from Fig. 33.3 that, the change of multipath error is repeated every day because the orbit of GEO satellite changes regularly and slowly. The standard deviation of multipath error is listed in Table 33.1. It can be seen that during that 3 days, the standard deviation of multipath error at both B1 and B2 is on the same order.

Therefore, the present multipath error can be estimated in real time according to the extracted multipath error while monitoring the Ionosphere delay of GEO satellite.

33.4 Real Time Estimation and Correction to the Pseudorange Multipath Error of the GEO Satellite

To estimate the multipath error in real time, firstly, a database is needed which stores the multipath error for the Ionosphere-monitoring GEO satellite in a period. Multipath error can be calculated as shown in formula (33.4) and (33.5). The ambiguity of carrier phase observation can be calculated precisely and the cycle

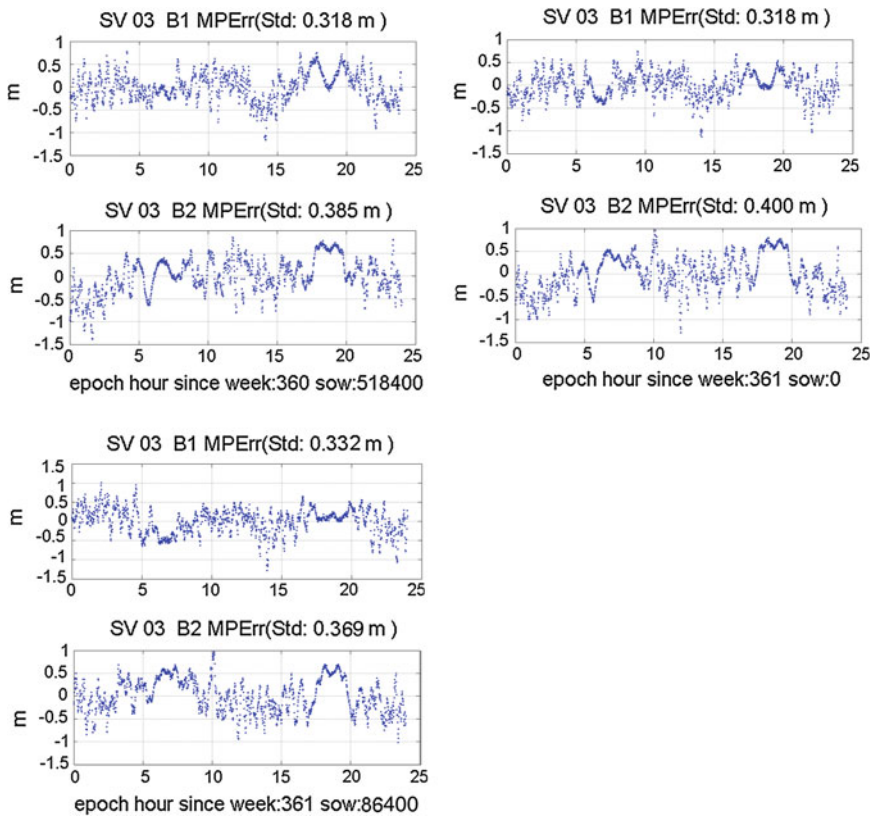

Fig. 33.3 Extracted multipath error of GEO satellite during 2012 Dec 1 to 2012 Dec 3

Table 33.1 The standard deviation of multipath error during Dec 1 to Dec 3

Frequency point	Dec 1	Dec 2	Dec 3
B1	0.318	0.283	0.332
B2	0.385	0.400	0.369

skip is removed after post processing. Extracted multipath error is stored as MP_1^k and MP_2^k for further use. Multipath error of GEO satellite can be estimated and corrected in real time as the following formula:

$$\begin{cases} \widetilde{\rho}_1^{k+1}(t) = \rho_1^{k+1}(t) - MP_1^k(t_{opt}) \\ \widetilde{\rho}_2^{k+1}(t) = \rho_2^{k+1}(t) - MP_2^k(t_{opt}) \end{cases} \tag{33.6}$$

$\rho_1^{k+1}(t)$, $\rho_2^{k+1}(t)$ is the pseudorange observation at present for B1 and B2 frequency, $MP_1^k(t_{opt})$, $MP_2^k(t_{opt})$ is the multipath error at t_{opt} the day before for B1 and B2 frequency, t_{opt} is the most close time to the present time the day before,

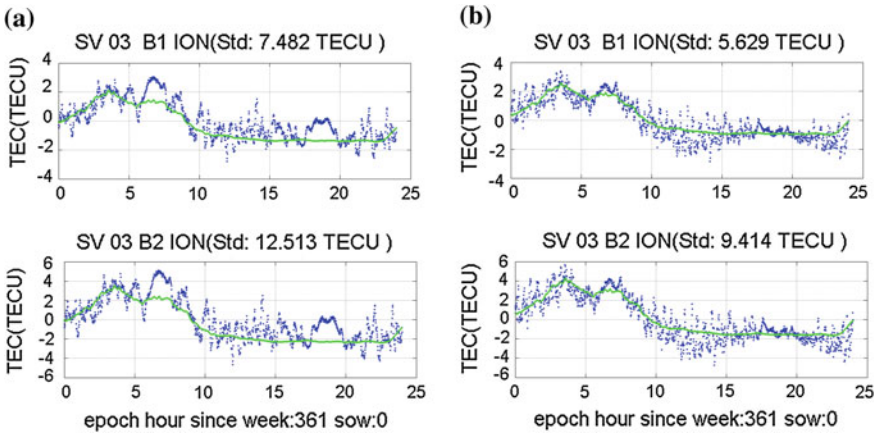

Fig. 33.4 Comparison of ionosphere delay results (**a**) before and (**b**) after correcting the multipath error for SV03

$\widetilde{\rho}_1^{k+1}(t)$, $\widetilde{\rho}_2^{k+1}(t)$ is the pseudorange observation after multipath error correcting for B1 and B2 frequency.

After multipath error correcting in real time, $\widetilde{\rho}_1^{k+1}(t)$, $\widetilde{\rho}_2^{k+1}(t)$ is used in formula (33.1) and (33.2), so we get more precise ionosphere monitoring results $\Delta\widetilde{Ion}_1$ and $\Delta\widetilde{Ion}_2$ by dual frequency pseudorange.

As shown in Fig. 33.3, the change of multipath error is almost the same in the adjacent 2 days for GEO satellites. However if more precise multipath error estimation is needed, the parameter t_{opt} should be more precise. t_{opt} can be calculated by searching the maximum of the following formula:

$$\widehat{\rho}(t_{opt}) \cdot \widehat{\rho}^{k+1}(t)^T, t_{opt} = t - T_{sd} + \delta_t(t) \tag{33.7}$$

In the above formula, $\widehat{\rho}^{k+1}(t)$ is the normalized 1×3 ECEF position vector, which stands for the present position of the satellite, T_{sd} is a sidereal, $\delta_t(t)$ is the time difference between 2 days when GEO satellite in the same position, $\widehat{\rho}(t_{opt})$ is a normalized $n \times 3$ ECEF position vector, which stands for the GEO position at t_{opt} a sidereal before. Because of the characteristic of GEO satellite, $\delta_t(t)$ is usually very small.

To verify the effect of multipath error correction in Ionosphere delay monitoring, the experiment data in Sect. 33.2 is analyzed. The Ionosphere monitoring results are computed using dual-frequency pseudorange observations and dual-frequency carrier phase observations of 24 h in the same time. Because the effect of multipath error to carrier phase observations is much smaller than pseudorange observations, we use the ionosphere delay computed by dual-frequency carrier phase observations as the standard to evaluate the Ionosphere delay computed by dual-frequency pseudorange observations. The Ionosphere delays before and after correcting the multipath error is shown in Fig. 33.4.

Table 33.2 Calculating errors of ionosphere delay before and after correcting the multipath error for SV03 (TECU)

Frequency point	Before correcting	After correcting	Improvement (%)
B1	7.482	5.629	24.8
B2	12.513	9.414	24.8

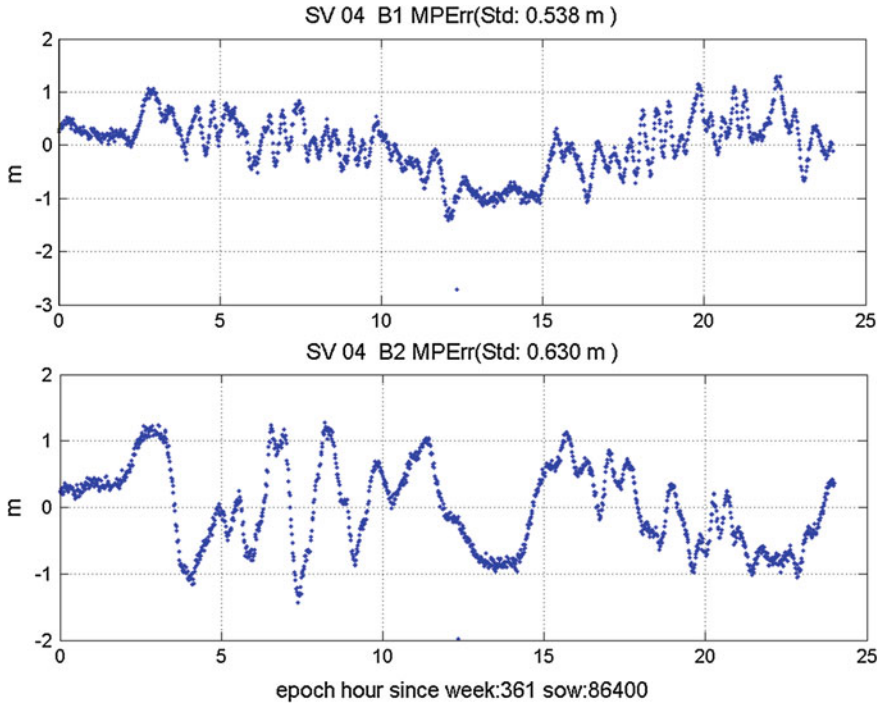

Fig. 33.5 The pseudorange multipath error of GEO SV04 relative to ground station

The results of calculating errors of ionosphere delay before and after correcting the multipath error for SV04 is listed in Table 33.2.

It can be seen from Fig. 33.4 and Table 33.2, by real time multipath estimation, the distinct fluctuation of dual-frequency pseudorange ionosphere delay error appeared at 7 o'clock and 18 o'clock is eliminated, the dual-frequency pseudorange ionosphere delay error of B1 reduces from 7.48TECU to 5.63TECU, error of B2 from 12.51TECU to 9.41TECU, both of the improvement ratios are 24.8 %.

The elevation of GEO SV03 selected in Sect. 3.2 is 32.23° relative to the ground station, to validate the multipath real-time estimation algorithm under low elevation situation, the GEO SV04 is chosen for applicability test, whose elevation is 21.02° relative to ground station. Generally, the pseudorange multipath error become larger in the circumstance of low elevation, the extracted multipath error of GEO SV04 is shown in Fig. 33.5.

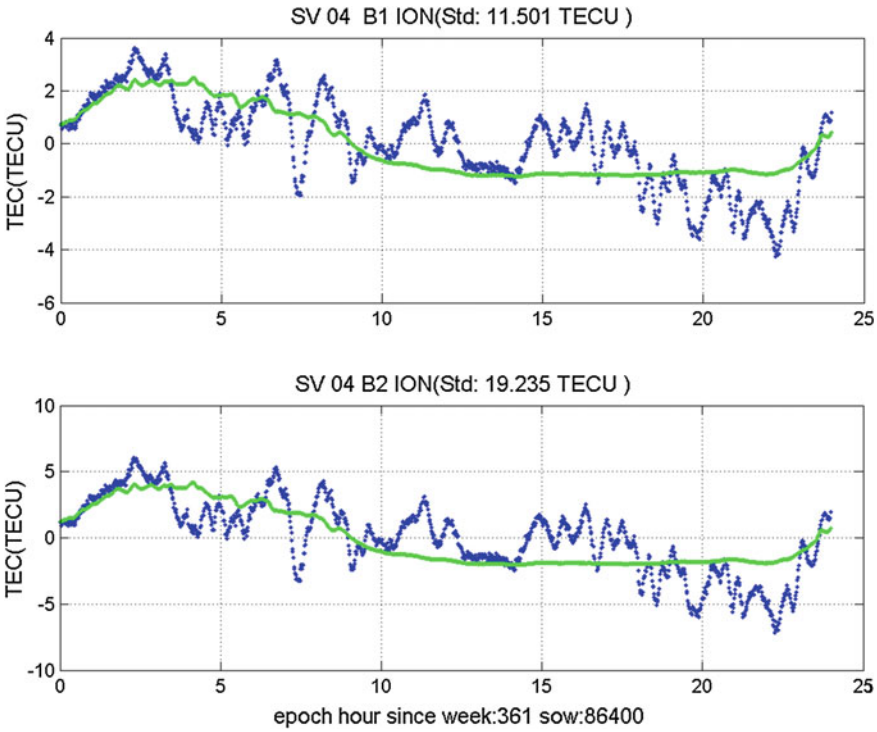

Fig. 33.6 Dual-frequency ionosphere delay monitoring results of SV04

Test results show that, In the condition of 10 lower degree elevation, the pesudorange multipath error of SV04 is 1.7 times larger than SV03, furthermore, the variation trends of multipath error are more severely, so it has greater influence on ionosphere delay monitoring results. The dual-frequency ionosphere delay monitoring results of SV04 are shown in Fig. 33.6, the calculation error of dual-frequency pseudorange ionosphere delay of B1 is 11.50TECU, B2 is 19.235TECU, and the error variation trends are drastic.

After corrected with real-time pseudorange estimation results, the monitoring results of dual-frequency ionosphere delay are as shown in Fig. 33.7.

The standard deviation of dual-frequency pseudorange ionosphere delay error before and after amended are listed in Table 33.3.

It can be seen from Fig. 33.7 and Table 33.3, after real-time pseudorange multipath error correction, the ionosphere delay error of B1 and B2 both have 55.7 % improvement ratio, the fluctuation in dual-frequency pseudorange ionosphere is eliminated basically, which proves this method is more effective for low elevation satellite in ionosphere delay monitoring.

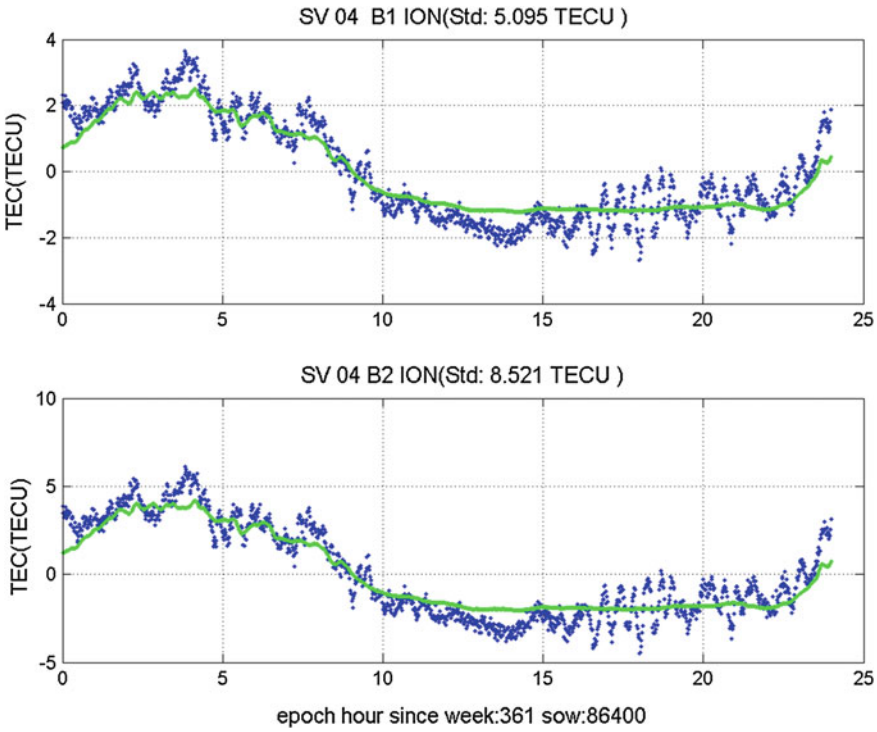

Fig. 33.7 Dual-frequency ionosphere delay monitoring results after multipath error corrected

Table 33.3 Calculating errors of ionosphere delay before and after correcting the multipath error for SV04 (TECU)

Frequency point	Before correcting	After correcting	Improvement (%)
B1	7.482	5.629	24.8
B2	12.513	9.414	24.8

33.5 Conclusions

The multipath error is the main factor affecting the ionosphere delay monitoring accuracy of dual-frequency pseudorange, in Compass system, affected by the obit characteristics; there is "coherent multipath error" in pseudorange of the GEO satellite, which degrades the dual-frequency pseudorange ionosphere monitoring accuracy seriously. This paper proposed a real-time multipath estimation and correction method, utilized multipath error of one sidereal day ago to estimate the current multipath error in real-time, thus the real-time estimation for current pseudorange multipath error is achieved. Test results show that, for GEO satellite whose elevation is 31.23°, the corrected ionosphere delay accuracy can be

improved by 24.8 %, for GEO satellite whose elevation is 21.02°, the corrected ionosphere delay accuracy can be improved by 55.7 %. Therefore, this algorithm can improve the calculation accuracy of dual-frequency pseudorange ionosphere delay effectively using low computational cost, so it is worthy to be widely spread.

References

1. Schempp T, Burke J, Rubin A (2008) WAAS benefits of GEO ranging. In: Proceedings of ION GNSS 2008, pp 1903–1910
2. Zhao W, Zhao N (2013) Analysis of the pseudorange multipath impact on dual-frequency ionospheric delay correction in compass system. In: Proceedings of the China satellite navigation conference (CSNC), LNEE 243, p 355 ff
3. Kaplan ED (2002) Understanding GPS principles and applications. Publishing House of Electronics Industry in 2002, Beijing, pp 208–210
4. Kee C, Parkinson B (1994) Calibration of multipath errors on GPS pseudorange measurements. In: Proceedings of the 7th international technical meeting of the satellite division of the institute of navigation, Salt Lake City, UT, 20–23 Sept 1994, pp 353–362

Chapter 34
The Realization of the RTK Algorithm Based on GPS/BDS OEM Board and the Test of its Performance

Conghui Du, Kaiwei Yang, Qiang Guo and Jianwei Zhang

Abstract Using the high-accuracy OEM board, which contains of BDS B1/B2/B3 and GPS L1/L2 frequency, this paper realized the embedded algorithm of RTK of BDS, GPS and BDS + GPS. Both static and ground kinematic tests were carried out to evaluate the precision of the embedded algorithm of RTK from BeiDou, GPS and BDS + GPS. In static mode, the results demonstrated that the accuracy of static zero-baseline was sub-mm for the horizontal component and 1 mm for vertical component using BDS. The proportion of the fix results were higher than 98 %. The accuracy of GPS for 10 km static baseline, whose difference of horizontal component was smaller than 1 cm and the vertical component was smaller than 3 cm, was better than BDS, whose difference for three component was better than 4 cm. The statistics accuracy of GPS for 10 km baseline was better than 4 mm for horizontal component and better than 2 cm for vertical component, and the BDS was better than 1.5 cm for horizontal component and better than 3.5 cm for vertical component. The proportion of the fix results were higher than 95 %. For kinematic baseline, the result of integration positioning was accordant to the real topography, and the standard deviation of adjustment of every epoch was better than 6 mm.

Keywords RTK · BeiDou · GPS · Integration positioning · High-accuracy board

C. Du (✉) · K. Yang · Q. Guo · J. Zhang
The 54th Research Institute of CETC, Shijiazhuang, China
e-mail: 734711301@qq.com

C. Du · K. Yang · Q. Guo · J. Zhang
Satellite Navigation Technology and Equipment Engineering Technology Research Center of Hebei, Shijiazhuang, China

J. Sun et al. (eds.), *China Satellite Navigation Conference (CSNC) 2014 Proceedings: Volume I*, Lecture Notes in Electrical Engineering 303,
DOI: 10.1007/978-3-642-54737-9_34,

34.1 Introduction

China is currently developing its own independent global navigation satellites system, that is, the BeiDou Navigation System, which can provide preliminary regional navigation and positioning service. At present, many scholars have done a lot of researches on BeiDou satellite system and related applications [1]. We can develop multiple applications of BeiDou system autonomously and easily based on the high-accuracy OEM board. Combined with computer, communications technology, the OEM board, which is embedded by high-accuracy RTK algorithm, can widely used in traditional mapping, driving school system, transportation, deformation monitoring, urban management and so on.

Integrated navigation can also provide stable, reliable positioning results in the case of poor observational environment, thereby increasing the operating distance. As the demand for high-precision positioning, the commercial production of the high-accuracy multi-frequency OEM board of BeiDou application is attracted more and more attention.

34.2 Embedded RTK Strategy Design

We design a kind of multi-frequency OEM board based on FPGA, whose the core parts are DSP and FPGA. The RTK algorithm is embedded in the DSP part.

34.2.1 Platform Introduction

The size of the OEM board is 88 mm × 57 mm, the power consumption is about 2.5 W. The DSP part uses the chip of TMS320C6416, whose maximum operating frequency is 720 MHz, the maximum addressable spaces 1M. The computational burden of DSP is focused on the information layer, including the extraction of raw observations, resolving navigation message, SPP and RTK task. The figure of the OEM board is presented in Fig. 34.1.

34.2.2 DSP Programming

RTK is a dynamic real-time relative positioning technology using the carrier phase observations [2].

Embedded RTK strategy content mainly consists combination of RTK tasks and stand-alone machine, real-time cycle slip detection, the ambiguity search for the increase or decrease satellites and ambiguity fixed when the reference satellite is

Fig. 34.1 The OEM board

changed. Its purpose is to ensure a high-accuracy and stable result output in complex environments or long time running conditions, without increasing operational complexity and space complexity. Successful strategy or not directly related to the stability of the OEM board and the quality of the data [3–5].

34.2.2.1 RTK Data Model

Dynamic relative positioning using dual-difference carrier phase observations, which eliminates the impact of the satellite clock error, receiver clock error, weakens the satellite orbit errors on the baseline solution. The dual-difference observation equation can be expressed as follows [1, 2]:

$$\begin{aligned}\Delta\nabla\phi(t)\cdot\lambda = \Delta\nabla\rho - \Delta\nabla N\cdot\lambda + \Delta\nabla d_{orb} \\ + \Delta\nabla Ion + \Delta\nabla Trop + \sum\delta\end{aligned} \tag{34.1}$$

where, $\Delta\nabla\phi(t)$ is the carrier phase measurements, λ is the wavelength of carrier phase, $\Delta\nabla d_{orb}$ is the track error, $\Delta\nabla Ion$ denotes the ionospheric delay, $\Delta\nabla Trop$ denotes the tropospheric delay, $\Delta\nabla\rho$ is the geometric distance between satellite position and BeiDou receiver position, $\Delta\nabla N$ is the integer ambiguity.

Suppose there are two simultaneous observation satellite station S^j and S^k, setting S^j reference satellite, we can get a linear form of the dual-difference observation equation [2]:

$$\Delta\nabla\phi^k\cdot\lambda = -[\nabla l_2^k\ \nabla n_2^k\ \nabla m_2^k]\begin{bmatrix}\delta X_2\\ \delta Y_2\\ \delta Z_2\end{bmatrix} - \Delta\nabla N^k\cdot\lambda + \Delta\nabla\rho \tag{34.2}$$

where the subscript "2" denotes the rover station, $\Delta\nabla\phi^k = \nabla\phi^k - \nabla\phi^j$, $\begin{bmatrix} \nabla l_2^k \\ \nabla n_2^k \\ \nabla m_2^k \end{bmatrix} = \begin{bmatrix} l_2^k - l_2^j \\ m_2^k - m_2^j \\ n_2^k - n_2^j \end{bmatrix}$

$(l_2^k, m_2^k, n_2^k), (l_2^j, m_2^j, n_2^j)$ is the direction cosine of the rover station to the two satellites. The error equation of Eq. (34.2) is rewritten as follow:

$$\upsilon^k(t) = \frac{1}{\lambda}[\nabla l_2^k(t)\ \nabla n_2^k(t)\ \nabla m_2^k(t)] \begin{bmatrix} \delta X_2 \\ \delta Y_2 \\ \delta Z_2 \end{bmatrix} + \Delta\nabla N^k + \Delta\nabla u^k(t) \tag{34.3}$$

where $\Delta\nabla u^k(t) = \Delta\nabla\phi^k(t) - \frac{1}{\lambda}\Delta\nabla\rho$.

As the rover position is constantly change, so the RTK operation only use one epoch observations. The integer ambiguity must be pre-calculated, which is the RTK initialization process. As long as the number of simultaneous observation satellites is greater than 4, we can conduct RTK task. After RTK initialization, we use the least squares method for positioning solving.

The flow chart of main RTK steps is expressed in Fig. 34.2.

34.2.2.2 Ambiguity Resolution

The key technology of RTK is maintaining the satellite measured on a continuous tracking in the dynamic observation process. Once the loss of satellites occurs, the job of initializing is need. According to Eq. (34.3), also because we use two frequency observations, so there are two dual-difference ambiguities of two frequencies need to fix. This paper adopts LAMBDA algorithm to search ambiguities. The statistical test is Ratio test method, when the ratio is greater than 3.5, giving the fixed results [2, 3].

34.2.2.3 Cycle Slip Detection

Accurate detection and repair cycle slip is the key to high-precision positioning, improving the continuity and reliability of positioning. For the DSP of the OEM board, we distribute 12 array space at most for RTK task, so the number of arrays must be control. Taking into account of the demand of the real-time application, we adopt the ionospheric residual method, which ionospheric residual continuous or not between two adjacent epoch, to detect cycle slip.

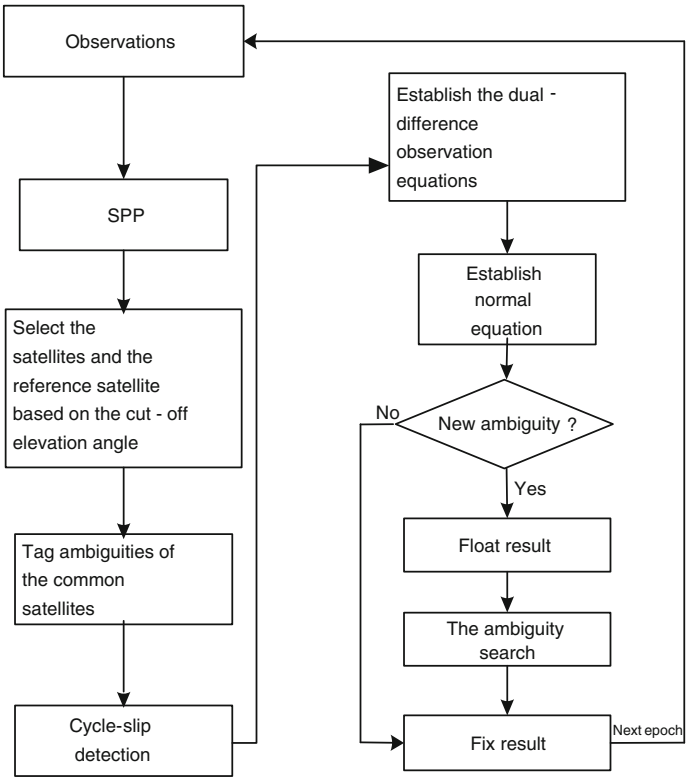

Fig. 34.2 Processing flow of RTK

For this paper, we just only detect cycle slip, without repairing. If there are cycle slips of non-reference satellites, we just need to fix the ambiguities of these satellites for this epoch again. But if there are cycle slips of the reference satellite, then we need to fix all the ambiguities.

34.3 Performance Test of the OEM Board

To assess the RTK accuracy of the OEM board, we designed three tests: static zero-baseline test, static 10 km baseline test and kinematic test.

34.3.1 Static Zero-Baseline Test

This measurements collected with two dual-frequency BeiDou/GPS receivers with 1 Hz sample rate and 10° cut-off elevation angle, which shared the same antenna

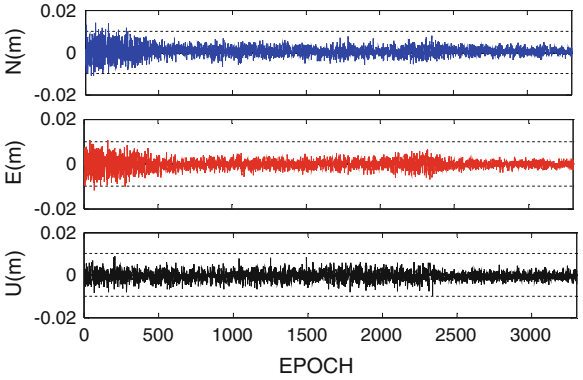

Fig. 34.3 L1L2 experiment of zero-baseline

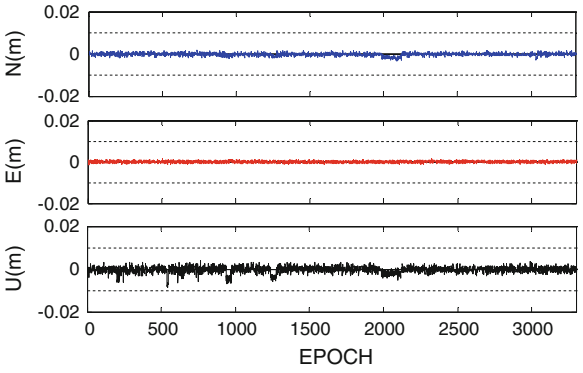

Fig. 34.4 B1B2 experiment of zero-baseline

installed on the a building roof. Suppose the two receivers are base station and rover station respectively, forming the task of RTK. The rover station receiver received the date of base station receiver, then dealt with the observations of two receivers real-timely and uploaded the results to computer with 1 Hz. We processed RTK algorithm for BDS, GPS and BDS + GPS respectively for 1 h and converted the results to North/East/Up orientation. The results of static zero-baseline data are compared with the truth value, "zero", to assess the accuracy. The results of each epoch of the N/E/U estimation are presented in Figs. 34.3, 34.4, 34.5, 34.6, 34.7. The statistics of the precision of the N/E/U results (1σ) and the proportion of fixed results are listed in Table 34.1.

It is indicated that the proportion of the fix results are higher than 98 %. The results of B1/B2 are the best, which the error of North and East are all most within ± 4 mm, and the vertical mostly within ± 5 mm. The statistics of the horizontal component is sub-millimeter and the vertical component is 1 mm. The error of GPS are all most within ± 8 mm of three-dimensional components and the statistics result is better than 3 mm.

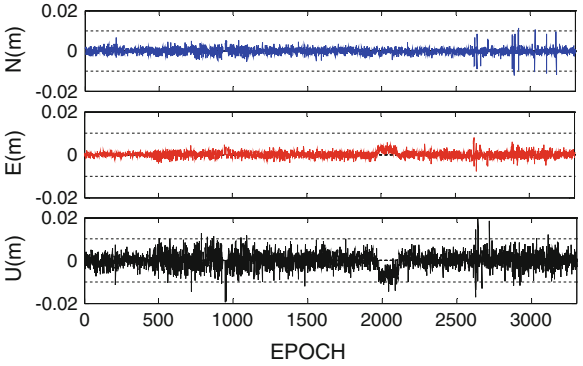

Fig. 34.5 B1B3 experiment of zero-baseline

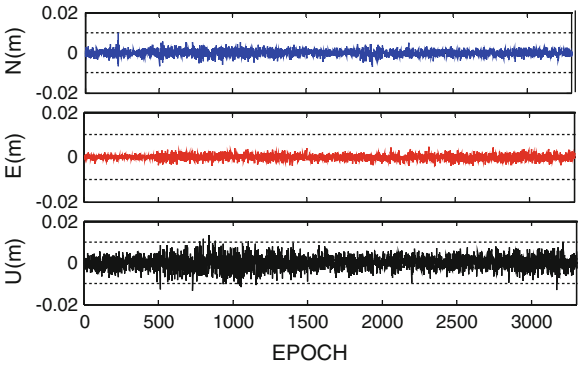

Fig. 34.6 B2B3 experiment of zero-baseline

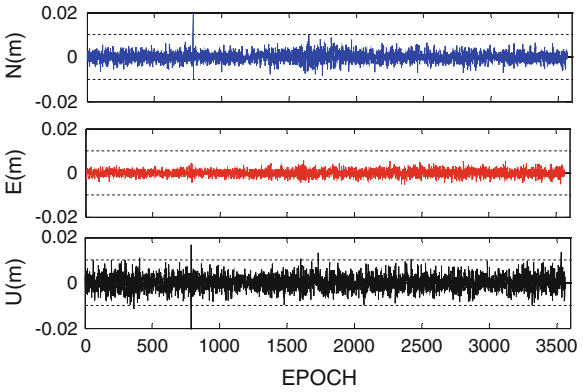

Fig. 34.7 GPS/BDS experiment of zero-baseline

Table 34.1 Processing precision of static zero-baseline (unit: mm)

Processing model	Proportion of the fix results (%)	N	E	U
L1L2	98.8	2.1	1.8	2.1
B1B2	99.9	0.6	0.4	1.0
B1B3	98.9	1.2	1.2	1.4
B2B3	99.0	0.5	1.2	2.9
GPS/BDS	99.7	2.1	1.3	3.0

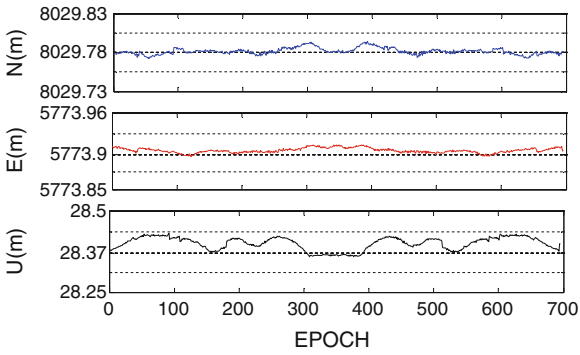

Fig. 34.8 L1L2 experiment of 10 km baseline

34.3.2 Static 10 km Baseline Test

This measurements also collected with two dual-frequency BeiDou/GPS receivers with 0.1 Hz sample rate and 10° cut-off elevation angle, which one antenna installed on the a building roof and another on a standard spot about 10 km far away. The rover station received the data of base station via the 3G module, forming the task of RTK, then dealt with the observations of two receivers real-timely and uploaded the results to computer with 0.1 Hz. We processed RTK algorithm for BDS, GPS and BDS + GPS respectively for 2 h and converted the results to North/East/Up orientation. The results of static 10 km baseline data are compared with the truth value, [8029.7816, 5773.9059, 28.4004], to assess the accuracy. The results of each epoch of the N/E/U estimation are presented in Figs. 34.8, 34.9, 34.10, 34.11, 34.12. The statistics of the precision of the N/E/U results (1σ) and the proportion of fixed results are listed in Table 34.2.

It is indicated that the proportion of the fix result is higher than 95 %. The results of GPS are the best, which the error of North and East are all most within ± 1 cm, and the vertical mostly within ± 3 cm. The statistics of the horizontal component is 4 mm and the vertical component is 2 cm. The error of B1/B2 are all most within ± 4 cm of three-dimensional components and the statistics result is better than 1.5 cm for horizontal component and 2 cm for vertical component.

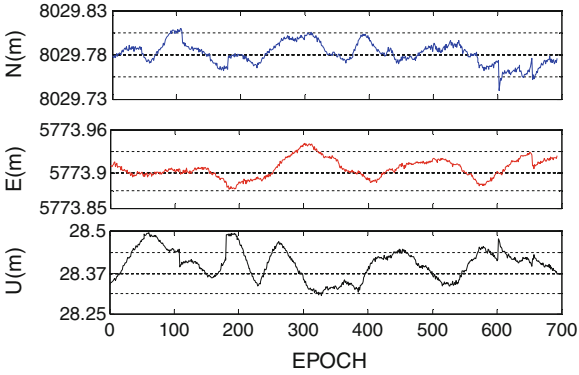

Fig. 34.9 B1B2 experiment of 10 km baseline

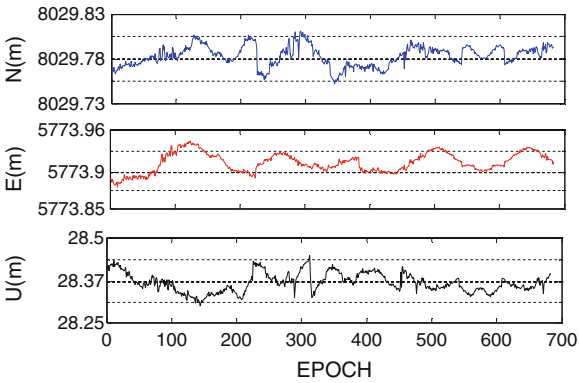

Fig. 34.10 B1B3 experiment of 10 km baseline

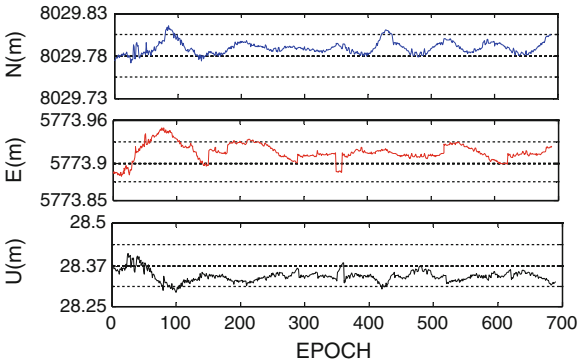

Fig. 34.11 B2B3 experiment of 10 km baseline

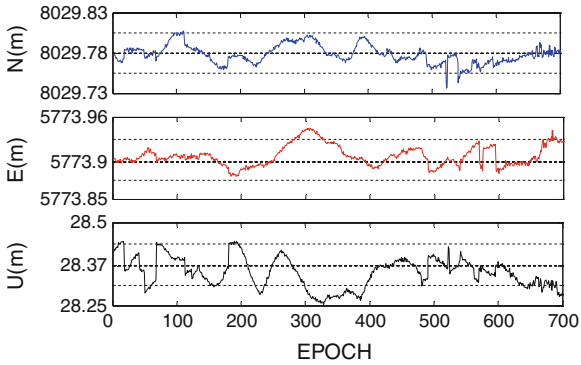

Fig. 34.12 GPS/BDS experiment of 10 km baseline

Table 34.2 Processing precision of static 10 km baseline (unit: mm)

Processing model	Proportion of the fix results (%)	N	E	U
L1L2	95.8	3.5	3.3	19.6
B1B2	97.1	11.5	12.7	31.6
B1B3	95.1	10.6	15.5	35.4
B2B3	96.0	9.5	15.0	65.3
GPS/BDS	95.7	12.5	13.1	45.1

34.3.3 Kinematic Test

The kinematic measurements collected with two dual-frequency BeiDou/GPS receivers with 1 HZ sample rate and 10° cut-off elevation angle, which one antenna installed on the a building roof and another running on the broad road about 1–2 km far away. The rover station received the data of base station via the broadcasting station, forming the task of RTK, then dealt with the observations of two receivers real-timely and uploaded the results to computer with 1 Hz, showed in Fig. 34.13. We processed RTK algorithm BDS + GPS for 1.2 h.

The test results and the actual map are very match, showed in Fig. 34.14 and the proportion of the fix results is 85.3 %. The standard deviation of adjustment of every epoch is depicted in Fig. 34.15. It is showed that the standard deviation is all in 6 mm.

Fig. 34.13 Rover station

Fig. 34.14 Test RTK result for road test of BD/GPS

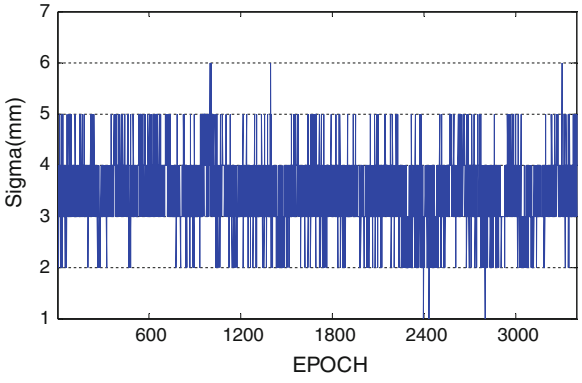

Fig. 34.15 Test std RTK result for road test of BD/GPS

34.4 Summary

Based on the high-accuracy OEM board, which contains of BDS B1/B2/B3 and GPS L1/L2 frequency, this paper realized the embedded algorithm of RTK of BDS, GPS and BDS + GPS. An assessment of the accuracy of the embedded RTK was done through both static and ground kinematic tests. The results showed that the accuracy of static zero-baseline was mm magnitude. The proportion of the fix results were higher than 98 %. The statistics accuracy of GPS for 10 km baseline was better than 4 mm for horizontal component and better than 2 cm for vertical component, and the BDS was better than 1.5 cm for horizontal component and better than 3.5 cm for vertical component. The proportion of the fix results were higher than 95 %. For ground kinematic baseline, the results of integration positioning were accordant to the real topography, and the standard deviation of adjustment of every epoch was better than 6 mm.

This paper was main realized the function of embedded RTK algorithm and the test of its performance was good. The accuracy of static test was better, but the stability of the results and practicability of long time running are need to test further. On the other hand, the strategies of cycle slip detection and ambiguity resolution are need to study to prove the accuracy and to reduce the operational complexity and the space complexity.

References

1. Shi C, Zhao Q, Hu Z, Liu J (2012) Precise relative positioning using real tracking data from COMPASS GEO and IGSO satellites. GPS Solution
2. Li Z, Huang J et al (2011) GPS surveying and data processing, vol 11. Wuhan University Publisher, pp P162–P168 (in Chinese)
3. Ren Z, Fan S, The basics of the embedded operating system. Beihang University Press (in Chinese)
4. Kaplan ED, Hegarty CJ (2010) Understanding GPS principles and applications. Publishing House of Electronics Industry (in Chinese)
5. Xie G (2010) Principles of GPS and receiver design. Publishing House of Electronics Industry (in Chinese)

Chapter 35
The Operation Fault Simulation and Availability Analysis of Navigation Satellite

Jintao Dang, Jianwen Li, Hai Huang and Fan Luo

Abstract When the operation faults of satellite navigation system occur, its navigation service performance will be affected. The regional satellite navigation constellation consists of GEO, IGSO and MEO. The space environments and orbit maneuvering situations of the satellites are different, because of their special orbit heights and types. Therefore, satellite fault situations need to be further refined and analyzed. The previous researches mostly discussed the two situations including orbit maneuvering and single event upset, but there is no considering about the randomness of orbit maneuvering or the fault situations of single event upset in different satellite work units. In this paper, the fault situations of single event upset are divided into four work units, including navigation task processing unit, spread spectrum receiver unit, satellite platform unit and satellite clock unit. Then, the specific fault simulation model is set up by the algorithm named Monte Carlo, and all the possible fault types of three kinds of satellites including GEO, IGSO and MEO are analyzed by simulation. Finally, the mathematical model of satellite availability is established, and then the satellite availabilities in different situations of fault types are analyzed comparatively.

Keywords Simulation · Satellite fault · Monte Carlo · Satellite availability

J. Dang (✉) · J. Li · H. Huang · F. Luo
The Institute of Surveying and Mapping, Information Engineering University, Zhengzhou, China
e-mail: jerrydawn@sina.cn

J. Li
e-mail: ZZLJW@126.com

J. Sun et al. (eds.), *China Satellite Navigation Conference (CSNC) 2014 Proceedings: Volume I*, Lecture Notes in Electrical Engineering 303,
DOI: 10.1007/978-3-642-54737-9_35,

35.1 Introduction

Satellite navigation system may fault in the operation course, and its navigation service performance will be affected during fault recovery. Researching satellite operation faults and establishing a more realistic simulation model will help to make a better evaluation on navigation service performance. For standard positioning service, the indicators of navigation service performance include constellation coverage, positioning accuracy, availability, integrity and continuity. Among them, availability is an important indicator closer to user demand, based on constellation coverage and positioning accuracy [1].

The previous discussions about orbit maneuvering situations, just put maneuvering interval and maneuvering recovery time as a constant, without considering maneuvering random characteristics. For single event upset, the previous researches only considered that the occurring probabilities of three kinds of satellites including GEO, IGSO and MEO are different, and the situations of single event upset were not divided into different work units of satellite. This paper intends to divide the fault situations of single event upset into four parts, including navigation task processing unit, spread spectrum receiver unit, satellite platform unit and satellite clock unit, and then all the possible fault types of three kinds of satellites are analyzed by simulation. Then, based on the simulation results, the satellite availabilities in different situations of fault types are analyzed comparatively.

35.2 Fault Types

The regional satellite navigation constellation consists of GEO, IGSO and MEO, with the characteristics of many satellite types, quantity, and complex constellation configuration [2]. Since three kinds of satellites have different orbit heights and types, the space environments and maneuvering situations of the satellites are different. The different space environments make their occurring probabilities of single event upset different. Simultaneously, the occurring probabilities of single event upset in different satellite work units are also different. Therefore, understanding and analyzing different fault types correctly have important theoretical value and engineering significance for constellation top-level design, evaluating constellation operation state and making maintenance strategies [3].

35.2.1 Single Event Upset

Single event effect is caused by a single high-energy proton or heavy proton passing through devices or microcircuit sensitive areas [4]. Analyzing from structural design, the products containing microcircuit devices in space environment, have the

risk of single event effect, whose effects mainly including single event upset, single event latch-up and so on. According to foreign applying statistics, the anti-radiation indicators provided by manufacturers and component irradiation experiments, the fact can be confirmed that single machine of satellite has almost no risk of single event latch-up, and the main risk is single event upset.

Since the space heights of GEO and IGSO are the same, the electromagnetic environments are basically the same. The occurring probabilities of single event upset are both about 1 times per 30 days, and the fault recovery times are both about 2 h. With regard to MEO, the occurring probability is about 1 times per 60 days, and the fault recovery time is about 12 h.

If single event upset can recover quickly after occurring, it will not basically affect the accuracy of satellite ephemeris and clock error, only affecting satellite availability. Single event upset in different work units has different effects on satellite service. If single machine of satellite measurement and control system and laser timer malfunction in short term, it will not basically affect navigation service. If reference frequency synthesizer and rubidium clock malfunction, the effects will be serious. However, the device performance used is relatively low, so the occurring probability is very low (not be found on experimental satellites during 2 years). The faults of spread spectrum receiver can recover quickly, only affecting the uplink continuous injection. If navigation task processing unit switches on-off, because of the principle of satellite-ground design, the fault recovery time is generally 3–7 h, which has great effects on satellite availability. According to satellite in-orbit observation data, single event upset can be divided specifically into different fault types, as shown in Table 35.1.

Wherein, P1, P2, P3, P4 are the occurring probabilities of single event upset of navigation task processing unit, spread spectrum receiver unit, satellite platform unit and satellite clock unit respectively. S0, S1, …, S15 are the occurring probabilities of 16 kinds of fault types. The occurring probability of single event upset for each satellite is equal to the combination of the occurring probabilities of different work units, calculated by the formula (35.1).

$$p_s = 1 - (1 - p_1)(1 - p_2)(1 - p_3)(1 - p_4) \tag{35.1}$$

Due to the limited observation data, the exact value cannot be yet calculated for the occurring probability of each fault type. Therefore, this paper simply considers that the occurring probability of each fault type is equal in the simulation analysis. Thus, the ratio of the occurring probabilities of single event upset of 4 work units is 90:40:10:2. Taking into account a lot of fault types, the simulation assumes that only one kind of fault occurs each time for each work unit, meaning that the fault probability of each work unit is equal to the sum of the probabilities of all fault types of the work unit.

Table 35.1 Single event upset fault classification

Work units	Fault types
Navigation task processing unit (P1)	Navigation message error (S0)
	I branch capture exception (S1)
	Frequency difference limit exceeding (S2)
	Q branch loss of lock (S3)
	Work conditions showing error (S4)
	I branch pseudorange occurring slowly (S5)
	I branch seconds of week counting error (S6)
	Downlink frequency occurring slips (S7)
	Uplink ranging stratification (S8)
Spread spectrum receiver unit (P2)	Uplink injection failed (S9)
	Uplink channel ranging values occurring steps (S10)
	Uplink channel Q branch capture failed (S11)
	Uplink channel ranging slips (S12)
Satellite platform unit (P3)	Platform work exception (S13)
Satellite clock unit (P4)	Clock automatically switching (S14)
	Rubidium clock light pressure parameters occurring exception (S15)

35.2.2 Orbit Maneuvering

High orbit satellites running in space, due to the combined effects of the Earth's non-spherical gravity, lunisolar gravity, solar radiation pressure and other perturbation, their orbit positions will gradually deviate from the nominal value, resulting in constellation configuration changing, thereby affecting navigation service performance. At the same time, due to the limited space orbit positions, the International Telecommunication Union (ITU) has made the regulation that GEO satellite point longitude must be controlled within $\pm 0.1°$ range. In order to maintain constellation service performance and comply with ITU rules, for regional constellation, the frequent orbit maneuvering is needed for GEO.

Orbit maneuvering is usually accomplished by using 10 N satellite engine (N is the thrust unit, Newton), including two work modes, continuous jet and pulsed jet. The work time of continuous jet is about tens of seconds, and the work time of pulsed jet is about a few seconds. For GEO, orbit maneuvering can be divided into two control modes including east–west position maintaining and north–south position maintaining. Among them, east–west position maintaining needs 20 min approximately, and north–south position maintaining varies by the size of the orbit inclination, needing a few hours. For IGSO and MEO, orbit maneuvering mainly needs to adjust the phase, and the recovery time is short relatively. The maneuvering situations of different orbit types are as shown in Table 35.2.

Table 35.2 The maneuvering situations of different orbit types

Orbit types		Maneuvering interval	Maneuvering recovery time
GEO east–west position maintaining	GEO-1	20 days	20 min
	GEO-2	40 days	20 min
	GEO-3	20 days	20 min
	GEO-4	60 days	20 min
	GEO-5	20 days	20 min
GEO north–south position maintaining		4 a	6 h
IGSO		100 days	2 h
MEO		200 days	2 h

35.3 Fault Simulation

In the simulation analysis, this paper assumes that the faults occur randomly and the fault recovery times obey normal distribution. Therefore, the generation of good random numbers is the key to fault simulation. In this paper, a linear congruential generator is used to generate random numbers, and Monte Carlo algorithm is used to simulate the fault distribution.

35.3.1 Monte Carlo Algorithm

Monte Carlo algorithm is a kind of calculating method based on random numbers, also called computer random simulation method. The generation of good random numbers is the key to Monte Carlo simulation. In the computer implementation, generally through a deterministic algorithm to generate random numbers, the sequences generated in this way are not random in nature, only a good imitation of random number characteristics (as can be checked by statistics), usually called pseudo-random numbers. Assume that random variables $U_1, U_2, \ldots, U_n$ are independent of one another in the $(0, 1)$ uniform distribution, according to the central limit theorem:

$$X = \left(\sum_{i=1}^{n} U_i - \frac{n}{2} \right) / \sqrt{\frac{n}{12}} \tag{35.2}$$

X obeys the normal distribution $N(0, 1)$ asymptotically, and generally $n = 10$ is proper. Let $n = 12$, and then the above formula can be simplified into the formula (35.3).

$$X = \sum_{i=1}^{12} U_i - 6 \tag{35.3}$$

Thus, by the formula $Y = \sigma X + \mu$, you can get the random number Y obeying the normal distribution $N(\mu, \sigma^2)$.

35.3.2 Simulation Analysis

Since single event upset belongs to unscheduled interruption, according to the occurring probability of single event upset, the satellite states can be divided into 0–1 (normal state or single event upset state), using Monte Carlo simulation method for generating 0–1 pseudo-random numbers.

Orbit maneuvering is short-term plan interruption, with a certain cyclicity. In addition, Adjustment timely is needed according to the satellite in-orbit situations. The cycle is assumed to m days, and the deviation is ξ between the maneuvering epoch and the nearest cycle. At the same time, assume that ξ obeys $N(0, \sigma^2)$, and σ is the standard deviation, which can be set to a certain value (determined by the 3σ principle that the probability of the adjustment time between the minimum and maximum value is 99.7 %).

Assume that the recovery times of all kinds of faults obey normal distribution (normal distribution is the most wide distribution in nature), that is $\eta \sim N(MTR, \sigma_\eta^2)$. Wherein, *MTTR* is the average value of fault recovery time, and σ_η is the standard deviation, which can be set to a certain value (determined by the 3σ principle that the probability of the recovery time between the minimum and maximum value is 99.7 %).

35.3.2.1 Single Event Upset Simulation

For different orbit types, the occurring probabilities of single event upset are different, and the fault recovery times are also different. The space electromagnetic environments of GEO and IGSO are the same, as the space heights are equal. Therefore, the situations of single event upset of both can be considered the same. This paper carries out the simulation analysis only for GEO and MEO, and the results are as shown in Figs. 35.1 and 35.2 (marks 0–15 represent the 16 kinds of fault types of single event upset, consistent with the sequence in Table 35.1).

Wherein, the simulation time starts from October 1, 1990 (Julian date 48165) to October 1, 2020 (Julian date 59123), and the time span is 30 years, 1 day set as the interval; The occurring probability of single event upset for GEO is 1/30 days. The average value of fault recovery time is 2 h, and the variance is 15 min; The occurring probability of single event upset for MEO is 1/60 days. The average value of fault recovery time is 12 h, and the variance is 30 min; The ratio of fault probabilities of 4 work units is 90:40:10:2, and the occurring probability of each work unit is equal to the sum of the occurring probabilities of all faults types of the work unit.

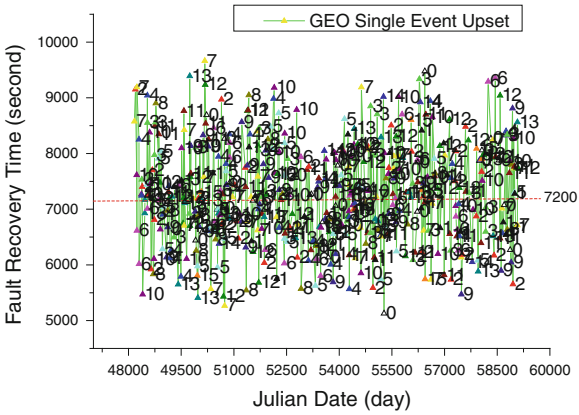

Fig. 35.1 GEO fault simulation of single event upset

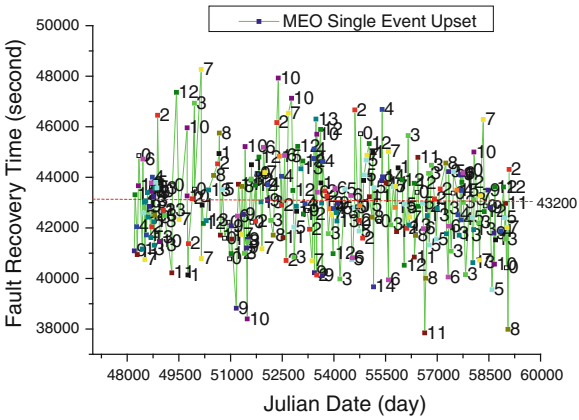

Fig. 35.2 MEO fault simulation of single event upset

As can be seen from the above two figures: (1) the fault recovery times are uniformly distributed around the average value, consistent with the random characteristics of normal distribution; (2) The transverse distribution of the faults of GEO are denser than MEO, which is corresponding to the fault probability size of both; (3) The maximum values of the fault recovery times of GEO and MEO are both basically within 3σ, in line with the 3σ principle of normal distribution; (4) The ratio of the fault recovery times of 4 work units is approximately equal to 90:40:10:2, that is the ratio of the fault probabilities of all work units; (5) For satellite clock unit, the faults occur only 8 times for GEO, only 5 times for MEO, indicating that the fault probability of satellite clock unit is very low, one time averagely 4–5 years.

35.3.2.2 Orbit Maneuvering Simulation

According to the input parameters of orbit maneuvering in Table 35.2, orbit maneuvering simulation is carried out, and the simulation time is the same as single event upset simulation. Since the situations of IGSO and MEO about orbit maneuvering are relatively simple, the simulation analysis in this paper is only for the more complex orbit maneuvering of GEO. The recovery time of east–west position maintaining is 20 min, setting the variance 100 s, and the recovery time of north–south position maintaining is 6 h, setting the variance 900 s. The results of orbit maneuvering simulation are as shown in Fig. 35.3.

Wherein, marks 1–5 represent the 1st to the 5th east–west position maintaining, and mark 6 represents north–south position maintaining in Fig. 35.3. As can be seen from Fig. 35.3: (1) The recovery times of east–west position maintaining are uniformly distributed around the average value, consistent with the random characteristics of normal distribution; (2) The times of east–west position maintaining is inversely proportional to maneuvering intervals; (3) The occurring probability of north–south position maintaining is very low, one time averagely 4–5 years, and the maneuvering recovery time is long relatively each time, spending several hours.

35.4 Satellite Availability Analysis

Availability is an important indicator of satellite navigation system service performance. Satellite availability is an annual time percentage of space signals that can be tracked and are "healthy", launched by the satellites occupying slots. Here the "healthy" signals mean that no warning indicators occur for navigation signals and satellite health word is "healthy". Therefore, satellite availability is directly related to the state of the satellite faults, and its value can be calculated by the information of the satellite faults.

Based on the average interval time of the faults *MTBF*and the average recovery time of the faults *MTTR*, the occurring probabilities of the satellite faults can be calculated as shown in the formula (35.4).

$$p_i = \frac{MTTR_i}{MTBF_i + MTTR_i}, \quad i = 1, 2, 3, \ldots \tag{35.4}$$

Assume that regional navigation constellation has $n(n \geq 4)$ navigation satellites, and each satellite is assumed that only one kind of fault occurs at every moment. It's easy to get the average availability of each satellite, as shown in the formula (35.5).

$$P = 1 - \sum_{i=1}^{n} p_i, \quad n \geq 4 \tag{35.5}$$

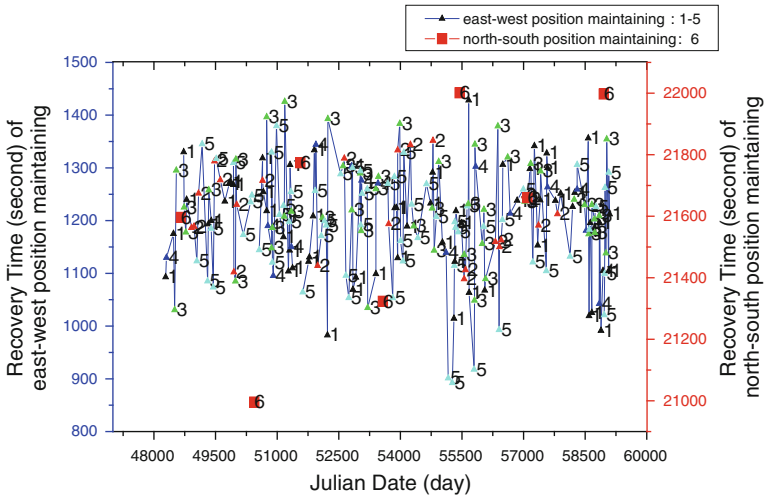

Fig. 35.3 GEO orbit maneuvering simulation

Table 35.3 The calculating results of satellite availability

Satellite	GEO-1 (%)	GEO-2 (%)	GEO-3 (%)	GEO-4 (%)	GEO-5 (%)	IGSO (%)	MEO (%)
Case 0	100	100	100	100	100	100	100
Case 1	98.43	98.43	98.43	98.43	98.43	98.43	98.59
Case 2	97.33	97.88	97.33	98.12	97.33	98.25	98.57
Case 3	97.02	97.75	97.02	97.99	97.02	98.13	98.44

According to the information of fault and maneuvering given in this paper, satellite availability is calculated and compared in different cases, as shown in Table 35.3. The four cases (Case 0–3) are corresponding separately to normal operation state, only considering single event upset, only considering orbit maneuvering and taking into account single event upset and orbit maneuvering simultaneously.

As can be seen from Table 35.3: (1) The effects of orbit maneuvering on satellite availability are larger than single event upset; (2) The satellite availabilities of IGSO and MEO are higher than GEO; (3) The satellite availability of MEO is the highest among three kinds of satellites.

35.5 Conclusions

In this paper, the situations of single event upset are classified into four parts, including navigation task processing unit, spread spectrum receiver unit, satellite platform unit and satellite clock unit for the simulation analysis. The fault

distributions obtained by simulation are more comprehensive and actual, and it is beneficial to evaluating satellite operating state and making maintenance strategy.

Meanwhile, the situations of three kinds of satellites, that is GEO, IGSO and MEO, are analyzed by simulation about orbit maneuvering, taking into account the cyclicity and randomness of orbit maneuvering, more consistent with the actual situations of orbit maneuvering.

Based on the results of fault simulation, satellite availability in different fault situations is compared and analyzed. The conclusion is that different maneuvering situations, orbit types, and fault types have great effects on satellite availability.

References

1. Li G, Li J, Jiao W et al (2010) Analysis of PDOP availability of navigation constellation based on satellite service intermittence. Geomatics Inf Sci Wuhan Univ 7:841–845
2. DoD US (2001) Global positioning system standard positioning service performance standard. Assistant secretary of defense for command, control, communications, and intelligence
3. Xu J (2008) Modeling and evaluation of effects of fault satellites distribution on PDOP availability of navigation constellation. Acta Aeronaut ET Astronaut Sin 29(5):1139–1143
4. William J (2007) Global positioning system (GPS) standard positioning service (SPS) performance analysis report. Federal Aviation Administration, Washington, DC

Chapter 36
Analysis of Characteristics of BDS Observable Combinations for Wide-Lane Integer Ambiguity Resolution

Guangxing Wang, Kees de Jong, Xiaotao Li, Qile Zhao and Jing Guo

Abstract The characteristics of BDS (BeiDou System) observables were analyzed with 30 days of observables collected at five stations distributed in Asia-Pacific area. Signal-to-noise ratio, phase-minus-code combination and MW (Melbourne-Wübbena) combination of BDS observables were investigated. Kalman filtering was employed to smooth the time series of MW combinations. The signal-to-noise ratios are different from satellite to satellite, while the differences among different frequencies are marginal. Diurnal fluctuations can be seen from the time series of phase-minus-code combinations, and they probably reflect the daily variations of ionospheric effects. Typical standard deviations of MW combination for GEO satellites are between 0.27 and 0.37 m, and those for IGSO satellites are around 0.42 m. Fractional parts of mean values of MW combination for different passes of IGSO satellites remain almost constant, while similar behavior is not shown in the case of BDS MEO satellites. For GEO satellites, daily fluctuations can be seen in the time series of MW combinations. Due to these different behaviors, the strategy of wide-lane FCB estimation may depend on the type of satellite, rather than simply averaging MW combinations for all of them.

Keywords BDS · GPS · MW combination · SNR · Ionospheric effects · Wide-lane · FCB

G. Wang (✉) · X. Li · Q. Zhao (✉) · J. Guo
GNSS Research Center of Wuhan University, Wuhan 430079, China
e-mail: gxwang0113@126.com

Q. Zhao
e-mail: zhaoql@whu.edu.cn

X. Li
e-mail: woailixiaotao@126.com

G. Wang · K. de Jong · J. Guo
Fugro Intersite B.V, Dillenburgsingel 69, 2263 HW, Leidschendam, The Netherlands

J. Sun et al. (eds.), *China Satellite Navigation Conference (CSNC) 2014 Proceedings: Volume I*, Lecture Notes in Electrical Engineering 303,
DOI: 10.1007/978-3-642-54737-9_36,

36.1 Introduction

On December 27, 2012, the BeiDou Navigation Satellite System (BDS, earlier referred to as COMPASS) officially started providing Positioning, Navigation and Timing (PNT) service in most of Asia-Pacific area. The BDS currently comprises a total of 15 satellites: five satellites in geostationary (GEO), five satellites in inclined geosynchronous orbits (IGSO) and five satellites in medium Earth orbits (MEO). Each satellite broadcasts signals at three frequencies simultaneously, which makes it possible to form combinations with favorable features, such as longer wavelength or moderate or no ionospheric effects.

Qualities and statistical behaviors of BDS original measurements, as well as their combinations, have been studied since the advent of BDS. Cheng et al. [1] compared the qualities of BDS and GPS ranging signals, and investigated the impacts of multi-path errors on the ambiguities of the phase-minus-code combination. The conclusion is that ranging signals from GEO satellites outperform those from IGSO satellites, and multi-path errors in signals from these two types of satellites contain long-periodic and short periodic trends, respectively. Proper triple-frequency combinations of BDS are able to enhance the detection of cycle slips and to accelerate ambiguity resolution. Some meaningful triple-frequency combinations of BDS were suggested by Shen et al. [7], based on the analysis of characteristics of different combinations. Experiments showed that the quality of BDS observables is marginally higher than that of GPS ones, especially when the elevation is lower [10]. However, characteristics of BDS observables collected by different types of receivers have not yet been extensively studied.

Methods of integer ambiguity resolution (IAR) in precise point positioning (PPP) with GPS were advanced [2, 3]. In these methods, the determination of uncalibrated phase delays (UPDs) or fractional cycle biases (FCBs) was a prerequisite of IAR. Firstly, the original ambiguities were transformed to wide-lane and narrow-lane. Then, wide-lane and narrow-lane UPDs or FCBs, determined successively at one or more reference sites, were utilized to help recover the integer properties of ambiguities at mobile site. Due to the special orbit design, GEO and IGSO satellites stay in view for a longer period in Asia-Pacific region, which makes it necessary to investigate the time-variant behaviors of FCBs before determining them by simply averaging over epochs.

As mentioned above, averaging over time is one of the methods for wide-lane FCB estimation of GPS satellites, due to their relative stability over long periods. BDS is composed of three different types of satellites, the observables and FCBs of which may have different behaviors over the longer term. These behaviors might play an important role in selecting proper strategy for FCB estimation of BDS. This paper aims at analyzing and comparing the characteristics of both BDS and GPS observables, in order to provide some reference for the signal design and wide-lane FCB estimation for BDS.

36.2 Fundamental Functional Models

For a receiver-satellite pair a - s, the undifferenced code and carrier phase observation equations on frequency i at epoch time t can be written as [5]

$$p_{i,a}^{s}(t) = \rho + \gamma_i I_a^s(t) + dp_{i,a} - dp_i^s \tag{36.1}$$

$$\phi_{i,a}^{s}(t) = \rho - \gamma_i I_a^s(t) + \lambda_i N_{i,a}^s + d\phi_{i,a} - d\phi_i^s \tag{36.2}$$

where $\rho = R_a^s(t) + T_a^s(t) + c\delta t_a(t) - c\delta t^s(t)$ is the sum of all time-dependent and frequency-independent (or non-dispersive) items, $R_a^s(t)$ is the receiver-satellite range, $T_a^s(t)$ is the zenith tropospheric delay, $\delta t_a(t)$ and $\delta t^s(t)$ are the receiver and satellite clock errors respectively, c is the speed of light, $I_a^s(t)$ is the (first-order) slant ionospheric delay the first frequency, $\gamma_i = f_1^2/f_i^2$, $N_{i,a}^s$ is the phase ambiguity, λ_i the wavelength of frequency i, $dp_{i,a}$ and dp_i^s are the frequency-dependent code hardware delays, while $d\phi_{i,a}$ and $d\phi_i^s$ are their phase counterparts. Note that all the bias terms are in units of meters. Not shown in the above equations are observation noise terms, with expectation equal to zero, and higher-order ionospheric effects. For the purpose of simplicity, subscripts for receiver, satellite and epoch time are omitted where it does not cause misunderstanding in the following sections.

36.2.1 Phase-Minus-Code Combination

Subtracting (36.1) from (36.2), the phase-minus-code combination can be expressed as [5, 9]

$$\phi_i - p_i = -2\gamma_i I + \lambda_i N_i + (d\phi_{i,a} - d\phi_i^s) - (dp_{i,a} - dp_i^s) \tag{36.3}$$

In this combination, the terms of receiver-satellite geometry and tropospheric delay, as well as receiver and satellite clock errors are eliminated, while ionospheric effect is amplified. As is explicit in Eq. (36.3), the first-order ionospheric term is doubled. In addition, the higher-order terms, although not shown in Eq. (36.3), would also be amplified according to their presence in the observation equations [4]. For a typical case, e.g. station WUHN (30.53°N, 114.36°W) in central China, the first-order ionospheric term on L1 frequency could be more than 50 m [6], and even more than 100 m in extreme conditions [4]. Compared with ionospheric delay, the magnitude and variation of hardware delay terms are much smaller. If no cycle slip occurs, the ambiguity will remain the same, and the combination mainly reflects the variation of ionospheric effects.

36.2.2 MW Combination

To construct the MW (Melbourne-Wübbena) combination between frequency i and j, we first define [2]

$$\frac{f_i}{f_i+f_j}p^s_{i,a}+\frac{f_j}{f_i+f_j}p^s_{j,a}=\rho^s_a+\frac{f_1^2}{f_if_j}I^s_a+dp_{MW,a}-dp^s_{MW} \tag{36.4}$$

$$\frac{f_i}{f_i-f_j}\phi^s_{i,a}-\frac{f_j}{f_i-f_j}\phi^s_{j,a}=\rho^s_a+\frac{f_1^2}{f_if_j}I^s_a+\lambda_{ij}N^s_{ij,a}+d\phi_{MW,a}-d\phi^s_{MW} \tag{36.5}$$

where $dp_{MW,a}$ and dp^s_{MW} are receiver and satellite code hardware delay, $d\phi_{MW,a}$ and $d\phi^s_{MW}$ are receiver and satellite phase hardware delay, λ_{ij} and N_{ij} are the wide-lane wavelength and ambiguity, with

$$\begin{cases}\lambda_{ij}=\dfrac{c}{f_i-f_j}\\ N_{ij}=N_i-N_j\end{cases} \tag{36.6}$$

Subtracting (36.4) from (36.5), the MW combination can be expressed as

$$\begin{aligned}&\frac{f_i}{f_i-f_j}\phi_i-\frac{f_j}{f_i-f_j}\phi_j-\left(\frac{f_i}{f_i+f_j}p_i+\frac{f_j}{f_i+f_j}p_j\right)\\&=\lambda_{ij}N_{ij}+d\phi_{MW,a}-d\phi^s_{MW}-\left(dp_{MW,a}-dp^s_{MW}\right)\end{aligned} \tag{36.7}$$

The above combination eliminates the effects of receiver-satellite geometry, tropospheric delay, receiver and satellite clock errors, and first-order ionospheric delay. Apart from observation noise, it only contains wide-lane ambiguity and hardware delays. For the convenience of discussion, *Nij* ($i, j = 1, 2, 3, i = j$) in the following sections represent the MW combinations for frequencies i and j divided by wide-lane wavelength. They are actually affected by the hardware delay residuals, and have no integer nature.

36.2.3 Single State Kalman Filtering

Recursive least-squares make it possible to update least-squares estimators for new observables without the need of having to save all past observables. Here, it is employed to reduce the random noise contained in MW combinations. The recursive estimation procedure is initialized with the computation of the initial least-squares estimate $\hat{x}_{0|0}$, i.e.

$$\begin{cases} \hat{x}_{0|0} = (A_0^T Q_0^{-1} A_0)^{-1} A_0^T Q_0^{-1} y_0 \\ Q_{\hat{x}_{0|0}} = (A_0^T Q_0^{-1} A_0)^{-1} \end{cases} \tag{36.8}$$

Once $\hat{x}_{0|0}$ is known, $\hat{x}_{k|k}$ can be computed from $\hat{x}_{k|k-1}$ and y_k ($k = 1, 2, \ldots$) as [8]

$$\begin{cases} \hat{x}_{k|k-1} = \Phi_{k,k-1} \hat{x}_{k-1|k-1} \\ Q_{\hat{x}_{k|k-1}} = \Phi_{k,k-1} Q_{\hat{x}_{k-1|k-1}} \Phi_{k,k-1}^T + q\Delta t I \end{cases} \tag{36.9}$$

$$\begin{cases} \hat{x}_{k|k} = \hat{x}_{k|k-1} + K_k v_k \\ K_k = Q_{\hat{x}_{k|k}} A_k^T Q_k^{-1} \\ v_k = y_k - A_k x_{k|k-1} \\ Q_{\hat{x}_{k|k}} = (Q_{\hat{x}_{k|k-1}}^{-1} + A_k^T Q_k^{-1} A_k)^{-1} \end{cases} \tag{36.10}$$

where y is the state to be filtered, $\hat{x}$ is the estimate of parameter, A is the design matrix, Φ is the state transmission matrix, Q is the covariance matrix of the observations, q is the spectral density factor, I is the unit matrix, K is the gain matrix and v is the predicted residual. The subscript $k|k-1$ denotes predicted value, $k|k$ denotes filtered value and $k, k-1$ denotes state transmission from epoch $k-1$ to k.

Equations (36.9) and (36.10) are time-update and measurement-update, respectively. In this work, only one state is filtered, so single state Kalman filtering is utilized. With y the state of MW combination at each epoch, the above matrices A and Φ are reduced to scalars 1, and Q_k ($k = 0, 1, 2, \ldots$) is calculated according to the empirical precision of observables. System noise can be taken into account by applying proper spectral density factor q.

36.3 Data Description

Thirty days of daily multi-GNSS data collected from May 19 (day of year 139) to June 17 (day of year 168), 2013 at five stations in Asia-Pacific area were analyzed. Stations F713, CUT0 and PFTP are located in Curtin, Australia, F783 in Manila, and F725 in Seoul, South Korea (see Fig. 36.1). Among the five stations, F713, F725, F783 and CUT0 are equipped with Trimble NetR9 receivers, while PFTP is equipped with a Unicore UR240-CORS receiver. Both GPS and BDS observables were processed. For BDS, observables on B1, B2 and B3 were available at all stations except PFTP, while for GPS, only observables on L1 and L2 were processed.

Shown in Fig. 36.2 are the elevation angles of BDS GEO satellites at each station. Generally, elevations of GEO satellites at F783 are greater than at the other four stations, since F783 is located near the equator. Elevations at F713, CUT0 and PFTP are nearly the same. Elevations of C03 and C01 are the largest for all five stations, while C05 is the lowest, especially at station F725.

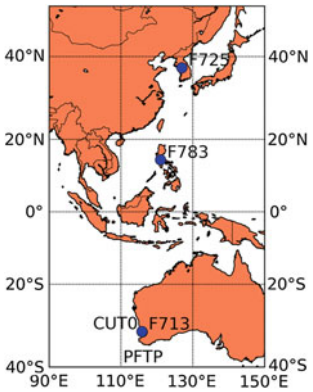

Fig. 36.1 Locations of five stations. Stations F713, CUT0 and PFTP are so close to each other that they seem to overlap in the figure

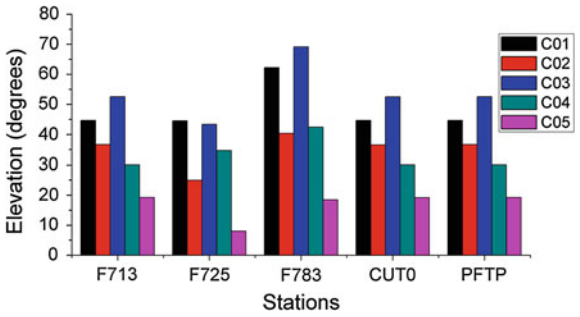

Fig. 36.2 The elevation angles of BDS GEO satellites at each station

Table 36.1 Values of frequencies and wavelengths of original signals and wide-lane combinations for GPS and BDS

System	Original			Wide-lane		
	Band	Frequency (MHz)	Wavelength (cm)	Combination	Wavelength (cm)	Variance (metric)
GPS	L1	1575.42	19.03	L1/L2	86.19	$33.0\ \sigma_{phs}^2 + 0.5\ \sigma_{code}^2$
	L2	1227.60	24.42	–	–	–
BDS	B1	1561.098	19.20	B1/B2	84.70	$31.1\ \sigma_{phs}^2 + 0.5\ \sigma_{code}^2$
	B2	1207.140	24.83	B1/B3	102.47	$47.3\ \sigma_{phs}^2 + 0.5\ \sigma_{code}^2$
	B3	1268.52	23.63	B2/B3	488.42	$813.9\ \sigma_{phs}^2 + 0.5\ \sigma_{code}^2$

Frequencies and wavelengths related to original signals and MW combinations for both systems are shown in Table 36.1. Variances were computed according to the frequency-dependent coefficients in Eq. (36.7) with the assumption that standard deviations for different frequencies are the same. σ_{phs}^2 and σ_{code}^2 represent the a priori variances of carrier phase and code range respectively.

Observables were employed to form MW combinations, and comparisons were conducted among different combinations, different site locations, different

satellites, as well as different receivers. In order to reduce observation noise and at the same time retain signal characteristics, single state Kalman filtering was applied to smooth the raw time series.

36.4 Results and Discussion

36.4.1 Signal to Noise Ratio

Signal-to-noise ratio (SNR), defined as the ratio of signal power to noise power, could be utilized to evaluate the quality of ranging signals, and therefore, indirectly, the precision of carrier phase observations. The time series of signal-to-noise ratios are shown in Fig. 36.3. Each panel represents a GEO satellite of BDS, and black, red and green dots represent the signal-to-noise ratios of frequency bands B1, B2 and B3. Generally speaking, satellites C03 and C01 have the highest signal-to-noise ratio, and satellite C05 the lowest. In addition, each time series of signal-to-noise ratio shows a daily periodicity. Signal-to-noise ratios of each satellite at station F725 are lower than their counterparts at the other four stations, especially for the spikes at frequency band B3. At station PFTP, signal-to-noise ratio of carrier phase B2 is obviously higher than that of carrier phase B1, which confirms the conclusion of Zhang and Ding [10]. Actually, the receiver equipped at station PFTP is of the same type (Unicore) as that used by Zhang and Ding [10] in their analysis. For most cases other than F725, the signal-to-noise ratio of band B3 is higher than those of the other two bands, but the differences among frequencies are marginal compared with those among satellites. In Fig. 36.3e, signal-to-noise ratios are different before and after the interruption, which might relate to the replacement of receiver.

36.4.2 Phase-Minus-Code Combination Analysis

Time series of phase-minus-code combinations at five stations are shown in Fig. 36.4. Each subplot represents one GEO satellite, and black, red and blue lines represent $(\varphi_1 - p_1)/\lambda_1$, $(\varphi_2 - p_2)/\lambda_2$, $(\varphi_3 - p_3)/\lambda_3$ respectively. As is shown in Table 36.1, the values of λ_1, λ_2 and λ_3 are 19.20, 24.83 and 23.63 cm, respectively.

Generally, diurnal variations can be seen in all time series. As discussed previously, the phase-minus-code combination mainly includes ambiguity, hardware delays and amplified ionospheric effect. Assuming hardware delays do not change much with time and ambiguities are constant if no cycle slip occurs, the diurnal fluctuations are probably due to the daily variation of ionospheric effects. Closer examination showed that all the peaks appear at around 2:00 pm local time when the ionosphere is usually considered the most active during a day.

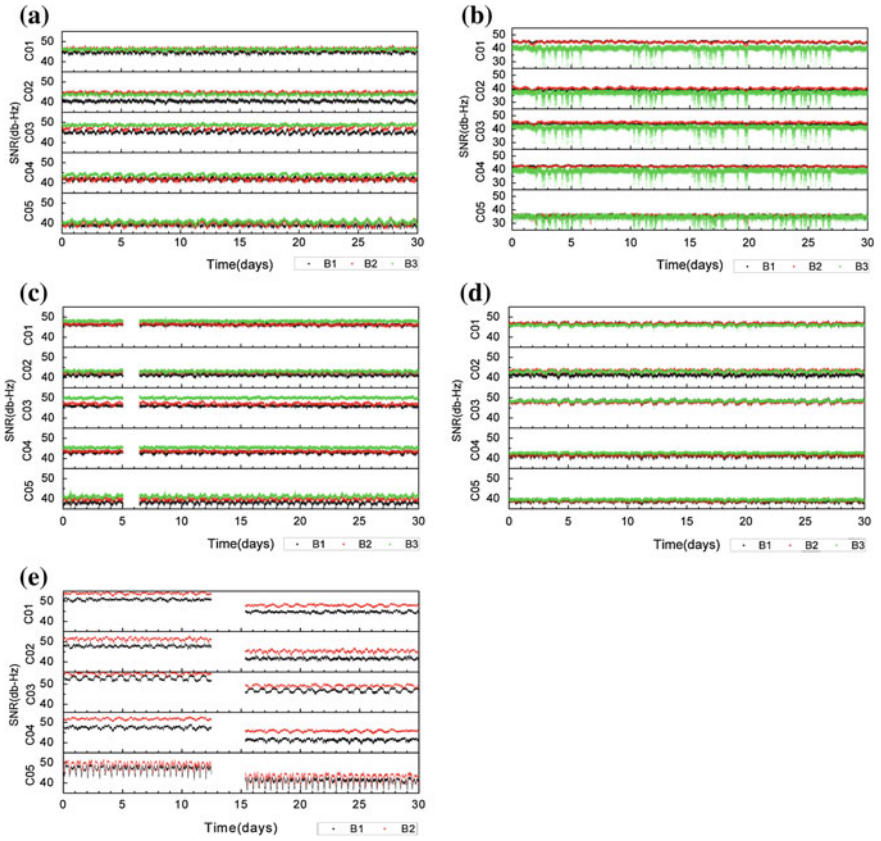

Fig. 36.3 Signal-to-noise ratio of BDS GEO satellites at five stations during 2013139～2013168. **a** F713. **b** F725. **c** F783. **d** CUT0. **e** PFTP

The patterns of time series in Fig. 36.4a, d, and e are nearly the same, while those in the other two figures have different shapes. This is because the stations used to generate Fig. 36.4a, d, and e are located in the same area in Australia, while the other two are located in Seoul and Manila, respectively, see Fig. 36.1. The ionospheric effects are different from area to area.

It is worth noting that there are several jumps and spikes in most of the time series. Since the variation of ionosphere should be continuous, these jumps and spikes are caused by jumps in ambiguities. What is more, the spikes occur at the same epochs as the jumps in the MW combinations, which will be discussed in the following section. In Fig. 36.4b, the bottom panel, which represents the phase-minus-code combination of C05 at station F725, is much noisier than any other satellite-station pair. This is caused by the high rate of missing data, since the numbers of epochs when no signals from C05 are available are around 200 or more every day. Frequent data missing leads to frequent resets of ambiguities, which offsets the time series. However, similar noise level is not shown in the time series of other satellites at station F725.

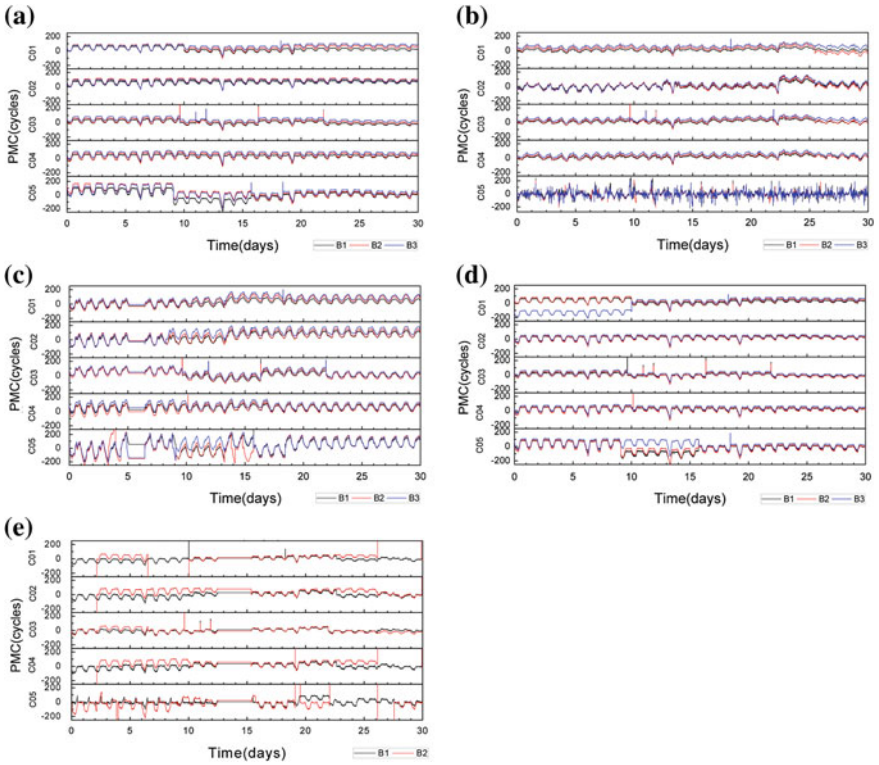

Fig. 36.4 Phase-minus-code combinations of BDS GEO satellites at five stations during 2013139 ∼ 2013168. **a** F713. **b** F725. **c** F783. **d** CUT0. **e** PFTP

36.4.3 MW Combination Analysis

Figure 36.5 shows the raw time series of MW combinations for five GEO satellites of BDS: the five panels of each figure represent five stations. Lines of different colors represent different MW combinations with different wide-lane wavelengths, i.e. black line for N12, red one for N13 and blue one for N23. The bottom subplot representing station PFTP in each figure has only one black line, since only observables on B1 and B2 are available at this station. Comparing vertically, it can be noted that time series of station PFTP have more jumps and interruptions than those of other four stations. This may be related to the observing conditions or receiver performance, since the type of receiver at PFTP is different from those installed at the other four sites. The time series for C05 at F725, i.e. the second panel in Fig. 36.5e, is much noisier both than any other satellite at the same station and than the same satellite at any other station, which may be caused by some abnormalities in the corresponding tracking channel of the receiver.

In addition, two significant jumps at around day 10 and day 18 respectively are shared by all five stations in Fig. 36.5a, which suggests jumps in satellite C01 at

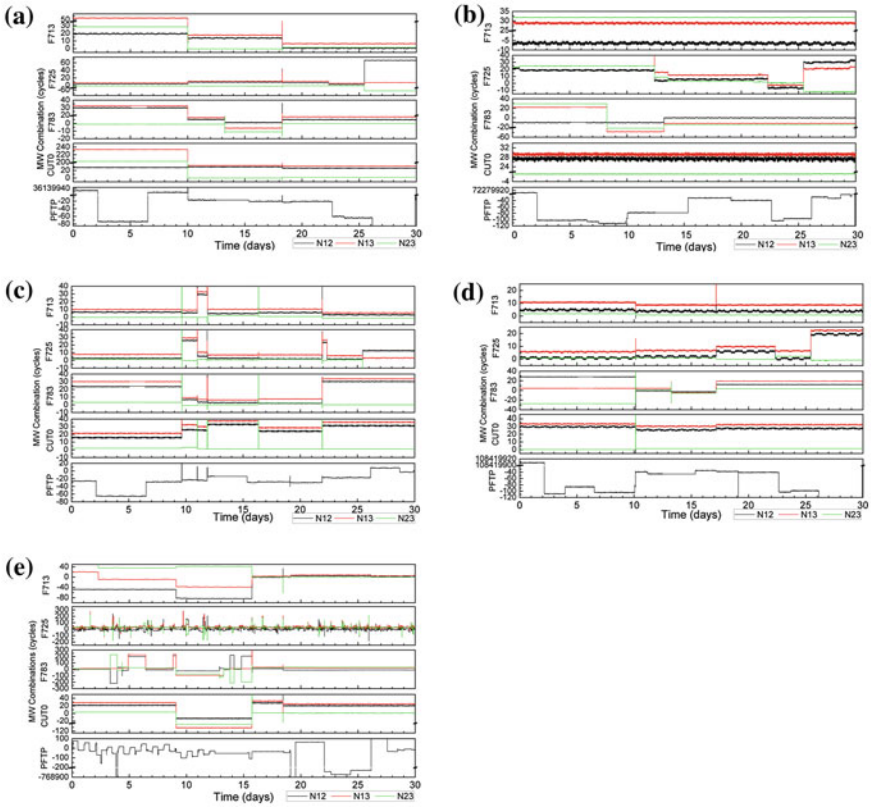

Fig. 36.5 MW combinations of BDS GEO satellites at five stations during 2013139 ∼ 2013168. Note the break in some vertical axis and different scales. **a** C01. **b** C02. **c** C03. d C04. e C05

corresponding epochs. Actually, similar coincidence could be seen in Fig. 36.5c and d, although the total numbers and epoch times at which the jumps occur are different from satellite to satellite. However, jumps in subplots of Fig. 36.5b never coincide, and the time series of C02 at F713 and CUT0 are continuous during the whole thirty-day period. This apagogically strengthen the point that the above mentioned jumps, shared by all five stations in other four figures, are related to abnormalities in satellites.

Taking the time series for C02 at F713 for example, and without loss of generality, the standard deviations for three MW combinations N12, N13 and N23 are 0.43, 0.26 and 0.08 cycle, i.e. 0.36, 0.27 and 0.37 m, respectively.

Similar analysis was conducted for IGSO satellites and MEO satellites of BDS, as well as GPS satellites for comparison. Figure 36.6 contains MW combination (B1/B2) time series of eight passes of C06 (IGSO) at F713. Shown in this figure is the MW combination between observables at frequencies B1 and B2, and

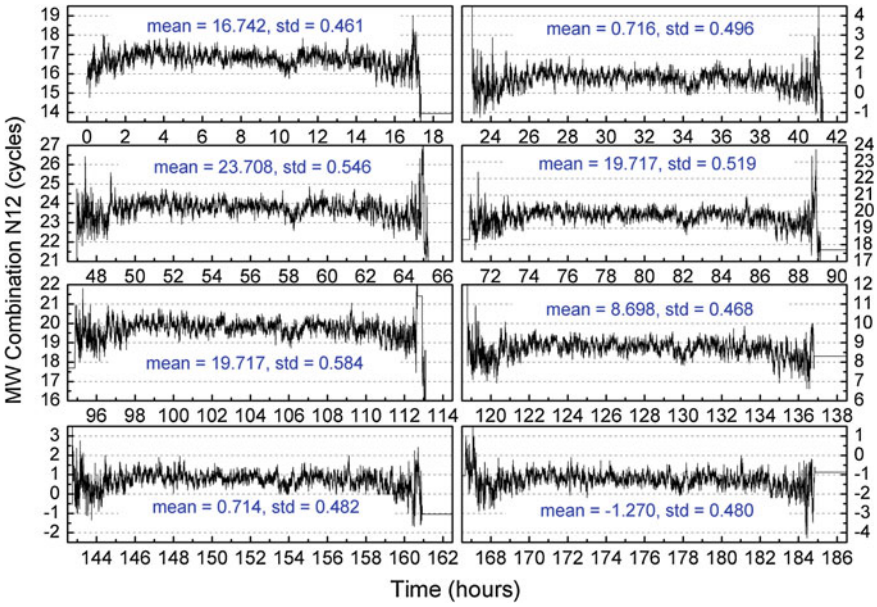

Fig. 36.6 MW combination of BDS IGSO satellite C06 at F713 during 2013139 ∼ 2013168

the wavelength for this combination is 84.70 cm, very close to wide-lane wavelength of GPS, i.e. 86.19 cm. Since the track of sub-satellite point for BDS IGSO satellite turns up with the shape of digit "8", the pass of IGSO satellites could last for a much longer period than that of MEO satellites. It can be seen that each pass of C06 over site F713 covers nearly 20 hours. Due to the variation of the elevation angle, the noise levels of MW combination are obviously higher at the beginning and the end of each pass. The standard deviation for each time series is around 0.50 cycle, i.e. 0.42 m. It is also worth noting the fractional part of the mean value for each pass. Although the mean values are significantly different from pass to pass, their fractional parts are very close, i.e. around 0.7 cycle (or −0.3 cycle).

MW combination (B1/B2) of MEO satellite C11 of BDS is shown in Fig. 36.7. Different from IGSO satellites, each pass of the MEO satellite lasts for only several hours or even shorter. In addition, the time series of MW combinations for the MEO satellite are not stable during one pass. They are much noisier and usually contain some jumps. Therefore, the consistence among fractional parts of MW combinations in different passes shall not be significant. However, data from more satellites may have to be analyzed before drawing any final conclusions.

For comparison, the time series of first eight passes of GPS satellite G01 at F713 is shown in Fig. 36.8. It can be seen that the time series are more stable except for noise at the beginning and end of each pass. The standard deviation for each time series is around 0.35 cycle, i.e. 0.30 m. Similarly, the fractional parts for different passes are also very close, i.e. around−0.6 cycle (or 0.4 cycle), which confirms the methods of GPS FCB estimation proposed in [2, 3].

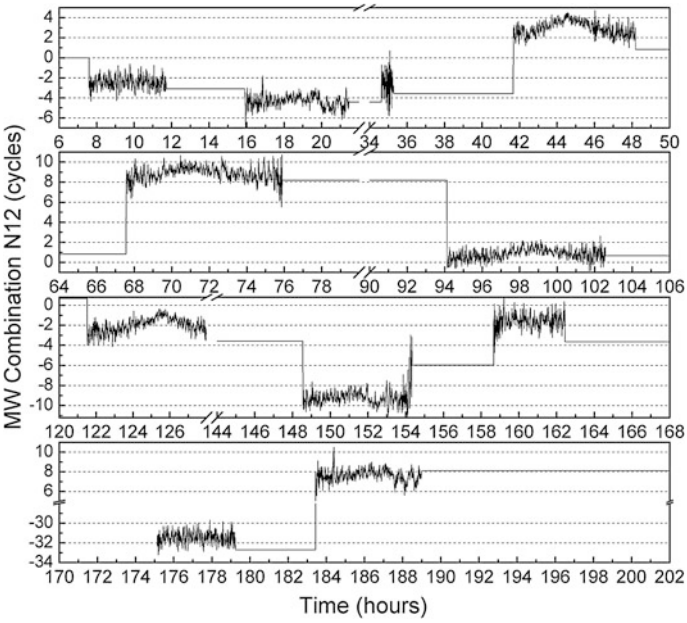

Fig. 36.7 MW combination of BDS MEO satellite C11 at F713 during 2013139 ∼ 2013146

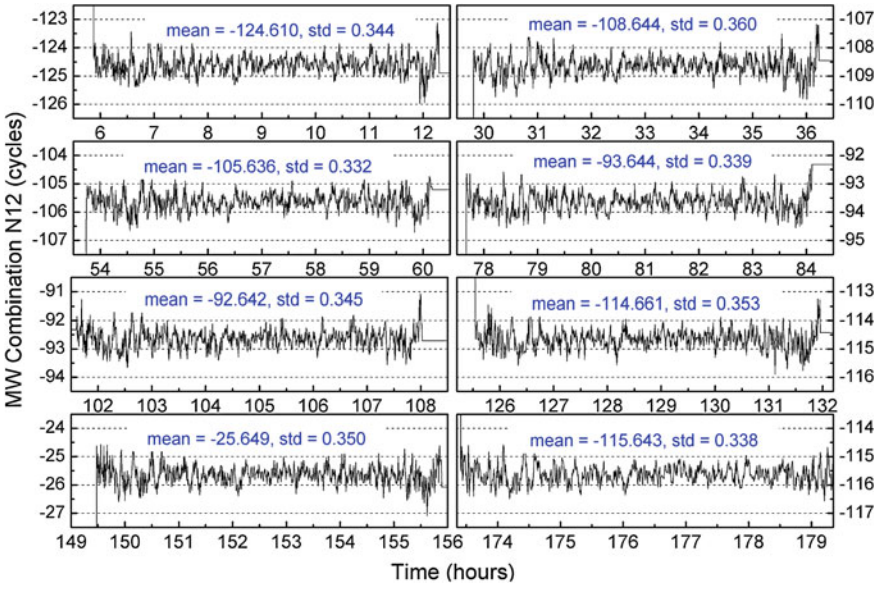

Fig. 36.8 MW combination of GPS satellite G01 at F713 during 2013139 ∼ 2013168

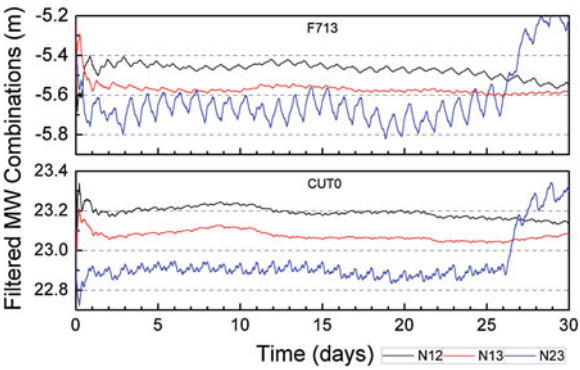

Fig. 36.9 Filtered MW combinations of BDS GEO satellite C02 at F713 (*top*) and CUT0 (*bottom*) during 2013139 ∼ 2013168. Note that wavelengths are taken into account and the unit of vertical axis is meter

To further investigate the long-term features of above MW combinations, recursive least-squares filtering as described in Sect. 36.2.3 was employed to reduce the noise and to smoothen the time series. The a priori precisions of code range and carrier phase were considered to be 0.4 m and 0.02 cycle, respectively. Uncertainties in the dynamic model were also taken into account by introducing a white-noise random function with spectral density factor $\sqrt{q} = 5 \times 10^{-6} s^{-1/2}$.

Figure 36.9 contains the filtered time series of MW combinations for BDS GEO satellite C02 at stations F713 and CUT0. Lines of different colors represent combinations of different frequency-pairs. Significant daily periodicity could be seen at both stations, although the amplitudes differ for different stations and combinations. At both stations, the amplitudes of combination $N23$ are remarkably larger than those of $N12$ and $N13$, while those of $N12$ are slightly larger than $N13$. The method of FCB estimation through averaging requires at least the stability of fractional part of MW combination. However, according to the above results, only GPS and BDS IGSO satellites can meet this requirement, which suggests that the method of FCB estimation for GPS might not work so well for BDS MEO and GEO satellites as for IGSO satellites.

36.5 Conclusions and Recommendations

In this paper, the characteristics of BDS observables were analyzed from the perspectives of SNR, phase-minus-code combination and MW combination. 30 days of observables were collected at five stations distributed in Asia-Pacific area; receiver types were not the same. Combinations of three different frequencies of BDS were investigated, and the different orbit types of BDS satellites were also taken into account. Since the GEO satellites of BDS are continuously visible in the sky, main attention was on these satellites.

Generally, the signal-to-noise ratio of band B3 is higher than those of the other two bands, but the differences among frequencies are marginal compared with

those among satellites. From the time series of phase-minus-code combinations, diurnal fluctuations can be seen, with the peaks usually appearing at around 2:00 pm local time, which reflects the daily variation of ionospheric effects. Since the ionospheric effects are related to the locations of stations, the patterns of stations nearby appear close to each other.

The standard deviations of MW combination time series for C02 (GEO) at F713 are 0.36 m, 0.27 m and 0.37 m for N12, N13 and N23, respectively, and those of N12 time series for C06 (IGSO) at F713 are around 0.42 m. The standard deviations of time series for GPS satellite G01 at F713 are around 0.30 m. With regarding to BDS IGSO and GPS satellites, further investigation shows that the fractional parts of mean values of MW combination for different passes remain stable, only with variations of less than 0.05 cycle only. However, the scenarios for GEO and MEO satellites of BDS are different.

Using a simple Kalman filter to reduce the noise in the MW time series revealed significant daily fluctuations, especially in the case of B2/B3 combination. This suggests that, for BDS, properly considering uncertainty in the dynamic model might bring better WL FCB estimates than simply averaging MW combinations, as is usually done.

Acknowledgments This work was partially sponsored by National Natural Science Foundation of China (Grant No. 41231174 and Grant No. 41204009), partially sponsored by National "863 Program" of China (Grant No. 2013AA122501), and partially sponsored by the "111 Project" of China (Grant No. B07037). The authors would like to thank the IGS Multi-GNSS Experiment (MGEX) for providing GNSS data. The first author gratefully acknowledges Dr. X. Liu at Fugro Intersite B.V. who provided pertinent advice and revised the manuscript. Thanks also go to the editor in chief and three anonymous reviewers for their valuable comments and improvements to this manuscript.

References

1. Cheng P, Li W, Bei J (2012) Precision Analysis of BeiDou Range Measurement Signals. Acta Geodaetica et Cartographica Sinica 41(5):690–695, 708
2. Ge M, Gendt G, Rothacher M, Shi C, Liu J (2008) Resolution of GPS carrier-phase ambiguities in precise point positioning (PPP) with daily observations. J Geodesy 82(7):389–399. doi:10.1007/s00190-007-0187-4
3. Geng J, Meng X, Dodson AH, Teferle FN (2010) Integer ambiguity resolution in precise point positioning: method comparison. J Geodesy 84(9):569–581. doi:10.1007/s00190-010-0399-x
4. Hoque MM, Jakowski N (2012) Ionospheric propagation effects on GNSS signals and new correction approaches. In: Jin S (ed) Global navigation satellite systems-signal, theory and applications. InTech, Rijeka
5. Kleusberg A, Teunissen PJG (1996) GPS for geodesy. Springer, Berlin
6. Liu X, Yuan Y, Huo X, Li Z, Li W (2010) Model analysis method (MAM) on the effect of the second-order ionospheric delay on GPS positioning solution. Chin Sci Bull 55(12):1162–1167
7. Shen J, He H, Guo H, Wang A (2012) Application Research of Linear Combination Based on Triple-frequency Observation. GNSS world of China 37(2):37–40

8. Teunissen PJG (2001) Dynamic data processing recursive least-squares. Delft University Press, Delft
9. Xia L, Liu J, Zhang S, Deng Y (1999) Analysis on code multipath mitigation by phase-aided smoothing. Geo-spat Inf Sci 2(1):73–77
10. Zhang X, Ding L (2013) Quality analysis of the second generation compass observables and stochastic model refining. Geomatics Inf Sci Wuhan Univ 38(7):832–836

Chapter 37
Research on GNSS System Time Offset Monitoring and Prediction

Huijun Zhang, Xiaohui Li, Lin Zhu and Xue Zhang

Abstract With the progress of Global Navigation Satellite System (GNSS), which mainly include GPS, GLONASS, GALILEO as well as BeiDou, multi-GNSS joint working mode has become a development and application trend. The System time offset between two satellite navigation systems is one of the most important aspects of their interoperability and compatibility. This paper introduces the research progress of GNSS System Time Offset Monitoring and prediction at NTSC. The reasons that GNSS system time offset monitoring is done by means of Signal-in-Space Reception are analyzed and the measurement principle is discussed in detail. Multi-GNSS receiver calibration is the key technology of GNSS system time offset monitoring with Signal-in-Space Reception. The causes of Inter-System biases and inter-frequency biases are researched and so does their calibration method. The calibration results are showed and analyzed. The key technologies of BDs system time offset monitoring are researched which include the algorithms related to satellite equipment group delay and dual-frequency ionosphere delay correction whose measurement result is illustrated. And then, the system time offset monitoring results of UTC(NTSC)-GPST and UTC(NTSC)-GLONASST by Signal-in-Space Reception for 6 months long are showed and their precisions is up to 2.10 and 3.24 ns respectively. Furthermore, the experiment results about BDS system time offset UTC(NTSC)-BDT calculated from all visible BDs satellites from 1 to 12 are displayed. Finally, the intentional application and development directions of GNSS system time offset monitoring are put forward.

H. Zhang (✉) · X. Li · L. Zhu · X. Zhang
National Time Service Center (NTSC), Chinese Academy of Sciences, Lintong, Xi'an, China
e-mail: zhj@ntsc.ac.cn

H. Zhang · X. Li · L. Zhu · X. Zhang
Key Laboratory of Precision Navigation and Timing Technology, National Time Service Center, Chinese Academy of Sciences, Xi'an 710600, China

X. Zhang
University of Chinese Academy of Sciences, Beijing 100039, China

J. Sun et al. (eds.), *China Satellite Navigation Conference (CSNC) 2014 Proceedings: Volume I*, Lecture Notes in Electrical Engineering 303,
DOI: 10.1007/978-3-642-54737-9_37,

Keywords GNSS · System time offset monitoring · Signal-in-space reception · BDs system time offset

37.1 Background and Significance

Currently GNSSs (Global Navigation Satellite Systems) has got into a new era of vigorous development, which mainly includes GPS, GLONASS, Galileo and BDs [1–3]. GNSS satellite navigation systems bring about tremendous space for development. Multi-GNSS which includes GPS, GLONASS, BDs as well as Galileo is expected to implement combination navigation and positioning [4]. Thus the limitations of stand-alone GNSS can be overcome. The advantages of multi-GNSS combination positioning are as following [5, 6]: (1) increasing the number of visible satellites; (2) enhancing the production efficiency; (3) making the positioning more reliable and more precise. The purpose of multi-GNSS navigation is that for each of the components of GNSS were implemented interoperability in the design, construction and operational aspects, so that they do not block each other and combination of these signals can provide the optimal navigation service [7].

Nevertheless, combined multi-GNSS positioning also will bring a series of complex issues, such as compatibility and interoperability between different systems, one of them is the system time and their mutual conversion problem. Every GNSS system has its own time reference system, the system time of GPS is GPST, which is traceable to UTC (USNO); GLONASS system time is GLONASST, traceable to UTC (SU); Galileo system time is GST which was controlled to the TAI or UTC by the Time Service Provider (TSP). BDs system time is referred as BDT, BDT using a continuous time scale which is no leap second insertion, and it traces to international TAI or UTC [8, 9]. In the multi-GNSS combined navigation applications, the satellite clock correction broadcasted by every GNSS is utilized to realize the processes of GPS pseudo-range correction to GPST, GLONASS psedo-ranges correction to GLONASST and BDs pseudo-range correction to the BDT. Thus, the system time offset between different GNSS will cause the deviation of positioning. It is necessary to use a unified system time in the user receiver [10, 11].

GPS and Galileo have already reached agreements between the two systems, and the advance of GGTO monitoring by two-way satellite time transfer and common view methods is in the process [12, 13]. Both these two methods can be used to monitor the system time offset between BDs and GLONASS or Galileo. However, these methods require both sides to negotiate firstly, and also including political factors as well as expensive fees, another important problem is the geographical constraints, because it needs to be observed with the same satellite whether it is two-way satellite time transfer method or common view method. Based on the above considerations, the best monitoring method of GNSS system time offset can turn to receive the Signal-in-Space.

National Time Service Center (NTSC) of CAS is the specialized research institute for Chinese national standard time production, maintain and dissemination. Since 2005, the deviation between UTC (NTSC) and Coordinated Universal Time (UTC) is within 20 ns. The platform of system time offset monitoring is based on the UTC (NTSC) standard time and frequency.

37.2 The Research Progresses of GNSS System Time Offset Monitoring and Prediction

There are two different monitoring methods for the platform of GNSS system time offset monitoring which are direct time comparison and signal-in-space reception respectively. The method of direct time comparison can be implemented by means of direct comparison link which is TWSTFT link or CV link between two places where system time or time base are produced. The method of signal-in-space reception can be implemented using multi-GNSS receiver. Then, GNSS system time can be obtained. Further, the system time offset between any two GNSS can be derived from the difference between two system time.

We can obtain direct or indirect comparison data UTC(NTSC)-GST/GPST/GLONASST through three TWSTFT link. The first is the link between NTSC and PTB. The second is the link between NTSC and SU. And the indirect link is between PTB and USNO. It is more important that not only TWSTFT link but also CV link have been set up between NTSC and time and frequency center of BDs. Thus, the direct comparison data of UTC(NTSC)-BDT can be acquired. The TWSTFT links and CV link described above have been carried out steadily for several years, but there is a disadvantage that system time offset results are generated with large delay. So GNSS system time offset monitoring and prediction cannot be done in real time and the practicability purpose also cannot be reached. Therefore, the method of GNSS system time offset monitoring by signal-in-space reception is attached importance. But several parts of error will be deducted when this method is utilized which include errors associated with satellite, errors introduced by signal propagation and errors with respect to receiver. The other aspects of errors are necessary to be considered such as inter-frequency bias and inter-system bias [14–16].

At NTSC, the research of signal-in-space reception has been carried out since 2008 [17, 18]. In 2011, the single system time offset monitoring system for UTC(NTSC)-GPST was set up and the precision is up to 5 ns. This monitoring system was updated and improved in 2008 and three multi-GNSS timing receivers were applied to set up a platform of GNSS system time offset monitoring which include three stations. The measurement precision of UTC(NTSC)-GPST is increased and changed from 2.8 to 1.1 ns. Subsequently, The monitoring function is expanded with adding UTC(NTSC)-GLONASST. In the meantime, several aspects of GNSS system time offset in the case of multi-station monitoring are

researched. They are as followings: (1) the method of time reference synchronization between two stations; (2) the method of GNSS system time offset data processing in the condition of multi-station combined monitoring; (3) the zero value calibration between one slave station and master station; (4) the calibration method of inter-system biases of multi-GNSS timing receiver.

On the one hand the system of multi-station combination GNSS system time offset monitoring for UTC(NTSC)-GPST/GLONASST has been test run since 2013. On the other hand primary testing results for UTC(NTSC)-BDT monitoring have been obtained in later 2013. Being the fact that it is not the monitoring values of system time offset but the prediction model parameter are applied by multi-GNSS user, the method of system time offset prediction based on of system time offset monitoring values is researched. So, prediction model parameters of UTC(NTSC)-GPST/GLONASST/BDT/GST are calculated. And we are planning to provide with those parameters for customer by communication satellites broadcasting or by FTP File located on the server in 2014. A special explanation is that UTC(NTSC)-UTC(PTB) measurement value from TWSTFT link is taken as UTC(NTSC)-GST temporarily at present.

37.3 The Principle of GNSS System Time Offset Monitoring

The system time offset monitoring principle by Signal-In-Space reception is as follows: we take the standard frequency signal of NTSC as a frequency reference, the standard time signal as the reference time scale, the difference between UTC (NTSC) and GNSST are measured (including UTC (NTSC)-GPST, UTC (NTSC)-GLONASST, UTC (NTSC)-BDT, UTC (NTSC)-GST, etc.). Figure 37.1 shows the measuring principle, take the GPS and GLONASS systems as an example, UTC (NTSC)-GPST and UTC (NTSC)-GLONASST can be measured at the NTSC, then we can obtain the GPST-GLONASST by that indirectly.

Figure 37.2 describes the core equipment of this monitoring method which is the receiver and the GNSS time interval counter. In the precise known of GNSS receiver antenna phase center, each navigation system spatial navigation signals received by timing receiver, the receiver pseudo-range and high-precision time interval counter measurement value are used so as to calculate the difference between UTC (NTSC) and each navigation system. GNSST (GPST, GLONASST, BDT, GST, etc.) can be calculated in Eq. (37.1) below:

$$\begin{aligned} UTC(NTSC) - GNSST = (\rho - \mathrm{r} + dt - \mathrm{pd} - \mathrm{d(ion)} - \mathrm{d(trop)} - \mathrm{Ep})/\mathrm{c} \\ - TIC\,Value - \Delta Ch\,Delay + \Delta ISDB \end{aligned} \tag{37.1}$$

Where GNSST is the GNSS system time, ρ indicates the pseudo-range from receiver to the satellite, r represents the real geometric distance between satellite and ground, dt is the satellite clock bias, pd is the orbit error, d (ion) is the

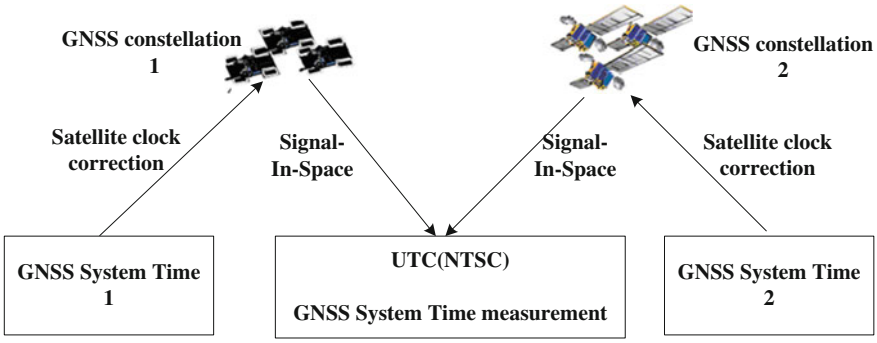

Fig. 37.1 Schematic diagram of system time offset monitoring by signal-in-space reception

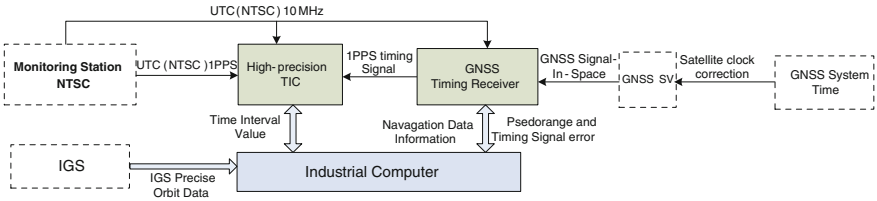

Fig. 37.2 Block diagram of receiving space signal to achieve the system time offset monitoring

ionospheric delay, d (trop) is the tropospheric delay, Ep indicate other errors, c is the speed of light, TIC Value is the measurement value of precision time interval counter, ΔChDelay indicates that the receiver relative channel delay bias, ΔISDB represents the inter-system hardware delay bias.

Since more than 5 satellites of every GNSS constellation can be received at a fixed position at NTSC, the average number of received GPS satellites and GLONASS satellites both over 8. In addition, the system time offset monitoring is done at one second interval, so we can use the following ways to further improve the monitoring precision: (1) Averaging the system time offset monitoring results for all visible satellite. (2) Smoothing monitoring data per minute.

37.4 Multi-GNSS Receiver Calibration

From formula (37.1) described above, we can see that inter-system biases and inter-frequency biases of multi-GNSS receiver must be deducted from pseudo-range when the data processing is done.

Simplified pseudo-range equation can be defined as:

$$P_i^k = \rho_i^k + b_i + \varepsilon^k \tag{37.2}$$

Where subscript i denotes one GNSS and superscript k is one satellite. ρ is true geometric range; b_i is the receiver clock bias. ε^k is the combined effect of all measurement errors. The different time reference epoch of pseudo-range measurement by receiver from each GNSS results in inter-system biases. We can express the clock bias the second GNSS relative to the first GNSS, that is ΔISDB:

$$\Delta ISDB = b_2 - b_1 \tag{37.3}$$

The receiver channel delay biases depend on the frequency of the satellite signal. For the GPS system, as the use of code division multiple access (CDMA) signal system, all the satellites use the same carrier frequencies the delay biases between each channel is very small, about sub-millimeter and can be neglected. However, the GLONASS system uses frequency division multiple access (FDMA) signal system, satellite signals of different frequencies generated the receiver channel delay are different from each other, and there is a certain deviation, called the inter-frequency bias [19]. Observed in the case of multi-GNSS, in order to improve the monitoring precision of GNSS system time offset, it is necessary to calibrate the GLONASS channel delay biases in advance for precision measurements.

The calibration arrange of inter-system bias and inter-frequency biases measurement by using GNSS simulator as shown in the Fig. 37.3. In the ideal case, the pseudo-range value output from receiver by different frequencies of GLONASS satellites should be the same value, nonetheless, due to the channel delay biases between GLONASS different frequencies, pseudo-range PR is biased at the receiver side for different frequency points of GLONASS satellites. Taking the receiver channel which receives the frequency number 0 GLONASS satellites as reference channel, the inter-frequency biases of other channels can be calculated relative to the reference channel. In the same way, calculating the pseudo-range difference between one GPS satellite and GLONASS reference satellite, the inter-system biases can be derived.

GLONASS has 14 frequency points, the sub-bands are identified by frequency numbers k, from −7 to 6. The GLONASS L1 carrier frequency, in hertz, at a frequency number k are defined by:

$$f_{L_1}^k = 1602\,\text{MHz} + k \times 562.5\,\text{MHz} \tag{37.4}$$

The use of GNSS simulator to test the GLONASS L1 carrier signal inter-frequency biases of Septentrio PolaRx4 receiver, thus the results were compared and analyzed.

The measurement results are as followings:

1. Inter-system biases for Spetentrio PolaRx4 receiver is 7.04 ns.
2. GLONASS inter-frequency biases for Septentrio PolaRx4 receiver and Novatel OEMV-3 receiver are shown in Fig. 37.4.

Figure 37.4 shows the measurement results of GLONASS infer-frequency biases on different frequency number. It can be seen from figure above that for the

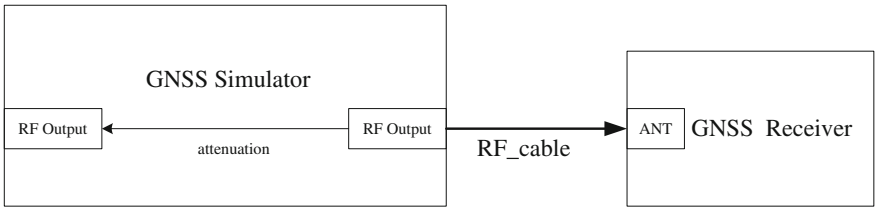

Fig. 37.3 Schematic diagram of using GNSS simulator to measure inter-system biases and GLONASS inter-frequency biases

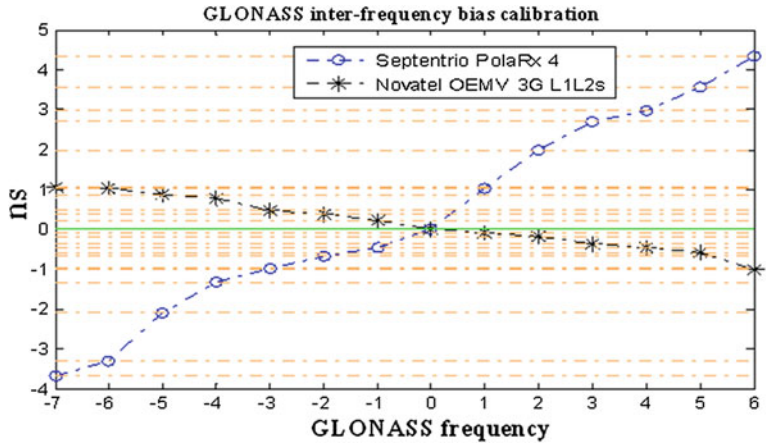

Fig. 37.4 Comparison of the inter-frequency biases value with different frequency number of GLONASS (L1)

Septentrio PolaRx4 receiver, the inter-frequency of GLONASS is vary with respect to the frequency number 0 of GLONASS satellites in −4 ns to +5 ns. Fortunately, for receiver of the same brand, the variation did not change with temperature change, it is the result of the carrier phase measurement in receiver DSP chain [20].

37.5 Research on UTC(NTSC)-BDT Monitoring by Receiving Signal-in-Space

The principle of monitoring UTC(NTSC)-BDT through receiving signal-in-space is the same as UTC(NTSC)-GPST and UTC(NTSC)-GLONASST. The basic method is approximately similar to the description of Eq. (37.1) and the difference is that the BDs receiver is utilized to monitor UTC(NTSC)-BDT instead of multi-GNSS receivers. So, inter-system biases of multi-GNSS receiver can be avoided.

In addition, the BDs calculation of satellite position, time group delay, dual-frequency ionosphere correction is also different from GPS and GLONASS [2, 21].

Satellite time group delay (TGD) is an important impact factor on GNSS system time offset monitoring, which is broadcasted through navigation message of GPS and BDs. BDs is a triple- frequency navigation system composed of B1, B2, B3, and the satellite clock bias is based on B3 [22]. Its navigation message broadcasts TGD1 and TGD2, which is the hardware delay offset of B1 and B2 respectively relative to B3. Therefore, the BDs user should consider TGD in system time offset monitoring. For example, if using B1 pseudo-range to calculate UTC(NTSC)-BDT, the user must add TGD1 in time offset modification.

As a triple-frequency navigation system, BDs dual-frequency ionosphere correction can be calculated by ionosphere-free combination of B_1/B_2 dual frequency pseudo-range. Due to the special processing of BDs satellite group delay in each frequency, it's dual-frequency ionosphere delay correction is different with GPS/GLONASS:

$$P_i^k = \rho^k + \delta t \cdot c - \delta t^k \cdot c + \frac{40.28}{f_i^2} \cdot d_{TEC} + d_{trop} + (\tau_i + \tau_i^k) \cdot c + \varepsilon_i \qquad (37.5)$$

P_i^k indicates the pseudo-range from the receiver to satellite (k) with frequency (i), ρ^k indicates the real geometric distance between the receiver and satellite (k), δt indicates the receiver clock bias, d_{TEC} is the sum of electron content in oblique path, d_{trop} is the troposphere delay, τ_i^k is satellite k channel delay, τ_i indicates the receiver channel delay of frequency (i), f_i indicates the carrier frequency of frequency (i), ε_i indicates the measurement errors, c is the speed of light. We can get B1 dual-frequency ionosphere delay according to the following formula:

$$I_1^k = \frac{f_2^2}{f_1^2 - f_2^2}\left(P_2^k - P_1^k + TGD_1^k - TGD_2^k\right) \qquad (37.6)$$

37.6 Measurement Results Analysis of GNSS System Time Offset

Measurement results of UTC(NTSC)-GPST and UTC(NTSC)-GLONASST are shown in Figs. 37.5 and 37.6 respectively. The blue spot represents original measurement result. The receiver delay is calibrated by a simple calibration method [23, 24]. The green curve represents smoothing results and the red star represents the reference value from Circular-T. Two reference values is derived from the differences between UTC-UTC(NTSC) and UTC-GPST/UTC-GLONASST separately in Circular-T.

But, there is a 215 ns difference between our measurement value and Circular-T measurement value. This is because GLONASS receiver in BIPM has not been

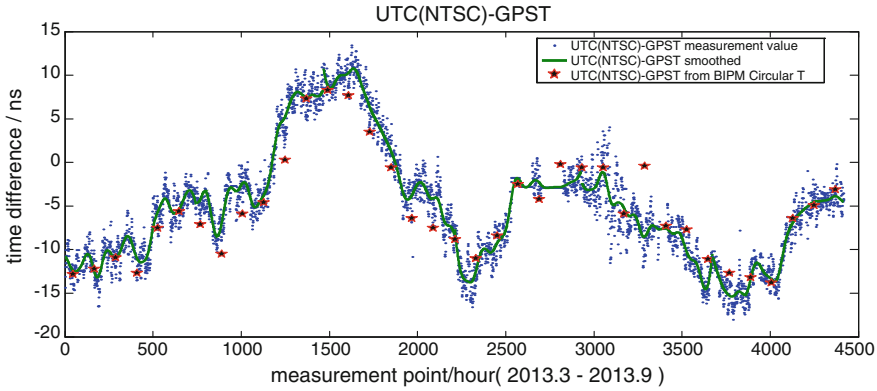

Fig. 37.5 UTC(NTSC)-GPST measurement value compared with those of Circular T

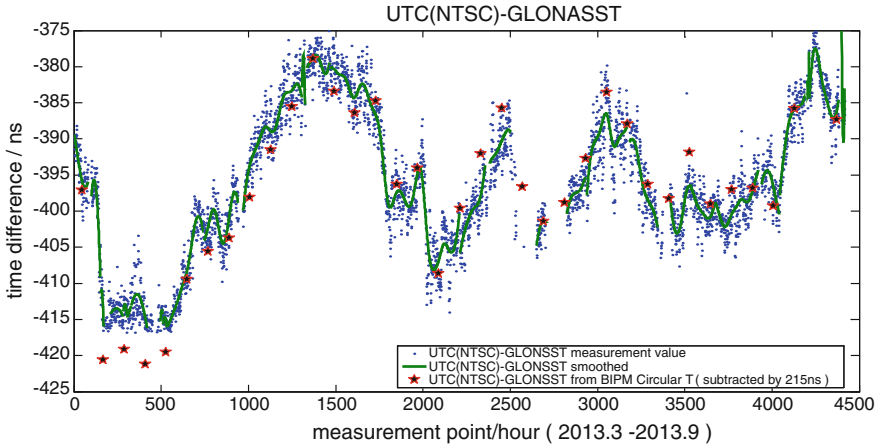

Fig. 37.6 UTC(NTSC)-GLONASST measurement value compared with those of Circular T

calibrated yet. UTC(NTSC)-GPST/GLONASS measurement values are compared with Circular T value. As a result the two RMS value, 2.1 and 3.24 ns, are calculated respectively.

In Fig. 37.7, the red line is GPST-GLONASST by subtracting the measurement value of UTC(NTSC)-GLONASST from UTC(NTSC)-GPST. The green circle is GPST-GLONASST broadcasted by GLONASS satellite. These two lines are showed close match.

Figure 37.8 is the weighted average of UTC(NTSC)-BDT measurement value of all visible BDs satellites from 1 to 11 at 7th November, 2013. Where channel delay biases are not considered.

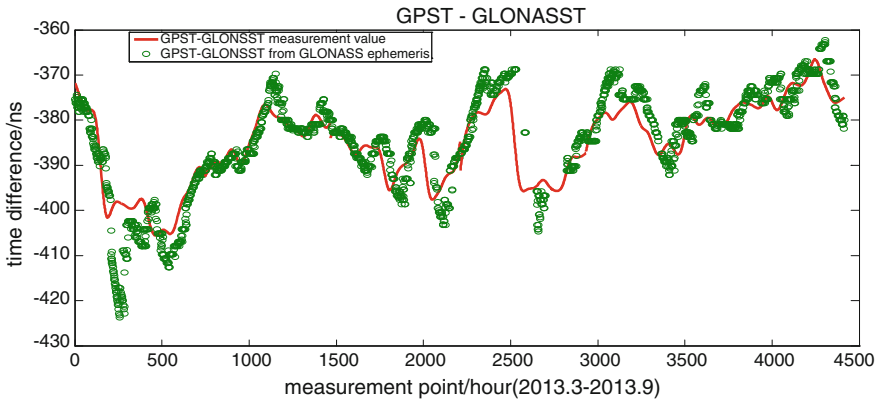

Fig. 37.7 GPST-GLONASST by subtracting UTC(NTSC)-GLONASST from UTC(NTSC)-GPST compared with those of GLONASS ephemeris

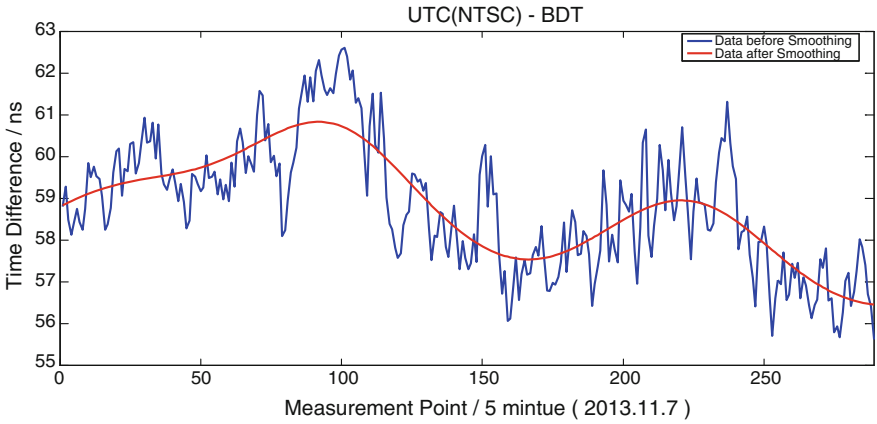

Fig. 37.8 UTC(NTSC)-BDT results calculated by weighted average from BDs 1 to 11 satellite

37.7 Conclusion and Outlook

The platform of multi-station combined system time offset monitoring and prediction has been constructed at NTSC. The method of receiving signal-in-space is taken as the main method because it possesses the advantages of real-time and high precision. However, various errors must be deducted from pseudo-range and the receiver calibrations must be done in advance.

In this paper, inter-system bias and inter-frequency of multi-GNSS receiver are analyzed and calibrated precisely by GNSS simulator. The calibration results show that, inter-system bias of Spetentrio PolaRx4 receiver is 7.04 ns and inter-frequency biases range from −4 ns to +5 ns for Spetentrio PolaRx4 receiver and

+1 to −1 ns for Novatel OEMV-3 respectively. These biases will influence GNSS system time offset monitoring and must be deducted. As a result, measurement results of both UTC(NTSC)-GPST and UTC(NTSC)-GLONASST can be less than 5 ns (1σ).

We have accomplished experiment for UTC(NTSC)-BDT monitoring in order to add this function to our monitoring and prediction platform.

A simple calibration method for receiver delay is used temporarily in GNSS system time offset monitoring and absolute delay calibration is considered to adopt in the further research. The absolute delay calibration will reach about 2 ns precision with GNSS signal simulator and high-speed oscilloscope [25, 26].

Above all, GNSS system time offset monitoring and prediction system has run for 1 year at NTSC. We are planning to open our service after further improvement by means of both communication satellite broadcasting and Internet publish.

References

1. MOSCOW (2008) GLONASS interface control document
2. Chinese satellite navigation system management office (2013) Beiyou satellite navigation system signal in space interface control document, 27 Dec 2013
3. European Union (2010) European GNSS open service signal in space interface control document, Sep 2010
4. Hein G, Avila-Rodriguez J, Wallner S, Pany T, Eissfeller B, Hartl P (2007) Envisioning a future GNSS system of system: part 2. Inside GNSS, March/April 2007, pp 64–72
5. Zinoviev A (2005) Using GLONASS in combined GNSS receiver: current status. ION GNSS, Long Beach, 13–16 Sept 2005
6. Rizos C (2008) Multi-constellation GNSS/RNSS from the perspective of high accuracy user in Australia. J Spat Sci 53(2):29–63
7. Dong S, Wu H, Li X (2008) The compass and its time reference system. Metrologia 45:S47–S50
8. Dong S, Li X, Wu H (2007) About compass time and its coordination with other GNSS. In: Proceedings of the 39th annual precise time and time interval (PTTI) metting, pp 21–24
9. Rizos C (2008) Multi-constellation GNSS/RNSS from the perspective of high accuracy user in Australia. J Spat Sci 53(2):29–63
10. Moudrak A, Konovaltsev A, Furthner J, Hammesfahr J, Bauch A, Defraigne P, Bedrich S (2004). Timing aspects of GPS-Galileo interoperability: challenges and solutions. In: Proceedings of the 36rd annual precise time and time interval (PTTI) metting, pp 279–292
11. Moudrak A, Konovaltsev A, Furthner J, Hammesfahr J, Defraigne P (2005) GPS Galileo time offset: how it affects positioning accuracy and how to cope with it. In: Proceedings of ION GNSS 2004, 21–24 Sept 2004, Long Beach, California
12. Vanschoenbeek I, Bonhoure B, Boschetti M et al (2007) GNSS time offset: effects on GPS-Galileo interoperability performance. Inside GNSS, pp 60–70
13. Hahn JH, Powers ED (2007) A report on GPS and Galileo time offset coordination efforts. In: Proceedings of IEEE international frequency control symposium, pp 440–445
14. Hegarty C, Powers E, Fonville B (2004) Accounting for timing biases between GPS, modernized GPS, and Galileo signals. In: Proceedings of 36th annual precise time and time interval (PTTI) systems and applications meeting, Washington, DC, 7–9 Dec 2004)
15. Neumann J, Bates M, Harvey R (2003) Method for reducing inter-frequency bias effects in a reciver. US Patent 6608998, 19 Aug 2003

16. Pei X, Chen J, Wang J, Zhang Y, Li H (2012) Application of inter-system hardware delay bias in GPS/GLONASS PPP. In: Chinese third navigation academic symposium
17. Zhang H, Li X, Li L (2010) GNSS system time offset monitoring and prediction. China Satellite Navigation Conference, May 2010
18. Zhang H, Li X, Xu L, Xue Y (2011) The method of receiver clock bias correction for GNSS system time offset monitoring. CSNC 2011, pp 832–837, Shanghai, May 2011
19. Yamada H, Takasu T, Kubo N, Yasuda A (2010) Evaluation and calibration of receiver inter-channel biases for RTK-GPS/GLONASS. ION GNSS, Portland, OR, Sept 21–24 2010
20. Sleewaegen J, Simsky A, De Wilde W, Boon F, Willems T (2012) Digital versus analog: demystifying GLONASS inter-frequency carrier phase biases. Inside GNSS, May/June 2012
21. Liu J (2012) Research on the method of GEO satellite position calculation. Surveying Mapp Geog Inf 37(5):10
22. Fan J, Wu X, Li Y, Wei G (2013) The method of DCB parameter evaluation based on BDs triple-frequency data. China space technologies 8(4):62–70
23. Li X, Zhang H (2008) A simple measurement method of GPS timing receiver delay. J Electron Meas Instrum 28(3):249–252
24. Li X, Zhang H, Shi S, Wang G (2009) Measurement of the time delay of GPS timing receiver based on UTC(NTSC). European frequency & time forum & IEEE international frequency control symposium
25. Plumb J, Larson K, White J, Powers E, Beard R (2003) Stability and error analysis for absolutely calibrated geodetic GPS receivers. In: Proceedings of the 34th annual precise time and time interval (PTTI) systems and applications meeting, pp 309–323
26. Tholert S, Grunert U, Denks H, Further J (2007) Absolute calibration of time receivers with DLR'S GPS/GALILEO HW simulator. In: Proceedings of the 39th annual precise time and time interval (PTTI) systems and applications meeting, pp 323–330

Chapter 38
Ionosphere Dispersion Effects on Wideband GNSS Signal Performance

Ying Liu and Yibo Chen

Abstract The ionosphere dispersion causes the distortions of wideband GNSS signals traversing the ionosphere, and thus impacts the signal performance. Its effects are comparatively analyzed and simulated in terms of time-domain waveform, correlation function, code loop lock point bias, and carrier phase tracking bias under different signal spectrum shapes, bandwidths and total electron content (TEC) conditions. The results show that the signals with split spectrum are more susceptible to ionosphere dispersions than concentrated spectrum, and the distortions and tracking biases increase with the increase of either the TEC or the signal bandwidth. The study provides a reference for the design and evaluation of wideband GNSS signals and the receiver compensation techniques.

Keywords Wideband signal · Ionosphere delay · Dispersion effect · Lock point bias · Carrier phase bias

38.1 Introduction

The ionosphere is an anisotropic and dispersive medium. When the spectrum of an electromagnetic wave spread over a wide band, its signal components with different frequencies propagate through the ionosphere with different phase speeds, and thus suffer different delays and yield different phases, which causes the corresponding signal deformations (e.g. pulse stretching) in time-domain and space-domain. This is called the ionosphere dispersion of wideband signals [1].

Y. Liu (✉)
Beijing Institute of Tracking and Telecommunication Technology, Beijing 100094, China
e-mail: yingliu2009@163.com; liu2ying@163.com

Y. Chen
School of Electronic and Information Engineering, Beihang University, Beijing, China

J. Sun et al. (eds.), *China Satellite Navigation Conference (CSNC) 2014 Proceedings: Volume I*, Lecture Notes in Electrical Engineering 303,
DOI: 10.1007/978-3-642-54737-9_38,

The ionosphere dispersion effects are usually negligible for traditional narrow-band GNSS signals. Single-frequency receivers correct the ionosphere delay by using the models corresponding to the broadcast navigation message, for example, the Klobuchar model [2] and the NeQuick model [3]; while dual-frequency receivers correct the ionosphere delay by using the delay relationship between the two carrier frequencies. However, these methods simply use the center frequency ionospheric delays to replace the total group delays of the GNSS signals with spectrums spread to certain bandwidths [4]. Since the ionosphere dispersion can cause severe signal deformations/distortions and thus extra biases in the code phase and carrier phase measurements, the above models and methods are only applicable to narrow-band signal cases [5]. With the popularization of wideband GNSS signals, it is important to quantitatively study the ionosphere dispersion effects on wideband GNSS signal performance.

Reference [5] proposed an ionosphere dispersion simulation method by transferring the time domain signal to the frequency domain, and analyzed the wideband signal distortions caused by the dispersive ionosphere in terms of signal waveform and correlation function. This paper compares and summarizes the signal distortions under different bandwidths, signal spectrum shapes and TEC. Moreover, the code phase tracking bias and carrier phase tracking bias caused by the ionosphere dispersion are numerically simulated. The objective is to provide a reference for wideband GNSS signal structure design, performance evaluation and receiver compensation techniques.

38.2 Modeling Ionosphere Dispersion on Wideband Signal

The ionosphere is a dispersive medium with its propagation velocity (or equivalently, refraction index) depending on the wave's frequency. The phase velocity v_p and group velocity v_g of the signal component with a frequency of f in the navigation signal traversing the ionosphere can be approximately expressed as [4, 6]

$$v_p = \frac{c}{n_p} = \frac{c}{1 - \frac{40.3 n_e}{f^2}}, \; v_g = \frac{c}{1 + \frac{40.3 n_e}{f^2}} \tag{38.1}$$

where c is the speed of light, n_p is the refraction index for the phase propagation in the ionosphere, and n_e is the number of electrons (i.e., electron density) along the satellite-to-user signal propagation path. The corresponding group delay/carrier phase advance is [6]

$$\tau(f) = \frac{40.3\mathrm{TEC}}{c \cdot f^2} \tag{38.2}$$

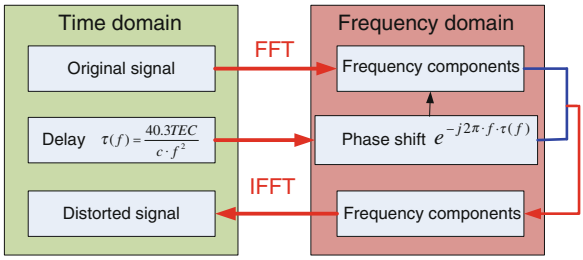

Fig. 38.1 Simulation model of ionosphere dispersion on wideband signals

where TEC is Total Electron Count along the path length:

$$\mathrm{TEC} = \int_{\mathrm{SV}}^{\mathrm{User}} n_e dl \tag{38.3}$$

For a narrow band signal such as GPS L1 C/A, the delays of different frequencies over the signal band are nearly identical. Therefore the ionosphere effects can be represented by a delay at the center frequency. For a wideband signal such as Galileo E5, however, the delays of different frequencies show large variation, non-linearity and asymmetry over the signal band, so that the signal distortion caused by the ionosphere dispersion is significant, and its effects on the ranging error cannot be ignored especially when a large TEC occurs [5].

The ionosphere dispersion on wideband signals can be modelled in Fig. 38.1 [5]. Assuming that the time domain input signal is $S(t)$, it can be converted into the frequency domain by using the Fast Fourier Transformation (FFT). Then the delay $\tau(f)$ of each frequency component can be calculated separately according to (2). Next, the phase of each frequency component of the distorted signal is shifted accordingly. Finally, through Inverse Fast Fourier Transformation (IFFT), the frequency domain signal is converted back to the time domain signal $S_{iono}(t)$. The equations of the ionosphere effect calculation are expressed as [5]

$$S_{iono}(t) = \mathrm{ifft}\left\{\mathrm{fft}[S(t)] \cdot e^{-j2\pi\cdot f\cdot\tau(f)}\right\} \tag{38.4}$$

$$S_{iono}(t) = \int_{-\infty}^{\infty}\left(\int_{-\infty}^{\infty} S(t)\cdot e^{-j2\pi\cdot f\cdot t}dt\right)\cdot e^{-j2\pi\cdot(40.3\cdot TEC/(c\cdot f)-f\cdot t)}df \tag{38.5}$$

38.3 Simulation of Dispersion Effect on AltBOC(15,10) Signal

This section investigates the signal characteristics, code phase and carrier phase tracking bias due to the ionosphere dispersion for the Galileo E5 AltBOC(15,10) signal through numerical simulation. The TEC is set to be a constant value of 100

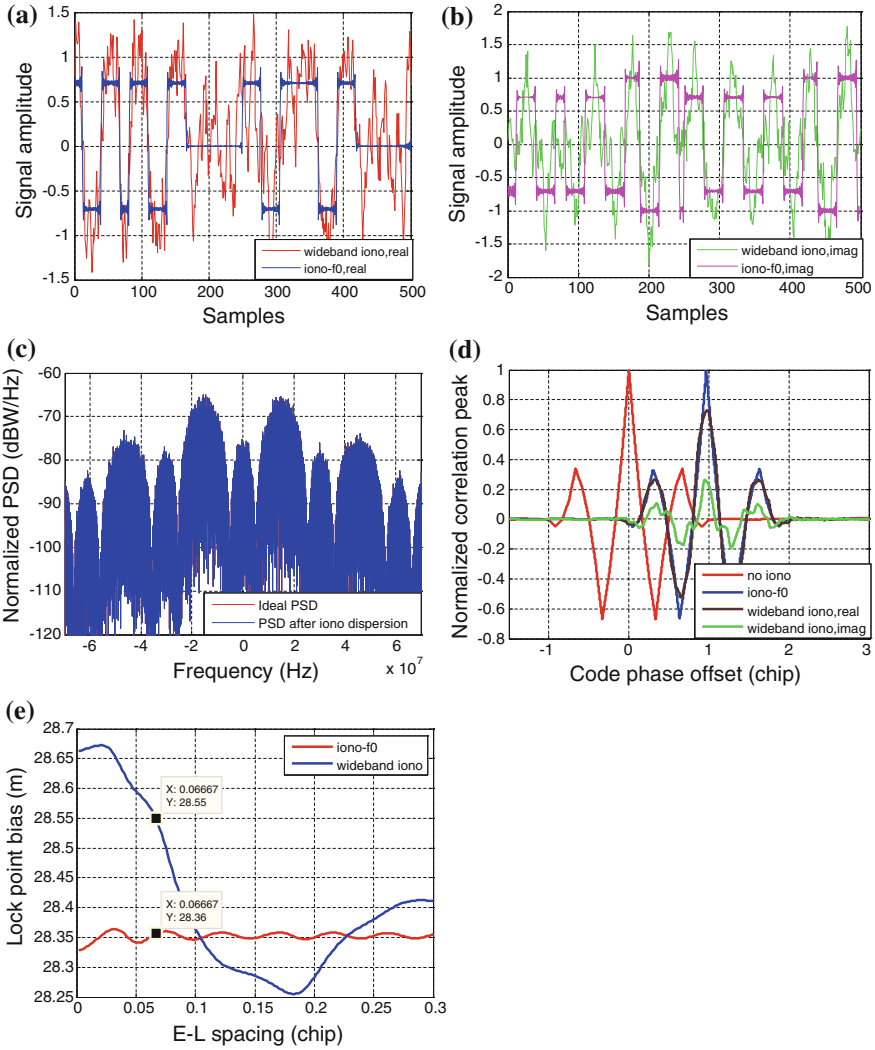

Fig. 38.2 Dispersion effects on E5 signal **a** real part (I component) waveform **b** imaginary part (Q component) waveform **c** PSD **d** correlation function **e** lock point bias

TECU, which is a typical daytime value in middle latitude area and corresponds to a delay of about 28.37 m (nearly one chip) for the E5 center frequency.

38.3.1 Signal Characteristics

The signal characteristics mainly include the time domain waveform, frequency domain spectrum, and correlation domain CCF (cross-correlation function). Since the baseband E5 signal is a complex signal [7], the dispersion effects on the real

part (I component) and the imaginary part (Q component) are shown in Fig. 38.2a and b respectively, where"iono-f0"denotes the non-dispersive ionosphere case using only the delay of the single frequency (f_0) tone to represent the ionosphere delay over the whole signal frequency band, and "wideband iono" denotes the dispersive ionosphere case considering the dispersion effect on wideband signals. It can be seen that the ionosphere dispersion causes severe signal deformations and fluctuations, so that correct logic values of some code chips cannot be identified from the distorted signal waveform.

Figure 38.2c compares the power spectral density (PSD) functions of the E5 signal before and after propagation through the dispersive ionosphere. It is shown that the ionosphere dispersion does not affect the signal power spectrum. Although the phase/delay response of the ionosphere channel depends on the frequency, the amplitude-frequency response of the ionosphere channel remains constant.

The performance of the navigation signal is closely related to the CCF between the incoming baseband signal and the ideal local reference code sequence. As shown in Fig. 38.2d, the ionosphere dispersion also leads to significant CCF distortions. The red line simulates the CCF without any ionosphere effects. The blue line shows the CCF with the ionosphere delay represented by the single-frequency tone delay at the center frequency. The brown line and the green line represent the real part and the image part of the CCFs of the wideband E5 signal traversing the dispersive ionosphere. The ionosphere delay of the single-frequency tone is near one code chip without considering the ionosphere dispersion effects. When considering the dispersion effects, the CCF of the distorted signal exhibits three other features besides the delay. First, the dispersion introduces asymmetry in the CCF peak and thus brings the tracking bias of the DLL (Delay Locked loop), which can be evaluated by the code loop lock point bias and the S-curve bias. Second, the dispersion induces the degradation of the CCF peak, which can be evaluated by the correlation peak loss. Third, the dispersion generates the imaginary part of the correlation function, which can introduce a certain phase shift into the receiver PLL (Phase Locked Loop) output. This will be detailed in Sect. 38.3.3.

38.3.2 Code Phase Tracking Bias

The distortion of the correlation function leads to the DLL lock point bias with respect to the true point of zero code phase difference between the local code and the incoming code. The effects of signal distortions on the code tracking bias can be evaluated by the lock point bias and the S-curve bias for single point positioning and differential positioning, respectively. The S-curve (discrimination curve) can be obtained from the above-mentioned CCF and the discriminator function (for example, the early-minus-late envelope discriminator), and the variation of the lock point bias (zero-crossing point bias) of the discriminator with different correlator spacing can be calculated. As shown in Fig. 38.2e, the lock point shifts nearly one code chip from the ideal location due to the ionosphere

delay, and the lock point bias varies significantly with the increase of the correlator spacing due to the deformation and asymmetry of the correlation function caused by the ionosphere dispersion. According to the auto-correlation characteristics of the E5 signal, the E-L spacing of the wideband-matched receiver should be less than 0.3 PRN code chips. The lock point biases with and without the ionosphere dispersion effects at a correlator spacing of 0.0667 PRN chip (i.e. 0.8 subcarrier chip) are indicated in the figure showing a difference of 0.2 m. And the S-curve bias, which is the difference between the maximum and the minimum values of the lock point biases under different correlator spacing, reaches 0.42 m.

38.3.3 Carrier Phase Tracking Bias

The ionosphere dispersion effects transfer part of the signal energy from the I component to the Q component. Consequently, an imaginary part appears in the correlation function, which leads to the phase bias of the carrier tracking loop. The carrier phase tracking bias can be calculated by

$$\Delta\phi_m(\Delta\tau_{m,\max}) = a\tan\left(\frac{imag(R(\Delta\tau_{m,\max}))}{real(R(\Delta\tau_{m,\max}))}\right) \tag{38.6}$$

where $R(\tau)$ is the complex correlation function, and $\Delta\tau_{m,\max}$ is the delay corresponding to the maximum of the real part of the correlation function. It can be calculated that the carrier phase bias caused by the dispersion reaches 18.5 degree (0.0129 m for the E5 carrier) with a TEC of 100 TECU.

38.4 Impacts of Different Bandwidths, Spectrum Shapes and TECs

According to Eq. (2), the ionosphere delay is directly related to TEC and signal frequency. This section will discuss the impacts of the following three aspects on the signal distortion: signal bandwidth, signal spectrum shape, and TEC.

38.4.1 Signal Bandwidth

The BPSK-R(1) signal centering at 1207.14 MHz and the E5b signal are compared to clarify the impact of signal bandwidth. The E5b signal can be regarded as a BPSK-R(10) signal. Therefore, the signal distortions of the two signals with the same modulation, the same center frequency, the same TEC of 100 TECU and

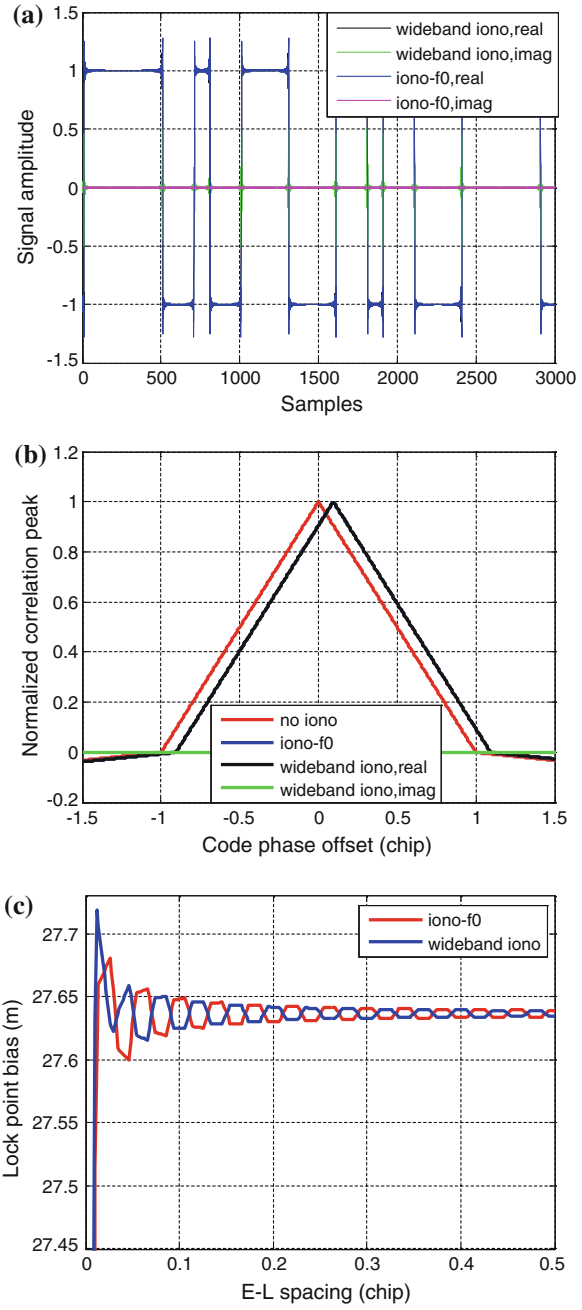

Fig. 38.3 Dispersion effect on BPSK-R(1) **a** time domain waveform **b** correlation function **c** lock point bias

different bandwidths are simulated and shown in Figs. 38.3 and 38.4. It can be seen that part of the signal energy is transferred from the I component to the Q component by the ionosphere dispersion and thus the non-zero imaginary part is

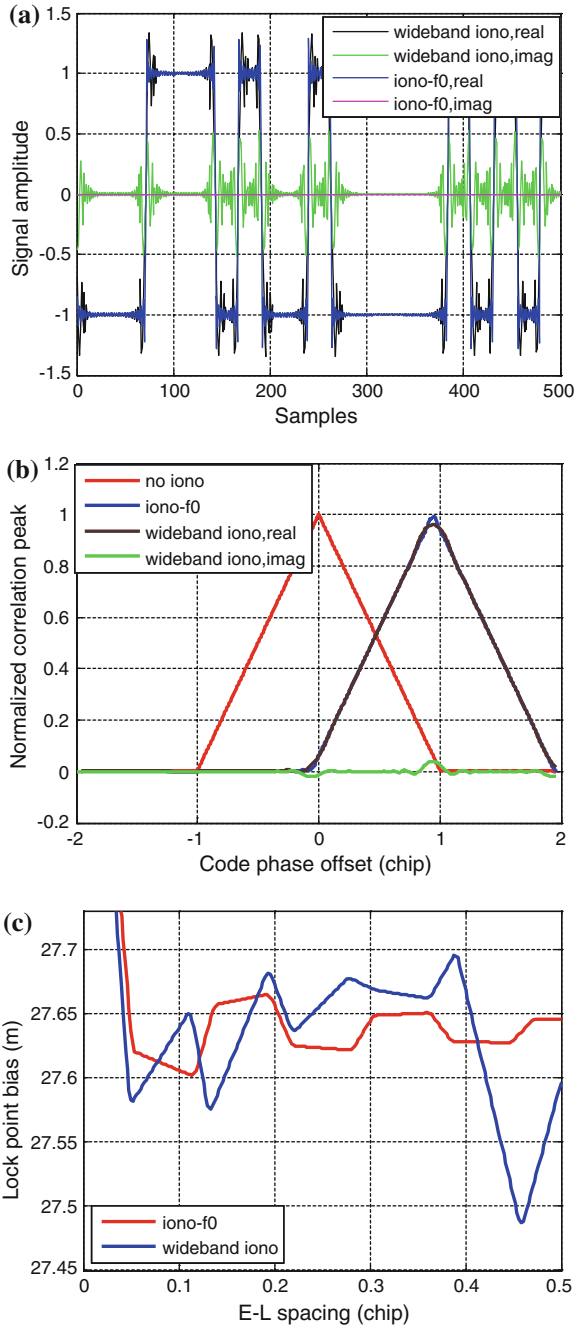

Fig. 38.4 Dispersion effect on E5b **a** time domain waveform **b** correlation function **c** lock point bias

produced in either the time domain baseband signal or the correlation function. The distorted E5b waveform ripples more severely than the BPSK-R(1) signal with higher amplitude of the imaginary part. As a result, the distortion of the E5b correlation function is more obvious with a correlation loss of 0.34 dB, whereas the loss for BPSK-R(1) is only 0.03 dB. Moreover, the DLL lock point bias for the E5b signal exhibits a larger variation than the BPSK-R(1) signal. The maximum difference of the lock point biases with and without the dispersion effect is nearly 0.15 m for the E5b signal and only 0.06 m for the BPSK-R(1) signal. Finally, the PLL carrier phase tracking bias caused by the ionosphere dispersion is 2.4° for E5b and 0.22° for BPSK-R(1). In a word, the signal distortion increases and the signal performance degrades as the signal bandwidth increases.

38.4.2 Signal Spectrum Shape

The BPSK-R(25) signal and the AltBOC(15,10) signal have the same main lobe null-to-null bandwidth of 51.15 MHz, but the spectrum of the BPSK-R(25) signal is centralized and that of the AltBOC(15,10) signal is split. With the same TEC of 100 TECU and the same center frequency of 1191.795 MHz, the effects of ionospheric dispersion on the BPSK-R(25) signal are shown in Fig. 38.5. Compared with the results of the AltBOC(15,10) signal in Sect. 38.3, the ionosphere dispersion effects on the BPSK-R(25) signal are weaker: the waveform fluctuations and CCF distortions are attenuated; the correlation loss is reduced from 2.3 to 0.86 dB; the maximum difference of the lock point biases with and without the ionosphere dispersion is reduced from about 0.35 m to only 0.1 m; meanwhile, the PLL phase shift is reduced from 18.5° to 6.95°. So it can be concluded that the split spectrum are more susceptible to the ionosphere dispersion-induced performance degradation than the concentrated spectrum.

38.4.3 TEC

The TEC value is changed to be 50 TECU and 150 TECU to evaluate its impacts on the distortions of the E5 AltBOC(15,10) signal. The correlation functions and the code tracking biases are depicted in Figs. 38.6 and 38.7 respectively. Compared with Fig. 38.2d, e, we can see that the CCF asymmetry, the correlation loss, and the variation of the DLL lock point biases all increase as the TEC increases. The real part of the correlation peak in Fig. 38.7 deviates from the “iono-f0”case and shifts leftwards obviously. Therefore appropriate pre-distortion techniques should be adopted in the receiver to compensate the phase shifts of the DLL and the PLL for high-accuracy measurements.

The typical mid-latitude nighttime TEC value is between 0 and 30 TECU, and the daytime TEC reaches up to 250 TECU. During active periods of the

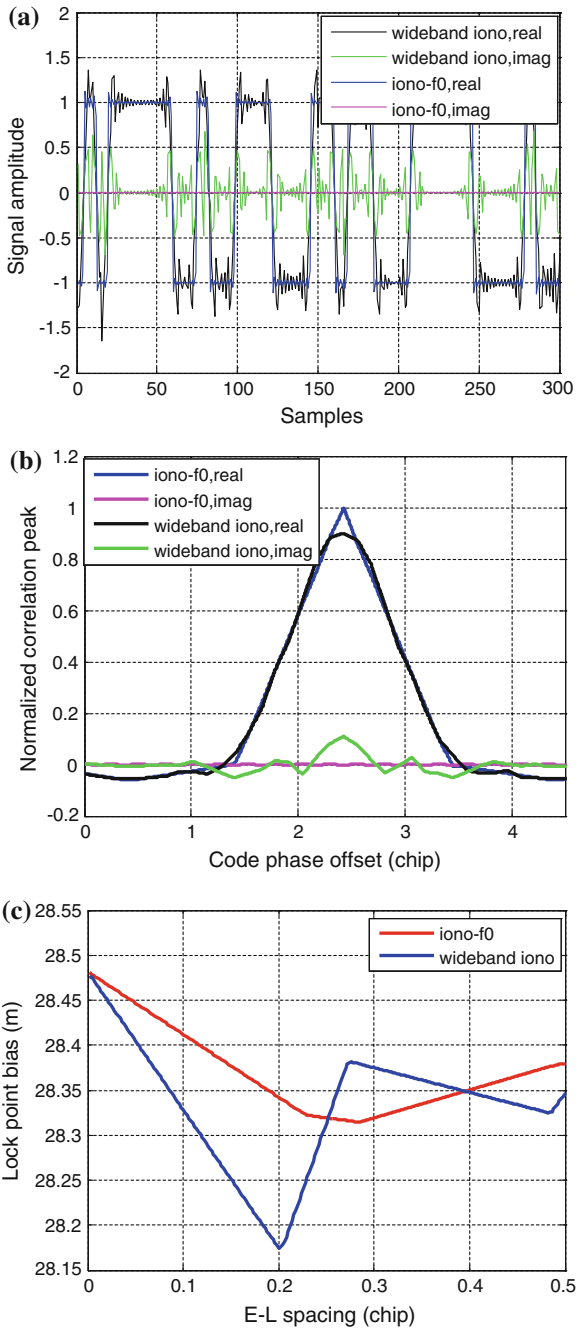

Fig. 38.5 Dispersion effects on BPSK-R(25) **a** time domain waveform **b** correlation function **c** lock point bias

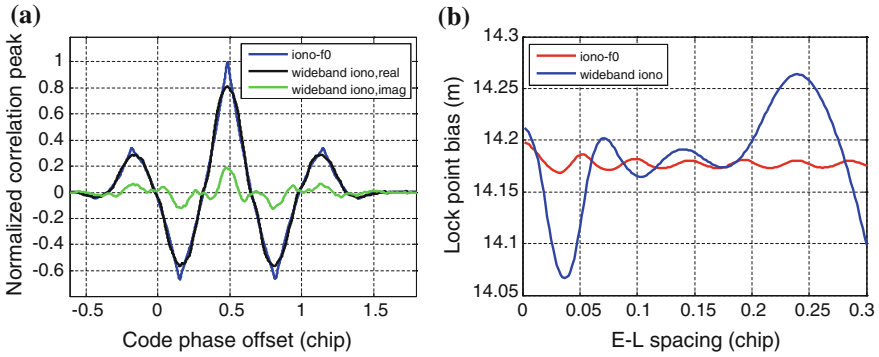

Fig. 38.6 CCF and code tracking bias of E5 with TEC = 50 TECU **a** correlation function **b** code tracking bias

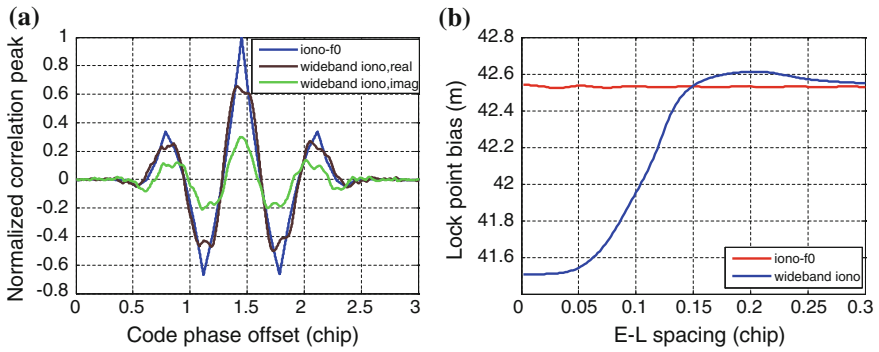

Fig. 38.7 CCF and code tracking bias of E5 with TEC = 150 TECU **a** correlation function **b** code tracking bias

ionosphere, the TEC value may be higher than 250 TECU. The variation of correlation power loss, code tracking bias, and PLL phase shift are simulated with the TEC values from 0 to 500 TECU in Fig. 38.8a–c, respectively. It can be seen that the all three curves present a rising trend with the TEC increasing. However, the correlation loss does not increase monotonically with TEC.

38.5 Conclusions

The paper investigated the ionosphere dispersion effects on wideband GNSS signal performance. The signal distortions caused by the dispersive ionosphere is analyzed and simulated in terms of time domain waveform, correlation function, code phase lock point bias and carrier phase tracking bias under different signal

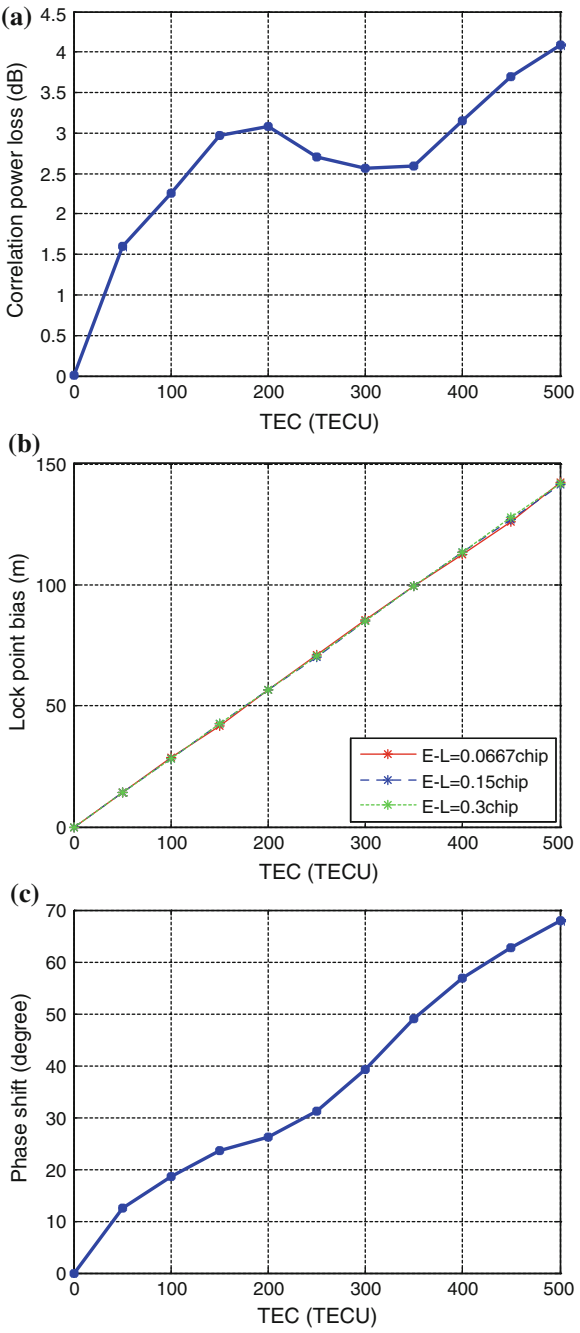

Fig. 38.8 E5 distortions versus TEC **a** correlation loss **b** code tracking bias **c** carrier tracking bias

bandwidths, different spectrum shapes, and different TEC values. The results indicate that: (1) The ionosphere dispersion produces severe distortions on wideband signal waveforms and correlation functions, and thus leads to non-negligible biases in receiver code phase tracking and carrier phase tracking; (2) The distortions due to the ionosphere dispersion increase as the bandwidth or the TEC increases; (3) The split spectrum is more susceptible to the ionosphere dispersion than the centralized spectrum; (4) It is recommended for the wideband GNSS signal receiver to compensate for the ionosphere dispersion in order to reduce the code phase and carrier phase tracking biases.

References

1. McIntosh R, Malaga A (1981) Frequency dispersion in the ionosphere. IEEE Trans Antennas Propag 29(6):970–972
2. Klobuchar JA (1987) Ionospheric time-delay algorithm for single-frequency GPS users. IEEE Trans Aerosp Electron Syst 23(3):325–331
3. Radicella SM, Nava B (2010) NeQuick model: origin and evolution. In: IEEE ISAPE, pp 422–425
4. Kaplan ED, Hegarty CJ (2006) Understanding GPS principles and applications, 2nd edn. Artech House, Washington
5. Gao GX, Datta-Barua S, Walter T, Enge PK (2007) Ionosphere effects for wideband GNSS signals. ION AM
6. Christie JRI, Parkinson BW, Enge PK (1996) The effects of the ionosphere and C/A frequency on GPS signal shape: considerations for GNSS-2. ION GPS
7. European Space Agency (2010) European GNSS (Galileo) open service signal in space interface control document (OS SIS ICD), Issue 1.1

Chapter 39
Analysis on Correction Accuracy of Ionospheric Model for BeiDou System

Wenjun Zhao, Qing Gao and Daliang Gong

Abstract The ionospheric error is the main error sources affecting positioning accuracy for single-frequency users. Parameters of ionospheric model are broadcast by satellite navigation systems for users, so the correction accuracy of the model has direct impact on positioning results. Based on continuous monitoring stations, Beidou system calculated and broadcast 8 parameters of Klobuchar under the geographic coordinate system, and they are updated every 2 h. In order to scientifically evaluate the correction effect of Beidou ionospheric model, firstly, the ionospheric model accuracy of different time periods and different latitudes was analyzed through the basis of GIM model provided by CODE based on Beidou latest observations. Secondly, the following positioning modes were calculated respectively. (1) Single frequency positioning without ionospheric corrections of Beidou. (2) Beidou Single-frequency + Beidou K8 model. (3) Beidou Single-frequency + GPS K8 model. The effect of residual ionospheric corrections was analyzed for positioning results. The results show that the northern hemisphere is better than the southern hemisphere for the accuracy of Beidou ionospheric model. Mid-latitudes regions can get the best correction, and the RMS of correction residuals was average about 0.6 m, and it showed a decreasing trend to the low-latitude and high-latitude regions. Beidou K8 model is better than GPS K8 model for single frequency positioning in Beijing.

Keywords Ionospheric model · Regional navigation system · Correction residuals · Correction rate

W. Zhao (✉) · Q. Gao · D. Gong
P.O. Box 5128, Beijing 100094, China
e-mail: qq1847921840@163.com

J. Sun et al. (eds.), *China Satellite Navigation Conference (CSNC) 2014 Proceedings: Volume I*, Lecture Notes in Electrical Engineering 303,
DOI: 10.1007/978-3-642-54737-9_39,

39.1 Introduction

With the development of GNSS positioning technology, ionospheric delay becomes one of the most serious error sources affecting GNSS measurements [1–4]. For GPS L1 pseudorange, the zenith direction ranging error caused by ionospheric delay is about 5–15 m on daytime in mid-latitudes regions, and about 3 m in the evening. But the effect can be up to hundreds of meters at the peak of solar activity. For dual-frequency receiver, the first-order term impact of the ionosphere can be eliminated by a combination of dual-frequency. For single-frequency receiver, it is only through differential or ionospheric correction model. Common models are Klobuchar model, NeQuick model, IRI2007 model and so on.

The correction effect of Ionospheric model has a direct impact on the positioning result. GPS broadcast 8 parameters of Klobuchar based on geomagnetic coordinates, and they are updated once a day, so the correction accuracy is about 60 % [5, 6]. Galileo system uses Nequick model, and designed correction accuracy is 70 % or less than 20 TECU in slant correction. BD II system uses 8 parameters Klobuchar model under the geographic coordinate system. Ionospheric delay of satellite-station direction and combination observations of satellite receiver and hardware delay can be get by the use of dual-frequency pseudorange, and satellite and receiver hardware delay can be deducted in combination observations, then the VTEC of corresponding puncture point can be get through projection function. The eight parameters can be solved with the VTEC as model observables, and it is broadcast to users. GPS ionospheric model has been researched sufficiently, but parameters meaning and calculating strategies are different for Beidou and GPS, so it is necessary to analyze the effect of the ionosphere model of Beidou system, which can provide a reference for the user and can provide data to support the construction of a global system. Firstly, the difference of ionospheric model parameters for Beidou and GPS was introduced. Secondly, the correction formula is given for Beidou regional ionospheric model. Then the ionospheric model accuracy of different latitudes was analyzed through the basis of GIM model provided by CODE. Lastly, the effect on positioning result was analyzed for correction accuracy of Beidou ionospheric model.

39.2 Ionospheric Model of Beidou

Beidou system uses eight parameters (α_n, β_n, $n = 1, 2, 3, 4$) Klobuchar model under geographic coordinates. Vertical ionospheric delay of B1I can be calculated as follows [7, 8]:

$$I_z(t) = \begin{cases} 5 \times 10^{-9} + A_2 \cos\left[\dfrac{2\pi(t - 50{,}400)}{A_4}\right], & |t - 50{,}400| < A_4/4 \\ 5 \times 10^{-9} & |t - 50{,}400| \geq A_4/4 \end{cases} \quad (39.1)$$

where, I_z is the vertical zenith ionospheric delay, the unit is second, and the corresponding frequency is B1. t is time of intersection between the line of receiver to satellite and the ionosphere (in the range of 0–86400), the unit is second. For different frequencies, they need to take a frequency-dependent factor *k(f)*.

A_2 is the amplitude of the cosine curve on the day, they are calculated by α_n coefficients.

$$A_2 = \begin{cases} \sum_{n=0}^{3} \alpha_n |\phi_M|^n A_2 > 0 \\ 0 \qquad A_2 < 0 \end{cases} \tag{39.2}$$

A_4 is the period of a cosine curve in seconds, they are calculated using the coefficients β_n.

$$A_4 = \begin{cases} 1{,}72{,}800 & A_4 \geq 1{,}72{,}800 \\ \sum_{n=0}^{3} \beta_n |\phi_M|^n & 1{,}72{,}800 > A_4 \geq 72{,}000 \\ 7{,}200 & A_4 < 72{,}000 \end{cases} \tag{39.3}$$

where, ϕ_M is the latitude of puncture point, and its unit is radians. ϕ_M and $\lambda_M$can be calculated as follows:

$$\phi_M = \arcsin(\sin\phi_u \cos\psi + \cos\phi_u \sin\psi \cos A) \tag{39.4}$$

$$\lambda_M = \lambda_u + \arcsin\left(\frac{\sin\psi \sin A}{\cos\phi_M}\right) \tag{39.5}$$

where, ϕ_u is the geographic latitude of user in radians. λ_u is the geographic longitude of user in radians. A is satellite azimuth in radians. ψ is geocentric opening angle between user and puncture in radians which is calculated as follow:

$$\psi = \frac{\pi}{2} - E - \arcsin\left(\frac{R}{R+h}\cos E\right) \tag{39.6}$$

where, R is the radius of the Earth, and the value is 6,378 km. E is satellite elevation angle in radians. h is the height of the ionosphere monolayer, and the value is 375 km.

$I_z(t)$ can be converted to $I_{B1I}(t)$ through $I_{B1I}(t) = \frac{1}{\sqrt{1-\left(\frac{R}{R+h}\cdot\cos E\right)}} \cdot I_z(t)$.

39.3 Evaluation on Correction Effect of Beidou Ionospheric Model

Ionosphere may be affected by both solar activity and the earth's magnetic field. The effect was different in different latitudes and different time periods, which showed significant spatial and temporal characteristics. Based on the measured data of Beidou, the characteristics of ionosphere were analyzed in detail.

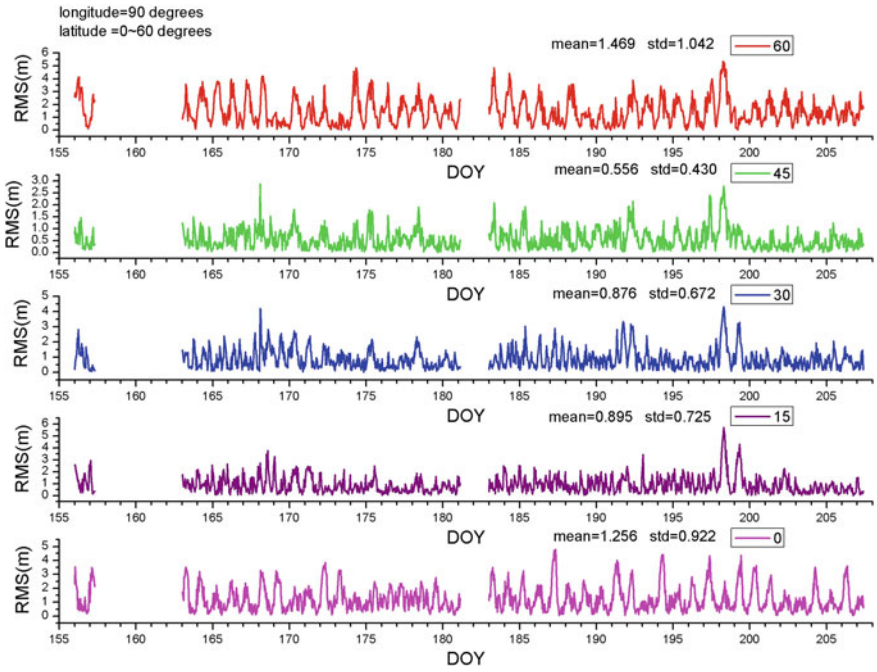

Fig. 39.1 East longitude 90°

39.3.1 Analysis of Correction Accuracy for Different Latitudes Regions

In order to investigate the correction accuracy of Beidou ionospheric model in different geographic regions, north latitude 0°, 15°, 30°, 45°, 60° and east longitude 90° , 105°, 114, and 125° were selected. The RMS of correction residual were shown in Figs. 39.1, 39.2, 39.3, 39.4 and Table 39.1.

From Table 39.1 and Figs. 39.1, 39.2, 39.3, 39.4, the following conclusions can be drawn:

1. The accuracy of the model in the mid latitudes was better than low latitudes and high latitudes, its RMS of correction residuals was about 0.6 m.
2. In the mid-latitudes, the correction accuracy was decreased from east longitude 90 ° to 125 °, and the maximum RMS was within 1.5 m.

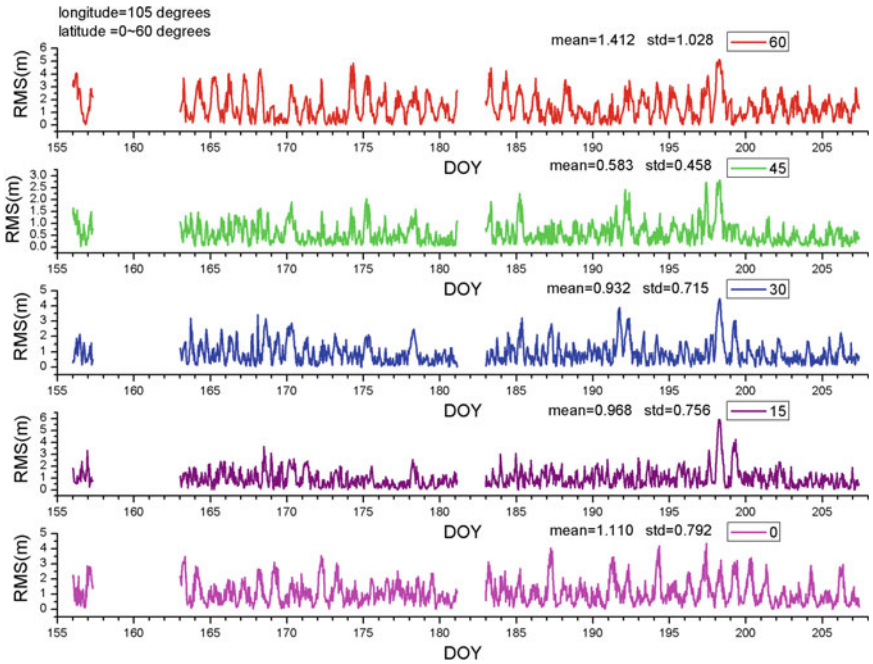

Fig. 39.2 East longitude 105°

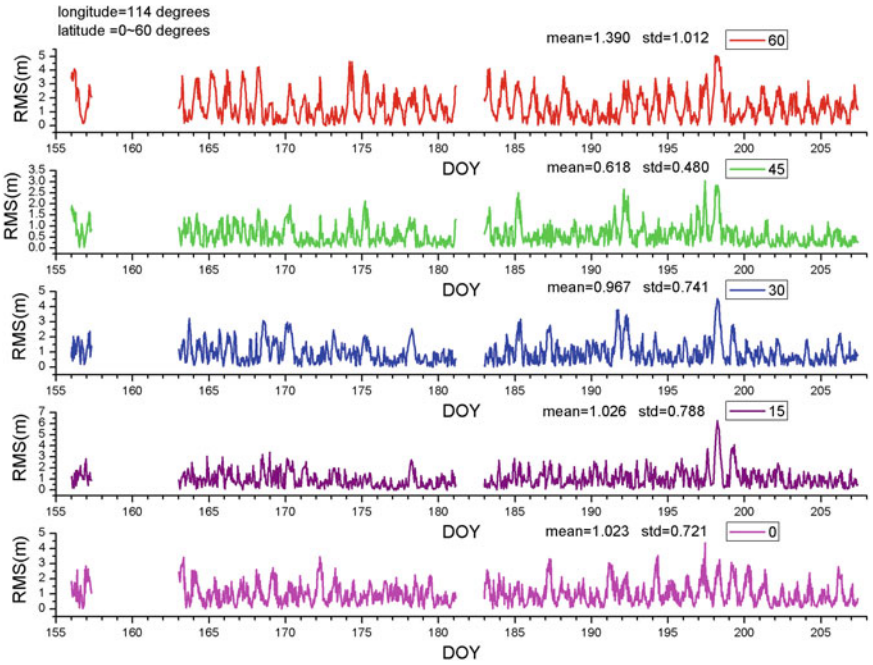

Fig. 39.3 East longitude 114°

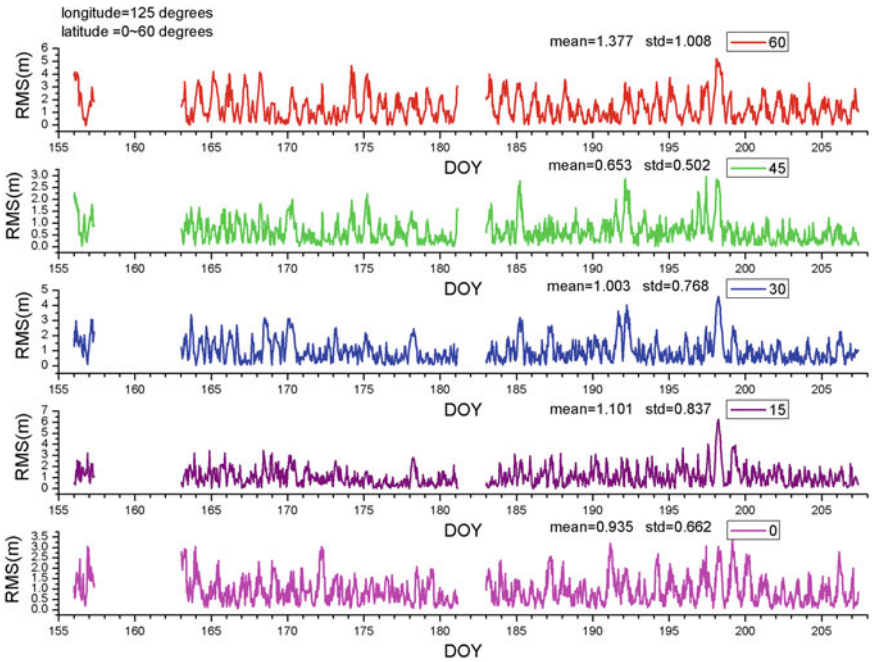

Fig. 39.4 East longitude 125°

Table. 39.1 The statistic result of correction residuals of Beidou K8 model

Lat	Lon			
	90	105	114	125
60	1.469	1.412	1.390	1.377
45	0.556	0.583	0.618	0.653
30	0.876	0.932	0.967	1.003
15	0.895	0.968	1.026	1.101
0	1.256	1.110	1.023	0.935

39.3.2 Analysis of Correction Accuracy for Different Observation Periods

Data comes from URUM, BJFS, SHAO, WUHN and KUNM, which are parts of 15 CORS stations of Wuhan University. Each station used measuring receivers. Measuring time was in July 2012. The height of cut-off angle was 5°, and the sampling interval is 30 s.

Firstly, based on parameters of ionospheric model from receivers, ionospheric delays were calculated in the view direction for all visible satellites. Secondly,

Fig. 39.5 Analysis of correction effect for Beidou K8 model

ionospheric delays were computed in the view direction using GIM model provided by CODE,which was considered as the reference value for Beidou K8 model. Finally, the correction rate of the Beidou K8 model relative to GIM model was computed.

In the analysis, the observation period is divided into two periods during the day and night, the results shown in Fig. 39.5.

In Fig. 39.5, correction rate of Beidou K8 model was generally above 70 %, and its mean was about 80 %. Correction rate in night was higher than day.

In order further analyze effect of time on ionospheric correction accuracy, the grids of 2° × 2° were designed from east longitude 60° to 160° and north latitude 60° to north latitude 60°. Tow time periods of July 22, 2012 19:00 and 07:00 in UTC were selected, which were corresponding to 15:00 (day) and 03:00 (night) in Beijing time. The RMS of correction residual of Beidou K8 relative to GIM was computed in meters. The results were shown in Figs. 39.6 and 39.7.

As can be seen from Figs. 39.6 and 39.7, the correction accuracy of Beidou K8 was within 1 m. The correction accuracy in night was better than day.

39.3.3 Analysis of Impact on User Positioning

Data came from measuring receivers on Beijing stations, which included B1I, B2I, GPS L1 and GPS L2. Measuring time was in July 22, 2012 17:50:00 to July 23, 2012 18:10:00. The height of cut-off angle was 5°, and the sampling interval is 1 s.

Based on the original observation data and ephemeris information, respectively, the following positioning modes were computed: (1) Single frequency positioning

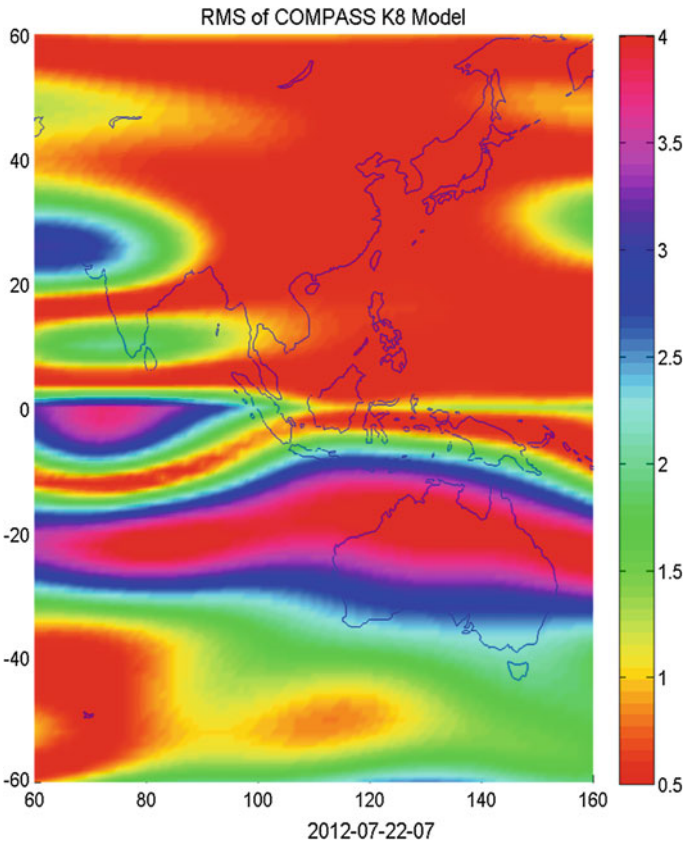

Fig. 39.6 15:00 in Beijing time

without ionospheric corrections of Beidou. (2) Beidou Single-frequency + Beidou K8 model. (3) Beidou Single-frequency + GPS K8 model. (4) Beidou dual frequencies. All epochs were sorted and taking the 95 % as results. Results are shown in Table 39.2 and Fig. 39.8, 39.9, 39.10.

The black box in figure was part of the night 00:00–04:00 in GMT. The results can be drawn:

1. Without correction of ionospheric model, the positioning accuracy of Beidou single-frequency was worse than dual-frequency, and the ionospheric errors on B2 frequency was larger than B1. Single-frequency positioning accuracies of B1 and B2 were greatly improved 5.6 and 11.1 m respectively using Beidou K8 model.
2. Beidou K8 model was better than GPS K8 model for single frequency positioning in Beijing.

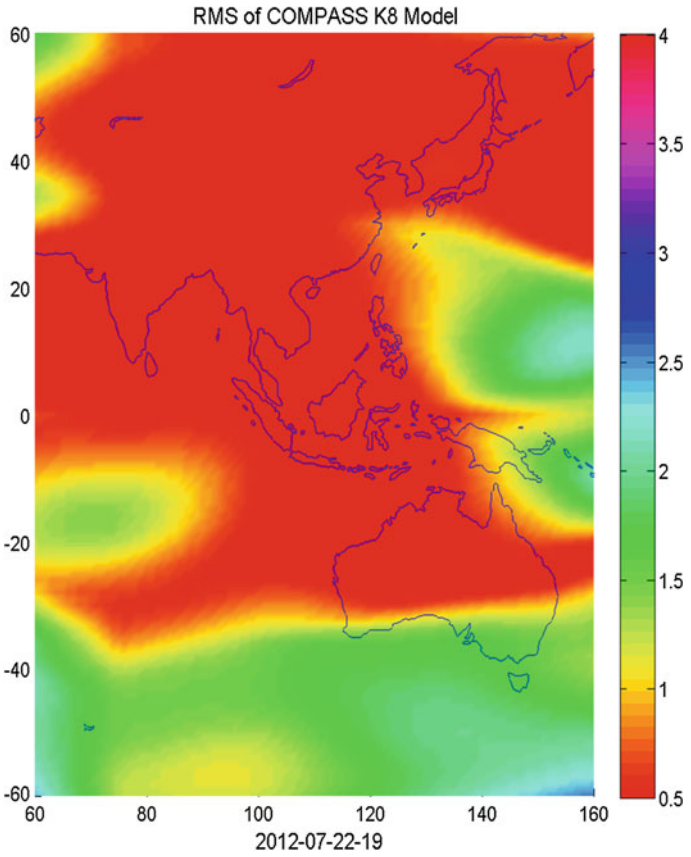

Fig. 39.7 03:00 in Beijing time

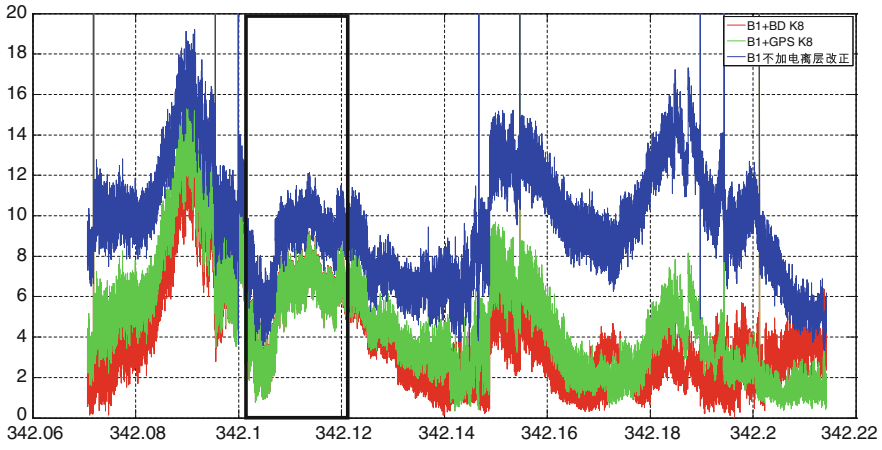

Fig. 39.8 Positioning error using different ionospheric model for B1

Table 39.2 Statistics of positioning based on the different ionospheric models

Positioning mode	Positioning error (95 %, m)		
	Level	Elevation	Position
B1+BD K8	4.0	8.03	8.91
B1+GPS K8	4.26	9.32	10.2
B1 without ionospheric correction	4.76	14.1	14.53
B2+BD K8	4.46	7.71	8.82
B2+GPS K8	4.85	9.19	10.05
B2 without ionospheric correction	6.46	19.64	19.89
B1+B2	5.89	12.09	13.07

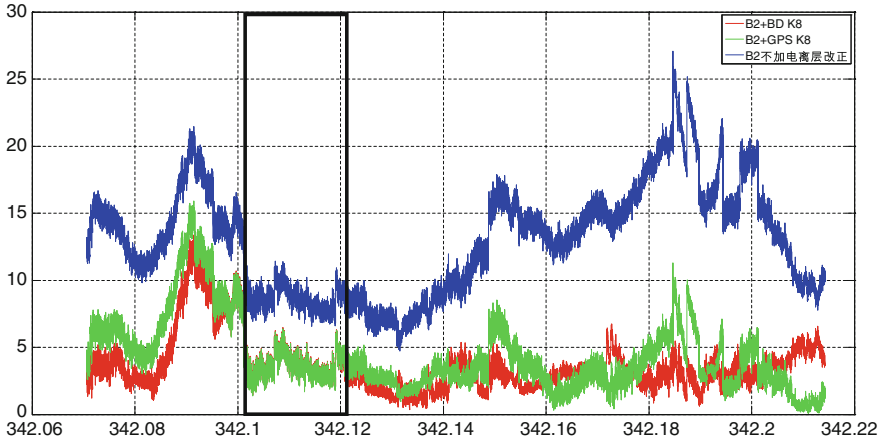

Fig. 39.9 Positioning error using different ionospheric model for B2

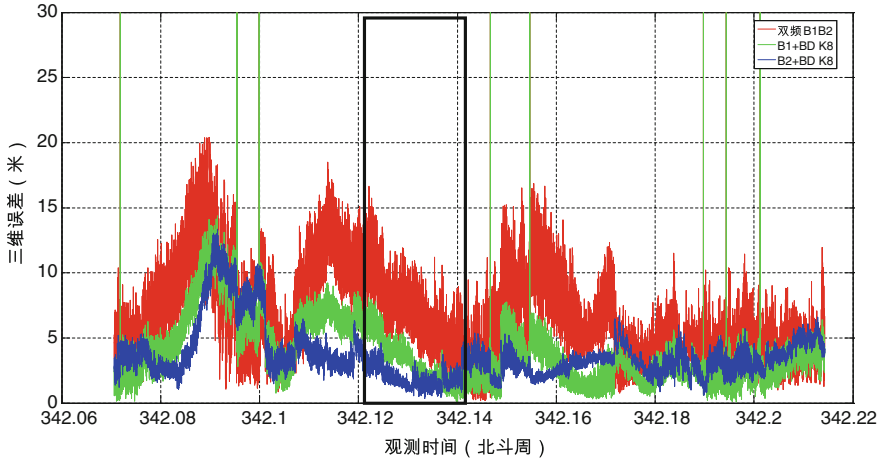

Fig. 39.10 Comparison of positioning error between Beidou single frequency and dual-frequency

3. Positioning accuracy of dual-frequency was worse than single frequency, which indicated that the amplifying error by dual-frequency combination was larger than residual error of ionospheric model.

39.4 Conclusion

In this paper, 15 CORS stations of Wuhan University and Beidou measuring data in Beijing were used. Based on GIM provided by CODE, Beidou regional ionospheric model was quantitatively analyzed. The results are as follows:

1. In Beijing test, correction rate of Beidou K8 model was generally above 70 %, and its mean was about 80 %. Correction rate in night was higher than day.
2. The accuracy of the model in the mid latitudes was better than low latitudes and high latitudes, its RMS of correction residuals was about 0.6 m. In the mid-latitudes, the correction accuracy was decreased from east longitude 90° to 125°, and the maximum RMS was within 1.5 m.
3. Single-frequency positioning accuracies of B1 and B2 were greatly improved 5.6 m and 11.1 m respectively using Beidou K8 model, and Beidou K8 model was better than GPS K8 model for single frequency positioning in Beijing.

References

1. Zhang H P (2006) Study on GPS based china regional ionosphere monitoring and ionospheric delay Correction. Ph.D. Dissertation, Shanghai Astronomical Observatory, ChineseAcademy of Sciences, Shanghai, China, May 2006
2. Wan W-x, Ning B-q, Liu L-b (2007) Nowcasting the ionospheric total electron content over china. J Prog Geophys 22(4):1040–1045
3. Klobuchar J (1987) Ionospheric time-delay algorithm for single-frequency GPS users. IEEE Trans Aerosp Eelectronic Syst AES-23:325–331 (ISSN 0018-9251)
4. Hofmann-Wellenhof B, Lichtenegger H, Collins J (2001) GPS—theory and practice, 5th edn. Springer, New York
5. ICD-GPS-200C-004 (2000) NAVSTAR GPS space segment/navigation user interfaces. Arinc Research Cooperation, April 2000
6. Journel AG, Huijbregts CJ (1978) Mining geostratistics. Academic Press
7. Prasad N, Sarma AD (2004) Ionospheric time delay estimation using IDW grid model for GAGAN. J Indian Geophys Union 8(4):319–327
8. Sharma S, Galav P (2011) Longitudinal study of the ionospheric response to the geomagnetic storm of 15 May 2005 and manifestation of TADs. Ann Geophys 29:1063–1070

Chapter 40
Optimization of GEO Navigation Satellite Station Shifts Impulsives

Ying Liu, Guoqiang Zhao and Jing Li

Abstract In order to increase system availability,optimization of control of the drift orbit of GEO navigation satellites for station shifts is studied. Given the orbit drift time, comparing to the traditional method that adjusts phase by changing the semimajor axis, we employ the primer vector theory and assess the whole improvement process. The detailed algorithm is presented to determine the number, time, and position of the impulsives. At the end of program, The numerical optimization method BFGS is used to improve the model. As shown by the problem analyzed, we can get better result by applying the presented method.

Keywords GEO station shifts · Primer vector theory · Trajectory optimization

40.1 Introduction

After a Geostationary Earth Orbit (GEO) navigation satellite is positioned at the initial geostationary orbit, station shifts will take place due to various reasons and the satellite and change the subsatellite longitude. Considering the key role of GEO satellites in Beidou navigation satellite constellation, it is of high significance to study issues related to drift control for the GEO satellites station shifts because this shall help save satellite propellants, increase the availability of GEO satellites and thus increase the overall system availability of the system.The literatures [1–3] introduce the traditional method of orbit control in detail. The traditional method

Y. Liu (✉)
Beijing Institute of Tracking and Telecommunications Technology, Beijing 100094, China
e-mail: liu2ying@163.com

G. Zhao · J. Li
State Key Laboratory of Astronautic Dynamics, Xi'an 710043, China
e-mail: sciwalker@126.com

J. Sun et al. (eds.), *China Satellite Navigation Conference (CSNC) 2014 Proceedings: Volume I*, Lecture Notes in Electrical Engineering 303,
DOI: 10.1007/978-3-642-54737-9_40,

adjusts the orbit semimajor axis and changes the relative angular velocity. Thus the satellite moves to the target position. Another orbit control is performed to reduce the satellite's relative drift speed and it is reinserts into another GEO. Given the mission requirements, different strategies are designed corresponding to different time durations.

Given the orbit drift time duration, the initial and the target position vector are specified. The essence of the traditional control strategy is to solve the Lambert problem. The literature [4] tells that the Lambert solution is not the optimal result of two position vector as the transfer time is fixed. The optimal trajectory should satisfy the necessary condition of the primer vector. The paper also gives the improvement process. The literature [5] analyze the optimization of evasion maneuvers. The literature [6] apply the feature to search the optimal multi-impluse launch opportunites.

We apply the primer vector theory to improve the GEO navigation satellite station shifts and present the detailed calculation procedure. The BFGS numerical method is employed to optimize the fuel consumption.

40.2 Primer Vector Theory

40.2.1 Problem Formulation

The primer vector is introduced by Lawden [4] in 1963. The primer vector is defined to be the costate variable associated with the velocity vector's. Consider the problem that the spacecraft is subject only to the central force of the Earth gravity and the thrust of its own propulsion system.

$$\dot{\boldsymbol{r}} = \boldsymbol{v} \tag{40.1}$$

$$\dot{\boldsymbol{v}} = \boldsymbol{g} + \Gamma \boldsymbol{u} \quad \boldsymbol{g} = -\frac{\mu}{r^3}\boldsymbol{r} \tag{40.2}$$

$$\dot{J} = \Gamma \tag{40.3}$$

where $\boldsymbol{r}$ and $\boldsymbol{v}$ denote the position and velocity vectors in the Earth centered inertial system. The Earth's gravitational constant is denoted by μ and its value is 398600.14 km^3/s^2. Γ is thrust acceleration $0 \leq \Gamma \leq \Gamma_{max}$ and $\boldsymbol{u}$ is the unit vector of control variables. For the assumption that the velocity change is finished at the negligible duration, the thrust capability of the satellite is not bounded and can be replaced by an impulsive without in any way affecting its position. That is $\Gamma = 0$ or $\Gamma \to \infty$. Generally, J is the characteristic velocity to be minimized expressed by

$$J(t_f) = \int_{t_0}^{t_f} \Gamma dt \tag{40.4}$$

where t_0 and t_f denote the initial and final time, respectively. Equation (40.1)–(40.3) is the formulation of the satellite under the control of gravity and thrust.

To obtain the optimal fuel consumption solution, we should solve the optimal control problem in the interval of $t_0 \leq t \leq t_f$.

40.2.2 Necessary Conditions for Optimal Orbit Transfer

According to the dynamic Eq. (40.1)–(40.3), the Hamilton function is constructed as

$$H = \boldsymbol{\lambda}_r^T \boldsymbol{v} + \boldsymbol{\lambda}_v^T \boldsymbol{g} + (\boldsymbol{\lambda}_v^T \boldsymbol{u} + \lambda_J)\Gamma \tag{40.5}$$

The symbol $\boldsymbol{\lambda}_r$, $\boldsymbol{\lambda}_v$, λ_J denote the corresponding costates of $\boldsymbol{r}$,$\boldsymbol{v}$ and J, respectively. The costate equation is as follows

$$\dot{\boldsymbol{\lambda}}_r = -\frac{\partial H}{\partial \boldsymbol{r}} = -G(\boldsymbol{r})\boldsymbol{\lambda}_v \tag{40.6}$$

$$\dot{\boldsymbol{\lambda}}_v = -\frac{\partial H}{\partial \boldsymbol{v}} = -\boldsymbol{\lambda}_r \tag{40.7}$$

$$\dot{\boldsymbol{\lambda}}_J = -\frac{\partial H}{\partial J} = 0 \tag{40.8}$$

where $\mathbf{G}(\boldsymbol{r})$ is called the Gravity Gradient Matrix

$$G(\boldsymbol{r}) = \mu(3\boldsymbol{r}\boldsymbol{r}^T - r^2\boldsymbol{I})/r^5 \tag{40.9}$$

and $\boldsymbol{I}$ is the identity matrix.

Due to the Pontryagin Maximization (or Minimization) Principle, $\boldsymbol{\lambda}_r$ and $\boldsymbol{\lambda}_v$ are determined by the boundary conditions. And

$$\boldsymbol{\lambda}_J = -1 \tag{40.10}$$

To maximizing the function (40.5), the dot product $\boldsymbol{\lambda}_v\, \boldsymbol{u}$ should be maximized. So the direction of $\boldsymbol{\lambda}_\mathbf{v}$ and u should be aligned. We denote $\boldsymbol{\lambda}_\mathbf{v}$ by $\boldsymbol{p}$ and call it the Primer Vector. According to the Eq. (40.7), we have

$$\dot{\boldsymbol{p}}(t) = -\boldsymbol{\lambda}_r(t) \tag{40.11}$$

The Hamilton function is formulated as

$$H = \boldsymbol{p}^T \boldsymbol{g} - \dot{\boldsymbol{p}}^T \boldsymbol{v} + (p-1)\Gamma \tag{40.12}$$

In the situation of impulsive $\Gamma \to \infty$, $(p-1)\ \Gamma$ should always be zero to make the expression meaningful. So the Eq. (40.12) can be written as

$$H = \boldsymbol{p}^T \boldsymbol{g} - \dot{\boldsymbol{p}}^T \boldsymbol{v} \tag{40.13}$$

The primer can be obtained by solving the equation as follows

$$\ddot{\boldsymbol{p}}(t) = G(\boldsymbol{r})\boldsymbol{p} \tag{40.14}$$

The following conditions must be satisfied over an optimal trajectory:

(1) The primer can be obtained by eq. (40.14). The primer and its first time derivative must be continuous everywhere.
(2) The magnitude p of the primer must not exceed 1 on the trajectory and $p = 1$ at the impulsive time.
(3) The impulsive direction must be aligned with the primer at the time.
(4) Due to the condition (2), The primer reaches a maximum at all interior impulsives. $\dot{p} = \dot{\boldsymbol{p}}^T \boldsymbol{p} = 0$.

40.3 Optimization Procedure of Orbit Transfer Design

Necessary conditions are already given in the previous section for optimal impulsive transfer orbit. The current section shall explain how to transform a non-optimal orbit into an optimal orbit. Lion and Handelsman demonstrated how to get an approaching solution to provide first-order propellant consumption with a method encompassing increase of intermediate impulsives and terminal glide, thus improving non-optimal impulsive orbits, when the main vectors computed for the non-optimal orbits do not meet necessary conditions. An iterative process is established to get solutions to converge to the necessary conditions.

40.3.1 Calculation of the Primer Vector

A reference trajectory should be ready before the primer vector calculation. The reference trajectory is usually not optimal. We calculate the primer vector along the nonoptimal orbit. Usually the lambert solution is used between the two point.

$$\boldsymbol{p}_0 = \frac{\Delta \boldsymbol{V}_0}{|\Delta \boldsymbol{V}_0|} \quad \boldsymbol{p}_f = \frac{\Delta \boldsymbol{V}_f}{|\Delta \boldsymbol{V}_f|} \tag{40.15}$$

where $\boldsymbol{p}_0$ and $\boldsymbol{p}_\mathrm{f}$ denote the primer vector at the initial and final time. $\Delta \mathbf{V}_0$ and $\Delta \mathbf{V}_\mathrm{f}$ denote the characteristic velocity at the initial and final time.

From the Eq. (40.14), the primer vector can be calculated by the transition matrix.

$$\begin{pmatrix} \boldsymbol{p}(t) \\ \dot{\boldsymbol{p}}(t) \end{pmatrix} = \begin{pmatrix} \phi_{11} & \phi_{12} \\ \phi_{21} & \phi_{22} \end{pmatrix} \begin{pmatrix} \boldsymbol{p}_0 \\ \dot{\boldsymbol{p}}_0 \end{pmatrix} \tag{40.16}$$

and we have

$$\dot{\boldsymbol{p}}_0 = \phi_{12}^{-1}\left(\boldsymbol{p}_f - \phi_{11}\boldsymbol{p}_0\right) \tag{40.17}$$

So we have known the initial primer vector state $\boldsymbol{p}_0, \dot{\boldsymbol{p}}_0$. Using the eq. (40.16), we can obtain the primer vector state at any time on the trajectory.

40.3.2 Procedure of Optimization

(1) Given the initial position, the final position and the orbit drift time, we can acquire the initial solution of the primer vector and the transition matrix.
(2) Then we check the primer magnitude of the whole trajectory. If the primer magnitude p(t) exceeds 1 at the interior point, the two impulsive transfers are not optimal. We should add the third impulsive at the time t_{m} when the magnitude p(t) is maximized.

$$\delta \boldsymbol{r}_m = cA^{-1}\frac{\boldsymbol{p}_m}{|\boldsymbol{p}_m|} \tag{40.18}$$

where

$$A = \phi_{22}\left(t_m, t_f\right)\phi_{12}^{-1}\left(t_m, t_f\right) - \phi_{22}(t_m, t_0)\phi_{12}^{-1}(t_m, t_0) \tag{40.19}$$

$$c = \frac{\beta\frac{\Delta \boldsymbol{V}_f}{|\Delta \boldsymbol{V}_f|} - \alpha\frac{\Delta \boldsymbol{V}_0}{|\Delta \boldsymbol{V}_0|} - 1}{\frac{\left[\alpha\cdot\alpha - \frac{(\alpha\cdot\Delta \boldsymbol{V}_0)^2}{|\Delta \boldsymbol{V}_0|^2}\right]}{|\Delta \boldsymbol{V}_0|} + \frac{\left[\beta\cdot\beta - \frac{(\beta\cdot\Delta \boldsymbol{V}_f)^2}{|\Delta \boldsymbol{V}_f|^2}\right]}{|\Delta \boldsymbol{V}_f|}} \tag{40.20}$$

$$\alpha = \phi_{12}^{-1}(t_m, t_0)A^{-1}\frac{\boldsymbol{p}_m}{|\boldsymbol{p}_m|} \tag{40.21}$$

$$\beta = \phi_{12}^{-1}(t_m, t_f)A^{-1}\frac{\boldsymbol{p}_m}{|\boldsymbol{p}_m|} \tag{40.22}$$

We can get t_{m} and p_{m} by check the trajectory process. And the transition matrix A can be calculated by the corresponding pieces of trajectory.

(3) Then we should slove two Lambert problems. One is the trajectory that is from the initial position to the position $\boldsymbol{r}_m + \delta \boldsymbol{r}_m$. And the corresponding

time duration is $t_m - t_0$. The other trajectory is from the position $\boldsymbol{r}_m + \delta\boldsymbol{r}_m$ to the end position. Now we get a three impulsive trajectory and we can make the characteristic velocity smaller by adjusting the interior impulsive's time and position. And the descent value can be expressed by

$$dJ = (\boldsymbol{p}_m^+ - \boldsymbol{p}_m^-)d\boldsymbol{r}_m - (\boldsymbol{p}_m^+\boldsymbol{V}_m^+ - \boldsymbol{p}_m^-\boldsymbol{V}_m^-)dt_m \tag{40.23}$$

The labels "+" and "–" denote the state before and after the impulsive.

(4) We check the primer magnitude of the whole trajectory again. If the primer vector satisfy the neccsary condition. Then the iteration process ends. Or the same improvement iteration should continue.

40.3.3 Numerical Optimization Algorithm

We propose the *Broyden–Fletcher–Goldfarb–Shanno* (BFGS) optimization algorithm with numerical stability.

(1) Given the initial point $\boldsymbol{x}^{(1)}$ and the tolerance *tol*.
(2) The matrix H_1 is the identity matrix. Calculate the gradient at $\boldsymbol{x}^{(1)}$.
(3) Make $\boldsymbol{d}^{(k)} = -\boldsymbol{H}_k\boldsymbol{g}_k$.
(4) From make one-dimension search at $\boldsymbol{x}^{(k)}$,

$$f(\boldsymbol{x}^{(k)} + \lambda_k\boldsymbol{d}^{(k)}) = \min_{\lambda \geq 0} f(\boldsymbol{x}^{(k)} + \lambda\boldsymbol{d}^{(k)})$$

and

$$\boldsymbol{x}^{(k+1)} = \boldsymbol{x}^{(k)} + \lambda_k\boldsymbol{d}^{(k)}.$$

(5) Check convergence criterion. If $\frac{\left|f(\boldsymbol{x}^{(k+1)}) - f(\boldsymbol{x}^{(k)})\right|}{|f(\boldsymbol{x}^{(k+1)})| + |f(\boldsymbol{x}^{(k)})|} < \frac{tol}{2}$ is satisfied, then stop the iteration. The end point is $\boldsymbol{x}^{(k+1)}$. Or continue the procedure (6).
(6) Make $\boldsymbol{g}_{k+1} = \nabla f(\boldsymbol{x}^{(k+1)})$, $\boldsymbol{p}^{(k)} = \boldsymbol{x}^{(k+1)} - \boldsymbol{x}^{(k)}$, $\boldsymbol{q}^{(k)} = \boldsymbol{g}_{(k+1)} - \boldsymbol{g}_k$. Calculate $\boldsymbol{H}_{(k+1)}$ using BFGS formula.

$$\boldsymbol{H}_{(k+1)} = \boldsymbol{H}_k + \frac{\boldsymbol{p}^{(k)}\boldsymbol{p}^{(k)T}}{\boldsymbol{p}^{(k)T}\boldsymbol{q}^{(k)}} - \frac{\boldsymbol{H}_k\boldsymbol{q}^{(k)}\boldsymbol{q}^{(k)T}\boldsymbol{H}_k^T}{\boldsymbol{q}^{(k)T}\boldsymbol{H}_k\boldsymbol{q}^{(k)}} + \left[\boldsymbol{q}^{(k)T}\boldsymbol{H}_k\boldsymbol{q}^{(k)}\right]\boldsymbol{u}\boldsymbol{u}^T$$

$$\boldsymbol{u} = \frac{\boldsymbol{p}^{(k)}}{\boldsymbol{p}^{(k)T}\boldsymbol{q}^{(k)}} - \frac{\boldsymbol{H}_k\boldsymbol{q}^{(k)}}{\boldsymbol{q}^{(k)T}\boldsymbol{H}_k\boldsymbol{q}^{(k)}}$$

The iteration continues until the specified number is achieved. Or return the procedure (3).

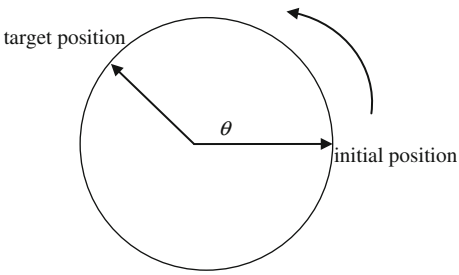

Fig. 40.1 GEO satellite station shifts

40.4 Numerical Example

Assume the satellite is at the initial position (Fig. 40.1) at the beginning. The phase difference between the target position and the initial position is θ. For computing convenience, the quantities about length, time, are nondimensionalized by GEO radius (42164 km), period (86164 s) and thus μ is $4\pi^2$. The initial position vector is (1,0,0), θ is 288°. The orbit drift time duration for station shifts is 2.3.

Computing the Lambert problem and we get the following parameters.

The first impulsive time: 0
The first impulsive vector: (0.5443, 0.3857, 0)
The second impulsive time: 2.3
The second impulsive vector: (–0.1987, –0.6369,0)
The whole impulsive magnitude: 1.3343

The primer magnitude varies as the following figure (Fig. 40.2).

According to the primer vector theory, an impulsive should be added at the time where the primer magnitude is maximal. Finishing the process and the primer magnitude is as Fig. 40.3.

In the later part of Fig. 40.3, the primer magnitude still exceeds 1 obviously. So another impulsive is added and the BFGS algorithm is performed to optimize the whole trajectory. The final primer magnitude trajectory is as Fig. 40.4.

From the Fig. 40.4, we can see that the primer magnitude is always not exceeds 1. The necessary conditions of optimal trajectory are satisfied. The final result is that the optimal station shifts should perform 4 impulsives. The characteristic velocity is 1.1884 and it is 0.1459 less than the two-impulsive station shifts. It is about 704 m/s after transformed into international standard. The four impulsives are summarized as follows:

The first impulsive time: 0
The first impulsive vector: (0.1815, 0.3987, 0)
The second impulsive time: 0.7941
The second impulsive vector: (0.0905, −0.1273, 0)
The third impulsive time: 1.5059
The third impulsive vector: (0.1498, −0.0483, 0)

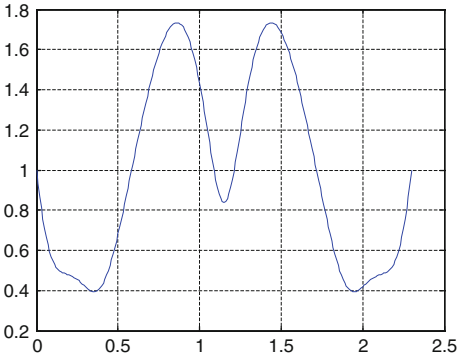

Fig. 40.2 The primer magnitude of the two-impulsive station shifts

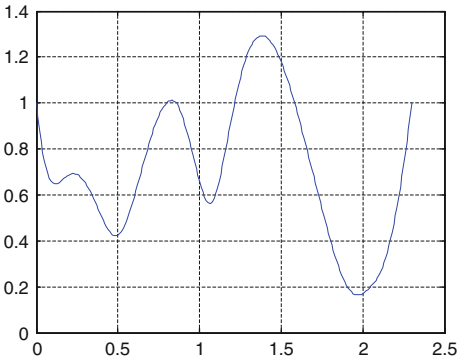

Fig. 40.3 The primer magnitude after adding an impulsive in interior part of the two-impulsive station shifts

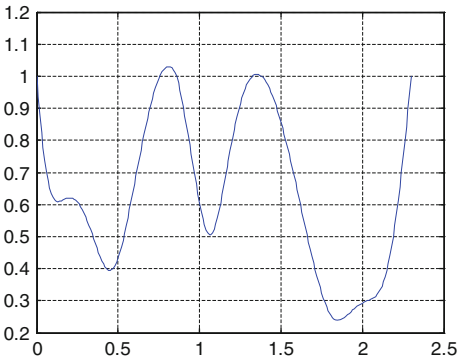

Fig. 40.4 The primer magnitude after adding two impulsives in interior part of the two-impulsive station shifts

The fourth impulsive time: 2.3
The fourth impulsive vector: (−0.3221, −0.2950, 0)
The whole impulsive magnitude: 1.1884

40.5 Conclusion

The paper focuses on optimization of GEO Navigation Satellite station shifts impulsives. According to the nonoptimal orbit drift trajectory, we employ the primer vector theory and present the detailed algorithm to determine the number, time, and position of the impulsives. Combining the numerical optimization method BFGS, we can get better orbit drift strategies for station shifts and reduce fuel consumption.

References

1. Li Hengnian (2011) Geostationary satellite orbital analysis and collocation design strategies [M]. National Defence Industrial Press, Beijing
2. Erik Mattias Soop (1999) Handbook of geostationary orbits [M]. National Defence Industrial Press, Beijing
3. Li Yuheng (2003) The principle of station-keeping and maneuver strategies of geostationary communication satellites. J Spacecraft TT&C Technol 22(04):53–61
4. Jezewski DJ (1975) Primer vector theory and applications. NASA-TR-R-454, Washington, D. C
5. Zhao Ruian (2008) Space weapon orbit design[M]. Chinese Astronautic Press, Beijing, Beijing, pp 203–303
6. Qiao D (2007) Study of transfer trajectory design method for deep space exploration and application to small body exploration, Harbin Institute of Technology, pp 30–34
7. Press WH, Teukolsky SA, Vetterling WT, Flannery BP (2005) Numerical recipes in c++: the art of scientific computing. Publishing House of Electronics Industry Press, Butterworths, London

Part III
BDS/GNSS User Terminal Technology

Chapter 41
A New Designed Navigation Microstrip Patch Antenna with Air Back Cavity

Liu Zheng and Li Feng

Abstract In this paper a new designed microstrip patch antenna with air back cavity will be mentioned, compared to the common microstrip patch antenna, it improves the narrow bandwidth and the poor radiation efficiency. The low precision machining requires and the flexible structure in project make the new antenna very fit to the multiband satellite navigation receivers. By the electromagnet simulation software HFSS, the scientific of this new design will be proved firstly for this paper, and a prototype will be produced to test and to prove the feasibility. The new designed microstrip patch antenna might widely replace the common microstrip patch antenna in many navigation applications.

Keywords Microstrip patch antenna · Air back cavity · Bandwidth · Radiation efficiency · Miniaturization

41.1 Introduction

Microstrip patch antennas were first proposed in the early 1970s and since then a plethora of activity in this area of antenna engineering has occurred, probably more than in any other field of antenna research and development. Microstrip patch antennas have several well-known integrated over other antenna structures, including their low profile and hence conformal nature, light weight, low cost of production, robust nature, and compatibility with microwave monolithic integrated circuits and optoelectronic integrated circuits technologies [1]. Because of these

L. Zheng (✉) · L. Feng
Beijing Automation Control Equipments Institute, Feihangstr. 1, Beijing 100074, China
e-mail: liu.zheng2312@gmail.com

L. Feng
e-mail: lifeng600@sohu.com

J. Sun et al. (eds.), *China Satellite Navigation Conference (CSNC) 2014 Proceedings: Volume I*, Lecture Notes in Electrical Engineering 303,
DOI: 10.1007/978-3-642-54737-9_41,

merits, forms of the microstrip patch antenna have been utilized in satellite navigation terminals for GPS, BD 2. generation, etc.

Despite the previously mentioned features, microstrip patch antennas suffer from several inherent disadvantages of this technology in its pure form, namely, they have small bandwidth and relatively poor radiation efficiency resulting from surface wave excitation and conductor and dielectric losses. With our self-developed BD2 navigation system got into the practical stage, multiband navigation receivers become more popular today. That needs a greater bandwidth, a higher gain for every navigation frequency, and better circular polarization characteristics from the navigation antennas urgently. In particular, the design requirements for miniaturization, the designers use more high dielectric constant materials for the microstrip patch antennas, this will result in a further decline bandwidth and radiation efficiency of the microstrip patch antennas.

The impedance bandwidth of the microstrip patch antennas can be extended with a wideband feed network, but not for the radiation bandwidth. Even because of the use of the feed network, the radiation efficiency of the antennas will be lower. If the received navigation signal is poor, a low gain from the navigation antenna makes the low sensitivity navigation receiver, which is designed for high dynamic application, not work in normal state. A main design for multiband navigation antennas is the aperture stacked microstrip patch antenna. But it is only fit for receive the signals with those center frequencies far away from each other, otherwise there is a crosstalk between the antennas on every substrate. The design of stacked microstrip patch antenna dose not extend the bandwidth of single patch on every substrate, there is no redundancy when the antennas work in a dramatic changed ambient temperature. In those applications the dielectric constant of the substrate will change, and it makes the work frequency bandwidth of the antenna change too. In this situation, the bandwidth of the microstrip patch antenna may not include the signal bandwidth without redundancy.

For the abovementioned disadvantages of common microstrip patch antennas, this paper presents a new designed microstrip patch antenna with a air reflection back cavity. The new designed microstrip patch antenna will be slightly larger than a common one, when they are printed on the same substrates. But it has much wider bandwidth for impedance and circular polarize radiation, and much higher radiation efficiency.

41.2 A New Designed Microstrip Patch Antenna with Air Back Cavity

41.2.1 Antenna's Structure and Work Principle

A microstrip patch antenna is a resonant-style radiator so one of its dimensions must be approximately $\lambda_g/2$, where λ_g is a guided wavelength taking into

consideration the surrounding environment of the printed antenna. It is apparent that the properties of the substrate, namely, its dielectric constant, ε_r and its height play a fundamental role in the performance of the printed antenna. For a detailed explanation of how a microstrip patch antenna conceptually operates in terms of equivalent slots, etc., please consult one of the many articles on this subject [2].

The microstrip patch antenna mounted on the low dielectric constant material is physically bigger than the antenna on the high dielectric constant laminate. It has a larger collecting area and therefore greater directivity. The directivity slightly increases as the thickness increases because of the increasing volume of the antenna. Please note that efficiency is not included. The higher the dielectric constant, the more power is lost to the surface wave and therefore the antenna is less efficiency. Please note there are no surface waves excited for the case when $\varepsilon_r = 1$. The thicker the material is, or the lower the dielectric constant, the greater the bandwidth [1].

So when a design of microstrip patch antenna requires a wideband, high radiation efficiency, and in a small size, the thickness of the antenna must be increased, simultaneously the equivalent permittivity of a high dielectric constant substrate must be reduced. A popular design today to change the equivalent permittivity of the microstrip patch antenna is the application of two stacked substrate with different dielectric constant. But because of the thickness norm up to the microwave materials facilities, the antenna engineers could not use two stacked substrate to get the ideal dielectric constant as they want for a microstrip patch antenna. And the thinner the material is, the greater the loss of radiation efficiency. The dielectric constant of air is 1, and the thickness of the air can be controlled with design of structure. When the air is stacked with a high dielectric constant, an ideal equivalent permittivity for a microstrip patch antenna could be achieved easily.

Because of the loss of electromagnetic signals is very low in the air, if only an air layer stacked back to the substrate, the rear and lateral radiation could be more. It is not conducive to anti-multipath reception, if the front to back ratio of the antenna is too small. Therefore the new designed microstrip patch antenna mentioned in this paper changes the air layer into an air cavity by the structure. This change can not only reduce the radiation to rear and lateral, but also reflect the rear radiation to front; thereby the radiation efficiency and the front gain of the antenna can be improved a lot.

By the abovementioned two steps, the thickness of the microstrip patch antenna will be increased without more electromagnetic loss in the stacked substrates, and the equivalent permittivity could be lowered. The directivity of the microstrip patch antenna can be greater, the radiation efficiency can be higher, and the bandwidth of impedance and circuit polarized radiation gain can be much wider.

41.2.2 Analysis by Electromagnet Simulation Software

The numerical methods for analysis of microwave were proposed in 1960s. Based on that, the first microwave EDA software HFSS (High Frequency Structure Simulator) from American company ANSOFT was born in 1980s. Nowadays the microwave EDA software is already becoming the most powerful and basic tools for the engineers in design of antennas, microwave circuits, and electromagnetic compatibility. As a three-dimensional electromagnetic simulation software, the HFSS analysis microwave engineering problems with finite element method (FEM). The HFSS has the unparalleled accuracy and reliability of the simulation, the fast simulation speed, the easy-to-use operator interface, and the stable, mature technology adaptive meshing. As a best choice of microwave design tools and standards, HFSS was widely used in aviation, aerospace, electronics, semiconductor, computer, communications and other fields, increases the design efficiency for many different microwave structures.

The author of this paper modeled a microstrip patch antenna with the above-mentioned air back cavity structure in HFSS, according to structural requirements of a real project. The high dielectric constant laminate is AD1000 from American Arlon with ε_r is 10.9; the thickness of the air back cavity is 3 mm. A common microstrip patch antenna was also modeled with the same laminate for contrast verification. In this project, a microstrip patch antenna with center frequency in 1,575 MHz, and works for the navigation frequencies GPS L1 (1,575 MHz), GLONASS L1 (1,602 MHz) and BD2 B1 (1,561 MHz) will be required. The material of the main structure of the antenna is aluminum, and the antenna cover will be made in PTFE.

According to the requirements in this project, the 3D model in HFSS of the new designed microstrip patch antenna with air back cavity will be shown in Fig. 41.1 (left). At the same time, the 3D model of the common microstrip patch antenna of the same dielectric constant laminate will be shown in Fig. 41.1 (right) also.

The two microstrip patch antennas are both designed in form rectangle; diagonal is cutaway for circular polarize radiation; single fed point is set to be match the impedance, and easy to obtain the property of the antenna. Among them, the substrate of the microstrip patch antenna with an air back cavity has a 60 mm side length, and the substrate of the common microstrip patch antenna has a 50 mm side length, 44 % shorter. The two antennas have the same size aperture.

By the software HFSS, a full wave simulation respectively computing is done for the two models. Figure 41.2 shows the −10 dB return loss bandwidth (impedance bandwidth) results of the two models.

The new designed microstrip patch antenna has a 132 MHz impedance bandwidth covering at least from 1,523 MHz to 1,655 MHz, and the common microstrip patch antenna on the high dielectric constant laminate has a 35 MHz impedance bandwidth. It is only 26.5 % to the new designed antenna.

Using the RealizedGainRHCP (realized gain is four pi times the ratio of an antenna's radiation intensity in a given direction to the total power incident upon

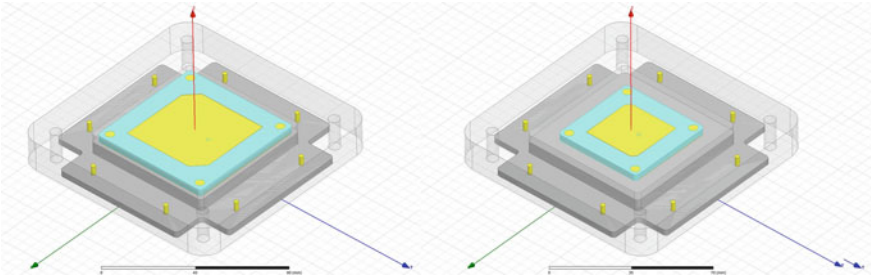

Fig. 41.1 3-D model in HFSS: new designed microstrip patch antenna with air back cavity (*left*) and the common microstrip patch antenna (*right*)

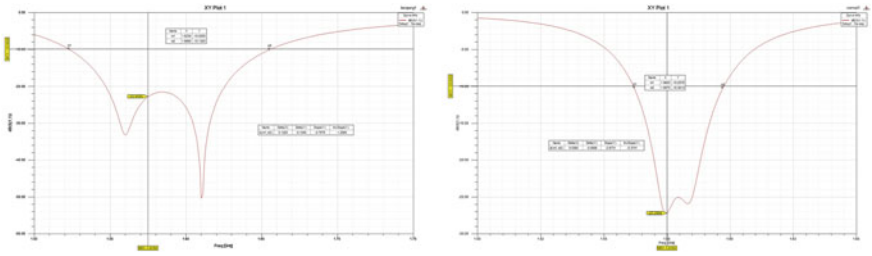

Fig. 41.2 Curve: return loss simulation results of the new designed microstrip patch antenna with air back cavity (*left*) and the common microstrip patch antenna (*right*)

the antenna port) in the result options, the 3 dB peak gain in front bandwidth can be obtained. And the results of Axial Ratio bandwidth of the two antennas, which is usually to be an indicator of the circular polarization judgment, can be also obtained.

Figure 41.3 shows the RealizedGainRHCP and Axial Ratio bandwidth simulation results of the two models.

By the results comparing from the Fig. 41.3, the 3 dB gain bandwidth of the common microstrip patch antenna is 33 % to the microstrip patch antenna with air back cavity, and the 6 dB circular polarization axial ratio is 26.7 %. The microstrip patch antenna with air back cavity has a very good circular polarization and higher gain in the whole work band. It can be used in the dramatic changing environmental temperature, and always covering the signal's frequency band.

The main reason of a higher gain of the new designed microstrip patch antenna is not upon the bigger substrate's size, but the reflection of rearward radiation, and the higher radiation efficiency. By the software HFSS, the antenna parameters at 1,575 MHz can be obtained. The radiation efficiency of the new designed microstrip patch antenna is 96.1 %, and the other one is 82.3 %; the front to back ratio of the new designed antenna is 34.5, and the other one is 17.4, as shown in Fig. 41.4. With the comparing between the two group parameters, the correctness of these reasons above can be confirmed.

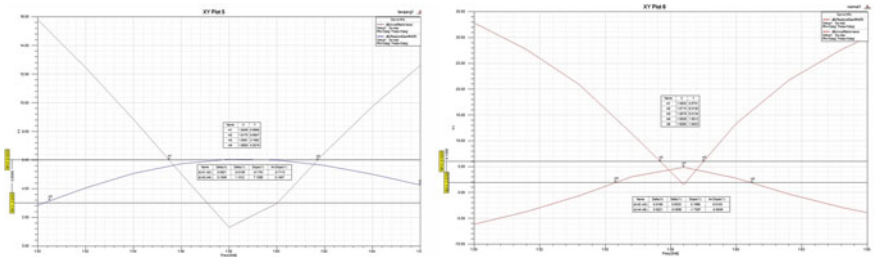

Fig. 41.3 Curve: the bandwidth of the RealizedGainRHCP and the axial ratio simulation results of the new designed microstrip patch antenna with air back cavity (*left*) and the common microstrip patch antenna (*right*)

Antenna Parameters:

Quantity	Value	Units
Max U	0.32297	W/sr
Peak Directivity	4.2438	
Peak Gain	4.0796	
Peak Realized Gain	4.0587	
Radiated Power	0.95638	W
Accepted Power	0.99487	W
Incident Power	1	W
Radiation Efficiency	0.96131	
Front to Back Ratio	34.504	
Decay Factor	0	

Antenna Parameters:

Quantity	Value	Units
Max U	0.24631	W/sr
Peak Directivity	3.7655	
Peak Gain	3.1007	
Peak Realized Gain	3.0953	
Radiated Power	0.82201	W
Accepted Power	0.99825	W
Incident Power	1	W
Radiation Efficiency	0.82345	
Front to Back Ratio	17.353	
Decay Factor	0	

Fig. 41.4 Data: the antenna parameters simulation results of the new designed microstrip patch antenna with air back cavity (*left*) and the common microstrip patch antenna (*right*)

To further prove that the air back cavity is truly reflects the rearward to front, the aperture side length of the antenna will be extended to 180 mm, and the air back cavity depth will not be changed. At this time, the peak gain of the new designed antenna is far higher than the common antenna, and the main lobe is narrower too. This can prove that the radiation directivity of the microstrip patch antenna with air back cavity is much greater than common microstrip patch antenna, because the air back cavity can reflect the rearward radiation forward.

The RHCP gain results of the two antennas are shown in the Fig. 41.5. The peak gain of the microstrip patch antenna is higher than common one almost 3 dB, and the main lobe width narrower almost 10°.

The compared results above proved that, the new designed microstrip patch antenna mentioned in this paper has a much better performance than the common, but with a bigger size. According to the actual structure of the project size requirements for the new microstrip patch antenna's back cavity depth adjustment for compromise design, also in engineering this design reflects the flexibility advantages.

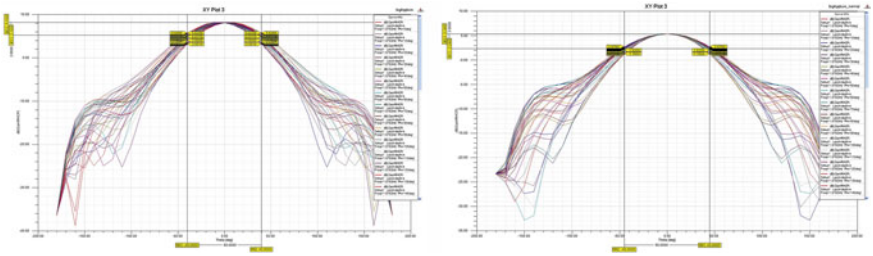

Fig. 41.5 Curve: gain directivity simulation results of the new designed microstrip patch antenna with air back cavity (*left*) and the common microstrip patch antenna (*right*)

41.2.3 Analysis of the Air Back Cavity Depth

By the software HFSS, the air back cavity depth of the microstrip patch antenna model will be changed without changing other parameters, from the simulation analysis found that: the center frequency of the antenna will work lower with the decreasing depth of the air back cavity, as the bandwidth is narrower. Of cause with the changing structure of the antenna without changing the fed position and notching size will cause the performance poor. But in this paper, the effect between the cavity depth and the antenna performance is the main research priorities. Therefore the changed antenna model will not be optimized.

Since this space limitations, not to list all the simulation results after every change of the air back cavity depth. Figure 41.6 shows the return loss simulation result when the air back cavity depth changed to 0.2 mm.

Figure 41.6 shows that, with the air back cavity depth decreasing the equivalent permittivity will be higher, and the center frequency of the same size antenna moves from 1,575 MHz to 1,326 MHz. The microstrip patch antenna size can be reduced to optimize the center frequency to 1,575 MHz again. If the air back cavity depth changes to 0 mm, the microstrip patch antenna is same as a common microstrip patch antenna. By the air back cavity depth decreasing, the new designed antenna's performance will approach the common microstrip patch antenna's, the bandwidth will be narrower, But the radiation efficiency is still much higher than the common microstrip patch antenna's with only 0.2 mm air back cavity depth.

Figure 41.7 shows the antenna parameters at frequency 1,326 MHz after the changing of the air back cavity depth. From the parameters found that, although the antenna is not optimized to the best performance at this frequency, the radiation efficiency is still higher than 90 %; because of the reduced reflection by the decreased air back cavity depth and the poor circular polarization, the front to back ratio is only 14.32.

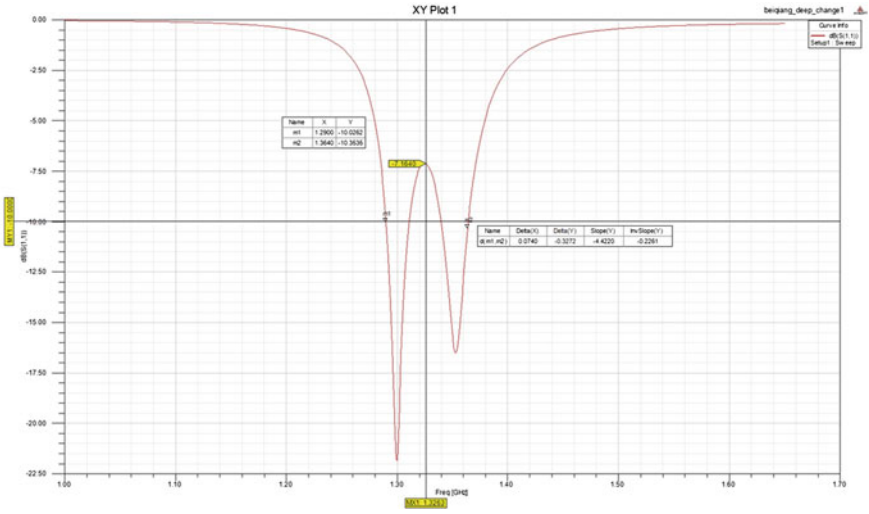

Fig. 41.6 Curve: return loss simulation result with a 0.2 mm air back cavity depth

Fig. 41.7 Data: the antenna parameters simulation result with a 0.2 mm air back cavity depth at 1,326 MHz

Antenna Parameters:

Quantity	Value	Units
Max U	0.22672	W/sr
Peak Directivity	3.8605	
Peak Gain	3.4897	
Peak Realized Gain	2.8492	
Radiated Power	0.73804	W
Accepted Power	0.81644	W
Incident Power	1	W
Radiation Efficiency	0.90397	
Front to Back Ratio	14.322	
Decay Factor	0	

41.3 Product Verification

A prototype of the new designed microstrip patch antenna with air back cavity as the model shown in Fig. 41.1 was produced firstly, the materials and the structure are all the same as the model. From the simulation found also that, the metal surface roughness of the air back cavity is not important for the model. Therefore for the precision requirement is not very high.

The impedance and radiation bandwidth in the test results of the new designed microstrip patch antenna prototype are almost same as the simulation results. A GNSS navigation receiver with the antenna prototype can get very good CNR

(carrier noise ratio), what can prove the design of the microstrip patch antenna with air back cavity is scientific and feasible.

41.4 Conclusion

In this paper, for the narrow bandwidth and low radiation efficiency of the common microstrip patch antenna, through a combination research of the stacked microstrip patch antenna to adjust the equivalent permittivity, and the antennas with reflect cavity to reflect the rearward radiation, a new designed microstrip patch antenna with air back cavity is proposed to extend the bandwidth and to improve the radiation efficiency. The microstrip patch antenna using this design has a bigger size than the common microstrip patch antenna, but the precision requirement is not high, the performance is much improved, the sizing is also very flexible. For the not very small size required application environments, it can widely replace the common microstrip patch antenna. When a ceramic substrate with very high dielectric constant could be used, the size of the new designed microstrip patch antenna with air back cavity can be much decreased for more miniaturization applications.

References

1. Godara LC (2004) Handbook of antennas in wireless communications. CRC Press, LLC, Boca Raton
2. Kuo J-S, Wong K-L (2000) A dual-frequency L-shaped patch antenna. Microw Opt Technol Lett 27:177–179
3. Xie Y, Liu Y, Li L, Ding H, Lei Z (2009) Principle and engineering applications. Science Press, Beijing

Chapter 42
A Method for Amplitude and Phase Calibration in a Spaceborne Multibeam Receiver

Zhigang Huang, Chunjie Qiao and Yueke Wang

Abstract This paper presents a method for amplitude and phase calibration in a spaceborne multibeam receiver, which is based on the satellite-ground link, to solve the inconsistent problem in amplitude and phase between different channels. In this method, the calibrating signal is firstly immitted by a ground control station, and then the discrepancy of amplitude and phase between different channels and the reference channel in the receiver are determined by signal processing. And self-calibration would finally be achieved by some inversion operations. Additionally, this paper adopted an advanced discrete fourier transform method to determine the parameters which is help to overcome the spectral leakage caused by the doppler frequency shift. Results denote that errors of amplitude and phase would heavily influence the beam pointing and beam shape for a spaceborne multibeam receiver which will lead to a distinct decline in performance. However, this problem is meliorated after our adapting the method in this paper to calibrate the amplitude and phase errors of the receiver.

Keywords Multibeam receiver · Digital beam forming · Calibration of amplitude and phase · Parameter estimation

42.1 Introduction

With the increasing capability of signal processing in electronic components and the mature development of antenna array technology and digital beam forming technology, multibeam receivers have got an extensive attention. Using multibeam

Z. Huang (✉) · C. Qiao · Y. Wang
College of Mechatronics Engineering and Automation of NUDT, ChangSha 410073, China
e-mail: h-zhigang@163.com

J. Sun et al. (eds.), *China Satellite Navigation Conference (CSNC) 2014 Proceedings: Volume I*, Lecture Notes in Electrical Engineering 303,
DOI: 10.1007/978-3-642-54737-9_42,

receivers on a satellite has many advantages. It is feasible to cover the ground area with a high gain or adjust the beam shape and point according to our aims, which is help to realize the spatial filtering and spatial orientation. And at the same time, it also has the ability to isolate the beam space and reuse multiple frequencies. However, all the advantages above for a multibeam receiver are determined by the consistency between different channels. Unfortunately, since the tolerance of manufacture and installation, the discrepance and drift in components' performance, the cosmic radiation and other factors, problem of channel inconsistency in the receiver will be inevitable after the orbiting for a long time. This will seriously affect the performance of the multibeam receiver.

Many scholars have taken much further researches on calibrating the amplitude-phase errors between different channels in a spaceborne multibeam receiver. Mano et al. first put forward the Rotating Electric field Vector method (REV) in 1982 to solve this problem. Although, it is widely used in satellite communication system for remote calibration, but it needs a lot of time to accomplish the calibration since the calibration factors are measured one by one [1, 2]. Silverstein proposed two methods, one called Uniform Transfer Encoding (UTE) method, and the other is named Control Circuit Encoding (CCE) method [3–5]. UTE method is, thereinto, considered more suitable for a multibeam receiver which is based on the digital beam forming technology. But it requires some additional hardwares and huge computation. Masayuki presented an orthogonal code method to calibrate the amplitude-phase errors in RF channel which is based on the satellite-ground loop [6]. Via digital parallel processing technology, this method can calibrate all of the channels at the same time which reduced the time of calibration greatly.

The methods based on satellite-ground loop are though vulnerable by the influence of the satellite-ground link. But on the premise of high Signal-to-Noise Ratio (SNR), this method can complete the calibration caused by both the antenna array and the RF front end. For a spaceborne multibeam receiver, however, we can but rely on the spaceborne system itself to calibrate the amplitude-phase errors in multiple channels. And limited by the hardware resources, volume and power, etc., method in Ref. [6] will not be practical due to the complexity computation. This paper proposed a more simple and valid method to achieve the calibration which is also based on the satellite-ground loop. But in our method, the ground control station was used to immit a single-frequency calibration signal with enough power to the spaceborne receiver. And if the incidence azimuth of the calibration signal is available to the receiver, the amplitude and phase parameters of the received signal in different channels would be determined by the receiver facilely through our method. Then the amplitude-phase calibration factors can be obtained by some matrix inverse operations, and the calibration can be accomplished finally. In addition, there do not need any additional hardware in our method. And the algorithm itself is stable and easy to be implemented.

42.2 Theory

42.2.1 System Model

The amplitude-phase errors in a multibeam receiver come mainly from the antenna array and the RF front end. The Intermediate Frequency (IF) signal, which is the output of the RF front end, is usually sampled directly by AD components. And the amplitude-phase errors caused by AD components would be negligible generally. There thus needs an external incentive to ensure the integrity of the calibration during the process of amplitude-phase error calibration. Figure 42.1 shows the system model in this paper where the GCS in Fig. 42.1a means the ground control station. When the satellite passes, a high power single-frequency calibration signal is immitted to the spaceborne receiver by the GCS. Due to the discrepancies in amplitude and phase caused by the antenna array and the RF front end in receiver, amplitude-phase errors would be introduced after the mixing process. In order to ensure the performance of the multibeam receiver, this paper designed an amplitude-phase calibration module between acquisition module and the beam-forming network to measure the amplitude-phase errors and calibrate them.

Figure 42.1b is the structure of calibration module, including calculation unit, verify unit and calibration unit. The first calculation unit is used to estimate the channel parameters and calculate the corresponding calibration coefficients. Verify unit is used to test the effectiveness of the calibration coefficients. Calibration unit is of curse used to accomplish the process of calibration.

42.2.2 Calibration Theory

Take the uniform circular array as an example, we suppose that the radius of the antenna array is r and the element number is $M + 1$ where the central array is chose to be the reference in phase calibration. If the receiver works with the DSS-BPSK signal and the pitching angle and azimuth angle for the signal is assumed as (ϕ, θ), then the DSS-BPSK signal can be expressed as

$$x(t) = A_0 \cdot d(t)m(t)\exp(\omega_0 t) \tag{42.1}$$

where, A_0 means the signal intensity. $d(t)$ denotes the symbol information. And $m(t)$ means the spread spectrum sequence.

If we ignore the influences of the doppler shift and the transmitting delay time, the received IF signal can be wrote as

$$y_i(t) = A_1^i d(t)m(t)\exp(j\omega_0 t)\exp\left(-j\phi_a^i\right)\exp\left(-j\phi_c^i\right), \quad i = 0, 1, \ldots M \tag{42.2}$$

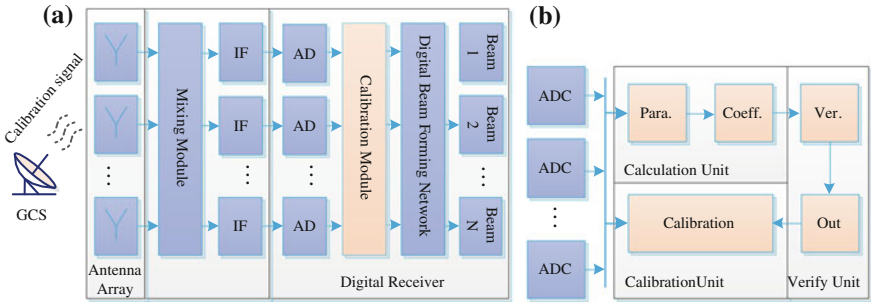

Fig. 42.1 System model and the structure of the calibration module: **a** for the system model and **b** for the structure of the calibration module. The GCS in figure (**a**) means the ground control station

where, A_1^i is the amplitude of the received signal. $\phi_a^i = \omega_0 r \cos(\theta_i - \theta)\sin\phi/c$ denotes the delay phase caused by the array manifold, while c is the speed of light and $\theta_i = 2\pi i/M$. ϕ_c^i is also the delay phase which caused by the amplitude-phase errors in antenna array and the RF front end.

Rewriting (42.2) as a matrix equation, there is

$$\mathbf{Y} = \mathbf{AXT} \tag{42.3}$$

where, $\mathbf{Y} = \mathrm{Diag}[y_i], \quad \mathbf{A} = \mathrm{Diag}[A_1^i],$

$\mathbf{X} = \mathrm{Diag}[d(t)m(t)\exp(j\omega_0 n)\exp(-j\theta_a^i)],$

$\mathbf{T} = \mathrm{Diag}[\exp(-j\phi_c^i)].$

The aim of the amplitude-phase calibration is to make the delay phase in different channels only correlative to the array manifold. As the signals in (42.3), that means $\mathbf{Y} = \mathbf{X}$. Thus, the calibration module must achieve the following transfer

$$\mathbf{Y} = \mathbf{A}^{-1}\mathbf{AXTT}^{-1} = \mathbf{IXI} = \mathbf{X} \tag{42.4}$$

But in practice, we just need to keep the amplitude and phase in different channels consistent. That means

$$\mathbf{Y} = \mathbf{A_1AXTT_1} = \mathbf{C_AXC_T} \tag{42.5}$$

where, matrix $\mathbf{A_1}$ and $\mathbf{T_1}$ are just the matrix of amplitude-phase calibration coefficients.

42.3 Method for Parameter Estimation

42.3.1 Amplitude-Phase Parameters Estimation

There are two kinds of methods to estimate the amplitude-phase parameters of signals in a receiver: DFT method and phase-locked loop method. The performance of the latter method is determined by its noise bandwidth, integral time and the filter parameters. When the input conditions are changed, it would make the loop losing lock undemandingly. However, the method for parameter estimation which based on the DFT technology is relatively simple and stable. Though, under the condition of low SNR, this method still has a good performance. So, we mainly use the DFT method to estimate the amplitude and phase parameters in this paper. However, because the influence of doppler shift, the traditional DFT method in parameter estimation will cause the problem of spectrum leakage which will lead the estimated parameters distortion. And we thus need to alter the traditional DFT method to eliminate the influence of spectrum leakage problem. Ref. [7] provided a useful method to solve it.

If the observed calibration signal in any channel is

$$s(n) = A \cdot \exp[j(2\pi f_0 Tn/N + \phi_0)], \quad n = 0, 1, \ldots N-1 \tag{42.6}$$

where, A, f_0 and ϕ_0 denote the amplitude, frequency and initial phase of the observed calibration signal respectively.

Divide the sampled sequence into two parts with the same length. Thus, there is

$$s_1(n) = A \cdot \exp[j(2\pi f_0 Tn/N + \phi_0)], \quad n = 0, 1, \ldots N/2-1 \tag{42.7}$$

$$s_2(n) = s_1(n) \cdot \exp j(2\pi f_0 T), \quad n = 0, 1, \ldots N/2-1 \tag{42.8}$$

After the operation of DFT with the length of N/2, their discrete spectrums and amplitudes and phases are shown as the following equations

$$S_1(k) = A_{1k}\exp(j\varphi_{1k}), \quad k = 0, 1, \ldots N/2-1 \tag{42.9}$$

$$S_2(k) = S_1(k)\exp(j\pi f_0 T), \quad k = 0, 1, \ldots N/2-1 \tag{42.10}$$

$$A_{1k} = \frac{A \cdot \sin[\pi(k - f_0 T/2)]}{2\sin[\pi(k - f_0 T/2)/N]} \tag{42.11}$$

$$\varphi_{1k} = \phi_0 + (1 - 2/N)(f_0 T/2 - k)\pi \tag{42.12}$$

Generally, the amplitude correction coefficients are some relative values. And otherwise, the doppler shift in an any receiving channel is nearly equal to each other. Thus, we can use the amplitude of the maximum spectrum to instead the real amplitude of this channel.

If the phases of $S_1(k)$ and $S_2(k)$ at the maximum spectrum point are expressed as φ_1 and φ_2 respectively, then their difference is

$$\Delta\phi = \varphi_2 - \varphi_1 = \pi f_0 T - 2m\pi \tag{42.13}$$

It is obvious than the range of f_0 belongs to $(m \pm 0.5) \cdot 2/T$. That means $\Delta\phi$ distribute in $[-\pi, \pi]$. Combining (42.12) and (42.13), we can obtain the phase parameter

$$\hat{\phi}_0 = \frac{3N-2}{2N}\varphi_1 - \frac{N-2}{2N}\varphi_2 \tag{42.14}$$

42.3.2 Calibration Coefficients Estimation

In order to make the receiver obtaining the maximum gain after calibration, we need to calibrate amplitude and phase with different reference channels. For amplitude calibration, we should choose the channel with biggest amplitude as the reference. And for phase calibration, we should choose the central channel as the reference.

If A_i, $(i = 0, 1, \ldots, M)$ is the estimated amplitude parameters using the advanced DFT method in this paper and $A_{\max}$ is the maximum one, it's easy to draw the amplitude coefficient matrix

$$\mathbf{A}_1 = \mathrm{diag}\left[\frac{A_{\max}}{A_i}\right], \quad i = 0, 1, \ldots, M \tag{42.15}$$

If $\varphi_i, (i = 0, 1, \ldots, M)$ is the estimated phase parameters obtained through (42.14), it contains three parts in practice: the delay phase caused by transmittion (ϕ_T), the delay phase caused by the array manifold expressed asϕ_i, $(i = 0, 1, \ldots, M)$ and the delay phase come from the inconsistency in different channels expressed as θ_i, $(i = 0, 1, \ldots, M)$. Relation between them is

$$\begin{cases} \varphi_0 = \phi_T + \phi_0 + \theta_0 \\ \varphi_1 = \phi_T + \phi_1 + \theta_1 \\ \vdots \\ \varphi_M = \phi_T + \phi_M + \theta_M \end{cases} \tag{42.16}$$

Normally, the location of the monitoring station is fixed on the ground, and the location of the satellite can be obtained through the orbit prediction. The incidence direction of the calibration signal can thus be determined through some certain geometric transforms. That means the unknown ϕ_i in (42.16) is available for the spaceborne receiver. And if we assume that the first channel is the reference one, there is $\phi_0 = 0$, the relative phase errors for all channels can be obtained through the following equation.

$$\begin{cases} \Delta\theta_1 = \theta_1 - \theta_0 - \phi_1 \\ \Delta\theta_2 = \theta_2 - \theta_0 - \phi_2 \\ \vdots \\ \Delta\theta_M = \theta_M - \theta_0 - \phi_M \end{cases} \tag{42.17}$$

So the phase calibration coefficient matrix is

$$\mathbf{T_1} = \mathrm{diag}[\exp(-j\Delta\theta_i)], \quad i = 0, 1 \ldots M \tag{42.18}$$

where, there is $\Delta\theta_0 = 0$.

42.4 Simulation

This paper has done some simulations to verify whether the proposed method is helpful to improve the performance of the multibeam receiver while there exist some amplitude-phase errors between different channels. In simulation, the antenna array of the multibeam receiver is a uniform circuit array with seven elements and seven beams. And the working carrier frequency of the antenna array is 1.5 GHz, and the radius is 0.545 λ. The calibration signal is a single-frequency signal at the carrier frequency. The range of the random amplitude errors between different channels is −3–3 dB, while their phases are shifting from −180° to 180°. And the length of DFT calculation is 8,192.

Figure 42.2 shows the standard deviations for amplitude and phase measurements which are derived from different SNR conditions (100 times measurement at each SNR). From which, we can see that the measurement precision of amplitude and phase are 0.2 dB and 1.5° while SNR = 0 dB. It is concluded that the method described in this paper can still provide a high precision of parameter estimation even though the SNR is much low. In addition, Fig. 42.3 also shows that with the increase of SNR, the detection accuracy of amplitude and phase parameters has improved significantly.

Figure 42.3 simulated the point change of the central beam before and after calibration. Comparing Fig. 42.3a and b, it can be seen that there are tremendous discrepancies between the ideal beam and the beam without calibration while there are some amplitude-phase errors in the received signals. This suggests that the amplitude-phase errors will seriously affect the performance of the spaceborne multibeam receiver. On the other hand, we can find that the beam after calibration is close to the ideal nearly by comparing Fig. 42.3a and c which proved that the proposed method is impactful.

Figure 42.4 is the profile curve of the central beam while the azimuth angle and pitching angle equal to 0° respectively. Both the two figures are zoomed in.

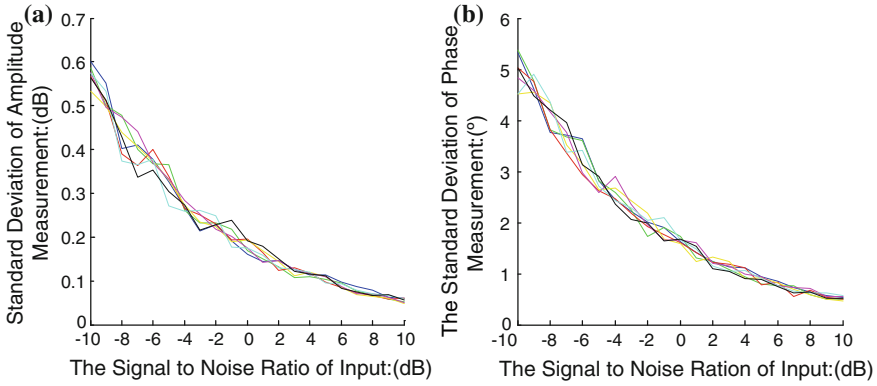

Fig. 42.2 The standard deviation of the parameter measurement results at different SNR: **a** for amplitude measurement results and **b** for phase measurement results

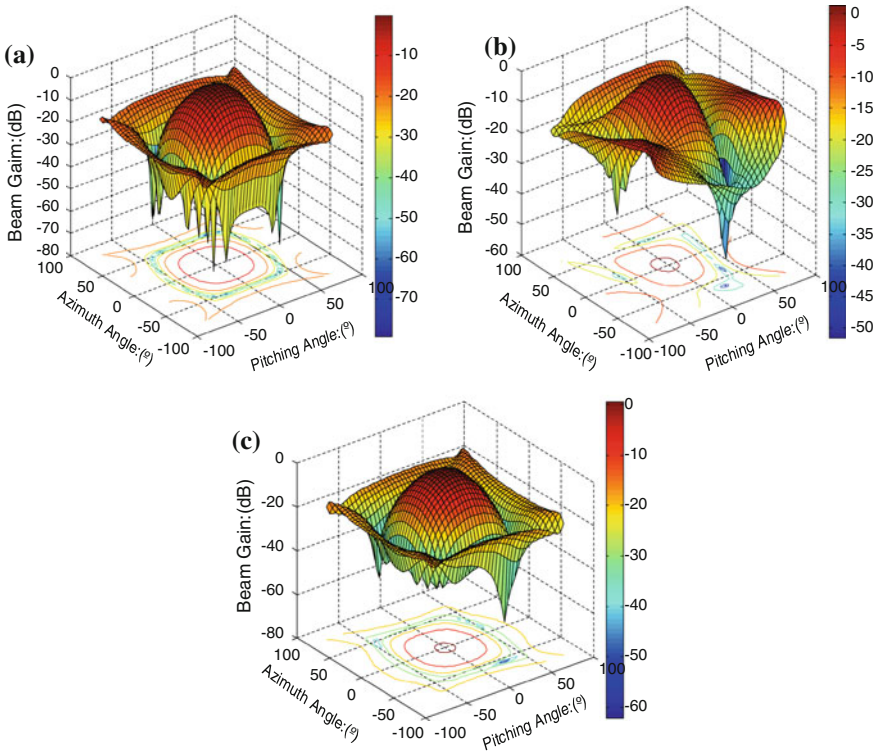

Fig. 42.3 The change of central beam before and after calibration: **a** for the ideal beam point, **b** for the beam point before calibration, **c** for the beam point after calibration

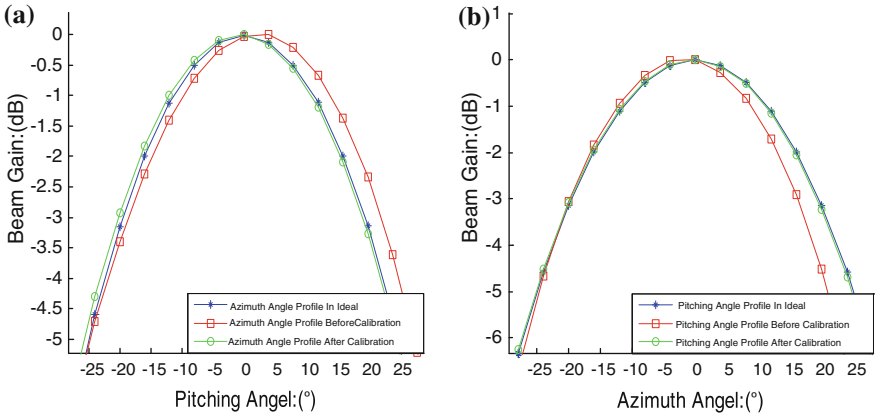

Fig. 42.4 The profile curve of central beam: **a** for azimuth profile curve at $\theta = 0°$, **b** for pitching profile curve at $\phi = 0°$. Where, θ and ϕ denote the azimuth angle and pitching angle respectively

Comparing Fig. 42.4a and b, it can be found that the point of the central beam, before calibration, shifts from (0°, 0°) to (0°, 4°). But it is modified after the process of calibration.

42.5 Conclusion

This paper proposed a simple and effective method for the calibration of amplitude-phase errors in a spaceborne multibeam receiver which is based on the satellite-ground link. In this method, a high power calibration signal with single frequency is imitted by the ground control station. And the receiver uses the advanced DFT technology to estimate the channel amplitude-phase parameters and the calibration coefficient matrix. Then the calibration coefficient matrix is used to compensate the channel amplitude-phase errors after the sampling module. The simulations proved the feasibility of our scheme. And results show that the method in this paper can effectively compensate the amplitude-phase inconsistency between the receiver antenna array and the RF front end. And under the condition of low SNR, our method still has a good calibration performance.

References

1. Mano S et al (1982) A method for measuring amplitude and phase of each radiating element of a phased array antenna. IEEE 555–560
2. Zhao H (2009) Research on satellite digital multi-beam phased array antenna key technique. Nanjing University of Science and Technology, China

3. Silverstein SD (1997) Application of orthogonal codes to the calibration of active phased array antennas for communication satellites. IEEE Trans Signal Process 206–218
4. Silverstein SD (1997) Remote calibration of active phased array antennas for communication satellites. In: IEEE international conference on acoustics, speech and signal processing, pp 4057–4060
5. Silverstein SD (1997) Algorithms for remote calibration of active phased array antennas for communication satellites. IEEE 1181–1186
6. Masayuki O et al (2001) A remote calibration for transmitting array antenna by using synchronous orthogonal codes. IEEE Trans Comm 689–693
7. Qi G (2010) Detection and estimation: principles and application. Publication House of Electronics Industry, China

Chapter 43
Dynamic Calculation Method of Satellite Elevation Mask with Rocket Onboard GPS Real-Time Positioning

Aishui Rao, Yonggang Li, Jian Hu, Junlei Bao and Zhenping Wang

Abstract According to the setting problem of satellite elevation mask of rocket onboard GPS real-time positioning, the influence of defilade angle on carrier rocked positioning precision is analyzed, and furthermore, the dynamics calculate method of satellite elevation mask based on the observable lowest elevation is put forward. Tested using the actual task data, the result shows that this method can utilize the most satellites to take part in rocket positioning, also, the position precision and the speed precision are all meet the demand. This method is especially propitious to the carrier rocket positioning calculate in the telemetry arc segment of Marine Tracking.

Keywords Lowest elevation · Positioning precision · Carrier rocket · GPS real-time positioning · Satellite elevation mask

43.1 Foreword

There are many papers discussing the satellite elevation mask of receiver installed on the Earth surface, but it is lack of paper which discussing the satellite elevation mask of receiver installed on the rocket, it's height is changing with time. Paper [1] studies the usability of the GPS horoscope with different defilade angle, pointing out that more satellites can be seen under lower defilade angle, and the horoscope usability will get an improvement, but that will lead to more atmosphere delay and many path effects; Paper [2] gives the calculation method of satellite elevation, points out that the modern GPS receivers all have a minimum elevation request(call

A. Rao · Y. Li · J. Hu (✉) · J. Bao · Z. Wang
Satellite Marine Tracking and Control Department of China, Jiangyin 214431, China
e-mail: mayfan11@163.com

A. Rao
e-mail: ras@ustc.edu

J. Sun et al. (eds.), *China Satellite Navigation Conference (CSNC) 2014 Proceedings: Volume I*, Lecture Notes in Electrical Engineering 303,
DOI: 10.1007/978-3-642-54737-9_43,

a satellite elevation mask) to the satellites of the participation positioning, and generally the value is 5°–10°; Paper [3] studies the influence of low elevation angle satellite to positioning precision, acquires the conclusion that the better troposphere delay and vertical precision with 5° defilade angle. GNSS tracking telemetry and command system have already been extensively applied to track and measure task of carrier rocket shoot and satellite shoot [4]. The carrier rocket loading GNSS receiver can real time calculate the trajectory of rocket. Its calculation result calls rocket onboard positioning result. In order to raise measuring precision, the special GNSS trajectory calculation software is developed. It real time receives the navigation message sending by the satellite navigation equipments which installed on the ship, then, combines with the pseudorange data which is transmitted from the rocket telemetering data to realizes the real-time positioning. This calculation result calls self locating result [5]. According to the setting problem of satellite elevation mask of rocket onboard GPS real-time positioning, the dynamics calculate method of satellite elevation mask is put forward, tested using the actual task data through GNSS trajectory calculation software.

43.2 The Influence of Satellite Elevation Mask to Positioning Precision

43.2.1 The Method of Positioning Precision Calculate of GPS Trajectory

GNSS trajectory calculation software adopts pseudorange point positioning of least square method. According to positioning principle, the positioning equation is as following:

$$V = AX - L \tag{43.1}$$

Among them, V is a measure noise vector, matrix A is a direction cosine matrix, X is a position and clock correction vector, L is an observed vector. According to the precision estimate formula relevant of the least square method, the precision of positioning the result is estimated as following [6]:

1. Root-mean-square error of pseudorange observed value

$$\sigma_0 = \pm\sqrt{\frac{V^T V}{n-4}} = \pm\sqrt{\frac{[vv]}{n-4}} \tag{43.2}$$

Among them, $[vv]$ is the square of residual error V, n is the observed satellite numbers.

2. The power inverse matrix Q_{xx} of unknown X

$$Q_{xx} = (A^T A)^{-1} = \begin{bmatrix} Q_{11} & Q_{12} & Q_{13} & Q_{14} \\ Q_{21} & Q_{22} & Q_{23} & Q_{24} \\ Q_{31} & Q_{32} & Q_{33} & Q_{34} \\ Q_{41} & Q_{42} & Q_{43} & Q_{44} \end{bmatrix} \tag{43.3}$$

Getting a positioning precision estimate formula:

$$\sigma_P = \pm\sigma_0 \sqrt{(Q_{11} + Q_{22} + Q_{33})} \tag{43.4}$$

According to formula 43.4, position precision can be obtained while calculating rocket's position. The calculation method of speed precision is similar to this [7].

43.2.2 An Example of Positioning Precision Calculate

We set the satellite elevation mask value of GNSS trajectory calculation software as below: Playback a certain rocket shoot task data to analyze and evaluate the positioning precision of the self locating result, statistics the minimum value of positioning precision, as well as the biggest value, average value, standard deviation and the numbers of satellite participation positioning. As Tables 43.1 and 43.2 show.

Some results can be obtained from Tables 43.1 and 43.2:

1. The higher the satellite elevation mask, the higher the positioning precision and the fewer the numbers of satellite participation positioning.
2. All positions precision obtains the guide line request(less than 10 m) that the rocket real time positioning. In addition to the defilade angle −90°, the rest speed precision obtains the guide line request (less than 0.1 m/s).
3. The standard variance of position precision exists a saltus with the satellite elevation mask's changing, from 1 to 3 m; The standard variance of speed precision also exists a saltus, from 0.01 to 0.2 m/s. It indicates that there is one critical point within satellite elevation mask between −10° and 15°.

43.2.3 The Reason of Positioning Precision Saltus

Figure 43.1 has drawn the satellite position precision at any time variety curve diagram, selected the calculation results when satellite elevation mask are −10°, −15°, and −90° apart. As a result from the diagram, when satellite elevation mask is −10°, the curve is smooth; when satellite elevation mask is −15°, there is a saltus at the curve where time is 1,388 s; when satellite elevation mask is −90°, there are two saltuses at the curve where time is 1,388 and 1,529 s; Around the time 1,388

Table 43.1 Statistics analytical data of position precision using GPS trajectory

Satellite defilade angle (°)	Average value	Minimum value	Biggest value	Standard deviation
15	2.38	0.07	8.90	1.64
10	2.51	0.15	8.90	1.55
5	2.57	0.15	6.01	1.08
0	2.55	0.27	4.99	0.89
−5	3.46	0.27	7.14	1.52
−10	4.13	0.80	7.14	1.26
−15	4.91	0.80	38.30	3.33
−90	5.33	0.80	47.64	4.30

Table 43.2 Statistics analytical data of velocity precision using GPS trajectory

Satellite elevation mask (°)	Average value	Minimum value	Biggest value	Standard deviation	Satellite numbers
15	0.028	0.001	0.123	0.017	6.780
10	0.026	0.001	0.119	0.017	7.431
5	0.023	0.002	0.119	0.017	8.130
0	0.023	0.002	0.119	0.016	8.485
−5	0.023	0.004	0.110	0.015	8.968
−10	0.022	0.003	0.105	0.015	9.306
−15	0.086	0.003	2.190	0.277	9.737
−90	0.140	0.003	4.081	0.448	9.795

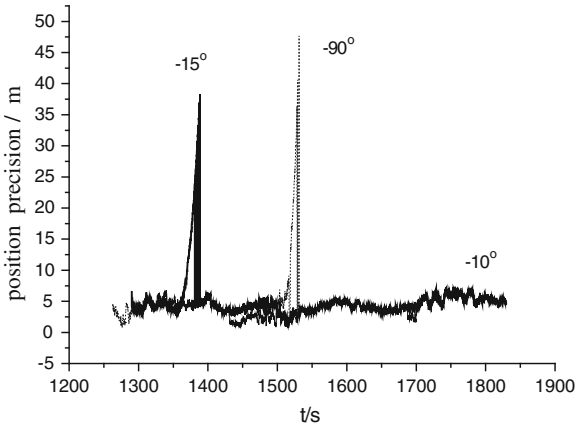

Fig. 43.1 Curve: position precision under the influence of satellite elevation mask

and 1,529 s, the satellite positioning precision dissatisfied carrier rocket positioning precision requests. Inside the task arc segment, the elevation of GPS satellite shows in Fig. 43.2, the elevation of satellite No. 5 is −14.3° at the time 1,388 s, the elevation of satellite No. 4 is −16.1° at the time 1,529 s. Therefore low elevation satellite participation positioning calculation is the reason that makes the positioning precision descended.

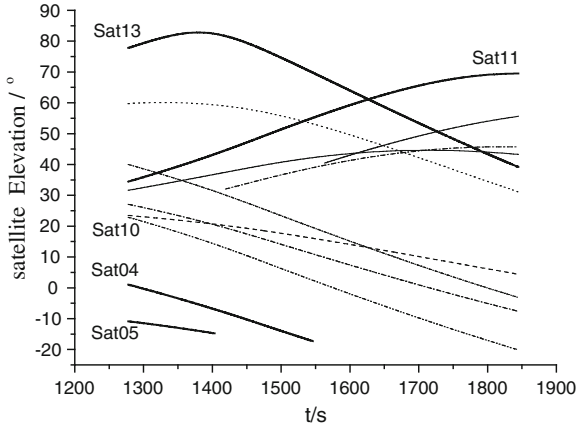

Fig. 43.2 Curve: satellite elevation

43.3 Dynamic Calculate Method with Satellite Elevation Mask

43.3.1 The Lowest Elevation of Observable Satellite

The radius of earth is a_e, the distance between carrier rocket and the origin of coordinates WGS84 is R, the lowest elevation of observation satellite is α. When the connecting line between satellite and rocket onboard receiver is a tangent line with the Earth, the satellite is the lowest elevation satellite for the rocket onboard receiver observated, one formula can be find $\cos = a_e/R$. Considering GPS satellite is under the rocket onboard receiver, we can get the formula as following:

$$\alpha = -\cos^{-1}\left(\frac{a_e}{R}\right) \tag{43.5}$$

The Earth is an irregular ellipsiod, according to the related parameter of ellipsiods WGS-84, the semi-major axis of the Earth is 6,378,137 m, the semi-minor axis of the Earth is 6,356,752 m. The a_e value in the formula should be real time calculated according to the concrete position of rocket. In the formula 43.5, the R equals the sum of radius of earth a_e and rocket flight height H, therefore giving rocket flight height, the lowest elevation of observable satellite can be calculated, parts of datas such as Table 43.3 show.

Figure 43.3 is the curve diagram of satellite elevation and lowest elevation of observable satellite, the lowest elevation at 1,388 s is −14.5° (at the time the elevation of No. 5 satellite is −14.3°), the lowest elevation at 1,539 s is −17.4° (at the time the elevation of No. 4 satellite is −16.8°).

Table 43.3 Lowest elevation of observable satellite change with rocket flight height

Rocket height (km)	0	5	10	50	100	200	300	500	1000
Lowest elevation (°)	0	−2.3	−3.2	−7.2	−10.1	−14.2	−17.2	−22.0	−30.2

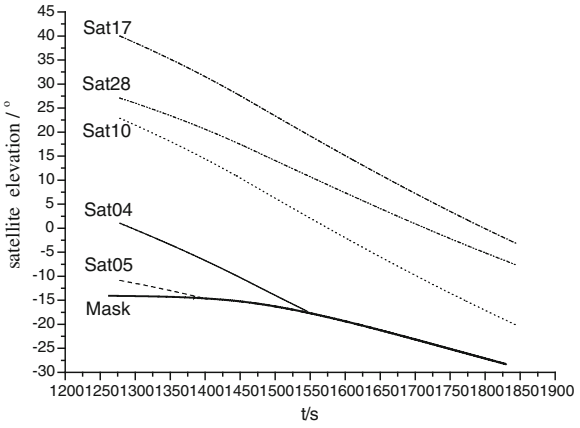

Fig. 43.3 Curve: satellite elevation and lowest elevation observable

43.3.2 Dynamic Calculate Method with Defilade Angle

The GPS receiver usually uses static setting method to set satellite elevation mask, its value is from 5° to 10°. But for the rocket onboard receiver, the method of static setting will causes a few problems:

1. The higher the rocket flight height, the lower the lowest elevation of observable satellite, the more the satellites whose elevation is less than 0°. If the defilade angle is setted from 5° to 10°, some satellites would be shielded. As showed by Table 43.3, when the height of rocket is 1,000 km, the lowest elevation is −30.2°.
2. There are some satellites contiguous to earth's surface, they can influence positioning precision, but can't be got rid of through artificial setting a static satellite elevation mask. For example, if satellite elevation mask is set by −15°, the positioning precision at 1,388 s is dissatisfied with the guide line request.
3. For high-speed carrier rocket, especially when it is under the tumbling abnormal condition, the GPS satellite under the rocket is so important to the positioning calculation that it can't be simply excluded.

Dynamic calculation method with satellite elevation mask is a kind of method which dynamically calculates satellite elevation mask according to the rocket flight height and real time sets its value. The satellite whose elevation is lower than the satellite elevation mask doesn't participate in positioning calculation. This method can let the most satellites participate in positioning calculation, and guarantee positioning precision. Because the reduced positioning precision is

Table 43.4 Data of position precision using dynamic setting satellite elevation mask

The value of *He* (km)	Average value	Minimum value	Biggest value	Standard deviation
0	5.01	1.44	30.10	2.70
5	4.72	1.44	21.42	1.67
10	4.54	1.44	14.08	1.10
15	4.50	1.30	8.52	1.01
20	4.48	0.80	7.43	1.01
25	4.47	0.80	7.43	1.02
50	4.44	0.80	7.43	1.10

mainly caused by the satellite which is contiguous to the earth's surface, this kind of satellite should be obviated. According to formula 43.5, it can be got a formula of calculation satellite elevation mask:

$$\alpha_{mask} = -\cos^{-1}\left(\frac{a_e + H_e}{R}\right)(R > = a_e + H_e) \tag{43.6}$$

Among them, *He* is the lowest rocket flight height that requested while adopting dynamic calculation method with satellite elevation mask.

43.3.3 The Positioning Result of Dynamic Setting Defilade Angle

In the arc segment of Marine Tracking, rocket flight height is over 100 km, therefore it can use formula 43.6 to dynamically calculate satellite elevation mask. The data of position precision and velocity precision in the task arc segment is shown in Tables 43.4 and 43.5, using dynamic setting satellite elevation mask. The semi-major axis of the Earth is 6,378,137 m, and the value of lowest rocket flight height is from 0 to 50 km. Some results can be known from Tables 43.4 and 43.5:

1. The higher the value of lowest rocket height *He*, the higher the positioning precision. When *He* is more than 15 km, the maximum position precision satisfies the task request (10 m), the maximum velocity precision also satisfies the task request (1 m/s).
2. Velocity precision changes quickly with *He* value. It changes from 0.35 to 0.015 m/s while *He* changes from 0 to 50 km. The value reduces lower than 20 times. Thus, when *He* equals to 50 km, its positioning precision can satisfy with carrier rocket task request, this height value exactly is the maximum height of the troposphere.

When the *He* value in formula 43.6 equals to 0 and 50 km, the curves of position precision at any time variety is shown in Fig. 43.4. In the diagram, while *He* equals to 50 km, the curve of position precision is smoother, the precision satisfies task request.

Table 43.5 Data of velocity precision using dynamic setting satellite elevation mask

The value of *He* (km)	Average value	Minimum value	Biggest value	Standard deviation	Satellite numbers
0	0.109	0.004	3.070	0.350	9.898
5	0.076	0.004	2.391	0.241	9.879
10	0.051	0.004	1.795	0.142	9.859
15	0.038	0.004	1.057	0.087	9.843
20	0.028	0.004	0.574	0.042	9.824
25	0.024	0.004	0.248	0.021	9.804
50	0.023	0.004	0.105	0.015	9.721

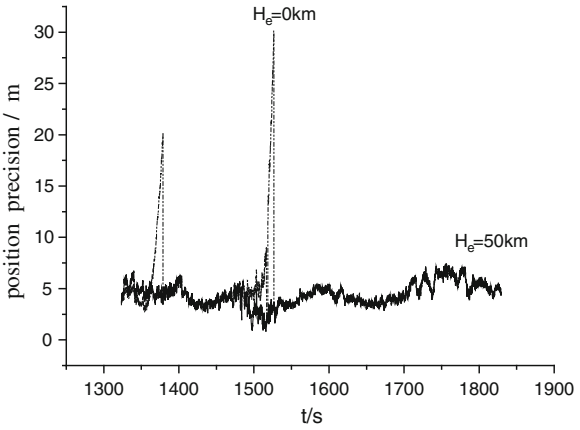

Fig. 43.4 Curve: position precision using satellite elevation mask with dynamics

43.4 Conclusion

Based on the calculation method of observable satellite's lowest elevation, the paper puts forward a dynamic calculate method of satellite elevation mask according to the rocket flight height. The method is validated using a certain task data. As a result of the calculation, it can make as more as possible satellites participate in positioning while is insure of positioning precision. When receiver is apart from ground over 50 km, the method can acquire satisfied precision, especially be suitable for positioning of the flying carrier rocket.

References

1. Kaplan ED (2001) Understanding GPS principles and applications. Publishing House of Electronics Industry, Beijing, pp 184–204
2. Yu L (2009) GPS global positioning receiver—principle and software implement. Publishing House of Electronics Industry, Beijing, pp 133–135(Ch)

3. Chao R et al (2011) Effects of low GPS satellite elevation mask angle on estimation of tropospheric delay. J Geodesy Geodyn 31(6):125–127(Ch)
4. Shuqiang Z, Aihua X (2005) The application of global positioning system in exterior ballistic measurement. GNSS World Chin 4:12–17(Ch)
5. Aishui R et al (2013) The analysis of scissors error between the GPS onboard positioning result and ship-borne locating result. J Telemetry Tracking Commad 34(2):41–45(Ch)
6. Shuqiang Z et al (2006) The precision estimate for real-time trajectory determination using on-board GPS. GNSS World Chin 31(2):19–22(Ch)
7. Shuqiang Z et al (2012) Rocket trajectory determination and precision analysis using on-board GLONASS data processing. J Astrodyn 2(2):27–32(Ch)

Chapter 44
Multipath Insensitive Delay Lock Loop in GNSS Receivers

Rong Si, Baowang Lian and Cha Li

Abstract The multipath effect introduces quite big errors to the traditional DLL-based code measurement. This paper presents a multipath insensitive delay lock loop (MIDLL). Then the paper analyzes the correlation model under multipath signal and introduces the discrimination function of MIDLL detailedly. Simulation results and analysis show that MIDLL improves the tracking error due to multi-paths dramatically, and tracking error is limited to 1 m on pseudorange in typical multipath environments. This loop predominantly applies to strong GNSS signals, because it is more sensitive than the typical delay lock loop to thermal noise.

Keywords GNSS · Multipath mitigation · MIDLL

44.1 Introduction

Multipath seriously affects the code phase and pseudorange measurement accuracy of the receiver, the pseudorange error caused by that can be up to a few meters. So, many researchers have been working on multipath mitigation, and lots of results have been promising. In general, the existing multipath mitigation techniques can be divided into three categories. The first is based on the discriminator design, Narrow Correlator [1] and Stroboscopic Correlator [2] is a typical representative of this design, which by reducing the multipath signal output of the discriminator, thus reducing the code phase tracking error and pseudorange error. The second is based on the design of multipath estimation, MEDLL [3] (Multipath Estimation Delay Lock Loop) combines the signal estimation and the tracking loop together, thus effectively reducing the multipath error. The third is based on the design of the receiver

R. Si (✉) · B. Lian · C. Li
Academy of Electronics Information, Northwestern Polytechnical University, Xi'an 710072, China
e-mail: woshisirong@126.com

J. Sun et al. (eds.), *China Satellite Navigation Conference (CSNC) 2014 Proceedings: Volume I*, Lecture Notes in Electrical Engineering 303,
DOI: 10.1007/978-3-642-54737-9_44,

front-end, it uses some antenna technology that can suppress multipath, such as the use of chock ring and ground plane, to suppress multipath signal reflected from the antenna reception on the ground. Compared with the standard delay lock loop, in the case of medium and long multipaths, these techniques dose improve code tracking accuracy. But they are not effective for short delay multipaths.

The new technique is based on the fact that there is an invariant point in the standard discriminator output when the latter is specifically normalized, the paper proposes a new discriminator that can mitigate multipaths whatever their delays. Then the paper analyzes the code phase tracking error in detail, and addresses the issues of the proposed discriminator. Finally, the paper describes the limitation of the proposed technique and gives simulation results.

44.2 Multipath Effect on Measurement

The receiver tracks the signal through the tracking loop, to get the code phase measurements. In the presence of multipath signals, these observations may be affected by multipath signals, in which may induce significant errors. Therefore, by analyzing the impact of tracking loop can describe measurement error and characteristic caused by multipath.

The received signal consists of the sum of the direct signal and the many reflected multipath signals, can be expressed as

$$s(t) = \sum_{k=0}^{N} A_k d(t) c(t - \tau_k) \cos(\omega_0 t + \varphi_k(t)) \tag{44.1}$$

where, k = 0 indicates that the signal is a direct satellite signal, others are for N multipath signals, A_0, A_k respectively represent the amplitude of the direct signal and the multipath signal, d(t) represents the navigation data signal, $c(t - \tau_k)$ represents different delays of the C/A code, ω_0 represents the frequency of satellite intermediate frequency signal, $\varphi_k(t)$ represents the phase of the kth signal. s(t), respectively, correlates with the early code $S_E(t) = c(t - \hat{\tau}_0 - \Delta/2)$ and late code $S_L(t) = c(t - \hat{\tau}_0 + \Delta/2)$, then

$$R_E(\varepsilon) = \sum_{k=0}^{N} A_k R(\varepsilon - \Delta\tau_k - \Delta/2) \cos(\varphi_k - \hat{\varphi}_0) \tag{44.2}$$

$$R_L(\varepsilon) = \sum_{k=0}^{N} A_k R(\varepsilon - \Delta\tau_k + \Delta/2) \cos(\varphi_k - \hat{\varphi}_0) \tag{44.3}$$

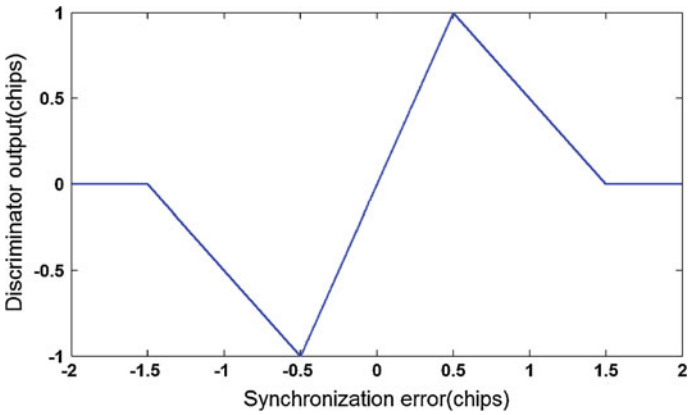

Fig. 44.1 Early minus late discriminator output for free multipath

where, Δ is the correlator spacing, R(t) is the correlation function of c(t). $\hat{\tau}_0$, $\hat{\varphi}_0$, they respectively represent the estimates of the direct signal code phase delay and carrier phase delay, $\Delta\tau_k = \tau_k - \tau_0$, defines the tracking lock error as $\varepsilon = \hat{\tau}_0 - \tau_0$, then the subtraction of the two equations is the discrimination function.

$$D(\varepsilon) = R_E(\varepsilon) - R_L(\varepsilon) \tag{44.4}$$

As shown in Fig. 44.1, in case of no multipath on the received signal, the discriminator outputs zero corresponding lock error $\varepsilon = 0$. DLL locks the signal through tracking the zero point of the discriminator. In the effect of multipath signal, the zero point shifts a little, therefore conducts the multipath error, as shown in Fig. 44.2. It describes the effect of receiver DLL discriminator output caused by different multipath signal. Table 44.1 gives the parameters of the multipath signals, including the short multipath (MP1 in phase, MP2 out-of-phase), the medium multipath (MP3, MP4), and the long multipath (MP5, MP6).

44.2.1 Multipath Insensitive Code Loop

Figure 44.2 shows there is an invariant point in the discriminator output whatever the multipath. The point corresponds the code synchronization input error $(-1 - \Delta/2)$ chips (i.e., $\varepsilon = -1 - \Delta/2$, $D_{E-L} = 0$). Assumed that the received signal is the sum of the direct signal and one multipath ray, then the values of the in-phase early (I_E),

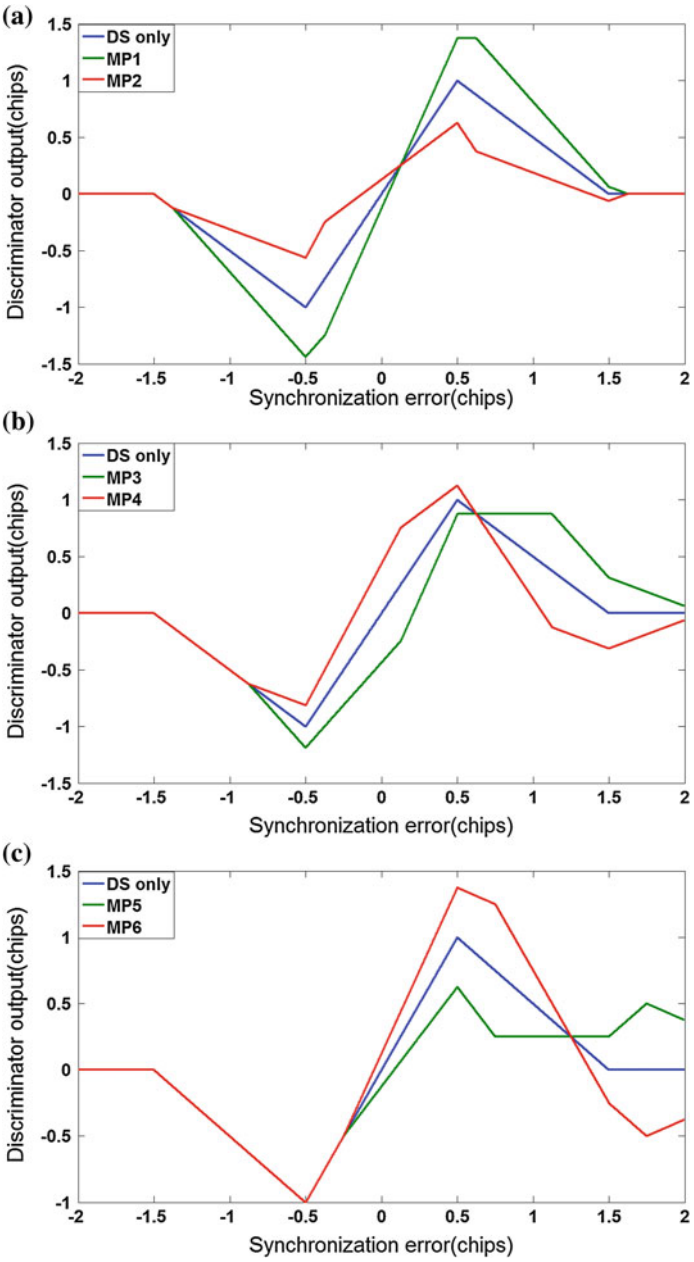

Fig. 44.2 Early minus late discriminator output for free multipath for different multipaths of Table 44.1. **a** Early minus late discriminator output for free multipath and MP1 and MP2. **b** Early minus late discriminator output for free multipath and MP3 and MP4. **c** Early minus late discriminator output for free multipath and MP5 and MP6

Table 44.1 Signal define *DS* direct signal, *MP* multipath signal

	Relative magnitude	Delay (chips)	Carrier phase
DS	1	0	0
MP1	0.5	0.125	0
MP2	0.5	0.125	π
MP3	0.5	0.625	0
MP4	0.5	0.625	π
MP5	0.5	1.125	0
MP6	0.5	1.125	π

the in-phase late (I_L), and the quadrature phase early (Q_E), the quadrature phase late correlation (Q_L) are given as follows, respectively,

$$I_E = A_0 \cos\left(\theta_0 - \hat{\theta}\right) R\left(\varepsilon - \frac{\Delta}{2}\right) \frac{\sin(\pi \Delta f_0 T)}{\pi \Delta f_0 T} + \sum_{1 \le k \le N} A_k \cos\left(\theta_k - \hat{\theta}\right) R\left(\varepsilon - \tau_k - \frac{\Delta}{2}\right) \frac{\sin(\pi \Delta f_k T)}{\pi \Delta f_k T} \tag{44.5}$$

$$Q_E = A_0 \sin\left(\theta_0 - \hat{\theta}\right) R\left(\varepsilon - \frac{\Delta}{2}\right) \frac{\sin(\pi \Delta f_0 T)}{\pi \Delta f_0 T} + \sum_{1 \le k \le N} A_k \sin\left(\theta_k - \hat{\theta}\right) R\left(\varepsilon - \tau_k - \frac{\Delta}{2}\right) \frac{\sin(\pi \Delta f_k T)}{\pi \Delta f_k T} \tag{44.6}$$

$$I_L = A_0 \cos\left(\theta_0 - \hat{\theta}\right) R\left(\varepsilon + \frac{\Delta}{2}\right) \frac{\sin(\pi \Delta f_0 T)}{\pi \Delta f_0 T} + \sum_{1 \le k \le N} A_k \cos\left(\theta_k - \hat{\theta}\right) R\left(\varepsilon - \tau_k + \frac{\Delta}{2}\right) \frac{\sin(\pi \Delta f_k T)}{\pi \Delta f_k T} \tag{44.7}$$

$$Q_L = A_0 \sin\left(\theta_0 - \hat{\theta}\right) R\left(\varepsilon + \frac{\Delta}{2}\right) \frac{\sin(\pi \Delta f_0 T)}{\pi \Delta f_0 T} + \sum_{1 \le k \le N} A_k \sin\left(\theta_k - \hat{\theta}\right) R\left(\varepsilon - \tau_k + \frac{\Delta}{2}\right) \frac{\sin(\pi \Delta f_k T)}{\pi \Delta f_k T} \tag{44.8}$$

where, A_0, A_k represents the amplitude of the direct signal and the kth multipath signal, τ represents the prompt code phase, τ_0 represents the direct signal transmission delay, τ_k represents the transmission delay of the kth multipath signal, θ_0, θ_k respectively refers to the carrier phase of the direct signal and the kth multipath signal, θ represents the phase of the local carrier, T refers to the predetection intergration time of the DLL, Δf_0 represents the frequency error of the direct signal, Δf_k refers to the frequency error of the kth multipath signal, $\varepsilon = \tau - \tau 0$

represents the synchronization error, Δ means the correlator spacing, R is the normalized autocorrelation function of the C/A code, expressed as follows,

$$R(\tau) = \overline{C(t)C(t+\tau)} \approx \begin{cases} 1 - |\tau| & |\tau| \le 1 \\ 0 & \text{otherwise} \end{cases} \tag{44.9}$$

The noncoherent early minus late envelope code loop discriminator is given by

$$D_{E-L} = \sqrt{I_E^2 + Q_E^2} - \sqrt{I_L^2 + Q_L^2} \tag{44.10}$$

Below, we derive the formula given by the discriminator output at the invariant point $\varepsilon = -1 - \Delta$ chips. Assume $\Delta < 1$ chip and ε as the following formula

$$-1 - \frac{\Delta}{2} \le \varepsilon < -1 - \frac{\Delta}{2} + \min\left(\frac{\Delta}{2}, \tau_1\right) \tag{44.11}$$

where, τ_1 represents the relative delay of the shortest multipath.

Then, we can get

$$-1 - \Delta \le \varepsilon - \frac{\Delta}{2} < -1 - \Delta + \min\left(\frac{\Delta}{2}, \tau_1\right) \tag{44.12}$$

Because $\min\left(\frac{\Delta}{2}, \tau_1\right) \le \frac{\Delta}{2}$

Thus

$$-1 - \Delta \le \varepsilon - \frac{\Delta}{2} < -1 - \frac{\Delta}{2} \le -1 \tag{44.13}$$

Consequently

$$R\left(\varepsilon - \frac{\Delta}{2}\right) \approx 0 \tag{44.14}$$

From (44.13), we can get

$$\varepsilon - \frac{\Delta}{2} - \tau_1 < \varepsilon - \frac{\Delta}{2} \le -1 \tag{44.15}$$

Thus

$$R\left(\varepsilon - \frac{\Delta}{2} - \tau_1\right) \approx 0 \tag{44.16}$$

On the other hand, from (44.11) we can get

$$-1 \le \varepsilon + \frac{\Delta}{2} < -1 + \min\left(\frac{\Delta}{2}, \tau_1\right) \tag{44.17}$$

Thus

$$-1 - \tau_1 \le \varepsilon + \frac{\Delta}{2} - \tau_1 < -1 + \min\left(\frac{\Delta}{2}, \tau_1\right) - \tau_1 \tag{44.18}$$

Because $\min(\frac{\Delta}{2}, \tau_1) \le \tau_1$, thus

$$-1 - \tau_1 \le \varepsilon + \frac{\Delta}{2} - \tau_1 < -1 + \min\left(\frac{\Delta}{2}, \tau_1\right) - \tau_1 \le -1 \tag{44.19}$$

Consequently, we get

$$R\left(\varepsilon + \frac{\Delta}{2} - \tau_1\right) \approx 0 \tag{44.20}$$

We replace the Eqs. (44.5)–(44.8) by Eqs. (44.15), (44.16) and (44.20), thus

$$\begin{aligned} &I_E \approx 0, Q_E \approx 0 \\ &I_L \approx A_0 \frac{\sin(\pi \Delta f_0 T)}{\pi \Delta f_0 T} \cos(\theta_0 - \hat{\theta}) R\left(\varepsilon + \frac{\Delta}{2}\right) \\ &Q_L \approx A_0 \frac{\sin(\pi \Delta f_0 T)}{\pi \Delta f_0 T} \sin(\theta_0 - \hat{\theta}) R\left(\varepsilon + \frac{\Delta}{2}\right) \end{aligned} \tag{44.21}$$

For $-1 - \frac{\Delta}{2} \le \varepsilon < -1 - \frac{\Delta}{2} + \min\left(\frac{\Delta}{2}, \tau_1\right)$, we can simplify the discriminator function as follows

$$\begin{aligned} D_{E-L}(\varepsilon) &\cong -\sqrt{I_L^2 + Q_L^2} \\ &= -A_0 \left| \frac{\sin(\pi \Delta f_0 T)}{\pi \Delta f_0 T} R\left(\varepsilon + \frac{\Delta}{2}\right) \right| \end{aligned} \tag{44.22}$$

From Eqs. (44.5) to (44.8) can be obtained, when $\varepsilon \le -1 - \Delta/2$, the discriminator outputs zero constantly. But this is not the fact, we should note that Eq. (44.9) is a approximation of the autocorrelation function, in fact, outside the [−1, 1] chip, the autocorrelation function is not a perfect zero . Therefore, at –1 − Δ/2, the autocorrelati-on function value is not zero (so the above (44.15, 44.16, 44.20, 44.21) are all approximation). However, at –1 − Δ/2, due to the early correlation value equals to the late correlation value, at this point the discriminator outputs zero, the point we called the invariant point. Thus, the discriminator always goes through the invariant point whatever the multipath.

Therefore, we synchronize the local signal to the direct signal by this invariant point, i.e., the discriminator tracks the signal in case of the prompt code is $1 + \Delta/2$ in advance of the direct signal, which means that the received signal will be synchronized to very late code finally (VL code, $1 + \Delta/2$ chip from the prompt code). Therefore, we are concerned about the characteristics of the discriminator curve within $[-1 - \Delta/2, -1 + \Delta/2]$.

Assuming a code phase search step of Δ used during acquisition, the code phase uncertainty we get from acquisition is $\pm\Delta/2$, therefore, the initial input tracking error is in the range $[-\Delta/2, +\Delta/2]$. But the range that we are concerned about is $[-1 - \Delta/2, -1 + \Delta/2]$, if we advance the code phase that get from acquisition by 1 chip, thus the initial tracking error will fall in the range $[-1 - \Delta/2, -1 + \Delta/2]$. Therefore, this new discriminator is defined as follows:

$$D(\varepsilon) = -D_{E-L}(\varepsilon) \quad \varepsilon \in [-1 - \Delta/2, -1 + \Delta/2] \tag{44.23}$$

The new discriminator that we called Multipath Insensitive Delay Lock Loop (MIDLL). From the above, when MIDLL reaches its steady state, the direct signal is synchronized to the VL code, therefore, when we calculate the pseudorange, the code phase value obtained from acquisition should minus 1 chip, and then plus $1 + \Delta/2$, then plus the NCO output value locked by the DLL in case of its steady state, then can get the actual pseudorange value. Furthermore, since the prompt code in lock state have noise, we refer to the VL code as the input of the PLL.

Here we discuss how to perform a particular discrimination normalization, the typical discrimination normalization is as follows.

$$Norm_{E-L}(\varepsilon) = \sqrt{I_E^2 + Q_E^2} + \sqrt{I_L^2 + Q_L^2} \tag{44.24}$$

This normalization is not applicable to MIDLL operational region (OR) = $[-1 - \Delta/2, -1 + \Delta/2]$ chips. Through simulation, we found the result obtained by the Eq. (44.25) is a constant in the OR, as shown in Fig. 44.3, so we can use it to normalize the formula (44.23), as shown in Fig. 44.3.

$$SUM = \sqrt{I_E^2 + Q_E^2} + \sqrt{I_L^2 + Q_L^2} + \sqrt{I_{VL}^2 + Q_{VL}^2} \tag{44.25}$$

Then the discriminator is defined as follows.

$$D = \frac{\sqrt{I_L^2 + Q_L^2} - \sqrt{I_E^2 + Q_E^2}}{\sqrt{I_E^2 + Q_E^2} + \sqrt{I_L^2 + Q_L^2} + \sqrt{I_{VL}^2 + Q_{VL}^2}} \tag{44.26}$$

Noted that the new discriminator requires three correlators (E, VL, L). Figure 44.4 is a normalized discriminator output by formula (44.26), respectively, $\Delta = 1$ chip and $\Delta = 0.25$ chip, it can be seen, when the input synchronization

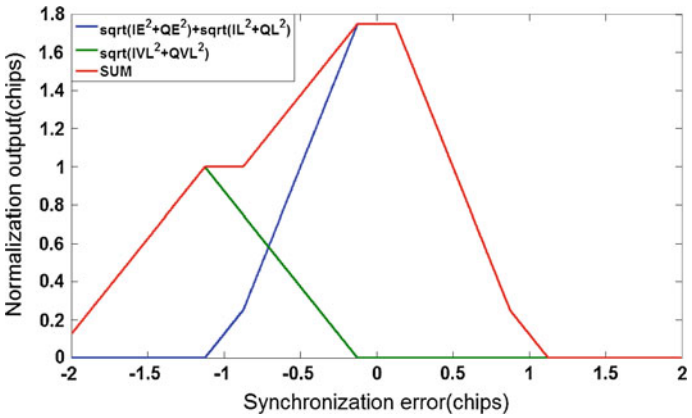

Fig. 44.3 Normalization output ($\Delta = 0.25$ chip)

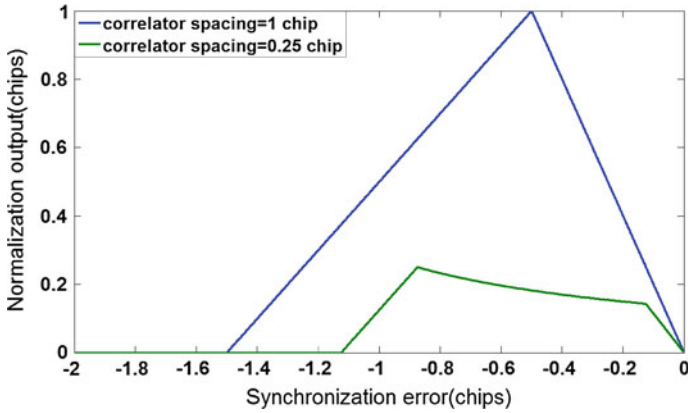

Fig. 44.4 Normalized discriminator output ($\Delta = 1$ chip and $\Delta = 0.25$ chip)

error $\varepsilon = -1 - \Delta/2$, the discriminator always outputs zero. In addition, we also made two sets of simulation, in which the first set of simulation condition is, correlator spacing $\Delta = 1$ chip, the relative amplitude of the multipath signal (in case of the magnitude ratio of the multipath signal and the direct signal, namely M/D $= A_1/A_0$) is 0.5, the delay is 0.125 chip, the phase is respectively 0 and π; the other set of simulations only displace the delay by 1 chip. The discriminator output of MIDLL is shown in Fig. 44.5, it shows that multipath does not affect the invariant point of the new discriminator, it merely affects the shape of the discriminator curve.

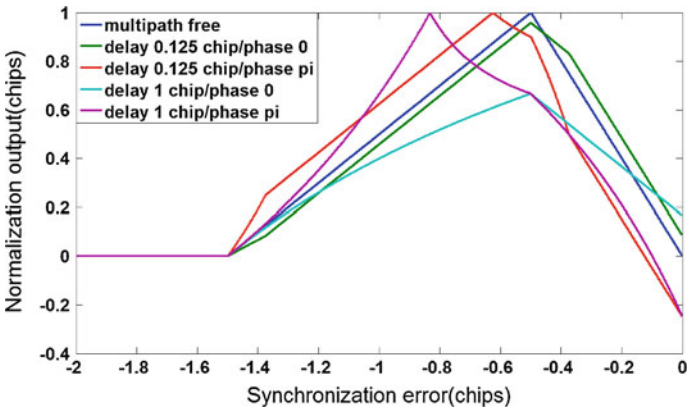

Fig. 44.5 New discriminator output in presence of different multipaths

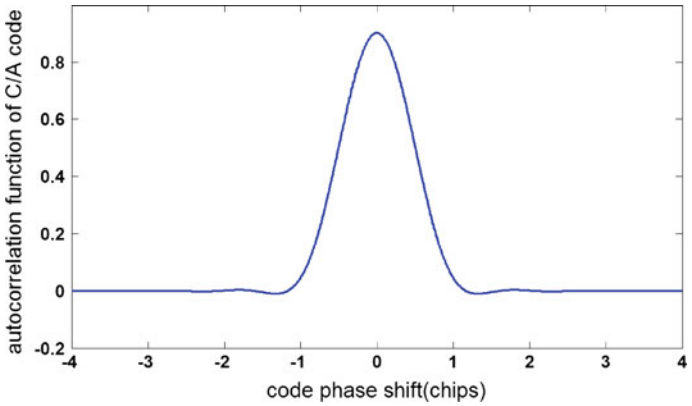

Fig. 44.6 Autocorrelation function of C/A code with 2 MHz filter

44.3 Analysis and Simulation

The preceding analysis assume the receiver bandwidth is unlimited, but in actual, in order to limit the noise and interference, the receiver bandwidth is limited. The limited bandwidth filters the high frequency component of the C/A code as well, resulting that the actual C/A code autocorrelation peak output which is formed by the noncoherent integration of the receiver code tracking loop is not as Eq. (44.9), but was similar to Fig 44.6, the shape of a limited bandwidth curve. Figure 44.6 shows the autocorrelation function curve, assuming a 2 MHz bandwidth, it can be seen that the peak of the angular portion is smoothed out [4, 5], but is still symmetrical, therefore it has no effect on the standard DLL, but for the proposed new discriminator, as shown in Fig. 44.7, the receiver bandwidth affects the

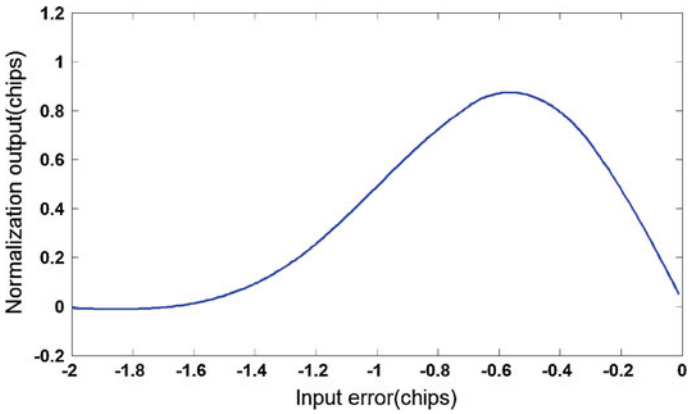

Fig. 44.7 Discriminator output of MIDLL. Receiver bandwidth = 2 MHz

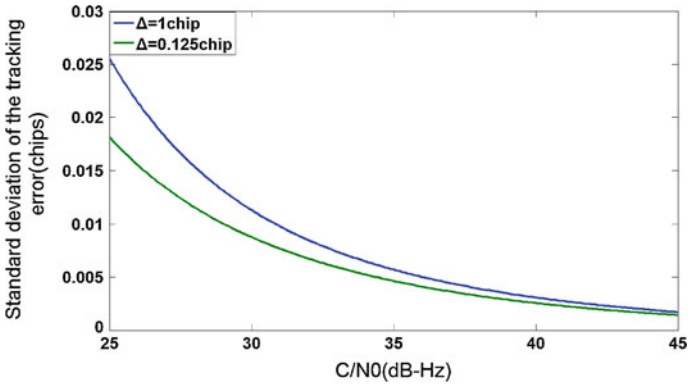

Fig. 44.8 Standard deviations of tracking error due to thermal noise for MIDLL

invariant point, because it depends on the zero output of the discriminator. As shown in the figure, in case of 2 MHz, correlator spacing $\Delta = 1$ chip, the invariant point shifts from $-1 - \Delta/2 = 1.5$ chips to -1.68 chips. Thus, the pseudorange value obtained by the MIDLL plus 0.18 chip (1.68 − 1.5 chips), in order to get the correct pseudorange value. This section first study the anti-noise performance and anti-multipath performance of MIDLL in case of 2 MHz bandwidth.

Thermal noise: in the case of white Gaussian noise, we study the effect of thermal noise on MIDLL. Figure 44.8 shows the anti-noise performance of MIDLL which the correlator spacing is 0.25 chip and 0.375 chip, respectively, it is clearly that the carrier to noise ratio is greater, the correlator spacing is smaller, the smaller is the tracking error. Figure 44.9 compares the anti-noise performance of DLL with that of MIDLL in case of correlator spacing is 0.25 chip, obviously, the

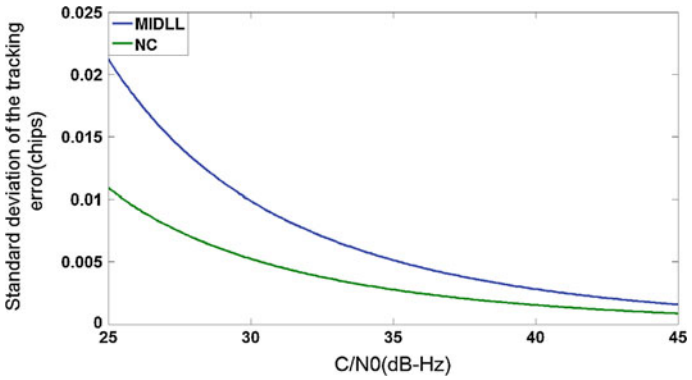

Fig. 44.9 Standard deviation comparison between MIDLL and NC

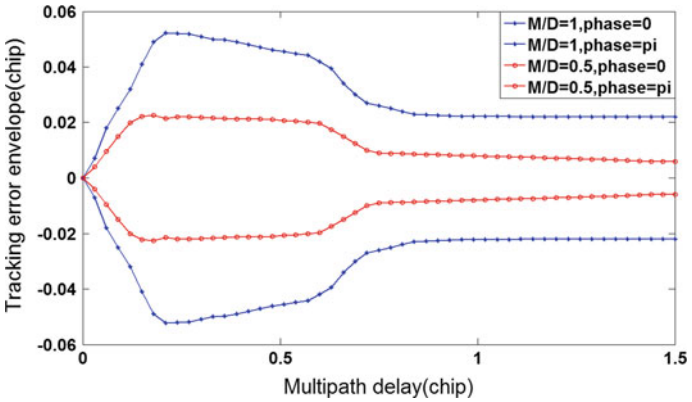

Fig. 44.10 Error envelopes of MIDLL due to single multipath ray (BW = 2 MHz, $\Delta = 1$ chip)

MIDLL is more susceptible to noise than DLL. Therefore, MIDLL should generally be used at higher SNR.

The results show that the use of MIDLL can degrade the anti-noise performance of the receiver. However the anti-multipath performance of MIDLL is remarkable, so when using $\Delta = 0.5$ chip and $\Delta = 0.375$ chip, the thermal noise performance degradation induced by the use of the MIDLL could be compensated for by its capacity to significantly reduce the multipath effect, generally most significant. Remember that the MIDLL is developed to cope with the multipath error on pseudorange.

Multipath: For MIDLL,the tracking error caused by multipath have strict analytical relationship with correlator spacing Δ, the relative magnitude of the multipath signal, delay and phase. Now we simulate and analyze the multipath code tracking error caused by these four parameters, as shown in Fig. 44.10,

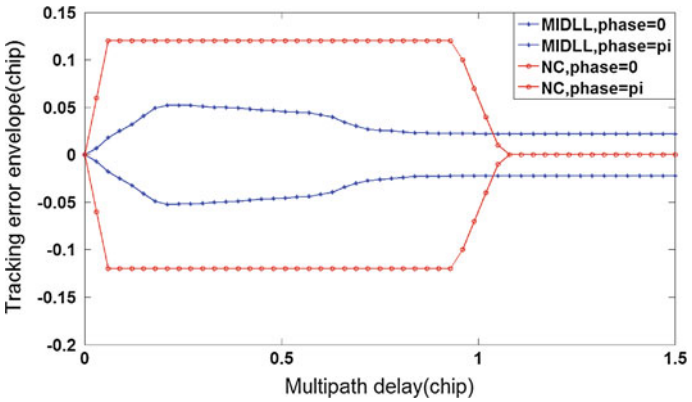

Fig. 44.11 Error envelopes due to a single multipath ray having M/D = 1 for MIDLL (BW = 2 MHz, Δ = 1 chip) and for NC (BW = 8 MHz, Δ = 0.125 chip)

respectively represents the code phase tracking error curve of MIDLL in M/D = 0.5 and M/D = 1, Fig. 44.11 respectively shows the code phase tracking error curve of Narrow Correlator (NC) and MIDLL in M/D = 1. The results show that when the multipath delay is less than 1 + Δ/2, the anti-multipath performance of MIDLL (BW = 2 MHz) is better than that of NC (BW = 8 MHz), the result is converse when the multipath delay is greater than 1 + Δ/2, this because multipath does not affect the late correlation value of DLL when the delay is greater than 1 + Δ/2. For short delay multipath (multipath delay is less than 0.1 chip), MIDLL and NC have the same performance. However, due to the short delay multipath will cause great pseudorange measurement error, we find that when using a large bandwidth, the MIDLL's anti-multipath performance for short delay increases significantly.

To achieve the theoretical performance of MIDLL, we use the RF front-end filter of 8 MHz. Under this condition, the discriminator output curve is very close to that of unlimited bandwidth. We do the same simulation analysis under the bandwidth of 8 MHz to MIDLL, simulation of multipath tracking error curve of MIDLL under different M/D, as shown in Fig. 44.12, the parameter is, Δ = 0.125 chip, BW = 8 MHz, M/D = 1 and M/D = 0.5, respectively. Figure 44.13 is the multipath tracking error curve of Narrow Correlator (NC) and MIDLL under M/D = 1, respectively. The results show that, MIDLL has a good anti-short delay multipath performance, and obviously better than the NC.

Furthermore, we also use the software GPS receiver to verify MIDLL's validity. The IF signal is generated from the GPS signal simulator, and its frequency is 9.55 MHz, signal sampling frequency is 38.192 MHz, other parameters are, Δ = 1 chip, C/N_0 = 45 dB Hz. The received signal is the sum of the direct signal and one multipath ray, assuming the multipath delay is 0.325 chip, M/D = 0.5. Compared the anti-multipath performance of MIDLL with the NC and

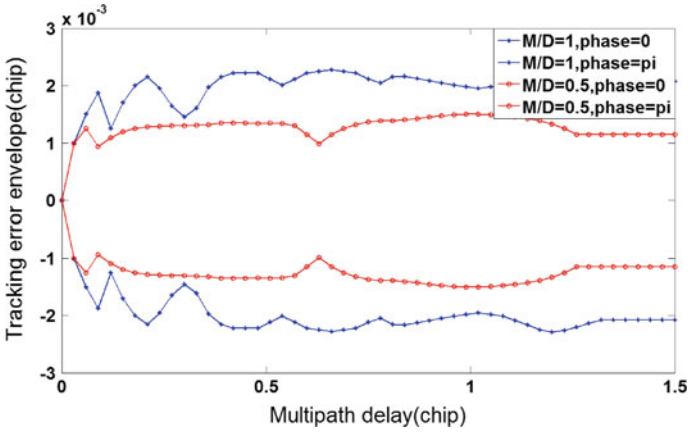

Fig. 44.12 Error envelopes of MIDLL due to single multipath ray (BW = 8 MHz, Δ = 0.125 chip)

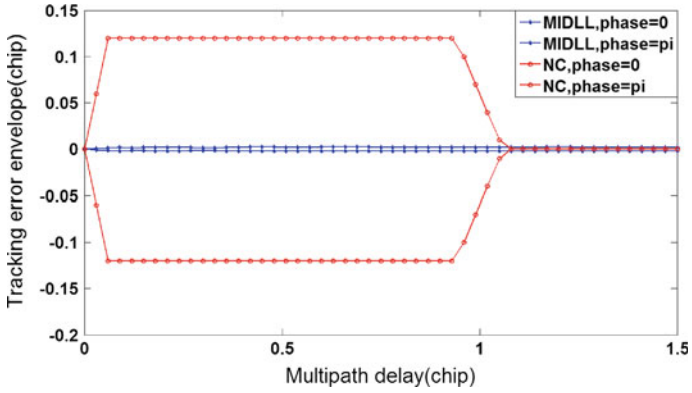

Fig. 44.13 Error envelopes due to a single multipath ray having M/D = 1 for MIDLL (BW = 8 MHz, Δ = 0.125 chip) and for NC (BW = 8 MHz, Δ = 0.125 chip)

the DLL, as shown in Fig. 44.14, the pseudorange error in the MIDLL remain about 1 m, while the NC (Δ = 0.1 chip) and the DLL pseudorange errors remain about 10 and 38 m, respectively. Thus, we have checked that the MIDLL is more precise than the NC, which is in turn more precise than the DLL. The stability and better anti-multipath performance of the MIDLL is also demonstrated through this test experiment.

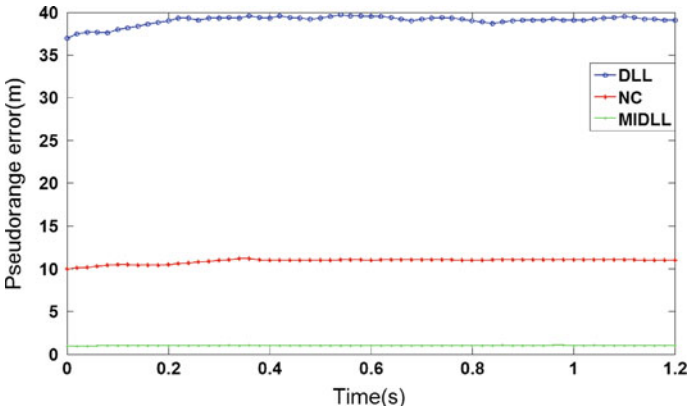

Fig. 44.14 Pseudorange error comparison

44.4 Conclusion

With the more and more application of high-precision positioning in GNSS, multipath has become one of the major errors that affect the positioning accuracy. Currently a variety of multipath mitigation techniques, such as MEDLL, Narrow Correlator (NC), Stroboscopic and other technology have been applied to the GNSS receiver, but the ranging accuracy of these technology is not high, and some techniques are complex to achieve. The proposed MIDLL, under a typical multipath, it can obtain very accurate pseudorange measurements, and which does not require postprocess of the observations or any additional hardware, and it is easy to implement. Theoretical analysis and simulation results show that, MIDLL can significantly suppress the multipath error, superior of the narrow correlation technology. However, the loop is more sensitive to noise, it is generally used for strong SNR. With the modernization of GPS, as well as the development of Galileo and other satellite navigation systems, the new signal system has been adopted, we need to further applied the MIDLL to these signals, and evaluate its effectiveness.

References

1. Ji Y, Sun X, Shi H (2009) Analysis of performance of GPS multipath mitigation error based in narrow correlator. J Wuhan Univ Technol 33(4):737–740
2. Ji Y, Shi H, Sun X (2007) Study of a multipath mitigation performance of Strobe correlator. J Astromautics 28(5):1094–1098
3. Van Nee RDJ (1992) The multipath estimating delay lock loop. In: Proceedings of the IEEE 2nd international symposium on spread spectrum techniques and applications, Yokohama Japan, pp 39–42, 29 Nov–2 Dec 1992

4. Kaplan ED, Hegarty CJ (2012) Understanding GPS: principles and applications. Publishing House of Electronics Industry, Beijing
5. Braasch MS (1996) Multipath effects. In: Global positioning system: theory and applications, vol 1, Chap. 14. AIAA, Washington, DC

Chapter 45
Joint Space-Time Interference Suppression Method of GNSS Receiver Based on the Maximum CNR Criterion

Guo Yi, Yang Sheng and Shen Rongjun

Abstract Joint space-time adaptive process (STAP) is an advanced interference suppression method for GNSS receiver. The STAP method based on power inversion (PI) and beam forming (BF) optimal criterion is widely used. We usually hope that anti-jamming processing not only null the interference direction, but also beam forming the satellite signal for antenna array processing gain. But satellite signal is too weak to hardly estimation the direction of arrive (DOA), and the estimation error cause anti-jamming performance drop quickly. Aim at this problem, a joint space-time anti-jamming method based on Maximum CNR criterion is proposed. Firstly, we use PI method to suppress interference primarily, and acquisition and tracking to get the desired code spread signal, and estimate the satellite signal direction vector. Then we compare the output CNR of PI and BF method, control the output to maximum the CNR of output signal. The proposed method not only avoid the complexity of traditional satellite DOA estimation, but also overcome the performance loss by the estimation error. The performance is much better than PI and BF method and the complexity is simple, it is benefit for engineer realization.

Keywords Space-time interference suppression · Power inversion · Beam forming · Carrier to noise ratio

National Natural Science Foundation (61201257)

G. Yi (✉) · Y. Sheng
Beijing Satellite Navigation Center, Beijing 100094, China
e-mail: guoyi_mail@163.com

G. Yi
School of Automation Science and Electrical Engineering of Beijing University of Aeronautics and Astronautics, Beijing 100191, China

S. Rongjun
The General Armament Department of PLA, Beijing 100720, China

J. Sun et al. (eds.), *China Satellite Navigation Conference (CSNC) 2014 Proceedings: Volume I*, Lecture Notes in Electrical Engineering 303,
DOI: 10.1007/978-3-642-54737-9_45,

45.1 Introduction

Joint space-time process is widely used as an advanced anti-jamming technique [1]. In space-time joint processing, PI (Power Inversion) and BF (Beam Forming) methods is widely used. Both of them have their advantages and disadvantages respectively. PI method need not a priori knowledge of the satellite signal direction, the algorithm is relatively simple, easy to engineering implement. But this method does not achieve the best reception for each satellite. BF method can achieve antenna array process gain, but need a priori knowledge of the satellite signal direction using INS, forecasting ephemeris or DOA estimation algorithm [2]. The receiver is complexity and high costs, the estimation error of space-time direction easily lead to the deterioration of the anti-jamming performance. Because of the above problems, BF method is often used in the engineering implementation. In this paper, a new joint space-time anti-jamming method based on the maximum CNR optimal criterion is proposed which combines PI and BF methods, Firstly, we use PI method to suppress interference initially, acquisition and tracking to get the desired spread code signal for the estimation of the satellite signal direction vector. Then we use BF method to anti-jamming and compare the output CNR of PI method for controlling the channel switch. At last we use the output results to position. Through compare, analysis and simulation, it is obviously that the proposed method not only avoid the complex computation of traditional satellite signal direction estimation, but also overcome the signal loss for estimation bias. The performance improves greatly compared with the traditional beam forming method.

In Sect. 45.2, the mathematical model of space-time processing was given. The BF and PI methods were unified to the same mathematic form. Based on above analysis, in Sect. 4.3, a new GNSS receiver space-time anti-jamming method is proposed based on the maximum CNR criterion, the flow diagram and structure diagram of the proposed method were given. In Sect. 45.4, Numerical simulation demonstrates that the proposed method is effective and efficient. The conclusion was given in Sect. 45.5.

45.2 Space-Time Adaptive Processing

The Structure of space-time adaptive processing is shown in Fig. 45.1. $\{w_{mn}\}$, $m = 1, 2, \ldots, M$; $n = 1, 2, \ldots, N$ are space-time two dimensional weight coefficients. $MN \times 1$ dimensional $\mathbf{W}$ denotes weight vector of processor. Then

$$\mathbf{W} = [w_{11}\, w_{21} \ldots w_{M1}\, w_{12}\, w_{22} \ldots w_{M2}\, w_{1N}\, w_{2N} \ldots w_{MN}]^{\mathrm{T}}$$

$\mathbf{R} = \mathrm{E}(\mathbf{X}\mathbf{X}^{\mathrm{H}})$ is the received data covariance matrix, where $\mathbf{X}$ is $MN \times 1$ dimensional received data vector.

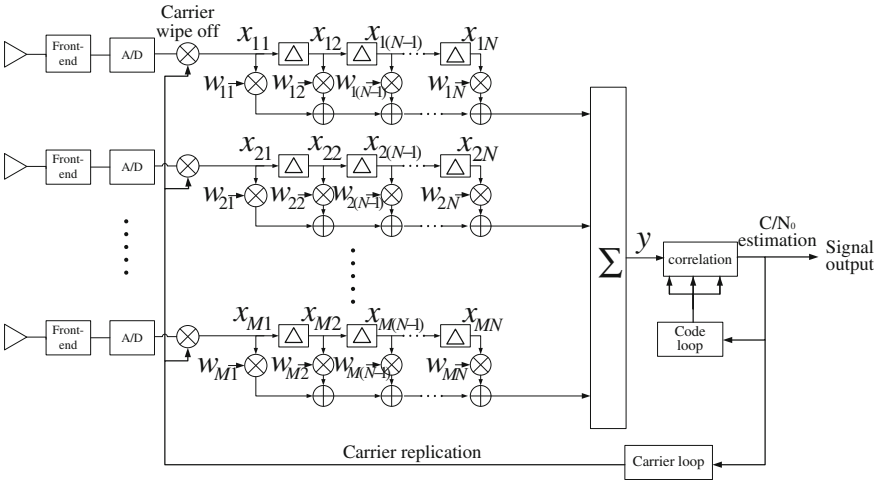

Fig. 45.1 Structure of space-time adaptive processing

$$\begin{aligned}\mathbf{X}(t) &= \mathbf{S}\cdot s(t) + \sum_{i=1}^{P}\mathbf{a}_i j_i(t) + \mathbf{n}(t) \\ &= \left[x_{11}\, x_{21}\ldots x_{M1}\, x_{12}\, x_{22}\ldots x_{M2}\ldots x_{1N}\, x_{2N}\ldots x_{MN}\right]^{\mathrm{T}}\end{aligned} \tag{45.1}$$

Which $s(t)$, $\mathbf{S}$ denote satellite signal and its space-time direction vector, $\mathbf{S} = \mathbf{S}_t \otimes \mathbf{S}_s$, $\mathbf{S}_t$ is time domain vector, $\mathbf{S}_s$ is space domain direction vector; $j_i(t)$, $\mathbf{a}_i$ denotes the i th interference and its space-time direction vector; $\mathbf{n}(t)$ denotes received noise vector. BF and PI methods can be unified to the same mathematic form.

$$\min_{\mathbf{W}}\left\{\mathbf{W}^{\mathrm{H}}\mathbf{R}_{\mathbf{X}}\mathbf{W}\right\} \quad \text{s.t.} \quad \mathbf{W}^{\mathrm{H}}\mathbf{S} = 1 \tag{45.2}$$

The Largrangian function is showed as follow

$$\mathrm{L}(\mathbf{W}) = \mathbf{W}^{\mathrm{H}}\mathbf{R}_{\mathbf{X}}\mathbf{W} - \lambda\left(\mathbf{g}^{\mathrm{H}} - \mathbf{C}^{\mathrm{H}}\mathbf{W}\right) \tag{45.3}$$

where λ is a constant. And

$$\nabla_{\mathbf{W}}(\mathrm{L}(\mathbf{W})) = 0 \tag{45.4}$$

The optimal weight is obtained.

$$\mathbf{W}_{opt} = \mathbf{R}_{\mathbf{X}}^{-1}\mathbf{S}\left(\mathbf{S}^{\mathrm{H}}\mathbf{R}_{\mathbf{X}}^{-1}\mathbf{S}\right)^{-1} = \mu\mathbf{R}_{\mathbf{X}}^{-1}\mathbf{S} \tag{45.5}$$

Assuming the space direction vector of the kth satellite can be obtained by INS, ephemeris or satellite signal DOA estimation. Defining

$$\mathbf{r}_k = [\cos\theta_k \cos\varphi_k, \quad \cos\theta_k \sin\varphi_k, \quad \sin\theta_k] \tag{45.6}$$

where φ_k, θ_k represent azimuth angle, elevation angle respectively. $\mathbf{S}_s = \mathbf{a}(\mathbf{r}_k)$ is space constraint vector. Furthermore, the space-time constraint vector $\mathbf{S}$ can be obtained. According to Eq. (45.5), the optimal weight of BF method can be obtained.

In the condition that a priori knowledge of the satellite signal DOA is unknown, the space-time constraint vector S sets as a column vector which first term is 1 and other terms are zeros, that is $\mathbf{S} = [1, 0, \ldots, 0]^{\mathrm{T}}$. According to Eq. (45.5), the optimal weight of PI method can be obtained.

Assuming the space direction vector of the kth satellite can be obtained by INS, ephemeris prediction or calculation of DOA estimation. Defining

$$\mathbf{r}_k = [\cos\theta_k \cos\varphi_k, \quad \cos\theta_k \sin\varphi_k, \quad \sin\theta_k] \tag{45.7}$$

where φ_k, θ_k represent azimuth angle, elevation angle respectively. $\mathbf{S}_s = \mathbf{a}(\mathbf{r}_k)$ is space constraint vector. Furthermore, the space-time constraint vector can be obtained. According to Eq. (45.5), the optimal weight of BS method can be obtained.

45.3 Joint Space-Time Interference Suppression Method Based on the Maximum CNR Criterion

In this paper, the joint space-time process method based on the maximum CNR criterion need take full advantage of BF method, get antenna array gain, obtain maximum CNR. The traditional space-time direction vector estimation methods are including in using the cyclostationarity of C code [2], using INS combined ephemeris information and so on. The computation is high. We derive from MMSE criterion and deduce a new space-time direction vector estimation method.

MMSE criterion is based on that useful signal has some priori knowledge, it is proposed that set a reference signal which has much correlation with useful signal in receiver, and make the mean square error be smallest between array output and reference signal. Assuming the reference signal is $d(t)$, array output error signal is

$$e(t) = d(t) - y(t) = d(t) - \mathbf{W}^{\mathrm{H}}\mathbf{X}(t) \tag{45.8}$$

Make the square error of $e(t)$ be the smallest, and the optimal weight vector is

$$\mathbf{W}_{opt} = \mathbf{R}_{\mathbf{X}}^{-1}\mathbf{r}_{\mathbf{X}d} \tag{45.9}$$

where $\mathbf{r}_{\mathbf{X}d}$ is correlation vector between reference signal and received signal vector

$$\mathbf{r}_{\mathbf{X}d} = \mathrm{E}[\mathbf{X}(t)d^*(t)] \tag{45.10}$$

On MMSE criterion, the selection of reference signal $d(t)$ is a key factor for the performance of the array. For GNSS receiver, the modulated pseudo code of the satellite signal is known. If we know exactly the phase of the code and Doppler shift, then the reference signal $d(t)$ is determined. Here we recover a local reference signal from carrier tracking loop and code tracking loop. The navigation data positive and negative polarity can be almost negligible [3].

When the ideal reference signal $d(t)$ is obtained, there is only a coherence μ_0 difference between $d(t)$ and received signal $s(t)$, take $d(t) = \mu_0 s(t)$ and formula (45.1) into formula (45.10), and

$$\begin{aligned}\mathbf{r}_{\mathbf{X}d} &= \mathrm{E}\left[\left(\mathbf{S}\cdot s(t) + \sum_{i=1}^{P}\mathbf{a}_i j_i(t) + \mathbf{n}(t)\right)\mu_0 s(t)\right] \\ &= \mu_0 p\mathbf{S} = \mu\mathbf{S}\end{aligned} \tag{45.11}$$

Take formula (45.11) into formula (45.9), and

$$\mathbf{W}_{opt} = \mu\mathbf{R}_{\mathbf{X}}^{-1}\mathbf{S} \tag{45.12}$$

Comparing Formula (45.12) and (45.5), it is known that after obtaining ideal reference signal $d(t)$, MMSE criterion and BF criterion are equivalent, and space-time direction vector can estimate as follows

$$\mathbf{S} = \mathbf{r}_{\mathbf{X}d} = \mathrm{E}(\mathbf{X}d) = \frac{1}{K}\sum_{k=1}^{K}\mathbf{X}_k d_k \tag{45.13}$$

It is avoided high complexity of using the cyclostationarity of navigation, INS combined with ephemeris information and so on.

The method above can be used in condition that reference signal $d(t)$ is absolutely correct, the signal acquisition and tracking is completely correct. In strong interference condition, acquisition and tracking may exist large deviation. It causes space-time direction vector estimation is not correct, and degrades the anti-jamming performance. The output signal CNR falls instead of rises. In literature [4], the code aided closed loop iterative convergence method can not converge in the same condition, and cause more serious consequences compared with the proposed open loop method.

From earlier derivation, we notice that the optimal weight vector is not affected by the direction vector error. Combined with BF method, it can remains a better anti-jamming performance in the harsh environment, acquisition and tracking exist large deviations and loss of locking. A new space-time interference suppression method based on maximum CNR criterion for GNSS receiver is proposed in this paper. The flow diagram is shown in Fig. 45.2. The hardware structure is shown in Fig. 45.3. The proposed method uses PI method to suppress interference initially, and acquisition and tracking to obtain the desired spreading code signal for

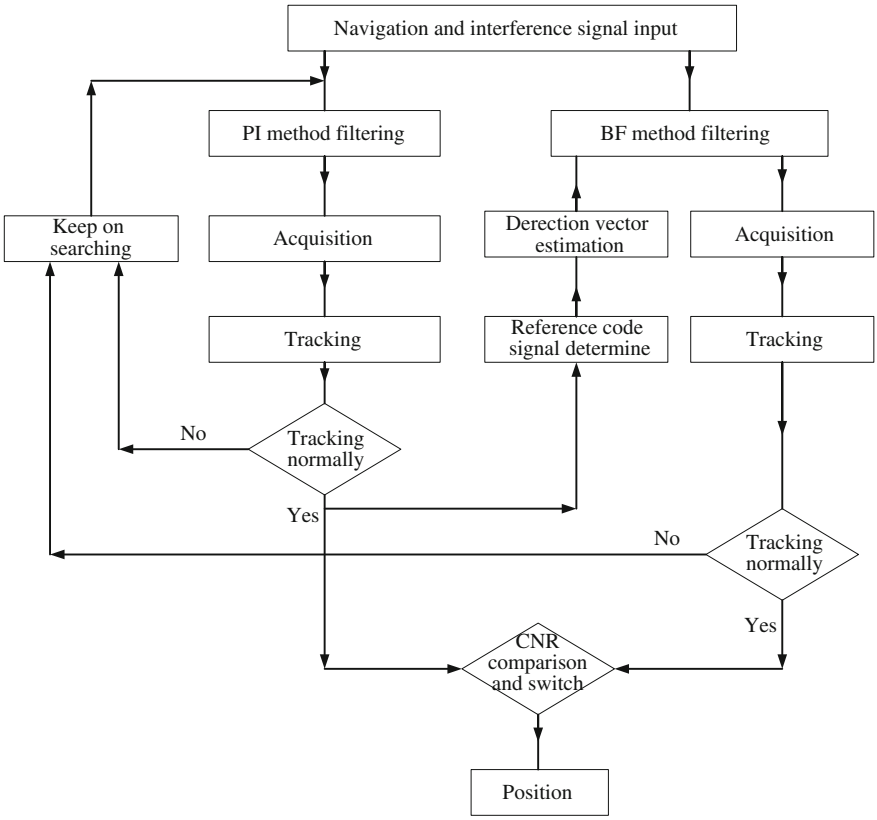

Fig. 45.2 Flow diagram of maximum CNR method

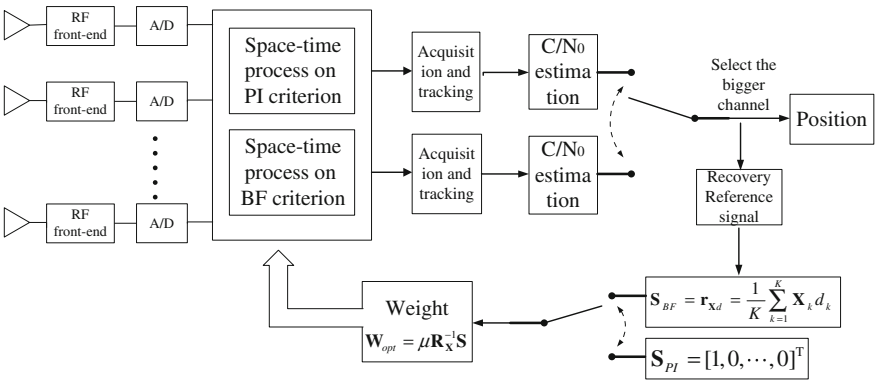

Fig. 45.3 Hardware structure of maximum CNR method

estimating the space-time direction vector; Then the BF method is used, the signal which has larger C/N_0 is output by estimating and comparing the two output C/N_0 [5], and use the output to position. It avoids the disadvantages of wrong estimation of space-time direction vector in strong interference condition and the disadvantages of PI method which do not make full use of the space-time direction vector information which is known exactly. For avoiding the case that the two channel CNR is similar and the output signal are frequently switched between the two channels, we can compare the output signal CNR of the two methods regularly, and switch in the condition that several consecutive comparison results are same.

45.4 Simulation and Analysis

In the following, the performances of PI, BF and the proposed method are analyzed by simulation. The simulation use five elements ULA (Uniform Linear Array). The array elements spacing is $d = \lambda/2$. The time delay node number is 7. The interference incident angle range is $0^\circ \sim 180^\circ$. The satellite signals incident angle is $\theta = 120^\circ$. The normalized time delay is satisfied that $B\Delta = 1$, where B is receiver processing bandwidth.

The L1 C/A code is adopted in the simulation. The received satellite signal power is -157 dBW. The C/N_0 formula is $C/N_0 = S_r + G_a - 10\log(kT_0) - N_f - L$, where Sr is received satellite signal power and $S_r = -157$ dBW; Ga is antenna gain and $G_a = 0$ dB; The receiver thermal noise density is $10\log(kT_0) = -205$ dBW/Hz, where k = 1.38×10^{-23} (W s/K) is the boltzmann constant, the thermal noise reference temperature $T_0 = 290$ K; $N_f = 4$ dB is receiver noise figure including the loss of antenna and cables. $L = 2$ dB is the loss of signal process and A/D quantization. $C/N_0 = 42$ dB/Hz in single antenna condition can be calculated. The sample rate is 2 times of chip rate. The receiver processing bandwidth is about 2 MHz. The in band white noise power is about -142 dBW. And SNR $\approx (-157) - (-142) = -15$ dB.

There are one broadband interference, one partial band interference and one single frequency interference. All kinds of interference J/N is 65 dB, the interference incident angle range is uniform from 0° to 180°.

Figure 45.4 shows the relationship between code estimation bias and output CNR when satellite signal space-time direction vector is estimated. The figure shows that BF method is more sensitive to the estimation bias of reference spreading code signal. When code estimation bias is larger than 0.7 chip, the performance of proposed method drops quickly; PI method has nothing to do with the space-time vector direction, the output CNR is more stable. At the same time, the beam form antenna array gain is loss. When the reference spreading code signal estimation bias is at [− 0.8, 0.8] chip, the BF method outperforms PI method. When the estimation bias is larger than 0.8 chip or less than − 0.8 chip, the PI method outperforms BF method.

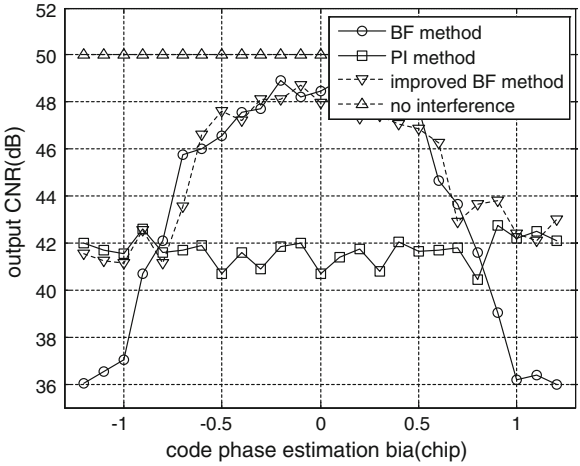

Fig. 45.4 Relationship between code estimation bias and output CNR

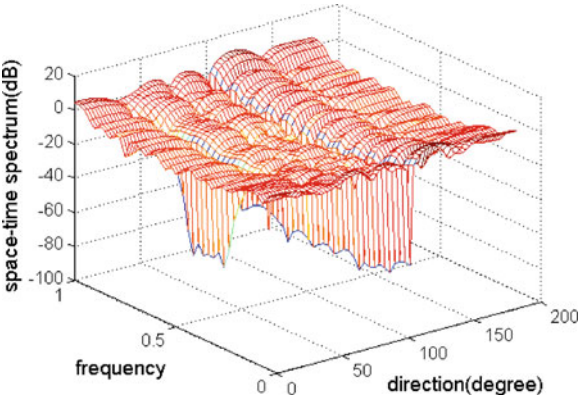

Fig. 45.5 Space-frequency response two-dimensional spectrum of weight

Figure 45.5 shows the space-frequency response two-dimensional spectrum of weight obtained by the proposed method. From the figure we can see that the space-time weight vector depression in the corresponding interference position to anti-jamming and heaving in the corresponding signal position to satellite signal position to better reception.

45.5 Conclusion

In this paper, a new space-time anti-jamming method based on the maximum CNR optimal criterion is proposed, aim at the shortcoming of traditional BF method. The proposed method combines PI and BF method, take their own advantages, and reduce complexity of estimating direction vector. Simulation demonstrates the method is effective.

References

1. Fante RL, Vaccaro JJ (2000) Wideband cancellation of interference in a GPS receive array. IEEE Trans Aerosp Electron Syst 36:549–564
2. Sun W, Amin MG (2005) A self-coherence anti-jamming GPS receiver. IEEE Trans Sig Process 53(10):3910–3915
3. Li M (2011) Study on key techniques of digital beamforming in satellite navigation receiver. National University of Defense Technology
4. Lu D, Wu R, Shi Q, A blind adaptive GPS interference suppression method based on the code structure. China, 20091006909.3
5. Falletti E, Pini M, Lo Presti L, et al (2008) Assessment on low complexity C/N0 estimators based on MPSK signal model for GNSS receivers, position, location and navigation symposium. In: 2008 IEEE/ION 5–8, Monterey, California

Chapter 46
Bit Synchronization Method for Highly Sensitive BeiDou Receiver

Zhifeng Han, Rongbing Li, Jianye Liu, Fei Xie and Ning Wang

Abstract As one of the high-performance receiver, high sensitivity receiver has gradually become a research hotspot in recent years. Increasing the PDI time can improve SNR (Signal to Noise Ratio) to track the weak signal on one hand, and reduce data rate and operand on the other hand, but it needs to consider the effect of data bits jump. BeiDou Navigation Satellite System (BDS) broadcasts D1 NAV message on B1I signal. D1 NAV message is modulated with 1 kbps secondary code of Neumann-Hoffman (NH) code, which can improve suppression of narrow-band interference and the cross correlation characteristic of satellite signals. Meanwhile, the NH code limits the pre-detection integration (PDI) time to be 1 ms. So that, to track the weak signal availably, the NH code must be solved to increase the PDI time. The common method so-called sliding correlation method is influenced by data bit jumps. A method of Bit synchronization which can also solve NH code and data bit jumps is designed, by using bits matching method in groups. Using the QuartusII 7.2 software, the method of Bit synchronization is designed. The simulation results show that the bit synchronization method is able to achieve signal synchronization stably and reliably. By bit synchronizing and NH code solving, the PDI time can be the maximum 20 ms and it will lay the foundation for the further research and application of weak signal tracking sensitivity.

Keywords Bit synchronization · NH code · Beidou receiver · High sensitivity · PDI

This work was partially supported by the National Natural Science Foundation of China (Grant No. 61374115, 61273057, 61328301, 61104188), Industry-Academy-Research Fund Project supported by AVIC.

Z. Han (✉) · R. Li · J. Liu · F. Xie
Nanjing University of Aeronautics and Astronautics, Nanjing 210016, China
e-mail: hanzhifeng@nuaa.edu.cn

N. Wang
Shenyang Aircraft Design and Research Institute, Shenyang 110035, China

J. Sun et al. (eds.), *China Satellite Navigation Conference (CSNC) 2014 Proceedings: Volume I*, Lecture Notes in Electrical Engineering 303,
DOI: 10.1007/978-3-642-54737-9_46,

46.1 Introduction

With the development of satellite navigation system, high-performance receivers have been the research hotspots at home and abroad. Highly sensitive receiver is one of the hotspots. SiRF, QinetiQ and u_blox have developed highly sensitive GPS receiver products [1]. In recent years, many colleges and universities have carried out research on highly sensitive GPS receiver. With the development of the Beidou navigation system, highly sensitive Beidou navigation receiver contains theoretical value and application prospect.

To extend the PDI time is the most common method used to enhance the loop SNR in highly sensitive receiver. At the same time, to extend the PDI time can reduce data rate and computational complexity. To extend the PDI time, there are two aspects need to be considered:

On one hand, the data of 50 bps decides the maximal PDI time to be 20 ms after bit synchronization in order to avoid data bits jump. How to solve the data bits jump is the key to realize PDI time extend.

On the other hand, the B1I signal of the MEO/IGSO satellites broadcasts D1 navigation message. D1 navigation message is secondarily modulated with 1 kbps NH code, which can improve the resistance ability of narrowband interference and improve the cross-correlation of satellite signals [2]. But at the same time, it limits the PDI time to be 1 ms by the influence of NH code phase jump. Therefore, NH code must be solved to eliminate the influence of NH code phase jump and extend the PDI time.

Thus, in order to improve the sensitivity of the Beidou receiver by extending the PDI time, the influence of data bits jump and NH code phase change must be eliminated. Therefore, how to realize bit synchronization of the Beidou signal and how to solve NH code are the main problems in this paper.

In recent years, Navigation Research Center of Nanjing university of Aeronautics and Astronautics have done much research on Beidou satellite navigation receiver, Beidou/Inertial integrated navigation and so on [3, 4]. Navigation Research Center has made good progress in theory research, software receiver design and hardware receiver. This paper is based on the open FPGA/DSP hardware navigation receiver platform to carry out related study.

46.2 Analysis of Beidou Bit Synchronization

46.2.1 Principle of Bit Synchronization

If the PDI time is 1 ms, tracking loop will output 1 kHz original navigation message binary data after the loop is stabilized. The binary data needs to be bit synchronization to find the edge of the data bits and convert 20 binary figures to 1 bit figure. Also it needs to be frame synchronization to find the starting edge of

every frame. Then according to the rules of arrangement, the navigation message can be got.

The common GPS bit synchronization method is histogram method [5]. The basic steps are shown in Fig. 46.1.

(1) Divide the loop output binary figures into groups with circularly number 1–20;
(2) Check data jump one by one. If there is a jump, the corresponding count value plus one.
(3) Judge bit synchronization according to the count value and the threshold.

46.2.2 The Influence of NH on Bit Synchronization

BDS broadcasts D1 NAV message on B1I signal. D1 NAV message is modulated with 1 kbps secondary code of NH code, as shown in Fig. 46.2. The width of NH code is equal to one bit navigation data, the width of one NH chip is equal to the cycle of ranging code.

Therefore, Beidou bit synchronization can't use the histogram method because of NH code phase jump affection.

46.2.3 Analysis of NH Code Stripping Technology

The common method to strip NH code is sliding correlation method. Similar to ranging code stripping, 20 ms binary data is related to the local NH code for sliding to find relevant peak. The loop structure of the sliding correlation method is shown in Fig. 46.3.

But in this method, the influence of the data bits jump must be considered [6]. In addition, NH sliding correlation increases the search time to be 20 time of the original. Therefore, the use of sliding correlation method is not very effective to strip NH code.

46.3 Bit Synchronization Method for Coherent Integral

In order to enhance the sensitivity of Beidou satellite navigation receiver, the PDI time is need to be extended to improve the SNR of the loop. In order to extend the PDI time, the influence of data bits jump and NH code phase change must be removed to achieve PDI time of 20 ms [7].

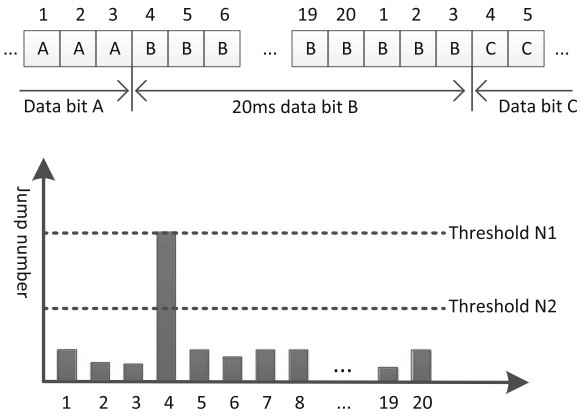

Fig. 46.1 A synchronous histogram method

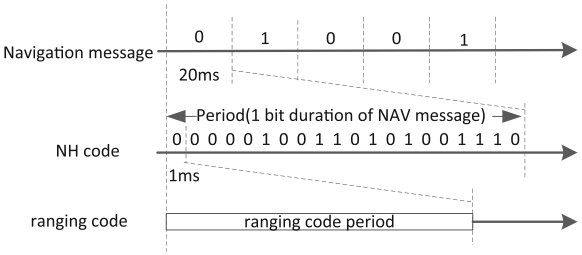

Fig. 46.2 Secondary coding schemes

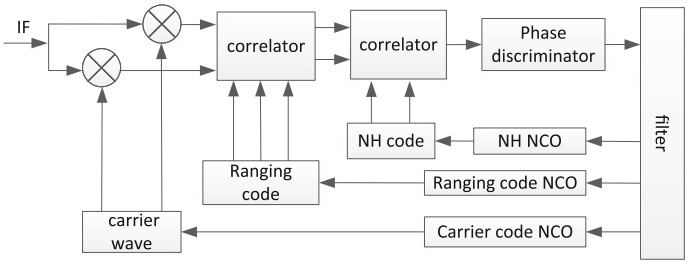

Fig. 46.3 Loop structure of NH code sliding correlation

46.3.1 Bit Synchronization Method

If the data bit edge can be found, stripping NH code will be very easy because of the immobility and repeatability of NH code. However, Beidou NH code phase changes cause that bit synchronization cannot be implemented by the histogram method. Therefore, new bit synchronization methods need to be designed.

Although NH code results in data bits jump, the relationship between the bits of data is all right because of repeatability of NH code. Navigation message is arranged with frame and the frame data starts with 11 bits frame flag having very strong reliability. Based on frame synchronization and grouping, Beidou bit synchronization method is put forward.

Divide binary data streams into 20 groups using 1–20 cyclical numbers and do bits matching detection in groups. If there are 20 consecutive groups and the 20 bits match with NH code, the edges of data bits and frame will be found. Bit synchronization is shown in Fig. 46.4.

In this bit synchronization method, the internal data of each group is checked not by the bit jump, so this bit synchronization method is not influenced by NH code phase jump.

Upon completion of bit synchronization and frame synchronization, the data bits edges and frame starting have been identified. The NH code starting edges and data bits edges are consistent, so NH code can be stripped directly. This will not increase additional time.

46.3.2 Procedure of Bit Synchronization

Common frame synchronization method is based on the preamble and parity detection.

The BDS NAV message in format D1 is structured in the superframe, frame and subframe. Every superframe is composed of 24 frames. Every frame is composed of 5 subframes. Every subframe is composed of 10 words. Every word has 30 bits and lasts 0.6 s. Every word consists of NAV message data and parity bits. In the first word of every subframe, the first 15 bits is not encoded and the following 11 bits are encoded in BCH (15,11,1) for error correction. So there is only one group of BCH code contained and there are altogether 26 information bits in the word. For all the other 9 words in the subframe both BCH (15,11,1) encoding for error control and interleaving are involved. Each of the 9 words of 30 bits contains two blocks of BCH codes and there are altogether 22 information bits in it (Fig. 46.5).

Based on the above characteristics of Beidou D1, 30 selected figures are checked by bits matching. The first 11 figures are checked by preamble and the last 15 figures are checked by BCH error correction.

Procedure of bit synchronization and frame synchronization method for coherent integral is shown in Fig. 46.6.

Procedure of bit synchronization mainly includes circulation packet, inspection, and NH code bits matching and stripping. Design registers with line width of 20 and depth of 30. Then 30 bits of each column data are detected, ensuring that test bits are from different data bits. Bits matching detection mainly includes preamble and BCH error correction to ensure the reliability of bit synchronization.

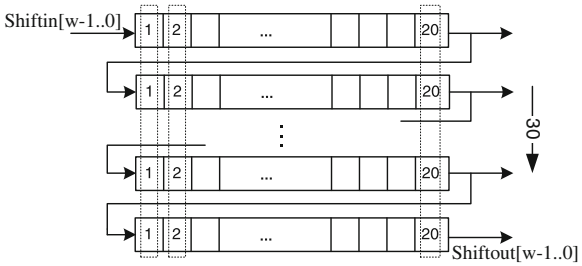

Fig. 46.4 Bit synchronous principle

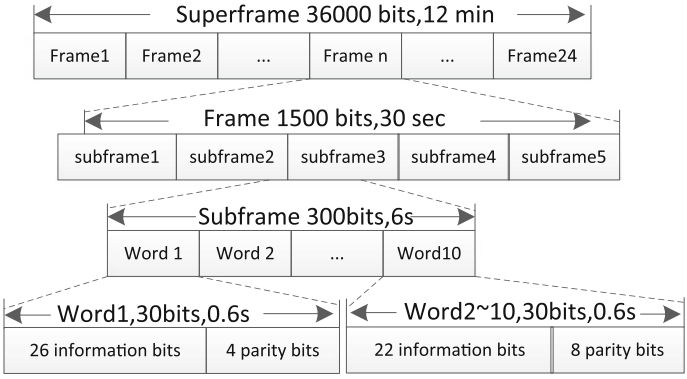

Fig. 46.5 D1 navigation message frame structure

46.3.3 The Gain of All Bits Coherent Integral

Coherent integral formula of I branch signal is shown as follows:

$$I_P(n) = \frac{1}{N_{coh}} \sum_{k=1}^{N_{coh}} i_P(nN_{coh} + k)$$

Among them, $i_P(n)$ is the output signal of correlator; N_{coh} is the count of related results during the PDI time.

$i_P(n)$ contains gauss white noise of mean zero and variance σ_n^2. Signal power of $\sum_{k=1}^{N_{coh}} i_P(nN_{coh} + k)$ enhances N_{coh}^2 times than the original. And noise power enhances N_{coh} times because the value can be positive or negative. Therefore, the SNR increases N_{coh} times after coherent integration.

$$G_{ci} = 10 \lg N_{coh}$$

Therefore, if the correlator cumulative time is 1 ms and PDI time is 20 ms, the coherent integral gain will be about 13.01 dB. Extending the PDI time can greatly improve the SNR of the loop and greatly enhance sensitivity.

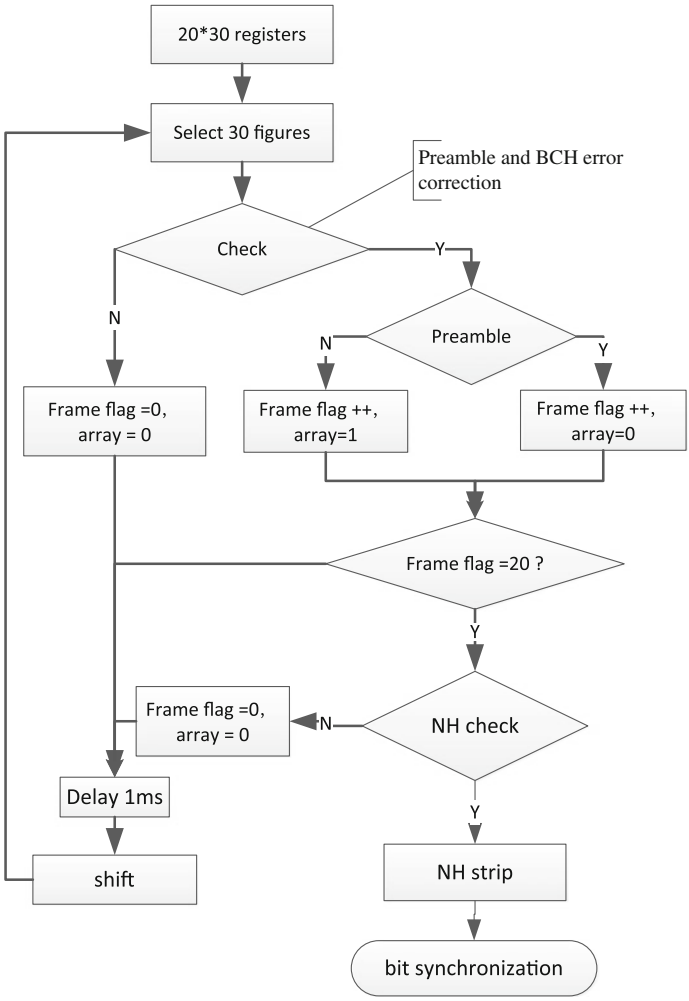

Fig. 46.6 Procedure of bit synchronization

46.4 The Simulation Analysis

46.4.1 The Simulation Platform

Receiver hardware platform was used to do some experiments to verify the bit synchronization method. The platform includes antenna unit, radio frequency unit and baseband unit. The baseband unit is made up with Altera FPGA chip EP2S6F484I4 and TI DSP TMS320C6713 chip. Programs in the FPGA contain carrier NCO module, code NCO module, carrier frequency mixing module, code

generation module, correlator module and frame synchronization module; Programs in DSP contain visible stars prediction, signal capture strategy, signal tracking loop and other functions.

46.4.2 Simulation Experiment

Use QuartusII 7.2 software to design this bit synchronization and frame synchronization as follows:

```
GPS_FRAME_SYNC_GEN
(
clock,
clock32×,
cs_gnss,
reset,
DUMP,
CHn_I_PROMPT_SIGN,
Frame_sync_flag,
Bit_sync_flag,
clock_1 ms
);
```

Among them, the clock32× is 32 times of the code NCO clock, as frame synchronization enable clock; cs_gnss works as module enabling signal input, high level can make the module work; DUMP is the output signal of code generation module and here works as input; CHn_I_PROMPT_SIGN is instant accumulation of I branch; Frame_sync_flag is frame synchronization signal output, cycle for 6 s, indicates the frame starting. Bit_sync_flag is bit synchronization flag signal. Clock_1 ms is created for the frame synchronization clock output.

46.4.3 Simulation Results

Bit synchronization and frame synchronization simulation results are shown in Fig. 46.7.

The data bits were divided into 20 groups. The bit_sync_flag is bit synchronization flag and the frame_sync_flag is frame synchronization flag.

From the simulation results, we can see that the bit synchronization and frame synchronization method is able to achieve stable and reliable signal synchronization and frame synchronization, and NH code can be quickly stripped.

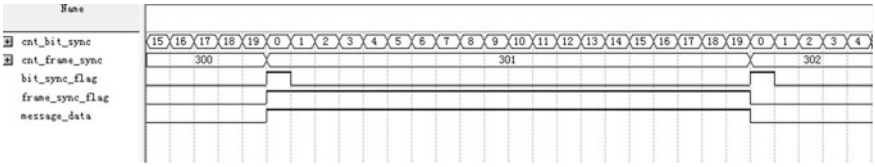

Fig. 46.7 Bit synchronization simulation results

46.5 Conclusion

The data bits jump and NH code phase change limit the extending of Beidou receiver PDI time. To solve this problem, a new method of bit synchronization and frame synchronization is put forward by grouping bits matching. On the receiver hardware platform, QuartusII software was used to verify this new method.

(1) This approach can achieve bit synchronization and frame synchronization at the same time, and is not affected by NH code phase jump;
(2) This method can strip NH code fast and conveniently and do not cause additional time delay.
(3) After bit synchronization and NH stripping, the PDI time can be extended to 20 ms. It will greatly improve the SNR and the sensitivity of weak signal.

References

1. Cai C, Pi Y (2006) The research progress of high sensitivity GPS technology. J glob positioning syst (GPS) 31(2):1–4
2. Zou D, Deng Z, Huang J, et al (2009) A study of neuman hoffman codes for GNSS application. In: Wireless communications, networking and mobile computing, 2009. WiCom'09. 5th international conference on, IEEE, pp 1–4
3. Tian B, Ning C, Ding F et al (2009) The GPS software receiver navigation message extraction research. J Commun Technol 42(03):212–215
4. Wen C, Yue F, Chou Y et al (2013) Under the environment of high rail BDS weak signal tracking technology research. J Aircr Measur Control 32(4):363–370
5. Shi X, Ba X, Chen J (2013) Beidou MEO/IGSO satellites B1 frequency signal capture method research. J Foreign Electron Measur Technol 32(4):19–21
6. Xie F, Liu J, Li R et al (2013) Deeply SINS/GPS integrated navigation algorithm based on tracking loop correlation measurements. J Chin Inertial Technol 21(004):472–477
7. Huang JY, Li R, Liu J et al (2012) High dynamic self-adjusting software receiver loop tracking technology research. In: The third China satellite navigation electronic corpus academic conference—S07 Beidou/GNSS user terminal technology

Chapter 47
On the Requirements of GNSS Intermediate Spoofing

Jian Wang, Meng Zhou, Hong Li, Xiaowei Cui and Mingquan Lu

Abstract Intermediate spoofing can control the target receiver successfully without interrupting tracking loop, so it is strongly secret, while it needs to know the accurate antenna position and channel condition of victim. In practical condition, position of victim is often fuzzy, which will influence the performance of spoofing. For a successful spoofing in actual scene with a lower detected probability, it is necessary to research the requirements of GNSS Intermediate spoofing. In this paper, according to the principle of intermediate spoofing, we establish the signal model of intermediate spoofing, and then we analyze the related influence factors based on a fix successful probability, including signals' interval, carrier-frequency difference, carrier-phase difference and code rate difference between authentic signal and spoofing signal. Monte Carlo simulations present the relationship between spoofing-to-noise ratio (SSR) and factors, which verify the reasonable of models and theoretical analysis. Thus, minimum SSR for successful spoofing is obtained in the case of fuzzy position of victim, which reduces the risk of being detected. Finally, requirements of successful intermediate spoofing are summarized. The research is based on actual scene, which extends the application range of intermediate spoofing, so it has a guiding significance for designing of GNSS spoofer.

Keywords Intermediate spoofing · Carrier-frequency difference · Carrier-phase difference · Code rate difference · Minimum spoofing-to-signal ratio

J. Wang (✉) · M. Zhou · H. Li · X. Cui · M. Lu
Department of Electronic Engineering, Tsinghua University, Beijing 100084, China
e-mail: tswangjian05@gmail.com

J. Sun et al. (eds.), *China Satellite Navigation Conference (CSNC) 2014 Proceedings: Volume I*, Lecture Notes in Electrical Engineering 303,
DOI: 10.1007/978-3-642-54737-9_47,

47.1 Introduction

With the extensive application of GNSS system, navigation warfare has becoming a hot issue gradually. Early in 2001, the US government has realized the vulnerability of GPS, and regarded spoofing as disaster in its internal file [1]. Today, research on spoofing has made great breakthrough in the US. In lab environment, spoofing has been proved to be reasonable [2], and in real sense, it has spoofed the aircraft and yachts successfully [3, 4]. Therefore, in future navigation warfare, spoofing will become an important and effective tool.

Intermediate spoofing is a kind of spoofing way. It can control the receiver to output wrong position and time information without interrupting the tracking loop, so it is extremely concealed. While it needs to know the accurate channel condition and 3D position of target receiver. In other words, to align the carrier phase completely, accuracy of 3D position must be centimetre, while it is almost impossible in real sense [5]. Spoofer could overcome this difficulty by enhancing power of spoofing signal, while this method also has limitations: higher signal power means higher probability to be detected, and lower signal power means lower spoofing successful probability. So research on the requirements of successful spoofing is necessary. Currently, there is little research on the requirements of intermediate spoofing. Humphreys et al. [3] declared a standard: when power of spoofing signal is 10 dB larger than that of authentic signal, it is a successful spoofing, while they didn't give the reason. Tippenhauer et al. [6] changed this standard to 2 dB by analysing pseudo-range, while they didn't consider the influence of carrier-phase difference. What's more, pseudo-range is influenced by multiple satellites, so it can't represent the condition of single channel.

In this paper, according to the principle of intermediate spoofing, we establish the signal model of intermediate spoofing. Then, for a successful spoofing, we analyze influence of signals' interval, carrier-frequency difference, carrier-phase difference and code rate difference to minimum spoofing-to-signal ratio (SSR). Monte Carlo simulations verify the reasonable of theoretical analysis. Finally, when in real sense, minimum SSR is presented, and requirements of intermediate spoofing is also summarized. Research in the paper relax restriction of intermediate spoofing, and make it closer to real sense, so it has a guiding significance for designing of GNSS spoofer.

47.2 Model and Influence Factors

47.2.1 Principle of Intermediate Spoofing

When in tracking mode, the tracking loop keeps tracking the correlation peak of authentic signal. If the two signals are aligned, spoofing signal tries to take over the tracking loop by higher power, until the loop tracks the spoofing signal. Ideal intermediate spoofing works as Fig. 47.1 [2]. First, spoofing signal enters the

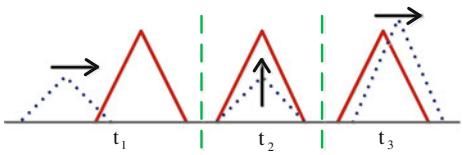

Fig. 47.1 Schematic diagram of intermediate spoofing

tracking loop with a low power and a different code rate (t_1); then, after it is aligned with the authentic signal, power of spoofing signal begins to increase until it is larger than that of authentic signal, in this case, the tracking loop locks on the spoofing signal (t_2); finally, the spoofing signal moves away from the authentic signal and take over the tracking loop, until the two signals are not overlap.

In real sense, due to the inaccurate position, code phase and carrier phase are difficult to align completely, estimating carrier Doppler is also inaccurate. Therefore, spoofer may be increasing its power at a wrong time (e.g. t_1), which weakens the performance of spoofing.

47.2.2 Signal Model

GPS intermediate frequency (IF) signal can be expressed as Eq. 47.1 [7]. Here, A is signal's amplitude; C(n) is GPS C/A code; D(n) is navigation message; f is carrier frequency; φ is carrier phase; w(n) is white Gaussian noise (WGN).

$$S(n) = AC(n)\,D(n)\,\cos\left(2\pi fn + \varphi\right) + w(n) \tag{47.1}$$

There are some differences on signal parameters between spoofing signal and authentic signal. After spoofing signal is added, signal received can be expressed as Eq. 47.2. Here, α is quotient of spoofing signal and authentic signal, which is another representation of SSR. $C'(n)$ is C/A code of spoofing signal, and it has tiny frequency difference with authentic signal; f' is carrier frequency of spoofing signal; φ' is carrier phase of spoofing signal; τ is signals' interval.

$$S'(n) = AC(n)\,D(n)\cos\left(2\pi fn + \varphi\right) + \alpha AC'(n-\tau)\,D(n)\cos\left(2\pi f'n + \varphi'\right) + w(n) \tag{47.2}$$

When in tracking stage, carrier loop generates local IF carrier signal $\cos\left(2\pi f_i n\right)$, and then it down-conversions the signal received to baseband; code loop generates local C/A code and dispreading the baseband signal. Then, envelop $I^2 + Q^2$ is formed and can be expressed as Eq. 47.3.

$$\begin{aligned} I^2 + Q^2 \approx \{&[R(t)\,\mathrm{sinc}\left(f_d T\right)]^2 + [\alpha R'(t-\tau)\,\mathrm{sinc}\left(f'_d T\right)]^2 \\ &+ 2\alpha R(t)\,R'(t-\tau)\,\mathrm{sinc}\left(f_d T\right)\mathrm{sinc}\left(f'_d T\right)\cos\left(2\pi\Delta f_d T + \Delta\varphi\right)\}A^2 + w_I^2 + w_Q^2 \end{aligned} \tag{47.3}$$

Here, R(t) is the correlation function and can be expressed as Eq. 47.4; $R^{'}(t)$ is also the correlation function but influenced by code rate difference, it can be expressed as Eq. 47.5 [8]; f_d and f'_d is residual carrier Doppler; $\Delta f_d = f'_d - f_d$ is carrier-frequency difference between spoofing signal and authentic signal; w_I and w_Q is WGN.

$$R(t) = \begin{cases} t+1, & -1 \le t < 0 \\ -t+1, & ;0 \le t \le 1 \\ 0, & \text{others} \end{cases} \tag{47.4}$$

$$R'(t) = \beta R(t) = R(t) * \begin{cases} 1 - 0.25|f_{d,c}T|, & |f_{d,c}T| \le 2 \\ 1/(f_{d,c}T), & |f_{d,c}T| > 2 \end{cases} \tag{47.5}$$

Known from Eq. 47.3, $I^2 + Q^2$ is still non-central chi-square distribution, and the non-central parameter reflects signals' interaction.

47.2.3 Influence Factors of SSR

47.2.3.1 Standard of Successful Spoofing

Because of the interaction between spoofing signal and authentic signal, power of hybrid signal is not simple overlay. In particular, when the carrier-phase difference is 180°, which means $\Delta\alpha = \pi$, power of the two signals cancels each other out as Eq. 47.3. Therefore, there is no significance to compare with power of signal separately. In the paper, we define the standard of successful spoofing as follows: if the correlation peak of hybrid signal is at least γ times than that of authentic signal, we say it is a successful spoofing.

Given the spoofing successful probability η, quotient of spoofing signal and authentic signal can be calculated by Eq. 47.6. Here, $P_d^s(z, d, \lambda)$ and $P_d^j(x, d, \lambda)$ are density probability of authentic signal and hybrid signal, and they can be got from Ref. [7].

$$\eta = \int_0^{\infty} \int_{\gamma x}^{\infty} P_d^s(z, d, \lambda) P_d^j(x, d, \lambda') d_z d_x \tag{47.6}$$

Equation 47.6 is very complicated and hard to get analytical expression explicitly, so the theoretical value can be calculated only by simulation. Note that spoofing is slow and we want to find the minimum SSR, so first we need to identify a minimum tolerable spoofing successful probability, in the following part, we consider it as 50 %.

When non-central parameter of chi-square distribution is large enough, the distribution is Gaussian distribution approximately. In this case, probability density function is symmetrical. In Fig. 47.2, if $J2 = \gamma S2$, we know that $J1 = \gamma S1$ and $J3 = \gamma S3$, and then when correlation peaks of authentic signal are S1 and S3,

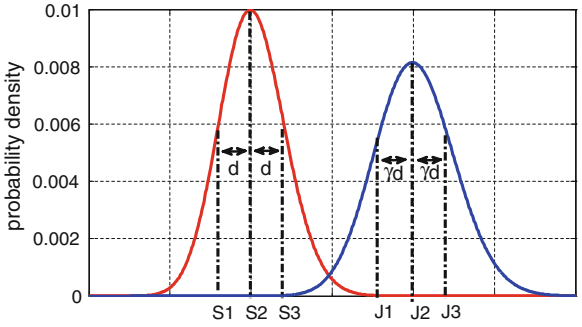

Fig. 47.2 Schematic diagram of probability density

spoofing successful probability can be expressed as Eq. 47.7. Thus, Eq. 47.6 can be simplified as Eq. 47.8. Obviously, if J2 > γS2, spoofing successful probability is larger than 50 %, and if J2 > γS2, spoofing successful probability is less than 50 %. In this case, if the standard above is established, mean of hybrid signal is γ times of that of authentic signal.

$$\begin{aligned}\eta' &= P_d^s(S1,d,\lambda)\int_{J1}^{\infty} P_d^j(x,d,\lambda')d_x + P_d^s(S3,d,\lambda)\int_{J3}^{\infty} P_d^j(x,d,\lambda')d_x \\ &= P_d^s(S1,d,\lambda)\left(\int_{J1}^{\infty} P_d^j(x,d,\lambda')d_x + \int_{J3}^{\infty} P_d^j(x,d,\lambda')d_x\right) = P_d^s(S1,d,\lambda)\end{aligned} \tag{47.7}$$

$$\eta = \int_0^{S2} P_d^s(x,d,\lambda)d_x = 50\,\% \tag{47.8}$$

Mean of non-central chi-square distribution equals to the no-central parameter approximately, which is also the signal-to-noise ratio (SNR). Known from Eq. 47.3, SNR of authentic signal and hybrid signal can be expressed as Eqs. 47.9 and 47.10. Here, σ is noise power.

$$\lambda = (AR(t)\ \mathrm{sinc}\ (f_d T)/\sigma)^2 \tag{47.9}$$

$$\begin{aligned}\lambda' \approx\ & \{[R(t)\,\mathrm{sinc}\,(f_d T)]^2 + [\alpha R'(t-\tau)\,\mathrm{sinc}\,(f_d' T)]^2 \\ & + 2\alpha R(t)R'(t-\tau)\,\mathrm{sinc}\,(f_d T)\,\mathrm{sinc}\,(f_d' T)\cos(2\pi\Delta f_d T + \Delta\varphi)\}(A/\sigma)^2\end{aligned} \tag{47.10}$$

Suppose that when there is no spoofing signal, local signal and authentic signal are aligned, and when spoofing is successful, local signal and spoofing signal are aligned. So in Eq. 47.9, t = 0, f_d = 0 and in Eq. 47.10, t = τ, f_d' = 0. Theoretical discriminant formula of successful spoofing is expressed as Eq. 47.11.

$$\begin{aligned}L(\Delta f_d, \Delta\varphi, f_{d,c}, \tau) &= \lambda'(t=\tau, f_d'=0)/\lambda(t=0, f_d=0) \\ &= [R(\tau)\,\mathrm{sinc}\,(\Delta f_d T)]^2 + (\alpha\beta)^2 \\ &\quad + 2\alpha\beta R(\tau)\,\mathrm{sinc}\,(\Delta f_d T)\cos(2\pi\Delta f_d T + \Delta\varphi) > \gamma\end{aligned} \tag{47.11}$$

47.2.3.2 Influence Factors

Equation 47.12 is the condition of Eq. 47.11, and it describes the influence effect of carrier-frequency difference, carrier-phase difference, code rate difference and signals' interval. Once $\gamma > 1$, the constraint succeeds. Following is influence effect of each factor.

$$\begin{aligned} \alpha > & [-R(\tau)\,\mathrm{sinc}\,(\Delta f_d T)\cos(2\pi\Delta f_d T + \Delta\varphi) \\ & + \sqrt{\gamma - R^2(\tau)\,\mathrm{sinc}^2(\Delta f_d T)\sin^2(2\pi\Delta f_d T + \Delta\varphi)}]/\beta \\ & s.t.\ \gamma - R^2(\tau)\,\mathrm{sinc}^2(\Delta f_d T)\sin^2(2\pi\Delta f_d T + \Delta\varphi) > 0 \end{aligned} \tag{47.12}$$

In an ideal condition, $\Delta\varphi = 0, f_{d,c} = 0, \tau = 0$, then we can get the influence of carrier-frequency difference due to Eqs. 47.4, 47.5, and 47.12, which can be expressed as Eq. 47.13.

$$\alpha > \sqrt{\gamma - \mathrm{sinc}^2(\Delta f_d T)\sin^2(2\pi\Delta f_d T)} - \mathrm{sinc}\,(\Delta f_d T)\cos(2\pi\Delta f_d T) \tag{47.13}$$

Let $\Delta f_d = 0, f_{d,c} = 0, \tau = 0$, we can get the influence of carrier-phase difference due to Eqs. 47.4, 47.5, and 47.12, which can be expressed as Eq. 47.14.

$$\alpha > \sqrt{\gamma - \sin^2(\Delta\varphi)} - \cos(\Delta\varphi) \tag{47.14}$$

Let $\Delta f_d = 0, \Delta\varphi = 0, \tau = 0$, we can get the influence of code rate difference due to Eqs. 47.4 and 47.12, which can be expressed as Eqs. 47.5 and 47.15.

$$\alpha > (\sqrt{\gamma} - 1)/\beta \tag{47.15}$$

Let $\Delta f_d = 0, \Delta\varphi = 0, f_{d,c} = 0$, we can get the influence of signals' interval due to Eqs. 47.5 and 47.12, which can be expressed as Eqs. 47.4 and 47.16.

$$\alpha > \sqrt{\gamma} - R(\tau) \tag{47.16}$$

47.3 Experiment Results

47.3.1 Condition of Experiments

A series of Monte Carlo simulations are made to research the influence effect of factors. In the experiments, IF signal of GPS No. 5 C/A code is generated by signal simulator, and its frequency is 3.563 MHz, SSR is −19 dB. Correlation peak of Prompt is mean of authentic signal. After adjudging parameters of spoofing signal,

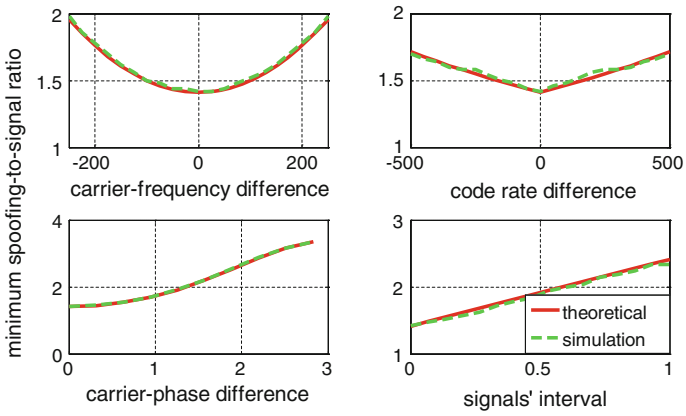

Fig. 47.3 Influence of single factor

we notice the correlation peak of Prompt, and simulate the spoofing successful probability by multiple-run. In particular, when the power of hybrid signal is 3 dB larger than the authentic signal, which means $\gamma = \left(\sqrt{2}+1\right)^2 \approx 5.8$, we regard a successful spoofing.

47.3.2 Analysis of Influence Factors

Equations 47.13–47.16 are theoretical formulas in an ideal condition, simulations can be made to verify their reasonability. Figure 47.3 is the comparison chart. We can see that the theoretical curve and simulation curve are almost superpose, and the slight difference are caused by finite Monte Carlo simulation times and points. So the results shows that the theoretical analysis is reasonable.

Figure 47.4 shows the influence effect of carrier-frequency difference and signals' interval. We can see that if there is carrier-frequency difference, tracking loop won't lock on the true frequency, which decreases correlation peak of authentic signal, thus, correlation peak of hybrid signal is also decreases. Therefore, in some range, if influence of carrier-phase difference is not considered, minimum SSR increases as the carrier-frequency difference increasing.

Figure 47.5 shows the influence effect of carrier-phase difference and signals' interval. As signals' interval increases, interaction between spoofing signal and authentic signal weakens. When carrier-phase difference is smaller than $\pi/2$, which means $\cos(\Delta\varphi) > 0$, it can prompt power's aggregation, so as signals' interval increases, SNR loss caused by interaction occupies the dominant position, and the minimum SSR increases; while when carrier-phase difference is between $\pi/2$ and π, which means $\cos(\Delta\varphi) < 0$, it can inhibit power's aggregation, so as signals' interval increases, this inhibition ability weakens gradually, and the minimum SSR

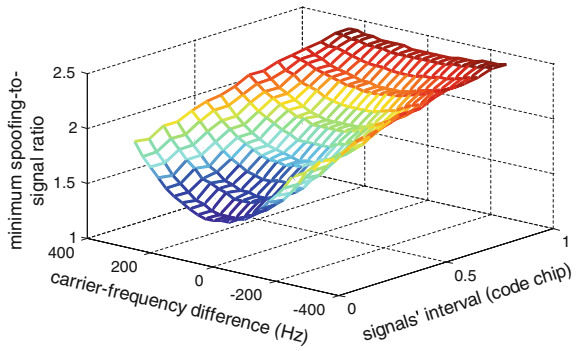

Fig. 47.4 Influence of carrier-frequency difference and signals' interval

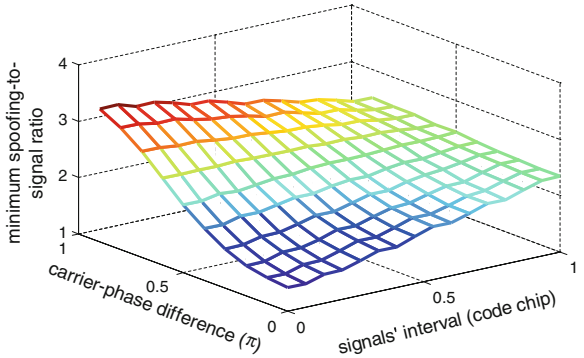

Fig. 47.5 Influence of carrier-phase difference and signals' interval

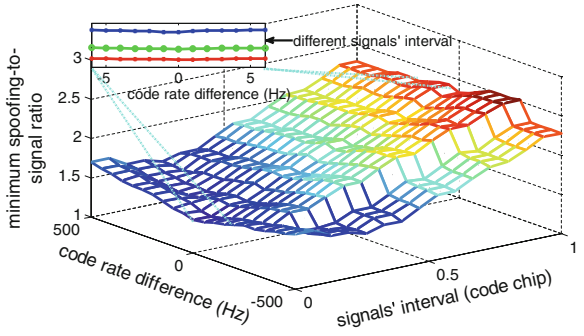

Fig. 47.6 Influence of code rate difference and signals' interval

decreases. What is more, when carrier-phase difference is in $[0, \pi]$,$\cos(\Delta\varphi)$ is monotone decreasing. So if fixing signals' interval, SNR of hybrid signal decreases, thus, minimum SSR increases as carrier-phase difference increasing.

Figure 47.6 shows the influence effect of code rate difference and signals' interval. We know that β changes slowly compared with code rate in Eq. 47.5, so influence of code rate difference is not explicit. On the whole, as the absolute value of code rate difference increases, the minimum SSR becomes larger. However,

code Doppler in the receiver belongs to [−3 Hz, 3 Hz], so code rate difference belongs to [−6 Hz, 6 Hz]. In Fig. 47.6, when code rate difference is in this range, it has little influence on the minimum SSR.

47.4 Requirements of Intermediate Spoofing

In the receiver, carrier loop involves frequency-locked loop and phase-locked loop, which ensures both the dynamic range and phase accuracy. Typically, frequency accuracy in acquisition is 500 Hz, so this is the range of carrier-frequency difference, thus, $-250\,\mathrm{Hz} < \Delta f_d < 250\,\mathrm{Hz}$; if the accuracy of receiver position is not centimeter-level, it is larger than the carrier wavelength, so carrier-phase difference may be any value, thus, $0 < \Delta\varphi < 2\pi$; if the carrier Doppler reaches 10 KHz, the code Doppler will be 6 Hz, so range of code rate difference is [−6 Hz, 6 Hz]; In tracking stage, if code phase offset is smaller than 1 code chip, code loop can deal with this successfully, so signals' interval is also in this range, thus, $\tau < 1$ code chipand the position accuracy is 300 m approximately.

After that, the minimum SSR can be calculated by Eq. 47.12. Let $x = R(\tau)\,\mathrm{sinc}\,(\Delta f_d T)$ and $y = \cos(2\pi\Delta f_d T + \varphi)$, range of x and y is easy to verified now. Therefore, calculating minimum SSR is an optimization problem, as Eq. 47.17.

$$\text{s.t.}\begin{cases} \max\left(\sqrt{\gamma - x^2 + x^2y^2} - xy\right)/\beta \\ -\frac{2}{3\pi} \le x \le 1 \\ -1 \le y \le 1 \\ \beta \approx 1 \end{cases} \tag{47.17}$$

The Maximum value can be selected form extreme points or boundary points, and the extreme points can be verify from Eq. 47.18. Easy to know when $x = 0$ and $y = 0$, extreme value is selected. Therefore, compared the function value in extreme point and boundary points, we can obtain the minimum SSR. Here, when $x = 1$ and $y = -1$, minimum SSR can be expressed as Eq. 47.19. In this condition, carrier-frequency difference is 0, carrier-phase difference is π and signals' interval is 0.

$$\begin{cases} \partial z/\partial x = x(y^2 - 1)/\sqrt{\gamma - x^2 + x^2y^2} - y = 0 \\ \partial z/\partial y = x^2y/\sqrt{\gamma - x^2 + x^2y^2} - x = 0 \end{cases} \tag{47.18}$$

$$\alpha \approx \sqrt{\gamma} + 1 \tag{47.19}$$

In particular, let $\gamma = \left(\sqrt{2} + 1\right)^2 \approx 5.8$, then $\alpha \approx 3.414$, which is 10.66 dB. The result is consistent with Fig. 47.5. Requirements of intermediate spoofing can be summarized as Table 47.1.

Table 47.1 Requirements of intermediate spoofing

Characteristic	Range
Carrier-frequency difference	[−250, 250] Hz
Code rate difference	[−6, 6] Hz
Position accuracy	<300 m
Spoofing-to-signal ratio	>10.66 dB

47.5 Conclusions

Through the attack model of intermediate spoofing, the paper presents a theoretical discriminant formula of successful spoofing, and analysis the influence of carrier-frequency difference, carrier-phase difference, code rate difference and signals' interval. Experiments shows the reasonability of theoretical analysis. What's more, when in a reasonable range, code rate difference can hardly influence the minimum SSR; when carrier-phase difference is between 0 and $\pi/2$, the minimum SSR increases as signals' interval increasing, while when it is between $\pi/2$ to π, the minimum SSR decreases as signals' interval increasing; influence of carrier-frequency difference and carrier-phase difference is closely intertwined, so it's difficult to evaluate separately. Finally, with an inaccurate condition, calculation formula of the minimum SSR is presented, which is independent on influence factors. Thus, requirements of intermediate spoofing are listed. Research in this paper extends the application range of intermediate spoofing and make it more suitable for real sense, so it has a guiding significance for designing spoofer.

References

1. Anonymous (2001) Vulnerability assessment of the transportation infrastructure relying on the global positioning system. Techecnical report, John A. Volpe National Transportation Systems Center
2. Humphreys TE et al (2008) Assessing the spoofing threat: development of a portable GPS civilian spoofer. In: Proceedings of ION GNSS meeting, 2008
3. Shepard DP, Bhatti JA, Humphreys TE, et al (2012) Evaluation of smart grid and civilian UAV vulnerability to GPS spoofing attacks. In: Proceedings of ION GNSS meeting, 2012
4. http://www.insidegnss.com/node/3659
5. Jafarnia-Jahromi A, Lin T et al (2012) Detection and mitigation of spoofing attacks on a vector based tracking GPS receiver. In: Proceedings of the ITM of the Institute of Navigation, 2012
6. Tippenhauer NO, Pöpper C, Rasmussen KB et al (2011) On the requirements for successful GPS spoofing attacks. In: Proceedings of the 18th ACM conference on computer and communications security. ACM, 2011, pp 75–86
7. Parkinson B et al (1996) The global positioning system: theory and application, vol 1. AIAA, 1996
8. Li CX, Wang FX, Guo G (2007) Correlation of PN spread spectrum signal under first-order dynamics. Acta Electronica Sinica 35(9):1789–1793

Chapter 48
Tracking Loop Model and Hardware Prototype Verification of GNSS/INS Deep Integration

Tisheng Zhang, Hongping Zhang, Yalong Ban, Xiaoji Niu and Jingnan Liu

Abstract There is no systematic and complete theoretical model for signal tracking loop of the GNSS/INS deep integration. And the performance of the deeply-coupled system based on hardware prototype hasn't been fully verified. These limitations block the progress and application of the GNSS/INS deeply-coupled technology. This paper studies the GNSS/INS deeply-coupled technology based on the scalar deep integration for GPS L1 receiver. It establishes the transfer functions between the error sources (including thermal noise, oscillator phase noise, inertial measurement unit (IMU) error, the delay of Doppler aiding information) and the tracking loop error of the deep integration. And then the steady state tracking model is proposed and analyzed. A hardware/software integrated GNSS/INS scalar deep-coupled prototype is successfully developed, and real-time optimizations are made in terms of the system operation and aiding information delay. The performance of the designed deeply coupled prototype is fully evaluated based on a GPS/IMU hardware simulator and outdoor tests. The result shows that the INS aiding could improve the steady state's tracking performance by extending the integration time to 20 ms and by compressing the bandwidth to 3 Hz under normal dynamic conditions. The proposed error models, designed methods, and hardware prototype developed in this paper can be further applied to the key performance study of the GNSS/INS deeply coupled system, such as the sensitivity and anti-interference under dynamic conditions.

Keywords GNSS/INS deep integration · INS aided tracking loop · Error transfer function · Deeply-coupled hardware prototype

T. Zhang (✉) · H. Zhang (✉) · Y. Ban · X. Niu · J. Liu
GNSS Research Center of Wuhan University, Wuhan, China
e-mail: zts@whu.edu.cn

H. Zhang
e-mail: hpzhang@whu.edu.cn

J. Sun et al. (eds.), *China Satellite Navigation Conference (CSNC) 2014 Proceedings: Volume I*, Lecture Notes in Electrical Engineering 303,
DOI: 10.1007/978-3-642-54737-9_48,

48.1 Introduction

Global navigation satellite system (GNSS) and inertial navigation system (INS) are highly complementary. Therefore the research and development of GNSS/INS integrated navigation have been a hot spot in the past two decades [1]. According to the GNSS information used for data fusion, GNSS/INS integrated navigation could be divided into loosely-coupled system that based on GNSS navigation results, tightly-coupled system based on GNSS observations, and deeply-coupled system based on GNSS baseband signals [2, 3]. The deeply coupled system, which was originally proposed at year 2000, could further take advantage of the dynamic characteristics of INS to improve the acquisition and tracking performance of satellite signals in the GNSS receivers [4].

According to the architecture of GNSS receiver's tracking loop, the deeply coupled systems are divided to scalar and vector mode [5]. The scalar deeply coupled system is based on the conventional GNSS receiver tracking loops, with independent tracking channels. The INS aiding information is inserted into each channel of tracking loop to help the signal tracking separately [6]. Therefore, the scalar deeply couple is relatively simple, reliable, and easy to implement. In the vector deeply coupled system, the INS data and the GNSS signal tracking data are integrated in a centralized navigation filter to make a centralized data fusion mechanism. Then the estimations from the filter are feedback to control every tracking channel, which forms a unified signal tracking strategy [7, 8]. Therefore, the vector deeply couple can make best use of the available information and get better performance. However, because of the system complexity and the heavy computation load, it is a challenge to develop a stable and reliable real-time vector deeply coupled system that can head for engineering and production. Moreover, for the estimation accuracy of the Kalman filter can't meet the needs of the carrier phase, the carrier phase must be tracked by scalar tracking loop. Therefore, this paper's work focuses on the modelling of the tracking loop, the hardware system implementation and the tests' verification.

The inertial-aided tracking loop is the key of the scalar deep integration. Scholars did some researches on the deeply-coupled technologies, including the model and analysis of the inertial-aided tracking loop, the affect of the crystal and the IMU quality, the synchronization of the INS information and the tracking loop, the system performance analysis. 2003 Alban from Stanford proposed a model of the inertial-aided tracking loop, in which the IMU model and the feed-forward branch model were oversimplified, and the transfer function could not be used for quantitative analysis of the tracking error and other performances of the tracking loop. However, the model has not been further improved [9]. In the deep integration hardware system, the INS information has more or less delay compared to tracking loop, but the delay was considered in the inertial-aided tracking loop model in no literature. 2008 Tang and Ye, respectively, studied the optimal bandwidth of the inertial aided tracking loop to provide bandwidth value for different IMU, different C/N. However, the specific model between IMU devices

error and tracking error was not given [10, 11]. The deeply-coupled system development requests a relatively high technical threshold, in which the receiver's baseband need be adjusted. Deeply coupled systems were developed on software platforms for research institutions at home and abroad, while companies developed hardware systems through cooperation [12, 13].

With GPS L1 single frequency receiver for example, based on GNSS/INS scalar deep integration, this paper builds the model between error sources (including thermal noise, oscillator phase noise, inertial measurement unit (IMU) error, and the delay of Doppler aiding information) and the tracking loop error of the deep integration. And then it proposes and analyzed the INS aided tracking loop's steady state error model. Moreover, it develops an integrated real-time GNSS/INS scalar deeply-coupled hardware prototype system, and optimizes the prototype for running real-time and INS information delay. Finally, the performance of the designed deeply coupled prototype is fully evaluated based on a GPS/IMU hardware simulator and tests.

48.2 Error Model of INS Aided Tracking Loop

48.2.1 Principle of INS Aided Tracking Loop

The scalar deeply coupled system structure is shown in Fig. 48.1. The upper part is the GPS receiver subsystem, while the lower part is the inertial navigation subsystem. The two subsystems assist each other through information exchanging. The system structure shows that the two subsystems in the scalar mode deep integration are relatively independent, whose internal structure need be adjusted relatively small. The difference between deeply coupled system and loosely coupled system, tightly coupled system is that the INS information is also sent to the receiver's baseband (red arrows in Fig. 48.1) in the deeply coupled system, realized the assistance to the receiver at signal level.

Since GPS receiver and INS are two sensors, they measure in different ways to calculate navigation information. The vehicle dynamic information is measured respectively by receiver and INS, so the INS results could be used to assist the receiver. Since the dynamic changes are responded by the tracking loops in the receiver, the INS measured dynamic information could be fed forward into the tracking loops.

The block diagram of the INS aided tracking loop is shown in Fig. 48.2 [14]. The lower part is the tracking loop branch, consistent with the normal structure of the carrier loop. Since the GPS antenna measures dynamic changes through receiving satellites' signal, the direct measured result is the relative dynamic changes of the GPS antenna and the satellite on line of their sight (LOS). Therefore, there is a LOS projection between the vehicle and the receiver RF. The upper part is the INS branch, the measurements of gyros and the accelerometers

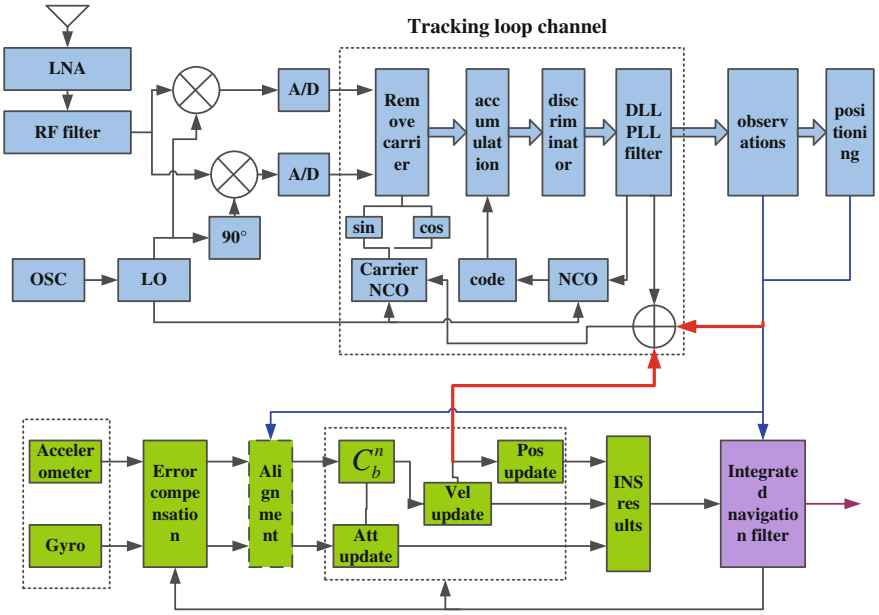

Fig. 48.1 Block diagram of scalar deeply coupled system

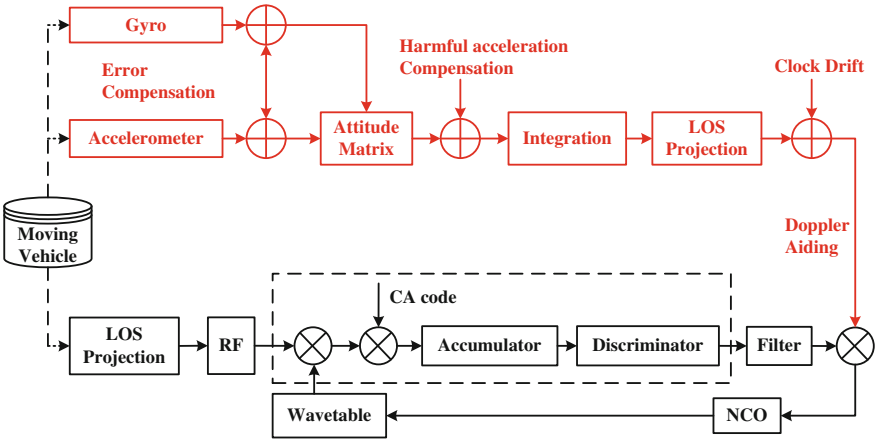

Fig. 48.2 Block diagram of INS aided tracking loop

are not dependent on external information, while the accelerometers directly measure the vehicle's acceleration (including earth's gravity), the gyros measure angular rate. The Doppler aiding information by combining the Doppler measured by INS after LOS projection and the receiver's clock drift, which as the feed forward part is sent into the receiver's carrier tracking loop. When the system is

realized, the update of the Doppler aiding information and the tracking loop can't be completely synchronous, so the time-delay is added before aiding the tracking loop.

48.2.2 Error Sources of Tracking Loop

Figure 48.2 shows that the error caused by feed forward branch includes INS measurement error and Doppler delay error. The INS measurement error could be divided into IMU bias type error which is unrelated with dynamic and IMU scale factor type error which is related with dynamic. While the IMU bias type error includes the IMU device error (constant bias, bias instability, white noise) and the initial navigation error which has been corrected by coupled navigation results (velocity error and attitude error), the IMU scale factor type error includes IMU scale factor error and non-orthogonal error. The Doppler delay error is the non-synchronization of aiding information and tracking loop, which is caused by the non-synchronization of IMU and GNSS data collection, INS information computing and transfer delay, the different update rate of aiding information and tracking loop information.

While the normal tracking loop's error sources include thermal noise, oscillator phase noise and vehicle dynamic, the INS aided tracking loop's error sources include thermal noise, oscillator phase noise, IMU bias type error, IMU scale factor type error and Doppler delay error. With the INS assistance, the affect of vehicle dynamic on the tracking loop is replaced by IMU bias type error, IMU scale factor type error and Doppler delay error. Figure 48.3 shows the block diagram of the INS aided tracking loop displaying the affection of different error sources [14].

It is sum of all the error sources affecting the tracking error $\delta\theta$. The thermal noise ω_φ and the oscillator phase noise θ_{clk_error} are independent of each other. While the oscillator phase noise is added to the input signal θ_i through the multiply of the local signal and the input signal, the thermal noise is superimposed on the input signal when the input signal flows through the tracking loop. Therefore, their affects on the tracking error are independent of each other, and the normal tracking loop's error is analyzed based on this condition. The Doppler aiding information output from INS is physically independent of tracking loop's error. The sum of Doppler aiding information and the output from loop filter is used to control the NCO, so the affect of the INS branch on the tracking error is independent from the affect of the thermal noise and the oscillator phase noise. The IMU bias type error Δf_{IMU}, the IMU scale factor type error K_a and the Doppler aiding delay e^{-st_0} are independent, and their contribution to the Doppler aiding information's error are additive. Therefore, the affects on the tracking error from all the error sources are independent and additive.

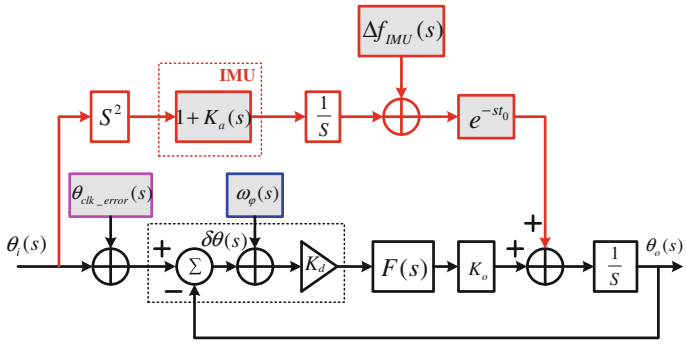

Fig. 48.3 Block diagram of INS aided tracking loop displayed the error sources affect

48.2.3 Error Transfer Function

Since the simple structure's normal tracking loop, the error transfer function can be deduced by the tracking loop model. The structure becomes more complex and the types of error sources increase after the INS aiding, and then the function between each error source and the tracking error can't be deduced directly. Because the error sources of the INS aided tracking loop are physically independent, and their affects on the tracking error are additive, the error transfer function between each error source and the tracking error could be researched individually.

The function between IMU bias type error and tracking error is analyzed as an example. Assuming there is only IMU bias type error in the feed-forward branch, the thermal noise and oscillator phase noise are also not considered, Fig. 48.4 shows the affect of the IMU bias on tracking error.

The function of $\delta\theta$ and Δf_{IMU} can be deducted based on Fig. 48.4:

$$\delta\theta(s) = \theta_i(s) - \theta_o(s) = -\frac{1}{s}\Delta f_{IMU}(s)(1 - H(s)) = -\frac{1}{s}\frac{1}{1 + \frac{K_d K_o F(s)}{s}}\Delta f_{IMU}(s) \tag{48.1}$$

$\frac{\Delta f_{IMU}(s)}{s}$ represents the IMU bias type error caused by the feed–forward branch, which needs the tracking loop to bear. And $(1 - H(s))$ is the error propagation function of the normal tracking loop. Therefore, the result matches with intuitive understanding.

The functions of other error sources and the tracking error can be analyzed using the same method. Since the affects of all the error sources on the tracking error are independent, the tracking error caused by all the error sources could be obtained by adding every error source's effect result.

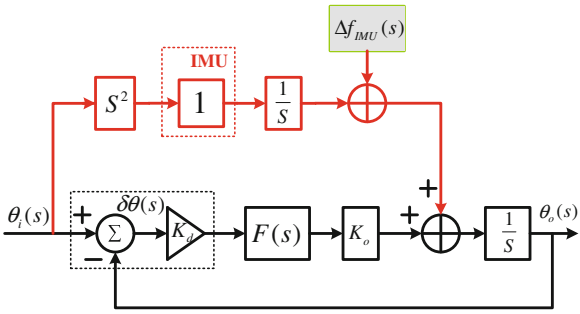

Fig. 48.4 Block diagram of INS aided tracking loop displayed IMU bias type error affect

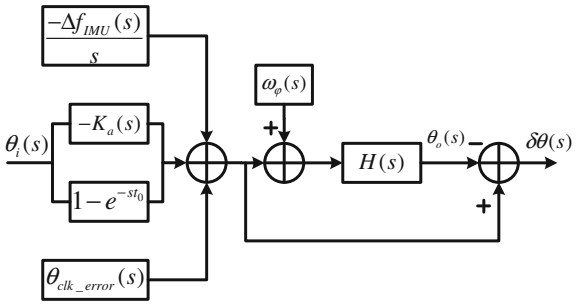

Fig. 48.5 Block diagram of INS aided tracking loop's error transfer function

$$\delta\theta(s) = (1 - H(s))\left(\theta_{clk\_error}(s) - K_a(s)\theta_i(s) - \frac{\Delta f_{IMU}(s)}{s} + (1 - e^{-st_0})\theta_i(s)\right) - H(s)\omega_\varphi(s) \tag{48.2}$$

The schematic diagram of INS aided tracking loop's error function is shown as Fig. 48.5 based on formula 48.2.

48.3 Error Analysis of Tracking Loop

48.3.1 Steady-State Error of Normal Second-Order PLL

Assuming σ_{PLL} represents a mean square error of the carrier phase measurement error, and σ_{tPLL} is the thermal noise, σ_{rv} is vibration-induced oscillator phase noise, σ_{rA} is Allan deviation oscillator phase noise, and θ_e is dynamic stress error. A conservative rule of thumb for tracking threshold is that the 3-sigma jitter must not exceed one-fourth of the phase pull-in range of the PLL discriminator [15].

$$\sigma_{PLL} = \sqrt{\sigma_{tPLL}^2 + \sigma_{rv}^2 + \sigma_{rA}^2} + \theta_e/3 \leq 15^\circ \tag{48.3}$$

The formula of the thermal noise's mean square error is

$$\sigma_{tPLL}^2 = \frac{0.53\omega_n}{C/N_0}\left[1 + \frac{1}{2T_{coh} \cdot C/N_0}\right] \tag{48.4}$$

The tracking error caused by the thermal noise is closely related to carrier to noise ratio C/N_0, noise bandwidth B_n, and coherent integration time T_{coh}.

For the second-order PLL, the vibration-induced oscillator phase noise could be expressed as [15]:

$$\sigma_{rv}^2 = \frac{\pi f_0^2 K_g^2 G_g}{2\sqrt{2} f_n} = \frac{\pi^2 f_0^2 K_g^2 G_g}{\sqrt{2}\omega_n} \tag{48.5}$$

In the formula, K_g is the g-sensitivity, and $G_g(f)$ is the power spectral density of vibration, f_0 is carrier frequency.

For the second-order PLL, the Allan deviation oscillator phase noise could be expressed as [16]:

$$\sigma_{rA}^2 = 2\pi^2 f_0^2 \left[\frac{\pi^2 h_{-2}}{\sqrt{2}\omega_n^3} + \frac{\pi h_{-1}}{4\omega_n^2} + \frac{h_0}{4\sqrt{2}\omega_n}\right] \tag{48.6}$$

h coefficient reflects the stability of the crystal.

For the second-order PLL, the dynamic stress error caused by frequency ramp dynamic $\Delta\Re$ could be expressed as [16]:

$$\Delta\Re\delta\theta = \frac{\Delta\Re}{3\omega_n^2} \tag{48.7}$$

Therefore, the steady-state error model of second-order PLL could be expressed as:

$$\sigma_{PLL} = \sqrt{\frac{0.53\omega_n}{C/N_0}\left(1 + \frac{1}{2T_{coh} \cdot C/N_0}\right) + \frac{\pi^2 f_0^2 K_g^2 G_g}{\sqrt{2}\omega_n} + 2\pi^2 f_0^2 \left(\frac{\pi^2 h_{-2}}{\sqrt{2}\omega_n^3} + \frac{\pi h_{-1}}{4\omega_n^2} + \frac{h_0}{4\sqrt{2}\omega_n}\right) + \frac{\Delta\Re}{3\omega_n^2}} \tag{48.8}$$

48.3.2 Steady-State Error of INS Aided Second-Order PLL

Under vehicle dynamic conditions, the IMU bias type error is the main aiding information error factor, so the IMU bias type error need be modeled in detail, and the IMU scale factor type error is simply modeled as a random constant. Starting from INS velocity differential equations, simplify and add error disturbance to get

error equations, and convert to Laplace domain. Then considering the IMU device error and the initial navigation error, assuming that the satellite is in the north of the vehicle, $\Delta f_{IMU}(s)$ can be expressed as [17]:

$$\Delta f_{IMU}(s) = \frac{2\pi}{\lambda}\left\{\frac{1}{s}\cdot\left[\frac{b_{ax\_c}}{s}+\frac{GM_{ax}(0)+w_{GMax}(s)}{s+\frac{1}{T_a}}+w_{ax}(s)\right]\right.$$
$$\left.+\frac{g}{s^2}\cdot\left[\frac{b_{gy\_c}}{s}+\frac{GM_{gy}(0)+w_{GMgy}(s)}{s+\frac{1}{T_g}}+w_{gy}(s)\right]+\frac{1}{s}\cdot\delta V_N(0)+\frac{g}{s^2}\cdot\phi_E(0)\right\} \tag{48.9}$$

Bringing Eqs. (48.9) into (48.1), the specific model that reflects the relationship of the IMU bias type error and the tracking error. In literature 14, the influence of each error component to the tracking error in the navigation update time interval was analyzed in detail based on the specific model. Its results showed that in the IMU bias type error, the initial velocity error component was the main factors to the tracking error. Because the tracking error caused by IMU bias type error periodically changes with the integration navigation updated, the maximum tracking error caused by the initial velocity error can be set as IMU bias type error's contribution to the loop steady-state error. The maximum tracking error caused by the initial velocity error can be obtained by converting its error transfer function into time domain and calculating its derivative.

$$\theta_{V0} = \frac{2\pi\cdot\delta V_N(0)}{\lambda\cdot e\cdot\omega_n} \tag{48.10}$$

For the INS aided second-order PLL, frequency ramp input could make IMU scale factor type error generate loop steady-state error. Starting from the transfer function of IMU scale factor type error and the tracking error, when the IMU scale factor type error is modelled as a random constant, the steady-state error could be obtained by calculating its derivative in time domain.

$$\theta_{K_a} = \frac{K_a\cdot\Delta\Re}{\omega_n^2} \tag{48.11}$$

Since the tracking error caused by the Doppler delay occurs only when the vehicle dynamic changes, and the error can quickly converge to zero, steady-state error analysis need not consider the Doppler delay. Therefore, the steady-state error model of the INS aided second-order PLL can be written as [14]:

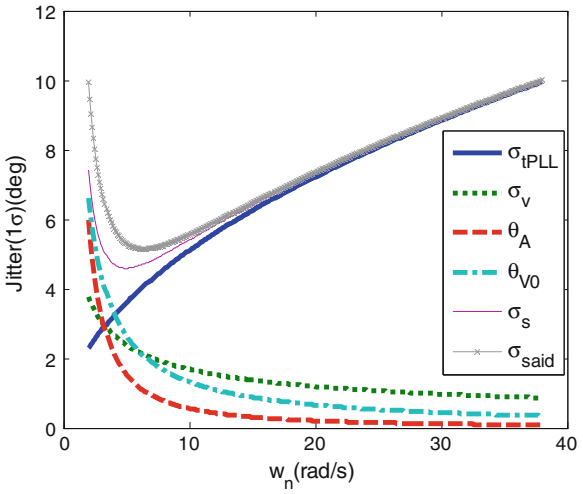

Fig. 48.6 Tracking loop's error with and without INS aiding in static conditions

$$\sigma_{Aid\_PLL} = \sqrt{\begin{array}{l}\dfrac{0.53\omega_n}{C/N_0}\left(1\dfrac{1}{2T_{coh}\cdot C/N_0}\right)+\dfrac{\pi^2 f_0^2 K_g^2 G_g}{\sqrt{2}\omega_n} \\ +2\pi^2 f_0^2\left(\dfrac{\pi^2 h_{-2}}{\sqrt{2}\omega_n^3}+\dfrac{\pi h_{-1}}{4\omega_n^2}+\dfrac{h_0}{4\sqrt{2}\omega_n}\right)+\left(\dfrac{2\pi\cdot\delta V_N(0)}{\lambda\cdot e\cdot\omega_n}\right)^2+\dfrac{K_a\cdot\Delta\Re}{3\omega_n^2}\end{array}} \tag{48.12}$$

48.3.3 Error Analysis of Steady-State

In order to analyze IMU impact on the tracking error, OCXO is selected, whose g-sensitivity is $1 \times e^{-10}$ (1/g), power spectral density of vibration is 0.05 (g^2/Hz). Figure 48.6 shows the relationship of the INS aided tracking loop's error and the bandwidth in the conditions that static, a low-grade IMU MTI-G, C/N0 30 dB-Hz, coherent integration time 1 ms. While the horizontal axis is the characteristic frequency of the PLL, the vertical axis is the tracking error (deg).

Figure 48.6 shows that the tracking error caused by the thermal noise σ_{tPLL} increases with bandwidth increasing, and the tracking errors caused by crystal reduce with bandwidth increasing, which are the same as in normal PLL. Meanwhile, the tracking error caused by the IMU bias type error θ_{V0} reduces with bandwidth increasing. Under static conditions, compared with normal PLL, the tracking error of low-grade IMU aided PLL is not significantly larger, so the contribution of the IMU bias type error to the tracking error can be ignored.

Under dynamic conditions, in addition to the static tracking error, the dynamic stress error appears in the tracking loop. The test condition is set as follow: the

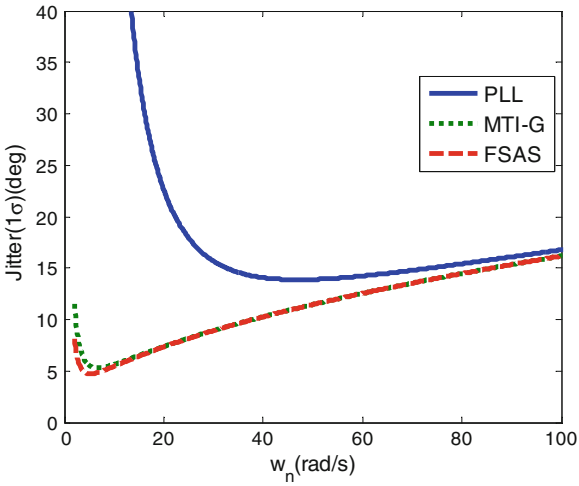

Fig. 48.7 Tracking loop's error with and without INS aiding in dynamic conditions

vehicle's acceleration is 1 g, the C/N0 is 30 dB-Hz, the coherent integration time is 1 ms, and the IMU includes low-grade IMU MTI-G, medium-grade IMU FSAS. Figure 48.7 shows the relationships of the steady-state tracking error and the bandwidth, including normal PLL, MTI-G aided PLL, FSAS aided PLL. When the vehicle's acceleration is 1 g, the optimal bandwidth of normal PLL is wider than 15 Hz, but the optimal bandwidth is narrower than 5 Hz with the INS aiding. With the INS aiding, even the low-grade INS, the tracking error is significantly improved.

48.4 Design and Optimization of Hardware Prototype

48.4.1 Hardware Prototype Design

Figure 48.8 is the self-built hardware integrated platform [18]. The main processor is TMS320C6713 DSP, and the coprocessor is EP2S60 FPGA, communication between them through the EMIF of DSP. The GNSS RF unit and the MEMS IMU unit are connected to the processor by the I/O of FPGA. Depending on the external device interface definition, FPGA can flexibly define its I/O and design program. All units on the platform share a common oscillator, which includes TCXO, OCXO and external interface.

Figure 48.9 shows the software architecture based on the deep integration hardware platform. Since it is good at high speed digital signal processing in parallel and the interface control, FPGA is responsible for GNSS IF data sampling, baseband signal processing, IMU data sampling, etc. However, DSP specializes in complex calculations and task scheduling, so it is used for GNSS baseband control,

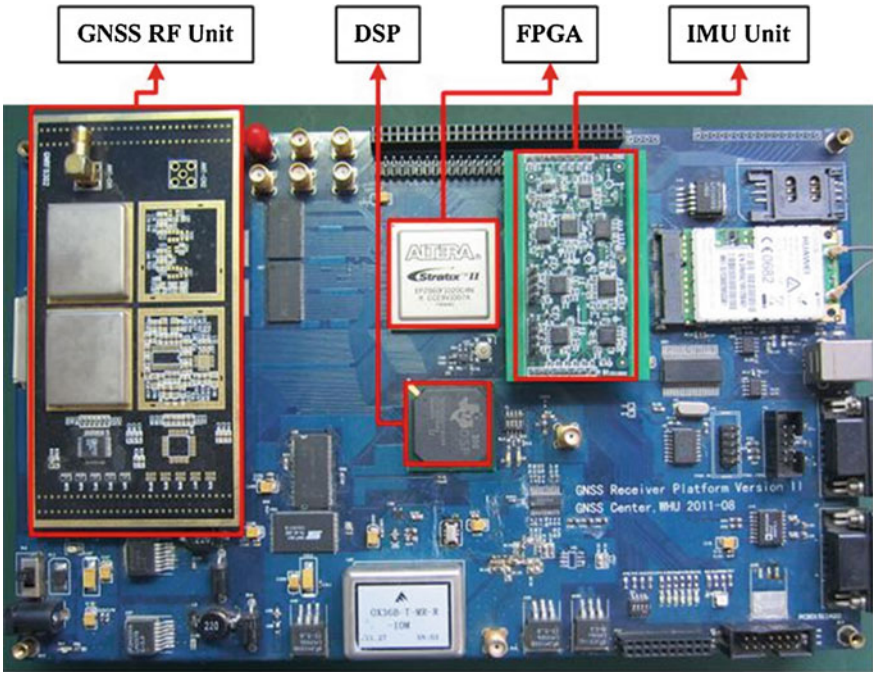

Fig. 48.8 Self-built hardware integrated platform

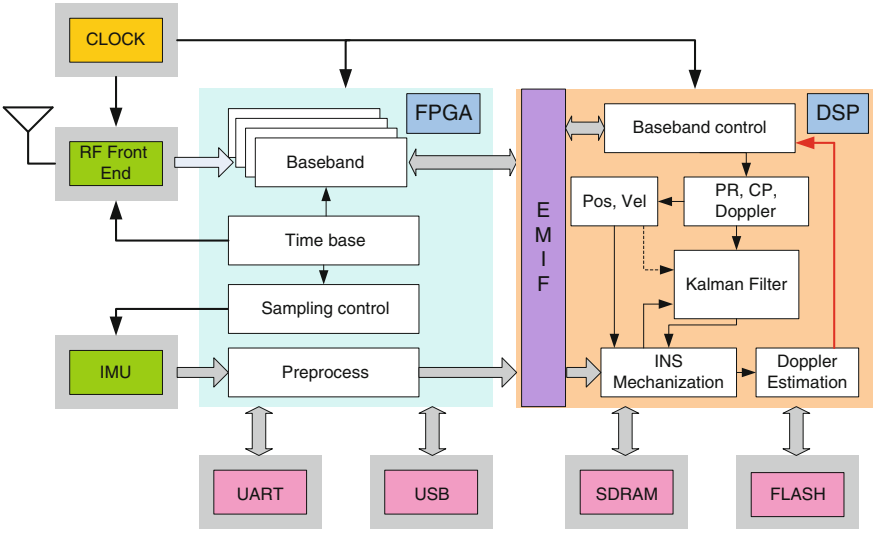

Fig. 48.9 Block diagram of integrated deeply coupled software architecture

satellite positioning, INS mechanization, Kalman filter algorithm, the LOS Doppler estimation and aiding tracking.

The advantage of the integrated prototype can be summarized as follows: (1) all the function units are triggered by the same clock; (2) the deep integration can choose different types of crystal as the system clock; (3) the platform's interface is high speed; (4) integrated software is suit for the deep integration; (5) it has GNSS/IMU raw data recording and playback function.

48.4.2 Hardware Prototype Optimization

Compared with deep integration on the software platform, the hardware prototype design need consider running real-time, GNSS/INS data synchronization. It specifically related to embedded software architecture, IMU and GNSS data sampling synchronization, and INS aiding information delay.

1. **Embedded software architecture**

DSP needs to respond GPS data, as well as IMU data, simultaneously process these data. Therefore, DSP needs to respond to two external interrupts, a higher priority interrupt (interrupt #1) used for receiving and processing GPS baseband data, and a lower priority interrupt (interrupt #2) used for receiving and processing IMU data. Since the correlators in the baseband update every millisecond, the interval time of interrupt #1 must be less than 1 ms to ensure not to miss integration results. Considering the processor computing power and the dynamic, the interval time of interrupt #1 is set as 0.707 ms, and the interrupt #2 is set as 50 ms.

When DSP enters an interrupt service routine, other interrupts are forbidden by default whatever their priority is. Then if the execution time of an interrupt exceeds 0.707 ms, some 0.707 ms interrupts will be missed. Therefore the interrupt priority level and interrupt nesting design of the software are necessary. The external interrupt 1 with 0.2 ms execution time has the highest priority, the external interrupt 2 with 10 ms execution time has the second highest priority, and the timer interrupt with 18 ms execution time has the lowest priority. At the same time, interrupt nesting is allowed in the two lower priority interrupts. Tests showed that the processor would be able to handle all tasks completed within limited time, even has free time [19].

2. **Synchronization of data sampling**

In order to ensure navigation performance, IMU data and GPS data must be synchronized. And the most effective method is to sample IMU data under GPS PPS trigger, which could realize the data synchronization essentially. It needs two conditions: i) GPS receiver can provide PPS, ii) the IMU sampling time could be controlled by the external. In the integrated prototype, the GPS receiver subsystem could provide PPS. And the IMU module is designed consists of gyroscopes and

accelerometers with analog interfaces, sampled by a multiplexing ADC with controllable sampling time.

The IMU data sampling control module is designed in FPGA. There is no additional cost of hardware for this platform, only an IMU sampling module needs to be designed on the FPGA. Six analog signals from sensors (gyroscopes and accelerometers) are sent to the input of ADC with multiplexer, and the ADC is triggered by the 200 Hz pulse train to sample IMU data. The PPS signal is generated in the time base module of the receiver on the FPGA. And the PPS signal is used to initialize the time-stamp counter. Then the counter could generate a pulse train to trigger the ADC. Finally, the time stamp is added to the IMU data. Tests showed that the maximum delay of IMU sampling was 22us, whose effects could be ignored.

3. **INS aiding information delay**

If the aiding information could not reflect the vehicle dynamics in time, its contribution will be greatly weakened, especially with strong dynamics. To ensure the performance of the system, the time delay of the aiding Doppler should be short enough.

Data transmission is carried out between FPGA and DSP in the integrated deeply-coupled system. On one hand, GNSS data and IMU data are using the same transmission channel (EMIF), which causes essentially the same delay. On the other hand, the EMIF can be efficient, seamless communication. Therefore, processing time difference between loop filter output and INS aiding information is mainly caused by different processing time of discriminator, loop filter, and INS mechanization, Doppler estimation. In addition, the Doppler estimation is executed once the INS mechanization is completed. Tests showed that the INS aiding information delayed 0.5 ms to the loop filter output, and the tracking error caused by delay could be ignored.

48.5 Tracking Performance Testing and Verification

48.5.1 Test Conditions and Methods

Figure 48.10 shows the testing conditions of the deeply coupled system. The GNSS/INS hardware simulator produced by NAVLABS in America is used to quantitatively evaluate the integrated deeply-coupled system. Since the simulator mainly applies in the vehicle navigation research, it can only output GPS L1, the MEMS IMU signal can output by SPI interface, high-grade IMU data can only obtain data files [20]. Table 48.1 shows the IMU configuration parameters in the simulator. Further dynamic tracking performance testing is carried out using vehicle, including self-built deeply coupled prototype, medium-grade INS (SPAN-FSAS), etc. The MEMS IMU on the prototype including a three axis accelerometer (LIS344ALH), a

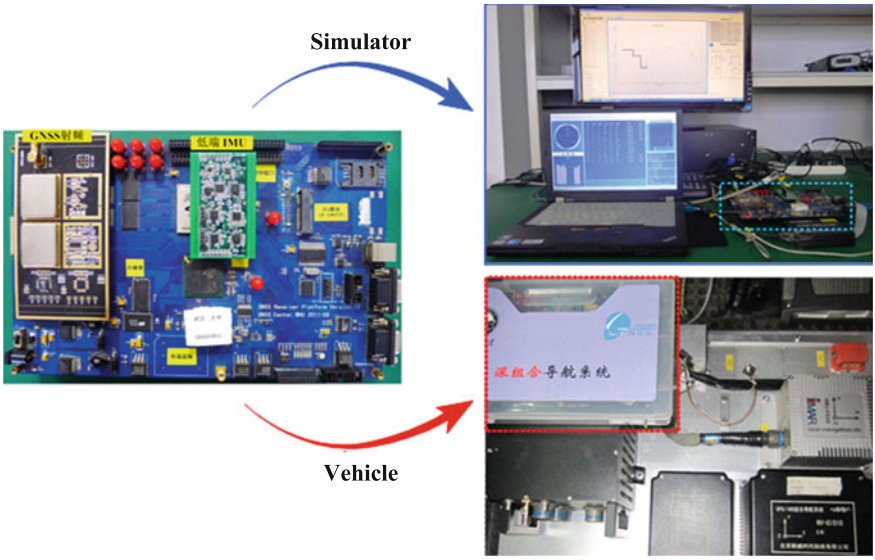

Fig. 48.10 Testing conditions of the deeply coupled system

Table 48.1 IMU configuration parameters in the simulator

Parameters	Low-grade IMU (MEMS)	Medium-grade IMU (IXSEA)	Parameters	Low-grade IMU (MEMS)	Medium-grade IMU (IXSEA)
Gyro bias(deg/h)	36	0.05	Accelerometer bias (m Gal)	2,000	102
Gyro white noise(deg/$\sqrt{}$hr)	3.0	0.003	Accelerometer white noise (m/s/$\sqrt{}$hr)	0.12	0.09
Gyro scale factor (ppm)	300	30	Accelerometer scale factor (ppm)	300	40

singly axis gyroscope (LPR510AL), and a double axis gyroscope (LY510ALH), is used for low-grade INS aided tracking loop, and the SPAN-FSAS is used for medium-grade INS aided tracking loop. TCXO and OCXO are provided on the platform, which could verify the effect of the crystal on the system.

On one hand, in order to verify deeply-coupled system's dynamic performance based on medium-grade INS, the problem that importing medium-grade IMU data to the hardware prototype need to be addressed. On the other hand, repeated vehicle tests should be avoided. In order to solve these problems, GPS IF/IMU raw data recording and playback unit is developed based on the hardware prototype. It not only could replay GPS/IMU data to debug the deeply coupled system, but also

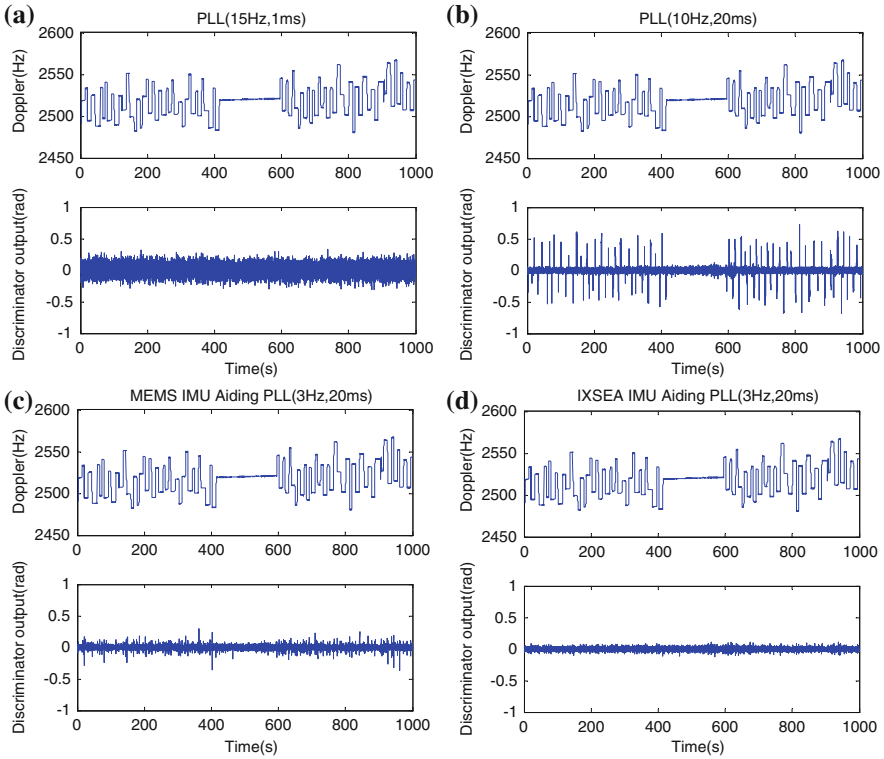

Fig. 48.11 Tracking error tested by simulator. **a** normal PLL (1 ms, 15 Hz). **b** normal PLL (20 ms, 10 Hz). **c** MEMS INS aided PLL (20 ms, 3 Hz). **d** Medium-grade INS aided PLL (20 ms, 3 Hz)

could replace the log IMU data by medium-grade IMU data and achieve medium-grade INS aided tracking loop testing [21].

48.5.2 Simulator-Based Testing and Verification

In the set simulator scenario, the dynamic changes are frequent including acceleration (maximum 2.5 g), deceleration and turning, etc. Here satellite PRN24 as an example is analyzed the tracking error, whose C/N0 is 50 dB-Hz, elevation is 34°. Figure 48.11 shows the tracking error of tracking loop with and without INS aiding, the upper part is the Doppler, and the lower part is the discriminator output.

Figure 48.11a shows the tracking error of the normal second-order PLL with 1 ms integration time and 15 Hz bandwidth. When the vehicle dynamic changes, the carrier phase error doesn't change, but the overall margin of phase error is big.

Table 48.2 Tracking error statistical results

	Normal PLL (1 ms, 15 Hz)	MEMS INS aided PLL (20 ms, 3 Hz)
PRN = 24(C/N0 = 50)	0.10 rad	0.068 rad
PRN = 22(C/N0 = 45)	0.26 rad	0.098 rad

Figure 48.11b shows the tracking error of the normal second-order PLL with 20 ms integration time and 10 Hz bandwidth. When the vehicle dynamic changes, the carrier phase error significantly increases. The result illustrates the normal PLL is not suitable for long time integration. Figure 48.11c shows the tracking error of the MEMS INS aided second-order PLL with 20 ms integration time and 3 Hz bandwidth. When the vehicle dynamic changes, the carrier phase error slightly increases. Figure 48.11d shows the tracking error of the medium-grade INS aided second-order PLL with 20 ms integration time and 3 Hz bandwidth. Even when the vehicle dynamic changes largely, the carrier phase error doesn't change. Test results show that: (1) when the vehicle dynamic changes, the normal PLL's integration time should not be too long, and it's bandwidth should not be too narrow. (2) with the INS aiding, while the tracking loop's dynamic accuracy is guaranteed, the tracking error could be reduced by compressing the bandwidth and lengthening the integration time. (3) when the vehicle dynamic changes largely, the medium-grade INS has better aiding effect. Therefore, the test results verify the error model analysis.

Table 48.2 statistically compares the tracking error (RMS) of the normal PLL with 1 ms integration time and 15 Hz bandwidth and the MEMS INS aided PLL with 20 ms integration time and 3 Hz bandwidth. For high elevation satellites with higher signal strength, the tracking error of INS aided PLL is 0.7 times the normal PLL's. And for low elevation satellites with higher signal strength, the tracking error of INS aided PLL is 0.4 times the normal PLL's. Therefore, while the INS aided tracking loop's dynamic accuracy is guaranteed, the tracking error could be reduced by compressing the bandwidth and lengthening the integration time.

48.5.3 Vehicle-Based Testing and Verification

The vehicle dynamic test under open sky is carried out on 21 June 2013 to further verify the tracking performance. Here the tracking error of satellite PRN13 as an example is analyzed, whose C/N0 is 48 dB-Hz, elevation is 45 deg. Figure 48.12 shows the tracking error of tracking loop with and without INS aiding.

Figure 48.12a shows the tracking error of the normal second-order PLL with 20 ms integration time and 10 Hz bandwidth. For the small vehicle dynamic changes, the carrier phase error doesn't significantly change. Figure 48.12b shows the tracking error of the normal second-order PLL with 20 ms integration time and

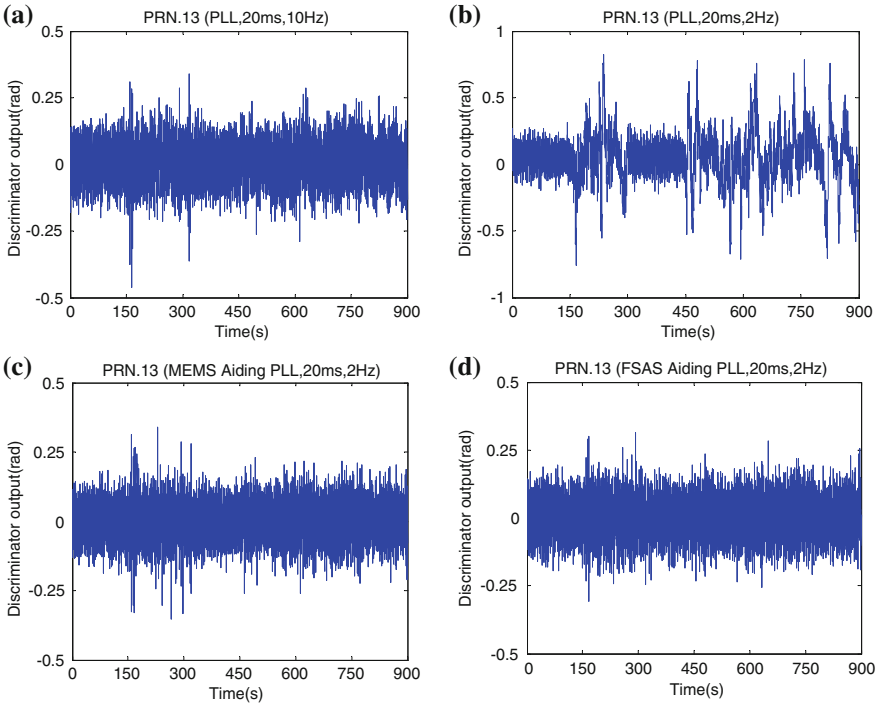

Fig. 48.12 Tracking error tested by vehicle. **a** Normal PLL (20 ms, 10 Hz). **b** Normal PLL (20 ms, 2 Hz). **c** MEMS INS aided PLL (20 ms, 2 Hz). **d** Medium-grade INS aided PLL (20 ms, 2 Hz)

2 Hz bandwidth. Even when the vehicle dynamic changes small, the carrier phase error significantly increases. These test results is the same as the simulator test results. Figure 48.12c, d respectively show the tracking error of the MEMS INS aided PLL and medium-grade INS aided PLL with 20 ms integration time and 2 Hz bandwidth. Since the alignment has not fully been achieved, the tracking error is bigger at the first dynamic change. And then the carrier phase error doesn't significantly increase. In addition, for the small vehicle dynamic, MEMS INS aiding effect is not an obvious disadvantage. The vehicle test results consistent with the simulator test results further validate the reasonableness of the error model.

48.6 Conclusions

GNSS/INS deeply-coupled system can realize INS aiding GNSS signal tracking, and improve the GNSS receiver's dynamic tracking performance essentially. In

order to improve the theory of the INS aided GNSS tracking loop and hardware system verification, this paper proposes an error model that could be used for quantitative analysis of error sources affecting the tracking error. And it deduces the steady-state tracking model. Then it develops and optimizes the real-time deeply-coupled prototype based on hardware platform for example with GPS L1. Finally tracking errors of tracking loops before and after INS aiding are tested by simulator and vehicle. The test results show that: (1) with the INS aiding, while the tracking loop's dynamic accuracy is guaranteed, the tracking error could be reduced by compressing the bandwidth and lengthening the integration time. (2) MEMS INS can significantly improve the dynamic tracking performance. The test results are consistent with the analysis results of the error model, verifying the reasonableness of the error model. The proposed error model and hardware prototype developed can be further applied to the key performance study of the GNSS/INS deeply coupled system, such as the sensitivity and anti-interference under dynamic conditions, and provide theories, methods for further deep integration study.

Acknowledgments The colleagues of the Navigation group from GNSS Research Center at Wuhan University who participated in the deep integration research and testing are thanked for their cooperation. And this work is supported by the National High Technology of China under contract 2012AA12A206, the National Natural Science Foundation of China under contract 41174028 and Opening project of Chinese Academy of Sciences under contract 2012PNTT10.

References

1. Grewal MS et al (2007) Global positioning systems, inertial navigation, and integration. Wiley Online Library, New Jersey, pp 252–264
2. Gautier JD, Parkinson BW (2003) Using the GPS/INS normalized evaluation tool (GIGET) for the comparison of loosely coupled, tightly coupled and ultra-tightly coupled integrated navigation systems. In: Proceedings of ION AM, pp 65–76
3. Huang X, Gao X et al (2009) INS/GPS ultra-tight coupled technique research status and prospect. Aerodynamic Missile. pp 42–47
4. Misra P, Enge P (2006) Global positioning system: signals, measurements, and performance, 2nd edn. Ganga-Jamura, Lincoln, MA, pp 1–20
5. Gao G, Lachapelle G (2007) INS-assisted high sensitivity GPS receivers for degraded signal navigation. In: Proceedings of ION GNSS, Fort Worth, TX, pp 2977–2989
6. Alban S et al (2003) Performance analysis and architectures for INS-aided GPS tracking loops. In: Proceedings of ION NTM, Anaheim, CA, pp 611–622
7. Parkinson B, Spilker JJ (1996) Global positioning system: theory and applications. AIAA, Washington, pp 6–15
8. Petovello MG, Driscoll CO, Lachapelle G (2008) Carrier phase tracking of weak signals using different receiver architectures. In: Proceedings of ION NTM, San Diego, CA, pp 781–791
9. Alban S (2004) Design and performance of a robust GPS/INS attitude system for automobile applications. Stanford University, Leland
10. Tang K (2008) Research on the key technology of embedded GPS/MIMU integrated navigation. National University of Defense Technology, Changsha, pp 113–120

11. Ye P (2011) MEMS IMU/GNSS ultra-tight integration navigation technology. Shanghai Jiao Tong University, Shanghai
12. Lin T, Driscoll CO, Lachapelle G (2011) Development of a context-aware vector-based high-sensitivity GNSS software receiver. In: Proceedings of ION NTM, San Diego, CA, pp 1043–1055
13. Kennedy S, Rossi J (2008) Performance of a deeply coupled commercial grade GPS/INS system from KVH and NovAtel Inc. PLANS, 2008 IEEE/ION, pp 17–24
14. Zhang T (2013) Research on the tracking technology of GNSS/INS Deep Integration based on Hardware prototype. Wuhan University, Wuhan
15. Kaplan E, Hegarty C (2006) Understanding GPS: principles and applications, 2nd edn. Artech House, Norwood, MA, pp 3–30
16. Irsigler M, Eissfeller B (2002) PLL tracking performance in the presence of oscillator phase noise. GPS Solutions 5(4):45–57
17. Ban Y (2013) INS error transmission under static conditions. Wuhan University, Wuhan
18. Zhang T, Niu X, Zhang H, Zhang D, Ban Y (2012) An integrated research platform for real-time deeply integration. In: Proceedings of ION GNSS. Nashville, TN, pp 1666–1673
19. Zhang T, Zhang H, Ban Y. Niu X (2013) Performance evaluation of a real-time integrated MEMS IMU/GNSS deeply coupled system. In: Proceedings of CSNC 2013, Springer, Berlin, pp 737–749
20. Zhang T, Zhang H, Yalong B, Kunlun Y, Xiaoji N, Jingnan L (2013) Hardware Implementation of a real-time MEMS IMU/GNSS deeply-coupled system. IEICE Trans Commun 96(11):2933–2942
21. Zhang T, Zhang H et al A GNSS IF data and IMU raw data recording device. 201210117657.7

Chapter 49
Characteristic Analysis and Fast Adaptive Synchronization Algorithm of GPS CNAV-2 Navigation Message Synchronization Code

Zhong-liang Deng, Jie-qiang Li, Chang-ming Li, Lu Yin and Yue Xi

Abstract In the navigation data processing, the speed and accuracy of the frame synchronization processing plays an important role in system efficiency and signal analysis. Unlike other navigation message which synchronized using a fixed sequence, In GPS L1C CNAV-2 navigation message, and the synchronization code uses the BCH (51, 8) code based TOI (Time of Interval) and is no longer fixed binary sequence. The TOI, in GPS L1C CNAV-2 navigation message, is the 18 s count value in every 2 h while indicated by ITOW (Interval Time of Week) and cyclically changes between 0 and 399. Thus, the BCH coding generated by the TOI is circular. Thus, the synchronization algorithm used in fixed binary sequence does not work anymore. Beside, circularity makes us have to count maximum correlation in the two adjacent frames simultaneously and traversal 256 pairs of sequences at last in each detection, which influence the speed of the frame detection and the real timeliness of receiver. To solve this problem, beginning with the shift registers which generate synchronized code of GPS L1C CNAV-2 navigation message, this paper analysis the three characteristics of the loop resistance, autocorrelation, and cross-correlation. Then, the paper designs the fast adaptive synchronization algorithm for GPS L1C CNAV-2 navigation message. In this synchronization algorithm, the first step is estimating the number of error bit in the front nine bit of 52 bit, an integral BCH coding. Then, filter and sort these possible pairs of sequences. When we count the maximum correlation in the two adjacent frames simultaneously, the pairs of sequences is detected based on the priority order. Thus, the fast adaptive synchronization algorithm makes the fast synchronization and low rate of false synchronization in different signal conditions.

Keywords GPS L1C · Synchronization codes characteristics · Adaptive · Synchronization algorithm

Z. Deng · J. Li (✉) · C. Li · L. Yin · Y. Xi
Beijing University of Posts and Telecommunications, Beijing 100876, China
e-mail: lijieq2@bupt.edu.cn; 413021607@qq.com

J. Sun et al. (eds.), *China Satellite Navigation Conference (CSNC) 2014 Proceedings: Volume I*, Lecture Notes in Electrical Engineering 303,
DOI: 10.1007/978-3-642-54737-9_49,

49.1 Introduction

With the development of technology, the Global Navigation Satellite System GNSS (Global Navigation Satellite System) has become the main method of autonomous orientation navigation by the use of measuring the radio distance between the user and satellites whose position has been known. From the beginning of the 1960s, U.S. led in building a global satellite navigation system GPS which was deployed completely in 1995 and has spawned many new industries [1]. The 21st century, the United States began the GPS modernization program. In the program, the new civilian navigation signals L2C, L5, L1C will be worldwide broadcast in the oncoming generation of GPS satellites. Among them, the GPS L1C signal modulated on the L1C\A RF carrier enhances interpretability between GPS and other GNSS systems [2]. The CNAV-2 navigation message modulated on the L1C signal is innovative and brings some different of frame format and Frame format frame synchronization.

49.2 CNAV-2 Navigation Message Synchronization Code Generation and Characteristic Analysis

49.2.1 CNAV-2 Navigation Message Frame Format and BCH (51, 8) Encoding

CNAV-2 navigation message frame consist of three sub-frame, namely, first sub-frame 52 bit, second sub-frame 1,200 bit, third sub-frame 548 bit, 1,800 bit totally [3]. The frame format of CNAV-2 navigation message is shown in Fig. 49.1.

The first sub-frame, which is used to extract TOI and synchronize navigation message, is as long as 52 bit generated by BCH (51, 8) based on the TOI (Time of Interval). The TOI is the 18 s count value in every 2 h while indicated by ITOW (Interval Time of Week). The difference between two TOI in the two adjacent frames is 1. The second sub-frame and the third sub-frames are generated by the original message after CRC check, LDPC coding, interleaving.

BCH code is a very important cyclic code. Cyclic code generating polynomial is expressed as follows [4]:

$$g(x) = LCM[m_1(x), m_3(x), \ldots m_{2t-1}(x)]$$

Among, mi(x) is a prime polynomial. LCM means to extract the least common multiple in the formula. The least common multiple is the generating polynomial of BCH code. BCH code can correct t random errors assuming d is the minimum code distance.

$$t = (d-1)/2$$

subframe1 52bit	subframe2 1200bit	subframe3 548bit

Fig. 49.1 Frame format of CNAV-2 navigation message

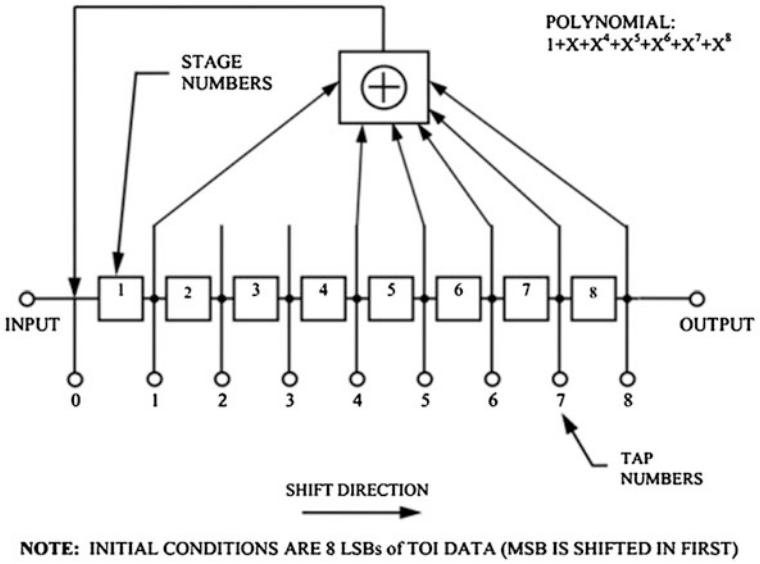

Fig. 49.2 Linear shift register of BCH (51, 8)

BCH (51, 8) linear shift register is shown in Fig. 49.2 [5]. The TOI data is the 18 s count value in every 2 h while indicated by ITOW (Interval Time of Week). TOI data period N is 400, which is calculated by expression as follow.

$$N = (2\,h * 3{,}600\,s/h)/18\ s = 400$$

TOI data, in the range of 0–399, is expressed by 9 bit binary number. TOI data bits 1–8 (8 LSBs) are loaded into the generator, Most Significant Bit (MSB) first, as initial conditions of the registers, which is then shifted 51 times to generate 51 encoded symbols. The ninth bit of TOI data (MSB) shall be modulo-2 added to the 51 encoded symbols and it shall also be appended as the MSB of the 52-symbol TOI message.

It was apparent from BCH (51, 8) linear shift register that the TOI and BCH (51, 8) encoding results is relational. The mapping diagram is shown in Fig. 49.3.

BCH (51, 8) encoding results of some TOI is shown in Table 49.1.

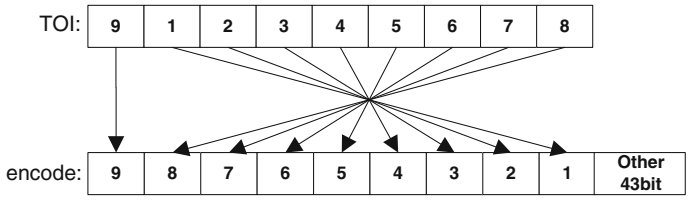

Fig. 49.3 Mapping diagram between TOI and BCH (51, 8) encoding results

Table 49.1 BCH (51, 8) encoding results of some TOI

TOI	BCH (51,8) encoding results
15	*011110000011001111010000110100010011011001100100011 0*
16	000001000101001111101100001110110111011100001001010 0
30	*001111000001100111101000011010001001101100110010001 1*
32	000000100010100111110110000111011011011100001001010
64	000000010001010011111011000011101101110111000010010 1
68	000100010100111110110000111011011011100001001010000
81	010001010011111011000011101101110111000010010100000 0
136	000010001010011111011000011101101110111000010010100 0
162	001000101001111101100001110110111011100001001010000 0

49.2.2 Autocorrelation and Cross Correlation

Similar to the auto-correlation curve and cross-correlation curve of L1C Ranging Codes [6], the 52 bit long TOI have good autocorrelation and cross correlation.

The Fig. 49.4 is the auto-correlation curve of 52 bit generated by BCH (51, 8) when TOI is 15. Through the figure, we can get that the autocorrelation value is maximum only when the offset is zero.

The Fig. 49.5 is the cross-correlation curve of 52 bit generated by BCH (51, 8) when TOI is 15 and 16. Through the figure, we can get that the cross-correlation value is low whether what the offset is zero.

Through the analysis above, if the navigation message has been synchronized, we can get the TOI data, the second-class time of this frame, by calculating the correlation value of 52 bit demodulated and 52 bit encoded by BCH (51, 8) with TOI ranging of 0–399.

49.2.3 Quasi-Cyclic Characteristics

Through analyzing the 52 bit BCH (51, 8) encoding result generated by TOI ranging of 0–399, we can get that it has quasi-cyclic characteristics. As the Table 49.1 shown, compared with the BCH (51, 8) encoding results when TOI is 30,

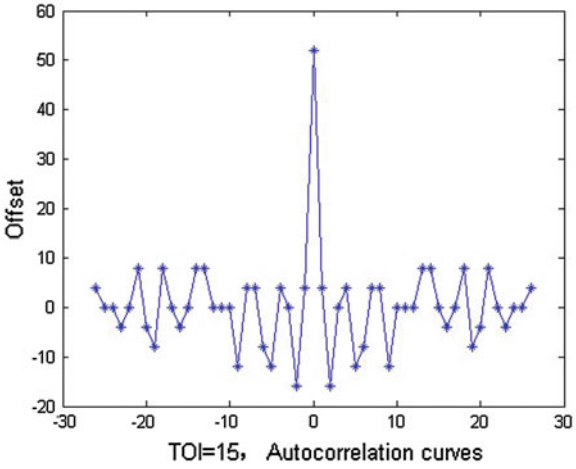

Fig. 49.4 Autocorrelation curves of BCH (51, 8) encoding results when TOI is 15

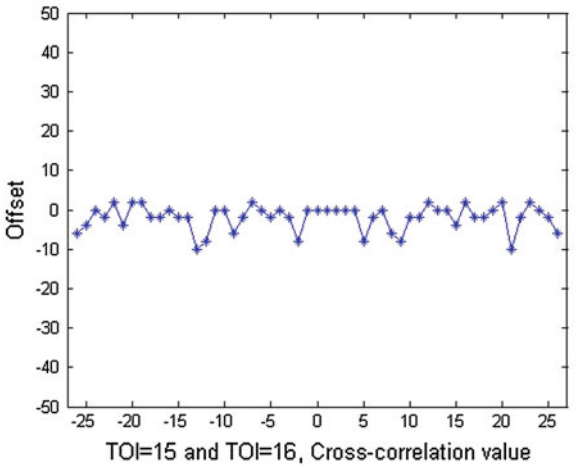

Fig. 49.5 Cross-correlation curve of BCH (51, 8) encoding results when TOI is 15 and 16

the BCH (51, 8) encoding results when TOI is 15 is 1 bit offset to the left. The other BCH (51, 8) encoding result in Table 49.1 also show the quasi-cyclic characteristics, as the following Fig. 49.6.

Quasi-cyclic characteristics cause the same correlation values in the adjacent bit. Assuming that we receive 53 bit, as shown in Fig. 49.7, the front 52 bit is exactly the BCH (51, 8) encoding result when TOI is 16, and the after 52 bit is exactly the BCH (51, 8) encoding result when TOI is 32. Thus, we can't confirm which the correct first bit of the navigation message is.

Consider that the difference of BCH (51, 8) encoding result by the TOI of the first sub-frame of the adjacent frame, we use BCH (51, 8) encoding result generated by (TOI, TOI + 1) to calculate the correlation values with the first

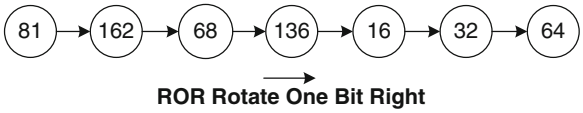

Fig. 49.6 Quasi-cyclic characteristics of BCH (51, 8) encoding results

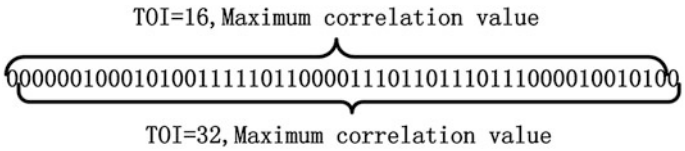

Fig. 49.7 Quasi-cyclic characteristics of BCH (51, 8) encoding results

sub-frame of the adjacent frame. If the correlation value is maximal, this bit is the correct first bit of the navigation message.

But TOI value ranges from 0 to 399. Figure 49.8 shows that we need 400 pairs (TOI, TOI + 1) to calculate the correlation values per bit, which spend a lot of time and resources and a fast synchronization scheme is needed.

49.3 Fast Adaptive Synchronization Algorithm Based on CNR

49.3.1 The Relationship of CNR and BER

To achieve positioning by GPS receiver, GPS receiver must extract the ephemeris representation, clock correction, and accuracy parameters to calculate the position of the satellite. But when the satellite signal is weak or when the interference is serious, the demodulated navigation message has higher error rate. Use the GPS L1C simulator simulate the signal whose navigation message has been known and use GPS L1C signal receiver demodulates the message and calculate the CNR.

Adjust the output power to output different simulator L1C signal with different carrier to noise ratio. Comparing the bits demodulated by the receiver under the different condition of the different CNR, with the standard known navigation message, we get the relationship between the CNR and BER, as shown in Table 49.2.

Due to the acquisition sensitivity of the most GPS receiver is −140 dB and the corresponding CNR is around 30. In this paper, we estimate error bit range and correlation value range in the MSB 9 bit of 52 bit we received, based on the actual CNR when the GPS L1C signal has been stably tracked., as shown in Table 49.3.

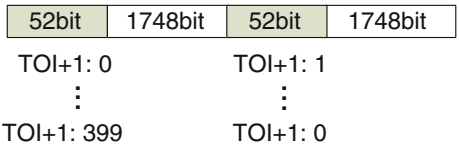

Fig. 49.8 Traversal 400 pairs of sequences in each detection

Table 49.2 BER under different CNR

C/N (dB)	10	15	20	25	30	35	40	45
BER/10e−6	31	30.3	29.4	27.7	24.2	18.5	9.8	2.3

Table 49.3 The error range forecast based on the CNR

CNR	Error bit range	Correlation value range
C/N (dB) ≥ 40	≤1	50
40 ≥ C/N (dB) ≥ 30	≤2	48

49.3.2 Traversal Sequence Filter and Synchronization Algorithm

In the process of frame synchronization, we locate error location based on the error range. Thus, inverse the corresponding bits to achieve filtering and sorting the 400 pairs TOIs. For example, the algorithm is introduced as follow when the CNR is not less than 40.

1. The adjacent two frames, calculated correlation value, are denoted as n and $(n + 1)$ frame. And the MSB 9 bit of 52 bit of the first sub-frame in the first frame is denoted as $a_9\ a_8\ a_7\ a_6\ a_5\ a_4\ a_3\ a_2\ a_1$.
   Assuming $a_i' = 1 \oplus a_i, \quad i \in [1, 9]$;
   Thus, According to the estimated error range, correct the error location of $a_9\ a_8\ a_7\ a_6\ a_5\ a_4\ a_3\ a_2\ a_1$ in order. Include the case of error-freely, it has ten possible sequences, as shown in Table 49.4.
2. Correct 9 bit data and calculate the TOI of first frame as the mapping relationship mentioned in Fig. 49.3. The results are recorded as $(TOI_0, TOI_0 + 1)$, $(TOI_1, TOI_1 + 1)$,⋯, $(TOI_9, TOI_9 + 1)$.
3. Calculate the correlation values of BCH (51, 8) generated by the first number of $(TOI_i, TOI_i + 1)$ and 52 bit of the first frame. Calculate the correlation values of BCH (51, 8) generated by the second number of $(TOI_i, TOI_i + 1)$ and 52 bit of the second frame. The case of error-free has the priority to calculate the correlation values. If these two correlation values exceed the preset threshold synchronously, then consider the bit detected now is the first bit of a frame. And

Table 49.4 TOI forecast based error bit range

Sort	Demodulation message	Correction message	Remark	N frame	n + 1 frame
1	$a_9\ a_8\ a_7\ a_6\ a_5\ a_4\ a_3\ a_2\ a_1$	$a_9\ a_8\ a_7\ a_6\ a_5\ a_4\ a_3\ a_2\ a_1$	No error	TOI_0	$TOI_0 + 1$
2	$a_9\ a_8\ a_7\ a_6\ a_5\ a_4\ a_3\ a_2\ a_1$	$a_9'\ a_8\ a_7\ a_6\ a_5\ a_4\ a_3\ a_2\ a_1$	First bit error	TOI_1	$TOI_1 + 1$
⋮	⋮	⋮	⋮	⋮	⋮
10	$a_9\ a_8\ a_7\ a_6\ a_5\ a_4\ a_3\ a_2\ a_1$	$a_9\ a_8\ a_7\ a_6\ a_5\ a_4\ a_3\ a_2\ a_1'$	Ninth bit error	TOI_9	$TOI_9 + 1$

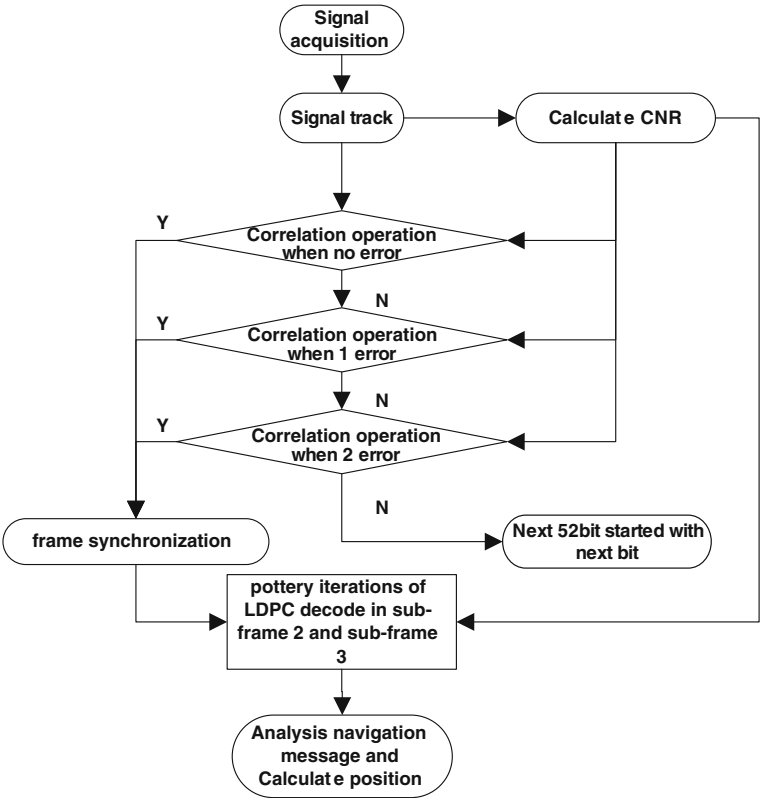

Fig. 49.9 Flowchart of fast synchronization algorithm

the TOI detected now is the second-class time of the frame based on the GPS-based time.

When the CNR is low than 40, it is need to consider the case of two bit error. In detail, we show the algorithm flowchart as Fig. 49.9.

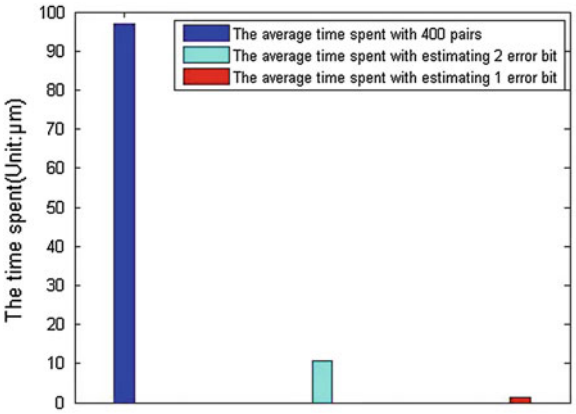

Fig. 49.10 Time-consuming of algorithm based on the error range forecast

49.3.3 Algorithm Verification

First, generate the stimulant GPS L1C signal as the test signal source by GPS L1C Signal Generator. Then, use the GPS L1C Software Receiver to achieve acquisition, tracking, frame synchronization algorithm simulation. Compute the total time and the total number of bits detected from achieving signal tracking to achieving frame synchronization. The average time per bit is defined by the quotient of the total time and the total number of bits detected, as shown in Fig. 49.10.

From the figure, it can be seen that the average time per bit is greatly reduced by using the Fast Adaptive Synchronization Algorithm.

49.4 Summary

In the paper, we, firstly, introduced the frame format of modern GPS L1C signal CNAV-2 navigation message. Secondly, this paper analyzes the autocorrelation, cross-correlation, quasi-cyclic of the synchronization code. Then the paper proposed a method that forecast error range based on the error range. The simulation results show that this Fast Adaptive Synchronization Algorithm improve efficiency distinctly.

References

1. Wei E-H, Shi G-J, Hu X-J (2005) GPS modernization and its influence. Bull Surv Mapp 07:24–28
2. Shaofeng JJB (2005) Progress in global positioning system (GPS) modernization of US. Ship Electron Eng 02:15–18

3. Liang X, Li Y, Tao X (2012) Research on Galileo and GPS L1C navigation message. In: The 3rd China satellite navigation conference electronic proceedings, vol 5
4. Huanyin Z, Lingzan ZHU (2006) Research on the coding of cyclic code. Mod Electron Tech 19:11–12
5. Zhao J-F, Chang J, Qian H, Liu Y (2011) On the application of error correction coding in navigation signals. In: The 2nd China satellite navigation conference electronic proceedings, vol 1
6. He C-L, Wang Y (2013) Weil code correlation performance of GPS L1C signal. Radio Commun Technol 01:32–35

Chapter 50
The Performance Analysis of Acquisition for GNSS Signal Over Frequency Non-selective Fading Channel

Lei Chen, Shuai Han and Weixiao Meng

Abstract As most research focuses on improving the acquisition sensitivity and speed in AWGN (Additive White Gaussion Noise) channel, this paper will present the theoretical analysis of acquisition performance for GNSS signal over frequency non-selective fading channel. The complementary cumulative distribution function for the correlation peak value higher than a threshold R_{th} is derived when the channel is slow and fast fading respectively. For the Rician fading, when the threshold R_{th} is larger than a special value, the acquisition performance over slow fading channel will surpass the performance over fast fading channel. Conversely, the performance for fast fading will be better. But, both of them are inferior to the performance over AWGN channel. For the Rayleigh channel, theoretical analysis shows that the acquisition performance for GNSS signal over slow fading channel exceeds the performance over fast fading channel. Finally, the acquisition for GPS signal transmitted over frequency non-selective fading channel has been simulated and the simulation results confirm the validity of the derivations and analysis.

Keywords Acquisition · Frequency non-selective fading channel

50.1 Introduction

With the development of Global Navigation Satellite System (GNSS), navigation and location have become indispensable service in daily life. The GNSS receiver, as major devices of user segment, is also gradually matured. To acquire the coarse delay of Pseudo-random Noise (PRN) code and estimate the Doppler frequency

L. Chen (✉) · S. Han · W. Meng
Key Laboratory of Police Wireless Digital Communication, Ministry of Publice Security, PRC; Communication Research Center, Harbin Institute of Technology, No. 2 Yikuang Street, Nangang District, Harbin 150080, China
e-mail: leichen@hit.edu.cn chen.naruto@gmail.com

J. Sun et al. (eds.), *China Satellite Navigation Conference (CSNC) 2014 Proceedings: Volume I*, Lecture Notes in Electrical Engineering 303,
DOI: 10.1007/978-3-642-54737-9_50,

bias of GNSS signal, the acquisition should be completed firstly in GNSS receiver. Then, the received signal will be imported into tracking loop to accomplish the precise synchronization.

As one of most important components in GNSS receiver, the acquisition technology of GNSS signal has been intensively studied. Most of researches focus on two targets: one is to accelerate the acquisition, such as the parallel acquisition algorithm [1] and the method based on FFT [2]; the other is to improve the sensitivity of acquisition, such as coherent accumulation [3], assisted acquisition [4] and combined acquisition [5]. However, all of above-mentioned researches hypothesize that GNSS signal transmitted over additive white AWGN channel. Actually, in the Urban canyons or indoor environment where consist of numerous reflectors and scatterers, the channel that GNSS signal transmitted will be multipath fading channel. Thus, in this study, we will analyze the performance of acquisition for GNSS signal over frequency non-selective fading channel.

The remainder parts of this paper are organized as follows: Sect. 50.2 introduces the signal model, the correlation peak for GNSS signal over frequency non-selective fading channel. In Sect. 50.3, Rician fast fading and slow fading scenarios are investigated. And the probability density function and the complementary cumulative distribution function for correlation peak value higher than a threshold R_{th} are derived. Followed in Sect. 50.4, Rayleigh fading channel are investigated. And the acquisition for GPS signal transmitted over frequency non-selective fading channel has been simulated in Sect. 50.5. Finally, Sect. 50.6 presents the conclusion and future works.

50.2 Signal Model

For the multipath fading channel, if the signal bandwidth is greater than the coherence bandwidth of the channel, the channel becomes frequency-selective and the multipath components are resolvable. On the other hand, if the signal bandwidth is less than the channel coherence bandwidth, the channel will be frequency-nonselective. In this condition, the multipath components in the received signal are not resolvable and the received signal appears to arrive at the receiver via a single fading channel [6]. The IF signal model of GNSS signal over frequency-nonselective fading channel is given by

$$s(t) = h(t)D(t)c(t)e^{j2\pi(f_{IF}+f_d)t} + n(t) \tag{50.1}$$

where $h(t)$ denotes channel fading parameter, $D(t)$ denotes navigation data, $c(t)$ denotes PRN code, f_d represents Doppler frequency bias and $n(t)$ represents Gaussian noise.

As our analysis focus on the relation between the fading channel and correlation peak exported from correlator, the navigation data and Gaussian noise can be neglected and we assume that the Doppler frequency bias is zero. Let $c(t - t_0)$

represent the duplicated PRN code of GNSS receiver. Then, the correlation result after correlation operation between received signal and local duplicated signal is expressed as

$$R(\tau) = \int_0^{NT_C} h(t)c(t)c(t - t_0 + \tau)dt \tag{50.2}$$

where N denotes the code length of PRN code, T_C is the period of one chip. And the correlation peak is the correlation value when $t = \tau$.

Similarly, for the discrete signal, the correlation result is written as

$$R(n) = \sum_{m=1}^{N} h(m)c(m)c(m - m_0 + n). \tag{50.3}$$

Due to $c(m) \in \{-1, 1\}$, the correlation peak when $n = m_0$ is

$$R(m_0) = \sum_{m=1}^{N} h(m). \tag{50.4}$$

As GNSS signal transmitted through frequency non-selective fading channel, the channel fading parameter $h(m)$ is random variable. So the correlation peak, being equal with the sum of series random variables, is also a random variable.

50.3 Rician Fading Channel

For the Rican fading channel, the channel parameter is given by

$$h(m) = \sqrt{\frac{\kappa}{1+\kappa}}\sigma + \sqrt{\frac{1}{1+\kappa}}\sigma x(m). \tag{50.5}$$

where, the parameter κ (also called K-factor) is ratio of the energy in the specular path (the line-of-sight path) to the energy in the scattered path (the aggregation of large number of reflected and scattered paths). And $x(m) \sim CN(0, 1)$ presents that $x(m)$ are circularly symmetric complex Gaussian variables.

Then, $|h(m)|$, the module of the channel fading parameter, is Rican distributed with the parameter (κ, σ^2). The probability destiny function is expressed as

$$f_{|h|}(x) = \frac{2(\kappa+1)x}{\sigma^2} e^{\left(-\kappa - \frac{(\kappa+1)x^2}{\sigma^2}\right)} I_0\left(2\sqrt{\frac{\kappa(\kappa+1)}{\sigma^2}}x\right) \tag{50.6}$$

where $I_0(\cdot)$ is the zero order modified Bessel function of the first kind.

50.3.1 Fast Fading Channel

The fast fading channel is defined as that the changing period of the channel parameter is equal to the period of GNSS PRN code chip and the channel parameter stay invariant within a PRN code chip period T_C. Then, we have the correlation peak as

$$R_{fast}^{Rician}(m_0) = \sum_{m=1}^{N} h(m) = N\sqrt{\frac{\kappa}{\kappa+1}}\sigma + \sqrt{\frac{1}{\kappa+1}}\sigma \sum_{m=1}^{N} x(m). \tag{50.7}$$

Let $X = \frac{1}{\sqrt{N}} \sum_{m=1}^{N} x(m)$, then, $X \sim CN(0,1)$, so we have

$$R_{fast}^{Rician}(m_0) = N\sqrt{\frac{\kappa}{\kappa+1}}\sigma + \sqrt{N}\sqrt{\frac{1}{\kappa+1}}\sigma X. \tag{50.8}$$

Then, $\left|R_{fast}^{Rician}(m_0)\right|$, the module of the correlation peak, is Rican distributed with the parameter $\left(N\kappa, \left(\frac{\kappa}{\kappa+1}N^2 + \frac{1}{\kappa+1}N\right)\sigma^2\right)$. The probability destiny function after simplification is shown as

$$f_{\left|R_{fast}^{Rician}\right|}(x) = \frac{2(\kappa+1)x}{\sigma^2 N} e^{\left(-N\kappa - \frac{(\kappa+1)x^2}{N\sigma^2}\right)} I_0\left(2\sqrt{\frac{\kappa(\kappa+1)}{\sigma^2}}x\right). \tag{50.9}$$

For a given threshold R_{th}, the complementary cumulative distribution function (CCDF) for correlation peak value higher than the threshold is

$$P_{fast}^{Rician}(x > R_{th}) = Q\left(\sqrt{2\kappa N}, \frac{R_{th}}{\sigma\sqrt{\frac{N}{2(\kappa+1)}}}\right) \tag{50.10}$$

where $Q(\cdot)$ is Marcum Q function, defined as

$$Q(a,b) = \int_{b}^{+\infty} x e^{-\frac{x^2+a^2}{2}} I_0(ax)dx. \tag{50.11}$$

50.3.2 Slow Fading Channel

In the slow fading channel, we assume that the changing period of the channel parameter is equal to the period of GNSS PRN code and the channel parameter stay invariant within a PRN code period NT_C. Then, we get the correlation peak as

$$R_{slow}^{Rician}(m_0) = \sum_{m=1}^{N} h(m) = N\sqrt{\frac{\kappa}{\kappa+1}}\sigma + N\sqrt{\frac{1}{\kappa+1}}\sigma x(m). \tag{50.12}$$

Then, $\left|R_{slow}^{Rician}(m_0)\right|$, the module of the correlation peak, is Rican distributed with the parameter $(\kappa, N^2\sigma^2)$. The probability destiny function is given by

$$f_{\left|R_{slow}^{Rician}\right|}(x) = \frac{2(\kappa+1)x}{N^2\sigma^2} e^{\left(-\kappa - \frac{(\kappa+1)x^2}{N^2\sigma^2}\right)} I_0\left(2\sqrt{\frac{\kappa(\kappa+1)}{N^2\sigma^2}}x\right) \tag{50.13}$$

For a given threshold R_{th}, the CCDF for correlation peak value higher than the threshold is obtained as

$$P_{slow}^{Rician}(x > R_{th}) = Q\left(\sqrt{2\kappa}, \frac{R_{th}}{N\sigma\sqrt{\frac{1}{2(\kappa+1)}}}\right). \tag{50.13}$$

50.3.3 General Case

For the general case, we assume that N denotes the length of PRN code and K is the coherence integration gain, ΔT is the period of channel parameter variation and $\mu = \Delta T/T_C$ is the channel variation factor. When $KNT_C/\Delta T$ is integer, the correlation value and the correlation peak of GNSS signal are shown as

$$R(n) = \sum_{k=0}^{K-1}\sum_{m=1}^{N} h(m+kN)c(m+kN)c(m-m_0+n), \tag{50.15}$$

$$\begin{aligned} R(m_0) &= \sum_{k=0}^{K-1}\sum_{m=1}^{N} h(m+kN) = \sum_{m=0}^{KN-1} h(m) = KN\sqrt{\frac{\kappa}{1+\kappa}}\sigma + \sqrt{\frac{1}{1+\kappa}}\sigma\sum_{m=0}^{KN-1} x(m) \\ &= KN\sqrt{\frac{\kappa}{1+\kappa}}\sigma + \mu\sqrt{\frac{1}{1+\kappa}}\sigma\sum_{m=0}^{KN/\mu-1} x(m). \end{aligned} \tag{50.16}$$

Let $X = \frac{1}{\sqrt{KN/\mu}}\sum_{m=1}^{KN/\mu-1} x(m)$, then $X \sim CN(0,1)$, and we can obtain that

$$R_{\mu,K}^{Rician}(m_0) = KN\sqrt{\frac{\kappa}{1+\kappa}}\sigma + \sqrt{\frac{KN\mu}{1+\kappa}}\sigma X \tag{50.17}$$

The module of the correlation peak, $\left|R_{\mu,K}^{Rician}(m_0)\right|$, is Rican distributed with the parameter $\left(\frac{KN\kappa}{\mu}, \frac{K^2N^2\kappa+KN\mu}{\kappa+1}\sigma^2\right)$. The probability destiny function is shown as

$$f_{\left|R_{\mu,K}^{Rician}\right|}(x) = \frac{2\left(\frac{KN\kappa}{\mu}+1\right)x}{\frac{K^2N^2\kappa+KN\mu}{\kappa+1}\sigma^2} e^{\left(-\frac{KN\kappa}{\mu}-\frac{\left(\frac{KN\kappa}{\mu}+1\right)x^2}{\frac{K^2N^2\kappa+KN\mu}{\kappa+1}\sigma^2}\right)} \cdot I_0\left(2\sqrt{\frac{\frac{KN\kappa}{\mu}\left(\frac{KN\kappa}{\mu}+1\right)}{\frac{K^2N^2\kappa+KN\mu}{\kappa+1}\sigma^2}}x\right). \tag{50.18}$$

For a given threshold R_{th}, the CCDF for correlation peak value higher than the threshold is given by

$$P_{\mu,K}^{Rician}(x > R_{th}) = Q\left(\sqrt{2\frac{KN\kappa}{\mu}}, \frac{R_{th}}{\sigma\sqrt{\frac{KN\mu}{2(\kappa+1)}}}\right). \tag{50.19}$$

50.4 Rayleigh Fading Channel

For the Rayleigh fading channel, the channel parameter $h(m) \sim CN(0, \sigma^2)$, the module of the channel fading parameter is Rayleigh distributed and the probability destiny function is presented as

$$f_{|h|}(x) = \frac{2x}{\sigma^2} e^{-\frac{x^2}{\sigma^2}}. \tag{50.20}$$

50.4.1 Fast Fading Channel

The fast fading channel is defined as above that the period of the channel parameter changing is equal to the period of GNSS PRN code chip and the channel parameter stay invariant within a PRN code chip period T_C. Then, we have the correlation peak as

$$R_{fast}^{Rayleigh}(m_0) = \sum_{m=1}^{N} h(m) \tag{50.21}$$

Then the correlation peak is the summation of N independent identically-distributed random variables which are distributed as $CN(0,\sigma^2)$. So the correlation peak is distributed as $CN(0,N\sigma^2)$. The module of correlation peak, $\left|R_{fast}^{Rayleigh}(m_0)\right|$, is Rayleigh distributed. Thus, the probability destiny function is given by

$$f_{\left|R_{fast}^{Rayleigh}\right|}(x)=\frac{2x}{N\sigma^2}e^{-\frac{x^2}{N\sigma^2}} \tag{50.22}$$

For a given threshold R_{th}, the CCDF for correlation peak value higher than the threshold is presented as

$$P_{fast}^{Rayleigh}(x>R_{th})=\int_{R_{th}}^{+\infty}f_{\left|R_{fast}^{Rayleigh}\right|}(x)dx=e^{-\frac{R_{th}^2}{N\sigma^2}} \tag{50.23}$$

50.4.2 Slow Fading Channel

In the slow fading channel, the assumption is same as above mentioned that the changing period of the channel parameter is equal to the period of GNSS PRN code and the channel parameter stay invariant within a PRN code period NT_C. Then, the correlation peak is

$$R_{slow}^{Rayleigh}(m_0)=Nh(m). \tag{50.24}$$

Hence, the correlation peak is $CN(0,N^2\sigma^2)$. The module of correlation peak, $\left|R_{slow}^{Rayleigh}(m_0)\right|$, is Rayleigh distributed. The probability destiny function is given by

$$f_{\left|R_{slow}^{Rayleigh}\right|}(x)=\frac{2x}{N^2\sigma^2}e^{-\frac{x^2}{N^2\sigma^2}}. \tag{50.25}$$

For a given threshold R_{th}, the CCDF for correlation peak value higher than the threshold is expressed as

$$P_{slow}^{Rayleigh}(x>R_{th})=\int_{R_{th}}^{+\infty}f_{\left|R_{slow}^{Rayleigh}\right|}(x)dx=e^{-\frac{R_{th}^2}{N^2\sigma^2}}. \tag{50.26}$$

50.4.3 General Case

For the general case of Rayleigh fading channel, we assume that N denotes the length of PRN code and K is the coherence integration gain, ΔT is the period of

channel parameter variation and $\mu = \Delta T/T_C$ is the channel variation factor. When $KNT_C/\Delta T$ is an integer, the correlation value and the correlation peak of GNSS signal are shown as

$$R(n) = \sum_{k=0}^{K-1}\sum_{m=1}^{N} h(m+kN)c(m+kN)c(m-m_0+n), \tag{50.27}$$

$$\begin{aligned} R(m_0) &= \sum_{k=0}^{K-1}\sum_{m=1}^{N} h(m+kN) = \sum_{m=0}^{KN-1} h(m) \\ &= \frac{\Delta T}{T_C}\sum_{m=0}^{KNT_C/\Delta T-1} x(m) = \mu \sum_{m=0}^{KN/\mu-1} x(m), \end{aligned} \tag{50.28}$$

where $x(m) \sim CN(0,\sigma^2)$. Let $X = \sum_{m=0}^{KN/\mu-1} x(m)$, then $X \sim CN\left(0, \frac{KN}{\mu}\sigma^2\right)$. So we have

$$R(m_0) = \mu X. \tag{50.29}$$

The module of correlation peak, $\left|R_{\mu,K}^{Rayleigh}(m_0)\right|$, is Rayleigh distributed with the parameter $\frac{\mu KN}{2}\sigma^2$. The probability destiny function is followed as

$$f_{\left|R_{\mu,K}^{Rayleigh}\right|}(x) = \frac{2x}{\mu KN\sigma^2} e^{-\frac{x^2}{\mu KN\sigma^2}}. \tag{50.30}$$

The expectation and variance are

$$E\left[\left|R_{\mu,K}^{Rayleigh}(m_0)\right|\right] = \frac{\sigma\sqrt{\mu KN\pi}}{2}, \tag{50.31}$$

$$Var\left[\left|R_{\mu,K}^{Rayleigh}(m_0)\right|\right] = \left(2-\frac{\pi}{2}\right)\frac{\mu KN}{2}\sigma^2. \tag{50.32}$$

And the CCDF for correlation peak value higher than the threshold R_{th} is expressed as

$$P_{\mu,K}^{Rayleigh}(x > R_{th}) = \int_{R_{th}}^{+\infty} f_{\left|R_{\mu,K}^{Rayleigh}\right|}(x)dx = e^{-\frac{R_{th}^2}{\mu KN\sigma^2}}. \tag{50.33}$$

50.5 Numerical Analysis and Simulation

We have analyzed the performance of acquisition for GNSS signal over frequency non-selective fading channel and derived the probability destiny function and the complementary cumulative distribution function of the module value for the

Table 50.1 The expectation and the standard variance of the correlation peak module for GPS C/A code

		Rayleigh fading	Rician fading		
			$\kappa = 1$	$\kappa = 3$	$\kappa = 5$
Fast fading	Expectation	28.3454	723.7238	886.0883	933.9582
	Standard variance	14.8168	15.9922	11.3082	9.2331
Slow fading	Expectation	906.61	927.3025	964.1131	982.0085
	Standard variance	473.9093	432.0175	342.0745	286.6850

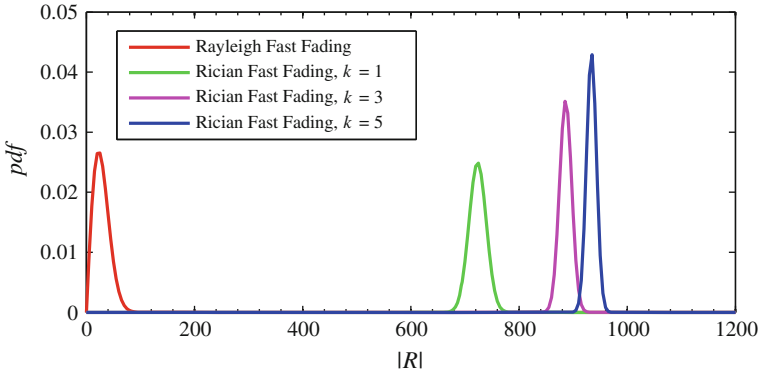

Fig. 50.1 The PDF of the correlation peak module for GPS signal over fast fading channel

correlation peak. In this section, the acquisition of GPS signal will be simulated to verify the correctness of derivation and analysis.

As the length of GPS C/A code is 1023, when 1 ms coherent accumulation is utilized, the expectation and standard variance of the correlation peak module value for GPS C/A code are listed in Table 50.1. And Figs. 50.1 and 50.2 show the probability destiny function when GPS signal transmitted over fast fading and slow fading channels, respectively. And the correlation peak of C/A code is no longer constant value. For the Rician fading channel, either the fast fading or slow fading, the expectation of the module value for the correlation peak increases and the standard variance decreases with the increasing of the Rician fading factor κ. While, for the Rayleigh fading channel, the expectation in fast fading is much less than the value in slow fading which illustrates that fast fading scenario has more disadvantage for GPS C/A code acquisition.

Figure 50.3 shows the theoretical and the simulated complementary cumulative distribution function for the module of the correlation peak when given a threshold R_{th}. The consistency between the theoretical results and the simulation results confirm the validity of the derivations and analysis in Sects. 50.3 and 50.4. For the Rician fading scenario, when $\kappa = 5$ and $R_{th} < 935$, the CCDF in fast fading is higher than the value in slow fading. On the contrary, when $\kappa = 5$ and $R_{th} > 935$,

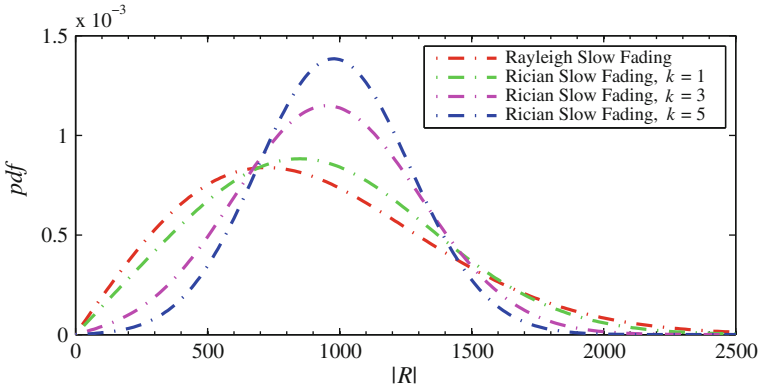

Fig. 50.2 The PDF of the correlation peak module for GPS signal over slow fading channel

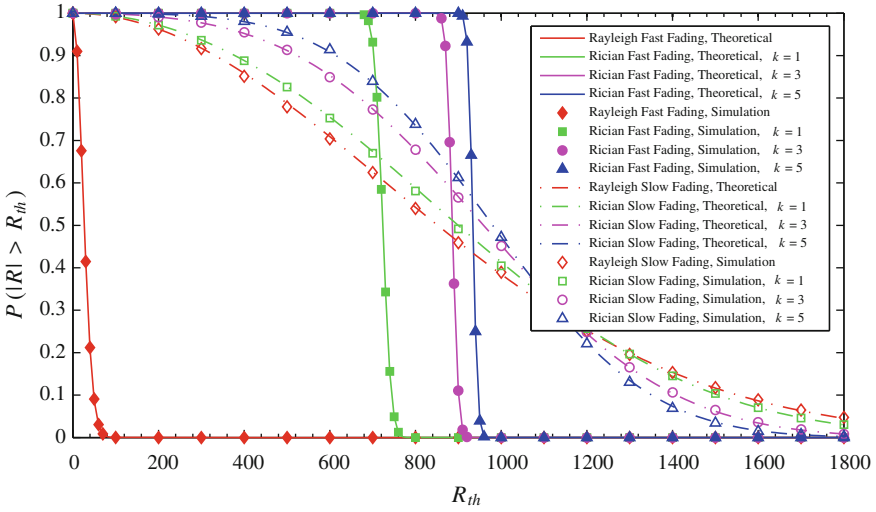

Fig. 50.3 The CCDF of the correlation peak module for GPS signal over fading channel

the CCDF in slow fading is higher. Hence, the same threshold will affect the acquisition performance for the signal transmitted over fading channel with different fading speed. While for the Rayleigh fading scenario, the performance in slow fading channel will be much superior to the fast fading channel. The reason is that there is no line-of-sight component in Rayleigh fading channel and the fast fading will completely destroy the auto-correlation properties of C/A codes.

The probability of detection for GPS signal over fading channel when C/N_0 is 44 dB-Hz is simulated in Fig. 50.4. The x-axis denotes the fading period of the channel and the measurement unit is millisecond. The 0.001 ms corresponds to

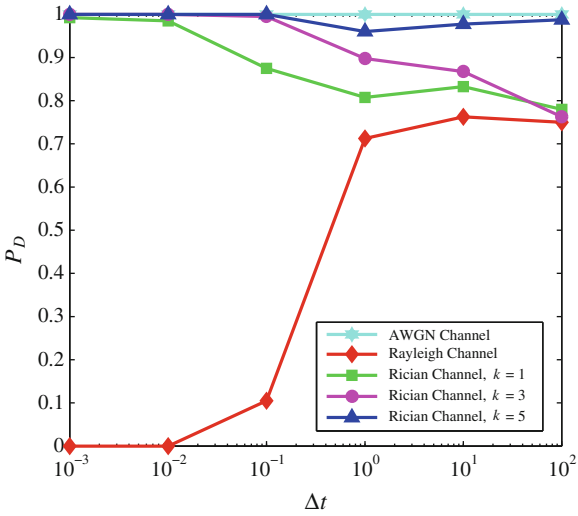

Fig. 50.4 The probability of detection for GPS signal as $C/N_0 = 44$ dB-Hz

fast fading period and 1 ms corresponds to slow fading period. In this simulation, the threshold is 1023/2, half of C/A code length. For Rician fading channel, the simulation results show that the detection probability in fast fading is superior to the probability in slow fading. But the simulation results in Rayleigh channel are just opposite. The simulation results in Fig. 50.4 coincide with the CCDF in Fig. 50.3 when threshold is 1023/2.

50.6 Conclusion

In this study, we have analyzed and simulated the performance of acquisition for GNSS signal over frequency non-selective fading channel. The probability density function and the complementary cumulative distribution function are derived when GNSS signal transmitted over Rician fading channel and Rayleigh fading channel respectively. The analysis and simulation show that the Rayleigh fading has more disadvantage than Rician fading. The effect of fading channel on the probability of false alarm is not considered in this study and this will be detailed study the future works.

Acknowledgments This research is sponsored by National High-technology Research and Development Program (863 Program) of China (project no. 2012AA120802) and the Fundamental Research Funds for the Central Universities (Grant No.HIT.NSRIF.2014022), also supported by the National Science and Technology Major Project (2012ZX03004003).

References

1. Burgi C, Mey E, Orzati V et al (2006) Higly integrated solution for ultra-fast acquisition and precise tracking of weak GPS and Galileo L1 signals. In: ION GNSS 2006, Fairfax, VA, pp 226–235
2. Van Nee D, Coenen A (1991) New fast GPS code-acquisition technique using FFT. Electron Lett 27:158–160
3. Chansarkar MM, Garin L (2000) Acquisition of GPS signals at very low signal to noise ratio. In: ION national technical meeting. Anaheim, CA, pp 731–737
4. van Diggelen F (2000) A-GPS: assisted GPS, GNSS, and SBAS. Artech House Inc., Boston
5. Moghaddam A, Watson R, Lachapelle G et al (2006) Exploiting the orthogonality of L2C code delays for a fast acquisition. In: ION GNSS 2006, Fairfax, VA, pp 1233–1241
6. Proakis JG, Salehi M (2008) Digital communications, 5th edn. McGraw-Hill Companies Inc., New York, pp 830–899

Chapter 51
Research on High Sensitivity Acquisition Methods for the BDS B1I Signal

Lei Chen, Hong Lei Qin and Tian Jin

Abstract As the BDS B1I signal transmitted by MEO/IGSO satellites is modulated with 1 kbps Neumann-Hoffman code (NH code), the coherent integration time is limited within 1 ms, which cause difficulties to acquire weak signals. To overcome the problems brought by high bit-flipping rate of NH code, this paper conducts research to improve PMF-FFT (partial matched filter and fast Fourier transform) methods [1, 2] according to the feature of the B1I signal. Firstly, the estimation of NH code phase is done during acquisition to remove the effect of NH code and extend coherent integration time. And then incoherent integration is done to further improving the processing gain. Finally, simulations are conducted, the results show that the revised PMF-FFT methods can successfully acquire B1I signal as weak as 23 dB-Hz.

Keywords BDS · NH code · High sensitivity acquisition · PMF-FFT

51.1 Introduction

The BeiDou Navigation Satellite System (BDS) is a satellite navigation system established and run independently by China, which has wide application prospect and important strategic significance. In some specific environments like forests, urban and canyon, satellite signal power declines seriously due to occlusion, which causes difficulties for receivers to acquire it. Thus needs high sensitivity acquisition methods to enhance the sensitivity of receivers.

Generally, acquisition methods can be divided into two categories as the serial search method and the parallel search method. The serial search method [3] means

L. Chen (✉) · H. L. Qin · T. Jin
School of Electronics and Information Engineering, BeiHang University,
Beijing 100191, China
e-mail: blue_aia@sina.cn; blue_aia@163.com

J. Sun et al. (eds.), *China Satellite Navigation Conference (CSNC) 2014 Proceedings: Volume I*, Lecture Notes in Electrical Engineering 303,
DOI: 10.1007/978-3-642-54737-9_51,

using digital correlators to scan for specific satellite signal in both Doppler frequency domain and code phase domain. This method costs few resources but has slow speed. The parallel search method [4] means using FFT method to realize parallel search in Doppler frequency domain or code phase domain. At present, high sensitivity acquisition is realized mainly by extending the coherent and incoherent integration time. As the BDS B1I signal transmitted by MEO/IGSO satellites is modulated with 1 kbps Neumann-Hoffman code (NH code), the coherent integration time is limited within 1 ms when using the methods mentioned above and so the acquisition sensitivity is limited.

To overcome the problems brought by high bit-flipping rate of NH code, this paper conducts research to improve partial matched filter and fast Fourier transform (PMF-FFT) methods [5] according to the feature of the B1I signal. The estimation of NH code phase is done during acquisition to remove the effect of NH code and extend coherent integration length. And incoherent integration is done to further improving the processing gain.

The paper is organized as follows. Section 51.2 presents an overview of the general structure of the received B1I signal. Section 51.3 introduces the traditional acquisition method and analyzed how NH code affects the sensitivity of traditional acquisition method. Section 51.4 presents the PMF-FFT combined NH code estimation and incoherent integration method, the frequency response and detection probability is derived. Section 51.5 presents the result of simulation experiments and Sect. 51.6 is the summary of the whole paper.

51.2 Signal Model

The BDS B1I signal is received by antenna and is demodulated to intermediate frequency through low noise amplifiers, filters and down-converters. The intermediate frequency signal $i(n)$ and $q(n)$ is shown as follows:

$$i(n) = AC(n+\tau)D(n)NH(n)cos\left(2\pi\left(f_0 + f_{dopp}\right)n\Delta T + \phi_0\right) + n_i(n) \tag{51.1}$$

$$q(n) = AC(n+\tau)D(n)NH(n)sin\left(2\pi\left(f_0 + f_{dopp}\right)n\Delta T + \phi_0\right) + n_q(n) \tag{51.2}$$

The two formulas above can be expressed in plural form as:

$$r(n) = AC(n+\tau)D(n)NH(n)\exp\left(j2\pi\left(f_0 + f_{dopp}\right)n\Delta T + \phi_0\right) + N_{noise} \tag{51.3}$$

where A is the received carrier amplitude, $C(n)$ is the C/A PRN of B1I signal, τ is the initial code phase, $D(n)$ is the navigation data, $NH(n)$ is the Neumann-Hoffman code, f_0 is the intermediate frequency, f_{dopp} is the Doppler frequency, ϕ_0 is the

carrier accumulated phase, ΔT is the Sampling interval, n_i and n_q are Gaussian white noise (GWN) following normal distribution which are independent of each other.

51.3 Signal Model

Take the serial acquisition [6] method as example to analyze the performance of the traditional acquisition method when acquiring B1I signal. Method diagram as shown in Fig. 51.1.

Firstly, the Doppler frequency and code phase range are divided by certain search step, composing multiple search units. In each unit, the code phase of local recurrence carrier frequency domain corresponds to the central position of the unit. Baseband signal and the local recurrence carrier are mixed to obtain the signal as follows:

$$r(n) = AC(n+\tau)D(n)NH(n)\exp(j2\pi f_d n\Delta T + \phi_0) + N_{noise} \tag{51.4}$$

Mixing result is correlated with the local recurrence spread spectrum code:

$$i(n) = AD(n)R(\tau)R_{NH}(\tau')\mathrm{sinc}\left(2\pi f_{dopp} n\Delta T\right)\cos(\phi_0) + n_i \tag{51.5}$$

$$q(n) = AD(n)R(\tau)R_{NH}(\tau')\mathrm{sinc}\left(2\pi f_{dopp} n\Delta T\right)\sin(\phi_0) + n_q \tag{51.6}$$

$R_{NH}(\tau')$ is the correlation result of the baseband signal and the local PRN code. The incoherent integral amplitude of each search unit can be calculated as follows:

$$\begin{aligned} |r(n)|^2 &= |i(n)|^2 + |q(n)|^2 \\ &= \left(AR(\tau)R_{NH}(\tau')\left|\mathrm{sinc}\left(2\pi f_{dopp}\Delta T\right)\right|\right)^2 \end{aligned} \tag{51.7}$$

If the amplitude of the maximum non coherent integration is above the preset capture threshold, it means that the acquisition is successful and the current frequency is the real frequency of the signal, and the initial code phase can be got by the peak position, otherwise means the signal does not exist or the acquisition fails.

It can be inferred from Eq. (51.7) that the amplitude of incoherent integration is influenced by the correlation result of NH code. The autocorrelation characteristic curve of the NH code modulated by BD B1I signal is shown in Fig. 51.2. It can be seen that $R_{NH}(\tau')$ reached its maximum when NH codes of the baseband signal and the local PRN are completely synchronized, otherwise it drops rapidly. So if the NH code is not striped, the coherent integration length will be limited in 1 ms, so that the acquisition sensitivity is limited. In order to improve the acquisition sensitivity, NH code stripping method is indispensable.

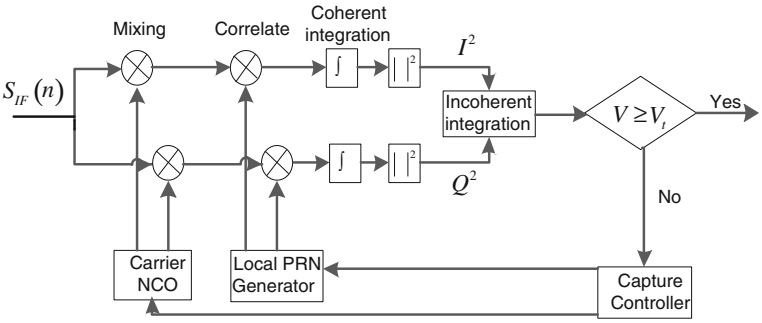

Fig. 51.1 Serial acquisition algorithm

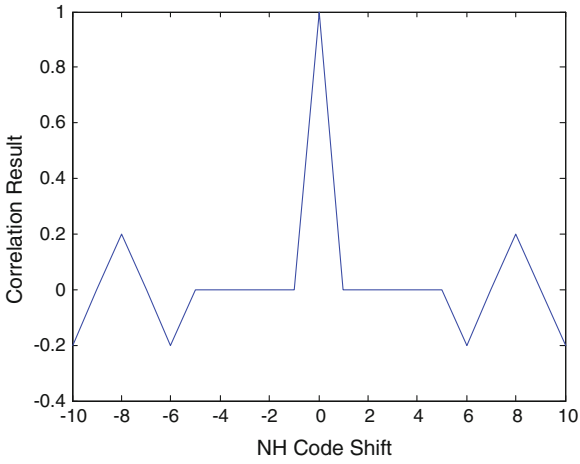

Fig. 51.2 Autocorrelation feature of NH code

51.4 Revised PMF-FFT Method Based on Incoherent Integration and NH Code Stripping

51.4.1 Acquisition Method Architecture

Figure 51.3 shows the structure of the Revised PMF-FFT method based on incoherent accumulation and release of NH code stripping. The revised method mainly contains four parts: NH code stripping, partial matched filtering, Fast Fourier Transform, and incoherent integration. The particular steps of the method are as follows:

1. Firstly, the number of partial matched filter P, the coherent integration length T_i and the incoherent accumulation times M are set before time.
2. The sampling frequency is denoted by f_s. So the total amount of sampling data needed for one time acquisition is $N_{total} = T_i \cdot M \cdot f_s$.

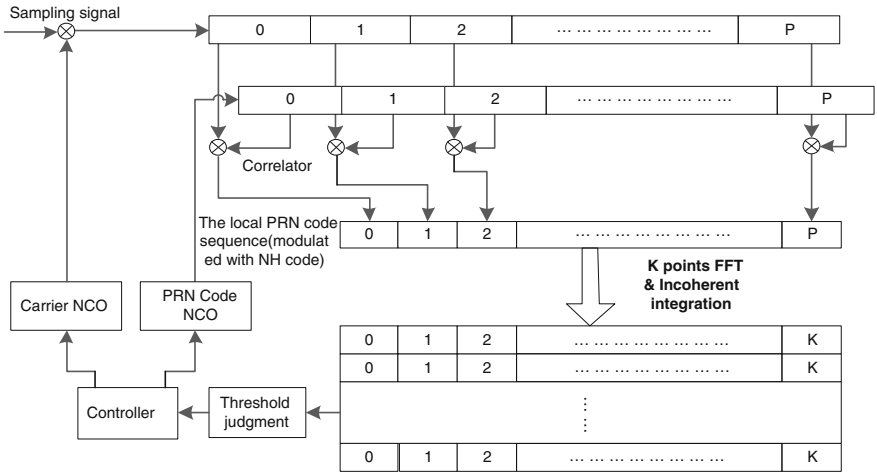

Fig. 51.3 Structure of the revised PMF-FFT methods

3. Generate the local C/A PRN with the length equal to T_i. Denote the NH code sequence as: $NH[20] = [0, 0, 0, 0, 0, 1, 0, 0, 1, 1, 0, 1, 0, 1, 0, 1, 0, 0, 1, 1, 1, 0]$. Assuming that the initial NH code phase of the input signal is $NH[0]$. Modulate the local C/A PRN and the NH code sequence together and divide the modulated sequence into P sections. Divide the input T_i long signal sampling sequence into P sections as well and correlate the corresponding PRN section and signal section to get the partial correlation results. Transfer the partial correlation results to the complex FFT (the whole number of FFT points is K) to resolve the residual carrier frequency between the receiver and the satellite.
4. Input the next T_i long signal sampling sequence and repeat step (2) until it has been done M times. Calculate the modulus of the FFT results and accumulate the corresponding M modulus respectively. Save the accumulation results.
5. Shift the local PRN sequence a few points and repeat step (2) to step (3) until the possible PRN code phase has been checked.
6. Set the initial code phase of the local NH code to NH[1], NH[2] … NH[19] successively and repeat step (2) to step (4). After all the accumulation results are got, find the peak result and compare with the threshold which is set before time. If the peak result is bigger than the threshold, that means the signal is successfully acquired.

51.4.2 System Model

Regardless of the initial carrier phase, the in- and quadrature-phase accumulations are shown in Eqs. (51.8) and (51.9).

$$i(n) = AC(n+\tau)D(n)NH(n)\cos(2\pi f_d n\Delta T) + n_i \tag{51.8}$$

$$q(n) = AC(n+\tau)D(n)NH(n)\sin(2\pi f_d n\Delta T) + n_q \tag{51.9}$$

Denote the number of the sampling data contained in every section as:

$$N = (T_i \cdot f_s)/P$$

The outputs of the partial matched filter are:

$$I_i = \sum_{k=Ni}^{N(i+1)-1} [AR(i)R_{NH}(i)D(i)\cos(2\pi f_d k\Delta T) + n_i(k\Delta T)] \tag{51.10}$$

$$Q_i = \sum_{k=Ni}^{N(i+1)-1} \left[AR(i)R_{NH}(i)D(i)\sin(2\pi f_d k\Delta T) + n_q(k\Delta T)\right] \tag{51.11}$$

$$R(i) = \frac{1}{N}\sum_{k=Ni}^{N(i+1)-1} C(k)C_p(k) \tag{51.12}$$

$$R_{NH}(i) = \frac{1}{N}\sum_{k=Ni}^{N(i+1)-1} NH(k)NH_p(k) \tag{51.13}$$

where $i = 0,1,2,\ldots,(P-1)$, $R(i)$ is the cross-correlation value of the signal PRN and local PRN, and $R_{NH}(i)$ is the cross-correlation value of the signal NH code and the local NH code.

Only consider of the condition when the signal PRN and local PRN, signal NH code and local NH code perfectly matched, when $R(i) = R_{NH}(i) = 1$ according the Eqs. (51.12) and (51.13). Assume that the navigation data remains unchanged during the coherent integration period, then Eq. (51.14) can be derived from Eqs. (51.10) and (51.11).

$$V(i) = \sum_{k=Ni}^{N(i+1)-1} [\exp(2\pi f_d k\Delta T) + n_s(k\Delta T)] \tag{51.14}$$

$$\begin{aligned} V(i) = &\left(\frac{\sin(\pi f_d N\Delta T)}{\sin(\pi f_d \Delta T)}\right)\cdot\left(\frac{\exp(j2\pi f_d iN\Delta T)\cdot\exp(j\pi f_d N\Delta T)}{\exp(j\pi f_d N\Delta T)}\right) \\ &+ \sum_{k=Ni}^{N(i+1)-1} n_s(k\Delta T) \end{aligned} \tag{51.15}$$

The outputs of the partial matched filters are then transferred to the complex FFT. The number of the complex FFT points is K. Calculate the modulus of the outputs of the complex FFT.

$$\begin{aligned}\left|\hat{V}^l(k)\right| &= \sum_{i=0}^{K-1}\left(\exp(-j2\pi ik/k)\cdot V(i)\right) \\ &= \left|\left(\frac{\sin(\pi f_d N\Delta T)}{\sin(\pi f_d \Delta T)}\right)\cdot\left(\frac{\sin(\pi f_d NP\Delta T-\pi Pk/K)}{\sin(\pi f_d N\Delta T-\pi k/K)}\right)\right| + N_s\end{aligned} \tag{51.16}$$

where $k = 0, 1,\ldots, (K-1)$, $l = 1,\ldots, M$, and N_s is the noise part. Square and accumulate the modulus, and the final results can be expressed as follows:

$$\left|\hat{V}^2(k)\right|_M = (1/M)\sum_{l=1}^{M}\left|\hat{V}^l(k)\right|^2 \tag{51.17}$$

Set the acquiring threshold before time and compare the peak output of Eq. (51.17) with it. If the peak output of Eq. (51.17) is larger than the acquiring threshold, then the signal is acquired successfully. The Doppler frequency of the signal can be derived according to the location of the peak as follows:

$$f_d = \frac{kP}{KT_i}.$$

51.4.3 Performance Analysis

When the searching signal does not exist or the signal PRN and local PRN do not matched, the output results $\left|\hat{V}^2(k)\right|_M$ behave according to center chi-square distribution with $2M$ degrees of freedom. The probability density function (PDF) of $\left|\hat{V}^2(k)\right|_M$ can be expressed as follows when $\sigma^2 = 1$.

$$f_{noise}(V) = \frac{1}{2^M\Gamma(M)}(V)^{M-1}e^{-V/2}, \quad V \geq 0 \tag{51.18}$$

When the searching signal exists, $\left|\hat{V}^2(k)\right|_M$ behave according to the noncentral chi-square distribution with $2M$ degrees of freedom and the PDF is as follows [7].

$$f_{\text{signal}}(V)\imath = \frac{1}{2}\left(\frac{V}{\lambda}\right)^{\frac{M-1}{2}}e^{\left(-\frac{\lambda+V}{2}\right)}I_{M-1}\left[(V\cdot\lambda)^{\frac{1}{2}}\right] \tag{51.19}$$

Where λ is the noncentral parameter and can be calculated as follows [8]:

$$\lambda = \frac{\left|\left(\frac{\sin(\pi f_d N\Delta T)}{\sin(\pi f_d \Delta T)}\right)\cdot\left(\frac{\sin(\pi f_d NP\Delta T-\pi Pk/K)}{\sin(\pi f_d N\Delta T-\pi k/K)}\right)\right|}{P\cdot N}$$

The false alarm probability of one $\left|\hat{V}^2(k)\right|_M$ can be calculated according to Eq. (51.18).

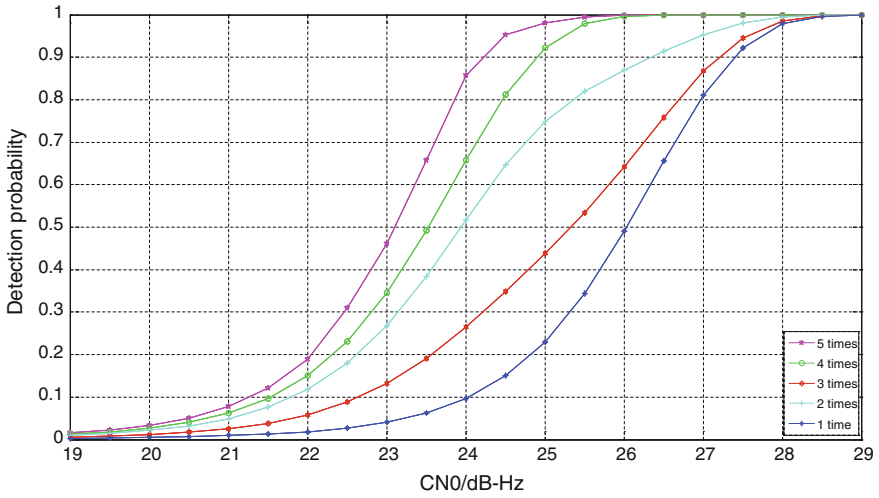

Fig. 51.4 Relation between detection probability and CN0 under different incoherent integration times

$$P_{fa} = \int_{V_t}^{+\infty} f_{noise}(V) \cdot dV \tag{51.20}$$

The false alarm probability of one time acquisition is as follows:

$$P_{FA} = 1 - \left(1 - P_{fa}\right)^K \tag{51.21}$$

The detection probability of one $\left|\hat{V}^2(k)\right|_M$ can be calculated according to Eq. (51.19).

$$P_d = \int_{V_t}^{+\infty} f_{\text{signal}}(V) \cdot dV \tag{51.22}$$

The detection probability of one time acquisition is as follows:

$$P_D = 1 - (1 - P_d)^K \tag{51.23}$$

Set the needed P_{FA} before time, the P_D can be calculated according to Eqs. (51.18)–(51.23).

Figure 51.4 shows the relation between detection probability and CN0 under different incoherent integration times. The detection probability is calculated under

Table 51.1 Acquisition result under different CN0 conditions

20 ms coherent integration, 5 time incoherent integration, with NH code stripping					
Signal CN0 (dB-Hz)	Carrier Doppler frequency	PRN code phase	Peak	Noise	Peak/noise ratio
25	*1 kHz*	*204.6*	*3.52E+07*	*4.98E+06*	*7.0679*
24	*1 kHz*	*204.6*	*2.92E+07*	*5.00E+06*	*5.8336*
23	*1 kHz*	*204.6*	*2.61E+07*	*4.98E+06*	*5.2313*
22	550	721.3	2.33E+07	4.98E+06	4.6691
21	850	84.9	2.30E+07	4.98E+06	4.6142

the condition that the false alarm probability $P_{FA} = 0.001$, the number of FFT points is 200 and the carrier Doppler frequency is $f_d = 0$ Hz. It shows that the detection probability rises as the incoherent accumulation time increases.

51.5 Simulation Results

Simulation experiment is carried out to prove the acquisition sensitivity of the revised PMF-FFT method. The signal data used in the experiment is generated by simulation method, so that the exact code phase and Doppler frequency can be known before time. The exact code phase of signal is 204.6, and the exact carrier Doppler frequency is 1 kHz. A series of signal data of different CN0 are generated for the test of acquisition sensitivity.

The parameters of the implemented method are as follows. The sampling frequency is $f_s = 50$ MHz. The coherent integration time is $T_i = 20$ ms. The number of partial matched filter is $P = 200$. The number of complex FFT points is $K = 200$. The frequency resolution is $f_{dis} = P/(T_i \cdot K) = 50$ Hz. The number of incoherent integration is $M = 5$.

Table 51.1 shows the results of the revised PMF-FFT method when the CN0 of input signal varies from 25 to 21 dB-Hz, where the italicized parts mean successfully acquired. Figure 51.5 shows that the output peak to noise ratio goes down when the CN0 of the signal decrease. Figures 51.6, 51.7 and 51.8 show the results of the method when the code phase of local PRN is set equal to the exact signal code phase and the signal CN0 varies from 22 to 24 dB-Hz. From these tree figures, it can be seen that there is a clear peak at the true location when CN0 $\geq$ 23 dB-Hz, and there is no obvious peak when CN0 $\leq$ 22 dB-Hz.

Two contrast experiments are carried out in order to verify the improvement of the acquisition sensitivity of the revised method. The first experiment is comparing the acquisition sensitivity of the method with or without NH code stripping. The second experiment is comparing the acquisition sensitivity of the method with or without incoherent integration when NH code stripping is included. The results are shown in Tables 51.2 and 51.3. Table 51.2 illustrates that the acquisition

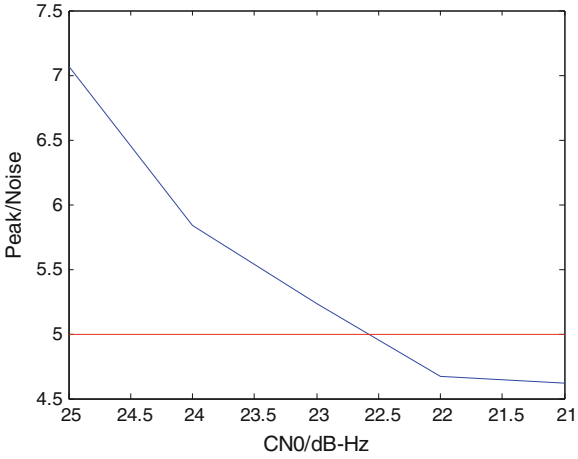

Fig. 51.5 Peak/noise under different CN0 conditions

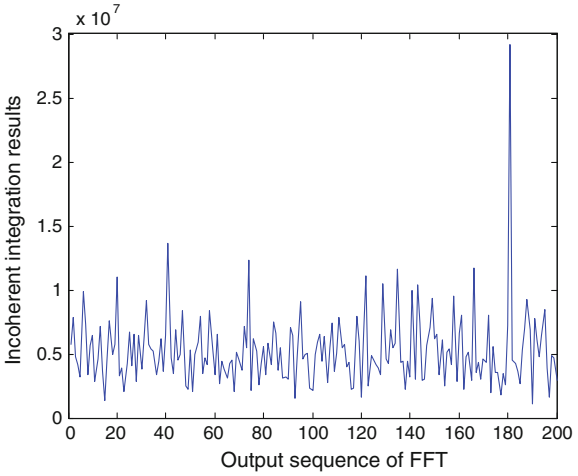

Fig. 51.6 FFT outputs at CN0 = 24 dB-Hz, code phase = 204.6

sensitivity of method with NH code stripping is 9 dB higher than method without NH code stripping when the coherent integration length is 20 ms. Table 51.3 illustrates that the acquisition sensitivity of method with five times incoherent accumulation is 5 dB higher than method without incoherent accumulation.

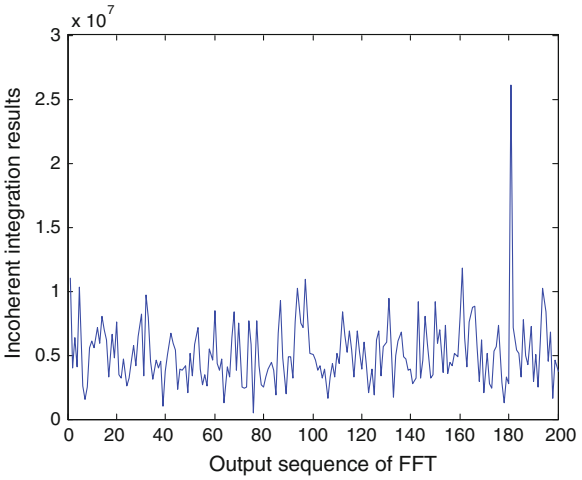

Fig. 51.7 FFT outputs at CN0 = 23 dB-Hz, code phase = 204.6

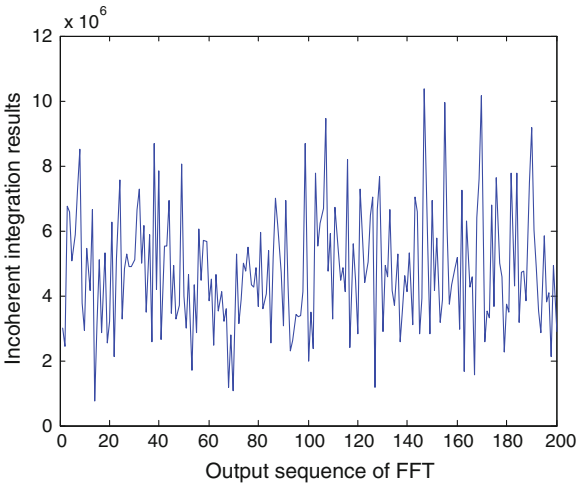

Fig. 51.8 FFT outputs at CN0 = 22 dB-Hz, code phase = 204.6

Table 51.2 Acquisition sensitivity of PMF-FFT without NH code estimation

Acquisition method	Acquisition sensitivity (dB-Hz)
20 ms coherent integration, 5 time incoherent integration, NH code stripping	36
1 ms coherent integration, no incoherent integration, no NH code stripping	41

Table 51.3 Relationship between acquisition sensitivity and incoherent integration times

Incoherent integration time	1	2	3	4	5
Acquisition sensitivity/dB-Hz	27	26	25	23	23

51.6 Conclusion

The BDS B1I signal transmitted by MEO/IGSO satellites is modulated with 1 kbps NH code, limiting the coherent integration time within 1 ms, which cause difficulties to acquire weak signals. Aiming at solving this problem, this paper presents a revised PMF-FFT acquiring method, combining the NH code stripping method and incoherent integration method together with the traditional PMF-FFT method. The effect of NH code on traditional acquisition method is analysed in Sect. 51.3. The structure of the revised method is presented and the system model is given in Sect. 51.4. The simulation experiment results are given in Sect. 51.5. It turns out that the revised PMF-FFT method can successfully acquire signal as weak as 23 dB-Hz in simulation environment, which is 9 dB higher than method without NH code stripping and 5 dB higher than method with NH code stripping but without incoherent integration. The future works include: (1) Implementing the revised PMF-FFT using FPGA and test the performance with actual signal; (2) Studying ways to compensate the PRN code phase according to the carrier Doppler frequency on the basis of the revised PMF-FFT method.

References

1. Spangenberg SM et al (2000) An FFT-based approach for fast acquisition in spread spectrum communication systems. Wirel Pers Commun 13(1–2):27–55
2. Chang L, Jun Z, Zhu Y, Qingge P (2011) Analysis and optimization of PMF-FFT acquisition algorithm for high-dynamic GPS signal. In: Proceedings of 2011 IEEE 5th international conference, 17–19 Sept 2011
3. Lin DM, Tsui JBY (2000) Comparison of acquisition methods for software GPS receiver. In: Proceedings of ION GPS, 2000
4. Li W, Huang X, Liu L (2013) New acquisition scheme with high sensitivity for long code. J Xidian Univ (Nat Sci) 40(4)
5. Shi X, Ba X, Chen J (2013) Research on acquisition methods for the B1 signal of MEO/IGSO in BDS. Foreign Electronic Measurement Technology 32(4)
6. Xie G (2009) Principles of GPS and receiver design. Electronic Industry Press, Beijing
7. Wang Y, Wang J (2009) Random signals analysis basics. Electronic Industry Press, Beijing
8. Qin Y, Zhang B-N, Guo D-S, Ye Z (2009) Research of P-code direct acquisition technology at low signal-to-noise rate in high dynamic condition. J Astronaut 30(2)

Chapter 52
Analyses of Ratio Test Technique for Satellite Navigation Receivers Anti-spoofing

Long Huang, Weihua Mou, Guangfu Sun and Feixue Wang

Abstract An effective method to attack GNSS receivers tracking the authentic satellite is to make the code phase of spoofing signals relatively slipping respect to the corresponding authentic ones. In this paper, a detection technique based on ratio test of correlation peak is proposed to the auto-aligned synthesis spoofing mode. By analyzing the distortion process of correlation peak, the maximum of the ratio test result and its position are calculated, and setting the threshold of ratio test accordingly. Simulation results show that the proposed ratio test method could achieve a detection probability of 90 % with a false alarm probability of 5 %, and could also avoid false alarm induced by multipath and signal fluctuations.

Keywords GNSS · Satellite navigation receiver · Spoofing interference · Ratio test · Anti-spoofing

52.1 Introduction

Spoofing is a kind of correlative interferes to CDMA systems. By transmitting similar signals with higher power, spoofing could induct target receivers and result in wrong time and position outputs or even no information out. Spoofing interferes can be divided into re-radiated and generated types. The re-radiated spoofing must be co-operated with suppressing interferes to conduct effective attacks, while generated spoofing could take effect alone by directly invading code tracking loops of receivers. Consequently, generated spoofing is more practical and becomes a main spoofing technique.

L. Huang (✉) · W. Mou · G. Sun · F. Wang
Satellite Navigation R&D Center, National University of Defense Technology, Changsha, China
e-mail: huangl386@hotmail.com

J. Sun et al. (eds.), *China Satellite Navigation Conference (CSNC) 2014 Proceedings: Volume I*, Lecture Notes in Electrical Engineering 303,
DOI: 10.1007/978-3-642-54737-9_52,

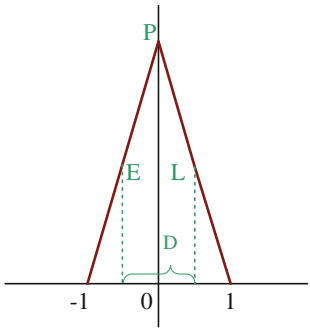

Fig. 52.1 CCF of authentic signal

To the application scenario of spoofing attacks to the receivers tracking the authentic signals, a ratio test technique is proposed in this paper to detect the invading process of generated spoofing interferes. The ratio test technique needs only add a small software module to the traditional GNSS receivers with nothing modified in hardware, and could achieve the detection probability (P_D) of 90 % with a false alarm probability (P_{fa}) of 5 %.

52.2 System Model

The code tracking loops of GNSS receivers usually take the structure of Delay Lock Loops (DLL), while $\tilde{I}_{early}$ $\tilde{I}_{prompt}$ and $\tilde{I}_{late}$ presenting the early channel, prompt channel and late channel respectively. As shown in Fig. 52.1, the correlations of early channel are basically equal to the late channel.

Define the ratio test detector as:

$$\Gamma(\Delta) = \frac{\tilde{I}_{late}}{\tilde{I}_{prompt}} = 1 - \frac{\Delta}{2} \tag{52.1}$$

It means that the ratio test detector is a constant related to the early-late space (Δ) when tracking the authentic signals.

The invading process of a generated spoofing to a GNSS receiver can be demonstrated in Fig. 52.2.

The grey triangle is the CCF (correlation function) of authentic signal and local replicated codes, and the black triangle is the CCF of spoofing signal and local replicated codes. The red dashed shows the synthesized plot of the authentic and spoofing CCFs.

Supposing that the spoofing signals moved from the late to the early relative to the authentic signals, it is obvious that the spoofing taking effect only when the mismatch of signals phases less than $1 + \Delta$. In this process, the correlation of late channel ascends while the correlation of prompt channel descends, which results in the ratio test outputs grows in the spoofing processing. Therefore, a generated

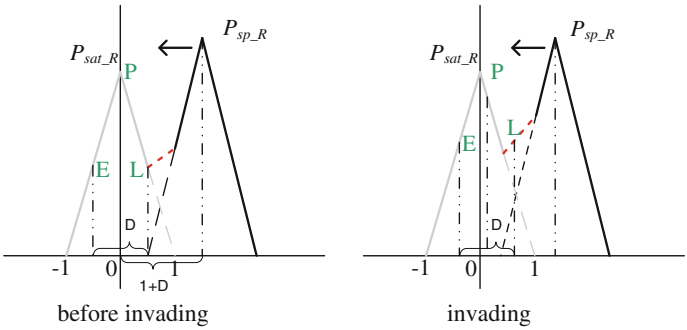

Fig. 52.2 Invading process of generated spoofing signal (Color figure online)

spoofing can be detected by comparing the ratio test results to the predefined threshold.

To conduct a effective attack, the generated spoofing signals should fill the following conditions:

- The spoofing signal power entering the target code loop should be higher than the authentic signal;
- The moving speed of spoofing signal relative to authentic signal should be less than the maximum dynamic range.

The following analyse is restricted to the code phase mismatch range between $1 + \Delta$ to 0. The characteristic of ratio test is just the same in the remaining process.

The focus of ratio test technique is to find the reasonable threshold, which guaranteeing the effective diction of spoofing which the false alarm probability is constricted.

In corroding to the position of late and prompt channels in the synthesized CCF, the invading process could be divided into the following phases.

52.2.1 Phase I of Spoofing Invading

Phase I is defined as that the prompt channel positioned in the authentic CCF area (grey real line in Fig. 52.3) and the late channel positioned in the synthesized CCF area (red dash line in Fig. 52.3).

In this phase, the correlations outputs of late channel ascend while the correlation outputs of prompt channel descend. Consequently, the ratio test detector is a increasing function, and the maximum comes in at the end of this phase:

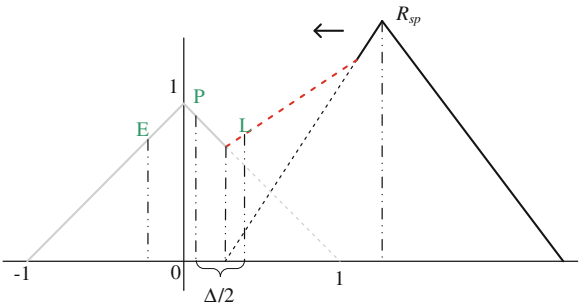

Fig. 52.3 Phase I of invading process of generated spoofing signal (Color figure online)

$$\Gamma_{L\_max}(\Delta)\begin{cases} = \dfrac{1-\frac{\Delta}{2}+\frac{\Delta}{4}R_{sp}}{1-\frac{\Delta}{4}R_{sp}} & 1<R_{sp}<2 \\ > 1+\left(R_{sp}-1\right)\frac{\Delta}{2} & R_{sp}\geq 2 \end{cases} \tag{52.2}$$

52.2.2 Phase II of Spoofing Invading

Phase II is defined as that the prompt channel and the late channel both positioned in the synthesized CCF area (red dash line in Fig. 52.4).

In this phase, the correlation outputs of late and prompt channel both ascend with time. The ratio test detector could be presented as:

$$\Gamma_L(\tau) = \frac{L_0 + \left(R_{sp}-1\right)\tau}{P_0 + \left(R_{sp}-1\right)\tau} \tag{52.3}$$

Derivative the upper equation,

$$\frac{\partial\Gamma_L(\tau)}{\partial\tau} = \frac{\left(R_{sp}-1\right)(P_0-L_0)}{\left[P_0+\left(R_{sp}-1\right)\tau\right]^2} < 0 \tag{52.4}$$

That is the ratio test is a decreasing function in phase II of spoofing invading process.

52.2.3 Phase III of Spoofing Invading

Phase III is defined as that the prompt channel positioned in the synthesized CCF area (red dash line in Fig. 52.5) and the late channel positioned in the spoofing CCF increasing area (black real line in Fig. 52.5).

In this phase, the correlation outputs of late and prompt channel both ascend with time as in phase II. The ratio test detector could be presented as:

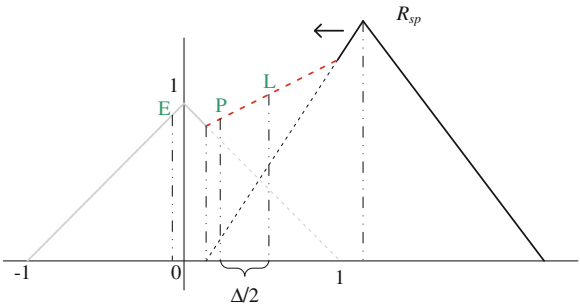

Fig. 52.4 Phase II of invading process of generated spoofing signal (Color figure online)

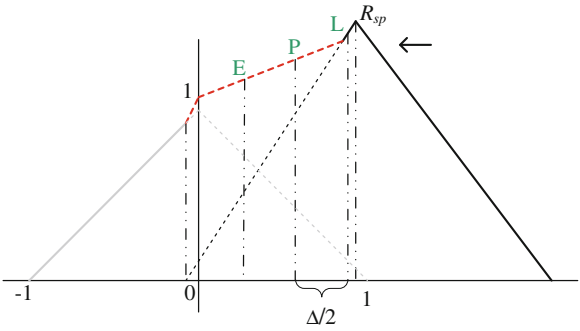

Fig. 52.5 Phase III of invading process of generated spoofing signal (Color figure online)

$$\Gamma_L(\tau) = \frac{P_0 + \left(R_{sp} - 1\right)\frac{\Delta}{2} + R_{sp}\tau}{P_0 + \left(R_{sp} - 1\right)\tau} \tag{52.5}$$

Derivative the upper equation,

$$\frac{\partial \Gamma_L(\tau)}{\partial \tau} = \frac{-\left(R_{sp} - 1\right)^2 \frac{\Delta}{2}}{\left[P_0 + \left(R_{sp} - 1\right)\tau\right]^2} < 0 \tag{52.6}$$

That is the ratio test is also a decreasing function in phase III of spoofing invading process.

52.2.4 Phase IV of Spoofing Invading

Phase IV is defined as that the prompt channel positioned in the synthesized CCF area (red dash line in Fig. 52.6) and the late channel positioned in the spoofing CCF decreasing area (black real line in Fig. 52.6).

In this phase, the correlation outputs of late descend with time while the correlation outputs of prompt ascend with time. Therefore, the ratio test is also a decreasing function in phase IV of spoofing invading process.

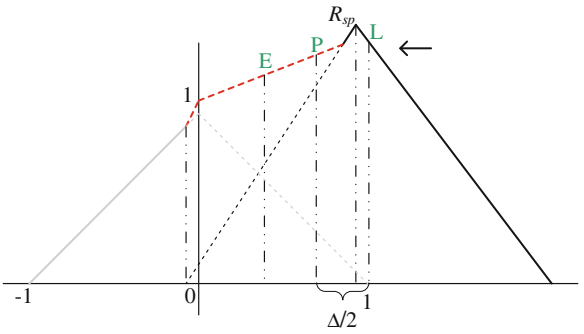

Fig. 52.6 Phase IV of invading process of generated spoofing signal (Color figure online)

In the all four invading phases, the ratio test detector ascends with time only in phase I, so the maximum of ratio test in the whole invading process is just the maximum in phase I.

$$\Gamma_{L\_max}(\Delta)\begin{cases} = \frac{1-\frac{\Delta}{2}+\frac{\Delta}{4}R_{sp}}{1-\frac{\Delta}{4}R_{sp}} & 1<R_{sp}<2 \\ > 1+\left(R_{sp}-1\right)\frac{\Delta}{2} & R_{sp}\geq 2 \end{cases} \tag{52.7}$$

52.3 Detection Method

According to the upper analyses, a dualistic hypothesis testing could be constructed based on the ratio test detector:
H0 spoofing is present;
H1 spoofing is absent.

The statistical characteristic of the correlation output of the late and prompt channels can be written as:

$$\begin{aligned} \tilde{I}_{L|H_0} &\sim N\left(1-\frac{\Delta}{2},\sigma^2\right) \\ \tilde{I}_{P|H_0} &\sim N\left(1,\sigma^2\right) \\ \tilde{I}_{L|H_1} &\sim \begin{cases} N\left(1-\frac{\Delta}{2}+\frac{\Delta}{4}R_{sp},\sigma^2\right) & 1<R_{sp}<2 \\ N\left(1+\left(R_{sp}-1\right)\frac{\Delta}{2},\sigma^2\right) & R_{sp}\geq 2 \end{cases} \\ \tilde{I}_{P|H_1} &\sim \begin{cases} N\left(1-\frac{R_{sp}}{4},\sigma^2\right) & 1<R_{sp}<2 \\ N\left(1,\sigma^2\right) & R_{sp}\geq 2 \end{cases} \end{aligned} \tag{52.8}$$

The ratio test detector is derived by dividing a normal random variable by another normal random variable, and the probability distributing function (PDF)

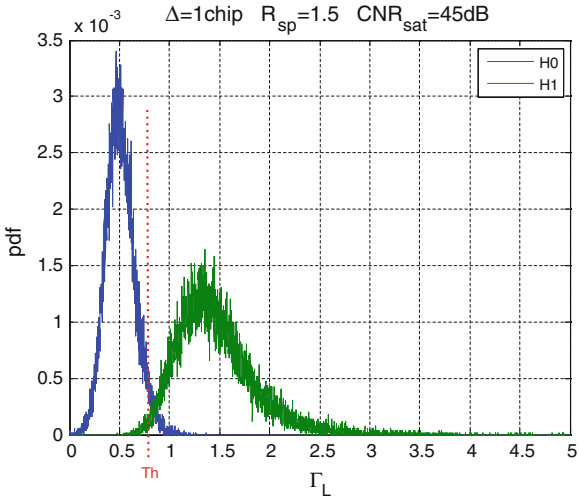

Fig. 52.7 Simulated PDF results of H0/H1

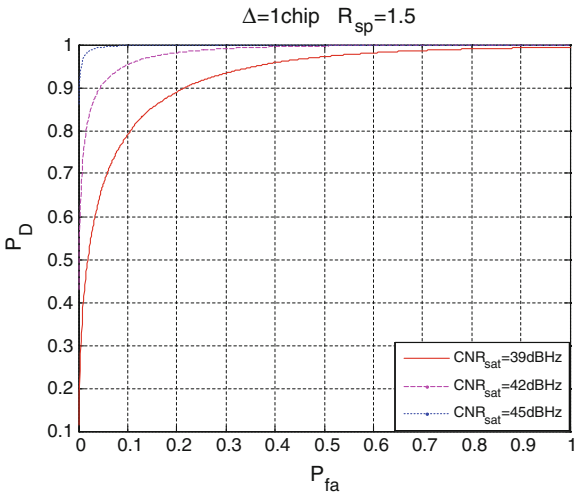

Fig. 52.8 ROC results of ratio test

can not be calculated directly. In this paper, the Monte Carlo is conducted to inquire the pdf of ratio test detector. It is plotted in Fig. 52.7.

The threshold of spoofing detection could be determined based on the Neyman–Pearson rule:

$$\begin{aligned} P_{fa} &= P\{\Gamma_L > \gamma_{Th} | H_0\} \\ P_D &= P\{\Gamma_L > \gamma_{Th} | H_1\} \end{aligned} \tag{52.9}$$

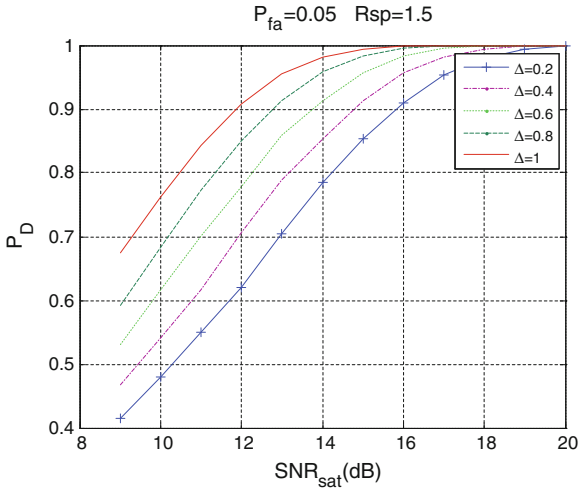

Fig. 52.9 P_D curves with different Δ when $R_{sp} = 1.5$

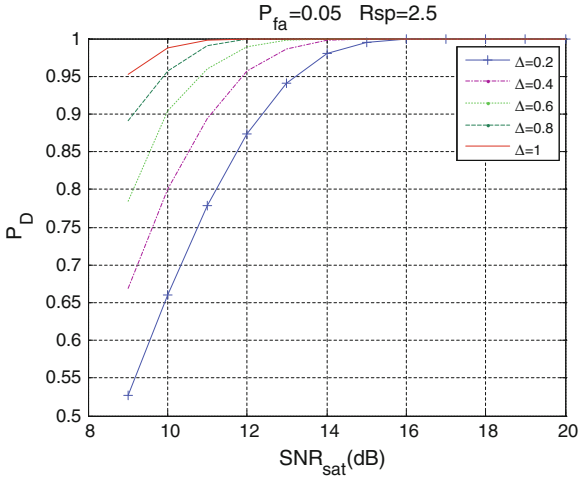

Fig. 52.10 P_D curves with different Δ when $R_{sp} = 2.5$

That is to a certain false alarm probability (P_{fa}), the decision threshold γ_{Th} can be concluded according to $p\ (\Gamma_L|H_1)$, and then the spoofing detection probability (P_D) can be calculated according to $p\ (\Gamma_L|H_1)$. The receiver-operation-characteristic (ROC) curves are figured in Fig. 52.8.

According to the Eqs. (52.8) and (52.9), to a certain false alarm probability $\left(P_{fa}\right)$, the decision threshold γ_{Th} is only related with the early-late space of receiver code tracking loops and the signal-to-noise rate (SNR) of the authentic signals. Figures 52.9 and 52.10 present the detection probability of ratio test in different conditions.

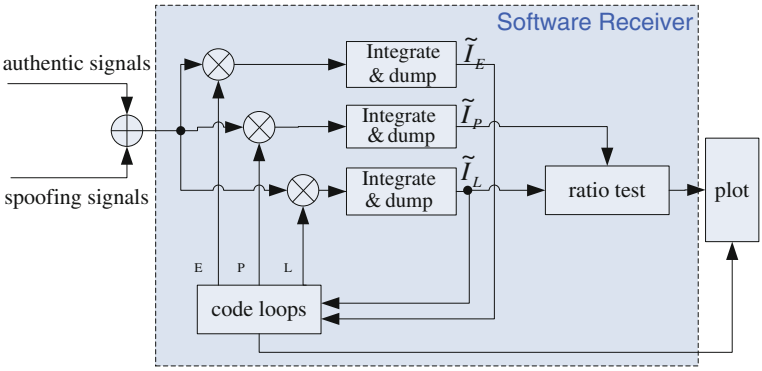

Fig. 52.11 Test platform of spoofing detection

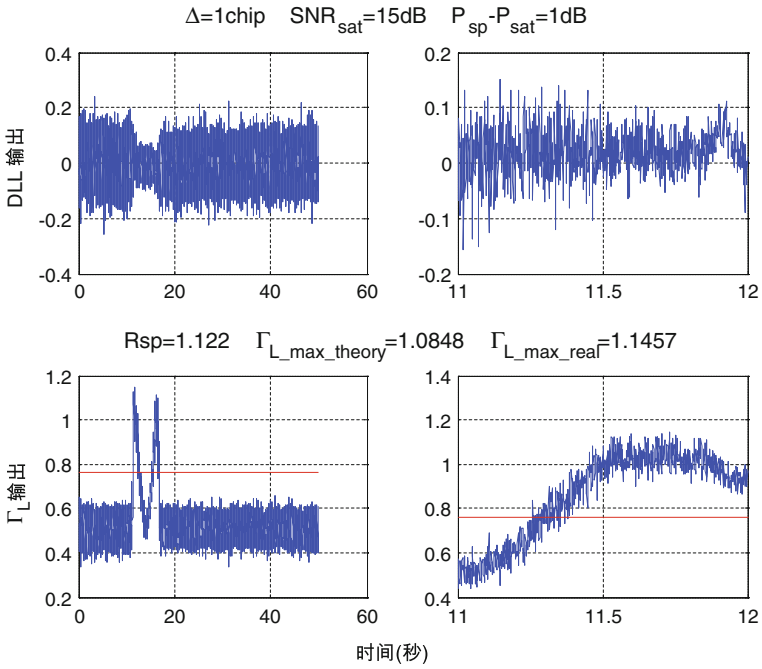

Fig. 52.12 Invading process when SAPR = 1 dB (Color figure online)

52.4 Simulation Verification

A simulation verification platform is build based on a software GNSS receiver, as shown in Fig. 52.11.

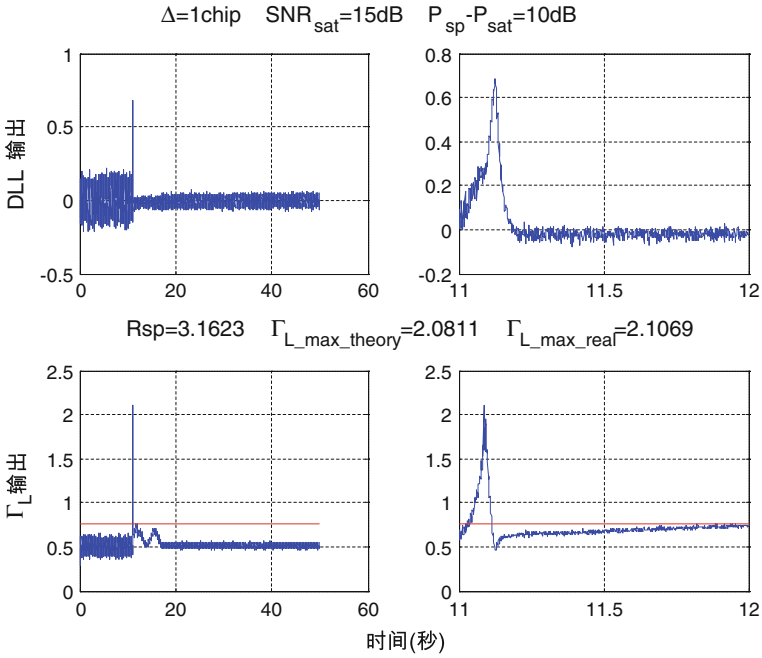

Fig. 52.13 Invading process when SAPR = 10 dB (Color figure online)

The basic parameters of the test platform are:

- Bandwidth of the carry tracking loop is 10 Hz;
- Bandwidth of the code tracking loop is 1 Hz;
- Accumulated time is 1 ms.

The software GNSS receiver kept tracking to the authentic signals in the first 10 min. And then, a spoofing signal with a relatively motion of 0.5 Hz was added in.

Figures 52.12 and 52.13 give the ratio test detector outputs with time in different scenarios, in which the right subplot is zoomed in the left one and the horizontal red line presents the detection threshold.

From the simulated results, it can be concluded:

1. The ratio test detector proposed in this paper can effectively detect the invading of generated spoofing with nearly no false alarm;
2. The simulated maximum of the ratio test is identical to the previous theoretical analyses;
3. The receiver could keep tracking to the synthesized signals when $R_{sp} < 2$ and is out of tracking state when $R_{sp} \geq 2$, which is also identical to the previous theoretical analyses.

52.5 Conclusions

A detection technique based on ratio test of correlation function is proposed to the generated spoofing attack. By analyzing the distortion process of correlation function, the maximum of the ratio test detector and its position are calculated, and setting the threshold of ratio test accordingly. Simulation results show that the proposed ratio test method could achieve a detection probability of 90 % with a false alarm probability of 5 %, and could also avoid false alarm induced by multipath and signal fluctuations.

References

1. Volpe JA (2001) Vulnerability assessment of the transportation infrastructure relying on the global positioning system. National Transportation Center
2. Best RE (2003) Phase-locked loops design, simulation, and applications, 5th edn. McGraw-Hill Press, New York
3. O'Hanlon BW et al (2010) Real-time spoofing detection in a narrow-band civil GPS receiver. In: Proceedings of ION GNSS
4. Psiaki ML (2011) Developing defenses against jamming and spoofing of civilian GNSS receivers. In: Proceedings of ION GNSS
5. Jafarnia-Jahromi A et al (2012) Detection and mitigation of spoofing attacks on a vector-based tracking GPS receiver. In: Proceedings of ION ITM

Chapter 53
Multitone-Based Non-linear Phase Variation Estimation for Analog Front-Ends in GNSS Receivers

Feiqiang Chen, Junwei Nie, Zhengrong Li and Feixue Wang

Abstract For high precision GNSS applications, accurate online measurements and calibrations of non-linear phase variation of analog front-ends at receivers is indispensable. Previous approaches are designed for off-line measurements, which rely on expensive instruments such as vector network analyzer (VNA). Therefore, they cannot facilitate online measurements, where the frequency response of analog front-end varies over time. Against this background, a novel multitone-based estimation method is proposed. Specifically, a multitone signal is injected into the front-end, while maximum likelihood (ML) estimation and least square (LS) linear fitting are performed at the output signals in order to estimate the non-linear phase variation. The proposed method could be conveniently realized at the GNSS receivers for online measurements. The accuracy of the proposed method is validated through comparisons with a benchmark Agilent VNA.

Keywords Non-linear phase variation · GNSS · Receiver · Multitone signal · Estimation

53.1 Introduction

The Global Navigation Satellite System (GNSS) is a space based radio navigation system. It provides 3D positioning and timing solutions to users anywhere in the world at any time. As reliance on GNSS receivers has increased, so too has the desire for precise positioning. When dealing with a sub-decimeter accuracy goal, every potential source of error must be accounted [1].

F. Chen (✉) · J. Nie · Z. Li · F. Wang
School of Electronic Science and Engineering, National University of Defense Technology, Changsha, China
e-mail: cfq01@126.com

J. Sun et al. (eds.), *China Satellite Navigation Conference (CSNC) 2014 Proceedings: Volume I*, Lecture Notes in Electrical Engineering 303,
DOI: 10.1007/978-3-642-54737-9_53,

It is well understood that the frequency-dependent amplitude and non-linear phase variation of antenna and analog front-end hardware can introduce biases into the code and carrier phase measurements of GNSS receivers [2, 3]. For high precision applications, precisely calibrating these biases is highly required. The effect of antenna on received signals could be taken into account by using measured reception patterns [4]. Unfortunately, due to the frequency difference between input and output signals caused by down-converter, obtaining the phase frequency response of the analog front-end hardware using conventional techniques is a daunting task. Moreover, front-end hardware consists of analog devices including bandpass filters, down-converter and so on, whose frequency response will change with the temperature, humidity and over life natural of devices. So, the frequency-dependent amplitude and non-linear phase variation of front-end hardware should be accurately estimated and calibrated on-the-fly.

Compared with linear, invariant system, phase response measurement for front-end hardware in GNSS receivers is much more complex and difficult due to the frequency-converting device. Several approaches are known to be able to overcome the problem caused by frequency-converting. Agilent Technologies uses PNA series Vector Network Analyzer (VNA) to measure the phase response of frequency-converting systems based on reference mixer method [5, 6]. Its major advantage is high precision and accuracy, while it requires complex calibration procedures and some additional components except the VNA. The Rohde & Schwarz Corporation proposed a two-tone method [7], it simultaneously measures the phase difference between the two carriers at the input and output of the frequency-converting system, then calculates the group delay using these phase differences and the carrier frequency offset. Frequency/amplitude modulation approach [8] measures the group delay based on phase comparison. The drawbacks of the above approaches are obvious. They all require expensive instruments such as VNA and complex calibration procedures, which made them difficult to integrated to the GNSS receivers for on-the-fly measurements.

In this paper, we proposed a novel estimation method to obtain the non-linear phase variation of analog front-end hardware in GNSS receivers. It need only a simple multitone signal generator, the estimator could be realized in the digital signal processor (DSP) of GNSS receivers. Thus it could be conveniently integrated to the receivers for the on-the-fly measurements. We demonstrate the accuracy of the proposed approach by comparing the estimated results with the measurement results obtained from Agilent VNA.

53.2 Front-End Hardware Model

Front-end hardware components of a common GNSS receiver contain bandpass filters, mixer, lowpass filters and so on. We could model the front-end hardware by cascade a down converter and an equivalent filters whose frequency response are

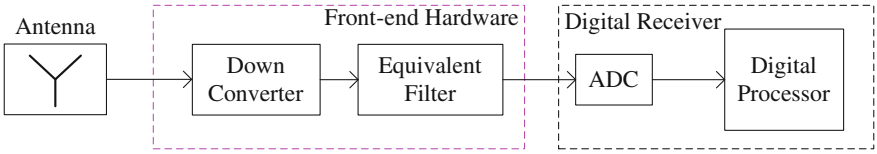

Fig. 53.1 Model of the front-end hardware

consist of bandpass filters, lowpass filters and other components. The model of the front-end hardware is shown in Fig. 53.1.

53.3 Estimation Method Based on Multitone

A multitone signal is given by

$$x(t) = \sum_{i=1}^{M} \cos(\omega_i t + \varphi_0) \tag{53.1}$$

It consists of M single tones, which have equivalent amplitude (Assume amplitude is 1) and initial phase φ_0, while ω_i is the frequency of the i-th tone.

Figure 53.2 shows the principle of the proposed estimation method. A multitone signal with the same initial phase is injected to the front-end hardware, the phases of input tones are constant. After passing the front-end hardware, the frequency of each tone will down-converted to a lower value. If the front-end hardware has linear phase frequency response, then the effect of front-end hardware on each tone is just adding an equivalent delay, the phases of output tones will keep linear versus frequency. While if the phase frequency response of the front-end hardware is not linear, the phases of output tones will not be linear versus frequency, and the phase deviations from line are the non-linear phase variation of the front-end hardware.

Define the frequency response of the equivalent filter as

$$H(\omega) = A(\omega)\exp\{j\phi(\omega)\} = A(\omega)\exp\{j(\omega\tau + \Delta\phi(\omega))\} \tag{53.2}$$

where $A(\omega)$ is the amplitude frequency response, $\phi(\omega)$ is the phase frequency response, and τ is the group delay of the equivalent filter, $\Delta\phi(\omega)$ is the non-linear phase variation which needs to be estimated and calibrated.

By injecting the multitone signal in Eq. (53.1) into the front-end, the output signal after the down converter is given by Eq. (53.3), Where ω_0 is the local oscillator frequency, φ_{mix} is a unknown constant phase of the down converter (the gain of the down converter has no effect on phase estimation, assume it is 1), $f(\omega_0, \omega_i)$ is the high frequency component introduced by down converting and will be filter by low-pass filter.

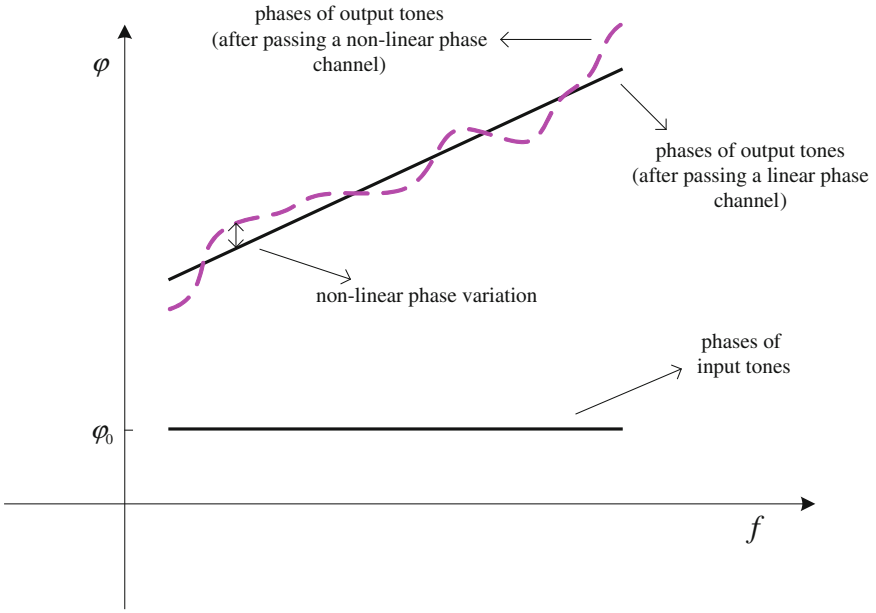

Fig. 53.2 Schematic of the proposed multitone-based estimation method

$$y_{mix}(t) = \sum_{i=1}^{M} A(\omega_i)\cos[(\omega_i - \omega_0)t + \varphi_0 + \varphi_{mix}] + f(\omega_i, \omega_0) \tag{53.3}$$

After passing the equivalent filter and analog-to-digital converter (ADC), the output signal at time n may be expressed in Eq. (53.4), Where τ_0 is a unknown constant delay determined by sampling time of ADC, $w(n)$ is narrowband Gaussian noise with zero mean and variance σ^2. When the ADC sampling rate satisfies the Nyquist sampling theorem, $w(n)$ may be treated as uncorrelated.

$$y(n) = \sum_{i=1}^{M} A(\omega_i)\cos[(\omega_i - \omega_0)n + \theta(\omega_i)] + w(n) \tag{53.4}$$

Where $\theta(\omega_i) = \omega_i\tau_0 + \varphi_0 + \varphi_{mix} + \phi(\omega_i)$.

53.3.1 ML Estimator for Phase Estimation

By applying the Maximum Likelihood (ML) estimation method in [9], the ML estimator for the output phase of the i-th tone $\theta(\omega_i)$ is expressed as

$$\hat{\theta}(\omega_i) = \arctan\left(\frac{-\beta_i}{\alpha_i}\right) \tag{53.5}$$

by defining the parameter vectors $\boldsymbol{\alpha} = [\alpha_1\ \alpha_2\ \ldots\ \alpha_M]^T$ and $\boldsymbol{\beta} = [\beta_1\ \beta_2\ \ldots\ \beta_M]^T$ as well as the observed data vector $\mathbf{Y} = [y(0)\ y(1)\ \ldots\ y(N-1)]^T$ of length N, $\boldsymbol{\alpha}$ and $\boldsymbol{\beta}$ could be formulated as

$$\begin{bmatrix} \boldsymbol{\alpha} \\ \boldsymbol{\beta} \end{bmatrix}_{2M\times 1} = (\mathbf{H}^T\mathbf{H})^{-1}\mathbf{H}^T\mathbf{Y} \tag{53.6}$$

According to Eq. (53.4), $\boldsymbol{H}$ can be expressed as $\boldsymbol{H} = [\boldsymbol{C}\ \boldsymbol{S}]$, where

$$\mathbf{C} = \begin{bmatrix} 1 & 1 & \cdots & 1 \\ \cos(\omega_1 - \omega_0) & \cos(\omega_2 - \omega_0) & & \cos(\omega_M - \omega_0) \\ \vdots & & \ddots & \\ \cos[(N-1)(\omega_1 - \omega_0)] & & & \cos[(N-1)(\omega_M - \omega_0)] \end{bmatrix}_{N\times M}$$

and

$$\mathbf{S} = \begin{bmatrix} 1 & 1 & \cdots & 1 \\ \sin(\omega_1 - \omega_0) & \sin(\omega_2 - \omega_0) & & \sin(\omega_M - \omega_0) \\ \vdots & & \ddots & \\ \sin[(N-1)(\omega_1 - \omega_0)] & & & \sin[(N-1)(\omega_M - \omega_0)] \end{bmatrix}_{N\times M}.$$

53.3.2 LS Linear Fit for Non-linear Phase Variation Estimation

Firstly, assume the ML estimator has no error, that is to say we could obtain $\theta(\omega_i)$ precisely. Let us rewrite $\theta(\omega_i)$ in Eq. (53.4) as

$$\theta(\omega_i) = \omega_i(\tau + \tau_0) + \varphi_0 + \varphi_{mix} + \Delta\phi(\omega_i) \tag{53.7}$$

where $\Delta\phi(\omega_i)$ is the non-linear phase variation which needs to be estimated and calibrated.Because the constant delay τ_0 and mixer phase φ_{mix} are unknown, we could not obtain $\Delta\phi(\omega_i)$ directly in Eq. (53.7).

Note that if the non-linear phase variation $\Delta\phi(\omega)$ is 0, then $\theta(\omega)$ will be linear versus ω. By performing Least Square (LS) linear fit on $\theta(\omega)$, we could obtain $\Delta\phi(\omega_i)$ using Eq. (53.8)

$$\Delta\phi(\omega_i) = \theta(\omega_i) - (a\omega_i + b) \tag{53.8}$$

where a and b are linear and constant term of the coefficients, which will minimize error, E, given by

$$E = \sum_{i=1}^{M} [\theta(\omega_i) - (a\omega_i + b)]^2 \tag{53.9}$$

that is to say, if there is no ML estimator error for phase estimation, we could obtain the non-linear phase variation $\Delta\phi(\omega_i)$ precisely.

Then, considering the ML estimator error, the ML estimator of the output phase of the i-th tone could be expressed as

$$\hat{\theta}(\omega_i) = \theta(\omega_i) + \Delta\theta(\omega_i) \tag{53.10}$$

where $\Delta\theta(\omega_i)$ is the phase estimation error of each output tone. From the output signal we may obtain the phase estimation of each tone, and thus obtain the data set $\left\{\left(\omega_i, \hat{\theta}(\omega_i)\right), i = 1, 2, \ldots, M\right\}$.

Therefore, the coefficients a and b may be estimated by

$$a = \frac{\sum_{i=1}^{M}\left[\omega_i - \frac{1}{M}\sum_{i=1}^{M}\omega_i\right]\left[\hat{\theta}(\omega_i) - \frac{1}{M}\sum_{i=1}^{M}\hat{\theta}(\omega_i)\right]}{\sum_{i=1}^{M}\left(\omega_i - \frac{1}{M}\sum_{i=1}^{M}\omega_i\right)^2} \tag{53.11}$$

$$b = \frac{1}{M}\sum_{i=1}^{M}\hat{\theta}(\omega_i) - \frac{a}{M} \tag{53.12}$$

Finally, we could obtain the estimator for non-linear variation given by

$$\hat{\Delta\phi}(\omega_i) = \hat{\theta}(\omega_i) - (a\omega_i + b) \tag{53.13}$$

According to ML estimation theorem, as the signal-to-noise (SNR) of multitone and sample data length increases, the precision of estimator in Eq. (53.13) will improve.

The proposed method introduced above is summarized in Table 53.1.

53.4 Field Test Results

In order to assess the performance of the proposed estimation method, field test have been carried out on front-end hardware of a GNSS receiver.

Firstly, we use Agilent VNA to measure the amplitude and group delay of the front-end under test, the reference mixer method have been used in order to

Table 53.1 Multitone-based non-linear phase variation estimation method

1) Generate multitone signal $x(t)$ as expressed in Eq. (53.1)
2) Inject the multitone into the front-end hardware under test, obtain output data $y(n)$
3) Estimate the phases of the output tones using Eq. (53.5)
4) Perform LS linear fit on data set $\left\{\left(\omega_i, \hat{\theta}(\omega_i)\right), i = 1, 2, \ldots, M\right\}$, obtain coefficient a and b
5) Estimate the non-linear phase variation using Eq. (53.13)

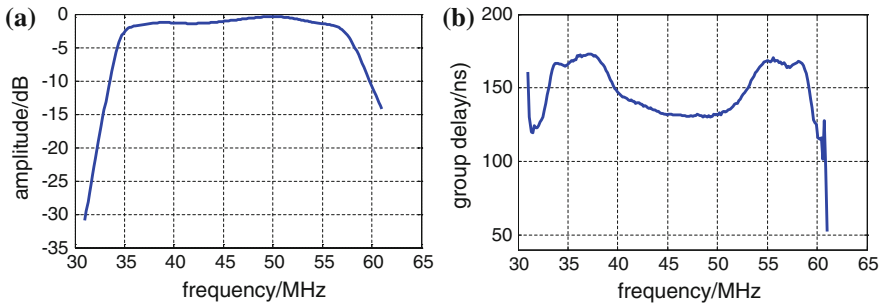

Fig. 53.3 Frequency response tested by Agilent VNA

improve the precision of the measurement results. The results are shown in Fig. 53.3.

Figure 53.3a is the amplitude response, Fig. 53.3b is the group delay response. We can see that, the bandwidth of the front-end hardware under test is about 20 MHz, and the center frequency is about 46.5 MHz. Moreover, its group delay are not constant over pass-band, it has group delay variation about 60 ns.

Secondly, calculate the non-linear phase variation from the group delay test results and regard it as a reference.

Finally, Estimate the non-linear phase variation using the proposed method, the multitone used in the experiment consists of 201 tones, whose frequencies are uniformly distributed between 31.5 and 61.5 MHz, the sample data length is 65,536, and SNR is about 30 dB here. Then compare the estimation results with those obtained from Agilent VNA. Test results are shown in Figs. 53.4 and 53.5.

Figure 53.4 shows the non-linear phase variation measurement results. Figure 53.5 shows the estimation error compared with Agilent VNA. It is obvious that the non-linear phase variation estimation results show a good agreement with those measured by Agilent VNA over the bandwidth of interest. The precision of non-linear phase variation estimation could reach 2°. Although the error becomes large out of the pass-band because of low SNR, it is acceptable, because there is little signal power out of the bandwidth of interest.

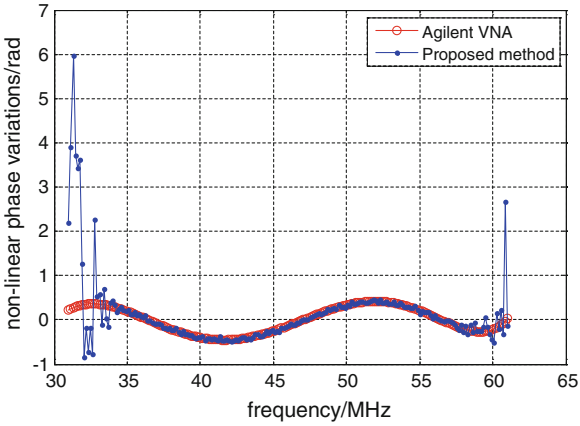

Fig. 53.4 Non-linear phase variation measured by Agilent VNA and the proposed method

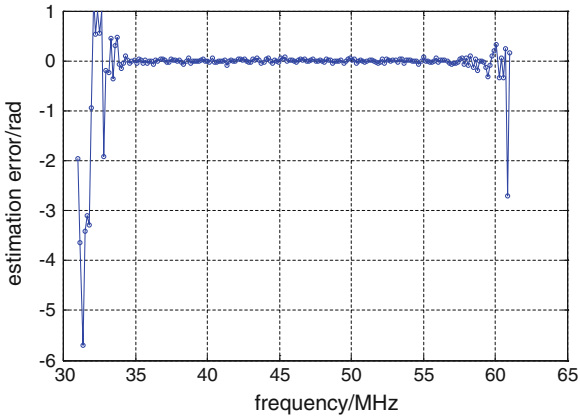

Fig. 53.5 Estimation error of non-linear phase variation

53.5 Conclusions

A novel approach has been presented to estimate the non-linear phase variation of analog front-end hardware in GNSS receivers. The approach is particularly suitable for high precision applications. It need only a simple multitone signal generator, the estimator could be realized in the DSP of GNSS receivers. Thus it could be conveniently integrated to the receivers for the on-the-fly measurements. In this paper, the accuracy of the proposed approach has been established by comparing the estimated results with those obtained from Agilent VNA.

References

1. Church CM (2009) Estimation of adaptive antenna induced phase biased in GNSS receiver measurements. Graduate School of The Ohio State University, Ohio
2. Kim US (2005) Analysis of carrier phase and group delay biases introduced by CRPA hardware. In: Proceedings of ION GNSS conference, Long Beach, CA
3. Gupta I, Church CM, O'Brien AJ (2007) Prediction of antenna and antenna electronics induced biases in GNSS receivers. In: ION NTM, San Diego, CA, pp 650–656
4. Konovaltsev A, Cuntz M et al (2010) Antenna and RF front end calibration in a GNSS array receiver. In: IEEE IMWS
5. Agilent Technologies (2007) Measuring group delay of frequency converters with embedded local oscillators. Application note 1408-18
6. Agilent Technologies (2004) Mixer conversion-loss and group-delay measurement techniques and comparisons. Application note 1408-2
7. Rohde & Schwarz Corporation (2009) Group delay measurements of frequency converters. Application note 1EZ60
8. Sha H (2009) Research and application of the group delay measurement method in transfer channel of satellite navigation system (in Chinese). Graduate School of National University of Defence Technology
9. Kay SM (1998) Fundamentals of statistical signal processing. Prentice Hall PTR, New Jersey

Chapter 54
Correlation Side-Peaks Cancellation Technique for Sine-BOC Signal Tracking

Bo Qu, Jiaolong Wei, Zuping Tang and Tao Yan

Abstract With the development of GNSS systems, BOC modulation signal has been widely used in the modernized GPS, Galileo, and Beidou. BOC signal has the split power spectrum density (PSD), which has better compatibility with GPS C/A signal. Furthermore, the PSD of BOC signal has more high frequency components, which results in better code tracking performance and multipath mitigation performance than BPSK signal. Because of the sub-carriers, the autocorrelation function (ACF) of BOC modulation signal has a main peak and some side peaks. The traditional delay locked loop (DLL) may be locked on the side peaks of ACF, which causes the extra tracking error. In this paper, an unambiguous tracking method is proposed for BOC modulation signal. The received BOC signal is correlated with two different local reference signals with the tailored waveform to obtain correlation outputs. Then the correlation outputs are combined to eliminate side peaks and obtain the combined correlation with one peak. The early minus late power (EMLP) discriminator can be used to lock on the sole peak of the combined correlation function. This unambiguous tracking techniques has been analyzed for BOC (1, 1) signal in the simulation. The simulation results show that this technique can achieve the unambiguous tracking for BOC signal and maintain the same level of the tracking performance as the traditional tracking loop.

Keywords GNSS · BOC modulation signal · Unambiguous tracking · Delay locked loop

B. Qu · J. Wei (✉) · Z. Tang · T. Yan
Department of Electronics and Information Engineering, Huazhong University of Science and Technology, Wuhan, China
e-mail: jlwei@mail.hust.edu.cn

J. Sun et al. (eds.), *China Satellite Navigation Conference (CSNC) 2014 Proceedings: Volume I*, Lecture Notes in Electrical Engineering 303,
DOI: 10.1007/978-3-642-54737-9_54,

54.1 Introduction

With the development of GNSS systems, BOC modulation signal has been widely used in the modernized GPS [1], Galileo [2], and Beidou [3]. Different from the traditional BPSK modulation signal, the sine-subcarrier or cosine-subcarrier is employed in BOC modulation signal to modulate the pseudo random noise (PRN) code so that it has the split power density spectrum (PSD) and more high frequency component. Thus, BOC modulation signal could provide better tracking accuracy and anti-jamming performance than BPSK modulation signal.

The traditional delay locked loop utilizes the autocorrelation function (ACF) of the PRN code to track the received signal. Due to the effect of the subcarrier, the ACF of BOC modulation signal has one main peak and multiple side peaks, and the number of correlation peaks grows with the increase in the order of BOC modulation signal. When DLL is used to track the received signal, it may lock on the side peak of the ACF, which causes a large tracking bias. This is the tracking ambiguity problem. In order to solve this problem, some unambiguous tracking methods have been proposed in recent years. The bump-jumping (BJ) technique based on the magnitude comparison between the prompt and its neighboring peaks, which can solve the tracking ambiguity problem of BOC modulation signal [4]. However, the BP method isn't suitable for the situation that carrier-to-noise ratio is low. Reference [5] proposed a BPSK-like method, in which the BOC modulation signal is treated as two BPSK modulation signals to implement the unambiguous tracking for BOC modulation signal. Nevertheless, the high frequency component in BOC modulation signal hasn't been utilized effectively, which reduces the tracking accuracy for GNSS receivers. Reference [6] proposed the ASPeCT method which subtracts the cross-correlation between the BOC modulation signal and BPSK modulation signal from the ACF of BOC modulation signals. Although ASPeCT implements the unambiguous tracking, it is only suitable for BOC(n, n) modulation signal. A dual estimate method has been proposed in [7] and improved in [8]. This unambiguous tracking method employs delay locked loop (DLL) and subcarrier locked loop (SLL) to track code phase and subcarrier phase, respectively. Compared with the traditional method, the dual estimate method needs the extra SLL, which increases the implementation complexity.

An unambiguous tracking technique is proposed for sine-BOC modulation signal in this paper. This unambiguous technique designs two reference waveforms and cancels the side peak of the correlation function by combining the cross-correlation between the received signal and two reference signals. Moreover, this technique needs the same number of correlators as that of BP method and ASPeCT method, which has low implementation cost.

The paper is organized as follows: In the Sect. 54.2, BOC modulation signal and the ambiguity problem are briefly introduced. Section 54.3 introduces the designed waveform and the unambiguous tracking method. Section 54.4 shows the tracking accuracy and multipath performance of the proposed method. Finally conclusions are drawn in Sect. 54.5.

54.2 Sine-BOC Modulation Signal

BOC modulation signal can be obtained by multiply the binary PRN code by square wave subcarrier. When the square wave subcarrier has sine phase, the BOC modulation signal is named as sine-BOC modulation signal. When the square wave subcarrier has cosine phase, the BOC modulation signal is named as cosine-BOC modulation signal. BOC modulation signal represented by the frequency of subcarrier and the PRN code is usually notated as BOC(m, n), where m represents that the subcarrier frequency is m × 1.023 MHz and n represents that the PRN code rate of BOC modulation signal is n × 1.023 MHz. m and n are positive integers, and m > n. k = 2 m/n is the order of BOC modulation signal, which is usually positive integer.

BOC modulation signal can be represented by the product of PRN code and the subcarrier:

$$s(t) = c(t)sc(t) \tag{54.1}$$

$c(t)$ is PRN signal, which can be denoted as

$$c(t) = \sum_{i=-\infty}^{+\infty} c_i p(t - iT_c) \tag{54.2}$$

where $\{c_i\}$ is the PRN code with the chip width T_c, $P(t)$ is chip waveform. $sc(t)$ is square subcarrier, which is denoted as

$$sc(t) = \mathrm{sgn}(\sin(2\pi f_s t + \varphi)) \tag{54.3}$$

where f_s is the subcarrier frequency. When φ is zero, the subcarrier is sine subcarrier; when φ is $\pi/2$, the subcarrier is cosine subcarrier.

When PRN code is modulated by the subcarrier, its power density spectrum (PSD) is split and the main power of BOC modulation signal is located at the subcarrier frequency, which can keep high separation degree from BPSK modulation signal. The PSD of sine-BOC modulation signal can be represented as:

$$G_{BOC(f_s,f_c)}(f) = f_c \left(\frac{\sin\left(\frac{\pi f}{2f_s}\right) \sin\left(\frac{\pi f}{f_c}\right)}{\pi f \cos\left(\frac{\pi f}{2f_s}\right)} \right)^2, \quad k = \frac{2f_s}{f_c} \text{ is even} \tag{54.4}$$

$$G_{BOC(f_s,f_c)}(f) = f_c \left(\frac{\sin\left(\frac{\pi f}{2f_s}\right) \cos\left(\frac{\pi f}{f_c}\right)}{\pi f \cos\left(\frac{\pi f}{2f_s}\right)} \right)^2, \quad k = \frac{2f_s}{f_c} \text{ is odd} \tag{54.5}$$

The ACF of BOC modulation signal can be obtained by Inverse Fourier transform of PSD:

$$R(\tau) = (-1)^{l+1}\left[\frac{1}{p}\left(-l^2 + 2lp + l - p\right) - (4p - 2l + 1)\frac{|\tau|}{T_c}\right], |\tau| < T_c \quad (54.6)$$

where $p = m/n$, $l = ceil(2p|\tau|/T_c)$, and $i = ceil(x)$ represents the smallest integer which meets the condition $i \geq x$.

The ACFs of BPSK modulation signal and BOC(1, 1) modulation signal are shown in Fig. 54.1.

From Fig. 54.1, we can see that the ACF of BPSK modulation signal has one peak. However, due to the effect of subcarrier, the ACF of BOC(1, 1) signal has a positive peak and two negative peaks. With the increase in the order of BOC signal, the number of ACF peaks grows. The ACF of BOC(1, 2) signal has three positive peaks and four negative peaks.

Because of the multiple peaks of ACF of BOC modulation signal, there are multiple zero-crossing points for the traditional early minus late power (EMLP). The EMLP discriminator output is shown in Fig. 54.2.

In Fig. 54.2, the correlator spacing of EMLP is 0.2 Tc. When the discriminator output for BPSK modulation signal is zero, there is a sole zero-crossing point. Therefore, BPSK signal can be tracked unambiguously by the traditional DLL. Beside a zero-crossing point at time delay 0, there are four zero-crossing points around 0.5 and −0.5 Tc. The BOC(1, 2) signal has more zero-crossing points than BOC(1, 1) signal. However, only when DLL is locked on the zero-crossing point at 0 Tc, the received navigation signal can be tracked accurately. When the DLL is locked on the other zero-crossing points, there is an estimate bias which causes the large ranging error.

54.3 Unambiguous Tracking Method for Sine-BOC Modulation Signal

The proposed unambiguous tracking method in this paper utilizes the correlation between two reference signals and the received signal to cancel the side peak of the cross-correlation so that the DLL can track the received signal unambiguously.

The waveform of the reference signal is designed as follows (Fig. 54.3):

This waveform $g(t)$ of the reference signals can be expressed as

$$s(t) = \begin{cases} 1 & 0 \leq t \leq w/2 \\ -1 & -w/2 \leq t \leq 0 \\ 0 & other \end{cases} \quad (54.7)$$

where w is the width of the waveform.

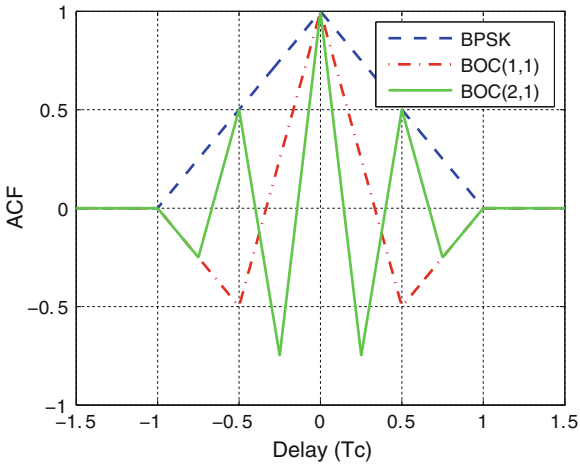

Fig. 54.1 Autocorrelation function of BPSK, BOC(1, 1) and BOC(1, 2) signals

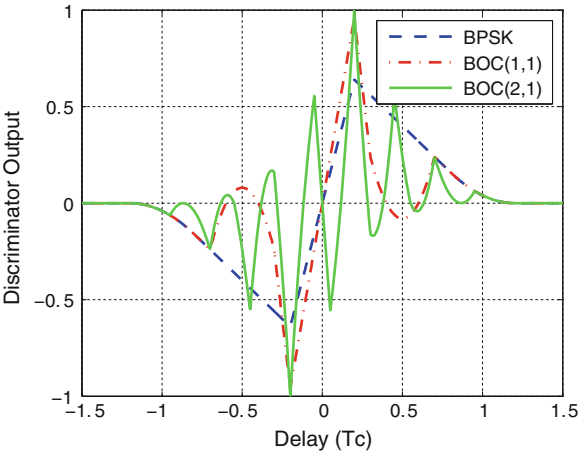

Fig. 54.2 EMLP discriminator output

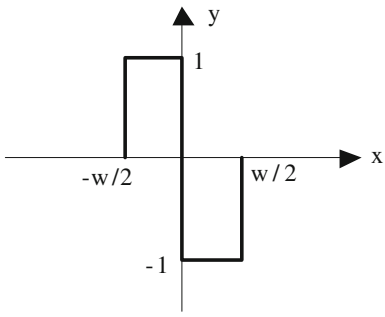

Fig. 54.3 Waveforms of local reference signals

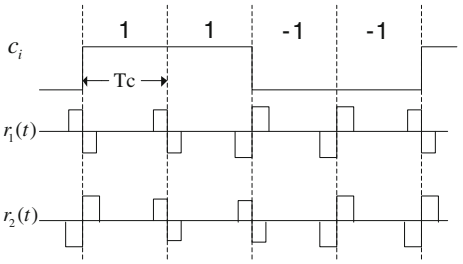

Fig. 54.4 Local reference signals

Then the waveform can be used to generate two local reference signals, as shown in Fig. 54.4.

The local reference signals in Fig. 54.4 can be denoted as

$$r_1(t) = \sum_{i=0}^{+\infty} c_i g(t - iT_c) \tag{54.8}$$

$$r_2(t) = \sum_{i=0}^{+\infty} c_i g(t - iT_c - T_c) \tag{54.9}$$

The reference signal $r_2(t)$ has 1 chip relative time delay to the reference signal $r_1(t)$.

The cross-correlations of the received signal with $r_1(t)$ and $r_2(t)$ are $R_1(\tau)$ and $R_2(\tau)$. We can cancel the side peak and obtain the combined correlation function with one peak.

$$R_{com}(\tau) = |R_1(\tau)| + |R_2(\tau)| - |R_1(\tau) - R_2(\tau)| \tag{54.10}$$

The combined correlation functions of BOC(1, 1) modulation signal and BOC(1, 2) modulation signal are shown in Figs. 54.5 and 54.6, respectively. The chip widths are 1 Tc for BOC(1, 1) modulation signal and 0.5 Tc for BOC(1, 2) modulation signal. We can see that the correlation functions $R_1(\tau)$ and $R_2(\tau)$ have multiple peaks. However, the combined correlation function $R_{com}(\tau)$ has the sole peak. Thus, this combined correlation function can be used to track the BOC modulation signal unambiguously by traditional EMLP discriminator.

54.4 Simulation Results

The tracking accuracy and multipath performance of the proposed tracking technique are analyzed in this section.

Figure 54.7 shows the tracking error versus the signal to noise power density (SNR) of the proposed method, ASPeCT, and the traditional DLL tracking method. The front-end bandwidth of the receiver is 4 MHz, the correlator spacing

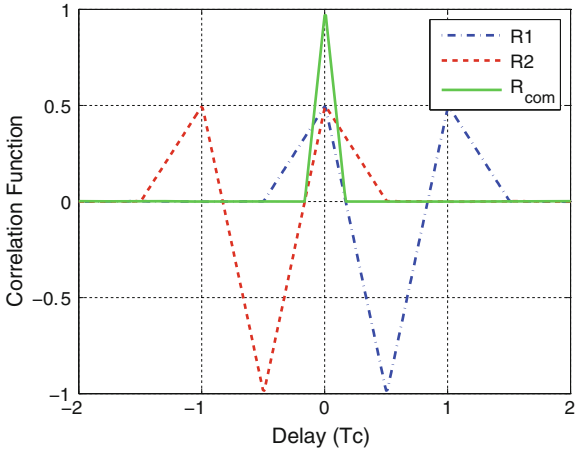

Fig. 54.5 Cross-correlation function and combined correlation of BOC(1, 1) signal

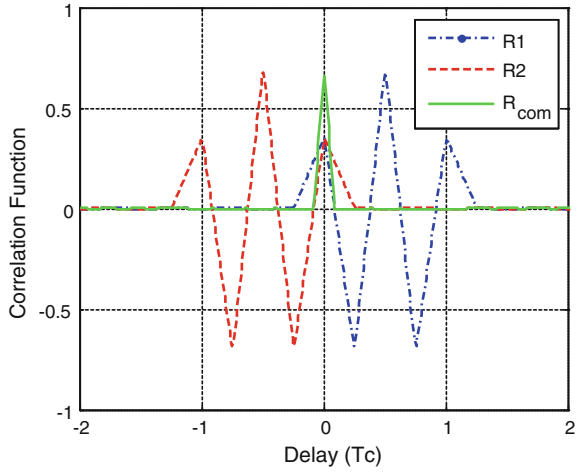

Fig. 54.6 Cross-correlation function and combined correlation of BOC(2, 1) signal

is 0.25 Tc, the tracking loop bandwidth is 1 Hz, and the integration time is 1 ms. The tailored waveform width is 1 Tc, and the received signal is BOC(1, 1) modulation signal. It can be seen that the proposed method can reach the same level accuracy as that of the ASPeCT and the traditional tracking method. Although the ASPeCT has also the high tracking accuracy, ASPeCT is suitable for BOC(n, n) modulation signal [6], and the proposed method has no limitation on the order of BOC modulation signal.

Figure 54.8 shows the tracking performance of the proposed method, ASPeCT, and the traditional DLL tracking method in multipath environment. The simulation employs the two-path model which contains one direct signal and one multipath signal. The multipath to direct ratio of amplitude is −10 dB, the time delay of multipath signal varies from 0 to 1.5 Tc. The front-end bandwidth is 4 MHz, the correlator is 0.25 Tc, the bandwidth of the tracking loop is 1 Hz, and the

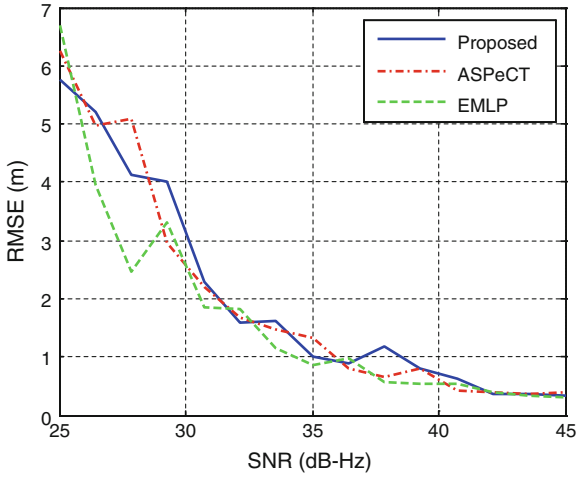

Fig. 54.7 Code delay RMSE versus SNR

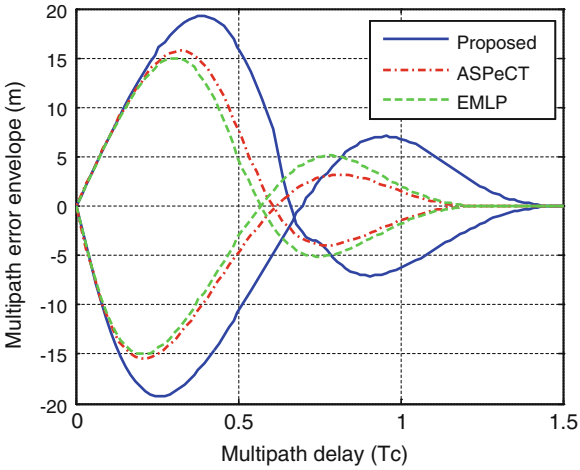

Fig. 54.8 Multipath error envelope versus multipath delay

integration time is 1 ms. The waveform width of the proposed method is 1 Tc. It is shown from Fig. 54.7 that the ASPeCT and the EMLP have the similar multipath performance, while the proposed method has slightly worse multipath performance than ASPeCT and EMLP. Therefore, the proposed method is suitable for the situation with less multipath signal.

54.5 Conclusions

An unambiguous tracking method has been proposed for BOC modulation signal to solve the tracking ambiguity problem. The proposed method utilizes two different reference signals composed by the tailored waveform to correlate with the

received signal and obtain two different correlation functions. Then these correlation functions can be combined to obtain the combined correlation function with the sole main peak, which can be used by EMLP to track BOC signal unambiguously. The tracking accuracy and multipath performance are analyzed in this paper. The analyzing results shows that the proposed method can track BOC modulation signal unambiguously, and reach the same tracking performance of the traditional tracking method.

References

1. Hudnut K, Titus WC, Captain U (2004) GPS L1 civil signal modernization (L1C). In: Final report of interagency GPS executive board stewardship project, vol 204
2. Hein GW, Godet J, Issler JL, Martin JC, Lucas-Rodriguez R, Pratt T (2002) The Galileo frequency structure and signal design. In: Proceedings of the 2002 ION, pp 1273–1282
3. Chong C (2009) The status of COMPASS BeiDou development. In: 2009 PNT challenges and opportunities symposium
4. Fine P, Wilson W (1999) Tracking algorithm for GPS offset carrier signals. In: Proceedings of the 1999 ION national technical meeting, pp 671–676
5. Martin N, Leblond V, Guillotel G, Eiries V (2003) BOC(x, y) signal acquisition techniques and performances. In: Proceedings of the 2003 ION GPS/GNSS, pp 188–198
6. Julien O, Macabiau C, Cannon ME, Lachapelle G (2007) ASPeCT: unambiguous sine-BOC(n, n) acquisition/tracking technique for navigation applications. IEEE Trans Aerosp Electron Syst 43(1):150–162
7. Hodgart MS, Blunt PD (2007) A dual estimate receiver of binary offset carrier modulated signals for global navigation satellite systems. Electron Lett 43(16):877–878
8. Hodgart MS Simons E (2012) Improvements and additions to the double estimation technique. In: Proceedings of satellite navigation technologies and European workshop on GNSS signals and signal processing. ESA workshop on IEEE, Noordwijk, pp 1–7

Chapter 55
Research on User Terminals' Acquisition Sensitivity Based on P2P Aiding

Dai Weiheng, Tian Shiwei, Sun Lipeng and Chang Jiang

Abstract With development of short range communication technology, P2P (Peer to Peer) networks are pervasive, and the nav-com user terminals become popular. The application of P2P networks provide the new method to improve positioning performances of user terminals. Compared to conventional A-GNSS augmentation, P2P aiding is completed by user terminals each other, which don't depend on preinstalled communication infrastructures (e.g., mobile communication base stations). In P2P networks, aiding sources are closer to aided users than conventional base stations aiding. The advantage can provide more accurate and reliable augmentation information, so the user terminals can get better augmentation performances. Now there are some groups research P2P aiding, but their topic is the mean acquisition times. But the acquisition sensitivity is very important metric for both military users and civil users. The paper researches performance of acquisition sensitivity in P2P networks. The aiding peer can receive both GNSS signals and the communication signals of aided peer. According to the real-time measurements of carrier phase and frequency offset, the aided peer can get real-time local frequency offset values. Based on these values, the peer can extend coherent integration time and improve the acquisition sensitivity. Simulation show that the aided user can complete coherent integration of several seconds, and the non-aided user only do for hundreds of milliseconds. The aided terminal can reliably work in low signal-noise ration, even in 10 dB Hz condition. The requirement of communication rate is less than 1 kps.

Keywords P2P aiding · Acquisition sensitivity · Coherent integration time

D. Weiheng (✉) · T. Shiwei · C. Jiang
College of Communication Engineering of PLA, University of Science and Technology, Nanjing 210007, Jiangsu, China
e-mail: dwh_526@163.com

S. Lipeng
Taiyuan Satellite Launch Center, Taiyuan 030027, Shanxi, China

J. Sun et al. (eds.), *China Satellite Navigation Conference (CSNC) 2014 Proceedings: Volume I*, Lecture Notes in Electrical Engineering 303,
DOI: 10.1007/978-3-642-54737-9_55,

55.1 Introduction

The navigational signal from satellites is extremely weak, and the sources of radiation are far way. On the earth, the civil signal power is only −133 dBm, and the signal get weaker 10–20 dB in house. So the availability of satellite navigation is limited, it can't be used in challenge environments. To resolve the problem, many methods have been researched, and these technologies can be separated into two categories. The first kinds are integrated navigation, the satellite navigation is used outdoor, and the inertial navigation or other terrestrial radio navigation is used in challenge environments. Through utilizing multiple methods, the availability of navigation system is improved. But the method require the user has many navigation sensors, the complexities and costs of user are also increased. The second methods improves the sensitivity of receivers by using advanced digital signal processing algorithm, adopting external augmentation technologies. The former ones are called high-sensitivity technologies, and the latter ones are called Assisted receiver technologies. For civil users, the sensitivity of high-sensitivity can achieve −155 dBm and the weaker signals. The assisted receiver has similar performance metric. High-sensitivity receiver needs more resources including computing ability, memory spaces, stable clock. The assisted receiver need communication module, and it can receive and send information to external server. With development of microelectronic technologies, GNSS receivers are usually integrated into smartphones, so the user can improve the performance of local GNSS receiver through communicating with cell stations. The users can get more sensitivity, shorted time-to-first-fixed, and more accuracy.

Recently, the development of short-distance communication system is rapid, for example, WLAN, UWB, and ZigBee, etc. Among the users, the information transmission rate is high, which is different from cell communications. In the background, the paper will research the way to improve the sensitivity of receivers. There are other papers discuss the improvement about time-to-first-fix, or accuracy, and these topics will not discussed in the paper.

55.2 A-GNSS Technology

55.2.1 The Principle of A-GNSS

There are major approaches to assist GNSS known as MS-assisted and MS-based GPS. "MS" stands for mobile station, means the GNSS receiver, in MS—assisted GNSS the position is calculated at a server, and the GNSS receiver's job is only to acquire the signals, and send the measurements to the server. In MS-based GNSS, the position is calculated by receiver itself. If the receiver is not going to compute position, then it does not necessarily need satellite orbit data. It is possible to keep these at the server, and the server can directly compute the acquisition assistance data and send it to receiver.

The frequency and time assistance data will be used to reduce uncertainty of time and frequency respectively. The receiver can get information about almanac, ephemeris or initial position, and to compute the expected observed satellite Doppler frequencies. It can reduce the frequency search space.

The A-GNSS time assistance partitions neatly as follows: CDMA networks have time accuracy of microseconds, enough to provide cod-delay assistance. GSM, UMTS and WCDMA networks have time accuracy of one to two seconds, not enough to provide code-delay assistance. If time assistance is better than 1 ms of accuracy, we call it fine-time assistance. Otherwise we call it coarse-time assistance.

55.2.2 Shortcomings of A-GNSS Technologies

The A-GNSS technologies now are based on cell stations and servers mainly. Mobile users receive assistance data or computation resources to complete using weak signals in challenge environments. But the improvement of sensitivity has close relationship to the accuracy of assistance information. When the accuracy of assistance time and frequency is high, the receiver can reduce the search scope more obviously. And we can improve sensitivity when the requirement of false alarm rate is fixed. The cell radius is usually several kilometers, So the accuracy of time assistance only achieves several chips. In the cell communication architecture, the possibility of improving sensitivity is low. The short-distance communication technologies can help to be a peer-peer (P2P) networks. Different from traditional cell networks, the P2P networks can result in assistance among the users [1]. The assistant data is produced by users, and this assistant model is called self-assistance.

55.3 The Principle of P2P Assistance

With the development of short-distance communication and NAV-COM integrated technologies, the smartphones are usually equipped the chips of GNSS receiver and short—distance communication modules now. Under these conditions, users can exchange measurements and message data each other. This is the physical foundation for P2P assistance. Compared with traditional A-GNSS technology, the assisted peer accepts the information which is sent by peer nearby, not cell stations. In the Fig. 55.1, the assisting peer is outdoor, so the quality of signal is good, and the peer can work normally. The outdoor peer can get information of position, time, frequency, navigation message and measurements. The assisted peer is indoor, so it doesn't work without the assistant data. The assisted peer can get these information through short-distance communication systems, so it can acquire weak signal in the house.

Comparing with the assistance provided by cell stations, the P2P assistance has two advantages [2]: (1) The assisting peer is closes to the assisted peer, and the

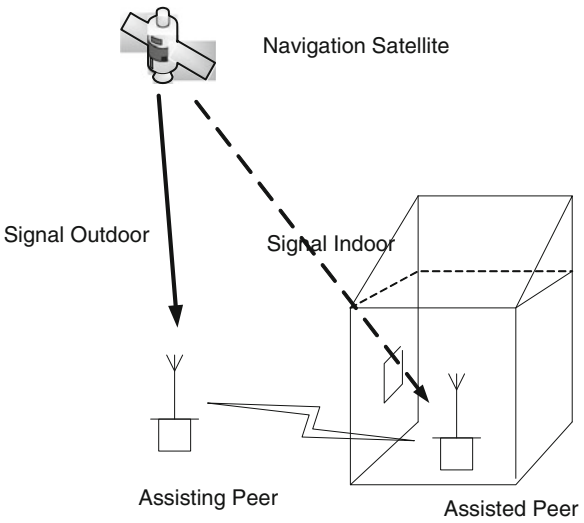

Fig. 55.1 System scheme of peer to peer assisting

similarity between both sides is high, so the accuracy of assistant data is high. (2) Short-distance communication systems can provide high speed communication channel between both sides, so assisted peer can get more information in the same time. Based on these advantages, P2P assistance can provide the better performance than A-GNSS technology, and the improvement of sensitivity is more.

The receiver must increase the coherent integration time to detect weak signals. But the increasing is limited by three factors: data bit length, user dynamic, and local clock stability. The influence of bit length can be resolved by assisted navigation message. And in the future, the pilot signals will be introduced in satellite navigation, so this restriction will disappear. So the limiting factors are only dynamic and clock stability.

To simply the problem, the paper only research the influence of the clock, so we suppose the user is static. In P2P assistance frameworks, the paper can improve clock stability to extend the coherent integration time (Fig. 55.2).

The communication modules and GNSS receiver use the same clock, and it is a reasonable assumption. Assisting peer can receiving both GNSS signals and short-communication signals. Assisted peer can communication with assisting peer, and both sides can to be time synchronized. So the peers can get carrier NCO value at the same time, named $\phi_{i,0}$, $\phi_{i,1}$, $\phi_{i,2}$, …, $\phi_{i,T}$, $\varphi_{i,0}$, $\varphi_{i,1}$, $\varphi_{i,2}$, …, $\varphi_{i,T}$ respectively. And the sampling time interval is set as ΔT.

$$\begin{aligned}\Delta f_{\text{peers}} &= \frac{\varphi_i - \varphi_{i-1}}{T} - \frac{\phi_i - \phi_{i-1}}{T} \\ &= f_{comm,a} + f_{DOPP,u} - f_{comm,d} - f_{DOPP,u} \\ &= f_{comm,a} - f_{comm,d}\end{aligned}$$

Fig. 55.2 The principle of P2P frequency transfer

Communicating the carrier NCO value between the peers, we can get the frequency offsets. $f_{comm,a}$ is communication frequency of assisting peer, and $f_{comm,d}$ is that of assisted peer.

The frequency standard of GNSS is very stable, so we can take this frequency as standard frequency. The assisting peer can receive GNSS signals, and get the frequency offset between assisting peer's clock and standard frequency. Because the communication and GNSS receiver module use one clock, we can get communicating frequency offset to standard frequency through simple projection operation. The communicating frequency offset between two peers is known in advance, and the communication frequency offset of assisted peer is also known. And we can use this frequency offset to assist the acquisition of weak GNSS signals.

From the former analysis, we can know the frequency of assisted peer is a bridge, and the frequency of assisting peer can be corrected in real time. So the frequency can be kept stable in scope, the influence of clock can be mitigated and the integration time is also extended.

Now we analysis the accuracy and influence factors of this assistance, and the assisted peer is static.

The accuracy is effected by accuracy of assisting peer frequency value, the frequency offset between two peers, ratio value α of communication frequency to GNSS frequency.

Through resolving the carrier Doppler frequency value from multiple satellites, we can get velocity and real-time clock frequency offset of user.

$$\Delta\dot{\mathbf{X}} = \left(\mathbf{H}^{\mathbf{T}}\mathbf{H}\right)^{-\mathbf{1}}\mathbf{H}^{\mathbf{T}}\Delta\dot{\boldsymbol{\rho}}$$

$\mathbf{H}$ is observing matrix, and $\Delta\bar{\dot{\boldsymbol{\rho}}}$ is measurements of Doppler frequency, and $\Delta\dot{\mathbf{X}}$ is a vector including three-dimension velocity and local clock's frequency offset value.

The estimation accuracy of frequency value of assisting peer can be computed by this formula:

$$\sigma_{\text{Doppler}} = \sqrt{\mathbf{2}} \cdot \sigma_{GNSScarrierphase} / T_{\text{interval}}$$
$$\sigma_{localfrequcnyoffset} = TDOP \cdot \sigma_{\text{doppler}}$$

The estimation accuracy of frequency offset between two peers is expressed as:

$$D\left(\Delta f_{\text{peers}}\right) = \frac{\left(D(\varphi_i - \varphi_{i-1}) - D(\phi_i - \phi_{i-1})\right)}{T_{\text{interval}}}$$
$$\sigma_{\text{peers}} = 2 \cdot \sigma_{commcarrierphase} / T_{\text{interval}}$$

So the accuracy of assisted frequency value is expressed as:

$$\sigma_{assistedfrequency} = \sigma_{\text{localfreoffset}} + \alpha \cdot \sigma_{\text{peers}}$$

Now the accuracy of tracking of PLL can achieve 0.02 cycle. When the time interval is 200 ms, the accuracy of Doppler frequency is 0.14 Hz. And the value of TDOP is usually between 1 and 2, we set TDOP to 1.5. Based on these assumption, the accuracy of assisting peer's frequency is 0.21 Hz, and the relative accuracy is 1.3e−10.

For high speed communication, communicating modules must do carrier phase tracking, and the accuracy is usually 0.05 cycle. When the observation time interval is 200 ms, the accuracy of frequency offset between peers is 0.35 Hz.

Based on the estimation of accuracy in former section, we know the accuracy of assisted frequency value is 0.41 Hz when the time interval is 200 ms. The energy loss due to frequency offset can be computed by the formula:

$$R(\Delta f) = \sin c(\Delta f T)$$

Δf is frequency offset value, and T is coherent integration time. If the frequency offset value is 0.41 Hz and integration time is 200 ms, the loss is only 1 %. The improvement of accuracy and time interval of assistance data can result in reduction of energy loss. But it need more communication overheads.

With the assistance data about frequency information, the assisted peer can increase the coherent integration time by accumulation of each segment's result (Fig. 55.3).

In the acquisition of weak signals, local signals will integrate with the input signals. Usually the peer uses TCXO, and its short-term stability is only 1e−9. There are large frequency offset, so the coherent integration time limited to 20 ms.

In the new algorithm, through compensating the local frequency offset of each segment, we can keep the stability of local frequency in a relative long time and extend integration time. When the time is extended to 2 s, the sensitivity will be improved 20 dB comparing to the sensitivity when integration time is only 20 ms. From references, we know the requirement of SNR is 11.7 dB when the false alarm rate is 0.001 and the success rate is 0.95. So when the integration time extend to 2 s, the accepted carrier-noise ratio is 8.7 dB Hz. And the time is extend to 20 s, the density of signal can less than 0 dB Hz.

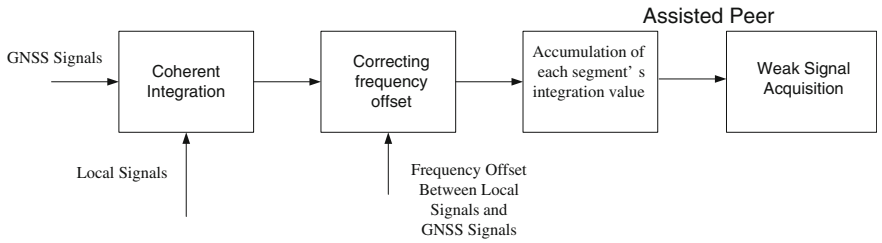

Fig. 55.3 The acquisition process based on accumulation of multiple-segments integration value

55.4 Algorithm Simulation and Performance Analysis

The paper validate the performance of algorithm about improving sensitivity based on P2P assistance. We do the computer simulation experiments which depend on the Matlab software, and integrated with semi-physical experiments.

We validate the frequency stability of TCXO by Beidou signal simulator and the receiver developed by ourself. The simulator transmits B1 signal that the center frequency is 1,561.098 MHz and the carrier-noise-ratio is 60 dB Hz. These parameter can reduce the influence of noise. Supposing the user is static, and operating model of receiver is multiple-satellites timing service with known position. By the measurements of carrier phases from PLL and averaging operations, we can get high-accuracy local clock frequency values. The signal simulator uses atomic clock, and the receiver use TCXO. Their stability have two orders of magnitude of difference. So the result of experiments is credible. Figure 55.4 gives a series of real time frequency value of TCXO, and the time interval of sampling is 200 ms.

From Fig. 55.4, we can know the short-term (hundreds of milliseconds) frequency stability of TCXO is 1e−11 order, and the stability in seconds is 1e−9 order [3]. The multiplication of coherent integration time and frequency offset can determine the performance of coherent accumulation. The energy loss can be computed as following formula [4]:

$$Loss = 20\log 10(\sin c(\Delta fT))\ (\mathrm{dB})$$

From the formula, we can see that the loss is 4 dB when frequency offset value is a half of reciprocal of integration time. In the designation of receiver, the frequency offset value usually is set as a quarter of reciprocal of integration time. So the frequency can't exceed 2.5 Hz when the integration time is 100 ms, and the frequency can't exceed 0.25 Hz when the integration time is 1 s. For B1 frequency signals, the stability of clock must be 1e−9 and 1e−10 order respectively.

We can deduce that the coherent integration time is limited to hundreds of milliseconds based on the stability of TCXO. The conclusion can do from references and out experiment data. When the integration time is extended to several

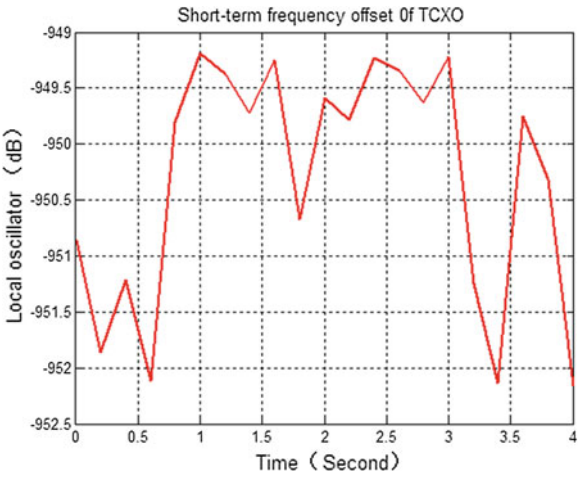

Fig. 55.4 TCXO short-term frequency values

seconds, the loss increases at the same time. It is not helpful to improve the pre-detection SNR.

We record the signal sent from simulator, and playback in the software receiver which is coded in matlab software. And the frequency information of local signal use the measuring data shown in former paper. The Doppler frequencies due to radial movement between satellite and users can be predicted and eliminated. So the reason of fluctuation of frequency is the frequency offset of local clock.

At first, we simulate the curve about pre-detection SNR for different coherent integration time without assistant information. The carrier-to-noise ratio of input signal is 10 dB Hz.

The Fig. 55.5 shows the pre-detection SNR for different integration time. With the increasement of integration time, the SNR increases at first and stop to improve later. Due to the frequency offset, the SNR can't to increase at all time. At last the SNR is only 5.6 dB that does not satisfy the requirement of acquisition.

In the new algorithm, user can correct the frequency offset in real time through P2P assistance. With the reduction of frequency offset, the users can extend the coherent integration time and improve the pre-detection SNR at last.

In Fig. 55.6, we can see that use can complete long time coherent integration operation by P2P assistance. The carrier-to-noise ratio of input signal is also 10 dB Hz. Compared to the Fig. 55.5, the pre-detection SNR increases with the extending of integration time. At last the SNR can achieve the need of reliable acquisition, and the sensitivity of receiver is also improved.

The paper also research the influence of assistant time intervals. From the Fig. 55.6, we can know the performance of improvement of sensitivity is better with the time interval is shorter, and the receiver can achieve the threshold of acquisition faster. But with the shorter time interval, the communication system must have higher information transmission rate. And in our algorithm, the exchanging information includes the frequency offset values and carrier phase

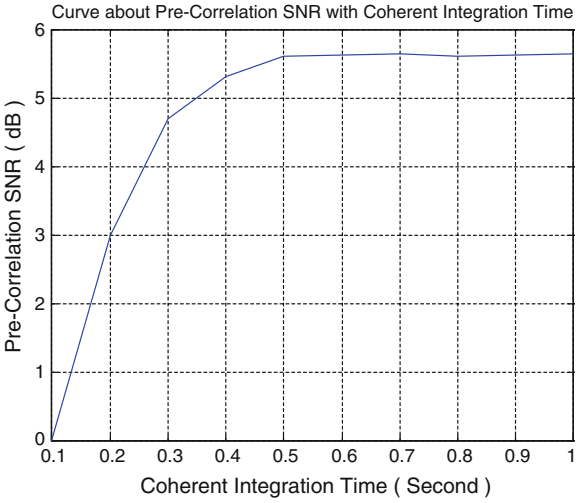

Fig. 55.5 Pre-correlation SNR with time of coherent integration without assistant data

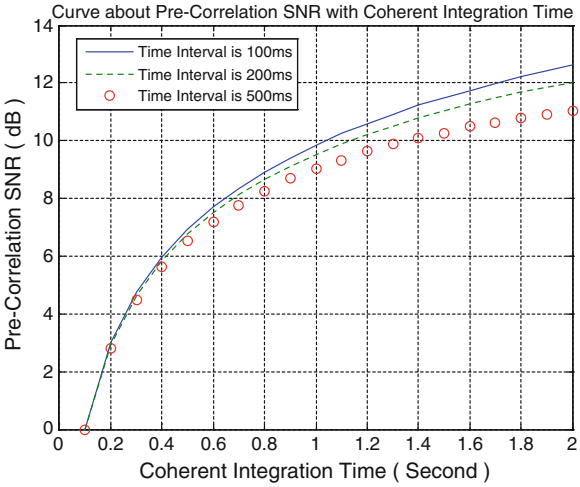

Fig. 55.6 Pre-correlation SNR with time of coherent integration with assistant data

measuring data. Even the assistant time interval is 100 ms, and the requirement of transformation rate is less than 1 kps. The communication overheads can be accepted in short-distance communication system totally.

55.5 Conclusion and Future Works

With the development of short-distance communication systems and P2P networks, the paper propose a real-time frequency offset corrected methods based on the P2P assistant frameworks. We describe the principles and process, and verify

the effectiveness by computer simulations. The results prove that the method can improve the sensitivity of receivers obviously, and the communication overheads are low.

In the future, we continue to research the method in multiple peers' assistant data, and the peers are dynamic.

References

1. Gabelli G, Deambrogio L et al (2012) Cooperative code acquisition based on the P2P paradigm. In: Proceeding of international technical meeting of ION, Newport Beach, CA, Jan 30–Feb 1 2012
2. Kassabian N, Lo Prestis L (2012) Technique for MAT analysis and performance assessment of P2P acqusition engines. In: Proceeding of IEEE conference of PLANS, Cambridge, USA, pp 980–988
3. Wesson KD et al (2010) Opportunistic frequency stability transfer for extending the coherence time of GNSS receiver clocks. In: Proceeding of 23rd international technical meeting of the satellite division of ION, OR, 21–24 Sept 2010
4. Morrison A (2009) Accurate millisecond level oscillator phase noise estimation for standalone GNSS. In: Proceedings of the ION GNSS conference Savannah, GA

Chapter 56
The Design and Analysis of BeiDou B1 Non-GEO Satellites High Sensitivity Acquisition

Hang Ruan, Zhou Zheng, Jian Li and Feng Liu

Abstract With the development of the BEIDOU satellite navigation system, its receiver sensitivity requirements continue to rise. Compared with tracking, it is difficult to improve the sensitivity for the reason that acquisition needs a larger amount of calculation and faces a high real-time requirement. As a result, acquisition is the key factors limiting the sensitivity. In this paper, in order to improve the Compass B1-frequency signal acquisition sensitivity, it designs a standard called the mean detection probability based on the analysis of the pseudo-code mismatch, Doppler mismatch, coherent integration, non-coherent accumulation, detection probability and false alarm probability. According to the standard, it achieves a high sensitivity of −147 dBm Compass B1 signal acquisition method and it is verified by simulation.

Keywords High sensitivity · Coherent accumulation · Non-coherent accumulation · The mean detection probability

56.1 Introduction

At present, the acquisition sensitivity of GPS L1CA navigation receiver can reach −147 dBm when there is no assistance from other resource. It is the cold start sensitivity of the receiver which will help a lot in common weak signal application.

H. Ruan (✉) · Z. Zheng · J. Li · F. Liu
School of Information and Electronics, Beijing Institute of Technology, Beijing, People's Republic of China
e-mail: ruanhang_bit@163.com

Z. Zheng
e-mail: zhengzhou@bit.edu.cn

J. Li
e-mail: lijian_551@bit.edu.cn

F. Liu
e-mail: bit_liufeng@bit.edu.cn

J. Sun et al. (eds.), *China Satellite Navigation Conference (CSNC) 2014 Proceedings: Volume I*, Lecture Notes in Electrical Engineering 303,
DOI: 10.1007/978-3-642-54737-9_56,

In contrast to the GPS L1CA signal for civil use, the non-GEO satellite of Compass B1 signal has similar properties in the aspect of signal modulation, the navigation data length and satellite dynamic. As a result, the acquisition sensitivity of B1 non-GEO satellite can also reach −147 dBm. Furthermore, the acquisition speed can be more or less slowed down to improve the sensitivity for the reason that the Compass satellite stay a long time in view so that it will almost not affect the location speed when acquiring the satellite out of view.

In the environment of weak signal, the main approach to improve the acquisition sensitivity is to expend the power accumulation length including coherent integration length, non-coherent accumulation length [1] and differential coherent process [2]. All of these methods are to increase the accumulation gain and enhance SNR so as to realize high sensitivity acquisition. On the other hand, satellite signal acquisition has the property of large searching range, high real-time request and high amount of data to process. It needs down sampling to reduce the complexity of calculation for the purpose of high efficiency process which will bring an extra power loss. Moreover, the Doppler frequency estimation error will also bring SNR loss [3]. Introduces a code phase bias compensation scheme but it is at the expense of efficiency which will increase a lot of steps. In total, the essential method to solve the problem is to further improve the sensitivity.

In this paper, according to the problem above, it designs a module of BEIDOU B1 non-GEO satellite signal in consideration of the mismatch of code phase and Doppler shift. Based on this module, the detection probability and false alarm probability of coherent integration and non-coherent accumulation is calculated. A design approach based on the mean detection probability is introduced and an acquisition module with the sensitivity of −147 dBm is devised. Simulation is carried out to validate the theoretical analysis.

56.2 Signal Module

The received satellite signal is frequency down-converted, filtered and sampled by the receiver and transferred to the immediate frequency signal whose expression is as (56.1)

$$s(nT_s) = \sqrt{2P}c(nT_s)d(nT_s)\cos(2\pi(f_{IF} + f_D)nT_s + \varphi) + n_w(nT_s) \tag{56.1}$$

where T_s is the sampling rate, P is the signal power, $c(\cdot)$ is the pseudo random noise code sequence, $d(\cdot)$ is the navigation data, f_{IF} is the local immediate frequency, f_D is the Doppler frequency, φ is the carrier phase, n_w is the additive Gaussian Write Noise. The noise power is σ_n^2. The digital discrete signal is then sent into the acquisition module to search the signal parameters which are Doppler frequency and code phase. The main methods of acquisition include parallel frequency search, parallel code phase search and match filter. The received signal is complex multiplied with local generated carrier, correlated and accumulated with

the local code to form the detection statistic variable. The expression of the signal after carrier complex multiplying and code correlation is as (56.2)

$$s_c(nT_s)=\sqrt{2P}d(n)R(\tau,\Delta f_d)\mathrm{sinc}(\pi\Delta f_d T_C)e^{j\varphi}+n_c(nT_c) \tag{56.2}$$

where $R(\tau,\Delta f_d)$ is the pseudo random code autocorrelation function which is a function of initial code phase delay τ and Doppler estimation error Δf_d. T_c is the coherent integration length, n_c is the noise component after accumulation. When the signal power can be detected, the code phase error is within a chip, so the expression of the autocorrelation is written in a chip as (56.3)

$$R(\tau,\Delta f_d)=\frac{1}{P_c}\sum_{n=0}^{P_c-1}R_{T_p}\left(\tau+n\cdot\frac{\Delta f_d}{f_{RF}}\right) \tag{56.3}$$

where $R_{T_p}(\cdot)$ is a triangle function with the width of $\pm T_p$ and amplitude of 1. T_p is the code chip period, f_{RF} is the signal radio frequency and P_c is the number of code chip during the integration period.

In the situation of common sensitivity with the relative short power accumulation, Δf_d nearly doesn't have influence on the shape of the code autocorrelation function. However, in the acquisition of weak signal, the coherent integration is long and the number of non-coherent accumulation is large so that the impact of Doppler estimation mismatch on autocorrelation cannot be ignored. Figure 56.1 illustrates the autocorrelation function of BEIDOU B1 signal with the Doppler mismatch of 500 Hz and different power accumulation length. It is clearly that the mismatched Doppler frequency changes the main peak location and brings power loss. The longer the power accumulation length is, the larger the power loss and the peak bias are. So the mismatched Doppler frequency cannot be ignored. Figure 56.2 gives out the power loss with different frequency shift and coherent integration length. When the power accumulation length extends 200 ms, Doppler frequency shift is over 500 Hz, the power loss is more than 0.5 dB. As a result, in the signal model of the paper, the impact of Doppler frequency on the autocorrelation function is considered.

In the real acquisition module, the input signal has to be further down-sampled in order to reduce the resource consumption, improve the instantaneity of hunting and accelerate the code chip searching speed. Consequently, the sampling rate of the acquisition input signal is really low which is usually the same as or twice as the code rate. The low sampling rate will bring an extra power loss and the expression of acquisition input signal is as (56.4)

$$S(nT_c)=\sqrt{P}d(n)R(kT_{sc}+\Delta\tau,\Delta f_d)\mathrm{sinc}(\pi\Delta f_d T_c)e^{j\varphi}+n_c(nT_c) \tag{56.4}$$

where T_{sc} is the signal sampling interval, k is the relative code phase error of sampling point within a chip, $\Delta\tau$ is the relative phase error between the sampling point and right phase with the range of $(-T_{sc}/2, T_{sc}/2)$.

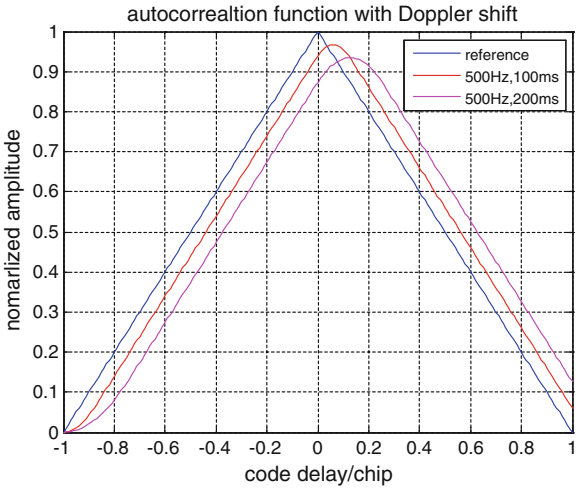

Fig. 56.1 Autocorrelation function with Doppler frequency shift

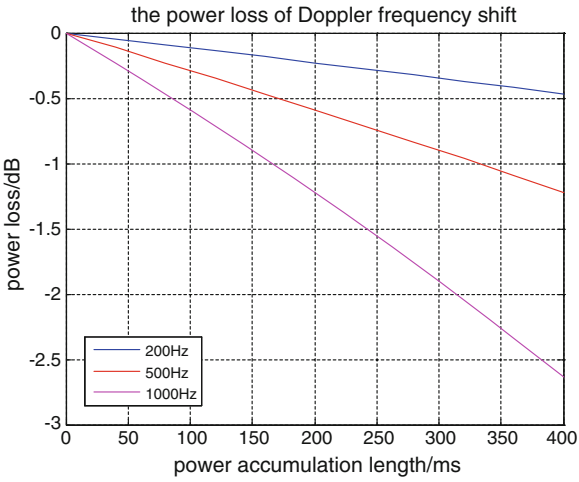

Fig. 56.2 The power loss of Doppler frequency shift

56.3 The Mean Detection Probability

56.3.1 Coherent Integration and Non-Coherent Accumulation

After orthogonal demodulation, the received signal is divided into in-phase branch and quadrature branch which can be expressed as (56.5) and (56.6)

$$I_c(nT_c) = \sqrt{P} \cdot d(n)R(kT_{sc} + \Delta\tau, \Delta f_d)\mathrm{sinc}(\pi\Delta f_d T_c)\cos\varphi + n_c(nT_c) \tag{56.5}$$

$$Q_c(nT_c) = \sqrt{P} \cdot d(n)R(kT_{sc}+\Delta\tau, \Delta f_d)\mathrm{sinc}(\pi\Delta f_d T_c)\sin\varphi+n_c(nT_c) \tag{56.6}$$

The acquisition module complex multiplies the local carrier and correlates the local code with the received signal and noise at the same time. Taking the noise of in-phase branch as an example, the processing is as (56.7)

$$I_n = \sum_{n=0}^{N-1} n_w(nT_{sc}) \cdot \cos\left(2\pi\left(f_{IF} + f_{e,d}\right) + \varphi\right) \cdot c(nT_{sc}), \varphi \sim U(-\pi, \pi) \tag{56.7}$$

where N is the number of sampling point in the coherent integration length. The noise variance after coherent integration is as (56.8)

$$\mathrm{var}(I_n) = E\left(I_n^2\right) - (E(I_n))^2 = \sigma_n^2/2T_c \tag{56.8}$$

The noise power of quadrature branch is the same as that of the in-phase branch. When the signal is absent, the correlation results of both in-phase branch and quadrature branch obey the Gaussian distribution with the mean value of 0 and variance of $\sigma_n^2/2T_c$. When the signal is present, the correlation result of in-phase branch and quadrature branch obey the Gaussian distribution with the variance of $\sigma_n^2/2T_c$ and means of $E(I_c)$ and $E(Q_c)$ respectively. The expression of the mean is as (56.9) and (56.10)

$$E(I_c) = \sqrt{P} \cdot d(n)R(kT_{sc} + \Delta\tau, \Delta f_d)\mathrm{sinc}(\pi\Delta f_d T_c)\cos\varphi \tag{56.9}$$

$$E(Q_c) = \sqrt{P} \cdot d(n)R(kT_{sc} + \Delta\tau, \Delta f_d)\mathrm{sinc}(\pi\Delta f_d T_c)\sin\varphi \tag{56.10}$$

The final detection variable after coherent integration and amplitude calculation is as (56.11)

$$D_e = I^2(nT_c) + Q^2(nT_c) \tag{56.11}$$

It is the square sum of two independent Gaussian random variables. It obeys the central χ^2 distribution with the freedom of 2 when the signal is absent and the non-central χ^2 distribution with the freedom of 2 when the signal is present. The expressions of detection probability and false alarm probability is as (56.12) and (56.13)

$$P_{fa}(\beta) = 1 - exp\left(\frac{\beta}{2\sigma^2}\right) \tag{56.12}$$

$$P_D(\beta) = Q_1\left(\frac{\sqrt{\alpha}}{\sigma}, \frac{\sqrt{\beta}}{\sigma}\right) \tag{56.13}$$

where β is the detection threshold, σ^2 is equal to $\sigma_n^2/2T_c$, $Q_1(\cdot)$ this the first order Marcum Q function, α is the square sum of the two independent Gaussian random

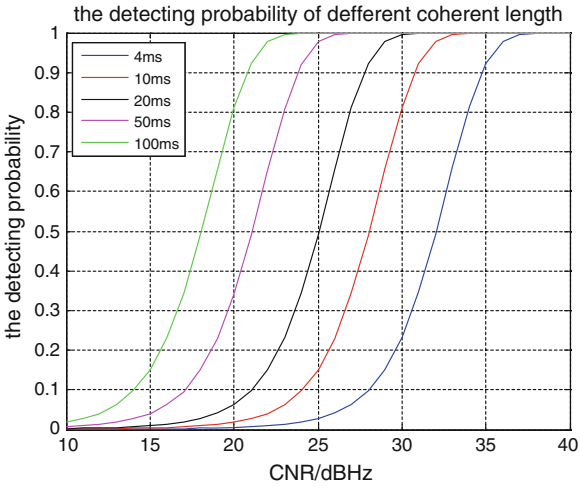

Fig. 56.3 The detection probability of different coherent length

variable which is expressed as (56.14). When the false alarm probability is 1e−3, the detection probability of different coherent integration length corresponding to different CNR is shown in Fig. 56.3. If it requests that the detection probability reaches 99 % when the signal power is −147 dBm, the coherent integration length should be set longer than 20 ms.

$$\alpha = P \cdot R^2(kT_{sc} + \Delta\tau, \Delta f_d) \cdot \mathrm{sinc}^2(\pi \Delta f_d T_c) \tag{56.14}$$

In the acquisition of BEIDOU B1 signal, the modulation of navigation data limits the expending of the coherent integration length. Even demodulated the NH code, the longest integration length is only 20 ms. For the purpose of further improve the sensitivity without assistance from other resource, non-coherent integration is introduced to increase the power accumulation. After non-coherent integration, the detection variable is as (56.15)

$$D_{nonc} = \sum_{n=1}^{N} \left(I^2(nT_c) + Q^2(nT_c) \right) \tag{56.15}$$

where N is the number of non-coherent accumulation, n is the start time of each segment of coherent integration. As they are independent from each other and obey Gaussian distribution, they obey central and non-central χ^2 distribution with the freedom of 2 N respectively when the signal is absent and present. The false alarm probability and detection probability is as (56.16) and (56.17)

$$P_{fa}(\beta) = Q_N\left(0, \frac{\sqrt{\beta}}{\sigma}\right) \tag{56.16}$$

$$P_D(\beta) = Q_N\left(\frac{\sqrt{\alpha}}{\sigma}, \frac{\sqrt{\beta}}{\sigma}\right) \tag{56.17}$$

where $Q_N(\cdot)$ is the Nth order Marcum Q function, $\sigma^2 = \sigma_n^2/2T_c$, α is the square sum of all the Gaussian random variable which form the detection statistic variable which is expressed as (56.18)

$$\alpha = \sum_{i=1}^{N} P \cdot R^2(n_i T_{sc} + \Delta\tau, \Delta f_d) \cdot \mathrm{sinc}^2(\pi \Delta f_d T_c) \tag{56.18}$$

In conclusion, the detection probability with different combination of coherent integration length and non-coherent accumulation time when both the code phase estimation error and frequency shift estimation error is zeros, false alarm probability is 1e−3 is drawn in Fig. 56.4. It shows that the difference between the detection performances of 100 ms coherent integration and 4 ms coherent integration, 25 non-coherent accumulation is 4 dB.

56.3.2 The Mean Detection Probability

The detection probability is a function of detection threshold, code phase estimating error and Doppler frequency estimating error. In the real signal acquisition model, as the description above, the code phase and Doppler frequency shift is searched discretely. In the process of detection, the parameters that is determined to characterize the signal corresponds to the search step which is most closed to the real signal parameters. It is a special result of all the situations that the detection result is totally the same as the signal parameters. As a result, the analysis of the acquisition detection performance should consider the power loss that discrete process brings besides the affection of the CNR on it. Since the signal parameter corresponding to the sampling point in the search space obey union distribution, a standard called MDP which is short for Mean Detection Probability is raised to evaluate the performance of acquisition model in discrete form.

In the domain of code phase, after the down-sampling of the signal, the $\Delta\tau$ in the expressions of in-phase branch and quadrature branch appears randomly in the sampling interval with the same probability. In other words, $\Delta\tau$ obey uniform distribution in the range of $(-T_{sc}/2, T_{sc}/2)$ [4]. In the domain of frequency, in order to reduce the impact of sin*c* envelop loss on the sensitivity, the frequency searching range of the detection is set as wide as $(-1/2T_c, 1/2T_c)$. The value of Δf_d randomly appear in the searching area with the equal probability so that it also obeys uniform distribution. As a result, in consideration of the whole acquisition

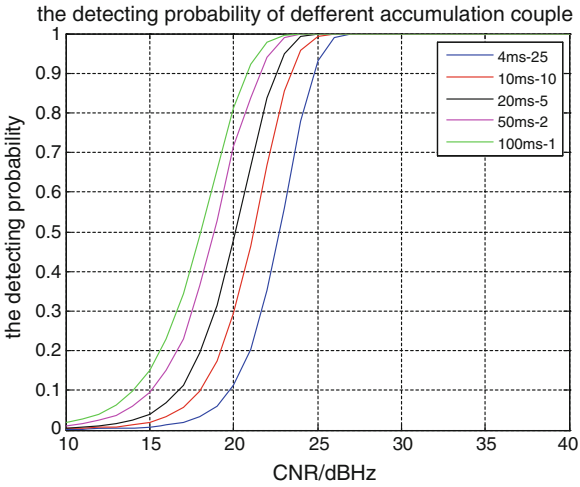

Fig. 56.4 The detecting probability of different accumulation couple

procedure according to the real model of acquisition described above, the Mean Detection Probability (MDP) is derived and expressed as (56.19)

$$P_{MDP}(\beta) = \frac{T_c}{T_{SC}} \int_{-T_{SC}/2}^{T_{SC}/2} \int_{-T_C/2}^{T_C/2} P_D(\beta, \Delta f_d, \Delta\tau, P) d\Delta f_d d\Delta\tau \tag{56.19}$$

where β is the detection threshold gained by fixed false alarm probability, $P_D(\beta, \Delta f_d, \Delta\tau, P)$ shows the detection probability of different carrier Doppler frequency and different code phase error. The MDP of coherent integration is gained by substituting (56.12, 56.13, 56.14 into 56.19) and that of non-coherent accumulation is gained by substituting (56.16, 56.17, 56.18 into 56.19).

According to (56.19), the MDP is a function of signal power, Doppler frequency error and code phase error in the conditional of that the threshold is determined by false alarm probability. If the signal power is confirmed, MDP is a function of code phase and Doppler frequency. As the expression above is really complex, the signal model is simplified by converting the digital discrete processing into SNR. The mean code phase error E_c and the mean acquisition Doppler frequency error E_f is expressed as (56.20) and (56.21) respectively.

$$E_c = \frac{1}{T} \int_{-T_{SC}/2}^{T_{SC}/2} |\tau| d\tau = \frac{T_{SC}}{4} \tag{56.20}$$

$$E_f = T_c \cdot \int_{-T_C/2}^{T_C/2} |\Delta f_d| d\Delta f_d = \frac{1}{4T_C} \tag{56.21}$$

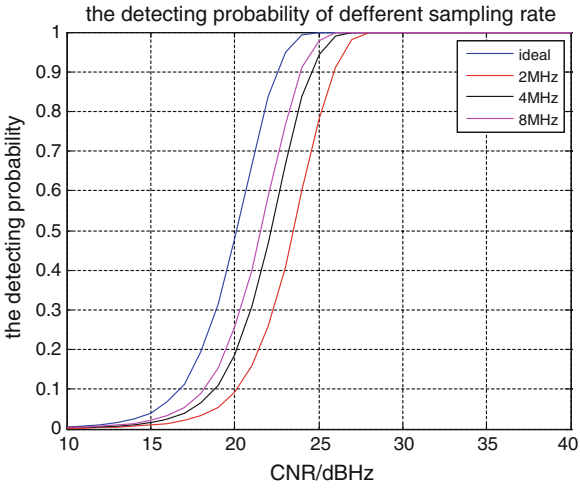

Fig. 56.5 The detection probability of different sampling rate

The mean signal power loss brought by code phase error and frequency mismatch error is as (56.22)

$$Loss_c = 20 \times \log\left(R\left(E_c, \frac{1}{4T_c}\right)\right) \tag{56.22}$$

The mean signal power loss brought by carrier frequency error is as (56.23)

$$Loss_f = 10 \times \log\left(\mathrm{sinc}^2\left(\frac{1}{4T_C 4}\right)\right) \tag{56.23}$$

Figure 56.5 illustrates the detection probability of different CNR and different sampling rate whose coherent integration length is 20 ms, non-coherent accumulation is 5 times, frequency searching step is 50 Hz and false alarm probability is 1e−3. In the ideal condition, the acquisition sensitivity can reach −150 dBm with 20 ms coherent integration and 5 times non-coherent accumulation. In consideration of the discrete sampling and Doppler frequency mismatching, the performance of detection is degraded. When the sampling rate is 2 MHz which is the same as the code rate of BEIDOU B1 signal, the detection probability cannot reach 99 % with the signal power of −147 dBm

As the direct coherent integration length is relative long, the acquisition frequency step is only 50 Hz and the Doppler mismatch loss in code domain is really small. The detection probability curve in Fig. 56.5 is without consideration of the code accumulation loss brought by Doppler estimation error.

In real application, the frequency searching step of 50 Hz is so small that it will seriously slow down the acquisition speed. Segment match filter with FFT will well solve the problem [5]. For example, if the coherent integration length is 20 ms and divided into 64 segments and the number of FFT points is 128, the

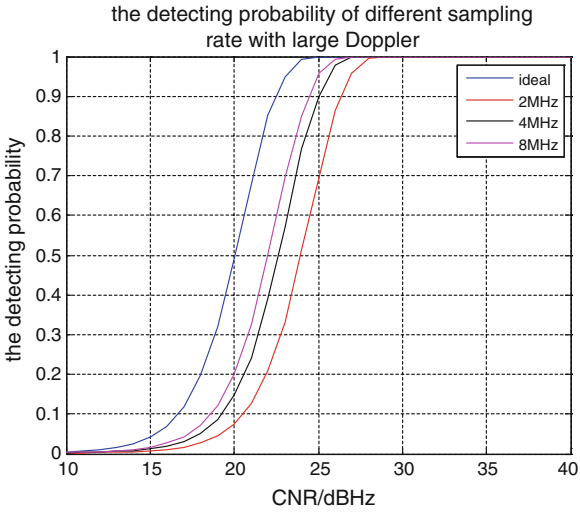

Fig. 56.6 The detection probability of different sampling with large Doppler

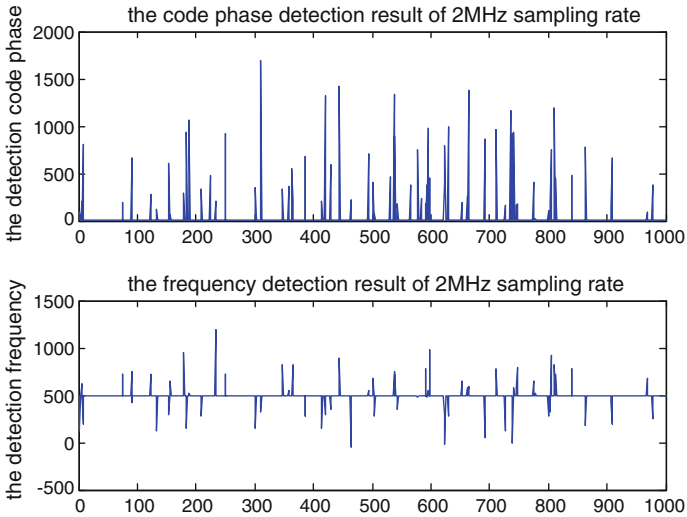

Fig. 56.7 The detection result with the sampling rate of 2 MHz

frequency search range is 1.6 kHz when the frequency estimation error loss is 0.9 dB. The mean frequency estimation error is 400 Hz. Since the accumulation is long, the code Doppler mismatching will lead a power loss that cannot be ignored. In addition, the fence effect of FFT will also bring an extra power loss of 0.9 dB. Figure 56.6 shows the detection probability of different sampling rate with the

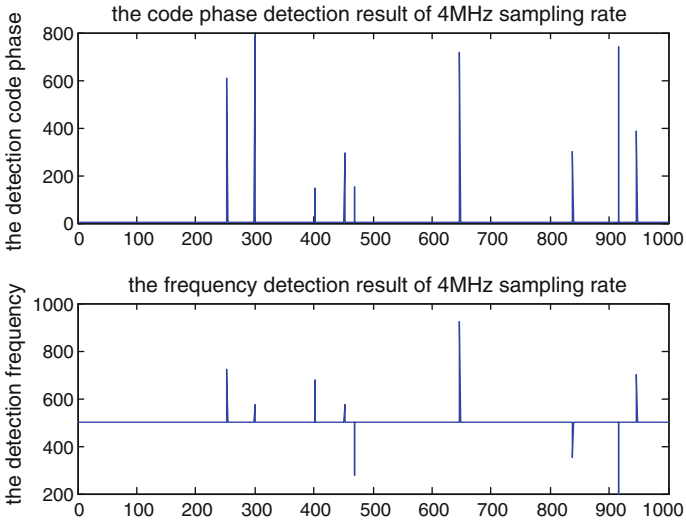

Fig. 56.8 The detection result with the sampling rate of 4 MHz

Doppler frequency shift of 400 Hz. The hence effect of FFT, Doppler frequency shift impact on carrier synchronization and code correlation is all considered in the figure. It concludes that the BEIDOU non-GEO satellite will reach the standard of 1e−3 false alarm probability and 99 % detection probability when the sampling rate is twice the code rate, coherent integration length is 20 ms and non-coherent accumulation number is 5.

56.4 Design and Simulation

In order to further verification the parameters analysis, the Mento Carlo simulation is done to test the high sensitivity acquisition of BEIDOU B1 non-GEO satellite with the acquisition parameter designed above. In the simulation, the acquisition engine is a segment match filter with FFT. The number of FFT points is 64, coherent length is 20 ms and non-coherent accumulation is 5 times which is determined according to the analysis. The coefficient of match filter is the B1 pseudo random noise code sequence modulated NH code. The signal power is −147 dBm, Doppler frequency shift obeys uniform distribution in the range of ±800 Hz and code phase obeys uniform distribution in sampling interval. The detection scheme is to find the maximum value and validate whether the corresponding parameter is right or not. The simulation result is as follow.

Figures 56.7 and 56.8 is the code phase detection and frequency detection result with the code sampling rate of 2 and 4 MHz respectively. The correct code phase is 1 and the Doppler frequency 500 Hz. It is clearly that the detection probability is only 92.77 % when the sampling rate is 2 MHz, coherent length is 20 ms and non-coherent

accumulation is 5 which is the same as the theoretical analysis. When the sampling rate is 4 MHz, coherent length is 20 ms and non-coherent accumulation number is 5, the detection probability is 99.07 %. It claims that the sensitivity of BEIDOU non-GEO acquisition reaches −147 dBm with the engine coefficient of 4 MHz sampling rate, 20 ms coherent integration and 5 non-coherent accumulations.

56.5 Conclusion

In this paper, for the purpose to fulfill the requirement of the BEIDOU B1 non-GEO satellite acquisition sensitivity, it numerically analyzes the main scheme to improve the acquisition sensitivity based on the property of the BEIDOU B1 non-GEO satellite. The basic power accumulation length to realize the sensitivity of −147 dBm is gained. At the same time, it introduce a conception of mean detection probability to evaluate the true performance of acquisition in consideration of code Doppler mismatch, carrier Doppler mismatch and the discrete process. Through model simplification, it calculates the detection probability and gain the digital acquisition method with the sensitivity of −147 dBm. The simulation has also been done to verify the acquisition performance.

References

1. Borio D, O'Driscoll C, Lachapelle G (2009) Coherent, non-coherent, and differentially coherent combining techniques for acquisition of new composite GNSS signals. IEEE Trans Aerosp Electron 45(3):193–206
2. Ta TH, Qaisar SU, Dempster AG, Dovis F (2012) Partial differential postcorrelation processing for GPS L2C signal acquisition. IEEE Trans Aerosp Electron 48(2):1287–1305
3. Ahmad U, Sik CW, Park S, Dong-Sun L (2011) Sample fraction & Doppler effect compensation algorithm for acquisition of weak GPS signals. In: International technical meeting of the institute of navigation, San Diego, CA, pp 826–833. 24–26 Jan 2011
4. Qaisar SU, Dempster AG (2012) Assessment of the GPS L2C code structure for efficient signal acquisition. IEEE Trans Aerosp Electron Syst 48(3):1889–1902
5. Zheng Y, Zhang Y (2010) An improved segmented match filters with FFT approach. In: 2010 2nd international conference on computer technology and development (ICCTD 2010)

Chapter 57
Robustness and Accuracy Analysis of a Compatible Narrow Correlation Assisted Double Delta Algorithm

Xinhui Lin, Lei Zhang, Hang Ruan and Feng Liu

Abstract Double Delta is an anti-multipath algorithm which is now widely used. It uses a set of narrow correlation and a set of wide correlation to correct phase function, and has a high resolution phase detector. It has the advantages that can effectively take up medium or long delays multipath with fewer resources. Previous studies and experiments have proved the anti-multipath performance of Double Delta algorithm, however the lack of studies that its poor traction easily lead to loss of lock and error code loop lock problem. In this paper, the above problem is considered, the multipath error envelope and the discriminator S-curve of Double Delta technical in BPSK and BOC signals is compared and it can be found that Double Delta technical also has good anti-multipath performance in BOC signal but error lock phenomenon is more prominent. Then a narrow correlation assisted Double Delta tracking method is put forward. The advantage in the robustness without the loss of tracking accuracy is proved through simulation and testing. It can detect false lock problem of Double Delta and make it suitable for the new GNSS signal such as BOC signal. The improved method enhances the robustness and compatibility of the tracking loop, and the consumption of additional hardware resources and the algorithm complexity is low. The results have a certain reference value of the receiver's anti-multipath channel design and engineering implementation.

X. Lin (✉) · L. Zhang · H. Ruan · F. Liu
School of Information and Electronics, Beijing Institute of Technology, Beijing, People's Republic of China
e-mail: linxinhui@bit.edu.cn

L. Zhang
e-mail: aerolong@bit.edu.cn

H. Ruan
e-mail: ruanhang_bit@163.com

F. Liu
e-mail: bit_liufeng@bit.edu.cn

J. Sun et al. (eds.), *China Satellite Navigation Conference (CSNC) 2014 Proceedings: Volume I*, Lecture Notes in Electrical Engineering 303,
DOI: 10.1007/978-3-642-54737-9_57,

Keywords Double delta · Narrow correlation · Robustness · False locked · Compatible channel

57.1 Introduction

Measurement error of modernized GNSS receiver consists of the following components: satellite orbit errors, satellite clock errors, ionospheric error, tropospheric error, the receiver clock error, receiver noise and multipath effects. With the development of differential technology, satellite and receiver clock errors, ionospheric and tropospheric errors can be eliminated by differential technology, receiver noise can be eliminate effectively through filtering techniques. Multipath error is different from these above errors, it is closely related to environmental conditions surrounding the receiver antenna, but is little related to the space. So it is difficult to eliminate by differential technique. Therefore, multipath error has become one of the main errors of the precision positioning.

The commonly used multipath error elimination techniques based on changes in the internal structure of the receiver [1] are narrow correlation technologies, ELS technology, Double Delta technology and MEDLL technology. Although MEDLL technology which can estimate the delay and amplitude parameters of the multipath signal, but it requires a lot of internal correlation resources, so it's not widely used in the receiver. The Double Delta technology which has the many advantages such as a small amount of computation, taking up small extra resources, low complexity, real-time, can be used to rapidly changing multipath occasions, has good effect on the medium or long delay multipath suppression and has better performance than narrow correlation and ELS technology, has been widely used.

Previous research on the Double Delta focused on its multipath performance. Literature [2] gives the Double Delta multipath error analysis and derives its code tracking error envelope expression. Literature [3] analyzed the multipath performance of Double Delta technology in the band-limited receiver channel. In fact, due to changes in the structure of the discriminator function, Double Delta technology easily occur false locked phenomenon. With the development of new GNSS signal such BOC, Double Delta algorithm also has a good multipath performance, but its false lock phenomenon is also more prominent [4]. Therefore, the study of the false lock phenomenon of Double Delta technology, improve its robustness has a very important engineering significance.

In this paper, the robustness of Double Delta discriminator is analyzed. The narrow correlation assisted Double Delta to detect the false lock is put forward. The simulation shows that this method can effectively improve the robustness of the Double Delta technology and improve the ability of the loop to adapt the dynamic. While this method can improve the application of Double Delta to the new system signal and make it suitable for the new GNSS signals.

57.2 Performance and False Lock Problem of Double Delta Technical

57.2.1 Multipath Performance Analysis Based on Multipath Error Envelope

Multipath error envelope is the direct relation between the multipath delay and the measurement error under ideal conditions. The ideal condition is that the relative amplitude of the multipath is known, there is only one way multipath signal and the direct signal is not blocked. Although multipath error envelope model simplifies the complex multipath environment, but it is still very suitable for the comparison between the multipath performances between different signals, because it directly reflects the modulation and code rate of the signals [5].

As Fig. 57.1a, by comparing multipath error envelope between the traditional width correlation, the narrow correlation and Double Delta in the BPSK signal, the following conclusions can be obtained: the narrower width the correlation is, the better the multipath performance the receiver has. Compared with the traditional width correlation, the narrow correlation can effectively reduce multipath error. For the 0.1–0.9 chip delay multipath signal which the multipath error increases obviously for the wide correlation, narrow correlation can suppress multipath error in a low level. Compared with the narrow correlation technique, Double Delta technique can suppress multipath error to zero for multipath signal of about 0.2–0.8 chip delay. It can be illustrate that Double Delta has better performance to the multipath signals of medium length chip delay and it's only sensitive to the multipath signal which is shorter than 0.2 chip or long than one chip delay.

Figure 57.1b is the multipath error envelope of wide correlation, narrow correlation and Double Delta technique in BOC (1,1) signal. The following conclusions can be drawn: the narrow correlation technique can also obtain good resistance to the narrow correlation technique using the BOC (1,1) signal may also be obtained good resistance to multipath effects in the BOC (1,1) signal. And when the multipath delay in the medium or long chips, the narrow correlation algorithm in BOC (1,1) signal has better effects than in BPSK signal, which is due to the BOC signal has more sharply correlation peaks than the BPSK signal. And multipath error magnitude of Double Delta technology is smaller than narrow correlation, so it can be demonstrated that the multipath suppression of Double Delta is also superior to the narrow correlation.

57.2.2 Analysis of False Lock Problem

Receiver uses EMLP discriminator when performing code tracking, it distributes a pair of correlation E and L on both sides of the correlation peaks. Figure 57.2a is the EML discriminator curve of wide correlation, narrow correlation and Double Delta in BPSK signal.

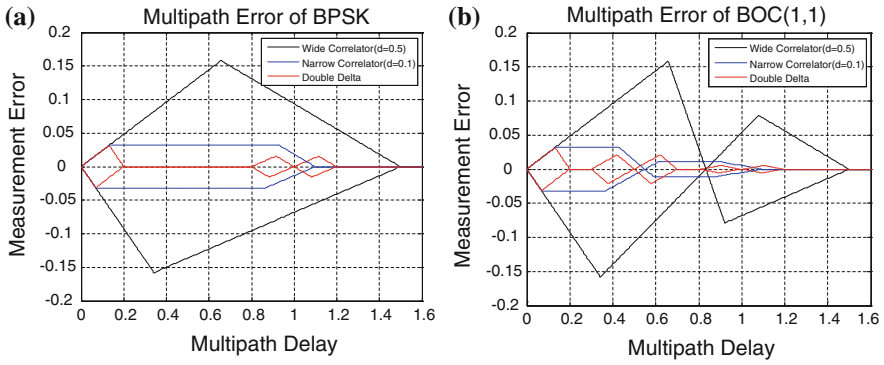

Fig. 57.1 Multipath error of wide correlation, narrow correlation and double delta. **a** *The black, blue and red curves* are multipath error envelop in BPSK signal. **b** *The black, blue and red curves* are multipath error envelop in BOC (1,1) signal

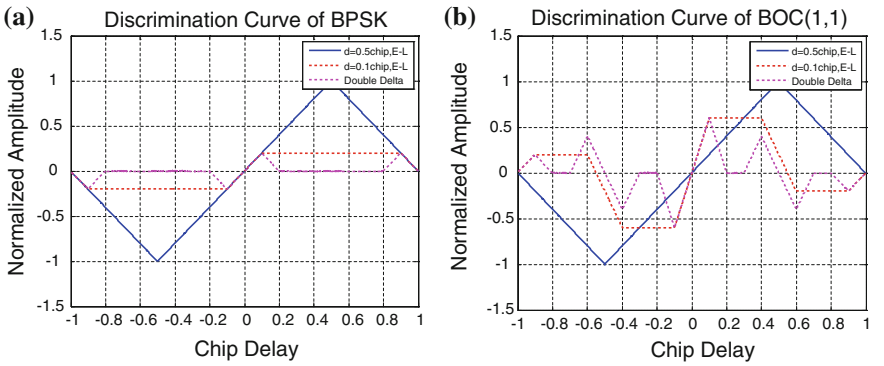

Fig. 57.2 Discrimination curve of wide correlation, narrow correlation and double delta. **a** *The black, blue and red curves* are EML discrimination curve in BPSK signal. **b** *The black, blue and red curves* are EML discrimination curve in BOC signal

As can be seen, the correlation spacing is smaller, the smaller the pulling range of the discriminator function has, the worse stability of the loop is, and it is easily to loss of lock. Compared with the traditional wide correlation, the pulling range of the discriminator of the narrow correlation is greatly reduced, which resulted in the problem that narrow correlation has worse stability than wide correlation. The phase detector result of Double Delta for more than 0.2 chip phase shift is zero. It is easily lead to instability and false lock of the loop.

Figure 57.2b is the EML discriminator curve of wide correlation, narrow correlation and Double Delta in BOC (1,1) signal. As can be seen, BOC (1,1) signal discriminator function has multiple zero crossing points, if large multipath delay may cause false locks, so a bump-jumping aided tracking is necessary. The autocorrelation function of BOC (1,1) signal has the auxiliary peak so when using

Double-Delta technique, it should be ensured that the spacing between the two outermost correlation is smaller than the width of the correlation peak function. And compared to the narrow correlation, the discriminator function of Double-Delta technology has more zero crossing points in BOC (1,1) signal. So the use of auxiliary detection technique is necessary to avoid false locks. Thus greatly increasing the resources consumption and complexity of the algorithm, making the Double Delta usefulness in the new GNSS signal

57.3 False Lock Detection Strategy Based on Narrow Correlation Assisted Double Delta

From the analysis of second chapter, the conclusion can be drew that: Double Delta technology has a good anti-multipath effect on both for BPSK signal or BOC signal, but there are false lock problems in both types of signals. False locking problem in the BOC signal is more prominent. In order to avoid false lock, bump-jumping detection algorithm is need to be used, thus the additional cost of the correlation resource is consumed, and this is a key reason Double Delta algorithm is restrict used in the new GNSS signal. Future new GNSS signal has two main characteristics: widely used BOC modulation and using the pilot channel assisted data channel for tracking. This provided the conditions for the detection of false lock of Double Delta.

57.3.1 False Lock Detection Model

The channel structure of a Narrow Correlation Assisted Double Delta (referred NADD) is shown in Fig. 57.3.

(1) Channel Structure
Three-way NCO of narrow correlation is used in pilot channel, while the data channel using the five-way NCO of Double Delta for tracking. The reason for this choice is because the power of the pilot channel signal is usually higher than the data channel (such as the power rate of GPS-L1C frequency is 3:1) or the same.(the power rate of GPS-L5 frequency is 1:1). While the pilot channel is not modulated message, the problem of the data sign bit flip is not need to be considered, which has higher tracking sensitivity. Stability of narrow correlation channel is generally better than the Double Delta channel and it has better advantage for tracking sensitivity.

(2) Loop control algorithm based on the joint tracking
The joint pilot and data channel tracking loop is used in this method, a three NCO combined five NCO weighted discriminator is used in loop control process, as shown in Eq. (57.1):

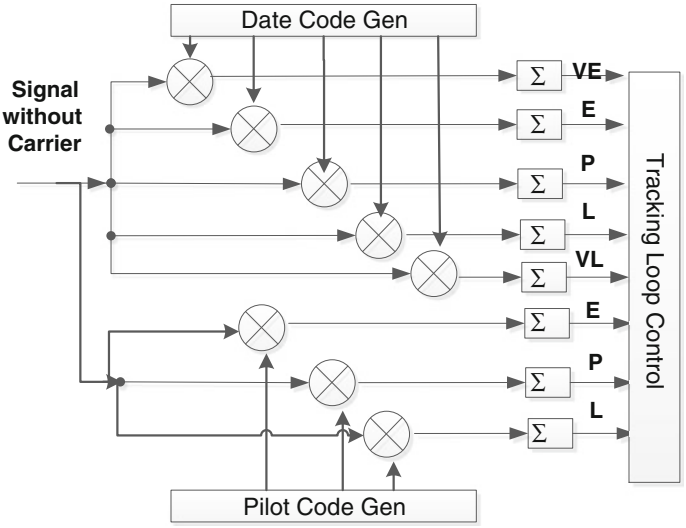

Fig. 57.3 Tracking channel structure of NADD

$$D = \alpha[2(E1 - L1) - (E2 - L2)] + (1 - \alpha)(E - L) \tag{57.1}$$

Overall loop control process is shown in Fig. 57.4. When that tracking loop starts, take a value 0, uses a three-way NCO discriminator for loop control, making the loop stable and fast locking to the correct point. After the loop is locked, enter the normal tracking mode, the value of a is one, uses a five-way NCO discriminator as a result for loop control, in order to enhance the pseudo-distance tracking accuracy of the loop in multipath environment. During normal tracking mode, the output of each discriminator is compared. Since signal of the pilot channel and the data channel is synchronization while the distribution of the noise is independent. If the false lock condition occurs on Double Delta channel, the discriminator output of narrow correlation channel will offset value 0. Detection method is set a counter, the counter initial value is 0, the lower limit of the counter is set to 0. The results of the phase statistics once every 100 ms, if the phase error exceeds the threshold, the counter is incremented by one, if not more than the threshold, the counter is decremented by one. Set counter threshold is T. When the counter value exceeds T, stop normal loop control, enter the false locked correction mode, set a value 0, restart the narrow correlation for loop control, traction the loop back to the right tracking point, making the Double Delta Technology lock in the right tracking point, and all counters are cleared. After the loop locks to the right point, and then resume a weight of one, switch back to the normal tracking mode.

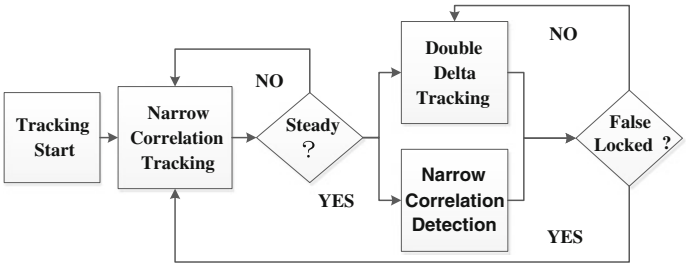

Fig. 57.4 Tracking strategy of NADD

57.3.2 Selection of the Decision Threshold

In this paper, the discriminator output of three-way narrow correlation is set as a standard to determine whether the loop is false locked. In addition to the effects of multipath, without the presence of other interference sources, the measurement error is mainly due to code phase jitter caused by the thermal noise. The variance of the code measurement errors due to thermal noise, for the traditional non-coherent early minus late method, the values σ_{tDLL} can be estimated by Eq. (57.2) [6].

$$\sigma_{tDLL} = \sqrt{\frac{B_L}{2C/N_o} D\left(1 + \frac{2}{(2-D)T_{coh}C/N_o}\right)}, \; D \geq \frac{\pi}{B_{fe}T_C} \tag{57.2}$$

Among them, the bandwidth for the RF front-end is Bfe, Tc is the pseudo-code yards wide.

The multipath error formula of narrow correlation, i.e. the relationship between code tracking error and correlation spacing d, multipath parameters [2] (relative amplitude, phase and delay) may be expressed as

$$\tau_e = \begin{cases} \frac{\tau\alpha\cos(\phi)}{1+\alpha\cos(\phi)}, & 0 < \tau \leq a \\ \frac{d\alpha\cos(\phi)}{2}, & a < \tau \leq b \\ \frac{\alpha\cos(\phi)}{2-\alpha\cos(\phi)}(T_C + \frac{d}{2} - \tau), & b < \tau \leq c \\ 0, & \tau > c \end{cases} \tag{57.3}$$

To sum up, the detection threshold of the narrow correlation discriminator output is

$$R = \sigma_{tDLL} + \tau_e \tag{57.4}$$

Table 57.1 Main civil signal of GPS and Galileo

Signal name	Modulation type	Multiplexed type
GPS-L1C/A	BPSK (1)	None
GPS-L1C	TMBOC (6,1/4/33)	Pilot/Data
GPS-L2CM/L2CL	TDDM-BPSK (1)	Time multiplexed
GPS-L5C	QPSK (10)	Two channels
Galileo-E1	CBOC (6,1,1/11)	Pilot/Data
Galileo-E5a/E5b	AltBOC (15,10)	Pilot/Data

When taking the space of the narrow correlation 0.1 chip, the variance of the code phase measurement error of the thermal noise are around 0.005, the code phase measurement error caused by multipath is about 0.04, so the threshold should be taken about 0.045.

Under normal circumstances, in order to avoid frequent switching occurs, the loop requires a low false alarm rate and a low false detection probability. Here a Tong detector is set which A is T +1, B is one [6]. Here the false alarm probability $<10-6$, and false detection probability $<10-7$ as a standard, under the medium carrier to noise ratio, the threshold value T of the counter takes 12.

57.3.3 Compatibility and Promotion of the Model

The major public civil signal of GPS and Galileo system is shown in Table 57.1. China's Beidou satellite navigation system will also follow several major modulation and multiplexing methods.

From several signals listed in Table, for those mainstream class new GNSS signal, the methods described herein can be completely compatible. For single-channel non-multiplexed signals, a five-way NCO weights combined discriminator based on a single channel can be built. For a dual-channel multiplexed pilot/data channel for BPSK or BOC signal, five-way NCO can be build on data channel and a three-way NCO can be built on pilot channel, using different phase detector according to different weights.

57.4 Simulation of NADD Performance

The advantage of the method in this paper is that avoiding the Double Delta anti-multipath algorithms false lock problems under the premise of keeping the same accuracy and multipath performance. Make the Double Delta algorithm can be applied to the new GNSS signals, meanwhile improve the robustness of the loop. The simulation is also considered from two aspects from the robustness and tracking accuracy.

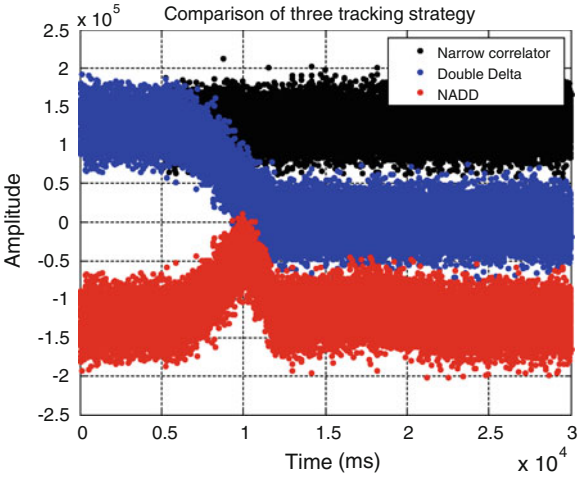

Fig. 57.5 Comparison of three tracking strategy *the black, blue and red curves* are tracking accumulation of narrow correlation, double delta and NADD

57.4.1 Loop Robustness Simulation

First consider the robustness of the loop, adds 0.2 chip offset when the loop is in a stable tracking process which makes Double Delta algorithm lock on the wrong point, while the narrow correlation can return to normal traction. After the simulation, record the accumulation of the three methods using a narrow correlation, Double Delta algorithm and the proposed method of NADD and the results shown in Fig. 57.5.

As can be seen from the figure, after the chip offset is added, the narrow correlation can be not affected, maintaining normal tracking. Double Delta affected by this offset and leads to false locks, then eventually leading to loss of lock loop. The proposed method NADD is able to detect this shift in time, and correct the false locks, use the narrow correlation loop to maintain the loop to the right tracking point, keep the loop a steady tracking.

The upper and lower in Fig. 57.6 is respectively the output of the weighted combination discriminator used for tracking and narrow correlation discriminator used for detection. As can be seen from the above figures, the weighted combination discriminator has such a process: start loop tracking, use the narrow correlation to traction, switch to the Double Delta for multipath tracking, adds the chip offset to make the false lock, switch back to narrow correlation for traction, re-lock to the correct tracking point, and then switch to the Double Delta for multipath tracking. As can be seen from the bottom of the figure, the narrow correlation has such a process: for the loop control, detect a large jitter exceeds the threshold, re-start to traction the loop back to the right tracking point.

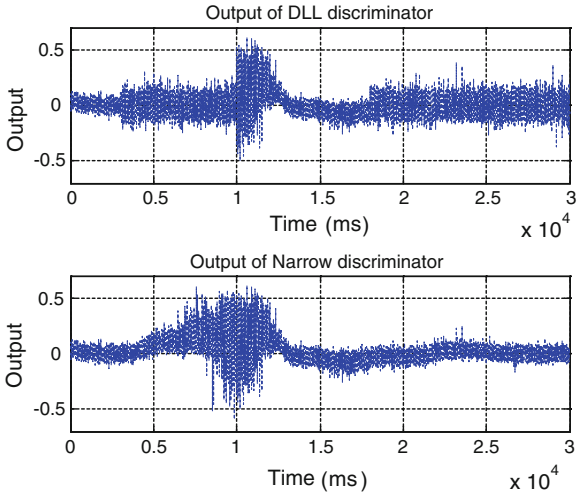

Fig. 57.6 Output of the combined and detection discriminator the *upper* is the combined discriminator, and the *bottom* is the detection discriminator

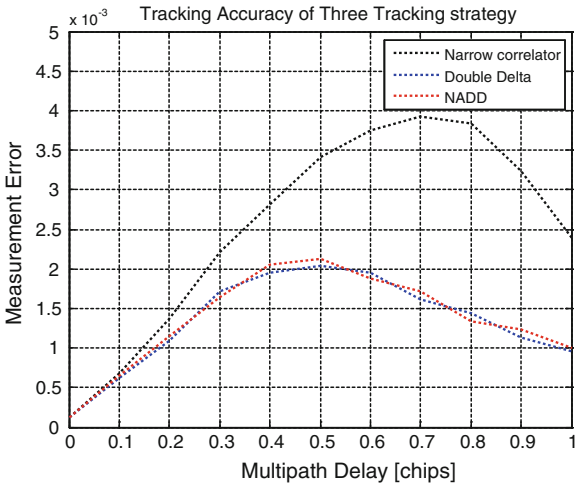

Fig. 57.7 Tracking accuracy of three tracking strategy *the black, blue and red curves* are tracking accuracy of narrow correlation, double Delta and NADD

57.4.2 Tracking Accuracy Test

Figure 57.7 is the comparative of three tracking accuracy under the multipath signal is 0.5 chip delay and the amplitude rate to the direct signal is 0.6. As can be seen from Fig. 57.7, in multipath conditions Double Delta algorithm performance is superior to the narrow correlation, and the methods NADD described in this paper use Double Delta algorithm for tracking after the initial phase of the narrow correlation traction. Tracking accuracy and multipath performance is approximate as Double Delta algorithm, improving the robustness of the loop without any tracking accuracy losses.

57.5 Conclusion

In this paper, a Narrow Correlation Assisted Double Delta is proposed to solve the problem of Double Delta technology easily gets false locked. In an effective solution solve the problem of Double Delta technology easily gets false locked meanwhile promote the Double Delta algorithm applied to the new GNSS signals. Compared with other anti-multipath method be aimed specially at new BOC signal, the feature which pilot channel assisted data channel of new GNSS signal is used in this method. And it can compatible with BPSK and BOC signals of new and old systems effectively. This method is mainly to increase the control of software algorithms level, and consumes no additional hardware, the impact on system resources and power is small. This improvement can have good performance on both loop robustness and anti-multipath, and has some practical value in the actual engineering.

References

1. Pany T, Irsigler M, Eissfeller B (2005) S-curve shaping: a new method for optimum discriminator based code multipath mitigation[C]. In: Proceedings of ION GNSS 18th international technical meeting of the satellite division, 13–16 September 2005, Long Beach, CA
2. Yuanfa JI, Huli SHI, Xi-yan S (2007) Study on multipath mitigation performance of strobe correlator. J Astronaut 28(5):1094–1099
3. Morrissey TN, Shallberg KW, Townsend B (2006) Code tracking errors for double delta discriminators with narrow correlator spacing and band limited receivers [C]. The Institute of Navigation NTM, Monterey, USA
4. Jovanovic A (2010) Requirements and analysis for a Robust E1 Galileo Tracking Algorithm In The Scope Of The GAMMA-A Project[C], In: Proceeding ION 2010 international technical meeting, 25–27 January 2010, San Diego, CA
5. Irsigler M, Eissfeller B. (2003) Comparison of multipath mitigation techniques with consideration of future signal structures[C]. Proceedings of ION GPS/GNSS 2003, pp 2584–2592
6. Kaplan ED, Hegarty CJ (2006) Understanding GPS principle and applications [M], 2nd edn. Artech House, Boston

Chapter 58
Dynamic Delay Generation Method Based on Variable Fractional Delay Filter

Hai Sha, Huaming Chen, Zhicheng Lv, Guozhu Zhang and Gang Ou

Abstract In the traditional dynamic delay generation method, the delay accuracy is difficult to increase and the wideband is very narrow. In this paper, a high-precision and wideband method is proposed. This method uses the VFD filter to achieve the fractional delay, through the Farrow structure the delay can be changed on line. The simulation shows that when the filter order is 50, the 0.01 sampling delay accuracy can be achieved in $\pm 0.9\pi$ bandwidth.

Keywords Satellite navigation · Dynamic delay generation · Variable fractional delay filter · Weighted least squares

58.1 Introduction

Dynamic delay generation method is a key technology in satellite navigation signal simulator, ground remote control system, anti-jamming antenna array receiver and other equipment. The accuracy of this method will determine the performance of the entire system. Meanwhile, with upgrading modern satellite navigation systems constantly, the signal bandwidth is greatly improved. Therefore, the study on high precision, wide bandwidth dynamic delay generation method has an important value of work for the construction and promotion of Chinese Beidou satellite navigation system.

Conventionally, traditional methods for generating dynamic delay can be divided into two categories, one is based on a numerically controlled oscillator (NCO) method [1], and the other is based on a fractional delay (FD) filter method [2, 3]. Wherein the structure of the former method is very simple, but it cannot

H. Sha (✉) · H. Chen · Z. Lv · G. Zhang · G. Ou
College of Electronic Science and Engineering, National University of Defense Technology, Changsha 410073, China
e-mail: sandhai@163.com

J. Sun et al. (eds.), *China Satellite Navigation Conference (CSNC) 2014 Proceedings: Volume I*, Lecture Notes in Electrical Engineering 303,
DOI: 10.1007/978-3-642-54737-9_58,

achieve the fractional point sampling delay; the latter method can only achieve a limited fractional point sampling delay, if improving accuracy, the filter resources need to be largely increased. Meanwhile the bandwidth of two methods is very narrow; the solution to generate the wideband signal delay can only increase the operating frequency. Hence this paper proposes a method to generate dynamic delay based on variable fractional delay (VFD) filter.

VFD filter can change the any fractional point sampling delay online, without redesigning a new filter, which is widely used in real-time signal processing system. Among the existing literature, [4] provide a comprehensive review of several standard FD filter design techniques; [5–11] proposed a variety of VFD filter design methods. Based on the analysis and comparison of the traditional methods, this paper is detailed discussed on the process on the method based on VFD filter, and through some examples, the superiority of proposed method is demonstrated.

58.2 Traditional Methods

58.2.1 Dynamic Delay Generation Method Based on NCO

In NCO, the output frequency is controlled by the phase control word, which principle is simply described as the periodic process of incremental and cumulative overflow back to zero. In satellite navigation system, the dynamic delay generation method based on NCO can be used in two ways, one way is that the NCO output pulse is used as a clock of pseudo-code generator; another way is that the NCO output pulse is generated the read address of pseudo-code sequence memory. The results of two methods are essentially the same, their principle are shown in Fig. 58.1.

Firstly the initial register value of pseudo-code generator or the initial address of pseudo-code memory is obtained by the initial delay value. Then, the phase control words calculated by code rate are real-time adjusted continuously, which achieved the dynamic delay generation.

58.2.2 Dynamic Delay Generation Method based on FD Filter

FD filter is used to delay fractional sampling signal, the dynamic delay generation method based on FD filter [2] is shown in Fig. 58.2. The pseudo-code signal generator produced the nominal frequency signal; according to the initial delay and Doppler information, the address of FD filter group is calculated by the

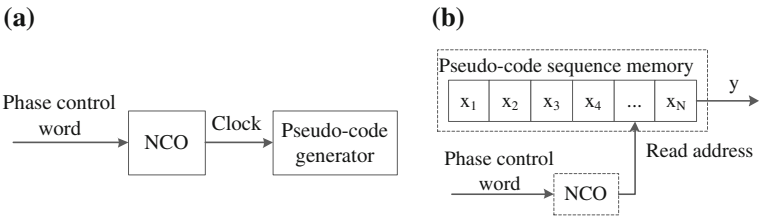

Fig. 58.1 The principle curve of the dynamic delay generation method based on NCO (**a**) is the way to control the clock of pseudo-code generator; **b** is the way to control the read address of pseudo-code generator

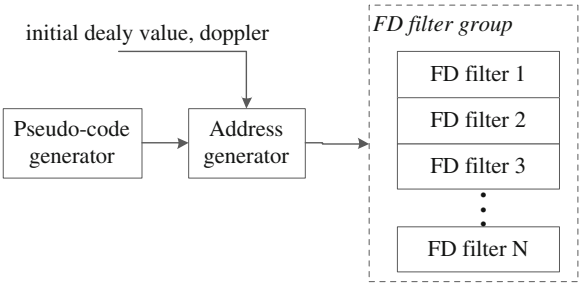

Fig. 58.2 The principle diagram of dynamic delay generation method based on FD filter

address generator, the address is responded to implement the different signal delay, thereby the dynamic delay generation is completed.

In Fig. 58.2, the accuracy of this method is related to the number of FD filters. When the FD filter number is N, the accuracy is $1/N$ sampling delay, the mth FD filter is m/N. Therefore, this method can achieve some fixed fractional sampling delay; the method is also so-called dynamic delay generation method based on fixed fractional delay (FFD) filter.

58.2.3 Comparison of the Traditional Methods

The difference between the two traditional methods is mainly reflected in the way to delay fractional sampling signal, the simulation is accomplished by the two methods respectively. The simulation is to delay C/A signal with 0.2 sample points in GPS system, the results are shown in Fig. 58.3.

For the NCO method, it cannot achieve the signal delay in less than the clock cycle; the simulation result is an average delay. Meanwhile, the delay result is the neighboring integral sampling data, this method can be considered as a zero-order interpolation. Then for the FFD filter method, each sampling points is delayed, the output value is calculated by known data, it can be assumed that the method is a multi-order interpolation.

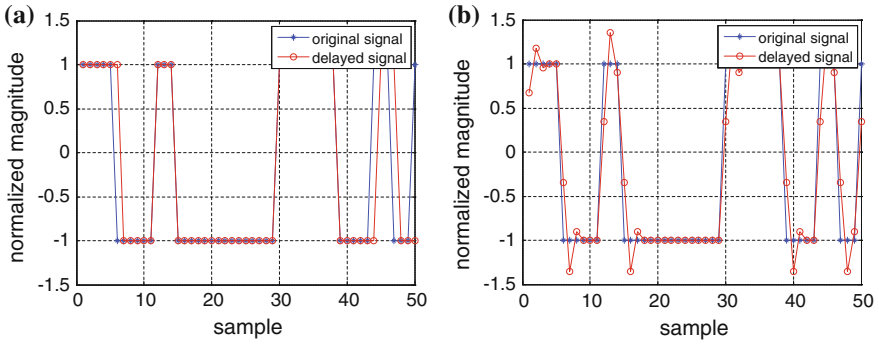

Fig. 58.3 Simulation result. **a** Result of the NCO method. **b** Result of the FFD filter method

In summary, the two methods are essentially to achieve the dynamic delay signal resampling; these are all the realization form of FD filter. For the NCO method, the delay value of FD filter is 0 or 1; for the FFD filter method, the delay value of FD filter is fixed m/N. Nevertheless for the VFD filter method, the delay of FD filter is any value among [0, 1], therefore, from the perspective of the FD filter, the three methods have a unified FD filter model,

$$H_d = e^{-jp\omega} = \begin{cases} p = 0, 1 & \text{for NCO method} \\ p = \frac{m}{N} & \text{for FFD filter method} \\ p = \text{any value} & \text{for VFD filter method} \end{cases} \tag{58.1}$$

where p is the fractional delay. From formula (58.1), the NCO and FFD filter methods are the special circumstance of VFD filter method.

58.3 Dynamic Delay Generation Method based VFD Filters

When the based VFD filter dynamic delay generation method is used to control the pseudo-code signal delay in satellite navigation system, the principle is shown in Fig. 58.4.

The sampled pseudo-code signals in nominal frequency were stored in the data buffer memory; and the current delay is calculated through pseudo-ranges and their derivatives, which were provided by external mathematical simulation software, the delay value is decomposed as integer sampling delay and fractional sampling delay. The integer sampling delay is achieved by changing the read address of data buffer memory, and then the fractional sampling delay is achieved by changing the delay of VFD filter.

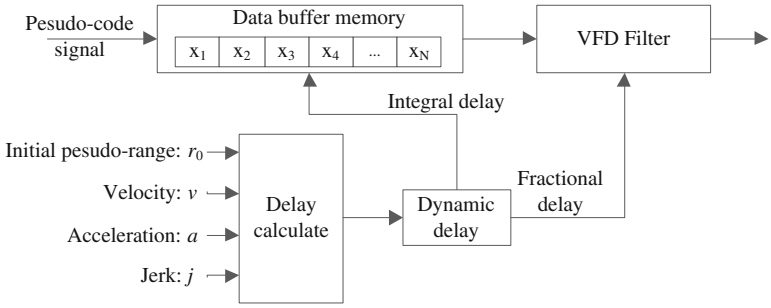

Fig. 58.4 Principle diagram of dynamic delay generation method based on VFD filter

58.3.1 Dynamic Delay Calculation Method

To obtain the delay at any time, the three-order Taylor function of the pseudo-range information was usually the model of dynamic delay, the function was expressed

$$r(t) = r_0 + vt + \frac{1}{2}at^2 + \frac{1}{6}jt^3 \tag{58.2}$$

where r_0 is the initial pseudo-range, v is the one-order derivative of pseudo-range or radial velocity, a is the two-order derivative of pseudo-range or radial acceleration, j is the three-order derivative of pseudo-range or radial jerk.

To implement the (58.2) function in hardware, the 3-order accumulator was used, which structure is shown in Fig. 58.5.

Where D_0, D_1, D_2 indicates the registers in three accumulators; k_0, k_1, k_2 represents the cumulative parameter; p_0, p_1, p_2 represents the output of the accumulators. The output of the third order accumulator p_0 is

$$p_0(n) = k_0 + nk_1 + \frac{1}{2}(n^2 - n)k_2 + \frac{1}{6}(n^3 - 3n^2 + 2n)k_3. \tag{58.3}$$

Let the system sampling frequency is f_s, the pseudo-code frequency is f_c, the register word length is N, then the relationship of r(t) and p_0(n) is

$$\frac{p_0(n)}{M}\frac{f_c}{f_s} = r\left(\frac{n}{f_s}\right), M = 2^N. \tag{58.4}$$

Contrasting with the coefficient of parameter n, it is solved for

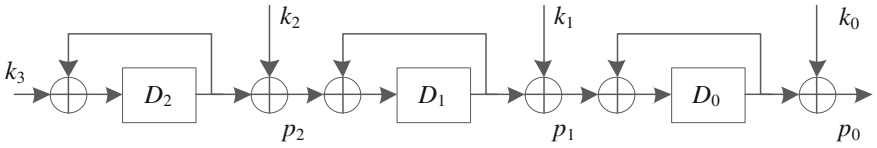

Fig. 58.5 Structure of 3-order accumulator

$$\begin{cases} k_0 = \left\lfloor \dfrac{Mf_c}{c} r \right\rfloor \\ k_1 = \left\lfloor \dfrac{Mf_c}{cf_s} \left(v + \dfrac{a}{2f_s} + \dfrac{j}{6f_s^2} \right) \right\rfloor \\ k_2 = \left\lfloor \dfrac{Mf_c}{cf_s^2} \left(a + \dfrac{j}{f_s} \right) \right\rfloor \\ k_3 = \left\lfloor \dfrac{Mf_c}{cf_s^3} j \right\rfloor \end{cases} . \tag{58.5}$$

58.3.2 VFD Filter Design Method

The ideal frequency response of VFD filter is

$$H_d(\omega, p) = e^{-j\omega\left(\frac{N}{2}+p\right)} = e^{-j\omega\frac{N}{2}} \cdot e^{-j\omega p} \quad -\omega_p \le \omega \le \omega_p, -0.5 \le p \le 0.5 \tag{58.6}$$

where N is the order number of the digital filter, p is the fractional delay value. And the transfer function of FIR filter can be described as

$$H(z, p) = \sum_{n=0}^{N} h_n(p) z^{-n} = \sum_{n=0}^{N} \sum_{m=0}^{M} h(n, m) p^m z^{-n} = \sum_{m=0}^{M} \left(\sum_{n=0}^{N} h(n, m) z^{-n} \right) p^m \tag{58.7}$$

where the coefficient $h_n(p)$ can be expressed as M-order polynomial, the Farrow structure [12] is used to achieve the formula (58.7), as shown in Fig. 58.6.

Therefore on the condition of minimum square error criterion, the design on VFD filter can be expressed as an unconstrained optimization problem,

$$\min \iint W(\omega) \left| H_d(\omega, p) - H\left(e^{j\omega}, p\right) \right|^2 d\omega dp \tag{58.8}$$

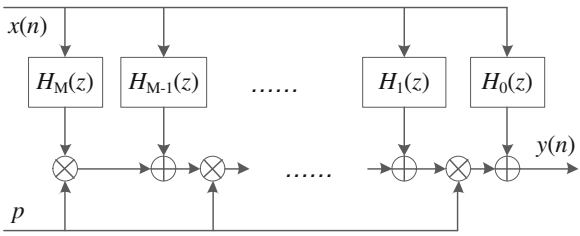

Fig. 58.6 Farrow structure of VFD filter

Currently, the simplest method is to design the Lagrange type VFD filter [4], which has the maximum flatness in the frequency $\omega = 0$, but the bandwidth is very narrow. For the wide-band applications, more efficient design method is iterative weighted least squares (IWLS) method, the details process of IWLS method is in [7].

58.4 Examples and Results

The biggest difference between the proposed method with others is utilizing the VFD filter, which has wide-band, high delay accuracy and low complexity characteristics.

58.4.1 Analysis of Accuracy

To evaluate the performance, the maximum absolute error of variable frequency response ε_m, the maximum absolute group delay error ε_τ are defined, respectively, by

$$\varepsilon_m = \max\left\{\left|H_d(\omega,p) - H\left(e^{-j\omega},p\right)\right|, \quad 0 \le \omega \le \omega_p, 0 \le p \le 0.5\right\} \tag{58.9}$$

$$\varepsilon_\tau = \max\left\{\left|\frac{N}{2} + p - \tau(\omega,p)\right|, \quad 0 \le \omega \le \omega_p, 0 \le p \le 0.5\right\} \tag{58.10}$$

To compute the errors in Eq. (58.9)–(58.10), frequency ω and parameter p are uniformly sampled at step sizes $\omega_p/200$ and 1/60, respectively in this section.

An $N = 50$, $M = 7$, and $\omega_p = 0.9\pi$ VFD filter is designed with IWLS method. Figure 58.7 shows that the absolute error of frequency response and absolute error of variable frequency response, respectively. The maximum error of ε_τ is located in the 0.9π cutoff frequency, and the ε_m is very small in the entire band.

However, if using the FFD filter method proposed by [2, 3], the bandwidth of pass band is only 0.6π, which cannot appease the demand of 0.9π bandwidth.

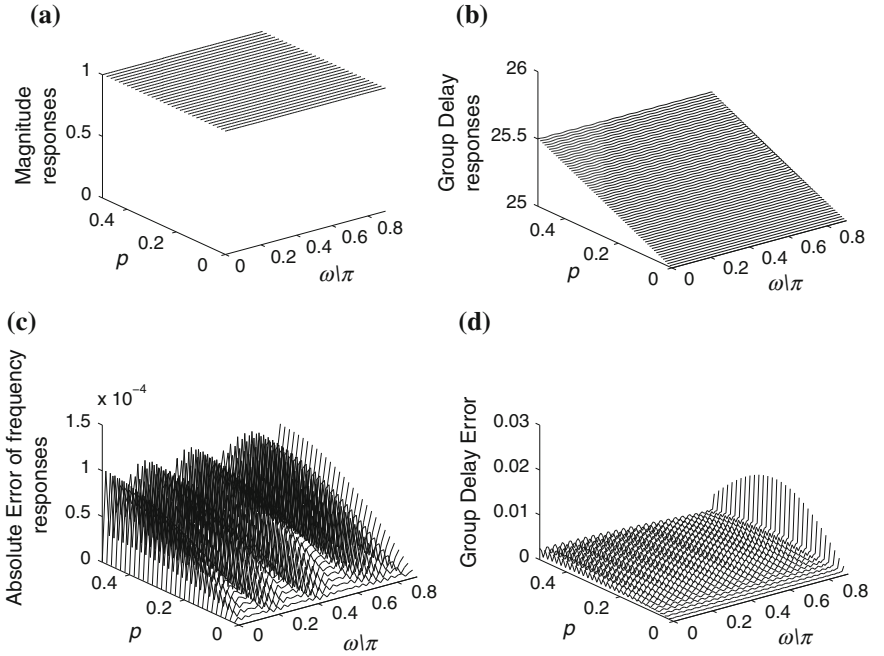

Fig. 58.7 Design of an $N = 50$, $M = 7$, and $\omega_p = 0.9\pi$ VFD FIR filter. **a** Magnitude response. **b** Variable fractional-delay response. **c** Absolute error of frequency response. **d** Absolute error of variable frequency response

Further, the Table 58.1 shows the results of VFD filter in the different order N. when $N = 40$, the delay accuracy is 0.1 sampling delay in the entire frequency band, the amplitude error is -65 dB; when $N = 60$, the accuracy is up to 0.01 sampling delay, the amplitude error is -93 dB.

58.4.2 Analysis of Algorithm Complexity

Because the Farrow structure is used by the VFD filter method, the parameter p is only reset on changing the filter delay characteristics. But for the FFD filter method, the all parameters of sub-filter is reset. On the other hand, according to the [2], if the accuracy requests the 0.001 sampling delay, the 1,024 filter coefficients need to be saved. Nevertheless, for the same requests of 0.001 sampling delay and 0.6π bandwidth, the only 250 filter coefficients need to be saved in the VFD filter method. Therefore, the complexity of the VFD filter method is far less than the FFD filter method.

Table 58.1 Results of VFD filter in different orders *N*. ($M = 7$, $\omega_p = 0.9\pi$)

N	ε_m	ε_τ
20	0.017328(−35 dB)	0.483923
30	0.002991(−50 dB)	0.163664
40	0.000541(−65 dB)	0.048835
50	0.000104(−79 dB)	0.012767
60	0.000021(−93 dB)	0.003155

58.5 Conclusions

This paper analyzes the principle and characteristics on the traditional dynamic delay generation method. In perspective of FD filter model, the NCO method and FFD filter method are all special cases of the VFD filter method. Meanwhile the proposed VFD filter method can solve the dynamic delay generation in high-precision, wide band conditions. The simulation results indicate that the proposed method can achieve the 0.01 sampling delay accuracy in the 0.9π pass band when the order of VFD filter is 50. The computational complexity is far less than the traditional method.

References

1. Qi W, Chang Q et al (2008) Arithmetic of doppler simulation in high dynamic signal simulator. Acta Aeronautica et Astronautica Sinica 29(5):1252–1257
2. Yang J (2007) The research of the signal simulation theory and technologies for satellite navigation. National University of Defense Technology, Changsha
3. Chen Z (2011) Research on the method of simulating navigation signals accurately based on BOC modulation. National University of Defense Technology, Changsha
4. Laakso T, Valimaki V et al (1996) Splitting the unit delay (FIR/all pass filters design). IEEE Signal Process Mag 13(1):30–60
5. Deng T, Chivapreecha S et al (2012) Bi-minimax design of even-order variable fractional-delay FIR digital filter. IEEE Trans Circuits Syst 59(8):1766–1774
6. Hon K, Jiang A (2009) FIR, allpass, and IIR variable fractional delay digital filter design. IEEE Trans Circuits Syst I Regul Pap 56(9):2064–2074
7. Jong S, Soo P et al (2008) Minimax design of variable fractional-delay FIR digital filters by iterative weighted least-squares approach. IEEE Signal Process Lett 15:693–696
8. Tian D, Yong L (2006) Weighted-least-squares design of variable fractional-delay FIR filters using coefficient symmetry. IEEE Trans Signal Process 54(8):3023–3038
9. Tian D (2011) Decoupling minimax design of low-complexity variable fractional-delay FIR digital filters. IEEE Trans Circuits Syst I Regul Pap 58(10):2398–2408
10. Hui Z, Jue Y (2006) A simple and efficient design of variable fractional delay FIR filters. IEEE Trans Circuits Syst II Express Briefs 53(2):157–160
11. Jong S, Soo P et al (2010) A new criterion for the design of variable fractional-delay FIR digital filters. IEEE Trans Circuits Syst I Regul Pap 57(2):368–377
12. Farrow C (1988) A continuously variable digital delay element. IEEE ISCAS in Processing, pp 2641–2645

Chapter 59
Spoofing Jamming Suppression Techniques for GPS Based on DOA Estimating

Yaotian Zhang, Lu Wang, Wenyi Wang, Dan Lu and Renbiao Wu

Abstract This paper studies GPS receiver anti-spoofing jamming problems. Unlike blanket jamming, spoofing jamming is hidden because its power level below noise floor. Besides, spoofing jamming has the same format with satellite signals. A designed spoofing jamming can guide GPS receiver positioning errors occurred and change its navigation line. The existing jamming suppression methods of satellite navigation systems are more suitable for blanket jamming suppression, while for spoofing jamming suppression, these methods are almost invalid. The current published literature make the spoofing jamming detection technology as the major research direction, and rarely involve how to suppress spoofing jamming. This paper analyzes the characteristics of repeater spoofing jamming. For one and multiple of repeater spoofing jamming scenarios, beam forming and RELAX algorithm are proposed to estimate the DOA (Direction of Arrival) of spoofing jamming respectively. After detecting the DOA of spoofing jamming, GPS receiver can steer nulling to the direction of spoofing jamming and suppress spoofing jamming by constructing the projection matrix of spoofing jamming. Simulation experiments prove the correctness and the effectiveness of the two methods.

Keywords GPS receiver · Spoofing suppression · Beam forming · RELAX algorithm

Y. Zhang (✉) · L. Wang · W. Wang · D. Lu · R. Wu
Tianjin Key Lab for Advanced Signal Processing, Civil Aviation University of China, Tianjin, China
e-mail: zyzbasketball@sina.com

J. Sun et al. (eds.), *China Satellite Navigation Conference (CSNC) 2014 Proceedings: Volume I*, Lecture Notes in Electrical Engineering 303,
DOI: 10.1007/978-3-642-54737-9_59,

59.1 Introduction

When GPS (Global Positioning System) signals arrival GPS receivers, its power really weakness about −160 dBW. GPS receivers vulnerable to blanket jamming and spoofing jamming. Unlike blanket jamming, spoofing jamming is hidden because its power level below noise floor and has the same or similar format with authentic satellite signals. Spoofing jamming can guide GPS receiver deviating from accurate navigation and positioning. Spoofing jamming has two forms: production spoofing jamming and repeater spoofing jamming. Repeater spoofing jamming cost lower and technically easy to achieve, is the most important way of spoofing jamming and gradually tends to intelligence. Spoofing jamming has become a major threat to satellite navigation systems. In 2010, the British London's global satellite navigation security conference pointed out that we should not only concerned about the precision of navigation but also more concerned about its reliability, security and robustness [1, 2].

Anti-spoofing jamming technology can be divided into two categories, namely spoofing detection and spoofing mitigation. Spoofing detection algorithms concentrate on discriminating the spoofing jamming signals but they do not necessarily perform countermeasures against the spoofing attack, while spoofing mitigation techniques mainly concentrate on neutralizing the detected spoofing jamming signals and help the victim receiver to retrieve its positioning and navigation abilities. Currently, the majority of anti-spoofing jamming technology proposed in the literature are belonging to spoofing detection, for the study of spoofing mitigation is relatively few. Spoofing mitigation technology mainly includes RAIM technology (Receiver Autonomous Integrity Monitoring) and multi-antenna technology. Ledvina proposes an extended RAIM technique that is able to detect and exclude the outlier measurements injected by the spoofing jamming. However, RAIM technology is effective only in cases where only one or two spoofing measurements are present among several authentic pseudo-ranges; otherwise, if the spoofed pseudo-range measurements are in majority, the RAIM technique might reject authentic measurements [3]. McDowell proposes an array antennas technology that is able to suppress spoofing jamming. This technology use the information which obtained after tracking satellite signals to estimate the DOA (Direction of Arrival) of each satellite signals and detect the DOA of spoofing jamming. After detecting the direction of spoofing jamming, antennas array can steer a null toward the spoofing jamming source and suppress its harmful effect. However, this technology is effective only in cases where only one spoofing jamming existing and needing feedback information [4]. Daneshmand proposes a double antennas array technology and multi-antennas array technology [5, 6]. These techniques make correlation operation between the data received from each antenna and the data from reference antenna to detect the direction of spoofing jamming. Finally, antennas array can steer a null toward the spoofing jamming source and suppress it. The disadvantage of these techniques is not applicable to the cases where multiple spoofing jamming existing. This paper proposes a multi-

antennas beam forming and null steering technology for the spoofing scenario of single and multiple repeater spoofing jamming sources (each repeater spoofing jamming source contains multiple repeater satellite signals).

59.2 Data Model

Assume a uniform linear array composed by N element. Antenna array received signals can be written as

$$\mathbf{x}(nT_s) = \sum_{m=1}^{N_a} \mathbf{a}_m \sqrt{p_m^a} F_m^a(nT_s) + \sum_{k=1}^{N_s} \mathbf{b}_k \sqrt{p_k^s} F_k^s(nT_s) + \mathbf{n}(nT_s) \tag{59.1}$$

where N_a and N_s are the number of authentic signals and spoofing jamming sources respectively. Note that, each repeater spoofing jamming source contains multiple repeater satellite signals, N_k are the number of repeater satellite signals for each repeater spoofing jamming source. $\mathbf{n}(nT_s)$ is the complex additive white Gaussian noise vector, T_s is the sampling interval.

$$F_m^a(nT_s) = D_m^a\left(nT_s - \tau_m^a\right) c_m^a\left(nT_s - \tau_m^a\right) e^{j\phi_m^a + j2\pi f_m^a nT_s} \tag{59.2}$$

$$F_k^s(nT_s) = \sum_{l=1}^{N_k} D_l^s\left(nT_s - \tau_l^s\right) c_l^s\left(nT_s - \tau_l^s\right) e^{j\phi_l^s + j2\pi f_l^s nT_s} \tag{59.3}$$

where a and s refer to the authentic signals and spoofing jamming respectively and ϕ, f, p and τ are the phase, Doppler frequency, signal power and code delay of the received signals respectively. $D(nT_s)$ and $c(nT_s)$ represent navigation data bits and PRN code. $\mathbf{a}_m$ is the logogram of $\mathbf{a}(\theta_m)$, representing steering vector of mth authentic signals,

$$\mathbf{a}_m = \mathbf{a}(\theta_m) = \left[1 \quad e^{-j\frac{2\pi}{\lambda}d\sin\theta_m} \quad \cdots \quad e^{-j(N-1)\frac{2\pi}{\lambda}d\sin\theta_m}\right]^T \tag{59.4}$$

$\mathbf{b}_k$ is the logogram of $\mathbf{b}(\theta_k)$, representing steering vector of kth spoofing jamming,

$$\mathbf{b}_k = \mathbf{b}(\theta_k) = \left[1 \quad e^{-j\frac{2\pi}{\lambda}d\sin\theta_k} \quad \cdots \quad e^{-j(N-1)\frac{2\pi}{\lambda}d\sin\theta_k}\right]^T \tag{59.5}$$

in (59.4) and (59.5), λ and d represents the wavelength of the satellite signal and the spacing between antenna arrays respectively.

59.3 Spoofing Jamming Suppression Techniques Based on DOA Estimating

59.3.1 Spoofing Jamming Suppression Techniques for Single Repeater Spoofing Jamming Source

Single repeater spoofing jamming source usually composed by a spoofing device which repeating multiple satellite signals, in the presence of single repeater spoofing jamming source, beam forming is proposed to estimate the DOA of spoofing jamming source. Actually, beam forming is matched filtering, a non-parametric algorithm and has a good effect on estimating the DOA of single repeater spoofing jamming source. Beam forming to estimate the DOA of spoofing jamming can be summarized as: searching the peak value of $\mathbf{a}^H(\theta)\mathbf{Ra}(\theta)$,

$$\hat{\theta}_k = \arg\max_{\theta} \mathbf{a}^H(\theta)\mathbf{Ra}(\theta) \tag{59.6}$$

where $\mathbf{a}(\theta)$ represent steering vector of the uniform linear array, $\mathbf{R}$ is the sample covariance matrix,

$$\mathbf{R} = E\{\mathbf{x}(nT_s)\mathbf{x}^H(nT_s)\} = \sum_{m=1}^{N_a} p_m^a \mathbf{a}_m \mathbf{a}_m^H + \sum_{k=1}^{N_s} N_k p_k^s \mathbf{b}_k \mathbf{b}_k^H + \sigma^2 \mathbf{I} \tag{59.7}$$

where $N_s = 1$ since there is only one spoofing jamming source, σ^2 represent the power of noise. The power of authentic signals, spoofing jamming and noise satisfy the following relationship,

$$p_m^a < p_k^s \ll \sigma^2 \tag{59.8}$$

Thus, to be directly estimating the DOA of spoofing jamming from (59.6) is impossible, because the authentic signals and spoofing jamming are drowned in the noise level. To solve this problem, the power of the noise must be subtracted from $\mathbf{R}$. Noise power is mainly distributed in the main diagonal of $\mathbf{R}$. If a unit matrix which has a similar power with noise subtracted from $\mathbf{R}$, then the power of the noise can remove from $\mathbf{R}$. Considering the power of noise much larger than the power of authentic signals and spoofing jamming, the power of the unit matrix can be decided by the average of the main diagonal elements of $\mathbf{R}$. $\tilde{\mathbf{R}}$ represents the sample covariance matrix after removing the power of the noise,

$$\tilde{\mathbf{R}} = \mathbf{R} - \zeta \mathbf{I} \tag{59.9}$$

where ζ is the average of the main diagonal elements of $\mathbf{R}$,

$$\zeta = trace(\mathbf{R})/N \tag{59.10}$$

by substituting $\tilde{\mathbf{R}}$ from (59.9) in (59.6),

$$\hat{\theta}_k = \arg\max_{\theta} \mathbf{h}^H(\theta)\tilde{\mathbf{R}}\mathbf{h}(\theta) \tag{59.11}$$

where $\mathbf{h}(\theta)$ represent steering vector of a uniform linear array.

After estimating the DOA of spoofing jamming source, the spoofing subspace $\mathbf{P}$ can be obtained,

$$\mathbf{P} = \mathbf{h}\left(\hat{\theta}_k\right)\mathbf{h}^H\left(\hat{\theta}_k\right)/N \tag{59.12}$$

According to the projection theory, the orthogonal projection matrix to the spoofing subspace can be obtained as

$$\mathbf{P}_\perp = \mathbf{I} - \mathbf{h}\left(\hat{\theta}_k\right)\mathbf{h}^H\left(\hat{\theta}_k\right)/N \tag{59.13}$$

Thus, if the orthogonal projection matrix is applied to vector $\mathbf{x}(nT_s)$ as

$$\begin{aligned}\mathbf{y}(nT_s) &= \mathbf{P}_\perp\mathbf{x}(nT_s) = \mathbf{P}_\perp\sum_{m=1}^{N_a}\mathbf{a}_m\sqrt{p_m^a}F_m^a(nT_s) + \mathbf{P}_\perp\sum_{k=1}^{N_s}\mathbf{b}_k\sqrt{p_k^s}F_k^s(nT_s) + \mathbf{P}_\perp\mathbf{n}(nT_s)\\ &\approx \mathbf{P}_\perp\sum_{m=1}^{N_a}\mathbf{a}_m\sqrt{p_m^a}F_m^a(nT_s) + \mathbf{P}_\perp\mathbf{n}(nT_s)\end{aligned} \tag{59.14}$$

the spoofing jamming is removed from the received antenna array signals. The derivation of spoofing jamming suppression of the formula (59.14) is as follows,

$$\mathbf{P}_\perp\mathbf{b}_k = \mathbf{b}_k - \mathbf{h}\left(\hat{\theta}_k\right)\mathbf{h}^H\left(\hat{\theta}_k\right)\mathbf{b}_k/N = \mathbf{b}_k - \rho\mathbf{h}\left(\hat{\theta}_k\right) \tag{59.15}$$

where $\rho = \mathbf{h}^H\left(\hat{\theta}_k\right)\mathbf{b}_k/N$, if $\hat{\theta}_k$ has sufficient accuracy with θ_k, then normalized correlation coefficient $\rho \approx 1$, namely $\mathbf{P}_\perp\mathbf{b}_k \approx 0$.

59.3.2 Spoofing Jamming Suppression Techniques for Multiple Repeater Spoofing Jamming Source

Multiple repeater spoofing jamming sources composed of multiple spoofing devices. Each spoofing device broadcasts several specific satellite signals. These spoofing devices composed by a pseudo-constellation. In the presence of multiple repeater spoofing jamming sources, relaxation (RELAX) algorithm is proposed to estimate the DOA of spoofing jamming sources. RELAX algorithm was proposed by Li and Stoica [7], it is a parametric algorithm to estimate signal parameters and has a good effect on estimation the DOA of multiple repeater spoofing jamming sources. By the following formula repeated iteration to obtained all DOA of spoofing jamming sources, $N^{'}$ is the number of samples,

$$\mathbf{x}_k(nT_s) = \mathbf{x}(nT_s) - \sum_{i=1, i\neq k}^{N_{spoof}} \mathbf{a}(\hat{\theta}_i)\hat{s}_i(nT_s) \tag{59.16}$$

$$\hat{s}_k(nT_s) = \left.\frac{\mathbf{a}^H(\theta_k)\mathbf{x}_k(nT_s)}{N}\right|_{\theta_k=\hat{\theta}_k}, \quad n = 1, 2, \ldots, N' \tag{59.17}$$

$$\hat{\theta}_k = \arg\min_{\theta_k} \sum_{n=1}^{N'} \left| \mathbf{I} - \frac{\mathbf{a}(\theta_k)\mathbf{a}^H(\theta_k)}{N}\mathbf{x}_k(nT_s) \right|^2 = \arg\max_{\theta_k} \sum_{n=1}^{N'} \left|\mathbf{a}^H(\theta_k)\mathbf{x}_k(nT_s)\right|^2 \tag{59.18}$$

After estimating the DOA of spoofing jamming sources, according to the projection theory, the orthogonal projection matrix to the spoofing subspace can be obtained as,

$$\mathbf{P}_{\perp} = \mathbf{I} - \mathbf{A}(\theta)\mathbf{A}^H(\theta)/N \tag{59.19}$$

where $\mathbf{A}(\theta) = \left[\mathbf{h}\left(\hat{\theta}_1\right) \quad \mathbf{h}\left(\hat{\theta}_2\right) \quad \cdots \quad \mathbf{h}\left(\hat{\theta}_k\right)\right]$ is the array manifold of spoofing jamming sources. The spoofing jamming is suppressed by applying the orthogonal projection matrix to antenna array received signals.

59.4 Simulation Results

For single spoofing jamming source, an antenna array with ten elements is used and the antenna configuration is chosen a uniform linear array with a half GPS L1 wavelength spacing. Authentic signal is PRN1, transmitted from the direction at azimuth of 0°, SNR = −20 dB. Spoofing jamming composed by PRN1, PRN2, PRN3, PRN14 from the direction at azimuth of 25°, INR = −18 dB.

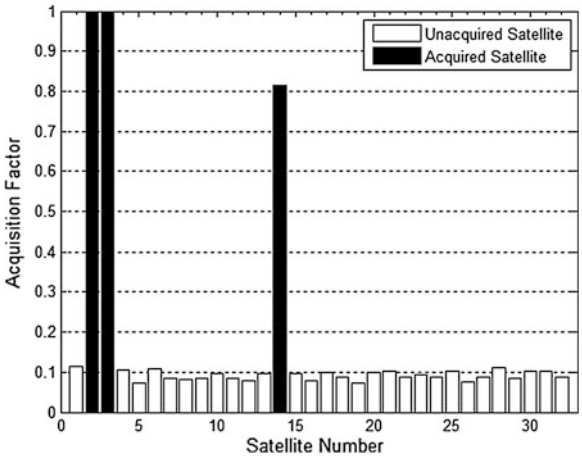

Fig. 59.1 The result of acquisition before spoofing suppression

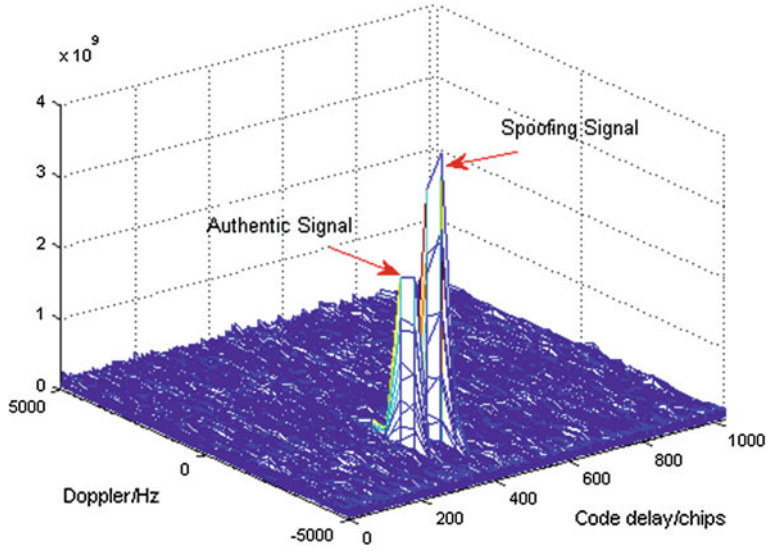

Fig. 59.2 PRN1's CAF before spoofing suppression

Figure 59.1 is the result of acquisition before spoofing suppression. It is observed that GPS receiver acquires three spoofing PRNs, namely PRN2, PRN3 and PRN14. It is indicated that the repeater spoofing jamming can indeed acquired by the receiver. Note that, PRN1 doesn't acquired in Fig. 59.1 due to antenna array received signals have both authentic PRN1 and spoofing jamming PRN1. The result of PRN1's cross ambiguity functions (CAF) contains two distinct correlation

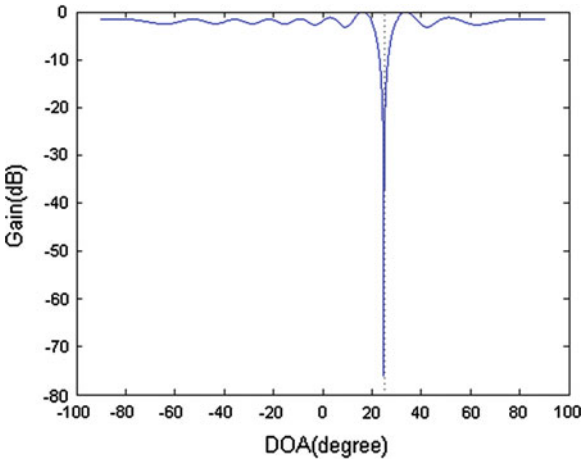

Fig. 59.3 The antenna array pattern of beam forming

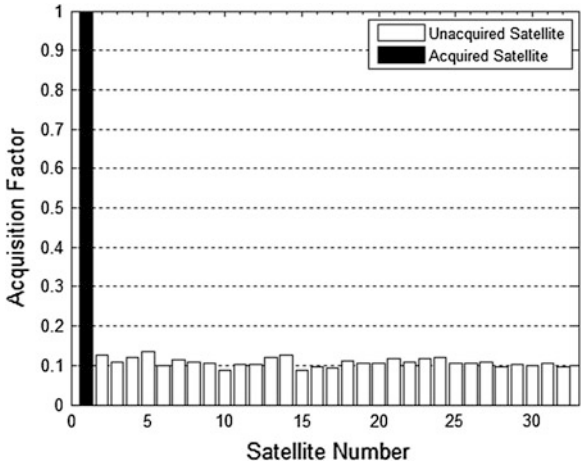

Fig. 59.4 The result of acquisition after spoofing suppression

peaks in Fig. 59.2, not met with the acquired conditions of GPS receiver, that's the reason which GPS receiver failed to acquire PRN1 in Fig. 59.1.

Figure 59.3 is the antenna array pattern of beam forming. We can see that the antenna array forming a deep null steering at the direction of spoofing jamming. Figure 59.4 is the result of acquisition after spoofing suppression. It is observed that GPS receiver only acquired PRN1. In order to certain whether the spoofing jamming suppression successfully, we can observe the PRN1's CAF after spoofing suppression.

Figure 59.5 is the PRN1's CAF after spoofing suppression. It can be observed by comparing the Figs. 59.5 and 59.2 that the PRN1's CAF only existing the authentic peak and the spoofing peak disappearing after spoofing suppression.

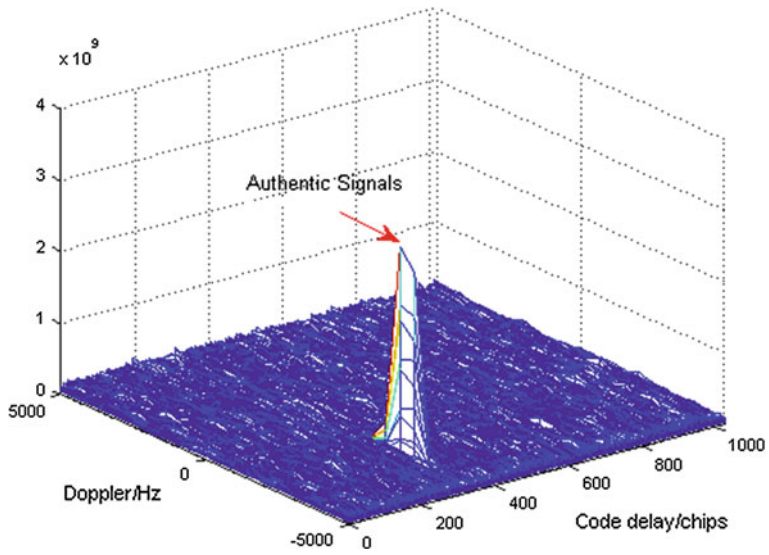

Fig. 59.5 PRN1's CAF after spoofing suppression

Fig. 59.6 The result of acquisition before spoofing suppression

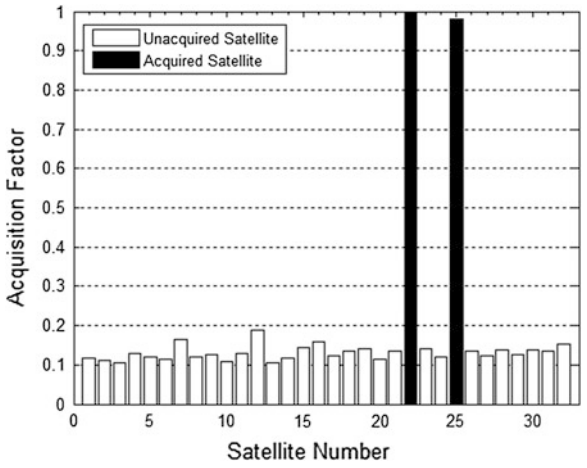

For multiple spoofing jamming sources, an antenna array with ten elements is used and the antenna configuration is chosen a uniform linear array with a half GPS L1 wavelength spacing. Authentic signal is PRN1, transmitted from the direction at azimuth of 0°, SNR $= -20$ dB. One spoofing jamming composed by PRN1, PRN2, PRN3, PRN6, PRN14, PRN20 and PRN22 from the direction at azimuth of 20°, INR $= -18$ dB. The other spoofing jamming composed by PRN1, PRN2, PRN3, PRN6, PRN14, PRN20 and PRN25 from the direction at azimuth of 70°, INR $= -18$ dB.

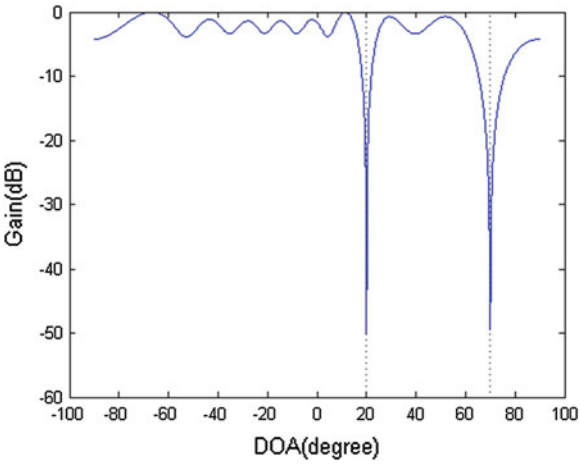

Fig. 59.7 The antenna array pattern of RELAX algorithm

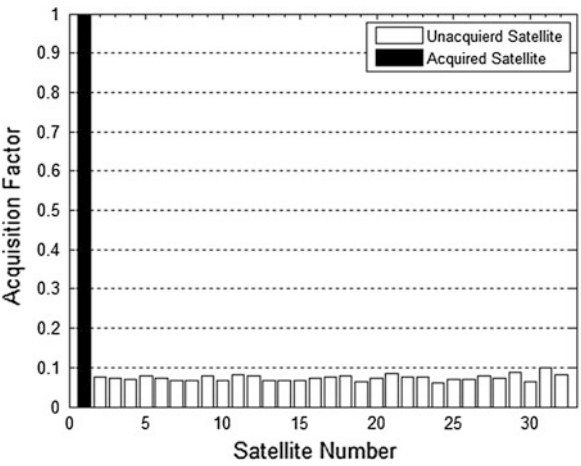

Fig. 59.8 The result of acquisition after spoofing suppression

Figure 59.6 is the result of acquisition before spoofing suppression. It is observed that GPS receiver acquired only two spoofing PRNs, PRN22 and PRN25. The results of PRN1's, PRN2's, PRN3's, PRN6's, PRN14's and PRN20's cross ambiguity functions (CAF) contains two distinct correlation peaks are similar to the result in Fig. 59.2 and not met with the acquired conditions of GPS receiver too. The GPS receiver fails to acquire PRN1, PRN2, PRN3, PRN6, PRN14 and PRN20.

Figure 59.7 is the antenna array pattern of RELAX algorithm. It is observed that the antenna array forming two deep null steering at the directions of two spoofing jamming. Thus the antenna array can suppress spoofing jamming effectively.

Figure 59.8 is the result of acquisition after spoofing suppression. It is observed that GPS receiver only acquires the authentic PRN1.

59.5 Conclusions

This paper analyzes the characteristics of repeater spoofing jamming, proposing estimating the DOA of spoofing jamming source first, then constructing the projection matrix of spoofing jamming and suppressing spoofing jamming. For one and multiple of repeater spoofing jamming scenarios, beam forming and RELAX algorithm are proposed to estimate the DOA of spoofing jamming respectively. Simulation results prove the correctness and the effectiveness of the two methods. Besides, the two methods need not change the structure of GPS receivers and navigation information solving. These two methods can directly suppress spoofing jamming in spatial, easy to implement and less calculation and have a certain significance to anti-spoofing GPS receiver. In the future, in order to achieve the adaptive switching between beam forming and RELAX algorithm in the presence of single and multiple spoofing jamming, the number of spoofing jamming must be detected by using spoofing jamming detection technology.

Acknowledgments The work of this paper is supported by the Project of the National Natural Science Foundation of China (Grant No. 61172112, 61179064 and 61271404), Tianjin Science and Technology Fund (Grant No. 10ZCKFGX04000), and the Fundamental Research Funds for the Central Universities (Grant No. ZXH2009A003, ZXH2012M006 and 3122013D020).

References

1. Last D (2010) GNSS: the present imperfect. DSKTN Conference, London
2. Basker S (2010) Jamming: a clear and present danger. GPS World 21(4):8–9
3. Ledvina BM, Bencze WJ, Galusha B, Miller I (2010) An in-line anti-spoofing device for legacy civil GPS receivers. In: Proceedings of the Institute of Navigation—international technical meeting (ITM '10), San Diego, Calif, January 2010, pp 698–712
4. McDowell CE (2007) GPS spoofer and repeater mitigation system using digital spatial nulling, US Patent 7250903
5. Daneshmand S, Jafarnia-Jahromi A, Broumandan A, Lachapelle G (2011) A low complexity gnss spoofing mitigation technique using a double antenna array. GPS World Magazine 22(12):44–46
6. Daneshmand S, Jafarnia-Jahromi A, Broumandan A, Lachapelle G (2012) A low complexity GPS anti-spoofing method using a multi-antenna array. ION GNSS'12 conference session B3, Nashville, TN, pp 1–11
7. Li J, Stoica P (1996) Efficient mixed-spectrum estimation with applications to target feature extraction. IEEE Trans Signal Process 44(2):281–295

Chapter 60
A High-Dynamic Null-Widen GPS Anti-jamming Algorithm Based on Statistical Model of the Changing Interference DOA

Yanxin Ma, Dan Lu, Wenyi Wang, Lu Wang and Renbiao Wu

Abstract The directions of arrival (DOA) of interference changes rapidly with time in high-dynamic satellite navigation system, which leads to the mismatch between weights training data and weights applying data during the adaptive processing. In this case, the conventional adaptive anti-jamming algorithms are invalid since jammers may easily move out of the array pattern nulls and could not be suppressed. In this letter, a novel method of null-widen is deduced based on the Laplace distribution model of the changing interference DOA in high-dynamic environment. By taking the moving interferences as discrete interference sources obey the Laplace distribution, the extension matrix can be obtained and the average covariance matrix can be calculated from matrix product to broaden the width of nulls. The new method does not alter the noise contribution to the covariance matrix and does not require information about interference DOA. The width of nulls is easy to control. In addition, by combining with the power minimization approach, the new null-widen method does not need the DOA of desired satellite signal. The proposed method can provide correctly acquisition.

Keywords GPS · High-dynamic · Interference suppression · Null widening · Adaptive array · Laplace distribution

60.1 Introduction

In satellite navigation system, because the satellite is usually far away, the satellite signal received by GPS receiver array is so weak that it is susceptible to interferences [1]. Various kinds of spatial adaptive processing algorithms have been proposed for

Y. Ma (✉) · D. Lu · W. Wang · L. Wang · R. Wu
Tianjin Key Lab for Advanced Signal Processing, Civil Aviation University of China, Tianjin, China
e-mail: myxwajm@163.com

J. Sun et al. (eds.), *China Satellite Navigation Conference (CSNC) 2014 Proceedings: Volume I*, Lecture Notes in Electrical Engineering 303,
DOI: 10.1007/978-3-642-54737-9_60,

interference cancellation in GPS, including the power minimization approach [2], minimum variance distortionless response method [3], adaptive as well as blind adaptive beamforming [4], which could effectively suppress interferences and improve the performance of the system when the receiver is mounted on static or low-dynamic platform. However, for high-dynamic GPS receiver, the DOA of interference changes rapidly with time, which leads to the mismatch between weights training data and weights applying data during the adaptive processing. In this case, the conventional adaptive anti-jamming algorithms are invalid since jammers may easily move out of the array pattern nulls and could not be suppressed.

Null-widen technology can extend the period of time for the interference moving out of the nulls and effectively solve the problem mentioned above. The derivative constraint [5] and covariance matrix taper (CMT) [6–9] are the two methods most studied at present. Gershiman have presented an algorithm in [5] which sets derivative constraints on jammer directions to broaden the width of nulls. But this method is computation-intensive and the control of null-width is not flexible. Mailloux and Zatman respectively proposed the null-widen methods by adding virtual interference sources and expanding the bandwidth of interference signal [6, 7], but the Mailloux's method may adds noise contribution to the covariance matrix. The statistical model of the changing interference DOA is discussed by Li Rongfeng. He proved that the result of the uniform distribution mode is equal to Zatman method [9]. However, the changing interference DOA doesn't simply obey the uniform distribution mode in high-dynamic environment. In this letter, a novel method of null-widen is deduced based on the supposed Laplace distribution model, which does not have to know the information about the directions of both the desired signal and the interference. The extension matrix obtained here does not alter the noise contribution to the covariance matrix and the width of nulls is easy to control.

60.2 Signal Model of the High-Dynamic Array

In high-dynamic satellite navigation system, not only velocity and acceleration, but also differential of acceleration of the receiver changes rapidly. However, because the satellite is usually far away, we can assume the DOA of the satellite signal remains constant in a short time for the stable GPS receiver. By contrast, the interference direction relative to the GPS receiver is rapidly changing due to the source-receiver distance is very close [10].

Consider a uniform linear array with M elements, the space between adjacent elements is half of the wavelength. Suppose there are L satellite signals and P interference signals, the data vector received array can be written as

$$\mathbf{x}(t) = \sum_{l=1}^{L} s_l(t)\mathbf{a}(\varphi_l) + \sum_{p=1}^{P} u_p(t)\mathbf{a}\left[\varphi_p(t)\right] + \mathbf{n}(t) \tag{60.1}$$

where, $s_l(t)$, φ_l, denote the lth satellite signal and its DOA ($l = 1, 2, \ldots, L$), $u_p(t)$ represents the pth interference, $\varphi_p(t)$ denotes the DOA of the pth interference which is changing with time ($p = 1, 2, \ldots, P$). $\mathbf{a}(\varphi)$ denotes the steering vector, $\mathbf{a}(\varphi) = [1, e^{-j\pi\sin\varphi}, \ldots, e^{-j(M-1)\pi\sin\varphi}]^T$, and $\mathbf{n}(t)$ denotes the Gaussian white noise. Assume the satellite signal, interference and noise are independent of each other.

Compared with the interferences and the noise, the satellite signal is so weak that it can be neglected. Then, the covariance matrix of received array data can be written as

$$\mathbf{R} = E\left[\mathbf{x}(t)\mathbf{x}^H(t)\right] \approx \sum_{p=1}^{P} \sigma_p^2 \mathbf{a}\left[\varphi_p(t)\right]\mathbf{a}^{\mathrm{H}}\left[\varphi_p(t)\right] + \sigma_n^2\mathbf{I} \tag{60.2}$$

where, E[·] is mathematical expectation $(\cdot)^{\mathrm{H}}$ is conjugate transpose, σ_p^2 denotes the power of pth interference, σ_n^2 denotes the power of noise, $\mathbf{I}$ is unit matrix.

During the practical adaptive processing, we usually use batch mode on account of the restriction of processing speed and algorithm convergence performance. The specific measure is applying the adaptive weight calculated by a block of sampling data snapshots to the next block. Because the signal must be stable during the adaptive processing, the required data snapshots which are collected for forming the adaptive weight are very short. So, Eq. (60.2) can be changed as follows

$$\hat{\mathbf{R}} = E\left[\hat{\mathbf{x}}(t)\hat{\mathbf{x}}^H(t)\right] \approx \sum_{p=1}^{P} \sigma_p^2\, \mathbf{a}(\varphi_p)\, \mathbf{a}^{\mathrm{H}}(\varphi_p) + \sigma_n^2\mathbf{I} \tag{60.3}$$

φ_p denote the current direction, $\hat{\mathbf{x}}(t)$ is the current short sampling data snapshots. Then the element (k, l) of $\hat{\mathbf{R}}$ can be obtained

$$\hat{\mathbf{R}}(k,l) \approx \sum_{p=1}^{P} \sigma_p^2 e^{-j\frac{2\pi}{\lambda}(x_k - x_l)\sin\varphi_p} + \sigma_n^2\delta_{kl} \tag{60.4}$$

As the sample data in formula (60.3) contains only the "current" interference information, the null of the adaptive beam pattern so obtained at this point by adaptive algorithm is extremely sharp and jammers may soon move out of the null in this case. The robustness of the algorithm is very poor. Null-widen technology can effectively solve the problem mentioned above. The general method of null-widen is to build a new covariance matrix $\bar{\mathbf{R}}$ [8] by extending interference sources. $\bar{\mathbf{R}}$ is the result of the sampling covariance matrix $\hat{\mathbf{R}}$ dot product the taper matrix $\mathbf{T}$.

$$\bar{\mathbf{R}} = \hat{\mathbf{R}} \odot \mathbf{T} \tag{60.5}$$

where, symbol $\odot$ denotes the Hadamard product. $\mathbf{T}$ is also called the extension matrix. In the next article, a new extension matrix is proposed based on the change of interference DOA to be Laplace distribution. And it can effectively broaden the width of nulls.

60.3 Method of Broadening Nulls

As the DOA of interference changes rapidly with time, $\varphi_p(t)$ can be described as an extension of the current direction φ_p

$$\varphi_p(t) = \varphi_p + \Delta\varphi_p \tag{60.6}$$

It is easy to explicate that the interference DOA is mainly in a state of constant or changed little during a very short period of time in high-dynamic movement processing. That is to say the value of $\Delta\varphi_p$ mainly concentrated in a small angle range around 0°. Therefore, the Laplace distribution model can be used to describe the change of interference DOA in high-dynamic environment. $f(\Delta\varphi_p)$ is the probability density function of $\Delta\varphi_p$.

$$f(\Delta\varphi_p) = \frac{1}{2\lambda_p} \mathrm{e}^{-\frac{|\Delta\varphi_p - \mu|}{\lambda_p}} \tag{60.7}$$

Here, the unit of φ_p and $\Delta\varphi_p$ is degree, $\mu = 0$, variance is $2\lambda_p^2$.

The average covariance matrix of the received array signal is

$$\bar{\mathbf{R}} = \sum_{p=1}^{P} \sigma_p^2 \int f(\Delta\varphi_p)\mathbf{a}[\varphi_p(t)]\mathbf{a}^{\mathrm{H}}[\varphi_p(t)]\mathrm{d}\Delta\varphi_p + \sigma_n^2\mathbf{I} \tag{60.8}$$

Then the element (k, l) of $\bar{\mathbf{R}}$ can be obtained

$$\bar{\mathbf{R}}(k,l) = \frac{1}{1 + \left(\Delta_{kl}\frac{\pi}{180}\right)^2} \sum_{p=1}^{P} \sigma_p^2 \mathrm{e}^{-j\frac{2\pi}{\lambda}(x_k - x_l)\sin\varphi_p} + \sigma_n^2\delta_{kl} \tag{60.9}$$

where, $\Delta_{kl} = \frac{2\pi}{\lambda}\lambda_p(x_k - x_l)\cos\varphi_p$.

Let

$$\mathbf{T}(k,l) = \frac{1}{1 + \left(\Delta_{kl}\frac{\pi}{180}\right)^2} \tag{60.10}$$

As is shown in the formula above, when $k = l$, $\mathbf{T}(k, l) = 1$, $\delta_{kl} = 1$

$$\begin{aligned} \bar{\mathbf{R}}(k,l) &= \sum_{p=1}^{P} \sigma_p^2 \mathrm{e}^{-j\frac{2\pi}{\lambda}(x_k - x_l)\sin\varphi_p} + \sigma_n^2\delta_{kl} \\ &= \hat{\mathbf{R}}(k,l) \times \mathbf{T}(k,l) \end{aligned} \tag{60.11}$$

When $k = l$, $\delta_{kl} = 0$,

$$\begin{aligned}\bar{\mathbf{R}}(k,l) &= \mathbf{T}(k,l)\sum_{p=1}^{P}\sigma_p^2 e^{-j\frac{2\pi}{\lambda}(x_k-x_l)\sin\varphi_p} \\ &= \hat{\mathbf{R}}(k,l)\times\mathbf{T}(k,l)\end{aligned} \tag{60.12}$$

According to the formula (60.11) and (60.12), $\bar{\mathbf{R}}$ can be rewritten as

$$\bar{\mathbf{R}} = \hat{\mathbf{R}}\odot\mathbf{T} \tag{60.13}$$

$\mathbf{T}$ is the extension matrix, but the interference DOA φ_p in $\mathbf{T}$ is hard to get in practical application.

According to the high-dynamic movement model we can know that when $|\cos\varphi_p| = 1$, the interference DOA has the fastest change, then the null width should to be extended is the biggest. Therefore, we select the parameter $\lambda_{\max}$ which can generate the required maximum null width instead of $\lambda_p\cos\varphi_p$ to form the extension matrix. Then

$$\overline{\mathbf{T}}(k,l) = \frac{1}{1+\lambda_{\max}^2\left[(x_k-x_l)\frac{\pi^2}{90\lambda}\right]^2} \tag{60.14}$$

It can be seen from the formula above that new extension matrix does not need the information about the directions of interference and does not alter the noise contribution to the covariance matrix as well.

Using the extended covariance matrix for interference suppression, there is the following optimization problem

$$\begin{aligned}&\min \mathbf{w}^H\bar{\mathbf{R}}\mathbf{w} \\ &s.t.\ \mathbf{w}^H\boldsymbol{\delta}_M = 1\end{aligned} \tag{60.15}$$

where, $\mathbf{w} = [w_1, w_2, \ldots, w_M]^T$ is the weight vector, $\boldsymbol{\delta}_M = [1,0,\ldots,0]^T$ is a M * 1 dimensional vector.

Equation (60.15) can be solved in Lagrange's multiplier method, then

$$\mathbf{w} = \frac{\bar{\mathbf{R}}^{-1}\boldsymbol{\delta}_M}{\boldsymbol{\delta}_M^{\mathbf{H}}\bar{\mathbf{R}}^{-1}\boldsymbol{\delta}_M} \tag{60.16}$$

60.4 Simulation

In this simulation experiment, consider a ULA with 7 elements (i.e., $M = 7$). The DOAs of the four satellite signals produced by high-dynamic simulator are $-40°$, $0°$, $20°$, $40°$, $SNR = -20$ dB. For the stable GPS receiver, because the satellite is

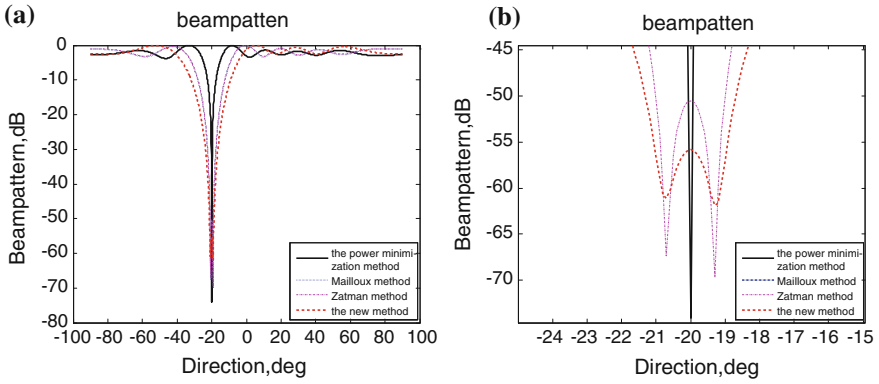

Fig. 60.1 Comparison of beam patterns obtained via the power minimization method and the null-widen methods of inter-frequency signal. **a** Comparison of the full beam patterns, **b** localized beam pattern of the null

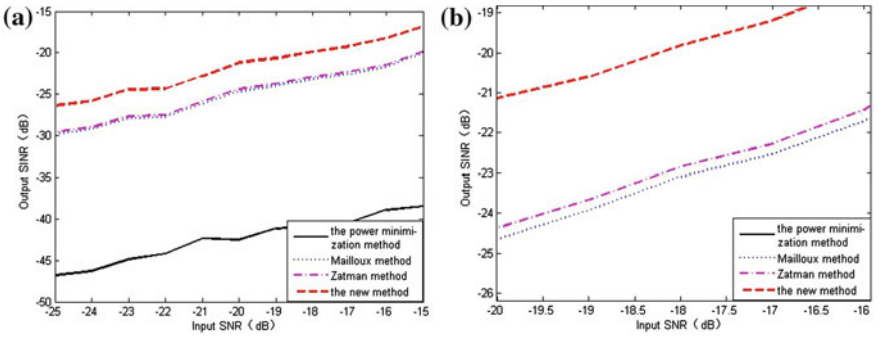

Fig. 60.2 Comparison of the interference suppression performance between the power minimization method and the null-widen methods. **a** Comparison of the output SINR, **b** the partial enlarged view of null-widen methods

usually far away, we can assume the DOA of the satellite signal remains constant in a short time, even in high-dynamic environment. According to the high-dynamic movement model given by Hinedi [11], assume the receiver moves along a straight trajectory and the distance between receiver trajectory and interference source is r. Then we can calculate that the DOA of interference could change 30° in 3 s, when the initial velocity is 1 km/s and r = 10 km. Suppose the great change of interference DOA is 3° during a period of time (weight updating time in batch process), and the interference impinges on the array in direction changing from −20° to −17° gradually, $INR = 40$ dB. The weight vector is calculated by the data sampled in the interference DOA −20°, $\lambda_p = 0.8$. Simulation result is obtained by averaging results of 100 Monte Carlo experiments using 10 data snapshots.

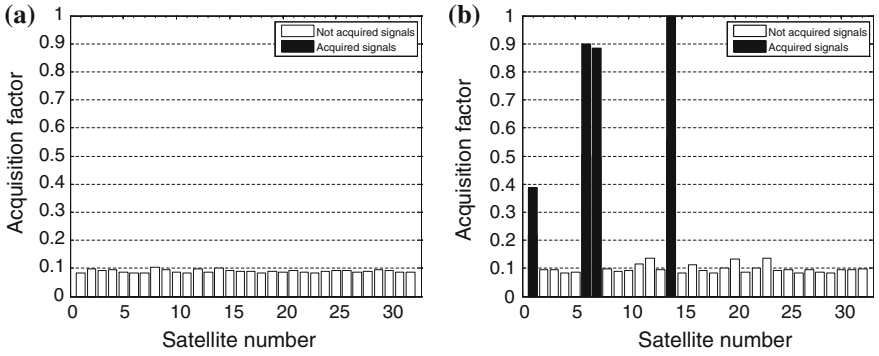

Fig. 60.3 Comparison of the acquisition performance between the power minimization method and the new method. **a** The power minimization method, **b** the new method

In Fig. 60.1a, the beam pattern formed via the null-widen power minimization method (dashed lines) is compared with that obtained via the power minimization method (solid line). For clarity, the magnified null part is shown in Fig. 60.1b. From the figure it can be noted that all the null-widen methods can explicitly broaden the width of the null, but the new method provide the deepest pattern null compared with the other two null-widen methods on the same width.

Figure 60.2 gives the comparison of the output signal to interference plus noise ratio (*SINR*) as a function of the input *SNR*, which is obtained by averaging results of 100 Monte Carlo experiments. From Fig. 60.2a it can be noted that significant improvement of interference suppression performance can be achieved by using the null-widen methods. And from Fig. 60.2b we can find that the result of Zatman method is slightly better than Mailloux method on the same null width, but the new method is the best.

To further verify the anti-jamming performance of the new method in high-dynamic environment, the acquisition of satellite signals are performed by using high-dynamic GPS receiver. Figure 60.3 gives the comparison of acquisition performance, from which it can be noted that the power minimization method fails, while the new method works well.

60.5 Conclusion

The directions of jammers changed rapidly in high-dynamic environment, hence the conventional adaptive anti-jamming algorithms were invalid and the GPS receiver failed to acquire satellites. In allusion to the problem, a new null-widen method based on Laplace distribution model is presented for interference mitigation. The proposed method does not have to know the information about the directions of both the desired signal and the interference, in addition, it doesn't alter noise contribution to the covariance matrix. The simulation results demonstrate the

validity of the method proposed in this paper, and it can provide correctly acquisition and accurately positioning.

Acknowledgment The work of this paper is supported by the Project of the National Natural Science Foundation of China (Grant No. 61179064, 61172112 and 61271404), Fundamental Research Funds for the Central Universities (Grant No. ZXH2009A003, ZXH2012M006, 3122013D020 and 3122013SY27) and the Tianjin Science and Technology Fund (Grant No. 10ZCKFGX04000).

References

1. Nesreen IZ, James LG (2004) Extended Kalman filter-based tracking of weak GPS signals under high dynamic conditions. In: Proceedings of the 17th international technical meeting of the satellite division of The Institute of Navigation. Proc ION-GPS, Long Beach, CA, pp 20–31
2. Ke XZ, Lu Y (2008) Research of GPS anti-jamming antenna based on power inversion algorithm. J Xi'an Univ Technol 24(2):149–152
3. Jay RS (2003) Interference mitigation approaches for the global positioning system. Lincoln Lab J 14(2):167–180
4. Li P, Lu D, Wu RB (2008) Adaptive anti-jamming algorithm based on the characteristics of the GPS signal. In: Proceedings of 2008 international symposium on intelligent signal processing and communication systems. IEEE Press, Xiamen, pp 181–184
5. Gershman AB, Serebryakov GV, Boehme JF (1996) Constrained hung-turner adaptive beamforming algorithm with additional robustness to wideband and moving jammers. IEEE Trans Antennas Propag 44(5):361–367 (MENG)
6. Zatman M (1995) Production of adaptive array troughs by dispersion synthesis. Electron Lett 31(25):2141–2142
7. Mailloux RJ (1995) Covariance matrix augmentation to produce adaptive array pattern troughs. Electron Lett 31(10):771–772
8. Guerci JR (1999) Theory and application of covariance matrix tapers for robust adaptive beamforming. IEEE Trans Signal Process 47(4):977–985
9. Li RF, Wang YL, Wan SH (2003) Research on adapted pattern null widening techniques. Mod Radar 25(2):42–45
10. Wu RB, Lu D, Li CH (2011) Power minimization with derivative constraints for high dynamic GPS interference suppression. Sci China 41(8):968–977
11. Hinedi S, Statman JI (1988) High-dynamic GPS tracking final report. JPL Publication 88-35, 15 Dec

Chapter 61
System Clock and Time Reference Ambiguity Solution Method Based on Clock Quartering

Lei Chen, Jingyuan Li, Yangbo Huang and Gang Ou

Abstract This paper researches a method of system clock and time reference ambiguity solution based on clock quartering. For satellite navigation receiver of satellite navigation system ground monitoring station, in the time-frequency digital signal processing section, phase ambiguity between time base and the input clock cause the time difference of the local time and time-frequency jumps. And this finally leads to pseudorange jumping problem. A solution is proposed in this paper that FPGA dividing the clock cycle into 4 equal portions, sampled 1PPS by using the given sampling frequency which is twice of input clock frequency, measured the portions where the rising edge of 1PPS signal is, get the phase difference between input clock and 1PPS signal, judge using falling or rising edge of clock for sampling edge by the distance between rising edge of 1PPS signal and the rising or falling edge of clock. As long as the connection of time reference and time-frequency system has not been changed, the sampling edge would not be changed once it was chosen. DSP save the portion number, and automatically choose the sampling edge each time system startup. And compare stored 1PPS signal phase portion number and FPGA output 1PPS signal phase portion number. If the monitor shows the difference of them is greater than or equal to 2, it means that the connection is changed or time-frequency signal problems occurred, then the monitoring software alarm and retests the phase portions and reset the portion number. By this way, the phase ambiguity of satellite navigation system ground monitoring station has been solved successfully.

Keywords Time reference · Phase monitoring · Ambiguity solution · Pseudorange jumping · Sampling edge

L. Chen (✉) · J. Li · Y. Huang · G. Ou
College of Electronic Science and Engineering, National University of Defense Technology, Changsha, People's Republic of China
e-mail: chenlei1025@nudt.edu.cn

G. Ou
e-mail: ougang_nnc@163.com

J. Sun et al. (eds.), *China Satellite Navigation Conference (CSNC) 2014 Proceedings: Volume I*, Lecture Notes in Electrical Engineering 303,
DOI: 10.1007/978-3-642-54737-9_61,

61.1 Introduction

Beidou satellite navigation ground station signal measuring communication systems used reference 1PPS (1 Pulse per Second) signal and the system clock (88.45 MHz) signal at the same time. In the time-frequency digital signal processing part, input 1PPS signal is sampled by sampling rate, which is system clock (88.45 MHz), to achieve synchronization of receiving terminal's local time and the system time of time-frequency [1].

With the development of satellite navigation systems, synchronization accuracy requirements of satellite navigation system has reached sub-nanosecond middleweight on the current time [2]. Clock is the most important and special signal part in the circuit since most of the devices within the system are acting on the clock on the edge. It requires a strictly small difference of clock signal delay, otherwise it may cause temporal logic state error. Thus clearly FPGA (Field Programmable Gate Array, Field Programmable Gate Array) factors that determine the system clock delay to minimize has a very important significance to ensure the stability of the design.

In digital communication system, stable transmission of data must meet setup and hold time requirements [3].

The so-called set-up time (Setup Time), refers to the data stability constant time before the trigger's rising edge of the clock signal arriving. If it's not so long enough that the data will not be at the rising edge of this clock into the flip-flop [3]. Figure 61.1 shows a set-up time tolerance. In which, T_{clk} is the system clock cycle. T_{ffpd} is the response time of trigger output. T_{comb} is the time required for the signal output of flip-flop passing combinational logic. T_{setup} is expressed settling time.

The so-called hold time (Hold Time), refers to the data stable constant time after the rising edge of the clock signal triggers. If the hold time is not enough, the data also can't be transported into the flip-flop [3]. The hold time tolerance is shown in Fig. 61.2. In which, T_{hold} is represents hold time.

In the receiving terminal of ground stations satellite navigation and positioning measurement and communication system, there is no constrain of phase relationship between the system clock (88.45 MHz) and the 1PPS signal. Therefore, when the 1PPS signal sampled by the system clock (88.45 MHz), it will not meet the requirements of setup and hold time, which will cause the relationship of local time and the time-frequency system changed, and eventually lead receiver pseudorange jump.

Shown in Fig. 61.3, when the rising edge of external 1PPS's phase and the system clock (88.45 MHz) substantially aligned, it may produces two kinds of phase relationship 1PPS signals inner FPGA after sampling by the rising edge. Each of them is shown in Fig. 61.3, "Internal detected second pulse signal I" and "internal pulse signal detected by the second II", so the local time generated by the 1PPS signal also has two types.

Based on the background above, this paper analyses the phase relationship between the system clock and the time reference (1PPS), proposes system clock and time reference ambiguity solution method based on clock quartering, points to solve the practical problems in engineering applications above.

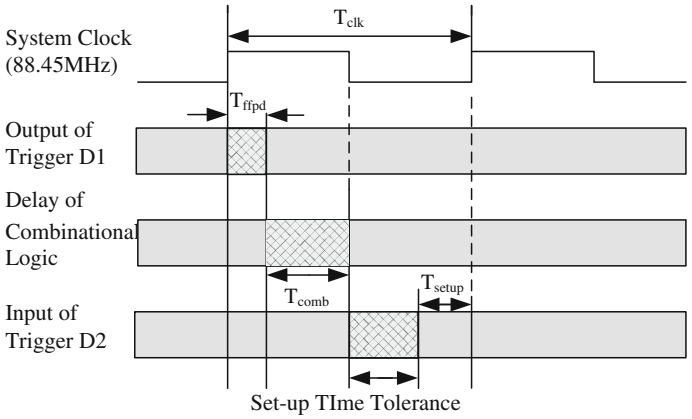

Fig. 61.1 Scheme: setup time margin

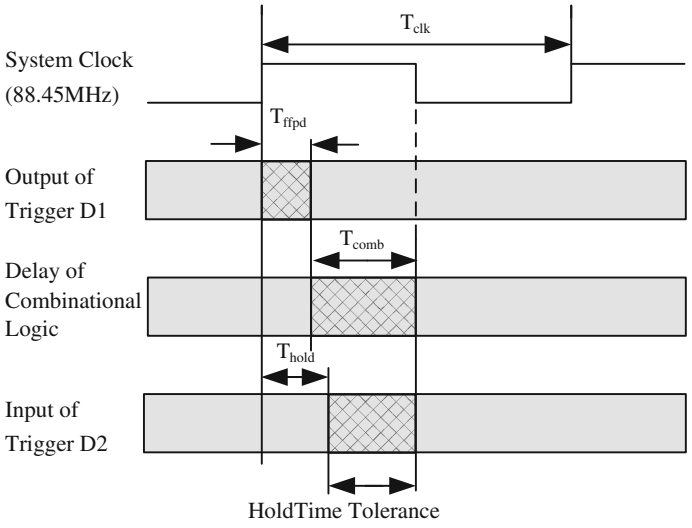

Fig. 61.2 Scheme: hold time margin

Fig. 61.3 Scheme: 1PPS signal sampling scheme

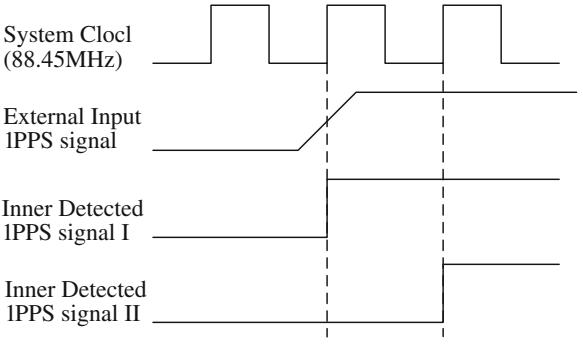

61.2 Model Designs of Phase Detection and Ambiguity Solution Method

61.2.1 Method Proposing

For solving the practical problems in engineering application, this paper proposes a method of system clock and time reference ambiguity solution based on clock quartering. The time reference (1PPS) and the phase of the system clock can be ensure to be monitored stably, if the connection of time-frequency signal lines has been changed and the time-frequency system operating well. By the clock monitoring and selection techniques, phase ambiguities between 1PPS signal and the system clock can be solved.

Figure 61.4 shows a block diagram of the achievement of digital orthogonal transformation. The IF digital signal, which exports form ADC (Analog/digital converter), is a real signal. And the sampling rate is 88.45 MHz. The signal passing digital orthogonal transformation module is separated into I signal and Q signal which are orthogonal complex signals. After the transformation, the signal sampling clock rate changes form system clock (88.45 MHz) to 22.1125 MHz. The signal after orthogonal transformation has been secondary quantitative. The high 4 bits output of I/Q branch signal after transformation is taken into use.

The phase relationship of time reference (1PPS) and the system clock has 4 kinds of possible relationships each time when system starting up. And at each time when starting up, we should avoid the phase ambiguity.

Digital signal sampled is controlled by the sampling phase counter, which is driven by the system clock (88.45 MHz). The counter has 4 kinds of value, 0, 1, 2, 3. Each time when DSP transports time reference to the terminal, the counter clears at the arriving edge of external 1PPS signal. Here's external 1PPS signal is generated by the input system clock (88.45 MHz) after sampling clock signal. The 1PPS signal above is sampled by system clock (88.45 MHz). When the external 1PPS signal phase is substantially aligned with the rising edge of the system clock (88.45 MHz), FPGA internally may produce two kinds of 1PPS signal with different phase relationship sampled by the rising edge. At the moment of DSP timing if the input system clock (88.45 MHz) and 1PPS signal occur phase jitter, the counter clearing time sequence will change, which results in the extraction phase of the signal transition. And ultimately reflects in the pseudorange jumping integral multiple of 11 ns. The problem solved by the 1PPS signal phase selection module by the following.

61.2.2 Design Ideas of Proposed Method

This design idea of the method is shown in Fig. 61.5. Measure the phase difference between the input clock signal and the 1PPS by some method, judge to use the falling edge of system clock to sample if the rising edge of 1PPS signal is closed to the rising

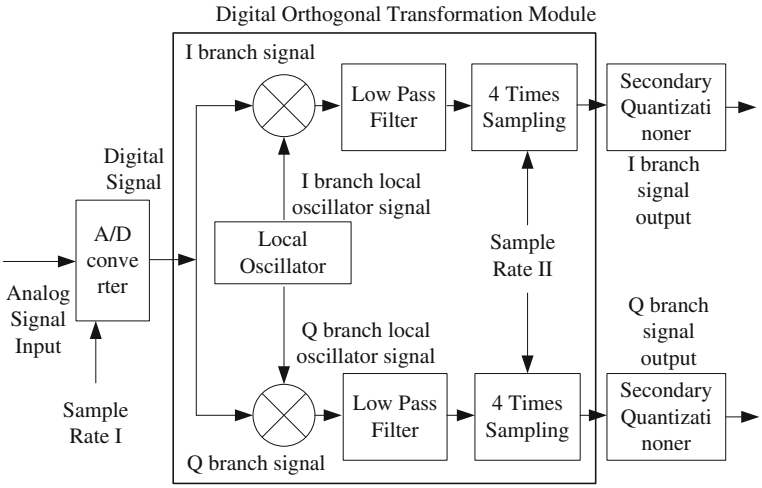

Fig. 61.4 Scheme: digital orthogonal transformation

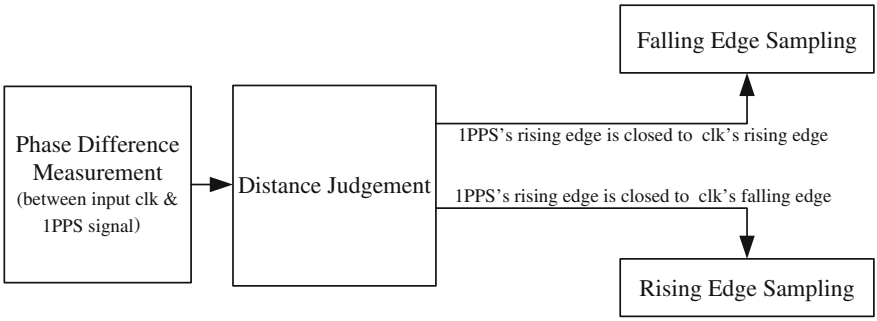

Fig. 61.5 Scheme: ideas of the designed method

Fig. 61.6 Scheme: dividing of clock phase

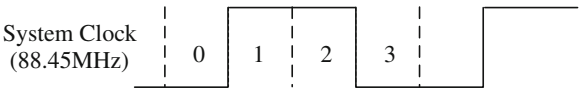

edge of system clock. Judge to use the rising edge of system clock to sample if the rising edge of 1PPS signal is closed to the falling edge of system clock. Once the sampling edge is determined, it will not be changed as long as the connection of time-frequency system and time-frequency signal. It should be ensured that the 1PPS phase drift relative to the system clock should be less than 1/4 clock cycles.

Figure 61.6 shows a schematic diagram of clock phases divided. Firstly, the clock cycle is divided into 4 divisions. FPGA samples 1PPS signal by using the frequency 4 times of the input clock's frequency, then the phase part in which 1PPS signal's rising edge occurs can be detected. And FPGA output the part

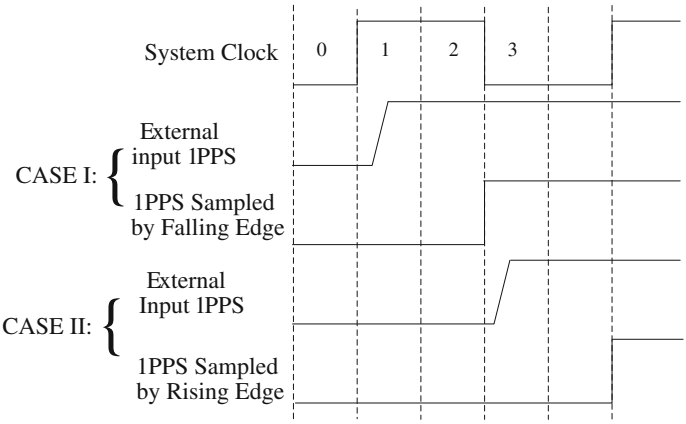

Fig. 61.7 Scheme: sampled 1PPS output signal timing

number to DSP (Digital Signal Processor). DSP reads the part number, and stored in FLASH (Flash Memory).

The 1PPS signal phase selection registers in the module are read-only, using 2 bit (D1, D0), which contains 4 states, 0–3. DSP control monitor software to display these registers to indicate the phase relation between input 1PPS signal and system clock (88.45 MHz). According to the state of the registers, we determine to use the rising or falling edge. If the state is 0 or 1, select the falling edge. If the state is 2 or 3, select the rising edge. This action done by the 1PPS signal sampling edge selection register in DSP interface. The register is available for writing at the least one bit as a terminal configuration parameter used to select the input clock of using rising or falling. This register is only set once when system installed on the station according to the actual to the relation of input 1PPS signal phase and the system clock (88.45 MHz) clock phase, later fixed.

The device's phase logical timing sequence diagram of 1PPS signal output selecting is shown in Fig. 61.7.

Each time when starting up, FPGA detects 1PPS signal's phase number and sends to register. If the rising edge of 1PPS located in 0 or 1, the falling edge is taken into use for sampling. Others, the rising edge is taken into use for sampling. Meanwhile, DSP compares the phase number stored in FLASH with the current phase number. If the difference between them is greater than or equal to 2, alarm to monitoring software to indicate that some problems occur in the time-frequency signal which needs to reset.

Through the FPGA and DSP we realize real-time monitoring of time reference (1PPS), eliminate the phase randomly changes at each time system starting up, solve the ambiguity between time reference (1PPS) and the system clock.

If an exception occurs, DSP alarms immediately and re-adjust the phase of system clock. Ultimately, DSP and FPGA ensure the determined a stable phase relationships of time reference (1PPS) and the system clock, and ensure the pseudorange output form the receiver do not jump.

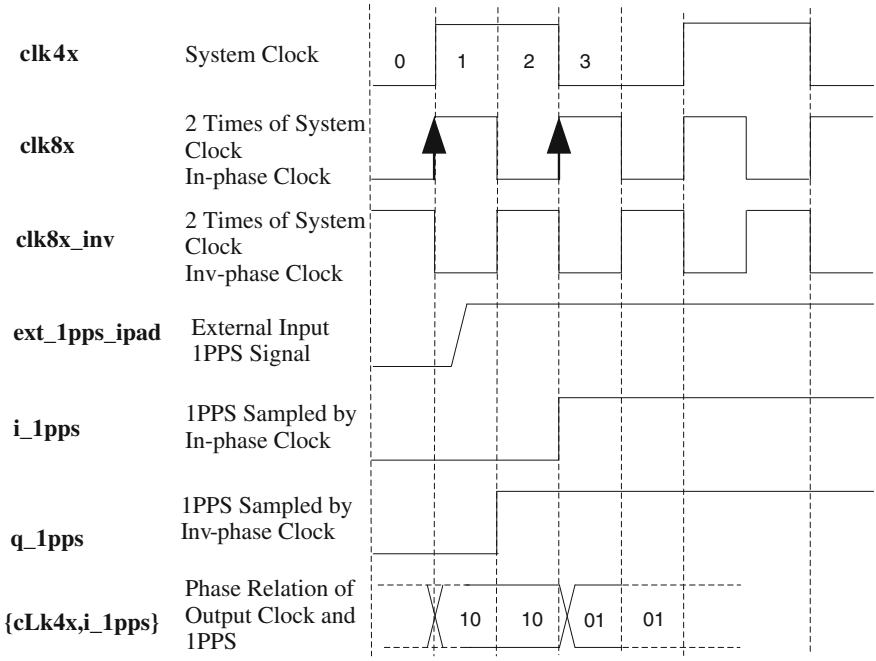

Fig. 61.8 Scheme: timing sequence of 1PPS signal phase selecting signal

61.3 Implementation Steps of Phase Detection and Ambiguity Solution Method

Step I: Firstly, FPGA divides input system clock's clock period into 4 equal portions, as shown in Fig. 61.8. FPGA generates in-phase clock (clk8x) and inverted clock (clk8x_inv) by twice of the system clock's frequency.

Step II: FPGA samples external 1PPS signal by the in-phase clock (clk8x) and inv-phase clock (clk8x_inv) to obtain the no inverting and inverting two kinds of 1PPS signal that i_1pps and q_1pps.

Step III: 1PPS's phase selection signal timing sequence is shown in Fig. 61.8, judging the value of {clk4x, i_1PPS} at the rising edge of clk8x. As the arrowheads shown in Fig. 61.8, according the different location of external 1PPS, {clk4x, i_1PPS} could be 4 different value, 10, 11, 01 and 00. The 4 values are corresponding to the 0, 1, 2, 3 location which is the number of system clock's quartering parts in which the rising edge of 1PPS may be. FPGA output the value to DSP. DSP reads the part number and store in FLASH.

Step IV: Each time when system starts up, DSP reads 1PPS signal phase number stored in the FLASH. If the number is 10 or 11, it means the rising edge of the 1PPS signal is within the range of 0 or 1, FPGA is set by DSP to use the falling edge to sample 1PPS and gets output signal i_1pps shown in Fig. 61.8. Others, if

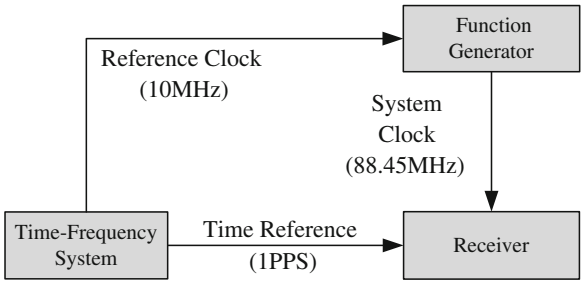

Fig. 61.9 Scheme: functional verification method

the number is 01 or 00, it means the rising edge of the 1PPS signal is within the range of 2 or 3, FPGA is set by DSP to use the rising edge to sample 1PPS and gets output signal q_1pps shown in Fig. 61.8.

61.4 Simulations and Validation of Phase Detection and Ambiguity Solution Method

Figure 61.9 shows a schematic of functional verification method. By using the function generator, simulate the state that phase relation of system clock (88.45 MHz) and 1PPS signal changes. Functional verification method scheme is shown in Fig. 61.9, note that the ranging measurement signal link is left out (not given) in Fig. 61.9 while the test states still follow the normal connection.

Validation steps are as follows.

Step I:

Adjusting the function generator output clock phase, interval 1 ns, checking whether FPGA query output 1PPS signal phase number changes through DSP to verify the FPGA 1PPS phase detector is functioning correctly (This step has been verified through software emulation).

Step II:

Adjusting the phase of the function generator to a critical point, and then determine the sampling edge. After that, adjusting the function generator phase between ± 2 ns, observing whether the output pseudorange jump or not. (On normal situation, pseudorange will produce a continuous change by the continual changing of clock phase, but should not result in jump). Here we verification the feasibility of this ambiguity method.

We select a measuring communication satellite uplink earth for the testing experiment. The initial phase is adjusted by function signal generator.

Case I: Phase monitoring value varies between 2 and 3; 1PPS signal edge value is set to rising edge. The results are shown in Table 61.1.

Case II: Phase monitoring values vary between 2 and 3; 1PPS signal edge value is set to falling edge. The results are shown in Table 61.2 (Jumping of Phase Ambiguity Occurred).

Table 61.1 Testing results on case I

DSP reset times	Phase monitor value	Pseudorange/m
0	3	−1100.616686
1	3	−1100.642458
2	3	−1100.616936
3	3	−1100.615113
4	2	−1100.619390
5	2	−1100.624828
6	2	−1100.612223
7	2	−1100.653630

Table 61.2 Testing results on case II (jumping of phase ambiguity occurred)

DSP reset times	Phase monitor value	Pseudorange/m
0	2	−1100.653630
1	2	−1100.624223
2	2	−1100.625056
3	2	*−1100.414395*
4	3	*−1111.890725*
5	3	−1111.773983
6	3	−1111.910657
7	3	−1111.749460

Analysis: The phase monitor value in test varies between 2 and 3, 1PPS signal's rising edge has aligned to and the system clock's falling edge.

On the first test experiment, 1PPS signal's sampling edge value is set to rising edge. When the phase monitoring values varied between 3 to 2, reset DSP (equivalent terminal re-timing), the pseudorange has not occurred jumping.

On the second test experiment, 1PPS signal's sampling edge value is set to falling edge, when the phase monitoring values varied between 2 to 3, reset DSP, the pseudorange has occurred jumping and the jump distance is integral numbers the clock system(88.45 MHz)'s cycles (see the italicised values in Table 61.2).

This result proves that: setting rising edge sample can solve phase ambiguity when monitor value between 2 and 3.

Case III is that phase monitor value varies between 0 and 1. The 1PPS signal's sampling edge value is set to rising edge. The testing results are as follows in Table 61.3.

Case IV is that phase monitor value varies between 0 and 1. The 1PPS signal's sampling edge value is set to falling edge. The testing results are as follows in Table 61.4.

Analysis: Monitoring value of the test phase changes between 1 and 0. In this case 1PPS signal's rising edge is aligned with the system clock's rising edge.

On the third test experiment, 1PPS signal's sampling edge value is set rising edge, when the phase monitoring values varied between 0 to 1, reset DSP, the pseudorange has occurred jumping and the jump distance is integral numbers the clock system(88.45 MHz)'s cycles (see the italicised values in Table 61.3).

Table 61.3 Testing results on case III (jumping of phase ambiguity occurred)

DSP reset times	Phase monitor value	Pseudorange/m
0	0	−1100.614998
1	0	−1100.611793
2	0	−1100.622224
3	0	*−1100.615765*
4	1	*−1111.934466*
5	1	−1111.914240
6	1	−1111.925013
7	1	−1111.908700

Table 61.4 Testing results on case IV

DSP reset times	Phase monitor value	Pseudorange/m
0	1	−1111.917356
1	1	−1111.930251
2	1	−1111.914522
3	1	−1111.926337
4	0	−1111.912413
5	0	−1111.923362
6	0	−1111.928137
7	0	−1111.914197

On the fourth test experiment, 1PPS signal's sampling edge value is set to falling edge. When the phase monitoring values varied between 0 to 1, reset DSP, the pseudorange has not occurred jumping.

This result proves that: setting falling edge sample can solve phase ambiguity when monitor value between 0 and 1.

61.5 Conclusions

These results demonstrate the correctness of the device for time reference (1PPS) and the system clock phase monitoring, and demonstrate the validity of the device for solving the phase ambiguity of system clock and time reference. For measurement and communication system, just by input correct settings through external signal, the phase ambiguity problems of system clock and time reference can be solved.

References

1. Wu Y (2011) Research and application of time measurement of satellite navigation system. National University of Defense Technology

2. Chen L, Li C et al (2012) Accuracy analysis of BOC signal dual sideband algorithm on non-ideal channel, satellite navigation conference (CSNC) 2012 proceedings, lecture notes in electrical engineering, vol 161, pp 415–427
3. Rabaey JM et al Digital integrated circuits-a design perspective, 2nd edn. Publishing House of Electronics Industry, pp 237–239

Chapter 62
Wavelet Packet Transformation Based Technique in Mitigation DME Pulsed Interference for GNSS

Liuli Li, Wenyi Wang, Dan Lu, Lu Wang and Renbiao Wu

Abstract The Galileo E5 and GPS L5 signals are important components of GNSS, however, the Galileo E5 and GPS L5 signals lie within the Aeronautical Radio Navigation Service (ARNS) band, where Distance Measuring Equipment (DME) works in, and strong pulsed interference originating from DME stations can degrade the performance of GNSS receivers. At high altitude, the worse DME interference environment is. Because the similarity between wavelet and DME pulse is higher than that of the GNSS signals, it is easier to detect and remove interference in wavelet packet domain. Although the wavelet packet transformation (WPT) based DME pulse mitigation had been proposed, but the parameters about WPT are not discussed systematically which pay important role in mitigation performance. This paper mainly discusses the parameters selection about WPT including wavelet, composition level, threshold rules and thresholding function. Mitigation Performance are assessed with respect to threshold rules and threholding function by numerical experiments.

Keywords GNSS · DME · Wavelet packet transformation · Pulsed interference mitigation

62.1 Introduction

Global Navigation Satellite System (GNSS) is a satellite system consists of global, regional and augmentation systems, it uses United States GPS, Russian GLONASS, European Union's Galileo, Compass of China, WASS (Wide Area Augmentation System), EGNOS (European Geostationary Navigation Overlay Service), MSAS (Multi-Functional Satellite Augment System) and other systems

L. Li (✉) · W. Wang · D. Lu · L. Wang · R. Wu
Tianjin Key Lab for Advanced Signal Processing, Civil Aviation University of China, Tianjin, China
e-mail: llli_hope@163.com

J. Sun et al. (eds.), *China Satellite Navigation Conference (CSNC) 2014 Proceedings: Volume I*, Lecture Notes in Electrical Engineering 303,
DOI: 10.1007/978-3-642-54737-9_62,

to allow receivers to determine their location to high precision, and providing Integrity Checking and navigation security alarms information.

The Galileo E5 signal and the GPS L5 signal are important components of the future GNSS, they are primarily serving the civil navigation, occupying a dedicated frequency band [1]. These signals lie within the ARNS band, they suffer interference from the services in this band, in particular, strong power pulsed signals from DME systems, which operate in the frequency span between 960 and 1,215 MHz. These pulsed interference degrades the SNR (signal-to-noise ratio) potentially causes the tracking loops of receivers to fail to converge [2]. At higher altitude, the more line-of-sight DME pulsed signals are received, the worse DME interference environment is [1].

A variety of approaches to DME pulsed interference mitigation have been proposed, among these, the time domain pulse blanking is the most common method [2]. The time domain pulse blanker removes the signal samples when the amplitude of the received signal sample exceeds the threshold indicating the presence of pulsed interference, so as the useful signal is removed. Because the similarity between wavelet and DME pulse is higher than that of the GNSS signals, in recent years, some researchers propose WPT based pulsed interference mitigation algorithm [3–5], which processing mitigation in wavelet coefficients domain through a pre-designed threshold. But they don't have a systematic analysis about parameters selection corresponding WPT, and these will pay important role in DME interference mitigation performance. This paper discusses parameters selections of WPT including wavelet, composition level, threshold rules and thresholding function. Mitigation Performance are assessed with respect to threshold rules and threholding function by numerical experiments.

62.2 Mathematical Model

The X-mode DME ground system transmits Gaussian-shaped pairs with a 3.5 μs half-amplitude pulse width and an inter-pulse interval of 12 μs. A pulse pair has the following expression [3],

$$s_{pulse\ pair}(t) = \mathrm{e}^{-\frac{\alpha}{2}t^2} + \mathrm{e}^{-\frac{\alpha}{2}(t-\Delta t)^2} \tag{62.1}$$

where $\alpha = 4.5 \times 10^{11}\ \mathrm{s}^{-2}$, $\Delta t = 12\ \mu\mathrm{s}$. Each pulse pair is modulated by a carrier has the following expression, which is illustrated in Fig. 62.1,

$$s_{DME}(t) = P \times \sum_{k=1}^{N} \left(\mathrm{e}^{\frac{-\alpha(t-t_k)^2}{2}} + \mathrm{e}^{\frac{-\alpha(t-\Delta t-t_k)^2}{2}}\right) \times \cos(2\pi f_I + \theta_I) \tag{62.2}$$

where P is the DME peak power at the receiver antenna level; $\{t_k\}$ is the set of pulse pair arrival times; f_I is the frequency of the received DME signal; θ_I is the

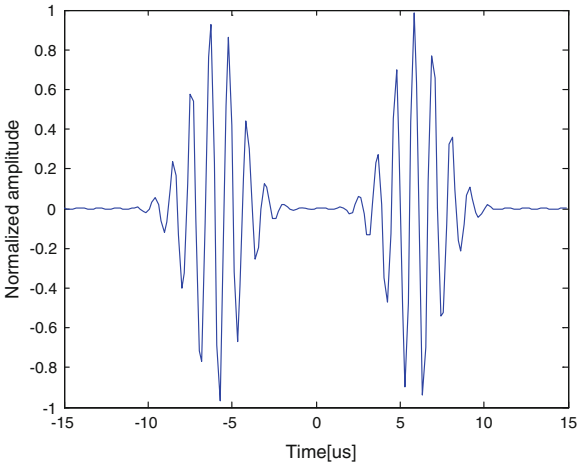

Fig. 62.1 Normalized DME modulated pulse pair

DME signal carrier phase at the antenna of the receiver; N is the total number of pulse pairs.

The received GNSS signal including interference from M DME stations can be expressed as following,

$$s_R(t) = s_{GNSS}(t) + \sum_{i=1}^{M} s_{DME_i}(t) + n(t) \tag{62.3}$$

where $s_{GNSS}(t)$ is useful GNSS signal; $s_{DME_i}(t)$ is modulated DME singles from one DME station; $n(t)$ is addictive white noise. The GNSS signals are buried under the noise level.

62.3 WPT Based DME Interference Mitigation

WPT is a time-frequency analytical tool for signal, which is an improvement to wavelet transformation (WT). Comparing with WT, WPT decomposes the high pass filter output which the WT doesn't, thus is used to get the advantage of better frequency resolution representation. The multi-resolution property of WPT which enables wavelets to extract information at different scales, making them a powerful tool for representing local characteristic of the signal, such as edge, spikes, breakpoints and so on. A depth-3 WPT tree of $s_R(t)$ is shown in the Fig. 62.2, where A represents high frequency, D represents low frequency, the index is the decomposition level.

The substance of WPT is a criterion function that measures the degree of similarity between wavelets basis and signals, the higher similarity, the bigger wavelet packet coefficient is. The coefficients which represent the DME interference signal

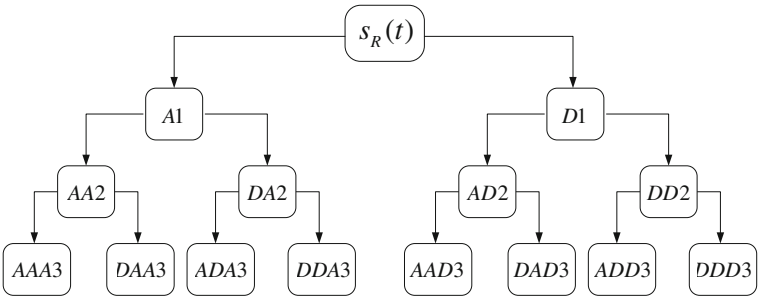

Fig. 62.2 Wavelet packet decomposition tree

are bigger than that represent the GNSS signal. Setting the coefficients that are above the pre-defined threshold to zero or shrinking it, while those below the threshold are preserved to extract the interference. WPT based DME interference mitigation includes three steps as following:

1. Wavelet Packet Transformation
The GNSS signal including DME interference is translated to the wavelet packet domain by selecting a proper wavelet and decomposition level L.
2. Threshold Selection and Processing
Rescale the wavelet packet coefficients in level L according to different threshold rules.
3. Inverse Wavelet Packet Transformation
The inverse wavelet packet transformation is performed by the modified coefficients to get output signal.

As can be seen from the above three steps, three parameters pay an important role in mitigation performance: the wavelet, the decomposition level and threshold.

62.3.1 Selection of Wavelet

In accordance with the definition of wavelet transform, the coefficient of wavelet decomposition will be more localized if the mother function is more similar to the analyzed signal. To perform Multi-Resolution Analysis, the compactness and the orthogonality of the wavelet is required. Transient and non-periodic signals are best extracted with an asymmetrical wavelet basis function, which provides a better match to the shape of the DME pulse than a symmetrical waveform. Daubechies, Symlet and Coiflet wavelets meet the three properties above. Db5 wavelet is recommended in DME pulsed mitigation [2], so the wavelet type used in this paper is db5.

62.3.2 Decomposition Level Selection

Since WPT is achieved through uniform bank filters where the frequency-response at each level is obtained through dyadic frequency-scaling operation of the previous level, the ideal wavelet packet frequency resolution BW_L is linked to the wavelet decomposition level L as [6]:

$$BW_L = \frac{f_s/2}{2^L} \tag{62.4}$$

where f_s is the sampling frequency. The number of decomposition level is up to the point where the wavelet packet frequency resolution is comparable with the interference bandwidth.

The maximum level depends on the two main operations in the procedure of wavelet packet decomposition: convolving with filter and down-sampling, which is determined as [7]:

$$L_M = R_0 \log_2[l_s/(l_w - 1)] \tag{62.5}$$

where the l_s and l_w are the length of original signal and filter respectively; R_0 is the round towards zero function. The proper decomposition level is determined by the consideration between wavelet packet frequency resolution and maximum level. In our case, sampling frequency is 5.714 MHz; 99 % of the DME pulsed interference energy falls within 800 kHz, the length of the interference detection window is 134 points. The length of filter corresponding db5 is 10. So 3 is selected as decomposition level in this paper.

62.3.3 Threshold Selection

Wavelet packet transformation has been used as a denoising technique in signal processing, and mainly there are two types of thresholding function: hard threshold and soft threshold [8]. In general, decomposed wavelet packet coefficients correspond to useful signal is bigger than that associated with noise, and setting the smaller coefficients can get the denoised signal. However, in our case, useful GNSS signal is under noise level while DME pulsed interference is of strong power. It is necessary to modify the classical thresholding function, meaning that the smaller wavelet packet coefficients are preserved while the bigger ones are zeroed or shrinking. The modified hard threshold function is:

$$\hat{w}_{j,k} = \begin{cases} 0 & |w_{j,k}| > \lambda \\ w_{j,k} & |w_{j,k}| \le \lambda \end{cases} \tag{62.6}$$

Table 62.1 Description of threshold selection rules

Rule name	Description
Rigrsure	Selection using the principle of Stein's unbiased risk estimate (SURE)
Sqtwolog	Fixed form threshold equal to the square root of two times the logarithm of the length of the signal
Heursure	Selection using a mixture of the first two options mentioned
Minimaxi	Threshold selection using the minimax principle

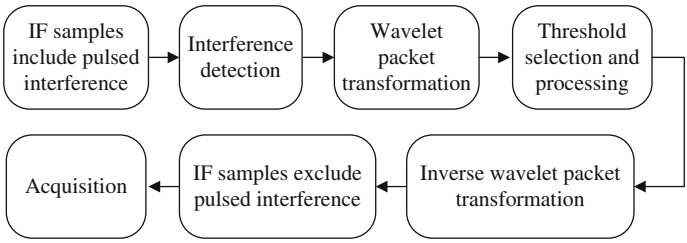

Fig. 62.3 Block diagram of WPT based mitigation technique

where λ is threshold and $w_{j,k}$ is the kth wavelet packet coefficient in level j, the $\hat{w}_{j,k}$ is the wavelet packet coefficient after thresholding.

The modified soft threshold function is:

$$\hat{w}_{j,k} = \begin{cases} \operatorname{sgn}(w_{j,k})\lambda & |w_{j,k}| > \lambda \\ w_{j,k} & |w_{j,k}| \leq \lambda \end{cases} \tag{62.7}$$

where $\operatorname{sgn}(\cdot)$ is the sign function.

MATLAB wavelet toolbox provides four threshold selection rules including: Stein's Unbiased Risk Estimate (SURE), fixed form threshold (Sqtwolog), Heuristic SURE and minimax principle [8]; and are listed in Table 62.1.

62.3.4 Interference Mitigation Scheme Design

Figure 62.3 shows the schematic of WPT based DME interference mitigation. Firstly, the incoming IF (Intermediate-Frequency) signal samples are passed through a moving window. The next step is time domain DME pulse detection. Once the DME signal is detected, it will be transformed into wavelet packet domain. Secondly, make threshold treatment with coefficients and get thresholded wavelet coefficients. The thresholded wavelet coefficients are then used to perform IWPT to obtain output signal excluding interference to replace detected interference samples.

Table 62.2 Acquisition performance comparison among different mitigation techniques for different JNR

JNR (dB) Method	10	15	20	25
Rigrsure(H)	7.7786	8.0282	7.9701	7.8162
Rigrsure(S)	8.1335	8.2714	8.1473	7.782
Sqtwolog(H)	7.0262	7.3615	7.3306	7.3498
Sqtwolog(S)	5.8339	5.2844	4.5515	4.1312
Heursure(H)	7.9033	7.6789	8.285	7.9301
Heursure(S)	7.6699	7.6552	8.0991	7.7493
Minimaxi(H)	7.6221	7.6474	7.9232	7.9849
Minimaxi(S)	7.3582	6.9587	6.2802	6.1579
TB	5.8801	6.4961	6.3274	6.8527
Original	4.925	2.5051	1.0808	1.0462

If no interference is detected, the sample is preserved. Finally, the output signal enters the acquisition block to estimate its mitigation performance.

62.4 Results and Discussion

In the MATLAB environment, we use correlation peak to next peak ratio (CPPR) [2] as acquisition merit to compare DME interference mitigation performance by different threshold rules and thresholding functions. The higher value of CPPR, the better performance of the acquisition is.

In the experiments, the satellite data from one satellite PRN1 (PRN: Pseudo Random Noise code) are interfered by one DME station, and are down-converted at the intermediate frequency of 4.309 MHz. The inter-frequency of the received DME signal is 4 MHz, and the pulse pair repetition rate of the DME station is 10,000 pulse pairs per second. Take 10 ms of data enters to acquisition block.

Defining the DME pulses peak power to noise ratio as JNR (Jammer-to-Noise Ratio); we compare WPT based mitigation by different threshold rules and time domain blanking with different JNR. The CPPR results are shown in Table 62.2, and each CPPR value is the mean CPPR value after 10 acquisition trails for each method. As shown in Table 62.2, H indicates hard thresholding and S indicates soft threholding; TB represents time domain blanking and Original represents original data without interference mitigation.

The successful acquisition is defined as CPPR greater than 2 in the receiver, otherwise unsuccessful. As shown in Table 62.2, the CPPR is smaller than 2 when JNR is 20 or 25 dB, meaning that the original data fail in acquisition. After apply different types mitigation methods listed in Table 62.2, the receiver can capture

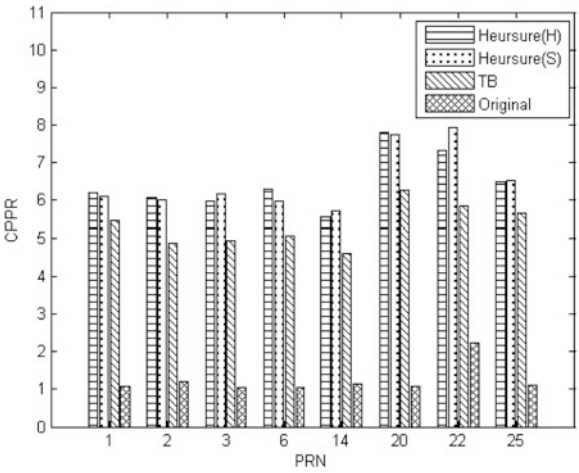

Fig. 62.4 CPPR of eight PRNs for different mitigation methods (JNR = 20 dB)

satellite successfully with different JNR. Under the condition of 3 stage WPT using db5 wavelet, the Rigrsure(H), Rigrsure(S), Sqtwolog(S), Heursure(H), Heursure(S), Minimax(H), Minimax(S) methods are perform better than time domain blanking expect Sqtwolog(S) method.

Considering another experiment, when JNR is 20 dB, 10 s of satellite date from eight satellites (PRN1, PRN2, PRN3, PRN6, PRN14, PRN20, PRN22, PRN25) is added to acquisition and tracking. CNR (Carrier to Noise Ratio) is used as the figure of merits based on the receiver tracking results, the higher CNR gain, the better performance of the tracking is. Compare with WPT based mitigation by threshold rules of Heursure using hard and soft thresholding respectively, time domain banking and original data. The acquisition results is shown in Fig. 62.4, and the tracking results in shown in Fig. 62.5, where each value is the mean value after 10 acquisition and tracking trails for each method. When the receiver fails in acquisition, the CNR is assumed to be zero.

As can been seen in Figs. 62.4 and 62.5, the original signal without mitigation can only capture one satellite but fail to capture seven satellites. After applying mitigation method, all the eight satellites can be capture and tracked successfully. Among the methods, Heursure rule based WPT performs better than time domain blanking in acquisition and tracking results.

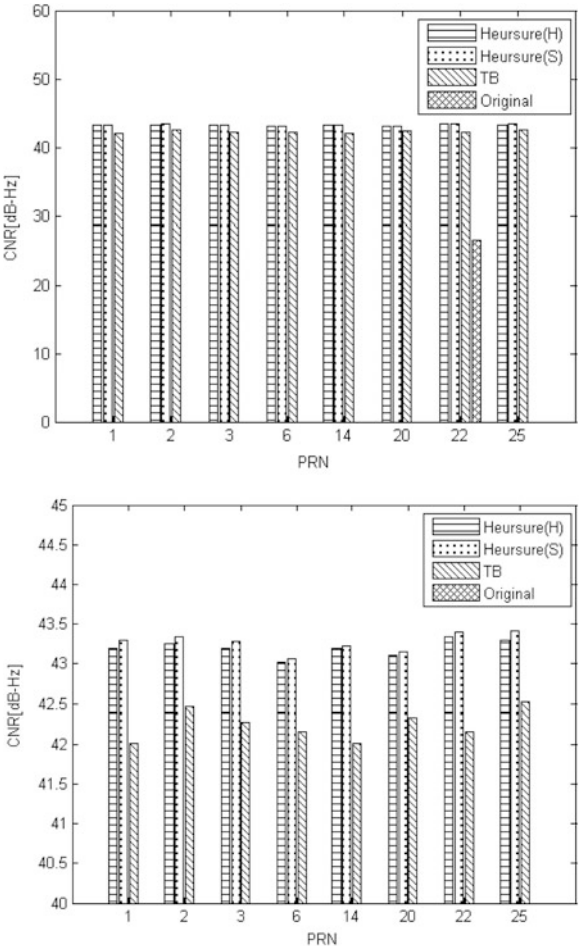

Fig. 62.5 CNR of eight PRNs for different mitigation methods (JNR = 20 dB) (*top*), zoom (*bottom*)

62.5 Conclusion

We describe wavelet packet transformation based DME pulse interference mitigation as well as discuss parameters including the selection of wavelet, decomposition level selection, threshold rules and thresholding. The acquisition and tracking results are used to evaluate interference mitigation performance. The numerical experiments show that wavelet packet transformation of db5 waveform and decomposition level 3 behaves better than time domain blanking. Among different threshold rules, Rigrsure, Heursure and Minimaxi give better results.

Acknowledgment The work of this paper is supported by the Project of the National Natural Science Foundation of China (Grant No. 61179064, 61172112 and 61271404), Fundamental Research Funds for the Central Universities (Grant No. ZXH2009A003, ZXH2012M006 and 3122013D020) and the Tianjin Science and Technology Fund (Grant No. 10ZCKFGX04000).

References

1. Denks H, Hornbostel A, Chopard V et al (2009) GNSS receiver testing by hardware simulation in an standardized pulsed and CW interference environment. In: Proceedings of ENC GNSS, Naples
2. Gao GX, Heng L, Hornbostel A et al (2013) DME/TACAN interference mitigation for GNSS: algorithms and flight test results. GPS Solutions 17(4):561–573
3. Anyaegbu E, Brodin G, Cooper J et al (2008) An integrated pulsed interference mitigation for GNSS receivers. J Navig 61(2):239–256
4. Paonni M, Jang JG, Eissfeller B et al (2010) Innovative interference mitigation approaches: analytical analysis, implementation and validation. In: Satellite navigation technologies and European workshop on GNSS signals and signal processing (NAVITEC), 2010 5th ESA workshop on IEEE, pp 1–8
5. Musumeci L, Samson J, Dovis F (2012) Experimental assessment of distance measuring equipment and tactical air navigation interference on GPS L5 and Galileo E5a frequency bands. In: Satellite navigation technologies and European workshop on GNSS signals and signal processing (NAVITEC), 2012 6th ESA workshop on IEEE, pp 1–8
6. Musumeci L, Dovis F (2013) Performance assessment of wavelet based techniques in mitigating narrow-band interference. In: Localization and GNSS (ICL-GNSS), 2013 international conference on IEEE, pp 1–6
7. Yang L, Judd MD, Bennoch CJ (2004) Denoising UHF signal for PD detection in transformers based on wavelet technique. In: Electrical insulation and dielectric phenomena, 2004. CEIDP'04. 2004 annual report conference on IEEE, pp 166–169
8. Abdel Fattah AS, Elramly S, Ibrahim M et al (2011) Denoising algorithm for noisy chaotic signal by using wavelet transform: comprehensive study. In: Internet technology and secured transactions (ICITST), 2011 international conference for IEEE, pp 79–85

Chapter 63
A GNSS Space-Time Anti-jamming Algorithm Based on Convex Optimization

Shunxiao Wu, Yangbo Huang, Feng Tian and Gang Ou

Abstract Traditional space-time adaptive processing algorithm can not well balance the demands between canceling jams and beam-forming. Aimed at this problem, A new algorithm based on convex optimization and multiple objectives programming is proposed for the designing of space-time filter. Two object functions are defined, and are combined via an object weight coefficient to form a single optimization goal. The relationship between the object weight coefficient and the optimization results is analyzed, and then proposed the criterion for judge the rationality of the object weight coefficient. The method for finding the optimal object weight coefficient is then developed. Results of computer simulation show that: the new method can form wide band main beam for useful signal direction under both strong and weak jams with a more low inserting loss compared with PI method; it overcomes the shortcomings of MSINR method that pass band of equivalent filter for useful signal direction will get narrower when the taps increase; especially when the signal and narrow-band jams come from the same direction the new method can still perform well.

Keywords STAP · Beam-forming · Convex optimization · MOP

63.1 Introduction

As the satellite navigation signal is vulnerable to interference, the demand for high anti-jamming performance is more urgent under the background of military application. So far, adaptive array based on joint space-time processing technology

S. Wu · Y. Huang · F. Tian · G. Ou (✉)
Satellite Navigation and Positioning R&D Center, School of Electronic Science and Engineering, National University of Defense Technology, Changsha 410073, China
e-mail: ougang_nnc@163.com

J. Sun et al. (eds.), *China Satellite Navigation Conference (CSNC) 2014 Proceedings: Volume I*, Lecture Notes in Electrical Engineering 303,
DOI: 10.1007/978-3-642-54737-9_63,

is mainly used for improving anti interference capacity of the satellite navigation system (GNSS) receivers. Joint space-time processing is an advanced signal processing technique, and it is widely used in the field of radar [1] and communication [2]. In 2000, R. L. Fante proposed to apply this technology to the GPS receiver's anti-jamming [3] for the first time, and achieved good results. Joint space-time processing is essentially designing the weighting coefficients of each space-time filter tap in the antenna array back-end based on certain optimization criterion. The usual anti-jamming criterions are power inversion (PI) criterion, maximum signal-to-noise ratio (MSINR) criterion and linear constrained minimum variance (LCMV) criterion. PI criterion is to minimize the space-time filter output signal's power under the constraint that the filter coefficients are not all zero. Without using direction information of GNSS satellites, PI method has an uncontrollable influence on the useful signal, so it can not achieve high anti-jamming performance, although it is relatively simple to implement. MSINR criterion is to maximize the Signal-to-Interference-plus-Noise Ratio (SINR) at the space-time filter output; it can put the main beam toward the useful signal while at the same time form nulls in the direction of strong interference. However, as literature [4] points out, under narrowband assumption and MSINR criteria the equivalent frequency response at the signal direction gradually becomes narrow and centered on signal carrier frequency when the number of time domain taps increase, so for the wideband GNSS signal the loss of array processing becomes large. LCMV criterion is to minimize the space-time filter output signal's power under some linear constraint, so PI and MSINR can be seen as special case of LCMV. Performance of LCMV is determined by specific adopted constraints, literature [5] proposes a special method to establish constraints for cancelling broadband interference which at first use space-time two-dimensional power spectrum to estimate the arrival direction of interferences, then put null response at those directions. This method can deeply depress interference signals; however, peaks of space-time power spectrum is find through direct searching, so large amount of calculation is needed, the method can not be universally used.

Boyd SP et al. [6] apply convex optimization algorithm to the design of antenna array beam pattern, namely finding the space-time filter weights which make the array response in each direction and each frequency approximate desired response as far as possible. Yan S. [7] point out that the space-time filter weights optimization design is a special class of convex optimization problems—second-order cone optimization problem which has effective solving algorithm, and get an uniform form to model and solve these problems which also supports interference cancellation on the basis of Boyd. The high effective algorithms for solving convex optimization problems brings great flexibility to space-time filters design, so the shortcoming of traditional PI and MSINR method can be well overcame. But in the open literature there is no method that can well balance the two demands of depressing interference and optimizing array response in the useful signal's arrival direction. The usual approach is to set one constraint for a target and then optimize another goal, it is difficult to determine parameters used in the constraints, so is the disadvantage of such method.

In this paper the idea of multiple objective optimizations is adopted to achieve the two goals of depressing interference and reducing useful signal loss simultaneously. The first object functions indicating the interference cancellation effect is proposed, and the second object function is to indicate the frequency response deviation between the actual and desired one at the useful signal arrival direction. The desired frequency response is designed to satisfy two goals, one is to minimize the Carrier power to noise density ratio (CNR) loss at the receiver's dispreading output point, and the other is to get good phase center consistency of the whole array. By introducing a weighting factor the two object functions is combined to a whole object function, and the optimization of the whole object function can be solved fast by convex optimization techniques if a weighting factor is given in premise. On this basis a novel criterion used for judging if the two optimization goals are sufficiently optimized for a given weighting factor is proposed, and then by using the criterion an optimal weighting factor can be searched out. The space-time filter weighting coefficients corresponds to the optimal weighted factor can guarantee deep null strap in the arrival direction of interference and forming a broadband main beam toward the useful signal, so the new methods effectively overcomes the defects of conventional PI and MSINR method.

63.2 Structure of Space-Time Filter and Its Convex Optimization Form

The common processing structure of space-time filter for a GNSS receiver with an anti-jamming antenna array is shown in Fig. 63.1, M is the num of antenna array elements, each array element is followed by N time domain taps, the tap interval is T, and ω_L is the down converting frequency. Let $\{w_{mn}\}$, $n = 1, 2, \ldots, N$, $m = 1, 2, \ldots, M$ to be the weighting coefficients of the time-space filter, usually expressed in a $MNX1$ dimension vector form: $W = [w_{11}, w_{12}, \ldots, w_{1N}, w_{21}, \ldots, w_{22}, \ldots, w_{M1}, \ldots, w_{MN}]$. T is required less than 1/B, B is bandwidth of the front end, and the total delay time of each array element is $(N-1)T$ which is required to cover different multi-path delays [5].

Traditional methods analyze space-time filter using narrowband assumption, while literature [8] points out that for the broadband GNSS signal the narrowband assumption can introduce obvious biases and proposed a more precision broadband model. Under the broadband model, the array response to a single frequency signal can be expressed as follows:

$$H(\omega, \phi_k, \theta_k) = W^H[v^t(\omega) \otimes v^s(\omega + \omega_L, \phi_k, \theta_k)] \tag{63.1}$$

In Eq. (63.1): the signal's direction of arrival (DOA) is donated as (ϕ_k, θ_k); $v^s(\omega + \omega_L, \phi_k, \theta_k) = \left[e^{-j(\omega+\omega_L)\tau_1}, \ldots, e^{-j(\omega+\omega_L)\tau_N}\right]^T$ is the space domain steering vector, $\tau_1, \ldots, \tau_N$ is the signal delay time difference at each array element;

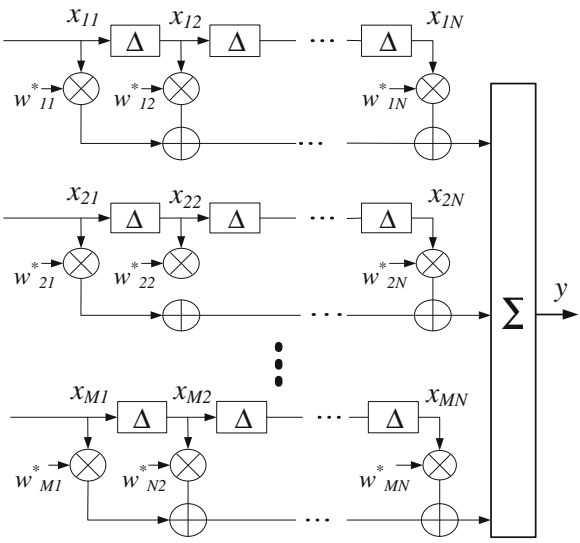

Fig. 63.1 Space-time filtering structure

$v^t(\omega) = \left[1, \ldots, e^{-j\omega(M-1)T}\right]^T$ is the time domain steering vector; $\otimes$ is Kronecker product. The product $a(\omega, \phi_k, \theta_k) = v^t(\omega) \otimes v^s(\omega + \omega_L, \phi_k, \theta_k)$ is defined as space-time joint steering vector. Let R_{xx} ($MN \times MN$ dimension) to be the covariance matrix of data at each taps, then output signal power of the space-time filter is $P_{out} = W^H R_{xx} W$. As the GNSS signal's power is far lower than the power of noise and jams, so minimizing P_{out} can realize interference cancellation.

Convex optimization problem is a very wide class of optimization problems, it only requires that the optimization object function is convex and the range of optimizing variable is a convex set. Although solution of convex optimization problem can not be always directly expressed as simple formula, there are efficient algorithms to find it, such as interior point methods [9]. In engineering practice, Matlab toolbox CVX is usually used to solve convex optimization problems [10]. Therefore, if convex optimization technique is used in space-time filter design, the key lies in forming the design problem in the convex optimization form. Under the broadband assumption, a uniformly convex optimization form for the antenna array space-time processing design is proposed in literature [7], its main results can be compactly expressed as the following object function and constraints:

$$\begin{aligned} & \min \mu_p, \quad p \in \{1,2,3,4\} \\ s.t. & \left\| \gamma(F_{PB}, \Theta_{ML} \right\|_{q1} \leqslant \mu_1 \\ & \left\| p(F_{PB}, \Theta_{SL}) \right\|_{q2} \leqslant \mu_2 \\ & W^H R_{xx} W \leqslant \mu_3 \\ & \|W\| \leqslant \mu_4 \\ & W^H a(f_0, \theta_s) = 1 \end{aligned} \tag{63.2}$$

In Eq. (63.2): the upper limit of difference between actual response and expected response within the main beam of the array is μ_1, and μ_2 is the upper limit of difference between actual response and expected response (usually take value 0) within the side lobes of the array, this two constraints is realized by sampling in frequency and DOA and then measured with 2 or ∞ norm. The upper limit of signal output power is μ_3, and μ_4 is upper limit of amplitude of the weight vector which is used to ensure robustness of the results. The last equality constraint is used to ensure that for useful signal the array response equals to 1. As the design goal in this paper is anti-jamming, μ_3 should be the object function. Therefore, other parameters for constraints should be assigned manually, so it's difficult to ensure achieve the optimal results.

63.3 Multi-objective Optimization of Interference Suppression and Beam Forming

63.3.1 Multi Object Optimization Function

For simplification of analysis, assume that antenna array elements are identical; the desired signal is only one satellite signal, and its DOA is (ϕ_0, θ_0). For the optimization goal of depressing interference the space-time filter output signal's power can be use as object function, so the first object function is $P_1(W) = W^H R_{xx} W$. At the DOA of signal each frequency will get a unique array response, thus forming an equivalent filter $H(\omega, \phi_0, \theta_0)$ for the useful signal, characteristics of the filter determines impact of the array on carrier to noise ratio, ranging accuracy, etc. of the spread spectrum GNSS signal. Firstly a desired filter $H_d(\omega, \phi_0, \theta_0)$ is constructed based on an ideal weight coefficient case which minimizes the signal's carrier to noise ratio loss and equivalent phase center consistency of the array, then use the deviation between the actual array response and the desired filter response as the second object function $P_2(W)$ corresponding to the optimization goal of minimizing CNR loss. Several kind of norm can be used to measure the degree of approximation of two filters. In this paper the 2-norm is chosen based on the consideration that when a narrow-band jamming come in the same or near DOA with the useful signal, $H(\omega, \phi_0, \theta_0)$ should have very low amplitude at some frequency points, therefore $P_2(W)$ can be expressed as follow:

$$P_2(W) = \frac{1}{F_s} \int_{-0.5F_s}^{0.5F_s} |H(\omega, \phi_0, \theta_0) - H_d(\omega, \phi_0, \theta_0)|^2 dw \tag{63.3}$$

In order to facilitate numerical calculation, taking samples in frequency, thus integration is converted to summation, namely:

$$P_2(W) = \frac{1}{K}\sum_{i=0}^{i=K-1} |H(\omega_i, \phi_0, \theta_0) - H_d(\omega_i, \phi_0, \theta_0)|^2 \tag{63.4}$$

In Eq. (63.4): ω_i, $i = 0, 1, \ldots, K-1$ are the uniformly spaced sampling points in the pass band, generally sampling point $K \approx 15\ N$ [11].

In order to ensure minimum distortion of signal, the desired filter should have the constant amplitude response of 1, and at the same time its group delay should be independent of signal's DOA. Choose an array element as the reference element, for this reference element set only one tap's coefficient to 1 other coefficient to 0, and for other elements set all coefficient to 0, in such configuration a good desired filter is obtained with its group delay has nothing to do with signal DOA. So the response of desired filter can be expressed as follow:

$$H_d(\omega, \phi_0, \theta_0) = e^{-jLTw} \tag{63.5}$$

In Eq. (63.5): L is the group delay, usually take the value of [N/2].

In order to take both consideration of interference depression and reduce of signal CNR, by introducing a positive weighting factor λ, functions corresponding to two optimization goals is combined to a total object function:

$$P(W, \lambda) = P_1(W) + \lambda P_2(W) = W^H R_{xx} W + \lambda P_2(W), \quad \lambda > 0 \tag{63.6}$$

Combining with (63.4) and (63.5), the total object function is as follow:

$$P(W, \lambda) = W^H R_{xx} W + \frac{\lambda}{K}\sum_{i=0}^{i=K-1} \left|W^H a(\omega_i, \phi_0, \theta_0) - e^{-jLT\omega_i}\right|^2 \tag{63.7}$$

Unlike ordinary weighting, weighting factor λ is a parameter need to be determined by some judging criterion and searching method.

63.3.2 Optimization of Weighting Factor

For a given λ, solving the following unconstrained optimization problem will get a weighting vector $W_{opt}(\lambda)$ for the space-time filter.

$$\min_W \quad P(W, \lambda) \tag{63.8}$$

It is easy to judge that Eq. (63.8) is a convex optimization problem, and can efficiently be solved. As $P(W, \lambda)$ reflects the two optimization goals, so the solution $W_{opt}(\lambda)$ embodies the two demands in different extend, but how to determine the value of λ is still a question. Therefore the rationality of λ need to be analyzed, and the optimal weighting factor λ_{opt} can thus be defined, and then $W_{opt}(\lambda_{opt})$ is the global optimal weighting vector.

When $\lambda \to 0$, the object function tends to $P_1(W)$, the solution $W_{opt}(\lambda) \to 0$, apparently, signal and interference are suppressed at the same time; when $\lambda \to +\infty$, the object function tends to $P_2(W)$, meanwhile the interference suppression goal is ignored. The two extreme cases are unreasonable. When value of λ traversing from 0 to $+\infty$, $P_1(W_{opt}(\lambda))$ and $P_2(W_{opt}(\lambda))$ can be viewed as two functions with variable of λ, and this two function can be shown as non reduce and non increasing functions respectively. Here is the proof process:

For the optimization problem (63.8), assume that solving values by traversing from 0 to $+\infty$ for λ, you can get two functions $P_1(W_{opt}(\lambda))$ and $P_2(W_{opt}(\lambda))$, it can be shown that the two functions are non reduced and non increasing functions respectively. Here is the proof process: take two weighting factors $0 < \lambda_1 < \lambda_2 < +\infty$, according to its definition the following two formulas can be obtained:

$$P_1(W_{opt}(\lambda_2)) + \lambda_1 P_2(W_{opt}(\lambda_2)) \geq P_1(W_{opt}(\lambda_1)) + \lambda_1 P_2(W_{opt}(\lambda_1))$$

and

$$P_1(W_{opt}(\lambda_1)) + \lambda_2 P_2(W_{opt}(\lambda_1)) \geq P_1(W_{opt}(\lambda_2)) + \lambda_2 P_2(W_{opt}(\lambda_2)).$$

According to the above two formulas:

$$\lambda_2(P_2(W_{opt}(\lambda_1)) - P_2(W_{opt}(\lambda_2))) \geq P_1(W_{opt}(\lambda_2)) - P_1(W_{opt}(\lambda_1))$$

and

$$P_1(W_{opt}(\lambda_2)) - P_1(W_{opt}(\lambda_1)) \geq \lambda_1(P_2(W_{opt}(\lambda_1)) - P_2(W_{opt}(\lambda_2))).$$

Because $\lambda_2 > \lambda_1$, thus $P_2(W_{opt}(\lambda_1)) \geq P_2(W_{opt}(\lambda_2))$ and $P_1(W_{opt}(\lambda_1)) \geq P_1(W_{opt}(\lambda_2))$, so the two function's reduction and not increasing properties are proved.

In anti-jamming applications, minimizing the first object function $P_1(W)$ should be a priority, therefore λ should choose as small as possible value under certain constraints, without the constraints the unreasonable situation $W_{opt}(\lambda) \to 0$ will appear. Taking MSINR method as reference, a reasonable constraint for λ is that there is one frequency sampling points where the actual array response approximates the desired filter's response. This constraint can not only prevent $\lambda \to 0$, but also give enough flexibility to depressing the narrow-band interference comes from the signal direction. Based on the above consideration, taking a positive number δ as the upper limit, a set for the feasible λ can be defined as follow:

$$S_\delta = \left\{ \lambda | \min_i |W_{opt}(\lambda)^H a(\omega_i, \phi_0, \theta_0) - e^{-jLT\omega_i}| \leq \delta \right\} \tag{63.9}$$

Therefore the optimal weighting factor is expressed as follow:

$$\lambda_{opt} = \inf S_{\delta}. \tag{63.10}$$

63.3.3 Searching the Global Optimal Weighting Vector

The solving process of the space-time filter's optimal weighting vector is also the calculation process of optimal weighting factor defined in formula (63.10). Before calculating formula (63.10), firstly the allowable deviation in formula (63.9) should be determined. The less the value of δ, the more stringent requirements of array response approximating desired filter is, general requirement is $\delta \leq 0.01$, meanwhile δ can not be infinitely close to 0, there should be a lower bound. When just minimize the second object function (corresponding to $\lambda \to +\infty$), the most approximation to desired filter can be got. So the solution of the following problem will produce weighting vector corresponding to $\lambda \to +\infty$, namely $W_{opt}(+\infty)$.

$$\min_{W} \quad P_2(W). \tag{63.11}$$

Apparently formula (63.11) is also a convex optimization problem. So the lower limit of can be defined as follow:

$$\delta_{\min} = \min_{i} |W_{opt}^{H}(+\infty)a(\omega_i, \phi_0, \theta_0) - e^{-jLT\omega_i}|. \tag{63.12}$$

The amount of computation and mathematics prove involved is difficult when solving the optimal weighting factor defined by formula (63.10), this paper uses the search method to find the approximate value $\bar{\lambda}_{opt}$. Considering that λ is a scale factor, and the larger λ is, the more easy to satisfy $\lambda \in S_{\delta}$, therefore searching is carried out by geometrically way. To sum up, the novel space-time filter design process for anti-jamming is as follows:

1. To solve the problem (63.11), and use formula (63.12) to obtain δ_{min};
2. To select allowable deviation $\delta(\delta_{min} < \delta \leq 0.01)$ and increasing rate $\alpha(\alpha > 1)$ of weighting factor, and initial weighting factor $\lambda_0 > 0$;
3. To solve the optimization problem (63.8), judge whether $\lambda_0 \in S_{\delta}$, if satisfied, stop the search, else transfer to step 4;
4. To solve the optimization problem (63.8), with increased $\lambda_k = \alpha\lambda_{k-1}$ and determine whether $\lambda_k \in S_{\delta}$, if satisfied, stopping searching, else continue step 4.

When searching is stopped, making $\bar{\lambda}_{opt} = \lambda_k$ and take the corresponding $W_{opt}(\bar{\lambda}_k)$ as the optimal weighting vector. In practical application, in order to reduce the search step, we can adjust the value of α and λ_0.

63.4 Performance Simulation

63.4.1 Performance Evaluation Method

To accurately assess anti-jamming performance, simulation experiments use equivalent array gain to measure space-time anti-jamming performance of the filter, the definition of equivalent array gain is as follow [11]:

$$G_e = \frac{CNR_e}{CNR_0}. \tag{63.13}$$

In Eq. (63.13): CNR_0 is the carrier to noise ratio got at despread spectrum point when a single element is used and no interference exist; CNR_e is the carrier to noise ratio got by a receiver after the space-time filter processing and with interference existing. As the sampled data at each element is generated by Matlab, so CNR_0 can be controlled, and CNR_e is estimated by a software receiver. In order to speed up the simulation speed, the generation of signal and noise, interference, and space-time filtering processing use Matlab, while the software receiver run on a dedicated hardware acceleration system of Cadence, namely PalladiumIII system. On PalladiumIII system, the HDL description of the receiver and its test bench is compiled and runs on many distributed processors parallel, thus the simulation rate is about 1/300 of the actual rate. So only 2–3 min of simulation time is consumed to complete the signal acquisition, tracking and carrier to noise estimation. The sensitivity of the receiver is 32 dB Hz.

63.4.2 Typical Examples and Performance Comparison

In the simulation: a 4 element phalanx array is used with the element space of $d = \frac{|k|}{2}$, $|k|$ is corresponding to the wavelength of the signal carrier frequency, the useful signal is the GPS L2P signal; data sampling rate is (62/3) MHz, using 1 ms data points to estimate the cross-correlation matrix R_{xx}; take 0.2 MHz as the interval, and take 101 uniformly distributed frequency sampling points in the signal bandwidth of 20 MHz as $\omega_i, i = 0, 1, \ldots, 100$.

Simulation experiment 1: there are 1 useful signals and 3 unrelated interference signal incident, the DOA of useful signal is (0°, 60°), DOAs of three interference are (45°, 15°), (165°, 20°), (285°, 25°). Interference signal is wideband interference with BPSK modulation, center frequency is the same as signal and bandwidth is 20 MHz. The CNR for signal is 43 dB Hz, three interferences have the Jam to signal power ratio (JSR) of 55 dBc. Solving the optimization problem (63.11) obtaining $\delta_{min} = 3.4077\text{e}{-}06$, setting $\delta = 0.005$, $\alpha = 1.5$, $\lambda_0 = 101$, and setting time tap number N to 21, and $L = 10$, after the 17 step search, obtain the optimal weighting vector. The software receiver gets $CNR_e = 38.04$, taking it into account

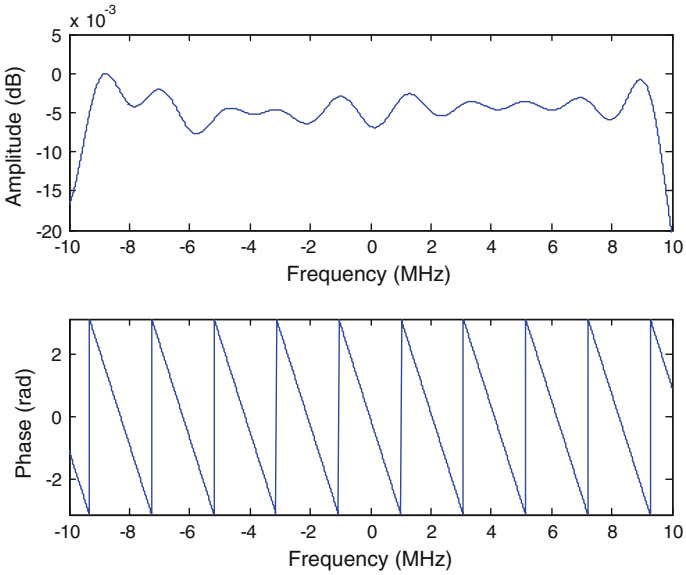

Fig. 63.2 The equivalent filter obtained by this paper's method in experiment 1

that the processing loss of the receiver is 0.5 dB, so $CNR_0 = 42.5$, $G_e = 38.04 - 42.5 = -4.46$ dB. Under the same signal interference configuration the equivalent array gain is $G_e = -6.85$ dB for the PI method, while for the MSINR method the array output signal can not be acquired, so $G_e < 32 - 42.5 = -8.5$ dB. The equivalent filter's responses at the signal's DOA got by three kinds of methods are as shown in Figs. 63.2, 63.3 and 63.4 respectively. The simulation results shows that when the number of interference is equal to the freedom of the array and the interference is strong, loss of CNR is large for the three methods, but the loss is relatively smallest by this novel method, and the array response in the signal's DOA is closer to desired filter compared to PI method, can better ensure the ranging precision and antenna array equivalent phase center consistency. For MSINR method, as literature [4] pointed out, its equivalent filter bandwidth in the signal direction is too narrow, serious loss of useful signal is caused. Reducing time domain tap number to 1, namely use pure spatial processing, $G_e = -0.4$ dB will be obtained by the MSINR method, but a pure spatial processing is too sensitive to channel adaptation and multipath interference, it has a poor robustness [1, 3].

Simulation experiment 2: the DOA of signal is (0°, 60°), the CNR of signal is 43 dB Hz, no interference exist, time domain tap number is 21. $G_e = 2.51$ dB is obtained by using the new novel method, $G_e = -3.34$ dB is obtained by using PI method, $G_e = -5.23$ dB is obtained by using MSINR method. The new novel method has positive array gain, while other method have negative gain, so it's broad-band beam-forming effect is obvious.

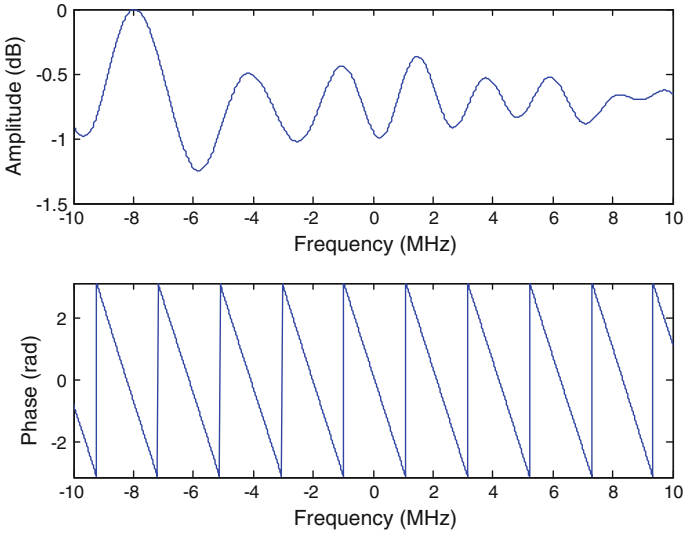

Fig. 63.3 The equivalent filter obtained by PI method in experiment 1

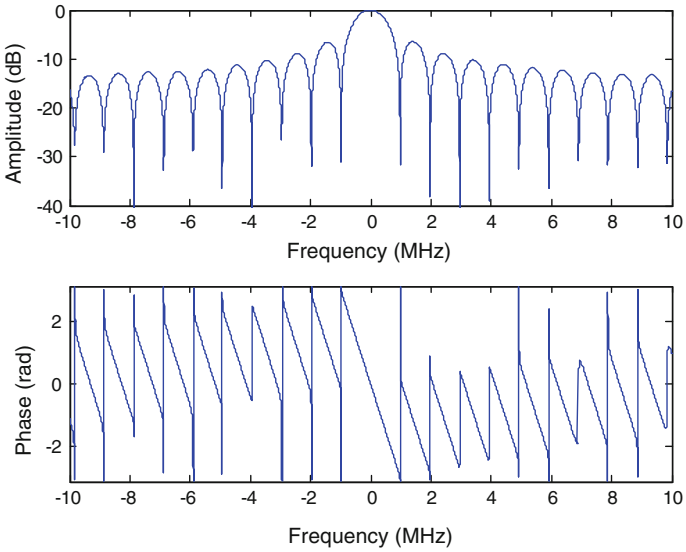

Fig. 63.4 The equivalent filter obtained by MSINR method in experiment 1

Simulation experiment 3: there is only one signal and interference, and both have the same DOA of (30°, 20°), the CNR of signal is 43 dB Hz, the JSR is 45 dBc, the interference is BPSK modulation, bandwidth is 0.2 MHz, time domain tap number is 21. $G_e = 1.89$ dB is obtained by using the new novel method, and

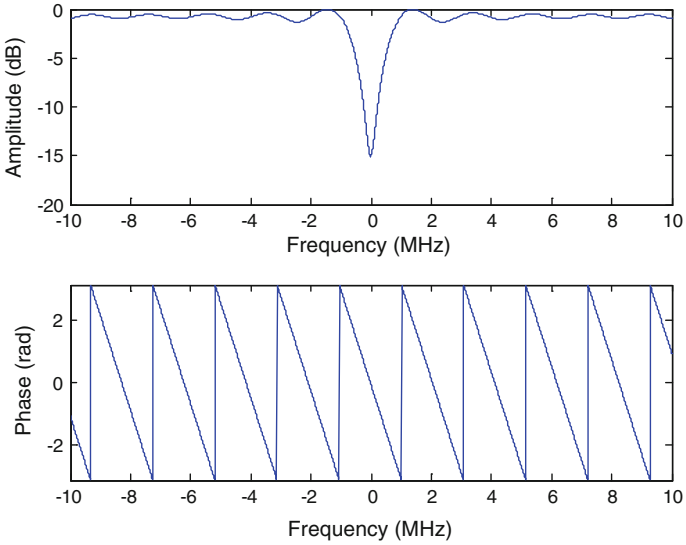

Fig. 63.5 The equivalent filter obtained by this paper's method in experiment 3 (JSR = 45 dBc)

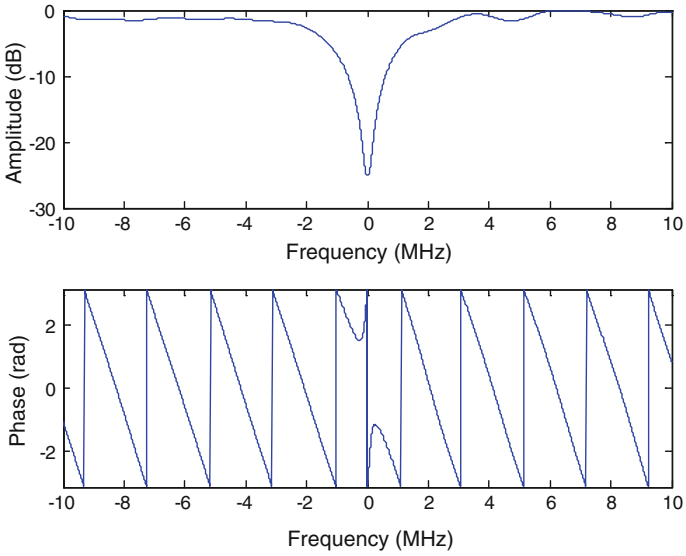

Fig. 63.6 The equivalent filter obtained by PI method in experiment 3 (JSR = 45 dBc)

the equivalent filter in signal direction is shown in Fig. 63.5, it is seen that narrowband interference that is in the same DOA of signal can also be effectively depressed. By using PI method, the array CNR loss was significantly higher than the new novel method. Equivalent filter's response at the signal's DOA is shown in Fig. 63.6, it is seen that as the goal of PI method is to reduce the output power, the

null of filter is too wide. For the PI method, with the JSR increasing to 70 dBc, the array's output signal cannot be acquired, namely $G_e = -8.26\,\text{dB}$, while the new novel method can effectively anti-interference, and $G_e = -4.19\,\text{dB}$ is obtained.

63.5 Conclusion

Traditional PI algorithm has shortcomings of high insertion loss and can hardly forming the main beam toward the signal direction, because it has not effectively balance the two goals of depressing interference and reducing CNR loss, and traditional MSINR algorithm will form very narrow bandwidth filter for useful signal when the number of the time domain tap is large, which leads to serious loss of CNR. The utilization of convex optimization techniques in antenna array adaptive processing provides a way to solve the problem. But there are problems like parameter selection and inconvenience to realize in engineering for the current convex optimization based anti-jamming methods. In this paper, the anti-jamming space-time optimal filter design problem is modeled as a two object programming problem. The MOP problem is solved by introducing a weighting factor to combine a total object function, and then the rationality criterion of the weighting factor is analyzed. Then a searching method is proposed to find the optimal weighting factor, and the global optimal weighting vector for the space-time filter is obtained at the same time. Combined with evaluation of numerical simulation and software receiver, it proves that the new novel method can effectively balance the two goals, in the premise of certain increase in computational cost; the method in this paper is superior to traditional PI and MSINR method.

References

1. Wang Y, Peng Y (2000) Space-time adaptive signal processing. Tsinghua University Press, Beijing
2. Haimovich PM, Shah A (1997) Applications of space-time adaptive processing in wireless communications. In: IEEE proceedings of MILCOM 97, vol 3. pp 1098–1102
3. Fante RL, Vaccaro JJ (2000) Wideband cancellation of interference in a GPS receive array. Aerosp Electron Syst IEEE Trans 36(2):549–564
4. Niu J, Ge R, Li M et al (2011) The influence analysis of narrowband hypothesis to GNSS antenna array anti-jamming performance evaluation. J Nat Univ Defense Technol 33(5):128–133
5. Ren C, Wu S, Ju WANG (2008) A novel wideband interference cancellation method for GPS receiver. J Electron Inf 30(8):1977–1980
6. Lebret H, Boyd S (1997) Antenna array pattern synthesis via convex optimization. Sig Process IEEE Trans 45(3):526–532
7. Yan S, Ma Y (2009). Sensor array beam optimization design and application. Science Press, Beijing China

8. Grant M, Boyd S, Ye Y (2009) cvx users' guide[R]. Technical Report Build 711, Citeseer. Available at: http://citeseerx.ist.psu.edu/viewdoc/download
9. Boyd SP, Vandenberghe L (2004) Convex optimization. Cambridge University Press, Cambridge, NY
10. Wu SP, Boyd S, Vandenberghe L (1997) FIR filter design via spectral factorization and convex optimization. In: Datta B (ed) Applied and computational control, signals, and communications. Birkhauser
11. Junwei NIU (2011) Study on GNSS antenna array anti-jamming algorithm and performance evaluation key techniques. National University of Denfense Technology, Changsha

Chapter 64
Research on Multipath Mitigation Based on the Variable Length Reduced Sigma Point Kalman Filter

Jing Peng, Yingxue Su, Jingyuan Li and Feixue Wang

Abstract In the modernized GNSS systems, multipath has become the major limitation to the application of high precision positioning and the performance of all sorts of receivers. Moreover, the characteristics of multipath of different satellites are different in the combined constellation. Towards the aim of multipath mitigation for the monitoring stations in Beidou navigation satellite system (BDS), this paper analyzes the characteristics of multipath of combined constellation in BDS system first, and an algorithm of multipath mitigation based on the variable length Reduced Sigma Point Kalman Filter (RSPKF) is put forward subsequently, which can be employed in the multipath mitigation for different kinds of satellites in the combined constellation. The results of field experiments implied that, the standard deviation of multipath residuals for all frequencies and all kinds of satellites were reduced more than 27 % by the proposed algorithm while compared with the multipath mitigation method based on the fixed data length RSPKF.

Keywords Satellite navigation and positioning · Multipath mitigation · Variable length reduced sigma point Kalman filter · Combined constellation

64.1 Introduction

In the future, the performance of global navigation satellite system will be improved dramatically, and demands for increased accuracy have lead to new signal system and enhancement such as elimination of systematic errors. Most of the systematic errors such as ionospheric delay, tropospheric delay, satellite orbit errors and clock bias can be reduced by the mathematical models or by the

J. Peng (✉) · Y. Su · J. Li · F. Wang
College of Electronic and Science Engineering, National University of Defense Technology, Changsha 410073, People's Republic of China
e-mail: jingpeng_nudt@163.com

J. Sun et al. (eds.), *China Satellite Navigation Conference (CSNC) 2014 Proceedings: Volume I*, Lecture Notes in Electrical Engineering 303,
DOI: 10.1007/978-3-642-54737-9_64,

difference method, and these improvements make multipath error, which is difficult to be eliminated by the model due to its diversity related to the environment, become the dominant error source in the application of high precision positioning, particularly in the combined GNSS systems [5].

With the development of Beidou Navigation System (BDS), multipath error has become the significant factor which limits the performances of all sorts of receivers and even the whole satellite navigation system. In the period of BDS experimental satellite, the field experiment analysis results showed that there was an obvious fluctuation in the pseudo-range observation. By the investigation of comparison experiments, the pseudo-code multipath was finally located as the primary reason of fluctuation. In order to improve the measurement precision of receiver, it is necessary to take measure to eliminate the multipath error. Besides, the main installation consideration for some urban monitoring stations has been primarily based on the accessibility, cost-saving and easy maintenance, and the multipath mitigation should be also considered to improve the data quality of observations in those urban monitoring stations.

Several techniques for multipath mitigation based on the data post-processing have been developed in the last decades due to their flexibility and easy realization [6, 13], these data processing techniques are the significant approaches for the analysis of multipath characteristic and data quality assessment as well. Moreover, the multi-carrier modulation is used in the modernized GNSS system [9]; Hein [3], and the combined constellation is employed by the BDS system [11], all these characteristics determine the data processing method of multipath mitigation in the modernized GNSS system will be different from the conventional method, particularly in the combined constellation BDS system. So far, BDS system is in operation, which provides the regional service to the Asia and the Pacific area. Considering the promotion of the industrialization of BDS, it is urgent to deal with the BDS regional experimental data to put forward an effective multipath mitigation method for modernized GNSS receivers and monitoring stations.

64.2 Multipath Extraction Method Based on the Optimal Dual Frequency Data Combination

64.2.1 Code Minus Carrier Phase Observation

Generally, the pseudo-range multipath observation can be obtained by the results of pseudo-code minus carrier phase [7, 8] without cycle slip (it is so-called CMC observation), which is not the real multipath as the errors caused by other effects such as carrier phase multipath, receiver noise, and etc. are combined in addition to pseudo-range multipath.

Only considering the correction of the first-order parameter of ionospheric error, assuming that the high-order parameter can be negligible, the observation

equations of pseudo-range and carrier phase can be described respectively as follows:

$$\rho_j = R + \frac{A_1}{f_j^2} + \delta_{trop} + c(\delta t_u - \delta T^s) + MP_{\rho_j} + \varepsilon_{\rho_j} \tag{64.1}$$

$$\lambda_j \varphi_j = R - \frac{A_1}{f_j^2} + \delta_{trop} + c(\delta t_u - \delta T^s) + \lambda_j N_j + mp_{L_j} + \varepsilon_{L_j} \tag{64.2}$$

where: j is the subscript which indicates a certain frequency of signal ($j = 1, 2, 3$); ρ is the pseudo-range observation; φ is the real carrier phase observation; N is the integer ambiguity; λ is the wavelength of carrier phase; R is the real range between satellite and receiver; A_1 is the first-order parameter of ionospheric delay; δ_{trop} is the tropospheric delay; δt_u and δT^s are the receiver clock bias and satellite clock bias respectively; MP_ρ and mp_L are the pseudo-range multipath and the carrier phase multipath respectively; ε_ρ and ε_L are the measurement noise of pseudo-code and carrier phase; and c is the vacuum speed of light.

Take triple frequencies GNSS system for example, the single frequency pseudo-range multipath can be described by the linear combination of pseudo-range and multi-carrier phase observations.

$$MP_{\rho_i} = \rho_i - \sum_{j=1}^{3} c_{i,j} \lambda_j \varphi_j + K_i \tag{64.3}$$

where: $i, j \in (1, 2, 3)$, which indicates the certain frequency of pseudo-range and carrier phase respectively, $\{c_{i,j} | i, j \in (1, 2, 3)\}$ represent the combination parameters, and K_i is the composite of the measurement noise, carrier phase multipath, interchannel delay for the ith frequency and integer ambiguities.

Substitute the pseudo-range and carrier phase equations into Eq. (64.3), it gets:

$$MP_{\rho_i} = MP_{\rho_i} + \left(1 - \sum_{j=1}^{3} c_{i,j}\right) S + \left(\frac{1}{f_i^2} + \sum_{j=1}^{3} \frac{c_{i,j}}{f_j^2}\right) A_1 \tag{64.4}$$

where: $S = R + \delta_{trop} + c(\delta t_u - \delta T^s)$.

64.2.2 Selection of the Optimal Dual Frequency Combination

Assuming the multipath observation could be extracted by dual frequency observations, the combination parameters can be calculated by Eq. (64.4) as follows:

$$\begin{cases} c_{i,n} + c_{i,m} = 1 \\ \frac{c_{i,n}}{f_n^2} + \frac{c_{i,m}}{f_m^2} = -\frac{1}{f_i^2} \end{cases} \tag{64.5}$$

where: $i, n, m \in (1, 2, 3)$, n and m indicate the selected dual frequency combination. The frequency factor is defined $\mu_{nm} \equiv f_n^2 / f_m^2$, and the analytical expressions of $c_{i,n}$ and $c_{i,m}$ can be obtained as:

$$\begin{cases} c_{i,n} = \dfrac{1 + \mu_{mi}}{1 - \mu_{mn}} \\ c_{i,m} = \dfrac{1 + \mu_{ni}}{1 - \mu_{nm}} \end{cases} \tag{64.6}$$

After the combination of dual frequency data, the variance of carrier phase measurement noise can be magnified as:

$$\sigma_{\phi_i}^2 = c_{i,n}^2 \sigma_{\phi_n}^2 + c_{i,m}^2 \sigma_{\phi_m}^2 \tag{64.7}$$

where $\sigma_{\phi_j}^2$ is the variance of the composite of carrier phase measurement noise and carrier phase multipath.

From Eq. (64.7), the magnification of carrier phase measurement noise is different when choosing different combination of dual frequency data. Thus, we suggest that the optimal dual frequency combination should be selected while extracting the multipath observation.

In the condition of same carrier loop noise bandwidth, predetection integration time, and carrier to noise ratio, after the dual frequency combination, the magnifying times to the standard deviation of carrier phase measurement noise for *i*th frequency can be described as:

$$v_i = \sqrt{c_{i,n}^2 \mu_{mn} + c_{i,m}^2} \tag{64.8}$$

And the dual frequency combination which makes Eq. (64.8) the smallest is the optimal dual frequency combination for the multipath extraction. Therefore, we can get the optimal dual frequency combination for GPS, BDS, and Galileo respectively, such as L1 and L5 for GPS, B1 and B2 for BDS, E1 and E5a for Galileo.

64.3 Multipath Estimation Based on the Adaptive Filtering

After extracting the multipath observation by the optimal double frequency combination, a short-term model can be involved to describe the multipath observation, and the pure multipath error can be obtained by the adaptive filter subsequently.

64.3.1 Process Model and Measurement Model

In this paper, a joint filter [12] is employed to estimate the multipath error and the parameters of multipath short-term model simultaneously. Assuming that the state random variable is $\boldsymbol{x}_k^* = [\boldsymbol{x}_k \quad \boldsymbol{w}_k]^{\mathrm{T}}$, where $\boldsymbol{x}_k$ is the state variable of multipath,

$\boldsymbol{w}_k = [\, w_{k,1} \quad \ldots \quad w_{k,M} \,]^{\mathrm{T}}$ is the parameter vector of multipath short-term model, $k \in \mathbf{N}$ is the discrete time index, and $\boldsymbol{y}_k$ is the observation vector.

The discrete process and measurement equations can be described as follows:

$$\begin{cases} \boldsymbol{x}_k^* = f(\boldsymbol{x}_{k-1}^*, \boldsymbol{n}_{k-1}^*) \\ \boldsymbol{y}_k = h(\boldsymbol{x}_k^*, \boldsymbol{v}_k) \end{cases} \tag{64.9}$$

Expand Eq. (64.9), it gets:

$$\begin{bmatrix} x_k \\ w_{k,1} \\ \vdots \\ w_{k,M} \end{bmatrix} = \begin{bmatrix} \mathrm{f}(x_{k-1}, \ldots, x_{k-M}, w_{k-1,1}, \ldots w_{k-1,M}) \\ w_{k-1,1} \\ \vdots \\ w_{k-1,M} \end{bmatrix} + \begin{bmatrix} n_{k-1} \\ r_{k-1,1} \\ \vdots \\ r_{k-1,M} \end{bmatrix} \tag{64.10}$$

$$\mathrm{f}(x_{k-1}, \ldots, x_{k-M}, w_{k-1,1}, \ldots w_{k-1,M}) = \sum_{i=1}^{M} w_{k-1,i} x_{k-i} \tag{64.11}$$

$$y_k = x_k + v_k \tag{64.12}$$

64.3.2 Reduced Sigma Point Kalman Filter

For an n_x-dimension state space, $2n_x + 1$ sigma points are required in the standard Sigma Point Kalman Filter (SPKF) to represent the statistical characteristic of the state distribution. This algorithm can be considered as the statistical linearization, which is able to overcome the inherent limitations such as nonlinear transformation error caused by the synthesis linearization in EKF. However, the number of sigma points is related to the dimension of state space, thereby the calculation of sigma points in SPKF might cause computational burden to the system when the dimension of state variable is very large.

To solve this problem, Julier and Uhlmann [4] proposed a Reduced Sigma Point Kalman Filter (RSPKF) which employs a spherical simplex method as the criterion of sigma point selection. Only $n_x + 2$ sigma points are required to represent the mean and covariance of state variable, which lie on a hypersphere with radius of $\sqrt{n_x}$.

In the RSPKF algorithm, the sigma points can be calculated as [4]:

$$\mathcal{X}_i = \overline{\boldsymbol{x}} + \sqrt{\boldsymbol{P}_{xx}}\mathcal{A}_i \tag{64.13}$$

where $\sqrt{\boldsymbol{P}_{xx}}$ is a matrix square root of the state covariance, $\mathcal{A}_i$is referred to as the sigma point matrix, which determines the distribution of sigma points in the hypersphere. The definition of $\mathcal{A}_i$ in details can be found in Julier and Uhlmann [4]

The weight of sigma point can be defined as:

$$W_i = \begin{cases} 0 \le W_0 \le 1 & i = 0 \\ \frac{1-W_0}{n_x+1} & i = 1, \ldots, n_x + 1 \end{cases} \tag{64.14}$$

The RSPKF algorithm can be described as the following steps.

1. Calculate the sigma points

$$\mathcal{X}_{i,k-1} = \hat{\boldsymbol{x}}_{k-1} + \boldsymbol{S}_{\boldsymbol{xx},k-1}\mathcal{A}_i \quad i = 0, \ldots, n_x + 1 \tag{64.15}$$

2. Time update stage

$$\mathcal{X}_{i,k|k-1} = \mathrm{f}(\mathcal{X}_{i,k-1}) \quad i = 0, \ldots, n_x + 1 \tag{64.16}$$

$$\hat{\boldsymbol{x}}_{k|k-1} = \sum_{i=0}^{n_x+1} W_i \mathcal{X}_{i,k|k-1} \tag{64.17}$$

$$\boldsymbol{S}_{\boldsymbol{xx},k|k-1} = \mathrm{qr}\left\{ \left[\sqrt{W_1}(\mathcal{X}_{1:n_x+1,k|k-1} - \hat{\boldsymbol{x}}_{k|k-1}) \quad \boldsymbol{S}_{\boldsymbol{ww},k-1} \right] \right\} \tag{64.18}$$

$$\boldsymbol{S}_{\boldsymbol{xx},k|k-1} = \mathrm{cholupdate}\left(\boldsymbol{S}_{\boldsymbol{xx},k|k-1}, \mathcal{X}_{0,k|k-1} - \hat{\boldsymbol{x}}_{k|k-1}, W_0\right) \tag{64.19}$$

3. Measurement update stage

$$\mathcal{Y}_{i,k|k-1} = \mathrm{h}(\mathcal{X}_{i,k|k-1}) \quad i = 0, \ldots, n_x + 1 \tag{64.20}$$

$$\hat{\boldsymbol{y}}_{k|k-1} = \sum_{i=0}^{n_x+1} W_i \mathcal{Y}_{i,k|k-1} \tag{64.21}$$

$$\boldsymbol{S}_{\boldsymbol{yy},k} = \mathrm{qr}\left\{ \left[\sqrt{W_1}(\mathcal{Y}_{1:n_x+1,k|k-1} - \hat{\boldsymbol{y}}_{k|k-1}) \quad \boldsymbol{S}_{\boldsymbol{vv},k} \right] \right\} \tag{64.22}$$

$$\boldsymbol{S}_{\boldsymbol{yy},k} = \mathrm{cholupdate}\left(\boldsymbol{S}_{\boldsymbol{yy},k}, \mathcal{Y}_{0,k|k-1} - \hat{\boldsymbol{y}}_{k|k-1}, W_0\right) \tag{64.23}$$

$$\boldsymbol{P}_{\boldsymbol{xy},k} = \sum_{i=0}^{n_x+1} W_i(\mathcal{X}_{i,k|k-1} - \hat{\boldsymbol{x}}_{k|k-1})(\mathcal{Y}_{i,k|k-1} - \hat{\boldsymbol{y}}_{k|k-1})^{\mathrm{T}} \tag{64.24}$$

$$\boldsymbol{K}_k = \left(\boldsymbol{P}_{\boldsymbol{xy},k}/\boldsymbol{S}_{\boldsymbol{yy},k}^{\mathrm{T}}\right)/\boldsymbol{S}_{\boldsymbol{yy},k} \tag{64.25}$$

$$\hat{\boldsymbol{x}}_k = \hat{\boldsymbol{x}}_{k|k-1} + \boldsymbol{K}_k(\boldsymbol{y}_k - \hat{\boldsymbol{y}}_{k|k-1}) \tag{64.26}$$

$$\boldsymbol{U}_k = \boldsymbol{K}_k \boldsymbol{S}_{\boldsymbol{yy},k} \tag{64.27}$$

$$\boldsymbol{S}_{\boldsymbol{xx},k} = \text{cholupdate}\left(\boldsymbol{S}_{\boldsymbol{xx},k|k-1}, \boldsymbol{U}_k, -1\right) \tag{64.28}$$

where $\sqrt{\boldsymbol{P}_{\boldsymbol{xx}}}$ can be obtained by the Cholesky factorization [10] $\boldsymbol{P}_{\boldsymbol{xx}} = \boldsymbol{S}_{\boldsymbol{xx}}^{\mathrm{T}} \boldsymbol{S}_{\boldsymbol{xx}}$, and $\boldsymbol{S}_{\boldsymbol{xx}}$ denotes the formal triangle matrix which is the Cholesky factor of $\boldsymbol{P}_{\boldsymbol{xx}}$. $\boldsymbol{S}_{\boldsymbol{ww},k-1}$ and $\boldsymbol{S}_{\boldsymbol{vv},k}$ denote the matrix square root of process noise and measurement noise matrix covariance respectively. qr$\{\cdot\}$ represents the QR decomposition, and cholupdate$(\cdot)$ represents the rank-one Cholesky update [2].

64.3.3 Variable Length Reduced Sigma Point Kalman Filter

64.3.3.1 Characteristic of Multipath in Combined Constellation

BDS system uses the combined constellation design which consists of GEO satellite, IGSO satellite and MEO satellite. Due to the different motions of different types of satellites, the multipath of different satellite will show different characteristics for the reference or monitoring station.

Figure 64.1 shows the comparison of Fast Fourier Transform (FFT) spectrum of multipath observations with three frequencies for the combined constellation in BDS system. The observation period is from UTC 09:15:28 to UTC 11:37:19, August 27, 2012. The monitoring receiver antenna is mounted on a building roof. The sampling rate is 1 Hz. The type of observation is the wide-correlated pseudorange. Moreover, the optimal dual frequency combination of B1 and B2 is chosen to extract the multipath observation data.

From Fig. 64.1, it implies that the frequency components of the multipaths of combined constellation are mainly concentrated within 0.01 Hz. In particular, the multipath of GEO satellite shows the characteristic of low frequency variety, and the frequency component of the multipath is mainly concentrated within 0.005 Hz in which the data from B3 frequency is obvious.

64.3.3.2 Variable Length RSPKF

To adapt the multipath mitigation algorithm to the combined constellation, a variable data length can be set for different kinds of satellites. If the observation data indicates GEO satellite, a process model with long data length is involved due to the characteristic of GEO multipath shows the low frequency variety. Otherwise, if the observation data indicates IGSO or MEO satellites, the data length M of process model will be set as a short one.

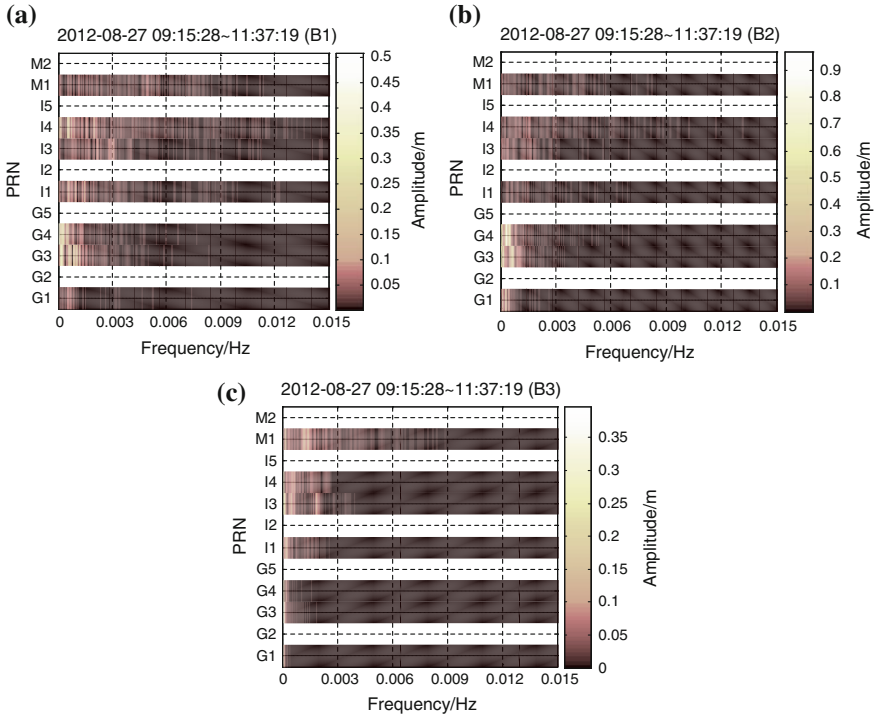

Fig. 64.1 FFT spectrum of multipath for BDS combined constellation. **a** B1. **b** B2. **c** B3

Considering the design idea of the Variable Length Least Mean Square (VLLMS) filter [1], the proposed filter in this paper is consisted of three parallel RSPKF filters. The control module adapts the data length by the output errors of the three RSPKF filters. The schematic structure of variable length RSPKF is showed in Fig. 64.2. Unlike VLLMS filter, it is not necessary to input a multipath signal in the proposed filter. This character can be used in the real-time estimation of multipath for all kinds of receivers and navigation terminals.

According to the order control principle in VLLMS [1] the data length of variable length RSPKF can be controlled as the following steps at instant k.

1. Calculate the output errors:

$$e_{k,i} = y_k - x_{k,i}, \quad i = 1, 2, 3 \tag{64.29}$$

2. Select the optimal data length by L times iteration.

$$m_i = \frac{1}{L} \sum_{j=k-L+1}^{k} e_i^2(j), \quad i = 1, 2, 3 \tag{64.30}$$

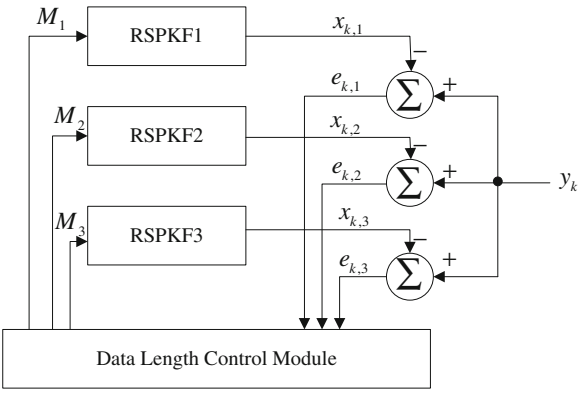

Fig. 64.2 Schematic structure of variable length reduced sigma Kalman filter

$$M_{k+1,1} = \begin{cases} M_{k,1} + 1 & \text{if } m_1 > m_2 > m_3 \\ M_{k,1} & \text{if } m_1 > m_2 \text{ and } m_2 \le m_3 \\ M_{k,1} - 1 & \text{otherwise} \end{cases} \tag{64.31}$$

$$\begin{cases} M_{k+1,2} = M_{k+1,1} + 1 \\ M_{k+1,3} = M_{k+1,1} + 2 \end{cases} \tag{64.32}$$

The selection of iteration times L is important to the proposed filter. If L is small, it will help the realization of the multipath mitigation in real-time process, and it might not find the optimal data length yet. If L is large, it guarantees the enough iteration times to find the optimal data length, but it also brings the heavy computational burden to the filter. Hence, the maximum iteration times is set to $L_{\max} = 5$ in this paper.

64.4 Experimental Results

Take the field experimental data of BDS as an example, a self-developing receiver and antenna are used to collect the data. The observation period is from UTC 06:11:21 to UTC 07:11:21, August 6, 2012. Analyzing the observation data selected from G1, I1, and M1 satellites respectively. The sampling rate is set to 1 Hz, and B1/B2 optimal dual frequency combination is selected for multipath extraction.

In the experiment, the matrices covariance of process noise and observation noise can be set as:

$$\boldsymbol{Q}_k^* = \mathrm{diag}\left(\boldsymbol{Q}_x \vdots \boldsymbol{Q}_w\right) \tag{64.33}$$

$$\boldsymbol{R}_k = \sigma_{mp}^2 \tag{64.34}$$

Table 64.1 Comparison of multipath residual of RSPKF filters with different data lengths (unit: m)

Frequency	PRN	Data length			
		Variable	10	20	50
B1	G1	0.0061	0.0095	0.0094	0.0095
	I1	0.0087	0.0153	0.0153	0.0155
	M1	0.0127	0.0214	0.0218	0.0217
B2	G1	0.0052	0.0081	0.0081	0.0081
	I1	0.0082	0.0147	0.0147	0.0147
	M1	0.0113	0.0199	0.0204	0.0211
B3	G1	0.0065	0.0092	0.0092	0.0093
	I1	0.0084	0.0133	0.0134	0.0134
	M1	0.0122	0.0201	0.0207	0.0212

Table 64.2 Comparison of positioning error before and after multipath mitigation (unit: m)

	RMS-X	RMS-Y	RMS-Z
Before mitigation	11.358	5.581	1.501
Fixed length RSPKF	11.159	4.707	0.648
Variable length RSPKF	11.147	4.636	0.648

where $\boldsymbol{Q}_x = 0.1^2$, $\boldsymbol{Q}_w = 0.5^2 \cdot \mathrm{diag}(1, \ldots, 1)_{M \times M}$, M is the data length, and σ_{mp} is the standard deviation of multipath error, which is set to 0.5 m.

Table 64.1 shows the performance comparison of variable data length and fixed data length RSPKF. It shows that the standard deviation of the residual of multipath with three frequencies for G1, I1 and M1. From Table 64.1, it implies that the residual of the proposed filter is smaller than which of the fixed data length RSPKF filters. The standard deviation of the residual of multipath with three frequencies in G1, I1 and M1 satellites reduced more than 27 % when compared with the fixed length RSPKF filters.

Table 64.2 shows the comparison of positioning error before and after multipath mitigation. It indicates that the positioning root mean square error of XYZ directions increased 1.9, 16.9 and 56.8 % for the experimental fixed station by using the proposed mitigating multipath algorithm.

64.5 Conclusion

In view of the characteristics of multipath in the combined constellation, a multipath mitigation algorithm based on the variable length RSPKF is put forward with a multipath short-term model. The field experimental results show that the self-controlling variable length RSPKF filter is more applicable in the multipath

mitigation of the combined constellation than the fixed one. As the proposed method can be applicated in multipath mitigation without storing large amount of data and it can adjust parameters adaptively, it shows the potential capability in real-time application for multipath mitigation of fixed stations in the condition of cycle slip being repaired and the integer ambiguity being resolved.

References

1. Bilcu RC, Kuosmanen P, Eguazarian K et al (2002) A variable length LMS algorithm: theoretical analysis and implementations. In: Proceedings of the 9th international conference on electronics, circuits and systems, vol 3, pp 1031–1034
2. Dongarra JJ, Bunch JR, Moler CB et al (1999) LINPACK users' guide. Philadelphia: SIAM, 1979
3. Hein GW (2002) Status of GALILEO signal design and frequency plan. In: Proceedings of ION GPS, pp 24–27
4. Julier SJ, Uhlmann JK (2002) Reduced sigma point filters for the propagation of means and covariances through nonlinear transformations. In: Proceedings of American control conference, pp 887–892
5. Leick A (2004) GPS satellite surveying, 3rd edn. Wiley, Hoboken
6. Liu H, Li X, Ge L, Rizos C et al (2009) Variable length LMS adaptive filter for pseudorange multipath mitigation based on SydNET stations. J Appl Geodesy 3:35–46
7. Liu W, Mou W, Wang F (2012) A new unequal-variance-based triple-frequency first order ionosphere correction algorithm and its application in BDS. Sci China Phys Mech Astron 55(3):546–552
8. Liu Z, Mou W, Pang J et al (2012) Analysis and comparison of extracting algorithms of pseudo-range multipath in three-frequency GNSS. Bull Surveying Mapp 5:10–13
9. McDonald KD (2002) The modernization of GPS: plans, new capabilities and the future relationship to Galileo. J Global Positioning Syst 1(1):1–17
10. Press WH, Teukolsky SA, Vetterling W et al (2007) Numerical recipes: the art of scientific computing, 3rd edn. Cambridge University Press, New York
11. Tan S (2008) Development and thought of compass navigation satellite system. J Astronaut 29(2):391–396
12. Wan E, Van der Merwe R, Nelson A (2000) Dual estimation and the unscented transformation. In: Solla S, Leen T, Müller K (eds) Neural information processing systems, vol 12. MIT Press, Cambridge, pp 666–672
13. Zheng DW, Zhong P, Ding XL et al (2005) Filtering GPS time series using a Vondrak filter and corss-validation. J Geodesy 79:363–369

Chapter 65
Implementation of a Software-Defined BeiDou Receiver

M. Zahidul H. Bhuiyan, Stefan Söderholm, Sarang Thombre, Laura Ruotsalainen and Heidi Kuusniemi

Abstract Satellite-based positioning is undergoing a rapid change. Both the GPS and the GLONASS systems are being modernized to serve better the current challenging applications in harsh signal conditions. These modernizations include increasing the number of transmission frequencies and changes to the signal components. In addition, the European Galileo and the Chinese BeiDou systems are currently under development for global operation. Therefore, the research and development of Global Navigation Satellite System receivers in view of these new upcoming systems has been experiencing a new upsurge. In this paper, the authors discuss the main functionalities of a GNSS receiver in view of BeiDou satellite navigation system. While describing the main functionalities of a software defined BeiDou receiver, the authors also highlight the similarities and differences between the signal characteristics of BeiDou B1 open service signal and the legacy GPS L1 C/A signal, as they both exhibit similar characteristics in general. In addition, the authors implement a novel acquisition technique for long coherent integration in the presence of NH code modulation in BeiDou D1 signal. Finally, the authors present a BeiDou-only navigation fix with the implemented software-defined BeiDou receiver.

Keywords BeiDou satellite navigation system · Software-defined receiver

65.1 Introduction

The Chinese satellite navigation system BeiDou has a mixed space constellation that has, when fully deployed, five Geostationary Earth Orbit (GEO) satellites, twenty-seven MEO satellites and three Inclined Geosynchronous Satellite Orbit

M. Z. H. Bhuiyan (✉) · S. Söderholm · S. Thombre · L. Ruotsalainen · H. Kuusniemi
Finnish Geodetic Institute, Geodeetinrinne 2 FI-02430 Masala, Finland
e-mail: zahidul.bhuiyan@fgi.fi

J. Sun et al. (eds.), *China Satellite Navigation Conference (CSNC) 2014 Proceedings: Volume I*, Lecture Notes in Electrical Engineering 303,
DOI: 10.1007/978-3-642-54737-9_65,

(IGSO) satellites. The GEO satellites are operating in orbit at an altitude of 35,786 km and positioned at 58.75°E, 80°E, 110.5°E, 140°E and 160°E respectively. The MEO satellites are operating in orbit at an altitude of 21,528 km and an inclination of 55° to the equatorial plane. The IGSO satellites are operating in orbit at an altitude of 35,786 km and an inclination of 55° to the equatorial plane. These satellites broadcast navigation signals and messages within 3 frequency bands. The BeiDou system has been in development for more than a decade, and it is estimated to be operational with global coverage at the latest in 2020. The BeiDou satellites transmit ranging signals based on the CDMA (Code Division Multiple Access) principle, like GPS and Galileo. The mixed constellation structure of BeiDou results in better observation geometry for positioning and orbit determination compared to current GPS and GLONASS, and future Galileo, especially in China and neighboring regions. The BeiDou system has already started contributing to the multi-GNSS benefits where increased accuracy, availability and integrity are possible when utilizing interoperable GNSS.

The characteristics of BeiDou B1I (B1 In-phase) signal can be compared with GPS L1 signal in order to realize the similarities and differences between the two systems. Both the civilian signals from these two systems have similar characteristics in general, for example, the periods of their spreading codes are both 1 ms long, and the coordinate systems and the navigation message structures are almost the same with minor differences [1, 2]. This eventually means that many algorithms that are implemented for the GPS receiver can be readily available to the BeiDou receiver without any major modification. But to improve the positioning performance, all the modern GNSS signals, including BeiDou and the GPS L5, introduce a second layer of modulation between the navigation data and the PRN code chips, known as Neumann-Hoffman (NH) code modulation. This ultimately improves the data bit rate of the modern GNSS signals. The legacy GPS L1 C/A signal has a data bit rate of 50 bps, which means that 1 bit data lasts for 20 ms (i.e., the PRN code cycle repeats 20 times for each data bit). The data bit rate of BeiDou D2 signal is 500 bps which means that 1 bit data lasts for only 2 ms (i.e., 2 spreading code cycles). The data bit rate of BeiDou D1 signal is 50 bps originally, but after modulated by NH code, the data bit rate becomes 1 kbps. So compared to the GPS signal, the data bit rate of BeiDou signal increases significantly. Particularly, the NH code modulated D1 signal has 1 kbps data bit rate which makes data bit transition possible within the data bit boundary. The use of NH code and the resultant increase in the data bit rate has pros and cons. On the positive side, the NH code can boost the ability of anti-narrowband interference and improve the cross-correlation property of satellite signals and the bit synchronization [3]; whereas on the negative side, the existence of NH code makes the acquisition and tracking of the modernized GNSS signals more challenging [4–7].

The use of a software-defined GNSS receiver is highly appreciated for its flexibility, re-configurability and diversity. These unique characteristics of a software-defined receiver make it possible to develop and then to validate new algorithms for optimizing the receiver performance at a low cost [8]. A number of software-defined receivers have already been developed for GNSS signal reception

and processing [8–11]. Most of these receives are capable of processing GPS, GLONASS and Galileo signals. Recently, a PC-based BeiDou software receiver is introduced in [12] with limited algorithmic details on how to acquire, track and process a NH code modulated BeiDou signal. Therefore, in this paper, the authors discuss the main functionalities of a BeiDou receiver considering the challenges introduced by the existence of NH code modulation.

The rest of this paper is organized as follows. Sect. 65.2 discusses the main functionalities of a software-defined GNSS receiver in view of BeiDou satellite navigation system. In Sect. 65.3, data collection scenarios and experimental configurations are presented and the positioning results are presented. Finally, conclusions and the future work lists are discussed in Sect. 65.4.

65.2 Software-Defined GNSS Receiver

A GNSS software-defined receiver consists of three major components, RF front-end unit, a signal processing unit, and a navigation processing unit. The RF front-end module is responsible for signal amplification, noise filtering, down-conversion, automatic gain control, and analogue-to-digital conversion. The front-end module converts the received analog data to digital Intermediate Frequency (IF) data at a rate which is several times more than the code chipping rate. A 26 MHz sampling frequency is used to generate the raw digitized IF samples in all the experimented cases of this work.

The digital IF data are then processed by a signal processing unit whose main responsibilities include signal acquisition, code and carrier tracking and data demodulation. The demodulated data and the resulting pseudorange measurements are then utilized by a navigation processing unit in order to offer a Position, Velocity and Timing (PVT) solution, along with some other relevant information. The software-defined receiver differs from a conventional receiver in the sense that the functions of the processing and navigation units, including correlation/tracking and navigation tasks, are delivered by software, leading to a more flexible design with potential savings in cost and power.

A software-defined GNSS receiver platform, named as FGI-GSRx, has been developed in Finnish Geodetic Institute for the analysis and validation of novel algorithms for an optimized GNSS navigation performance. The basic version of FGI-GSRx is based on an open-source software receiver platform [8], and it has been adapted recently to be BeiDou-compatible with a dual-frequency front-end from Nottingham Scientific Limited (NSL) [13]. The NSL front-end, ‘stereo v2’ is used to capture the BeiDou data. The stereo front-end configuration is presented in Table 65.1. The BeiDou B1I signal spectrum, time-domain plot and bin distribution of the digitized IF samples are shown in Fig. 65.1.

Table 65.1 NSL stereo v2 front-end configuration for BeiDou B1I signal reception

Intermediate frequency	6.5 MHz
Front-end bandwidth	4.2 MHz
Sampling frequency	26 MHz
Number of quantization bits	2 bits

65.2.1 BeiDou Signal Acquisition

The main purpose of signal acquisition is to determine which of the satellites are visible to the user and then, to coarsely estimate the carrier Doppler and the code frequency of those visible satellites. In other words, signal acquisition is a three dimensional search, where the satellite PRN number, the carrier Doppler and the code phase are coarsely estimated. An FFT-based signal acquisition technique is implemented in the receiver. The traditional coherent acquisition techniques used for GPS L1 C/A signal cannot directly be applied to BeiDou D1 signal acquisition due to the presence of NH-code modulation. In case of BeiDou D1 signal, the sign changes occur more frequently than that of a GPS L1 C/A signal due to the presence of NH code. Therefore, an acquisition scheme for BeiDou D1 signal with more than 1 ms coherent integration period may appear dangerous, if sign information is not consistently preserved. In view of this sign transition problem, a novel acquisition technique is implemented for BeiDou D1 signal that preserves the total useful signal energy in the presence of a sign transition, and hence, makes a correct acquisition decision on the presence of the satellite, and its carrier Doppler and the corresponding code phase. The working principle of the novel BeiDou D1 acquisition technique is depicted in the following.

1. For a coherent integration period of T_{coh} ms, a (T_{coh}*1000 =) X_{bit} number of NH code bits is selected first. For example, for a coherent integration period of 5 ms, the first 5 bits of NH code, i.e., [−1−1−1−1−1] can be selected. Also, a long incoming BeiDou signal of (T_{coh} + 20−1) ms is required to carry out the FFT-based acquisition. In case of T_{coh} = 5 ms, the acquisition metric will be consisted of 24 ms long incoming signal.
2. The frequency resolution is chosen such that the frequency bin size is less than $2/3T_{coh}$, where T_{coh} is the coherent integration time. In case of a 5 ms integration time, the frequency bin size should be less than or equal to 133.33 Hz.
3. The chosen X_{bit} long NH code sequence is then multiplied with the locally generated BeiDou PRN codes in order to form a X_{bit} long NH-code-modulated-PRN-code-cycles.
4. An FFT-based correlation is then performed on each T_{coh} ms blocks of incoming BeiDou signal with the locally generated X_{bit} long NH-code-modulated-PRN-code-cycles (i.e., the output of step 3.) with an incoming signal index increment of 1. An example on how the incoming BeiDou D1 signal is structured for acquisition is shown in Fig. 65.2 below for a coherent integration period of T_{coh} = 5 ms.

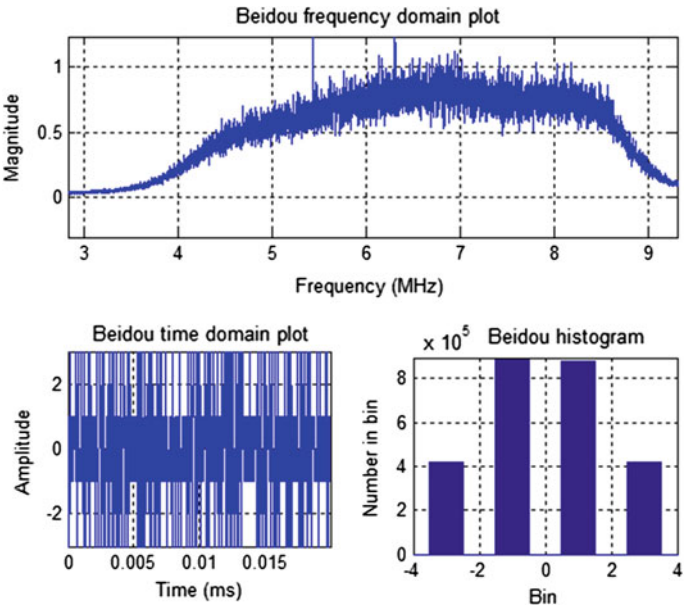

Fig. 65.1 BeiDou signal spectrum (*up*), time-domain plot (*lower-left*), and bin distribution of the digitized IF samples

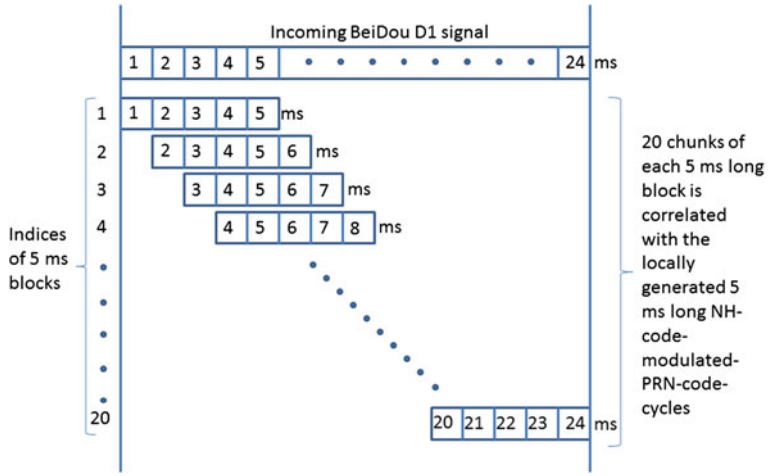

Fig. 65.2 24 ms long incoming BeiDou signal is structured into 20 chunks of 5 ms long block with an index increment of 1

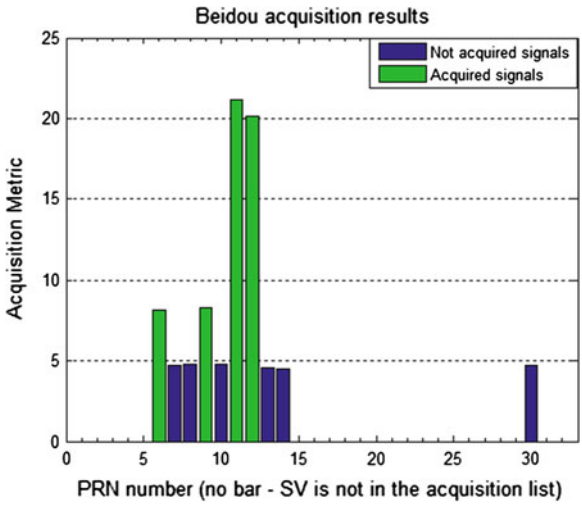

Fig. 65.3 Acquisition metric for BeiDou IGSO and MEO satellites

5. As the NH code length is 20 bits, there are altogether 20 chunks of correlation matrices with all possible code delay and carrier Doppler combinations for a specific BeiDou satellite. The winning index is the one which has the maximum correlation peak, and therefore, it can then be used for detecting the presence of the satellite, along with the estimation of the carrier Doppler and the code phase via a pre-detection threshold computed against a certain probability of false alarm.

The above acquisition technique is used in the software receiver in order to acquire the BeiDou IGSO and MEO satellites. The resultant acquisition metric is shown in Fig 65.3.

65.2.2 BeiDou Signal Tracking

The acquisition approach discussed above gives the initial estimates of the carrier Doppler and the code offset. After the acquisition, the control will be handed over to tracking loops to track the variations of carrier phase and code offset due to the line of sight movement between the satellites and the receiver. Conventional DLL and FLL-assisted PLL tracking loops [14] are implemented in the software receiver. The main objective of signal tracking is to wipe off the code and the carrier. The DLL synchronizes the code phase of the local replica with the incoming signal, whereas the carrier tracking loop synchronizes the carrier frequency and phase with those of the incoming signals. Figure 65.4 below shows the tracking status of BeiDou PRN 11 for a 99 s long data.

Bit boundary detection: Once the BeiDou receiver keeps tracking the carrier phase and the code offset of the incoming signal, the next phase is to detect the bit

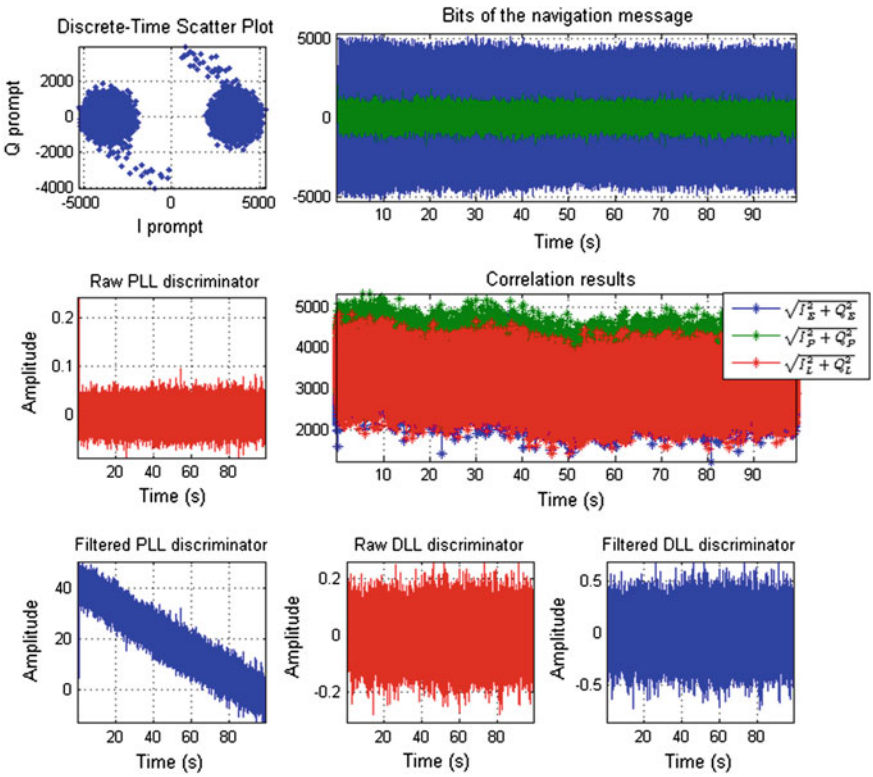

Fig. 65.4 Channel tracking status for PRN 11

boundary and then to wipe off the NH code. The purpose of bit boundary detection is to avoid integration across a data bit-edge which might cause errors in the navigation message detection. Algorithms for the bit boundary detection can be found in [10, 15, 16]. The Histogram Method, for instance, senses the bit sign changes and keeps a statistic of their position. But this approach will not work with the BeiDou D1 signal due to the presence of NH code. The sign changes in this code within the data bit boundary would in fact be detected as data bit changes affecting the statistics that this method uses for the bit boundary detection. On the other hand, as the data bits are now modulated with the NH code, a simple correlation of the incoming NH code modulated data with the locally generated NH code can then be used to estimate the bit edge. The index with a maximum correlation peak of 20 will be perfectly aligned with the NH code, and it can then be used as the bit boundary index.

C/N_0 estimation: The Carrier-to-Noise density ratio (C/N_0) in the receivers is often calculated based on the ratio of the narrowband and the wideband power [15]. If this C/N_0 estimation technique is used, the NH code must have to be wiped off before the narrowband power is calculated. Otherwise, the narrowband power

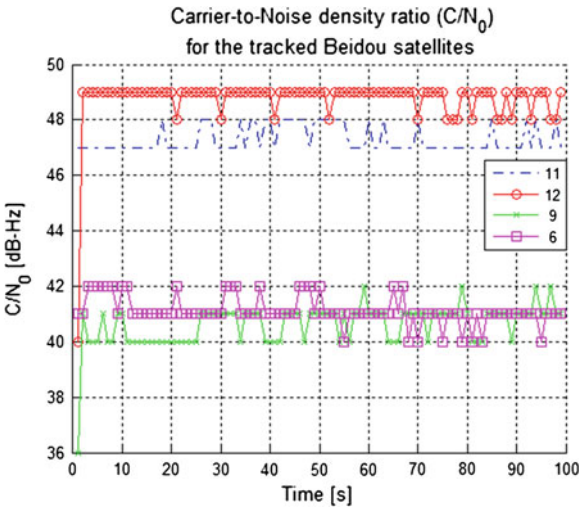

Fig. 65.5 C/N_0 for the tracked BeiDou satellites

calculation will be erroneous due to the presence of bit transition within the 20 ms bit boundary. In the implemented software-defined BeiDou receiver, the C/N_0 is estimated based on the ratio of the signal's narrowband power to its wideband power as mentioned in [15]. Figure 65.5 shows the C/N_0 of the tracked BeiDou satellites. As shown in the figure, the C/N_0s of the IGSO satellites' signals are lower than the MEO satellites' signals, as they have to traverse longer distance than the MEO ones.

Navigation solution: At the navigation message decoding phase, the first step is to detect the sub-frame preambles on the demodulated data. The BeiDou navigation message has both error correction coding and data interleaving. The error correction is performed by the Bose, Chaudhuri, and Hocquenghem (BCH 15, 11, 1) codes, which are capable of correcting one-bit error within every block of 15 bits. After successfully decoding the navigation message, a receiver position can be calculated via a least-square method with at least 4 visible satellites with decoded ephemerides.

65.3 Live Data Collection and Results Analysis

A dual-frequency front-end from NSL is used to capture the real BeiDou data. The maxim 2,769B front-end [13] is configured according to the details mentioned in Table 65.1. The BeiDou B1I signal spectrum, time-domain plot and bin distribution of the digitized IF samples were already shown in Fig. 65.1 of Sect. 65.2.

The latest BeiDou data was collected on November 27 at around 5:40 AM UTC time at a static position with a roof antenna in Finnish Geodetic Institute,

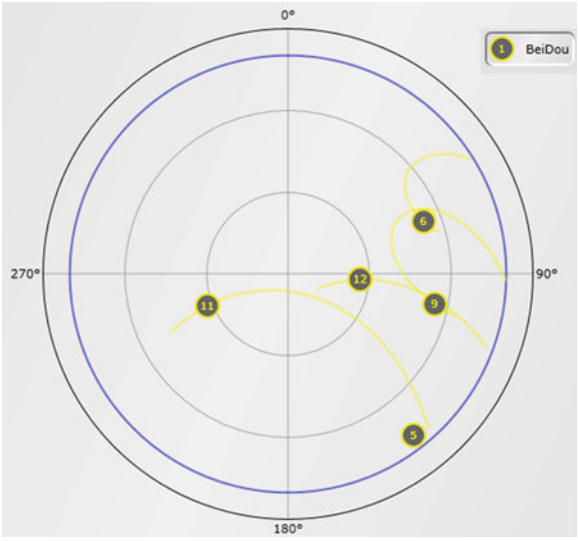

Fig. 65.6 Sky-plot of BeiDou satellite navigation system at UTC time 5:40 AM at Finnish Geodetic Institute with elevation cut-off angle 10°

Kirkkonummi, Finland. The data was collected for about 99 s. The sky-plot at the time of data collection is shown in Fig 65.6. There are 1 GEO satellite (PRN 05), 2 IGSO satellites (PRNs 6 and 9), and 2 MEO (PRNs 11 and 12) satellites. At the moment, the FGI-GSRx BeiDou receiver can acquire, track and offer a navigation solution with BeiDou D1 signal from IGSO and MEO satellites. The authors have been working to include GEO satellites' (D2) signal reception capability in their software-defined BeiDou receiver.

The horizontal error scatter plot is shown in Fig. 65.7, and the position error variations in ENU frame is shown in Fig. 65.8. The position error statistics is finally presented in Table 65.2.

The error statistics were computed for a stand-alone code-phase based position solution without applying any environmental error corrections. Among the few collected data sets, the error statistics are shown also with one other old data set from Aug 21, 2013. Both the data sets were 99 s long, and they were collected with the same front-end configuration as mentioned earlier in Table 65.1. The position error statistics were computed with respect to true known position. The horizontal and vertical mean errors for Nov 27, 2013 dataset were 4.66 and 4.88 m respectively with a mean PDOP of 5.96. And, the horizontal and vertical mean errors for Aug 21, 2013 dataset were 5.94 and 9.74 m respectively with a mean PDOP of 4.75.

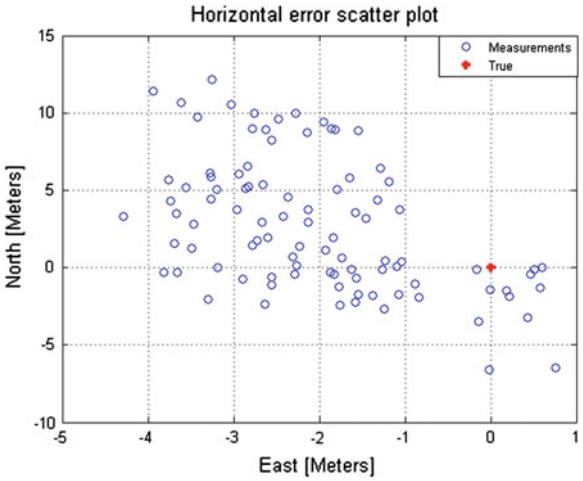

Fig. 65.7 Horizontal error scatter plot

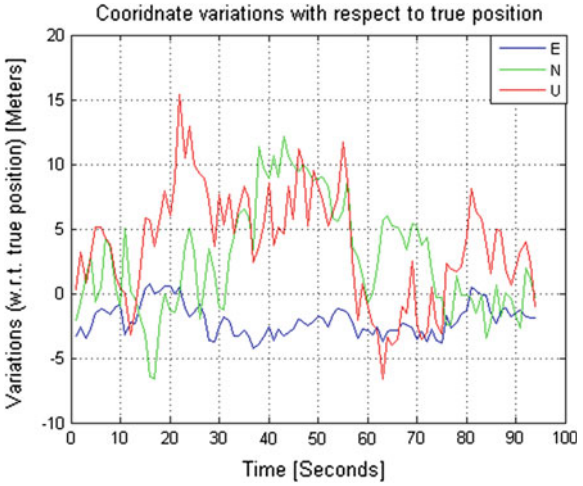

Fig. 65.8 Position error variations with respect to true position in ENU frame

Table 65.2 Position error statistics with respect to true position

Data collection date	Horizontal				Vertical			
	Std. Dev.(m)	Mean (m)	Max (m)	Mean HDOP	Std. Dev. (m)	Mean (m)	Max (m)	Mean VDOP
Nov 27, 2013	3.02	4.66	12.58	3.83	3.19	4.81	15.39	4.56
Aug 21, 2013	3.48	5.94	16.47	3.40	3.74	9.74	16.75	3.33

65.4 Conclusions

This paper presents the main functionalities of a software-defined BeiDou B1I receiver, while highlighting the similarities and differences of BeiDou B1I signal has with the existing GPS L1 C/A signal. A novel acquisition technique for long coherent integration in the presence of NH code was also presented and implemented. Real data was collected with a front-end, which is then processed with the implemented software-defined BeiDou receiver. BeiDou-only positioning results were presented for a static scenario with two 99 s long datasets. The performance of the software-defined BeiDou receiver was presented with different statistical parameters. Future work includes acquisition, tracking and decoding of BeiDou D2 signals from GEO satellites. In addition, the authors are currently working to achieve a multi-GNSS navigation solution with GPS, BeiDou and Galileo navigation systems.

References

1. BeiDou Navigation Satellite System Signal In Space Interface Control Document (2012) Open service signal B1I (Version 1.0), China Satellite Navigation Office
2. IS-GPS-200G (2012) Navstar GPS space segment/navigation user interfaces. global positioning systems directorate
3. Zou D, Deng Z, Huang J, Liu H, Yang L (2009) A study of Neuman Hoffman codes for GNSS application. In: Wireless communications, networking and mobile computing, 2009
4. Mongrédien C, Lachapelle G, Cannon M E (2006) Testing GPS L5 acquisition and tracking algorithms using a hardware simulator. In: Proceedings of ION GNSS, pp 2901–2913
5. Hegarty C, Tran M, van Dierendonck AJ (2003) Acquisition algorithms for the GPS L5 signal. In: Proceedings of the 16th international technical meeting of the satellite division of The Institute of Navigation, pp 165–177
6. Zheng B, Lachapelle G (2004) Acquisition schemes for a GPS L5 software receiver. In: Proceedings of GNSS. pp 1035–1040
7. Yang C, Hegarty C, Tran M (2004) Acquisition of the GPS L5 signal using coherent combining of L5 and Q5. In: Proceedings of the 17th international technical meeting of the satellite division of The Institute of Navigation, pp 2184–2195
8. Borre K, Akos DM, Bertelsen N, Rinder P, Jensen SH (2007) A software-defined GPS and Galileo receiver: a single-frequency approach. In: Applied and numerical harmonic analysis, 1st edn. Birkhäuser Verlag GmbH, Boston
9. Tsui J (2000) Fundamentals of global positioning system receivers: a software approach. In: Wiley series in microwave and optical engineering, Wiley, New York
10. Ma C, Lachapelle G, Cannon ME (2004) Implementation of a software GPS receiver. In: Proceedings of ION GNSS, pp 21–24
11. Normark P-L, Christian S (2005) Hybrid GPS/Galileo real time software receiver. In: Proceedings of the 18th international technical meeting of the satellite division of The Institute of Navigation, pp 1906–1913
12. Juanga J-C, Tsaia C-T, Chena Y-H (2013) Development of a PC-Based software receiver for the reception of Beidou navigation satellite signals. J Navig 66(05):701–718
13. Nottingham Scientific Limited (2013) Delivering Reliable and robust GNSS, http://www.nsl.eu.com/datasheets/stereo.pdf available online (retrieved on 10 November, 2013)

14. Kaplan ED (2006) Understanding GPS—Principles and Applications, 2nd edn. Artech House Publishers, Boston
15. Parkinson BW, Spilker JJ (1996) Global positioning system: theory and applications. In: American Institute of Aeronautics, vol. 1, 370 L'Enfant Promenade, SW, Washington, DC
16. Ziedan NI, Garrison J (2003) Bit synchronization and doppler frequency removal at very low carrier to noise ratio using a combination of the Viterbi algorithm with an extended Kalman Filter. In: Proceedings of ION GPS/GNSS 2003

Chapter 66
GNSS Spoofing Mitigation Based on Joint Detection of Code Doppler and Carrier Doppler in Acquisition

Dingbo Yuan, Hong Li and Mingquan Lu

Abstract GNSS spoofing is extremely deceitful and destructive because it can lead victim receivers to output misleading time and position information. Therefore, timely and low cost spoofing detection and mitigation is of great importance for critical GNSS applications and services. This paper presents a method for GNSS spoofing mitigation based on joint detection of code Doppler and carrier Doppler in acquisition. Subsequently, the performance of the method is evaluated. Theoretical and simulation results demonstrate that the method is effective, and it does not require additional hardware.

Keywords Spoofing mitigation · Code Doppler · Acquisition

66.1 Introduction

Nowadays, Global Navigation Satellite System (GNSS) is becoming more and more predominant, since an increasing number of applications and services rely on precise location information and time synchronization, such as communications networks, emergency response and financial transactions [1]. However, GNSS signals are vulnerable to interference and jamming because of being extremely weak signals over wireless channels. In addition, GNSS signal structures are open to the public, so they are more susceptible to disruptive attacks. Among them, spoofing is extremely deceitful and deadly, because it can generate misleading position and time information and it is difficult to be detected by users [2–4]. Hence, reliable spoofing detection and mitigation is of great importance for GNSS applications and services.

D. Yuan (✉) · H. Li · M. Lu
Department of Electronic Engineering, Tsinghua University, Beijing 100084, China
e-mail: ydb12@mails.tsinghua.edu.cn yuandingbo90@163.com

J. Sun et al. (eds.), *China Satellite Navigation Conference (CSNC) 2014 Proceedings: Volume I*, Lecture Notes in Electrical Engineering 303,
DOI: 10.1007/978-3-642-54737-9_66,

As is described in [5–7], spoofing attacks could be classified into three categories depending on their design complexity and the corresponding anti-spoofing techniques: simplistic spoofing, intermediate spoofing and sophisticated spoofing. Simplistic spoofing just generates and broadcasts GNSS signals, but does not attempt to make spoofing signals consistent with genuine signals from the satellites. Intermediate spoofing generates spoofing signals and attempts to synchronize them with the current genuine signals from the satellites. As for sophisticated spoofing, it generates several spoofing signals and it not only makes them consistent with genuine signals, but also makes themselves consistent with each other.

A lot of methods for spoofing detection and anti-spoofing have been proposed in the past years [8–12]. And they could be described briefly as follows. Amplitude (power) test and time-of-arrival test could be implemented easily in GNSS receivers and they turn out to be very effective for simplistic spoofing. Angle-of-arrival test and consistency test between GNSS and inertial measurement unit (IMU) would be more protective but they require additional hardware. Cryptographic authentication would be the most protective but it has to modify current GNSS receiver and GNSS signal structure.

As for simplistic spoofing attacks, because of spoofing signal not being consistent with genuine signal necessarily and the relative movement between the spoofer and victim receiver, the code Doppler and carrier Doppler between the spoofing and genuine signals are not consistent any more. As for intermediate spoofing [5], it has to make the victim receiver lock the spoofing signal without breaking the current tracking loop. The spoofer has to adjust the code phase and carrier frequency of the spoofing signal to align with the genuine signal. Consequently, the code Doppler and carrier Doppler between the spoofing and the genuine signals are not consistent any more. Generally, in order to align with genuine signal, the code Doppler of the spoofing signal is higher than that of the genuine signal.

In addition, acquisition is the first step of baseband signal processing, so spoofing detection and mitigation at this stage is of great importance and alarm could be set as early as possible. Given this, a method for GNSS spoofing detection and mitigation based on joint detection of code Doppler and carrier Doppler in acquisition is proposed in this paper. Meanwhile, performance evaluation of the proposed method is presented as well. We give a detailed discussion about how genuine signal-to-noise ratio (called signal-to-noise ratio, as well, SNR), spoofing-to-genuine ratio (SGR), acquisition number and acquisition time interval affect the spoofing mitigation performance. At the end of the paper, simulation results are provided to demonstrate the theoretical results.

66.2 Signal Model

Let $s(t)$ denote the received intermediate frequency composite signal, and then it can be expressed as

$$s(t) = s_S(t) + s_G(t) + n(t) \tag{66.1}$$

where $n(t)$ represents the additive white Gaussian noise (AWGN) while $s_S(t)$ represents spoofing signal and $s_G(t)$ represents genuine signal, and they are expressed as follows [13].

$$\begin{aligned} s_S(t) &= \sqrt{2P_S c}\left(\left(f_{code} + f_{S,code}^{dop}\right)t + \phi_{S,code}\right)\cos\left(2\pi\left(f_{IF} + f_{S,carrier}^{dop}\right)t + \phi_{S,carrier}\right) \\ s_G(t) &= \sqrt{2P_G c}\left(\left(f_{code} + f_{G,code}^{dop}\right)t + \phi_{G,code}\right)\cos\left(2\pi\left(f_{IF} + f_{G,carrier}^{dop}\right)t + \phi_{G,carrier}\right) \end{aligned} \tag{66.2}$$

Here P_S and P_G are the power of the spoofing and genuine signals, respectively, $c(.)$ is the pseudo noise code, f_{IF} is the carrier frequency and f_{code} is the nominal PN code chip rate. $f_{S,code}^{dop}$ and $f_{S,carrier}^{dop}$ are the code Doppler and carrier Doppler of the spoofing signal, respectively, while $f_{G,code}^{dop}$ and $f_{G,carrier}^{dop}$ are the code Doppler and carrier Doppler of the genuine signal, respectively. $\phi_{S,code}$, $\phi_{S,carrier}$, $\phi_{G,code}$ and $\phi_{G,carrier}$ are the initial code phase and carrier phase of the spoofing signal and genuine signal, respectively.

Let α and β denote SNR and SGR. Let σ^2 denote the power of noise. Then, they can be expressed as follows,

$$\alpha = \frac{P_G}{\sigma^2}, \quad \beta = \frac{P_S}{P_G} \tag{66.3}$$

For a simplistic spoofing attack, spoofing signals do not have to be consistent with genuine signals. Moreover, there may be a relative movement between the spoofer and the victim receiver. Consequently, $f_{S,code}^{dop}$ and $f_{S,carrier}^{dop}$ would not be consistent with $f_{G,code}^{dop}$ and $f_{G,carrier}^{dop}$ either.

As for an intermediate spoofing attack, it has to make the victim receiver lock the spoofing signal without breaking the current tracking loop [14]. So the spoofer has to adjust the code phase and carrier frequency of the spoofing signals continuously to align with the genuine signals. Usually, there are two strategies for the spoofer to align with the genuine signals received by the victim receivers [14]. Strategy 1 in Ref. [14] maintains the consistency between the carrier Doppler and the code Doppler, and it aligns with the genuine signals by changing the code Doppler and carrier Doppler simultaneously. In this way, both $f_{S,code}^{dop}$ and $f_{S,carrier}^{dop}$ would not be consistent with $f_{G,code}^{dop}$ and $f_{G,carrier}^{dop}$ any more. Strategy 2 in Ref. [14] breaks the consistency between the code Doppler and carrier Doppler. The code Dopplers of the spoofing signals and genuine signals are not the same any more while the carrier Dopplers of them are still consistent. In this way, the consistency between $f_{S,code}^{dop}$ and $f_{S,carrier}^{dop}$ is not maintained.

66.3 The Principle of the Algorithm

As is described above, the code Doppler and carrier Doppler of the spoofing signals are not consistent with the genuine signals any longer. Hence we try to monitor the code Doppler and carrier Doppler of the received signals to detect and mitigate the spoofing signals. As is known to us, acquisition is the first step of GNSS baseband signal processing. It would be timely and alarm could be raised as early as possible if we can make spoofing detection and mitigation at acquisition stage. Hence, we will present the principle of the method for spoofing mitigation based on joint detection of code Doppler and carrier Doppler in acquisition.

The method could be divided into two parts: baseband signal acquisition and spoofing mitigation. They are described in detail as follows.

66.3.1 Baseband Signal Acquisition

Like traditional signal acquisition, baseband signal acquisition here mainly does coherent and non-coherent integrations of received and local signals. And then compared with a preset threshold which is derived from a desired false alarm probability according to Neyman-Pearson criterion [15], we search the code phase domain and the frequency domain to get a peak. However, it is a little different here.

Generally, we can just get coarse code phase and carrier Doppler in acquisition. In order to make spoofing mitigation, we need to get accurate code Doppler and carrier Doppler. Thus, we should do acquisition more than once. Let us denote the acquisition number as N. The time interval between each acquisition would be constant and it is denoted as δ. For each acquisition, let T_{coh} and K denote the coherent integration time and non-coherent integration number, respectively.

Firstly, we can get the non-coherent integration of each acquisition. Meanwhile, after the desired false alarm probability is preset, we can get the corresponding threshold [15]. Then we can get the non-coherent results which are over the threshold. And we record the corresponding code phase and carrier Doppler as,

$$C_n = [c_{n1}, \ldots, c_{nL}], \quad F_n = [f_{n1}, \ldots, f_{nL}] \tag{66.4}$$

Here n represents the nth acquisition and L represents numbers of non-coherent results which are over the threshold. As we know that the ideal code autocorrelation function is a delta impulse function, if sample rate f_s is very high, there may be more than one point over the threshold. We should just retain one point from each delta impulse peak by

$$\left|c_{ni} - c_{nj}\right| \geq f_s / f_{code}, \quad 1 \leq i,\ j \leq L,\ i \neq j \tag{66.5}$$

At each acquisition, we would get two code phases and corresponding carrier Dopplers. If there is only one point over the threshold, then the two code phases

and carrier Dopplers would be the same. Otherwise, if there is more than one point over the threshold, then we should get two code phases and carrier Dopplers whose corresponding correlation results are the first and second maximum. The code phase and corresponding carrier Doppler at the nth acquisition would be denoted as

$$C_n = [c_{n1}, c_{n2}], \quad F_n = [f_{n1}, f_{n2}] \tag{66.6}$$

After N acquisition, we obtain a code phase matrix and a carrier Doppler matrix, which are expressed as follows,

$$C = \begin{bmatrix} c_{11} & c_{12} \\ c_{21} & c_{22} \\ \cdots & \cdots \\ c_{N1} & c_{N2} \end{bmatrix}_{N\times 2,} \quad F = \begin{bmatrix} f_{11} & f_{12} \\ f_{21} & f_{22} \\ \cdots & \cdots \\ f_{N1} & f_{N2} \end{bmatrix}_{N\times 2} \tag{66.7}$$

66.3.2 Spoofing Mitigation

In baseband signal acquisition, after several acquisitions, we get the code phase matrix and carrier Doppler matrix. Then in spoofing mitigation stage, we would identify spoofing signal and genuine signal based on two matrix in Eq. (66.7). As we all know, the code Doppler is proportional to the carrier Doppler for genuine signal, because the Doppler effect is caused by the relative motion between the satellite and the receiver. Generally, for civilian receivers and L1 C/A signal, the motion is not highly dynamic, so relative velocity is less than 2 km/s, the corresponding carrier Doppler is less than 10 KHz. And the C/A code rate is 1.023 MHz, so the corresponding code Doppler is less than 6 Hz. As for the spoofing signal, in order to align with the genuine signal, its code Doppler is usually higher and it is not consistent with the carrier Doppler any more. Therefore, we should firstly find out the code Dopplers and carrier Dopplers of both genuine and spoofing signals so that we can distinguish them. Generally, the code and carrier Doppler of the genuine signal and spoofing signal vary slowly and we can treat them as constant in a short time. Given this, in order to find out the code Doppler of the genuine signal and spoofing signal, we should actually find out two straight lines from the code phase matrix C, the slope of each line is actually the desired code Doppler. And the intercept of each line is actually their corresponding initial code phase. Similarly, we could find out two straight lines from the carrier Doppler matrix F, the average intercept of each line is actually the corresponding carrier Doppler.

Let t_n denote the start time of each acquisition, we can easily see that $t_n - t_{n-1} = \delta$. In order to fit two straight lines from the given code phase matrix C, we should firstly get the classification line of the code phase matrix by

$$A = \frac{\sum_{n=1}^{N} (c_{n1} + c_{n2} - 2\bar{c})(t_n - \bar{t})}{2\sum_{n=1}^{N} (t_n - \bar{t})^2} \tag{66.8}$$

$$B = \bar{c} - A\bar{t} \tag{66.9}$$

where

$$\bar{t} = \frac{1}{N}\sum_{n=1}^{N} t_n \tag{66.10}$$

$$\bar{c} = \frac{1}{2N}\sum_{n=1}^{N} (c_{n1} + c_{n2}) \tag{66.11}$$

With the parameter A and B, we can easily calculate the point of the classification line at time t_n. They can be expressed as the following equation.

$$c_n = At_n + B \tag{66.12}$$

In case that the two lines would intersect each other, we should get the possible intersection point and it can be denoted as m.

$$m = \underset{1 \le n \le N}{\arg} \min\{\min(c_{n1} - c_n, c_{n2} - c_n)\} \tag{66.13}$$

Then we could divide the code phase matrix into two separate sets by checking whether the code phase at time t_n is below the classification line or not. That is to say, the two separate code phase sets could be expressed as follows.

$$\begin{aligned} C_1 &= \{c_{ni} | c_{ni} > c_n, 1 \le n \le m, 1 \le i \le 2\} \\ &\quad \cup \{c_{ni} | c_{ni} \le c_n, m < n \le N, 1 \le i \le 2\} \\ C_2 &= \{c_{ni} | c_{ni} \le c_n, 1 \le n \le m, 1 \le i \le 2\} \\ &\quad \cup \{c_{ni} | c_{ni} > c_n, m < n \le N, 1 \le i \le 2\} \end{aligned} \tag{66.14}$$

Correspondingly, we could divide the carrier Doppler matrix into two separate sets using the same rules. They can be expressed as the following equations.

$$\begin{aligned} F_1 &= \{f_{ni} | c_{ni} > c_n, 1 \le n \le m, 1 \le i \le 2\} \\ &\quad \cup \{f_{ni} | c_{ni} \le c_n, m < n \le N, 1 \le i \le 2\} \\ F_2 &= \{f_{ni} | c_{ni} \le c_n, 1 \le n \le m, 1 \le i \le 2\} \\ &\quad \cup \{f_{ni} | c_{ni} > c_n, m < n \le N, 1 \le i \le 2\} \end{aligned} \tag{66.15}$$

For convenience, we would rewrite the above four sets as follows.

$$\begin{aligned} C_1 &= \{c_1(n) | 1 \le n \le N\}, \quad C_2 = \{c_2(n) | 1 \le n \le N\} \\ F_1 &= \{f_1(n) | 1 \le n \le N\}, \quad F_2 = \{f_2(n) | 1 \le n \le N\} \end{aligned} \tag{66.16}$$

Then we can get the corresponding code Doppler and carrier Doppler by

$$f_{i,code}^{dop} = \frac{\sum_{n=1}^{N}\left(c_i(n) - \frac{1}{N}\sum_{n=1}^{N} c_i(n)\right)(t_n - \bar{t})}{\sum_{n=1}^{N}(t_n - \bar{t})^2}, \quad 1 \le i \le 2 \tag{66.17}$$

$$f_{i,carrier}^{dop} = \frac{1}{N}\sum_{n=1}^{N} f_i(n), \quad 1 \le i \le 2 \tag{66.18}$$

For genuine signal, the code Doppler should be proportional to the carrier Doppler, and the relationship between them could be expressed as $f_{G,code}^{dop}/f_{G,carrier}^{dop} = R$. Take civil L1 C/A signal as an example, R would be 1/1540. Thus, we should test the ratio between the code Doppler and carrier Doppler. The ratio of the spoofing signal would be farther from R than that of the genuine signal. Then we can find out the spoofing signal by a preset threshold R_T. If the ratio is over the threshold, we declare that it is spoofing signal. Otherwise, it is genuine signal. That is to say, if $\left|f_{i,code}^{dop}/f_{i,carrier}^{dop} - R\right| > R_T$, then corresponding C_i and F_i would be the code phase and carrier Doppler of spoofing signal, and the tracking loop would not lock it. Otherwise, it would be the code phase and carrier Doppler of genuine signal. In this way, we successfully mitigate the spoofing signal.

66.4 Performance Analysis and Evaluation

As we know, the performance of the proposed method is influenced by many factors, such as SNR, SGR, acquisition number, acquisition time interval and sampling rate, etc. Here we would give a detailed analysis about how SNR, SGR and acquisition number affect the spoofing mitigation performance.

66.4.1 SNR and SGR

We would regard spoofing mitigation probability as a parameter to evaluate the performance of the proposed method. Since the first step of the proposed method is baseband signal acquisition, it is obvious that the power of the genuine signal and spoofing signal will influence the spoofing mitigation probability.

Here we assume that the spoofing signal is independent with the genuine signal. We know that the signal acquisition is set up as a hypothesis test, testing the hypothesis H_1 that genuine signal is present, the hypothesis H_2 that spoofing signal is present versus the hypothesis H_0 that the signal is not present. Thus the corresponding general probability density of each acquisition could be expressed as follows [15], where f_s is the data sample rate and $I_{K-1}(.)$ is a modified Bessel function of the first kind.

$$
\begin{aligned}
f(x;H_0) &= \frac{1}{2^K(K-1)!}x^{K-1}\mathrm{e}^{-x/2}; \quad x \geq 0 \\
f(x;H_1) &= \frac{1}{2}\left(\frac{x}{2K\alpha f_s T_{coh}}\right)^{\frac{1}{2}(K-1)}\mathrm{e}^{-\frac{1}{2}(x-2K\alpha f_s T_{coh})} \\
&I_{K-1}\left(\sqrt{2K\alpha f_s T_{coh}x}\right); \quad x \geq 0 \\
f(x;H_2) &= \frac{1}{2}\left(\frac{x}{2K\alpha\beta f_s T_{coh}}\right)^{\frac{1}{2}(K-1)}\mathrm{e}^{-\frac{1}{2}(x-2Kf_s\alpha\beta T_{coh})} \\
&I_{K-1}\left(\sqrt{2K\alpha\beta f_s T_{coh}x}\right); \quad x \geq 0
\end{aligned}
\tag{66.19}
$$

Let P_d denote the probability of successful detection of the two desired code phases and carrier Dopplers, then it could be expressed as Eq. (66.20).

$$
P_d = \int_{TH}^{\infty}\int_{TH}^{\infty} f(x_2;H_2)f(x_1;H_1)dx_1dx_2 \tag{66.20}
$$

According to Neyman-Pearson criterion, TH is a threshold which is related to the preset probability of false alarm. And it could be derived by the following equation,

$$
f(x;H_0) = \frac{1}{2^K(K-1)!}x^{K-1}\mathrm{e}^{-x/2}; \quad x \geq 0 \tag{66.21}
$$

From Eqs. (66.20) and (66.21) we can see that, if the power of the genuine signal and the spoofing signal is stronger, the probability of successful detection would be higher. However, although the spoofing signal is independent with the genuine signal, if the power of the genuine signal (spoofing signal) is much stronger than the spoofing signal (genuine signal), the probability of successful detection would be very low. That is because the actual cross correlation of the genuine signal and spoofing signal is not zero. If the power difference of the genuine signal and spoofing signal is significant, then the cross correlation would be very large. As a consequence, the threshold would rise up, and the probability of successful detection would fall down.

Take L1 C/A signal as an example, the initial code phase of the genuine signal and spoofing signal is 250 and 247, correspondingly. The code Doppler of the genuine signal and the spoofing signal is 2.6 and 10 Hz while the carrier Doppler of them is 4,000 Hz. The parameters for the mitigation method is as follows, baseband signal sample rate is 1.023 MHz, coherent integration time $T_{coh} = 1$ ms, non-coherent number $K = 4$. And the acquisition number $N = 25$. Probability of false alarm is 1e−3 and the threshold R_T is 1.25e−3. The simulation result is illustrated in Fig. 66.1. We can declare that, the probability would decrease if SGR is too large or too small. If SGR is 0, which means the genuine signal has the same power with the spoofing signal, the probability would be the highest. And we can also find that the probability would monotonically increase as SNR increases when

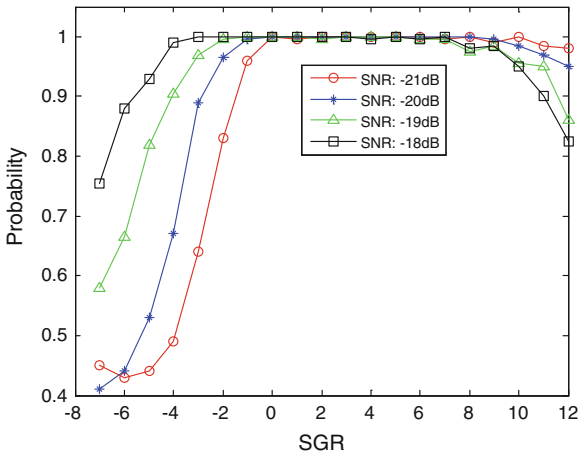

Fig. 66.1 Probability of successful spoofing mitigation

spoofing signal is weaker than genuine signal. And it is actually the opposite when spoofing signal is stronger than genuine signal. That is because of the influence of the cross correlation as is described above.

66.4.2 Acquisition Number

The core idea of the proposed method is spoofing identification by joint detection of code Doppler and carrier Doppler in acquisition. However, as we all know, we can just get coarse code phase and carrier Doppler in acquisition. In order to get accurate code Doppler and carrier Doppler, we need to do acquisition several times. The time interval between each acquisition should be not too large or too small. If it is smaller than the hardware computation time, then we can't get correct result without additional hardware. If it is too large, it may take a long time to identify the spoofing signal, which is not available for some critical applications and services. Moreover, for the intermediate spoofing attack, if the time interval is too large, maybe the code phase of the spoofing signal would not change any more since it has aligned with the genuine signal.

As the code phase and carrier Doppler of each acquisition is not accurate enough because of the noise and limited sample rate. As the acquisition number increases, carrier Doppler derived through Eq. (66.18) would be much more accurate. And if we get more code phases, we can get more precise code Doppler through Eqs. (66.8–66.17).

On one hand, larger acquisition number would result in more precise result. On the other hand, if acquisition number is too large, it would take more time to identify the spoofing signal for each channel. Here we still take L1 C/A signal as an example, SNR and SGR are −20 and 0 dB, correspondingly. The time interval is 40 ms, the threshold R_T is 1.25e−3, as acquisition number varies from 15 to 40,

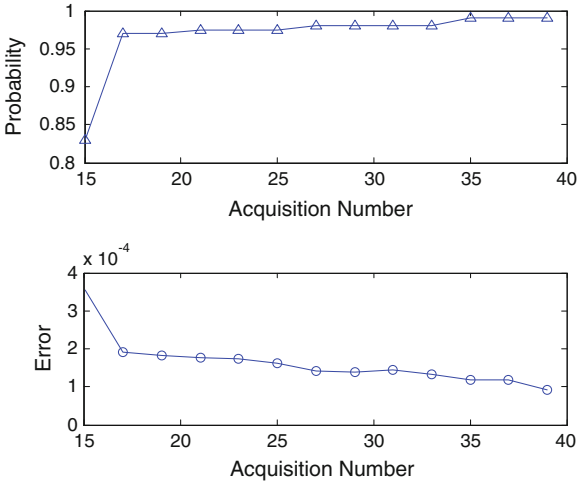

Fig. 66.2 Probability of successful spoofing mitigation and computation error of the method with acquisition number increasing

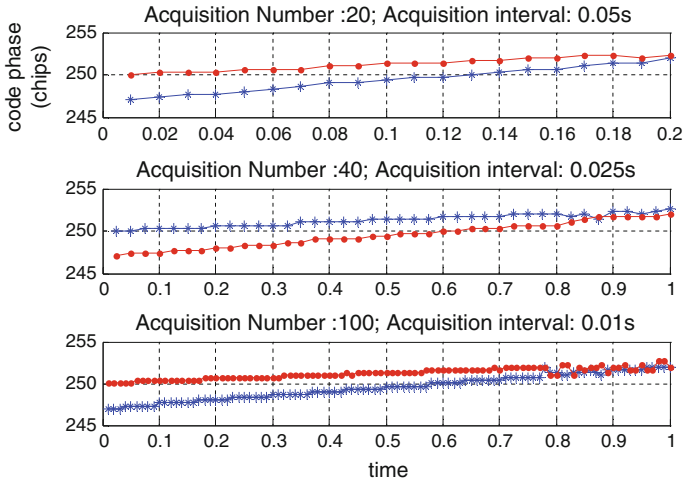

Fig. 66.3 Code phases of genuine and spoofing signals with different acquisition numbers and intervals

and probability of successful spoofing mitigation is listed as the upper part of Fig. 66.2. We find that the probability monotonically increases as the acquisition number increases. And computation error of the method is listed as the lower part of Fig. 66.2. We find that the error is becoming smaller while the acquisition number increases.

Meanwhile, by setting different acquisition numbers and acquisition intervals, code phases of genuine and spoofing signals are illustrated in Fig. 66.3. When

acquisition number is 40 and acquisition interval is 25 ms, the result would be more accurate than the case when acquisition number is 20 and acquisition interval is 50 ms. However, when acquisition number is 100 and acquisition interval is 10 ms, the performance is not improved so much. That is because the interval is too small.

66.5 Conclusion

An increasing attention is focused on GNSS spoofing attacks and anti-spoofing recently. Many anti-spoofing methods are proposed in the past few years, but they are mainly focused on spoofing detection. In this paper, we present a method for spoofing mitigation in acquisition by joint detection of code Doppler and carrier Doppler. The proposed method in this paper can not only detect but also mitigate spoofing signal. And the method make spoofing mitigation in acquisition, which is timely and alarm can be raised up earlier compared with other anti-spoofing methods. As the method is implemented in acquisition, it doesn't require any additional hardware and it can make spoofing mitigation continuously without interrupt the normal tracking loop.

Future research will focused on a much more complete performance analysis of the method, including the influence of sample rate and the threshold R_T. How to set the threshold R_T adaptively should also be investigated.

References

1. U. S. Government (2010) Global positioning system. http://www.gps.gov
2. Cavaleri A, Motella B, Pini M, Fantino M (2010) Detection of spoofed GPS signals at code and carrier tracking level. In: Proceedings of the 5th ESA workshop on satellite navigation technologies and European workshop on GNSS signals and signal processing (NAVITEC '10), pp 1–6, December 2010
3. Humphreys TE, Ledvina BM, Psiaki ML, O'Hanlon BW, Kintner PM (2008) Assessing the spoofing threat: development of a portable GPS civilian spoofer. In: Proceedings of the ION GNSS international technical meeting of the satellite division
4. Warner JS, Johnston RG (2002) A simple demonstration that the global positioning system (GPS) is vulnerable to spoofing. J Secur Adm
5. Humphreys TE et al (2008) Assessing the spoofing threat: development of a portable GPS civilian spoofer. In: The proceedings of ION GNSS 2008, Savannah, GA, 16–19 Sept 2008
6. Ledvina BM et al (2010) An in-line anti-spoofing device for legacy civil GPS receivers. In: The proceedings of national technical meeting—ION NTM 2010, San Diego, CA, 25–27 Jan 2010
7. Nicola M, Musumeci L, Pini M, Fantino M, Mulassano P (2010) Design of a GNSS spoofing device based on a GPS/Galileo software receiver for the development of robust countermeasures. In: ENC GNSS 2010, Braunschweig, Germany, 19–21 Oct 2010
8. O'Hanlon BW, Psiaki ML, Humphreys TE et al (2012) Real-time spoofing detection using correlation between two civil GPS receiver. In: Proceedings of the 25th international

technical meeting of The Satellite Division of the Institute of Navigation (ION GNSS 2012), vol 2001, pp 3584–3590
9. Meurer M, Konovaltsev A, Cuntz M, Hättich C () Robust joint multi-antenna spoofing detection and attitude estimation using direction assisted multiple hypotheses RAIM. In: Proceedings of the 25th international technical meeting of The Satellite Division of the Institute of Navigation (ION GNSS 2012), Nashville, TN, Sept 2012, pp 3007–3016
10. Montgomery P, Humphreys TE (2009) A multi-antenna defense: receiver-autonomous GPS spoofing detection. Inside GNSS (March/April):40–46
11. Humphreys TE, Ledvina BM, Psiaki ML et al (2008) Assessing the spoofing threat: development of a portable GPS civilian spoofer. In: Proceedings of the ION GNSS international technical meeting of the satellite division
12. Ledvina BM, Bencze WJ, Galusha B et al (2001) An in-line anti-spoofing device for legacy civil GPS receivers. In: Proceedings of the 2010 international technical meeting of the Institute of Navigation, pp 698–712
13. Kaplan ED, Hegarty CJ (2005) Understanding GPS: principles and applications, 2nd edn. Artech House, Boston
14. Gao Y, Li H, Lu M et al (2013) Intermediate spoofing strategies and countermeasures. Tsinghua Sci Technol 18(6):599–605
15. Parkinson BW, Spilker JJ (eds) (1996) Global positioning system: theory and applications, vol 1. AIAA

Chapter 67
Demonstration of Signal Tracking and Scintillation Monitoring Under Equatorial Ionospheric Scintillation with a Multi-Frequency GNSS Software Receiver

Tao Lin and Gérard Lachapelle

Abstract Ionospheric scintillations can degrade the performance of GNSS receivers by causing fading in the amplitude and phase of trans-ionospheric GNSS signals. Considering the current solar maximum, a research project was established between the Brazilian Institute of Geography and Statistics (IBGE), the University of the State of Rio de Janeiro, and the Position, Location and Navigation (PLAN) Group at the Department of Geomatics Engineering, University of Calgary (UofC), to investigate the effects of equatorial ionospheric scintillation on GNSS signal tracking performance and measurement quality with the latest receiver technology. A so-called shared-channel architecture, which supports the inter-frequency and inter-satellite code/carrier aiding, has been proposed in this paper. Based on the data collected during this project, the proposed shared-channel architecture has been proven to provide significant benefits over standard receiver processing architecture.

Keywords Equatorial scintillation · GNSS signals · GNSS software receiver · Satellite and frequency diversity

67.1 Introduction

The solar maximum of the current Sunspot Cycle 24 was predicted to happen in 2013. As a result of the higher Sun activity, ionospheric scintillation causing amplitude fading and phase fluctuation of the received GNSS signals is expected to happen more often and strongly. A research project was consequently established in 2012, by the Brazilian Institute of Geography and Statistics (IBGE), the

T. Lin (✉) · G. Lachapelle
University of Calgary, Calgary, AB, Canada
e-mail: tlin@ucalgary.ca

J. Sun et al. (eds.), *China Satellite Navigation Conference (CSNC) 2014 Proceedings: Volume I*, Lecture Notes in Electrical Engineering 303,
DOI: 10.1007/978-3-642-54737-9_67,

University of the State of Rio de Janeiro, and the Position, Location and Navigation (PLAN) Group of the Department of Geomatics Engineering, University of Calgary (UofC), to investigate the effects of equatorial ionospheric scintillation on GNSS signal tracking performance and measurement quality with the latest receiver technology. The multi-constellation multi-frequency GNSS Software Navigation Receiver (GSNRx^{TM}) developed by the UofC PLAN Group was used in this project due to its multi-constellation multi-frequency processing capability and its flexibility to adopt the latest receiver technology for GNSS signal tracking under strong equatorial scintillation.

This paper first introduces so-called shared-channel architecture for signal acquisition and tracking under scintillation. The scintillation parameter estimation implemented in GSNRx^{TM} are then described, as well as the data collection approaches. The assessment of the proposed architecture is evaluated based on results in the observation domain, through detecting dual frequency cycle slips and in the position domain by submitting the GSNRx^{TM}-derived observations to the Natural Resources Canada (NRCan) Canadian Spatial Reference System Precise Point Positioning (CSRS-PPP) Service. The results are also compared with those obtained using the RIOD station observations with a commercial hardware receiver to assess the performance of the GSNRx^{TM}.

67.2 Shared-Channel Architecture

Ionospheric scintillations are rapid temporal fluctuations in both amplitude and phase of trans-ionospheric GNSS signals caused by the scattering of irregularities in the distribution of electrons encountered along the radio propagation path. The occurrence of scintillation has large day-to-day variability. The most severe scintillations are observed in the polar (at auroral latitudes) and near the equator ($\pm 20°$ of geomagnetic equator).

Equatorial amplitude scintillation affects both code/carrier tracking and degrades pseudorange and carrier phase measurements. Deep amplitude fades over sufficient duration can cause loss of lock in both code and carrier tracking within a GNSS receiver. Equatorial phase scintillation adversely affects the operation of a receiver's phase lock loop (PLL) and leads to carrier cycle slips, navigation data bit errors, and completely loss of carrier lock. Carrier phase tracking is very sensitive to scintillation due to its stringent tracking threshold. Therefore one solution for the scintillation problem is to employ a frequency lock loop (FLL) to replace a PLL for carrier tracking, due to its better robustness to signal attenuation and signal dynamics. However, many GNSS applications require (multi-frequency) carrier phase measurements, which a FLL cannot provide.

Despite the challenge of phase tracking under strong equatorial scintillation, several signal processing techniques can be used to improve the carrier tracking robustness. The common ones are FLL-assisted-PLL, adaptive-bandwidth PLL, and data stripping. Given the robustness of a FLL, it is wise to consider using a

FLL to aid a PLL. This combined carrier tracking loop is called FLL-assisted-PLL. In a typical implementation of a FLL-assisted-PLL, a FLL and a PLL operate in parallel to jointly control the carrier numerical controlled oscillator (NCO). The overall performance of such a FLL-assisted-PLL is between a standalone FLL and a standalone PLL depending on the loop noise bandwidths. An adaptive-bandwidth PLL is another popular option for carrier tracking under scintillation. The use of a wide PLL bandwidth can help maintain phase tracking during periods of phase scintillation by tracking rapidly changing phase. On the other hand, a narrow PLL bandwidth is desirable to tolerate amplitude scintillation with the ability to track at low carrier to noise-density (C/N_0) conditions. The adaptive-bandwidth PLL is typically implemented by a Kalman filter with a time-varying Kalman gain based on the C/N_0 conditions, because Kalman filter explicitly models the receiver clock and optimally adapts its bandwidth based on C/N_0.

It is well-known that a pure PLL discriminator provides an improved signal tracking threshold by up to 6 dB compared to a Costas discriminator. Modernized GNSS signals provide a pilot (data-less) component and a data component. Although tracking only the pilot component can bring a 3 dB loss due to the power sharing of data and pilot component, there is still a net gain of 3 dB due to the pure PLL. Therefore, it is recommended to track the pilot component of modernized GNSS signals (e.g., GPS L2C and L5) under scintillation. For the GNSS signals which do not have a pilot component, it is still possible to utilize a pure PLL discriminator with data stripping. For example, for the GPS L1 C/A signal, after storing a complete copy of the full navigation data bits, or with external aiding, it is possible to predict the navigation data bits until the navigation message changes. This is so called data stripping. With the help of data stripping, it is still possible to use a pure PLL discriminator instead of a Costas discriminator in short-term for better carrier tracking under scintillation.

The techniques discussed above focus on improving the carrier tracking in a single-frequency scalar-based receiver. Carrier tracking under scintillation can be improved by using multi-satellite and multi-frequency aiding. This is because scintillation rarely occurs on all visible satellites simultaneously on account of isolated nature of the electron irregularities mentioned above. In addition, scintillation is carrier frequency dependent. Both amplitude and phase scintillation level has an inverse relation with the signal carrier frequency. The lower the carrier frequency, the stronger the scintillation it is. In other words, if the same GPS signal was broadcast on L1, L2 and L5 frequencies at same power, it is more likely that scintillation will impact the L2 and L5 signals more than the L1 signal.

For the benefits of both frequency diversity and satellite diversity, it is important to implement the multi-satellite and multi-frequency aiding in a multi-frequency GNSS receiver. A typical implementation of such a processing architecture—herein referred to Shared-Architecture A—is shown in Fig. 67.1.

For the purpose of a better illustration, only the processing for GPS L1 C/A and L2C signals is shown in the figure. Each satellite has multiple channels for tracking signals on different frequencies. Each channel has a Doppler removal and correlation (DRC) unit, a local signal generator unit, and a PLL. In this

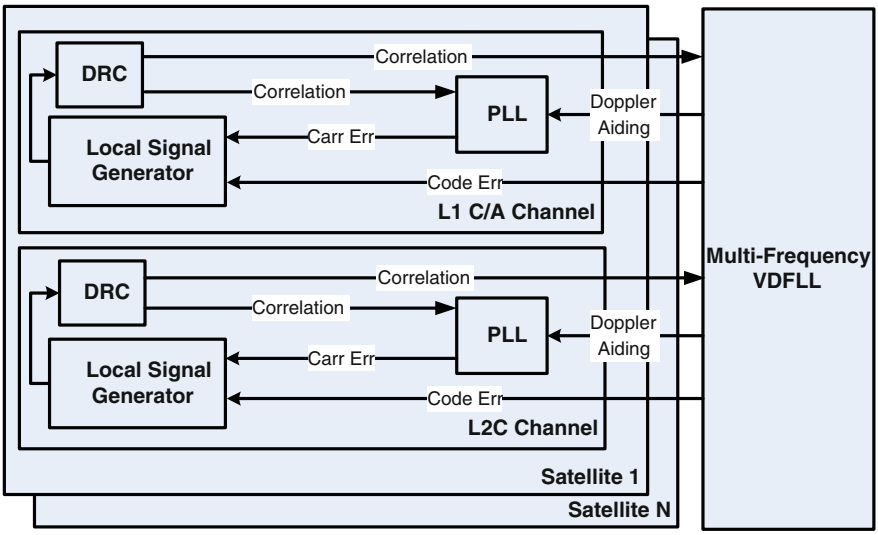

Fig. 67.1 Shared-Architecture A

architecture, the key component is the multi-frequency vector delay and frequency lock loop (VDFLL). It receives the correlation from all channels and track the code and frequency of all signals from all satellites jointly. Regardless the implementation variations, a VDFLL should include a local PVT (Position, Velocity, and Time) engine which accepts multi-frequency code and Doppler measurements. The most common choice of this local PVT engine is an extended Kalman filter.

The VDFLL provides two feedback signals for each channel. One is the code phase error or the code Doppler to control the code NCO in the local signal generator, and the other is the carrier Doppler to aid the PLL in each channel. These code phase errors and the carrier Doppler values are derived from the local PVT engine. With the carrier Doppler aiding from the VDFLL, the PLL in each channel only needs to track the residual Doppler (i.e., that induced by scintillation). The main implementation challenge of Shared-Architecture A is a reliable multi-constellation multi-frequency PVT engine, as implementation of multi-frequency aiding and multi-satellite aiding are dependent upon it.

An alternative processing architecture, named Shared-Architecture B, is shown in Fig. 67.2. Compared to Shared-Architecture A, this architecture utilizes a delay lock loop (DLL) for code tracking in each channel and the multi-frequency VDFLL is replaced by a single frequency VFLL and a code phase estimator. In this architecture, DLLs are carrier-aided by PLLs to provide low noise pseudorange measurements. As the carrier aiding from PLLs are fused by a VFLL, the multi-satellite aiding still propagates to DLLs indirectly from the PLLs in L1 C/A channels, even though a vector delay lock loop (VDLL) is not used in this case. Instead of being used for controlling the code NCOs, the code phase estimates

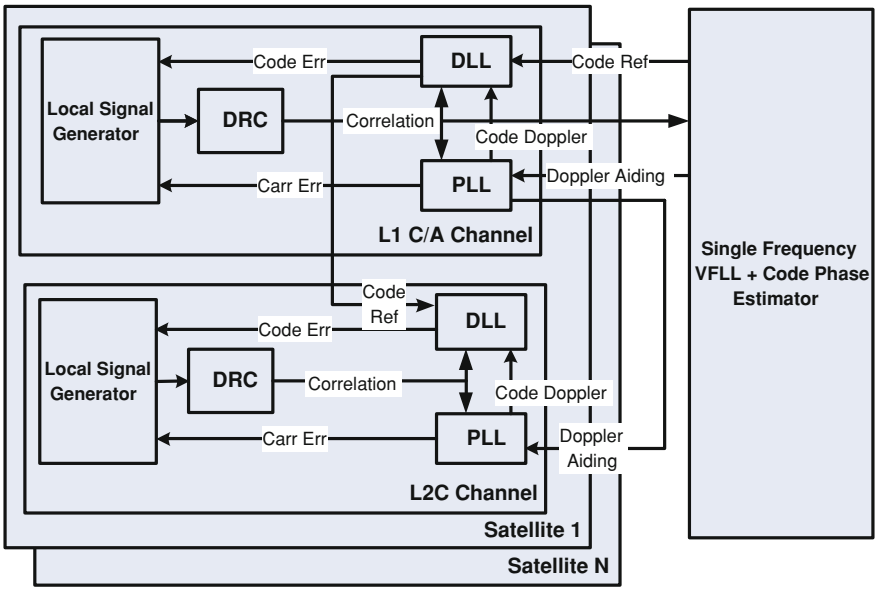

Fig. 67.2 Shared-Architecture B

derived from the single frequency PVT engine are applied to detect loss of code lock on L1 C/A signals and to steer the DLLs when loss of code lock does occur.

In Shared-Architecture B, because the L1 C/A signal is more resistant to equatorial scintillation than the L2C signal, the L2C PLLs are aided by the L1 C/A PLLs. Since the carrier Doppler from the L1 C/A channels is already fused by the VFLL, the L2C PLLs are benefiting from the satellite diversity as well. In the L2C channels, similar to the L1 C/A channels, the carrier-aided DLLs are used for code tracking. The estimated L2C code phases based on the L1 C/A timing information are only used for detecting the loss of code locks and for code steering after loss of locks. Shared-Architecture B also has the advantage of implementing multi-satellite aiding and multi-frequency aiding separately. For example, if only the multi-frequency aiding mode is needed, the receiver can simply disable the VFLL aiding and keep the L1-to-L2 aiding, which Shared-Architecture A cannot.

For signal acquisition, both architectures only acquire the signal on a single frequency (referred to the master frequency signal here), since the code phase and carrier Doppler parameters of other frequency signals can be directly estimated by the carrier Doppler and timing information of the master frequency signal. In order words, the timing information and carrier Doppler from the master frequency signal can be used to directly initialize the code and carrier tracking loops of other frequency signals. The typical choice of the master frequency signal is the GPS L1 C/A signal, due to its shorter ranging code and stronger scintillation resistance compared to others.

Both Shared-Architecture A and Shared-Architecture B were implemented in a multi-constellation multi-frequency GNSS software receiver. Only the results of the Shared-Architecture B with the intermediate frequency (IF) data affected by equatorial ionospheric scintillation are presented in this paper, but results with Shared-Architecture A were similar.

67.3 Scintillation Monitoring

Scintillation monitoring capability is one of the key features, which has been added into GSNRx^{TM} during this research. It is useful not only for scientific research on scintillation but also for signal and measurement quality control. The amplitude scintillation index (S4) and phase scintillation variance are commonly used to indicate the level of the scintillation activity. The S4 index can be computed as [1]:

$$S4 = \sqrt{S4_T - S4_N} \tag{67.1}$$

where the total $S4_T$ index includes both the intensity variation and noise effect, and $S4_N$ is the noise impact on the S4 index, which can be computed as [1]

$$S4_N = \sqrt{\frac{100}{C/N_0}\left(1 + \frac{500}{19C/N_0}\right)} \tag{67.2}$$

The phase scintillation variance is the typical parameter used to reflect the phase scintillation level. The key step of computing the phase scintillation variance is the phase de-trending process. The purpose of the phase de-trending process is to remove the low frequency effect on carrier phase, such as satellite motion, satellite clocks, receiver clock, tropospheric delay, ionospheric delay, unwanted multipath and possible user motion if the antenna is not static. As shown in Van Dierendonck et al. [1], various phase de-trending methods are possible to achieve this goal. The one implemented in GSNRx^{TM} is the high pass filtering method, which is proposed by Van Dierendonck et al. [1]. It utilizes a 6th order Butterworth high pass filter with a cut-off frequency of 0.1 Hz to de-trend the carrier phase measurements.

In the equatorial region, the rapid phase changes, which are reflected on the phase scintillation variance, may be associated with signal fades, which are reflected on S4 (but not necessarily the contrary), as shown by SBAS-IONO Group [2] and Xu et al. [3]. Therefore the S4 index values are more commonly used to identify the occurrence of equatorial scintillation. Usually the S4 index values of below 0.3 associated with weak scintillation and those above 0.6 with strong scintillation.

67.4 Data Collection

In order to collect the IF data affected by equatorial scintillation necessary to perform this study, a narrow-band dual-frequency front-end (GPS L1/L2) was installed at the facilities of IBGE Coordination of Geodesy in Rio de Janeiro. The front-end has a bandwidth of 8 MHz and collects complex I/Q samples at 10 MHz. The station (referred to RIOFE herein) is located under the Southern lobe of the equatorial anomaly's daily path, which is located on average ±15° around the Geomagnetic Equator. Data was collected daily after sunset (20:00–24:00 local time, 23:00–3:00 Universal Time), from June 4, 2012 to March 29, 2013, whenever equatorial scintillation occurred. The actual occurrence of strong scintillation was verified by checking the S4 values measured by a Septentrio PolarRxS ionospheric scintillation monitoring receiver belonging to the Concept for Ionospheric Scintillation Mitigation for Professional GNSS in Latin America (CIGALA) network. Based on the S4 values measured by the closest operational CIGALA stations to Rio de Janeiro, the IF data collected the previous day at RIOFE was deleted or saved.

Due to the front-end bandwidth limitation, the dual-frequency front-end cannot capture GPS L2P signal. In order to examine the impact of equatorial scintillation on L2P and provide a reference for the IF data, the navigation measurements from a Trimble NetRS hardware receiver, which is located at the RIOD station at IBGE Coordination of Geodesy in Rio de Janeiro only 5 m away from the site (RIOFE) where IF data was collected for this research. From the IF data collection available, three session files strongly affected by scintillation were selected for processing and analysis: October 24 and November 17, 2012, and February 20, 2013. In addition to these files, two more were selected corresponding to a quiet scintillation time period (this one from 22:10 to 2:10 local time on June 04–05, 2012) and to a session with fewer satellites affected by scintillation (March 28, 2013).

67.5 Performance Assessment

The performance of the proposed shared-channel architecture implemented in GSNRx^{TM} is assessed in terms of the number of valid measurements and solution accuracy. The results presented in this paper is based on Shared-Architecture B. Figure 67.3 shows the percentile of valid L1 C/A and L2C phase observations with the Shared-Architecture B and a standard architecture (without using multi-frequency and multi-satellite aiding). Valid phase observations are defined as those where the carrier phase observations have phase lock indicator (PLI) value larger than 0.6 (see Further Reading) and no cycle slips are detected. The results are based on 8 h of data using 2 Hz measurements collected on October 24 and November 17, 2012. The S4 values in this figure are the S4 estimates with the S4 estimator presented earlier. As shown, due to the benefits of multi-frequency

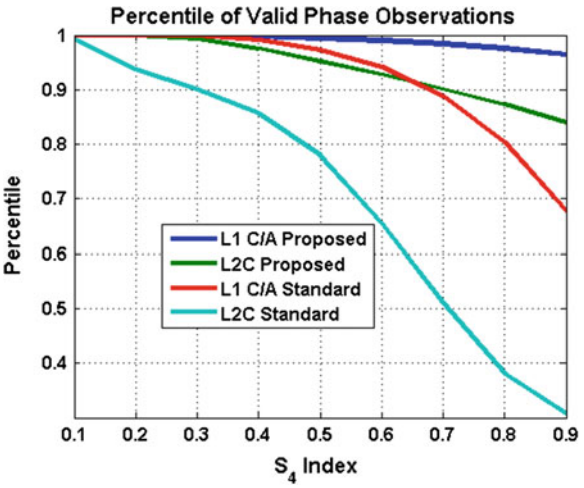

Fig. 67.3 Percentile of valid phase observations ("L1 C/A proposed" and "L2C proposed" refers to the L1 C/A and L2C carrier phase observations from the proposed Shared-Architecture B; "L1 C/A standard" and "L2C standard" refers to the L1 C/A and L2C carrier phase observations from a standard architecture)

multi-satellite aiding, Shared-Architecture B provides significantly more valid measurements than a standard architecture over the entire S4 range, especially for the L2C carrier phase. This demonstrates the importance of the multi-frequency multi-satellite aiding for a multi-frequency GNSS receiver.

In order to assess the performance of GSNRx^{TM} in the position domain, the L1 and L2 code and phase measurements generated by GSNRx^{TM} for the five sessions at RIOFE were submitted to the NRCan CSRS-PPP Service. This service can perform single or dual frequency static or kinematic positioning. The measurements collected at RIOD were also submitted to this service for comparison. All measurements were processed by NRCan CSRS-PPP Service in kinematic mode to allow the necessary degree of freedom for the coordinates to be affected by the ionosphere through epoch by epoch estimation. PPP L1 code solutions were generated for all five sessions using RIOFE and RIOD measurements. The solutions using both GSNRx^{TM}-derived measurements and Trimble NetRS-derived measurements have similar accuracy regardless the occurrence of scintillation. The solution using GSNRx^{TM}-derived measurements is noisier mainly due to the front-end bandwidth limitation. There is a strong correlation between both solutions when scintillation occurs. In both receivers, to reduce the code noise, the DLL was aided by the carrier Doppler from the PLL, which is influenced by scintillation. Thus the accuracy of both solutions is degraded by scintillation.

The dual frequency measurements (L1 and L2 carrier phase and code) can be generated by GSNRx^{TM} for IIR-M and IIF satellites. CSRS-PPP requires a minimum of five satellites with all four types of measurements for at least one epoch in order to initialize a dual frequency (i.e., ionospheric-free) processing. Once the solution is initialized, the number of satellites' requirement is reduced to four. The November 17, 2012 dataset fulfilled these requirements for 1 h 38 min 45 s, thus CSRS-PPP was able to generate a precise dual frequency PPP solution using this subset. Considering the higher accuracy of this type of solution, the PPP

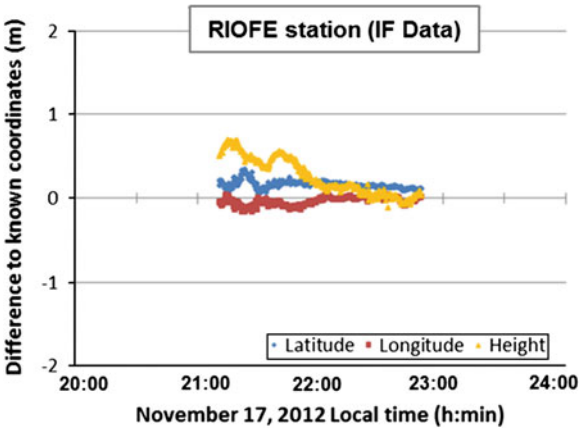

Fig. 67.4 Position errors with GSNRx™ measurements

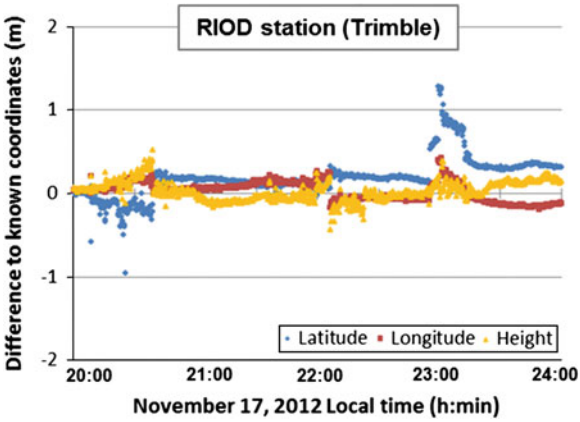

Fig. 67.5 Position errors with Trimble NetRS measurements

processing estimated residual tropospheric parameters and corrected for ocean loading effects, as the stations are relatively close to the Brazilian coast. Figure 67.4 shows the position errors processed by dual frequency CSRS-PPP. The same type of solution using measurements collected at the RIOD station for all visible satellites during the entire 4-h session is shown in Fig. 67.5. The PPP solution for RIOFE was generated using measurements of only four to five satellites per epoch for less than 2 h, whereas the solution for RIOD was produced using observations for all visible satellites in each epoch for 4 h, since the front-end used at RIOFE is a narrow-band front-end, which cannot capture L2P signals, while Trimble NetRS at RIOD can generate L2P measurements for all satellites in view. The corresponding RMS and mean values of the position errors for all observation sessions at RIOFE and RIOD are listed in Table 67.1. The RMS and mean values for all sessions are generally very similar for RIOFE and RIOD. PPP L1 code position difference RMS values range from a sub-metre level (horizontal) and a metre level (vertical) in a session with no scintillation to a 5-m level

Table 67.1 RMS and mean values of the position errors at RIOFE and RIOD

Station	Type of PPP solution	Difference to known coordinates (m)					
		Latitude		Longitude		Height	
		RMS	Mean	RMS	Mean	RMS	Mean
RIOFE	L1 code	0.7	0.2	0.8	−0.4	1.9	−0.3
RIOD	L1 code	0.4	0.2	0.3	−0.1	0.9	−0.2
RIOFE	L1 code	3.9	−2.1	3.8	3.1	7.9	−1.6
RIOD	L1 code	4.2	−2.3	4.0	3.2	6.9	−1.3
RIOFE	L1 code	3.2	−1.5	2.8	1.5	4.3	1.4
RIOD	L1 code	3.3	−1.7	3.1	2.0	4.2	1.5
RIOFE	L1 L2C code and phase	0.16	0.15	0.07	−0.05	0.33	0.25
RIOD	L1 L2P code and phase	0.24	0.03	0.13	0.06	0.12	0.01
RIOFE	L1 code	2.5	−1.6	2.2	1.8	3.8	2.1
RIOD	L1 code	2.6	−1.6	2.1	1.7	4.2	2.2
RIOFE	L1 code	4.6	−3.6	2.0	1.3	8.1	5.8
RIOD	L1 code	4.8	−3.8	1.8	1.4	8.2	5.8

(horizontal) and an 8-m level (vertical) in a session with strong scintillation, i.e., a factor up to 12. PPP L1 code position differences are biased by up to four (horizontal) and six (vertical) metres in all sessions under strong scintillation; the best positioning accuracies are those given by the dual frequency PPP solutions. For November 17, 2012, accuracies at the level of centimetres to a few decimetres for both RIOFE and RIOD are obtained.

In Fig. 67.4, the convergence period of the PPP solution (necessary for the float ambiguities to converge to or close to integer values) can be seen with no discontinuities. On the other hand, discontinuities can be observed in Fig. 67.5. The discontinuities are mainly due to cycle slip occurrence in phase measurements. Although there more L2P phase measurements than L2C phase measurements, cycle slips caused by scintillation on the hardware receiver observations forced the ambiguity resolution process to re-start several times along the 4-h session, generating a final coordinate difference RMS at the decimetre level. In case of the software receiver, GSNRx^{TM}, the availability of fewer dual frequency phase measurements caused the solution not to converge to centimetre level during the duration of the sub-session.

67.6 Conclusions

This paper proposes a new baseband signal processing architecture, shared-channel architecture for GNSS signal processing under strong equatorial scintillation. This processing architecture has been implemented in a multi-constellation multi-frequency GNSS software receiver, GSNRx^{TM}. The performance of GSNRx^{TM}, which utilizes the proposed architecture, in the observation domain was excellent under

severe scintillation scenarios. This indicates that the proposed shared-channel architecture is highly resistant to equatorial ionospheric scintillation.

Submitting L1 code observations generated by the software receiver, GSNRx™ at RIOFE and by the hardware receiver, Trimble NetRS at RIOD to CSRS-PPP service gave very similar results in the position domain in all cases, with the ionospheric delay being responsible for degrading solution accuracies from the session with no scintillation to those with strong scintillation. The best positioning accuracies were those given by the dual frequency PPP solutions, at the centimetre to few decimetres level for both RIOFE and RIOD. Cycle slips caused by scintillation on the hardware receiver observations forced the ambiguity resolution process to re-start several times along the session, which did not happen when CSRS-PPP processed the software receiver cycle slip-free observations.

Acknowledgments The authors would like to acknowledge Dr. Luiz Paulo Souto Fortes at IBGE and the University of the State of Rio de Janeiro for the scintillation data collection and NRCan CSRS-PPP data processing.

References

1. Van Dierendonck AJ, Klobuchar J, Hua Q (1993) Ionospheric scintillation monitoring using commercial single frequency C/A code receivers. In: Proceedings of the 6th international technical meeting of satellite division of the institute of navigation (ION GPS 1993), pp 1333–1342
2. SBAS-IONO Group (2010) Effect of ionospheric scintillations on GNSS—a white paper. SBAS ionospheric working group. http://waas.stanford.edu/papers/IWG/sbas_iono_scintillations_white_paper.pdf. Accessed 13 Oct 2013
3. Xu R, Liu Z, Li M, Morton Y, Chen W (2012) An analysis of low-latitude ionospheric scintillation and its effects on precise point positioning. J Glob Position Syst. doi:10.5081/jgps.11.1.22

Author Biographies

Tao Lin holds a BSc in Geomatics Engineering (University of Calgary 2008) and a PhD in Geomatics Engineering (University of Calgary 2013). He works as a post-doctoral fellow and senior research associate in PLAN group at University of Calgary since 2013. His research expertise includes GNSS software receiver and navigation algorithm design.

Professor Gérard Lachapelle holds a Canada Research Chair in Wireless Location in the PLAN Group of the University of Calgary. He has been involved with GPS developments and applications since 1980. His research ranges from precise positioning to GNSS signal processing. More information is available on the PLAN Group website (http://plan.geomatics.ucalgary.ca).

Chapter 68
Rapid Reacquisition Algorithm with Vector Tracking Loop in Indoor Pseudolite Applications

Yang-yang Liu, Bao-wang Lian, Yu-long Song and Hao-wei Xu

Abstract The tracking loop always loses its lock in the indoor independent pseudolite positioning system when the weak signals are blocked by the strong signals frequently. Aiming at solving this problem, this paper proposes a rapid reacquisition algorithm with vector tracking loop (VTL). The algorithm utilizes the tracking information from all channels to aid the processing of individual channel through the extended Kalman filter (EKF), and it can obtain a stable tracking control input. A simulation has been made to compare the tracking ability of the blocked signals between scalar tracking loop (STL) and vector tracking loop (VTL). Furthermore, an independent indoor pseudolite positioning system has been set up. The experiments prove that, in rapid reacquisition lost signals, the performance of VTL is much more effective than the STL's.

Keywords Vector tracking loop · Pseudolite · Rapid reacquisition algorithm

68.1 Introduction

In recent years, the demand for indoor navigation is more and more, and the accuracy requirements are also increasing. However, because of its complexity of the environment, little or no GNSS signals can be directly into the room. The use of pseudolite (PL) can provide effective GNSS satellite signals for indoor environment, which makes indoor high-precision positioning possible. But it will also bring serious near-far problem, the tracking loop always loses its lock when the weak signals are blocked by the strong signals, affecting the positioning accuracy and even leading to failure position.

Y. Liu (✉) · B. Lian · Y. Song · H. Xu
Department of Electronics Engineering, Northwestern Polytechnical University,
127 Youyi Xilu, Xi'an 710072, China
e-mail: liu_yang90@163.com

J. Sun et al. (eds.), *China Satellite Navigation Conference (CSNC) 2014 Proceedings: Volume I*, Lecture Notes in Electrical Engineering 303,
DOI: 10.1007/978-3-642-54737-9_68,

The basic idea of vector tracking loop (VTL) is to use the correlation between channels. In order to improve the performance of receiver, it uses the strong signals tracking results to aid the channel tracking weak signals. In 1995, Spilker [1] puts forward the concept of "vector tracking" firstly, and elaborates its ideas, structure and characteristics. In [2–4], VTL is described in detail and the performance of continuous tracking interrupt signal is verified. The ability of VTL for weak GPS signals in high dynamics is analysed in [5]. The tracking performance of different dynamic models has been compared in [6]. The advantages of VTL to STL is compared in [7]. The deviation mechanism of code tracking loop in VTL is studied in [8, 9]. In previous studies, the performance of VTL is analysed and simulated based on the theoretical, not for actual applications.

This paper analyses the performance of VDFLL in rapid reacquisition from its own characteristics. Firstly, the structures of the VTL and STL are described and we focus on analyzing the extended kalman filter (EKF) for the VTL algorithm model. A simulation has been made to compare the tracking ability of the blocked signals among VTL and STL. Finally, an independent indoor pseudolite positioning system has been set up. And through the experiments, the correctness of the theoretical analysis is verified.

68.2 System Structure Model

68.2.1 Structure of VTL

The tracking loop of tradition receiver is STL, carrier tracking using Costas loop and pseudo-random noise sequence (PRN) tracking using the delay locked loop (DLL). In STL, each channel becomes a tracking loop alone and provides the tracking results for the navigation module independently, such as pseudo-range and pseudo-range rate. VTL structure adopts vector delay/frequency lock loop (VDFLL) to complete the pseudo-range and pseudo-range rate measurements, calculation and navigation at the same time.

Figure 68.1 shows the basic structure of the VTL. In this structure, the tracking loop is no longer formed by each channel independently, but by all the channels with navigation module together to form a large tracking loop. The observation vectors are composed by the tracking results, such as pseudo-range and pseudo-range rate, from all the tracking channels, and transferred to the navigation module. The navigation module filters the observation vectors with EKF and then gets the user's position, velocity and the clock information. Every channel achieves the feedback from the filter results to generate the local signals.

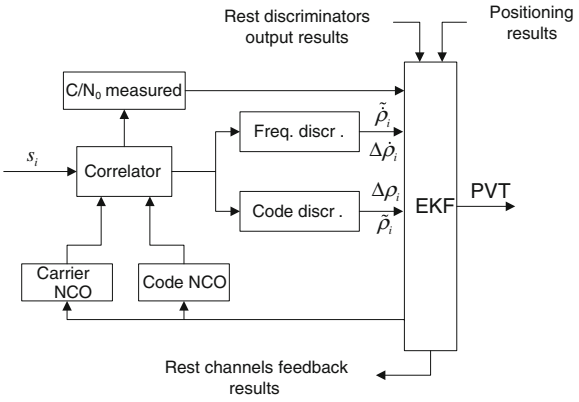

Fig. 68.1 Basic structure of VTL

68.2.2 Model of VTL

In Fig. 68.1, the correlation outputs of I, Q form correlator module are:

$$\begin{cases} I(n) = aD(n)R(\varepsilon)\sin c(f_e + T_s)\cos\theta_e + \eta_I \\ Q(n) = aD(n)R(\varepsilon)\sin c(f_e + T_s)\sin\theta_e + \eta_Q \end{cases} \tag{68.1}$$

τ is the estimation error of code phase; f_e is carrier frequency estimation error and carrier phase estimation error is θ_e; η is a white gaussian noise, and $D(n)$ is the navigation data; $R(\varepsilon)$ is related to the correlation function.

Frequency discriminator is a four quadrant arctangent function identifier, differential function is:

$$\Delta f_i = \frac{\arctan[(I_{i-1}Q_i + I_iQ_{i-1}) + j(I_{i-1}Q_i + I_iQ_{i-1})]}{t(n) - t(n-1)} \tag{68.2}$$

Phase discriminator is early-minus-later power discriminator, the output of the discriminator is:

$$\Delta\tau = \frac{1}{2}\frac{E^2 - L^2}{E^2 + L^2} \tag{68.3}$$

The early power of correlator is $E^2 = I_E^2 + Q_E^2$, and the later is $L^2 = I_L^2 + Q_L^2$.

The pseudo-range measurement error and pseudo-range rate measurement error are:

$$\begin{cases} \Delta\tilde{\rho} = \Delta\tau \cdot c/f_{C/A} \\ \Delta\tilde{\dot{\rho}} = -\Delta f \cdot c/f_{L1} \end{cases} \tag{68.4}$$

$\Delta\tau$ and Δf are the code phase error and carrier frequency error of the output of channel discriminator, respectively; $f_{C/A}$ and f_{L1} are the C/A code rate and L1 carrier frequency; c is the speed of light.

Calculate the estimated values of pseudo-range and pseudo-range rate:

$$\begin{cases} \hat{\rho}_i = \sqrt{(x_i - \hat{x}_u)^2 + (y_i - \hat{y}_u)^2 + (z_i - \hat{z}_u)^2} + c\hat{t}_k \\ \hat{\dot{\rho}}_i = \frac{1 - \frac{1}{c}[v_i - \hat{v}_u \cdot a_i]}{1 + \dot{\hat{t}}_k} \cdot \lambda_{L1} \end{cases} \tag{68.5}$$

where $\hat{\rho}_i$ and $\hat{\dot{\rho}}_i$ are the estimated values of pseudo-range and pseudo-range rate from the ith satellite to users; $[x_i, y_i, z_i]^T$ and v_i are the position and velocity of the satellite; $[\hat{x}_u, \hat{y}_u, \hat{z}_u]^T$ and $\hat{v}_u$ are the position and velocity of the user; λ_{L1} is the carrier wavelength of L1; and c is light speed.

In VDFLL, the observation vector is $Z_k = [\Delta\rho_1, \ldots, \Delta\rho_N, \Delta\dot{\rho}_1, \ldots, \Delta\dot{\rho}_N]^T$, where N is the number of pseudolite receiver observed. $\Delta\rho_i$and$\Delta\dot{\rho}_i$ are pseudo-range and pseudo-range rate respectively. The dynamic of the user is low in the indoor pseudolite positioning system, so this paper does not consider its acceleration information. $X_k = [\Delta x_k, \Delta y_k, \Delta z_k, \Delta\dot{x}_k, \Delta\dot{y}_k, \Delta\dot{z}_k, t_k, \dot{t}_k]^T$ is the state vector, where $[\Delta x_k, \Delta y_k, \Delta z_k]^T$ is position error, and $[\Delta\dot{x}_k, \Delta\dot{y}_k, \Delta\dot{z}_k]^T$ is the velocity error; t_k and $\dot{t}_k$ are the clock bias and clock drift respectively.

In the EKF, making a status update time T, the system is decentralized process written as:

$$X_k = \Phi X_{k-1} + W_{k-1} \tag{68.6}$$

$W_{k\text{-}1}$ is the process noise vector, zero mean.
And the measurement equation is written as:

$$Z_k = H_k X_k + V_k \tag{68.7}$$

V_k is the observation noise vector, zero mean.
Φ is the state transition matrix:

$$\Phi = \begin{bmatrix} I_{3\times3} & T \times I_{3\times3} & 0 & 0 \\ 0 & I_{3\times3} & 0 & 0 \\ 0 & 0 & 1 & T \\ 0 & 0 & 0 & 1 \end{bmatrix} \tag{68.8}$$

H is the observation matrix:

$$H = \begin{bmatrix} a_x^1 & a_y^1 & a_z^1 & 0 & 0 & 0 & -1 & 0 \\ \vdots & \vdots & \vdots & \vdots & \vdots & \vdots & \vdots & \vdots \\ a_x^N & a_y^N & a_z^N & 0 & 0 & 0 & -1 & 0 \\ 0 & 0 & 0 & a_x^1 & a_y^1 & a_z^1 & 0 & -1 \\ \vdots & \vdots & \vdots & \vdots & \vdots & \vdots & \vdots & \vdots \\ 0 & 0 & 0 & a_x^N & a_y^N & a_z^N & 0 & -1 \end{bmatrix}_{2N\times8} \tag{68.9}$$

I is the unit matrix, and $a_i = \left[a_x^i, a_y^i, a_z^i\right]$ is the unit vector cosine of the user to the ith pseudolite.

Calculate the error estimated values of pseudo-range error and pseudo-range rate:

$$\begin{bmatrix} \Delta\hat{\rho} \\ \Delta\hat{\dot{\rho}} \end{bmatrix} = H \cdot \hat{X} \tag{68.10}$$

Calculate tracking loop input

$$\begin{cases} \Delta\hat{\rho}^+ = \hat{\rho} + \Delta\hat{\rho} - \tilde{\rho} \\ \Delta\hat{\dot{\rho}}^+ = (\hat{\dot{\rho}} + \Delta\hat{\dot{\rho}} - \tilde{\dot{\rho}}) \cdot \dfrac{1}{\lambda_{L1}} \end{cases} \tag{68.11}$$

where $\Delta\hat{\rho}^+$ and $\Delta\hat{\dot{\rho}}^+$ are code loop input and carrier tracking loop input.

According to the system model, the implementation process of EKF is as follows [10]:

Predict the error variance:

$$P_{k|k-1} = \Phi P_{k-1|k-1}\Phi^T + Q_k \tag{68.12}$$

Step prediction equation:

$$\hat{X}_{k|k-1} = \Phi\hat{X}_{k-1} \tag{68.13}$$

Kalman gain:

$$K_k = P_{k|k-1}H_k^T\left(H_k P_{k|k-1}H_k^T + R_k\right)^{-1} \tag{68.14}$$

Estimation error variance:

$$P_{k|k} = (I - K_k H_k)P_{k|k-1} \tag{68.15}$$

State estimation equation:

$$\hat{X}_k = \hat{X}_{k|k-1} + K_k\left(Z_k - H_k\hat{X}_{k|k-1}\right). \tag{68.16}$$

68.3 Experiments and Results

In order to test the performance of VTL in the rapid reacquisition, the experiments are divided into two parts. In the first part, the satellite signals are generated by the commercial GPS signal source. The scene of the satellite signal obscured can be simulated through the satellite signal open and close. Through this experiment, we can evaluated the continuous tracking ability of VTL.

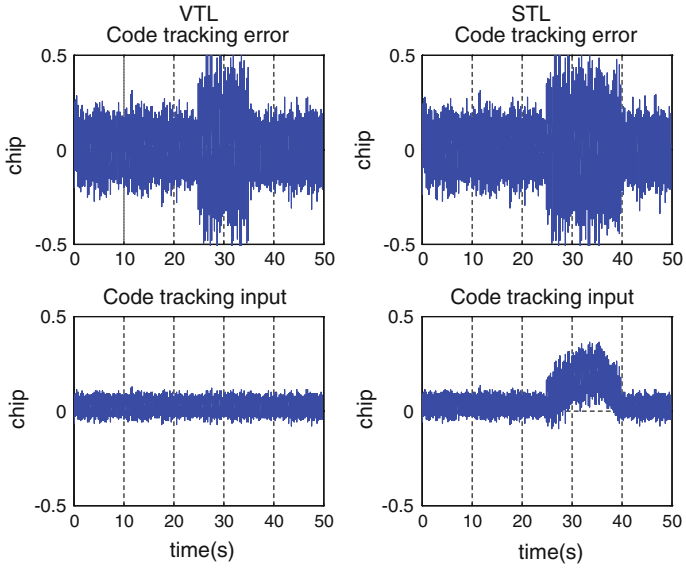

Fig. 68.2 Code tracking results of PRN 14: VTL (*left*) and STL (*right*)

In the second part of the experiments, we built an indoor pseudolite positioning system. We use three pseudolites for two-dimensional localization. In this experiment, we can test the performances of the continuous tracking ability for weak signal and the rapid reacquisition ability when the signals are loss of lock.

68.3.1 GPS Simulation

Fifty seconds intermediate frequency data is generated by commercial GPS signal source. There are 6 visible satellites, 4, 6, 10, 12, 14 and 15. The user's receiver is static. Initially, the carrier to noise ratio (C/N_0) of the received GPS signals is 44 dB Hz. In the whole experiment processing, the 14th satellite is open normally in addition to 25–35 s. The other five satellites are open normally throughout the experiment.

Figure 68.2 shows the code tracking results of PRN 14 and Fig. 68.3 is the frequency tracking results. In Figs. 68.2 and 68.3, the first column is the tracking results of VTL and the second is STL. In Fig. 68.2, the first row is the code tracking error and the second is code tracking input. In Fig. 68.3, the first row is frequency tracking error and the second is frequency tracking input.

We can see from Figs. 68.2 and 68.3, in the 0–25 s, the tracking results of PRN 14 with VTL and STL are normally and similarity. Within 25–35 s, the 14th satellite signal is closed. The tracking errors of VTL and STL increases dramatically, and the two loops lost the lock. But due to the aids of other channels, VTL

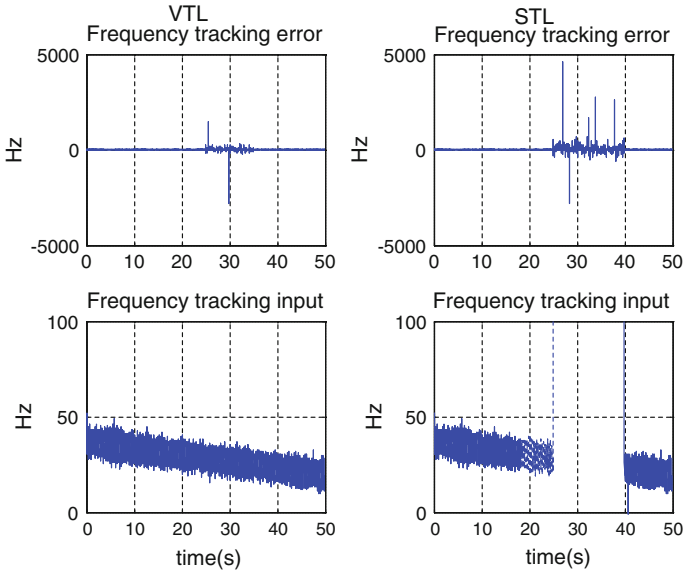

Fig. 68.3 Frequency tracking results of PRN 14: VTL (*left*) and STL (*right*)

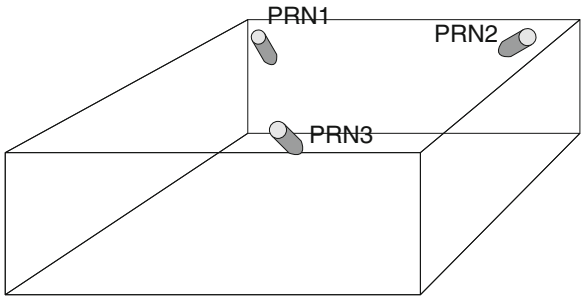

Fig. 68.4 Independent indoor pseudolite positioning system

can generate stable code tracking input and stable frequency tracking input, while the STL can not.

After 35 s, the signal of PRN 14 is reopened. The receiver with VTL reacquires the PRN 14 almost at the same time while the STL is about 39 s. In this experiment, in rapid reacquisition of shade satellite signals, the VTL is faster than the STL nearly 4 s.

68.3.2 Experiment of Indoor Pseudolite Positioning

In the indoor independent pseudolite position system, the GPS signal is provided by the pseudolite. Using the near-far problem in the process of indoor position, we test the tracking performance for weak signal and blocked signal of VTL.

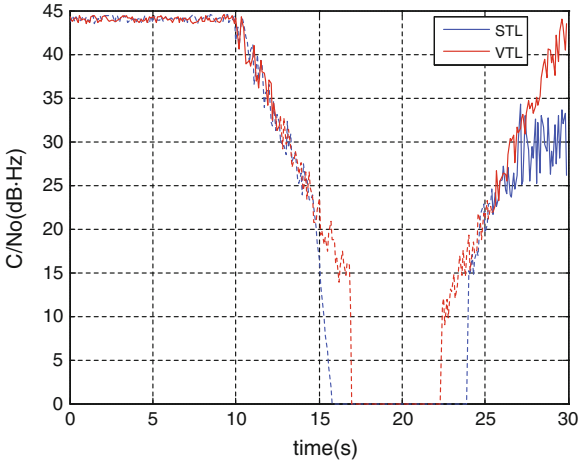

Fig. 68.5 Carrier to noise ratio comparison of 3rd pseudolite

In the experiment, the available space of laboratory size is 8 × 8 m plane and 4 m height. Figure 68.4 shows the detailed layout of pseudolites indoor, and we fix up three pseudolites for two-dimensional horizontal position. The receiver is fixed at the center of the triangle to collect the intermediate frequency data. We process the intermediate frequency data in software receiver with VTL and STL, respectively.

The experiment is divided into three states. The first stage is 0–10 s, three pseudolites transmit the GPS signals with a normally power; the second is 10–20 s, the power of 3rd pseudolite is gradually reducing until it to zero; the third is 20–30 s, the power of 3rd pseudolite is gradually increasing until it to normal.

In the experiment, because of the large computation, we cannot use VTL to realize real-time position. Therefore, we process the intermediate frequency data with software receiver.

Figure 68.5 shows the C/N_0 of the 3rd pseudolite throughout the experiment. Can be seen from the figure, in the first stage, the C/N_0 of VTL and STL are similarity, but in the second stage, about 15 s when the C/N_0 is reduced to 20 dB Hz, the STL loses its lock. In the third stage, about 25 s, the STL reacquire the 3rd pseudolite. About 17 s, when the C/N_0 is reduced to 15 dB Hz, the VTL loses its lock, and about 23 s, the VTL reacquire the 3rd pseudolite.

It can be seen from the experiment, the tracking performance for weak signals, relative to STL, VTL is lower than STL about 5 dB Hz. And when the weak signals are recovery, the VTL can reacquire signals faster than STL.

68.4 Conclusion

This paper studies the rapid reacquisition algorithm with the VTL and implement it into the indoor independent pseudolite positioning system. First through the simulation, we verify that when the signal is weakened and even disappeared

suddenly, the receiver with VTL can provide stable tracking input for the tracking channel to generate stable local signal. And when the signal is recovery, the receiver can reacquire the signal fast. Finally, an indoor independent pseudolite positioning system has been established. The experiment prove that the tracking ability for weak signals, the VTL is lower than STL about 5 dB Hz, and when the weak signal is recovery, the VTL can reacquire the signal faster than STL. The results show that the VTL has superior performance in rapid reacquisition and great application prospect.

References

1. Spilker JJ (1995) Vector delay lock loop processing of radiolocation transmitter signals. U.S. Patent 5398034, 14 Mar 1995
2. Lashley M, Bevly DM (2007) Analysis of discriminator based vector tracking algorithms. In: Proceedings of ION NTM 2007, San Diego, CA, 22–24 Jan 2007, pp 570–576
3. Pany T, Eissfeller B (2006) Use of a vector delay lock loop receiver for GNSS signal power analysis in bad signal conditions. In: Proceedings of ION PLANS, San Diego, CA, Apr 2006, pp 893–903
4. Zhao S, Akos D (2011) An open source GPS/GNSS vector tracking loop-implementation, filter tuning, and results. In: Proceedings of ION ITM 2011, San Diego, CA, 24–26 Jan 2011, pp 1293–1305
5. Lashley M, Bevly DM, Hung JY (2009) Performance analysis of vector tracking algorithms for weak GPS signals in high dynamics. IEEE J Sel Top Sign Process 3(4):661–673
6. Sousa FMG, Nunes FD (2012) Characterization and performance analysis of a VDFLL GNSS receiver architecture. In: 2012 6th ESA workshop on satellite navigation technologies and European workshop on GNSS signals and signal processing (NAVITEC), Noordwijk, The Netherlands, 5–7 Dec 2012, pp 1–8
7. Lashley M, Bevly DM, Hung JY (2010) A valid comparison of vector and scalar tracking loops. In: Proceedings of IEEE/ION position location and navigation symposium conference (PLANS), Indian Wells/Palm Spring, Indian Wells/Palm Springs, CA, 4–6 May 2010, pp 464–474
8. Xiao Z, Tang X, Pang J et al (2010) The study of code tracking bias in vector delay lock loop. SCIENTIASINICA: Phys Mech Astron 05:568–574
9. Luo Y, Wang Y, Luo H et al (2013) Study on vector tracking loop based on extended kalman filter. J Electron Inf Technol 06:1400–1405
10. Qin Y, Zhang H, Wang S (1998) Kalman filter and principles of integrated navigation. Northwestern Polytechnical University Press, Xi'an (In Chinese)

Chapter 69
An Optimized Capture Algorithm for GPS Receiver

Kun Zhai, Zhongliang Deng, Yuezhou Hu, Le Yang and Zhuang Yuan

Abstract The paper studies and designs a differential guess-check capture algorithm. This paper first makes a brief overview on coherent, incoherent and differential integration, then it contrasts effects of longer coherent integral time and incoherent integral time on the baseband loop, furthermore analyzes their features and shortcomings. The paper continues to discuss traditional capture algorithm, half-bits algorithm and full-bits algorithm. After analyzing theory and shortcomings, the paper proposes a kind of optimized differential guess-check capture algorithm. Through theoretical analysis and MATLAB software simulation verification, the paper simulated and compared the optimized algorithm with traditional loop algorithm on different data length 80, 180, 280 ms. The result indicates the optimized one has bigger correlation peak and smaller noise fluctuation. Moreover, as the processed data lengthens, the optimized algorithm has more obvious advantage. Finally, the methods to reduce the capture time are analyzed and simulated. This shows that the scheme design is effective and feasible.

Keywords Baseband receiver · Integration time · Guess-check capture algorithm · High sensitivity

69.1 Introduction

Coherent integration and incoherent integration are key technologies for receiving weak GPS signals. Although the operation of incoherent integration can enhance the signal-to-noise ratio, the square calculation before integration can bring in square loss, which doesn't exist in coherent integration.

K. Zhai (✉) · Z. Deng · Y. Hu · L. Yang · Z. Yuan
School of Electronic Engineering, Beijing University of Posts and Telecommunications, Beijing 100876, China
e-mail: 365936364@qq.com

J. Sun et al. (eds.), *China Satellite Navigation Conference (CSNC) 2014 Proceedings: Volume I*, Lecture Notes in Electrical Engineering 303,
DOI: 10.1007/978-3-642-54737-9_69,

In reverse, coherent integration is affected by data bits jumping and frequency tracking deviation, while the incoherent process won't be influenced by these two factors. Since the above, receiver can do long time (e.g. several hundred milliseconds, or even some seconds) incoherent integration.

For this problem, this page presents an optimization algorithm. The algorithm can effectively avoid square loss, at the same time reduce the influence of data bits jumping, thereby increases the capture sensitivity, which furthermore improves the performance of the receiver.

69.2 Basic Algorithms for GPS Signal Acquisition

69.2.1 Coherent and Non-coherent Integration Algorithm

Data is multiplied with complex scrambling code's conjugate and the pilot after spread spectrum, so as to obtain accumulative result of different time slots. Coherent integration is done through this method. Mathematical formula [3] is shown as (69.1)

$$R_{COH}(\tau, f_d) = \left| \sum_{k=1}^{N} y_k(\tau, f_d) \right| \tag{69.1}$$

Incoherent integration is done through additive accumulation of self-correlation amplitude, formula as shown as (69.2)

$$R_{NCH}(\tau, f_d) = \sum_{k=1}^{N} |y_k(\tau, f_d)|^2 \tag{69.2}$$

Coherent integration time is quite a key parameter of receiver's design and its value is a compromising process: In one hand, to improve filtering effect, reduce noise and enhance tracing accuracy, integration filter's bandwidth must be fairly narrow, that is, in order to support customer's high dynamics, make tracking loop tolerate frequency tracking error caused by customer's movement and limit its loss to a maximum degree, the bandwidth of integration filter must be quite wide, that is to say, the coherent integration time must be as short as possible.

Therefore, the receiver can choose the number of coherent and incoherent integral different pairs, so that reconcile the contradiction between the attenuation of frequency error and square loss and optimize the noise performance of the receiver.

69.2.2 Differential Coherent Accumulation Algorithm

This algorithm [2, 4] conjugates multiplicities the coherent integration result of two adjacent segments. This not only avoids the square loss of incoherent integration,

but also reduces effect of data bits flip, thus improving capture performance. Explicit formula as shown in (69.3)

$$R_{DCH}(\tau,f_d) = \left| \sum_{k=1}^{N-1} y_k(\tau,f_d) y_{k+1}^*(\tau,f_d) \right| \tag{69.3}$$

Among them, $y_k(\tau,f_d)$ indicates the integration result of the Kth coherent integration, $y_{k+1}^*(\tau,f_d)$ indicates $y_{k+1}(\tau,f_d)$'s complex conjugate, τ is phase delay of C/A code, f_d for Doppler shift.

This method is superior to incoherent integration because the latter's square operation magnifies noise, while differential coherent accumulation conjugate multiplicities adjacent point's noise, of which the amplifying of noise is much less, which will do much favour to improving signal-to-noise ratio.

69.3 Traditional GPS Capture Algorithm

69.3.1 Half-Bits Algorithm

This method [1] used one point of data as the beginning, then segments it continuously by 10 ms, and tabs them successively. Do coherent integration of data inside each segment, and then respectively do incoherent integration of the coherent integration result in odd segment and even segment. Compare the integral result of odd segment and even segment; get out the bigger group of data. These can ensure at least one group won't flip. Detailed algorithm schematic as shown in Fig. 69.1.

69.3.2 Full-Bits Algorithm

The difference between the half-bits method and the full-bits is that the latter one increases the time of coherent integration from 10 to 20 ms. But considering the flip of the data, they should be divided into 20 ms segments, and then delayed in unit of 1 ms, which results in 20 groups of data [1].

Then, does coherent integration in each group, mark the results with Y_m^b, and incoherently accumulate the result as (69.4)

$$Y^b = \sum_{m=1}^{m+1} Y_m^b \tag{69.4}$$

In the end, use $Y = \max\{Y^1, Y^2, Y^3, \ldots, Y^{20}\}$ to be the final result to judge.

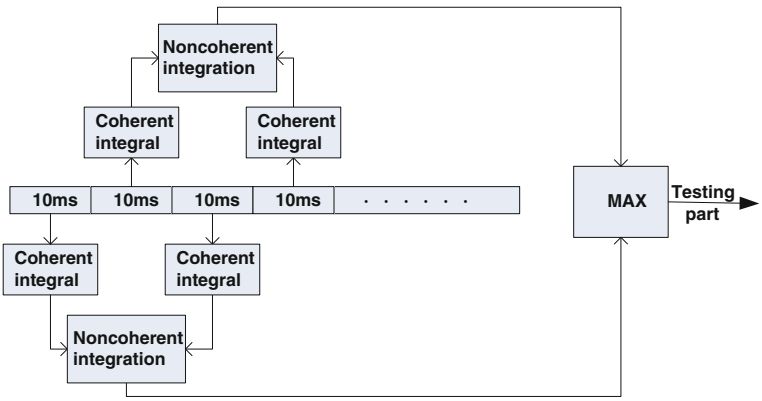

Fig. 69.1 Schematic of half-bits algorithm

69.4 Differential Coherent Guess-Check Optimized Algorithm

With guess-check optimized algorithm, receiver can solve the data bit jumping problems in coherent integration, and also avoid the square loss caused by incoherent integration, together with less calculation process. First, considering each data bit can only be 0 or 1, guess-check optimized algorithm continues the former coherent integration after guessing the bit value. One of the coherent integration does add operation while the other one does subtraction. Then as one of the guess must be right, with the other one wrong, guess-check optimized algorithm checks and compares the two results, considering the one having bigger absolute value to be the correct guess. Combined with the differential coherent integration method, an optimization algorithm can be forwarded.

Data will be divided into $M + 1$ sections, through delay time, fall into b groups, which are used to find the beginning of data. Using $Y_k^b(\tau, f_d)$ to present the coherent accumulation results of the Kth section for each groups, then the matrix of coherent accumulate can be represented as (69.5):

$$C_k^b(\tau, f_d) = \left[Y_k^b(\tau, f_d)\right]^* Y_{k+1}^b(\tau, f_d) \tag{69.5}$$

τ represents the phase delay of C/A code, f_d is the Doppler shift. The algorithm flow chart is in Fig. 69.2.

Concrete steps as follows:

Step 1: Use $a_1^b, a_2^b \ldots, a_M^b$ to represent the different combination of navigation data bits and product sign bits which are contiguous in b groups, and make $a_1^b = 1$ with:

$$S_1^b(\tau, f_d) = C_1^b(\tau, f_d) \tag{69.6}$$

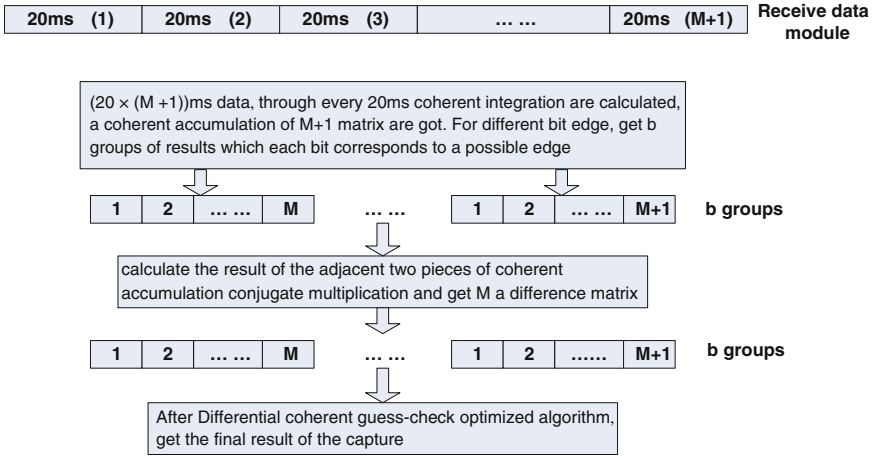

Fig. 69.2 Algorithm flow chart of differential coherent guess-check optimized algorithm

Step 2:

$$S_{2,0}^{b}(\tau,f_d) = S_1^{b}(\tau,f_d) - C_2^{b}(\tau,f_d) \tag{69.7}$$

$$S_{2,1}^{b}(\tau,f_d) = S_1^{b}(\tau,f_d) + C_2^{b}(\tau,f_d) \tag{69.8}$$

Step 3: Compare $\left|S_{2,0}^{b}(\tau,f_d)\right|$ with $\left|S_{2,1}^{b}(\tau,f_d)\right|$, if $\left|S_{2,0}^{b}(\tau,f_d)\right| > \left|S_{2,1}^{b}(\tau,f_d)\right|$, it means the adjacent navigation data bits have opposite signs, then make $a_2^b = -1$

$$S_2^{b}(\tau,f_d) = S_{2,0}^{b}(\tau,f_d) \tag{69.9}$$

Otherwise, if $\left|S_{2,0}^{b}(\tau,f_d)\right| < \left|S_{2,1}^{b}(\tau,f_d)\right|$, it means adjacent navigation data bits have same-phase sign, then make $a_2^b = +1$, so

$$S_2^{b}(\tau,f_d) = S_{2,1}^{b}(\tau,f_d) \tag{69.10}$$

Step 4: Similar to Step 3, make

$$S_{i,0}^{b}(\tau,f_d) = S_{i-1}^{b}(\tau,f_d) - C_i^{b}(\tau,f_d) \tag{69.11}$$

$$S_{i,1}^{b}(\tau,f_d) = S_{i-1}^{b}(\tau,f_d) + C_i^{b}(\tau,f_d) \tag{69.12}$$

Compare $\left|S_{i,0}^{b}(\tau,f_d)\right|$ with $\left|S_{i,1}^{b}(\tau,f_d)\right|$, get the sign polarity of adjacent navigation data bits with the way in Step 3, then get $S_i^{b}(\tau,f_d)$, a_i^b, then determine the final $a_1^b, a_2^b \ldots, a_M^b$ and $S_N^{b}(\tau,f_d)$ of each group.

Step 5: Get the values of the following equation, so we can consider the maximum result of each group to be its differential coherence accumulated value.

$$Z_{\max}^{b}(\tau, f_d) = \sum_{l=1}^{M} a_l^b \times C_l^b(\tau, f_d) \tag{69.13}$$

Maximum value in the earlier calculation result for each group is as differential coherent accumulation value as.

Step 6: Get the final result from the following equation as (69.14).

$$Z_{\max}(\tau, f_d) = \{Z_{\max}^{1}(\tau, f_d), Z_{\max}^{2}(\tau, f_d), \cdots, Z_{\max}^{b}(\tau, f_d)\} \tag{69.14}$$

Based on the method above method, differential coherence integral method combine with guess-check optimized algorithm, not only increases the integral time regardless of the limit within 20 ms, enhances the filtering effect, reduces noise while increases precision, but also avoids the square loss caused by incoherent integration, which leads to high sensitivity of capture.

69.5 Matlab Simulations

According to the analysis above, Matlab simulation compared the optimization algorithm with the half-bits algorithm and full-bits algorithm. In the simulation, sample frequency is 5 MHz; intermediate frequency is 1.25 MHz, segmentation coherent accumulation integral time is 20 ms.

69.5.1 Performance Comparison

Based on the result of Figs. 69.3 and 69.4, the full-bits gets the order of magnitudes of 10^6, while the optimization algorithm gets 10^{12}, with more distinct correlation peak and lower fluctuate of noise, which lead to higher sensitivity.

69.5.2 Performance Comparison with Different Data Length

The test results of the comparison among data length in 80, 180, 280 ms are as follows, with the mentioned three methods.

From Figs. 69.5, 69.6 and 69.7, with the increase of data length, acquisition probability of 3 methods all increase. Under the same data length and signal-to-noise ratio, the optimization algorithm gets higher acquisition probability than

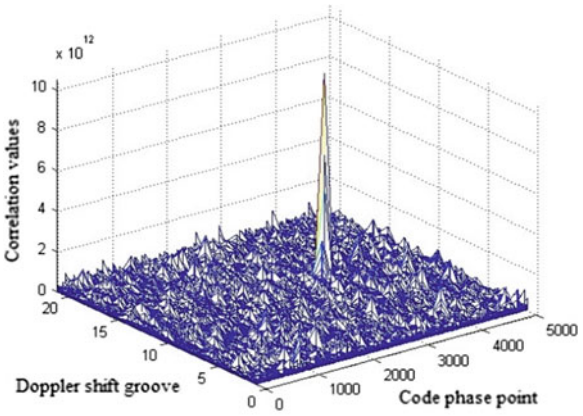

Fig. 69.3 Capture result of differential coherent guess-check optimized algorithm

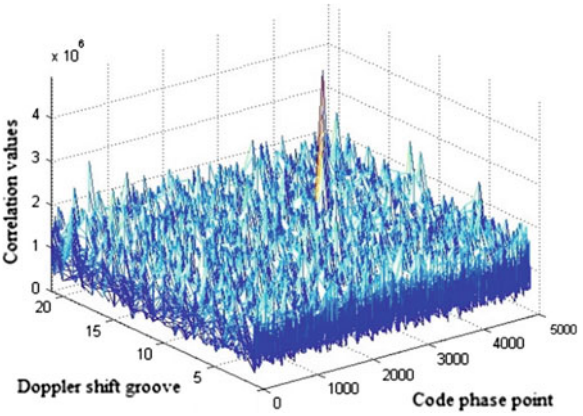

Fig. 69.4 Capture result of full-bits algorithm

the other two. And the advantage gets greater with longer data length. It's because the traditional methods encounter square loss during incoherent integration which is effectively avoided in the optimization algorithm.

69.6 Analysis to Reduce the Capture Time

Since the GPS signal acquisition time is largely determined by amount calculation of the capture algorithm. For the FFT capture mode, the length of the capture time depends on the number of FFT points captured.

For capture algorithms of this paper, only the adjacent polar judgment is calculated compared with amount calculation of the full-bits algorithm, when the coherent integration time is 20 ms and the frequency search step is same. For the case of large M, a new method is discussed in combination with the half-bits

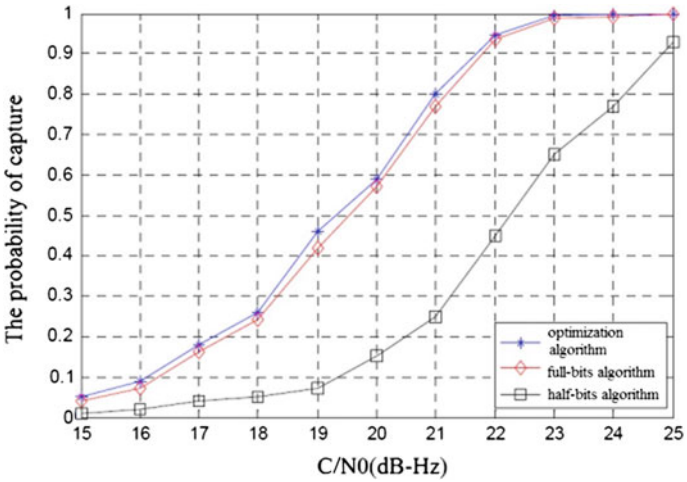

Fig. 69.5 The capture probability of data length 80 ms

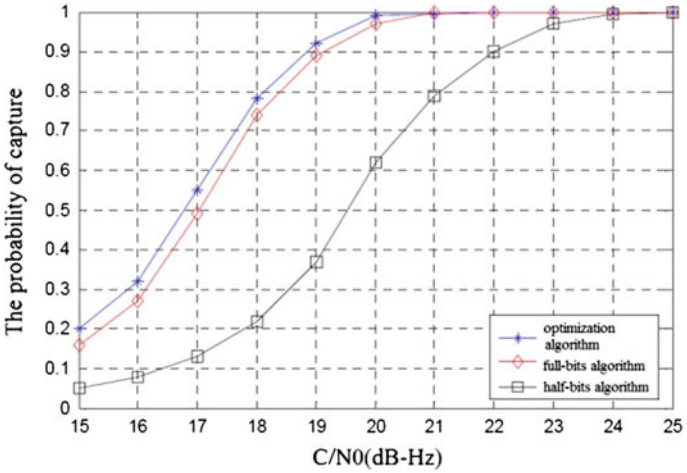

Fig. 69.6 The capture probability of data length 180 ms

algorithm and optimized algorithm. Firstly the data is divided into 10 ms long according to half-bits algorithm. Secondly they are differentially coherent integrated. Thirdly the odd and even segments are respectively coherent accumulated by the guess-check optimized algorithm. At last the largest group is selected as the capture results.

During the simulation, the data of length 180 ms is separately operated by the half-bits algorithm and the traditional differential coherent. The capture results of three algorithm are shown as Fig. 69.8.

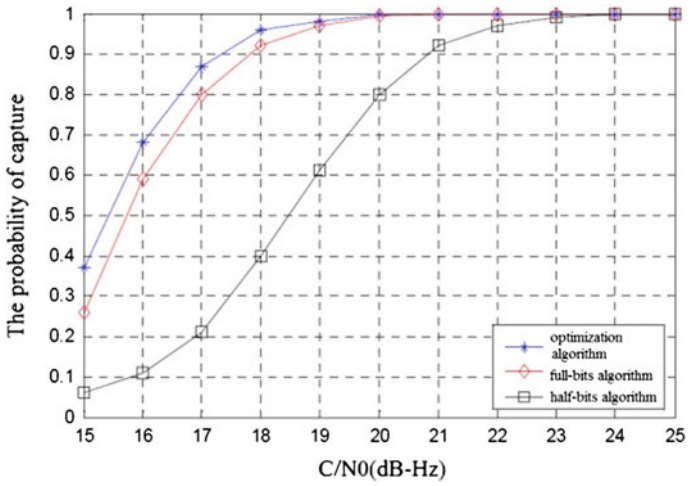

Fig. 69.7 The capture probability of data length 280 ms

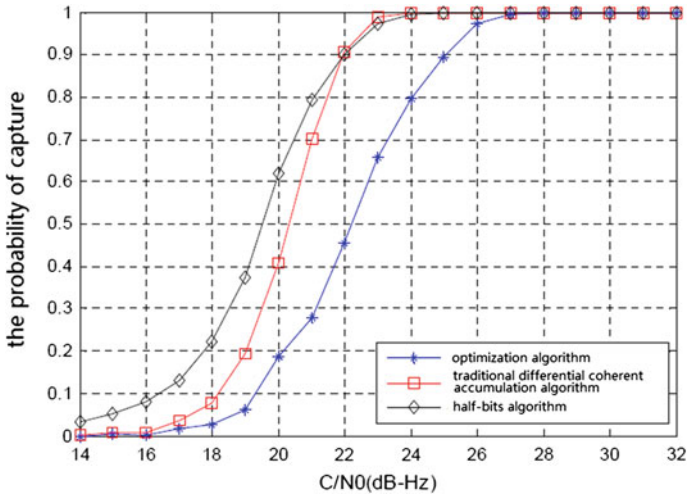

Fig. 69.8 Comparison performance of three capture algorithm

It can be seen the half-bits algorithm is optimal performance from Fig. 69.8, while the improved algorithm is relatively poor performance. But at a lower carrier-to-noise ratio of the case, it can still maintain a high probability of capture and be feasible. In the calculation, the improved method's amount is much smaller than the other methods. This can reduce the acquisition time. For the weaker capture probability, further research is needed.

References

1. Fan J (2012) Research on the high-sensitivity acquisition technology for GPS weak signal. Thesis (Master). Chongqing University
2. Ma R (2010) Research on acquisition algorithm of weak GPS signal and its realization on software receiver platform. Thesis (Master). Harbin Institute of Technology
3. Xie G (2011) Principles of GPS and receiver design. Publishing House of Electronics Industry, Beijing
4. Yu W, Zheng B, Watson R et al (2007) Differential combining for acquiring weak GPS signals. Signal Process 87(5):824–840